

RECENT ADVANCES in MECHATRONICS

Proceedings of the 2nd International Conference on Recent Advances in Mechatronics
ICRAM'99, May 24-26, 1999, Istanbul, Turkey

Abstracts of Plenary Papers
Regular Papers

Editors:
Okyay Kaynak
Feza Kerestecioğlu
M. Önder Efe
Cem Ünsalan

DISTRIBUTION STATEMENT A
Approved for Public Release
Distribution Unlimited

19990629 129



AQF99-09-1690

REPORT DOCUMENTATION PAGE			Form Approved OMB No. 0704-0188	
<p>Public reporting burden for this collection of information is estimated to average 1 hour per response, including the time for reviewing instructions, searching existing data sources, gathering and maintaining the data needed, and completing and reviewing the collection of information. Send comments regarding this burden estimate or any other aspect of this collection of information, including suggestions for reducing this burden to Washington Headquarters Services, Directorate for Information Operations and Reports, 1215 Jefferson Davis Highway, Suite 1204, Arlington, VA 22202-4302, and to the Office of Management and Budget, Paperwork Reduction Project (0704-0188), Washington, DC 20503.</p>				
1. AGENCY USE ONLY (Leave blank)		2. REPORT DATE		3. REPORT TYPE AND DATES COVERED
		1999		Conference Proceedings
4. TITLE AND SUBTITLE			5. FUNDING NUMBERS	
2nd International Conference on Recent Advances in Mechatronics: ICRAM 99			F61775-99-WF029	
6. AUTHOR(S)				
Conference Committee				
7. PERFORMING ORGANIZATION NAME(S) AND ADDRESS(ES)			8. PERFORMING ORGANIZATION REPORT NUMBER	
Bogazici University Faculty of Engineering, Bebek Istanbul 80815 Turkey			N/A	
9. SPONSORING/MONITORING AGENCY NAME(S) AND ADDRESS(ES)			10. SPONSORING/MONITORING AGENCY REPORT NUMBER	
EOARD PSC 802 BOX 14 FPO 09499-0200			CSP 99-5029- /	
11. SUPPLEMENTARY NOTES				
Two different volumes of abstracts.				
12a. DISTRIBUTION/AVAILABILITY STATEMENT			12b. DISTRIBUTION CODE	
Approved for public release; distribution is unlimited.			A	
13. ABSTRACT (Maximum 200 words)				
<p>The Final Proceedings for 2nd International Conference on Recent Advances in Mechatronics: ICRAM 99, 24 May 1999 - 26 May 1999</p> <p>This is an interdisciplinary conference involved with the synergistic integration of mechanical engineering with electronics and intelligent computer control for design and manufacture of products and processes. Topics include: mechatronics design, distributed systems, vision and sensors, robots and mobile machines, vibration and control, computational intelligence in mechatronics, embedded real-time systems, micro-mechatronics, motion control, hardware/software co-design, and intelligent manufacturing systems</p>				
14. SUBJECT TERMS			15. NUMBER OF PAGES	
EOARD, Robotics, MEMs, Space Technology			488 and 589	
			16. PRICE CODE	
			N/A	
17. SECURITY CLASSIFICATION OF REPORT	18. SECURITY CLASSIFICATION OF THIS PAGE	19. SECURITY CLASSIFICATION OF ABSTRACT	20. LIMITATION OF ABSTRACT	
UNCLASSIFIED	UNCLASSIFIED	UNCLASSIFIED	UL	

NSN 7540-01-280-5500

Standard Form 298 (Rev. 2-89)
Prescribed by ANSI Std. Z39-18
298-102

The Editors

**Okyay Kaynak
Feza Kerestecioğlu
M. Önder Efe
Cem Ünsalan**

Boğaziçi University
Electrical and Electronic Engineering
Bebek 80815
İstanbul, TURKEY

Organized by

UNESCO Chair on Mechatronics, Boğaziçi University
Mechatronics Research and Application Center, Boğaziçi University

Co-sponsored by

IEEE Industrial Electronics Society
IEEE Robotics and Automation Society

In Technical Co-operation with

ASME Dynamic and Control Sys. Div.
ASME Design Engineering Division
IEEE Control Systems Society
Institute of Electrical Engineers of Japan
Japanese Society of Mechanical Engineers
Robotics Society of Japan
Soc. of Inst. and Cont. Engineers of Japan

Cataloging-in-Publication Data

Kaynak, Okyay.
Icram '99: sempozyum tebliğleri/
Okyay Kaynak.
p.; cm.

1. Mechatronics. 2. Simulation methods.
3. Robotics. I. Title
629.892

ISBN: 975-518-131-8

Publication No: 656
Printed at Boğaziçi University Printhouse

© UNESCO Chair on Mechatronics, Boğaziçi University, İstanbul Turkey

This publication is secured by copyright. All rights reserved. No part of this book, either in part or in whole may be reproduced or transmitted in any form or by any means in other languages, reprinting, withdrawal of illustrations, recording, electronic, photographic, mechanical, or by any information storage and retrieval system, without prior written permission of the publisher.

Responsibility for the accuracy of all statements rests solely with the authors and not the publisher.

CONTENTS

Preface	v
A Message from the Chairman	vii
Acknowledgements	viii
List of Papers	ix
Abstracts of Plenary Papers	1
Regular Papers	3
Author Index	

ORGANIZATION COMMITTEE

General Chair:

O. KAYNAK (Bogazici University, Turkey)

Program Co-chairs:

M. H. ANG JR. (N. U. of Singapore, Singapore)

S. TOSUNOGLU (Florida Int. Univ., USA)

Special Sessions/Tutorials Chair:

H. HASHIMOTO (University of Tokyo, Japan)

Advisory Committee:

T. FUKUDA (Nagoya University, Japan)

F. HARASHIMA (TMIT, Japan)

M. H. LEE (Pusan National University, Korea)

M. TOMIZUKA (UC Berkeley, USA)

R. ISERMANN (T. Univ. of Darmstadt, Germany)

Plenary Speakers:

T. FUKUDA (Nagoya University, Japan)

G. HIRZINGER (DLR-Institute of Robotics and System Dynamics, Germany)

M. TOMIZUKA (UC Berkeley, USA)

R. ZOBEL (DG-III-Industry, Commission of the European Communities, Belgium)

National Organization Committee:

L. AKIN (Bogazici University, Istanbul)

Y. DENIZHAN (Bogazici University, Istanbul)

M. O. EFE (Bogazici University, Istanbul)

A. ERCIL (Bogazici University, Istanbul)

A. ERKMEN (Middle East Tech. Univ., Ankara)

Y. ISTEFANOPULOS (Bogazici Univ., Istanbul)

S. IPLIKCI (Bogazici University, Istanbul)

F. KERESTECIOGLU (Bogazici Univ., Istanbul)

A. B. KOKU (Vanderbilt University, USA)

O. TURKAY (Bogazici University, Istanbul)

C. UNSALAN (Bogazici University, Istanbul)

International Program Committee:

Y. ABE (Shinryo Corporation, Japan)

M. ACAR (Loughborough University, UK)

M. AIRILA (Helsinki Univ. of Tech., Finland)

S. E. ALPTEKIN (Cal Poly, USA)

K. ARBTER (DLR, Germany)

E. BERMAN (Ben-Gurion U. Negev, Israel)

A. BOURJAULT (U. de Franche-Comté, France)

W. J. BOOK (Georgia, A. Inst. of Tech., USA)

F. CACCAVALE (UC Davis, USA)

N. CAPLAN (NSF, USA)

C. COUTO (Universidade do Minho, Portugal)

K. C. CRAIG (Rensselaer Poly. Inst., USA)

P. DARIO (Scuola Superiore S. Anna, Italy)

C. W. DE SILVA (U. of British Col., Canada)

M. DRAMAN (Bogazici University, Turkey)

P. DREWS (RWTH-Aachen, Germany)

T. EMURA (Tohoku University, Japan)

K. ERBATUR (TUBITAK MAM, Turkey)

J. M. FERNANDES (U. Fed. de Uberlandia, Brazil)

E. FREUND (University of Dortmund, Germany)

M. HILLER (Gerhard-Mer.-U. Duisburg, Germany)

T. C. S. HSIA (UC Davis, Germany)

H. P. HUANG (National Taiwan Univ., Taiwan)

K. JEZERNIK (University of Maribor, Slovenia)

M. KONEKO (Hiroshima University, Japan)

N. KASABOV (University of Otago, New Zealand)

K. KAWAMURA (Vanderbilt University, USA)

S. KAWAMURA (Ritsumeikan University, Japan)

O. KHATIB (Stanford University, USA)

T. KING (University of Birmingham, UK)

T. A. LASKY (UC Davis, U.S.A.)

T. H. LEE (N. Univ. of Singapore, Singapore)

T. S. LOW (N. Univ. of Singapore, Singapore)

J. A. T. MACHADO (Univ. of Porto, Portugal)

H. KOIVO (Helsinki Univ. of Tech., Finland)

S. LEE (Pusan National Univ., Korea)

K. B. LIM (N. Univ. of Singapore, Singapore)

R. LUO (North Carolina State University, USA)

R. V. MAYORGA (University of Waterloo, Canada)

K. OHNISHI (Keio University, Japan)

F. PFEIFFER (Tech. Univ. of Munich, Germany)

B. RAVANI (UC Davis, USA)

I. RUDAS (Banki Donat Polytechnic,)

G. SCHMIDT (Tech. U. of Munich, Germany)

B. SICILIANO (Napoli University, Italy)

C. C. SMITH (Brigham Young University, USA)

T.-J. TARN (Washington University, USA)

D. TESAR (U. of Texas at Austin, USA)

K. YUCEF-TOUMI (MIT, USA)

S. K. TSO (City Univ. of Hong Kong, Hong Kong)

G. ULISOY (University of Michigan, USA)

S. VELINSKY (UC Davis, USA)

B. M. WILAMOWSKI (Univ. of Wyoming, USA)

R. ZURAWSKI (Cyberonics, USA)

PREFACE

The word mechatronics was first coined by a senior engineer of a Japanese company; Yaskawa, in 1969, as a combination of "mecha" of mechanisms and "tronics" of electronics and the company was granted the trademark rights on the word in 1971 [1-2]. The word soon received broad acceptance in industry and, in order to allow its free use, Yaskawa elected to abandon its rights on the word in 1982 [3]. The word has taken a wider meaning since then and is now widely being used as a technical jargon to describe a philosophy in engineering technology, more than the technology itself. For this wider concept of mechatronics, a number of definitions has been proposed in the literature, differing in the particular characteristics that the definition is intended to emphasize. The most commonly used one emphasizes synergy and is as follows: Mechatronics is the synergistic integration of mechanical engineering with electronics and intelligent computer control in the design and manufacture of products and processes. The embedded intelligence may vary from programmed behaviour to self organization and learning.

The development of mechatronics has gone through three stages. The first stage corresponds to the years around the introduction of the word. During this stage, technologies used in mechatronic systems developed rather independently of each other and individually. With the start of the eighties, a synergistic integration of different technologies started taking place, the notable example being in optoelectronics (i.e. an integration of optics and electronics). The concept of hardware/software co-design also started in these years. The third and the last stage starts with the early nineties. The most notable aspect of this stage is the increased use computational intelligence in mechatronic products and systems. It is due to this development that we can now talk about Machine Intelligence Quotient (MIQ). Another important development in the third stage is the possibility of miniaturization of the components; in the form of microactuators and microsensors (i.e. micromechatronics).

The field of mechatronics is now widely recognized in all parts of world. Various undergraduate and graduate degree programs on mechatronic engineering are being offered at different universities. Journals dedicated to the field of mechatronics are being published, dedicated conferences are being held. One such conference is the one organized in Turkey during August 14-16, 1995, with the title, "International Conference on Recent Advances in Mechatronics: ICRAM'95," under the technical co-operation of ASME (American Society of Mechanical Engineers), IEEE (Institute of Electrical and Electronics Engineers) Industrial Electronics Society, IEEE Robotics and Automation Society, IEEJ (Institute of Electrical Engineers of Japan), IFAC (International Federation of Automatic Control), IFToMM (Int. Fed. for the Theory of Machines and Mechanisms), JSME (Japanese Society of Mechanical Engineers), RSJ (Robotics Society of Japan) and SICE (Society of Instr. and Control Engineers of Japan). The conference was highly successful, it had more than 200 participants from 34 different countries. Four years has since then passed and in order to discuss the most recent advances, it has been decided to hold another similar conference during 24-26 May 1999, again in Istanbul, Turkey, under the title 2nd International Conference on Recent Advances in Mechatronics: ICRAM'99. It is organized by UNESCO Chair on Mechatronics and Mechatronics Research and Application Center of Bogazici University, Istanbul, co-sponsored by IEEE Industrial Electronics Society and IEEE Robotics and Automation Society, and in technical co-operation with ASME Dynamic and Control Systems Division, ASME Design Engineering Division, RSJ, IEEJ, JSME and SICE.

Two kind of papers have been solicited for this conference, "long papers" and "regular papers." The former ones have been collected in an edited book, published by Springer-Verlag (ISBN 981-4021-34-2), under the name Recent Advances in Mechatronics (Eds. Okyay Kaynak, Sabri Tosunoğlu and Marcelo Ang Jr.). The regular papers (90 of them) appear in this volume.

We would like to take this opportunity to thank all the authors for their valuable contributions. We are confident that the readers will find the contents of the proceedings interesting and beneficial.

Editors

References

1. Japan Trade Mark Kohhoku, Class 9, Shou 46-32713, 46-32714, Jan. 1971.
2. Japan Trade Registration No. 946594, Jan. 1972
3. N. Kyura, The Development of a Controller for Mechatronics Equipment, IEEE Transactions on Industrial Electronics, (1996), 43 (1), 30-37

A MESSAGE FROM THE CHAIRMAN

ICRAM'99 is being organized by UNESCO Chair on Mechatronics and Mechatronics Research and Application Center of Bogazici University, Istanbul, co-sponsored by IEEE (Institute of Electrical and Electronics Engineers) Industrial Electronics Society and IEEE Robotics and Automation Society, and in technical co-operation with ASME (American Society of Mechanical Engineers) Dynamic and Control Systems Division, ASME Design Engineering Division, RSJ (Robotics Society of Japan), IEEJ (Institute of Electrical Engineers of Japan), JSME (Japanese Society of Mechanical Engineers) and SICE (Society of Instr. and Control Engineers of Japan).

The support of the prestigious organizations listed above has resulted in a wide interest in the meeting. We have about 130 high quality presentations in the final program and 4 plenary presentations by very well known experts in their fields. Additionally, 2 panel discussions are planned during which a group of American and Turkish scientists will present their latest research endeavors with the purpose of identifying possible research collaboration areas.

Many colleagues from many different countries of the world have given their support to ICRAM'99. We have been trying to deserve this attention by doing our best to make the meeting both scientifically and socially rewarding to all the participants. In addition to the scientific program of the meeting, we are offering some tours of Istanbul to acquaint you with some of the cultural and historical riches that this city has to offer. Additionally, a post conference tour into Cappadocia is organized which, we hope, will promote not only long lasting friendship but also in-depth technical discussions in an expert group of limited size.

I would like to take this opportunity to acknowledge the tremendous effort invested in this meeting by many colleagues, students and others in many committees of the meeting. My special thanks go to the Program Chairs; Professors Tosunoglu and Ang, Jr., and to the members of the Advisory Committee and International Program Committee. I would also like to thank all the speakers, authors and participants for joining us and making ICRAM'99 a success.

Finally I wish you all a very pleasant stay in Turkey and a safe return back home. I hope that ICRAM'99 will be a meeting you will pleasantly remember for years to come.

Okyay Kaynak
General Chair

ACKNOWLEDGMENTS

The Organizing Committee of ICRAM'99 wish to thank the following for their contribution to the succes of this conference:

- UNESCO
- Bogazici University Foundation
- European Office of Aerospace Research and Development, Air Force Office of Scientific Research, United States Air Force Research Laboratory
- European Research Office, United States Army
- Turkish Airlines

LIST OF PAPERS

ABSTRACTS OF PLENARY PAPERS

Computational Intelligence for Robotic Systems	1
<i>Toshio Fukuda, Naoyuki Kubota, Nagoya University (JAPAN)</i>	
Mechatronics in the EU Fifth Framework Programme	2
<i>Rosalie Zobel, European Commission (BELGIUM)</i>	
Challenges in Mechatronics Research and Education	2
<i>Masayoshi Tomizuka, UC Berkeley (USA)</i>	
Advances in Robotics	2
<i>Gerd Hirzinger, DLR (German Aerospace Center, GERMANY)</i>	

MODELING AND SIMULATION

An Efficient Simulation Platform for the Development of Anti-Lock Brake System Using Hardware in-the-Loop System (HILS)	3
<i>S. Y. Yang¹, S. T. Park¹, K. S. Cho¹, M. H. Lee², ¹University of Ulsan, ²Pusan National University (KOREA)</i>	
Modeling of Wet Clutches in Automatic Transmissions	9
<i>Ali Haj-Fraj, F. Pfeiffer, Technische Universitaet München (GERMANY)</i>	
Modeling and Analysis of a Piezo-Actuated Positioning Mechanism	16
<i>Han. J.M.T.A. Adriaens, Willem L. de Koning, Reinder Banning, Delft University of Technology (THE NETHERLANDS)</i>	
The Shape of Multi-Body Motion	22
<i>William A. Wolovich, Mustafa Unel, Brown University (U.S.A.)</i>	

TRAJECTORY PLANNING AND CONTROL

Optimal System Inversion Based Motion Planning for Servosystems With Elastic Transmission	28
<i>Aurelio Piazzi¹, Antonio Visioli², ¹University of Parma, ²University of Brescia (ITALY)</i>	
Trajectory Control of a Robotic Manipulator Using Artificial Neural Networks	34
<i>Guney Devrim Ildiri¹, Osman Turkay², ¹Galatasaray University, ²Bogazici University (TURKEY)</i>	
Trajectory Generation and Obstacle Avoidance for Mobile Non-Holonomic Robots	40
<i>Zoran M. Gacovski¹, G.M. Dimirovski², Tatjana D. Kolemisevska², ¹Ministry of Defence, ²St. Cyril & St. Methodist University (MACEDONIA)</i>	
Reduction of Path Errors for Industrial Robots by Trajectory Precorrection	46
<i>Martin Grotjahn, Bodo Heimann, Axel Thiemann, University of Hannover (GERMANY)</i>	

VARIABLE STRUCTURE CONTROL SYSTEMS

Development of a Sliding Mode Controller Based on Neural Networks for the Semi-Suspension System	52
<i>Chang-Goo Lee, Hyung-Soon Lim, Kwang-Hyun Song, Chonbuk National University (KOREA)</i>	
Intelligent Signal Estimation Using Cosine Neural Networks with Variable Structure Systems Based Training Procedure	57
<i>M. Onder Efe, Okyay Kaynak, Feza Kerestecioglu, Bogazici University (TURKEY)</i>	
Practical Evaluation of V.S.C. with Varying Bounds of Robot Manipulator	62
<i>Pierre Nigrowsky¹, Antonio Visioli², Peter Turner¹, ¹Brunel University (UNITED KINGDOM), ²University of Brescia (ITALY)</i>	
Gaussian Neuro Sliding Mode Controller	68
<i>Hasan Palaz¹, Kemal Sarioglu², Ertugrul Akbas¹, Meliksah Ertugrul¹, ¹TUBITAK, ²Istanbul Technical University (TURKEY)</i>	

CONTROL OF MECHATRONIC SYSTEMS

Research Concerning the Improvement of Performances of Automatic Control Systems Based on the Optimization of Feeding and Transport Process	74
--	----

<i>Luciana Cristea¹, Adrian Dumitriu¹, Dorel Cristea², ¹Transilvania University of Brasov, ²S C. BRAFOR S.A. (ROMANIA)</i>	
Determining Maximal Asymptotic Stability region of Mechatronic Systems	78
<i>G.M. Dimirovski¹, Okyay Kaynak², A. Mojsovski¹, M.J. Stankovski¹, Y.W. Jing³, ¹St. Cyril & St. Methodist University (MACEDONIA), ²Bogazici University (TURKEY), ³Northeastern University (CHINA)</i>	
Cross-coupling Controller Design for 2-DOF Platform	84
<i>Oren Masory, Daoxi Xiu, Florida Atlantic University (U.S.A.)</i>	
DSP Based Position Control of PMSM with Real-Time Cycloidal Path Generation for Intelligent Motion Applications	88
<i>Francesco Parasiliti, Roberto Petrella, Marco Tursini, University of L'Aquila (ITALY)</i>	

PRODUCTION AUTOMATION

A Safety and Dexterity Design Strategy for Human Symbiotic Robots	94
<i>Toshio Morita, Hiroyasu Iwata, Shigeki Sugano, Waseda University (JAPAN)</i>	
Robot Assisted Polishing Using Nonprogrammable Active End Effectors	100
<i>Levent Guvenc, Istanbul Technical University (TURKEY)</i>	
The Economic Benefits of Integration Internet with Business Operations in Smart Manufacturing Management	106
<i>Ergun Gide, Fawzy Soliman, University of Technology Sydney (AUSTRALIA)</i>	
Design of Real Time Decision Support Systems on the Basis of the Tools G2+GDA	112
<i>Vadim N. Vagin, Alexander P. Yeremeyev, Moscow Power Engineering Institute(RUSSIA)</i>	

MACHINE VISION

Virtual Image Cancellation in a New Binocular Stereovision System	117
<i>Juichi Takeno, Zichuan XU, Meiji University (JAPAN)</i>	
A Study on Intelligent Control of Robot Manipulator Based-on Visual Servoing with Stereo Vision	123
<i>Sung-Hyun Han¹, Man-Hyung Lee², Jong Il Bae³, ¹Kyungnam University, ²Pusan National University, ³Pukyong National University (KOREA)</i>	
Error Recovery of Autonomous Mobile Robot with Vision Based Navigation System	129
<i>Yasunori Abe¹, Yoshio Tanaka¹, Shintaro Sakamoto¹, Toshio Fukuda², Fumihito Arai², Masaru Shikano², ¹Shinryo Corporation, ²Nagoya University (JAPAN)</i>	
Mechatronics in Agriculture - Robust Recognition of Plant Rows	135
<i>Björn Astrand, A. J. Baerveldt, Halmstad University (SWEDEN)</i>	

ADAPTIVE CONTROL

Adaptive Trajectory Tracking Control for Robot Arms with Motor Dynamics	142
<i>Jung-Hua Yang, Yungta College of Technology and Commerce (TAIWAN)</i>	
Neural Networks Adaptive Controller for Rigid Manipulators	148
<i>Reza Fotouhi-C, Peter N. Nikiforuk, University of Saskatchewan (CANADA)</i>	
Adaptive Motion Control of Mechatronic Systems	153
<i>Vasil A. Balavessov¹, V. Galabov², I. Avramov², Y. Deyanov², ¹Bulgarian Academy of Sciences, ²Technical University of Sofia (BULGARIA)</i>	
Neural Decomposed Computed Torque/Adaptive Control of Robot Manipulators	159
<i>M. Kadri¹, Brahim Bouzouia², N. Louam¹, ¹Ecole Nationale Polytechnique (FRANCE) ²Centre de Developpement des Technologies Avancees (ALGERIA)</i>	
Adaptive Control for Flexible Manipulators	165
<i>Reza Fotouhi-C, Walerian Szyszkowski, Peter N. Nikiforuk, University of Saskatchewan (CANADA)</i>	

DESIGN OF MECHATRONIC SYSTEMS

An Implementation of Automatic Container Transporter	170
<i>Young Jin Lee¹, Nam Huh¹, Young Jin Yoon¹, Man-Hyung Lee¹, Jong Il Bae², ¹Pusan National University, ²Pukyong National University (KOREA)</i>	

Robotized Palletizing of Wine Glasses	175
<i>Dilek Bilgin Tukul, Hakan Altinay, Can Bayar, Gokhan Gok, Gokay Hurmalı, Agan Simsek, Altinay Robotics & Automation Inc. (TURKEY)</i>	
High Mobility Hand Prosthesis; A Mechatronic Approach	473
<i>J. L. Pons, R. Ceres, L.A. Perez, H. Rodriguez, Instituto de Automatica Industrial, CSIC (SPAIN)</i>	
An Example of Failure Tolerance Through Active Braking	181
<i>James D. English, Antony A. Maciejewski, Purdue University (U.S.A.)</i>	
Holonic Distributed Grasping System	
<i>M. Durna, A.E. Turgut, I. Erkmen, A. Erkmen, A. Erden, Middle East Technical University (TURKEY)</i>	

MEASUREMENT TECHNOLOGY

Measurement of Dynamic Characteristics of Traction Drive and High-Precision Control of Traction Servomechanism	187
<i>Lei Wang, Takashi Emura, Syuichi Oomori, Tohoku University (JAPAN)</i>	
A Data Structure for the Organization by a Robot of Sensory Information	193
<i>Ahmet Bugra Koku, Richard Alan Peters, Vanderbilt University (U.S.A.)</i>	
Design of a MEMS Six DOF Accelerometer	199
<i>Oren Masory, Jean-Pierre Alfano, Florida Atlantic University (U.S.A.)</i>	
Three-Dimensional Target Tracking Using An Adjustable Infrared Sensor Configuration	203
<i>Ali Safak Sekmen, Mark Cambron, Mitch Wilkes, Vanderbilt University (U.S.A.)</i>	
Radius of Curvature and Location Estimation of Cylindrical Objects with Sonar Using a Multi Sensor Configuration	207
<i>Ali Safak Sekmen¹, Billur Barshan², ¹Vanderbilt University (U.S.A.), ²Bilkent University (TURKEY)</i>	

INTELLIGENT SYSTEMS

A Study of Q-Learning Method in Multi-Agent System	213
<i>Fang Yuan, Shao Shihuang, Geng Zhao Feng, China Textile University (CHINA)</i>	
The Improvement of Genetic Algorithm Using Boltzmann Selection	217
<i>Yoo-Shin Kim, Gi-Souk Yoon, Jae-Woo Kim, Pusan University (SOUTH KOREA)</i>	
Designing Intelligent Multiparameterized Devices: Mechatronics Field	223
<i>Genevieve B. Coilliot¹, Jean-Louis Tournier², ¹Universite d'ARTOIS, ²ENSEEIH (FRANCE)</i>	
An Expert System for the Prediction of Faults and Wearing in Gears, Roller Bearings and Drill Bits via Signature Analysis in the Frequency Domain	228
<i>Ata Mugan, Alper Bozdogan, Murat Dogan, Muzaffer Erdal, Istanbul Technical University (TURKEY)</i>	
The Intelligent Environment for Real-Time Systems Design	234
<i>Golovina Elena, Moscow Power Engineering Institute (RUSSIA)</i>	

CONTROL OF ROBOT MANIPULATORS

Decentralized Controllers for SCARA Robot Trajectory Tracking: An Experimental Comparison	239
<i>Antonio Visioli, Bruno Zappa, Giovanni Legnani, University of Brescia (ITALY)</i>	
A Novel Approach to Computed Torque Based Robot Control	245
<i>Meliksah Ertugrul¹, Okyay Kaynak², M.Ragip Basbug³, ¹TUBITAK, ²Bogazici University, ³Gebze Institute of Technology (TURKEY)</i>	
Neural Network Based Robot Controllers	251
<i>Ertugrul Akbas¹, Meliksah Ertugrul¹, Okyay Kaynak², Yagmur Denizhan², ¹TUBITAK, ²Bogazici University, (TURKEY)</i>	
Fuzzy Identifier based Inverse Dynamics Control of a Direct Drive Manipulator	257
<i>Kemalettin Erbatur¹, Okyay Kaynak², ¹TUBITAK, ²Bogazici University, (TURKEY)</i>	

FLEXIBLE MANUFACTURING SYSTEMS

Development of a Model for Internet Commerce Implementation in Intelligent Manufacturing

Management	263
<i>Ergun Gide, Fawzy Soliman, University of Technology Sydney (AUSTRALIA)</i>	
Gain-Scheduled Adaptive Control of Unreliable Manufacturing Systems with Variable Demands	269
<i>Brian Porter, Pik Yin Mok, The University of Hong Kong (HONG KONG)</i>	
The Use of Electronic Commerce as a Strategic Tool in Intelligent Manufacturing	275
<i>Ergun Gide, Fawzy Soliman, University of Technology Sydney (AUSTRALIA)</i>	
Contributions of ICT on Machine and Machine System Concepts	281
<i>Mauri Airila, Helsinki University of Technology (FINLAND)</i>	

EDUCATION AND TRAINING IN MECHATRONICS

Training on Programmable Instrumentation for a Curriculum of Electronic Engineering	285
<i>Perfecto Marino, Juan Nogueira, Heriberto Hernandez, University of Vigo (SPAIN)</i>	
Method and Software for Teaching Multibody System Dynamics in Mechatronics Courses	291
<i>Doru Talaba, Ion Visa, University of Transilvania of Brasov (ROMANIA)</i>	
Development of a Parallel Inverted Pendulum for Control Theory Education	297
<i>Jae Weon Choi, Un Sik Park, Joo Ho Kim, Pusan National University (KOREA)</i>	
Remote Learning: World-Wide-Web Operated Robot Arm	303
<i>Matanya Elchanani, Tarek Sobh, University of Bridgeport (U.S.A.)</i>	

NEURAL NETWORKS AND APPLICATIONS

Interferogram Analysis with Neural Networks	307
<i>A. S. Yak¹, A. N. Poo², S. S. Keerthi², ¹Philips Singapore Pte Ltd, ²National University of Singapore (SINGAPORE)</i>	
Lane Recognition Neural Network	313
<i>Suk Lee¹, Jang Myung Lee¹, Man-Hyung Lee¹, Jong Il Bae², ¹Pusan National University, ²Pukyong National University (KOREA)</i>	
Neural Network Control of a Fieldbus Pilot Plant System	319
<i>Fazlur Rahman M. H. R., Philip S. M. Chin, Yang Rong Huan, Pee Suat Hoon, Singapore Polytechnic University (SINGAPORE)</i>	
Sequential Task Execution in a Prosthetic Limb Using an Artificial Neural Network	325
<i>S. Srinivasan¹, A. Bradley², ¹Singapore Polytechnic University (SINGAPORE), ²RMIT (AUSTRALIA)</i>	
A Neuro-Fuzzy Controller for a Single Link Arm	
<i>S. Bogosyan, M. Gokasan, Istanbul Technical University (TURKEY)</i>	

FUZZY SYSTEMS

A Robust Fuzzy Controller for a Class of Multiple Hyperredundant Cooperative Robots	330
<i>Mircea Ivanescu¹, Alina Nirvana Popescu², Decebal Popescu², ¹University of Craiova, ²University Politehnica (ROMANIA)</i>	
Linearization of the Load Characteristics of a Converter Through a Fuzzy Compensation	336
<i>Amr El-Zawawi, Manal Ahmed Wahba, O. A. Sebakhy, University of Alexandria (EGYPT)</i>	
Do Fuzzy Controllers Have Advantages over Neural Controllers in Microprocessor Implementation	342
<i>Bogdan Wilamowski, Jeremy Binfet, University of Wyoming (U.S.A.)</i>	
Grey-Fuzzy Implementation of a DSP-Based Induction Motor Drive	348
<i>Hung-Ching Lu, Cheng-Hung Tsai, Tatung Institute of Technology (TAIWAN)</i>	
UPS Systems Feeding Nonlinear Loads Using Fuzzy Reasoning	354
<i>Hung-Ching Lu, Cheng-Hung Tsai, Tatung Institute of Technology (TAIWAN)</i>	

HYDRAULIC AND PNEUMATIC APPLICATIONS

Importance of Mechanical Flexibility on Behaviour of a Hydraulic Driven Log Crane	359
<i>Salvador Esque, Timo Kappi, Asko Ellman, Tampere University of Technology (FINLAND)</i>	
Analysis and Synthesis of Electrohydraulic Servomechanisms	366
<i>Alexandru Marin, Paul Svasta, Petrin Drumea, "POLITEHNICA" University (ROMANIA)</i>	

Force Transducer with Integrated Electronics for Hydraulic Cylinder	370
<i>Ionica Cristea², Mircea Comes¹, Marian Blejan¹, Adrian Mirea¹, Andrei Drumea², ¹Hydraulic and Pneumatic Research Institute, ²Politehnica University of Bucharest (ROMANIA)</i>	
Binary Mini - Robot Pneumatically Driven	
<i>Constantin Nitu, Nicolae Alexandrescu, Constantin Daniel Comeaga, Mihai Avram, Bogdan Gramescu, Politehnica University of Bucharest (ROMANIA)</i>	
Design of an Electropneumatic Micro Robot for In-pipe Inspection	374
<i>Cedric Anthierens, Maurice Betemps, INSA of Lyon (FRANCE)</i>	

MOBILE ROBOTS

Flexible Strategy and Theory for Identification With Hybrid Adaptation Application to Mobile Robotics	380
<i>Amar Khoukhi, F. Ait Saadi, Institut d'informatique USTHB University (ALGERIA)</i>	
Dynamically Stable Control of a Biped Robot	385
<i>Klaus Löffler, M. Gienger, F. Pfeiffer, Technische Universität München (GERMANY)</i>	
Reliable Mobile Robot Localization and Navigation Using Incremental Odometry, A Compass and A Gyroscope	
<i>Levent Yenilmez¹, Hakan Temeltas², ¹Turkish Air Force Academy, ²Istanbul Technical University (TURKEY)</i>	
Multi-Agent Based Strategy for Motion Control of Biped	391
<i>A. Khoukhi¹, L. Khoukhi¹, R. Ouiguini², ¹Institut d'informatique USTHB University, ²CDTA (ALGERIA)</i>	
Flexible Mini-Robot with Autonomous Motion	396
<i>Claude Laurent¹, Francis Munerato¹, Doru Mihalachi¹, Constantin Nitu², Constantin Daniel Comeaga², Waldemar Oleksiuk³, Wieslaw Czerwicz³, ¹University of Metz (FRANCE), ²Politehnica University of Bucharest (ROMANIA), ³Warsaw University of Technology (POLAND)</i>	
Active Video Modules for Launchable Reconnaissance Robots	478
<i>Kemal B. Yesin, Bradley J. Nelson, Nikolaos Papanikolopoulos, Richard Voyles, Donald Krantz, University of Minnesota (USA)</i>	

CONTROL APPLICATIONS

A Comparison of Controller Performance for an Autonomous Underwater Vehicle	402
<i>Ching-Chaw Chiok, Hariharan Krishnan, Chee-Leong Teo, National University of Singapore (SINGAPORE)</i>	
A Novel Speed Control Technique for Single-Phase Induction Motor	408
<i>A. S. Zein El-Din, A. E. El-Sabbe, Menoufia University (EGYPT)</i>	
Design of LMI Based H-Infinity Servo Controller for Cold Tandem Mill	413
<i>In Soo Kim¹, Yu Shin Chang¹, I. Cheol Hwang², Man Hyung Lee¹, Jong Il Bae³, ¹Pusan National University, ²Donggeui University, ³Pukyong National University (KOREA)</i>	
Intelligent Control of Multiple Mobile Robots Handling a Single Object in Coordination	419
<i>Kazuhiro Kosuge¹, Yasuhisa Hirata¹, Manabu Sato¹, Hajime Asama², Hayato Kaetsu², Kuniaki Kawabata², ¹Tohoku University, ²RIKEN (JAPAN)</i>	
ROBOPAINT: Multi-Robot Painting System for Glass Bricks	425
<i>Nazik Kurtuldu, Hakan Altinay, Can Bayar, Gokay Hurmalı, Gokhan Gok, Agan Simsek, Emin Tahrali, Dilek Bilgin Tukul, Altinay Robotics & Automation Inc. (TURKEY)</i>	
Development of an Active Worktable for Force Control of Robot Manipulators	430
<i>Shin-ichi Nakajima, Niigata Institute of Technology (JAPAN)</i>	

SENSORS AND ACTUATORS

Development of a Soft Planar Actuator Using Pneumatic-Rubber Balls	435
<i>Toshiro Noritsugu, Daijyu Kaneshiro, Okayama University (JAPAN)</i>	
Design and Performance of a New Tactile Sensor for Robotic Underwater Application	441
<i>Alessandro Bruno, G. Cannata, G. Casalino, University of Genoa (ITALY)</i>	
Development of the Actuator for an Automatic Drum Playing With a Moving Coil Type in Drive Motors	447

<i>Eiji Hayashi¹, Masami Yamane², ¹Kyushu Institute of Technology, ²Waseda University (JAPAN)</i>	
A Flexibility Operated Electro-Mechanical Fine Stepper Motor	452
<i>E. Wong Chun Kay¹, W. A. Bullough², E.C. Partington¹, ¹University of Sheffield (UNITED KINGDOM), ²University of Hong Kong (HONG KONG)</i>	
Design of a Capacitive and Perceptible Tactile Sensor for Robot Hand	456
<i>Francisco Flavio, Mauro F. E. Coss, F. F. Cordova Quiroz, M. Fransisco, Universidad del Valle de Mexico, Campus Tlalpan (MEXICO)</i>	
Dynamic Characteristics of Piezoelectric Multilayer Stack Actuators	461
<i>Pozzi M., King T., University of Leeds (UNITED KINGDOM)</i>	

ANALYSIS OF MECHATRONIC SYSTEMS
--

Nonlinear System Identification of a Micromanipulator	467
<i>Zhou Quan¹, Pasi Kallio¹, Heikki N. Koivo², ¹Tampere University of Technology, ²Helsinki University of Technology (FINLAND)</i>	

Challenges in Mechatronics Research and Education

Masayoshi Tomizuka

*Department of Mechanical Engineering, University of California
Berkeley, California 94720-1740, U.S.A., E-mail: tomizuka@me.berkeley.edu*

The term "mechatronics" was introduced in the late 1960s by the Yaskawa Electric Company (Japan) based on their observation of the synergy achieved through the integration of mechanical and electronic technologies. Yaskawa subsequently released trademark rights to the name and it has been used since then in education and industry to describe systems derived from this heritage.

Today, that heritage has come to include a broad variety of physical systems operating under computer and electronic control. The term "intelligence" might be applied to these systems, but its anthropomorphic implications lead to too many arguments as to appropriate definition. What we can observe, however, is that these systems employ a complexity of decision-making that is primarily limited by engineering economics rather than technology. This is a distinctive break from the past and serves as a defining characteristic of mechatronic systems. Using this perspective broadens the modern view of mechatronics to include any kinds of decision-making technologies although digital computers dominate today.

A major driver of mechatronics comes from the needs of industry. Masten of Texas Instrument summarizes the general trends in industry by listing 1) knowledge is king, 2) innovation is essential, 3) cost (what is "new" today becomes a "commodity" tomorrow, 4) products are more complex and system based with higher performance, 5) short design cycle, 6) markets are global and more competitive and 7) "design teams" are a preferred approach. Mechatronics offers the *best practice* to meet these challenges.

There have been numerous innovations in the 1980s such as adding intelligence to industrial products. We may call such trends as infusion of "information technology" to industrial products. Mechatronics in the 1980's was no longer a simple integration of mechanics and electronics. The availability of economically affordable and reliable microprocessors and new types of sensors had influenced the design and manufacturing of industrial products as well as the products themselves.

These developments also set the background for various definitions of mechatronics introduced in the late 1980's and the early 1990's. The International Federation for the Theory of Machines and Mechanism (IFTMM), provided a definition, "Mechatronics is the synergistic combination of precision mechanical engineering, electronic control, and systems thinking in design of products and manufacturing processes." The IEEE/ASME Transactions on Mechatronics, which was launched in 1996, adopted a similar definition, "Mechatronics is the synergetic integration of mechanical engineering with electronic and intelligent computer control in the design and manufacture of industrial products and processes."

It was mentioned that a major driver of mechatronics is the needs of industry, and that mechatronics offers the best practice. This does not mean that mechatronics refers to how things should be done in the development of products at industry. In fact, mechatronics provides a series of interesting research issues to university researchers. Mechatronics research in academia should be at the forefront and yet remain relevant to needs of industry. Mechatronics research examples appropriate as university research appear in many areas such as advanced vehicle control and safety systems (AVCSS), design and control of hard disc drives for high aerial density, biomedical systems and MEMS (micro-electro-mechanical systems).

Engineering education is facing challenges in the midst of rapid progress of IT. IT is important in mechatronics, but we need to recognize that in a field as dynamic as ITs, no set of vocational skills has any significant longevity. Having said above, our undergraduate students should be exposed to mechanical design, information technology (software and hardware), modeling and feedback control, integration of mechanical devices and computers, dealing with complexity and team work. Furthermore, students should be trained to be forward looking and curious and good communicators. Issues surrounding integration as well as working in team cannot be taught in lecture courses. Students must experience them, and in this regard laboratory courses are essential in mechatronics education. Many high school students have a simple equation Information Technology = Computer Science Department and do not realize how other engineering disciplines are changing by IT. In this regard, the role of educators must go beyond how mechatronics should be taught. It is important that we direct the attention of high school students and college freshmen and sophomores to the exciting field of mechatronics. Mechatronics is the field, which may attract a number of talented undergraduate students, and in fact mechatronics thinking should be exposed to all engineering students, in particular, in mechanical engineering and electrical engineering. Mechatronics thinking is the basics of the modern engineering education.

Computational Intelligence for Robotic Systems

Toshio Fukuda¹ Naoyuki Kubota²

*¹Center for Cooperative Research in Advanced Science and Technology,
Dept. of Mechano-Informatics and Systems &
Dept. of Micro System Engineering, Nagoya University,
1 Furo-cho, Chikusa-ku, Nagoya, 464-8603, JAPAN*

*²Dept. of Mechanical Engineering, Osaka Institute of Technology
5-16-1 Omiya, Asahi-ku, Osaka 535-8585, JAPAN*

This paper introduces recent topics of computational intelligence. The intelligent capabilities will be required to the various systems to adapt a system to dynamically changing environment. First, we introduce the computational intelligence including evolutionary computing, neural computing and fuzzy computing. Next, some of the important problems including the system architecture, structured intelligence, emerging system and implementation methods is discussed in this paper from the viewpoint of coevolution.

Mechatronics in the EU Fifth Framework Programme

Rosalie Zobel

*European Commission, DG XIII, Rue de la Loi 200 – N105 5/25, B-1049
Brussels, Belgium*

Mechatronics, as an intelligent integration of different engineering disciplines, can also play a pivotal role as a model for inter-disciplinary R&D that is supported by the European Commission's 5th Framework Programme for research & technological development.

The presentation will offer an overview of the R&D priorities relevant to mechatronics, as covered by the Information Society Technologies programme, (Key Actions II and IV), Key Action I of the Competitive and Sustainable Growth programme, as well as the Intelligent Manufacturing Systems initiative.

Advances in Robotics

Gerd Hirzinger

*Director, Institute of Robotics and System Dynamics, DLR-Oberpfaffenhofen
P.O.Box 11 16, 82230 Wessling, Germany*

Future robots presumably are the most challenging mechatronic systems. The talk tries to outline recent advances in the field of industrial robots as well as in the design of a new generation of lightweight robots and articulated multisensory hands for service applications in space and on earth.

Powerful man-machine interfaces and skill-transfer-techniques combined with sensor-based world model generation and update are key elements for new programming and task-learning concepts. And in surgery, mechatronic and robotic systems stand for the final break-through in minimally invasive operations and telesurgery.

An Efficient Simulation Platform for the Development of Anti-Lock Brake System Using Hardware-In-the-Loop System (HILS)

S. Y. Yang, S. T. Park and K. S. Cho
Department of Automotive Engineering
University of Ulsan
San 27 Mugue-dong, Nam-gu
Ulsan, 680-749, Korea
soonyy, spark@uou.ulsan.ac.kr

M. H. Lee
Department of Mechanical Engineering
Pusan National University
San 30 Jangjeon-dong, Kumjung-gu
Pusan, 609-735, Korea
mahlee@hjewon.pusan.ac.kr

Abstract

An efficient simulation platform for the development of anti-lock brake system (ABS) is presented. To reduce computational burden due to the rigidity of brake hydraulics, the actual hydraulic brake assembly is taken from the target vehicle and linked to a virtual 18-dof vehicle dynamics model. The latter is used to describe dynamical behavior of the target vehicle under extreme maneuvers. The hardware-in-the-loop system thus built allows the investigation of not only the dynamic behavior but also hydraulic responses of the vehicle with a complete assess to all system parameters and state variables.

1 Introduction

Simulation analysis has become an indispensable tool in the design of a control system, where parameters to be tuned affect dynamics of a plant in motion. This is because a small change in dynamics of the moving plant may reduce the stability margin significantly, thereby resulting in the loss of stability. The typical example is an electro-mechanical chassis control system which supports a driver to maintain steerability when braking on slippery roadways, such as Anti-Lock Brake System (ABS), Traction Control System (TCS) and Vehicle Dynamics Control (VDC).

Such control systems provide the control input in the form of braking pressure which is, in turn, resulting in different dynamical behaviors depending on the amount of braking energy absorbed by the road surface conditions. It is therefore very dangerous to tune the underlying control systems without knowing consequent physics of the vehicle motion. Moreover, uncoupling dynamical responses to rectify the source of undesirable maneuvers hard to attain due to difficulties

in defining the nominal motion among a set of road-test results. Furthermore, the growing demand for the rapid development has laid a tight limit on the time required for weather-dependent road tests.

In an effort to reduce the number of road tests, various simulation approaches have been introduced. Among them, a hardware-in-the-loop approach seems to be most promising in the sense that computationally expensive components could be substituted with the actual hardware [1]. Consequently, one can reduce the great deal of the numerical complexity in modeling, while narrowing down the gap between the simulation and experiment results. In this respect, we present an efficient simulation platform for the rapid prototyping of ABS.

The simulation platform thus constructed consists of two parts: a 18-dof virtual vehicle model and the actual hydraulic brake assembly of the target vehicle. The former is used to describe dynamical behavior of the target vehicle under extreme maneuvers, while the latter to reduce computational burden due to the rigidity of hydraulic units comprising brake system. By establishing a link between the actual hardware and the virtual vehicle model, one can artificially generate the road surface conditions inducing ABS involvement. Once tuned properly, the resulting simulation platform exhibits a very high degree of reliability, making many road tests obsolete.

2 Virtual Model of the Target Vehicle

The target vehicle under consideration employs a typical power steering system and a MacPherson strut front suspension, along with a semi-trailing arm rear suspension. To reduce the degree of complexity in modeling, these mechanical systems are simplified; namely, a 6-bar steering linkages for the power steering, a spring

and damper system with 2 closed kinematic chains for the front suspension, a simple spring and damper system without suspension kinematics for the rear. Finally, the governing equations of motion having minimal order, while taking into account imposed kinematic constraints, are derived by applying multibody formalism based on Kane's approach [2].

We resort to AUTOSIM to drive the governing equations of motion. Unlike the other commercial packages endowed with easy-to-use graphical interfaces, such as ADAMS and DADS, AUTOSIM requires a designer to establish interrelation between bodies and to incorporate them into dynamics model while taking into account kinematic constraints, thereby allowing the modeling of highly coupled multibody systems. Furthermore, AUTOSIM automatically generates platform-free numerical codes which is amenable to real-time applications.

2.1 The Six-Bar Steering Mechanism

Considering that the basic principle of steering action can be explained using the classical steering mechanism of Ackermann type, a 6-bar steering linkages optimizing Ackermann's turning geometry, as shown in Figure 1, is used to model the power steering system.

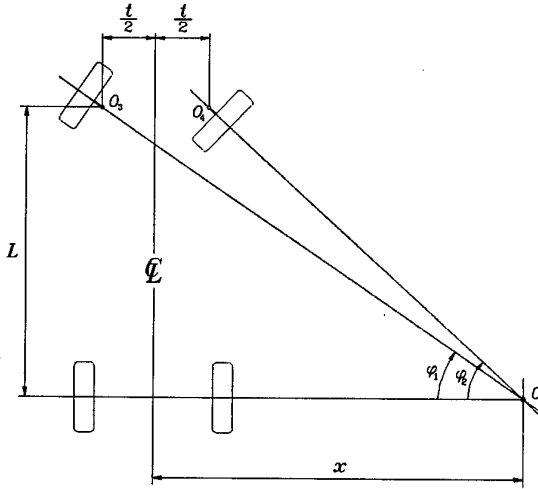


Figure 1: Ackerman geometry

The condition for correct steering requires the centerlines of the four wheels to meet at a single point, O , along the axis of the rear wheels. The steer angles according to the said correct steering condition are then given by

$$\tan \varphi_1 = \frac{L}{x + t/2} \quad (1)$$

$$\tan \varphi_2 = \frac{L}{x - t/2} \quad (2)$$

where x denotes the distance of O from the centerline L of the vehicle. Upon eliminating x from eqs. (1 and 2), the condition for correct steering can be derived as

$$f(\varphi_1, \varphi_2) = \sin(\varphi_2 - \varphi_1) - \rho \sin \varphi_1 \sin \varphi_2 = 0 \quad (3)$$

where $\rho = L/t$. It is, however, well known that the ideal steering satisfying the foregoing relation is difficult to achieve. Instead, we choose the six-bar steering linkages which optimizing the condition for ideal steering [3], as shown in Figure 2.

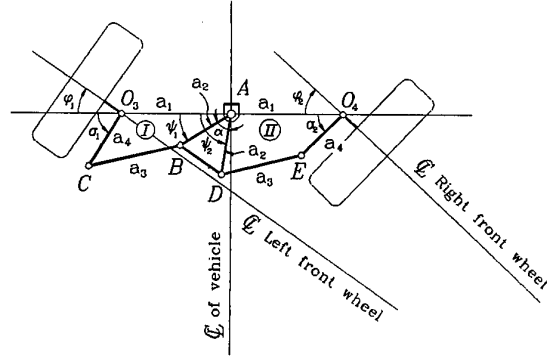


Figure 2: 6-bar steering mechanism

2.2 MacPherson Strut Suspension

The underlying MacPherson strut suspension consists of 5 bodies and 3 independent kinematic loops, as shown in Figure 3. Each body forming the loops is then analyzed independently to assign the appropriate degrees of freedom depending on its kinematic role in the system. For simplicity, a kinematic loop associated with the tension strut of the front suspension is neglected by defining a ball joint connecting the lower control arm and the wheel carrier as a rotational joint [4]. The idle degrees of freedom arising from the rotation of the rods about the line connecting the centers of their spherical joints are also neglected [5].

Integrating each body into a single dynamical system gives rise to a set of highly coupled kinematic constraints. These constraints, in turn, allows us to eliminate dependent generalized speeds, so that the resulting equations of motion can be expressed in terms of independent generalized speeds. The loop closure conditions obtained by disconnecting the loop at P , as shown in Figure 4, give rise to the following constraints equations [6]

$$\mathbf{r}^{B_P C_P} = \mathbf{0} \quad (4)$$

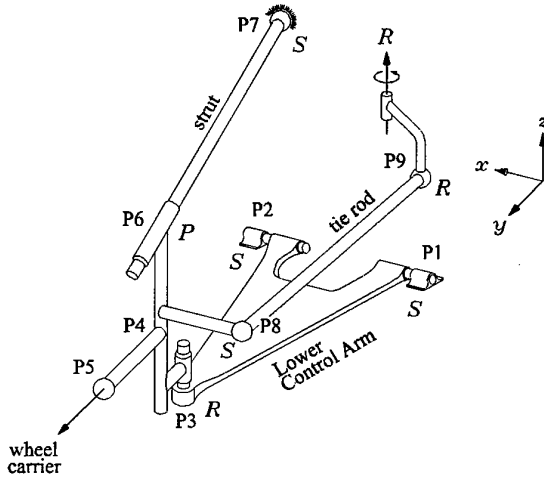


Figure 3: Architecture of a MacPherson strut

$$\mathbf{v}^{B_P C_P} = 0 \quad (5)$$

The foregoing equations can then be verified the vector equation connecting two open chains, namely,

$$\mathbf{a} + \mathbf{b} = \mathbf{c} + \mathbf{d} \quad (6)$$

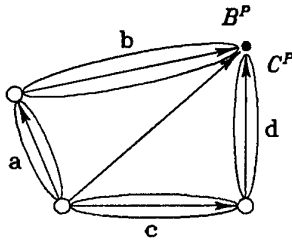


Figure 4: Loop closure conditions

2.3 Chassis Dynamics Model

For chassis dynamics model, the 18-dof vehicle model provided by MSC [7] is customized such a way that the resulting equations of motion includes the MacPherson strut front suspension, the linearized semi-trailing arm rear suspension, along with the 6-bar steering linkages. Figure 5 shows the characteristic curves of the front and rear suspensions damping. In addition, the dynamical properties used in simulation are listed in Table 1.

3 Construction of the HILS

The hardware used for the simulation is a hydraulic circuit comprising the braking system. The actual

Table 1: Dynamical properties used for simulation

Spring coefficient [N/m]	23530
of the front coil spring	
Spring coefficient [N/m]	20286
of the rear coil spring	
Spring coefficient [N/m]	180000
of the tire (vertical)	
Weight distribution (front:rear)	1.6:1
Moment of inertia (Rolling) [Kg-m ²]	300
Moment of inertia (Pitching) [Kg-m ²]	2000
Moment of inertia (Yawing) [Kg-m ²]	2800

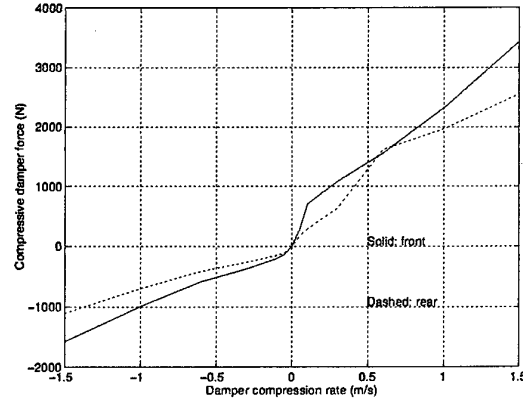


Figure 5: Damping forces (Front and Rear)

brake assembly including a hydraulic modulator for ABS is integrated into the simulation platform. The measured brake line pressures are then converted into the speed signals by virtue of the virtual vehicle model. Numerical integration of the governing equations of motion gives rises to the speed signals in discrete form, where the resulting wheel speed signals are determined by the amount of the brake line pressures and the given road surface conditions. To emulate the magnetic pick-up type speed sensor, the sine waves are generated through the built-in 4-channels function generator. Upon receiving the emulated speed signals, it is possible for ECU to determine the road surface conditions and provide appropriate control action to prevent brakes from locking. Hence, a loop including the brake assembly can be successfully constructed. Figure 6 shows the complete system layout.

3.1 Brake Hydraulics

Instead of the brake pedal effort, a pneumatic actuator is designed to initiate the brake system, as shown in

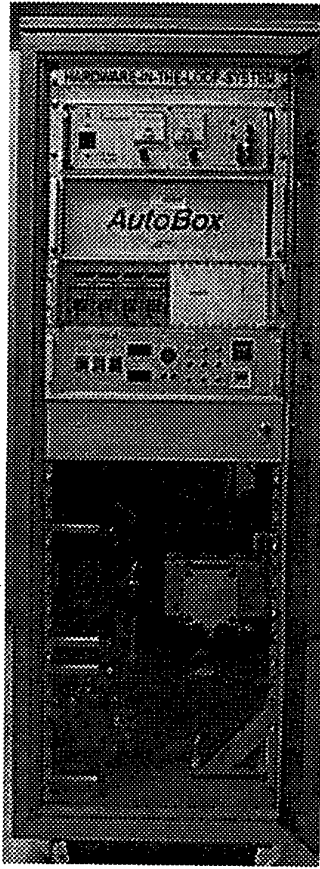


Figure 6: Front view of the HILS

Figure 7. The brake pressure distribution corresponding to the full braking condition can be obtained by controlling the stroke of the actuator. Figure 8 shows the pressure distribution for full braking. Moreover, a speed controller is attached to regulate the rise time of the brake pressure. This setup allows us to minimize the possible discrepancies due to repeated experiments, unlike the road-tests where the nominal motion has been chosen collectively.

The hydraulic brake assembly taken from the target vehicle is integrated into the simulation platform. This includes the vacuum booster master cylinder assembly, proportioning valve and the hydraulic modulator for ABS, as shown in Figure 9. To substitute the vacuum provided by the engine manifold, an additional vacuum pump is used to assist the booster. The pressure modulation in the wheel brakes can be achieved by the use of the sol-sol type 8-channel hydraulic modulator. Finally, the brake line pressures are measured through pressure transducers installed at each brake line. The underlying brake pressure signals are then transferred

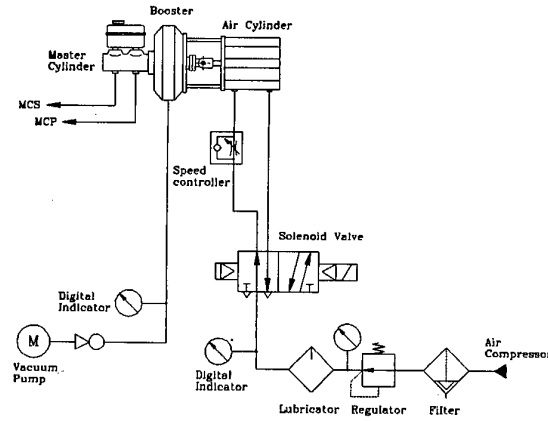


Figure 7: Design of the pneumatic actuator for braking

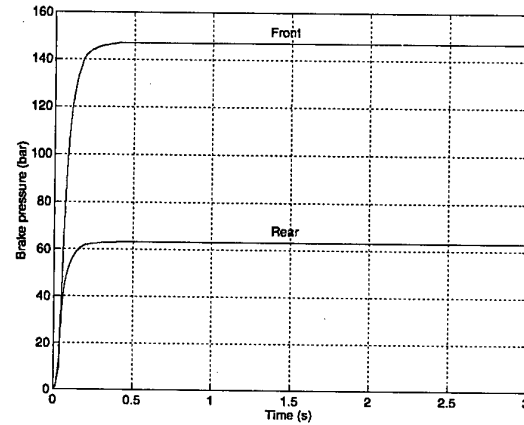


Figure 8: Brake pressure distribution

to the brake forces by [8]

$$F_b = (P_l - P_o) A_{wc} \eta_c BF (r/R) \quad [N] \quad (7)$$

where

- P_l = brake line pressure
- P_o = pushout pressure
- A_{wc} = wheel cylinder area, $[cm^2]$
- η_c = wheel cylinder efficiency
- BF = brake factor
- r = effective disk radius $[mm]$
- R = tire radius $[mm]$

3.2 Data Acquisition & Processing

The sensed brake line pressures are passing through the signal conditioner having the cutoff frequency of 100 Hz and, then, to be sent to ds2001 multi I/O board (dSPACE), where these signals are sampled at

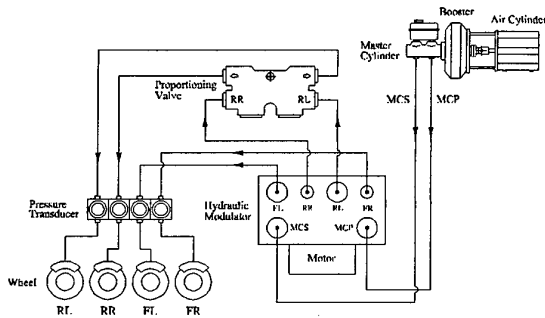


Figure 9: Brake hydraulic circuit

200 Hz. The latter sampling frequency corresponds to the solenoid firing frequency of the hydraulic modulator. Under the given road surface conditions, the system of non-linear equations of motion, which are coded in C and downloaded in ds1003 DSP board (dSPACE), takes the measured brake forces as the system input and produces the corresponding wheel speed signals after carrying out numerical integration with the minimum achievable sampling rate of 200 Hz. It should be emphasized that the loop time for the simulation has to be bounded within the specified sampling rate to secure successful data handshaking between the actual hydraulic module and the virtual vehicle model. In such a way, a link between two different systems can be established.

The discrete wheel speed signals thus obtained from numerical integration are converted into sine waves according to the characteristics of the magnetic pick-up type wheel speed sensor, namely,

$$S(f, t) \approx A(f) \sin(2\pi f t) \quad (8)$$

while satisfying

$$|A(f_1)| > |A(f_2)| \leftrightarrow f_1 > f_2, \quad (f_{\min} \leq f \leq f_{\max}) \quad (9)$$

where f and $A(f)$ denotes the wheel speed frequency and its corresponding magnitude, respectively. As discussed already, the vehicle model gives rise to the discrete speed values at every 5 [msec] when integrating with the 200 Hz sampling frequency. Note that the said wheel speed signal is too rough to emulate the continuous speed wave, which is, in turn, used to calculate the acceleration of the rotating wheel—the most crucial parameter in determining ABS engagement—. For example, the ECU might fire solenoid valves even in the normal situation due to surges induced by numerical noises associated the underlying procedure. To resolve the problem with numerical noises, we forcefully introduce one-step delay, i.e., save the previous

two values in the memory and use the numerical interpolation scheme to produce smooth sine waves. The sampling rate used for the interpolation is 1000 Hz, five times faster than the sampling frequency for the system integration.

4 System Validation

The off-line simulations have been conducted to verify the reliability of the 18-dof vehicle model. With the existing road-test results at hand, the brake pressure signals are taken as the input for the system of nonlinear equations of motion and the resulting wheel speed signals are compared with the measured wheel speed signals. Then, the system parameters including the road-surface conditions are tuned to minimize the difference between the simulation and road-test results as illustrated by Figures 10 and 11.

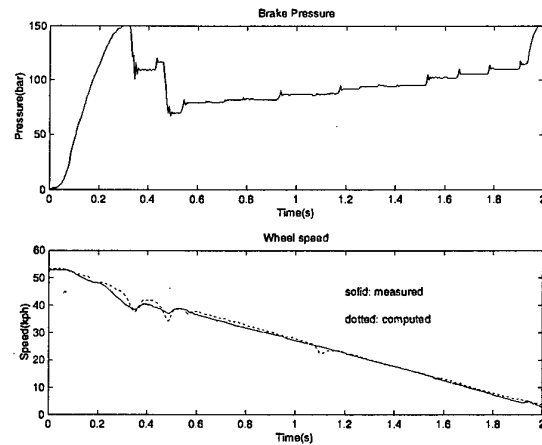


Figure 10: Wheel speed and corresponding brake pressure when ABS engaged (Front)

Figure 12 shows simulation errors after such tunings. It has been shown that the speed error of the front wheel is larger than that of the rear. This is because the front wheel has been affected by the uncertainty arising from the inertia variation in the drive train during braking. To reduce the gap, the drive train model must be included in the vehicle model. However, the increased complexity in modeling might reduce real-time capability. Instead, the wheel speed signals measured during braking directly are sent to the vehicle model so that chassis dynamics can be implemented using the measured signals, rather than the computed values. The latter approach is known to be a Vehicle-In-the-Loop System (VILS). The VILS is currently under construction at Ulsan University.

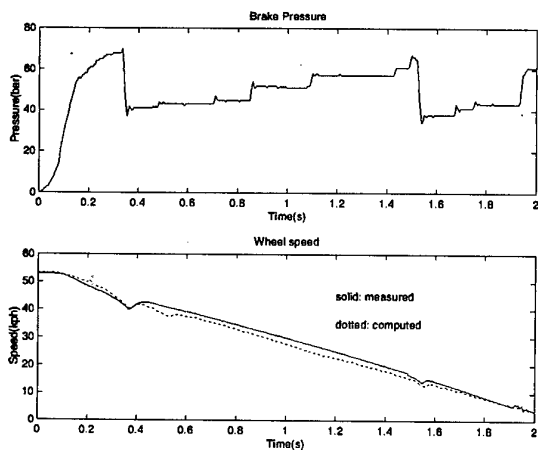


Figure 11: Wheel speed and corresponding brake pressure when ABS engaged (Rear)

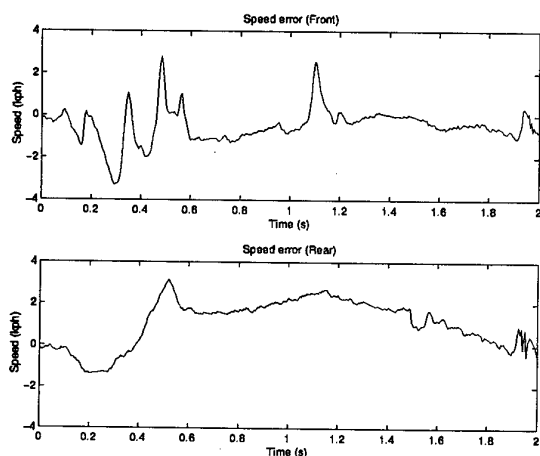


Figure 12: Simulation errors

5 Concluding Remarks

The efficient simulation platform for the rapid prototyping of Anti-Lock Brake System has been constructed. The 18-dof vehicle model is formulated to describe dynamics of the target vehicle under extreme maneuvers. The vehicle model consists of the MacPherson strut front suspension, linearized semi-trailing arm rear suspension and 6-bar steering linkages. To reduce computational burden arising from the rigidity of brake hydraulics, the actual brake system is linked to the virtual vehicle model. The loop including the hardware and the virtual vehicle model is then closed by the use of data acquisition and processing boards. The hardware-in-the-loop system makes it possible for engineers to assess the capabilities of the control scheme

long before the actual road-tests are carried out, boosting the grade of innovativeness and providing more flexibility in incorporating various control techniques.

6 Acknowledgement

The research work reported here was supported by the Korea Science and Engineering Foundation (KOSEF) through the Research Center for Machine Parts and Materials Processing at University of Ulsan.

References

- [1] M. Alexander, M. Elwell and S. Floyd, "An Overview of the LucasVarity Simulation Laboratory", SAE #970813, pp. 23-35, 1997.
- [2] T. R. Kane and D. A. Levinson, *Dynamics: Theory and Applications*, McGraw-Hill, New York, 1985.
- [3] K. E. Zanganeh, J. Angeles and A. Kecskeméthy, "On the Optimum Design of a Steering Mechanism", *Proc. 9th World Congress on the Theory of Machines and Mechanisms*, Milan, pp. 2524-2528, 1995.
- [4] J. Angeles and A. Kecskeméthy, *Kinematics and Dynamics of Multi-Body Systems*, Springer-Verlag, New York, 1995.
- [5] D. M. Spinelli and A. Costa, "Modeling and Simulation of a MacPherson Vehicle Suspension Concept Using Multibody System Techniques", SAE #962341, pp. 1-11, 1996.
- [6] M. W. Sayers, 1990, *Symbolic Computer Methods to Automatically Formulate Vehicle Simulation Codes*, Ph.D. dissertation, The University of Michigan, Ann Arbor, MI.
- [7] M. W. Sayers and D. S. Han, "A Generic Multibody Vehicle Model for Simulating Handling and Braking", *the 1995 Symposium of the International Association of Vehicle System Dynamics*, Ann Arbor, 1995.
- [8] R. Limpert, *Brake Design and Safety*, Society of Automotive Engineers, Inc., Warrendale, 1992.
- [9] AUTOSIM "Reference Manual: Version 2.0", Mechanical Simulation Corporation, Ann Arbor, MI, 1996.

Modelling of Wet Clutches in Automatic Transmissions

A. Haj-Fraj and F. Pfeiffer

Lehrstuhl B für Mechanik

TU-München, 85747 Garching, Germany

e-mail: ahf@lbm.mw.tu-muenchen.de

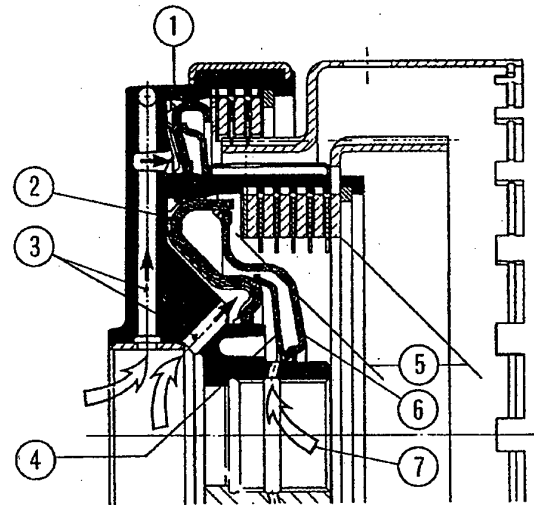
Abstract

The engagement behaviour of wet clutches used in automatic transmissions is analysed. A comprising model including all the components of the clutch is developed. The friction transmission mechanism consists of three phases: clearance phase, mixed contact phase and steady contact phase. The clearance phase describes the squeezing process of the oil film between the discs before they reach contact under the assumption that the lining material is porous, elastically deformable and has a rough surface. During the mixed contact phase the discs are partly in contact and the contact area increases smoothly due to the deformation of the surface asperities of the lined discs. The steady contact phase occurs when the disc package is pressed together and a static equilibrium in the axial direction has been established. The engagement behaviour of a wet clutch is discussed with variations of the main parameters.

1. Introduction

The transmission behaviour of wet clutches (figure 1) is affected by friction characteristic, oil viscosity, separation clearance, manufacturing tolerances, friction between the housing and the discs, etc. Therefore simplified models neglecting the presence of the oil film between the discs and the axial motion of the piston are not eligible for realistic prediction and simulation of the engagement behaviour of wet clutches. The model needed for this purpose must include the effects mentioned above.

In [1] and [2] the engagement behaviour of two clutch plates is analysed. The model used in [1] takes into account the clutch lining porosity. The transition from hydrodynamic to boundary lubrication is assumed to occur abrupt at a prescribed critical film thickness, which leads to a discontinuity in the torque curves. In [2] the surface roughness of the lining material is considered. A squeeze film phase and a consolidating con-



1 piston housing, 2 piston, 3 oil passages,
4 return spring, 5 disc package,
6 compensating plate, 7 lubrication passage

Figure 1: Wet clutch

tact phase are analysed but the mixed contact phase is not investigated. A simple and physically comprehensive model is used in [3] to simulate the transition from viscous to dry friction.

The above mentioned models do not include differences between each pair of friction discs, manufacturing tolerances and friction between discs and tangs. These effects are considered in detail in the model presented in this paper.

2. Description of the mechanical model

Figure 2 shows a comprising wet clutch model including the outer and inner tang, the piston, the return spring and the steel (inner) and lined (outer) plates.

Furthermore the oil film between each pair of friction surfaces is considered. At the beginning of a clutch engagement the control pressure is applied to the piston, which starts to press the disc package. Consequently the discs start approaching and the oil has to be squeezed out before the friction surfaces can make contact. The increasing squeeze pressure in the oil film prevents the discs from making instantaneous contact and the torque transmitted during this phase is purely due to viscous friction. Once the discs reach contact a transition from viscous to dry friction occurs. In order to describe this transient phase, the geometry and elasticity of the lined disc asperities must be taken into account.

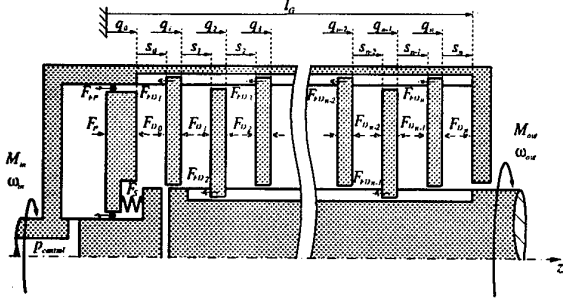


Figure 2: Wet clutch model

3. Equations of the two-discs model

3.1 Clearance phase model

We consider the squeeze oil film between a rotating steel disc and a lined disc while approaching each other (\$q_j\$ coordinate of the disc \$j\$). Taking into account the lining's elastic deformation and its surface roughness, the oil film thickness \$H\$ in figure 3 may be written as

$$H = h + \delta + h_s \quad (1)$$

with

- \$h = s + \bar{z}\$ the mean unstressed film thickness.
- \$s = q_{j+1} - b - q_j\$ the minimal unstressed film thickness.
- \$\delta = \frac{p_{oil} h_B}{E_B} (1 - \frac{2\nu_B^2}{1 - \nu_B}) = \frac{p_{oil} h_B}{E'_B}\$ the elastic deformation of the porous lining.
- \$h_s\$ the stochastic thickness difference from the nominal level defined by \$(h + \delta)\$ due to the asperities.

Here \$b\$ is the disc thickness, \$\bar{z}\$ is the mean height of the asperities, and \$h_B\$, \$E_B\$ and \$\nu_B\$ are the lining thickness, Young's modulus and Poisson's ratio respectively.

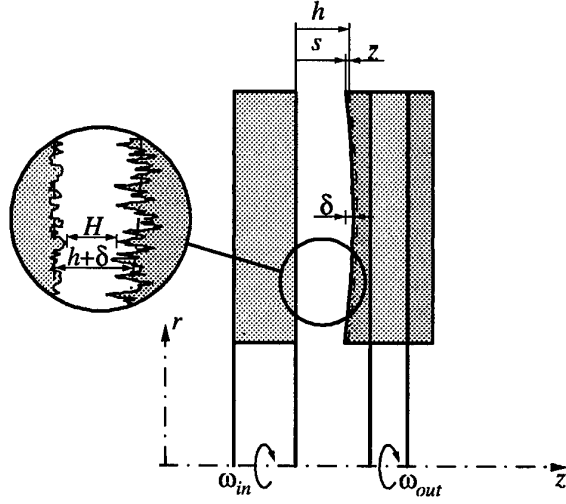


Figure 3: Clearance phase model

Assuming a homogenous and isotropic porous lining material and an incompressible fluid, the squeeze pressure can be described by the modified Reynold's equation [2, 4]

$$\frac{1}{r} \frac{d}{dr} \left[(H^3 + 12\phi h_B) r \frac{dp_{oil}}{dr} \right] = 12\eta \dot{H} + 24\phi h_B \rho \omega_{in}^2 + \frac{\rho \omega_{in}^2}{10} \left[3 + 4 \frac{\omega_{out}}{\omega_{in}} + 3 \left(\frac{\omega_{out}}{\omega_{in}} \right)^2 \right] \frac{1}{r} \frac{d}{dr} (r^2 H^3) \quad (2)$$

where \$\phi\$ represents the permeability of the lining material and \$\eta\$ and \$\rho\$ are the oil viscosity and density respectively.

We assume a uniform and isotropic surface roughness structure and a disappearing mean stochastic thickness \$h_s\$. Using the expectancy operator

$$E(X) = \int_{-\infty}^{\infty} x f(x) dx \quad (3)$$

where \$X\$ is a random magnitude with the density \$f(x)\$, the expected values of \$H\$ and \$H^3\$ can be calculated as

$$E(H) = (h + \delta) \quad (4)$$

$$E(H^3) = (h + \delta)^3 + 3(h + \delta) \int_{-\infty}^{\infty} h_s^2 f(h_s) dh_s + \int_{-\infty}^{\infty} h_s^3 f(h_s) dh_s$$

$$E(H^3) = (h + \delta)^3 + 3(h + \delta)\sigma^2 + \epsilon \quad (5)$$

where σ is the variance of the film thickness H and ϵ is a symmetry factor of its stochastic distribution, which equals zero for a symmetric distribution. Substituting H and H^3 in eq. (2) by eq. (4) and eq. (5) and solving the modified Reynolds equation with respect to the pressure p_{oil} leads to the squeeze pressure in the oil film, which can be integrated over the disc surface to [5]

$$\begin{aligned} F_{oil} &= 2\pi \int_{r_i}^{r_a} p_{oil} r dr \\ &= -\frac{\eta \dot{h} r_i^4}{h^3} \left\{ \frac{3\pi \alpha}{2\beta} \left[R^4 - 1 - \frac{(R^2 - 1)^2}{\ln R} \right] \right. \\ &\quad + \frac{9\pi \alpha^2 \bar{\delta}}{4\beta^3} \left[1 + \left(\frac{\sigma}{h} \right)^2 \right] (R^2 - 1) \\ &\quad \left. \cdot \left[\frac{R^4 + R^2 + 1}{6} - \frac{3}{8} \frac{(R^4 - 1)}{\ln R} + \frac{1}{4} \left(\frac{R^2 - 1}{\ln R} \right)^2 \right] \right\} \end{aligned} \quad (6)$$

where

$$\begin{aligned} \alpha &:= 1 + \frac{4S}{\bar{\gamma}} \left[1 + 3 \left(\frac{\sigma}{h} \right)^2 + \frac{\epsilon}{h^3} \right] \\ \beta &:= 1 + 12\psi + 3 \left(\frac{\sigma}{h} \right)^2 + \frac{\epsilon}{h^3} \\ S &:= \frac{\rho \omega_{in}^2 r_i^2}{20p_a} \left[3 + 4 \frac{\omega_{out}}{\omega_{in}} + 3 \left(\frac{\omega_{out}}{\omega_{in}} \right)^2 \right] \\ \psi &:= \phi \frac{h_B}{h^3}; \quad \gamma := \frac{12\eta \dot{h} r_i^2}{p_a h^3}; \quad \zeta := \frac{24\phi h_B \rho \omega_{in}^2 r_i^2}{h^3 p_a} \\ \bar{\gamma} &:= \gamma + \zeta; \quad \bar{\delta} := \frac{p_a h_B}{h E'_B}; \quad \bar{\delta} := \bar{\delta} \bar{\gamma}; \quad R := \frac{r_a}{r_i}; \end{aligned}$$

with the disc's inner and outer radii r_i and r_a and the reference ambient pressure p_a .

Assuming a Newtonian fluid, the shear stress can be written as

$$\tau(r) = \eta \frac{\omega_{in} - \omega_{out}}{h + \delta} r = \eta \frac{\Delta\omega}{h + \delta} r \quad (7)$$

The torque due to viscous shear is then obtained by integrating the shear stress over the disc surface

$$M_{vis} = \int_0^{2\pi} \int_{r_i}^{r_a} \tau r^2 dr d\varphi \quad (8)$$

$$= \frac{1}{2} \eta \pi \Delta\omega \left(r_a^4 - r_i^4 \right) \frac{1}{h} \quad (9)$$

3.2 Mixed contact phase model

Once the discs have made contact ($s = 0$), we have to deal with mixed friction as we have viscous friction in the area between the asperities and dry friction in the contact area between them and the steel disc (figure 4). In order to calculate the part of the torque due to dry friction, we have to determine the contact force F_{cont} between the asperities and the steel disc. Using the

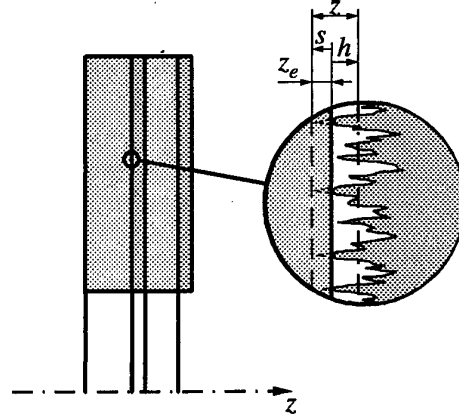


Figure 4: Mixed contact phase model

Hertzian theory the contact force F_{cont} and the ratio ξ of the contact area A_{cont} to the total friction area A_n can be expressed in terms of the compliance z_e (figure 4) [6, 7] as

$$F_{cont} = \frac{4}{3} E' A_n n_0 \bar{R}^{1/2} \sigma^{3/2} F_{3/2} \left(\frac{z_e}{\sigma} \right) \quad (10)$$

$$\xi = \frac{A_{cont}}{A_n} = \pi n_0 \bar{R} \sigma F_1 \left(\frac{z_e}{\sigma} \right) \quad (11)$$

with the definitions

$$F_{3/2} \left(\frac{z_e}{\sigma} \right) = \int_0^{z_e/\sigma} \left(\frac{z_e}{\sigma} - \frac{z_a}{\sigma} \right)^{3/2} f \left(\frac{z_a}{\sigma} \right) d \frac{z_a}{\sigma} \quad (12)$$

$$F_1 \left(\frac{z_e}{\sigma} \right) = \int_0^{z_e/\sigma} \left(\frac{z_e}{\sigma} - \frac{z_a}{\sigma} \right) f \left(\frac{z_a}{\sigma} \right) d \frac{z_a}{\sigma} \quad (13)$$

$$n_0 = \frac{N}{2l_s \bar{a}_e} \quad (14)$$

$$\frac{1}{E'} = \frac{1 - \nu_B}{E_B} + \frac{1 - \nu_S}{E_S} \approx \frac{1 - \nu_B}{E_B} \quad (15)$$

where $z_a = 2\bar{z}$, N is the number of asperity summits within a defined traverse length l_s , \bar{a}_e and \bar{R} are the

mean basis radius and the mean curvature radius of the asperity summits, E_S and ν_S are the Young's modulus and the Poisson's ratio of the steel disc.

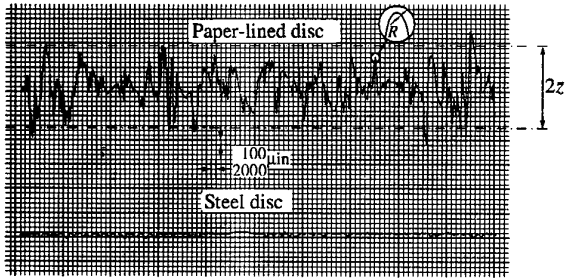


Figure 5: Profile traces of a steel and a paper-lined clutch disc

The probability density distribution $f(\frac{z_a}{\sigma})$ (figure 6) can be ascertained from a profile trace of the surfaces of lined clutch discs as shown in figure 5. Figure 5 shows that the surface roughness variation of the steel disc is negligible compared to the lined disc. Using the polynomial approximation of the surface roughness distribution

$$f\left(\frac{z_a}{\sigma}\right) = \frac{35}{96} \left[1 - \frac{1}{9} \left(\frac{z_a}{\sigma} - 3 \right)^2 \right]^3 \quad (16)$$

shown in figure 6, the integral functions (12) and (13) can be evaluated analytically.

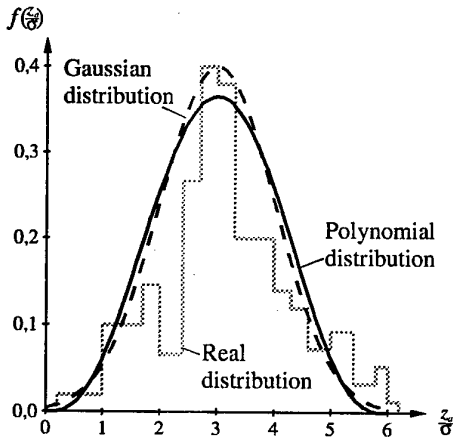


Figure 6: Surface roughness distribution of a lined disc

The part of the force due to the squeeze pressure in

the cavities between the asperities can be calculated using eq. (6) after redefining the thickness h as

$$h = \bar{z} + \frac{1}{2}s \quad (17)$$

The total force between the two discs is given as

$$F_D = (1 - \xi)F_{oil} + F_{cont} \quad (18)$$

Analogously we obtain for the torque transmitted between the two discs

$$M_D = (1 - \xi)M_{vis} + M_{dry} \quad (19)$$

The viscous torque M_{vis} results from eq. (9) and the redefined thickness h in eq. (17). To determine the dry torque M_{dry} , we use the Coulombian friction law

$$M_{dry} = r_m \mu \Delta \omega F_{cont} \quad (20)$$

where

$$r_m = \frac{2}{3} \frac{r_a^3 - r_i^3}{r_a^2 - r_i^2}$$

The coefficient of friction μ is assumed to be a function of the angular sliding velocity (figure 7) but constant over the friction surface.

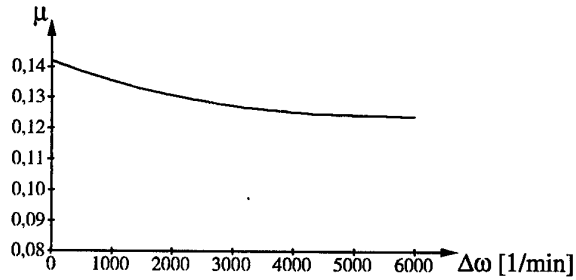


Figure 7: Characteristic of the friction coefficient

3.3 Steady contact phase model

This phase begins when the static equilibrium in the axial direction has been achieved. It is reasonable to expect the film thickness to not disappear completely because the asperities cannot be perfectly flattened. For numerical reasons, it is also expected that the velocities as well as the accelerations of the discs do not become zero exactly. Therefore, when a minimal film thickness h_{min} is reached, the accelerations \ddot{q}_j and \ddot{q}_{j+1} and the velocities \dot{q}_j and \dot{q}_{j+1} are set to zero. The computation of the contact force and of the transmitted

torque is performed according to section 3.2 as long as the discs slip.

When the relative angular velocity between the two discs disappears, the sticking state occurs. In this case the clutch torque represents a constraint torque

$$M_D \leq \mu_0 r_m F_{cont} \quad (21)$$

where μ_0 represents the coefficient of static friction.

4. Equations of motions of the multi-disc-clutch

4.1. Equations of translational motions

The axial motion of the piston is described by the generalized coordinate q_0 . The equation of motion of the piston can be written as

$$m_P \ddot{q}_0 = F_P - F_{FP} - F_S - F_{D_0} \quad (22)$$

Furthermore we obtain an equation of motion for each disc

$$m_j \ddot{q}_j = F_{D_{j-1}} - F_{D_j} - F_{FD_j} \quad (23)$$

4.1.1. The actuating force F_P . The hydraulic device provides the clutch with the necessary control pressure $p_{control}$. The oil has to flow through the orifice before it enters the piston chamber. The oil pressure in the piston chamber consists of a static and a dynamic part. The static pressure p_{sta} can be calculated using the classical orifice equation given by

$$p_{sta} = p_{control} - \text{sgn}(\dot{q}_0) \frac{\rho}{2} \dot{q}_0^2 \frac{A_P^2}{(A_d \alpha_d)^2} \quad (24)$$

where A_P is the piston abutting face, A_d and α_d are the orifice area and the discharge coefficient respectively.

The dynamic pressure p_{dyn} results from the rotation of the oil mass in the piston chamber

$$p_{dyn}(r) = \frac{1}{2} \rho v_{oil}^2(r) = \frac{1}{2} \rho \omega_{oil}^2 r^2 \quad (25)$$

The total force acting on the piston may be written as

$$\begin{aligned} F_P &= \int_{A_P} (p_{sta} + p_{dyn}(r)) dA_P \\ &= p_{sta} A_P + \frac{\pi}{4} \rho \omega_{oil}^2 (r_{P_o}^4 - r_{P_i}^4) \end{aligned} \quad (26)$$

with r_{P_i} and r_{P_o} representing the inner and outer radii of the piston. The angular velocity of the oil can be assumed to equal the piston housing velocity

$\omega_{oil} = \omega_{in}$. In the case of a dynamic compensated piston, for example, when it is double-sided pressurised or in the case of a brake clutch with a static piston housing, the dynamic part of the pressure has to be set to zero.

4.1.2. The return spring force F_S . The spring force is responsible for moving the piston back while disengaging the clutch. The spring usually has a degressive characteristic, which can be found from measurements (figure 8). The spring force depends on the piston displacement and can be calculated as

$$F_S(q_0) = F_{S_0} + c(q_0)q_0 \quad (27)$$

where F_{S_0} is the prestressing force and c is the spring stiffness.

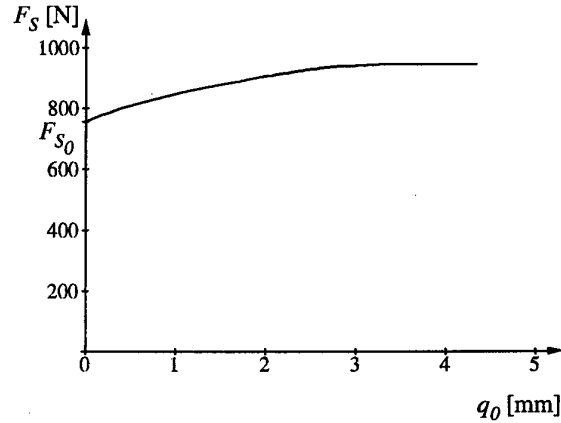


Figure 8: Characteristic of the return spring

4.1.3. The friction force of the piston seal F_{FP} . The piston seals cause friction forces between the inner and outer sides of the piston and the housing (friction coefficient μ_P). For a given inner stress force F_{P_i} and outer stress force F_{P_o} , the friction force of the piston seal can be written as

$$F_{FP} = \text{sgn}(\dot{q}_0) \mu_P (F_{P_i} + F_{P_o}) \quad (28)$$

4.1.4. The friction forces between tang and discs F_{FD} . The friction force between a disc and the tang can be written as

$$F_{FD_j} = \mu_i \frac{M_{D_{j-1}} + M_{D_j}}{r_{T_i}} \quad \text{for inner discs} \quad (29)$$

and

$$F_{FD_j} = \mu_o \frac{M_{D_{j-1}} + M_{D_j}}{r_{T_o}} \quad \text{for outer discs} \quad (30)$$

with μ_i and μ_o respectively the corresponding friction coefficients, r_{Ti} and r_{To} respectively the operative radii of the inner and outer tangs.

4.1.5. The disc force F_D . The disc forces can be calculated according to section 3.

4.2. Equations of rotational motions

Making use of the principle of the angular momentum the rotational motions of the inner and outer tang with the mating discs are written as

$$J_{in}\ddot{\varphi}_{in} = M_{in} - M_C \quad (31)$$

$$J_{out}\ddot{\varphi}_{out} = M_C - M_{out} \quad (32)$$

where M_{in} and M_{out} are the drive and load torques respectively. The clutch torque is given as

$$M_C = \sum_{j=1}^{n-1} M_{D_j} \quad (33)$$

where n is the number of discs.

4.3. Equation of the viscosity

Since the engagement process of a wet clutch is dissipative, it is coupled with an increase of the oil temperature. This has a great influence on the oil viscosity and consequently on the squeeze pressure and the shear stress of the oil film. Considering only the temperature dependence, the viscosity can be given by the following empiric equation [8]

$$\eta = \eta_0 e^{-\beta T_{oil}} \quad (34)$$

The change in the temperature results from the balance between the thermal load

$$\dot{Q}_{in} = M_C (\omega_{in} - \omega_{out}) \quad (35)$$

which is developed during the engagement process, and the thermal power

$$\dot{Q}_{out} = \lambda (T_{oil} - T_G) \quad (36)$$

which is conducted by the steel discs to the housing. Thus we can write

$$\dot{T}_{oil} = (\dot{Q}_{in} - \dot{Q}_{out}) \frac{1}{c_D} \quad (37)$$

Here λ , c_D and T_G represent the housing heat conductivity, the disc heat capacity and the housing temperature respectively.

5. Simulation results

Figure 9 shows some simulation results of the engagement of a wet clutch with 11 discs. The curve 9 (a) represents the plots of the viscous and the dry torques as well as the resulting transmitted torque in the clutch for the reference parameters (a) as written in table (1). At the beginning only the viscous torque is present. It increases until the discs get in contact. After the dry torque is developed, the viscous torque decreases with increasing contact area and oil temperature due to the thermal dissipation in the clutch.

A simulation with a smaller initial film thickness $s_j = 0.02 \text{ mm}$ is shown in figure 9(b). It is obvious that although the initial film thickness does effect the drag torque during the clearance phase, it does not influence the time at which contact occurs.

The tolerance of the disc thickness has indeed an influence on the duration of the engagement process as shown in figure 9(c). The higher level of the dry torque results from the dynamic pressure p_{dyn} because of the delayed deceleration of the clutch drive side.

Compared with the reference, a lower initial oil temperature leads to a higher drag torque and a longer engagement process. This results from the higher value of the viscosity, which increases with decreasing oil temperature.

A comparison of the torque curve with the experimental results given in [9] shows a good qualitative agreement.

	$p_{control} [\text{bar}]$	$s_j [\text{mm}]$	$b [\text{mm}]$	$T_{oil} [^\circ\text{C}]$
a)	1.4	0.9 mm	1.25	90
b)	1.4	0.02 mm	1.25	90
c)	1.4	0.9 mm	1.23	90
d)	1.4	0.9 mm	1.25	0

Table 1: Parameter variation

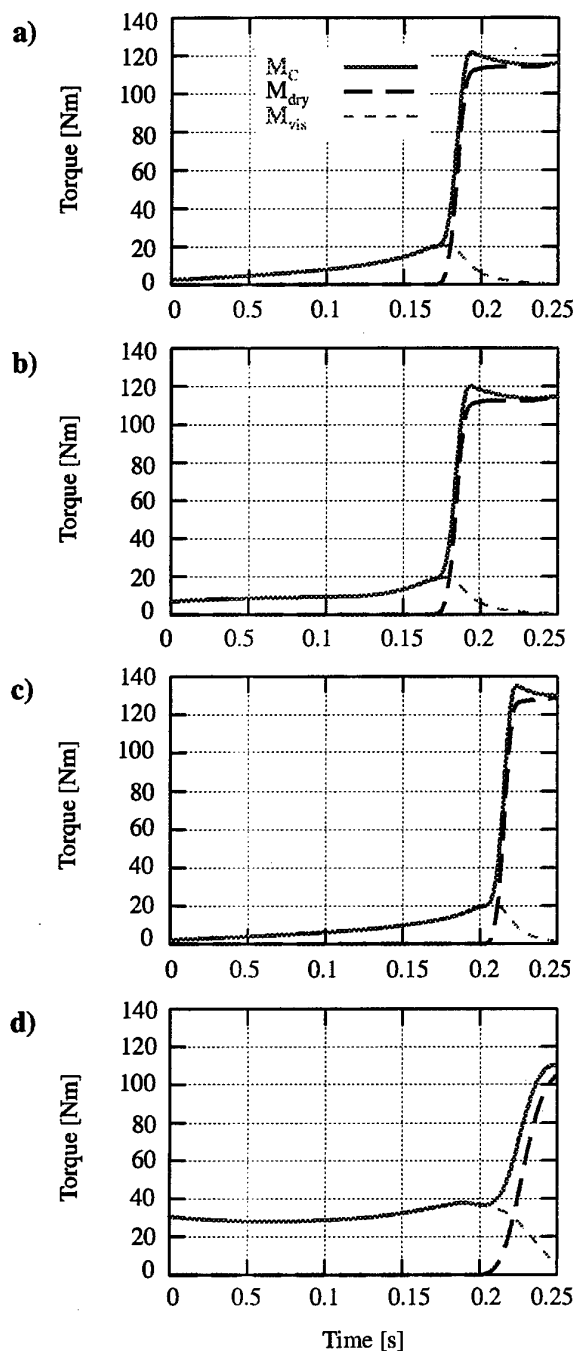


Figure 9: Simulation results of an engagement of a wet clutch with 11 discs

6. Conclusions

A detailed model has been developed to simulate the engagement behaviour of wet clutches. Effects like lining porosity, surface irregularities as well as clearance tolerances have been considered. The model equations have been deduced from the porous squeeze film and the Hertzian theory. The model showed that the drag torque during the engagement process is affected by the initial thickness of the oil film as well as by the initial oil temperature, whereas the duration of the engagement is influenced by the clearance tolerances and the initial oil temperature. The simulation results of the presented model agree qualitatively with the experimental tests.

References

- [1] H. Wu: *An Analysis of the Engagement of Wet-clutch Plates*; Wear 24 (1973) pp. 23-33.
- [2] L.L. Ting: *Engagement Behaviour of Lubricated Porous Annular Disks*; Wear 43 (1975) pp. 159-182.
- [3] B. JACOBSON: *Engagement of Oil Immersed Multi-disc Clutches*; 6th Int. Power Transmission and Gearing Conference, ASME, Scottsdale, USA, September 13-16, 1992, Volume 2, pp. 567-574.
- [4] J.L. Gupta, K.H. Vora, M.V. Bhat: *The Effect of Rotational Inertia on the Squeeze Film Load Between Porous Annular Curved Plates*; Wear 79 (1982) pp. 235-240.
- [5] A. Hoesl: *Modellierung des Schließvorganges einer Lamellenkupplung*; Thesis, Lehrstuhl B für Mechanik 1998.
- [6] J.A. Greenwood, J.B.P. Williamson: *Contact of Nominally Flat Surfaces*; Proc. R. Soc. London, Ser. A, 295 (1966) pp. 300-319.
- [7] K. Yamada, N. Takeda, J. Kagami, T. Naoi: *Mechanisms of Elastic Contact Between Rough Surfaces*; Wear 48 (1978) pp. 15-34.
- [8] T. A. Harris: *Rolling Bearing Analysis*; John Wiley & Sons (1991).
- [9] W. Beisel: *Untersuchungen zum Betriebsverhalten naßlaufender Lamellenkupplungen*; Dissertation, Technische Universität Berlin (1983).

Modeling and Analysis of a Piezo-Actuated Positioning Mechanism*

Han J.M.T.A. Adriaens[†], Willem L. de Koning[‡], and Reinder Banning[‡]

[†]Department of Information Technology and Systems, Delft University of Technology
Mekelweg 4, 2628 CD Delft, The Netherlands
Fax: +31-15-2787209, E-mail: h.adriaens@twi.tudelft.nl

[‡]Delft Institute of Microelectronics and Submicronotechnology
Department of Applied Natural Sciences, Delft University of Technology
Lorentzweg 1 2628 CJ Delft, The Netherlands

Abstract

The piezoelectric actuator is a common device for realizing extremely small displacements. In the behavior of a piezo-actuated mechanism the actuator dynamics play an important role. Therefore, in order to be able to design a high performance model-based controller the actuator dynamics must be taken into account in the system model. Based on the literature a physical model is derived. In this model the hysteresis effect is represented by a first-order differential equation. The model is analyzed in great detail and compared to another model from the literature. It turns out that the derived physical model is equally accurate for a number of characteristics. Furthermore, preliminary experiments have shown that the physical model more accurately describes the rate of convergence of hysteresis loops.

1 Introduction

The piezoelectric actuator (PEA) is a well-known commercially available device for realizing extremely small displacements in the range of 10 pm (1 pm = 10^{-12} m) to 100 μ m. The ratio of the input voltage and the output elongation is very favorable for this. A disadvantage however is its highly nonlinear input/output behavior. More specifically, a PEA shows hysteresis behavior. In simple terms this means that for a certain input there is no unique output. Instead, the output depends on the input history. For high accuracy positioning and tracking systems the piezo-actuated positioning mechanism should therefore be equipped with a controller. Modern controller design is based on a model of the system to be controlled. For piezo-actuated positioning mechanisms the dynamical aspects of the PEA

play a dominant role. In this paper we focus on the modeling of the dynamics of a piezo-actuated positioning mechanism.

In [8] a typical servomotor model is presented that is completely based on physical principles. In [7] an improvement to this model has been described. Instead of a combination of elementary elements the hysteresis is modeled by a nonlinear first-order differential equation, which has been proposed in [5]. In [1] a second improvement has been described. Instead of a mass-spring-damper system the mechanical behavior is modeled by a partial differential equation. In [6], [9], [8], [7] and [1] it is shown that in case of charge steering no hysteresis behavior is encountered in the input-output behavior, i.e. inbetween the electrical input and the displacement. A different way of dealing with the hysteresis effect is to do less complicated voltage steering and to take the hysteresis effect into account in the model on which you base the controller design. In [3] the series connection of linear time-invariant second order dynamics and the differential equation of hysteresis has been analyzed in great detail. Based on this model controllers have been developed and successfully applied to an already existing set-up in [2] and [4].

In this contribution we will derive a physical model for the case of voltage steering. This model will be analyzed in great detail and will be compared to the series connection. In section 2 the physical model will be derived and normalized. The series connection will be considered in section 3. In section 4 we will show that hysteresis loops converge. The model characteristics of the series connection are related to the ones of the normalized physical model in section 5. In section 6 the influence of the two feedback loops, which are present in the physical model, will be determined analytically. Finally, in section 7 we will summarize the results and draw some conclusions.

*This research is supported by the Dutch Technology Foundation (STW).

2 The physical model

In this section we will present the physical model for the case of voltage steering. The model will be based on the work in [8], [7], and [1]. Contrary to the case of charge steering, in the case of voltage steering we will have to deal with the hysteresis effect.

For a piezo-actuated mechanism that is fixed at one side the electromechanical model is presented in Figure 1. This model has been proposed in [8] and improved in [7] and [1].

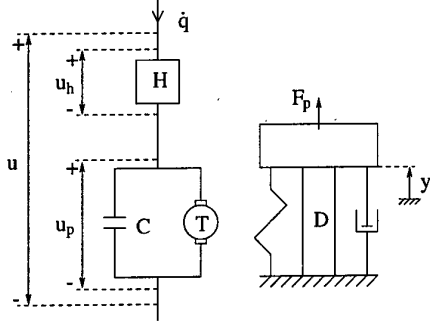


Figure 1: The electromechanical model of PEA and positioning mechanism together.

Here the hysteresis and piezo effect are separated. H represents the hysteresis effect and u_h is the voltage due to this effect. The piezo effect is represented by $C - T$, which is a DC permanent-magnet motor with electromechanical transformer ratio T and with parallel capacitance C . The voltage u_p is the back-electromotive-force (back-emf) from the mechanical side. The total voltage over the PEA is u . This voltage can be considered to be the input of the total system. The current flowing through the circuit is \dot{q} . The force F_p is generated by the PEA and drives the mechanics of PEA and positioning mechanism together, which is denoted by D . This mechanism is designed such that it is accurately modeled by a linear mass-spring-damper system. The resulting displacement y is the output of the total system.

The set of electromechanical equations is given by:

$$u = u_h + u_p \quad (1)$$

$$\dot{q} = \alpha |u_h| (a u_h - q) + b u_h \quad (2)$$

$$q = C u_p + T y \quad (3)$$

$$F_p = T u_p \quad (4)$$

$$m \ddot{y} + c \dot{y} + k y = F_p \quad (5)$$

The second equation is the hysteresis equation, which is proposed in [5] in a little more general form. This specific form has been used in [3], [7], and [1]. According to [3], for physically correct hysteresis it is required

that $\alpha > 0$ and that $\frac{1}{2}a \leq b \leq a$. We remark that q may be seen as the total charge in the PEA. The mechanical properties m , c , and k are a compound of the mechanical properties of both PEA and positioning mechanism together. Namely, in [1] it has been shown that the mechanical behavior of a well-designed piezo-actuated positioning mechanism can be accurately modeled by a single mass-spring-damper system. After simple manipulations the following set of equations may be obtained:

$$u_h = u - \frac{1}{C} q + \beta_o y \quad (6)$$

$$\dot{q} = \alpha |u_h| (a u_h - q) + b u_h \quad (7)$$

$$m \ddot{y} + c \dot{y} + k_o y = \beta_o q \quad (8)$$

with k_o and β_o defined as in [7]:

$$k_o = k + \frac{T^2}{C} \quad (9)$$

$$\beta_o = \frac{T}{C} \quad (10)$$

Before performing model analysis we will simplify the model by reducing the number of parameters. To this purpose we make the static gain of Eq. 8 equal to one. To do so we substitute $q = \frac{k_o}{\beta_o} v$, with v a new variable, in the model. After simple manipulations the following model may be obtained:

$$u_h = u - \beta_i v + \beta_o y \quad (11)$$

$$\dot{v} = \alpha |u_h| (a' u_h - v) + b' u_h \quad (12)$$

$$\ddot{y} + c' \dot{y} + k'_o y = k'_o v \quad (13)$$

where the new parameters are defined as:

$$\beta_i = \frac{1}{C} \frac{k_o}{\beta_o}, \quad a' = a \frac{\beta_o}{k_o}, \quad b' = b \frac{\beta_o}{k_o} \quad (14)$$

$$c' = \frac{c}{m}, \quad k'_o = \frac{k_o}{m} \quad (15)$$

In this set of equations the number of parameters is maximally reduced while all dynamical properties are captured.

In Figure 2 the normalized physical model is represented in a block-diagram form. Here H' represents the normalized hysteresis of Eq. 12 and D' represents the normalized linear dynamics of Eq. 13. Clearly, two feedback loops are present.

3 The series connection

In this section we will consider the series connection of linear dynamics and hysteresis in somewhat more detail. A much more extensive discussion may be found in [3].

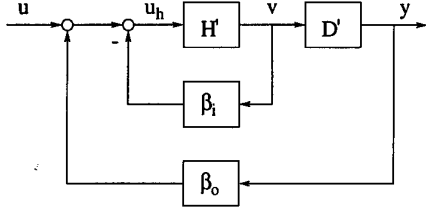


Figure 2: Block-diagram of the normalized physical model.

In Fig. 3 the series connection of linear time-invariant second-order dynamics D_s with static gain 1 and hysteresis H_s is represented in a block-diagram form.

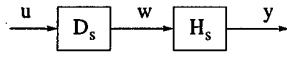


Figure 3: Block-diagram of the series connection of linear dynamics D_s and hysteresis H_s .

The equations describing the series connection are:

$$\ddot{w} + c'_s \dot{w} + k'_s w = k'_s u \quad (16)$$

$$\dot{y} = \alpha_s |\dot{w}| (a_s w - y) + b_s \dot{w} \quad (17)$$

where an index s is added to the parameters to indicate that we deal with the series connection and where the accent in c'_s and k'_s refers to the fact that the parameters are divided by the mass.

A hysteresis loop is defined as the stationary loop in the input/output plane, i.e. in the u/y plane, for a quasi-static monotone oscillating input, e.g. a low frequency sinusoid. In [3] the convergence of hysteresis loops has been proved for the series connection. Note that in the quasi-static case the series connection is similar to only hysteresis H_s , because the dynamics D_s reduces to the simple transfer of 1.

In [3] expressions have been derived for the center point and the average slope of a hysteresis loop:

$$\frac{y_{max} + y_{min}}{2} = a_s \frac{u_{max} + u_{min}}{2} \quad (18)$$

$$y_{max} - y_{min} = b_s (u_{max} - u_{min}) \quad (19)$$

where u_{max} and u_{min} , and y_{max} and y_{min} are the maximum and minimum inbetween which the input and output oscillate.

The hysteresis area is defined as the area enclosed by a hysteresis loop in the u/y plane. In [3] it has been derived that the hysteresis area is given by:

$$\varepsilon = \frac{4}{3} (a_s - b_s) \alpha_s \left(\frac{u_{max} - u_{min}}{2} \right)^3 \quad (20)$$

In Fig. 4 a realistic hysteresis loop is shown in which the characteristics center point, average slope, and hysteresis area are visualized.

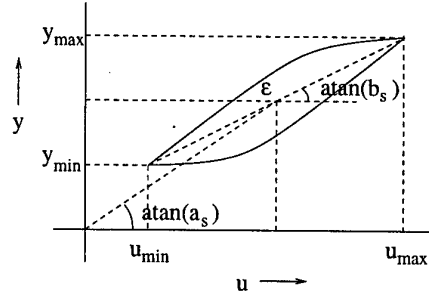


Figure 4: A realistic hysteresis loop where several hysteresis characteristics are visualized.

For decreasing deviations from a center point it follows from the previous expression that, because of the power three, the hysteresis area decreases faster. This has first been noted in [7]. As a result, for small deviations the nonlinearity is well approximated by its average slope. Therefore the total model of the series connection is well approximated by:

$$\Delta \ddot{w} + c'_s \Delta \dot{w} + k'_s \Delta w = k'_s \Delta u \quad (21)$$

$$\Delta y = b_s \Delta w \quad (22)$$

where Δ is used to indicate that we deal with deviation variables. The above model can be simplified to:

$$\Delta \ddot{y} + c'_s \Delta \dot{y} + k'_s \Delta y = k'_s b_s \Delta u \quad (23)$$

4 Convergence of hysteresis loops

In this section we will show that the hysteresis loops of the physical model converge to stable loops. Furthermore, we will compare the speed of convergence with that of the series connection.

Consider solely the hysteresis equation in the physical model, i.e. Eq. 12. From [3] we learn that the progress of the so-called left- and right-turning-points of a hysteresis loop in the u_h/v plane are given by:

$$v_{i+1}^L = e^{-2\alpha(u_{h,max} - u_{h,min})} v_i^L + L \quad (24)$$

$$v_{i+1}^R = e^{-2\alpha(u_{h,max} - u_{h,min})} v_i^R + R \quad (25)$$

with L and R constant for particular $u_{h,min}$ and $u_{h,max}$. Clearly, for convergence it is required that $\alpha > 0$ and $u_{h,max} - u_{h,min} > 0$. The latter is the difference of the maximum and minimum inbetween which u_h oscillates.

However, our goal is to prove convergence in the u/y plane. To this purpose we only need to prove convergence in the u/v plane, because inbetween v and y there

is only the dynamics D' (Fig. 2) which will only cause a transformation of the hysteresis loop but which has no influence on the speed of convergence.

A change in u will cause changes in u_h , v , and y . According to Eq. 11 the changes satisfy:

$$\Delta u_h = \Delta u - \beta_i \Delta v + \beta_o \Delta y \quad (26)$$

where Δ is used to indicate that we deal with changes in the variables. For clarity both β_i and β_o are positive constants. Suppose that a $\Delta u > 0$ gives a $\Delta u_h < 0$. Due to the monotony of the hysteresis equation (section 2) we then have $\Delta v < 0$. It is now easy to derive that Eq. 26 is only satisfied for a $\Delta y < 0$. In other words Δv and Δy have the same sign. For arbitrary Δv this is only the case when there is no phase shift between Δv and Δy , or in other words in case of a quasi-static experiment. It is just in this case that it is easy to show that the scenario sketched above leads to a contradiction. In quasi-static operation we have $\Delta v = \Delta y$, because the static gain of the dynamics has been normalized to 1 in section 2. By substituting this in Eq. 26 we obtain:

$$\Delta u_h = \Delta u - (\beta_i - \beta_o) \Delta y \quad (27)$$

In terms of the original parameters it can be derived that $\beta_i - \beta_o = \frac{k}{T} > 0$. Again suppose that a $\Delta u > 0$ gives a $\Delta u_h < 0$. For Eq. 27 to be satisfied we need $\Delta v = \Delta y > 0$. However, due to the monotony of the hysteresis equation this is not possible.

Concluding, in the general case a $\Delta u > 0$ gives a $\Delta u_h > 0$ which gives a $\Delta v > 0$. Depending on the frequency/phase shift Δy can be positive or negative. Let us consider three examples. 1) In quasi-static operation we have no phase shift and therefore $\Delta y = \Delta v$. 2) If the system we deal with was linear we would have that at the resonance frequency the phase shift was 90 degrees and as a result that $\Delta y = 0$ for $\Delta v = v_{max} - v_{min}$. However due to the hysteresis the 90 degrees phase shift occurs for a somewhat smaller frequency. The exact value depends on the amount of hysteresis. 3) For very high frequencies the phase shift is 180 degrees. Thus for $\Delta v > 0$ we have $\Delta y < 0$. However the amplitude drops to zero for very high frequencies, i.e. $\Delta y = 0$. These three examples show that Eq. 26 is satisfied for all frequencies. This equation may also be written as follows:

$$u_{h,max} - u_{h,min} = \frac{u_{max} - u_{min}}{\beta_i (v_{max} - v_{min}) + \beta_o \Delta y} \quad (28)$$

We now have an expression for $u_{h,max} - u_{h,min}$ which is an important term in the exponent of Eq. 24. Note that if $\Delta y > 0$ the outer feedback loop (β_o)

speeds up convergence because $u_{h,max} - u_{h,min}$ becomes larger due to this positive feedback. The inner feedback loop (β_i) slows down the convergence because $u_{h,max} - u_{h,min}$ becomes smaller due to this negative feedback. The terms positive and negative feedback are visualized in the block-diagram of Fig. 2. If overall convergence is speeded up or slowed down depends on the input frequency, i.e. on the magnitude and phase shift of the transfer function of the dynamics. However the three examples given above indicate that generally convergence is slowed down. In practice the input frequency will be well below the eigenfrequency of the linear dynamics, i.e. in practice we deal with the quasi-static case. In quasi-static operation the convergence behavior is slowed down according to Eq. 27. Concluding, for this model hysteresis loops will converge, but the speed of convergence differs from that of the series connection. In general the speed of convergence is slower and in the quasi-static case it is surely slower.

5 Relations between the parameters of the two models

In [3] the parameters of the series connection have been identified from experiments. Therefore in this section we will derive relations between all parameters of the series connection and the normalized physical model. To this purpose we will derive expressions for the center point, the average slope, and the hysteresis area for the normalized physical model.

Consider solely the hysteresis equation of the physical model, i.e. Eq. 12. Analogous to Eq. 18 and 19 the expressions for center point and average slope are given by:

$$\frac{v_{max} + v_{min}}{2} = a' \frac{u_{h,max} + u_{h,min}}{2} \quad (29)$$

$$v_{max} - v_{min} = b' (u_{h,max} - u_{h,min}) \quad (30)$$

To determine the center point for our total model we replace H' by a' in Fig. 2 and because we consider quasi-static operation the dynamics D' may be replaced by 1. The following expression may now be derived:

$$\frac{y_{max} + y_{min}}{2} = \frac{a'}{1 + a'(\beta_i - \beta_o)} \frac{u_{max} + u_{min}}{2} \quad (31)$$

To determine the average slope, H' is replaced by b' and D again by 1. The following expression may now be derived:

$$y_{max} - y_{min} = \frac{b'}{1 + b'(\beta_i - \beta_o)} (u_{max} - u_{min}) \quad (32)$$

Again consider solely the hysteresis equation, i.e. Eq. 12. Analogous to Eq. 20 the expression for the hysteresis area in the u_h/y plane is given by:

$$\varepsilon_{u_h/y} = \frac{4}{3} (a' - b') \alpha \left(\frac{u_{h,max} - u_{h,min}}{2} \right)^3 \quad (33)$$

Because we are interested in an expression for the hysteresis area in the u/y plane we have to find an expression for $u_{h,max} - u_{h,min}$ as a function of $u_{max} - u_{min}$. Here Eq. 28 may serve as a start. Because we consider quasi-static operation we have $\Delta y = y_{max} - y_{min} = v_{max} - v_{min}$. After substituting Eq. 32 the following relation may be derived:

$$u_{h,max} - u_{h,min} = \frac{1}{1 + b'(\beta_i - \beta_o)} (u_{max} - u_{min}) \quad (34)$$

Substitution of Eq. 34 in Eq. 33 and scaling by a factor $1 + b'(\beta_i - \beta_o)$ gives the relation for the hysteresis area in the u/y plane:

$$\varepsilon = \frac{4}{3} \frac{(a' - b') \alpha}{(1 + b'(\beta_i - \beta_o))^2} \left(\frac{u_{max} - u_{min}}{2} \right)^3 \quad (35)$$

Analogous to section 3 we note that for small deviations from a center point the nonlinearity is well approximated by its average slope. The total physical model is therefore well approximated by:

$$\Delta u_h = \Delta u - \beta_i \Delta v + \beta_o \Delta y \quad (36)$$

$$\Delta v = b' \Delta u_h \quad (37)$$

$$\Delta \ddot{y} + c' \Delta \dot{y} + k'_o \Delta y = k'_c \Delta v \quad (38)$$

where Δ again indicates that we deal with deviation variables. The above model can be simplified to the following equation:

$$\Delta \ddot{y} + c' \Delta \dot{y} + k'_c \Delta y = \beta'_c \Delta u \quad (39)$$

where

$$k'_c = k'_o \frac{1 + b'(\beta_i - \beta_o)}{1 + b'\beta_i} \quad (40)$$

$$\beta'_c = \frac{k'_o b'}{1 + b'\beta_i} \quad (41)$$

In terms of the original physical parameters k'_c and β'_c are, as in [7], derived to be given by:

$$k'_c = \frac{1}{m} \left(k + \frac{T^2}{b + C} \right) \quad (42)$$

$$\beta'_c = \frac{1}{m} \frac{b T}{b + C} \quad (43)$$

Comparing Eq. 18-20 and 23 with Eq. 31, 32, 35, and 39 after some manipulations leads to the following relations between the parameters:

$$a' = \frac{a_s}{1 - a_s(\beta_i - \beta_o)} \quad (44)$$

$$b' = \frac{b_s}{1 - b_s(\beta_i - \beta_o)} \quad (45)$$

$$\alpha = \alpha_s \frac{1 - a_s(\beta_i - \beta_o)}{1 - b_s(\beta_i - \beta_o)} \quad (46)$$

$$k'_o = k'_s (1 + b_s \beta_o) \quad (47)$$

$$c' = c'_s \quad (48)$$

All parameters of the normalized physical model have now been related to the ones of the series connection. The relations are convenient when we want to determine the parameters of the normalized physical model from experiments, because the parameters of the series connection are directly related to the experimental characteristics center point, average slope, and hysteresis area. From the relations above we can conclude that these characteristics are equally accurately described by both models.

6 The feedback parameters

In section 4 it is shown that the speed of convergence of hysteresis loops is different for the physical model as for the series connection. The feedback parameters β_o and β_i determine the difference in convergence. These parameters are still unknown in the expressions derived in the previous section. Therefore, in this section we will present a way to identify the feedback parameters from experiments.

The progress of left- and right-turning-points, i.e. the convergence behavior, is given by Eq. 24 and 25. In quasi-static operation $\Delta y = \Delta v$. Substituting $\Delta y = v_{max} - v_{min}$ in Eq. 28 and the resulting equation in the exponent of Eq. 24 gives:

$$2\alpha(u_{h,max} - u_{h,min}) = 2\alpha(u_{max} - u_{min} - (\beta_i - \beta_o)(y_{max} - y_{min})) \quad (49)$$

Substitution of Eq. 19 and 46 in the just obtained equation gives:

$$2\alpha(u_{h,max} - u_{h,min}) = 2\alpha_s(1 - a_s(\beta_i - \beta_o))(u_{max} - u_{min}) \quad (50)$$

The value of the exponent of convergence can be experimentally determined, enabling us to determine the value of $\beta_i - \beta_o$ because α_s and a_s are already known.

In section 4 we noted that for a frequency somewhat smaller than the resonance frequency we have a phase

shift of 90 degrees and as a result we have $\Delta y = 0$ for $\Delta v = v_{max} - v_{min}$. In this case Eq. 28 simplifies to:

$$u_{h,max} - u_{h,min} = u_{max} - u_{min} - \beta_i(v_{max} - v_{min}) \quad (51)$$

For not too large amplitudes we have $v_{max} - v_{min} = b'(u_{h,max} - u_{h,min})$. Substituting this gives:

$$u_{h,max} - u_{h,min} = \frac{1}{1 + b'\beta_i} (u_{max} - u_{min}) \quad (52)$$

Substituting this expression and Eq. 46 in the exponent of Eq. 24 gives:

$$2\alpha(u_{h,max} - u_{h,min}) = 2\alpha_s \frac{1 - a_s(\beta_i - \beta_o)}{1 + b_s\beta_o} (u_{max} - u_{min}) \quad (53)$$

The only unknown in the above expression is β_o which can thus be determined if this exponent is also experimentally determined.

For the series connection the exponent is $2\alpha_s(u_{max} - u_{min})$. For low frequency (lf) and frequencies somewhat smaller than the resonance frequency = high frequency (hf) the ratio of the rate of convergence of the physical model and the series connection, denoted by τ , may be derived to be:

$$\tau_{lf} = 1 - a_s(\beta_i - \beta_o) \quad (54)$$

$$\tau_{hf} = \frac{1 - a_s(\beta_i - \beta_o)}{1 + b_s\beta_o} \quad (55)$$

Preliminary experiments have shown that the convergence behavior is more accurately described by the physical model.

7 Conclusion

Based on the literature we derived a physical model for a voltage-driven piezo-actuated positioning mechanism. The hysteresis nonlinearity that plays an important role here has been modeled by a nonlinear first-order differential equation. The total model consists of the series connection of the differential equation of hysteresis and a linear time-invariant second order differential equation and two feedback loops with constant gains.

A second, less complicated, model consists of the series connection of a linear time-invariant second-order differential equation and the differential equation of hysteresis. For this model convergence of hysteresis loops has been proven in the literature. In this contribution we have proved convergence of hysteresis loops for the physical model. Furthermore we showed that convergence is slower for the physical model than for the series connection.

In the literature the model parameters of the series connection have been identified from experiments. This model describes very well the center point, average slope, and area of a stationary hysteresis loop. The physical model describes these characteristics equally well. The difference between the two models is the speed of convergence of hysteresis loops. Analytical expressions have been derived relating the feedback parameters to the exponent of the speed of convergence. Preliminary experiments have shown that the physical model describes the convergence behavior more accurately.

Based on the series connection we have already developed two controllers and successfully applied them to an existing set-up in [2] and [4]. In the near future we will investigate whether the physical model can be used as a basis for controller design.

References

- [1] J.M.T.A. Adriaens, W.L. de Koning, and R. Banning, "Modeling piezoelectric actuators," *Tech. Rep. Delft Univ. of Tech., The Netherlands*, TWI rep. 98-31, 1998. (submitted to IEEE/ASME Trans. on Mechatr.)
- [2] J.M.T.A. Adriaens, W.L. de Koning, and R. Banning, "Feedback-linearization control of a piezo-actuated positioning mechanism," *Proc. 5th Eur. Contr. Conf.*, Karlsruhe/Germany, Aug.31-Sept.3, 1999. (accepted)
- [3] R. Banning, W.L. de Koning, and J.M.T.A. Adriaens, "How to cope with hysteresis in dynamic systems," *Tech. Rep. Delft Univ. of Tech., The Netherlands*, TWI rep. 98-19, 1998. (submitted to Automatica)
- [4] R. Banning, W.L. de Koning, and J.M.T.A. Adriaens, "Discrete-time tracking control for hysteretic systems," *Proc. 5th Eur. Contr. Conf.*, Karlsruhe/Germany, Aug.31-Sept.3, 1999. (accepted)
- [5] B.D. Coleman and M.L. Hodgdon, "A constitutive relation for rate-independent hysteresis in ferromagnetically soft materials", *International Journal of Engineering Science*, vol. 24, no. 6, pp. 897-919, 1986.
- [6] R.H. Comstock, "Charge control of piezoelectric actuators to reduce hysteresis effects", United States Patent #4,263,527. Assignee: The Charles Stark Draper Laboratory, Cambridge/ MA, 1981.
- [7] W.L. de Koning, J.M.T.A. Adriaens, and R. Banning, "Physical modeling of piezoelectric actuators for control purposes", *Proc. IFAC Workshop on Motion Control*, Grenoble/France, Sept. 21-23, 1998, ISBN 0 08 043044 9 (spring 1999)
- [8] M. Goldfarb and N. Celanovic, "Modeling piezoelectric stack actuators for control of micromanipulation", *IEEE Contr. Syst. Mag.*, vol. 17, no. 3, pp. 69-79, 1997.
- [9] C.V. Newcomb and I. Flinn, "Improving the linearity of piezoelectric ceramic actuators", *Electronics Letters*, vol. 18, no. 11, pp. 442-444, 1982.

The Shape of Multi-Body Motion

William A. Wolovich

Brown University

Division of Engineering
Providence, RI 02912, USA
waw@lems.brown.edu

Mustafa Unel

Brown University

Division of Engineering
Providence, RI 02912, USA
mu@lems.brown.edu

Nancy Pollard

Brown University

Department of Computer Science
Providence, RI 02912, USA
nsp@cs.brown.edu

Elena Zattoni

Department of Electronics, Systems and Computer Science
University of Bologna, Italy
ezattoni@deis.unibo.it

Abstract

This paper addresses robotics, humans and virtual or simulated characters, multi-body systems¹ which have important similarities and differences. In robotics, speed and precision are often of primary concern, while in virtual character simulation, realistic performance may be most important. In all cases, however, the goals of classifying and retrieving motion information from example situations and modifying that motion to meet the goals of new situations are common. We present preliminary results for problems in motion classification and control using the simple but powerful analogy that motion sequences, just like visually observed objects, have characteristic shapes.

1. Introduction

Many studies have been directed toward understanding and modeling the way biological systems, particularly humans and animals, perform motion tasks such as walking, running, typing and lifting. Such research is fundamental to the development of procedures for improving the way humans and future robots will be able to perform complex tasks. This paper addresses robotics, humans and virtual or simulated characters, *multi-body systems* which have important similarities and differences. In robotics, speed and precision are often of primary concern, while in virtual character simulation, realistic performance may be most important. In all cases, however, the goals of classifying and retrieving motion information from example situations and

modifying that motion to meet the goals of new situations are common.

We anticipate an explosion in the availability of measured motion data over the next ten years, which is an exciting trend. Motion databases may be useful in themselves for purposes of studying human motion. For example, researchers in medicine may use databases of normal versus abnormal motion to develop diagnostic procedures and investigate treatment strategies. Ergonomic investigators could study the finger motions in repetitive typing tasks, for different individuals and/or keyboards, to quantify the muscle strain that produces carpal tunnel syndrome.

Motion databases also may be useful in learning how to recognize motion. For example, one might want to distinguish running from walking or performing some other activity. There is a considerable amount of research being performed in recognizing gestures within the context of specific applications (see [5] for an overview). The ability to construct large motion databases with relatively little effort will provide additional information for these efforts. The results have the potential to dramatically change the way we interact with the computer.

To classify and modify motion sequences, we employ the simple but powerful analogy that **motion sequences, just like visually observed objects, have characteristic shapes**. The specific idea is that motion sequences can be classified based on "signature curves" formed by plotting important parameters of the motion against one another. For example, Figure 1 (left) shows a plot of the knee angle vs. the hip angle of a simulated male running character described in [6]². This particular type of phase space plot

¹A multi-body system is one that is composed of several connected parts or bodies[15].

²The runner data is being used with the permission of Jessica Hodgins at Georgia Tech.

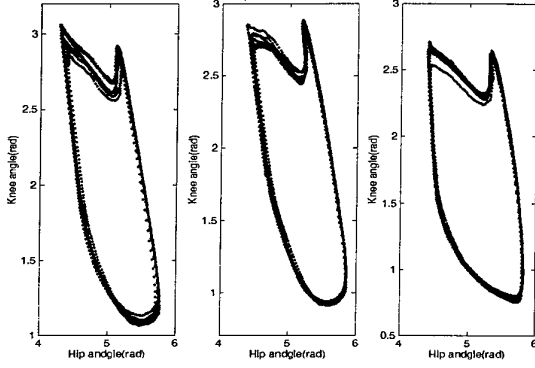


Figure 1. Right leg knee vs. hip plots for man, half-man/woman and woman with superimposed algebraic curves

has been used for diagnostic purposes by the biomechanics community (e.g. [2]). Section 2 outlines our general approach to motion classification and retrieval using plots such as these.

To allow users to modify motion sequences, we employ primitive signature curve shape alterations and motion surface interpolation, as detailed in Section 3. The key idea is that motion signature curves that have good discriminatory power may also be the most important aspects of the motion to get right when creating a new motion sequence.

Motion signature curves depict a static 2D picture of dynamic movement. Therefore, to obtain a more complete description of motion, we introduce time as an additional parameter, which is the focus Section 4. We conclude with some summary observations and an outline of our proposed future efforts in Section 5.

2. Motion Signature Curves as Implicit Algebraic Models

In this section we show how to describe motion sequences using two-dimensional (2D) *phase plots*, which are plots of one motion parameter (e.g. a joint angle value) versus another. We will focus on motions that are cyclic or repetitive in nature, which will give us plots with characteristic 2D shapes. Once appropriate sets of 2D phase plots have been determined, we quantify them using *algebraic curves*, as in [16], which will define our new *motion signature curves*.

An *algebraic curve* of degree n can be defined in the $\{\alpha, \beta\}$ phase plane by the implicit equation

$$F_n(\alpha, \beta) = a_{n0}\alpha^n + a_{n-1,1}\alpha^{n-1}\beta + \dots + a_{0n}\beta^n + a_{n-1,0}\alpha^{n-1} + a_{n-2,1}\alpha^{n-2}\beta + \dots + a_{01}\beta + a_{00} = 0 \quad (1)$$

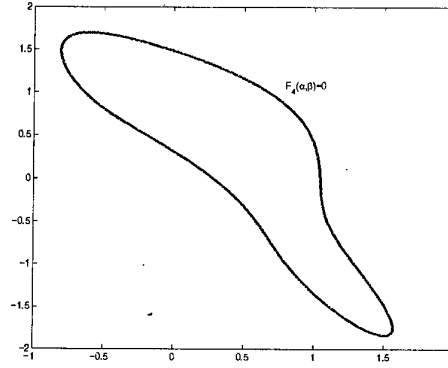


Figure 2. A typical signature curve

Since (1) can be multiplied by any non-zero scalar without changing the zero set, we often will find it convenient to deal with *monic curves*, which are defined by the condition that $a_{n0} = 1$. Figure 2 depicts a typical signature curve defined by a *quartic* (4th degree) algebraic curve.

We formally prove in [11, 17] that *any signature curve defined by (1) can be expressed as a finite sum of geometric primitive products, namely*

$$F_n(\alpha, \beta) =$$

$$Q_n(\alpha, \beta) + Q_{n-2}(\alpha, \beta) + Q_{n-4}(\alpha, \beta) + \dots + Q_{1 \text{ or } 2}(\alpha, \beta), \quad (2)$$

where each

$$Q_k(\alpha, \beta) = \prod C_{ki}(\alpha, \beta) \prod L_{kj}(\alpha, \beta) \quad (3)$$

is a unique conic-line product. Moreover, each (primitive) conic factor $C_{ki}(\alpha, \beta) = \alpha^2 + q_{ki}\alpha\beta + r_{ki}\beta^2 + s_{ki}\alpha + t_{ki}\beta + v_{ki}$ of (3) has a unique center $p_{ki} = (\alpha_{ic}, \beta_{ic})$, which is easily determined by the relations [10] $2\alpha_{ic} + q_{ki}\beta_{ic} + s_{ki} = 0$ and $q_{ki}\alpha_{ic} + 2r_{ki}\beta_{ic} + t_{ki} = 0$. The intersections of the real (primitive) line factors $L_{kj}(\alpha, \beta) = \alpha + l_{kj}\beta + k_{kj}$ are also easily obtained.

In the special case of closed-bounded quartics, it can be shown that [12]

$$F_4(\alpha, \beta) = \underbrace{(\alpha^2 + q_1\alpha\beta + r_1\beta^2 + s_1\alpha + t_1\beta + v_1)}_{C_1(\alpha, \beta)} \underbrace{(\alpha^2 + q_2\alpha\beta + r_2\beta^2 + s_2\alpha + t_2\beta + v_2)}_{C_2(\alpha, \beta)} + \underbrace{\kappa(\alpha^2 + \beta^2 + s_3\alpha + t_3\beta + v_3)}_{C_3(\alpha, \beta)} = 0, \quad (4)$$

the product of conics $C_1(\alpha, \beta)$ and $C_2(\alpha, \beta)$ (ellipses in this case), plus a third conic $\kappa C_3(\alpha, \beta)$ (a circle in this case).

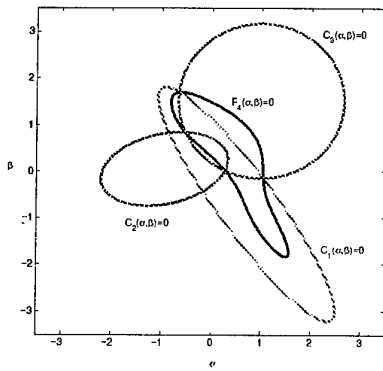


Figure 3. E^2C Representation of the same signature curve

Figure 3 displays this unique E^2C representation for the signature curve depicted in Figure 2.

Quartic curves and their E^2C representations define 10 *geometric invariants*, namely the 4 major/minor half-axes lengths of the two ellipses, the radius of the circle, the 3 distances between the centers of the ellipses and the circle, and the two angles that define the orientation of the ellipses relative to the circle. One can also define two alternative invariants as the ratio of the major and minor axes of the ellipses. These two *elliptical ratio invariants* were used in [12] to identify various objects by the relative positions of their ratio invariants in a two-dimensional *invariant space*, since these invariants change only slightly with small changes in the signature curve.

Our investigations have shown that it is possible to model some motion signature curves by quartic equations, where elliptical ratio invariants can be used to quantify corresponding motions. In other cases, higher degree algebraic curves will have to be employed to accurately model motion data. In these cases, alternative ratio invariants can be defined and employed. In particular, the ratios of $F_n(\alpha, \beta)$ at any two conic factor centers or line factor intersections, namely

$$I_{ij} \stackrel{\text{def}}{=} \frac{F_n(p_{ki})}{F_n(p_{kj})}, \quad (5)$$

are *related-point ratio invariants* [17] which also can be defined and used to quantify and uniquely identify motion signature curves of any degree n [14].

We next note that it is possible to separate and uniquely identify a number of different motions by an automatic, quantitative analysis of our signature curves. For example, Figure 1 depicts the data points and the corresponding signature curves, using the fitting algorithm [8], defined for the male and female runners, as well as a half-man/woman character created as part of a geometric morphing operation

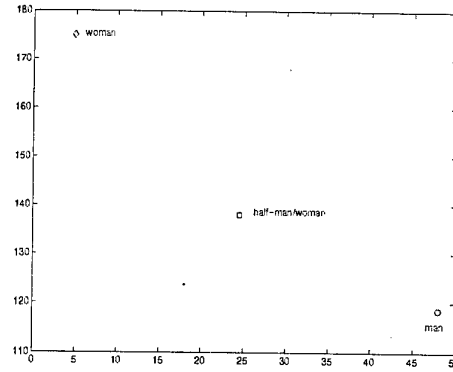


Figure 4. Relative positions of three characters in 2D invariant space

described in [7]. In this case, 6th degree curves were necessary to obtain the depicted accuracy of fit. Moreover, in this particular case, $Q_6(\alpha, \beta) = C_1(\alpha, \beta)C_2(\alpha, \beta)C_3(\alpha, \beta)$ in (2), the product of three conics whose centers were substituted into (5) to define two related-point ratio invariants for each character. Note that the relative positions of these invariants in the 2D invariant space depicted in Figure 4 clearly and (somewhat) uniformly differentiate these 3 virtual characters.

3. User Interaction: Modifying Existing Motion

Not only are signature curves useful for discriminating between character motions, they also are useful for modifying motion. The following subsections describe two approaches for allowing a user to modify a motion sequence: curve shape alterations based on primitive changes and an automation interpolation of motion signature surfaces. Our approach differs from previous work in that we use motion signature curves, rather than joint angles or joint torques as a basis for modifying motion and/or interpolating between two motion sequences.

3.1. Curve and Pose Modification

Many desired motions will not be attainable through interpolation or blending of other motions; the user will need to modify an existing motion sequence. One approach is to allow a user to change the phase plots by modifying the descriptive parameters of these phase plots. Recall the E^2C representation of the signature curve depicted in Figure 2. As illustrated in [13], the base ellipses can be transformed to their *canonical form*, with their centers at the origin and their major and minor axes coincident with the horizontal

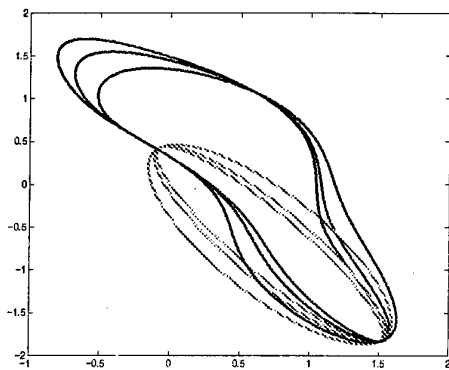


Figure 5. Signature curve shape modifications via primitive elliptical axis changes

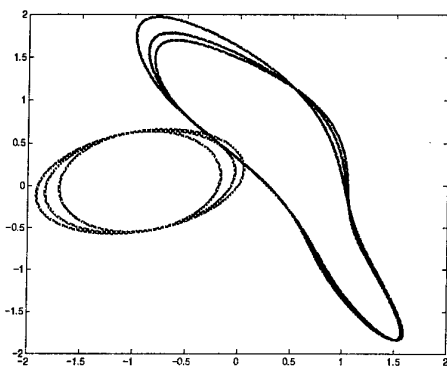


Figure 6. Signature curve shape modifications via primitive elliptical axis changes

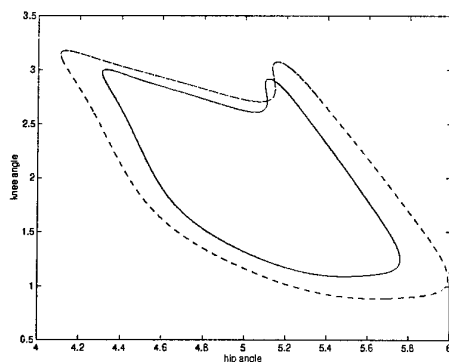


Figure 7. Original(solid) and modified (dashed) signature curves for a simulated runner

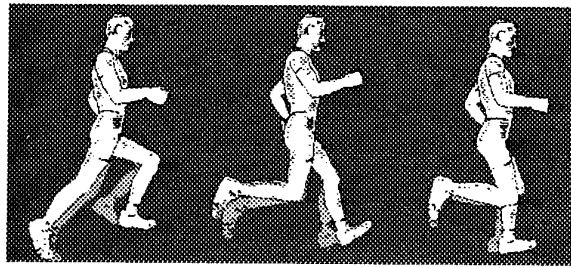


Figure 8. A user-modified running motion is shown. The original running motion is "ghosted" behind the new motion

and vertical axes, respectively. Multiplicative factors can then be used to scale either or both eigenvalues of their *canonical matrices* to produce appropriate shape changes along their major/minor axes. An inverse transformation to the original ellipses produces corresponding changes to the original signature curve. Using such a procedure, a designer could produce significant changes to initial signature curves by varying such parameters in an *interactive environment*. Figure 5 depicts the effect that such modifications along the minor axis of $C_1(\alpha, \beta)$ has on the shape of the original signature curve, while Figure 6 depicts the shape changes produced by analogous modifications along the major axis of $C_2(\alpha, \beta)$. Figures 7 and 8 illustrate how such curve modification techniques can be used. In Figure 7, the plot of knee vs. hip angle has been modified to produce a slightly larger range of motion for both the hip and the knee. Figure 8 shows a filmstrip of the results. The new motion is shown in white and the original motion is "ghosted" in grey. The rendering technique is taken from [9]; it is fast enough to play back the running motion in real-time (see Section 4) so that the user can immediately see the effects of a modification.

3.2. Automatic Interpolation of Motion Surfaces

The motion signature curves associated with various phase plots will vary by the type of motion, by the style or speed of the motion, and by the individual performing the motion. Controlled variations in a motion, such as running at different speeds, lifting various objects, or the gradual transition from (say) walking to running, will create families of signature curves. Once we have established a database of 2D signature curves for different character motions, we propose the automatic interpolation of 3D *motion signature surfaces* defined between two or more 2D signature curves, as in [13]. Different interpolation algorithms will produce different interpolated motions that "exist" between the base motions, as our preliminary investigations

have shown.

For example, the middle plot in Figure 1 represents a character geometrically halfway between the character represented in the left and right plots, but the shape of the curve is not what we would expect from a straightforward interpolation of joint angles from one character to the next. However, if we plot the same information in one invariant space (Figure 4), we see that a logical interpolation function within this space can easily be defined.

Generally speaking, there can be problems with interpolating general planar curves or *profiles*; e.g. how can one interpolate a (three-sided) triangle and a (four-sided) rectangle? As noted in [1], there is no guarantee that a non-self-intersecting polyhedral surface can be found which interpolates between polygon profiles. A measure of the “goodness” of any particular interpolation is also lacking, as are general techniques for including more than two consecutive profiles in a single interpolation strategy. For such reasons, we have developed new strategies for generating 3D signature surfaces which interpolate the individual (second degree) conic factors of our signature curves, rather than the curves themselves[13].

For example, a single implicit equation can be used to model an entire 3D signature surface defined by (say) three quartic signature curves that are perpendicular to a “ t ” axis of orientation, where t could denote particular “times” when a given signature curve would be dynamically active. If $C_a(\alpha, \beta) = \sum a_{ij} \alpha^i \beta^j = 0$ at $t = t_F$, $C_b(\alpha, \beta) = \sum b_{ij} \alpha^i \beta^j = 0$ at $t = t_G$, and $C_c(\alpha, \beta) = \sum c_{ij} \alpha^i \beta^j = 0$ at $t = t_K$ define any three corresponding³ conics of these signature curves, a *conic interpolated implicit signature surface* through these three conic profiles could be defined by setting the coefficients a_{ij} of $C_a(\alpha, \beta)$ equal to $a_{ij}(t) = d_{ij} + e_{ij}t + f_{ij}t^2$, where each

$$[d_{ij} \quad e_{ij} \quad f_{ij}] = [a_{ij} \quad b_{ij} \quad c_{ij}] \begin{bmatrix} 1 & 1 & 1 \\ t_F & t_G & t_K \\ t_F^2 & t_G^2 & t_K^2 \end{bmatrix}^{-1},$$

because $a_{ij}(t = t_F) \Rightarrow C_a(\alpha, \beta) = 0$, $a_{ij}(t = t_G) \Rightarrow C_b(\alpha, \beta) = 0$ and $a_{ij}(t = t_K) \Rightarrow C_c(\alpha, \beta) = 0$.

We expect that interpolation of motion signature curves will give more accurate results than a simple, linear interpolation between joint angle curves. One advantage of the proposed interpolation scheme is that it continuously alters global shape parameters rather than locally defined state vectors. One area of future work is to explore the utility of this interpolation scheme for allowing a user to blend a number of different motion sequences to create new motion.

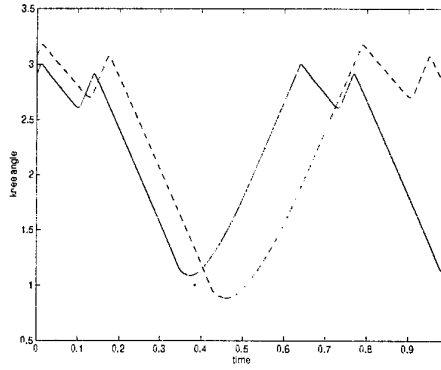


Figure 9. Knee angle vs time for the original(solid) and modified(dashed) runner

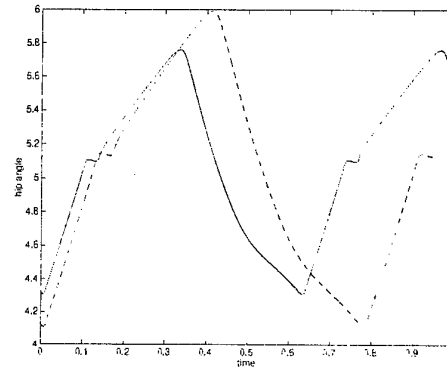


Figure 10. Hip angle vs time for the original(solid) and modified(dashed) runner

4. Simulated Motion

Clearly, motion signature curves depict a static 2D picture of dynamic movement. Therefore, to obtain a more complete description of motion, we must introduce time as an additional parameter, which is the focus of this section. To do this, we first sequentially order all of the boundary points defined around a motion signature curve. Time can then be defined to be proportional to the distance between any base point (starting at $t = 0$) and the increasing distance to all subsequent ordered points. Using this procedure, we have defined a periodic time-varying function for both the knee angle and the hip angle shown in Figures 9 and 10 for both signature curves depicted in Figure 7.

However, such plots may not imply realistic, human-like motion. Therefore, to produce more realistic motion, we could use the time intervals defined between actual motion data points to specify the relative velocity at any point on a

³Note that changes in the correspondence among the conics would produce different 3D surfaces.

closed signature curve as a function of that particular position on the signature curve, thereby producing a data-based *time-scaling curve*. When we then modify motion by altering the shape of a (static) motion signature curve, we can employ this same time-scaling curve to define a velocity function that would more realistically reproduce the new motion.

5. Concluding Remarks

We have outlined some new, quantitative procedures for modeling and analyzing various motion tasks involving temporal and spatial relationships in multi-body systems. Motion databases, which play an important role in these ongoing investigations, have been employed in the creation of 2D phase plots for depicting various types of human and human-like motion. Motion signature curves, or implicit algebraic models of these phase plots, have been defined and used for the first time to classify and identify the shapes of various motion tasks. Primitive decompositions of our signature curves have been used to both modify existing curves and to interpolate signature surfaces for different tasks and/or different individuals. These static signature curves are then parameterized in various ways to produce dynamic, time-varying motion. Future investigations will focus on expanding many of our investigations using other motion parameters and interpolating them in higher dimensions.

References

- [1] Chazelle, Bernard, "Application Challenges to Computational Geometry," CG Impact Task Force Report, Department of Computer Science, Princeton University, Princeton, NJ, 1997.
- [2] Enoka, R. M., D. I. Miller, and E. M. Burgess, "Below-Knee Amputee Running Gait," *American Journal of Physical Medicine*, Vol. 61, 1982, pp. 66-84.
- [3] Ens, Mark T., Duane W. Storti and Mark A. Ganter, "Implicit Methods for Geometry Creation," *International Journal of Computational Geometry and Applications* Vol. 8 (6), 1998, pp. 509-536.
- [4] Gavril, D. M. and L. S. Davis, "Tracking of Humans in Action: A 3D Model-Based Approach," *Proceedings of the ARPA Image Understanding Workshop*, February, 1996.
- [5] Gavril, D. M. "The Visual Analysis of Human Movement," *Computer Vision and Image Understanding*, Vol. 73, Jan. 1999, pp. 82-98.
- [6] Hodgins, Jessica K., W. L. Wooten, D. C. Brogan and J. F. O'Brien, "Animating Human Athletics," *ACM SIGGRAPH*, 1995, pp. 71-78.
- [7] Hodgins, Jessica K. and Nancy S. Pollard, "Adapting Simulated Behaviors for New Characters," *ACM SIGGRAPH*, 1997, pp. 153-162.
- [8] Lei, Z., M. M. Blane, and D. B. Cooper, "3L Fitting of Higher Degree Implicit Polynomials," *Proceedings of Third IEEE Workshop on Applications of Computer Vision*, Sarasota, FL, December 1996.
- [9] Markosian, L. E., M. A. Kowalski, S. J. Trychin, L. D. Bourdev and D. Goldstein, "Real-Time Nonphotorealistic Rendering," *ACM SIGGRAPH*, 1997.
- [10] Selby, Samuel M., *CRC Standard Mathematical Tables*, The Chemical Rubber Company, 30th Edition, 1996.
- [11] Unel, Mustafa and W. A. Wolovich, "A Unique Decomposition of Algebraic Curves," Technical Report LEMS-166, Brown University, October 1997.
- [12] Unel, Mustafa, "Polynomial Decompositions for Shape Modeling, Object Recognition and Alignment," Ph.D. Dissertation, Brown University, May 1999.
- [13] Unel, Mustafa and W. A. Wolovich, "Shape Control Using Primitive Decompositions," *Proceedings of Shape Modeling International '99*, Aizu-Wakamatsu, Japan, 1-4 March, 1999.
- [14] Unel, Mustafa and W. A. Wolovich, "A Complete Set of Geometric Invariants for Algebraic Curves," *Proceedings of the 1999 International Conference on Industrial and Applied Mathematics*, Edinburgh, Scotland, July 5-9, 1999.
- [15] Wendlandt, J. "A Recursive Workspace Balancing Controller for a 3D Multi-body Model of a Biped," 36th IEEE Conference on Decision and Control, San Diego, Ca. December 10-12, 1997.
- [16] Wolovich, W. A. and Mustafa Unel, "The Determination of Implicit Polynomial Canonical Curves," *IEEE Transactions on Pattern Analysis and Machine Intelligence*, Vol. 20 (10), October, 1998, pp. 1080-1090.
- [17] Wolovich, W. A., and Mustafa Unel, "Vision-Based System Identification and Control," **The Confluence of Vision and Control**, Springer Lecture Notes in Control and Information Sciences 237, 1998, pp. 171-182.

Optimal System Inversion Based Motion Planning for Servosystems with Elastic Transmission *

Aurelio Piazzì[¶] Antonio Visioli[§]

[¶]Dipartimento di Ingegneria dell'Informazione
University of Parma - Italy
e-mail: aurelio@ce.unipr.it

[§]Dipartimento di Elettronica per l'Automazione
University of Brescia - Italy
e-mail: visioli@bsing.ing.unibs.it

Abstract

In this paper we present a new methodology for the residual vibration reduction in point-to-point motions of mechanical systems endowed with elastic transmissions. The approach consists of selecting a smooth polynomial motion function for the load, which assures the absence of oscillation during and at the end of the motion, and then determining the corresponding input function by means of a noncausal dynamic system inversion. An optimization procedure can be applied in this context in order to minimize the motion time subject to actuator constraints and to select the system inversion point that minimizes the worst-case residual vibration in presence of parameter uncertainties. Simulation results show the significant robustness properties of this methodology, in spite of the simplicity of the overall open-loop control scheme.

1 Introduction

High-performances positioning servosystems such as robot manipulators, can be significantly limited by the presence of elasticities in the transmissions, which cause vibrations at the end of a point-to-point motion. In fact, if the elasticity is neglected in the motion planning phase, to accurately achieve the final position, a delay time has to be added at the end of the motion, in order for the residual oscillation to vanish. Hence, the total motion time necessarily increases.

In order to cope with this problem two different strategies can be applied: a feedback control, which may require the knowledge of the state of the system at any time, or a feedforward control, which implies that the

motion law is determined in advance, taking into account the parameters of the elastic transmission [1]. In the latter case, a further closed-loop can be added to the system in order to cope with system uncertainties and parameter variations. Regarding the motion planning aspect, many solutions have been provided in the literature. The most well-known technique is the input-shaping one, developed in the last decade (e.g. see [2]-[10]), which consists of convolving a sequence of impulses (the input shaper) with the desired system command in order to generate the system command that is then actually employed to drive the system. The input shaper is determined upon the natural frequency and the damping of the vibratory system and further developments have been devised to increase robustness.

In a previous paper [11], we proposed an alternative approach based on system inversion. Specifically, an arbitrarily smooth closed-form motion law for the load of the system has to be defined so that there are no oscillations during and at the end of the motion. Then, by means of a noncausal system inversion, the corresponding actuator input is determined. Polynomial functions are suitable to be adopted as output functions for this method since monotonicity can be easily obtained and they assure the smoothness of the input function and its derivatives until an arbitrarily prefixed order. Furthermore, in this context, the motion time can be effectively minimized, taking into account actuator constraints, by means of a simple bisection algorithm.

In this paper we significantly improve the above methodology by optimizing, in addition to the motion time, also the choice of the system inversion point so that it is minimized the worst-case amplitude of the

*Partial support for this research has been provided by MURST.

residual vibration in presence of significant uncertainties on the values of the stiffness constant and damping ratio of the system. In other words, by means of a simple iterative procedure, the worst-case amplitude of the residual vibration is reduced in a point-to-point motion whose duration is minimized subject to actuator constraints.

The paper is organized as follows. In Section 2 the system inversion based motion planning is explained. In Section 3 the optimization algorithm is described and in Section 4 simulation results are presented. Conclusions are drawn in the last section.

2 System inversion based methodology

An elastic transmission can be simple represented by the mass-spring-damper model depicted in Figure 1, where y is the motor shaft displacement, x is the load displacement, m is the load mass, k the stiffness constant and c the damping of the transmission [12]. The model is described by the following simple differential equation which links x and y :

$$m\ddot{x} + c\dot{x} + kx = c\dot{y} + ky \quad (1)$$

which can be re-written as:

$$\ddot{z} + 2\xi\omega_n\dot{z} + \omega_n^2 z = -\ddot{y}$$

where $z = x - y$, $\omega_n = \sqrt{k/m}$ rad/s is the frequency of the oscillatory mode and $\xi = c/2m\omega_n$ is the damping ratio.

Laplace transform operator can be applied to equation (1), resulting in the following transfer function:

$$G(s) = \frac{cs + k}{ms^2 + cs + k} \quad (2)$$

When the elasticity of the transmission is neglected, the motion planning is accomplished on $y(t)$, without taking into account the actual motion $x(t)$ of the load. This might represent a major drawback when the servosystem is required to have high performances. The basic idea proposed in this paper is to adopt a system inversion based methodology to calculate the input function $y(t)$ that determines a desired output function $x(t)$ without oscillations. In this context, it appears that the choice of the load motion law $x(t)$ is a crucial issue. Polynomial functions present important properties that render them particularly suitable for this purpose. Hence, we define

$$x(t) = a_n t^n + a_{n-1} t^{n-1} + \dots + a_1 t + a_0 \quad (3)$$

The choice of the order n is a direct consequence of the following property (whose proof can be found in

[11]), regarding the differentiability of the input of the system. Denote by $C^{(h)}$ the class of functions which have a h -th continuous derivative. Let also the i -th derivatives $y^{(i)}(t)$ and $x^{(i)}(t)$ be equal to zero for all $t < 0$ and all $i \in \mathbb{N}$ (at time $t = 0^-$ all initial conditions are equal to zero).

Property 1 Assume that $h \geq 1$. For the system described by the differential equation (1), if $x(t) \in C^{(h)}$ then it is functional reproducible by a unique $y(t) \in C^{(h-1)}$.

Hence, the degree h of the polynomial output function has to be selected to guarantee that $y(t) \in C^{(h-1)}$. The $n = 2h + 2$ coefficients a_n, \dots, a_0 can be determined by considering the point-to-point motion from position zero to position q that has to be completed in the time interval $[0, \tau]$ with τ being the free parameter that defines the motion duration time. Imposing that $x(t; \tau) \in C^{(h)}$ means that the following linear algebraic system has to be solved:

$$\begin{cases} x(0; \tau) = 0 & x(\tau; \tau) = q \\ x^{(1)}(0; \tau) = 0 & x^{(1)}(\tau; \tau) = 0 \\ \vdots & \vdots \\ x^{(h)}(0; \tau) = 0 & x^{(h)}(\tau; \tau) = 0 \end{cases} \quad (4)$$

It comes out that the general closed-form expression of $x(t; \tau)$ with $t \in [0, \tau]$ that results from (4) is given by:

$$x(t; \tau) = \alpha(h, \tau) q \int_0^t v^h (\tau - v)^h dv \quad (5)$$

with positive coefficient $\alpha(h, \tau) = (\int_0^\tau v^h (\tau - v)^h dv)^{-1}$. The above formula (5) can be easily proven taking into account that

$$\dot{x}(t; \tau) = \alpha(h, \tau) q t^h (\tau - t)^h. \quad (6)$$

From the above expression (6) it is also apparent that $x(t; \tau)$ is monotonically increasing, since $\dot{x}(t; \tau)$ is positive all over $(0, \tau)$, so that no oscillations occurs during the whole motion of m .

At this point, the input function $y(t; \tau)$ can be calculated by means of the noncausal system inversion, that is:

$$y(t; \tau) = \mathcal{L}^{-1}[Y(s; \tau)] = \mathcal{L}^{-1}[G^{-1}(s)X(s; \tau)] \quad (7)$$

where $X(s; \tau)$ is the Laplace transform of $x(t; \tau)$. After a few passages, the closed-form expression of $y(t; \tau)$ for $t \geq 0$ can be derived (obviously $y(t; \tau) = 0$ if $t < 0$):

$$y(t; \tau) = \frac{m}{c} \dot{x}(t; \tau) + (1 - \frac{mk}{c^2}) x(t; \tau) + \frac{mk^2}{c^3} e^{-(k/c)t} \int_0^t e^{(k/c)v} x(v; \tau) dv. \quad (8)$$

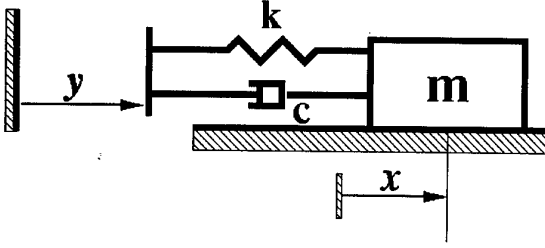


Figure 1: Model of system with elastic linkage.

Considering that $x(t; \tau) = q$ and $\dot{x}(t; \tau) = 0$ for $t \geq \tau$, expression (8) can be significantly simplified for $t \leq \tau$, obtaining:

$$y(t; \tau) = q + [y(\tau, \tau) - q]e^{-(k/c)(t-\tau)}. \quad (9)$$

From (9) it appears how $y(t; \tau)$ is all over bounded because the excited zero mode $e^{-(k/c)t}$ is stable.

3 Optimization procedure

In the application of the methodology described in Section 2, it is sensible to consider constraints on the actuators and therefore on the input function and its time derivatives, and that the linkage parameters are not exactly known. Hence, we propose to minimize the motion time, subject to actuator constraints, and the worst-case residual vibration amplitude. Specifically, we assume that the values of the linkage parameters c and k are uncertain, but it is known that $c \in [c^-, c^+]$ and $k \in [k^-, k^+]$, with known interval endpoints. Using another notation, we consider the uncertain parameter vector $\mathbf{p} = [c, k]^T$ belonging to $\mathcal{P} := [c^-, c^+] \times [k^-, k^+]$. In this context, we define the input function as

$$y(t; \tau_d, \mathbf{p}_d) = \mathcal{L}^{-1}[G^{-1}(s; \mathbf{p}_d)X(s; \tau_d)]$$

where $\tau_d \in \mathbb{R}^+$ and $\mathbf{p}_d \in \mathcal{P}$ are design parameters. The problem is to optimally choose τ_d^* and \mathbf{p}_d^* according to:

1.

$$\tau_d^* := \min_{\tau_d \in \mathbb{R}^+} \tau_d$$

subject to:

$$|y^{(i)}(t; \tau_d, \mathbf{p}_d)| \leq y_{max}^{(i)}, \quad \forall t \geq 0$$

$$\forall \mathbf{p}_d \in \mathcal{P} \quad i = 1, \dots, l \quad (l \leq h).$$

2. $\mathbf{p}_d^* = [c_d^*, k_d^*]$ is the minimizer of the following problem:

$$\min_{\mathbf{p}_d \in \mathcal{P}} \max_{\mathbf{p} \in \mathcal{P}} \{ \max_{t \geq \tau_d^*} |x(t; \tau_d^*, \mathbf{p}_d, \mathbf{p}) - q| \} \quad (10)$$

where

$$x(t; \tau_d^*, \mathbf{p}_d, \mathbf{p}) = \mathcal{L}^{-1}[G(s; \mathbf{p})Y(s; \tau_d^*, \mathbf{p}_d)].$$

It comes out that the optimal input motion function is:

$$y(t; \tau_d^*, \mathbf{p}_d^*).$$

Define the residual vibration amplitude as:

$$V(\tau_d^*, \mathbf{p}_d, \mathbf{p}) := \max_{t \geq \tau_d^*} |x(t; \tau_d^*, \mathbf{p}_d, \mathbf{p}) - q| \quad (11)$$

The proposed minimization of the worst-case residual vibration with minimum time motion planning is a problem that is very difficult to solve. Hence, we look for a suboptimal solution that can however be very useful in practical cases. This can be obtained by relaxing the worst-case search in the dense \mathcal{P} with a discrete finite search over the vertexes of \mathcal{P} plus the nominal midpoint of \mathcal{P} given by (c_o, k_o) . In this case, expression (11) is substituted by:

$$V(\tau_d^*, \mathbf{p}_d, \mathbf{p}_i) = \max_{t \geq \tau} |x(t; \tau_d^*, \mathbf{p}_d, \mathbf{p}_j) - q| \quad (12)$$

$$j = 1, \dots, 5$$

where $\mathbf{p}_1 := [c^- \ k^-]^T$, $\mathbf{p}_2 := [c^- \ k^+]^T$, $\mathbf{p}_3 := [c^+ \ k^-]^T$, $\mathbf{p}_4 := [c^+ \ k^+]^T$, and $\mathbf{p}_5 := [c_o \ k_o]^T$. Defining

$$M_v(\tau_d^*, \mathbf{p}_d) := \max\{V(\tau_d^*, \mathbf{p}_d, \mathbf{p}_j) : j = 1, \dots, 5\} \quad (13)$$

permits to rewrite expression 10 as follows:

$$\min_{\mathbf{p}_d \in \mathcal{P}} M_v(\tau_d^*, \mathbf{p}_d). \quad (14)$$

The value of the minimum time τ_d^* and the minimizers of problem (14) can then be found by means of the following optimal system inversion (OSI) algorithm, which can logically be divided in two parts, as well as the problem. The first is a typical bisection algorithm which is devoted to the search of τ_d^* which guarantees that limits on the input derivatives are satisfied for any $\mathbf{p}_d \in \mathcal{P}$, that is for $\mathbf{p}_d = \mathbf{p}_j$, $j = 1, \dots, 5$, since we consider again the relaxed problem. Then, a local search procedure is applied to find c_d^* and k_d^* that solve problem (14).

OSI Algorithm

First part

1. Set $\tau_{min} = 0$.
2. Determine an initial value for $\tau_{d_{max}}$ such as $\max_{t \geq 0} |y^{(i)}(t; \tau_{d_{max}}, \mathbf{p}_j)| \leq y_{max}^{(i)}$, $i = 1, \dots, l$ and $j = 1, \dots, 5$.

3. Set $\tau_d = (\tau_{d_{min}} + \tau_{d_{max}})/2$.
4. If $\max_{t \geq 0} |y^{(i)}(t; \tau_d, \mathbf{p}_j)| \leq y_{max}^{(i)}$, $i = 1, \dots, l$ and $j = 1, \dots, 5$ then set $\tau_{d_{max}} = \tau_d$ else set $\tau_{d_{min}} = \tau_d$.
5. If $(\tau_{d_{max}} - \tau_{d_{min}}) > \varepsilon$ then goto 3.
6. Set $\tau_d^* = \tau_{d_{max}}$.

Second part

7. Set $k_d^* = k_o$, $c_d^* = c_o$, $\text{flag}=0$.
8. Set $I := M_v(\tau_d^*, \mathbf{p}_d^*)$ and set $I^+ = I$.
9. Set $k^* = (1 + \gamma)k_d^*$. If $k_d^* > k^+$ then set $k_d^* = k^+$.
10. Set $I := M_v(\tau_d^*, \mathbf{p}_d^*)$.
11. If $I < I^+$ then set $\text{flag}=1$ and go to 9.
12. If $\text{flag}=1$ go to 16.
13. Set $k_d^* = (1 - \gamma)k_d^*$. If $k_d^* < k^-$ then set $k_d^* = k^-$.
14. Set $I := M_v(\tau_d^*, \mathbf{p}_d^*)$.
15. If $I < I^+$ then go to 13.
16. Set $\text{flag}=0$.
17. Set $c_d^* = (1 + \gamma)c_d^*$. If $c_d^* > c^+$ then set $c_d^* = c^+$.
18. Set $I := M_v(\tau_d^*, \mathbf{p}_d^*)$.
19. If $I < I^+$ then set $\text{flag}=1$ and go to 17.
20. If $\text{flag}=1$ go to 18.
21. Set $c^* = (1 - \gamma)c_d^*$. If $c_d^* < c^-$ then set $c_d^* = c^-$.
22. Set $I := M_v(\tau_d^*, \mathbf{p}_d^*)$.
23. If $I < I^+$ then go to 21.
24. End.

It has to be noted that parameter ε is a precision parameter that can arbitrarily fixed and γ determines the velocity of the descent to the minimum and the precision in determining c_d^* and k_d^* . It is easy to make it adaptive in order to decrease the overall computational time of the algorithm.

Finally, it has to be stressed that in practical cases, limits on the first and on the second derivative of the input function, which correspond to limits on the maximum velocity and acceleration (torque) provided by the actuator, are generally considered. In some cases, also the limit on the third derivative (jerk) is worthy to be taken into account.

4 An illustrative example

As an illustrative example, we consider an elastic transmission with $c_o = 8[\text{kg}\cdot\text{s}^{-1}]$, $k_o = 2000[\text{N}\cdot\text{m}^{-1}]$ and a load mass $m = 3[\text{kg}]$, which corresponds to a nominal frequency of $25.82[\text{rad}\cdot\text{s}^{-1}]$ and a nominal damping ratio of 0.05. The parameter range of uncertainty is $\pm 50\%$, i.e. $c \in [4, 12]$ and $k \in [1000, 3000]$. The motion is from $0[\text{m}]$ to $1[\text{m}]$. We fixed $h = 2$, so that the output function results to be $(t \in [0, \tau])$:

$$x(t; \tau) = \frac{6}{\tau^5}t^5 - \frac{15}{\tau^4}t^4 + \frac{10}{\tau^3}t^3.$$

We also fixed $l = 2$ and $y_{max}^{(0)} = 1.2$, $y_{max}^{(1)} = 4$ and $y_{max}^{(2)} = 5$. The resulting values of the OSI algorithm (setting $\varepsilon = 0.01$ and $\gamma = 0.001$) are $\tau_d^* = 1.65\text{s}$, $c_d^* = 12[\text{kg}\cdot\text{s}^{-1}]$ and $k_d^* = 1389.3[\text{N}\cdot\text{m}^{-1}]$, which corresponds to a maximum vibration amplitude of $5.6 \cdot 10^{-4}$ for the case where $c = c^+ = 12[\text{kg}\cdot\text{s}^{-1}]$ and $k = k^- = 1000[\text{N}\cdot\text{m}^{-1}]$. The corresponding input function $y(t; \tau_d^*, \mathbf{p}_d^*)$ is plotted in Figure 2 and its first and second time derivatives are plotted in Figures 3 and 4 respectively. Not that for the sake of clarity the input function starts at $t = 0.1\text{s}$. It can be seen how the constraints are not exceeded. Figure 5 shows the motion of the load corresponding to the maximum vibration amplitude over the relaxed uncertain domain, i.e. it is plotted $x(t; \tau_d^*, \mathbf{p}_d^*, \mathbf{p}_3)$. Figure 6 reports the value of the maximum amplitude vibration for different values of the system parameters. In order to verify the effectiveness of the proposed approach, we also evaluated the amplitudes of the residual vibration, for different values of system parameters, in case the input function is determined using a system inversion performed on the nominal model, i.e. $y(t; \tau_d^*, \mathbf{p}_d^o)$ is the input with $\mathbf{p}_d^o := [c_o, k_o]^T$. These results are reported in Figure 7. It appears how the maximum value of the amplitude of the residual vibration, attained when $c = c^+ = 12[\text{kg}\cdot\text{s}^{-1}]$ and $k = k^- = 1000[\text{N}\cdot\text{m}^{-1}]$ is $1.1 \cdot 10^{-3}$. The output motion corresponding to the maximum amplitude of the residual vibration is plotted in Figure 8. From the above results it appears a neat improvement (reduction of about 49% in the worst-case amplitude vibration) of the optimal system inversion based motion planning over the nominal system inversion based one.

5 Conclusions

In this paper we proposed a new optimization procedure in the system inversion based point-to-point motion planning for servosystems endowed with elastic transmissions. Once the motion time has been minimized subject to actuator constraints, the system inversion point is optimally chosen in order to minimize

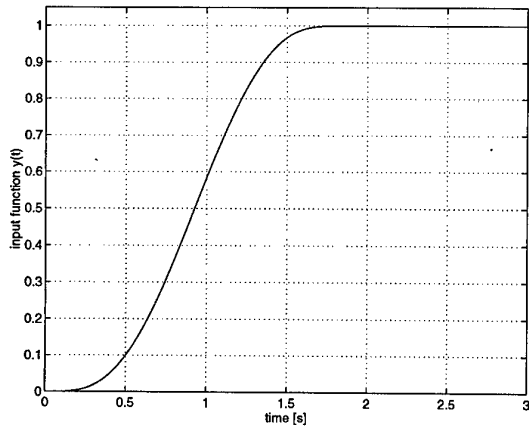


Figure 2: Optimal input function.

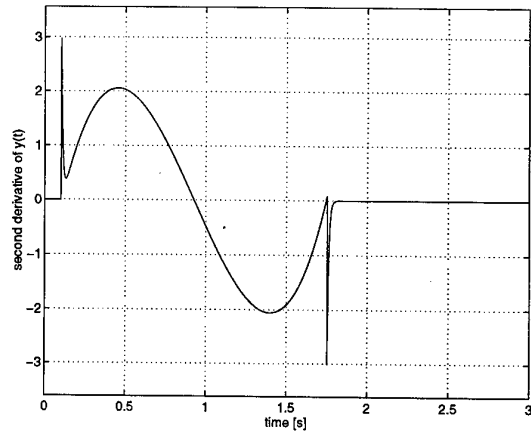


Figure 4: Second derivative of the optimal input function.

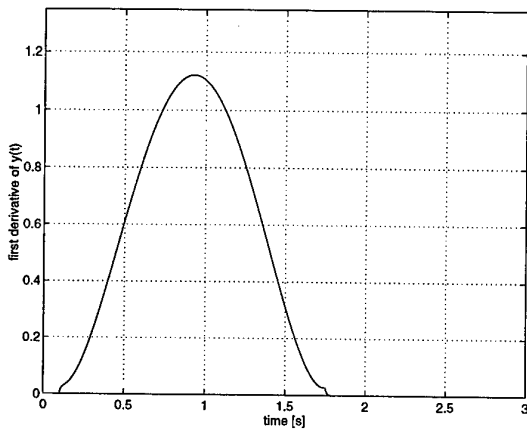


Figure 3: First derivative of the optimal input function.

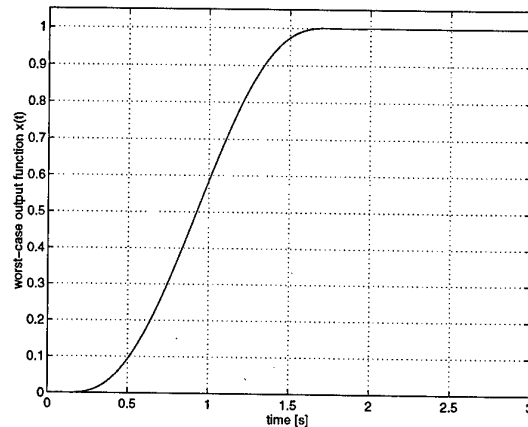


Figure 5: Worst-case output with the optimal system inversion.

the worst-case residual vibration in presence of parametric uncertainties. Results have shown the effectiveness of the overall method, despite its simplicity.

References

- [1] D. M. Aspinwall, "Acceleration profiles for minimizing residual response", *ASME Journal of Dynamic Systems, Measurement, and Control*, Vol.102, pp.3-6, Mar. 1980.
- [2] P. Meckl, W. Seering, "Active damping in a three-axis robotic manipulator", *ASME Journal of Vibration, Acoustics, Stress, and Reliability in Design*, Vol.107, pp.38-46, Jan. 1985.
- [3] P. Meckl, W. Seering, "Minimizing residual vibration for point-to-point motion", *ASME Journal of Vibration, Acoustics, Stress, and Reliability in Design*, Vol.107, pp.378-382, Oct. 1985.
- [4] N. C. Singer, W. P. Seering, "Preshaping command inputs to reduce system vibration", *ASME Journal of Dynamic Systems, Measurement, and Control*, Vol.112, pp.76-82, Mar. 1990.
- [5] J. M. Hyde, W. P. Seering, "Using input command pre-shaping to suppress multiple mode vibration", *Proc. IEEE Int. Conf. on Robotics and Automation*, Sacramento (CA), Vol.3, pp.2604-2609, 1991.
- [6] T. Singh, G. R. Heppler, "Shaped input control of a system with multiple modes", *ASME Journal of Dynamic Systems, Measurement, and Control*, Vol. 115, pp.341-347, Sep. 1993.

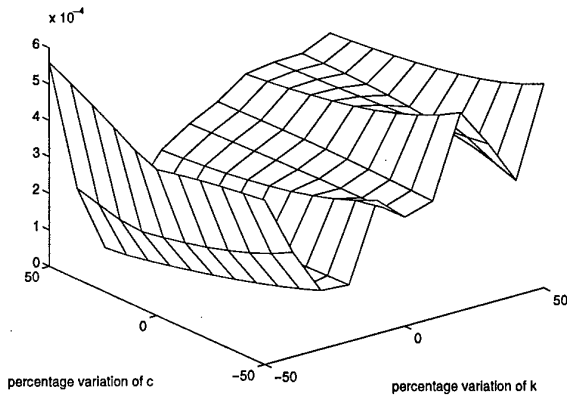


Figure 6: Amplitude of the residual vibration for different values of the system parameters (optimal system inversion).

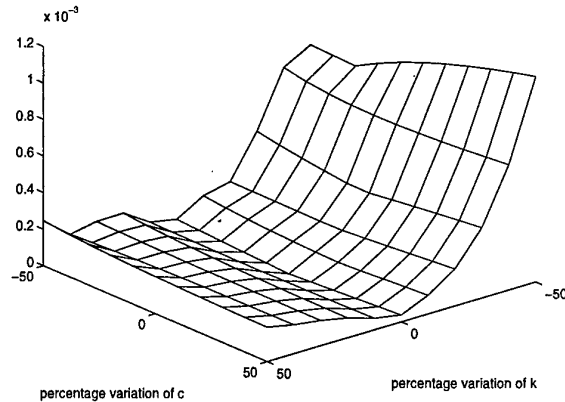


Figure 7: Amplitude of the residual vibration for different values of the system parameters (nominal system inversion).

- [7] W. Singhose, W. Seering, N. Singer, "Residual vibration reduction using vector diagrams to generate shaped inputs", ASME Journal of Mechanical Design, Vol.116, pp.654-659, June 1994.
- [8] W. E. Singhose, L. J. Porter, T. D. Tuttle, N. C. Singer, "Vibration reduction using multi-hump input shapers", ASME Journal of Dynamic Systems, Measurement, and Control, Vol.119, pp.320-326, June 1997.
- [9] W. Singhose, E. Crain, W. Seering, "Convolved and simultaneous two-mode input shapers", IEE Proceedings - Control Theory and Applications, Vol.144, No. 6, pp. 515-520, Nov. 1997.
- [10] W.E. Singhose, W.P. Seering, N.C. Singer, "Time-optimal negative input shapers", ASME Journal of Dynamic Systems, Measurement, and Control, Vol.119, pp.198-205, June 1997.
- [11] A. Piazzoli, A. Visioli, "Minimum-time open-loop smooth control for point-to-point motion in vibratory systems", Proc. IEEE Int. Conf. on Robotics and Automation, Leuven (B), pp. 946-951, 1998.
- [12] R. Adamini, R. Faglia, G. Incerti, "Parametric motion planning techniques for servosystems endowed with elastic transmission", Machine Vibration, Vol.4, pp.14-21, 1995.

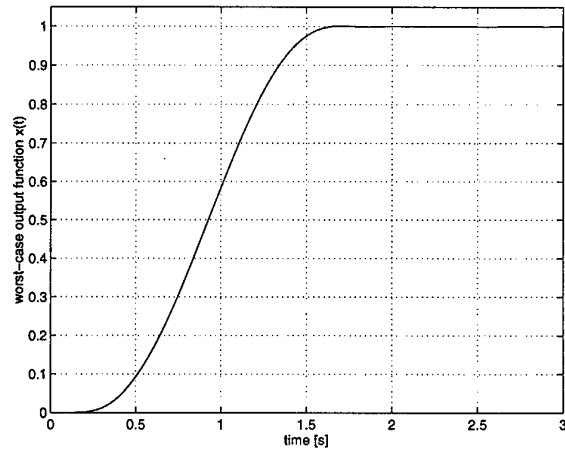


Figure 8: Worst-case output with the nominal system inversion.

Trajectory Control of a Robotic Manipulator Using Artificial Neural Networks

Güney Devrim İldiri* and Osman S. Türkay**

**Systems and Control M.Sc. Program, Boğaziçi University
Res. Ass., Industrial Eng. Dept., Galatasaray University, Istanbul, Turkey
e-mail : ildiri@hotmail.com*

***Mechatronics Applied Research Center, Mechanical Eng. Dept.,
Boğaziçi University, Istanbul, Turkey
e-mail : turkay@boun.edu.tr*

Abstract

This paper addresses the tracking control problem of a robotic manipulator with unknown and changing dynamics. A neuro-control architecture including a nonlinear compensator using an adaptive neural network is presented. The proposed scheme is simulated and successfully tested for the path tracking problem of a two-link planar arm. The fast adaptation capability of the proposed neuro-controller to changes in manipulator dynamics is satisfactory.

Keywords: *Robotic Manipulators, Trajectory Control, Artificial Neural Networks, Neuro-Adaptive Control.*

1. INTRODUCTION

Trajectory control problem of the robotic manipulators have become increasingly important because of their essential role in today's flexible automation and manufacturing strategies [1]. However, manipulators are subject to structured and/or unstructured uncertainties in industrial applications. Structured uncertainty involves variations in the manipulator link properties, unknown loads and inaccuracies in the torque constants of the actuators. Typical unstructured uncertainties are unmodeled dynamics caused by the presence of high-frequency modes, neglected time-delays and nonlinear friction [2]. Highly nonlinear, complex and coupled dynamics of a robotic structure hinder the efficient use of the well-known linear control techniques. Although an acceptable path tracking performance can be achieved using the linear controllers, nonlinear model based controllers offer a better efficient control technique. It has become

widely recognized that the tracking performance of the conventional control methods in high-speed operations is severely affected by the uncertainties [2]. Thus, the need of new control strategies capable of dealing with highly complex and nonlinear systems even under uncertainties has appeared. Towards this end the use of artificial neural networks appear very attractive.

Due to the natural properties of the artificial neural networks, they are ideally suited for path tracking control process. They are able to learn, to approximate any function to a high degree of accuracy and to classify patterns [3]. Moreover, a neuro-controller needs significantly less priori knowledge about the system. Using these attractive features, artificial neural networks have been shown to be very efficient in identification and control of a two-link planar robot arm.

This paper presents a nonlinear compensator using an inverse neuro-model which incorporates the computed torque method implemented to a two-link planar arm. While realizing the computed torque strategy, instead of using an inverse mathematical model of the robot dynamics, a neuro-model is employed. Before adopting the neuro-model in the control loop, its weights are adjusted off-line. Pre-training process of the neuro-model needs recording data of actual robot arm operation. The pre-trained neuro-model which is substituted in the control loop has obviously faster error convergence in responding to an untrained trajectory including strong uncertainties. Consequently the control architecture has better trajectory following performance. Thus, on-line adaptation of the network parameters enables the control system to react properly and effectively under changing or unknown dynamics.

2. ROBOT DYNAMICS MODEL

The two-link planar manipulator is shown in Fig. 1. The rigid body links are jointed together with two revolute joints and actuated by two separate motors at each joint.

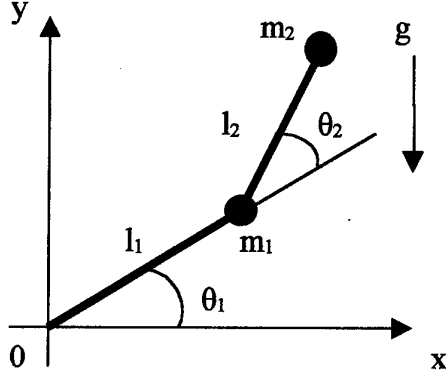


Fig. 1. Two-link planar arm.

The dynamic equation of the manipulator is given by:

$$\tau = M(\theta)\ddot{\theta} + V(\theta, \dot{\theta}) + G(\theta) \quad (1)$$

where τ is the 2×1 vector of joint torques supplied by actuators, M is the 2×2 positive definite manipulator inertia matrix, θ is the 2×1 vector of joint angular positions, $\dot{\theta}$ is the 2×1 vector of joint angular velocities, V is the 2×1 vector function representing centrifugal and Coriolis effects and G is the 2×1 vector function representing torques due to the gravity.

3. COMPUTED TORQUE METHOD

Computed torque method is commonly and efficiently used for the path tracking control process of a robotic manipulator [4].

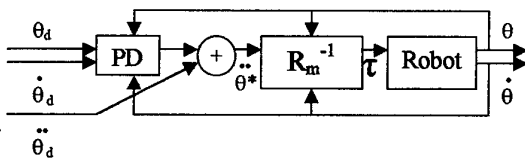


Fig. 2. Computed Torque Method

The control law consists of two parts; a linear feedback term and a feedforward term concerning the robot inverse dynamics. The feedback controller, which is an independent-joint PD controller with velocity reference, plus the desired acceleration,

sends its output through the dynamic model (see Fig. 2). This leads to a corrected acceleration which is used as an input to the inverse dynamics model [4]:

$$\tau = R_m^{-1}(\ddot{\theta}^*, \dot{\theta}, \theta) \quad (2)$$

where,

$$\ddot{\theta}^* = \ddot{\theta}_d + K_p(\dot{\theta}_d - \dot{\theta}) + K_d(\theta_d - \theta) \quad (3)$$

Computed torque control is a form of control method called non-linearity cancellation, because if the dynamic model is exact ($R_m = R$), the nonlinear dynamic perturbations are exactly cancelled. The rest of the system is a decoupled linear system that can be controlled according to standard techniques [4]. Fortunately, while implementing the computed torque method high control gains are not needed for a secure stability.

The computed torque method has been shown to make the overall system stable with a very low tracking error level if an exact model of the robot dynamics is available. However if such a model is not available, the system dynamics have to be adaptively identified in order to achieve a feedforward non-linear compensation. In such a case, artificial neural networks (ANNs) which provide the learning ability can be used to generate the necessary torque commands. However, its performance especially in high-speed operations is severely affected by uncertainties. Adaptive approaches may be proposed to obtain more robust control architecture in presence of structured uncertainties.

4. NEURO-CONTROL

This section presents a nonlinear compensator using neural networks incorporating the computed torque method for trajectory control of the robotic manipulator. The proposed control architecture is shown in Fig. 3.

Basically, the control architecture has the same structure as that of the computed torque method described in section 3. Instead of using an inverse mathematical model of the plant (R_m^{-1}), an inverse dynamics neuro-model (NN_{INV}) is used to compensate the system non-linearities as shown in Fig. 3.

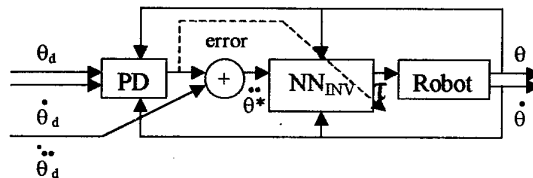


Fig.3. Neuro-controller based on computed torque method.

The ANN model which is used to model the real inverse dynamics structure of the robotic system for non-linear compensation has a simple structure. It is a three-layer fully connected feedforward neural network.

Indeed, even with neural network modeling identification, robot inverse dynamics can not be modeled including structured uncertainties and unexpected changes in properties of the robot and its environment. To make the overall control system be more robust, an adaptive control scheme must be associated with the present control architecture. An on-line adaptation of the neuro-controller structure is realized through an on-line learning process.

As a result of analyzing feedback control techniques and integrating them with the neuro modeling method, the "Feedback Error Learning" scheme is introduced in order to provide the necessary information to perform the on-line training of the neuro-controller [5]. The "Feedback Error Learning" scheme does not require a teaching signal, the feedback torque is used as the error signal for the on-line training process of the network. On-line training process of the proposed neuro-control architecture uses basically the same idea with an additional but necessary scaling factor, as shown in Fig. 3. The connection strength between node from i and to node j , W_{ji} is changed by an amount given by

$$\Delta W_{ji} = \eta \cdot \partial_j \cdot f'(O_j) \cdot i_i \quad (4)$$

where η is the learning rate, f' is the derivative of the activation function, i_i is the weighted sum of the outputs of the previous layer and O_j is the output signal of the node j . Besides ∂_j is given by

$$\partial_j = K \cdot (K_p(\dot{\theta}_d - \theta) + K_d(\theta_d - \theta)) \quad (5)$$

where K is the matching gain for adjusting the network output to the real range of actuator torques [1]. The activation function f is a bipolar sigmoidal function expressed by

$$f(x) = \frac{2}{1 + e^{-\lambda x}} - 1 \quad (6)$$

where $\lambda > 0$ and determines steepness of the continuous function $f(x)$ near $x=0$.

Note that the control and learning are performed simultaneously. Furthermore, as the on-line learning proceeds, convergence of the feedback signal towards zero is expected [2].

The neuro-controller which identifies the robot inverse dynamics is trained first off-line using the history of input and output recorded from the actual

robot motion [2]. This permits the construction of an approximate inverse neuro-model of the system which is then substituted into the control architecture where the training process will continue on-line making use of the feedback error signal. Hence faster adaptation of the neuro-controller becomes possible and more robust control strategies may be achieved.

5. SIMULATION RESULTS

To analyze the various features of this neuro-control system, the two-link robotic manipulator shown in Fig. 1 is simulated. The governing dynamic equations of the system ignoring the friction term is available in a number of references (see e.g. 1).

The two-link planar arm has been modeled as two rigid links of lengths $l_1=1$ m and $l_2=0.8$ m with lumped masses of $m_1=10$ kg and $m_2=5$ kg. The simulation has been carried out using fourth order Runge-Kutta algorithm with a sampling interval of $T=0.005$ sec, while the control time interval is chosen as 0.01 s.

The robotic arm is assumed to have the physical constraints of maximum and minimum joint angular positions values of,

$$\begin{aligned} \theta_{1\max} &= 90^\circ & \theta_{1\min} &= -90^\circ \\ \theta_{2\max} &= 120^\circ & \theta_{2\min} &= 10^\circ \end{aligned} \quad (7)$$

It is assumed that the maximum and minimum torque values provided by each actuator located on each revolute joint are as,

$$\begin{aligned} \tau_{1\max} &= \tau_{2\max} = 500 \text{ kgm}^2 / \text{s}^2 \\ \tau_{1\min} &= \tau_{2\min} = -500 \text{ kgm}^2 / \text{s}^2 \end{aligned} \quad (8)$$

In all the simulations the desired trajectories of the joints are specified in the joint space as the following sinusoidal motions (see Fig. 4.):

$$\theta_1 = 1.34 \sin(0.77t) \text{ and } \theta_2 = 0.78 \cos(0.91t) + 1.13$$

The angular velocities and angular accelerations are simply the derivatives.

The end-effector trajectory that corresponds to the above desired angular trajectories in the operational space is a curvilinear motion enduring about six seconds (see Fig. 5).

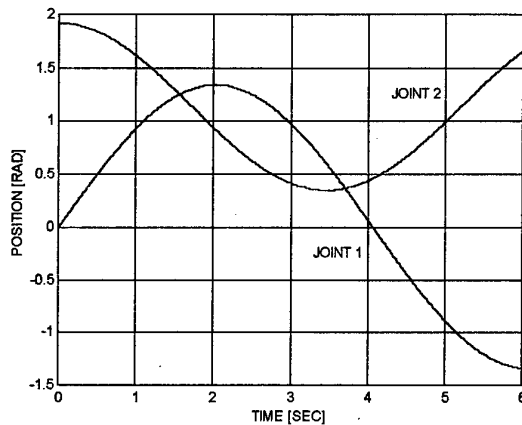


Fig. 4. Desired angular trajectories.

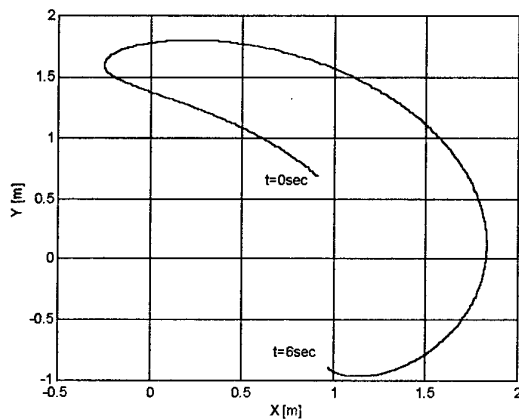


Fig. 5. Desired trajectory of the end-effector.

There are two simulation types carried out. The simulations type A correspond to the well-known desired trajectory tracking objective without any disturbances and changing dynamics. In simulations type B, the objective is the same but the controller has to overcome changing plant dynamics by adapting itself.

There is not yet a well-defined procedure for the determination of the optimum network architecture for a given control problem. The common approach is the trial and error method where the goal is to have good learning with the simplest network architecture. The neural network used in the simulations consisted of one hidden layer with 25 nodes, 2 nodes in the input layers and 6 nodes in the output layer (2-25-6).

The simulation type A is implemented with the feedback gains set to $k_p=200$ and $k_d=40$ for both joints. Since the robot dynamics is nonlinear, the Ziegler-Nichols tuning method is not implemented to determine the optimum k_p and k_d parameters. Instead, the "best" k_p and k_d values are determined by trial and error such that the error is minimum, the response is

fast and possibly well damped. Large feedback gains caused instability in the adaptation phase of the controller.

In Fig.6. and Fig.7, the desired trajectories, the actual trajectories and the position errors of joints θ_1 and θ_2 are displayed respectively. It is seen that the proposed controller is very effective.

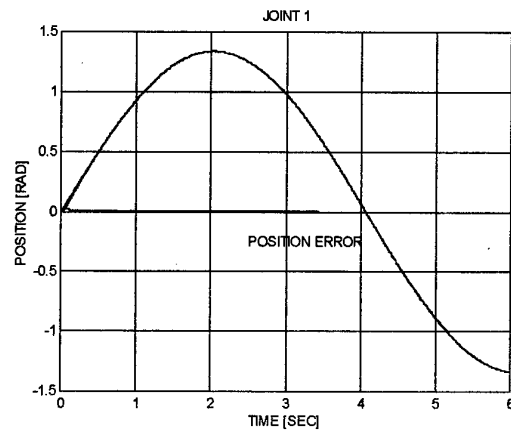


Fig. 6. Angular position θ_1 for simulation type A.

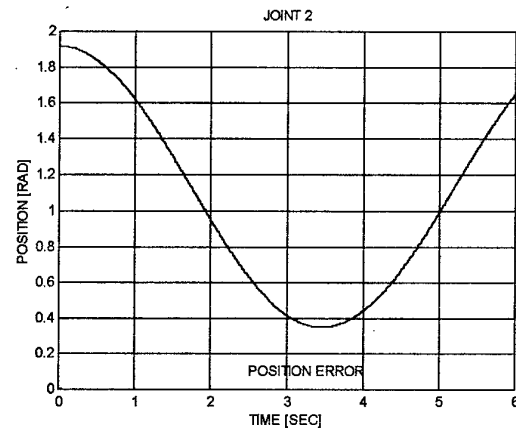


Fig. 7. Angular position θ_2 for simulation type A.

Since the positioning errors are very small they are plotted separately in Fig.8 and Fig.9, respectively.

Since the neuro-model is pre-trained off-line with the data collected during the actual motion of the robot arm, the path tracking performance is achieved even at the very beginning of the simulation. Figure 8 and Figure 9 show that the negligible positioning errors occur during the whole duration of the robot motion. It is observed that the relatively big errors occurring at the start of the motion converge rapidly towards zero.

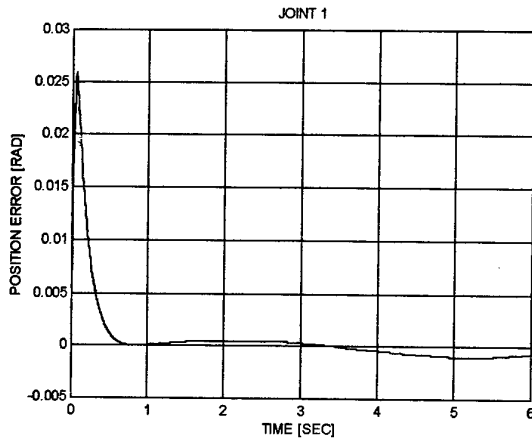


Fig. 8. Position error θ_1 for simulation type A

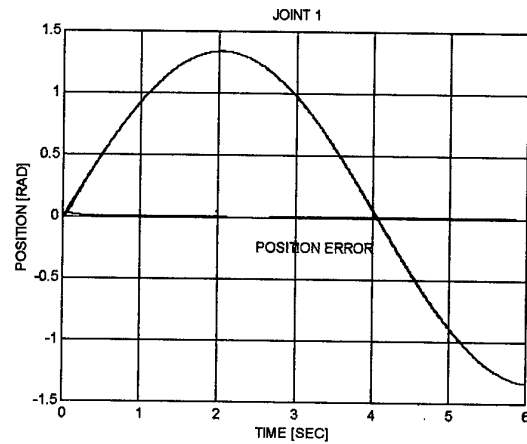


Fig. 10. Angular position θ_1 for simulation type B

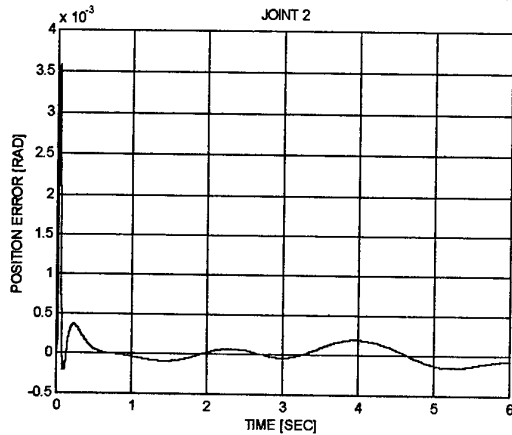


Fig. 9. Position error θ_2 for simulation type A

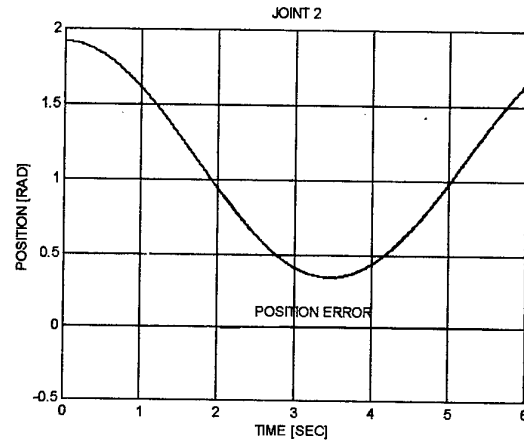


Fig. 11. Angular position θ_2 for simulation type B.

In simulation type B, the robot arm picks up a load of 5 kg at $t=2$ sec. In other words, the point mass at the end of robot arm, m_2 is increased by 100%. The resulting plots of the trajectory tracking performance of the joint positions θ_1 and θ_2 are displayed in Fig. 10 and Fig. 11, respectively. It is observed that the desired and actual trajectories agree extremely well.

Since the position errors θ_1 and θ_2 are very small they are plotted separately in Fig. 12 and Fig. 13. It is observed that overshoots in positioning errors occur at $t=2$. However, the on-line adaptation feature of the proposed controller become effective in decreasing the positioning errors θ_1 and θ_2 which converge towards zero. This demonstrates the capability of the controller to adapt to sudden changes in dynamics while providing necessary motor commands to reach the desired final position following a path close to the desired one.

The adaptation process of the controller is fast enough to give a satisfactory path tracking performance for both simulation types and even under strong uncertainties. The learning rate used during the on-line training process of the network was set to 0.02 value. The network weights are adjusted using backpropagation algorithm.

Note that the significant success in the tracking performance is mainly due to the close approximation of the inverse dynamics by the neuro-model using both off-line and on-line training procedures. Simulation results show that the proposed architecture is capable of tracking the desired path and of compensating unstructured uncertainties.

6. CONCLUSIONS

This work presented a nonlinear compensator using an inverse neuro-model for trajectory control of a two-link planar robot arm. Using a two stage training process, off-line and on-line learning, the neural network is capable of approximating nearly the

exact inverse dynamics of the manipulator and of adapting itself to the structured effects.

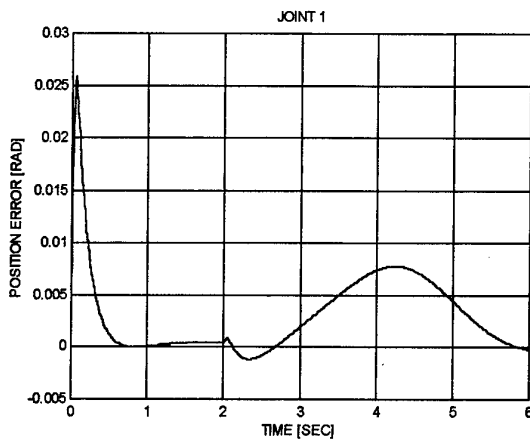


Fig. 12. Position error θ_1 for simulation type B

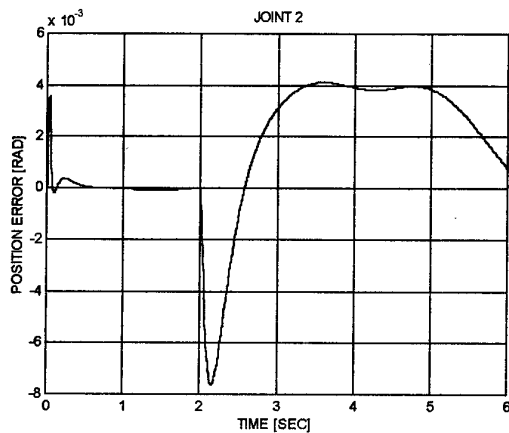


Fig. 13. Position error of θ_2 for simulation type B.

Simulation results indicate that the neuro-controller is able to track the sinusoidal trajectory with a high degree of accuracy. The simulations showed that better the approximation of the inverse dynamics, the lower are the tracking errors since the bounds on the tracking errors are directly proportional to the ones of the neuro-model approximation errors.

Another significant result is the effective adaptation capability of the proposed scheme. It is shown that a sudden change in the manipulator dynamics can be overcome by using the neuro-adaptive scheme which make use of on-line NN training. This is interesting for real-time applications where manipulator dynamics is often faced with sudden changes due to the parameter variations, load changes and possible external disturbances. As an example in this paper the end-effector mass was doubled during the robotic motion. The controller

acted immediately to recover the sudden jumps in tracking errors. Moreover, the error recovery time is satisfactory since an off-line training of the network has been realized first by using the data collected from the real-time motion of the robot arm. The efficiency and the adaptive capability of the artificial neural network controller based on the computed torque method has been proved. The fast adaptation capability of the proposed neuro-controller to changes in manipulator dynamics is also remarkable.

The advent of neuro-adaptive techniques, with optimization and adaptive critics, might pose the next step in the area of the neuro-control in robotics applications. On the other hand, theoretical studies concerning stability and convergence are still in the initial stages and numerous questions have yet to be answered. These titles are all prospective popular research topics of the future concerning neural network controllers and their implementations to robotics.

REFERENCES

1. Ozaki, T., T. Suzuki, T. Furuhashi, S. Okuma, and Y. Uchikawa, "Trajectory Control of Robotic Manipulators Using Neural Networks," *IEEE Transactions on Industrial Electronics*, Vol.38, No.3, pp.195-202, June 1991.
2. Khemaisia, S., and A.S. Morris, "Neuro-Adaptive Control of Robotic Manipulators," *Robotica*, Vol. 11, pp. 465-473, 1993.
3. Lin, C-T., and G.C.S. Lee, *Neural Fuzzy Systems*, Prentice Hall, Upper Saddle River, NJ, 1996.
4. An, C.H., Atkenson, C.G. and Hollerbach, J.M. *Model-Based Control of Robot Manipulator*, the MIT Press, Massachusetts, 1988.
5. Thomas, W., R.S. Sutton, and P.J. Werbos (editors), *Neural Networks for Control*, MIT Press, Cambridge, Massachusetts, 1990.

Trajectory Generation and Obstacle Avoidance for Mobile Non-Holonomic Robots

Zoran M.Gacovski¹, Georgi M.Dimirovski^{2*} and Tatjana D.Kolemisevska²

¹*Information Technology Dept. at Ministry of Defence, Skopje, Rep. of Macedonia*

²*Institute of Automation & Systems Engineering (ASE) at Faculty of Electrical Engineering
St.Cyril and St.Methodius University, Karpos 2 BB, PO box 574, 91000 Skopje, R. of Macedonia
Fax: ++ 389-91-112 163, e-mail: dimir@cerera.etf.ukim.edu.mk*

Abstract - The constraints of non-holonomic mobile robots are expressed as a non-integrable equations. For solving of trajectory generation problem, we have developed computer-aided technique by means of a composite analytical and heuristic method which is based on geometric reasoning and provides deterministic trajectories for all pairs of initial and final configurations and positions. In the cases of obstructed environment we have extended this work by adding some intelligence to automatically guided vehicle / mobile robot via fuzzy-logic supervisory controller. A number of simulation experiments on various PCs using this technique have been done, and run time takes only a few milliseconds. It has become apparent that this approach is quite attractive for application to real-time motion planning of factory-floor AGV/MR.

Keywords: Automatically Guided Vehicles, Mobile robots, Non-holonomic Motion Planning, Trajectory Generation, Obstacle Avoidance, Fuzzy-logic control.

I. INTRODUCTION

A number of both scientific, and engineering and technological results in the area of analysis, simulation modelling, design and implementation of AGVs/MRs have been achieved during the last decade (e.g., see references in this paper and references therein). However, non-holonomic considerations, due to their theoretic complexity, only recently have been subject to both theoretic and applied research (e.g., see [1], [2], [7], [9], [10], [12], [14]). In general, taking into consideration the aspect of steering non-holonomic systems by definition and right from the basic modelling stage is of rather recent date [11], [10], [7].

The complexity of AGVs/MRs control and navigation problems has stimulated various approaches. One way of overcoming the difficulties encountered and of ameliorating practical, though non-analytical, solutions to these problems is via the application of fuzzy systems modelling and control as in [3]-[6], [13]. One of analytical approaches is the use of Pontryagin's

maximum principle optimal control to solve these problems as in [10], which appears to be of more academic importance. It turned out, however, the analytical approach, which is based on differential-geometric formalism and on non-linear control theory [1], [2], [7], [10], [14], to be promising. For it is the solely one to provide for proper inclusion of non-holonomic aspects. Following our previous studies [8], [9] along these lines, in this we present a geometric based, analytic-simulation technique resolving the problem of concern. In the presence of obstacles fuzzy control becomes an attractive proposition, because such algorithms are flexible, robust and effective due to machine intelligence so that can adapt to almost environments within the motion horizon. Again following our previous studies reported in [3], [4], we have adopted fuzzy logic control approach to AGV/MR navigation for obstacle avoidance in a 2D-world with predefined horizon.

*) Author responsible for all correspondence.

II. ON NON-HOLONOMIC MOTION PLANNING

Traditional robot motion planning considers equality or inequality constraints over the configuration variables. These constraints are holonomic, i.e. topological properties of the configuration space are altered, or the robot is constrained to a lower dimensional manifold of the configuration space. Non-holonomic constraints, on the other hand, are imposed on the velocities instead of on the position variables of a system. A non-holonomic constraint is expressed as a non-integrable equation involving derivatives of the configuration parameters and it can not be reduced to equality constraint on the position parameters. Such constraints are expressed in the tangent space at each configuration defining allowable velocities of the system. For example the equation $w(x)x'=0$ expresses a linear velocity constraint, where $x(t) \in R^n$ represents configuration of the system and x' belongs to the tangent space of the configuration space at x .

Consider a problem where we wish to move the system from one configuration to another. There are many systems that are not capable to move between two arbitrary configurations for the kinematics constraints limit the set of reachable configurations to a space of lower dimension. Unlike such systems, we are interested in the cases in which the kinematics constraints do not restrict the reachable configurations. (An example of such a system is an automobile - front wheel drive cart). Its kinematics is constrained because the front wheels can only roll and spin, but not slide sideways. Despite this, we can park a car at any position and orientation. It is convenient to convert the problem of finding a path between two given configurations subject to k constraints of form $w(x)x'=0$ into the problem in control theory. Namely, we are interested in describing the directions in which, by means of control, we can move our AGV/MR instead of those in which we cannot.

There are two different kinds of techniques to the problem of generating trajectories for AGVs/MRs with non-holonomic constraints. Following the first kind of methodological techniques, a geometric reasoning is utilized to construct feasible trajectories by assembling arcs of simple curves (see Pin and Vasseur, [14]). In contrast, the philosophy within the second type relies on generating paths by searching the configuration space of the robot via

applying the non-holonomic constraint as an additional heuristic at every step of the search. Barraquand and Latombe [2], have proposed an elegant method along these lines based on hierarchical bit-map discretization and potential field functions. Their method may be generalized to robots with large number of degrees of freedom, however, its significant drawback is in large memory and computation time required, and is limited to bounded domains because search in configuration space is necessary. Our analytic-simulation technique belongs to the first type of techniques, and it is extended with fuzzy-logic control for the case of obstructed environment.

III. ON KINEMATICS OF A MOBILE ROBOT

"Car-like mobile robot" is a front-wheel-drive four-wheel vehicle (Figure 1). The fact that the two rear wheels are not steerable and roll without slipping on the ground introduces a constraint on the vehicle motion expressing that the velocity of the center of the rear axle is colinear with the orientation axis of the vehicle base. This constraint is of a non-holonomic type, i.e. it is not integrable, and does not allow a closed form analytical resolution for the vehicle trajectory.

We denote by L the distance between the 2 axes of the wheels, by θ the angle between the major axis of the robot and the x axis of the absolute reference frame, by ϕ the steering angle (i.e. the orientation of the front wheels with respect to the major axis of the robot), by x_M, y_M , and V_M the coordinates and the velocity of M , the middle of the axle of the rear wheels. We assume that there is no slipping of the rear wheels, therefore the velocity vector of M is always colinear with the major axis of the robot:

$$(dx_M/dt) \sin \theta - (dy_M/dt) \cos \theta = 0 \quad (1)$$

This equation is not integrable. It is a constraint on the velocity of the robot but does not affect the dimension of the space of configurations. On the other hand, for a given configuration, the space of achievable velocities has a dimension of only two. These are therefore a non-holonomic constraint. Another characteristic of the car-like robots is that the steering angle is constrained:

$$|\phi| \leq \phi_{max} < \pi/2 \quad (2)$$

Let us denote by N the middle of the front axle. Let x_N and y_N be the coordinates, and V_N the velocity of N (see Figure 1).

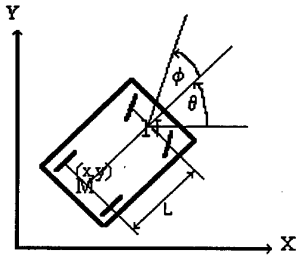


Fig.1. Schematic of car-like mobile robot.

Since we assumed no slipping of the front wheels,

$$\begin{aligned} V_N &= \begin{bmatrix} V_N \cos(\theta + \phi) \\ V_N \sin(\theta + \phi) \end{bmatrix} \end{aligned} \quad (3)$$

and since

$$\underline{ON} = \underline{OM} + \underline{MN} \quad (4)$$

we have:

$$\underline{V}_N = \underline{V}_M + d\underline{MN}/dt \quad (5)$$

Hence, we obtain:

$$\begin{aligned} V_N \cos(\theta + \phi) &= x'_M - \theta' * L * \sin \theta \\ V_N \sin(\theta + \phi) &= y'_M - \theta' * L * \cos \theta \end{aligned} \quad (6)$$

Combining these two equations with the non-holonomic constraint, we obtain:

$$L\theta' = V_N \sin \phi \quad (7)$$

This equation can be rewritten as:

$$ds/d\theta = L/\sin \phi \quad (8)$$

In here, s is the curvilinear distance along the trajectory. The previous equation provides for R , the radius of curvature of the trajectory, according to the steering angle. Given the constraint on the steering angle ϕ_{max} , we have an expression for the minimum radius of turn of the vehicle:

$$|R| \geq R_{min} = L/\sin \phi_{max} \quad (9)$$

IV. GEOMETRIC TRAJECTORY GENERATION

A mobile robot moving in a 2D-world with given horizon, such as a factory-floor, has 3 degrees of freedom: the coordinates of a given point of the robot, and the orientation of the robot itself. A path is a curve joining 2 points and providing a change in the robot orientation.

Changing the orientation of the vehicle can be done only when the vehicle is moving. To change the orientation θ of the vehicle with a minimum length of trajectory, we need to maximize the curvature of the trajectory. This is achieved when the vehicle is moving along a circle the radius of which is the minimum radius of curvature. The problem is that circles take a heavy toll on the length of the trajectory: for a long trajectory, a straight line segment is really needed. Hence the idea of combining arcs of circles and straight line segments. Therefore the trajectories are designed the following way: the robot moves along one of the circles related to the initial configuration in order to be oriented towards the goal, no matter what the final orientation must be. Then, it moves along a straight line in the direction of the goal.

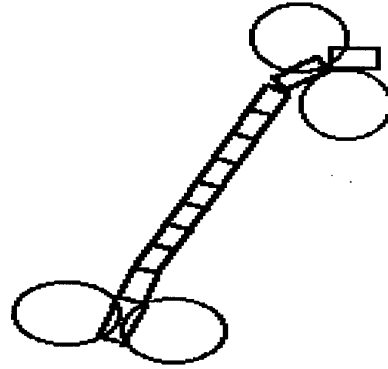


Fig.2. Example of trajectory joining two configurations and positions.

The last part of the trajectory is meant to provide the desired final orientation: the robot moves along one of the circles related to the final configuration. To be physically achievable, the trajectory must provide a continuous orientation to the robot. Therefore, the straight line segment must be tangential to the circles (Figure 2).

If the distance between the center of 2 circles is greater than the sum of their 2 radii, there are 4 common tangents to the circles. Since there are 4 possible couples of circles, there are 16 possible paths. The 16 paths provide the right orientation modulo π . Only 8 provide the desired orientation, the others lead to the opposite. Among the remaining paths, the preferred trajectory is selected using a criterion, e.g. shortest length of the path. If the distance between the 2 chosen circles is smaller than $2 * R_{min}$, then the circles have only 2 common tangents but the principle remains the same. When the initial and final positions of the robot are very near each other, backing control and maneuvering are often involved.

The geometric method provides a continuous orientation to the robot because the circles and the segment are tangent. However, the curvature of the obtained curve is discontinuous: it is a non-zero constant on the circles, and zero on the straight line segments.

As an example, we consider a mission in a 2D world of a non-holonomic MR that has its starting position at point (0.2, 0.9) (in relative spatial units) and its target position at (0.9, 0.2). In addition, it is known that MR has an initial orientation of 30 deg., and at the end point it should take a parking orientation of 180 deg. Note that, no matter what is the aimed trajectory of MR motion, due to non-holonomic constraints, velocity coordinate has to change according to a control law similar to time-optimal control, in order to realize the required orientation coordinate.

Our simulation software technique for trajectory generation is written in C++ language for a PC platform. The graphic device is mapped into frame $x=[0,1]$, $y=[0,1]$ by the header file "starbase.h", and the orientation can be given in degrees $[0-360]$. The coordinates of position are (de)incrementing by 0.04, and the orientation by 15 degrees at each moving step.

V. OBSTACLE AVOIDANCE USING FUZZY CONTROL

In the case of obstructed environment, mobile robot will be treated as an automatically guided vehicle (AGV) which can operate in camera mode and trajectory generation will be based on fuzzy logic control. The work covers situations in which sensor information is either incomplete or unreliable. The predefined fuzzy regions have

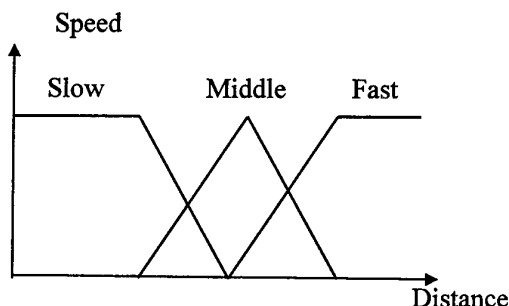


Fig.3. Example of fuzzy regions for AGV speed

triangular form, and they define three files covering distance from an object, orientation and speed. Clearly, the first two files are directly linked with obstacle detection whereas the last

one determine the strategy for steering. The location of a vehicle may be specified as a set $A=\{\text{near distance, middle distance, far distance, no obstacles}\}$.

To obtain the required orientation, this is concatenated with one of the following set $B=\{\text{more left, slightly left, straight, slightly right, more right}\}$. A third set C is defined to cover three speeds $C = \{\text{slow, middle, fast}\}$. The the movement of the vehicle is defined as:

depending on A move B at speed C

One simple control strategy can be defined as follows:

- if no obstacles, go to the end position fast;
- if there is an obstacle at far distance more to the left, then go slightly right with medium speed;
- if there is an obstacle at middle distance more to the left, then go slightly right with slow speed;
- if there is an obstacle at far distance slightly left, go more to the right with medium speed;
- if there is an obstacle at middle distance slightly left, go more to the right with slow speed;
- if there is an obstacle at far distance more to the right, go slightly left with medium speed;
- if there is an obstacle at middle distance more to the right, go slightly left with slow speed;
- if there is an obstacle at middle slightly right, go more to the left with slow speed.

It should be noted that for such predefined fuzzy system the following holds:

$$N=(\sum_{i=0,\dots,p} C_i^p)^k \quad (10)$$

where N is number of different situations, p is number of obstacle angle fuzzy regions and k is number of obstacle distance fuzzy regions. For the present work, $N=32768$ different situations may be accommodated. However, it is clear that such fuzzy rule base is not efficient for control strategies. This leads to the development of a tree-structured fuzzy rule base with no more than 32 'if-then-else' rules.

VI. CONCLUSIONS

The use of conventional path planners for generating trajectories for AGVs/MRs, and any non-holonomic system, easily cause incorrect results. Though the standard approach in path

planning is to use a planner for finding a trajectory without taking into account non-holonomic constraints, and then steering the system as close by as possible to this trajectory along an physically admissible trajectory.

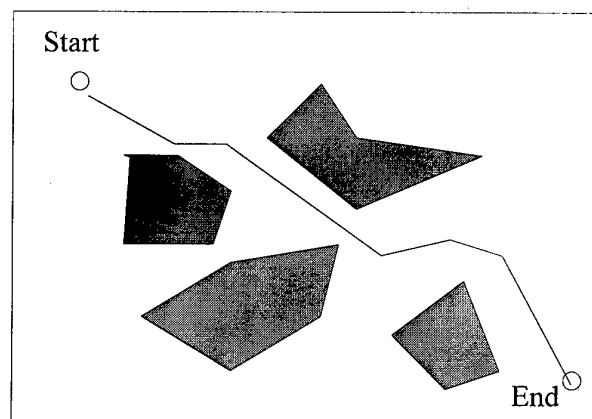
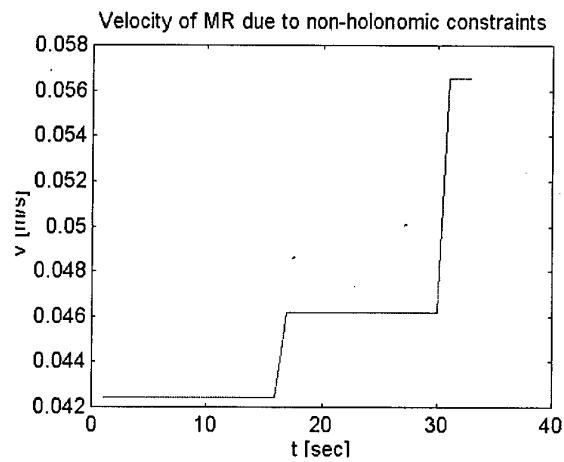
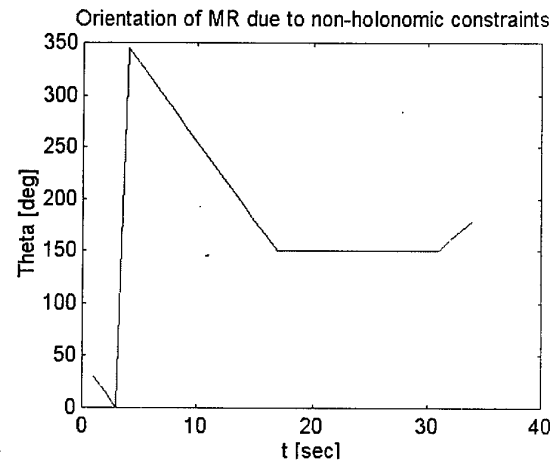
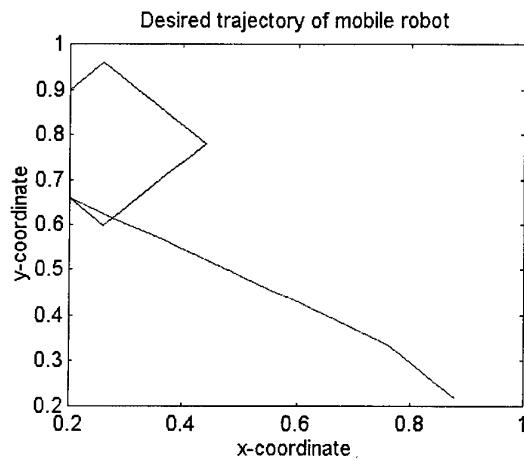
A more appropriate approach is via simultaneous consideration of the integrability and the control-lability aspects of non-holonomic systems. The main advantage of the geometric method is in being a deterministic methodology, and providing trajectories joining all pairs of configurations of AGVs/MRs in motion. The method also takes advantage of the forward and reverse mode of motion of the vehicle as well as of the combination of these on trajectory requiring maneuvering. The purpose of application of fuzzy control in obstructed environment is to realize a control performance using the experience of expert (control rules) with 'if ... then ...' rules.

Our algorithmic software structure can be easily used by an operator: simply, he has only to specify the desired final configuration of the vehicle. This point along with the fact that only a few miliseconds of run time on a PC are necessary to generate the trajectories makes this methodology quite attractive for real-time navigation and motion planning in an obstructed and/or a priori unknown environment.

REFERENCES

- [1] Barraquand, J., and J.C.Latombe, "Nonholonomic multibody mobile robots: Controllability and motion planning in the presence of obstacles", in *Proceed. of IEEE Intl. Conference on Robotics and Automation*, Sacramento (USA), pp.2328-35, 1991.
- [2] Brockett, R.W., "Lie theory and control systems defined on spheres", *SIAM J. Applied Maths.*, vol.25, no.2, pp. 45-56, 1973.
- [3] Dimirovski, G.M., O.L.Iliev, V.N.Burzevski, N.E.Gough, A.Zakeri, I.H.Ting, and R.M.Henry, "Fuzzy-logic control algorithms in navigation of a factory floor vehicle robot", in *IEE Conference Publication No.389* (Selected Papers), The IEE, London (UK), Vol.1, pp.282-287, 1994.
- [4] Dimirovski, G.M., O.L.Iliev, N.E.Gough, A.T. Dinibutun and O Kaynak, "A contribution to fuzzy-logic analytical-simulation methods for AGV motion navigation", in *Proceed. of Intl. Conf. on Recent Advances in Mechatronics*, Bogazici University, Istanbul (TR), Vol. II, pp. 678-683, 1995.
- [5] Iliev, O.L., G.M.Dimirovski, N.E.Gough, G.K. Stojanov, and A.Zakeri, "Obstacle avoidance for intelligent AGVs based on fuzzy control and expectation", in *Prepr. of 13th IFAC World Congress*, San Francisco (USA), Vol.Q Automotive, Marine, Autonomous Vehicles, pp.441-446, 1996.
- [6] Dimirovski, G.M. and T.D.Kolemisevska-Gugulovska, "On fuzzy-relational modelling of Prespa-Ohridean Lakes systems for ecological studies". *Journal of E.C.&T. Engineering*, vol.2, no.1, pp. 41-50, 1996.
- [7] Fernandes, L., L.Gurvits, and Z.X. Li, *Foundations of Nonholonomic Motion Planning*, Res. Rep. C of Robotics Research Laboratory, Courant Institute of Math. Sciences, New York University, New York (USA), pp. 1-106, 1990.
- [8] Gacovski, Z.M., *On Non-holonomic Motion Planning: Controlability and Trajectory Generation for Mobile Robots*, Res. Rep. of Inst. of Automation & Systems Engng., Faculty of Electrical Engineering, St.Cyril & St.Methodius University, Skopje (MK), pp. 1-29, 1996.
- [9] Gacovski, Z.M., B.R. Percinkova and G. M. Dimirovski, "On trajectory generation for mobile robots with nonholonomic constraints", in *Proc. SINTES-9, Int. Symp. on System theory, Robotics, Computers and Process Automation*, University of Craiova (RO), Vol. IX, pp. 235-242, 1998.
- [10] Hejase, A.J., "Optimal motion synthesis of a mobile robot", in *Proceed. of IEEE Intl. Workshop on Intelligent Motion Control*, Istanbul (TR), The IEEE, New York, Vol.II, pp.897-901, 1990.
- [11] Lafferiere, G. and H.J.Sussman, *Motion Planning for Controllable Systems without Drift*, Res. Rep. of Rutgers Center for Systems and Control, Rutgers University (USA), 1990.
- [12] Laumond, J.P., *Singularities and Topological Aspects in Nonholonomic Motion Planning*, Research Rep. of Department of Computer Science, Stanford University (USA), pp. 1-30, 1987.
- [13] Luo, R.C., T.-J.Pan, and C.M.Aras, "Intelligent motion control system for autonomous vehicles operating on a factory floor", in *Proceed. of IEEE Intl. Workshop on Intelligent Motion Control*, Istanbul (TR), The IEEE, New York, Vol.II, pp.419-423, 1990.
- [14] Pin, F.G., and H.A.Vasseur, "Autonomous trajectory generation for mobile robots with nonholonomic and steering angle constraints", in *Proceed. of IEEE Intl. Workshop on Intelligent Motion Control*, Istanbul (TR), The IEEE, New York, Vol.I, pp.295-300, 1990.

SIMULATION RESULTS



AGV Simulation - Fuzzy controlled

Reduction of Path Errors for Industrial Robots by Trajectory Precorrection

Martin Grotjahn, Bodo Heimann, Axel Thiemann

*Institute of Mechanics, University of Hannover, D-30167 Hannover
grotjahn@ifm.uni-hannover.de; heimann@ifm.uni-hannover.de*

Abstract

Simple linear joint controllers are still used in typical industrial robotic systems, although there exists a multitude of sophisticated non-linear control algorithms. The use of these controllers leads to non-negligible path deviations for applications that require high speed motions.

In this paper a method is proposed which reduces path deviations by pre-correction of the desired trajectory. The corrections are calculated with respect to a non-linear dynamic model of the robot and transferred to the robot. The method is applicable to typical industrial robots on condition that an interface for path corrections exists and that joint angles and torques are measurable.

Experimental investigations for the 6-dof industrial robot Siemens manutec-r15 show reductions of path errors that are much larger than for linear pre-correction which was proposed in [1, 2]. The results exhibit the robustness of the method with respect to different interpolation cycle times.

1. Introduction

Nowadays there is a large gap between the sophisticated control algorithms developed in robotics research and the simple control techniques used in industrial robotic applications. Typical industrial controllers disregard the non-linearities of robot dynamics, like friction and couplings of the different joints. Therefore, robust independent joint controllers are implemented which are sufficient for applications that require only high positioning accuracy.

Although such applications are still the main field of industrial robots' tasks, applications requiring high path accuracy — e.g. laser-cutting — are becoming more and more important. Many powerful control algorithms, like computed-torque [3] and adaptive methods [4, 5], have been developed in robotics research. By these algorithms the tolerances of such demanding applications can be complied. But they usually require

a centralized control architecture which is not existent in typical industrial controllers due to its complexity and the minor share of demanding applications.

However, common industrial robots have an interface which is designed for handing over path corrections from external sensor signals. An algorithm is proposed in [1, 2] which uses this interface for the reduction of path deviations. Corrections of the desired trajectory are calculated with respect to a linear model of the closed loop system and 'wrong' trajectories are fed into the controller. Due to the robot dynamics the resulting trajectory is closer to the original desired path than it would have been otherwise. The snag with this method is that only linear models of the over-all system are used.

In this paper another approach is presented which bases on a complete non-linear model of the robot. It combines the main ideas and advantages of the computed-torque method and the mentioned pre-correction algorithm. Like in the computed-torque method the inverse dynamics of the robot is used to calculate the expected torques from the desired joint motions. Since no torque interface is available for feed-forward control, the resulting values are transferred into trajectory corrections by an inverted controller model. The robot model is divided into two parts which are separately identified. For the identification it has only to be assumed that joint angles and torques are measurable.

The points in time for the transfer of path corrections are usually set by the interpolation cycle. Experimental investigations with different cycle times exhibit the robustness and the wide applicability of the proposed method. The achieved reduction of path deviations is impressing. The results are much better than for the linear pre-correction scheme.

2. Inverse robot dynamics

The inverse dynamic model of robots is usually divided into a gear and a rigid body model.

2.1. Gear model

Concerning the modelling of gears in robot dynamics, normally only the losses are taken into account by velocity dependent friction torques. Other effects like elasticity and backlash are neglected.

Often a physically motivated model is used combining dry friction and viscous damping [6]:

$$\tau_{f1,i} = a_1 \dot{q}_i + a_2 \text{sign}(\dot{q}_i). \quad (1)$$

Although this model is sufficient for many applications, a more precise model should cover the degressive characteristic of friction for higher velocities, which is shown in figure 1 where the normalized over-all friction characteristics for different axes of the industrial robot *Siemens manutec-r15* are plotted. To regard this the inclusion of an additional term is suggested in [7]:

$$\tau_{f2,i} = a_1 \dot{q}_i + a_2 \text{sign}(\dot{q}_i) + a_3 \arctan(a_4 \dot{q}_i). \quad (2)$$

A great difficulty in friction modelling for industrial robots is the dependence on the time-varying operating conditions, especially on the gear temperature [7]. Therefore 'warm-up' motions are often used to reach stationary conditions. Figure 2, however, shows that this is not sufficient. During a continuous 'back-and-forth'-motion of one gear the friction is measured every 12s at the same angle. Even after a long period no stationary condition is reached and after short interruptions friction increases significantly. This shows that not only the temperature but also the distribution of the lubricants has a large influence. Therefore, an exact prediction of friction is almost impossible. This can lead to errors not only for correction but also for rigid body identification.

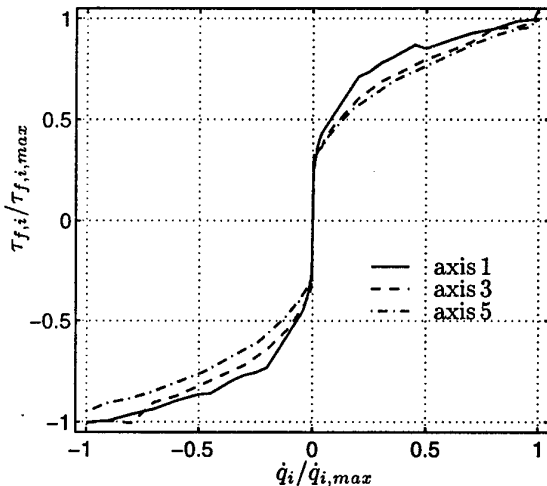


Figure 1. Normalized friction characteristics for different axes of the *Siemens manutec-r15*.

2.2. Rigid body model

The dynamic equation of the robot's rigid body model can be written as

$$\tau = M(q)\ddot{q} + c(q, \dot{q}) + g(q) \quad (3)$$

$$\Leftrightarrow \tau = A(q, \dot{q}, \ddot{q})p. \quad (4)$$

Equation (3) represents the usual form of the dynamic equation with the mass matrix $M(q)$ as well as the vectors of centrifugal and Coriolis forces $c(q, \dot{q})$, gravitational $g(q)$ and joint torques τ . Equation (4) is the corresponding parameter linear form. The base parameter vector p consists of the inertial and gravitational parameters of the links, e.g. masses and moments of inertia, and linear combinations of them. It has minimal order to guarantee identifiability of all elements p_i and can be derived automatically for any serial robot [8]. For typical industrial robots $\dim(p)$ is relatively small because of the symmetric link structure.

3. Identification

The friction characteristics are assembled by measuring the friction torques at different constant velocities. Subsequently, the friction model 2 is adapted by a non-linear optimization.

There exists a vast amount of literature on rigid body identification. However, most of the methods are variations of the same identification scheme. The robot is moved along a trajectory which is optimized to guarantee maximum 'excitation' of the parameters.

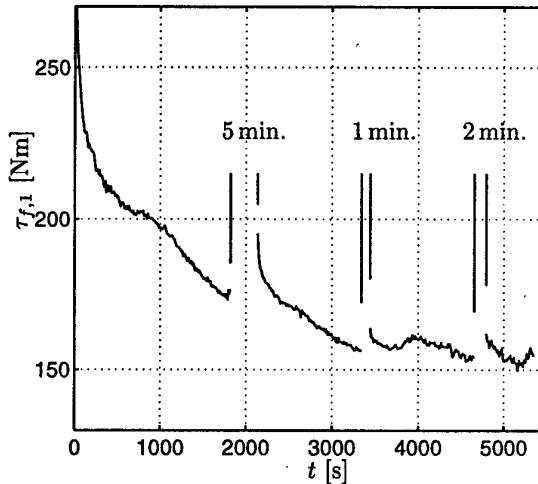


Figure 2. Variation of friction with time during continuous operation and brakes.

Joint motion and torque are measured and friction is compensated by a model determined in advance.

Here, a different method is used. The identification is done by a two-step algorithm. In the first step the elements of g and M are determined for a significant number of different configurations of the robot. In the second step the parameters are estimated by a weighted LS-method. A more detailed description of the procedure and the application to the robot *Siemens manutec-r15* is given in [9].

This identification procedure has two main advantages. On the one hand the implementation is easy since no optimized trajectories are needed. On the other hand no compensation of friction is required. So, the method is robust with respect to lack of knowledge about and variations of friction conditions.

4. Trajectory precorrection

For trajectory precorrection a model of the robot is inverted to compute the position commands that are necessary to track the desired trajectory. In the next section, the linear precorrection scheme [1, 2] is presented for comparison. Subsequently, the precorrection scheme is depicted which bases on the non-linear model presented in the sections before.

4.1. Linear precorrection scheme

In [1, 2] Lange and Hirzinger proposed the use of linear decoupled impulse response models of each joint's closed loop for reduction of path deviations. The model predicts the actual joint positions $q_i(k)$ based on the position commands $u_i(k-l)$ for $l = m_{d,i}, \dots, m_i$

$$\hat{q}_i(k) = \sum_{l=m_{d,i}}^{m_i} \hat{g}_i(l) u_i(k-l). \quad (5)$$

Here $\hat{g}_i(l)$ denotes the estimate of one impulse response coefficient and $m_{d,i}$ the relative degree of the system. Theoretically, m_i must be infinite but for stable systems the first few $\hat{g}_i(l)$ are sufficient. The joint index i is dropped for simplicity in the following.

The impulse response can be estimated using the LS-method applied to one short (500 sampling points) trajectory. No additional knowledge about the structure of the system or the controller is used during the identification process. This is an advantage on the one hand because the procedure can be implemented on unknown systems. On the other hand it can result in inferior model quality since available information about the controller and the physics of the system is not taken into consideration. Due to its linearity, the

model of the robot is incapable of incorporating the non-linear effects such as friction and the couplings between different joints.

Given the desired trajectory $q_d(k)$ for $k = 1, \dots, N$, and letting $q_d(N+j) = q_d(N)$ for $j \geq 1$, it is possible to formulate a system of equations to estimate the necessary position commands $\hat{u}_n(k)$ for $k = 1 - m_d, \dots, N$:

$$\begin{pmatrix} \hat{g}(m_d) & & & 0 \\ \vdots & \ddots & & \\ \hat{g}(m) & & \ddots & \\ 0 & \hat{g}(m) & \dots & \hat{g}(m_d) \end{pmatrix} \begin{pmatrix} \hat{u}_n(1 - m_d) \\ \vdots \\ \vdots \\ \hat{u}_n(N) \end{pmatrix} = \begin{pmatrix} q_d(1) \\ \vdots \\ \vdots \\ q_d(N + m_d) \end{pmatrix} \quad (6)$$

$$\Leftrightarrow \hat{G} \hat{u}_n = q_d. \quad (7)$$

It is not possible to simply invert G to calculate \hat{u}_n because the linear model is not guaranteed to be minimum-phase. That means the zeros of the system can be outside of the unit circle of the Z -plane. In that case, the inverted model is unstable and the estimated necessary commands \hat{u}_n are likely to contain large variations. Therefore, \hat{u}_n is computed using an Inverse-Covariance Kalman Filter [10] for the system

$$\begin{aligned} u_n(k+1) &= E u_n(k) \\ q_d(k) &= G_{k,1..N+m_d} u_n(k) + v(k). \end{aligned} \quad (8)$$

Given the covariances of the first estimate $\hat{u}_{n,0} = q_d$ and of the measurement noise $v(k)$, the ICKF computes the position commands. Small deviations of the desired robot path $\hat{q}_d = q_d + v$ are accepted in order to keep the modifications of the position commands $\Delta u_{cor} = \hat{u}_n - q_d$ small and thus to produce a smooth corrected trajectory.

To reduce the computational effort, it is desirable to keep the number of sampling points as low as possible. Experiments with the testbed *Siemens manutec-r15* have shown that the method works satisfactorily with sampling times up to $\Delta T = 20 \text{ ms}$, the resulting corrected trajectory can be transformed to the necessary sampling interval using spline interpolation. Therefore, the method is suitable for different interpolation cycle times. For the results shown in section 4.3 $\Delta T = 10 \text{ ms}$ was used.

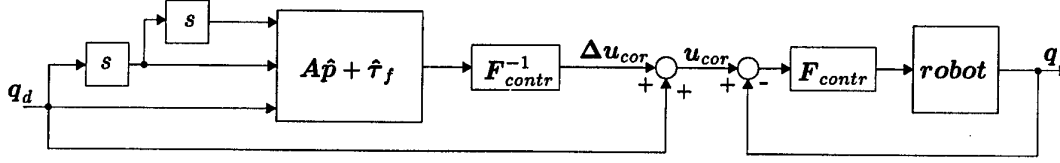


Figure 3. Structure of the complete robot system with non-linear trajectory precorrection.

4.2. Non-linear precorrection scheme

Instead of using a simple linear decoupled model of the robot and the controller to calculate a corrected trajectory, it is possible to use a model of the closed loop system based on the inverse robot dynamics and the known controller parameters. The necessary torques for all joints $\hat{\tau}_n$ for a given trajectory q_d can be estimated using equations (2) and (4):

$$\begin{aligned}\hat{\tau}_n &= \hat{M}(q_d)\ddot{q}_d + \hat{c}(q_d, \dot{q}_d) + \hat{g}(q_d) + \hat{\tau}_f(\dot{q}_d) \\ &= A(q_d, \dot{q}_d, \ddot{q}_d)\hat{p} + \hat{\tau}_f(\dot{q}_d).\end{aligned}\quad (9)$$

The inverted controller can convert the desired torques into deviations $\Delta u_{cor} = F_{contr}^{-1}\hat{\tau}_n$ that have to be added to the desired trajectory to achieve maximum path accuracy. The structure of the complete system can be observed in figure 3.

The over-all structure of the trajectory precorrection resembles the well known computed torque control [3]:

$$\begin{aligned}\tau_{act} &= F_{contr}(\Delta u_{cor} + q_d - q_{act}) \\ &= \hat{\tau}_n + F_{contr}(q_d - q_{act}) \\ &= A(q_d, \dot{q}_d, \ddot{q}_d)\hat{p} + \hat{\tau}_f(\dot{q}_d) \\ &\quad + F_{contr}(q_d - q_{act}).\end{aligned}\quad (10)$$

The results of the trajectory precorrection are not expected to be as good as the ones achieved with computed torque control, where the controller can be optimized to reduce the remaining path errors that are caused by model errors and outside disturbances. The advantage of trajectory precorrection is that one only

Table 1. Results of precorrection for trajectory 1, vertical circle

		uncorrected	linear	non-linear
E	$[10^{-3}]$	1.63	0.94	0.37
$\Delta_{abs,max}$	$[mm]$	2.22	0.80	0.41
$\Delta_{x,max}$	$[mm]$	0.57	0.43	0.12
$\Delta_{y,max}$	$[mm]$	2.09	0.75	0.40
$\Delta_{z,max}$	$[mm]$	1.16	0.52	0.24

needs to convey path information to the robotic system and no additional torque information. So, only a path interface is necessary.

The non-linear model is much more accurate than the linear model presented in the previous section and the resulting path accuracy is expected to be better.

4.3. Results

The results for the two previously introduced approaches are presented for three different trajectories:

- Trajectory 1: vertical circle, gripper vertical, diameter 40 cm, $0.6 \frac{m}{s}$.
- Trajectory 2: horizontal circle, gripper down, diameter 40 cm, $0.6 \frac{m}{s}$.
- Trajectory 3: 90° edge in x-y-plane.

In order to quantify the results of the precorrection five measures are given: the absolute maximum cartesian path error, the maximum cartesian path error for the x , y and z -direction, and the results of the following criterion evaluating the performance for the whole trajectory:

$$E = \sum_{i=1}^6 \sqrt{\frac{1}{m} \sum_{j=1}^m (q_{d,i}(j) - q_i(j))^2}, \quad (11)$$

where m is the number of sampling points.

The tables 1 to 3 show that the path accuracy measured by E is decreasing due to the precorrection for all tested trajectories. As expected the results are better for the non-linear precorrection scheme (reduction

Table 2. Results of precorrection for trajectory 2, horizontal circle

		uncorrected	linear	non-linear
E	$[10^{-3}]$	1.90	1.15	0.42
$\Delta_{abs,max}$	$[mm]$	1.92	0.86	0.41
$\Delta_{x,max}$	$[mm]$	0.62	0.47	0.10
$\Delta_{y,max}$	$[mm]$	1.88	0.85	0.41
$\Delta_{z,max}$	$[mm]$	0.96	0.54	0.30

Table 3. Results of precorrection for trajectory 3, horizontal edge

		uncorrected	linear	non-linear
E	$[10^{-3}]$	1.43	0.97	0.60
$\Delta_{abs,max}$	$[mm]$	0.99	0.68	0.36
$\Delta_{x,max}$	$[mm]$	0.21	0.27	0.22
$\Delta_{y,max}$	$[mm]$	0.98	0.68	0.15
$\Delta_{z,max}$	$[mm]$	0.49	0.50	0.24

of at least 57%) than for the linear (reduction of at least 31%).

Experiments have shown that the main reason for the performance difference is the inability of the linear model to incorporate friction. In figure 4 measurements of joint 2 for trajectory 1 are shown. It is clearly visible that the linear model does not compensate the changing sign of friction torque at the maximum. Therefore, its corrections are much worse than the ones of the non-linear model. Nevertheless, the resulting path of the manipulator is closer to the desired trajectory than without precorrection.

In figure 5 the break-away behaviour of the robot is presented for trajectory 1 in cartesian coordinates. Both models reduce the initial deviation impressively compared to the uncorrected path. Tables 1 to 3 show that the decrease of the maximum absolute error in cartesian coordinates for the linear model is considerable (at least 31% reduction) but inferior to the decrease for the non-linear model (at least 63% reduction).

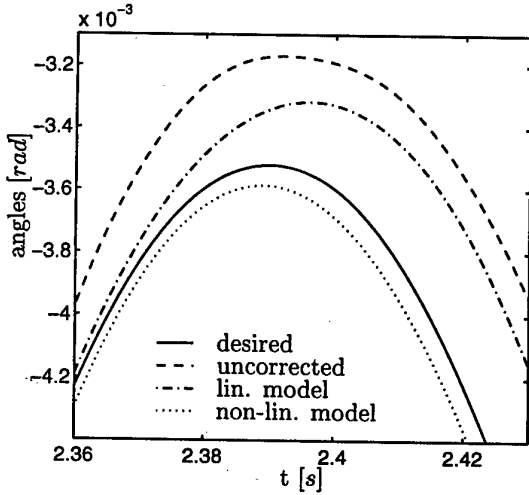


Figure 4. Results of precorrection for trajectory 1 in joint coordinates for axis 2, speed-reverse.

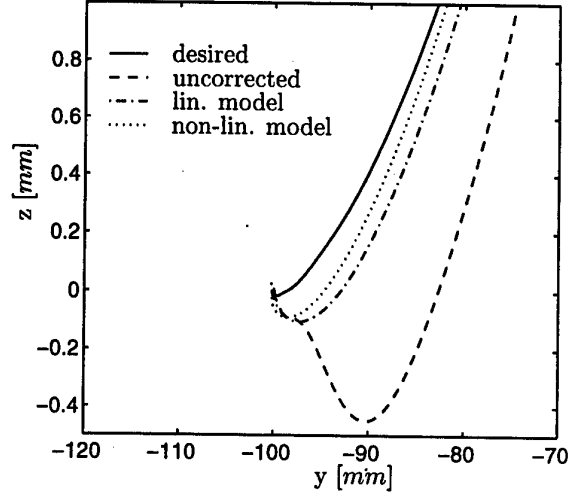


Figure 5. Results of precorrection for trajectory 1 in cartesian coordinates, break-away behaviour.

Figure 6 shows the absolute cartesian error for trajectory 2. It is reduced for almost the whole length of the trajectory except for two points (0.5 s and 1.5 s) where the accuracy for the uncorrected trajectory is high. Here also can be seen again (especially at 0.7 s and 1.4 s) that the non-linear model precorrection is much better than the correction using the linear model.

The tracking improvements for trajectory 3 are the least significant for all three trajectories according to the 3 tables - the maximum error in x-direction even

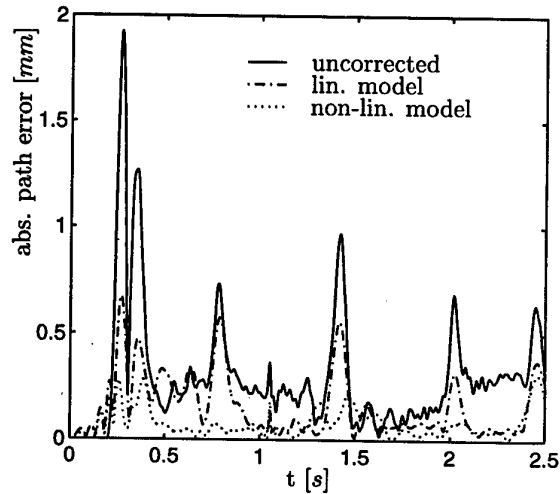


Figure 6. Results of precorrection for trajectory 2, absolute error in cartesian coordinates.

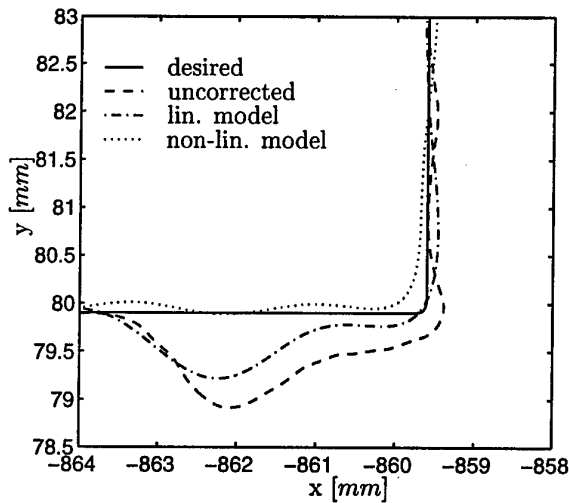


Figure 7. Results of precorrection for trajectory 3 in cartesian coordinates.

increases slightly due to precorrection. Nevertheless, the path-accuracy is impressive, which can be seen in figure 7 for trajectory 3. The linear model reduces the deviations to a certain degree, while the more sophisticated model improves drastically the path accuracy.

For most industrial robot controllers the interpolation cycle time and the controller cycle time differ from each other. The controller of the *Siemens manutec-r15* generates path data with $\Delta T_{IPO} = 32\text{ ms}$ and then interpolates for the 6 individual joint controllers using $\Delta T_{contr} = 2\text{ ms}$. The new non-linear precorrection scheme was tested for robustness with $\Delta T_{IPO} = 10\text{ ms}$, $\Delta T_{IPO} = 20\text{ ms}$ and $\Delta T_{IPO} = 32\text{ ms}$. Even though the interpolation leads to a loss of path-information especially at the points of speed-reverse, the results presented in table 4 show that the method is robust with respect to the interpolation for all three test trajectories. The path accuracy achieved by the precorrection only changes marginally.

Table 4. Results of non-linear precorrection for different interpolation cycle times

E [10^{-3}]	traj. 1	traj. 2	traj. 3
corrected, non-linear	0.37	0.42	0.60
$\Delta T = 10\text{ ms}$, uncor.	1.52	0.77	1.44
$\Delta T = 10\text{ ms}$, cor.	0.36	0.48	0.60
$\Delta T = 20\text{ ms}$, uncor.	1.55	1.78	1.43
$\Delta T = 20\text{ ms}$, cor.	0.39	0.47	0.62
$\Delta T = 32\text{ ms}$, uncor.	1.54	1.78	1.44
$\Delta T = 32\text{ ms}$, cor.	0.40	0.49	0.62

5. Conclusion

Trajectory precorrection is suitable for manipulators that provide no access to control algorithms but have an interface for path corrections. In this paper a trajectory precorrection method is presented which leads to impressive reductions of path deviations for typical industrial robots. The method is based on an over-all, non-linear model of the robot which can be automatically formulated and identified by means of the presented modelling and identification approach. An experimental comparison to a linear precorrection scheme for the 6-dof robot *Siemens manutec-r15* shows that the consideration of non-linearities leads to better results. However, the linear scheme combines also remarkable improvements with simplicity. Furthermore, it provides the possibility of learning which is not presented in this paper so that it is an alternative to non-linear modelling.

References

- [1] Lange, F.; Hirzinger, G., "Learning to improve the path accuracy of position controlled robots," in *Proceedings of Intelligent Robots and Systems*, vol. 10, pp. 494-501, 1994.
- [2] Lange, F.; Hirzinger, G., "Learning of a controller for non-recurring fast movements," *Advanced Robotics*, vol. 10, no. 2, pp. 229-244, 1996.
- [3] Asada, H.; Slotine, J.-J. E., *Robot Analysis and Control*. Wiley-Interscience Publication, 1986.
- [4] Slotine, J.-J. E.; Li, W., "On the adaptive control of robot manipulators," *International Journal of Robotics Research*, vol. 6, no. 3, pp. 147-156, 1987.
- [5] Craig, J. J., *Adaptive Control of Mechanical Manipulators*. Addison-Wesley, 1988.
- [6] Armstrong-Hélouvry, B., *Control of Machines with Friction*. Boston: Kluwer Academic Publishers, 1991.
- [7] Daemi, M.; Heimann, B., "Identification and compensation of gear friction for modeling of robots," in *Proc. of the 11th CISM-IFTOMM Symp.*, pp. 89-96, 1996.
- [8] Gautier, M.; Khalil, W., "Direct calculation of minimum set of inertial parameters of serial robots," *IEEE Transactions on Robotics and Automation*, vol. 6, no. 3, pp. 368-373, 1990.
- [9] Daemi, M.; Heimann, B., "Separation of friction and rigid body identification for industrial robots," in *Proc. of the 12th CISM-IFTOMM Symp.*, pp. 35-42, 1998.
- [10] Maybeck, P., *Stochastic Models, Estimation and Control*, vol. 1. Mathematics in Science and Engineering, Academic Press, 1979.

Development of a Sliding Mode Controller based on Neural Networks for the Semi-Suspension System

Chang-Goo Lee , Hyung-Soon Lim^o , Kwang-Hyun Song
Department of Control & Instrumentation Engineering
Chonbuk National University, Korea
E-mail : changgoo@moak.chonbuk.ac.kr

Abstract

In this paper, a new neural networks system modeling and sliding mode suspension controller are proposed. The new neural networks are an error self-recurrent neural networks which use a recursive least squares method for the fast on-line learning. The proposed neural networks converge considerably faster than the back-propagation algorithm and have advantages of being less affected by the poor initial weights and learning rate. The controller for suspension system is designed according to sliding mode technique based on new proposed neural networks. In order to adapt sliding mode control method, each frame distance between ground and vehicle body is estimated and controller is designed according to estimated neural model.

1. Introduction

Neural networks have been applied to various areas including the estimation of nonlinear systems and control application because of being strong on nonlinear modeling [1]. However, there are many disadvantages such as local minima, long time of learning and the slow convergence rate in the neural networks and back-propagation algorithm[2] used in the estimation of systems and controls. In order to improve these disadvantages, many researches has been reported. Representatively Singhal and Wu incorporated extended Kalman filter in the BP algorithm. However, the computational complexity of this algorithm becomes intractable as the size of multilayer neural networks increases. Recently, Scalero and Tepedelenlioglu, Lou and Perez derived another modified algorithm[3]. This algorithm divided neural networks into linear and nonlinear portion and then apply Kalman filter to improve the rate of convergence and also not sensitive to initial weights. However, it is still sensitive to learning rates because it computes the desired values of hidden layer based on the BP algorithm[4].

The key point of this work is to develop a new algorithm which does not require any pre-information about the system and architecture. In order to accomplish this goal, the desired values of hidden layers are computed by optimal method directly and each weight is updated by RLS(recursive least square). Specially in architecture, self-recurrent time delayed error as a bias is offered. This neural networks improve the disadvantages mentioned above.

We also estimate 7 degree of freedom vehicle model in realtime; in fact estimate each frame distance between ground and car body which is mentioned later and develop an adaptive sliding mode suspension controller based on this neural networks.

2. Error self-recurrent neural networks

The proposed neural networks have inputs as following; the time delayed output of plant and error between plant and output of neural networks. Generally, a bias or threshold is fixed to +1 or -1 which just increases or decreases the output of each neuron. But there is no exact theory available yet how to select this value according to system.

In this paper, in order to solve this vagueness and estimate a fast variable system, we suggest new model like Figure 1b. in which one-step previous error is feedback into input, where the weights have a positive value

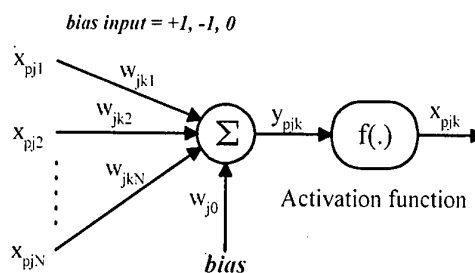


Figure 1a. Conventional Neural Network model

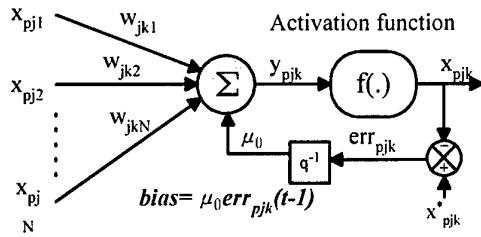


Figure 1b. Error Self-Recurrent Neural Network

Figure 1a. and Figure 1b. represent a conventional neural networks and the proposed one, respectively. Because the new neural networks described by Figure 1b. have error as bias which is different from Figure 1a. This solves vagueness and also estimates a fast variable system.

2.1. Learning algorithm

First, divide neural networks with linear portion and nonlinear one and then compute desired values of hidden layers in the linear portion with an optimal method.

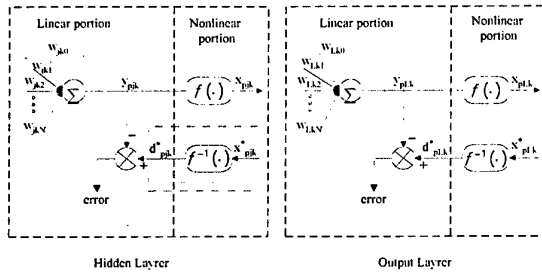


Figure 2. Division of Neural

The learning algorithm is as follows;

$$\begin{aligned}
 E &= \frac{1}{2} \sum_{k=0}^K (d_{pl,k}^* - w_{L,k} x_j)^2 \\
 d_{pl,k}^* &= f^{-1}(x_{pl,k}^*) \\
 \frac{\partial E}{\partial x_j} &= 0 \Rightarrow \sum_{k=1}^K d_{pl,k}^* w_{L,k} = w_{L,k} w_{L,k} x_j \\
 w_{L,k}^T d_{pl,k}^* &= w_{L,k}^T w_{L,k} x_j \\
 x_j^* &= w_{L,k}^T (w_{L,k} w_{L,k}^T)^{-1} d_{pl,k}^*, \quad \text{if } N \geq K \\
 x_j^* &= (w_{L,k}^T w_{L,k})^{-1} w_{L,k}^T d_{pl,k}^*, \quad \text{if } N < K
 \end{aligned} \quad (1)$$

In the every node of each layer, compute the gain vector k_k and then update weight vectors as follows;

$$\begin{aligned}
 d_{pl,k}^* &= f^{-1}(x_{pl,k}^*) \\
 K_k &= P_k x / (\lambda + x^T P_k x) \\
 P_k &= (I - K_k x^T) P_k / \lambda \\
 w_{L,k} &= w_{L,k} + k_K (d_{pl,k}^* - y_{pl,k} + \mu_0 e_{pl,k}(t-1)) \\
 w_{jk} &= w_{jk} + k_j (d_{pl,k}^* - y_{pl,k} + \mu_0 e_{pl,k}(t-1))
 \end{aligned} \quad (2)$$

2.2. The estimation of a fast varying nonlinear system

In order to evaluate the performance of the error self-recurrent neural networks and the learning algorithm, the test is executed like shown in Figure 3.

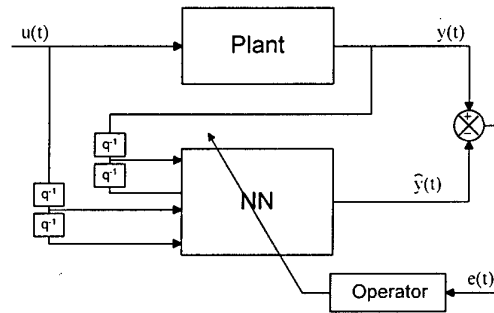


Figure 3. System modeling block diagram

The complex nonlinear plant model and input signal are selected as equation (3)

$$\begin{aligned}
 u(t) &= 0.5 \sin(2\pi / 50) + 0.5 \sin(2\pi / 120) \\
 y(t) &= (0.85y(t-1)y(t-2) + 0.16u(t-1) + \\
 &\quad 0.25u(t-2)) / (1 + y^2(t-1))
 \end{aligned} \quad (3)$$

The randomized weights were between 0 and 0.5 and the learning rate was selected as 0.05 for BP and Scalero algorithm. Figure 4. and Figure 5. show the result of BP and Scalero algorithm, respectively. Figure 4. and Figure 5. show that Scalero algorithm converges faster than BP algorithm. Figure 6. is the output response of neural networks trained by suggested algorithm. It converges faster than Scalero algorithm.

3. Real-time Identification of 7-DOF Vehicle Suspension System

A vehicle model for simulation is shown in Figure 7. which has 7 degree of freedom. The state of system considered here is heave, pitch, roll motion and 4 wheels' suspension strokes due to vibration of 4 wheel by road

disturbance. If we consider each motion, we assume that the order of this system is second.

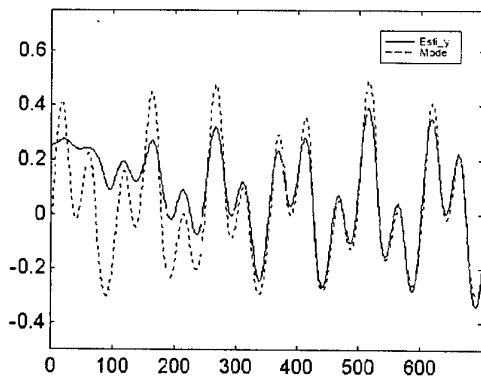


Figure 4. Output by BP algorithm (Bias=+1)

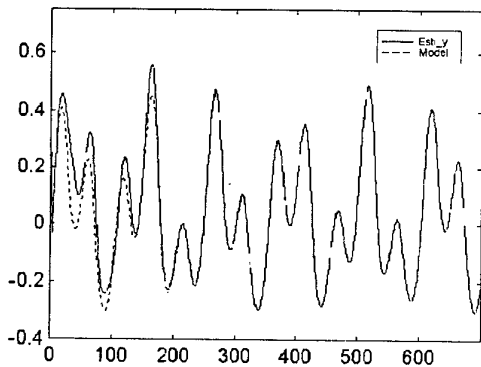


Figure 5. Output by Scalero's algorithm (Bias=+1)

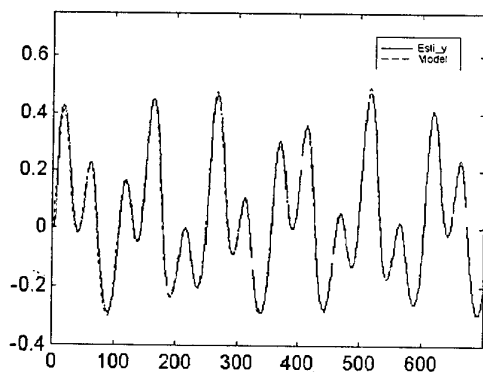


Figure 6. Output of proposed algorithm (Bias=e(t-1))

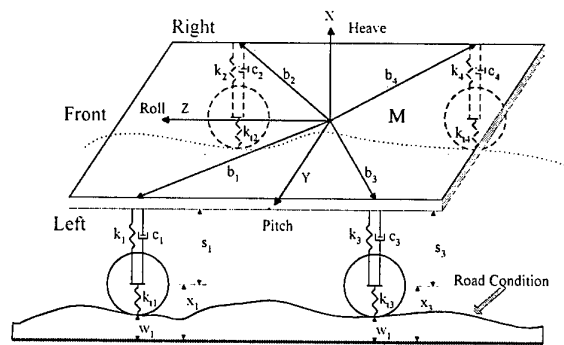


Figure 7. 7-degree of freedom vehicle model

Figure 8. show the block diagram for identifying vehicle suspension system.

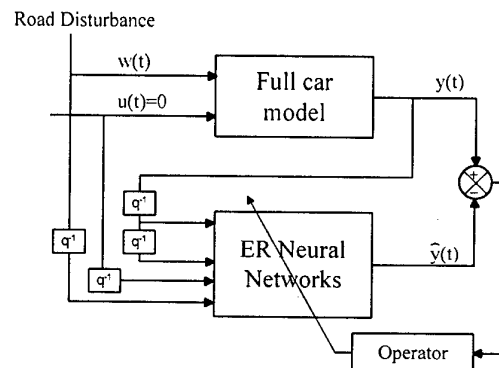


Figure 8. The method for Estimating a Full car

Inputs of neural networks are composed of 1 and 2 step time-delayed plant output and 1 step time-delayed road disturbance. $y(t)$ is the frame distances which mean distances between ground and car body, $s_i + x_i$ in Figure 7.

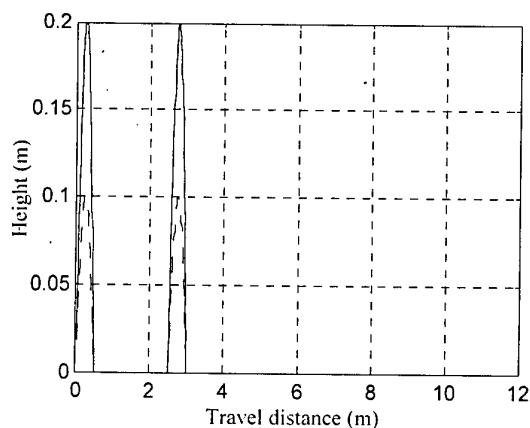


Figure 9. Road condition(left:0.2, right:0.1)

Frame distances should be selected to estimate and control suspensions, because sliding mode control method consider single input and multi output system.

The initial weights were selected between 0 and 0.5 and weights to error were fixed to 0.05. Figure 10., Figure 11., Figure 12. and Figure 13. show the estimation results of each frame distance when road conditions are given such as Figure 9. The estimation errors almost converge to zero at travel distance of 0.5m

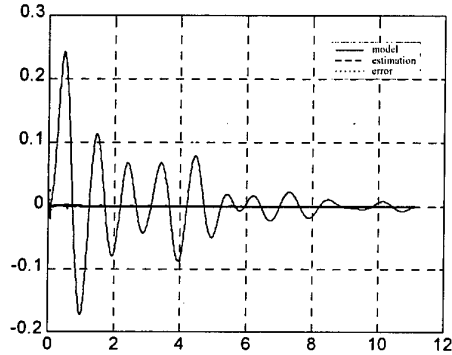


Figure 10. Front Left Frame Distance (m)

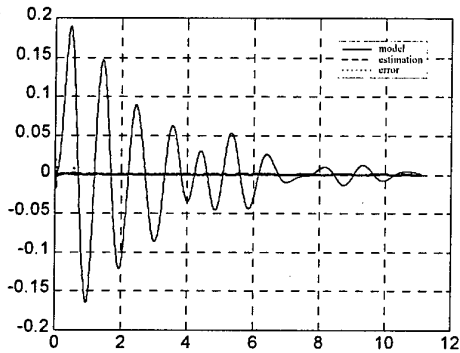


Figure 11. Front Right Frame Distance (m)

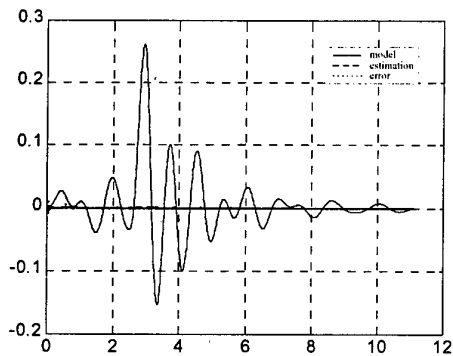


Figure 12. Rear Left Frame Distance (m)

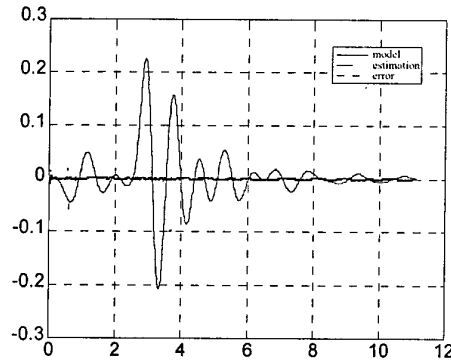


Figure 13. Rear Right Frame Distance (m)

4. Adaptive Sliding mode Suspension Controller

Controller based on neural networks model were derived by A.J. Morris, Keyser[7]. But this kind of neural networks can't be applied at real-time control, because most control responses are sensitive to neural network model and a long time of learning[4]-[7].

In this paper, we developed adaptive sliding mode suspension controller based on suggested new neural networks. Sliding mode control method is a kind of robust control which has a high performance in spite of model uncertainty and advantages of fast response feature and including nonlinear equations in controller.

The typical equation of sliding mode control is $x^{(n)} = f(x) + b(x)u$. But in this paper, because a controller is based on estimated neural networks, we just make an adaptation that method.

The output of neural networks is equation (4) which describe system.

$$y_j^{nn}(t) = F[\hat{A}y^p(t-1) + \hat{B}y^p(t-2) + \hat{C}u(t-1) + \hat{D}w(t-1) + \hat{E}e(t-1)] \quad (4)$$

As mentioned above, we assume that full-car model is second order. So sliding mode controller could be equation (5)

$$\begin{aligned} u &= -\hat{f} + \ddot{x}_d - \lambda \dot{\tilde{x}} - k \text{sat}(s/\phi) \\ \hat{f} &= F[\hat{A}y^p(t) + \hat{B}y^p(t-1) + \hat{C}u(t) + \hat{D}w(t) + \hat{E}e(t)] \\ \ddot{x}_d &= x_d = 0, \quad \lambda = 50 \\ k &= F + \eta = 10 \times |y(t)|^2 + 0.1, \quad \phi = 40 \end{aligned} \quad (5)$$

Since \dot{x} can not be computed directly, so we must estimate it as follows;

$$\begin{aligned}\hat{\ddot{x}}(t+1) &= \frac{y(t+1) - y(t)}{h} = \frac{y'''(t+1) - y(t)}{h} \\ y'''(t+1) &= F[\hat{A}y''(t) + \hat{B}y'(t-1) + \hat{C}u(t) + \hat{D}w(t) + \hat{E}e(t)]\end{aligned}\quad (6)$$

Figure 10. explains system identification and control at the same time

We estimate frame distances by proposed neural networks in these simulations. Then design the controller based on suggested neural networks model which makes 4 control output. To evaluate control performance, heave, pitch and roll motion are monitored instead of each frame distance.

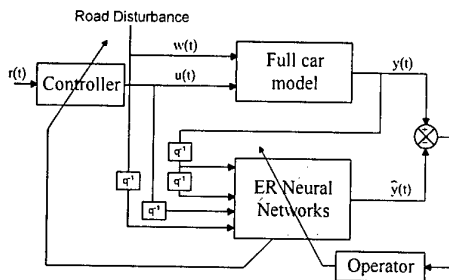


Figure 14. System control block diagram

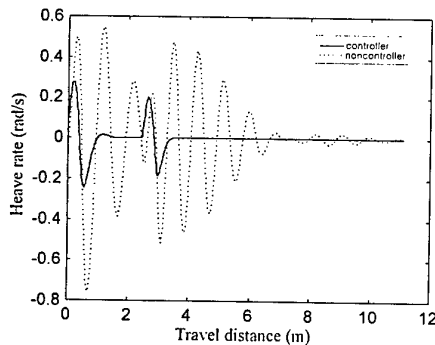


Figure 15. Heave motion

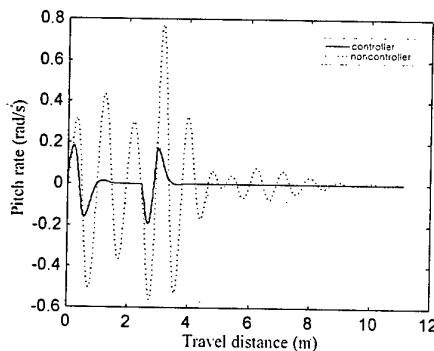


Figure 16. Pitch motion

Figure 15., Figure 16. and Figure 17. show each motion controlled by sliding mode controller, equation (5) when road condition is given as Figure 9. The result of different road disturbance such as sine wave, 2 bound sigmoid, etc was good, too.

5. Conclusion and Consideration

In this paper, new recurrent neural networks for improving convergence rate which have time delayed errors as a bias is suggested. And the performance is proved to be effective to estimation of fast variable system by computer simulations.

In order to get this results we compute desired values of hidden layer directly instead of transferring desired values by back-propagation and develop algorithm which updates weights by RLS in online.

According to the various testing results, new algorithm makes the real-time controller design based on neural networks easy, because the suggested algorithm is not so sensitive to initial weights, solves the problem of selecting learning rate and make a convergence fast.

The adaptive sliding mode controller for vehicle suspension is developed based on the suggested neural networks model. For more reality, we estimate frame distances instead of suspension strokes. According to computer simulations this controller was proved to be effective to suspension control.

References

- [1] Narendra. K. S. and Patthasarathy, "Identification and control of dynamical systems using neural networks", *IEEE Trans. Neural Networks*, Vol 1, pp. 4-27, 1990
- [2] Rumelhart, D. E. and McClelland, J. L., *Parallel Distributed Processing*, Vol. 1, MIT Press, Cambridge, MA, 1986
- [3] Scalero, R. S. and Tepedelenliouglu, N., "A fast new algorithm for training feedforward neural networks", *IEEE Trans. Signal Processing*, Vol. 40, pp. 202-210, 1992
- [4] Haykin, S., *Neural Networks : A Comprehensive Foundation*, Macmillan College Publishing Company Inc., NY, 1994
- [5] G.A.Montague, M.J.Willis and Morris, "Artificial neural network model based control", *ACC'94*, pp. 2134-2138, 1994
- [6] R. D. Keyser and Yonghong Tan, "Adaptive PID control with neural network based predictor", *CONTROL'94*, pp.1490-1494, 1994
- [7] A.Draeger, S.Engell, and H.Ranke, "Model predictive control using neural networks", *IEEE Control society*, October 1995, pp.61-66

Intelligent Signal Estimation Using Cosine Neural Networks with Variable Structure Systems Based Training Procedure

M. Onder Efe, Okay Kaynak and Feza Kerestecioglu

Bogazici University, Electrical and Electronic Engineering Department

Bebek, 80815 Istanbul, Turkey

{efemond, kaynak, kerestec}@boun.edu.tr

Abstract

This paper demonstrates the estimation of signals by using a neural network structure composed of cosine neurons. The building blocks of the architecture are cosine components with adjustable amplitude, frequency and phase. The training procedure is based on the mixture of gradient descent with a method utilizing sliding mode control philosophy. The proposed use of mixed information in training dynamics leads to the minimization of the cost of estimation as well as the cost of stability. Two application examples are presented in the paper. The first example considers the reconstruction of a time signal having finite frequency components in the spectrum. The second example shows the reconstruction of the frequency plot of a FIR filter.

1. Introduction

Signal estimation is an interdisciplinary area, the techniques of which are required in most engineering practice. The main issue in estimation theory is to construct an appropriate estimator, which gives descriptive information about the signal or system to be identified. Some approaches dealing with signal estimation adopt methods in the least squares sense [1].

Artificial neural networks have been studied extensively in the context of least squares [2]. Various applications mentioned in the literature utilize the least squares based training procedures. A common property of the neural systems is their mathematical tractability in the sense of evaluating the sensitivity derivatives easily. In this study, a simple way for the estimating the spectra of unknown signals is proposed with the introduction of a new neuron model, which we call *cosine neurons*. The proposed estimation scheme is carried out in time domain and operates on-line. The use of cosine neurons provides an important information about the shape of the frequency spectrum of the input signal. In general, if there is no closed-form time-domain equation of the input signal, it is considerably difficult to obtain its frequency domain

representation. Therefore a need arises for the use of an intelligent technique. The proposed approach has this characteristic and the fact that it can operate on-line makes it especially attractive.

At this point, the mechanism introducing the intelligence determines the overall performance of the estimator. Typically, the methods using the sensitivity derivatives of the cost function suffer from the shape of the cost surface, which is a multidimensional surface. In tuning the parameters, the information is extracted from the partial derivative of the cost function with respect to an adjustable parameter, along which the derivative may assume large values. Therefore, imposing a stabilizing force on training dynamics can eliminate the local unstability of gradient based techniques. This could be achieved by the use of Sliding Mode Control (SMC) philosophy in the training phase.

Earliest notion of SMC strategy was constructed on a second order system in the late 1960s by Emelyanov [3]. The work stipulated that a special line could be defined on the phase plane, such that any initial state vector can be driven towards the plane and then be maintained on it, while forcing the error dynamics towards the origin. The concept introduced by Emelyanov has first been applied to simple systems of order two. Since then, the theory has greatly been improved and a well defined design framework has been established. The sliding line has taken the form of a multidimensional surface, called the sliding surface and the function defining it is called the switching function. The main advantage introduced by the use of SMC approach is its robustness to unmodeled dynamics of the system under control. In this paper the system corresponds to the training dynamics.

Latest studies consider SMC approach with adjustable design parameters [4-5]. In [4], Kaynak *et al* demonstrate that the redesign of sliding surface can improve the performance of the overall control mechanism. The use of such techniques can therefore offer a practical alternative for stable training of intelligent systems. In [6-8], Efe and Kaynak demonstrate the distinguished performance introduced

by using Variable Structure Systems (VSS) analogy in the training of neuro-fuzzy systems.

The organization of this paper is as follows. The second section describes the problem and the conventional solution. The third section demonstrates the modified training procedure. In the fourth section simulation examples are presented. Conclusions constitute the last part of the paper.

2. Estimation by Cosine Neural Networks

The approach presented in this section is based on the matching of two signals in time-domain. A natural consequence of this is the similarity in the frequency views. For this reason, an estimator composed of finite number of cosine components is constructed as described by (1).

$$x_s(t) = \sum_{i=1}^{\text{neurons}} C_i \cos(w_i t + p_i) \quad (1)$$

where, x_s is the response of the estimator. C_i , w_i and p_i denote the amplitude, frequency and the phase of the i^{th} unit respectively. Let x_d and e denote the desired signal and estimation error respectively. In order to minimize the instantaneous cost defined by (2), gradient descent based update formula given by (3) is employed.

$$J = \frac{1}{2}(x_d - x_s)^2 = \frac{1}{2}e^2 \quad (2)$$

$$\Delta\phi_{GD} = -\eta_{GD} \frac{\partial J}{\partial \phi} \quad (3)$$

In (3), ϕ is a generic parameter of the neuroestimator and η_{GD} is the learning rate from the interval (0,1). The subscript GD denotes the gradient descent. Having this in mind, the update formulas for i^{th} unit can be described in (4) through (6).

$$\Delta C_i = \eta e \cos(w_i t + p_i) \quad (4)$$

$$\Delta w_i = -\eta e C_i \operatorname{rem}\left(t, \frac{2\pi}{w_i}\right) \sin(w_i t + p_i) \quad (5)$$

$$\Delta p_i = -\eta e C_i \sin(w_i t + p_i) \quad (6)$$

3. Variable Structure Systems Based Extraction of Stabilizing Information

The methods of computational intelligence frequently utilize the gradient based training procedures for parameter tuning. As mentioned earlier,

the most crucial point in training of a neuro-fuzzy system is the fact that the training procedure tries to minimize the cost, which is a function of the realization error. However, during the training phase, there is no force ensuring the parametric stability or convergence. The approach analyzed here demonstrates how a VSS based stabilizing information could be incorporated into the learning strategy adopted.

The parameter tuning formula given by (3) can be approximated by a first order system given by (7). In (7), T_s denotes the sampling period. If the parametric displacement $\Delta\phi$ is defined as the sliding line for parameter ϕ , adopting the reaching law in (8) and equating (7) and (8) yields the solution in (9).

$$\dot{\Delta\phi} = -\frac{1}{T_s} \Delta\phi + \frac{\eta e}{T_s} \frac{\partial x_s}{\partial \phi} \quad (7)$$

$$\dot{\Delta\phi} = -\frac{Q_\phi}{T_s} \tanh(\Delta\phi) - \frac{K_\phi}{T_s} \Delta\phi \quad (8)$$

$$\Delta\phi = \eta e \frac{\partial x_s}{\partial \phi} + Q_\phi \tanh(\Delta\phi) + K_\phi \Delta\phi \quad (9)$$

For the stability of the proposed solution, (10) is chosen as a Lyapunov function. Parametric stability is ensured if the inequality in (11) holds true.

$$V_\phi = \frac{1}{2}(\Delta\phi)^2 \quad (10)$$

$$\dot{V}_\phi = \left(\dot{\Delta\phi} \right) \Delta\phi < 0 \quad (11)$$

If (7) and (9) are substituted into (11), the following selection of learning rate satisfies the negative definiteness of the time derivative of the Lyapunov function in (10). This selection of η is given by (12).

$$\eta_\phi = \beta \min \left(\left| \frac{\Delta\phi}{N_\phi} \right|, \left| \frac{A_\phi}{N_\phi} \right| \right) \quad (12)$$

where,

$$N_\phi = e \frac{\partial x_s}{\partial \phi} \quad (13)$$

Define the following quantity;

$$A_\phi = Q_\phi \tanh(\Delta\phi) + K_\phi \Delta\phi \quad (14)$$

with β being a constant from the interval (0,1).

If this choice of η_ϕ is used in the approximate model of training dynamics (7), the stabilizing component of parameter update formula, which is given by (15), is obtained.

$$\Delta\phi_{VSS} = \beta \min(|\Delta\phi|, |A_\phi|) \text{sgn}(N_\phi) + A_\phi \quad (15)$$

At this point, one might argue that whether this rule leads to the minimization of realization error or not. Clearly, the rule described above will enforce the adjustable parameters to settle down but will not minimize the cost in (2). An appropriate combination of this rule and gradient technique can result in the minimization of both the realization error and the displacement magnitude of the relevant parameter. This mixture can be performed by utilizing a weighted average as described in (16).

$$\Delta\phi = \frac{\alpha_1 \Delta\phi_{VSS} + \alpha_2 \Delta\phi_{GD}}{\alpha_1 + \alpha_2} \quad (16)$$

In (16), α_1 and α_2 are positive weights and determine the influence of each approach in the final value of the parameter change vector.

4. Simulation Results

Two simulation examples are presented. In the first example, a signal having finite frequency components in the spectra is reconstructed. The second example reveals the performance of the proposed scheme in extracting the frequency plot of a FIR filter.

4.1. Reconstruction of a Signal

In this part the signal described by (17) is reconstructed by the proposed structure and the training procedure. The desired and estimated signals are illustrated in Fig. 1.

$$x_d(t) = \sum_{j=1}^4 \frac{\sin[(2j+1)t]}{2j+1} \quad (17)$$

In Fig. 2, the discrepancy between desired and estimated signals is depicted. For each period of the desired signal, a 628-point Fast Fourier Transform (FFT) is evaluated and corresponding to each period, results are given in Fig. 3 where the upper limit of the horizontal axis is adjusted such that the nonzero frequency components are easily seen. In this figure, the top row is the FFT of the desired signal (17). Subsequent plots in Fig. 3 illustrate the 628-point FFT

of the estimated signal, which corresponds to 2π seconds in time-domain. Starting from the second period, the estimated spectral view and the desired one become nearly indistinguishable.

In (18), the cost of stability is formulated. In Fig. 4, the time behavior of this quantity is illustrated whereas Figs. 5 and 6 demonstrate the realization error and the cost of stability without using parameter stabilizing information derived in the third section.

$$J_s = \sum_{i=1}^n \Delta C_i^2 + \Delta w_i^2 + \Delta p_i^2 \quad (18)$$

During the simulations of signal reconstruction example, following parameters are used as the simulation settings.

Table 1. Simulation Settings for Signal Reconstruction

#Neurons	5
β	0.99
η_{GD}	0.01
Q	0.10
K	0.10
α_1	3.00
α_2	1.00
T_s	10 msec

4.2. Extraction of Frequency Plot of a FIR Filter

In this section, the average power spectral density (PSD) plot of a FIR filter is extracted by the use of the algorithm presented. The filter has the following transfer function.

$$H(z) = 1 + 0.999z^{-2} \quad (19)$$

In Fig. 7, the averaged power spectral density graph is illustrated for an intermediate step. As the input signal, a white noise sequence generated by Matlab is used. For this case following parameters are used as the simulation settings.

Table 1. Simulation Settings for Frequency Plot Extraction

#Neurons	3
β	0.01
η_{GD}	0.90
Q	0.10
K	0.10
α_1	1.00
α_2	1.00
T_s	10 msec

5. Conclusions

The method reported in this paper demonstrates that the conventional training procedures for computationally intelligent systems, such as neural networks, fuzzy systems or methods adapted from artificial intelligence can be incorporated with methodologies leading to parametric stability.

Variable Structure Systems technique or Sliding Mode Control philosophy is one of the methods which is well-known with its robustness to unmodeled internal dynamics of the system under investigation. A suitable combination of traditional training methods with VSS technique can offer much preferable solutions in the sense of safety. This is apparent from the comparison of estimation error trends illustrated in Figs. 2 and 5, and the cost of stability plots depicted in Figs. 4 and 6.

In this study, the performance of the proposed approach has been demonstrated on the estimation of signals and extraction of frequency plot of a FIR filter. The strategy is based on the matching of signals in time-domain. Naturally, if two signals have similar views in time-domain, their frequency plots are similar. The estimator studied in this study comprises cosine-like basis functions with adjustable parameters. The developed method tunes the parameters on-line.

Various identification and control oriented applications of the proposed approach clearly stipulate that the method is capable of eliminating the locally divergent behavior of gradient based training approaches. This study demonstrates that the method can also be used in signal processing applications.

6. References

- [1] T. Söderström, *Discrete-time Stochastic Systems*, Prentice Hall, New Jersey, 1994.
- [2] S. Haykin, *Neural Networks*, Macmillan College Printing Company, New Jersey, 1994.
- [3] S. V. Emelyanov, *Variable Structure Control Systems*, Moscow, Nauka, 1967.
- [4] O. Kaynak, F. Harashima and H. Hashimoto, "Variable Structure Systems Theory, as Applied to Sub-time Optimal Position Control with an Invariant Trajectory," *Trans. IEE of Japan*, Sec. E, v.104, no.3/4, pp.47-52, 1984.
- [5] N. Bekiroglu, "Adaptive Sliding Surface Design for Sliding Mode Control Systems," Ph.D. Thesis, Bogazici University, 1996.
- [6] M. O. Efe and O. Kaynak, "A Novel Optimization Procedure for Training of Fuzzy Inference Systems By

Combining Variable Structure Systems Technique and Levenberg-Marquardt Algorithm," *Fuzzy Sets and Systems* (Submitted for publication).

[7] M. O. Efe and O. Kaynak, "Stable Training of Computationally Intelligent Systems By Using Variable Structure Systems Technique," *IEEE Transactions on Industrial Electronics* (Submitted for publication)

[8] M. O. Efe and O. Kaynak, "A Hybrid Training Procedure for Artificial Neural Networks Leading to Parametric Stability and Cost Minimization," The 7th Int. Conf. on Emerging Technologies and Factory Automation, ETFA'99, Spain (Submitted for publication)

6. Acknowledgments

This work is supported by the Bogazici University Research Fund (Grant No: 97A0202 and 99A202) and Foundation for Promotion of Advanced Automation Technology, FANUC.

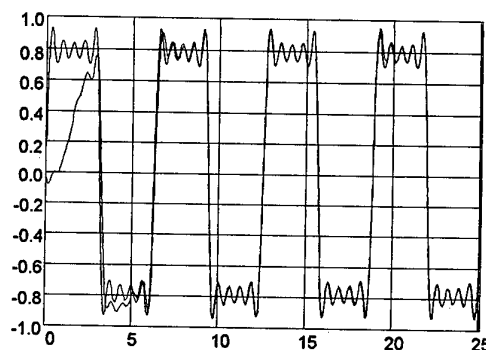


Figure 1. Desired and Estimated Signals

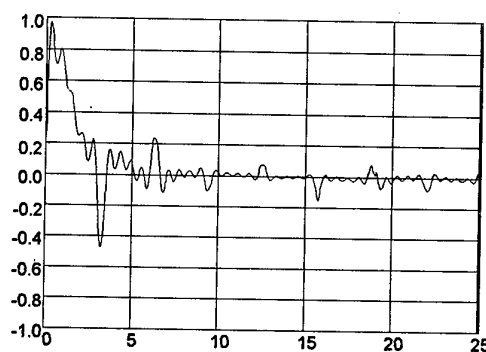


Figure 2. Estimation Error

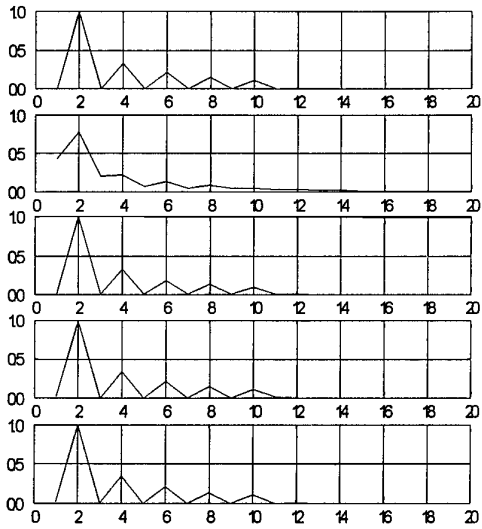


Figure 3. 628-Point FFT of the Desired Signal (top row) and Time Evolution of 628-Point FFT of Estimated Signal Corresponding to Each 2π Seconds

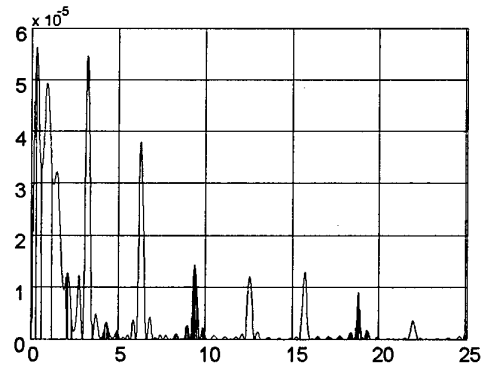


Figure 4. Cost of Stability with VSS and Gradient Descent Based Training Information Mixture

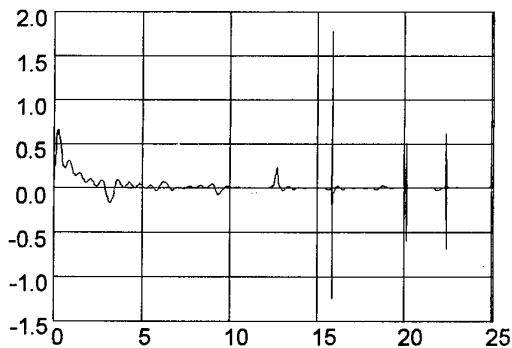


Figure 5. Estimation Error without VSS Based Component in Training Information

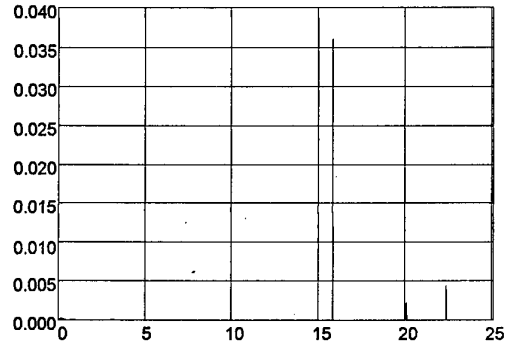


Figure 6. Cost of Stability without VSS Based Component in Training Information

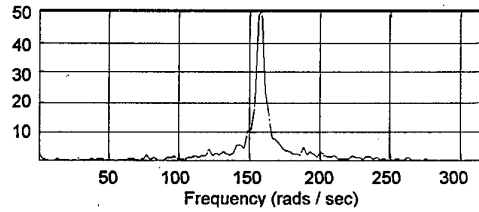
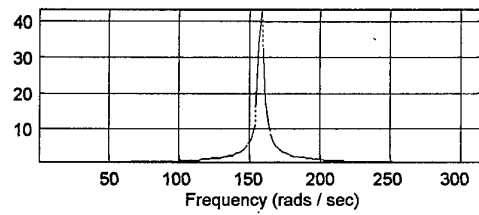


Figure 7. Desired Average Power Spectral Density and Estimated Average Power Spectral Density

Practical Evaluation of V.S.C. with Varying Bounds of Robot Manipulator *

Pierre Nigrowsky[¶] Antonio Visioli[§] Peter Turner[¶]

[¶]Electrical and Electronic Engineering Dept.
Brunel University - U.K.
e-mail: pierre.nigrowsky@brunel.ac.uk

[§]Dipartimento di Elettronica per l'Automazione
University of Brescia - Italy
e-mail: visioli@bsing.ing.unibs.it

Abstract

In this paper we present an experimental evaluation of a new type of Variable Structure Control with sliding mode for robot manipulators. The controller design is based on a Lyapunov approach and engineering considerations about the robot model are adopted in order to limit the chattering effect. Experiments are performed by means of an industrial SCARA robot, whose dynamic model parameters are estimated according to a simple procedure. Tracking errors have been evaluated accomplishing different kinds of trajectories and the obtained results show the valuability of the devised controller which appears to be better than other standard methodologies.

1 Introduction

Robot manipulators are highly nonlinear systems, traditionally controlled by assuming that the joints are independent of each other and interactions between them are considered as disturbances. This assumption is valid when there is a large reduction ratio between the actuator and the joint, and when the performances are not too demanding; in this case PID like controllers are generally sufficient. However, the requirements for robot manipulators nowadays can not be satisfied anymore with such approaches. This has lead to the development of new types of controllers that take into account the joint couplings. In the model based methodology [1], the dynamic equations of robot are integrated in the controller as a feedforward term. The implementation of such equations results in a overall linearized system. The linearization is efficient as long as the model used perfectly matches the robot system [2]. In practical applications, such an ideal situation is not obtained, since the adopted model has some pa-

rameter uncertainties as well as unmodeled structures. To deal with that, the controller must be made adaptive or robust so that it copes with the uncertainties and/or mismatches.

Variable structure with sliding mode is a robust control methodology that can deal with large disturbances [3]. It has gained popularity in the recent years, because of its versatile nature and inherent robustness properties. The scheme can be applied to linear as well as to nonlinear systems and it can provide consistent responses in presence of large uncertainties and disturbances. Since the first application of variable structure control with sliding mode to robotics by Young [4], the number of reported applications in this field has kept increasing (see, for example, [5, 6, 7]).

In the initial control scheme used by Young [4], hierarchical methodology [3], is adopted for the controller design. The sliding mode on each sliding surface takes place in a specific order; this requirement necessarily slows down the convergence of the tracking error. Furthermore, to achieved this result, the control laws are complicated and do not take advantage of the robot dynamic structure and are therefore not very effective. Slotine [8] proposes to use a computed torque feedforward term to somehow linearize the overall system and he compensates the uncertainties of the feedforward term with a VSC element. The sliding manifolds are considered to be independent, hence sliding mode occurs on the manifolds in a free order thereby increasing the speed of convergence of the tracking errors. The controller is designed so that the sliding condition is guaranteed for each sliding surface [3, 8]. This requires an estimate of the inverse of the inertia matrix, and results in a complex set of equations to be satisfied for the control law. The scheme has shown to be effective for trajectory tracking of robot manipulator, but the control effort is however conservative, which results in large chattering. Slotine addresses this problem by

*Partial support for this research has been provided by E.P.S.R.C. and M.U.R.S.T.

replacing the discontinuous function by a variable saturation one (referred as suction control [9]). The chattering problem is solved at the price of the robustness and sliding mode is no more guaranteed. Bailey *et al.* [10] propose to design a controller by using a Lyapunov function that characterizes the overall tracking error behaviour of the system. The resulting equations to be satisfied for the controller design are much simpler than in Slotine's proposal. With this approach the sliding mode on each sliding surface is however not anymore guaranteed. Instead, sliding mode occurs at the intersection of all the sliding surfaces. The chattering problem still occurs but in a reduced form. Bailey *et al.* tackles it by using a saturation function instead of the pure discontinuous function.

Even if Slotine and Bailey schemes depart from different perspectives, the resulting controller structure is similar, and both address the chattering problem after the controller designed has been completed.

The controller proposed in this paper addresses the problem of chattering directly in its design. The design is based on engineering considerations of the robot manipulator equations and structure. The scheme is tested on the ICOMATIC SCARA 03 robot manipulator installed in the Applied Mechanics and Robotics Laboratory of the University of Brescia.

2 Variable Structure Control with varying bounds

The most significant limitation with robot control algorithms employing VSC with sliding mode is the chattering phenomenon, which can damage the overall electromechanical structure, as well as reduce the motion performances. The general approach to overcome it is to replace the switching function by a smoother one [9, 10, 11]. This general approach however seriously alters the performances of the controller. The controller proposed in this paper addresses chattering during its design stage.

The well-known dynamic model of a n -joint robot manipulator can be written as follows:

$$T = M(\theta)\ddot{\theta} + C(\theta, \dot{\theta})\dot{\theta} + G(\theta) + F(\dot{\theta}) \quad (1)$$

where θ is the $n \times 1$ joint angle vector, T is the $n \times 1$ input torque vector (control variable), $M(\theta)$ is the $n \times n$ inertia matrix, which is symmetric positive definite, $C(\theta, \dot{\theta})$ is the $n \times n$ matrix representing the centrifugal and Coriolis terms, $G(\theta)$ is the $n \times 1$ vector of the gravity terms and $F(\dot{\theta})$ is the friction term. Note that $C(\theta, \dot{\theta})$ is defined such that it verifies the skew-symmetric property:

$$x^T [\dot{M}(\theta) - 2C(\theta, \dot{\theta})]x = 0 \quad \forall x \in \mathbb{R}^n.$$

Similarly to [10], the controller design relies on a pseudo-energy Lyapunov function:

$$V = \frac{1}{2} S^T M S \quad (2)$$

where $S = [S_1 \dots S_n]^T$ is the column vector for the sliding surfaces where each sliding surface S_i is defined as ($i = 1, \dots, n$):

$$\begin{aligned} S_i &= (\dot{\theta}_i - \dot{\theta}_{di}) + \lambda_i(\theta_i - \theta_{di}) \\ &= \tilde{\dot{\theta}}_i + \lambda_i \tilde{\theta}_i \end{aligned} \quad (3)$$

where θ_i and $\dot{\theta}_i$ are the angular position and velocity of the i -th joint, θ_{di} and $\dot{\theta}_{di}$ are the desired position and velocity respectively for the i -th joint and λ_i is a constant that defines the slope of the i -th sliding surface. We consider the following general controller structure:

$$T = \widehat{M}(\theta)\dot{e} + \widehat{C}(\theta, \dot{\theta})e + \widehat{G}(\theta) + \widehat{F}(\dot{\theta}) + Ts \quad (4)$$

where $\widehat{(\cdot)}$ is the parameter estimate, $e = (\dot{\theta}_d - \dot{\tilde{\theta}})$, which is the velocity demand augmented by the position error and similarly $\dot{e} = (\ddot{\theta}_d - \ddot{\tilde{\theta}})$ represents the acceleration demand augmented by the velocity error (note that $\tilde{\theta} = \theta - \theta_d$). As shown by Nigrowsky *et al.* [12], the controller must satisfy the following equation:

$$\dot{V} = S^T [\tilde{F}(\dot{\theta}) + \tilde{G}(\theta) + \tilde{C}(\theta, \dot{\theta})e + \tilde{M}(\theta)\dot{e} + Ts] \leq 0 \quad (5)$$

where $\tilde{(\cdot)}$ is the parameter error. Bounds on each elements $\tilde{F}(\dot{\theta})$, $\tilde{G}(\theta)$, $\tilde{C}(\theta, \dot{\theta})$, $\tilde{M}(\theta)$, e and \dot{e} in the above equation can be established by considering their physical natures. For a robot manipulator, the positions of the joints are physically bounded, and since $\tilde{M}(\theta)$ and $\tilde{G}(\theta)$ are functions of the joint position, they are also bounded. In a similar way, bounds on $\tilde{C}(\theta, \dot{\theta})$ and $\tilde{F}(\dot{\theta})$ are established by assuming the boundness of the joint position and its physically possible velocity. Indeed, the terms $\tilde{F}(\dot{\theta})$, $\tilde{G}(\theta)$, $\tilde{C}(\theta, \dot{\theta})$ and $\tilde{M}(\theta)$ can be bounded by a constant term K_1 . The bounds for e can simply be taken as a constant term with a velocity error, i.e. $k_1^e + k_2|\tilde{\theta}|$. Similarly, \dot{e} is bounded by $k_1^{\dot{e}} + k_3|\tilde{\dot{\theta}}|$. Hence, the inverse dynamic error $|\tilde{F}(\dot{\theta}) + \tilde{G}(\theta) + \tilde{C}(\theta, \dot{\theta})e + \tilde{M}(\theta)\dot{e}|_i$ can be bounded as follows ($i = 1, \dots, n$):

$$|\tilde{F}(\dot{\theta}) + \tilde{G}(\theta) + \tilde{C}(\theta, \dot{\theta})e + \tilde{M}(\theta)\dot{e}|_i < k_{1i} + k_{2i}|\tilde{\theta}_i| + k_{3i}|\tilde{\dot{\theta}}_i| \quad (6)$$

where k_{1i} , k_{2i} and k_{3i} are positive constant terms. Let define:

$$K_i(\tilde{\theta}_i, \tilde{\dot{\theta}}_i) = k_{1i} + k_{2i}|\tilde{\theta}_i| + k_{3i}|\tilde{\dot{\theta}}_i| \quad (7)$$

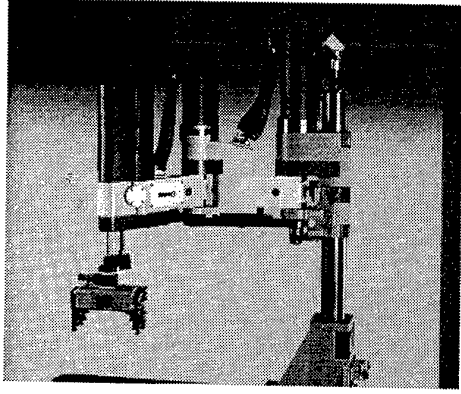


Figure 1: The SCARA ICOMATIC 03 situated in the Applied Mechanics and Robotics Laboratory of the University of Brescia.

The negativeness of \dot{V} can be guaranteed by taking

$$Ts_i = -K_i(\tilde{\theta}_i, \dot{\tilde{\theta}}_i) \text{sgn}(S_i).$$

With such bounds on the system uncertainties, the chattering magnitude is greatly reduced. Chattering is however not completely overcome because of the term k_{1i} , and the magnitude of the chattering is directly proportional to the magnitude of k_{1i} . To overcome this problem, k_{1i} is removed and k_{2i} and k_{3i} are slightly overestimated to compensate for the missing term. In this way, a problem occurs when $\tilde{\theta}_i$ and $\dot{\tilde{\theta}}_i$ are close to zero; since the boundness of the uncertainties is not anymore guaranteed, an offset occurs at the regulation point [12]. To remove it, an integral action is used. Hence, the control law is:

$$T = \hat{M}(\theta)\dot{e} + \hat{C}(\theta, \dot{\theta})e + \hat{G}(\theta) + \hat{F}(\dot{\theta}) + K(\tilde{\theta}, \dot{\tilde{\theta}}) \text{sgn}(S) + K_I \int_0^T \tilde{\theta} dt, \quad (8)$$

where

$$K(\tilde{\theta}, \dot{\tilde{\theta}}) = [K_1(\tilde{\theta}_1, \dot{\tilde{\theta}}_1), K_2(\tilde{\theta}_2, \dot{\tilde{\theta}}_2), K_3(\tilde{\theta}_3, \dot{\tilde{\theta}}_3), \dots]^T$$

and

$$K_i(\tilde{\theta}_i, \dot{\tilde{\theta}}_i) = k_{1i}|\tilde{\theta}_i| + k_{2i}|\dot{\tilde{\theta}}_i|.$$

The term K_I is column vector of constant terms for the integral action.

3 Estimation of the dynamic model of a SCARA robot

To test the devised Variable Structure Controller with varying bounds, we adopted a two degrees-of-freedom

SCARA robot, which is widely adopted in industrial environments for assembly tasks. Specifically, the SCARA ICOMATIC 03 robot manipulator has been employed. It has been built by Icomatic of Gussago (Brescia, Italy) and installed in the Applied Mechanics and Robotics Laboratory of the University of Brescia. The robot, shown in Figure 1, has actually three degrees-of-freedom, but the third link, which is devoted to move the gripper up and down, has not been involved in the experiments since its dynamics is completely decoupled from the others. The first two links are actuated by means of two direct current motors endowed with Harmonic Drive reduction gears (the reduction ratio is $\tau = 1/100$). The positions of the two joints are measured by means of incremental encoders (with a resolution of $\pi \cdot 10^{-5}$ rad/step) and the velocity measurements are provided by tachometers. The torque applied to the motors can be measured by a current test-point in the drive.

The robot is controlled by means of an open PC-based control architecture with QNX real-time operating system, which assures a closed-loop control frequency of 1kHz. In order to implement the controller, an estimate of the dynamic model is required [13]. Assuming that no external forces and torques are applied, the dynamic model of the robot can be written as follows (note that no gravity terms are present):

$$\begin{bmatrix} T_1 \\ T_2 \end{bmatrix} = \begin{bmatrix} m_{11} & m_{12} \\ m_{21} & m_{22} \end{bmatrix} \begin{bmatrix} \ddot{\theta}_1 \\ \ddot{\theta}_2 \end{bmatrix} + \begin{bmatrix} f_1(\dot{\theta}_1) \\ f_2(\dot{\theta}_2) \end{bmatrix} + \begin{bmatrix} -m_2 g_2 c(\dot{\theta}_1^2 + 2\dot{\theta}_1 \dot{\theta}_2) - m l_2 c(\dot{\theta}_1^2 + 2\dot{\theta}_1 \dot{\theta}_2) \\ m_2 g_2 c \dot{\theta}_1^2 + m l_2 c \dot{\theta}_1^2 \end{bmatrix} \quad (9)$$

where T_1 and T_2 are the torques applied to the links, l_1 and l_2 are the lengths of the links, m , m_1 and m_2 are the masses of the payload and of the two links and f_1 and f_2 are the dynamic friction functions of the two links. The elements of the inertia matrix have the following expressions:

$$\begin{aligned} m_{11} &= m\lambda^2 + m_1 g_1^2 + m_2 r^2 + J + J_{G1} + J_{G2}; \\ m_{12} &= m_{21} = m l_2 \mu + m_2 g_2 b + J + J_{G2}; \\ m_{22} &= m l_2^2 + m_2 g_2^2 + J + J_{G2}. \end{aligned}$$

where g_1 and g_2 are the distances of the centres of mass of the two links from the related joint and J , J_{G1} and J_{G2} are the inertia moments of the payload and of the two links with respect to the centre of mass. Finally, r^2 , b , c , λ^2 , μ^2 are geometric parameters that depend on the links position:

$$\begin{aligned} r^2 &= l_1^2 + g_2^2 + 2l_1 g_2 \cos(\theta_2); \\ b &= g_2 + l_1 \cos(\theta_2); \\ c &= l_1 \sin(\theta_2); \\ \lambda^2 &= l_1^2 + l_2^2 + 2l_1 l_2 \cos(\theta_2); \\ \mu^2 &= l_2^2 + l_1 \cos(\theta_2). \end{aligned}$$

Taking into account the presence of the reduction gears, the dynamic model can also be written with respect to the actual torque generated by the motors. With this aim, some simplifying assumptions can be made. Since the motors of the second and third links are located at the end of the first and second link respectively, the masses of the first and second link can be considered as lumped at the end of the same links (i.e. $g_1 \cong l_1$ and $g_2 \cong l_2$ and the values of J_{G1} and J_{G2} can be neglected). Then, considering also $l_1 = l_2 = l$ we have:

$$\begin{bmatrix} T_{m1} \\ T_{m2} \end{bmatrix} = \begin{bmatrix} J_1 + \tau^2 m_{11} & \tau^2 m_{12} \\ \tau^2 m_{12} & J_2 + \tau^2 m_{22} \end{bmatrix} \begin{bmatrix} \ddot{\theta}_{m1} \\ \ddot{\theta}_{m2} \end{bmatrix} + \tau m_2 l c \begin{bmatrix} -\dot{\theta}_{m1} & -\dot{\theta}_{m1} \\ \dot{\theta}_{m1} & 0 \end{bmatrix} \begin{bmatrix} \dot{\theta}_{m1} \\ \dot{\theta}_{m2} \end{bmatrix} + \begin{bmatrix} f_1(\dot{\theta}_{m1}) \\ f_2(\dot{\theta}_{m2}) \end{bmatrix}, \quad (10)$$

where T_{mi} is the torque applied to the i -th motor, $\dot{\theta}_{mi}$ and $\ddot{\theta}_{mi}$ are the velocity and acceleration respectively of the i -th motor, J_i is the sum of the known inertia moments of the i -th motor and the i -th reduction gear ($i = 1, 2$), and:

$$\begin{aligned} m_{11} &= m_1 l^2 + m_2 r^2; \\ m_{12} &= m_2 l b; \\ m_{22} &= m_2 l^2; \\ r^2 &= 2l^2(1 + \cos \theta_2); \\ b &= l(1 + \cos \theta_2); \\ c &= l \sin \theta_2. \end{aligned}$$

The first estimation that can be performed is the one regarding the dynamic friction. From equation (10), it appears that the inertia effects can be set to zero by simply moving the joints at a constant velocity (i.e. the acceleration is zero). Moreover, setting to zero the velocity of a single joint, the dynamic term representing the Coriolis and centrifugal torques is cancelled, so that only the term regarding the friction of the other joint is present. The above functions f_i ($i = 1, 2$) for the two joints have been numerically evaluated by executing different motions of single joints with different constant velocities and measuring the torque. The resulting numerical values have been subsequently interpolated by polynomial functions.

Once the friction functions have been estimated, the approximate values of the inertial parameters can be determined. The method consists of executing different experiments in which the two links are moved separately with piecewise constant accelerations, so that $C(\theta, \dot{\theta})\dot{\theta} = 0$ and the only unknown values in equations (10) are the elements of the inertia matrix. Since the element m_{11} depends on the position of the second link, it appears that the motor torque T_{m1} depends on the position of the second link too. For this reason, we fixed $\theta_2 = 0$, evaluating $J_{r1} = J_1 + \tau^2(m_1 l^2 + 4m_2 l^2)$.

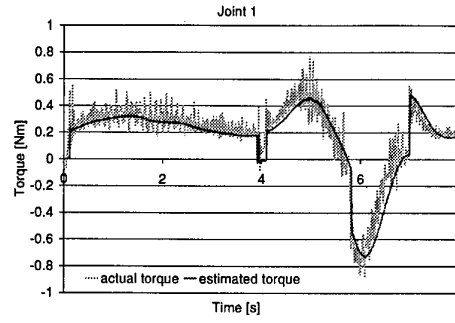


Figure 2: Estimated and actual torque for the joint 1 motion.

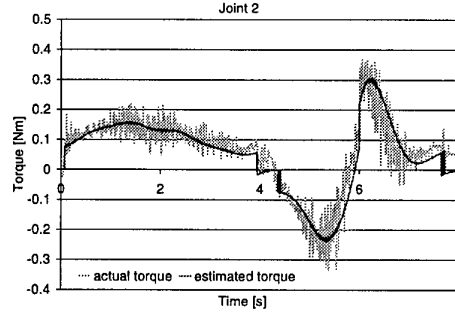


Figure 3: Estimated and actual torque for the joint 2 motion.

Note that for the motor of the second joint, the value of $J_{r2} = J_2 + \tau^2 m_{22}$ does not depend on the position of the first one. From the experimentally obtained values of J_{r1} and J_{r2} , it is easy to determine the values of m_1 and m_2 and consequently the values of the elements of the matrix representing the Coriolis and centrifugal torques.

To see how accurate the obtained model is, in Figures 2 and 3 are reported the estimated and the actual torque for a point-to-point motion followed by a circular torque, which covers a large portion of the robot workspace. It appears that, in spite of the simplifying assumptions, the obtained model is accurate.

4 Results

Various trajectories have been used to evaluate the tracking error. Specifically, a point to point motion from $(\theta_1^1, \theta_2^1) = (0, 0)$ to $(\theta_1^2, \theta_2^2) = (\pi/2, \pi/2)$ in 2s has been performed on the robot, with a piecewise constant acceleration profile (see Figure 4). Then, a linear trajectory in the Cartesian space from $(x_1, y_1) = (-0.3, 0.54)$ to $(x_2, y_2) = (0.6, 0.16)$ has been accomplished in 4s (see Figure 5). Finally, a circular trajectory in the Cartesian space, centered in $(x_c, y_c) = (0, 0.5)$ and with radius equal to 0.1m has been performed in 4s (see Figure 6). It has to be observed that

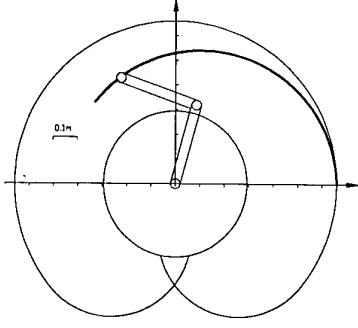


Figure 4: Cartesian space representation of the point-to-point trajectory, to be accomplished in 2s.

these trajectories require different torque levels.

Regarding the tuning of the parameters k_{1i} , k_{2i} and k_{Fi} ($i = 1, 2$), in order to assure a low tracking position error, the value of k_{1i} has to be much greater than the other two values. For each trajectory, the maximum and the mean absolute position tracking error of the end-effector has been evaluated. The end-effector position has been determined by applying the direct kinematics to the joint positions and therefore the presence of elasticities in the mechanical structure and calibration errors have not been taken into account. Note that, according to the ISO standard [14], the tracking error for the linear and circular trajectories have been calculated as the minimum difference between the real end-effector position and the reference trajectory. Furthermore, an additional parameter, inspired by the concept of accuracy and repeatability [14], has also been evaluated: it is defined as

$$E_i = \bar{e} + 3\sigma_e$$

where \bar{e} is the average value of the absolute error and σ_e is the standard deviation of e . Results are shown in Table 1. It has to be stressed that for all the experimented motions, the resulting final error is zero.

It appears that in general the adopted controller assures a low tracking error, since its maximum value for the linear and circular trajectory, where the tracking is of major concern, is about 0.1mm and the mean absolute error is not much greater than 0.01mm; hence it is close to the maximum performance achievable by the encoder resolution (note that an error of one encoder step for each joint corresponds to a maximum error on the end-effector of 0.01mm). To better evaluate the achieved performances, it is interesting to compare them with the ones obtained by the typical computed-torque controller [15] and the typical PID-based controller, which consists of two nested loops: the inner (which is analogically built in the drive), is devoted to control the velocity of the joint and the outer (imple-

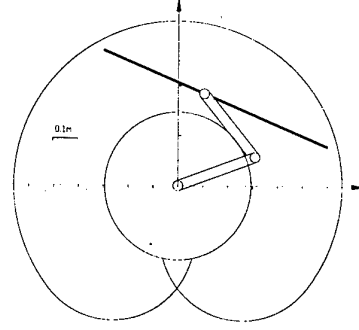


Figure 5: Cartesian space representation of the linear trajectory, to be accomplished in 4s.

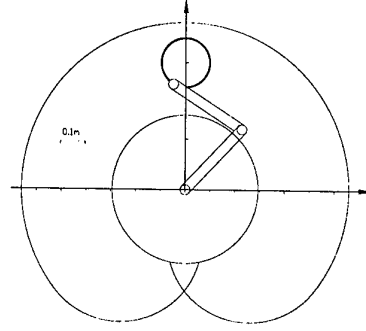


Figure 6: Cartesian space representation of the circular trajectory, to be accomplished in 4s.

mented digitally in the PC) is devoted to control the position. For these two controllers, results obtained performing the circular trajectory are shown in Table 2. It turns out that the variable structure control assures overall better performances with respect to the standard methodologies.

Regarding the chattering, it comes out that no particularly significant vibrations are introduced by the controller. To verify it, the torque signal relative to the first joint during the linear trajectory has been directly read from the current test point of the drive and not filtered. It has been plotted in Figures 7 and 8 for the VSC and the PID-based controller respectively. It has also to be stressed that chattering can be reduced by detuning the sliding mode controller and allowing a larger tracking error.

Trajectory	max	mean	E_i
point-to-point	0.253	0.048	0.023
linear	0.081	0.016	0.056
circular	0.104	0.019	0.069

Table 1: End-effector tracking errors (in [mm]) for the different experimented trajectories.

Controller	max	mean	E_i
PID	0.430	0.132	0.526
computed-torque	0.172	0.039	0.102

Table 2: End-effector tracking errors (in [mm]) for the PID-based and computed-torque control laws.

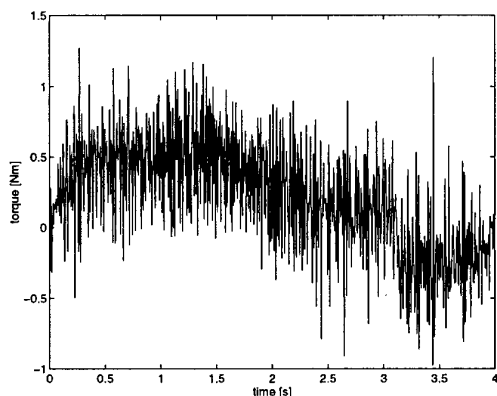


Figure 7: Torque signal for the variable structure controller performing the linear trajectory (joint 1).

5 Conclusions

In this paper we have presented an experimental evaluation of a new type of variable structure controller for robot manipulators. Engineering considerations are used in the design of the controller, which is based on a Lyapunov approach, and to limit the chattering effect the bounds are made variable. The tracking errors obtained for the different trajectories by means of an industrial SCARA robot show the effectiveness of the devised controller. It is also observed that the obtained results outperformed standard control algorithms, without significantly increasing the chattering.

References

- [1] C.H. An, C.G. Atkeson, J.M. Hollerbach "Model-Based control of a robot manipulator", The MIT Press, 1988.
- [2] P.K. Khosla, T. Kanade, "Real-Time Implementation and Evaluation of Computed-Torque Scheme", IEEE Trans. on Rob. and Aut., Vol. 5, No. 2, 1989.
- [3] V.I. Utkin, "Sliding Mode Control and its Applications to Variable Structure Systems", Mir (Moscow), 1978.
- [4] K.K.D. Young, "Controller design for a manipulator using the theory of variable structure systems", IEEE Trans. Syst. Man Cybern., Vol. 8, No. 2, pp. 1079-1085, 1978.
- [5] M. Hiroi, M. Hojo, Y. Hashimoto, Y. Abe, Y. Dote, "Microprocessor-Based Decoupled Control of Manipulator Using Modified Model-Following Method with Sliding Mode", IEEE Trans. Indus. Elect., Vol. IE-33, No. 2, pp. 110-113, 1986.
- [6] S. R. Habibi, R. J. Richards, "Sliding mode control of an electrically powered industrial robot", IEE Proc. D, Vol. 139, No. 2, pp. 207-225, 1992.
- [7] P. Nigrowsky, P.J. Turner, "Hybrid Controller Algorithms for the purpose of fast Tracking of a Non-linearly Actuated Robotic Arm", 3rd Int. ICSC Symp. on IIA and SOCO, Genova (I), 1999.
- [8] J. J. Slotine and S.S. Sastry, "Tracking control of nonlinear systems using sliding surfaces, with application to robot manipulators", Int. J. Control, Vol. 38, No. 2, pp. 465-492, 1983.
- [9] J. J. Slotine, "The Robust Control of Robot Manipulators", Int. J. of Robotics Research, Vol. 4, No. 2, pp. 49-64, 1985.
- [10] E. Bailey, A. Arapostathis, "Simple sliding mode control scheme applied to robot manipulators", Int. J. Control, Vol. 45, No. 4, pp. 1197-1209, 1987.
- [11] B. Yao, M. Tomizuka, "Smooth Robust Adaptive Sliding Mode Control of Manipulators With Guaranteed Transient Performance", Trans. ASME J. Dyn. Syst. Meas. and Control, Vol. 118, pp. 764-775, 1996.
- [12] P. Nigrowsky, P.J. Turner, "Variable Structure Control of Robot Manipulators with Varying Bounds", 7th IEEE Med. Conf. on Cont. and Aut., Haifa, 1999.
- [13] A. Visioli, "Control strategies for industrial robot manipulators", PhD thesis, Univ. of Brescia (I), 1999.
- [14] ISO 9283:1991, "Manipulating industrial robots: performance criteria and related testing methods".
- [15] L. Sciacivco, B. Siciliano, "Modelling and control of robot manipulators", McGraw-Hill, 1995.

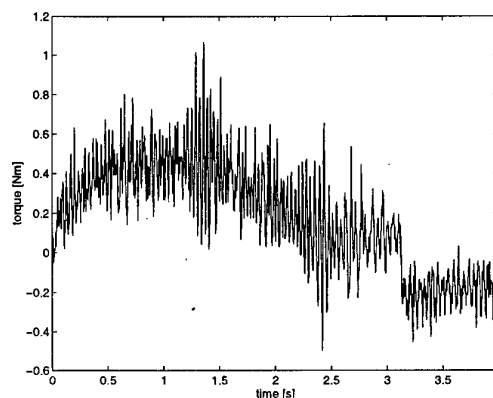


Figure 8: Torque signal for the PID-based controller performing the linear trajectory (joint 1).

Gaussian Neuro Sliding Mode Controller

Hasan Palaz

TUBITAK, UEKAE,
41470, Gebze, TURKEY

palaz@mam.gov.tr

Kemal Sarioğlu

Istanbul Technical
University, Electric-
Electronic Faculty,
Istanbul -TURKEY

Ertuğrul Akbaş

TUBITAK, UEKAE, 41470,
Gebze, TURKEY

ertugrul@mam.gov.tr

Melikşah Ertuğrul

TUBITAK MRC, ITRI,
41470, Gebze, TURKEY

melik@mam.gov.tr

Abstract

In this paper, Gaussian Neuro Sliding Mode Controller (GNSMC) is proposed to overcome difficulty in the calculation of the equivalent control. In sliding mode controllers, a whole knowledge of the plant dynamics is required for this purpose. In the GNSMC, Gaussian function based adaptive RBF neural network is used to compute the equivalent control signal of sliding mode controller. The performance of the proposed schemes is verified by simulation results on two dof direct drive manipulator. Simulation studies show that the novel approach ensures good trajectory following performance with payload variations and eliminates chattering without need a priori knowledge about plant. These characteristics make the proposed control technique an attractive solution for motion control applications

1. Introduction

Variable structure control (VSC) with sliding mode control (SMC) is a special type of control technique that is capable of making a control system very robust with respect to system parameter variations and external disturbances [1]. In addition, the technique provide good control performance and an easy way to design the control law for a wide spectrum of system types including linear systems, nonlinear systems, multi-input/multi-output systems, discrete-time models, large-scale and infinite dimensional systems, and stochastic systems. Because of these properties, today, research and development continue to apply SMC to a wide variety of engineering systems [2].

The first disadvantage of SMC is the chattering, which is the high frequency oscillation of the controller output. The second one is the difficulty in the calculation of the equivalent control. A thorough knowledge of the plant dynamics is required for this purpose.

In the literature, classical and intelligent approaches are used to overcome these problems. The first classical approach is the use of a saturation function instead of the sign function to eliminate chattering [3]. The second one

is the use of an averaging filter for avoiding the difficulty in the calculation of the equivalent control [4].

The intelligent approaches are combinations of soft computing technologies such as fuzzy logic or neural network (NN), and SMC theory. The first idea is based on fuzzy adaptation scheme for tuning sliding mode controller parameters in real time. These schemes avoid chattering without the need of off-line tuning of controller parameters and improve control performance of SMC for two degree of freedom (dof) direct drive manipulator [5]. The second idea is NN controller with learning rule based on sliding mode algorithm for calculation of unknown part of the equivalent control in presence of the plant uncertainties [6].

Last intelligent approach in the SMC literature is a synergistic combination of NN and sliding mode control to be able to obtain a robust neuro-controller with less system knowledge. They used a feed-forward NN to compute the equivalent control term in sliding mode. Thus, the requirements for the knowledge of dynamics and parameters are eliminated in the computation of the equivalent control [7].

Radial base function neural networks (RBFNN) have recently played a significant role in the NN domain. Many researchers are working on the theoretical investigation of this type NN. On the other side, it has potential to classification, time series prediction and also intelligent controller applications. The main reasons for this result are universal approximation ability, but also have the so-called "best approximation" property, comparative simplicity and computational efficiency [8].

In this paper, a new intelligent approach to sliding mode controller for n-link industrial robot manipulators is developed. In this approach, Gaussian function based adaptive RBFNN to compute the equivalent control signal of sliding mode controller is used. The performance of the proposed schemes is verified by simulation results on two dof direct drive manipulator. These studies show that adaptive RBFNN based sliding mode controller avoid chattering without need a priori knowledge about plant, ensure a fast system response and fast convergence of system states to the sliding surface and good trajectory

following performance with payload variations. These characteristics make the proposed control technique an attractive solution for trajectory control of robot manipulators.

The organization of the paper is as follows. In Section II, the classical SMC design and the base of our proposed controller are presented. In section III, the structure of the Gaussian Neuro Sliding Mode Controller (GNSMC), the structure and the on-line weight adaptation algorithm of RBFNN are discussed in detail. In section IV, the performance verification of the GNSMC system is presented by extensive simulation studies on a direct drive two dof SCARA type manipulator. The paper concludes with the presentation of some typical simulation results obtained for the control of a direct drive SCARA type robot.

2. Design of sliding mode controller

The control mechanism will be derived for a nonlinear, non-autonomous, multi-input multi-output system in the following form :

$$\dot{x}_i^{(a_i)} = f_i(X, t) + \sum_{j=1}^m b_{ij}(X, t) u_j \quad (1)$$

where the vector U of components u_j is the control input vector and the state X is composed of the x_i 's and their first (a_i-1) derivatives. Such systems are called square systems since they have as many control inputs u_j as outputs to be controlled x_i [3]. The system can be written in a more compact form as letting

$$X = [x_1 \ \dot{x}_1 \ \dots \ x_1^{a_1} \ \dots \ x_m \ \dot{x}_m \ \dots \ x_m^{a_m}]^T, \quad U = [u_1 \ \dots \ u_m]^T \quad (2)$$

and the system equation becomes,

$$\dot{X}(t) = F(X, t) + B(X, t)U(t) \quad (3)$$

where the system state vector is $X \in \mathbb{R}^n$, control signal vector is $U \in \mathbb{R}^m$, t is time and B is $(n \times m)$ input gain matrix. The aim is to drive the states of the system into sliding surface S $(m \times 1)$ defined by

$$S = \{X : \sigma(X, t) = \varphi(t) - \sigma_a(X) = 0\} \quad (4)$$

where, $\varphi(t) = GX^d(t)$ is the time dependent part of the sliding function $\sigma(X, t)$ and consists of desired (reference) state vectors X^d and slope matrix of sliding surface G $(m \times n)$. $\sigma_a(X) = GX(t)$ denotes the state dependent part of sliding function $\sigma(X, t)$.

The derivation of the control involves the selection of a Lyapunov function $V(S)$ and a desired form \dot{V} the

derivative of Lyapunov function. The selected Lyapunov function is

$$V = \frac{1}{2} \sigma^T \sigma \quad (5)$$

Therefore,

$$\dot{V} = \sigma^T \dot{\sigma} \quad (6)$$

It is desired that

$$\dot{V} = -\sigma^T D \text{sign}(\sigma) \quad (7)$$

thus, equation (7) equals to (8)

$$\sigma^T \dot{\sigma} = -\sigma^T D \text{sign}(\sigma) \quad (8)$$

where D is $(m \times m)$ positive definite diagonal gain matrix. Thus, the derivative of the Lyapunov function will be negative definite and this will ensure stability.

The expression for the derivative for the sliding function is

$$\dot{\sigma} = \dot{\varphi} - \frac{\partial \sigma_a}{\partial X} \dot{X} = \dot{\varphi} - G(F(X, t) + B(X, t)U(t)) \quad (9)$$

and by putting (9) into (8), the sliding mode control input signal can be obtained as follows,

$$U(t) = U_{eq}(t) + (GB)^{-1} D \text{sign}(\sigma) = U_{eq}(t) + \Delta U(t) \quad (10)$$

where $U_{eq}(t)$ is the equivalent control and it is written as,

$$U_{eq}(t) = -(GB)^{-1} (GF(X, t) - \dot{\varphi}) \quad (11)$$

and $\Delta U(t)$ is the additional control term and it is written as,

$$\Delta U(t) = (GB)^{-1} D \text{sign}(\sigma) = K \text{sign}(\sigma) \quad (12)$$

The equivalent control equation (11) and the additional control term equation (12) are starting point to design Gaussian function based adaptive RBFNN for computing the equivalent control signal of sliding mode controller (SMC).

3. Gaussian neuro sliding mode controller (GNSMC)

The equivalent control equation (11) contains $F(X)$ and B system matrices. Therefore this is difficult to compute exact value of the equivalent control without strong a priori knowledge about the system. In other words, a whole knowledge of the system dynamics (or inverse dynamics) and the system parameters is required to be able to compute the equivalent control. This is actually

very rare in practice. To be able to solve this problem, one can use a RBFNN to compute the equivalent control.

In the proposed structure, the equivalent control term in sliding mode control is computed by an adaptive RBFNN. The additional term in sliding mode is also computed and summed with the output of the RBFNN to form the control signal. The output of the secondary controller is accepted as a measure of error to update the weights of the RBFNN. The overall system with the proposed controller is given in Fig. 1.

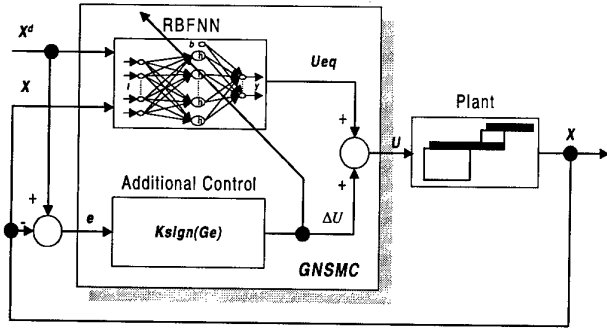


Figure 1. Illustration of the structure of the proposed GNSMC system

The structure of RBFNN is shown in figure 2 and consists of only three layers. The first layer is connection to the desired and the actual states. The second layer is the only hidden layer. It performs non-linear transformation from the input vector space to the internal vector space. The last layer is the output layer that equals to the number of inputs of the robot and transforms internal vector space into an output one in linear manner. Neurons of the hidden layer are radial base functions. The type of these functions is theoretically unimportant and Gaussian functions

$$h(I) = e^{-\frac{1}{2} \frac{\|I-c\|^2}{\lambda^2}} \quad \lambda > 0 \quad (13)$$

are used. Neurons in the output layer calculate linear function

$$f_i(I) = w_{i0}b + \sum_{j=1}^z w_{ij}h_j(I) \quad i = 1, \dots, m \quad (14)$$

where index i denotes output neuron i , index j runs through all the hidden layer neurons, I is an input vector, c is the center of RBF neurons of the hidden layer, λ is the width of RBF in neurons, b is a bias input and w_{ij} is a connection weight from hidden neuron j to output neuron i [8].

In order to obtain a high performance GNSMC solution to control of nonlinear system, it is essential to define the proper RBFNN architecture. The network architecture is determined by the number of nodes in each layer and the location of the function centers. The determination of the number of nodes in input layer and output layer is selected from the equivalent control equation (11). In the computation of the equivalent control, all the desired and actual states are used. Therefore, the number of nodes in input layer are the number of desired and the actual states. And the number of nodes in output layer are the number of control inputs to plant. For example in application of robot control, the number of nodes in the output layer are determined by the number of the actuators of the robot.

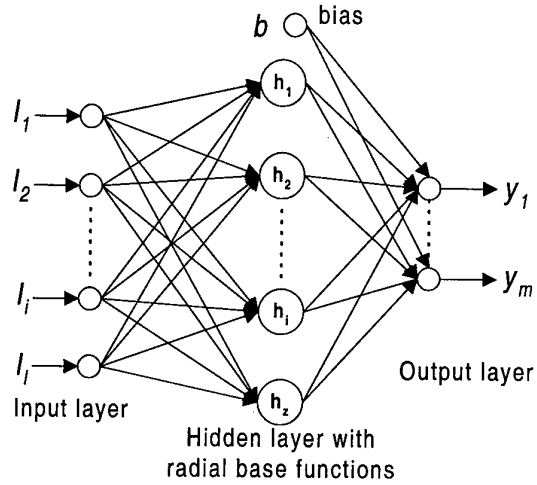


Figure 2. Illustration of the RBFNN structure

The selection of the number of hidden layer nodes and the location of centers will have profound effects on the performance of the RBFNN in GNSMC. The number of neurons in the hidden layer should be selected such that the RBFNN has mapping capability for inverse dynamics of the plant. The learning of RBFNN is divided into two parts usually because the hidden layer differs from the output one. First, the non-linear hidden is determined by some kind of clustering algorithm and then the output one is optimized either by gradient-descent procedure that represents a generalization of the least mean square (LMS) algorithm. K-means clustering algorithm is used to find the proper location of centers in hidden layer. And p-nearest neighbour heuristic rule is used to determine the width of basis functions [8][9].

The inputs of RBFNN I consist of desired and actual states.

$$I = \begin{bmatrix} (x^d)^T & x^T \end{bmatrix}^T \quad (15)$$

The output of RBFNN is equivalent control term Ueq . And it can be computed as follows,

$$Ueq_i = w_{i0}b + \sum_{j=1}^z w_{ij}h_j(I) \quad i = 1, \dots, m \quad (16)$$

The first step in the development of such learning procedure of RBFNN is to define the instantaneous value of the cost function. The cost function is selected as,

$$e = \frac{1}{2} \sum_{j=1}^m (Ueq_j^d - Ueq_j)^2 \approx \frac{1}{2} \sum_{j=1}^m (\Delta U_j)^2 \quad (17)$$

The weight adaptation algorithm of RBFNN is a combination of two learning phase. In first phase, positions of the radial base functions of the hidden layer is set by k-means clustering algorithm. Then, p-nearest neighbour heuristic rule is used to determine their widths. This phase is off-line and a part of the construction of RBFNN.

The second part of learning is based on gradient-descent procedure for the optimizing of all free parameters of RBFNN. The phase is on-line progress. The requirement is to find the free parameters w_{ij} , c_j and λ_j so as to minimize e . The result of this minimization are given as follows [8] [9].

Adaptation formulas for the linear weights,

$$\frac{\partial e(t)}{\partial w_{ij}(t)} = -e_i(t)h_j(I) \quad (18)$$

$$w_{ij}(t+1) = w_{ij}(t) - \eta_1 \frac{\partial e(t)}{\partial w_{ij}(t)} \quad j = 0, 1, \dots, z \quad (19)$$

Adaptation formulas for the positions of RBF centers,

$$\frac{\partial e(t)}{\partial c_j(t)} = -\frac{1}{\lambda_j^2} \sum_{i=1}^m e_i(t)w_{ij}(t)h_j(I)[I - c_j(t)] \quad (20)$$

$$c_j(t+1) = c_j(t) - \eta_2 \frac{\partial e(t)}{\partial c_j(t)} \quad j = 1, \dots, z \quad (21)$$

Adaptation formulas for the width of standard Gaussian functions,

$$\frac{\partial e(t)}{\partial \lambda_j(t)} = -\sum_{i=1}^m e_i(t)w_{ij}(t)h_j(I) \frac{\|I - c_j(t)\|^2}{\lambda_j^3(t)} \quad (22)$$

$$\lambda_j(t+1) = \lambda_j(t) - \eta_3 \frac{\partial e(t)}{\partial \lambda_j(t)} \quad j = 1, \dots, z \quad (23)$$

In adaptation formulas, μ_1 , μ_2 , μ_3 denote the learning rate.

4. GNSMC system verification by simulation

The performance of the GNSMC system presented in Section 3 is verified by extensive simulation studies on a direct drive two dof SCARA type manipulator sketched in Fig. 3.

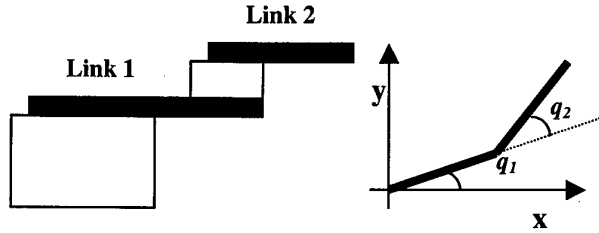


Figure 3. Illustration of the SCARA type manipulator

4.1. Manipulator Dynamics

The dynamical equations of this manipulator are given by the following equation [10]:

$$M(q)\ddot{q} + V(q, \dot{q}) + f_c = U \quad (24)$$

where, q is the vector of joint angles q_1 and q_2 shown in Fig.3. U is the torque vector applied to the joints, M is the inertia matrix, V is the vector of centripetal and coriolis forces, f_c stands for coulomb friction and M and V can be written explicitly as

$$M(q) = \begin{bmatrix} p_1 + 2p_3 \cos(q_2) & p_2 + p_3 \cos(q_2) \\ p_2 + p_3 \cos(q_2) & p_2 \end{bmatrix}, \quad (25)$$

$$V(q, \dot{q}) = \begin{bmatrix} -\dot{q}_2(2\dot{q}_1 + \dot{q}_2)p_3 \sin(q_2) \\ \dot{q}_1^2 p_3 \sin(q_2) \end{bmatrix}, \quad (26)$$

where $p_1 = 3.1877$, $p_2 = 0.1168$ and $p_3 = 0.1630$ [10].

4.2. Application of the GNSMC scheme to the control of the manipulator

The states are selected as the angular positions and their derivatives:

$$x_1 = q \text{ and } x_2 = \dot{q}.$$

Then the following state-space form representation of the robot manipulator is obtained:

$$\begin{bmatrix} \dot{x}_1 \\ \dot{x}_2 \end{bmatrix} = \begin{bmatrix} x_2 \\ -M^{-1}(x_1)(V(x_1, x_2) + f_c) \end{bmatrix} + \begin{bmatrix} 0 \\ M^{-1}(x_1) \end{bmatrix} U. \quad (27)$$

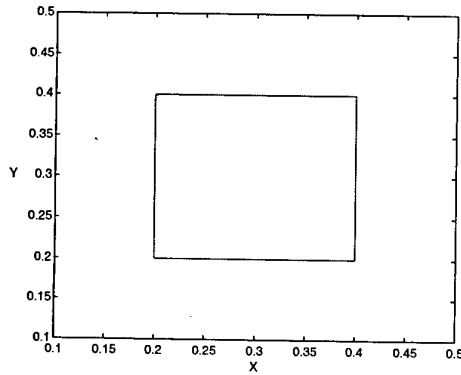


Figure 4. Desired trajectory of end effector on x-y plane

to compute additional control term in equation (12), proper selection of gain matrices (G and D) should be done. In our simulation studies G and D were selected as follows,

$$G = \begin{bmatrix} 5 & 0 & 1 & 0 \\ 0 & 5 & 0 & 1 \end{bmatrix} \text{ and } D = \begin{bmatrix} 2 & 0 \\ 0 & 2 \end{bmatrix}.$$

In addition, to eliminate chattering, shifted sigmoid function is used for computing additional control term as follows,

$$\Delta U(t) = (GB)^{-1} D\phi(\sigma) = K\phi(\sigma) \quad (28)$$

Where $\phi(\cdot)$ is a shifted sigmoid function and it is defined as,

$$\phi(\sigma_j) = \frac{2}{1 + e^{-\sigma_j}} - 1 \quad (29)$$

For computing the equivalent control term, we employed three layer RBFNN with $l = 8$ (number of input nodes), $z = 8$ (number of hidden nodes) and $m=2$ (number of output nodes). The initial weight of RBFNN have to enable the system to satisfy stability criterion. In our simulation random small initial weights are selected to make RBFNN output insignificant at initial stage of the control process. Moreover, all adaptation rates (μ_1, μ_2, μ_3) of RBFNN is selected as 0.01.

The desired end effector trajectory used for simulation studies in Fig. 4. It corresponds to the state references shown in Fig. 5. The simulation results are presented in Fig. 6. The solid and dashed lines belong to first and second link, respectively. The robot perfectly follows the desired trajectory.

In order to compare the effects of payload change while the robot is working 40 kg payload was added and the effects of this payload to trajectory control were examined. The payload was added at $t=10$ sec while the whole task of the manipulator takes 20 sec. Actual

trajectory of end effector on x-y plane is shown in Fig.6.(d)-(e). It shows that GNSMC satisfies robust control to payload variations.

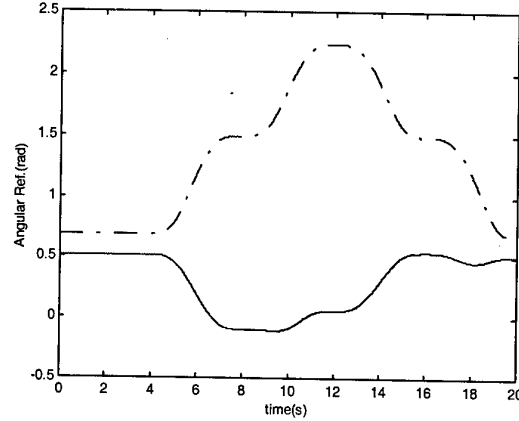
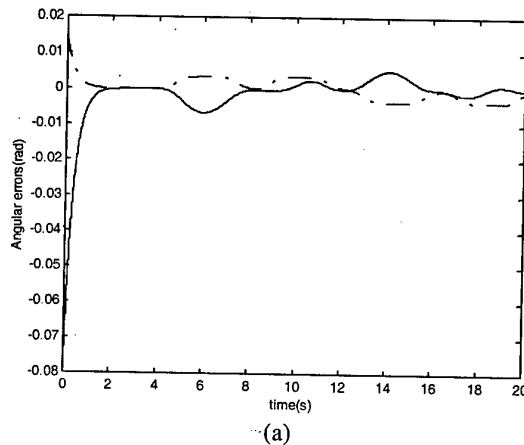


Figure 5. Angular position references

5. Conclusions

In this paper, a new intelligent approach to sliding mode controller for n-link industrial robot manipulators is developed. In this approach, we used Gaussian function based on-line adaptive RBFNN to compute the equivalent control signal of sliding mode controller. And also it has one great advantage that is an on-line controller which means that control and learning takes place at the same time.

The simulation studies show that GNSMC avoid chattering without need a priori knowledge about plant, ensure a fast system response and fast convergence of system states to the sliding surface and good trajectory following performance with payload variations. These characteristics make the proposed control technique an attractive solution for trajectory control of robot manipulators.



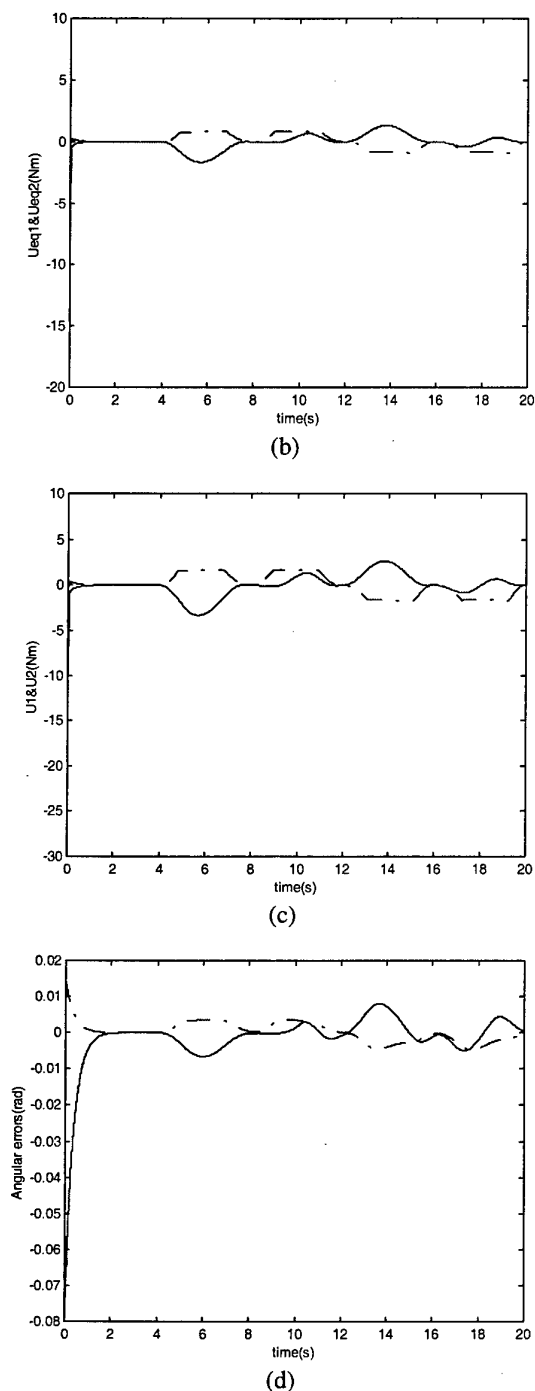


Figure 6. GNSMC performance during 20s trajectory tracking of the direct drive two dof SCARA type manipulator. (a) Angular tracking errors, (b) Equivalent control signals, (c) Control signals, (d) Angular tracking errors with payload, (e) Actual trajectory with payload variation.

6. References

- [1] Utkin, V.I., "Sliding Modes in Control Optimization", Springer-Verlag, 1981.
- [2] Hung J. Y., "Variable Structure Control: A survey", IEEE Transaction on industrial Electronics, Vol.40, no.1, February, 1993.
- [3] J. J. Slotine and W. Li, "Applied Nonlinear Control", Prentice Hall, 1991.
- [4] Ertugrul M., Kaynak O., Sabanovic A., Ohnishi K. "A Generalized Approach For Lyapunov Design Of Sliding Mode Controllers For Motion Control Applications", Advanced Motion Control Conference, AMC'96, Mie, Japan, 1996.
- [5] Erbatur K., Kaynak O., Sabanovic A., Rudas I., "Fuzzy adaptive sliding mode control of a direct drive robot", Robotics and Autonomous System, Vol.19, pp.215-227, 1996.
- [6] Sabanovic A., Jezernjk K., Rodic M., "Neural Network Application in Sliding Mode Control Systems", IEEE Workshop on variable Structure Systems, VSS'96, Tokyo, Japan, 1996.
- [7] Ertugrul M., Kaynak O., "Neuro-Sliding mode control of Robotic manipulators", International conference on advanced robotics, pp. 951-956, July 1997, California, USA
- [8] Haykin S., "A Neural Networks: A Comprehensive Foundation", Macmillan College Publishing Co., Inc., 1994.
- [9] Bishop C.M., "Neural Networks for Pattern Recognition", Oxford University Press, Oxford, 1995.
- [10] "Direct Drive Manipulator R&D package User Guide", Integrated Motion Incorporated, Berkeley CA.

Research Concerning the Improvement of Performances of Automatic Control Systems Based on the Optimisation of Feeding and Transport Process

Authors:

LUCIANA CRISTEA

Associate Professor, Ph.D.

Department of Fine Mechanics
and Mechatronics, Faculty of
Mechanics,

Transilvania University of
Braşov, Romania

email: lcristea unitbv.ro;

ADRIAN DUMITRIU

Associate Professor, Ph.D

Department of Fine Mechanics
and Mechatronics, Faculty of
Mechanics,

Transilvania University of
Braşov, Romania;

DOREL CRISTEA Msc.

Department of Transports,
S.C. BRAFOR S.A. Braşov,
Romania.

Abstract

The paper attempts to present a few results obtained during the research work sustained by the author within the domain of control automatic systems. The results presented in here illustrate some possibilities of structural optimisation and functioning in case of dimensional control automatic systems used in the bearing industry plainly in the case of ball bearing.

1. Introduction

The research objectives have been underlined within the frame of solving a specific problem raised in the field of machine manufacturing industry- automatic systems for dimensional control productivity improvement characteristics and performances.

The analysis of feeding systems has been initiated within the frame of scientific research objectives proposed by the author for which the obtained results have imposed an approach of the problem from a theoretical as well as a practical point of view.

In this paper are being approached a few aspects concerning the statistical and dynamic behaviour of automatic systems for ball control with the aim of achieving the best structures from the efficiency point of view. Theoretical studies consist of mathematical models for different types of feeding and transport structures. Their analyses aimed at the static and dynamic behaviour of spherical components during the different manipulating conditions.

In such circumstances, there have been underlined a series of influence factors that influence both the static and the dynamic behaviour of the spherical parts in different systems like the ones for feeding, transport and

dozing. During the research work numerical simulations of the movement laws by changing the main influence factors have been done.

The analysis of the results obtained during the optimisation process lead to the elaboration of new possibilities of assuring the structures of optimum automatization feeding from the efficiency and energy consumption point of view, for different types of pieces.

2. Theoretical aspects

The static analyses have underlined a group of forces acting upon the half - finished products during their feeding process (in other words, in contact with the catching elements).

In the case of feeding systems having disks with nets there has been analysed the general case in that the disk has an inclination with a γ angle with respect to the horizontal, the parts being captured from the tub in its inferior position and released in the superior one.

The spherical piece, located in the inferior position of the tub and disk, is being stressed by a system of forces. The disk, through the nest wall, provides the force F , force whose influence on the part depends on the nest geometry as well as the dimensional characteristics of its walls (see Fig. 1.).

Equation (1) shows the condition that has to be fulfilled by the disk through the force developed and that acts upon the piece, in order to achieve a rotational movement in the case of the latter.

$$F \geq \frac{G(\mu \cos \gamma + \sin \gamma (\mu \cos \psi - \sin \psi))}{\cos \delta - \mu \sin \delta} \quad (1)$$

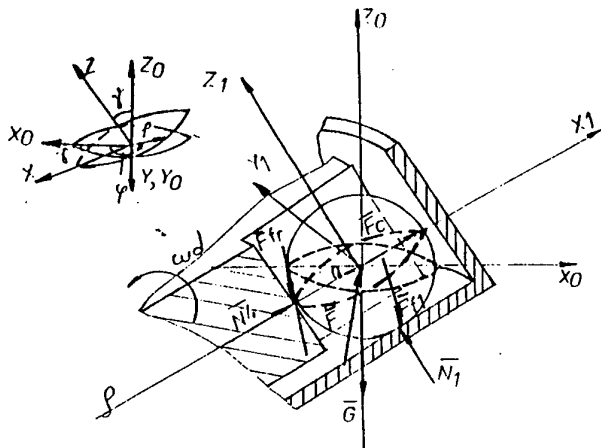


Figure 1. Static behaviour of spherical pieces on feeding disk with nest.

An important aspect that arises during the working process of the feeding systems refers to parts' (half-finished components) behaviour in the tub before their trapping by the catching and transport elements. From a static point of view the analysis of this behaviour can focus on finding the coupling forces and the limit equilibrium conditions among the pieces.

In the feeding tubs, the half-finished components are being located in a bulk shape, actually in a random position, so finally this has to reach in the neighbourhood of the catching and transport elements in order to be released from the system. In order to get a simplification of the analysis there has been taken into account only the homogeneous, spherical shapes for the half-finished components, and those that are into a tangent position related to one another.

Isolating two pieces from the tub (see figure 2) and taking into account their tangential position and the fact that they are relying on two planes (imaginary ones) that intersect after a horizontal axis having the α_1 and α_2 angles related to the horizontal plane (these imaginary planes are materialising in fact the pieces from the tub on which the parts considered are relying on), the equilibrium position has been deduced, considering the equation (2) and coupling forces as in equation (3).

$$\operatorname{tg} \beta = \frac{1}{2} (\operatorname{ctg} \alpha_1 - \operatorname{ctg} \alpha_2); \quad (2)$$

$$L = \frac{mg \sqrt{\sin^2 \alpha_1 + \sin^2 \alpha_2 - 2 \sin \alpha_1 \sin \alpha_2 \cos(\alpha_1 + \alpha_2)}}{\sin(\alpha_1 + \alpha_2)}. \quad (3)$$

$$t = \ln \left(\rho + \sqrt{\rho^2 + \frac{(r_c - r)^2 (l^2 \sin \delta - G \sin \gamma)}{m_o (G \sin \gamma \cos \phi - F \sin \delta)}} \right) - \ln \left(l + \sqrt{l^2 - \frac{l}{m_o}} \right) - \ln(r_d - r); \quad (4)$$

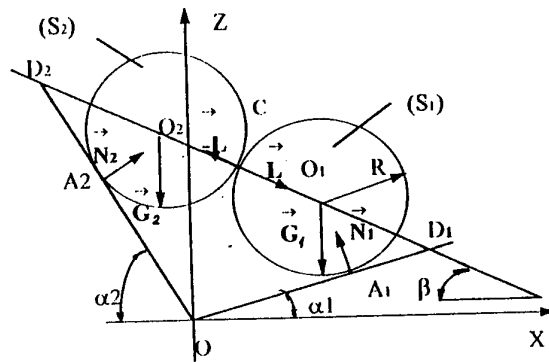


Figure 2. Static behaviour of the pieces in the bunker tub.

The β angle is known as natural breaker angle. Half-finished components movement is achieved mainly because of superior layers displacement influenced by the natural breaker β angle and only in a small amount because of the displacement of the whole quantity of pieces located at the bottom inside the bunker. As one can see in the equation (2), the natural breaker β angle can be influenced by the tub walls profile, respectively by its inclination angle.

Dynamic behaviour analysis, respectively the writing of the spherical piece movement governing equations with respect to a fixed coordinate system can be done based on analytical mechanics, namely, Lagrange's equations. Consequently the coordinate system $Ox_0y_0z_0$ (fixed) was considered to be the relating one in order to determine the movement governing equations for a spherical piece having the radius and mass m_o and which is being displaced by the conveyer disk from the inferior position of the tub to the conveyer disk from where it will be released to the exhaust sewer. As well as before, these feeding systems with disk having nests, respectively with rotor having horizontal palettes, can be considered particular types of the one with disks having inclined nests. Also, in this case can be written Lagrange's equation with respect to the coordinate system $Ox_0y_0z_0$.

In the dynamic behaviour analysis of the spherical piece in these feeding systems of the spherical piece in these feeding systems one assumes that the ball has two degrees of freedom: - a rotation around Oz_0 axis, because of the conveyer disk; - radial displacement because of the interstice between palettes, respectively

because of the relative displacement among piece, tub and conveyor as a consequence of manufacturing characteristics of the latter. Next, two generalized coordinates were chosen: the rotational angle ϕ and radius ρ . Lagrange's equations related to the fixed system Oxyz, taking into account the generalised coordinated: radius ρ and rotational angle ϕ can be written as follows to get the equation governing the movement in radial direction (see eq. 4).

In order to analyse the dynamical behaviour of the half-finished components in the inclined tub there had been considered a half-finished (rigid) in movement inside the feeding tub forced to stay in a permanent contact with the latter. The relative displacement of both rigid bodies being in contact can be done through gliding or rolling. Lagrange's equation with multipliers has been used to write the equation of movement, together with the nonholonomic couplings leading to a system with 1+s equations having 1+s unknowns: $q_1, \dots, q_s; \lambda_1, \dots, \lambda_s$. In case the piece is a spherical (homogeneous) one and it is rolling (with a swivel movement) without gliding between piece and tub a nonholonomic coupling is being achieved. Choosing the horizontal plane like the xOy plane of the fixed coordinate system (Oxyz), having Oz in the upper direction of the vertical and Gx'y'z' coordinate system jointly with the sphere one can see that the point G will be permanently in plane z=R (figure 3.).

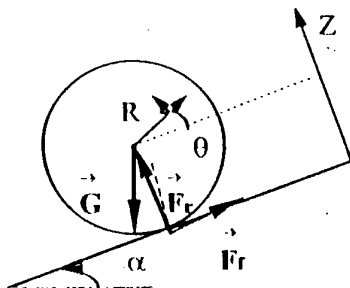


Figure 3. Dynamic behaviour of the piece in the bunker tub.

The generalised coordinates $x_G, y_G, \theta, \psi, \phi$ Satisfied two coupling connections unintegrable, therefore we get a nonholonomic system, a sclerenome one, having three degrees of freedom. In case the tub is inclined the coupling between both bodies becomes holonomous because the rotational axis, at a rolling of the piece without gliding in the plane of inclined tub, keeps a constant direction. From Lagrange's equations have been obtained three prime integrals (5) that allow a reduction of the problems to quadratics.

$$\begin{cases} \dot{\phi} + \dot{\psi} \cos \theta = C_1; \\ \dot{\theta}^2 + \dot{\psi}^2 \sin^2 \theta = C_2; \\ \dot{\psi} \sin^2 \theta = C_3 (1 + \cos \theta). \end{cases} \quad (5)$$

After calculations have been obtained the movement laws in the case of spherical pieces located on the inclined disk having an angle γ with respect to horizontal.

$$x_G = \frac{5}{14} g t^2 \sin \gamma; \quad \theta = \frac{5}{14 R} g t^2 \sin \gamma. \quad (6)$$

In case in that between piece and disk there is both gliding friction (having a coefficient μ) and rolling friction (having a coefficient s), the movement law can be written as in (7) for pieces moving on the bunker's disk.

$$x_G = \frac{GR(R \cdot \sin \gamma - s \cdot \cos \gamma)}{(mR^2 + I_G)} t^2. \quad (7)$$

One can consider that in case of a fast acceleration in movement, a ratio s/R as small as possible it will be favourable. In the same case can be accomplished the condition for a rolling movement only, without friction. In case of a cylindrical piece this condition becomes, as follows:

$$\mu \geq \frac{1}{3} \left(\tan \gamma + 2 \frac{s}{R} \right). \quad (8)$$

Considering the theoretical results, the authors have perfected a new testing plant to realise the static and dynamic characteristics' correlation with the specific functional characteristics and to determine the main and the most important optimal working parameters. The authors have based their studies on the automatic processing and dimensional control systems used in the bearing and assembling component production [1].

All these studies are very important in the field of precision mechanics and mechatronics systems.

The theoretical studies have generated some conclusions that led the authors to elaborate the rollers' laws of motion in different operating conditions [2]:

- Spherical parts inside the rotating and inclined feed hopper of the feeding systems;
- Spherical parts transported by holding elements;
- Spherical parts coming out from the feeding and transporting systems;
- Cylindrical parts coming out from the feeding and transporting systems;
- Cylindrical parts transported by holding elements;
- Cylindrical parts inside the rotating and inclined feed hopper of the feeding systems.

Considering the theoretical analysis, the authors give emphasis to the influence factors that can determine the optimised structure realisation [2].

Some of the most important factors are:

- the holding elements rotative speed;
- the tank rake;
- the parts' dimensional characteristics;
- the parts' features of constructions;
- the parts' quality coefficient;
- the holding elements dimensional characteristics;
- the holding elements features of constructions;
- the looping unit mechanical characteristics.

3. Experimental aspects

In order to analyse the correlation of the static and dynamic characteristics and the specific functional conditions, the authors devised and realised an original testing plant. The law-chart of this equipment is presented in figure 4. The computer traces the whole process of deposition, catching, handling, transport and exhaust of the parts from the tank, analysing the necessary information and signals from the sensors and generates the decisions on the optimised conditions of the feeding system.

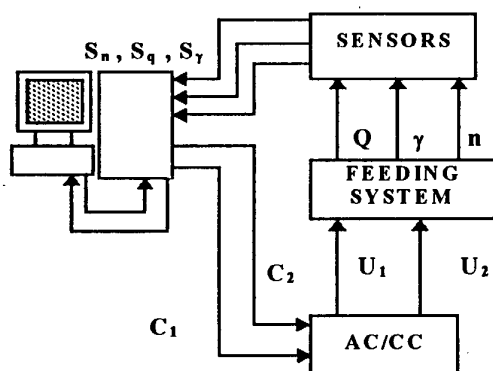


Figure 4. Testing plant law-chart.

This testing plant reproduces the mechanical structure of a feeding system with varied transporting rotors (hooked disks, carved disks and catch pin disks). The theoretical study imposed conditions on the experimental parameters. The handling, catching and transporting elements must turn round with a rotation speed with a variation range among 1 and 18 rotations per minute. The tank rake must vary among 0 and 90 degrees, namely from horizontal position to vertical position. The primary data that will be processed by the computer are: the rotation speed of the manipulation elements (S_n), the tank rake (S_r), the time (t), the working productivity (S_q) and the part characteristics (shape, dimensions, appearance and material). Figure 5 presents an example of a chart generated inside the experimental process for the spherical parts. This example presents the productivity variation dependent

on the tank rake and the rotation speed. It also presents the correlation among the static, dynamic behaviour and the specific functional characteristics. Analysing this chart, the authors can remark the tank rakes and the rotation speeds that assure a the high productivity for each of part types. The main purpose of this research is to generate optimised feeding, transport, proportioning and alignment systems for more mechanical efficiency.

The computer processes all the information, testing the analysed system and setting the working parameters to obtain an optimised mechanical system.

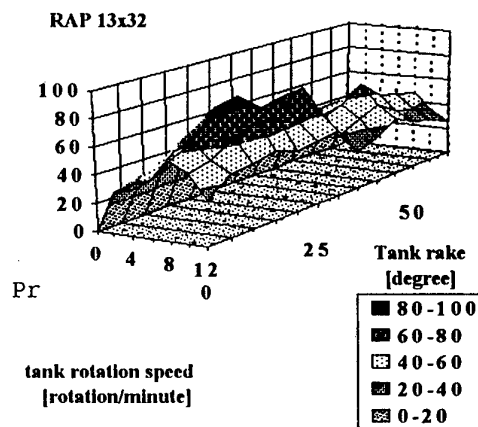


Figure 5. The chart of the productivity variation.

4. Conclusion

This method provides an automatic process control as well as a data base for the select on of the working parameters that can assure the most efficient mechanical structure used in the automation of dimensional control systems.

In conclusion, an important data base was gained and an automatic process control for optimising the feeding, transport, proportioning and alignment systems achieved. For further research the authors want to test the system with the aid of neuronal-networks. For the catching probability increase and the analyse of all dynamic aspects a fuzzy method will be proposed.

5. References

- [6.] Cristea, L.: *The Analysis of the Forces, considered in the Study of Feeding, Transport and Proportioning Systems in Automatic Dimensional Control*. In: Proceedings of - ICCE/3, New Orleans, 1996, pp. 197-198
- [7.] Cristea, L.: *Theoretical and experimental contributions at the static and dynamic optimisation of the feeding, transport alignment and proportioning systems used in the dimensional control automata's systems*. In: PhD. paper title, sustained with Transilvania University of Brasov, 1997.

Determining Maximal Asymptotic Stability Region of Mechatronic Systems

G.M. Dimirovski¹, O. Kaynak², A. Mojsovski¹, M.J. Stankovski¹ and Y.-W. Jing³

1 Automat. & Syst. Eng. Inst., Faculty of EE, St.Cyril & St.Methodius University, P.O.B. 574, 91000 Skopje, R.Macedonia; Fax#: ++389-91-112-163; E-mail: dimir@cerera.etf.ukim.edu.mk

2 UNESCO Chair of Mechatronics, Dept. of Electrical & Electronic Engineering, Bogazici University, Bebek, 80815 Istanbul, R.Turkey, Fax#: ++90-212-287-24-65; E-mail: kaynak@boun.edu.tr

3 Automatic Control Dept., Northeastern University, P.O.B. 135, Shenyang, Liaoning, 110006, P.R.China; Fax#: ++86-24-389-0448; E-mail: ywjing@ramm.neu.edu.cn

Abstract: This paper presents a contribution to E.J.Davison's computational method for stability analysis of mechatronic systems, which are essentially non-linear dynamic systems, via numerical construction of quadratic Lyapunov functions. It makes use of E.J.Davison's main algorithm and H.H.Rosenbrock's method for finding extremum (max./min.) values of a function, while contributing to the derivation of numerical scheme via appropriate algorithmic expansion of matrix equations involved. This way an expanded and improved estimate of the approximating hypervolume of asymptotic stability sub-domain is obtained that is closer to the stability and/or the bifurcation boundary.

Keywords: Mechatronic systems; non-linear systems; autonomous dynamics; asymptotic stability; Lyapunov approach; computational methods.

1. INTRODUCTION

The asymptotic stability is one the structural properties of general dynamic systems is required as a sine-qua-non condition in any engineering system, and so is the case of motion and, in general, of mechatronic control systems. It should be noted, however, mechatronic control systems are essentially non-linear as is the motion dynamics they are aimed to control. Therefore their stability too has to be addressed as such if the design and implementation constitute the actual goal of their investigation from the viewpoint of applied science.

Almost half a century has elapsed since the re-discovery of Lyapunov's 1892 dissertation (A.M. Lyapunov, *Probleme General de la Stabilité du Mouvement*, Annals of Mathematical Studies No. 17. Princeton N.J.: Princeton University Press, 1949), and a number of research studies for the extension of Lyapunov stability theory and novel theoretical findings have been elaborated (via differential geometric approach, e.g., A. Isidori, 1989, J.-J.E. Slotine & W.Li, 1991; H.K. Khalil, 1992). In practical applications, however, it is rather important to have techniques to establish guaranteed asymptotic stability in a wider feasible region in order to design control systems. The main concern, due to the essence

of Lyapunov's second or direct method to the stability of motion, is the construction of most appropriate Lyapunov function that guarantees the largest possible asymptotic stability region in terms of magnitude departures from the equilibrium state vector. Hundreds of contributions may be found in the literature, and therefore is impossible to cite them in here. From the applications point of view, however, the ones that may be efficiently used in a computer-assisted environment, in particular on a PC based platform, appear to be of substantial value.

In our investigations along these lines [6]-[9] and with regard to non-linear behaviour of the wide class of mechatronic systems, recently we have revisited some of the early developments which draw from the very sources of A.M.Lyapunov and his many followers in systems and control science and engineering; just to name a few, V.I.Zubov (1955), W.Hahn (1959), R.E.Kalman and J.E. Bretram (1960), J.LaSalle and S.Lefschetz [11], A.M. Letov [12], S. Margolis and W. Vogt (1963), F.N. Bailley [1], S. Barnett [2].

The works of E.J. Davison and his collaborators [3]-[5] are particularly important, for they resulted in a computer-assisted method which is known to give the largest approximate of asymptotic stability sub-domain for a given non-linear systems model.

Moreover, Davison's work has been motivated by the goal of deriving a constructive computational method which would give automatically (that is, without trial-and-error iteration) the largest, numerically attainable region of asymptotic stability for a given systems model of arbitrary order via quadratic Lyapunov functions [5].

In our research, we have found these contributions to be of particular value in applications and worth re-elaborating within the information processing potential of nowadays standard PC platform [13]. In doing so, we have found that H.H. Rosenbrock's results [14] on using rotating-co-ordinates and hill-climbing strategy for static minimisation are rather instrumental [5], though other similar techniques can be employed. This paper gives a summarised presentation of our results; due to space limitation, results of a number of computer simulation experiments will be given in the course of presentation (Figures 1, 2, 3). The comparison analysis has been worked out with respect to the original examples used in Davison-Kurak [5]: Van Der Pol's dynamic systems; second-order bang-bang servo-mechanisms; and a third-order, analytical non-linear dynamic system.

II. AN OUTLINE OF DAVISON'S TECHNIQUE [5]

It is well known, there is no general method for determining the best suitable Lyapunov function for the purpose of guaranteeing asymptotic stability for non-linear dynamical systems of arbitrary order because Lyapunov theory gives sufficient conditions only. Solely in the case of linear models these conditions are known to be necessary as well. Moreover, the problem of computationally oriented methods for asymptotic stability investigation is even more involved. Nevertheless, there exist a number of contributions to computer-assisted determination of the largest sub-domain of the domain of asymptotic stability for non-linear dynamical models of motion in mechatronics systems such as represented by the quite general class (1). Firstly, Davison and Man have given a computational solution to the well-known matrix equation occurring in Lyapunov stability analysis [3] while Davison and Cowan for stability region of any second-order system [4]. Secondly, in [5], Davison and Kurak gave a constructive computational method for asymptotic stability via the class of quadratic Lyapunov functions and demonstrated that this approach yields by far better estimates than all previously derived computer-assisted techniques. The main idea behind Davison's method is to convert the problem of finding the "best" quadratic Lyapunov function, yielding the maximum stability boundary on the grounds of LaSalle and Lefschetz theorem [9] on sufficient

conditions for determining a sub-domain in the asymptotic stability domain, into a parameter minimisation problem and then to resolve it by using Rosenbrock's method [14]. In the case of discontinuous system models, the first step is to find a most appropriate equivalent continuous model approximating the original one [5], [6].

It is assumed that a motion or dynamics of mechatronic systems is represented in the form of the well known general model of vector differential equation

$$\dot{x} = f(x), f(0) = 0 \quad (1)$$

and its equilibrium position around the zero-vector, $x = 0$, in the n -dimensional linear space having a well-defined Euclidean norm (the output equation is not of particular concern here).

The great potential of Lyapunov functions and Lyapunov theory lies in its applicability for analysis and design of non-linear dynamic systems provided a quality estimate of system's asymptotic stability sub-domain within the respective domain can be determined [1], [2], [5], [14].

It is assumed that a model of non-linear system of type (1) and fulfilling the above quoted assumptions is available. Therefore a mechatronic system of the class (1) can be assumed to be locally asymptotically stable in the vicinity of the equilibrium, and that the eigenvalues of the Jacobean matrix at the equilibrium vector are in the left-hand part of the complex plane. Then LaSalle-Lefschetz theorem, which is given below, may be applied.

Theorem [11]

The equilibrium point $x = 0$ of system (1) is asymptotically stable, if there exist a scalar function $V(x)$, a Lyapunov Function, having continuous first-partial derivatives, and a domain Ω containing the equilibrium point, such that:

- (1) $V(x) > 0, \forall x \in \Omega, x \neq 0$
- (2) $V(0) = 0$
- (3) $\dot{V}(x) = f'(x) \text{grad} V(x) < 0, \forall x \in \Omega, x \neq 0$
- (4) $\dot{V}(0) = 0$

and if C is positive constant such that the surface $V(x)=C$ is contained in Ω , then the domain which is defined by $V(x) < C$ is in the domain of asymptotic stability for the system (1).

This theoretical result clearly suggests the conclusion that for a particular Lyapunov function $V(x)$, the surface with the largest value, say $V(x) = C_{max}$, which satisfies LaSalle-Lefschetz Theorem, gives the boundary of the largest asymptotic stability domain for the system. It is desirable therefore to find

a particular Lyapunov Function $V^*(x)$ such that the hypervolume, contained in Ω and defined by $V^*(x) = C_{\max}^*$, is a maximum.

The candidate for an appropriate Lyapunov function to system class (1), which fulfils conditions (1), (2) and (4) obviously, is the quadratic one:

$$V(x) = x^T \bar{A} x, \quad (2)$$

where $\bar{A} = \bar{A}^T$, and \bar{A} is a positive definite matrix (usually denoted by $\bar{A} > 0$). Then it remains to ensure that condition (3) of the theorem above is fulfilled. It is readily obtained from (1) and (2) that

$$\dot{V}(x) = 2f^T(x) \bar{A} x. \quad (3)$$

For this purpose, it is desired to determine matrix \bar{A} and positive constant C , so that the condition (3) in the theorem holds in a way that the volume contained in the closed surface

$$x^T \bar{A} x = C \quad (4)$$

in the state space of the system is maximum, that is "best" approximation of the asymptotic stability region for the system. It may be assumed that the matrix in Eq. (4) is scaled by constant C to give matrix A , and therefore the problem reduces to find a positive definite matrix A so that the condition (3) holds and so that the volume is contained in the closed surface

$$x^T A x = 1, \quad (6)$$

and given by equation

$$\text{volume} \propto \frac{1}{\sqrt{\prod_{i=1}^n \lambda_i(A)}}, \quad (7)$$

is the maximum one. Here, $\lambda_i(A)$, $i = 1, 2, \dots, n$ represent the eigenvalues of matrix A , and the maximum sought is obtained via the minimum of the product of all eigenvalues.

The equivalent parameter minimisation problem may be defined in the following way: Find $A = A^T$ so as to minimise product $\prod_{i=1}^n \{\lambda_i(A)\}$ subject to the constraints given below:

$$(1) \quad \min_{i=1,2,\dots,n} \lambda_i(A) > 0 \quad (8)$$

and

$$(2) \quad f^T(x) A x < 0, \quad \forall x \in \Omega, \quad (9)$$

where $\Omega = \{x | x^T A x \leq 1, \quad x \neq 0\}$

That is, a minimisation type of organised search for a positive definite matrix A which will satisfy condition (3) of LaSalle-Lefschetz theorem while maximising the volume of the asymptotic stability sub-domain of the system.

In general, there may exist many local minima to the above posed minimisation. Therefore it is very important that the starting values for the unknown parameters be chosen as close as possible to those values which correspond to the global minimum of

product $\prod_{i=1}^n \{\lambda_i(A)\}$. It is this feature that gives rise

to the essential importance of using Rosenbrock's method [14], and to the importance of proper choice of initial value A_0 for the matrix sought [5]. For proofs and more detail, see the original works [3], [5], [14].

III. A SUMMARY OF THE IMPLEMENTED ALGORITHMIC PROCEDURE

As a rule, the whole constructive, computational analysis of Davison's method is performed via double-precision arithmetics. In addition, a fine grid constructed using of rotating co-ordinates [14], [5] is needed.

Step 1. Once, an autonomous non-linear model of the system investigated, which satisfies the basic requirements of LaSalle-Lefschetz theorem, is available in terms of vector state equation

$$\dot{x} = f(x)$$

represented by means of its state variables and their time derivatives:

$$\dot{x} = \{\dot{x}_1, \dot{x}_2, \dot{x}_3, \dots, \dot{x}_n\},$$

and for which it is fulfilled $f(0) = 0$ and its Jacobean matrix at $x=0$ is stable, then, provided the condition

$$\text{Re} \left\{ \lambda_i \left(\frac{\partial f}{\partial x} \right) \right\}_{x=0} < 0, \quad \text{for } i = 1, 2, 3, \dots, n,$$

is also satisfied, the constructive computations for the "best" appropriate Lyapunov Function may begin.

The respective Lyapunov function for the system investigated is sought within the class represented by the well-known matrix-vector formula

$$V(x) = x^T A_0 x.$$

Note that here, vectors x and x^T may be viewed as generating the uniformly dense sets of respective n -dimensional space. Also, at the beginning they may be viewed as giving the intersecting points of the unit vectors within the sub-domain of asymptotic stability. The positive definite matrix A_0 is obtained by solving the Lyapunov equation

$$J^T A_0 + A_0 J = -C$$

where matrix J is the system Jacobean evaluated at the equilibrium point $x=0$:

$$J = \left(\frac{\partial f}{\partial x} \right)_{|x=0}$$

(All derivatives are obtained via Newton interpolation formula). Matrix C is an arbitrary positive-definite matrix which may be taken to be the unity matrix I . LaSalle and Lefschetz have shown that, under the conditions stated, the above Lyapunov equation has got a unique positive-definite solution. Therefore the equation

$$x^T A_0 x = \varepsilon_0,$$

where ε_0 is an arbitrary small positive constant (usually taken to be $\varepsilon_0 = 0^{-5}$ or smaller for satisfactory results) leads to obtaining an initial asymptotic stability boundary for the non-linear system. It should be noted that the choice of the initial value for ε_0 is rather important. This initial region, determined in the vicinity of the equilibrium point, represents a starting ground for further steps 2, 3, and 4 for determining the maximum volume of the region surrounding the equilibrium within which the asymptotic stability of the system is guaranteed.

Step 2. Further enlargement of the initial sub-domain of asymptotic stability is achieved by means of ℓ -dimensional search for maximising the value of the positive constant ε subject to the constraints

$$\max_{j=1,2,\dots,N_n} f \left(\frac{y_j}{\sqrt{y_j (A_0 / \varepsilon) y_j}} \right) A_0 y_j < 0$$

beginning with the initial starting value $\varepsilon = \varepsilon_0$. This eventually results in obtaining the value ε_{\max} as a solution, and then the boundary of asymptotic stability sub-domain is given by the following equation

$$x^T A_0 x = \varepsilon_{\max}$$

This encompasses the whole region, enlarged this way, for which it is guaranteed that the original non-linear system has got stable solutions for any initial state vector. Further computations evolve around Davison's fundamental idea of maximum expansion of the volume of guaranteed asymptotic stability sub-domain via approaching the real asymptotic stability boundary from the inside of the region, which is expressed by means of mathematical formulation given in term of representation (7)-(9).

Step 3. Further enlargement of the asymptotic stability region, established in the previous step, proceeds by using the positive constant ε_{\max} in order to determine the new (temporary) initial matrix value \bar{A} which, in turn, is used in the computational analysis within Step 4 to obtain matrix A that defines the surface of the maximum attainable rapprochement to the real asymptotic stability boundary. This constructive computational analysis is a kind of optimisation procedure for the elements of matrix \bar{A} , taking as initial starting value for \bar{A} the re-evaluated $(A_0 / \varepsilon_{\max})$, proceeding further via the minimising the respective eigenvalues of \bar{A} ; the eigenvalues are computed via well-known either QR or SVD method [13]. This minimisation is performed by implementing Rosenbrock's method of hill-climbing for the searching procedure needed as follows:

$$\min_A \lambda_{\max}(\bar{A})$$

where $\lambda_{\max}(\bar{A})$ is the largest eigenvalue of matrix \bar{A} while satisfying the inequality constraints

$$(1) \quad \min_{i=1,2,\dots,n} \lambda_i(A) > 0$$

$$(2) \quad \max_{\substack{i=1,2,\dots,N_n \\ k=1,2,\dots,p}} \left\{ f \left(\frac{k}{p} \frac{y_j}{\sqrt{y_j A y_j}} \right) A y_j \right\} < 0.$$

This procedure results in determining matrix \bar{A}^* by means of which the boundary of asymptotic stability sub-domain

$$x^T \bar{A}^* x = \varepsilon$$

is evaluated.

It should be noted that this step is rather important in Davison's method. For it gives the initial starting value which is needed in Step 4 which computes the minimisation of the product of the eigenvalues of A , defining the final hypersurface of

asymptotic stability sub-domain for the non-linear dynamic system investigated.

Remark. By minimising the maximum eigen-value of matrix \bar{A} , which is inversely proportional to the square of the length of the smaller minor axis of the n-dimensional quadratic surface, the quadratic surface is forced to become less eccentric [5]. Our experiments have confirmed Davison-Kurak statement that if this step is omitted in the computational analysis as a whole and the product of the eigenvalues of A is used as the cost function, then the minimum eigenvalue of the initially chosen matrix

\bar{A} decreases rapidly with a little change in the remaining eigenvalues. This corresponds to local minimum of the function $\prod_{i=1}^n \{\lambda_i(A)\}$ and, as a

consequence, the n-dimensional quadratic surface defines a typical region with a large eccentricity and small volume.

Step 4. Parameter minimisation by using Rosenbrock's method [14] within this step performs a kind of optimisation of the elements of the initial starting matrix \bar{A} by means of the minimisation procedure defined as follows:

$$\min \prod_{i=1}^n \{\lambda_i(A)\}$$

while satisfying the constraints

$$(1) \quad \min_{i=1,2,\dots,n} \lambda_i(A) > 0$$

$$(2) \quad \max_{\substack{i=1,2,\dots,n \\ k=1,2,\dots,p}} \left\{ f \cdot \left(\frac{k}{p} \frac{y_j}{\sqrt{y_j A y_j}} \right) A y_j \right\} < 0$$

to obtain $x^* A x = 1$, where matrix A is the resulting matrix, representing the final asymptotic stability boundary for the non-linear system investigated.

Step 5. It should be noted, provided LaSalle-Lefschetz theorem is fulfilled, then the boundary surface that is evaluated at the end of Step 4 is guaranteed to be contained within the exact, real boundary of asymptotic stability for this large class of non-linear dynamic systems considered in here. It is necessary therefore to test the negativity of the first

time derivative of Lyapunov function $\dot{V}(x)$, which is constructed in previous computation, at all points within the stability domain

$$x \in \{x | x^* A x < 1, x \neq 0\}$$

by using an extremely fine grid of p points (number of grid points between the origin and a given point at the quadratic surface) and N unity vectors within Euclidean state space of the systems. Due to limitations, this detail is omitted, but it is pointed out the grid is formed by storing pre-determined unit vectors such that they uniformly span the n-dimensional space following to the concept of rotating unit vectors and evaluating their number needed via Gregory-Newton formula [14]. If a non-negative value $\dot{V}(x)$ occurs at some point(s), then N and p are increased and steps 2, 3, 4, and 5 repeated.

IV. BASIC DATA ON THE SOFTWARE IMPLEMENTATION

The program package, implementing this improved Davison's method, has been developed as a DOS--WINDOWS application on a PC 486 platform using Borland C++ and the philosophy of object-oriented programming. It is constituted by a two subprograms VOVED.CPP and REALIZ.CPP, the former one via VOVED.EXE and using class 'edit' creates datafiles FUNC.CPP and FUNC.FPP which are then used by the latter, after being called-in and complied by compiler bcc.exe.

A separate subprogram MATRIX.CPP and a class 'matrix' are performing all matrix manipulations and operations. Subprogram REALIZ.CPP makes use of object-programming functions NAJDI_J.CPP, NAJDI_Ao.CPP, EMAX.CPP, VECTOR.CPP, MINLAM.CPP, EIGENVAL.CPP, and MINPRLAM.CPP for computational procedures within Davison's method.

Program function L_GRAFIK.CPP enables graphical presentation of projections of the asymptotic stability volume on co-ordinate planes of the state space, while datafile REPORT.DAT enables printouts. For systems up to 10th order, a perfect man-machine co-operative symbiosis is achieved; thereafter some noticeable computational delay is taking place following the increase of the order of system dynamics.

V. CONCLUDING REMARKS

The essential requirement is that the right-hand side vector function of the model be continuous and sufficiently structured so as to guarantee uniqueness of solution to the model equation. If not, as in the case of Davison's example [5] on second-order bang-bang servomechanisms, a most adequate approximation must be sought beforehand. All other work is performed by this constructive computational method. The use may be extended to complex systems [9].

REFERENCES

- [1] F.N.Bailey, "Application of Lyapunov second method to interconnected systems". *SIAM J. Control*, vol.3, pp.443-462, 1966.
- [2] S.Barnett, *Matrix Methods in Stability Theory*. London: Nelson, 1970.
- [3] E.J.Davison and F.T.Man, "The numerical calculation of $A^TQ + AQ = C$ ". *IEEE Trans. Automatic Control*, vol. AC-13, pp. 448-449, 1968.
- [4] E.J.Davison and K.Cowan, "A computational method for determining stability region of a second order non-linear autonomous system". *Intl. J. Control*, vol. 9, pp. 349-357, 1969.
- [5] E.J.Davison and E.M.Kurak, "A computational method for determining quadratic Lyapunov functions for non-linear systems". *Automatica*, vol.7, pp. 627- 636, 1971.
- [6] G.M.Dimirovski, N.E.Gough and S.Barnett, "Categories in systems and control theory". *Intl. J. Syst. Sci.*, vol. 8, no.9, pp.1081-1090, 1977.
- [7] G.M.Dimirovski, "Analysis of dynamic stability of electrical power systems using k-time matrices". In *Proceedings 15th Conf. of Electr. Power Engrs. of Yugoslavia*, Yugoslav Committee CIGRE, Zagreb-Belgrade, vol. III, pp. 177-187, 1981.
- [8] G.M.Dimirovski, R.M.Henry, N.E.Gough and O.L.Iliev, "Internal model approach to the stability problem of interconnected deterministic systems and CAD technologies: 1. System analysis; 2. Sub-system analysis." In V.Kecman (ed.) *Proceed. JUREMA 6th Symp. on Process Control Systems*. Zagreb: The JUREMA Association, Lectures A.1.8/9, 1990.
- [9] G.M.Dimirovski and Y.-W. Jing, "On decentralised observer-based stabilisation of a class of interconnected nonlinear systems." In A. Isidori & F.Allgower (eds.) *Proceed. ESF COSY Workshop on Non-linear and Uncertain Systems*. Zurich: Institut fur Automatik - ETH, pp. 211-220, 1997.
- [10] W. Hahn, *Theorie und Anwendungen der direkten Methoden von Liapunov*. Berlin: Springer-Verlag, 1959.
- [11] J.LaSalle and S.Lefschetz, *Stability by Lyapunov's Direct Method with Applications*. New York: Academic, 1961.
- [12] A.M.Letov, *Stability of Controlled Non-Linear Systems* (in Russian). Moscow: FIZMATGIZ, 1962.
- [13] A.Mojsovski, G.M.Dimirovski and M.Stankovski, Methods of E.J. Davison and H.H. Rosenbrock in Determining Lyapunov Functions, *Techn.Res.Rep. ILS-17/ASE-ETF*. Skopje: ASE -Faculty of EE, Sts. Cyril & Methodius University, March 1998
- [14] H.H.Rosenbrock, "An automatic method of finding the greatest or least value of a function". *Computer J.*, vol. 3, pp. 175-184, 1960.
- [15] J.-J.E. Slotine and W.Li, *Applied Nonlinear Control*. Prentice Hall, Englewood Cliffs N.J., 1991.

Cross-coupling Controller Design for a 2-DOF Platform

Oren Masory and Daoxi Xiu

Robotics Center
Florida Atlantic University
Boca Raton, FL 33431
Masoryo@fau.edu

Abstract.

This paper proposes a cross-coupling controller for a two degrees-of-freedom platform. The cross-coupling controller is fed with the contour error along the trajectory, and in turn produces correcting signals, which fed as additional input for each axis, so that the magnitude of the error is reduced. The relationship between the cross-coupling controller gains, the trajectory and the PID controller gains of each axis is determined by pole placement. Simulation results show that the cross-coupling controller is capable of reducing the contour error by 30%.

1. Introduction

Recently, several prototypes of CNC machine tools, based on six Degrees-of-Freedom (DOF) parallel manipulators such as Stewart platform [1-4], have been proposed. This kind of machine tools possess the advantages of high force/torque capacity, high structural rigidity and better accuracy [5-9].

In order to ensure the high accuracy of the CNC machine tools, appropriate controllers or control schemes are needed. Several methods have been proposed and many advances have been accomplished for conventional CNC machine tools [10]. One of these methods is the cross-coupling controller, first proposed in [11].

The idea behind the cross-coupling controller is that as the system tracks a given contour, the contour error can be determined and then used to produce a compensation signals to the system's axes so that the error will be reduced or eliminated. In order to perform this task, a real-time model of the contour error as well as an effective compensating control law should be employed.

Since the mathematical treatment of a six DOF platform is rather very complex [5-7], the above methodology will be demonstrated on a two DOF platform. A two DOF platform differs from the conventional six DOF platform in its upper plate, which is reduced to a mass point located at the revolute joint that connects its two legs. Although some characteristics

of conventional platforms may not be revealed using this two DOF platform, the results of this investigation are still applicable.

2. Two DOF Platform Description, Kinematics and Control

The structure of a 2-DOF platform, shown in Figure 1, is a triangle where one side, called base, has a fixed length and attached to ground. The other two sides are actuated by hydraulic cylinders and are called legs. The legs are connected to ground and to each other by revolute joints. The platform is vertical and as such subjected to gravity.

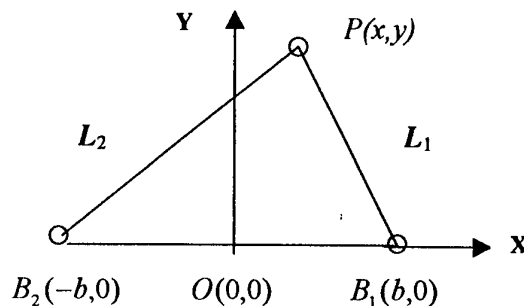


Figure 1. 2-DOF platform Architecture

The base of the 2-DOF platform is aligned with the X axis, while the actuation legs are in the XY plane. The origin of the coordinate system is chosen at the midpoint of the base. The legs L_1 and L_2 move $P(x, y)$ in 2-DOF space.

The inverse kinematics is given by:

$$\begin{bmatrix} L_1 \\ L_2 \end{bmatrix} = \begin{bmatrix} \sqrt{(b-x)^2 + y^2} \\ \sqrt{(b+x)^2 + y^2} \end{bmatrix} \quad (1)$$

The forward kinematics is given by:

$$\begin{bmatrix} x \\ y \end{bmatrix} = \begin{bmatrix} \frac{L_2^2 - L_1^2}{4b} \\ \frac{\sqrt{(4bL_1)^2 - (4b^2 + L_1^2 - L_2^2)^2}}{4b} \end{bmatrix} \quad (2)$$

The differential relation between leg length and the position $P(x, y)$ is given by

$$\begin{bmatrix} dL_1 \\ dL_2 \end{bmatrix} = \begin{bmatrix} \frac{x-b}{L_1} & \frac{y}{L_1} \\ \frac{x+b}{L_2} & \frac{y}{L_2} \end{bmatrix} \begin{bmatrix} dx \\ dy \end{bmatrix} \quad (3)$$

Each axis is implemented by a hydraulic cylinder and controlled by a PID controller the same as described in [9]. ITAE (the Integral of Time multiplied by Absolute Error) performance index was selected for the design of the PID controller. The transfer function of each leg is in the form:

$$L_i(s) = \frac{W_1(s)}{W(s)} L_i^*(s) - \frac{W_2(s)}{W(s)} F_i(s) \quad i = 1, 2 \quad (4)$$

where: L_i^* The reference position of each leg
 L_i The leg displacement of each leg.
 F_i The external disturbance to each leg.
 W 's Polynomials in s

3. Contour Error Model

The contour error is the deviation between the required and the actual contour produced during the machining process [9-11]. The contour error for an arbitrary curve is illustrated in Figure 2.

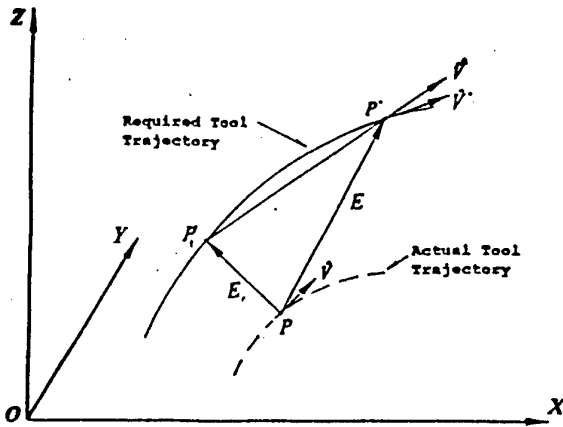


Fig. 2. Contour error for an arbitrary curve

Denote the following position vectors: P^* a position vector of a point on the planned contour; P a position vector of the corresponding point on actual contour; and P_1^* a position vector of a point on the planned contour which is closest to P .

The following error vector, E , is given by:

$$E = P^* - P \quad (5)$$

The contour error vector, E_r , is given by:

$$E_r = P_1^* - P = E - (P^* - P_1^*) \quad (6)$$

Let \hat{V}^* and \hat{V} be the unit vectors of velocities associated with P^* and P respectively, and $\hat{\bar{V}}$ is the unit vector of velocity associated with the chord $P^* - P_1^*$. Since the contour error, E_r , is normal to the planned contour, the direction of the chord $P^* - P_1^*$ and the tangent of the planned contour at P_1^* are almost the same for a small sampling segment. Thus, the contour error, E_r , is almost normal to $P^* - P_1^*$, and therefore $P^* - P_1^*$ can be approximated by the projection of the following error, E , along the unit vector $\hat{\bar{V}}$:

$$P^* - P_1^* \approx (E \cdot \hat{\bar{V}}) \hat{\bar{V}} \quad (7)$$

Then, Eq. (11) can be approximated as follows.

$$E_r \approx E - (E \cdot \hat{\bar{V}}) \hat{\bar{V}} \quad (8)$$

Since displacement during one sampling time of the controller is very small, and the difference between \hat{V}^* and \hat{V} is very small too. Also $\hat{\bar{V}}$ is not available in real time, therefore by replacing $\hat{\bar{V}}$ by \hat{V}^* , Eq. (8) becomes

$$E_r \approx E - (E \cdot \hat{V}^*) \hat{V}^* \quad (9)$$

4. Cross-Coupling Controller Design

From kinematics viewpoint, the contour error of a platform must be reflected as the deviation of all the axes from their desired displacements. As discussed above, the Jacobean matrix, J_p , provides the relationship between the motions in the world and

the joint coordinate systems. Thus the cross-coupling control law can be expressed as:

$$\varepsilon = K_c J_p E_r \quad (10)$$

where

$$\varepsilon = [\varepsilon_1 \quad \varepsilon_2]^T \quad \text{The cross-coupling control signal}$$

$$K_c = \begin{bmatrix} K_{c11} & K_{c12} \\ K_{c21} & K_{c22} \end{bmatrix} \quad \text{The cross-coupling controller gain}$$

The block diagram of the cross-coupling controller for a 2-DOF platform is shown in Figure 3.

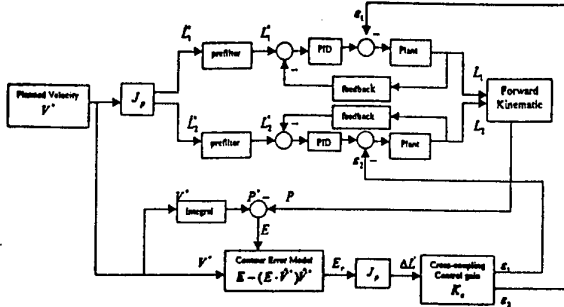


Fig. 3. Architecture of 2-D cross-coupling controller

To determine a relationship between the PID gains and the cross-coupling controller gains, it is assumed that the external force and internal dynamic force are negligible (omitting the second term in Eq. 4):

$$L_i(s) = \frac{W_1(s)}{W(s)} L_i^*(s) - \frac{W_3(s)}{W(s)} \varepsilon_i(s) \quad i = 1, 2 \quad (11)$$

where $W_3(s)$ is a polynomial in s .

At this point, there is a need to express ε_1 and ε_2 and their derivatives, depends on the order of $W(s)$, in term of leg variables in order to achieve an explicit transfer function between the reference leg length and the system output (actual leg length). Substitute Eq. 9 in Eq. 11 yields:

$$\varepsilon = \begin{bmatrix} \varepsilon_1 \\ \varepsilon_2 \end{bmatrix} = K_c J_p (E - (E \cdot \hat{V}^*) \hat{V}^*) \quad (12)$$

The expression for ε and its derivatives in term of leg variables L_i ($i = 1, 2$) is obtained by solving for E as shown in Figure 2.

$$E = P(x, y) - P^*(x^*, y^*) \quad (13)$$

where

$$P(x, y) = \begin{bmatrix} x \\ y \end{bmatrix} = \begin{bmatrix} \frac{L_2^2 - L_1^2}{4b} & \frac{\sqrt{\Gamma}}{4b} \end{bmatrix}^T$$

$$P^*(x^*, y^*) = \begin{bmatrix} x^* \\ y^* \end{bmatrix} = \begin{bmatrix} \frac{L_2^{*2} - L_1^{*2}}{4b} & \frac{\sqrt{\Gamma^*}}{4b} \end{bmatrix}^T$$

$$\Gamma = (4bL_1)^2 - (4b^2 + L_1^2 - L_2^2)^2$$

$$\Gamma^* = (4bL_1^*)^2 - (4b^2 + L_1^{*2} - L_2^{*2})^2$$

and

$$\hat{V}^* = V^* / \|V^*\|$$

where

$$V^* = \begin{bmatrix} \dot{x}^* \\ \dot{y}^* \end{bmatrix} = \begin{bmatrix} -\frac{L_1^*}{2b} & \frac{L_2^*}{2b} \\ \frac{L_1^*(4b^2 - L_1^{*2} + L_2^{*2})}{2b\sqrt{\Gamma^*}} & \frac{L_2^*(4b^2 + L_1^{*2} - L_2^{*2})}{2b\sqrt{\Gamma^*}} \end{bmatrix} \begin{bmatrix} \dot{L}_1^* \\ \dot{L}_2^* \end{bmatrix}$$

The following error, E , is linearized and high order terms are neglected. The contour error is expressed as:

$$\varepsilon = \begin{bmatrix} \varepsilon_1 \\ \varepsilon_2 \end{bmatrix} = C_p (L - L^*) \quad (14)$$

where C_p is a matrix of terms which are function of the pose and the velocity of the platform as well as K_c . C_p is selected by choosing the poles and zeros of the system in order to insure a certain performance.

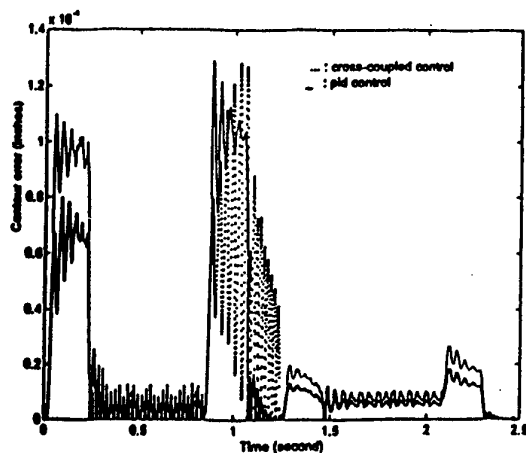
5. Simulation Results

Two trajectories were used for the simulation: a 5" square and a circle with 10" diameter.

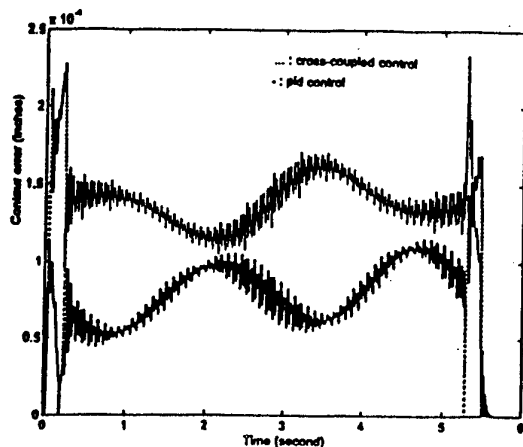
The cross-coupling controller gain, K_c , varies along the trajectory, but in these simulations an average constant value is used:

$$K_c = \begin{bmatrix} 4.249 & -0.415 \\ -0.782 & 6.068 \end{bmatrix} \quad (15)$$

The mismatched system is assumed to have deviation of $\pm 2\%$ in gain and $\pm 5\%$ in natural frequency.



(a)



(b)

Fig. 4. The contour error for mismatched system (a – Square, b – Circle)

Figure 4 illustrate the effect of the cross-coupling controller on the contour errors. As shown, the contour error along the circular trajectory was reduced by about 30%, and by 50% along the square trajectory.

6. CONCLUSION

The cross-coupling controller was designed by giving the contour error model and cross-coupling control law. Since the cross-coupling controller is related to the real-time contour error feedback, the cross-coupling controller gain is closely related to the position and velocity of the platform along the trajectory. The average values should be chosen for constant controller gain.

The simulation results illustrate that the cross-coupling control system has the ability to substantially reduce the

contour errors. Thus, the application of this method to a six DOF platform is very promising.

7. REFERENCES

- [1] Murry, C. J., "A floating revolution for automation", *Design News*, Aug. 1994
- [2] "The cutting edge of machine tools", *Manufacturing Engineering*, Nov. 1993
- [3] Fitzgerald, J. M., Lewis, F. L., "Evaluating the Stewart platform for manufacturing", *Robotics Today*, Vol. 6, No. 1, 1993
- [4] "Space frame design enhances metal-cutting machine tool", *R&D Magazine*, Sept. 1995, pp.62
- [5] Stewart, D., "A platform with six degrees of freedom", *Proceedings of the Institution of Mechanical Engineering*, Vol. 180, Part 1, No.15, 1965-1966, pp.371-386
- [6] Fitcher, E. F., "A Stewart platform-based manipulator: general theory and practical consideration", *Journal of Robotics Research*, Summer 1986, pp. 152-182
- [7] Hunt, K. H., "Structural kinematics of in-parallel-actuated robot-arms", *ASME Journal of Mechanisms, Transmissions, and Automation in Design*, Vol. 105, Dec. 1983, pp. 705-711
- [8] Yang, D. C. H. and Lea, T. W., "Feasibility study of a platform type of robot manipulators from a kinematic viewpoint", *ASME Journal of Mechanisms, Transmissions, and Automation in Design*, June, 1984, Vol. 106, pp. 191-198
- [9] Masory O. and Xiu, D., "Contour errors in a new class of CNC machine tools", *The 1998 World Automation Congress*, Anchorage, Alaska, USA, May 1998
- [10] Ulsoy, A. G. and Koren, Y., "Control of machining processes", *Journal of Dynamic System, Measurement, and Control*, Vol. 115, June 1993, pp. 301-323
- [11] Koren, Y., "Cross-coupled biaxial computer control for manufacturing systems", *ASME Journal of Dynamics systems, Measurement, and Control*, Vol. 102, Dec. 1980, pp. 265-272
- [12] Koren Y. and Lo, C. C., "Evaluation of servo-controller for machine tools", *Proc. of the American Control Conference*, 1992, pp. 370-374
- [13] Masory, O. and Wang, J., "Improving contouring system accuracy by two-state actuation", *Transactions of NAMR/SME*, Vol. 2, 1991, pp. 274-280
- [14] Srinivasan, K. and Kulkrani, P. K., "Optimal contouring control of multi-axial feed drive servomechanisms", *ASME Journal of Engineering Industry*, Vol. 111, May, 1989, pp. 140-148
- [15] Chuang, H.Y. and Liu, C. H., "Cross-coupled adaptive feedrate control for multi-axis machine tools", *ASME Journal of Dynamics Systems, Measurement, and control*, Vol. 113, Sept. 1991, pp.451-457
- [16] Matlab® Control Toolbox User Guide, The Mathworks, Inc., Dec. 1996
- [17] Jamshidi, M., *Large-Scale Systems*, Elsevier Science Publishing Co., Inc, 1983

DSP Based Position Control of PMSM with Real-Time Cycloidal Path Generation for Intelligent Motion Applications

Francesco Parasiliti, Roberto Petrella, Marco Tursini

Department of Electrical Engineering
University of L'Aquila

67040 Monteluco di Roio, L'Aquila - Italy

rock@ing.univaq.it – petrella@ing.univaq.it – tursini@ing.univaq.it

Abstract

This paper presents the implementation of an intelligent position controller for a PMSM drive based on a last generation μ C DSP (TMS320F24x) suitable for multiple axes motion control systems. The problem of path generation with variable target position and movement constraints is considered and solved in real-time by the same drive controller. Specific profiles for the torque and speed based on parametric sinusoidal acceleration are used. On the fly changes of target position as well as of other parameters of the movement are allowed and real-time calculation and tracking of the new position path are done. Experimental results showing the system performance for different movement characteristics are presented.

1. Introduction

Motion control systems exist in all classes of machines especially in those for the execution of co-ordinated motion in two or more axes, such as industrial robot manipulators, packing machines, etc.. The motion control of a machine or a system consists in principle of the following tasks: optimised speed control of the axis, position control in every axis, path generation for each axis and co-ordination of the motion among the axes [1].

With regard to the position control, different problems arise depending on the kind of motion to be performed (kind of target, speed, number of axes), the required dynamic and precision. One of the most difficult situations is certainly the positioning with variable target position and movement constraints. A typical case is represented by a packing machine which uses a thin PVC film to pack objects of different sizes. This is an example of multiple axes motion control system where the speed and position of the target are variable (depending on the size and weight of the object to be packed). Smooth speed changes are needed in order to limit the maximum jerk and to avoid the

breaking of the film. Thus specific profiles for the torque and speed must be generated in real-time depending on the characteristics of the movement, that is target position and movement constraints (limitations on mechanical speed and accelerations reached during the movement). Moreover on the fly changes of target position as well as other parameters of the movement should be allowed and real-time calculation and tracking of the new position path should be done.

One of the profiles that could be used to satisfy the previously stated needs is the one which uses a parametric sinusoidal acceleration. In this case smooth speed and position following a cycloidal trajectory are obtained and different paths can be generated by varying both the peak value and the period of the acceleration.

Until now the classical motion control system structure allocated the path generation task in an intelligent master controller and considered the drives as actuators being able to control the position, the speed and the torque in the corresponding axis [2][3]. This leads to unavoidable problems when complex paths for multiple axes are being generated. Particularly, both the demand for real-time calculation and the requirements for high communication throughputs of the master increase dramatically. Fast and accurate motion control cannot be achieved without the recourse to improved, high performance control systems.

With the introduction of μ C DSPs (Digital Signal Processors) dedicated to control of electrical drives, the task of path generation can be performed by the same drive controller in real-time. Consequently the task of co-ordination of the different axes can be executed by a low-cost general purpose μ C.

In this paper the implementation of an intelligent position controller for a PMSM based on a last generation μ C DSP (TMS320F24x) is presented. The problem of cycloidal path generation with variable target position and movement constraints is considered and solved in real-time by the same drive controller. All the parameters of the drive system can be changed in

real-time through a standard RS-232 serial link. Experimental results showing the system performance for different movement characteristics are presented.

2. Path generation problem

A one axis generic movement could be decomposed in an acceleration phase (A), a constant speed phase (C) and a deceleration phase (D) (see Figure 1).

By assuming for phases A and D a parametric sinusoidal acceleration, it is possible to establish the following relations:

$$\begin{cases} a_A(t) = \frac{\pi \cdot h_A}{t_{sA}^2} \cdot \sin\left(\pi \frac{t}{t_{sA}}\right) \\ v_A(t) = \int_0^t a_A(\xi) d\xi = \frac{h_A}{t_{sA}} \cdot \left[1 - \cos\left(\pi \frac{t}{t_{sA}}\right)\right] + v_0 \\ \theta_A(t) = \int_0^t v_A(\xi) d\xi = h_A \cdot \left[\frac{t}{t_{sA}} - \frac{1}{\pi} \sin\left(\pi \frac{t}{t_{sA}}\right)\right] + v_0 t + \theta_{0A} \end{cases} \quad (A)$$

$$\begin{cases} a_C(t') = 0 \\ v_C(t') = \int_0^{t'} a_C(\xi) d\xi = \frac{h_C}{t_{sC}} \\ \theta_C(t') = \int_0^{t'} v_C(\xi) d\xi = h_C \cdot \frac{t'}{t_{sC}} + \theta_{0C} \end{cases} \quad (C)$$

$$\begin{cases} a_D(t'') = -\frac{\pi \cdot h_D}{t_{sD}^2} \cdot \sin\left(\pi \frac{t''}{t_{sD}}\right) \\ v_D(t'') = \int_0^{t''} a_D(\xi) d\xi = -\frac{h_D}{t_{sD}} \cdot \left[1 - \cos\left(\pi \frac{t''}{t_{sD}}\right)\right] + \frac{h_C}{t_{sC}} \\ \theta_D(t'') = \int_0^{t''} v_D(\xi) d\xi = -h_D \cdot \left[\frac{t''}{t_{sD}} - \frac{1}{\pi} \sin\left(\pi \frac{t''}{t_{sD}}\right)\right] + h_C \cdot \frac{t''}{t_{sC}} + \theta_{0D} \end{cases} \quad (D)$$

where different time axes have been considered for simplicity in each phase. In the previous relations, h_i

and t_{si} ($i = A, C, D$) are a set of parameters characterising the movement, whose significance is indicated in the list of used symbols.

Analytically it is possible to relate these parameters to the basic physical characteristics of the movement (a_{maxA} , a_{maxD} and v_{max}) as follows:

$$h_A = \frac{\pi}{4} \cdot \frac{(v_{max} - v_0)^2}{a_{maxA}}, \quad t_{sA} = \frac{\pi}{2} \cdot \frac{(v_{max} - v_0)}{a_{maxA}} \quad (1)$$

$$h_C = v_{max} \cdot t_{sC} \quad (2)$$

$$h_D = \frac{\pi}{4} \cdot \frac{v_{max}^2}{a_{maxD}}, \quad t_{sD} = \frac{\pi}{2} \cdot \frac{v_{max}}{a_{maxD}} \quad (3)$$

Moreover the position increments that is possible to obtain in each phase are given by:

$$\Delta\theta_A = h_A + 2h_A \frac{v_0}{v_{max} - v_0} \quad (4)$$

$$\Delta\theta_C = h_C \quad (5)$$

$$\Delta\theta_D = h_D \quad (6)$$

and the total positions increment that is possible to obtain by the sequencing of the phases A, C and D is

$$\Delta\theta = \Delta\theta_A + \Delta\theta_C + \Delta\theta_D = h_A + 2h_A \frac{v_0}{v_{max} - v_0} + h_C + h_D \quad (7)$$

Hence a possible formulation of the path generation problem is to find out the $\theta_i(t)$, $v_i(t)$ and $a_i(t)$ profiles (in term of the parameters h_i , t_{si}) in order to have the total movement $\Delta\theta$ (refer to Figure 1 and (7))

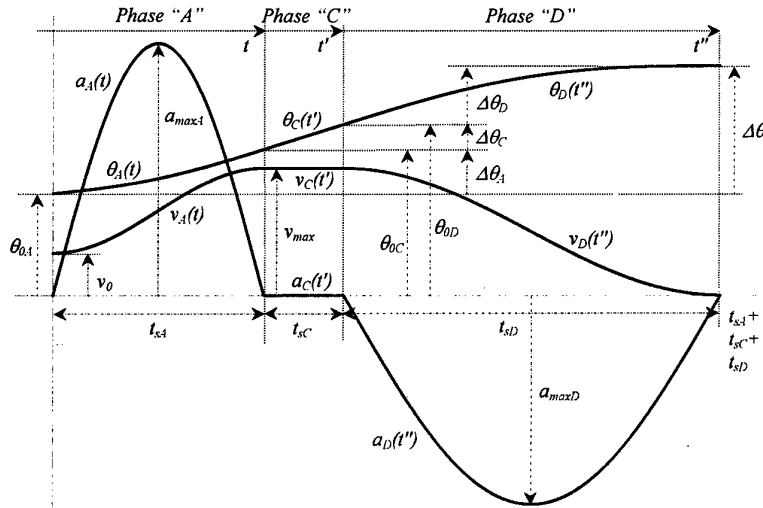


Figure 1. Generic movement.

equal to a target $\Delta\theta^*$. Input parameters of this problem are: the initial condition of speed v_0 , the assumed constraints on the acceleration ($a_{\max A}$) and deceleration ($a_{\max D}$) and the maximum allowable speed ($v_{\max 0}$) during the movement. The situation is resumed in Figure 2.

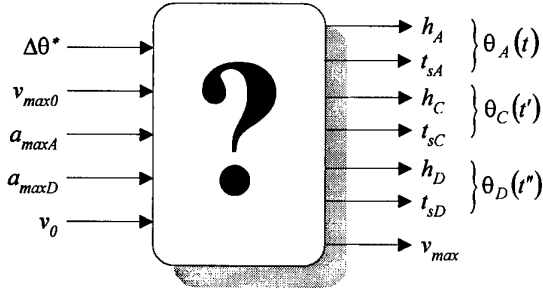


Figure 2. Path generation problem.

We think it right to point out that $a_{\max A}$ and $a_{\max D}$ are the exact values of the maximum accelerations during phases A and D while $v_{\max 0}$ is an upper bound. Thus, depending on the particular movement characteristic, this limit should be reached or not. In this sense v_{\max} is considered an output parameter of the problem.

Moreover depending on the sign of the initial speed v_0 and on target position $\Delta\theta^*$, four kinds of movement are possible, as it is summarised in Table 1.

Table 1. Possible kind of movements.

Positive movement without direction inversion	$\Delta\theta^* > 0$	$v_0 > 0$
Negative movement without direction inversion	$\Delta\theta^* < 0$	$v_0 < 0$
Positive movement with direction inversion	$\Delta\theta^* > 0$	$v_0 < 0$
Negative movement with direction inversion	$\Delta\theta^* < 0$	$v_0 > 0$

3. A solution of path generation problem

The general solution of the previously stated problem exist, is unique and will be given in the case of a positive movement without direction inversion. It is easy to extend the obtained results to the other three cases indicated in Table 1.

We can firstly notice that the solution of path generation problem depends on the value of the target

$\Delta\theta^*$ with respect to the position increment obtained by using only phases A and D ($t_{sC} = 0$) and the maximum allowed value of the speed ($v_{\max} = v_{\max 0}$). This increment is given by

$$\Delta\theta_{AD} = \Delta\theta_A + \Delta\theta_D = h_A + 2h_A \frac{v_0}{v_{\max} - v_0} + h_D \quad (8)$$

If the target $\Delta\theta^*$ is equal to $\Delta\theta_{AD}$, then the problem is simply solved by using the values of h_i and t_{si} ($i = A, D$) given by (1) and (3).

The situation is more complex when $\Delta\theta^* > \Delta\theta_{AD}$ or $\Delta\theta^* < \Delta\theta_{AD}$.

In the first case the values of $v_{\max 0}$, $a_{\max A}$ and $a_{\max D}$ are not high enough to allow the required position increment to be generated without introducing a constant speed phase. Hence, by assuming $v_{\max} = v_{\max 0}$, the position increment that must be introduced during this phase is

$$h_C = \Delta\theta^* - \Delta\theta_{AD} = \Delta\theta^* - h_A + 2h_A \frac{v_0}{v_{\max} - v_0} + h_D \quad (9)$$

its application time being

$$t_{sC} = \frac{h_C}{v_{\max}} = \frac{\Delta\theta^* - \Delta\theta_{AD}}{v_{\max}} = \frac{\Delta\theta^* - h_A + 2h_A \frac{v_0}{v_{\max} - v_0} + h_D}{v_{\max}} \quad (10)$$

In the second case the position increment that is possible to obtain by using only phases A and D and the maximum speed ($v_{\max} = v_{\max 0}$) is greater than the required one. Then the maximum value of speed reached during the movement must be properly reduced to a value $v_{\max} < v_{\max 0}$ small enough to satisfy $\Delta\theta^* = \Delta\theta_{AD}$. By substituting in (8) the values of h_A and h_D given by (1) and (3) and imposing $\Delta\theta^* = \Delta\theta_{AD}$, it is possible to obtain:

$$v_{\max} = \sqrt{\frac{4/\pi a_{\max A} a_{\max D} \cdot \Delta\theta^* + a_{\max D} v_0^2}{a_{\max A} + a_{\max D}}} \quad (11)$$

It could be noted that (11) is independent on the sign of v_0 and always gives a positive value for v_{\max} .

The last consideration allows us to unify the solution of path generation problem: we always evaluate v_{\max} given by (11) but we limit this value to $v_{\max 0}$ in the case $v_{\max} > v_{\max 0}$. The values of h_i and t_{si} are given by (1), (3), (9) and (10). Figure 3 shows the block

diagram of the algorithm solving the path generation problem in the considered case.

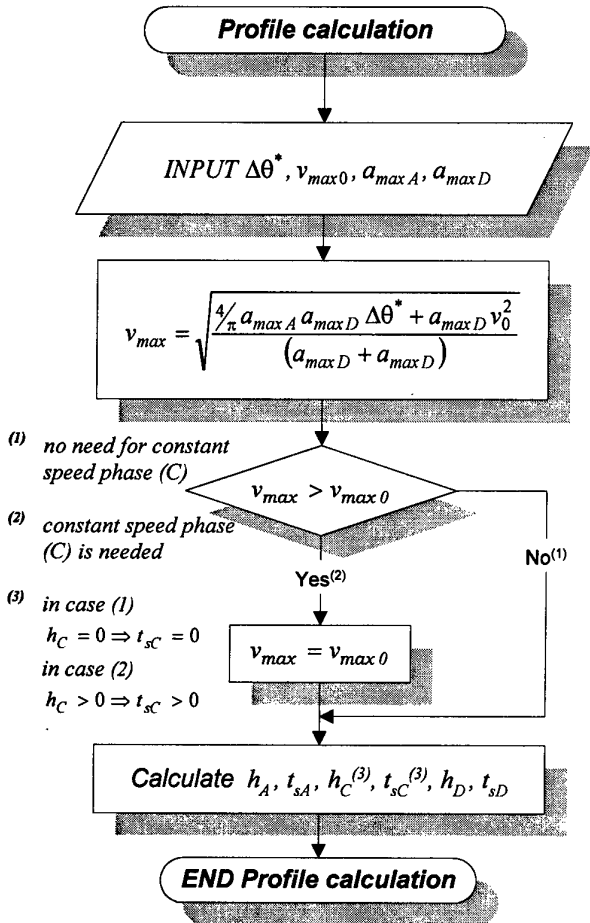


Figure 3. Solution of path generation problem in case of positive movement without direction inversion.

4. Control scheme

The PMSM based drive controller is shown in Figure 4. It is based on the field-oriented control principle arranged in the dq rotating frame aligned with the rotor flux. The motor currents in the two-phase stator reference frame $\alpha\beta$ are calculated by the measurement of two of the actual phase currents and a three-phases to $\alpha\beta$ transformation. Hence, the dq components are obtained using the rotor position information. The mechanical speed and the quadrature i_q component are controlled respectively to the reference values given by the position and speed controllers, whilst the direct i_d component is controlled at zero in order to minimise the current vs. torque ratio of the motor. The outputs of the current controllers, representing the voltage references, are then impressed to the motor using the Space Vector Pulse Width Modulation technique (SVPWM), once an inverse transformation from the rotating to the fixed stator reference has been performed. Position path feeding the position regulator is generated starting from the target position and taking into account the constraints on mechanical speed and accelerations. Almost all the used controllers are standard PI regulators except for the position controller where only a proportional regulator has been added and a feed forward component has been added to increase the dynamic response of the system.

5. Control hardware

The control hardware used to implement the intelligent position controller is based on a Texas Instruments TMS320F240 μC Digital Signal Processor control board dedicated to control of electrical drives which also integrates an IGBT based Intelligent Power Module (Figure 5).

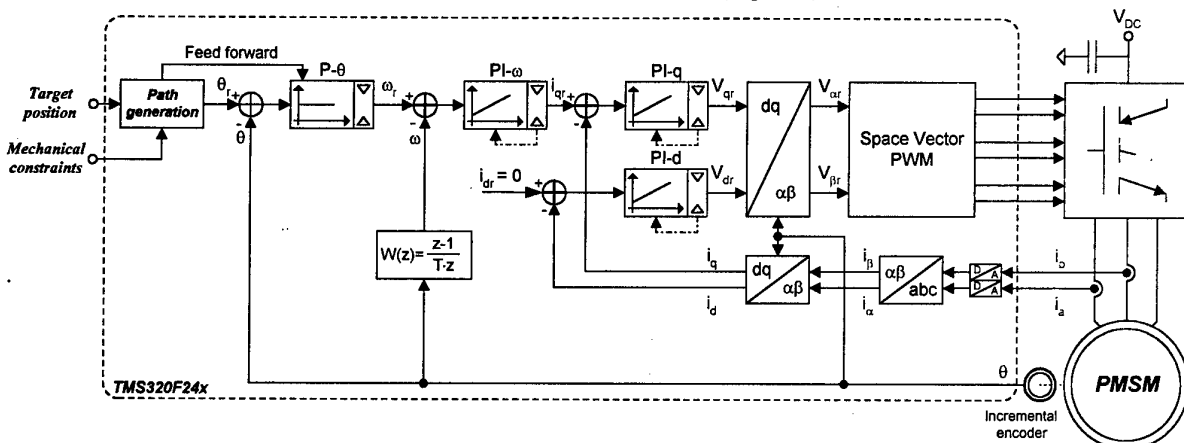


Figure 4. Control scheme.

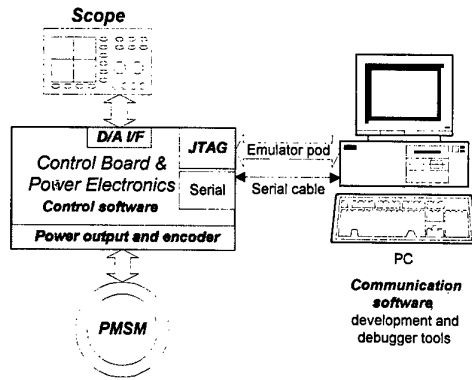


Figure 5. Control hardware.

A host PC is used to run both the DSP development and debugger tools and to simulate the behaviour of a master controller in a motion control system. A scope has been used to display in real-time the variables calculated inside the control algorithm by means of a 4 channels digital to analog interface mapped on the I/O addressing space of the μC DSP.

The μC is provided with 544 words (16-bit) of data Dual Access RAM (used to store control variables) and 16Kwords of program Flash-EEPROM (used to store control program and look-up tables) thus allowing a single-chip solution for motor control.

6. Software architecture

The control software has been designed according to the multi-process structure reported in Figure 6.

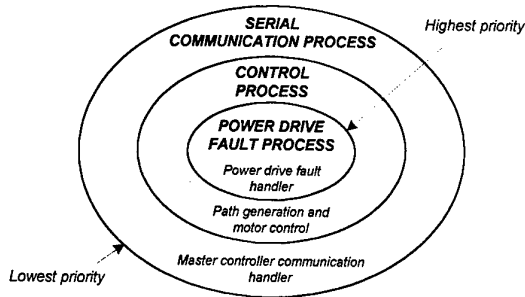


Figure 6. Multi-process software organisation.

The control process is executed every sampling period (100 μs) performing both motor control and real-time path generation based on the parameters and reference values received through the concurrent serial communication process. A power drive fault process has also been included to protect the power module. All the software has been implemented using assembly language and fixed precision numerical representation.

7. Experimental results

Figure 7 to Figure 10 present some of the results obtained by using the proposed system. The base values of 3000 rpm for speed and 3000 rad/s^2 for accelerations are assumed. Figure 7 shows speed and position during a movement where the speed limitation $v_{\max 0}$ is reached, that is phase "C" (constant speed phase) is present. Figure 8 shows the same variables during the same movement where the speed limitation $v_{\max 0}$ has been increased to a value high enough that phase "C" is not present. Finally an on the fly target position change without movement inversion has been considered in Figure 9 and Figure 10. Speed, position, quadrature component and phase currents are shown.

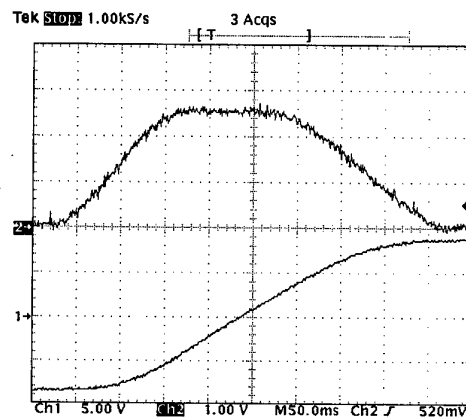


Figure 7. Speed (up) and position (down) (speed limitation is reached and constant speed phase is present ($\Delta\theta^*=\theta^*-\theta_0=14\pi$, $v_{\max 0}=0.5$, $a_{\max A}=0.5$, $a_{\max D}=0.35$)).

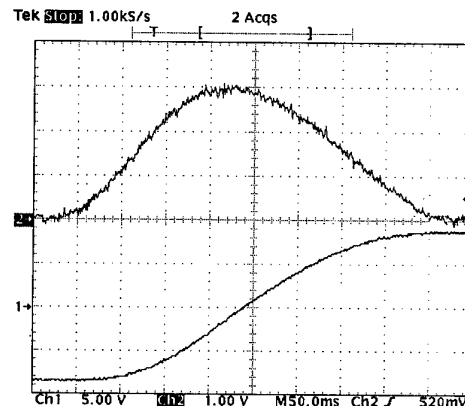


Figure 8. Speed (up) and position (down) (speed limitation is not reached and constant speed phase is not present) ($\Delta\theta^*=\theta^*-\theta_0=14\pi$, $v_{\max 0}=0.7$, $a_{\max A}=0.5$, $a_{\max D}=0.35$)).

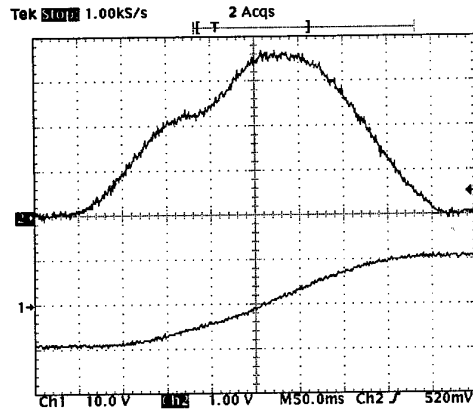


Figure 9. Speed (up) and position (down) during an on the fly target position change ($\Delta\theta_1^*=\theta_1^*-\theta_0=6\pi$, $\Delta\theta_2^*=\theta_2^*-\theta_0=14\pi$, $v_{max0}=0.7$, $a_{maxA}=0.5$, $a_{maxD}=0.6$).

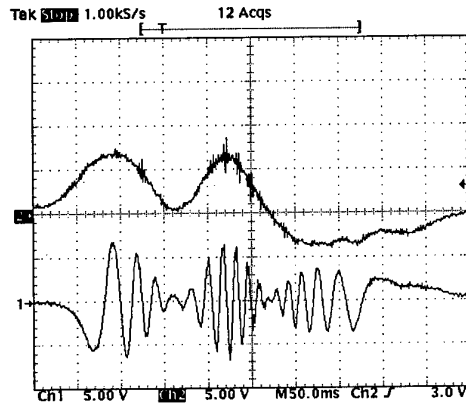


Figure 10. q-axis current (up) and phase current (down) during an on the fly target position change ($\Delta\theta_1^*=\theta_1^*-\theta_0=6\pi$, $\Delta\theta_2^*=\theta_2^*-\theta_0=14\pi$, $v_{max0}=0.7$, $a_{maxA}=0.5$, $a_{maxD}=0.6$).

7. Conclusions

In this paper the implementation of an intelligent position controller for a PMSM drive based on a last generation μ C DSP (TMS320F24x) has been presented, suitable for multiple axes motion control systems. The problem of path generation with variable target position and movement constraints is considered and solved in real-time by the same drive controller. Specific profiles for the torque and speed are used based on parametric sinusoidal acceleration. Experimental results showing the system performance for different movement characteristics are presented.

8. References

- [1] A. John, J.M. Pacas, "Intelligent motion: the new challenge for electrical drives", *Proc. of 7th European Conference on Power Electronics and Applications*, Trondheim, 1997, vol.3 pp.918-921.
- [2] T. Ohmae, M. Watanabe, "Microprocessor systems for motion control", *Proc. of IFAC Workshop on Motion Control for Intelligent Automation*, Perugia, Italy, October 27-29, 1992, pp. 253-258.
- [3] S. Di Gennaro, M. Tursini, "Control Techniques for Synchronous Motors with Flexible Shaft", *Proc. of 3rd IEEE Conference on Control Applications*, Glasgow, UK, August 24-26, 1994, pp. 471-476.

List of used symbols

- x_i ($i = A, C, D$): value of x during acceleration phase "A", constant speed phase "C" and deceleration phase "D" respectively.
- t, t', t'' : time references within phases A, C and D respectively.
- $\theta_i(\cdot)$, $v_i(\cdot)$, $a_i(\cdot)$: respectively position (rad), speed (rad/s) and acceleration (rad/s²) profiles within phase i .
- θ_{0i} : initial position within phase i .
- v_0 : initial condition for speed.
- t_{si} : time duration of phase i .
- h_A : position increment within phase A but considering $v_0 = 0$.
- h_C, h_D : position increment within phases C and D respectively.
- a_{maxi} : maximum value of acceleration within phase i .
- v_{max0} : speed upper bound.
- v_{max} : maximum speed reached within the movement.
- θ^* : target position.
- $\Delta\theta^*$: target position increment.
- $\Delta\theta$: position increment obtained within a generic movement.
- $\Delta\theta_{AD}$: position increment obtained within a movement which uses only phases A and D.

A Safety and Dexterity Design Strategy for Human Symbiotic Robots

Toshio MORITA Hiroyasu IWATA Shigeki SUGANO

Dept. of Mechanical Engineering, Waseda University
3-4-1 Ookubo, Shinjuku, Tokyo 169-8555, Japan
URL: <http://www.sugano.mech.waseda.ac.jp>

Abstract

An objective of this study is to find out design requirements for developing human symbiotic robots, which share working space with human, and have the ability of carrying out physical, informational, and psychological interaction. This paper mainly describes design strategies of the human symbiotic robots, through the development of a test model of the robots, WENDY (Waseda ENgineering Designed sYmbiont).

In order to develop WENDY, safety and dexterity of a humanoid robot Hadaly-2, which was developed in 1997, are improved on. The performances of WENDY are evaluated by experiments of object transport and egg breaking, which requires high level integration of whole body system.

1. Introduction

The development of humanoid robots which can support human labor by several combined communication channels, such as physical interaction and informational interaction, are expected to be a measure against labor shortages in aging societies. Such robots are distinctively called "human symbiotic robots", for they must have additional abilities of sharing behavioral space, working space, and thinking space with human.

In designing of the human symbiotic robots, capabilities of ensuring safety while interacting with human must be given top priority. Under this assumption, the Humanoid Project at the Advanced Research Institute for Science and Engineering (RISE), Waseda University has developed Hadaly-1 [1] and Hadaly-2 [2] as prototypes of the human symbiotic robots.

Among these robots, Hadaly-1 was developed as an informational assistant robot in 1995. Hadaly-1 can realize informational interaction with human by combining with audio-visual information, voice dialogue, and gesture motion using manipulator. Hadaly-2 was developed in 1997, from motivations for improving physical interaction ability of Hadaly-1. The Working condition of Hadaly-2 is shown in Figure 1.

In designing Hadaly-2, an anthropomorphic shape is adopted, since the human symbiotic robots must work in human's living space, which is designed to suit with daily life. Hadaly-2 can carry blocks in reference to the

operator's demands, by combing audio-visual information, voice dialogue, and gesture motion. Design requirements and system integration strategy were clarified through the development of Hadaly-2.

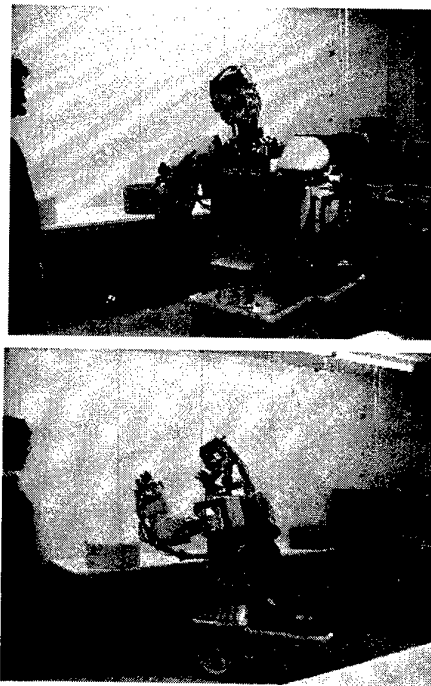


Figure 1 Working Condition of Hadaly-2

Based on the successful results, this paper aims to construct a new human symbiotic robot named WENDY (Waseda ENgineering Designed sYmbiont). First, this paper describes mechanism design strategies for improving dexterity of Hadaly-2. Next, the design strategies are implemented into WENDY. Finally, performances of WENDY are evaluated by experiments, such as picking up object on the floor and breaking eggs.

2. Design Strategy for Human Symbiotic Robots

2.1 Assurance of Safety and Dexterity

Human-robot interaction, which inevitably occur in human-robot symbiotic situation, can be mainly classified

into physical interaction and informational interaction.

Among these two interaction, physical interaction is particularly important, because human-robot symbiosis requires that robot must directly contact and collaborate with human. For realization of these physical interactive tasks, the important technical point is that manipulator can adapt to human's motion, while ensuring human's safety.

Based on this consideration, this section shows the design strategy for ensuring safety and dexterity in a human symbiotic robot.

(1) Safety

Many studies have been conducted on the safety of industrial robots, however, the working conditions of the robots whose key feature the symbiosis with humans are different from those of industrial robots, precluding the spatial separation of robots and humans. Consequently, taking more positive safety measures with the robot itself is required. As an approach for solving the problem, this study categorizes the safety measures of human symbiotic robot into two phases, such as impact safety and after collision safety.

In regards to impact safety, our previous study has shown the effectiveness of a double safety measure, which employs viscoelastic surface cover, and reflex movement of joints. Concretely, collision situations (subjective and objective collision) and control modes of manipulators (joint Impedance control and emergency stops) are classified, and the effect which those parameters exert on shock absorption is clarified by computer simulation. The simulation results are shown in Figure 2.

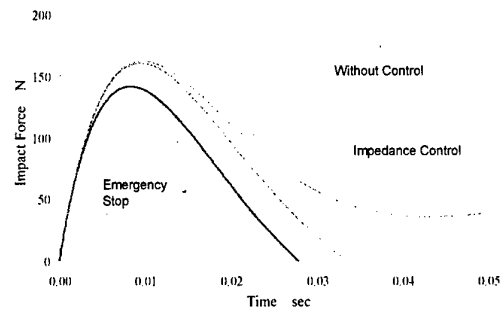
First, attention is paid to the effect of emergency stops. In subjective collisions, it was recognized that emergency stops had the effect of reducing both the peak force and the duration time from the levels of collisions without control. However, in objective collisions, the duration time rather increased, in contrast to what happened in subjective collisions. Compliance control did not have any peak force reduction effects comparable with emergency stop in subjective collisions, but it had effects in reducing the duration time in objective collisions.

From these remarks, the authors think that the adoption of design and control method in accordance with functions of each body part is effective for improving total performances of human symbiotic robots.

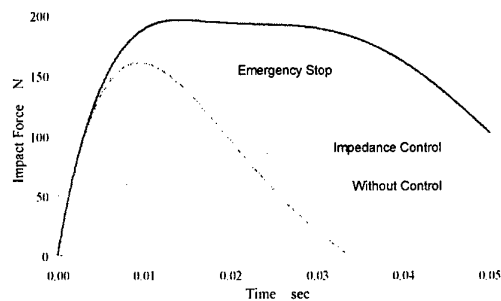
In addition to the measurement for impact safety, adaptive motions for realizing after collision safety, by coordinating whole limb systems are important for carrying out cooperative tasks with human. In the case, capabilities of object recognition by using visual and tactile information and coordinated motion of whole body are required.

These remarks are reflected in the design strategy of a head and a body-vehicle part of WENDY, shown in the

following paragraph.



(a) Subjective Collision Case:
(A robot unilaterally collides with a human)



(b) Objective Collision Case
(A human unilaterally collides with a robot)

Figure 2 Impact Safety Effect by Control Modes

(2) Dexterity

In addition to safety measures, dexterity is important for realizing human robot symbiosis. For practical use, human symbiotic robots must have capabilities of handling daily necessities. Assistance of cooking, for example, requires ability of handling of cookware and foods by using abilities of object recognition and coordination of whole body motion.

From these remarks, this study regards that dexterity of human symbiotic robot can be improved by realizing mobility of arm-hand systems and body-vehicle systems. Based on this concept, Hadaly-2 has carried out simple tasks in human's living space. As a next stage, we aim to advance dexterity of Hadaly-2 by the following design strategies.

For designing human symbiotic robot, motion space in both horizontal and vertical plane is required, because human's living space has unevenness. However, most of conventional mobile manipulators that contain Hadaly-2 are designed in consideration of mobility in horizontal plane. A measure on this problem is utilized in the mechanism design of waist and vehicle.

In addition to mobility, performance of arm-hand system must improve in order to perform the several tasks

which human is doing in the daily life. In the case, abilities of object recognition and coordinated control of arm and hand become more important.

In reference to the design concepts, limb mechanisms of Hadaly-2 are improved focusing on the integrity of the whole body system. The following chapters describe concrete design strategies.

2.2 Mechanisms of Head and Neck

A head subsystem of human symbiotic robots should act as not only visual information sensor, but also interface for collaborative tasks with human. For example, it was confirmed that operators infer the working condition of Hadaly-2 from the motions of its eyes. So, this study improves resolution of visual information processing, by developing a new head mechanism that employs two color CCD cameras for detecting objects and humans. An assembly drawing of the seven D.O.F. head mechanisms is shown in Figure 3.

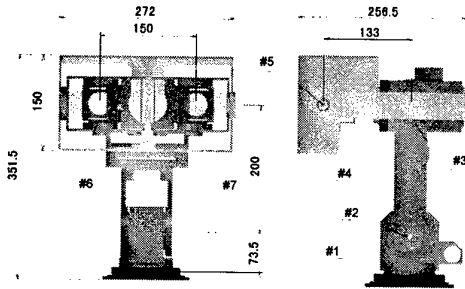


Figure 3 Head Mechanisms

The head mechanism consists of a three D.O.F. eye mechanism and a four D.O.F. neck mechanism. In regard to the eye part, locations of the CCD cameras are important, because the distance between two eyes affects both image processing and human's impression. Two cameras are separated as possible, under the conditions that the vision system can catch objects which are located at 10 [cm] from the face. And, in order to observe objects which are located on the floor, the neck mechanism employs two degrees of freedom in the direction of flexion and extension.

2.3 Mechanisms of Waist

Waist mechanisms are utilized for expanding the working spaces in vertical plane. Moreover, evacuating motions using redundancy of whole body are effective for suppressing the impact forces, which generate in the case of collision between humans and robots. In order to realize the motions stable, a waist mechanism that employs three degrees of freedom is developed.

The waist mechanisms consist of one rotation axis (joint #1) and two pitching axes (joint #2 and #3). By

rotating joint #2 to the opposite direction of joint #3, the waist can bend without stumbling over. Consequently, the end point of the WAM-10 manipulator [2] that is attached to the body mechanism can reach to the point on the floor, at a distance of 260[mm] from the rotation axis of the body. An overview of the developed waist mechanism is shown in Figure 4.

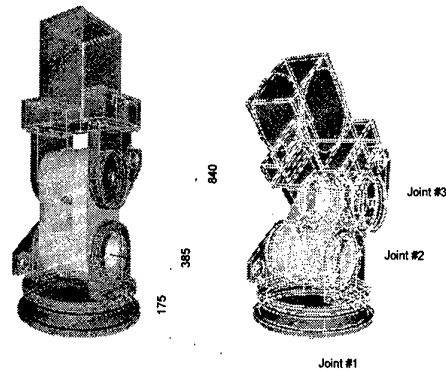


Figure 4 Waist Mechanisms

2.4 Mechanisms of Vehicle

Mobility in horizontal plane is necessary for human symbiotic robots to extend working space. In that case, however, stability of the mobile mechanisms is the most essential, because human-robot collaboration requires insurance of operator's safety. From these remarks, this study adopted wheeled vehicle mechanisms among many forms of the mobile mechanisms.

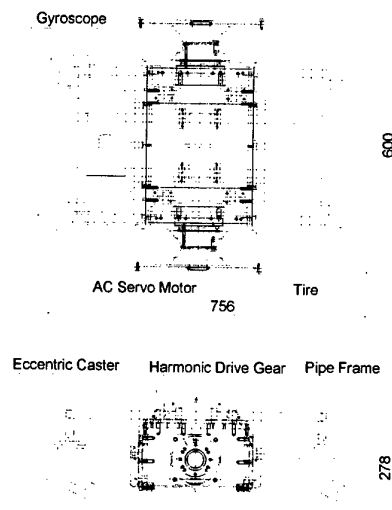


Figure 5 Vehicle Mechanisms

Figure 5 shows the assembly drawings of the developed two-wheeled vehicle mechanisms. In designing the mechanisms, the eccentric casters with suspensions are located at each vertex of rectangle, since vehicle must climb over bumps without stumbled over.

The developed vehicle has enough power for dragging the cables which connects the internal actuators to the external controllers, by utilizing combination of high power motor (300[W], AC) and harmonic drive gear (reduction ratio 1/33). Specification of the vehicle is as follows; maximum velocity, 5[km/h]; maximum payload, 120[kg]; climbable height, 1[cm]; weight, 53[kg]; maneuvering error, 1[%].

2.5 Mechanisms of Arm and Hand

Manipulators of the human symbiotic robots are utilized as interface between humans and robots, while carrying cooperative tasks. So, safety and adaptive manipulation is essential for constructing human symbiotic robots. In consideration of these problems, the authors have developed the WAM-10 (Waseda Automatic Manipulator #10), and design requirements for carrying out several tasks which involves physical interactions between robots and humans were clarified [3]. In this study, the hand mechanisms of the WAM-10 are improved by focusing on dexterity of pinching motion.

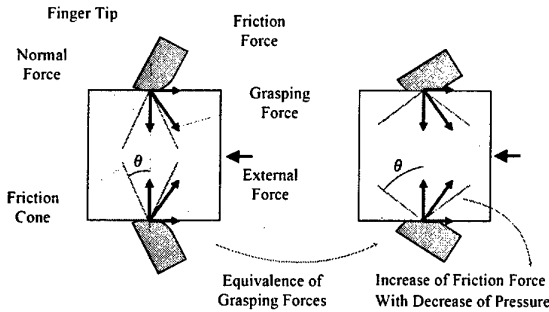


Figure 6 Adjustment of Friction by Pressure Control

Human changes the poses of fingertips with adapting to the shapes of objects. This motion can be regarded as control of friction by adjusting pressure, which is shown in figure 4. Coefficient of adhesive friction μ is changeable by adjusting areas of contact, in reference to following equation [4].

$$\mu = \frac{As}{W} = \frac{A(s_0 + \alpha p)}{W} = \frac{s_0}{p} + \beta \quad (1)$$

$$\theta = \tan^{-1} \mu \quad (2)$$

where, A : contact Area, W :contact force, s, s_0 : shearing stress, p : pressure, α, β : constants, and θ : acute angle of friction cone.

From these remarks, this study focuses on the design parameters of fingertips, such as shape, structure, material, and size. For continuously adjustment ability of contact conditions from point to area, curved shapes of the fingertip are designed by using rubber and bone. A nail is also attached to the fingertip, in order to realize extremely high pressure on the contact point.

3. Construction of WENDY

3.1 Mechanical Hardware and Functions

By combining the head, the waist, the vehicle and the arm-hand system, a limb mechanism of WENDY (Waseda ENgineering Designed sYmbiont) is constructed. An assembly drawing and an overview are shown in Figure 7, and 8. Specifications are arranged in Table 1.

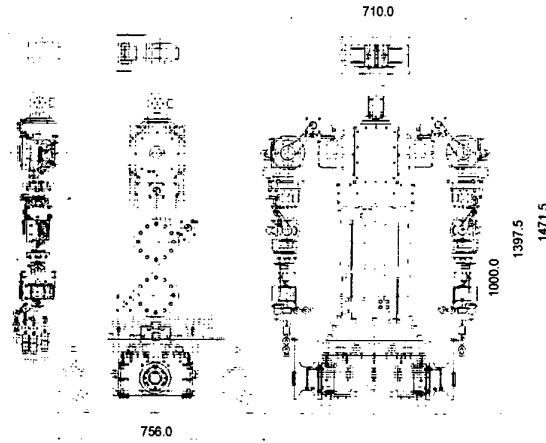


Figure 7 Assembly Drawing of WENDY

WENDY improves Hadaly-2 in the human interaction ability, since whole body motion control and visual-auditory information processing are implemented into design concept. In the system, image processing part is utilized for measuring the relative position from the base of WENDY to the target objects, by using stereo vision. In the process, shapes of the objects is recognized by visual images (512×480[pixel], 8×3[bit]RGB) through GPB-J board, which is on the market. The limb mechanisms of WENDY have the possibility of handling small sized object, which is located in human's living space. And it can turn around on the position while maintaining the end point positions of manipulators.

3.2 Control Systems and Algorithms

For development of control systems of WENDY, control architectures of Hadaly-2 is succeeded. In the

system, the host computer generates behavior codes by using visual, and voice dialogue information, through CAAD (Creating Actuator Angle Data) operating system.

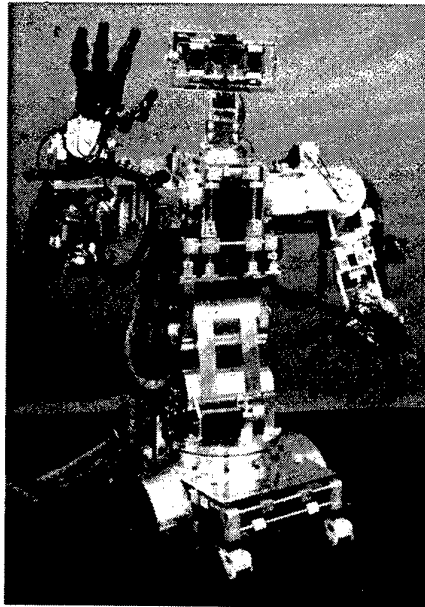


Figure 8 Overview of WENDY

The CAAD operating system was developed for arm-hand coordination control of Hadaly-2. The system is similar to finite state machine or petri-net. Therefore, environmental conditions, such as scenarios of dialogues and arrangements of objects, must be previously measured and installed into the behavior models. Each motion is created by using graphical user interface, and implemented into the CAAD. Then, the CAAD produces the limb motions in reference to the environmental situations, by combining the several motion patterns that involve gestures. Each body control system is received the behavior codes from the host computer through DP-RAM.

In this system, mobility are produced by combining straight line and rotation of the vehicle.

4. Evaluation Experiments

4.1 Image Processing and Head Motion

For evaluation of the head system, experiments on visual image processing and arm-head coordination are conducted, respectively. In regard to the visual image processing, recognition of objects shape, and measurement of distance are adopted for evaluation items. Contents of the experiments are listed as follows;

(1)Mission: Search a target object from any number of objects, which are located on the chair. Then, measure distance between the object and the base of WENDY.

(2)Environment: Objects are located at 1.0[m] (x-axis) from the base. Background color is blue. Sizes, shapes and its color are previously defined. (object #1; sphere; white, object #2; cube; red, object #3; pyramid; yellow)

From the experimental results, it is confirmed that the ratio of success of object recognition is approximately 90 [%], the measuring errors are 5 [cm] (z-axis) and 1 [cm] (x, y-axis), and the time for processing is 250 [ms].

Table 1 Specifications of WENDY

DOF	Finger	13 × 2
	Arm	7 × 2
	Neck	4
	Eye	3
	Waist	3
	Vehicle	2
	Total	52
Size [mm]	Height	1471.5
	Width	930.0
	Depth	756.0
Weight [kg]	Hand	2.0 × 2
	Arm	25.0 × 2
	Neck + Eye	8.0
	Waist	46.0
	Vehicle	53.0
	Total	161.0

Next, servo responses of the head mechanisms are evaluated by the head-arm coordination experiments. In the experiments, mechanical compliance coefficient of the manipulator is set to maximum, and operator shakes the manipulator. The applied external force is approximately 0.5 [Hz] sine curve. The eyeshot of WENDY is controlled to follow the end point of the manipulator, by calculating DK of the arm and IK of the head. The distance between hand and eye is set to 1.0 [m], and the angle of joint #4 is 0.0 [deg]. The experimental result on x axis, is shown in Figure 9. It is confirmed that fine following motions of head mechanisms are achieved by head-arm coordination.

4.2 Safety

The shock absorption cover is constructed according to the proposed design method, and it evaluated whether the developed arm can satisfy impact safety. In designing of a shock absorption cover, a material named Memoryfoam M-38, which is excellent in shock absorption, is adopted. Moreover, as conditions of a collision experiment, subjective collision case of 1 [m/sec] is

selected. The developed arm and a measuring instrument that equips a load cell are made to collide, and time histories of contact force is measured.

A simulation result and an experimental result are shown in Figure 10 (a) and (b). Since the simulation result and the experiment result are in agreement, it was confirmed that the manipulator equipped with safety can be developed in reference of the proposed design strategies.

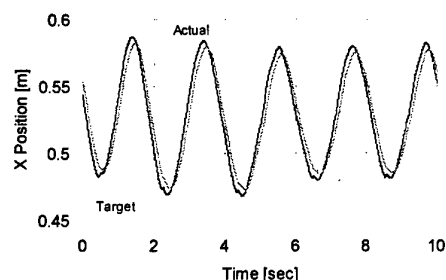
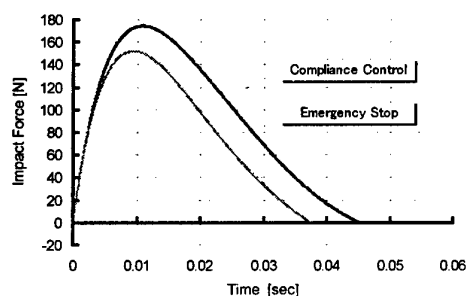
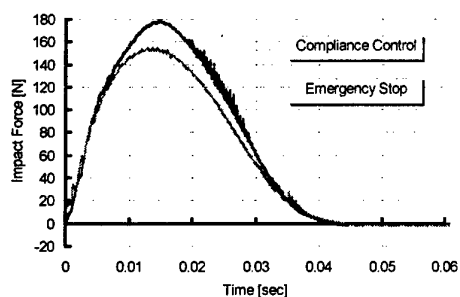


Figure 9 Following Motion of Head System



(a) Simulation Result



(b) Experimental Result Effect

Figure 10 Shock Absorption Effect of Manipulator

4.3 Dexterity

To evaluate dexterity of WENDY, object picking up and egg breaking are selected for experimental tasks. In the object picking up task, WENDY approaches to the target object by using the vehicle, and picks the object up.

Maneuvering path is generated from the object

position, with combination of linear lines and curves. Size of the object is 8 [mm] in width, 10 [mm] in depth, 20 [mm] in height, and 100 [g] in weight. The block is located at 700 [mm] in front, and 300 [mm] to the right. The ratio of success of picking up object is almost 100 [%]. This result shows that WENDY can realize accurate mobile manipulation by using whole body motion.

In regard to the egg breaking tasks, information from force sensor is not utilized, because the experiment mainly focuses on the evaluation of the mechanical characteristics of the fingertips. The experimental setup is shown in Figure 11. In the experiment, motion patterns are previously produced. The ratio of success becomes 20 [%] by using the new fingertip, while the ratio of success is 0[%] by using the conventional hemispheric fingertips. This result shows that the pressure control method using fingertip is effective for improving the dexterity of handling.



Figure 11 Experiments of Egg Breaking

5. Conclusion

This paper proposes design strategies of human symbiotic robots which has the possibilities for ensuring safety and dexterity. By using the strategies, a human symbiotic robot, WENDY is developed.

Effectiveness of the design strategies are confirmed from the results of several evaluation experiments, such as object picking up and egg breaking, which require high completeness of whole system.

References

- [1] S. Hashimoto et al., "Humanoid Robot -Development of an Information Assistant Robot Hadaly-," Proc. of 6th Roman, pp.106-111, 1997.
- [2] T. Morita, and S. Sugano, "Design and Control of Mobile Manipulation System for Human Symbiotic Humanoid: Hadaly-2," Proc. of ICRA'98, pp. 1315-1320, 1998.
- [3] T. Morita, and S. Sugano, "Development and Evaluation of Seven-D.O.F. MIA ARM," Proc. of ICRA'97, pp.462-467, 1997.
- [4] F. P. Bowden, and D. Tabor, "The Friction and Lubrication of Solids," Pt.II, Oxford University Press, 1964.

Robot Assisted Polishing Using Nonprogrammable Active End Effectors

Levent Güvenç

Associate Professor

Department of Mechanical Engineering

Istanbul Technical University

Gümüşsuyu, Taksim 80191, İstanbul - Turkey

E-mail: guvenc@burgaz.mkn.itu.edu.tr

Abstract

One of the major aims in an automated polishing system is to keep the polishing force and hence the material removal rate constant. The easiest way of achieving this in robot assisted polishing is to use through-the-arm force control where real time trajectory modifications result in all robot axes being moved simultaneously for the required fine end point motion. The main problem encountered in this approach is low steady state accuracy and low bandwidth of industrial robots. The solution is to use an active end effector for the fine manipulation required for keeping the polishing force constant in the presence of robot tracking errors while the gross motion is provided by the robot. Of the two types of available active end effector technologies nonprogrammable active end effectors are treated here by considering two such devices and evaluating them in the context of robot assisted material removal as they offer cheaper solutions to programmable ones even though they are less adaptable to changes in operating conditions.

1. Introduction

One of the major aims in an automated polishing system is to keep the polishing force constant since experimentally determined material removal rates and transient polishing force are seen to be highly correlated [3]. The easiest way of achieving this in robot assisted polishing is to use through-the-arm force control where real time trajectory modifications in world coordinates are used to achieve the required fine endpoint motions by moving all robot axes simultaneously. The main problem encountered in this approach is low steady state accuracy as industrial robots do not have high positioning accuracy. Also, the reliance on the robot's own controller results in large time lags associated with robot joint servo responses and a large dead time because of the required coordinate

transformations, both of which limit the achievable bandwidth in through-the-arm force control.

The solution is to use an active end effector for the fine manipulation required for keeping the polishing force constant in the presence of robot tracking errors while the gross motion is provided by the robot. Active end effectors can be divided into the two categories of programmable and nonprogrammable active end effectors. Nonprogrammable active end effectors usually use a pressure regulator to indirectly control the polishing force by keeping pressure constant in pneumatic cylinder(s). Programmable active end effectors use sensory information from position and force transducers which is fed back to a microcomputer that calculates the control action to be taken based on a suitable control law. While preferable due to their adaptability to changes in operating conditions, programmable active end effectors are also costly due to the need for sensors, the associated signal conditioning circuitry and a control computer. Hence, it is beneficial to use cheaper nonprogrammable active end effectors if they can maintain satisfactory performance.

Two nonprogrammable active end effectors are evaluated in this paper in the context of robot assisted polishing. The first one which will be abbreviated as CFD (meaning constant force device) here was designed to provide real time control of applied tooling force in robotic deburring and surface conditioning applications [1]. The pneumatic circuitry and mechanical parts of the CFD are analyzed here in detail and used in constructing a mathematical model. The model parameters of the pneumatic circuitry have been identified previously using maximum likelihood estimation by [4]. This identified model is used to demonstrate the adequacy of the response of the pneumatic circuitry of the constant force device for polishing tasks that are not too demanding. The bandwidth of the mechanical part of the CFD is also determined to be adequate for polishing tasks. Contact force measured during polishing is given to demonstrate this adequacy.

The second nonprogrammable active end effector treated here also uses regulation of pressure in a pneumatic cylinder. This device is attached to a SCARA type robot without vertical motion capability and is called robot polisher here [2]. The robot polisher is useful for fast polishing of large flat surfaces or surfaces of slowly varying curvature. The robot polisher is evaluated here and compared with the CFD regarding polishing performance.

The organization of the rest of the paper is as follows. The introduction is followed by two sections on the CFD and the robot polisher, respectively. A comparison of the two devices and comments on the use of nonprogrammable active end effectors is presented in the next section. The paper ends with conclusions.

2. The CFD constant force device

The CFD constant force device uses a high precision pressure regulator to indirectly control polishing force by keeping pressure constant in two opposing low friction air cylinders. The difference of the constant pressures in the two cylinders multiplied by the piston cross-sectional area and a geometric factor results in the static applied load. The desired force level is set by adjusting the pressure regulators. The CFD is termed a *rotary* constant force device since a counterbalance mechanism with rotational bearings is used instead of linear bearings. A constant force is applied on the part under static conditions, regardless of tool orientation as the tool weight is balanced by the counterbalance weight. This device has been used in deburring inner holes on a jet engine casing using compliant polishing wheels (Graf, 1988).

The CFD utilizes a pneumatic pressure regulator with a resolution of 0.0045 psi to regulate pressures in its two opposing cylinders. The reason for using two instead of one cylinder is to be able to use the device *upside down* as well. Each single acting cylinder has a glass body for low friction and ball and socket joints on the piston connecting rod to ensure linear piston motion.

2.1. CFD pneumatic model

The pneumatic circuit for a cylinder-regulator combination of the CFD is shown schematically in Figure 1. The derivation of the pneumatic model of this cylinder, pressure regulator combination has been given in [4] and is shown in block diagram form in Figure 2. p_d and p are the desired and actual cylinder pressures in this figure. There is a time lag with time constant τ due to the regulator's pressure sensing feedback path. The switch which chooses the charging or discharging path with a consequent change in the flow coefficient from K_v to K_{sv} and vice versa is the only nonlinearity in this model, all

other nonlinearities having been simplified using small signal linearization. Robot tracking error and workpiece surface irregularities enter the feedback loop through the disturbance input x_c .

The pneumatic model parameters K_v , K_{sv} , K_x and τ for the regulator, cylinder combination of the CFD have been identified in [4] by comparing experimental step displacement test results with simulated ones and using a maximum likelihood estimation scheme. It is clear due to the nonlinearities involved that the pneumatic model parameters should be identified for displacement levels consistent with those the pistons will be subjected to during actual polishing. During polishing, piston displacements arise from workpiece surface irregularities and robot tracking errors. The effect of robot tracking errors is given more attention here since the workpiece surface irregularities are not very large in magnitude for polishing tasks.

An experimentally determined robot tracking error profile is shown in Figure 3 for the six-axis GMF S-400 industrial robot used here to hold the CFD during polishing passes. This profile has a low frequency component with a half wave type shape and lower amplitude components at 1 to 2 Hz superimposed. The peak to peak (abbreviated p-p in the following) amplitude of the 1 to 2 Hz component is of the order of 1 mil. This 1-2 Hz component of the robot tracking error will not even excite the pressure regulation mechanism because the corresponding changes in pressure are within the finite resolution of the pressure regulator. The larger displacements that the pistons will be subjected to during the beginning and end of the robot motion occur gradually rather than in a stepwise fashion and the pressure regulator response should be fast enough to compensate for them. In short, the pneumatic circuitry of the CFD is expected to reject this robot tracking error profile which enters the loop at the disturbance input after being scaled down due to the geometry of the CFD. In order to test this assertion directly, a high precision linear positioning stage under closed loop position control was connected directly to one of the CFD cylinders under regulated pressure control to subject it to the robot tracking error input. The measured cylinder pressure response shown in Figure 4 has a maximum change in pressure that is less than the pressure regulation system's resolution of 0.005 psi, showing successful pressure regulation.

2.2. CFD mechanical model

The mechanical structure of the CFD consists of a parallelogram mechanism fixed to the robot or a stationary base through two hinged joints (O_1 and O_2 in Figure 5). The tool weight $M_t g$ is balanced by the counterbalance weight $M_{cw} g$ and the difference in cylinder pressure forces

F_{pd} and F_{pu} is used to obtain a constant workpiece interaction force in the static case. The simplified equivalent model of the CFD mechanical structure shown in Figure 6 is used in deriving the equations of motion. In this figure, all the mass has been lumped into the tool mass M_t and the counterweight mass M_{cw} , assuming massless links. The normal contact and pressure forces are given by

$$F_n = K_{pr}(x_n + x_{tr} + x_{wp}) \quad (1)$$

$$F_p = A_c(p_{cd} - p_{cu}) \quad (2)$$

where x_{tr} is the robot tracking error, x_n is the tool position relative to the CFD, and K_{pr} is the equivalent stiffness of the polishing tool and robot-tool holder. Modeling the dynamics of this device and using (1) and (2) results in

$$(M_t + M_{cw}(l_1/l_3)^2)\ddot{x}_n + K_{pr}x_n = -K_{pr}(x_{tr} + x_{wp}) + (l_2/l_3)A_c(p_{cd} - p_{cu}). \quad (3)$$

The mechanical model of the CFD given by (3) is, thus, seen to be a mass-spring system excited by robot tracking errors, workpiece surface irregularities and dynamic pressure forces. When typical numerical values are substituted in Equation (3), the bandwidth of the mechanical system is determined as 14 Hz

2.3. The overall model

The whole CFD model is shown in block diagram form in Figure 7. Robot tracking errors, workpiece surface irregularities and any net pressure changes act as inputs to the mechanical mass-spring structure which compensates for them in the 0 to 14 Hz frequency range. Robot tracking errors and workpiece surface irregularities cause the CFD pistons to move inside the cylinders causing transient changes in pressures and hence a change in the pressure force in (3), but the regulators adjust the pressures to the set point values and x_n follows the negative of $x_{tr} + x_{wp}$ resulting in a constant force F_n if the disturbances occur at low enough frequencies.

The adequacy of the pneumatic circuitry of the CFD in accommodating robot tracking errors was pointed out earlier. The mechanical model of the CFD with a resonance at 14 Hz will also not cause any problems at the much lower robot tracking error frequencies. Hence, good force regulation performance in polishing is expected from the CFD constant force device.

2.4. Force control experiments

The normal component of the polishing force recorded during a polishing pass with a compliant polishing wheel

is displayed in Figure 8 on a magnified scale. There are low frequency waviness (0.06 Hz) and 1-2 Hz components of 0.2 lbf and 0.06 lbf p-p magnitude, respectively. The higher frequency component is at the same frequency as the robot tracking error. These normal force fluctuations suggest that the CFD is not capable of compensating for robot tracking errors during polishing. This contradicts earlier results since the CFD device does a poorer job of regulating the polishing force than would be expected by the performance of the single cylinder, regulator combination and the large bandwidth of its mechanical structure.

After carefully considering several possibilities in order to explain the presence of unexpected polishing force fluctuations, it has been determined experimentally that the problem results from clearances and backlash in the hinged and ball and socket joints of the rotary mechanical structure of the CFD giving rise to residual tool motion of up to 0.55 mils that stays as a net tool-workpiece interference but is not transmitted to the pistons. A residual tool displacement of 0.55 mils during polishing corresponds to a 0.22 lbf change in force for a compliant polishing wheel with a 400 lbf/in stiffness, explaining the reason for the force fluctuations observed during polishing tests. This is mainly due to the rotary construction of the CFD, necessitating the presence of several joints. Due to clearances and backlash in these joints, displacements of up to 0.55 mils at the tool plate are not transmitted back to the pistons and remain as polishing wheel-workpiece interference.

The disturbance rejection frequency response of the CFD shown in Figure 9 is determined next, based on its quasilinear mathematical model which is linearized by assuming that the charging and discharging coefficients are the same. A comparison of Figure 9 with the disturbance rejection characteristic of through-the-arm force control for the GMF S-400 robot used here (see [3]) shows the enhanced disturbance rejection obtained when using the CFD. In theory, this nonprogrammable active end effector will effectively compensate for robot tracking errors in the frequency range of 0 to 5 Hz and achieve tight force control. This is not seen in practice since the joint clearance effects are not present in the model used to obtain Figure 9. This is still a useful result showing what could be achieved in the limiting case of a typical nonprogrammable, pneumatically powered active end effector if the design of its mechanical structure could be improved.

3. The robot polisher

The robot polisher SMR-100H is a three-axis die polishing machine which uses a pneumatically powered, nonprogrammable active end effector to achieve force

control indirectly through cylinder pressure regulation. Its force control system is shown schematically in Figure 10. The robot polisher uses a double acting cylinder and a pressure regulator to keep cylinder pressure constant. Although the connection between the piston and movable polishing head on the robot polisher end effector is a direct one, there are still some clearances in the linear drive rail mechanism. Also, a high amount of compliance is introduced by the belt drive utilized in powering the reciprocation mechanism. So, low frequency force fluctuations can be expected with this device as well. This is seen in the polishing force plot of Figure 11, where a reciprocating stone is moved over the workpiece by the robot polisher. The higher frequency force fluctuations in Figure 11 are mainly due to the reciprocating motion of the stone used. Note that the effect of polishing force fluctuations above 0.2 Hz will not be reflected on the workpiece surface as uneven material removal rate as they are averaged out by the reciprocating stone.

4. Comparison of the CFD and the robot polisher

First, it should be pointed out that well polished workpiece surfaces were obtained experimentally using both the CFD held by the GMF S-400 robot and the robot polisher. Even though both devices achieve results superior to the through-the-arm technique, they both suffer from disadvantages some of which could be corrected by appropriate modifications. This will enable both devices to be used satisfactorily in automated polishing.

As for the robot polisher, since the force plot obtained during polishing with the robot polisher does show force fluctuations at lower frequencies, the material removal rate achieved will not be uniform. Moreover, the end effector mechanism of the robot polisher does not have any tool weight cancellation mechanism like the one in the CFD. Hence, the tool orientation cannot be changed during polishing, a major limitation in the polishing of three dimensional sculptured die surfaces. This is an advantage of using a six degrees of freedom industrial robot, with the ability to position the tool at a desired orientation on any point on the workpiece surface. The major advantage of this device is that large flat surfaces can be polished very fast with little programming.

The responses of the force control loop obtained using the CFD nonprogrammable active end effector are better than the corresponding responses achieved by through-the-arm force control. Moreover, the CFD is capable of performing polishing force regulation with hard polishing tools like grinding wheels and reciprocating stones, an impossibility with through-the-arm robot force control. These two points clearly show the benefits achieved

through the use of an independently controlled active end effector. A further benefit of using the CFD device in comparison to the robot polisher is not having to deal with orientation dependent force sensor offsets due to the presence of its mechanical tool weight cancellation mechanism. In short, a rotary pneumatic constant force device like the CFD can be used satisfactorily in robot assisted die polishing, provided that its design could be improved.

A major disadvantage of nonprogrammable active end effectors is their nonadaptability to large changes in polishing process requirements due to their nonprogrammability and their inability to follow commanded force trajectories. The use of a programmable active end effector becomes a necessity in such cases.

5. Conclusions

Nonprogrammable active end effectors have been evaluated here as an alternative to through-the-arm and programmable active end effector control strategies in robot assisted polishing. Through-the-arm robot force control offers the easiest implementation but suffers from its reliance on the dynamic response of the massive robot arm for fine motion manipulation in tool coordinates. Programmable active end effector usage offers the most versatile and adaptable solution at the sake of increasing the overall cost.

Nonprogrammable active end effector usage has been shown to be a less adaptable but cheaper solution. Two examples of nonprogrammable active end effectors have been analyzed in detail here regarding their performance in robot assisted polishing. It has been shown that satisfactory polishing performance can be achieved using both devices for operating conditions that do not show wide variations. Improvements to both devices have been suggested.

6. References

- [1] Alvite, J.G., and Gearman, T.A., "Four New Constant Force Devices," Technical Paper, Mecanotron Corporation, Roseville, Minnesota.
- [2] Anonymous, "Robo Polisher Model SMR-100H," Operator's Manual, Showa Precision Machinery, Amagasaki, Japan.
- [3] Güvenç, L., and Srinivasan, K., 1995, "Force Controller Design and Evaluation for Robot Assisted Die and Mold Polishing," *Journal of Mechanical Systems and Signal Processing*, Vol. 9, No. 1, pp. 31-49.
- [4] Güvenç, L., and Srinivasan, K., 1999, "Modeling and Parameter Evaluation for a Pneumatic Constant Force Device," *Turkish Journal of Engineering and Environmental Sciences*, submitted.

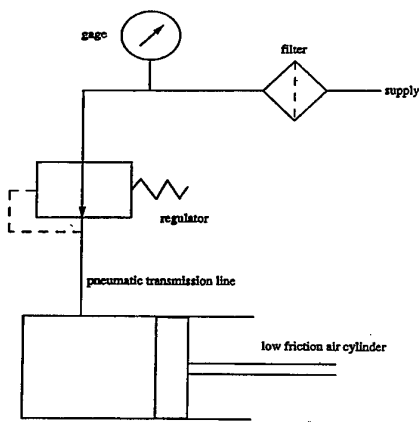


Figure 1. CFD pneumatic circuit

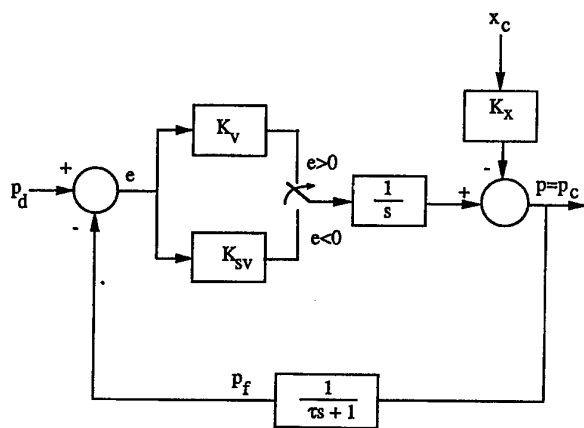


Figure 2. Pneumatic model

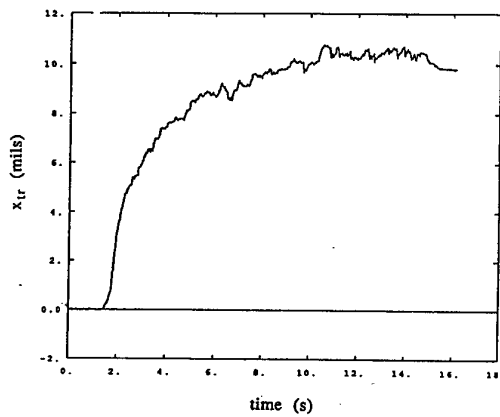


Figure 3. Robot tracking error profile

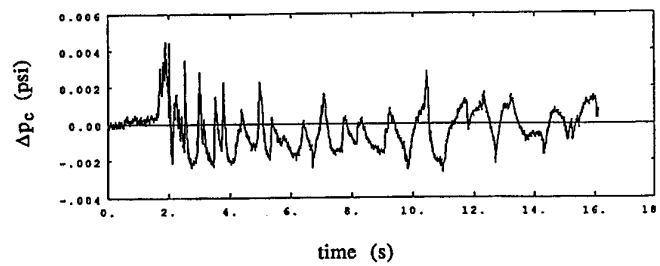


Figure 4. Cylinder change in pressure

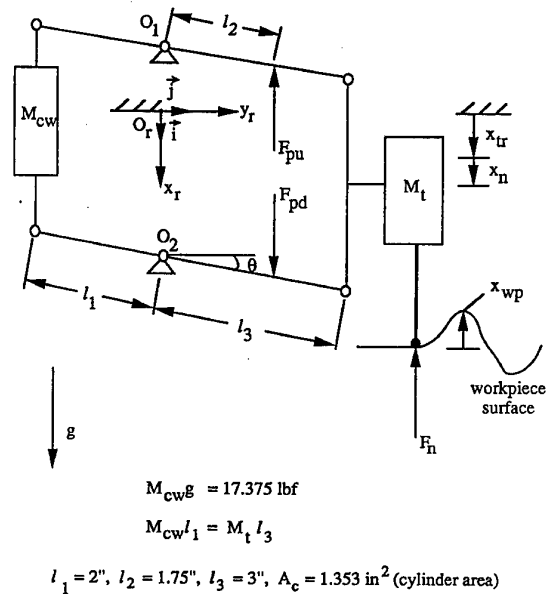


Figure 5. CFD mechanical structure

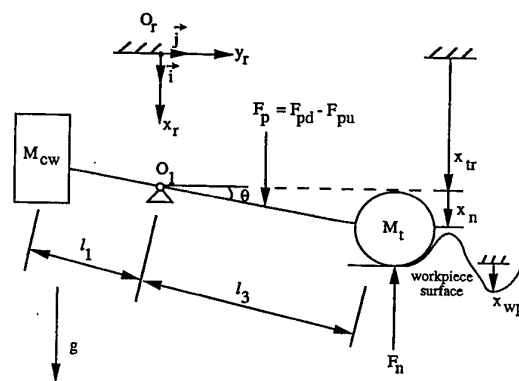


Figure 6. Simplified CFD mechanical model

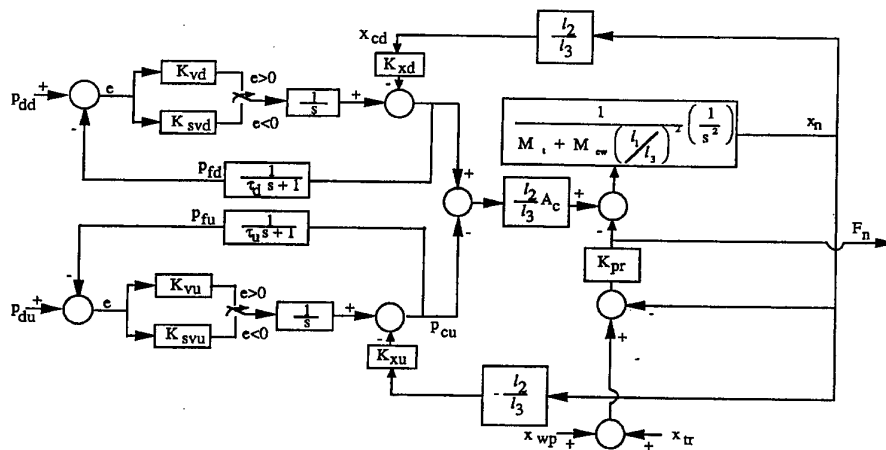


Figure 7. Overall CFD model

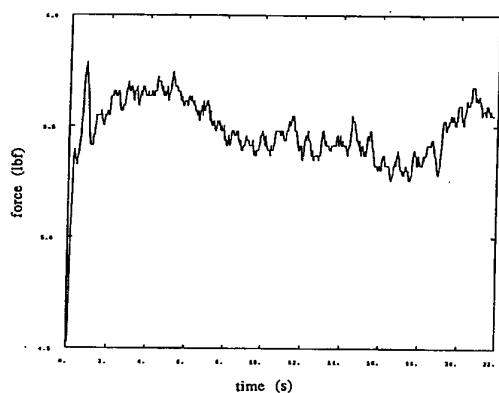


Figure 8. Normal force during polishing with the CFD

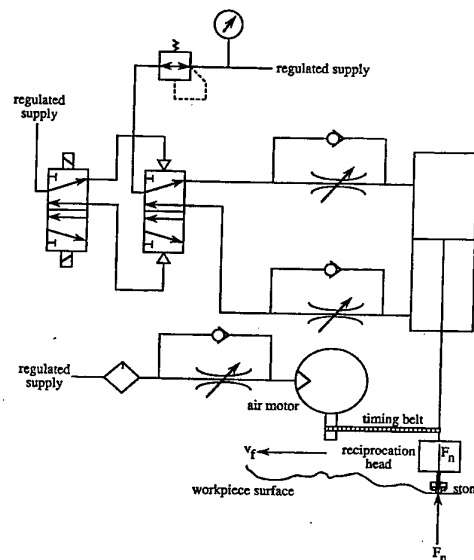


Figure 10. Robo polisher pneumatic force control schematic

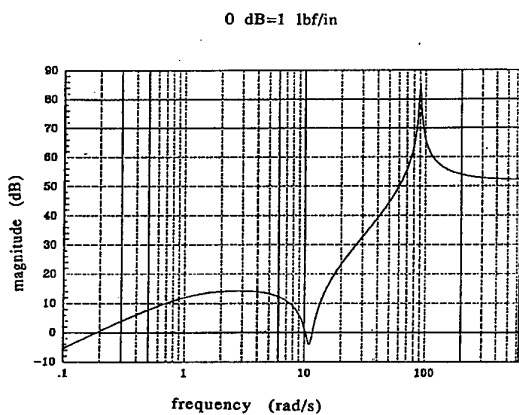


Figure 9. CFD disturbance rejection

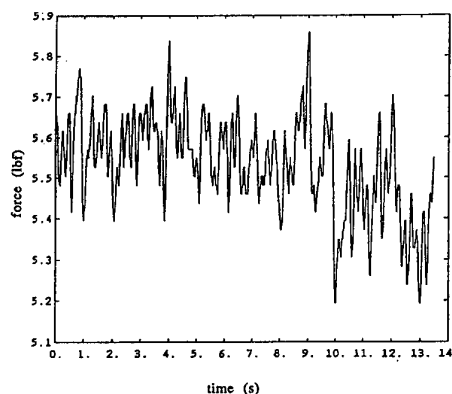


Figure 11. Normal force during polishing with the robot polisher

The Economic Benefits of Integration Internet with Business Operations in Smart Manufacturing Management

Ergun Gide

School of Management

University of Technology, Sydney, Australia

E-mail: Ergun.Gide@uts.edu.au

Fawzy Soliman

School of Management

University of Technology, Sydney, Australia

E-mail: Fawzy.Soliman@uts.edu.au

Abstract

The current dynamic and turbulent business environment and the approaching 21st century have put pressure on business operations all around the world to change traditional methods of conducting business to Internet-Based Electronic Commerce (or Internet Commerce). Electronic Commerce has been an idealised trading concept for many years. But the lack of integrated applications and the unavailability of universally accepted methods of communication have been a constant plague. As the Internet develops there is every possibility that e-mail and applications-based technologies will take over from traditional telephony as the common method of communications. Furthermore, the Internet provides an unprecedented infrastructure for moving information. This will have immense repercussions within the commercial world. This paper analyses the key drivers and economic values of integration Internet with business operations in smart manufacturing management.

1. Introduction

The market place of the twenty-first century is evolving into one of merging national markets fragmented consumer market, and rapidly changing product/service technologies. These changes are driving firms to compete, simultaneously, along several different dimensions: design, manufacturing, distribution, communication, marketing, sales, advertisement, and others. To effectively compete in global markets, firms must be quick and flexible in their response to customer needs. Businesses are beginning to use the Internet for such things as shortening the development cycle of new products, communicating with experts from around the world, receiving customer feedback on software, and accessing

supercomputers for industrial research and development (Gide and Soliman, 1997).

The Internet will be one of the most important business tools that will drive the formation of integrated supply chains that concepts are already evident in many initiatives for just-in-time manufacturing, continuous replenishment, vendor-managed inventory and electronic commerce. A successful supply-chain strategy depends to a large extent on the information system backbone that supports it. The Internet is a key part of that infrastructure, promoting business-to-business integration, ultimately resulting in global market expansion and increased control over working.

On the other hand, in a recent survey conducted by Arthur Andersen's Enterprise Group and National Small Business United in the US to determine what small companies (entrepreneurs) really do on the Internet, it was revealed that they were engaged in global business (Table 1).

Table 1. Percent of respondents who indicated the following Internet uses apply to them.

	Small Firms Overall (%)	Importers (%)	Exporters (%)
Use of the Internet	23	35	39
Conduct research on the Internet	17	21	26
Host/have a Web page	8	14	17

In industry, the efficient and effective management, manipulation and use of information is essential to economic vitality and growth. According to some experts, the use the integration of information

technologies, in an infrastructure of communication networks, hardware and software applications, databases, bulletin boards and other services, is a critical ingredients in production operations management success. Staying competitive in the next decade will require the development of, and commitment to, a strategy focused on improving manufacturing (or service) cost and quality (Gide & Soliman, 1997).

2. What does Internet Commerce Mean for Manufacturing?

Electronic Commerce, Electronic Trading and Electronic Business are often used interchangeably and many times there is a perception that these terms principally refer to the procurement cycle - the ordering and paying for goods or services either via electronic commerce technologies such as EDI or, more recently and growing in popularity, on-line Internet shopping.

Internet-Based E-Commerce is not an extension of EDI (Electronic Data Interchange) which has been primarily limited to computer-to-computer transactions, and has not been associated with major transformations of firms. There is no formal definition of the Internet-Based E-Commerce. Since, Internet commerce is still immature, so is the definition. However, one definition made by Kalakota (1996), as *"the process of converting digital inputs into value-added outputs"*. Basically, this process involves taking information as raw material and producing value added information-based products or services out of the original raw information.

So, electronic commerce refers to an on-line production process owned by intermediaries. Producers of information interact with services and other processed information, such as orders, payments or instructions. In reality, Internet Commerce is about businesses and consumers adopting a new process or methodology in dealing with each other. These processes are in essence supported by electronic interactions that replace close physical presence requirements or other traditional means (Soliman & Gide, 1997).

Internet-Based E-Commerce is giving a new way to electronic commerce, with different characteristics than traditional EDI. Internet Commerce is not a repeat of EDI, but rather is an evolution from the EDI. The Internet offers the greatest potential for Electronic Commerce known to date. According to Steel (1996) "there are less than 100,000 EDI (Electronic Data Interchange) users world-wide after 40 years or so of endeavour", but Nielsen Media Research and

CommerceNet survey shows that 78 million people used the Web during the first six months of 1998, and 20 million of those users made purchases via the Web. Businesses are aggressively adopting inter-company trade over the Internet because they want to cut costs, reduce order-processing time, and improve information flow. According to the Internet marketing research firm ActivMedia (1997) projections indicate that global Web sales through 2002 could total \$1.5 trillion, or about 3% of combined Gross Domestic Product (GDP) for all countries worldwide.

The phenomenal predictions of the size of the Internet market should be interpreted with some other factors in mind. The Internet is beginning to generate new sales channels, especially for products and services, which can be delivered digitally over the net. And there is no doubt that bank-assumed risk from credit card transactions through SET processes will accelerate traditional retail sales over the Internet. But these sales are still generally no more than sales substitution, or sales that would previously have been made by personal visits, mail order or the like. An interesting report on Web shopping and purchasing is new data taken from a Nielsen Media Research/CommerceNet study on Internet demographics released to researchers in August 1998 (Table: 2).

Table 2. Top items purchased on the Web, June, 1998 vs. September, 1997

Items Purchased	June, 1998 (million people)	September, 1997 (million people)
Books	5.6	2.3
Computer Hardware	4.4	2.0
Computer Software	4.0	2.8
Travel (airline tickets, hotel & car reservations)	2.8	1.2
Clothing	2.7	0.9

3. The Key Economic Values of E-Commerce

There are various types of key measurements that must be tracked prior to embarking on a full implementation. Some of the important key elements to measure business value are:

- **Improving customer service:** Providing customers self-access to their accounts, transactions and orders, is a valuable service (Mougayar, 1997). The level of satisfaction for those customers interacting electronically will undoubtedly rise.

- **Reducing costs:** The most basic cost reductions could be related to publishing costs, which include the cost of production, printing and distribution (Mougayar, 1997). Furthermore, marketing and selling costs are also lower in an electronically enabled commerce environment.
- **Providing Business Intelligence:** In the electronic commerce world businesses need to know much more about their clients. Electronic commerce makes it possible to market to specific individuals based on their patterns of (purchasing and browsing) behaviour. Hence they need to capture, and to analyse, as much information as possible about each individual purchase (or cancelled purchase) in order to build up customer's profiles. This is achieved in much the same way that neighbourhood stores once did, through personal acquaintance with the consumer and continuous contact. The use of this analysed data leads to what is being called "market response" systems or "adaptive marketing".
- **Process simplification:** Instead of using paper, using the World Wide Web (WWW) simplifies and speeds the approval process (Mougayar, 1997).
- **Generating new revenue:** The new Internet-Based Electronic Marketplace generates new revenue by selling new products and services specifically designed for the electronic marketplace (Mougayar, 1997). Existing product or services can also be sold on the Internet.
- **Taking faster decisions:** By receiving information about competition through an Intranet information retrieval database, it would be possible to develop a competitive strategy much faster than otherwise. The drivers for manufacturing are customer's needs and time. Time is a major source of competitive advantage and competitive pressures requiring production schedules to be shortened.

4. Manufacturing Value of Internet Commerce

The cost-benefit justification of Internet access and Information Systems in general is, and always be, a difficult one to prove but due to access of real time data, this would provide long term benefit of immeasurable value. To be able to analyze the value of Internet Commerce usage, it is helpful to have a measuring ruler. For individuals, one can compare the cost of an Internet

connection to the cost of using the telephone. It has been demonstrated that e-mail is cheaper than phone to communicate long distance with a number of people.

The Internet Commerce usage can make it possible to reduce the amount of time or effort required to perform certain tasks: cost savings and benefits from providing sales and customer support online and increase the potential of collaborative partnerships established over the Internet. The primary reasons for implementation of Internet Commerce is illustrated below in Table 3.

Table 3. The Main Reasons for Implementation of Internet Commerce (Source: Computerworld 1998)

Reason for Using Internet Commerce	Percentage (%)
Cost Savings	35
Customer Service	32
Revenue Generation	18
Marketing	13
Others	2
Total	100

Many businesses are using the Internet to contain long-distance telephone and mailing costs. Recent studies have shown that businesses can save thousands of dollars using e-mail, in lieu of some long distance phone calls and postal deliveries. For example, with first-class letters costing 45 cents each, a mailing of 1,000 pieces to customers would cost \$450 for postage alone, whereas the same information sent by e-mail would cost 2 to 3 cents each - and the messages would arrive in seconds as opposed to days or weeks. Overnight mail (which typically costs at least \$4-\$6 for each delivery) can not compete with e-mail for speed or cost. Long distance telephone charges, particularly international charges, are reduced by use of e-mail.

Businesses spend much more money than individuals on their phone. As an example, one provider's estimated cost of an Internet connection for a site of 15,000 users was about 8 cents per month per user. The same Internet connection for 100 users would cost about \$12.50 per month which is smaller than the cost of \$15 per month for a phone. In most cases, the cost of an Internet will be far less than an equivalent telephone connection and far more valuable in the long run. An average individual user spends \$20 to \$30 monthly on an Internet

connection which compares favourably with the cost of a telephone line (Estrada, 1993).

According to Mougayar (1997) there are various types of key measurements that must be tracked prior to embarking on a full implementation. The old adage "if you can't measure it, you can't tract it" applies. Some of the important key elements to measure business value are: reducing costs, process simplification, improving customer service, generating new revenue and taking faster decisions.

5. Current Challenges to Internet-Based E-Commerce

There are two main drawbacks or challenges in using Internet-Based E-commerce, these are: security issues and payment tools (Soliman & Gide, 1997). These two issues are receiving the highest priority and the best attention they deserve, both from vendors and users and implementers.

5.1. Security and Privacy Issues

While EDI users enjoy a high level of reliability and security, they are often restricted to the exchange of data with users of the same Value Added Network (VAN). For Internet commerce to really transform the way we do business a secure solution that works globally is required. To achieve this, a series of international standards needs to be agreed and vendors need to carry out a rigorous program of interoperability tests. Moreover, as trade moves beyond national boundaries, a common legal infrastructure must be agreed. For example, a contract that has been digitally signed in one country needs be recognised in other countries. Recent researches show that there is a growing confidence in solving the Internet security issues that have been very widely publicised. Even though security is a challenge it is not the main barrier to E-Commerce adaptation.

5.2. Payment Methods

There is confusion over the availability and choice of Internet payments tools. In addition, there are no interoperability standards to make one work with another. Over the past two years, new payment tools from small companies have emerged. The difficulty with E-Commerce-at the moment-is that all on line payment methods are new and relatively untested. It is vital that the business obtains payment at no less favourable terms than it currently does. Similarly the banks involved in the

process want to be sure about security and costs of processing the transaction within their existing security and operating restraints. Some of the new E-Commerce payment tools that can be used in manufacturing and business operations are:

Electronic Cash (Digital Cash)- It is a token-based currency which translates into equivalent real currency units that are guaranteed by a bank. (eg DigiCash).

Smart Cards- Smart Cards can be used with or without a stored value. If they have a stored value which contains "real digital cash", they are known as "Cash Cards" because they replace carrying cash (eg Mondex).

Electronic Cheques- These are the equivalent of paper based cheques. Authentication and verification are usually performed instantaneously by using digital signatures and time-stamping controls during the transaction (eg CheckFree).

Encrypted Credit Cards- There are varying degrees of encryption implementations credit of credit cards over the Internet, with the SET (Secure Electronic Transactions) holding the most promise (eg CyberCash).

6. Integrating Internet with Business Operations:

At the moment, according to many E-Commerce experts generally there are 3 types of Internet-based E-Commerce applications:

- Business to Business
- Business to Consumer, and
- Business to Employee.

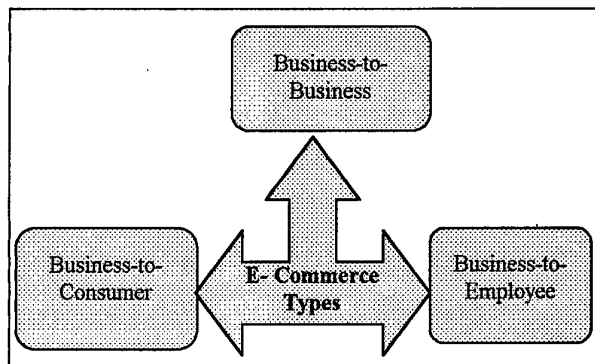


Figure 1. Electronic commerce application types in the virtual market.

6.1. Business-to-Business E-Commerce

Business-to-Business E-Commerce is complementary to EDI in that it is beginning to be used for non-production, non-replenishment applications. The widely used current terms used to describe the function of E-Commerce are "Business to Business" and "Business to Consumer". The expression "business-to-business" is inexact and sometimes misleading. In E-Commerce systems it is not always possible to tell who is accessing the automated point of sale/point of contact. It could be a retail consumer buying in wholesale quantities; it could be a business buying in retail quantities-and many other variants. Business-to-Business electronic ordering processes are generally designed to empower business managers. The business server can normally be accessed through the corporate Intranet, or an Extranet. Once the log on process is completed then the appropriate catalogue is selected. Ultimately all authorised suppliers' catalogues will be accessible by this business server. Suppliers' sites are not normally publicly promoted or advertised; they are trade sites, limited to their own closed user group of clients. Payment is made using a bank purchase card selected from an electronic wallet.

6.2. The Business-to-Consumer E-Commerce

The Business-to-Consumer E-Commerce is designed to complement normal retail shopping, mail order and direct marketing. It can accommodate delivery of soft, or digital goods, such as published material, software, audio and video products.

6.3. Business-to-Employee E-Commerce

Business-to-Employee E-Commerce is beginning to develop a new market place. Many companies now allow employee to buy using the corporate Intranet. A variant from an emulated business-to-consumer application is where employees may have purchases deducted from the payroll, or from allowances. Allowances or entitlements for clothes or equipment are often the norm in the armed services, police, fire services, airlines, banks, health services and so on. Not only do these systems have to keep track of entitlements and usage, but accounts, sizes and up to date measurements, location and other variables. This application promises to be an important hybrid of business-to-consumer and business-to-business.

7. Economic Benefits of E-Commerce for Business Operations

To date the major benefits from the Internet include improved internal and external communications. The Web has specifically brought a new marketing medium and enhanced information resource. Innovative applications are starting to appear which allow for sales and database interrogation. Other benefits such as e-mail and file transfer functionality, Web utilisation gave many companies 'Internet presence' and provided them with opportunities to develop and expand new services. A framework for realising the optimum level of benefits from using the E-Commerce over the Internet is illustrated below in Figure 2.

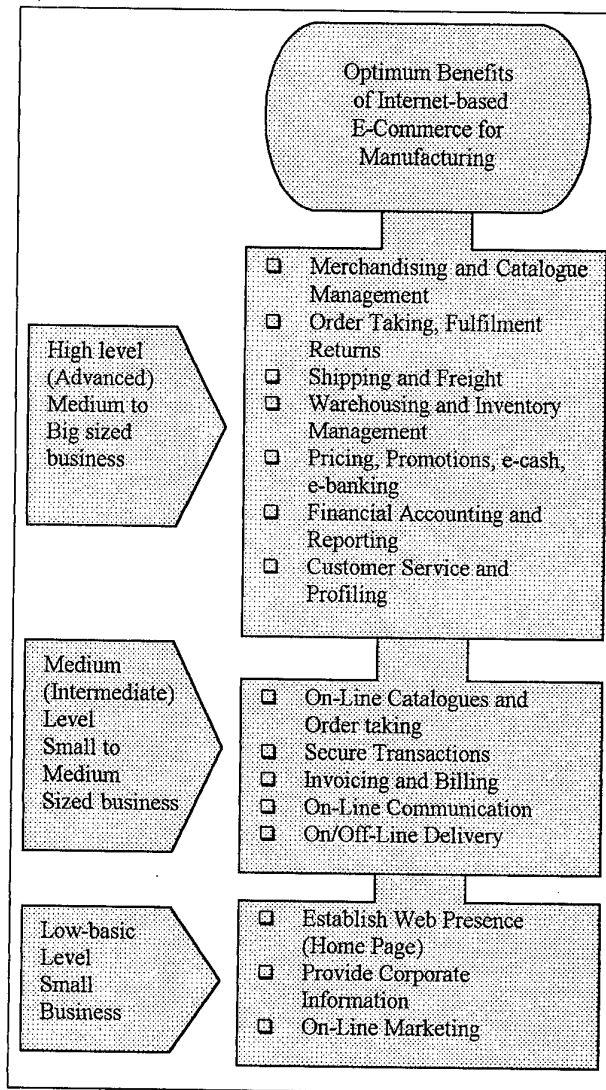


Figure 2. Framework for optimum level of adaptation and benefits of e-commerce over the Internet.

According to the Cisco Systems Inc., the leading maker of Internet equipment, more than \$1 trillion to \$2 trillion worth of goods and services will be sold on the Net by 2002. On the other hand, Gartner, a top industry consulting firm, has estimated business-to-business electronic commerce will be 12 to 15 times larger than consumer markets for the next few years, with consumer sales only catching up with business markets midway into the next decade. Businesses-to-business e-commerce involves companies and their suppliers while consumer markets include home shopping, banking, health care and broadband communications to the home. Although sales between businesses will dominate electronic commerce in the near term, Cisco estimates that by 2002 consumer-oriented business would represent 50 percent of the Internet economy.

8. Conclusions

This paper analysed the key drivers and economic values of integration Internet with business operations in smart manufacturing management.

Even though E-Commerce makes sense theoretically for business activities, the reality is that it has to integrate with internal and external processes that are already in place. Sometimes, this integration is a challenge linked to a major re-engineering exercise accompanied by resistance to change.

Despite the benefits and success stories a number of issues remain to be resolved such as security, privacy, and payment tools. It is believed that this concern regarding security will be lessened due to a series of international developments (Gide & Soliman, 1997). Other issues regarding the growth of the Internet are the lack of: a public key infrastructure (particularly for international trade), governmental stance, access, reliability (service levels), integrated applications and understanding/awareness of the Internet-Based E-Commerce capabilities, and finally the relative cost of required technologies.

9. References

1. ActiveMedia (1996), www.activemedia.com
2. Cisco Systems Inc. (1998), www.cisco.com
3. CommerceNet (1998), www.commerce.net
4. Cronin, M. J., *Global Advantage on the Internet*, Van Nostrand Reinhold, USA, 1996.
5. Cronin, M. J., *The Internet Strategy Handbook: Lessons from the New Frontier of Business*, Harvard Business Press, USA, 1996.
6. Dahl, A., and Lesnick, L., *Internet Commerce*, New Riders, USA, 1996.
7. Estrada, S., *Connecting to the Internet*, O'Reilly & Associates, Inc, Sebastopol, CA, 1993.
8. Forrester Research's Business Trade & Technology Strategies Service, (<http://www.internetnews.com/ec-news/cur/1997/07/3005-bb.html>)
9. Gartner (1998), www.gartner.com.
10. Gide, E., and Soliman, F., "Analysis of Conducting Business on the Internet," in *the Proceedings of Inet-tr'97 Conference*, Ankara, 21-23 November 1997.
11. Gide, E., and Soliman, F., "Key Drivers for Using the Internet in Australia," in *the Proceedings of Inet-tr'97 Conference*, Ankara, 21-23 November 1997.
12. Kalakota, R., and Whinston, A. B., *Frontiers of Electronic Commerce*, Addison Wesley, USA, 1996.
13. Kalakota, R. 'Debunking Myths About Internet Commerce', University of Rochester, USA, 1997.
14. Mougayar, W., *Opening Digital Markets*, CyberManagement, Canada, 1997.
15. Nielsen Media Research (1998), www.nielsen.com
16. Soliman, F., and Gide, E., "Impact of Internet-based E-Commerce on Manufacturing and Business Operations," in *the Proceedings of Inet-tr'97 Conference*, Ankara, 21-23 November 1997.
17. Steel, K., University of Melbourne, Australia, Private Communication, 1996.

DESIGN OF REAL TIME DECISION SUPPORT SYSTEMS ON THE BASIS OF THE TOOLS G2+GDA

VADIM N. VAGIN, ALEXANDER P. YEREMEYEV
Moscow Power Engineering Institute (Technical University)
Applied Mathematics Department
Krasnokazarmennaya str.14, Moscow, 111250, Russia
E-mail: vagin@apmsun.mpei.ac.ru
eremeev@srv-m.mpei.ac.ru

Key words: real time decision support system, decision making person, semiotic system, knowledge base, solver, information representation.

Topic: Embedded real-time systems.

Abstract

This paper describes the architecture and base concepts of building the real time decision support expert systems on the example of a prototype for monitoring and management of some complex objects (the main circulating pump, capacitor plant, ejector plant) of a nuclear power block, implemented on the basis of the tools G2+GDA.

1. Introduction

Real time decision support systems (RTDSS) are hardware-software complexes, intended for the help to the decision making persons (DMP) at management of complex objects and processes of a various nature in conditions of rigid temporary restrictions. When searching the decisions, expert models, constructed on the basis of expert knowledge, and heuristic methods of decision search, are used. According to a modern classification of software, RTDSS are a class of integrated intelligent (expert) systems of a semiotic type, combining strict mathematical decision search methods with nonstrict, heuristic methods, based on expert knowledge [1-3].

The necessity of creating RTDSS is caused by continuously growing complexity of controlled objects and processes with simultaneous time reduction, yielded by DMP on problem situation analysis and acceptance of necessary managing actions.

Conceptually joining the approaches and methods of the decision support theory, theory of information systems, artificial intelligence and using the objective and subjective information. RTDSS provides to DMP with the analysis of a soluble problem and directs him during decision search for increasing of a decision efficiency.

One of the basic problems at designing RTDSS is a choice of the suitable formal apparatus for a description of the decision support process and a construction on its base of an adequate (correct) decision making model (DMM). As such apparatus the production systems are usually used. However, available design tools of expert systems are oriented towards static problem domains, i.e. on situations, not requiring the corrections of DMM and decision support strategies during decision search [2].

2. Specificity of RTDSS

Peculiarities of problems, solved by RTDSS, are:

- the necessity of the temporary factor account at the problem situation description and during decision search;
- the necessity of decision making in conditions of temporary restrictions, determined by a real controlled process;
- impossibility of obtaining all objective information, necessary for the decision, and, in this connection, use of subjective, expert information;
- complexity of a search, the necessity of an active participation of DMP;
- presence of nondeterminism, the necessity of a correction and an introduction of additional information during decision search.

A basic purpose of RTDSS is to help to DMP at the control of complex objects and processes, revealing and prevention of dangers, development of the recommendations, i.e. to help

in the support of an abnormal regime before it will become irreversible. Developed RTDSS for operative-dispatching monitoring and management of a nuclear station power block and, in particular, its subsystems for monitoring and management of the main circulating pump (MCP), capacitor (CAP) and ejector plant (EJ), concern just such class [4].

The choice of the tools G2 for implementing RTDSS is caused by integration in it of basic high-effective technologies of complex program product development: object-oriented programming; open system technology and client-server one; the active object graphics; structured natural language and hypertext for information representation; decision search, based on production rules, procedures, dynamic (imitative) models; parallel fulfillment in real time of independent processes; the friendly interface with various types of the users (DMP, system manager, expert, knowledge engineer, programmer); a combination of technology of intelligent (expert) systems, based on knowledge, with technology of traditional programming.

The structure of base tools G2+GDA, necessary for RTDSS designing, consists of the interactive editor, tools of the graphic interface with the user, object-oriented graphics, graphic real time monitoring windows and animation, tools for display of connections between objects, interaction with external environment, imitative modeling and processing of complex rules and procedures, tools for messages and explanations.

3. The Architecture of RTDSS

Such objects as MCP, CAP and EJ of a nuclear station power block are not made serially. Each object is unique and, hence, RTDSS for object management is also unique. But at designing RTDSS for various objects it is possible to use the same hardware platform and tools. Moreover, within the framework of G2 class tools it is possible to design a tool environment of the same type of RTDSS. Such tools should give limited, but rather complete set of primitives for knowledge representation about an allocated class of objects and processes and about methods of management by them. Naturally, the tool environment, oriented towards dynamic RTDSS, should be open for updating by new constructive elements.

The generalized architecture RTDSS is given in fig. 1. In contrast with traditional expert systems in RTDSS it is necessary to include additional modeling blocks and forecasting blocks for analysis and estimation of accepted decision

consequences and choice of the best recommendations. These blocks are implemented on the basis of the imitative modeling system of G2.

We shall briefly view the basic concepts of RTDSS base module realization at the example of the prototype for monitoring and management of MCP of a power block [4].

Data base (DB) is a storehouse of object management information, acting with gauges from a subsystem of modeling and from DMP. The data in DB represent a set of continuous and discrete parameters of MCP (CAP, EJ). For database representation, the class hierarchy is realized. The class definition is given by means of the special tables, including such attributes as: a name of a class (Class name), a name of a parent class (Superior class), description of class specific attributes (Class specific attributes).

A base class of MCP parameters is a class of *gcn-parameter* – a successor of a class "object". Each MCP parameter has a developed name represented by DMP, what is reflected by attribute "fullname". For displaying continuous and discrete parameters two subclasses of a class "gcn-parameter" – *continuous-parameter* and *discrete-parameter* – are defined. All parameters are displayed as icons. The color of an icon of continuous parameters is changed in depending on a position of a current parameter value. In a normal condition the icon color is green, at an abnormal condition – red color. The change of color occurs according to production rules as whenever at obtaining the value by attribute "state", for example:

whenever the state of any continuous-parameter CP receives a value and when not (the state of CP is normal) then change the body icon-color of CP to red.

The value is also given to attribute "state" on a rule "whenever" at obtaining of a current value of a continuous parameter. For example:

whenever the cur-value of any continuous-parameter CP receives a value and when the cur-value of CP is the top-set of CP then conclude that the state of CP is upper.

DMP can change the current value of any parameter, if for any reasons, a source of parameter data (gauge) has ceased to function.

Knowledge base (KB) contains expert knowledge, on the basis of which analysis of object state will be carried out. The kind, in which knowledge in KB is presented, is determined by a knowledge representation model. The greatest spread in intelligent systems has received a production model with rules of the type:

If antecedent then consequent1 [, else consequent2].

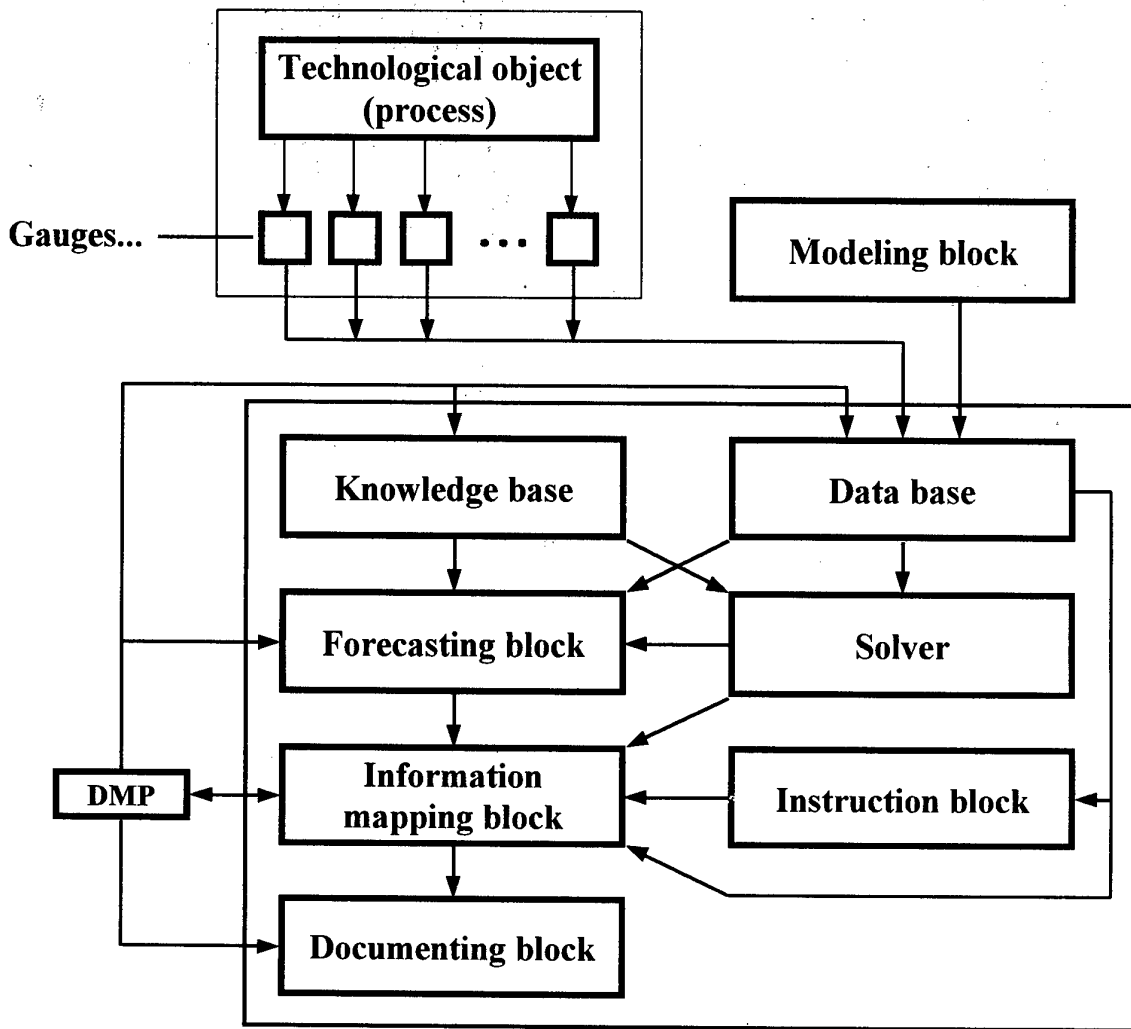


Fig. 1. The Generalized Architecture of RTDSS

In RTDSS an antecedent represents a logic expression concerning parameters of an object state. A consequent describes some action, which should be undertaken in case of the validity (consequent1) or not validity (consequent2) of an antecedent. These actions can consist in distribution of a command to the information block, in a change of information about object state, in activation of some knowledge from KB. The state estimation and the result distribution are a total of such action sequence. KB of RTDSS should satisfy to a number of the requirements, among which: presence of knowledge, allowing to carry out the analysis state of an object at incomplete information; presence for DMP of an opportunity of updating KB in a working mode, and, hence, presence of advanced means of the checking up entered data on correctness, when the

faulty changes in KB at functioning an object are inadmissible.

The instruction block directs actions of DMP in planned transitive modes. It works automatically (on a situation) at switching on the appropriate mode. The information on a mode of functioning of object acts from DB. The above requirements cause a necessity of information representation in KB in the most convenient for DMP recognition a graphic form. The example of a fragment of external representation of KB for DMP as the decision tree with the necessary explanatory is presented in fig.2, where the polyscreen for DMP is given.

A solver is a procedure which implement the algorithms (strategies) of application of knowledge from KB to data from DB. Solver as well as KB is a component of DMM.

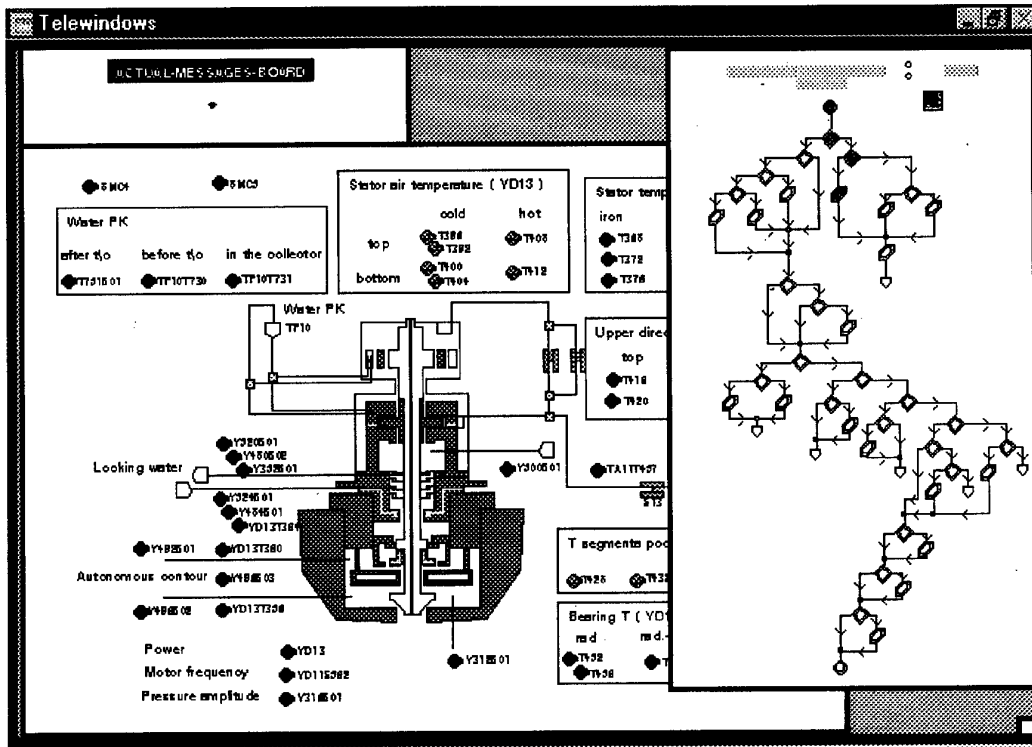


Fig. 2. The example of poly-screen for DMP (prototype for MCP)

Under designing RTDSS for monitoring and controlling the sophisticated objects, in particularly, the semiotic systems of operative-dispatching control by nuclear stations, traditional methods of information search are impossible in principle due to huge amount of interrelated and sometimes inconsistent facts and laws describing these objects. Therefore for manipulating and processing knowledge, representing by a collection of production rules, it is necessary to have an inference engine which implements decision-making procedures and forms a control recommendation list for such systems.

We have focused on parallel inference methods and procedures because only parallelism of inference procedures allows to increase the speed of inference processes and to treat a huge amount of productions. As the inference method we have chosen the parallel inference method on a special type semantic networks, possessing several types of parallelism (or-parallelism, and-parallelism, dcdp-parallelism).

As semiotic systems are open ones, they must take into account semantic and pragmatic aspects of knowledge processing. Moreover they assume the support of commonsense reasoning, the methods of plausible inference based on the apparatus of non-traditional logics (nonmonotonic,

modal, fuzzy and abductive ones). To operate with exceptions of knowledge base, it is suggested to apply default logic by R. Reiter [5].

The forecasting block carries out functions of forecasting of abnormal situations and consequences of managing actions. The forecasting is made on a DMP command on the basis of data on a current state of controlled object, acting from DB, and on the basis of knowledge, stored in KB. The managing action is either a set by DMP, or the recommendation given by G2 solver.

The information mapping block carries out functions of information representation to DMP. Initial data for it are data from DB, results of an estimation of a object state, received by a solver, results of the forecasts, made by the forecasting block, and instructions, given out by the instruction block.

The information, on the one hand, should be displayed in the form convenient for a fast recognition by DMP and, on the other hand, should be as it possible more complete. These requirements contradict each other, as the increasing of volume of the sign information decreases an ability of the person to perceive it. The problem is decided by means of the multilevel circuit of information mapping with application of

a hypertext technology and cognitive graphics. The information mapping unit for a prototype is the display of a workstation. The motionless image on the screen corresponds to a static object state, and the movement displays transition of an object in a new condition.

For mapping the information a number of working spaces is entered (fig.2):

1. Working space with the scheme of MCP (CAP, EJ), its auxiliary systems and gauges. MCP is submitted by an icon of a class gen. The given class has a few ports for connection with elements of the pump auxiliary subsystems: an independent contour, circulation of oil in bearings, locking water, cooling liquids. The gauges are represented on groups by graphic images of parameters fixed by them MCP. The working space of parameter becomes visible at pressing of a mouse key on an icon of parameter. Dynamics of processes, occurring in MCP, is displayed by change of graphic images color of parameters. Looking on the scheme, DMP can qualitatively estimate a state of MCP and define, which parameters are outside of a range of allowable values (these parameters are allocated by red color). For more detailed acquainting with a state of MCP, the operator has access to the parameter workspaces.

2. Working space of the urgent messages. At a normal condition in the working space of the urgent messages there is only one message "System MCP is in norm". This message has a green background and does not signal about any anomaly. At occurrence of abnormal situations in working space there are the appropriate messages on a red background.

3. Working space of KB. In it the decision tree of DMM is located. In basic this space is intended for the expert and knowledge engineer for creating and testing KB. In a decision making mode the means for a choice, concealment, moving and change of the size of the specified working spaces are given to DMP. With the help of these means he can design project interface with the application. In addition to DB the messages base is realized which contains all diagnostic messages, that can be given to the operator in a decision making mode. The message base places in separate working space and consists of copies of a class "gcn-message", being a subclasses of a built-in class G2 message with attribute "text". The class "gcn-message" is complemented by integer attribute "message-number" and logic attribute "message actuality".

Modeling block simulates behavior of an object. It can act as the agent of data about an object state at a stage of system testing and at a decision making stage for comparison with data, acting from gauges. The modeling block can also

be used together with the forecasting block for the forecast of abnormal situations and consequences of managing actions.

4. Conclusion

During implementation of the RTDSS prototype for monitoring and management of a nuclear station power block [4], 31 classes of objects, 12 subclasses of variables, 2 subclasses of connections between objects, 7 relations between objects were defined; 38 generalized rules, 45 procedures and 4 functions were written. DB about MCP includes 33 parameters, about CAP – 21 parameters, about EJ – 32 parameters. For each continuous parameter, a subworkspace and objects for graphic display of dynamics of changing its values are defined. The internal representation of the prototypes occupies 860K.

This work was supported by the Russian Fund of Fundamental Researches (project 99-01-00049).

References

1. Vagin V.N., Yeremeyev A.P. Implementing a conception of distributed artificial intelligence and multiagent systems in decision support systems based on the tools G2 + GDA // Proc. of the International Workshop "Distributed Artificial Intelligence and Multi-Agent Systems", DAIMAS'97, June 15-18, 1997, St. Petersburg, Russia, pp.249, 262-268.
2. Yeremeyev A.P. Organization of semiotic type knowledge representation model for dynamic decision support systems // Proc. of Seventh International Conf. "Artificial Intelligence and Information-Control Systems of Robots", AIICSR'97, Second Workshop on Applied Semiotics, Sept. 15, 1997, Smolenice Castle, Slovakia, pp.77-81.
3. Vagin V.N., Yeremeyev A.P. Parallel inference in knowledge representation models // Proc. of the Symposium on Robotics and Cybernetics, CESA'96, IMACS Multiconference, July 9-12, 1996, Lille-France, pp.184-188.
4. Yermeev A.P., Chibizova N.V. The prototype of a real time decision support system on the basis of the tool complex G2 // Proc. of Second Joint Conf. on Knowledge Based Software Engineering, JCKBSE'96, Sept. 21-22, 1996, Sazopol, Bulgaria, pp.128-133.
5. Reiter R. A logic for default reasoning // Artificial Intelligence 13, 1980, pp.81-132.

Virtual Image Cancellation in a New Binocular Stereovision System

Junichi Takeno, o.-Prof. of Meiji University

Zichuan XU, Graduated Student of the University

Meiji University, School of Science and Technology,

Faculty of Computer Science, Robots and Science Laboratory

takeno@cs.meiji.ac.jp

Abstract

This paper announces the world's first binocular stereovision system for robots that solves the problem of the virtual image which occurs when the viewed object consists of repeated patterns. This new technique, which was invented by the principal author, is called the rotation disparity mechanism. The technique also addresses occlusion, a problem unique to stereovision systems, making it possible to extract occlusion areas from images. The new binocular vision system comprises four CCD cameras, two for each eye.

1. Virtual Image Problem and Rotation Disparity Mechanism

The virtual image problem has long been considered a critical defect of usual binocular stereovision systems and has posed difficulties for researchers trying to create highly functional artificial vision systems. Some researchers have noted that virtual images seldom occur in typical working environments while others have declared that, since even human vision cannot overcome the virtual image problem, it is an acceptable defect of robot vision. The former statement simply admits the total absence of a safety mechanism should a virtual image occur. The latter statement is utterly unacceptable considering the fact that humans are in fact not annoyed by virtual images.

Two methods are currently available to solve the virtual image problem.

One is to discard the idea of usual binocular stereovision and instead develop a stereovision system with three or more eyes. The other is to improve on the concept of a binocular system, and attempt to enable a binocular vision robot to detect by its own movement any virtual images that may occur.

With the former method, researchers typically study techniques to discriminate virtual and real images with the third vision component. Since the positional information on the detected object is used to distinguish between virtual and real images, such a system does not guarantee, in principle, that all virtual

images will be eliminated. With the latter method, safe robot motion cannot be guaranteed unless virtual images are detected before the robot starts to move.

The principal author therefore concluded that when using a binocular system similar to human vision, a technique to detect virtual images would be required to be built in to the binocular stereovision system itself and called this technique the rotation disparity mechanism.

The rotation disparity mechanism is essentially based on the high-speed movement of at least one of the two eyes of the system, rather than increasing the number of eyes from two to three or more (a multi-eye system). The motion of this one eye will bring about the motion of virtual images and by detecting this motion, virtual images are discriminated. Importantly, real images do not move when a single eye is moved at high speed (Figure 1). Any form of high-speed motion generates similar effects. The authors selected rotational movement because rotation can be controlled more easily and both horizontal and vertical parallax information can be evaluated simultaneously.

The authors' technique is different from multi-eye vision, a conventional research theme, because the motion of at least one eye is controlled. The new technique further does not physically require a number of imaging cameras. It is also different from vision research that uses saccadic movement because the vibration of saccadic movement is fixed in one particular direction, and for this reason it is not actively used to eliminate virtual images.

2. Robot Vision System Featuring the Proposed Rotation Disparity Mechanism

The robot vision system proposed by the authors comprises four CCD cameras, two DC motors, two rotary encoders, and six DC servo motors.

Two CCD cameras are paired to create two eyes in the system. One camera in each pair, with a zoom function and a narrow focal field, is used to recognize objects. The other camera in each pair, with a wide-angle lens, captures 3-dimensional space in the line of sight using

the rotation disparity mechanism. The first camera thus has a function equivalent to the central vision of human eyesight, and the latter is equivalent to peripheral vision (Figure 2). This vision system has a three-tier structure. The bottom tier accommodates one DC motor and one rotary encoder which are used to move the cameras installed horizontally on the top tier. The middle tier holds one DC servo motor to precisely move the cameras in synch with the DC motors on the bottom tier. The top tier also holds the pan and tilt mechanism for the cameras and measures rotation disparity with the peripheral vision camera. Specifically, the peripheral vision camera is rotated about the center axis of the central vision camera while the direction of the central line of sight is kept synchronized with that of the central vision camera. The peripheral vision camera is initially positioned directly above the central vision camera. The direction of rotation is such that the base distance between the right and left cameras increases, or the peripheral vision cameras rotate in opposite directions. The cameras start rotating when a virtual image is detected in an image.

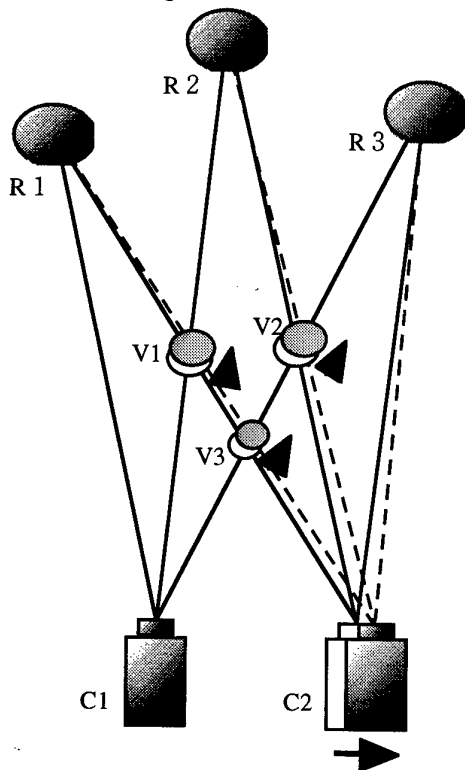


Fig.1 Principle of virtual image cancellation by the rotation disparity mechanism

R1,R2,R3: Real Objects

V1,v2,v3: Virtual Images

C1,C2: Peripheral Cameras of New Stereovision

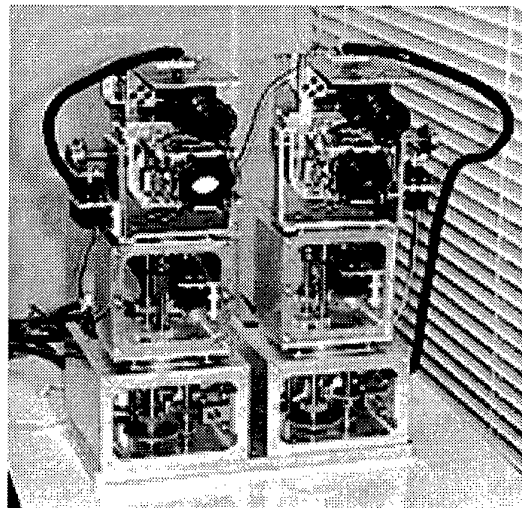


Fig. 2 A Prototype of New Binocular Stereovision

3 Virtual Image Cancellation Techniques

This section defines the meaning of virtual images and describes a technique to cancel virtual images using our new mechanism.

3.1 Occurrence of Virtual Images

A virtual image occurs when one attempts to calculate the distance in a 3-dimensional space using two or more image data captured from different positions.

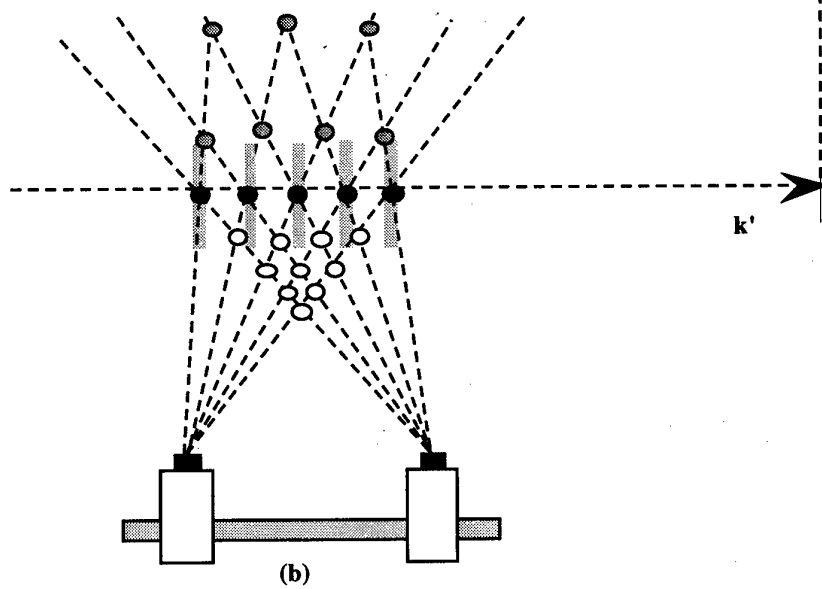
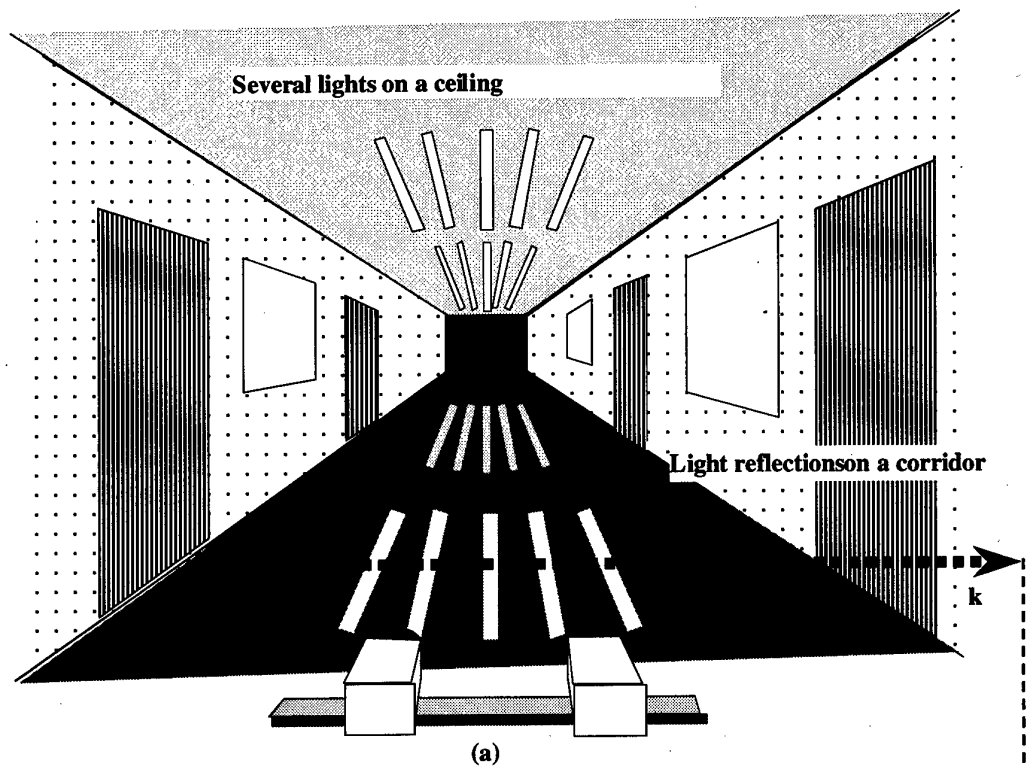
A distance calculation technique is comprised of finding a certain same image which is only partially included in two or more image data and performing the necessary calculations based on the position of the detected image and the position of the imaging equipment used (Figure 3).

Virtual images can occur for the following reasons:

1. Noise in image information
2. Ambiguous interpretation caused by quantization errors
3. Repetitive information on an image

Virtual images can occur due to 1), however, noise information can never be permanent. Noise can be eliminated within a time period that is small enough not to obstruct real-time observation.

As for 2), two or more image data, which are actually different from each other, can be interpreted as the same information due to quantization errors during image capture. Such errors occur due to the quantization characteristics of the imaging equipment and variables of the external environment. Thus, like 1), the ambiguous information cannot be permanent and can therefore be



- unreal image below the corridor
- real image on the corridor
- unreal image above the corridor

Fig. 3 Binocular stereo vision and the virtual images

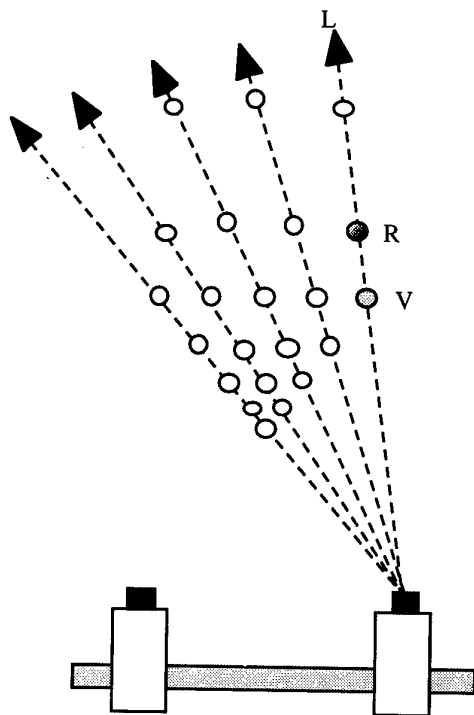


Fig4. Candidates of the Virtual Image eliminated. Quantization errors can also be reduced by combining data when searching for the same information.

As for 3), virtual images cannot be avoided if the image information is repetitive.

Thus, points 1 and 2 relate to noise rather than the occurrence of virtual images, and point 3 is the true virtual image issue.

3.2 Techniques for Canceling Virtual Images

This section describes three techniques for canceling virtual images using the binocular stereovision system incorporating the rotational disparity mechanism proposed by the authors. The first technique is used for observing a static 3-dimensional space. Static space here means that the object space does not change substantially. The second technique is used for observing a changing space. The last technique involves the use of a neural network.

3.2.1 Observing Static Space

A moving vision system may be classified into this category provided the movement information is clearly known. Static space observation includes cases where the motion of the object is very slow compared with the motion of the camera by the rotation disparity mechanism.

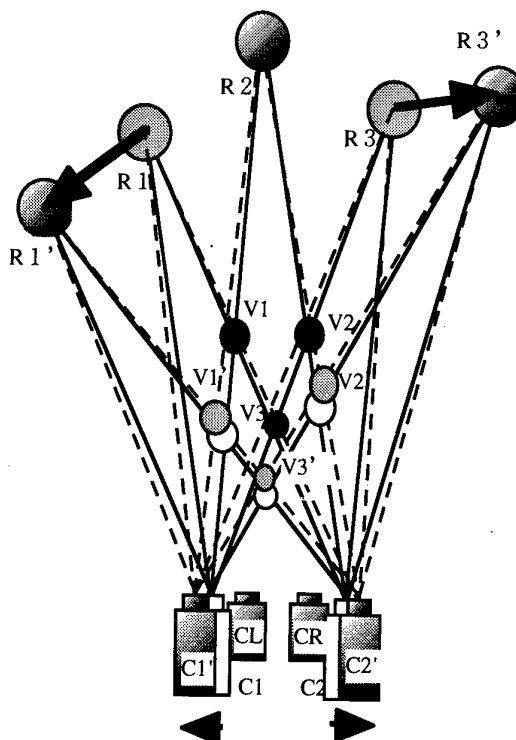


Fig. 5 Principle of virtual image cancellation by the rotation disparity mechanism
C1,C2: Peripheral Cameras
CL,CR: Central Cameras

The basic concept for identifying virtual images was described in section 1 using an example of a 2-dimensional plane. Specifically, this technique detects positional information in the 3-dimensional space using a vision system, then detects positional changes in the 3-dimensional space using the rotation disparity mechanism.

Candidate virtual images can easily be identified when two or more objects are in the same line of sight (Figure 4). In Figure 4, three objects are present on line of sight L. It is unknown which is the real image. It is obvious that at least one real image exists.

3.2.2 Observing Dynamic Space

The dynamic space problem can be reduced to the 3.2.1 problem if changes in the object space are detectable. Such changes can easily be detected using the central vision camera of the new vision system proposed by the authors in combination with a technique for detect floating points or by other techniques. When the object space changes, information derived from both central and peripheral vision cameras is integrated to identify virtual images (Figure 5). This, however, applies only when the object is moving at a relatively high speed. One may

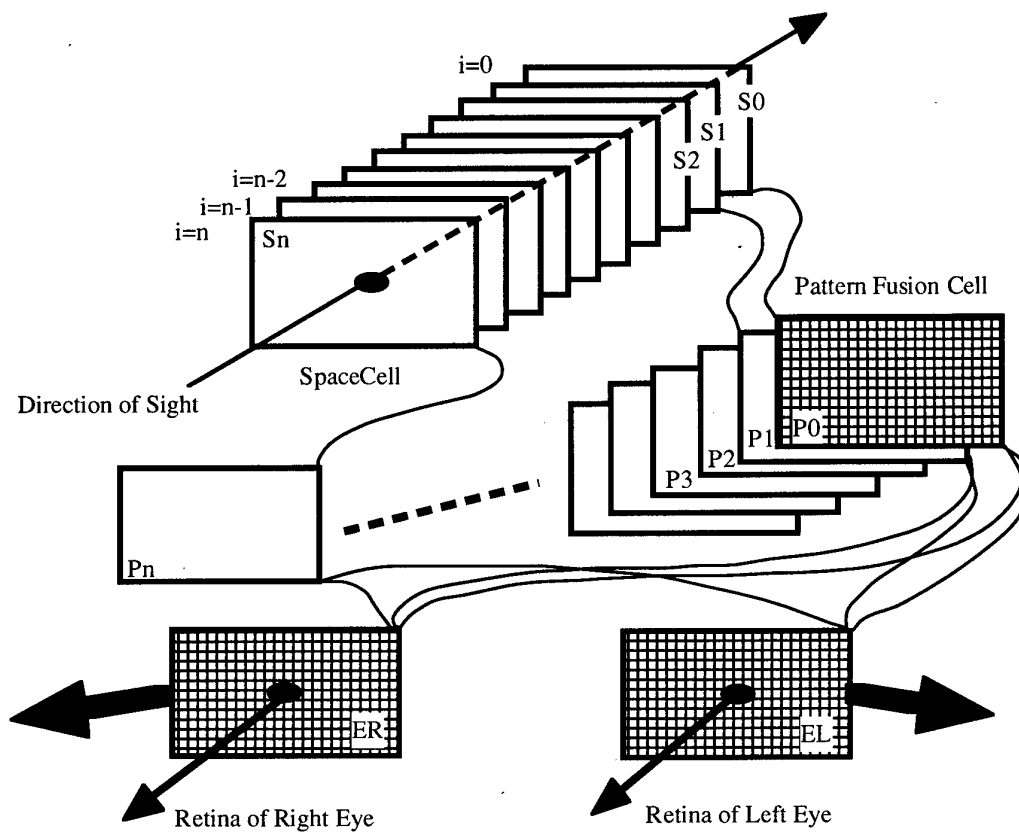


Fig.6 General Design of the Stereovision

thus believe that it is more natural for the vision system to track the object with the central vision camera rather than attempting to capture solid information. In this figure, C1 and C2, and CL and CR are the peripheral and central vision cameras, respectively. C1' and C2', representing the rotation disparity mechanism, show the result of the individual motion of C1 and C2 cameras. In this example, the motion of the rotation disparity mechanism from C1 to C1', or from C2 to C2' is slow compared with the motion of the object from R1 to R1', so it is necessary to measure the motion of the object using the CL and CR central vision cameras.

3.2.3 Using a Neutral Network

This technique is described only for an object which is moving very slowly compared with the motion of the camera by the rotation disparity mechanism, or when the object space is static.

The technique devised by the author comprises the following steps:

- (a) Detect solid information using binocular parallax
- (b) Find virtual images using the rotation disparity

mechanism

- (c) Delete the virtual image portions of the solid information of step (a) using the information derived in step (b)

The technique adopted here is similar to the technique described in 3.2.1 except that the former employs a sequential calculation technique while this technique is a kind of conditioned reflex technique using a parallel processing neutral network. In step (a), solid information is calculated using image information derived from the right and left eyes. The basic portion of this technique resembles the famous research by Prof. Paul M. Churchland at the University of California, San Diego. However, the authors' research is different in that the solid information has the same resolution as the number of picture elements. Furthermore, different objects in the same line of sight can be managed separately. In other words, our system can measure, so far as the functionality is concerned, the solid information for all objects in the nearest measurable position to those located at the point of infinity. In reality, however, distant solid information contains quantization errors. In step (b), the peripheral vision cameras are turned at high speed using the rotation disparity mechanism to identify

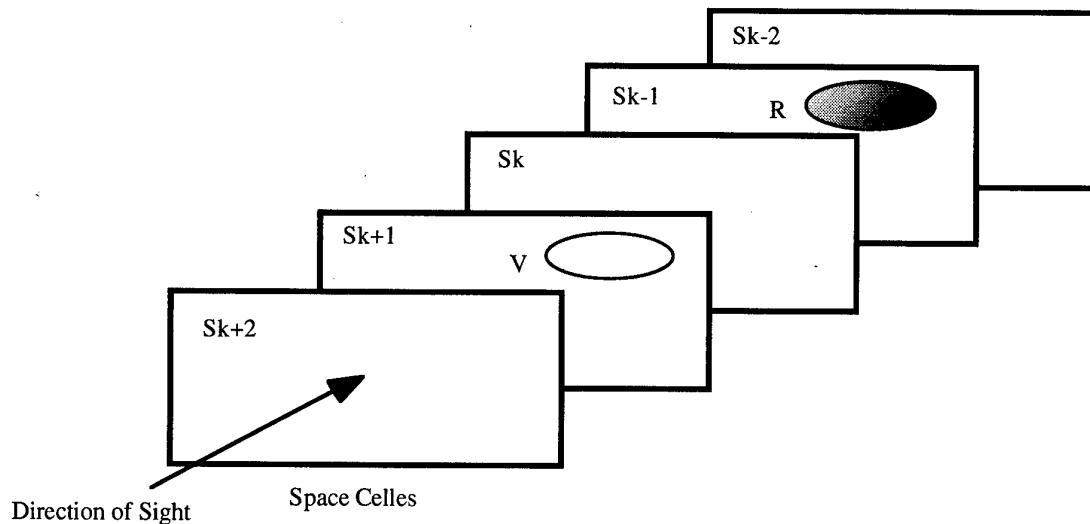


Fig.7 Virtual and Real Images on the Spece Celles

any virtual images. The virtual images are then canceled at step (c). To be specific, the processing system comprises a right and a left retina, pattern fusion cell and space cell (neutral network). The pattern fusion cell P_i determines the coincidence of an image projected on the two retinas with the horizontal parallax value of "i." The result is transmitted to the space cell S_i . S_i records the position of the object located at a distance corresponding to the parallax value "i" in the relevant vision system. For $i = 0$, the S_i information suggests that the object is located at the point at infinity. All information from S_0 to S_n can be calculated. We can calculate the direction of the line of sight and distance of all objects visible between the point at infinity in the environment viewed by the vision system and the distance equivalent to the parallax value "n." If in this information, two or more objects are observed in the same line of sight, we then have to determine if they are real or virtual images (Figure 7). In Figure 7, objects R and V are observed on the space cells S_{k-1} and S_{k+1} , respectively. The rotation disparity mechanism is now identifying whether they are real or virtual. If, for example, the object V on S_{k+1} is virtual, and R real, the object V is moving in the S_k side while R is static. Suppression signals are sent to object V on S_{k+1} of the space cell, which deletes object V in step (c).

4 Future Development Prospects

The basic concept described in this paper was announced at the annual academic lecture meeting of the Robotics Society of Japan in September 1998. [1] [2] At this time, however, the authors have not yet completed this study. We have so far manufactured a prototype of the hardware section of the binocular stereovision system with a rotation disparity mechanism. The relevant software is still under development. The neutral network

is in the concept stage, and we are currently manufacturing a prototype for the basic portion of the network.

Afterword

This paper reported on a new-type binocular stereovision system to solve the problem of virtual images. It introduced the principle of the rotation disparity mechanism, the theoretical principle of detection and elimination of virtual images, and a technique to detect occlusion. An experimental prototype system was introduced to demonstrate these principles.

The authors wish to acknowledge that this research was supported in part by the "Intelligent Robot," a Priority Area Research of the Ministry of Education, Science, Sports and Culture; the Sophisticated Dynamic Stereovision for Intelligent Autonomous Field Vehicle Project of Meiji University Comprehensive Research; the "High-Tech Research Center," a Private University Grant of the Ministry of Education, Science, Sports and Culture, and other aids.

A patent application for this research method has already been filed in Japan and preparations are underway for patent applications in the United States and Europe.

References

- [1] Zichuan XU, Junichi Takeno and others " Research of Visual Sense for Mobile Robots -Stereo Vision by Using Four CCD Cameras-", Annual Meeting for Robotics Society of Japan, Hokkaido Japan, 2N12, pp.885-886.
- [2] Atsushi Ichikawa, Junichi Takeno and others " Research on a vision system for autonomous mobile robots -Proposal for stereovision by rotation disparity", Annual Meeting for Robotics Society of Japan, Hokkaido Japan, 2N23, pp.897-898.

A Study on Intelligent Control of Robot Manipulator Based-on Visual Servoing with Stereo Vision

Sung Hyun Han¹, Man Hyung Lee², Jong Il Bae³

1. School of Mechanical Engineering, Kyungnam Univ., Masan City, Korea.

E-mail: shhan@kyungnam.ac.kr, TEL: +82-551-49-2624, FAX: +82-551-43-8133

2. School of Mechanical Engineering, Pusan National Univ., Pusan City, Korea.

E-mail: mahlee@hyowon.cc.pusan.ac.kr, TEL: +82-51-510-1456, FAX: +82-51-510-2331

3. Department of Electrical Engineering, Pukyong National Univ., Pusan City, Korea.

E-mail: jibae@pine.pknu.ac.kr, TEL: +82-51-620-1437, FAX: +82-51-620-1426

Abstract

This paper presents a new approach to visual servoing with the stereo vision. In order to control the position and orientation of a robot with respect to an object, a new technique is proposed using a binocular stereo vision. The stereo vision enables us to calculate an exact image Jacobian not only at around a desired location but also at the other locations. The suggested technique can guide a robot manipulator to the desired location without giving such priori knowledge as the relative distance to the desired location or the model of an object even if the initial positioning error is large. This paper describes a model of stereo vision and how to generate feedback commands. The performance of the proposed visual servoing system is illustrated by the simulation and experimental results and compared with the case of conventional method for a SCARA robot.

The abstract is to be in fully-justified italicized text, at the top of the left-hand column as it is here, below the author information. Use the word "Abstract" as the title, in 12-point Times, boldface type, centered relative to the column, initially capitalized. The abstract is to be in 10-point, single-spaced type, and may be up to 3 in. (7.62 cm) long. Leave two blank lines after the abstract, then begin the main text. All manuscripts must be in English.

1. Introduction

There are mainly two ways to put the visual feedback into practice. One is called look-and-move and the other is visual servoing. The former is the method which transforms the position and orientation of an object

obtained by a visual sensor into those in the world frame fixed to an environment and guides the arm of the manipulator to a desired location in the world frame [1,2]. In this method, precise calibration of a manipulator and camera system is needed. On the contrary, visual servoing uses the Jacobian matrix which relates the displacement of an image feature to the displacement of a camera motion and performs a closed-loop control regarding the feature as a scale of the state. Therefore, we can construct a servo system based only on the image and can have a robust control against the calibration error because there is no need to calculate the corresponding location in the world frame [2,3,4]. A hand eye system is often used in visual feedback and there are two ways of arranging the system. One is placing a camera and a manipulator separately; the other is placing the camera at the end-tip of the manipulator. The former motion strategy of the manipulator becomes more complicated than the latter. In the latter, it is easy to control the manipulator using a visual information because the camera is mounted on the manipulator end-tip. In this paper, we deal with the latter method. In the conventional works, some researches have presented methods to control the manipulator position with respect to the object or to track the feature points on an object using a hand eye system as the application of visual servoing [3,4]. These methods maintain or accomplish a desired relative position between the camera and the object by monitoring feature points on the object from the camera [5,6].

However, these have been all done by the hand eye system with monocular visions and it is necessary to compensate for the loss of information because the original three-dimensional information of the scene

is reduced to two-dimension information on the image. For instance, we must add an information of the three-dimension distance between the feature point and the camera in advance or use a model of object stored in the memory. Besides, a problem that the manipulator position fails to converge to a desired value arises depending on the way of selecting feature points or when the initial positioning error is not small. It is because some elements of the image Jacobian cannot be computed with only the information of the image and substituting approximate values at the desired location for them may result in large errors at the other locations.

This paper presents a method to solve this problem by using a binocular stereo vision. The use of stereo vision can lead to an exact image Jacobian not only at around a desired location but also at the other locations. The suggested technique places a robot manipulator to the desired location without giving such priori knowledge as the relative distance to the desired location or the model of an object even if the initial positioning error is large. This paper deals with modeling of stereo vision and how to generate feedback commands. The performance of the proposed visual servoing system was evaluated by the simulations and experiments and obtained results were compared with the conventional case for a SCARA robot.

2. Stereo Vision Model

We define the frame of a hand-eye system with the stereo vision and use a standard model of the stereo camera whose optical axes are set parallel each other and perpendicular to the baseline. The focal points of two cameras are apart at distance d on the baseline and the origin of the camera frame Σ_c is located at the center of these cameras. Fig. 1 represents the schematic diagram of a suggested visual servoing system. In Fig. 1 two DSP vision boards (MVB03) are used, which were made Samsung Electronics Company in Korea based-on the TMS320C30 chips.

An image plane is orthogonal to the optical axis and apart at distance f from the focal point of a camera and the origins of frame of the left and right images Σ_l and Σ_r , are located at the intersecting point of the two optical axes and the image planes. The

origin of the world frame Σ_w is located at a certain point in the world. The x , y , and z axes of the coordinate frames are shown in Fig. 2.

Now let ${}^l p = ({}^l x, {}^l y)$ and ${}^r p = ({}^r x, {}^r y)$ be the projections onto the left and right images of a point p in the environment, which is expressed as ${}^c p = ({}^c x, {}^c y, {}^c z)^T$ in the camera frame. Then the following equation is obtained (see Fig. 2).

$${}^l x \quad {}^c z = f ({}^c x + 0.5d) \quad (1-a)$$

$${}^r x \quad {}^c z = f ({}^c x - 0.5d) \quad (1-b)$$

$${}^l y \quad {}^c z = f \quad {}^c y \quad (1-c)$$

$${}^r y \quad {}^c z = f \quad {}^c y \quad (1-d)$$

Suppose that the stereo correspondence of feature points between the left and right images are found. In the visual servoing, we need to know the precise relation between the moving velocity of camera and the velocity of feature points in the image, because we generate a feedback command of the manipulator based on the velocity of feature points in the image.

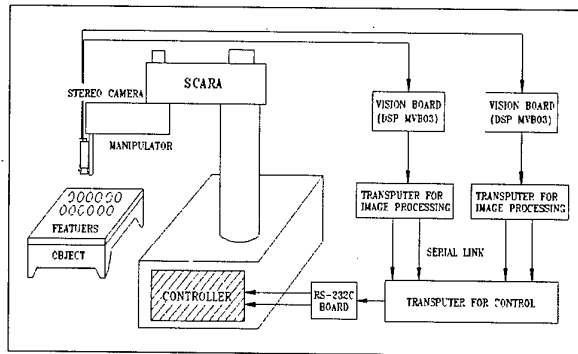


Fig. 1 Schematic diagram of visual servoing system.

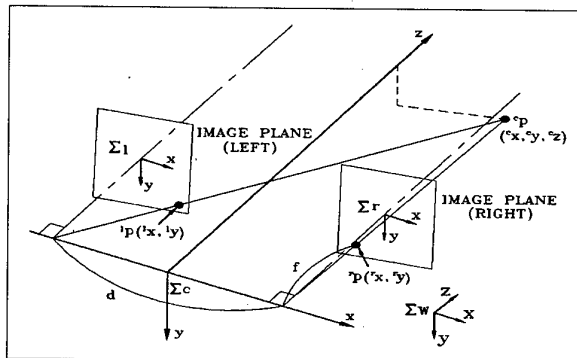


Fig. 2 The coordinates system of stereo vision model.

This relation can be expressed in a matrix form which is called the image Jacobian. Let us consider n feature points $p_k (k=1, \dots, n)$ on the object and the coordinates in the left and right images are ${}^l p_k ({}^l x_k, {}^l y_k)$ and ${}^r p_k ({}^r x_k, {}^r y_k)$, respectively. Also define the current location of the feature points in the image ${}^l p$ as

$${}^l p = ({}^l x_1 \ {}^r x_1 \ {}^l y_1 \ {}^r y_1 \ {}^l x_n \ {}^r x_n \ {}^l y_n \ {}^r y_n)^T \quad (2)$$

where each element is expressed with respect to the virtual image frame \sum_p .

First, to make it simple, let us consider a case when the number of the feature points is one. The relation between the velocity of feature point in image ${}^l \dot{p}$ and the velocity of camera frame ${}^c \dot{p}$ is given as

$${}^l \dot{p} = {}^p J_c {}^c \dot{p} \quad (3)$$

where ${}^p J_c$ is the Jacobian matrix which relates the two frames. Now let the translational velocity components of camera be σ_x, σ_y , and σ_z and the rotational velocity components be w_x, w_y, w_z then we can express the camera velocity V as

$$\begin{aligned} V &= [\sigma_x \ \sigma_y \ \sigma_z \ w_x \ w_y \ w_z]^T \\ &= [{}^c v_c \ {}^c w_c]^T \end{aligned} \quad (4)$$

Then the velocity of the feature point seen from the camera frame ${}^c \dot{p}$ can be written

$$\begin{aligned} {}^c \dot{p} &= \frac{d {}^c p}{dt} \\ &= \frac{d}{dt} {}^c R_w ({}^w p - {}^w p_c) \\ &= {}^c R_w \{ -{}^w w_c \times ({}^w p - {}^w p_c) \} + {}^c R_w ({}^w \dot{p} - {}^w \dot{p}_c) \end{aligned} \quad (5)$$

where ${}^c R_w$ is the rotation matrix from the camera frame to the world frame and ${}^w p_c$ is the location of the origin of the camera frame written in the world frame. As the object is assumed to be fixed into the world frame, ${}^w \dot{p} = 0$. The relation between ${}^c \dot{p}$ and V is

$$\begin{aligned} {}^c \dot{p} &= {}^c R_w \{ -{}^w w_c \times ({}^w p - {}^w p_c) \} - {}^c R_w {}^w \dot{p}_c \\ &= -{}^c w_c \times {}^c p - {}^c \dot{p}_c \\ &= \begin{bmatrix} -w_y {}^c z + w_x {}^c y - v_z \\ -w_z {}^c x + w_x {}^c z - v_y \\ -w_x {}^c y + w_y {}^c x - v_z \end{bmatrix} \end{aligned} \quad (6)$$

Therefore, substituting Eq. (6) into Eq. (3), we have the following equation.

$$\begin{aligned} {}^l \dot{p} &= {}^l J_c {}^c \dot{p} \\ &= J V \end{aligned} \quad (7)$$

In Eq. (7) matrix J which expresses the relation between velocity ${}^l \dot{p}$ of the feature point in the image and moving velocity V of the camera is called the image jacobian.

From the model of the stereo vision Eq. (1), the following equation can be obtained.

$${}^c x (2 {}^l x - {}^r x) = d {}^l x + {}^r x \quad (8)$$

$${}^c y ({}^l x - {}^r x) = {}^l y d = {}^r y d \quad (9)$$

$${}^c z ({}^l x - {}^r x) = f d \quad (10)$$

Above discussion is based on the case of one feature point. In practical situation, however, the visual servoing is realized by using plural feature points. When we use n feature points, image Jacobian J_1, \dots, J_n are given from the coordinates of feature points in the image. By combining them, we express the image Jacobian as

$$J_{im} = [J_1 \ \dots \ J_n]^T \quad (11)$$

Then, it is possible to express the relation of the moving velocity of the camera and the velocity of the feature points even in the case of plural feature points, that is,

$${}^l \dot{p} = J_{im} V \quad (12)$$

where we suppose that the stereo and temporal correspondence of the feature points are found.

In the case of the monocular, the image Jacobian J has the following form.

$$J = f \begin{vmatrix} -\frac{1}{c_x} & 0 & \frac{c_x}{c_z^2} & \frac{c_x c_y}{c_z^2} & -(1 + \frac{c_x^2}{c_z^2}) & \frac{c_y}{c_z} \\ 0 & -\frac{1}{c_x} & \frac{c_y}{c_x^2} & 1 + \frac{c_y^2}{c_z^2} & -\frac{c_x c_y}{c_z^2} & -\frac{c_x}{c_z} \end{vmatrix} \quad (13)$$

We now introduce the positional vector of the feature point in the image of monocular vision using the symbol ${}^mP = ({}^mx, {}^my)$. This is the projection of the point expressed as ${}^cP = ({}^cx \ {}^cy \ {}^cz)^T$ in the camera frame into the image frame of the monocular vision, and has the following relation.

$${}^mx = f \ {}^cx \ {}^cz^{-1} \quad (14-a)$$

$${}^my = f \ {}^cy \ {}^cz^{-1} \quad (14-b)$$

Substituting Eq.s (14-a) and (14-b) into Eq. (13) yields another expression of the image Jacobian for the monocular vision.

$$J = f \begin{vmatrix} -\frac{1}{c_z} & 0 & \frac{{}^mx}{c_z} & \frac{{}^mx {}^my}{f} & -\frac{{}^mx^2 + f^2}{f^2} & \frac{{}^my}{f} \\ 0 & -\frac{f}{c_x} & \frac{{}^my}{c_x} & 1 + \frac{{}^my^2 + f^2}{f^2} & -\frac{{}^mx {}^my}{f} & -\frac{{}^mx}{f} \end{vmatrix} \quad (15)$$

A disparity which corresponds to the depth of the feature point, is included in J in the case of the stereo vision, but s -term expressed in the camera frame cz is included in J in the case of the monocular vision.

3. Feedback Command

In the visual servoing, the manipulator is controlled so that the feature points in the image reach their respective desired locations.

We define an error function between the current location of the feature points in image ${}^l p$ and the desired location ${}^l p_d$ as

$$E = Q({}^l p - {}^l p_d) \quad (16)$$

where Q is a matrix which stabilizes the system. Then the feedback law is defined as following equation

$$V = -G E \quad (17)$$

where G corresponds to a feedback gain.

To realize the visual servoing, we must choose Q so that convergence is satisfied with the error system can be satisfied with

$$\begin{aligned} \dot{E} &= \frac{\partial E}{\partial t} \\ &= Q \frac{\partial {}^l p}{\partial t} \\ &= Q {}^l \dot{p} \\ &= Q J_{im} V \\ &= -G Q J_{im} E \end{aligned} \quad (18)$$

We use pseudo-inverse matrix of the image Jacobian J_{im} for Q to make $Q J_{im}$ positive and not to make an input extremely large, that is,

$$Q = J_{im}^+ = (J_{im}^T J_{im})^{-1} J_{im}^T \quad (19)$$

Therefore, the feedback command is given as

$$V = -G J_{im}^+ ({}^l p - {}^l p_d) \quad (20)$$

Fig. 3 shows a block diagram of the control scheme described by Eq. (20). Note that the feedback command u is sent to the robot controller and both the transformation of u to the desired velocity of each joint angle \dot{q}_d and its velocity servo are accomplished in the robot controller as show in Fig. 3.

Futhermore, as J_{im} is a $4n \times 6$ matrix and pseudo-inverse matrix J_{im}^+ is a $6 \times 4n$ matrix, a feedback command Eq. (20) of 6 degrees of freedom is obtained.

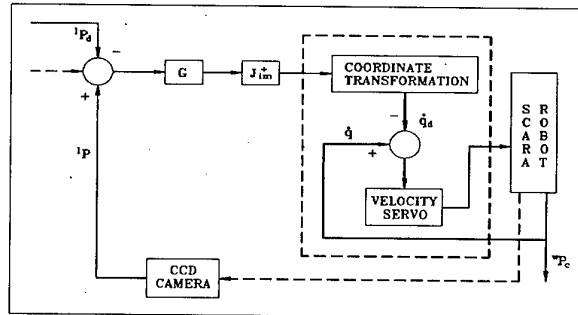


Fig. 3 Block diagram of visual feedback system.

4. Simulation and Experiments

4.1. Simulation

We have compared the visual servoing using the monocular vision with that using the stereo vision by the simulation. In the simulation, feature points of an object are the four corners of a square whose side dimension is 300 mm. In the same condition, we used four feature points even in the stereo vision. Parameters used the focal length, $f=16$ mm, baseline $d=130$ mm, sampling time of 50 msec, gain $\lambda=1$, desired location ${}^cP_d = (100\ 100\ 500)^T$ mm desired orientation in Euler angle $(\varphi, \theta, \psi) = (0, 0, 0)$ rad, initial error $(-50\ -50\ -50)^T$ mm in the translation and $(\varphi, \theta, \psi) = (20, 20, 20)$ rad in the orientation. error image. We select the four corners of a rectangle whose size is 200×200 mm as the feature points and set the translational error as $(-150\ -150\ -450)$ mm and the other values are the same as before (Fig. 4).

In Fig. 4, we can see that the result diverges in the case of the monocular vision, but converges in the case of the stereo vision. This is because the image Jacobian is fixed at the desired location in case of the monocular vision. Therefore, a correct feedback command can not be generated when the initial error is large. On the other hand, the image Jacobian can be updated at every in the case of the stereo vision, thus it is possible to generate a correct feedback command which assures the stability visual servoing.

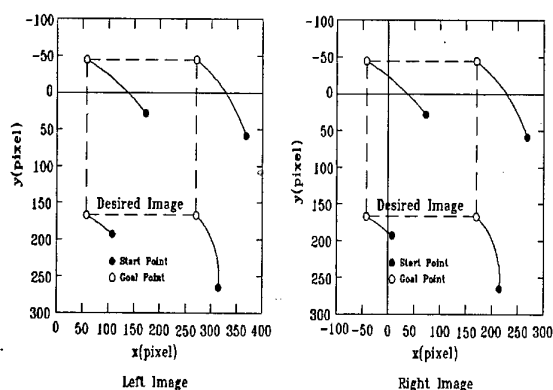


Fig. 4 Trajectories of the feature points on the images.

4.2. Experiments

In experiments, we used a four-axis SCARA Robot (SM5 Model) made in Korea with a stereo camera attached to the end tip of the arm. The feature points are three circular planes of 20 mm radius on three corners of an equilateral triangle, one side 87 mm and are placed on the board. Precise calibration had not been done for the stereo camera attached to the end-tips.

Two stereo images were taken and transformed to the binary images in the real time and in parallel by two image input devices and the coordinate of the gravitational center of each feature point was calculated in parallel by two transputers. We gave the stereo correspondence of the feature point in the first sampling. However, the stereo and temporal correspondence of the feature points in the succeeding sampling were found automatically by searching a nearby area where there were the feature points in the previous sampling frame. The coordinates of the feature points were sent to a transputer for motion control and it calculated a feedback command for the robot. The result was sent to the robot controller by using RS-232C, and the robot was controlled by a velocity servo system in the controller.

The sampling period of visual servoing was about 50 msec. Details were 16 msec for taking a stereo images, about 1 msec for calculating the coordinates of the feature points, 3 msec for calculating feedback command, about 16 msec for communicating with the robot controller. If we send a feedback input to the robot controller without using RS-232C, the faster visual servoing can be realized.

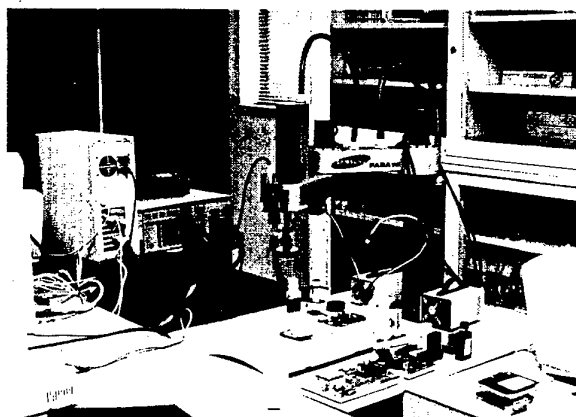


Fig. 5 The Experimental equipment set-up.

The desired location was $(0, 0, 500)^T$ mm and the desired orientation in Euler angle, $(\phi, \theta, \psi) = (0, 0, 0)$ degree and the initial error was $(50, 50, 50)^T$ mm for translation. The other parameters were the same as in the simulation. The error of current and desired location of the feature points are shown in Fig. 7. From these experimental results, we can see that the manipulator converges toward a desired location even if the calibration is not precise.

5. Conclusion

This paper proposes a new method of visual servoing with the stereo vision to control the position and orientation of a SCARA robot with respect to an object. The method overcomes the several problems associated with the visual servoing with the monocular vision. By using the stereo vision, the image Jacobian can be calculated at any position. So neither shape information nor desired distance of the target object is required. Also the stability of visual servoing is assured even when the initial error is very large. We have shown the effectiveness of this method by simulation and experiments.

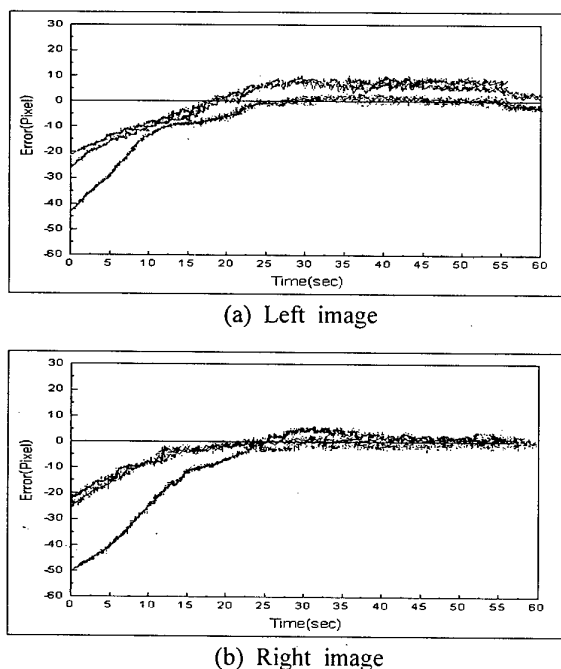


Fig. 6 Position Error in x and y axes.

To use this visual servoing in practical tasks, there still exist many problems such as the number of feature points to reduce noise or the quantization error and the way to choose feature points. Nevertheless, this method overcomes the several problems in visual servoing with the monocular vision.

References

- [1] Allen, P. K., Toshimi, B., Timcenko, A., "Real-Time Visual Servoing". In Proceeding of the IEEE International Conference on Robotics and Automation(1991), pp. 851-856.
- [2] Hashimoto, K., Kimoto, T., Edbine, T., and Kimura, H., "Manipulator control with image-based visual servo". In Proceedings of IEEE International Conference on Robotics and Automation(1991), pp. 2267-2272.
- [3] Chaumette, F., Rives, P., and Espiau, B., "Positioning of a robot with respect to an object, tracking it and estimating its velocity by visual servoing". In Proceedings of the IEEE International Conference on Robotics and Automation(1991), pp. 2248-2253.
- [4] Hashimoto, K., Edbine, T., and Kimura, H., "Dynamic visual feedback control for a hand-eye manipulator". In Proceedings of the IEEE/RSJ International Conference on Intelligent Robots and Systems(1992), pp. 1863-1868.
- [5] Bernard, E., Francois, C., and Patrick, R., "A new approach to visual servoing in robotics". IEEE Transactions on Robotics and Automation(1992), pp. 313-326.
- [6] Weiss, L. E., Sanderson, A. C., and Neuman, C. P., "Dynamic sensor-based control of robots with visual feedback". IEEE Journal of Robotics and Automation(1987), pp. 404-417.

Error Recovery of Autonomous Mobile Robot with Vision Based Navigation System

Yasunori Abe, Yoshio Tanaka and Shintaro Sakamoto
Shinryo Corporation
Toshio Fukuda, Fumihito Arai and Masaru Shikano
Nagoya University

Abstract

This paper proposes a new navigation system for an autonomous mobile robot. An earlier version of the robot navigated by recognizing a single landmark at a time. But, the landmark was often lost sight of, and as a result, the robot's self-position was lost. The authors propose a method that enables the robot to recover from such an error. The method determines the self-position by using information on the corner, windows and doors of the room simultaneously if the single landmark is lost.

1. Introduction

Autonomous mobile robot that has vision sensor is very useful in many industry fields. The good navigation method is to recognize the landmarks by the vision sensor to detect a self-location[1]. However, it was impossible that the robot recognizes the landmarks perfectly in the actual world for the various obstruction. Therefore, it is necessary that the robot can make recovery the error that the robot itself occurred in. It is very important that the robot detects the error, repairs the condition and prevents the recurrence of the error to make recovery. Therefore, authors propose the control architecture HALAS. In this paper, the Global Matching method that is located at the highest rank in the sensing behavior included into the HALAS is stated. The Global Matching is how to recognize its self-position, it does not depend on the landmark. When the landmark is lost sight of during the work, the Global Matching can navigate the robot to the set course by using the position information such as corner in the room, the doors, the windows, and the walls. The robot combines a wide-ranging recognition by the Global Matching and the local recognition by the landmark with the HALAS. Then, it can move with making recovery the error.

Wang proposed how to estimate the self-position at the indoor from the matching rate of the model and the edge screen gotten by the image processing[2]. However,

it is impossible to decide the self-position of the robot only using the result of the edge detection, because there are few geometrical characteristics in the big square room where the robot works easily. Tonaki proposed the method which the position was decided by using two laser luminous units[3]. This method can be expected precise measurement. But, the operator needs to work more because the measurement unit must be installed precisely every time. Furthermore, Ando[4] and Oriolo[5] proposed how to detect the self-position by using the ultrasonic sensor to measure distance from the wall. But, the measurement range of the ultrasonic sensor is so short that the method can not measure the distance directly in a large room. These techniques can not give full play to its ability regarding self-position measurement in the large office room. So, the authors propose this technique. It is stated about the algorithm, the position measurement precision and the result of the movement experiment in this paper.

2. Autonomous mobile robot

We have developed the robot that had the navigation system using the air diffusers as the landmarks and it was able to inspect the air flow rate and temperature[6]. The ceiling air diffuser is called Anemo and it is shown in Fig.1. The robot was equipped two CPUs and two CCD cameras. The robot consists of four submodules; the vision system, the vehicle system, the sensor system and the lift-up system. One CPU manages the vision system that recognizes the landmark and calculates the robot's position, and the other one manages the vehicle system, the sensor system and the lift-up system. The vision system has two CCD cameras. One is main CCD camera, and the other is small CCD camera. The main CCD camera, which is installed on a pan-tilt table, collects the image of an Anemo on the ceiling. This image is processed, and the robot calculates the distance to under the Anemo. The small CCD camera is installed for adjustment of self-location[7]. The robot moves according to the instruction that is transferred from the

vision system to the vehicle system. The vehicle system is composed of two driving wheels and two caster wheels. The driving wheels have two DC servo motors and the left wheel and the right wheel move independently. This robot is operated under point to point control of motion. The pattern of the robot motion is that it takes spin turns and faces in the direction of the Anemo, then it moves straight forwards until right under the Anemo and, finally it adjusts the position with the spin turn again. The lift-up system lifts the sensor system before measuring the rate of air flow. While the robot is moving, the hood is 500mm below the ceiling in order to avoid any obstacle. As the system changes to the measurement mode, the hood is lifted until the distance between the ceiling and the hood is in the range of 70mm to 200mm. Then the photoelectric switch turns on, and the lift-up speed slows down to avoid a shock when hitting the ceiling. As the hood touches the ceiling, the touch switch on the attachment hood is activated and the lift-up operation is ended. This whole process takes about 30 seconds. The robot does these measurements over again unless all measurements in same floor are finished. We show the autonomous mobile robot in Fig.2.

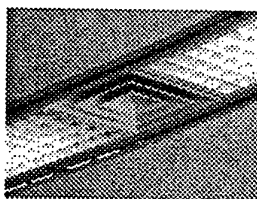


Fig.1 Anemo

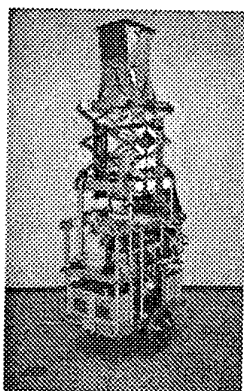


Fig.2 Autonomous mobile robot

3. Error recovery

The error of the autonomous robot is not the same as the trouble of the mere machine. It is the same kind of the error of human behavior based on the recognition.

There are these six kinds of errors; (1) Commission error, (2) Omission error, (3) Repetition error, (4) Imperfect, (5) Sequential error and (6) Extraneous act. In this research, we are going to deal with from (1) to (3). When the error recovery is carried out, three points of the following becomes important.

- (1) How does the robot discover the error ?
- (2) How does the robot restore the error ?
- (3) How does the robot prevent the recurrence of the error ?

The purpose of this research finds an answer in these problems.

4. HALAS

The authors propose HALAS (Hierarchical Adaptive and Learning Architecture System) as the control architecture of the navigation system of the autonomous mobile robot in consideration of the error recovery (Fig.2)[8]-[10]. The structure of the HALAS has the voluntary movement and the involuntary movement of vertebrate animal. The HALAS prevents the recurrence of the error by the voluntary movement. And the involuntary movement can discover the error and repair it. The involuntary movement consists of four action sets by the sensing level.

They are (1) Confident Action Set, (2) Discreet Action Set, (3) Reconsideration Action Set, and (4) Reconstruction Action Set.

The voluntary movement can choose the action set which is suitable for the error recovery by the reinforcement learning. The wind that the robot can get when it reaches an Anemo is being used as the reward of the reinforcement learning. Then the action set that has the highest evaluation function value is chosen at that time.

5. Global matching

The robot that lost sight of an Anemo gets lost the path it should go along. So, this robot does the Global Matching, and detects its position, and reverts in the course of the base. This Global Matching Method is one of the action sets including above mentioned (4) Reconstruction Action Set in HALAS. The Global Matching is the behavior that the robot can recognize the self-location absolutely by the coordinates system of the large room at the any positions. The self-location is shown in the two-

dimensional coordinates x and y , and the posture angle θ . In this research, the robot searches the position on the corner inside the room by the main camera. Then, the robot calculates its position with the corner.

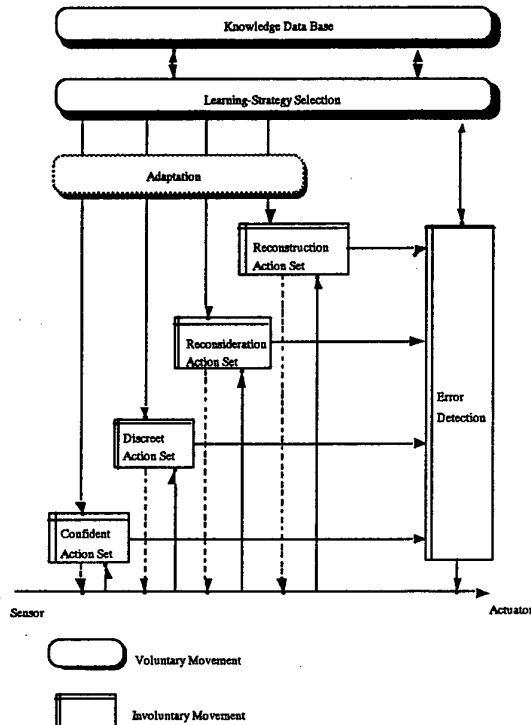


Fig.3 HALAS

5.1 Environmental condition

The environment that the Global Matching is done, and the precondition are explained here. The experimental environment was the room 26m by 11m is shown in Fig.4. This is the room that generally the air conditioning equipment inspection robot is used for. The robot has the design chart at this room. Therefore, the dimension of the room is known well. For example, the height of the ceiling, the position and size of the Anemo, the windows and the doors and so on are known well. The route of inspection was determined by human in advance. Furthermore, other environment conditions and preconditions in this technique are shown in the following.

- (1) The room is large rectangle office room and there are system lines where the Anemo and so on are arranged on the ceiling.
- (2) There is at least one wall side that there are not a pattern, a line, and a structure thing in the room. Then, there is at least one corner where the outline is clear and

it touches the wall. There can be window, door and so on in other walls.

- (3) The condition that it was lost sight of the self-location was as the following.

When the Anemo is not found even if the error recovery techniques included the involuntary movement were used. When the number of the Anemo was different from the map information.

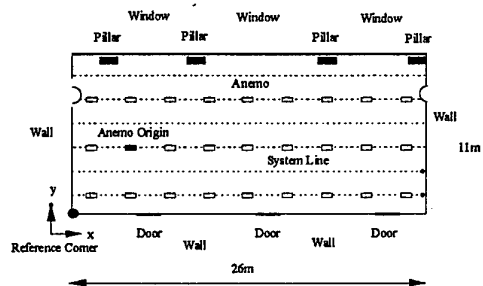


Fig.4 Experimental room

5.2. Orientation modification

To begin with this process, the robot turns to the wall for the corner detection. The robot detects the self-posture angle θ by using the system line on the ceiling. Then, the robot faces in the system line, and it makes the posture parallel to the system line. The process of the orientation modification is as the following. The robot takes pictures of the top by using the small camera which is set upright. Then, it confirms whether a system line exists. It is known from the past experiment that the small camera can find out the goal object if it is inside the range in every direction 300mm from the center of the robot. But, when the robot judges that a system line does not exist in this range because a straight line is not extracted as a result of the image processing, it looks up at the ceiling with the other vision sensor, the main camera which is set on the pan-tilt table. Then, it does the search of a system line again turning the table. After that, the robot calculates the distance to the system line and the direction, and it moves to right under the system line. The robot detects the angle of the posture of the system line with the small camera after the arrival, and it rotates to become parallel in the system line.

Then, the authors did the posture compensation experiment of the robot, and confirmed the error of posture matching. The initial position of the robot in this experiment was divided into two cases. One is Case (a) Right under the system line, the other one is Case (b) Between the system line and the system line. Then, each initial posture it was inclined to 0° , 45° and 90° . Then, the robot paralleled the system line from these position and postures. The result is shown in Table 1.

The orientation modification movement could be finally completed in less than $\pm 1^\circ$.

Table 1 Results of Orientation Modification (degree)

Case (a) Result		Case (b) Result	
Initial Small Camera	Main Camera	Small Camera	
0	-0.7	5.3	0.4
45	0.6	7.7	-0.1
90	0.5	6.6	-0.1

5.3 Corner Detection

The robot detects the corner to calculate its position expressed by x, y coordinates. The robot can use the corner of the ceiling side and the wall or the corner of the floor side and the wall. The corner of the ceiling side was used by this research. The images taken by the main camera for the corner detection treatment are shown in order by Fig.5. This method is explained concretely in the following. As the authors explained so far, the robot faces to the wall that a pattern is not in. First, the robot controls the pan-tilt table and the zooming of the lens to make the main camera face to the wall straightly at this position, Fig.5(a). The histogram that image pixel was projected on the Y axis is made in the taken image at this time. This histogram shows the straight line that crosses the inside of the screen horizontally. The straight line which was done like is the boundary line of the wall and the ceiling side. Next, the robot controls the pan angle of the main camera so that this straight line comes in the center of the screen, Fig.5(b). Thirdly, the robot extracts the boundary line that crosses the center of the screen by Hough change. Then, it calculates the center of gravity and adjusts the pan-tilt table so that the center of gravity comes in the center of the screen of the Fig.5(c). Fourthly, the robot detects the left end point of this straight line in this image. Then, it chases the line in the left with controlling pan-tilt table so that the end point becoming in the center of the camera again, Fig.5(d). This operation is repeated. Fifthly, the robot recognizes the straight terminal. The movement of the camera is to stop when the left end point on the boundary line comes in the center of the image, Fig.5(e). Finally, the robot confirms that there is a straight line that extends in the vertical bottom from this end point. This shows the boundary line of the wall and the wall. The angle of the pan and tilt are the directions of the corner seen from the robot.

Then, the coordinate of the corner is shown by the equations (1) and (2) in the coordinates system of Fig.6.

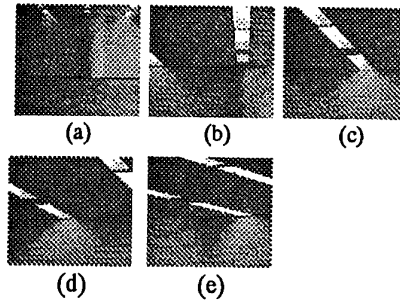


Fig.5 Image of Corner Detection

x_c, y_c : The x, y coordinate of the corner in the room

x_r, y_r : The x, y coordinate of the robot in the room

θ_r : The posture of the robot in the room

θ_t, ϕ_t : The pan and tilt angle of the camera

x_i, y_i : The x, y coordinate of the corner in the image

f : The focal distance

x_v, y_v, z_v : The x, y, z coordinate of the view point

$$x_c = \frac{x_v - \cos\left(\theta_r + \theta_t - \tan^{-1} \frac{x_i}{f}\right)}{\tan\left(\tan^{-1} \frac{y_i}{f} + \phi_t\right)} (z_c - z_v) \quad (1)$$

$$y_c = \frac{y_v - \sin\left(\theta_r + \theta_t - \tan^{-1} \frac{x_i}{f}\right)}{\tan\left(\tan^{-1} \frac{y_i}{f} + \phi_t\right)} (z_c - z_v) \quad (2)$$

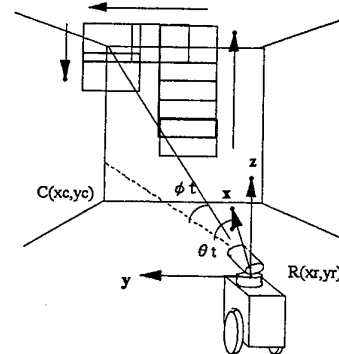


Fig.6 Coordinates System of Corner Detection

5.4 Evaluation of Position Error

When the self-location measurement is done by using this technique, five of the next are thought as factors of the error.

- (a) Inclination toward the vertical angle
- (b) The orientation modification error of the robot
- (c) The error of the corner detection by the image processing
- (d) The control error of the pan-tilt table of the main camera
- (e) Architectural error

The influence which the error of (a) - (d) gives to the self-position measuring was thought and the result of (a) is shown as a representative. It is shown in the maximum error circle of the self-position detection in each position inside the room in Fig.7. But, the error circles change magnification, and it is expanded to put emphasis on the result. The data shows the diameter of the maximum error circle. The corner in the coordinate origin (0,0) was detected, and the self-position was computed with the robot in each position.

The purpose of the Global Matching is that it makes the robot revert in the movement course when the robot deviated the course because an Anemo was lost sight of once. Therefore, the robot should have moved from the point where the corner detection had been done to the nearest Anemo that was in the course. However, as for the self-position measuring value, it was found out that it had the big error in the far point from the corner as a result of the error analysis. Therefore, there is area where the robot can not reach the nearby Anemo directly, when the robot measures the position by only the corner detection. So, the robot moves once to the range that the precision of position measuring by the corner detection is within $\pm 300\text{mm}$. Then, it does the self-position measuring again at the point. The Anemo to approach at this time is called an Anemo Origin, and the robot reverts from this Anemo Origin to the movement course.

The robot was put on the same places where the error analysis was done on the actual office floor. Then, the self-position measuring was done at the 12 places. The results are shown as the maximum error circles in Fig.8. The experimental results showed the tendency which was the same as the error analysis. The error became as big as a distance from the corner was far.

From these results, it becomes clear that an Anemo Origin should be a (5000, 5000) neighborhood Anemo.

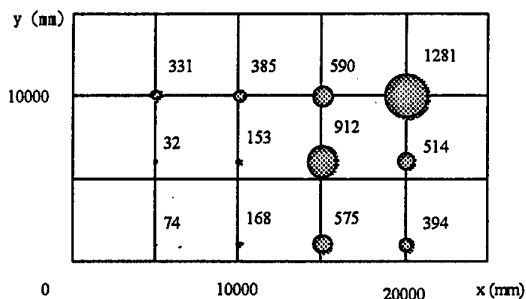


Fig.7 Error caused by Inclination of Robot

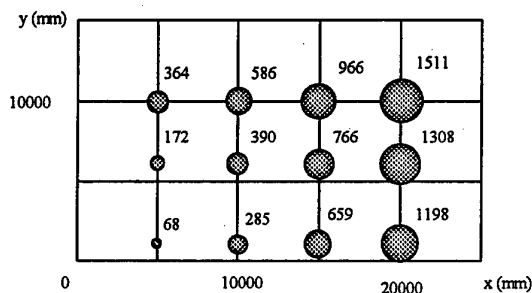


Fig.8 Experimental Result

5.5 Topological Matching

The coordinate of the robot based on the corner was calculated, and then the robot was moved to the Anemo Origin. However, it has not been confirmed yet if the robot was moved to the Anemo Origin or in the reverse direction. So, the robot does a final decision on the self-position by this technique. If the robot is in the position of Fig.9 (a), it can decide the self-position using the map information that describes where the door and windows are. But, the door and the windows shown in the map can not be discovered if the robot faces an opposition direction in Fig.9 (b). Therefore, modification on the position is necessary. The existence of the window and the door is judged by histogram on the edge in the vertical direction in the image. The robot recognized the window, door and wall.

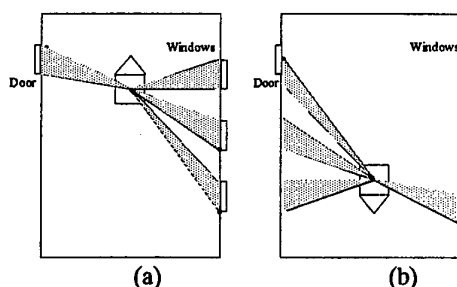


Fig.9 Topological Matching

6. Locomotive experiment

The proposed technique was applicable to this robot, and the error recovery movement experiments to revert to the Anemo Origin from four positions were done. The movement path at that time is shown in Fig.10. The robot was moved first with Case 1 and Case 2 in the y direction. This shows that the robot moved under the system line during the orientation modification was done. It had the self-position measurement error of 246mm with Case 2 by the first Global Matching movement after the orientation modification was done. The robot moved to the Anemo Origin (4400, 4480) based on this value. But, it gained the error of the dead reckoning. The error therefore to arrive was 1435mm. But, because it could approach the corner enough, the robot reduced the error by 1177mm by the 2nd Global Matching. When the robot came to this area, the Anemo Origin could be caught in the small camera, and the position error could be finally under 20mm.

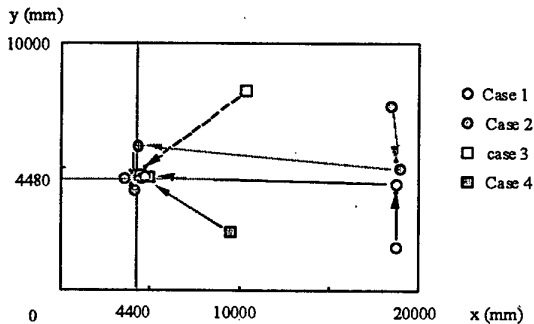


Fig.10 Trajectory of Global Matching

7. Conclusion

It was proposed how to recognize the self-position by the Global Matching that did not depend on the landmark, Anemo. And it was an error recovery method when an Anemo was lost sight of. After the robot did the orientation modification first and faced in the wall, the boundary line of the wall and the ceiling side was extracted. Then, the robot found the end of this straight line, and confirmed that there was other straight line that extended in the vertical bottom. This was confirmed as a corner and the self-position was calculated with the corner. It was confirmed that the robot could revert to the Anemo Origin set up around the neighborhood (5000,5000) of the coordinates of the corner as a result of the experiment. Even if an Anemo was lost sight of during the work and the robot deviated from the course,

it was shown by this technique that the robot could revert in the movement course from the Anemo Origin.

References

- [1] C. Becker et al., "Reliable Navigation Using Landmarks", Proceedings of the IEEE International Conference on Robotics and Automation, Vol.1, pp. 401-406 (1995)
- [2] Ling-Ling Wang, et al., "Model-based guidance by the longest common subsequence algorithm for indoor autonomous vehicle navigation using computer vision", Automation in Construction, vol.2, pp.123-137 (1993)
- [3] S. Tonaki, et al., "Communication of Realtime Two-dimensional Position Data with Scanning Beam", Proceedings of the 13th International Symposium on Automation and Robotics in Construction, pp.555-560 (1996)
- [4] Y. Ando, et al., "Following a Wall by an Autonomous Mobile Robot with a Sonar-Ring", Proceedings of the IEEE International Conference on Robotics and Automation, vol.3, pp.2599-2606 (1995)
- [5] G. Oriolo, et al., "On-Line Map Building and Navigation for Autonomous Mobile Robots", Proceedings of IEEE International Conference on Robotics and Automation Vol.3, pp.2900-2906 (1995)
- [6] Y. Abe, K. Tanaka, Y. Tanaka, T. Fukuda, F. Arai and S. Ito, "Development of Air Conditioning Equipment Inspection Robot with Vision Based Navigation System", Proceedings of The 11th International Symposium on Automation and robotics in Construction, pp.665-674 (1994)
- [7] Yasunori Abe, Toshio Fukuda, Kouetsu Tanaka, Yoshio Tanaka, Fumihito Arai, Koji Shimojima, Shigenori Ito "Navigation System for Air Conditioning Equipment Inspection Robot", Journal of Robotics and Mechatronics, Vol.7, No.5, pp.354-366 (1995)
- [8] Toshio Fukuda, Yasunari Yokoyama, Fumihito Arai, Koji Shimojima, Shigenori Ito, Yasunori Abe, Kouetsu Tanaka, Yoshio Tanaka, "Navigation System Based on Ceiling Landmark Recognition for Autonomous Mobile Robot - Position / Orientation Control by Landmark Recognition with Plus and Minus Primitives -", Proceedings of the 1996 IEEE International Conference on Robotics and Automation, Vol.2, pp.1720-1725(1996)
- [9] Yasunori Abe, Toshio Fukuda, Fumihito Arai, Yasunari Yokoyama, Yoshio Tanaka "Vision Based Navigation System Considering Error Recovery for Autonomous Mobile Robot", Proceedings of the 1997 IEEE International Conference on Robotics and Automation, Vol.3, pp.1993-1998 (1997)
- [10] Yasunori Abe, Masaru Shikano, Toshio Fukuda, Fumihito Arai and Yoshio Tanaka "Variable Template Matching for Autonomous Mobile Robot with Hierarchical Control System", Proceedings of The 5th International Conference on Intelligent Autonomous Systems, pp.368-375, (1998)

Mechatronics in Agriculture - Robust Recognition of Plant Rows

B. Åstrand and A.J. Baerveldt

Centre for Computer Systems Architecture, Halmstad University

Box 823 S-301 18 Halmstad, Sweden

E-mail: bjorn.astrand@cca.hh.se, Albert-Jan.Baerveldt@cca.hh.se

Abstract

In the future, mobile robots will most probably navigate through the fields autonomously to perform different kind of agricultural operations. As most crops are cultivated in rows, an important step towards this long-term goal is the development of a row-recognition system, which will allow a robot to accurately follow a row of plants. In this paper we describe a new method for robust recognition of plant rows based on the Hough transform. Our method adapts to the size of plants, is able to fuse information coming from two rows or more and is very robust against the presence of many weeds. The accuracy of the position estimation relative to the row proved to be good with an error variance between 0.6 and 1.2 cm depending on the plant size. Extensive field tests also showed that the system is sufficiently fast, about 10 images per second, to be used in a closed-loop control system.

1. Introduction

Increasing cost of chemicals and the soil pollution caused by the herbicide residues ask for alternative methods of crop protection. A potential way of reduction of chemicals is the use of precision techniques for various types of agricultural operations, so that the chemicals can be placed where they have an optimal effect with minimum quantity. For some operations it will even be possible to abandon the use of chemicals and apply other methods, e.g. mechanical weed-control. Our vision is that in the future, autonomous mobile robots will navigate through the fields to perform these operations. As most crops are cultivated in rows, an important step towards this long-term goal is the development of a row-recognition system, which will allow a robot to accurately follow a row of plants.

To derive guidance information from planting structures has been investigated by others. Marchant [1] and Marchant and Brivot [2] perform several steps of image processing based on near-infrared images to

discriminate weeds from plants. They calculate the center of each object in the image and use a Hough transform to calculate the offset and orientation relative to the row structures. They combine information coming from three row segments to increase performance.

Billingsley and Schoenfish [3] use the chrominance signal from a colour camera to acquire an image based on the "greenness" in the image. To threshold the image they use an adaptive method based on the expected plant material in the image. To find line structures they used linear regression based on information from three row segments to find the best fit. Slaughter, Chen and Curley [4] use a Bayesian classifier based on information from a color camera to discriminate weed from plants. The camera was centered above the row and they sum up all pixels in every column thus forming a histogram of the row structure. They use the median value of the histogram to estimate the position of the row.

Common for the above described methods is that they work for larger plants (>5 cm in diameter) or small plants with low weed density (3 weed/plant). In our case the system must be able to work even when the size of the plants and weeds are the same and the weed-density is high (>3 weed/plant). In this paper we present a new robust image-processing algorithm to detect the position of a row of plants. Our method is able to adapt to the size of the plants and is not disturbed by the presence of many weeds.

2. Row-recognition system

A problem for the development of a row recognition system is the fact that there might be a lot of weed which disturbs the appearance of a nice clear row structure of green plant material coming from the crops. One approach is to first classify every plant as crop or weed and then find a row structure based on the crops only. Another approach is to consider weed as noise and to find a row structure based on both crops and weeds. We use the last described method and to get a good signal to noise ratio, which means the ability to handle large weed pressure, we

look at a row segment of about four meter long. To be able to deal with missing crops in the rows and to increase robustness and accuracy we look at two rows at the same time.

We use a gray-scale camera with a near-infrared filter to detect plants. Using the filter gives a high-contrast image, where living plant material is bright and the soil is dark [5]. However due to disturbances, in form of different light conditions and due to the fact that all white pixels do not correspond to crops, some additional image-processing has to be done.

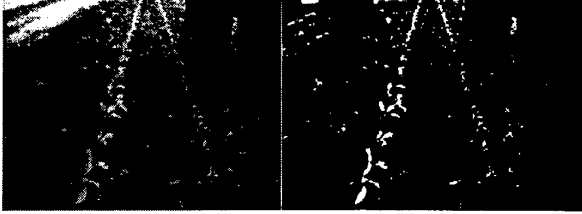


Figure 1. Original and threshold image

To decrease the effect of different light conditions we perform an opening operation on the image [7] and subtract the result from the original image. This results in an intensity-independent gray-level image from which a binary image can be derived with a fixed threshold. In the resulting binary image, plant material from both weeds and crops is white and the rest, coming from soil, stones and residues is black (figure 1).

$$\text{Image}_{\text{intensity}} = \text{Image}_{\text{opening}} - \text{Image}_{\text{original}} \quad (1)$$

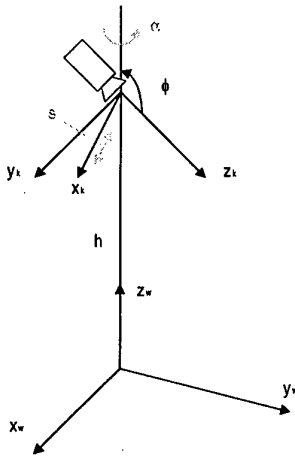


Figure 2. World-Camera Coordinate System

2.1 Geometric model

Based on the binary image the next step is to detect the row of crops in the image. To control for example a mobile robot or other tool, we must know the offset and the heading angle of the camera relative to the row structure. To be able to extract this information from the image we must have a geometric model of the row structures and know the transformations between the world coordinate system and the image coordinate system. To start with we assume that a line can approximate the row of crops. The world coordinates of the row can first be transformed to camera coordinates and finally to image coordinates through a perspective transformation. Figure 2 shows the geometry of the world and camera coordinate system. The heading angle, α , and the offset, s , are the unknown parameters which need to be found. It is assumed that the field can be approximated by a plane and the world coordinate system is chosen in such a way that this plane can be described as $z_w = 0$ and that the rows are lying in parallel with the y_w -axis. The camera angle, ϕ , and its height above the ground, h , are fixed.

The transformation from a position expressed in the camera coordinate system k to a position expressed in the world coordinate system w is in general [6]:

$$\begin{bmatrix} x \\ y \\ z \end{bmatrix}^w = [R]_k^w \begin{bmatrix} x \\ y \\ z \end{bmatrix}^k + \begin{bmatrix} t_x \\ t_y \\ t_z \end{bmatrix}_{k_{ORG}}^w \quad (2)$$

Where R is the rotation-matrix between world coordinate and the camera coordinate system. In our case R is a function of ϕ and α :

$$[R]_k^w = \begin{bmatrix} \cos(\alpha) & -\sin(\alpha)\cos(\phi) & \sin(\alpha)\sin(\phi) \\ \sin(\alpha) & \cos(\alpha)\cos(\phi) & -\cos(\alpha)\sin(\phi) \\ 0 & \sin(\phi) & \cos(\phi) \end{bmatrix} \quad (3)$$

In our case the translation-vector is a function of α , s and h :

$$\begin{aligned} t_z &= h \\ t_x &= s \cdot \cos(\alpha) \\ t_y &= s \cdot \sin(\alpha) \end{aligned} \quad (4)$$

The inverse transformation is:

$$\begin{bmatrix} x \\ y \\ z \end{bmatrix}^k = [R]_w^k \begin{bmatrix} x \\ y \\ z \end{bmatrix}^w + [t]_{w_{ORG}}^k \quad (5)$$

where:

$$[R]_w^k = [R]_k^w \text{ and } [t]_{w_{ORG}}^k = -[R]_w^k [t]_{k_{ORG}}^w \quad (6)$$

which gives:

$$\begin{bmatrix} x \\ y \\ z \end{bmatrix}^k = \begin{bmatrix} \cos(\alpha) & \sin(\alpha) & 0 \\ -\cos(\phi)\sin(\alpha) & \cos(\alpha)\cos(\phi) & \sin(\phi) \\ \sin(\alpha)\sin(\phi) & -\cos(\alpha)\sin(\phi) & \cos(\phi) \end{bmatrix} \begin{bmatrix} x \\ y \\ z \end{bmatrix}^w + \begin{bmatrix} -s \\ -h\sin(\phi) \\ -h\cos(\phi) \end{bmatrix} \quad (7)$$

As said before, the row structure can be regarded as a line lying in the plane $z_w = 0$, which gives us the three following equations from (7):

$$\begin{aligned} x_k &= \cos(\alpha)x_w + \sin(\alpha)y_w - s \\ y_k &= -\cos(\phi)\sin(\alpha)x_w + \cos(\alpha)\cos(\phi)y_w - h\sin(\phi) \\ z_k &= \sin(\alpha)\sin(\phi)x_w - \cos(\alpha)\sin(\phi)y_w - h\cos(\phi) \end{aligned} \quad (8)$$

The camera can be simply modeled as a pinhole camera where f is the so-called focal length [7]. The x_i, y_i coordinate system is the image-sensor coordinate system of which the axis are parallel to x_k and y_k respectively.

$$x_i = -f \cdot \frac{x_k}{z_k} \quad y_i = -f \cdot \frac{y_k}{z_k} \quad (9)$$

Equations 8 and 9 together give:

$$x_i = -f \frac{\cos(\alpha)x_w + \sin(\alpha)y_w - s}{\sin(\alpha)\sin(\phi)x_w - \cos(\alpha)\sin(\phi)y_w - h\cos(\phi)} \quad (10)$$

$$y_i = -f \frac{-\cos(\phi)\sin(\alpha)x_w + \cos(\alpha)\cos(\phi)y_w - h\sin(\phi)}{\sin(\alpha)\sin(\phi)x_w - \cos(\alpha)\sin(\phi)y_w - h\cos(\phi)} \quad (11)$$

Given a known position in the field described as x_w, y_w equation 10 and 11 give the position in the image described as x_i, y_i assuming we know the position and orientation of the camera described by α, s, h, ϕ . In our case we know that every pixel belonging to a plant row has a certain fixed position x_w which depends on the row distance but generally we do not know the value y_w . Therefore we eliminate y_w from equation 10 and 11 which gives:

$$\begin{aligned} s \cdot \cos(\alpha) \cdot (-f \cos(\phi) + y_i \sin(\phi)) &= \\ -fx_w \cos(\phi) + hx_i \cos(\alpha) - hy_i \cos(\phi) \sin(\alpha) & \\ + x_w y_i \sin(\phi) - fh \sin(\alpha) \sin(\phi) & \end{aligned} \quad (12)$$

For small values of α we can simplify the equation by

assuming that:

$$\sin(\alpha) = \alpha \text{ and } \cos(\alpha) = 1. \quad (13)$$

which gives:

$$\begin{aligned} a(-hy_i \cos(\phi) - fh \sin(\phi)) + s(f \cos(\phi) - y_i \sin(\phi)) \\ - x_w(f \cos(\phi) - y_i \sin(\phi)) + hx_i = 0 \end{aligned} \quad (14)$$

This can also be written as:

$$A\alpha + Bs + C = 0 \quad (15)$$

where: $A = (-hy_i \cos(\phi) - fh \sin(\phi))$

$$B = (f \cos(\phi) - y_i \sin(\phi))$$

$$C = -x_w B + hx_i$$

Finally, a straightforward transformation from image-sensor coordinates to image-pixel coordinates is needed:

$$x_i = -(x_p - x_c) \text{dpixelx}, \quad y_i = -(y_p - y_c) \text{dpixely} \quad (16)$$

Where dpixelx and dpixely is the size of the sensor elements in the x- and y- direction of the CCD-array. x_c and y_c are the coordinates of the optical center of the camera in pixels and set to half the size of the image.

This gives the following equation:

$$x_p = \frac{A}{h \cdot \text{dpixelx}} \cdot \alpha + \frac{B}{h \cdot \text{dpixelx}} \cdot s - \frac{B}{h \cdot \text{dpixelx}} \cdot x_w + x_c \quad (17)$$

This equation plays a central role to find the heading angle, α , and the offset, s , which is described in the next section. Please note that x_w is known as it is the position of the row in world coordinates.

2.2 Finding row-structures

The Hough transform is a well-known and robust method to find lines, especially if the lines cover the whole image as in our case [7]. Normally the lines are found with their equation in the image space e.g. $y_p = ax_p + b$, where the coefficients a and b are found with the Hough transform. We could also do this based on the binary image of plant material. All pixels coming from the crops contribute to the line and all pixels from the weeds are just noise. By using equation 17 for two points on this line we are able to calculate the heading angle, α , and the offset, s .

However, as shown in equation 17, there is a linear

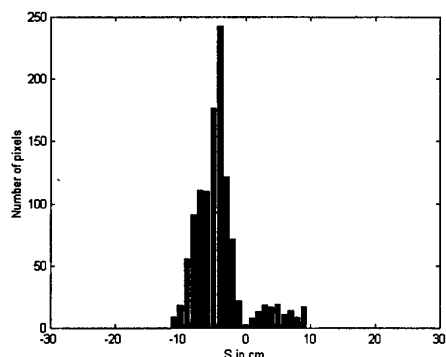


Figure 3. Distribution of s for a specific α

relation between s and α for a given pixel (x_p, y_p). This means that we directly can perform the Hough transform for s and α based on equation 17.

The Houghspace, $H(s, \alpha)$, is then an accumulator where each pixel coordinate (x_p, y_p) in the binary image, which is on, contributes even if it is belonging to a weed plant. The recognition of the row of crops among the weeds is achieved due the fact that weeds are uniformly distributed in the field, whereas all the crops grow exactly in a row, thus leading to a peak in the Houghspace.

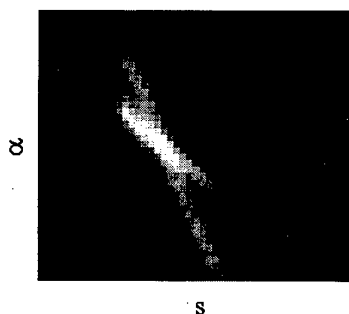


Figure 4. Houghspace accumulator

In the world model a plant row can better be described by a rectangular box rather than a line. The width of the box is equal to the average width of the plants and the length of the box is "unlimited" as it fills the whole image. The rectangular box can be described by a set of parallel adjacent lines. The number of lines is the width of the box divided by the line thickness, which is determined by the pixel size of the image. In our Houghspace this means that for one value of α the rectangular box corresponds to a number of adjacent s -cells. By summing up the contributions of the adjacent s -cells we obtain the support for a rectangular box, i.e. for the row of plants. The best estimate of s and α is found by searching for the maximum of the sum of adjacent s -cells in our

Houghspace. We can easily adapt to different size of the plants, by reducing or increasing the number of adjacent s -cells.

Figure 4 shows an example of the Houghspace and figure 3 shows the corresponding distribution of s for the correct value of α . In this example we look at the sum of three adjacent s -cells to find the most likely values of s and α .

If more than one row is used each row has then its own corresponding Houghspace. Information from the different rows can be fused together by calculating the average of s and α derived from the individual Houghspaces. Another possibility is to sum up the contributions from all Houghspaces for each cell (s, α), thus forming a common Houghspace and extract the most likely value of s and α from this one. The resolution of the Houghspace, i.e. the size of the cell (s, α) must be chosen carefully, where the resolution of the camera plays a major role. Figure 5 shows the sensitivity of s and α as function of the top and bottom pixels. The top pixel is the x -pixel coordinate of the row at the top of the image, and the bottom pixel is the x -pixel coordinate at the bottom. The size of s and α are chosen so that this corresponds to at least one pixel difference. In our case the resolution of s was set to 1 cm and of the heading angle, α , to 0.2 degrees.

3. Evaluation of the row-recognition system

The row recognition system was implemented on an industrial PC, equipped with a Pentium II 333 MHz processor and a Matrox Meteor II framegrabber. The vision system is a COHU CCD camera equipped with a near-infrared filter and a lens with 8.5 mm focal length. The camera was placed about 800mm above the ground and the camera angle was 68°. This means that we look at a segment of the rows from 1 to 5 meter in front of the camera.

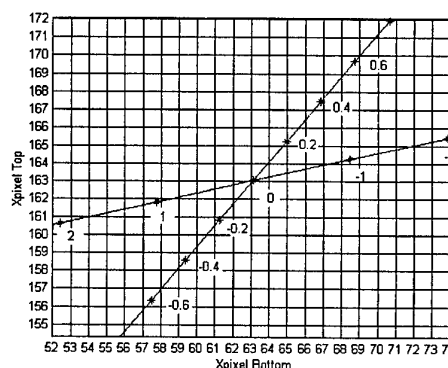


Figure 5. Resolution in image

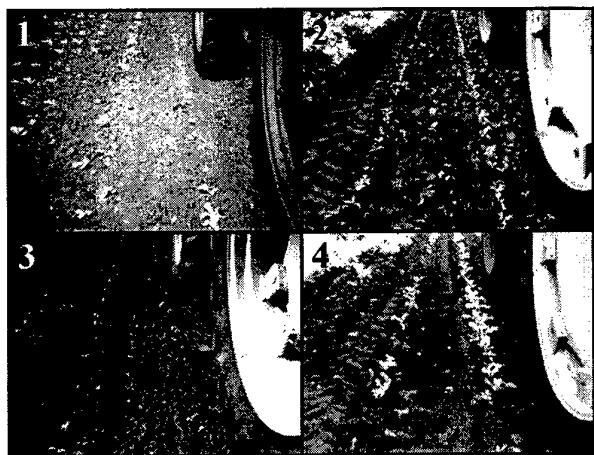


Figure 6. Four sets of real images

To evaluate the row-recognition system a number of real images were used to verify the system. Three sets of images from sugar-beet plants at three different stage of growth were included. Also one set of images from a rape field was used. From each set of images a subset of 70 spatially distributed images was chosen. The most relevant properties of each set are given in table 1 and one example image of each set is shown in figure 6. Ten of the images were used to calibrate the camera angle, ϕ , and the camera height above the ground, h . The number of adjacent s-cells was set to a value smaller than the plant size. Simulations have shown that the best performance is achieved when the number of adjacent s-cells is set smaller than the plant diameter. The opening kernel was also adjusted based on the plant size. We look at two rows simultaneously to increase the performance and robustness against missing crops, outliers and high weed densities (>3 weed/plant).

Table 1. Four sets of real-images

Set	Stage	ϕ cm	$\frac{\text{Weed}}{\text{Plant}}$
1	first true leaf (rape)	7-10	1
2	first-second true leaf	7	3.5
3	cotyledon	5	< 1
4	second true leaf	10-13	< 1

For all images the real position of the camera relative to the rows was estimated as follows. A human-operator marked the rows with a mouse based on which the estimation of the real heading α and offset s could be calculated. All images were treated twice and the average value from the two observations was taken as the final estimate of the real values and used to evaluate the performance of the row recognition system. As we look at two rows simultaneously, a left and right one, each row

has its own corresponding Houghspace, leading to two different observations for s and α . The Houghspaces of the left and right row are also fused together in a common Houghspace by summing up the entry of each corresponding cell. In table 2 the variance of the error of the measured offset s based on the left and right row separately, and based on the common Houghspace are shown. Another method to combine the result from the two rows is to take the average result from the left and right row. The result of this is also shown in table 2. Based on the result reported in table 2 we may conclude that the row-recognition system has a good performance ranging from 0.6 cm variance of error for set 2 to 1.2 cm for set 1. Moreover, it is shown that by using two rows instead of one the accuracy is improved significantly. Finally, it seems that fusion of the information from the two rows should be done in the Houghspace directly rather than by averaging the final results, as this leads to slightly less error variance.

To evaluate the robustness against calibration errors, errors of the values of the camera height and camera angle were introduced. To evaluate the robustness in plant size variations, the number of adjacent s-cells has been varied. The results are presented in form of extreme errors of s , shown in figure 7-9, and of the variance of the error of s in figure 10-12. All these results are based on the output from the common Houghspace. From the figures we may conclude that the system shows a satisfying robustness against calibration errors and that the number of adjacent s-cells must be chosen rather small compared to the expected plant size as a to large number of adjacent s-cell result in a poor performance.

Table 2. Variance of error of S in cm

Set	S_{right}	S_{left}	S_{common}	$\frac{S_{\text{right}} + S_{\text{left}}}{2}$
1	1.6	2.3	1.2	1.4
2	1.0	0.8	0.6	0.7
3	1.1	1.4	0.9	0.9
4	1.0	1.4	0.8	0.9

4. Field tests

The row-recognition system has been tested on a so-called inter-row cultivator, able to perform mechanical weed control between rows of plants. The system consists of a tractor that drives along the rows with the cultivator mounted at the rear of the tractor. The accuracy of the driver is not sufficient to come close to the plant rows. So a row-recognition system is desired which is able to guide the cultivator closer to the plants without damaging them. A steering-unit based on a very thin steering wheel, which

cuts through the soil, is used to control the position of the cultivator. A regulator has been implemented which gets its position feed-back from our row-recognition system and gives a control signal to the steering-unit.

The system was tested on two types of crops: sugar beet plants and rape. The row distance was typically 48 cm and the distance between the plants in the row was about 12 cm for the sugar beet plants and 15 cm for the rape. The weed density varied from field to field and could reach a level up to 12 weed/plants.

A number of field tests have been done to verify the row-recognition system, including tests under different light conditions, weed density and size of plants. The system was able to process 8-12 images/s (depending on plant size and weed density) and to cultivate at a speed of 2 km/h. The cultivator, cultivating several rows simultaneously, had a spacing left between the tools of 9 cm for the crops. As no crops were damaged, we may conclude that we were able to control the cultivator within ± 4.5 cm. These results confirm very well the results from the evaluation described in section 3, where the extreme errors were +3 and -4 cm (figure 8).

5. Conclusions and Outlook

In this paper we have presented a new method for the recognition of plant rows. The system proved to be able to effectively fuse information coming from two rows, and proved to be robust against calibration errors and to be robust against high weed densities. The accuracy of the position estimation relative to the row proved to be good with an error variance between 0.6 and 1.2 cm depending on the plant size and with a maximum error of ± 4 cm. Extensive field tests also showed that the system is sufficiently fast, about 10 images per second, to be used in a closed-loop control system. In future work we will develop an automatic calibration procedure and an end of row detection function. Moreover we plan to use the row-recognition system to guide a mobile robot through the field.

6. References

- [1] Marchant, J.A, "Tracking of Row Structure in Three Crops Using Image Analysis", *Computer and Electronics in Agriculture, Elsevier*, 1996(15), pp. 161-179.
- [2] Marchant, J.A, and R. Brivot, "Real-Time Tracking of Plant Rows Using a Hough Transform", *Real-Time Imaging , Academic Press Limited*, 1995(1), pp. 363-371.
- [3] Billingsley, J, and M. Schoenfisch, "Vision-Guidance of Agricultural Vehicles", *Autonomous Robots, Kluwer Academic Publishers*, Boston, 1995(2), pp. 65-76.
- [4] Slaughter, D.C, P. Chen and R.G. Curley, "Computer Vision Guidance System for Precision Cultivation", *ASAE Meeting Presentation*, Minneapolis, Minnesota, August 10-14, 1997.
- [5] Baerveldt, A.J, "Vision-Guided Mechanical Weed-Control", *The 2nd International Workshop on Mechatronical Computer Systems for Perception and Action (MCPA'97)*, Pisa, Italy, February 10-12, 1997, pp. 135-138.
- [6] Craig, J.J., *Introduction to Robotics Mechanics and Control*, Addison-Wesley Publishing Company Inc., 1989.
- [7] Shapiro, L.G., and R.M Haralick, *Computer and robot vision volume I and II*, Addison-Wesley Publishing Company Inc., 1992-1993.

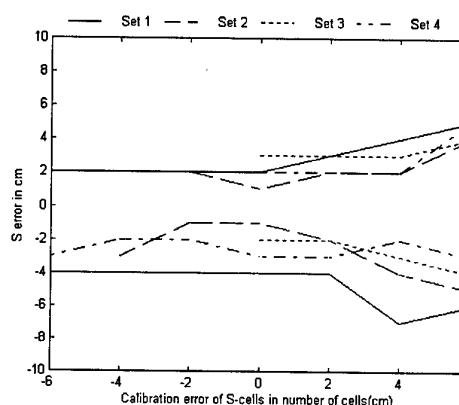


Figure 7. Error of s-cells in cm

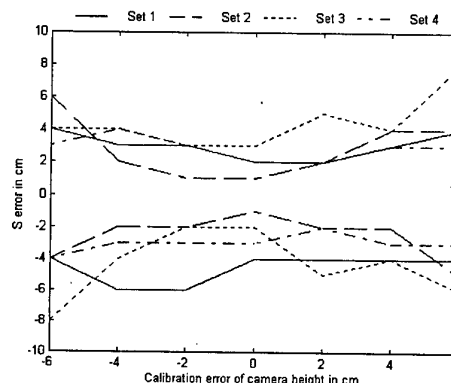


Figure 8. Error of height in cm

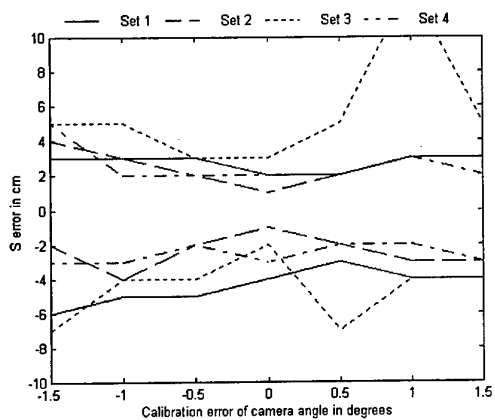


Figure 9. Error of camera angle in degrees

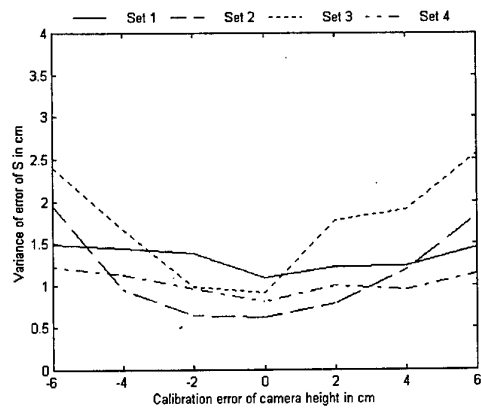


Figure 11. Error of camera height in cm (variance)

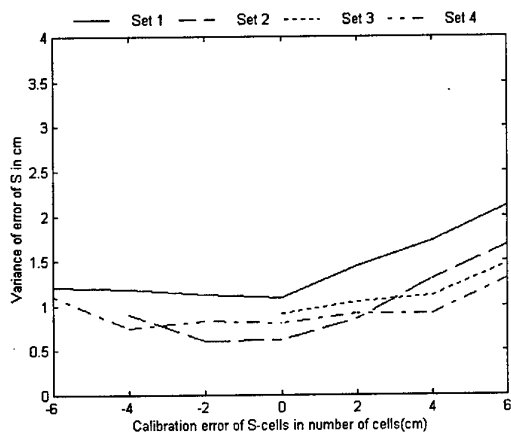


Figure 10. Error of s-cells in cm (variance)

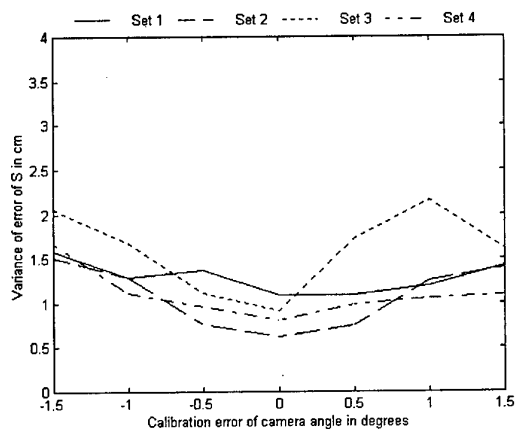


Figure 12. Error of camera angle in cm(variance)

Adaptive Trajectory Tracking Control for Robot Arms with Motor Dynamics

Jung-Hua Yang

Dept. of Electrical Engineering
Yungta College of Technology and Commerce, Pingtung, Taiwan.

Abstract

To achieve high performance robot control system, the inclusion of actuator dynamics in the controller design will be inevitable. Nonetheless, the consideration of actuator dynamics in the robot control system may complicate the controller structure and its corresponding stability analysis. Moreover, on-line computation of the regressor matrix in conventional adaptation mechanism is always time-consuming and expensive. Therefore, this study presents a novel approach to circumvent the above-mentioned drawbacks. In this scheme, the regressor matrix merely contains the desired trajectories which can be calculated a priori, and hence, the computational burden is largely reduced. The so-called semi-global asymptotical stability is guaranteed via Lyapunov analysis and simulation results also show the effectiveness of the controller.

1 Introduction

Intensive studies have been carried out in the literatures on the rigid robot represented by a set of second-order differential equations, charactering the dynamic behavior of the robot and assuming the inputs to be the torques or the forces acting on the joints. In reality, however, the actuator dynamics constitutes an important part in the robot dynamics, especially when high operation speed is required, as pointed out by Good *et al* [1]. Nonetheless, the consideration of actuator dynamics in the robot control system may complicate the controller structure and its corresponding stability analysis.

Recently the problem of controlling the motion of robots with motor dynamics has attracted considerable attention [2]-[13]. In [2] and [3], the controller is designed to compensate for the uncertainty in the robot and actuator dynamics by using robust control schemes. Nonlinear feedback linearization and decoupling is studied in [4] for robot containing motor dynamics. A third-order model is considered and a nonlinear feedback linearization in Cartesian space is investigated theoretically and

experimentally in [5], and [6] proposes an adaptive control scheme to account for the parametric uncertainty with the need of acceleration signals. Later on some other adaptive control approaches [7]-[8] are also advocated without the acceleration feedback. In [9]-[11], adaptive robust control schemes are designed to compensate for the parametric and nonparametric uncertainties. Moreover, the adaptation mechanism always require the on-line computation of regressor matrix, which would be very time-consuming and expensive. Although an adaptive control algorithm is proposed [12]-[13] to avoid the velocity measurement in the feedback, the on-line position measurement is still involved in the regressor matrix calculation. Therefore, this study presents a novel approach to circumvent the above-mentioned drawbacks. In this scheme, only position signal is needed in the feedback law, and the regressor matrix merely contains the desired trajectories which can be calculated a priori, and hence, the computational burden is largely reduced. The so-called semiglobal asymptotical stability is guaranteed via Lyapunov analysis and simulation results also show the effectiveness of the controller.

This paper is organized as follows : In section 2, brief description of the dynamic model and its basic properties are given. In section 3, an adaptive controller is provided for the model described in section 2. The design procedure of the control algorithm is splitted into two stages, namely, mechanical and electrical stages. Moreover, Lyapunov stability proof is also given in this section. In section 4, a case study on a two-link robot arm is made, and simulation results show the validity of the proposed controller. Finally, some concluding remarks are provided.

2 Dynamic Model

In this section, the dynamic model of a robot system and some of its intrinsic properties will be briefly reviewed. All the properties described are very useful in adaptive controller design and can be found in the literatures.

Consider the dynamics of an n -link robot manipulator with D.C. motor embedded in each joint to be :

$$\begin{aligned} M(q)\ddot{q} + C(q, \dot{q})\dot{q} + G(q) &= K_n I \\ LI + RI &= u \end{aligned} \quad (1) \quad (2)$$

where $q \in R^n$ represents the vector of joint angle and I is the vector of armature currents in D.C. motors, and $M(q) \in R^{n \times n}$, $C(q, \dot{q}) \in R^n$, and $G(q) \in R^n$ are denoted as the moment of inertia matrix, Coriolis and centrifugal terms, and gravitational torques, respectively, $K_n = \text{diag}[K_{n1}, K_{n2}, \dots, K_{nn}]$, $L = \text{diag}[L_1, L_2, \dots, L_n]$, and $R = \text{diag}[R_1, R_2, \dots, R_n]$ are diagonal matrices representing the equivalent torque constants; armature induction, and resistance, respectively, and $u \in R^n$ is defined as the control voltage input variable. It should be noted that (1) can be viewed as the mechanical part of the whole system while (2) can be treated as the corresponding electrical part. In the subsequent controller design, these two sub-systems will be analyzed separately. Furthermore, the following statements are held for general robot systems and are very useful in the stability analysis.

Property 1 : The right-hand side of dynamic equation (1) can be rewritten in a regression matrix form as follows :

$$M(q)\ddot{q} + C(q, \dot{q})\dot{q} + G(q) = W(q, \dot{q}, \ddot{q})\theta \quad (3)$$

where $W(q, \dot{q}, \ddot{q}) \in R^{n \times m}$, denoted as the regressor, is a matrix of known functions constituting the system dynamics, and $\theta \in R^m$ consists of the kinematic and dynamic parameters of the manipulator system.

Property 2 : $\dot{M}(q) - 2C(q, \dot{q})$ is skew-symmetric, i.e., $x^T(\dot{M} - 2C)x = 0, \forall x \in R^n$

Property 3 : For a robot system, the time derivative of the inertia matrix and the Coriolis centrifugal matrix can be bounded by the following inequalities :

$$\begin{aligned} \left\| \frac{d}{dt} M(q) \right\| &\leq \alpha_{11} \|\dot{e}\| + \alpha_{12} \\ \|C(q, \dot{q})\| &\leq \alpha_{21} \|e\| + \alpha_{22} \end{aligned}$$

where $e = q - q_d$ and q_d is some prespecified bounded trajectory function vector with bounded first- and second-time derivatives, and α_{ij} , $i, j = 1, 2$ are some positive constants.

3 Adaptive Controller Design

In this section, the adaptive control algorithm is devised under the assumption that all the system parameters are not known a priori and, the design procedure is performed separately on the basis of two stages, namely, the mechanical stage and the electrical stage.

First Stage Design :

Consider the mechanical part of the dynamic model, as shown in (1), which can be reformulated as :

$$M(q)\ddot{e} + C(q, \dot{q})\dot{e} = -M(q)\ddot{q}_d - C(q, \dot{q})\dot{q}_d - G(q) + K_n I \quad (4)$$

where q_d , \dot{q}_d , and \ddot{q}_d have been defined previously. Since there is no actual control input involved we further define a virtual control input I_d for this subsystem. Thus, if $I \rightarrow I_d$, we can have the subsystem to behave as if the virtual input I_d is the true input. Moreover, the on-line computation of the regressor matrix is very time-consuming and would lead to large computational cost. To remedy this problem, all the measured signals in the regressor matrix will be replaced by their desired forms, that is, let the virtual control input I_d adaptive control algorithm be devised as :

$$\begin{aligned} I_d &= \hat{K}_{nv} [\hat{M}(q_d)\ddot{q}_d + \hat{C}(q_d, \dot{q}_d)\dot{q}_d + \hat{G}(q_d) - \beta^2 k - \beta^2 e] \\ &= \hat{K}_{nv} [W(q_d, \dot{q}_d, \ddot{q}_d)\hat{\theta} - \beta^2 k - \beta^2 e] \\ &= \hat{K}_{nv} [W_d \hat{\theta} - \beta^2 k - \beta^2 e] \\ &= \hat{K}_{nv} \tau_d \end{aligned} \quad (5)$$

where \hat{K}_{nv} is the estimate of K_n^{-1} , $W_d \equiv W(q_d, \dot{q}_d, \ddot{q}_d)$, $W_d \hat{\theta} - \beta^2 k - \beta^2 e = \tau_d$, and β is the design parameter which will be properly selected to guarantee the asymptotical stability. And the adaptive parameter $\hat{\theta}$ and k satisfy the following equations :

$$\dot{k} = -2\beta k + \beta^2 \dot{e} \quad (6)$$

$$\dot{\hat{\theta}} = \Gamma \left(\frac{1}{\beta} W_d^T k - \frac{1}{\beta} W_d^T e - W_d^T \dot{e} \right) \quad (7)$$

$$\dot{\hat{K}}_{nv} = \text{diag}[\dot{\hat{K}}_{nv1}, \dot{\hat{K}}_{nv2}, \dots, \dot{\hat{K}}_{nvn}]$$

$$\dot{\hat{K}}_{nvi} = \left(\frac{1}{\beta} k_i - \frac{1}{\beta} e_i - \dot{e}_i \right) \tau_{di}, \quad i = 1, 2, \dots, n \quad (8)$$

where Γ is some positive-definite matrix, and x_i denotes the i th element of vector x .

Then, substituting the above control law (5) into the dynamics (4) along with the adaptation laws (6)-(8), we obtain

$$\begin{aligned} &M(q)\ddot{e} + C(q, \dot{q})\dot{e} + \beta^2 k + \beta^2 e \\ &= [\hat{M}(q_d) - M(q)]\ddot{q}_d + [\hat{C}(q_d, \dot{q}_d) - C(q, \dot{q})]\dot{q}_d \\ &+ [\hat{G}(q_d) - G(q)] + K_n e_I + K_n (\hat{K}_{nv} - K_n^{-1}) \tau_d \\ &= W_d \hat{\theta} - W\theta + K_n e_I + K_n \tilde{K}_{nv} \tau_d \\ &= W_d \tilde{\theta} + (W_d - W)\theta + K_n e_I + K_n \tilde{K}_{nv} \tau_d \end{aligned} \quad (9)$$

where

$$W\theta = M(q)\ddot{q} + C(q, \dot{q})\dot{q} + G(q)$$

$$e_I = I - I_d$$

$$\tilde{K}_{nv} = \hat{K}_{nv} - K_n^{-1}$$

Before proceeding with the stability analysis we have, based on the properties mentioned in section 2, the following proposition :

Proposition 1: The bounds of the vector norm $\|(W_d - W)\theta\|$, $\|\frac{d}{dt}M\|$, and $\|C(q, \dot{q})\|$ satisfy the following inequalities:

$$(1) \quad \|(W_d - W)\theta\| \leq \alpha_1 \|e\| + \alpha_2 \|\dot{e}\| \quad (10)$$

$$(2) \quad \|\frac{d}{dt}M\| \leq \alpha_3 \|\dot{e}\| + \alpha_4 \quad (11)$$

$$(3) \quad \|C(q, \dot{q})\| \leq \alpha_5 \|\dot{e}\| + \alpha_6 \quad (12)$$

Proof: The proof is straightforward and omitted due to limited space.

Q.E.D.

Accordingly, through Lyapunov stability analysis, the following theorem can be readily derived on the basis of the error dynamics (6)-(9) by incorporating proposition 1.

Proposition 2: Consider the closed-loop system dynamics (6)-(9), then the position error e and the velocity error \dot{e} will asymptotically decay to zero if the armature current I equals the virtual control input I_d and the control gain β is chosen large enough.

Proof : The evaluation of the closed-loop system stability will be made on the basis of the Lyapunov analysis. Before proceeding with the stability analysis of the closed-loop system, we first define a Lyapunov function candidate as follows :

$$\begin{aligned} V_1 &= \frac{1}{2}\beta^2 e^T e + \frac{1}{2}\dot{e}^T M(q)\dot{e} + \frac{1}{2}k^T k + \frac{1}{2}\sum_{i=1}^n K_{ni}\tilde{K}_{nvi}^2 \\ &\quad + \frac{1}{\beta}e^T M(q)\dot{e} - \frac{1}{\beta}k^T M(q)\dot{e} + \frac{1}{2}\tilde{\theta}^T \Gamma^{-1}\tilde{\theta} \\ &= \frac{1}{2}X^T P X + \frac{1}{2}\sum_{i=1}^n K_{ni}\tilde{K}_{nvi}^2 \end{aligned} \quad (13)$$

where

$$\begin{aligned} X &= [e^T \quad \dot{e}^T \quad k^T \quad \tilde{\theta}^T]^T \\ P &= \begin{bmatrix} \beta^2 I & M(q)/\beta & 0 & 0 \\ M(q)/\beta & M(q) & -M(q)/\beta & 0 \\ 0 & -M(q)/\beta & I & 0 \\ 0 & 0 & 0 & \Gamma \end{bmatrix} \end{aligned} \quad (14)$$

Due to the structural symmetry and positive-definiteness of $M(q)$ and Γ , it can be verified that, if the control gain β is chosen large enough as required, the Lyapunov function candidate V is a positive-definite function.

Then, by taking the time derivative of V_1 along the error dynamics (6)-(9), we obtain

$$\begin{aligned} \dot{V}_1 &= \beta^2 e^T \dot{e} + \dot{e}^T [-C\dot{e} - \beta^2 k - \beta^2 e + W_d \tilde{\theta} \\ &\quad + (W_d - W)\theta + K_n e_I + K_n \tilde{K}_{nv} \tau_d] \\ &\quad + \frac{1}{2}\dot{e}^T \dot{M}\dot{e} + k^T (-2\beta k + \beta^2 \dot{e}) + \frac{1}{\beta}\dot{e}^T M\dot{e} + \frac{1}{\beta}e^T \dot{M}\dot{e} \\ &\quad + \frac{1}{\beta}e^T [-C\dot{e} - \beta^2 k - \beta^2 e + W_d \tilde{\theta} \\ &\quad + (W_d - W)\theta + K_n e_I + K_n \tilde{K}_{nv} \tau_d] \\ &\quad + \frac{1}{\beta}\dot{e}^T M(-2\beta k + \beta^2 \dot{e}) - \frac{1}{\beta}k^T \dot{M}\dot{e} \\ &\quad - \frac{1}{\beta}k^T [-C\dot{e} - \beta^2 k - \beta^2 e + W_d \tilde{\theta} \\ &\quad + (W_d - W)\theta + K_n e_I + K_n \tilde{K}_{nv} \tau_d] \\ &\quad - \tilde{\theta}^T W_d^T (\frac{1}{\beta}k - \frac{1}{\beta}e - \dot{e}) + \sum_{i=1}^n K_{ni}\tilde{K}_{nvi}\dot{K}_{nvi} \end{aligned}$$

Next, we can have the upper bound for \dot{V} by using the properties described in section 2 and the inequalities derived in proposition 1 to yield:

$$\begin{aligned} \dot{V}_1 &\leq -\beta \|e\|^2 - (\beta - \frac{1}{\beta})\lambda_m(M)\|\dot{e}\|^T - \beta \|k\|^2 \\ &\quad + \|\dot{e}\|(\alpha_1 \|e\| + \alpha_2 \|\dot{e}\|) + \frac{1}{\beta}\|e\|(\alpha_3 \|\dot{e}\| + \alpha_4)\|\dot{e}\| \\ &\quad + \frac{1}{\beta}\|e\|(\alpha_5 \|\dot{e}\| + \alpha_6)\|\dot{e}\| + \frac{1}{\beta}\|e\|(\alpha_1 \|e\| + \alpha_2 \|\dot{e}\|) \\ &\quad + 2\alpha_7 \|\dot{e}\|^2 \|k\| + \frac{1}{\beta}\|k\|(\alpha_3 \|\dot{e}\| + \alpha_4)\|\dot{e}\| \\ &\quad + \frac{1}{\beta}\|k\|(\alpha_5 \|\dot{e}\| + \alpha_6)\|\dot{e}\| + \frac{1}{\beta}\|k\|(\alpha_1 \|e\| + \alpha_2 \|\dot{e}\|) \\ &\quad - (\frac{1}{\beta}k - \frac{1}{\beta}e - \dot{e})K_n e_I \\ &\leq -(\beta - \frac{\alpha_1}{\beta})\|e\|^2 - \beta \|k\|^2 \\ &\quad - \left[(\beta - \frac{1}{\beta})\lambda_m(M) - \alpha_2 - (\frac{\alpha_3}{\beta} + \frac{\alpha_5}{\beta})\|e\| \right. \\ &\quad \left. - (2\alpha_7 + \frac{\alpha_5}{\beta} + \frac{1}{\beta})\|k\| \right] \|\dot{e}\|^2 \\ &\quad + (\alpha_1 + \frac{\alpha_4}{\beta} + \frac{\alpha_5}{\beta} + \frac{\alpha_2}{\beta})\|e\|\|\dot{e}\| \\ &\quad + \frac{\alpha_1}{\beta}\|k\|\|\dot{e}\| + (\frac{\alpha_4}{\beta} + \frac{\alpha_6}{\beta} + \frac{\alpha_2}{\beta})\|\dot{e}\|\|k\| \\ &\quad - (\frac{1}{\beta}k - \frac{1}{\beta}e - \dot{e})K_n (I - I_d) \\ &\leq -\eta_1 \|e\|^2 - \eta_2 \|\dot{e}\|^2 - \eta_3 \|k\|^2 \\ &\quad + \eta_4 \|e\|\|\dot{e}\| + \eta_5 \|k\|\|\dot{e}\| + \eta_6 \|\dot{e}\|\|k\| \\ &\quad - (\frac{1}{\beta}k^T - \frac{1}{\beta}e^T - \dot{e}^T)K_n e_I \end{aligned}$$

$$\begin{aligned} \leq & -(\eta_1 - \frac{1}{2}\eta_4 - \frac{1}{2}\eta_5)\|e\|^2 - (\eta_2 - \frac{1}{2}\eta_4 - \frac{1}{2}\eta_6)\|\dot{e}\|^2 \\ & -(\eta_3 - \frac{1}{2}\eta_5 - \frac{1}{2}\eta_6)\|k\|^2 \\ & -(\frac{1}{\beta}k^T - \frac{1}{\beta}e^T - \dot{e}^T)K_n e_I \end{aligned}$$

where $\lambda_m(M)$ denotes the smallest eigenvalue of M , and

$$\begin{aligned} \eta_1 &= \beta - \frac{\alpha_1}{\beta} \\ \eta_2 &= (\beta - \frac{1}{\beta})\lambda_m(M) - \alpha_2 - \frac{1}{\beta}(\alpha_3 + \alpha_5)\|e\| \\ &\quad - \frac{1}{\beta}(2\alpha_7\beta + \alpha_5 + 1)\|k\| \\ \eta_3 &= \beta \\ \eta_4 &= \alpha_1 + \frac{1}{\beta}(\alpha_2 + \alpha_4 + \alpha_6) \\ \eta_5 &= \frac{\alpha_1}{\beta} \\ \eta_6 &= \frac{1}{\beta}(\alpha_2 + \alpha_4 + \alpha_6) \end{aligned}$$

Obviously, all the terms in $\eta_i, i = 1, 2, \dots, 6$ involving $\frac{1}{\beta}$ can be made negligible if β is chosen large enough. Therefore, we can infer, under the condition that $I = I_d$, that all the signals in the closed-loop system are bounded and, in addition,

$$e \in L_2, \dot{e} \in L_2$$

As a result, by invoking Barbalat's Lemma, we have

$$\begin{aligned} \lim_{t \rightarrow \infty} e &= 0 \\ \lim_{t \rightarrow \infty} \dot{e} &= 0 \end{aligned}$$

which completes the proof.

Q.E.D.

Second Stage Design :

In this stage, an adaptive control algorithm is provided for the electrical subsystem (2). It is noteworthy that in the first stage we have define a virtual control input I_d , and hence, an error term e_I between the armature current and the virtual control input arises at the right-hand side of (9). Therefore, we are trying, in this stage, to design an adaptive control approach for the dynamics of the error term e_I . Before doing this, we first construct the error dynamics of e_I . Consider the electrical dynamics (2),

$$L\dot{I} + RI = u, \quad (15)$$

then after some mathematical arrangements we have

$$L\dot{e}_I + K_I e_I = -L\dot{I}_d - RI + K_I e_I + u \quad (16)$$

If we let the control voltage input be

$$u = \hat{L}\dot{I}_d + \hat{R}I - K_I e_I + v \quad (17)$$

where

$\hat{L} = \text{diag}[\hat{L}_1, \hat{L}_2, \dots, \hat{L}_n]$ and $\hat{R} = \text{diag}[\hat{R}_1, \hat{R}_2, \dots, \hat{R}_n]$ denote the estimates of L and R , respectively, and v is the auxiliary control, which will be define later. Then, (17) becomes

$$L\dot{e}_I + K_I e_I = \tilde{L}\dot{I}_d + \tilde{R}I + v \quad (18)$$

where $\tilde{L} = \hat{L} - L$ and $\tilde{R} = \hat{R} - R$ are the estimation errors. Now, let the parameter estimates be

$$\dot{\hat{L}}_i = \gamma_1 e_{Ii} \dot{I}_{di}, \quad i = 1, 2, \dots, n \quad (19)$$

$$\dot{\hat{R}}_i = \gamma_2 e_{Ii} I_i, \quad i = 1, 2, \dots, n \quad (20)$$

where e_{Ii} , I_i , and \dot{I}_{di} denote the i th element of e_I , I , and \dot{I}_d , respectively, and γ_1 and γ_2 are the adaptation gains which are positive. Under such design philosophy, there exists a Lyapunov function V_2 such that the following proposition hold:

Proposition 3 : Consider the electrical subsystem (17). If the control input u is design as (18) incorporating with the adaptation laws (20)-(21) and K_I is selected to be postive-definite then a Lyapunov function

$$V_2 = \frac{1}{2}e_I^T L e_I + \frac{1}{2} \sum_{i=1}^n (\gamma_1^{-1} \tilde{L}_i^2 + \gamma_2^{-1} \tilde{R}_i^2) \quad (21)$$

exist and its time derivative along the dynamics (19)-(21) satisfies

$$\dot{V}_2 \leq -e_I^T K_I e_I + e_I^T v$$

Proof : Obviously, differentiating V_2 with respect to time we obtain

$$\begin{aligned} \dot{V}_2 &= e_I^T L \dot{e}_I + \sum_{i=1}^n (\gamma_1^{-1} \tilde{L}_i \dot{\tilde{L}}_i + \gamma_2^{-1} \tilde{R}_i \dot{\tilde{R}}_i) \\ &= -e_I^T K_I e_I + \sum_{i=1}^n (e_{Ii} \tilde{L}_i \dot{I}_{di} + e_{Ii} \tilde{R}_i I_i) \\ &\quad + e_I^T v + \sum_{i=1}^n (\gamma_1^{-1} \tilde{L}_i \dot{\tilde{L}}_i + \gamma_2^{-1} \tilde{R}_i \dot{\tilde{R}}_i) \end{aligned}$$

Upon the substitution of (20)-(21), the above equation can then be rewritten as:

$$\dot{V}_2 \leq -e_I^T K_I e_I + e_I^T v$$

which completes the proof.

Q.E.D.

In the sequel, the main theorem concerning the overall closed-loop system is to be proposed based on **Proposition 2** and **Proposition 3**.

Theorem 1 Consider the overall closed-loop system (1)-(2). If the control input u and the adaptation laws are elaborated as (18) and (6)-(8), (20), (21), respectively, with large enough β and K_I , and the auxiliary input v is designed as

$$v = \hat{K}_n \left(\frac{1}{\beta} k - \frac{1}{\beta} e - \dot{e} \right) \quad (22)$$

$$\dot{\hat{K}}_n = \text{diag}[\dot{\hat{K}}_{n1}, \dot{\hat{K}}_{n2}, \dots, \dot{\hat{K}}_{nn}]$$

$$\dot{\hat{K}}_{ni} = \gamma_3 \left(\frac{1}{\beta} k_i - \frac{1}{\beta} e_i - \dot{e}_i \right) e_{Ii}, \quad i = 1, 2, \dots, n \quad (23)$$

where \hat{K}_n is the estimate of K_n , then all the signals in the closed-loop system will be stable in the sense of Lyapunov. Moreover, the tracking errors e and \dot{e} will converge to zero asymptotically.

Proof : Consider a composite Lyapunov function $V = V_1 + V_2 + \frac{1}{2} \sum_{i=1}^n \gamma_3^{-1} \hat{K}_{ni}^2$ as shown in (13) and (22), then take its first time derivative along the closed-loop system dynamics (9) and (19) and substitute (23) and (24) into V to yields :

$$\begin{aligned} \dot{V} \leq & -(\eta_1 - \frac{1}{2}\eta_4 - \frac{1}{2}\eta_5) \|e\|^2 \\ & -(\eta_2 - \frac{1}{2}\eta_4 - \frac{1}{2}\eta_6) \|\dot{e}\|^2 \\ & -(\eta_3 - \frac{1}{2}\eta_5 - \frac{1}{2}\eta_6) \|k\|^2 - \lambda_m(K_I) \|e_I\|^2 \end{aligned}$$

where $\lambda_m(K_I)$ denotes the smallest eigenvalue of K_I . Again, by using the results developed in **Proposition 2** and **Proposition 3** and invoking Barbalat's Lemma, we can conclude that e , \dot{e} , k , and e_I will decay to zero asymptotically, which ends the stability proof.

Q.E.D.

Remark : The stability result shown above is also called the "semi-global asymptotic stability" which means that the domain of attraction of the closed-loop system can be made infinitely large by way of proper selection of β , although it seems that only local result is guaranteed in the Lyapunov analysis.

4 Simulation Studies

In this section, the advocated adaptive tracking control algorithm is applied to a two-link rigid robot manipulator with D.C. motor dynamics as an illustrated example. Several simulations are studied and shown below. The desired position trajectories are $q_{d1} = \frac{180}{\pi}(\cos(3t) - 1)$ degree and $q_{d2} = \frac{180}{\pi}(\cos(2t) - 1)$ degree, and the control gain β is selected to be 10. The following plots demonstrate the simulation results. Fig.(1) and Fig.(2) show the

position tracking errors. It noteworthy that if the initial conditions on the position errors are small and the control gain β is made large enough, the tracking responses will converge to zero very fast within 0.8 second which confirms the well-suited performance. However, it must be paid at the expense of large control force. Unfortunately, no systematic approach can be used to select the control gain β . It must be chosen by iterative simulations, and a trade-off between the system response and the control gain β should be made. Finally, Fig.(3) and Fig.(4) depict the velocity tracking responses.

5 Conclusion

In this paper, we have proposed an adaptive trajectory tracking control method for a multi-link rigid manipulator including electrical motor dynamics. No prior knowledge on the system parameters is required in the control algorithm. Moreover, the adaptive controller can be easily implemented, and hence, save a large amount of time from the practical point of view since the regressor matrix only contains the desired trajectory which can be calculated off-line. Simulation results also the effectiveness of the devised algorithm.

References

- [1] M. C. Good, L. M. Sweet, and K. L. Strobel, "Dynamic Models for Control System Design of Integrated Robot and Drive Systems", *J. Dyn. Syst., Meas., Contr.*, Vol. 107, pp. 53-59, 1985.
- [2] D. M. Dawson, Z. Qu, and J. J. Carrol, "Tracking Control of Rigid-Link Electrically-Driven Robot Manipulator", *Int. J. Contr.*, Vol. 56, pp. 911-1006, 1992.
- [3] C. Y. Su and Y. Stepanenko, "On the Robust Control of Robot Manipulators Including Actuator Dynamics", *J. Robot. Syst.*, Vol. 13, pp. 1-10, 1996.
- [4] R. Beekman and K. Lee, "Nonlinear Robotic Control Including Drive Motor Interactions", *Proc. Amer. Contr. Conf.*, pp. 1338-1338, 1988.
- [5] T. J. Tarn, A. K. Bejczy, X. Yun, and Z. Li, "Effect of Motor Dynamics on nonlinear Feedback Robot Arm Control", *IEEE Trans. Robot. and Automat.*, Vol. 7, pp. 114-122, Feb. 1991.
- [6] S. S. Ge and I. Postlethwaite, "Nonlinear Adaptive Control of Robots Including Motor Dynamics", *Proc. Instn. Mech. Engrs.*, Vol. 208, pp. 89-99, 1994.

- [7] J. Yuan, "Adaptive Control of Robotic Manipulators Including Motor Dynamics", *IEEE Trans. Robot. Automat.*, Vol. 11, pp. 612-617, 1995.
- [8] R. Colbaugh and K. Glass, "Adaptive Regulation of Rigid-Link Electrically-Driven Manipulators", *Proc. Int. Conf. Robot. Automat.* 1995.
- [9] R. Guenther and L. Hsu, "Variable Structure Adaptive Cascaded Control of Rigid-Link Electrically-Driven Robot Manipulators", *Proc. IEEE Conf. Dec. Contr.*, 1993.
- [10] Y. Stepanenko and C. Y. Su, "Adaptive Motion Control of Rigid-Link Electrically-Driven Robot Manipulators", *Proc. IEEE int. Conf. Robot. Automat.*, 1994.
- [11] C. Y. Su and Y. Stepanenko, "Hybrid Adaptive/Robust Motion Control of Rigid-Link Electrically-Driven Robot Manipulators", *IEEE Trans. Robot. Automat.*, Vol. 11, pp. 426-432, 1995.
- [12] T. Burg, D. Dawson, J. Hu, and M. de Queiroz, "An Adaptive Partial State-Feedback Controller for RLED Robot Manipulators", *IEEE Trans. Automat. Contr.*, Vol. 41, pp. 1024-1030, 1996.
- [13] C. Y. Su and Y. Stepanenko, "Redesign of Hybrid Adaptive/Robust Motion Control of Rigid-Link Electrical-Driven Robot Manipulators", *IEEE Trans. Robot. Automat.*, Vol. 14, pp. 651-655, 1998.

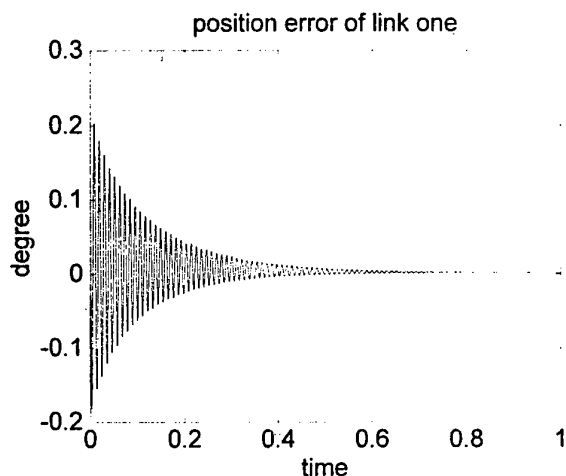


Fig.(1) Position tracking error of link 1

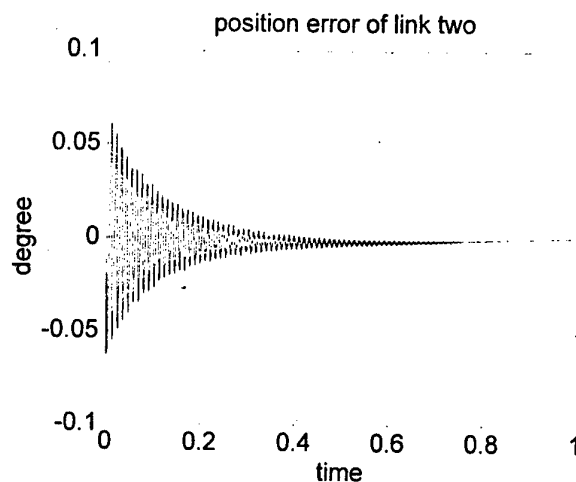


Fig.(2) Position tracking error of link 2

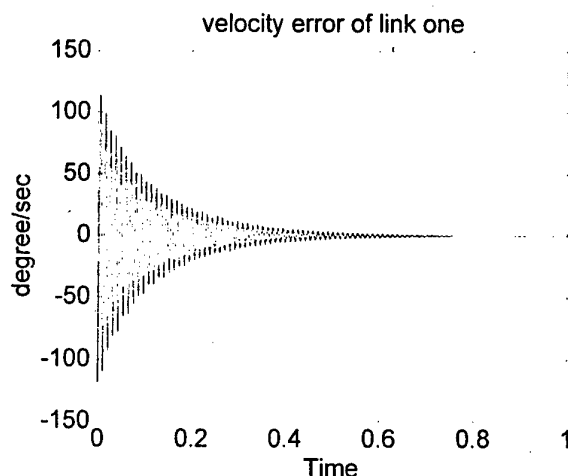


Fig.(3) Velocity tracking error of link 1

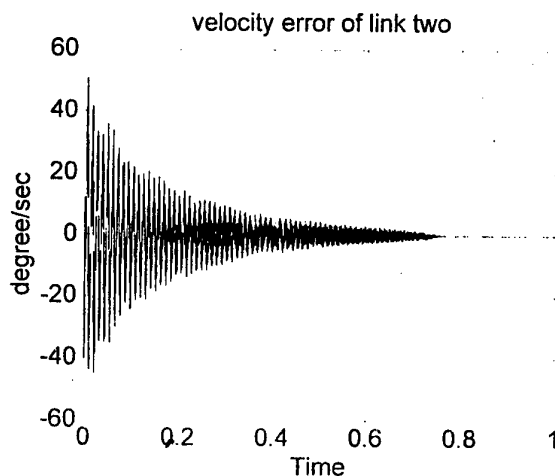


Fig.(4) Velocity tracking error of link 2

Neural Networks Adaptive Controller for Rigid Manipulators

Reza Fotouhi-C.

Mechanical Engineering Dept., University of Saskatchewan, Saskatoon, Canada S7N 5A9
ref260@engr.usask.ca

Peter N. Nikiforuk

nikiforu@engr.usask.ca

Abstract

A controller based on neural networks (NN) is proposed to achieve trajectory tracking for rigid manipulators. The NN used here has three layers with one hidden layer. Elements of a dynamics model of manipulator are approximated by this neural networks. These approximation form a stable adaptive control law. The NN weights are tuned on-line. Performance of the NN presented is compared with that of conventional adaptive controller.

1. Adaptive inverse dynamics

In the 1980s several globally convergent adaptive control schemes for rigid link manipulators appeared in the literature [1, 2]. These schemes belong to several distinct categories which were discussed in detail in [3]. The research described in [4] and [5] uses the adaptive inverse dynamics and the tracking error to drive the update law.

An important property for rigid manipulators is that the dynamics are linear in terms of a suitably selected set of robot parameters, sometimes called the *linear-in-parameters property* [6], such that the equation of motion can be written as

$$\tau(t) = M(\varphi, P)\ddot{\varphi} + C(\varphi, \dot{\varphi}, P)\dot{\varphi} + G(\varphi, P) = Y(\varphi, \dot{\varphi}, \ddot{\varphi})P$$

This property is widely used in adaptive inverse dynamics algorithms for rigid manipulators and other adaptive schemes. Here, the $m \times m$ mass matrix M is a function of the m -vector of degrees of freedom, φ , and the r unknown parameters P ; $C\dot{\varphi}$ is the m -vector of the centrifugal and Coriolis forces and G is the m -vector of the gravitational force; τ is the m -vector of controls; and $Y(\varphi, \dot{\varphi}, \ddot{\varphi})$ is an $m \times r$ regressor matrix.

For controlling the motion of the manipulator so as to follow a given path, φ_d , an inverse dynamics adaptive controller (model-based adaptive controller [4]) shown in Figure 1, was used. In [4], it was assumed

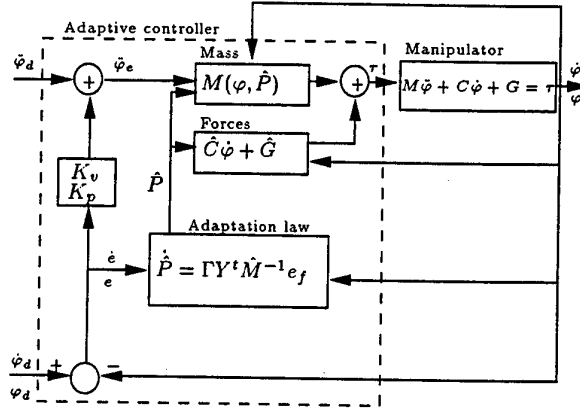


Figure 1: Inverse dynamics adaptive controller.

that the system with the estimated parameters \hat{P} was driven by the following control law

$$\tau(t) = M(\varphi, \hat{P})\ddot{\varphi}_e + C(\varphi, \dot{\varphi}, \hat{P})\dot{\varphi} + G(\varphi, \hat{P}) \quad (1)$$

where \hat{M} , \hat{C} and \hat{G} were estimates of M , C and G respectively and

$$\ddot{\varphi}_e(t) = \ddot{\varphi}_d + K_v \dot{e} + K_p e \quad e(t) = \varphi_d - \varphi \quad (2)$$

where K_v and K_p were $m \times m$ positive constant diagonal-gain matrices and $e(t)$ was the tracking error. The adaptation law was determined as

$$\dot{\hat{P}}(t) = \Gamma Y^T \hat{M}^{-1} e_f \quad (3)$$

where $\Gamma_{r \times r}$ was a positive constant diagonal matrix and e_f was the filtered tracking error given as

$$e_f(t) = \dot{e} + \Psi e \quad (4)$$

where $\Psi_{m \times m}$ also was a positive constant diagonal matrix.

The adaptive inverse dynamics approach is an efficient means for trajectory control of manipulators. However, there are some drawbacks with this and other

adaptive methods. Most of all, the dynamics model of the controlled plant should be known. Their tracking performance in high speed operation may be affected by unmodeled dynamics if they are not taken into account.

2. Neural networks adaptive controller

In recent years, neural networks (NN) have attracted the attention of many researchers [7, 8, 9, 10, 11, 12, 13, 14]. Some of the recent reviews of applications of the NN in robotics can be found in [15, 16, 17]. The learning capability of the NN can be used for learning the nonlinear functions associated with the dynamics of rigid manipulators. Upon learning, the NN would be able to generalize and respond effectively to unfamiliar situations. This type of NN, which sometimes is referred to as back propagation, is widely used for off-line learning of the inverse dynamics of manipulators. After the off-line learning period, the NN controllers can learn uncertainties of manipulators on-line. Many of the NN used for manipulators have three layers (input, hidden, output), in which the units in each layer are connected through weights. The weights are usually initialized randomly and modified by error back propagation. The tracking error decreases as the number of learning trials increases. In comparison with adaptive controllers some researchers say that NN offer better trajectory tracking performance.

Some of the drawbacks of NN are as follows: Randomly initialized weights may result in poor control and may cause stability problem. The number of neurons required has to be determined experimentally. It is not guaranteed that the learning algorithm will converge. In other words, the networks may take an indefinite amount of time to be trained. For large systems, with high degrees of freedom, slow adaptation will arise. The solutions of NN is in general not accurate [16]. Retraining is needed when the trajectory is changed. This is a serious disadvantage compared with adaptive and robust controllers.

An adaptive neural based controller for trajectory following of rigid manipulators was studied here as shown in Figure 2. One of the advantages of this NN controller is that there is no need to replace the NN when the rigid link manipulator is changed. A three layer nonlinear NN with arbitrary activation functions is used. The neural network weights are tuned on-line. The global asymptotic stability of the position tracking error as well as the boundedness of NN weight updates are guaranteed.

A three layer NN with one hidden layer has an output $y_i, i = 1, \dots, n_3$

$$y_i = \sum_{j=1}^{n_2} \left(w_{ij} \sigma \left(\sum_{k=1}^{n_1} v_{jk} x_k + \theta_{vj} \right) + \theta_{wi} \right) \quad (5)$$

where $x \in R^{n_1}$ is an input vector, σ is the activation function, v_{jk} the 1st-to-2nd layer interconnection weights, w_{jk} the 2nd-to-3rd layer interconnection weights; θ_{vj} and θ_{wi} are threshold offsets of the second and third layers respectively; n_1 and n_3 are the number of neurons in input and output layers respectively, and n_2 is the number of neurons in hidden layer.

Equation (5) in the matrix form is

$$y = W^t \sigma(V^t x) \quad (6)$$

in which

$$x^t = [1 \quad x_1 \quad \dots \quad x_{n_1}] \quad y^t = [y_1 \quad \dots \quad y_{n_3}]$$

$$V^t = \begin{bmatrix} \theta_{v1} & v_{1,1} & \dots & v_{1,n_1} \\ \vdots & \vdots & & \vdots \\ \theta_{vn_2} & v_{n_2,1} & \dots & v_{n_2,n_1} \end{bmatrix}$$

$$W^t = \begin{bmatrix} \theta_{w1} & w_{1,1} & \dots & w_{1,n_2} \\ \vdots & \vdots & & \vdots \\ \theta_{wn_3} & w_{n_3,1} & \dots & w_{n_3,n_2} \end{bmatrix}$$

A continuous function $f(x)$ can be constructed as

$$f(x) = W^t \sigma(V^t x) + \epsilon(x) \quad (7)$$

where $\epsilon(x)$ is a NN error vector.

2.1. Manipulator dynamics

As before, the dynamics an m -link rigid manipulator with revolute joint can be written as

$$\tau(t) = M(\varphi)\ddot{\varphi} + C(\varphi, \dot{\varphi})\dot{\varphi} + G(\varphi) + F(\dot{\varphi}) \quad (8)$$

where the $m \times m$ mass matrix M is a function of the m -vector of degrees of freedom, φ ; $C\dot{\varphi}$ is the m -vector of the centripetal and Coriolis forces; G is the m -vector of the gravitational force; F is the m -vector of the friction force; and τ is the m -vector of controls. It should be noted that the rigid manipulators hold the following properties.

Property 1. The inertia matrix $M(\varphi)$ is symmetric positive definite, and bounded by

$$m_1 I \leq M(\varphi) \leq m_2 I \quad (9)$$

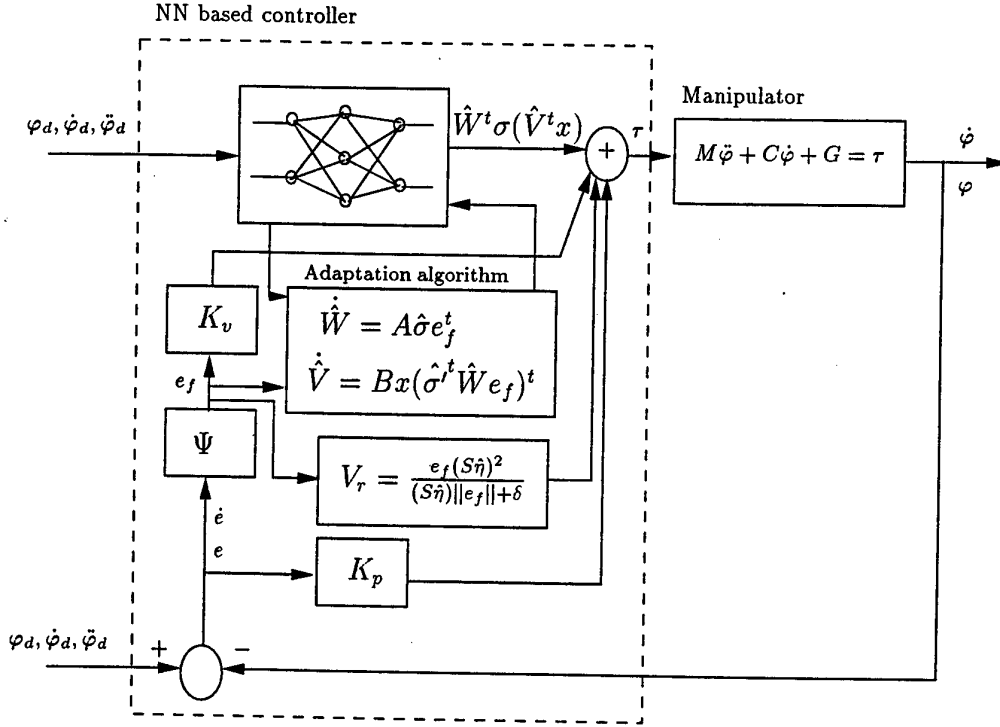


Figure 2: NN based adaptive controller.

where m_1 and m_2 are known positive constants and I is an unit matrix.

Property 2. The centripetal/Coriolis matrix, $C(\varphi, \dot{\varphi})$, may be chosen such that the matrix $\dot{M} - 2C$ is skew-symmetric and consequently the following holds

$$\varphi^t (\dot{M} - 2C) \varphi = 0 \quad (10)$$

where \dot{M} is time derivative of the inertia matrix.

Property 3. The following three layer neural network was used to approximate a nonlinear function

$$f_d(\varphi_d, \dot{\varphi}_d, \ddot{\varphi}_d) = W^t \sigma(V^t x) + \epsilon(x) \quad (11)$$

$$f_d(\varphi_d, \dot{\varphi}_d, \ddot{\varphi}_d) = M(\varphi_d) \ddot{\varphi}_d + C(\varphi_d, \dot{\varphi}_d) \dot{\varphi}_d + G(\varphi_d) + F(\dot{\varphi}_d)$$

where $x^t = [\varphi_d^t \ \dot{\varphi}_d^t \ \ddot{\varphi}_d^t]$; also V, W are constants with $n1 = n$ and $n3 = m$. It was assumed that the desired trajectory, $\varphi_d^t, \dot{\varphi}_d^t, \ddot{\varphi}_d^t$ is bounded; that is,

$$\|\epsilon(x)\| \leq \epsilon_b \quad (12)$$

in which ϵ_b is a positive constant.

2.2. The controller

The objective here is to track the motion of the manipulator with an inexact knowledge of the manipulator

dynamics. Using the definitions of e and e_f which were given in (2) and (4) respectively, the dynamics of manipulator, (8), can be written as

$$M \dot{e}_f = f(\varphi, \dot{\varphi}, \varphi_d, \dot{\varphi}_d, \ddot{\varphi}_d) - C e_f - \tau \quad (13)$$

$$f(\varphi, \dot{\varphi}, \varphi_d, \dot{\varphi}_d, \ddot{\varphi}_d) = M(\varphi)(\ddot{\varphi}_d + \Psi \dot{e}) + C(\dot{\varphi}_d + \Psi e) + G + F$$

where $\Psi_{m \times m}$ was a positive constant diagonal matrix.

The control input was selected as

$$\tau = \hat{W}^t \sigma(\hat{V}^t x) + K_v e_f + K_p e + V_r \quad (14)$$

where \hat{W}, \hat{V} are the dynamic estimates of W, V respectively, K_v and K_p are $m \times m$ positive constant diagonal-gain matrices, and $V_r(t)$ is a nonlinear term which compensate for robustness and disturbance given by

$$V_r = \frac{e_f (S \hat{\eta})^2}{(S \hat{\eta}) \|e_f\| + \delta} \quad (15)$$

where

$$\dot{\delta} = -\gamma \delta \quad (16)$$

with $\delta(0), \gamma$ as positive constants. The vectors S, η and z are defined as

$$\begin{aligned} \eta^t &= [\eta_0 \ \eta_1 \ \eta_2 \ \eta_3 \ \eta_4 \ \eta_5] \\ S &= [1 \ \|z\| \ \|z\|^2 \ \|\hat{W}\|_f \ \|\hat{V}\|_f \ \|\hat{W}\|_f \|\hat{V}\|_f] \\ z &= [e^t \ e_f^t] \end{aligned}$$

where $\|W\|_f^2$ is Frobenius norm defined as

$$\|W\|_f^2 = \text{trace}(W^t W) = \sum_{i,j} w_{ij}^2$$

The parameters η_i 's are positive bounding constants which depend on the desired trajectory, physical properties of the manipulator, the disturbance bound, error bound and also on control gain matrix Ψ . The parameter tuning law for η is

$$\dot{\tilde{\eta}} = \Lambda S^t \|e_f\| = -\dot{\tilde{\eta}} \quad (17)$$

where Λ is a symmetric positive definite matrix and $\tilde{\eta} = \eta - \hat{\eta}$.

As assumed in (12), the desired trajectory is bounded ($\|x\| \leq Q_d$ in which Q_d is a positive scalar constant). With the control input given by (14), (15) and (17), the neural network weights are updated by

$$\dot{W} = A \hat{\sigma} e_f^t \quad (18)$$

$$\dot{V} = B x(\hat{\sigma}^t \dot{W} e_f)^t \quad (19)$$

where $A \in R^{n^2 \times n^2}$, $B \in R^{n \times n}$ are symmetric positive definite constant matrices, and $\sigma' = |d\sigma(z)/dz|_{z=\hat{z}}$ and $\hat{\sigma}' = \sigma'(\hat{V}^t x)$. It was assumed here that the ideal weights are bounded such that

$$\|V\|_f \leq V_m \quad \|W\|_f \leq W_m \quad \|Z\|_f \leq Z_m$$

where V_m , W_m , Z_m are positive constants and

$$Z = \begin{bmatrix} W & 0 \\ 0 & V \end{bmatrix}$$

With these definitions tracking error e , \dot{e} goes to zero and the weight estimates \hat{V} , \hat{W} are bounded ([7, 18]).

The controller (14) may be used for any revolute joint rigid link manipulator. In this approach no weight initialization problem exists. The weights $\hat{V}(0)$, $\hat{W}(0)$ are initialized as zero which takes the NN out of the circuit. The PD terms $K_v e_f$ and $K_p e$ can stabilize the manipulator until the NN begins to learn. This means no off-line learning phase is required for this NN controller.

3. Conclusion

Neural network controllers have distinct adaptive and learning features when dealing with uncertainties and unmodeled dynamics. With sufficient learning a small tracking error and fast error convergence can be expected from the networks. Their drawbacks are that there are no guarantees in the convergence of learning

algorithms, and they need retraining when the trajectory is changed.

A NN adaptive controller for the motion control of rigid manipulators was studied here. The NN was used to approximate the nonlinear dynamics of the manipulators. This means that the robot dynamics does not need to be known exactly. Compared to adaptive control, this NN needs fewer assumptions and fewer calculation of explicit long expressions.

4. References

- [1] Romeo Ortega and Mark W. Spong. Adaptive motion control of rigid robots: a tutorial. *Automatica*, 25(6):877-888, 1989.
- [2] C. Abdallah, D. Dawson, P. Dorato, and M. Jamshidi. Survey of robust control for rigid manipulators. In *Proceedings of American Control Conference*, San Diego, California, USA, May 23-25 1990.
- [3] Reza Fotouhi-C., Walerian Szyszkowski, and Peter N. Nikiforuk. Adaptive control of rigid and flexible manipulators: a survey. *IEE Proceedings-Control Theory and Applications*, 1998. submitted.
- [4] John J. Craig, Ping Hsu, and S. Shankar Sastry. Adaptive control of mechanical manipulators. *The International Journal of Robotics Research*, 6(2):16-28, 1987.
- [5] Mark W. Spong and Romeo Ortega. On adaptive inverse dynamics control of rigid robots. *IEEE Transactions on Automatic Control*, 35(1):92-95, 1990.
- [6] Jean-Jacques E. Slotine and Weiping Li. Adaptive manipulator control: a case study. *IEEE Transactions on Automatic Control*, 33(11):995-1003, 1988.
- [7] Chiman Kwan, Frank L. Lewis, and Darren M. Dawson. Robust neural-network control of rigid-link electrically driven robots. *IEEE Transactions on Neural Networks*, 9(4):581-588, 1998.
- [8] Young H. Kim and Frank L. Lewis. Output feedback control of rigid robots using dynamic neural networks. In *Proceedings of IEEE International Conference on Robotics and Automation*, pages 1923-1928, Minneapolis, MN, USA, April 22-28 1996.
- [9] D.Y. Meddah and A. Benallegue. A stable neuro-adaptive controller for rigid robot manipulators. *Journal of Intelligent and Robotic Systems*, 20(2-4):181-193, 1997.
- [10] Weiying Cheng and John Ting-Yung Wen. A two-time-scale neural controller for the tracking control of rigid manipulators. *IEEE Transactions on Systems Man Cybernetics*, 24(7):991-1000, 1994.
- [11] Frank L. Lewis, Aydin Yesildirek, and Kai Liu. Multilayer neural-net robot controller with guaranteed tracking performance. *IEEE Transactions on Neural Networks*, 7(2):388-399, 1996.

- [12] Ahmet Karakasoglu, S. I. Sudharsanan, and M. K. Sundareshan. Identification and decentralized adaptive control using dynamical neural networks with application to robotic manipulators. *IEEE Transactions on Neural Networks*, 4(6):919-930, 1993.
- [13] R. Fierro and Frank L. Lewis. Control of a non-holonomic mobile robot using neural networks. *IEEE Transactions on Neural Networks*, 9(4):589-600, 1998.
- [14] Frank L. Lewis, Kai Liu, and Aydin Yesildirek. Neural net robot controller with guaranteed tracking performance. *IEEE Transactions on Neural Networks*, 6(3):703-715, 1995.
- [15] Keigo Watanabe. Intelligent control for robotic and mechatronics systems - a review. In *IEEE International Conference on Systems, Man and Cybernetics*, volume 1, pages 322-327, Beijing, China, Oct 14-17 1996.
- [16] Spyros G. Tzafestas. Neural networks in robotics: state of the art. In *IEEE International Symposium on Industrial Electronics*, volume 1, pages 12-19, Athens, Greece, July 10-14 1995.
- [17] M.J. Er, S.M. Yap, C.W. Yeaw, and F.L. Luo. Review of neural-fuzzy controllers for robotic manipulators. In *IEEE Industry Applications Conference 32nd IAS Annual Meeting*, volume 2, pages 812-819, New Orleans, LA, USA, Oct 5-9 1997.
- [18] Chiman Kwan, Darren M. Dawson, and Frank L. Lewis. Robust adaptive control of robots using neural network: global tracking stability. In *Proceedings of the 34th IEEE Conference on Decision and Control*, volume 2, pages 1846-1851, New Orleans, LA, Dec 13-15 1995.

Adaptive Motion Control of Mechatronic Systems

V. A. Balavessov,

Assoc. professor, Institute
of Mechanics, Bulgarian
Academy of Sciences,
balaves@bgcict.acad.bg

V. B. Galabov,

Assoc. professor,
Technical University of
Sofia, Bulgaria
vgalabov@vmei.acad.bg

I. I. Avramov,

Assoc. professor,
Technical University of
Sofia, Bulgaria
iavramov@vmei.acad.bg

J. M. Deianov

Postgraduate student,
Technical University of Sofia,
Sofia, Bulgaria

Abstract.

The present article deals with simple adaptive motion control of mechatronic systems. The direct adaptive control approach is used, as long as theoretically it does not require controller-embedded model of the plant, thus yielding simplified control realization. The adaptation is based on adaptive variation of signals rather than gains. As a result, fixed-gain controllers can be readily implemented, which is an unusual issue in adaptive control. Such control can be easily implemented, since the demands on computer power are significantly reduced and the sampling rate can be kept sufficiently high.

1. Introduction

Robots are typical representatives of mechatronic systems. One aspect that will not be treated here concerns the design of the mechanical system, as well as the tools and techniques for type-dimensional synthesis, analysis and optimization of robot mechanisms. A mechatronic concept for structural and functional design of such mechanisms can be found in [12].

There are certain difficulties in realizing of fast motions with robots. The problems come from the strong couplings between individual joint motions. Non-adaptive compensation of the couplings requires time-consuming computations, since accurate enough dynamic models are bulky. From one hand, there is some decrease of the sampling rate associated with the increased amount of computations. From the other hand, too slow sampling may deteriorate the performance, especially in the case of fast motions. Actually, decentralized fixed-gain control is used with all commercially available controllers. Such type of control results in an inherently parallel modular structure of the controller, which is most practical.

Adaptive control is a label assigned to a wide group of approaches, which are based on variations of the

control inputs adequately to *a priori* unknown variations of the plant's dynamics [1]. There are two widely recognized groups of adaptive control: direct and indirect ones [2].

Adaptive control schemes based on the *indirect* approach use a controller-embedded model of the plant. The model is with a known structure but with unknown parameters. During the normal operation of the system the model parameters are updated on-line in order to minimize the mismatch between the outputs of the model and the plant when they are subjected to one and the same control input. Subsequently, the control is generated according to the model. This approach is often referred to as *identification-based adaptive control*, as well as *explicit adaptive control*. However, explicit adaptive control may be used within the frame of direct adaptive control approach, too.

Direct adaptive control schemes (see Fig. 2) are based on controllers with previously defined structure but with unknown parameters. During the normal operation the controller's parameters are updated *directly* with the goal to minimize the error, or some other qualifier of the closed-loop system performance.

2. Some previous results

The equation of motion of an n degree-of-freedom rigid-body manipulator is described by

$$\mathbf{M}(\mathbf{q}) \ddot{\mathbf{q}} + \mathbf{C}(\mathbf{q}, \dot{\mathbf{q}}) \dot{\mathbf{q}} + \mathbf{g}(\mathbf{q}) = \mathbf{u}, \quad (1)$$

where \mathbf{q} is the $n \times 1$ vector of joint (generalized) coordinates; $\mathbf{g}(\mathbf{q}) \in \mathbb{R}^n$ is the vector of gravity forces; $\mathbf{M}(\mathbf{q}) \in \mathbb{R}^{n \times n}$ is the generalized inertia matrix; $\mathbf{C}(\mathbf{q}, \dot{\mathbf{q}}) \in \mathbb{R}^{n \times n}$ is the matrix of *Coriolis* and centrifugal effects; $\mathbf{u}(t) \in \mathbb{R}^n$ is the vector of generalized forces; it is also the control.

Basic properties. The generalized inertia matrix, $\mathbf{M}(\mathbf{q})$, is positive definite and bounded [3], i. e. $\exists m_1 > 0$ and $\exists m_2 \geq m_1$ such that

$$\forall \mathbf{q} \in Q \Rightarrow \underline{m} \mathbf{I}_n \leq \mathbf{M}(\mathbf{q}) \leq \bar{m} \mathbf{I}_n, \quad (2)$$

where Q denotes the allowed joint space, and the matrix inequalities imply positive definiteness rather than component-wise inequalities. The matrix of Coriolis and centrifugal effects is not uniquely defined [5]. However, it can be represented in a unique form [3] such that

$$\mathbf{C}(\mathbf{q}, \dot{\mathbf{q}}) + \mathbf{C}^T(\mathbf{q}, \dot{\mathbf{q}}) = \frac{d}{dt} \mathbf{M}. \quad (3)$$

Inverse dynamics control. The goal of gross motion robot control is to achieve closed-loop performance that meets some previously defined criteria. A widely spread control scheme is based on a computer-embedded inverse dynamics model. This is illustrated on the following figure (see Fig. 1). The approach requires precise inverse model (denoted by P^{-1}) of the plant (P), as well as a properly chosen feedback controller (C), that stabilizes the closed-loop system.

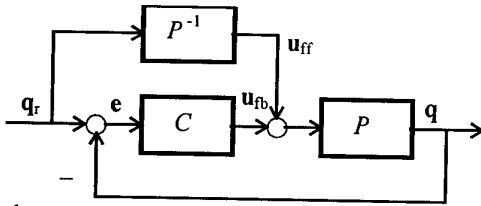


Fig. 1. Generalized scheme of inverse dynamics control.

The control comprises two components: feedback and feed-forward ones. The reference trajectory, $\mathbf{q}_r(t)$, has to be available together with its first and second order derivatives. Unlike the computed torque method, the generalized inertia matrix, $\mathbf{M}(\mathbf{q})$, is not used as a gain matrix here, and this is most suitable for use with direct adaptive control schemes. The computation of the feed-forward component, \mathbf{u}_{ff} , presents certain difficulties, since inverse models of complex mechatronic systems are rather bulky and uncertain to some extent. The feedback component, \mathbf{u}_{fb} , may be realized in a decentralized way. The following theorem [3, 5] helps to find such a control.

Theorem 1. The equilibrium state $\mathbf{e}(t) = \mathbf{0}$ of the system (1) is globally asymptotically stable under the control

$$\mathbf{u} = \mathbf{M}(\mathbf{q}) \ddot{\mathbf{q}}_r + \mathbf{C}(\mathbf{q}, \dot{\mathbf{q}}) \dot{\mathbf{q}}_r + \mathbf{g}(\mathbf{q}) + \mathbf{u}_{fb} \quad (4)$$

where $\mathbf{u}_{fb} := \mathbf{K}_p \mathbf{e} + \mathbf{K}_d \dot{\mathbf{e}}$ is a PD feedback control, $\mathbf{e}(t) := \mathbf{q}_r(t) - \mathbf{q}(t)$ is the tracking error, and the gain matrices, \mathbf{K}_p and \mathbf{K}_d , are constant and positive definite. \square

The gain matrices in (4) may be chosen diagonal, which is an important issue in decentralized control. In addition, the closed-loop system is exponentially stable provided the feedback gains are properly chosen, as stated by the following theorem.

Theorem 2. Let $\Lambda > 0$ be a constant and diagonal $n \times n$ matrix. Then the equilibrium state $\mathbf{e}(t) = \mathbf{0}$ of the system (1) is exponentially stable under the control (4), where the gain matrices are related by

$$\mathbf{K}_d = \Lambda \mathbf{K}_p$$

if there exists $\sigma > 0$ such that the inequality

$$\mathbf{K}_d - \frac{1}{2} (\Lambda \mathbf{M}(\mathbf{q}) + \mathbf{M}(\mathbf{q}) \Lambda) - \frac{1}{4} (\mathbf{C} \mathbf{K}_d^{-1} \mathbf{C}) > \sigma \mathbf{I}_n \quad (5)$$

verifies along the actual trajectory. \square

This theorem gives sufficient conditions for exponential stability and may be used for initial (off-line) setting of the gains. For lack of space proofs of Theorem 1 and Theorem 2 are not quoted here. The reader is kindly directed to references [5, 6] instead. It should be noted that the direct method of *Lyapunov* is used to the purpose. Energy-like *Lyapunov* functions prove to be very suitable for stability analysis of mechanical systems, and the identity (3) is essential in the proofs. In the case of Theorem 2, a *Lyapunov* function is found in the form

$$V_{exp} = \frac{1}{2} (\dot{\mathbf{e}} + \Lambda \mathbf{e})^T \mathbf{M}(\mathbf{q}) (\dot{\mathbf{e}} + \Lambda \mathbf{e}) + \mathbf{e}^T (\Lambda \mathbf{K}_d + \mathbf{K}_d \Lambda - \Lambda \mathbf{M}(\mathbf{q}) \Lambda) \mathbf{e} \quad (6)$$

This function is positive definite if inequality (5) holds.

The feed-forward component of the control (4) cannot be computed unless the structure and the parameters of the inverse model are known. The "true" values of the process parameters are often not known with sufficient accuracy. In addition, some of them may vary during operation in *a priori* unknown manner.

3. Adaptive control approaches

Some of the approaches exploit the linear-in-parameters representation of the inverse dynamics [3]

$$u_{ff} = Y(\ddot{q}_r, \dot{q}_r, \dot{q}, q) \hat{p} = M \ddot{q}_r + C \dot{q}_r + g$$

where \hat{p} is an estimate of the vector of dynamical parameters. Subsequently, the closed-loop system error, $e(t) = q_r(t) - q(t)$, is a function of the parameters error, $\tilde{p} = p - \hat{p}$, and this is used to tune the estimates to their "true" values. Although this is essentially an explicit adaptive control approach, it falls into the group of direct adaptive control, as long as it is based on computer-embedded inverse dynamics model. The generalized scheme of direct adaptive control is shown in Fig. 2. The goal is to reduce the mismatch between the plant output and the output of a reference model (*RM*) when subjected to one and the same reference input q_r . As it is usually assumed, the reference model is identity. The filter (*F*) is essentially of differentiating character and it is designed with respect to closed-loop stability. When the reference model is identity, then the goal $e_f = 0$ relates actually to stable reference phase-plane trajectories. In the particular case under consideration, these trajectories are described by the equation $\dot{e} + \Lambda e = 0$. The guidance of the closed-loop system along these phase-plane trajectories is performed by proper variations of the controller's parameters, p_c , according to the rules of a properly chosen adaptation algorithm (*AA*).

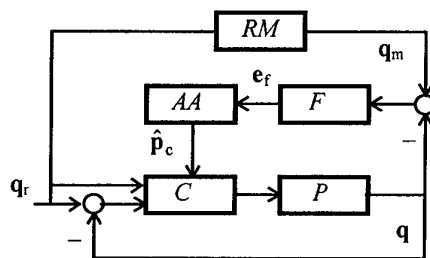


Fig. 2. Direct adaptive control scheme.

Typically, explicit adaptive control is used within the group of indirect adaptive control approaches. An example is the work of Craig *et al.* [1], where the

control synthesis is related to the computed-torque method.

The common advantage of the methods that are based on structurally perfect dynamical model is the opportunity to prove the asymptotical stability of the closed-loop system. However, the amount of calculations, that is necessary to be performed in real time, is too large to allow effective implementations. In addition, the synthesized controller is robot-dedicated and it is with centralized structure.

Actually, decentralized controllers are used with all commercially available robots. Therefore, the development of decentralized adaptive controllers is of practical interest. The prevailing part of adaptive control approaches make use of simple dynamical models of individual joint motions, and they are usually models of a second order plant. The parameters of the model are estimated on-line, and subsequently the control is synthesized on the base of the current estimates. Thus, most of these adaptive control approaches are indirect ones.

4. A simple adaptive control

In this section a simple direct adaptive control is discussed. The approach is essentially of the type shown in Fig. 2. However, instead of tuning the controller gains in compliance with the widely accepted practice, here the adaptive tuning relates to the generation and tuning of adaptive signals. This is obtained through some simplifications that prove to be quite adequate.

As a clear result, the gains may be kept constant, so they may be tuned off-line. Thus, it is possible to reduce the undesired effects during the transients, and robust controller design may be used.

The controller in a direct control scheme is with a previously defined structure, but with unknown (or not *a priori* tuned) parameters. The structure of the controller is adopted using the available information about the plant or the experience in the control of similar plants. Concerning mechatronic systems, *PD*, *PI* or *PID* controllers are used quite often. Generally, the feedback control is obtained in the form

$$u = Y(s) p_c, \quad (7)$$

where \mathbf{s} is the vector of output signals, $\mathbf{Y}(\mathbf{s})$ is a known matrix-valued function, defined by the adopted controller structure, and \mathbf{p}_c is the vector of controller parameters.

In case of decentralized control, which is of major interest in this paper, the individual control actions are generated in accordance with the generalized law

$$u_i = \mathbf{g}_i^T \mathbf{s}_i, \quad (8)$$

where u_i is the i -th local control action, \mathbf{g}_i is the vector of local gains, and \mathbf{s}_i is the vector of local signals (outputs) used. For instance, in the case of *PD* control we have

$$u_i = k_{pi} e_i + k_{di} \dot{e}_i \Rightarrow \mathbf{g}_i = \begin{bmatrix} k_{pi} \\ k_{di} \end{bmatrix}; \mathbf{s}_i = \begin{bmatrix} e_i \\ \dot{e}_i \end{bmatrix}. \quad (9)$$

An approach to adaptive adjustment of the *PD* gains is proposed by *Dubowsky* and *DesForges* [9]. Similar issues in direct adaptive control are considered in other references, too, e. g. see [5, 6]. Here we utilize a different approach, which is aimed at the use of the rigorous results for inverse dynamics control, presented in Section 2. The control is generated in accordance with a governing law that bears resemblance with the law (8):

$$u_i = \mathbf{g}_i^T (\mathbf{s}_i + \mathbf{p}_i) = \mathbf{g}_i^T \mathbf{s}_i + \mathbf{g}_i^T \mathbf{a}_i(t), \quad (10)$$

where the second component of the local control is destined to emulate the corresponding entry in the output of the inverse dynamics model, and \mathbf{a}_i is the vector of additional (auxiliary) signals [8], that is to be adaptively tuned in order to obtain stable closed-loop performance. In particular, assume that the local feedback control is with the structure given by (9), where $k_{pi} = \lambda_i k_{di}$, and $\lambda_i > 0$, $i=1,2, \dots, n$, are the diagonal entries of the Λ matrix in (5), chosen in such a way that the inequality (5) of Theorem 2 holds for the particular device and for a set of desired trajectories. Then the control may be represented in the form:

$$\mathbf{u} = \mathbf{K}_p \mathbf{e} + \mathbf{K}_d \dot{\mathbf{e}} + \mathbf{Y} \mathbf{p}_c - \mathbf{Y} \tilde{\mathbf{p}}_c, \quad (11)$$

where $\mathbf{p}_c^T = [\mathbf{a}_1^T, \mathbf{a}_2^T, \dots, \mathbf{a}_n^T]$ is the vector of "true" parameters, $\mathbf{Y} = \text{diag} [k_{d1}, k_{d2}, \dots, k_{dn}]$ is a constant matrix, and $\tilde{\mathbf{p}}_c := \mathbf{p}_c - \hat{\mathbf{p}}_c$ is the parametric error.

Note, that the "true" parameters may be chosen theoretically in such a way that the $\mathbf{Y} \mathbf{p}_c$ component of the control (11) emulates the output of the inverse dynamics model, since the \mathbf{Y} matrix is non-singular. If this is the case, the undisturbed closed-loop system must be exponentially stable, as it follows from Theorem 2. The use of the *decentralized inverse dynamics* model concept [5, 6] is quite satisfactory to the purpose. For lack of space we do not discuss it in details. The concept requires that \mathbf{a}_i ($i=1,2, \dots, n$) be functions of the local reference joint accelerations and velocities. However, in order to simplify the controller structure, the simplest possible structure of these adaptive signals may be assumed. This reduces significantly the number of adaptive parameters per joint, while the performance does not degrade dramatically.

The adaptive adjusting of the adaptive parameters \mathbf{a}_i , $i=1,2, \dots, n$, is performed according to stability requirements, and it is treated in the following section. Actually, these parameters may be treated as additional inputs that are fed into the system.

5. Stability issues

Note that with the control (11) the system (1) may be represented in the generalized closed-loop form

$$\dot{\mathbf{x}} = \mathbf{A}(\mathbf{x}, \mathbf{p}_c) \mathbf{x} + \mathbf{B}(\mathbf{x}, \mathbf{p}_c) \tilde{\mathbf{p}}_c \quad (12)$$

where $\mathbf{x}^T = [\mathbf{e}^T, \dot{\mathbf{e}}^T]$ is the system state. By virtue of Theorem 1 and Theorem 2 this system is stable, provided the "true" parameters emulate perfectly the output of the inverse dynamics model, and the parametric error is zero, i. e. if $\tilde{\mathbf{p}}_c = \mathbf{0}$. Naturally, the "true" parameters should not be constant. However, they are small in amplitude, as demonstrated by previous researches [7, 8]. In order to develop the adaptive tuning of the controller parameters we need a result, outlined by the following lemma.

Lemma. Consider the system (12) where \mathbf{p} is assumed to be a vector of constant but unknown parameters. Let $\Gamma > \mathbf{0}$ be a constant positive definite matrix, and let for the undisturbed system there exists the positive definite quadratic function

$$v = \frac{1}{2} \mathbf{x}^T \mathbf{V} \mathbf{x} \quad (13)$$

where $V = V(x, p_c)$ is a positive definite matrix, such that its derivative is negative definite along the actual trajectory:

$$\dot{V} = -\frac{1}{2} x^T W x \quad (14)$$

where $W = W(x, p_c)$ is a positive definite matrix. Then the application of the updating law

$$\dot{\hat{p}}_c = \Gamma B^T V x(t) \quad (15)$$

makes the state $x = 0$ an asymptotically stable equilibrium of the closed-loop system. \square

Proof. The direct method of *Lyapunov* is used and the proof is given schematically. Consider the quadratic positive definite function

$$v_a = \frac{1}{2} x^T V x + \frac{1}{2} \tilde{p}_c^T \Gamma^{-1} \tilde{p}_c$$

which is a legitimate *Lyapunov* function candidate. Its derivative proves to be

$$\dot{v}_a = -x^T W x + \tilde{p}_c^T (B^T V x + \Gamma^{-1} \dot{\tilde{p}}_c) \quad (16)$$

Taking into account that $\dot{\tilde{p}}_c = -\dot{\hat{p}}_c$, since the "true" parameters are constant, as well as the updating law (15), the derivative reduces down to

$$\dot{v}_a = -x^T W x.$$

Thus, the derivative is a negative definite function of x . Therefore, $x(t)$ tends to zero asymptotically. \square

It is important to note that if the "true" parameters are not constant, then the derivative (16) is

$$\dot{v}_a = -x^T W x + \tilde{p}_c^T \Gamma^{-1} \dot{\tilde{p}}_c.$$

Therefore, the equilibrium $x = 0$ is no longer asymptotically stable. However, it proves to be practically stable, i. e. the state tends to some vicinity of the origin as the time tends to infinity. The corresponding region depends on the parametric error, as well as on its derivative.

Taking into account the result outlined by the *lemma*, and on the base of the energy-like *Lyapunov*

function (6), applied to the system (1) with the control parameterization (10)–(11), the adjusting of the parameters is obtained in the form

$$\dot{\hat{p}}_c = \Gamma Y^T e_f(t), \quad (17)$$

where Γ is a properly chosen diagonal positive definite matrix and $e_f(t) := \dot{e}(t) + \Lambda e(t)$ is the "filtered error" (Λ is the diagonal and constant positive definite matrix introduced earlier).

Usually, the adaptation gains are considered as "magic" parameters, and their proper values are found by experience. However, the adaptation gains may be subjected to adaptive variations, too. This aspect is not considered here, since the related theory is too complex.

6. Self-learning issues

The perfect match of adaptive and self-learning (or repetitive) control has been put forward by some authors, e. g. see [11]. The type of control presented here has a very easy and natural issue to self-learning control [10]. Note that the adaptive control parameters may be treated as signals additional to the reference inputs.

The main idea is illustrated by a simple paradigm. Using fixed gains and no adaptation in the control there should be tracking error, i. e. the actual trajectory will differ from the reference one. However, there exists a *modified* reference trajectory such that it will result in exactly the goal (non-modified) trajectory.

This *modified* trajectory can be obtained on the base of the adaptive control. The modified trajectory is obtained in the following iterative way

$$\bar{q}_r(t, k) = \bar{q}_r(t, k-1) + \bar{a}(t, k)$$

where k is the pass number, $\bar{q}_r(t, 0) = q_r(t)$, and the additive component is obtained on the base of the adaptive control. In the case of *PD* control, where the gain matrices are related by $K_p = \Lambda K_d$, the additive component proves to be a solution of the following differential equation:

$$\dot{\bar{a}}(t, k) = \hat{p}_c(t, k-1) - \Lambda \bar{a}(t, k)$$

where $\hat{p}_c(t, i)$ is the vector of adaptive parameters obtained during pass i . The use of self-learning control in a combination with adaptive control of the type presented here yields very good results especially with smooth reference trajectories.

An important advantage comes from the fact that the additional inputs can be easily truncated in order to keep the transients within the limits. Unlike the typical self-learning techniques, here the feed-forward component of the control is expressed in terms of additive reference trajectory.

7. Conclusion

The article treats a direct adaptive control technique that is based on decentralized fixed-gain control, alike the one used with all commercially available robot controllers. Such type of control results in an inherently parallel modular structure of the controller, which is most practical. The technique falls into the group of *simplified adaptive control* [4], and it can be easily implemented, since there is no need of extensive computational capacity and the sampling rate can be easily kept sufficiently high.

The control presented here is based on adaptive variation of signals rather than gains and it is closely related to standard fixed-gain feedback control, in contrast to the well known adaptive control approaches with proven asymptotically stable equilibrium state (see [1] – [3]), where the use of computer-embedded model is essential. The experimental investigations show that the adaptive control based on auxiliary signals is a much better choice, when compared to decentralized control with variable adaptive gains.

Better experimental results are obtained with higher sampling rates. The computational scheme is rather simple, and it allows higher sampling rates be realized easily.

Acknowledgments

This work is supported by the National Research foundation of Bulgaria under grant No. TH 501/95, as well as by the National Fund for Technology policy of Bulgaria under grant No. 5033/99.

References

- [1] J. J. Craig, P. Hsu, and S. S. Sastry, "Adaptive control of mechanical manipulators", *The Int'l J. of Robotics Research*, 6, No. 2, pp. 16–28, 1987.
- [2] C. A. Canudas de Wit, *Adaptive Control of Partially Known Systems: Theory and Applications*, Vol. 7 of *Studies in Automation and Control*, Elsevier, 1988.
- [3] J.-J. Slotine and W. Li, "Putting physics in control: The example of robotics", *IEEE Control Systems Magazine*, 8, No. 6, pp. 12–77, 1988.
- [4] I. Bar-Kana and A. Guez, "Simplified techniques for adaptive control of robotic systems", *J. of Control and Dynamic Systems*, No. 40, pp. 147–203, 1991.
- [5] V. Balavessov, *Decentralized Direct Adaptive Control of Manipulation Robots*, Ph. D. Thesis, Institute of Mechanics, Bulgarian Academy of Sciences, 1994.
- [6] V. Balavessov, "Predictive adaptive control of robots with unknown dynamics", *J. Theoretical and Appl. Mechanics*, 1993, Year XXIV, No. 4, pp. 35–45.
- [7] V. Balavessov, "Adaptive control of mechatronic systems", *Proc. NATO ASI on Computational methods in Mechanisms*, Varna, Bulgaria, June, 1997, Vol. 2, pp. 451–460.
- [8] V. Balavessov, "Direct adaptive control of robots by means of auxiliary signals", *Problems of Engineering Cybernetics and Robotics*, 47, Sofia, 1998, pp. 3–10.
- [9] S. Dubowsky and D. DesForges, "The application of model-referenced adaptive control to control of robotic manipulators", *ASME J. of Dynamical Systems, Meas., and Control*, 101, 1979, pp. 193–200.
- [10] S. Arimoto, S. Kawamura, and F. Miyazaki, "Bettering operations of robot arms by learning", *J. of Robotic Systems*, 1984, 1, pp. 123–140.
- [11] M.-C. Tsai, and M. Tomizuka, "Model-referenced adaptive control and repetitive control for robot manipulators", *Proc. IEEE International Conf. on Robotica and Automation*, 3, pp. 1650–1655.
- [12] V. Galabov, I. Avramov, Z. Sotirov, V. Michailov, and J. Deianov, "Mechatronic concept in the structural and functional design of mechanisms", *Proc. International Conf. On Recent Advances in Mechatronics, ICRAM'95*, Vol. 2, 1995, Istanbul, Turkey, pp. 784–789.

Neural Decomposed Computed Torque/Adaptive Control of Robot Manipulators

M.Kadri, B.Bouzouia and N.Louam

*Centre de Développement des Technologies Avancées.
Laboratoire de Robotique et d'Intelligence Artificielle
128 Chemin Mohammed Gacem, BP 245 El-Madania Alger.
E-mail. bouzouia@hotmail.com*

Abstract

This paper presents a new robot controller based on artificial neural networks (ANNs) and capable to compensate changes in inertial model parameters. The approach involved uses a decomposition of the computed torque method into two parts, fixed and variable. The both fixed and variable torque are generated by an ANN. Another ANN is employed to estimate the inertial parameters. The inputs are fed to ANN to the variable torque as in the case of a conventional feedforward controller. To reduce the tracking error due to unmodeled dynamics and frictions we use a decentralized adaptive PD controller. High tracking performance from the proposed control approach are shown by the results of simulation and compared with the conventional computed torque method.

1. Introduction

For the past several years, the neural computation approach has emerged [1, 2, 3, 4, 5] to tackle problems for which several conventional computational approaches have been proven ineffective. Hence, there have been a lot of interests in applying artificial neural networks (ANNs) to solve the problems of identification and control of complex nonlinear system by exploiting the nonlinear abilities of the ANN [3, 5, 6, 7].

The robot manipulator control is often confronted with the highly complex nature of robot dynamics which present uncertainties like [8, 9, 10]:

- Imprecision on the inertial and geometrical parameters.
- Payload variations.
- Imprecision on the unmodeled dynamics.

The fundamental approach for robot manipulator control is the model-based computed torque control scheme [11] as shown in Figure 1. This control

technique can offer some required qualities, of robustness and precision if the robot model will be accurate. Variations of this basic idea can be found in other designs [12, 13]. ANN can also be trained off-line to learn the nonlinear robot dynamics, and then is used to implement the computed torque controller with further on-line modifications to account for uncertainties. However, the difficulty in implementing this approach is met in the important time required to update on-line the weights. Furthermore, this approach can not overcome the large variation of parameters in the dynamic model.

The adaptive control could be felt an attractive solution to control robot manipulator since it does not require an accurate model [14, 15]. However, as well known, it can not perform good results at high speed. In addition, a general drawback of an adaptive scheme is that the computational requirements for real-time parameters identification, and sensitivities to numerical precision and observation noise, increases undesirably with the number of the system state variables [7].

To include parameter estimation in the derivation of the robot control scheme, Leahy et al [16] have proposed an adaptive model-based neural network controller (AMBNNC) incorporating a neural network trained to provide a feedforward model with a payload mass estimator.

The feedforward torque adaptation is performed using the tracking error. But, this can mislead payload mass estimation since this error may be due to other perturbations such as frictions.

In this paper we investigate a new robot control technique as depicted in Figure 2. This control approach is different from that of Figure 1. It is proposed in the present work a decomposition of dynamic model into parts, fixed and variable. ANNs, are used to map the both parts. The fixed part, containing the constant term provide the nominal torque based on the dynamic model. The variable part, permits the tracking of the inertial parameters variation. This decomposition should

provide benefits in the reduction of the ANN size and avoid the need for an on-line adaptation of the ANN weights. Also, to reduce influence of other perturbations, like wise unmodeled dynamics, a decentralized adaptive proportional-derivative (PD) controller has been used and its output is added to the feedforward torque.

The structure of the paper is as follows. In Section 2 the robot dynamic model is mentioned. Section 3 presents the computed torque control. The proposed Neural Decomposed Adaptive Dynamic Control is described in Section 4. Simulation results of the proposed technique and a comparison with the computed torque method of a two-link direct drive manipulator are given in section 5. Section 6 draws some conclusions.

2. Robot Dynamic Model

The dynamics of an n -joints robot manipulator can be described by the nonlinear and coupled second order vector differential equation:

$$T = M(\theta)\ddot{\theta} + C(\theta, \dot{\theta}) + G(\theta) + F(\dot{\theta}) \quad (1)$$

where θ is the $n \times 1$ vector of joint angular positions, T is the $n \times 1$ vector of applied joint torque, $M(\theta)$ is the $n \times n$ symmetric positive-definite inertia matrix, $C(\theta, \dot{\theta})$ is the $n \times 1$ coriolis and centrifugal torque vector, $G(\theta)$ is the $n \times 1$ gravity loading vector, and $F(\dot{\theta})$ is the $n \times 1$ frictional torque vector. For convenience, let us denote $H(\theta, \dot{\theta}) = C(\theta, \dot{\theta}) + G(\theta)$ so that (1) can be rewritten as :

$$T = M(\theta)\ddot{\theta} + H(\theta, \dot{\theta}) + F(\dot{\theta}) \quad (2)$$

The robot dynamic equation (2) is highly nonlinear and coupled multi-input multi-output system. In most practical cases, the model is affected by some uncertainties due to the imprecision on the model parameters [17].

3. Neural Computed Torque Control

The model-based computed torque method [12, 13, 17] is the basic approach to robot control. The control law can be written as :

$$T = \hat{M}(\theta)u + \hat{H}(\theta, \dot{\theta}) \quad (3)$$

where $\hat{M}(\theta)$ and $\hat{H}(\theta, \dot{\theta})$ are estimates of $M(\theta)$ and $H(\theta, \dot{\theta})$, and u is given by

$$u = \ddot{\theta} + K_p(\theta_d - \theta) + K_v(\dot{\theta}_d - \dot{\theta}) \quad (4)$$

where K_p and K_v are $n \times n$ symmetric positive definite gain matrices. Combining (2), (3), and (4) yields the closed loop dynamic equation

$$\ddot{e} + K_v\dot{e} + K_p e = \hat{M}^{-1}(\Delta M(\theta)\ddot{\theta} + \Delta H(\theta, \dot{\theta}) + F(\dot{\theta})) \quad (5)$$

where

$$\Delta M(\theta) = M(\theta) - \hat{M}(\theta), \Delta H(\theta, \dot{\theta}) = H(\theta, \dot{\theta}) - \hat{H}(\theta, \dot{\theta}), \text{ and } e = (\theta_d - \theta). \text{ If } \hat{M} = M, \hat{H} = H, \text{ and } F = 0 \text{ then equation (5) becomes the following ideal second order equation :}$$

$$\ddot{e} + K_v\dot{e} + K_p e = 0 \quad (6)$$

where K_p and K_v can be chosen to achieve decoupled critically-damped or over-damped system response.

Since there are always uncertainties in the robot dynamic model, the ideal error response (6) can not be achieved and the performance is degraded as indicated in (5). Thus the computed torque based control is not robust in practice[17].

4. Neural Decomposed Adaptive Computed Torque Control

A new robot control scheme is proposed in this paper as depicted in Figure 2. The basic concept of this scheme is that the dynamic model of robot is decomposed into two parts :

Part-1 is fixed and contains terms with fixed inertial parameters.

Part-2 is variable and contains terms with variable inertial parameters.

Thus, the feedforward torque is given by :

$$T = T_1 + T_2 \quad (7)$$

$$T_1 = M_1(\theta_d, P_f)U + H_1(\theta_d, \dot{\theta}_d, P_f) \quad (8)$$

$$T_2 = M_2(\theta_d, P_v)U + H_2(\theta_d, \dot{\theta}_d, P_v) \quad (9)$$

Where T_1 is the $n \times 1$ vector of the fixed torque and T_2 is the $n \times 1$ vector of the variable torque. M_1 and H_1 are respectively, the inertial matrix and the coriolis and centrifugal vector containing fixed parameters. M_2 and H_2 are, respectively, the inertial matrix and the coriolis and centrifugal vector containing parameters. P_f is the vector of the fixed inertial parameters, and P_v is the vector of variable inertial parameters as a function of time. U is given by

$$U = \ddot{\theta} + T_{fb} \quad (10)$$

This decomposition has the advantage of simplifying the problem by avoiding the need of a precise model. In that, the partial robot dynamic knowledge can be sufficient for the fixed part to provide the nominal torque. The variable part, based on parameter estimation, compensates high changes in the system dynamic during the robot motion.

Two ANNs are trained off-line to map M_1 and H_1 of the fixed torque T_1 . The variable torque T_2 is determined as a conventional feedforward controller using the propriety of being linear in its parameters [9,10]. Consequently, equation (10) can be rewritten as

$$T_2 = (M_{2inf}(\theta)U + H_{2inf}(\dot{\theta}, \ddot{\theta}))P_v \quad (11)$$

where $M_{2inf}(\theta) + H_{2inf}(\dot{\theta}, \ddot{\theta})$ represents the $n \times m$ kinematic information matrix that describes the motion of links and also referred to, in the literature, as the observation matrix. Each element P_{vi} of the vector P_v can be an independent parameter or a linear combination of others parameters.

In the present case an ANN can be used as usual to map the variable torque. However, it will necessary be of an important size which may further increase with the complexity of the variable torque terms.

But, by employing the linear propriety in the parameters of the variable torque one can reduce the neural network size. Hence, the ANNs are not used to map the whole variable torque as in [18] but only M_{2inf} and H_{2inf} which includes the nonlinear terms [19]. So, as shown in equation (11), the variable torque will be computed with the ANN output and the parameters estimation.

The parameter estimator uses a multilayer ANN trained off-line in order to determine the value of the variable parameters during manipulator motion. The inputs, fed to the neural nets during the training, are vectors containing normalized values of the position, velocity, acceleration and applied torque. Notice that the parameters estimation acts here as a dynamical control since it allows the variable torque to track changes in the system dynamic.

To deal with unmodeled uncertainties and other perturbation on the robot system a decentralized adaptive PD control action is added to the feedforward control part. This adaptive action has been used by Seraji [20] who considered each joint as a subsystem with inertial coupling, Coriolis, centrifugal, friction, and gravity terms as in the equation (2).

The adaptive feedback independent joint controller dedicated to the i th joint is described by

$$T_{fb_i} = k_{pi}(t)e_i(t) + k_{vi}(t)\dot{e}_i(t) \quad (12)$$

where $e_i(t)$ and $\dot{e}_i(t)$ are the position and velocity tracking errors of the i th joint.

The feedback controller adaptation law which ensures asymptotic trajectory tracking is based on the weighted error $r_i(t)$ described as follows [20]:

The weighted error and the feedback gains are given by the expressions below :

$$r_i(t) = G_{pi}e_i(t) + G_{vi}\dot{e}_i(t) \quad (13)$$

$$k_{ij}(t) = k_{ij}(0) + \alpha_{ij} \int_0^t r_i(t)e_i^{(j)}(t)dt \quad j=0,1 \quad (14)$$

where α_{ij} are any positive scalar integral adaptation gains, and $\{G_{pi}, G_{vi}\}$ are positive scalar weighting factors which reflect the relative significance of the position and velocity errors. The superscript " (j) " denote the j th derivative with respect to the time parameter, and is $e_i^{(1)} = de_i/dt$.

In our case $e_i^{(0)}$ and $e_i^{(1)}$ are the position error e_i and the velocity error \dot{e}_i , respectively.

In digital control implementation, the auxiliary signal and the feedback gains controller, at each sampling instant N , are obtained from equations (9) and (10) by the following simple recursive adaptation procedure [20]:

$$r_i(N) = G_{pi}e_i(N) + G_{vi}\dot{e}_i(N) \quad (15)$$

$$\begin{aligned} k_{pi}(N) &= k_{pi}(N-1) + \alpha_{pi}[r_i(N)e_i(N) + r_i(N-1)e_i(N-1)] \\ k_{vi}(N) &= k_{vi}(N-1) + \alpha_{vi}[r_i(N)\dot{e}_i(N) + r_i(N-1)\dot{e}_i(N-1)] \end{aligned} \quad (16)$$

This decentralized feedback control can highly fast be computed since the controller gains are obtained from simple adaptation laws. Also, here the feedback control action can be evaluated very rapidly than the conventional adaptive algorithms. Finally, this feedback controller has a very simple structure with an auxiliary signal and an adaptive position-velocity feedback gain.

5. Simulation Results

Simulations were done to verify the proposed approach and to compare it with the neural computed torque method. A two link robot manipulator whose parameters are taken from the first two links of PUMA 560 robot are used for simulation studies [20]. For our

application we consider only the payload mass variation as parameter to estimate and the friction parameters as perturbation on the system. To implement the computed torque control two different ANNs NN1, NN2 are used to identify the inertial matrix, the coriolis and centrifugal term, respectively. Both the two networks are multilayered where the structures are (2/8/4) and (4/20/10/2) for NN1 and NN2, respectively. The PD gains are selected as $k_p=100$ and $k_v=60$ for each joint. To implement the proposed approach we use multilayer neural networks to map M_1 and M_{2inf} , have the same size with 2 input nodes, 8 nodes in the hidden layer and 4 nodes in the output layer. Also H_1 , and H_{2inf} have the same size with 4 input nodes, 20 hidden nodes and 2 output nodes. The neural network estimator must provide the payload mass value. It consist of 6 input nodes, 20 nodes per each of two hidden layers, and 1 output node. The all ANNs are trained on a random data uniformly distributed. After more trial, the adaptation gains for the decentralized adaptive PD action are chosen as show in table I.

Table I.
Adaptation gains parameters.

Joint	G_p	G_v	k_{p0}	k_{v0}	r_0	α_0	α_1
1	40	30	40	30	0	100	800
2	40	30	40	30	0	100	800

Figures (3-10) show the simulation results of trajectories control by the computed torque method and the proposed control approach. For comparison, Figure 3 and 4 show the obtained position trajectory for joint 1 and 2. We establish that the both methods provide a good trajectory tracking. But the neural adaptive dynamic control performed better than the computed torque method as prove in Figures 5 and 6, where the errors position obtained by the computed torque method is more important than those obtained by the proposed approach. These performances were again confirmed by the velocity trajectories as show in Figures (7-10). We have remarked that maximum errors correspond with the abrupt change in the payload mass.

6. Conclusion

A new neural network control for robot manipulator is presented in this paper. Unlike the classic computed torque method the decomposition of the robot dynamic model, in the proposed approach, into fixed and variable parts has provide a better robustness via the change in the variable dynamic parameters. The decentralized adaptive PD compensator was able to overcome the

errors due to the unmodeled dynamic (frictions in our case) and the estimation errors.

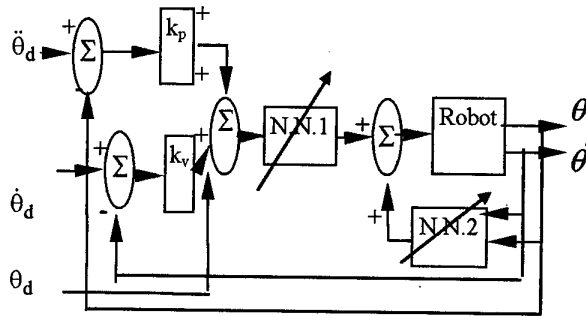


Figure 1. Neural Computed Torque Control.

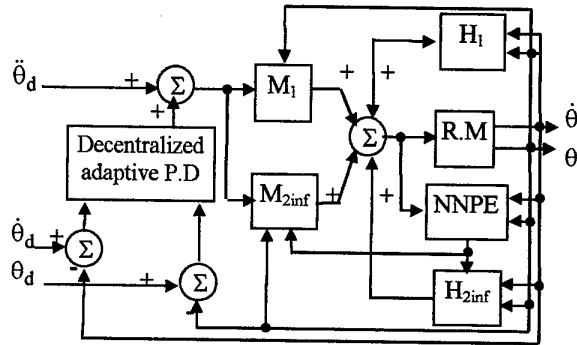


Figure 2. Neural Decomposed Adaptive Computed Torque Control.

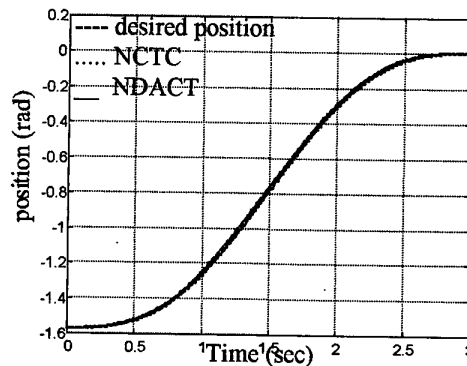


Figure 3 position of joint 1

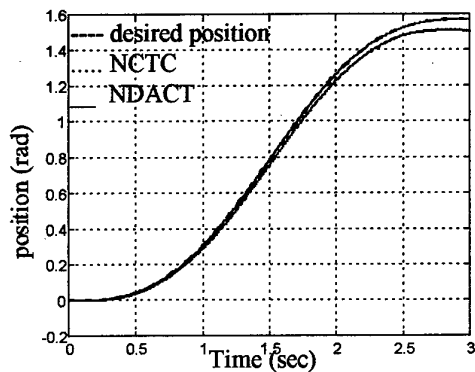


Figure 4 position of joint 2

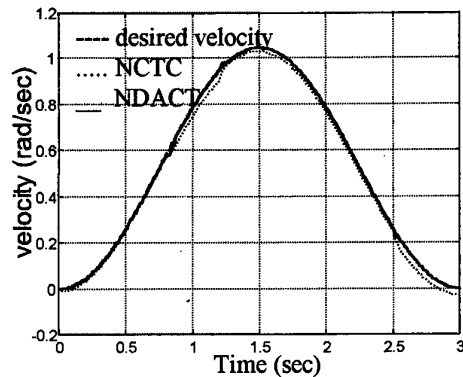


Figure 8 velocity of joint 2

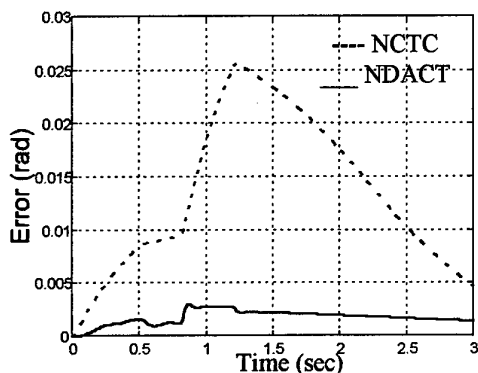


Figure 5 position error of joint 1

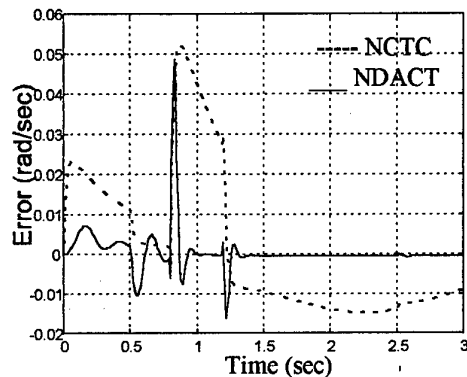


Figure 9 velocity error of joint 1

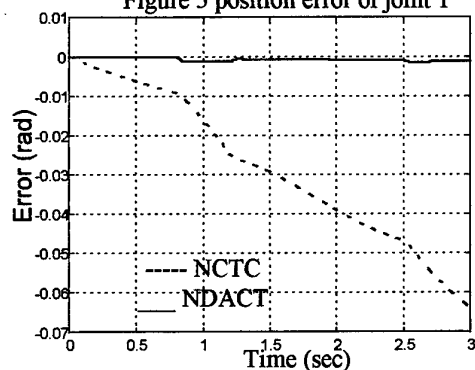


Figure 6 position error of joint 2

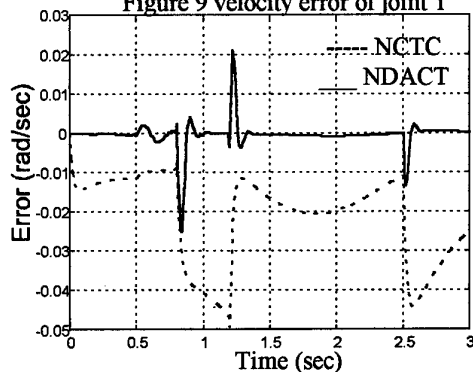


Figure 10 velocity error of joint 2

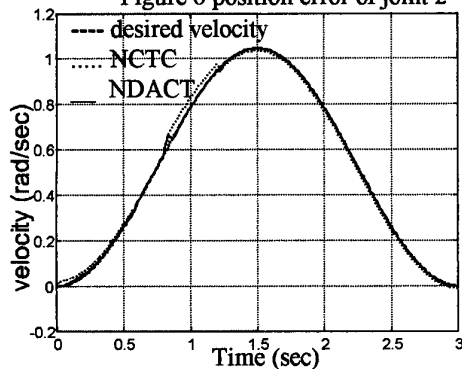


Figure 7 velocity of joint 1

7. References

- [1] B. Widrow, and M.A. Lehr, "30 years of adaptive neural networks : Perceptron, madaline, and backpropagation" *Proc. of IEEE*, Vol 78, pp 1415-1441, 1990.
- [2] R. P. Lippmann, " An introduction to computing with neural nets" *ASSP. Mag.*, Vol 4, pp 4-22, Apr 1987.
- [3] K.S. Narandra, and K. Parthasarathy, "Identification and Control of Dynamical System Using Neural Networks", *IEEE Trans. on NN*, Vol.1, No.1, pp 4-27, 1990.
- [4] T. T. Jervis, *Connectionist Adaptive Control*, PhD thesis, Cambridge University, Engineering Department, Trumpington Street, Cambridge, England, 1993.

- [5] D. Psaltis, A. Sideris, and A. Yamamura, "A multilayered Neural Network Controller", *IEEE Control Systems Magazine*, Vol 8, No.2, pp 17-21, 1988.
- [6] M. Kawato, Y. Uno, M. Isobe, and R. Suzuki, "Hierarchical Neural Network Model for Voluntary Movement with Application to Robotics", *IEEE Control Syst. Magazine*, Vol.8, No.2, pp8-16, 1988.
- [7] W.T. Miller, R.P. Hewes, F.H. Glanz, and L.G. Kraft, "Real-Time Dynamic Control of an Industrial Manipulator Using a Neural Network Based Learning Controller", *IEEE Trans. On Rob. and Aut.*, Vol.6, No.1, 1990, pp 1-9.
- [8] P. K. Khosla, "Categorization of parameters in the dynamic robot model," *IEEE Trans. on Rob. and Aut.*, 5, 261-268, 1989.
- [9] Z. Lu, K. B. Shimoga, and A. A. Goldenberg, "Experimental Determination of Dynamic Parameters of Robotic Arms," *J. of Rob. Syst.*, vol 10, No 8, pp1009-1029, 1993.
- [10] B. Bouzouia, "Identification of constant and variable parameters of robot manipulator", *Research Report LAAS*, No. 87 054, 1987.
- [11] R.P. Paul, *Robotic Manipulators - Mathematics, Programming and Control*, MIT Press, 1981.
- [12] T. Ozaki, T. Suzuki, T. Furuhashi, S. Okuma, and Y. Uchikawa, "Trajectory Control of Robotic Manipulators Using Neural Networks" *IEEE Trans. On Ind. Elec.*, Vol. 38, No. 3, pp 195-202, 1991.
- [13] A. Ishiguro, T. Furuhashii, S. Okuma and Y. Uchikawa, "A Neural Networks Compensator for Uncertainties or Robot Manipulator" *IEEE Tans. On Industrial Electronics*, 39, pp 61-66, Dec. 1992.
- [14] S. Tosunoglo and D. Tesar, "A Survey of Adaptive Control Technology in Robotics," *NASA Workshop on Space Telerobotics*, Pasadena, California, January 1987.
- [15] T. C. Hsia, "Adaptive Control of Robot Manipulators - A Review," *Proc. IEEE Conf. On Rob. and Aut.*, pp 183-189, 1986.
- [16] M.B.Jr. Leahy, M.A. Johnson, and S.K. Rogers, "Neural Network Payload Estimation for Adaptive Robot Control", *IEEE Trans. on NN*, Vol.2, No.1, 1990, pp93-100.
- [17] S. Jung and T.C. Hsia, "A new neural network control technique for robot manipulators", *Robotica*, Vol. 13, 1995, pp 477-484.
- [18] J.D. Yegerlehner, P.H. and Meckel, "Experimental Implementation of Neural Network Controller for robot undergoing Large Payload changes", *Proc IEEE Int. Conf Rob. and Aut.*, 1993, Vol.2, pp 744-749.
- [19] D. Katić, and M. Vokobratović, "Decomposed Connectionist Architecture for Fast and Robust Learning of Robot Dynamics," *Proc. IEEE Conf. On Rob. and Aut.*, pp 2064-2069, 1992.
- [20] H. Seraji, "Decentralized Adaptive Control of Manipulators: Theory, Simulation, and Experimentation." *IEEE. Trans. on Robotics and Automation*, Vol.5, No.2, 1989, pp 189-201.

Adaptive Control for Flexible Manipulators

Reza Fotouhi-C.

Walerian Szyszkowski

Peter N. Nikiforuk

Mechanical Engineering Dept., University of Saskatchewan, Saskatoon, Canada S7N 5A9

ref260@engr.usask.ca

szyszkow@engr.usask.ca

nikiforu@engr.usask.ca

Abstract

This paper provides a summary of research done on the adaptive control of flexible manipulators. Such manipulators, due to their generally lighter masses, should be of particular interest in space applications.

1. Introduction

Rigid robot control is based on the assumption that the transmissions are stiff and that the links are rigid. Such manipulators are heavy (load-carrying capacity is typically 5% to 10% of their own weight [1]), consume considerable power, and are generally impractical for high speed maneuvers. On the other hand, light manipulators have links that deform significantly in high speed operations and therefore their flexibility cannot be ignored. Flexibility can also be present in the joints; that is, gear elasticity, flexibility in the transmissions between actuators and links, shaft wind up, etc. Mechanical flexibility often generates severe problems for such controllers due to structural vibrations. Two approaches have been used for vibration reduction: input command pre-shaping [2] and closed-loop feedback [3]. If the controller was designed with the assumption of perfect rigidity, flexibility in the links or joints can decrease tracking capabilities and cause instability. Therefore flexibilities should be taken into account in the controller design. In addition, for flexible systems the number of degrees of freedom, which theoretically for a continuous system becomes infinite, exceeds significantly the number of actuators and the number of output variables. This introduces some extra constraints affecting the control strategy (under-actuated control system).

2. Control of flexible manipulators

Due to the complexity of the dynamics of manipulators with both joints and links flexibility, many researchers have considered only link flexibility [2, 4, 5, 6, 7], or

only joint flexibility [8, 9, 10, 11, 12], or some special case with only one flexible link [13, 14, 15, 16]. However, some have considered both joint and link flexibility [17, 18].

Several general approaches to the control of flexible robots have been reported such as feedback linearization [19] which is computationally expensive, and singular perturbation techniques [3] which are applicable to manipulators with small flexibility effects. Some more specific methods have been presented in [20], where the transfer function approach was used for single-link flexible arm control and in [21], where a pseudo-link approach was employed. A method called adaptive computed reference computed torque control was proposed in [17]. This approach will be discussed here in detail.

A digital adaptive controller for a two-link flexible manipulator with one rigid link and one flexible link was given in [16]. The manipulator operates in a gravitational field and a finite element model with three elements represented the flexible link. The adaptive control algorithm was indirect; that is, the control law at each sampling time was based on a prediction model of the plant whose time-varying parameters were estimated adaptively. A composite adaptive control (a mixture of joint subsystem-based adaptive control and simple flexible fixed-gain feedback) for flexible-link manipulators was presented in [5]. Linear parameterization was used to design an adaptive law for identifying the unknown parameters (payload mass) of a flexible manipulator. In [4] an adaptive controller, based on an approximate set of dynamic equations, was developed for a flexible manipulator with revolute joints carrying a rigid large uncertain payload. Given these equations, a globally stable tracking of the end-effector was established. The concepts of filtered error and a passivity theorem were used in developing the adaptive law. Experimental results for a two-link flexible manipulator with adaptive nonlinear control and pre-shaping were reported in [2]. The input pre-shaping scheme, which is an open-loop controller, adjusted the input command to the manipulator so that vibrations were eliminated.

Hybrid adaptive control algorithms for two-link flexible manipulators were presented in [14]. The authors claimed that the hybrid adaptive control is superior to pure continuous-time or discrete-time adaptive control, because the infrequent adjustment of the control parameters makes it more robust than these adaptive control techniques. The hybrid adaptive control systems operate in continuous time, while the control parameters are updated only at discrete instants. In [6] a task-level learning control problem was considered. This control problem can be formulated as an online nonlinear least square parametric optimization problem. The learning was performed in the course of the normal operation of the manipulator. An adaptive control scheme for flexible joint robot manipulators was presented in [9]. Asymptotic stability was ensured regardless of the joint flexibility using the passivity property. In [22] an adaptive variable structure scheme was proposed for the control of a flexible robot manipulator. All of the nonlinear dynamics of the system were all taken into account in the design of the control system. To alleviate chattering, a phenomenon that is commonly experienced in variable structure type of control, a saturation type adaptive scheme was proposed. In [23] the adaptive hybrid control of constrained nonlinear robots with flexible links was studied. For the analysis and the design of a controller for the flexible manipulator, a singular perturbation approach was used. According to the physical properties of a flexible manipulator, a two time-scale approach, namely the singular perturbation approach, was further utilized for analysis and general controller design. For demonstration of the controller performance, experiments of a two-link flexible manipulator were performed for the proposed controller and satisfactory results observed. In [15] the control of the tip position of a flexible manipulator carrying variable payload was considered. An approach to adaptive decentralized control for flexible joint robots based on adaptive observer technique was presented in [10]. A two-level adaptive control scheme was used to guarantee the trajectory tracking and the stability of the control system. The problem of endpoint position control for a planar manipulator which has two very flexible links was considered in [7]. The experimental model was used in a fixed controller as well as in a self-tuning one with unknown mass at the tip of manipulator. The design of a hybrid passive/adaptive controller for a single flexible link manipulator with a payload mass was discussed in [13]. A robust adaptive design procedure for flexible joint manipulators was developed in [8]. It was claimed that the scheme guarantees a robust performance even if the Coriolis, centrifugal, and friction terms in the manipulator dynamics were unknown.

2.1. Manipulators with flexible joints and links

A control technique for the motion of flexible manipulators presented in [17] took into account both joint and link flexibility. This technique can be applied in adaptive form if the slow changing robot parameters were unknown. The method was called *adaptive computed reference computed torque control*. The proposed method resulted in trajectory tracking while all state variables remained bounded. A block diagram of adaptive computed reference computed torque control for trajectory following is shown in Figure 1. The idea of computed torque control used for flexible manipulators in [17] was originally proposed in [24] for rigid manipulators.

The following is a brief description of the technique taken from [17]. Due to link/joint flexibility the number of degrees of freedom, n , is larger than the number of actuators, m . A general model for the dynamics of m -link flexible manipulators with revolute joints can be written in the form

$$H\tau = M\ddot{\varphi} + C\dot{\varphi} + G \quad (1)$$

where φ is the generalized coordinates, $\tau \in R^m$ is vector of the actuator torques, $H = H(\varphi)$ is the distribution matrix with the full rank m , the vector $G = G(\varphi, \dot{\varphi}, P)$ includes the gravity, damping, link and joint flexibility, $M = M(\varphi, P)$ is symmetric positive definite inertia matrix, $C = C(\varphi, \dot{\varphi}, P)$ accounts for the Coriolis and centrifugal forces and P is the r -vector of unknown parameters. Like for the rigid manipulator, the matrix $Y = M - 2C$ is skew-symmetric; that is, $Y_{ij} = -Y_{ji}$, and consequently $\dot{\varphi}^T Y \dot{\varphi} = 0$.

To eliminate problems related to the under-actuated systems, the generalized coordinates can be chosen such that $\varphi_k \in R^m$ is referred to as the vector of the rigid-body coordinates and $\varphi_u \in R^{n-m}$ is the vector of flexible coordinates such that

$$\varphi = L_k \varphi_k + L_u \varphi_u \quad (2)$$

where $[L_k \ L_u]$ is a permutation matrix. Then, the goal is that φ_k tracks the desired trajectory φ_{kd} , while φ_u and $\dot{\varphi}_u$ remain bounded. If $e_k = \varphi_{kd} - \varphi_k$ is the tracking error, then the reference trajectory, φ_{kr} , and reference error, e_{kr} , are defined as

$$\dot{\varphi}_{kr} = \dot{\varphi}_{kd} + \Psi_k e_k \quad e_{kr} = \varphi_{kr} - \varphi_k \quad (3)$$

where Ψ_k is a positive definite matrix, and $\varphi_{kr}(0) = \varphi_k(0)$. Similarly, assuming that a bounded desired trajectory φ_{ud} can be determined, and that $e_u = \varphi_{ud} - \varphi_u$ is the associated tracking error, the reference trajectory, φ_{ur} , and reference error, e_{ur} , can be defined then

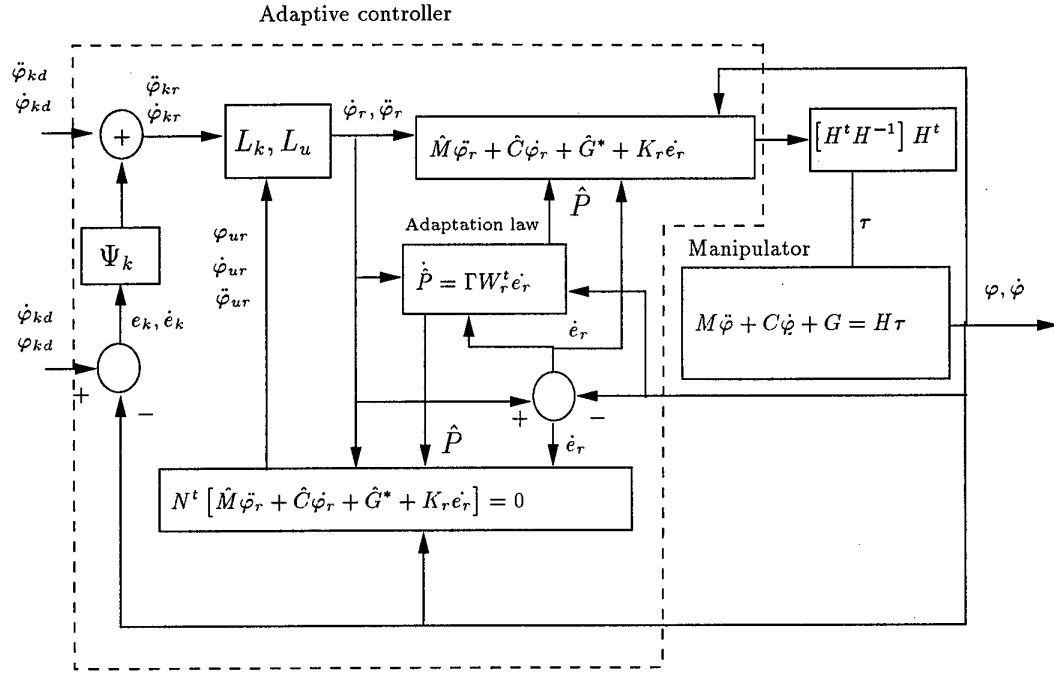


Figure 1: An adaptive controller for flexible manipulators.

as

$$\dot{\varphi}_{ur} = \dot{\varphi}_{ud} + \Psi_u e_u \quad e_{ur} = \varphi_{ur} - \varphi_u \quad (4)$$

where Ψ_u is a positive definite matrix, and $\varphi_{ur}(0) = \varphi_u(0)$. The total reference trajectory, φ_r , and total reference error, e_r , were given as

$$\varphi_r = L_k \varphi_{kr} + L_u \varphi_{ur} \quad (5)$$

$$e_r = \varphi_r - \varphi = L_k e_{kr} + L_u e_{ur} \quad (6)$$

The control objective is to find a bounded input, τ , such that e_r and \dot{e}_r are bounded and $\dot{e}_r \rightarrow 0$ when $t \rightarrow \infty$.

Using the linear-in-parameters property for rigid manipulators which partially holds for flexible manipulators, the right-hand side of Equation (1) can be written as

$$M(\varphi, P)\ddot{\varphi} + C(\varphi, \dot{\varphi}, P)\dot{\varphi} + G(\varphi, \dot{\varphi}, P) = W(\varphi, \dot{\varphi}, \ddot{\varphi})P + W_1(\varphi, \dot{\varphi}, \ddot{\varphi}) \quad (7)$$

where $W \in R^{n \times r}$ and $W_1 \in R^n$. The control law was given as

$$\tau(t) = (H^T H)^{-1} H^T [\hat{M}\ddot{\varphi}_r + \hat{C}\dot{\varphi}_r + \hat{G}^* + K_r \dot{e}_r] \quad (8)$$

where $M = M(\varphi, \hat{P})$, $\hat{C} = C(\varphi, \dot{\varphi}, \hat{P})$, and K_r is a positive definite gain matrix. The unknown reference trajectory φ_{ur} was determined from

$$N^T [\hat{M}\ddot{\varphi}_r + \hat{C}\dot{\varphi}_r + \hat{G}^* + K_r \dot{e}_r] = 0 \quad (9)$$

where $N \in R^{n \times (n-m)}$ is a matrix of full rank that satisfy

$$N^T H = 0$$

The new function $\hat{G}^* = G^*(\varphi, \dot{\varphi}, \varphi_r, \dot{\varphi}_r, \hat{P})$ was introduced, and it was assumed that it was possible to determine such functions such that the set (8), (9) produced a bounded solution for φ_{ur} and τ . As an example \hat{G}^* can be

$$G^*(\varphi, \dot{\varphi}, \varphi_r, \dot{\varphi}_r, \hat{P}) = K\varphi_r + B\dot{\varphi}_r + G_n(\varphi, \dot{\varphi}, \hat{P}) \quad (10)$$

where K and B are respectively the symmetric positive definite stiffness and damping matrices. If the function \hat{G}^* is linear in \hat{P} , then the error equation for the closed-loop system would be

$$M\ddot{e}_r + C\dot{e}_r + G^* - G + K_r \dot{e}_r = W_r \Phi \quad (11)$$

$$W_r(\varphi, \dot{\varphi}, \varphi_r, \dot{\varphi}_r, \ddot{\varphi}_r)\Phi = (M - \hat{M})\ddot{\varphi}_r + (C - \hat{C})\dot{\varphi}_r + (G^* - \hat{G}^*) \quad (12)$$

where $\Phi = P - \hat{P}$ is the parameters estimation error.

The proof of stability can be obtained by choosing the following Lyapunov function candidate

$$e_g(t) = \frac{1}{2} \dot{e}_r^T M \dot{e}_r + \Omega + \frac{1}{2} \Phi^T \Gamma^{-1} \Phi \quad (13)$$

where $\Omega = \Omega(\varphi, e_r, P)$ is a semi-positive definite matrix and Γ is a known positive constant diagonal matrix.

Differentiating (13) with respect to time and using the skew-symmetric property, $\dot{e}_r^T(\dot{M} - 2C)\dot{e}_r = 0$, and (11) results in

$$\dot{e}_g(t) = -\dot{e}_r^T K_r \dot{e}_r - R + \Phi^T(W_r^T \dot{e}_r + \Gamma^{-1} \dot{\Phi}) \quad (14)$$

where $R = R(\varphi, \dot{\varphi}, e_r, \dot{e}_r, P) \geq 0$ and if (15) is satisfied. If $G = K\varphi + B\dot{\varphi} + G_n(\varphi, \dot{\varphi}, P)$, using (10), and assuming $\Omega = \frac{1}{2}e_r^T K e_r$ and $R = \dot{e}_r^T B \dot{e}_r$, the following equation can be satisfied.

$$\dot{e}_r^T(G^* - G) = \dot{\Omega} + R \quad (15)$$

Choosing the following parameter adaptation law

$$-\dot{\Phi}(t) = \dot{P}(t) = \Gamma W_r^T \dot{e}_r \quad (16)$$

makes \dot{e}_g semi-negative. This implies that $\dot{e}_r \rightarrow 0$ when $t \rightarrow \infty$. However, it is not guaranteed that the estimated parameters \hat{P} converge to their true values P [17]. The estimated parameters converge to their true values if the desired trajectory is persistently exciting; that is, if the matrix $W_d = W_r(\varphi_d, \dot{\varphi}_d, \varphi_d, \dot{\varphi}_d, \ddot{\varphi}_d)$ is persistently exciting and uniformly continuous where W_r is given in (12) with $\varphi, \dot{\varphi}_r$ replaced by φ_d . This means there should exist positive constants $\alpha_1, \alpha_2, \beta$ such that for all $t_1 \geq 0$ (see [25])

$$\alpha_1 I \leq \int_{t_1}^{t_1+\beta} W_d^T W_d dt \leq \alpha_2 I \quad (17)$$

3. Concluding remarks

Adaptive control for rigid manipulators is well represented in the literature [26].

Despite many published works on the adaptive control of flexible manipulators during the past few years, part of which was discussed in this paper, its development seems to be still in its initial stages. Significant progress should be expected in the next few decades in understanding the fundamentals and in developing practical strategies for such manipulators to be used in industry and elsewhere.

4. References

- [1] Anthony R. Fraser and Ron W. Daniel. *Perturbation Techniques for Flexible Manipulators*. Kluwer Academic Publishers, Boston, Massachusetts, 1991.
- [2] F. Khorrami, S. Jain, and A. Tzes. Experimental results on adaptive nonlinear control and input preshaping for multi-link flexible manipulators. *Automatica*, 31(1):83-97, 1995.
- [3] P.J. Nathan and S.N. Singh. Sliding mode control and elastic mode stabilization of a robotic arm with flexible links. *ASME Journal of Dynamic Systems, Measurement, and Control*, 113:669-676, 1991.
- [4] C.J. Damaren. Adaptive control of flexible manipulators carrying large uncertain payloads. *Journal of Robotic Systems*, 13(4):219-228, 1996.
- [5] Lih-Chang Lin and Sy-Lin Yeh. A composite adaptive control with flexible quantity feedback for flexible-link manipulators. *Journal of Robotic Systems*, 13(5):289-302, 1996.
- [6] D. Gorinevsky. An application of on-line parametric optimization to task-level learning control. In *Proceedings of American Control Conference*, Seattle, WA, USA, June 21-23 1995.
- [7] Stephen Yurokovich, Anthony P. Tzes, Iewen Lee, and Kenneth L. Hillsley. Control and system identification of a two-link flexible manipulator. In *Proceedings of IEEE International Conference on Robotics and Automation*, volume 3, pages 1626-1631, Cincinnati, Ohio, May 13-18 1990.
- [8] S. Jain and F. Khorrami. Robust adaptive control of flexible joint manipulators. *Automatica*, 34(5):609-615, 1998.
- [9] Rogelio Lozano and Bernard Brogliato. Adaptive control of robot manipulators with flexible joints. *IEEE Transactions on Automatic Control*, AC-37(2):174-181, 1992.
- [10] J.S. Yu, R. Hu, and P.C. Mueller. An approach to adaptive decentralized control of flexible joint robots. In *Proceedings of IEEE/RSJ International Conference on Intelligent Robots and Systems*, pages 8-13, Yokohama, Japan, July 26-30 1993.
- [11] Ghorbel Fathi and Mark W. Spong. Adaptive integral manifold control of flexible joint robot manipulators. In *Proceedings of The IEEE International Conference on Robotics and Automation*, volume 1, pages 704-714, Nice, France, May 12-14 1992.
- [12] S. Nicosia and P. Tomei. A method to design adaptive controllers for flexible joint robots. In *Proceedings of The IEEE International Conference on Robotics and Automation*, volume 1, pages 701-706, Nice, France, May 12-14 1992.
- [13] Mauro Rossi and David W.L. Wang. Hybrid passive/adaptive control of a single flexible link manipulator with a payload. In *Proceedings of IEEE International Conference on Robotics and Automation*, pages 2109-2116, Minneapolis, Minnesota, April 1996.
- [14] Ying Chen and Adel H. Eltimsahy. Hybrid adaptive control of two-link flexible manipulators grasping a payload. In *The Fourth IEEE Conference on Control Applications (CCA)*, Albany, NY, September 28-29 1995.
- [15] D.K. Anand, M. Anjanappa, and K.H. Sung. Adaptive control of a flexible manipulator with varying payload. In *Proceedings of the 12th Triennial World Congress*

- of the International Federation of Automatic Control, Sydney, NSW, Australia, July 18-23 1993.
- [16] Y. P. Yang and J.S. Gibson. Adaptive control of a manipulator with a flexible link. *Journal of Robotic Systems*, 6(3):217-232, 1989.
 - [17] I.M.M. Lammerts, F.E. Veldpaus, M.J.G. Van de Molengraft, and J.J. Kok. Adaptive computed reference computed torque control of flexible robots. *ASME Journal of Dynamic Systems, Measurement, and Control*, 117(1):31-36, 1995.
 - [18] Lih-Chang Lin. State feedback H_∞ control of manipulators with flexible joints and links. In *Proceedings of IEEE International Conference on Robotics and Automation*, pages 218-223, Sacramento, CA, USA, April 1991.
 - [19] D. Wang and M. Vidyasagar. Control of a class of manipulators with a single flexible link-part i: Feed-back linearization. *ASME Journal of Dynamic Systems, Measurement, and Control*, 113:655-661, 1991.
 - [20] D. Wang and M. Vidyasagar. Transfer functions for a single flexible link. *The International Journal of Robotics Research*, 10(5):540-550, 1991.
 - [21] J.O. King, V.G. Gourishankar, and R.E. Rink. Composite pseudolink end-point control of flexible manipulators. *IEEE Transactions on Systems Man Cybernetics*, 20(5):969-977, 1990.
 - [22] Jung-Hua Yang, Feng-Li Lian, and Li-Chen Fu. Adaptive robust control for flexible manipulators. In *Proceedings of IEEE International Conference on Robotics and Automation*, Nagoya, Japan, May 21-27 1995.
 - [23] Jung-Hua Yang, Feng-Li Lian, and Li-Chen Fu. Adaptive hybrid position/force control for robotic manipulators with compliant links. In *Proceedings of IEEE International Conference on Robotics and Automation*, Nagoya, Japan, May 21-27 1995.
 - [24] Jean-Jacques E. Slotine and Weiping Li. On the adaptive control of robot manipulators. *The International Journal of Robotics Research*, 6(3):49-59, 1987.
 - [25] Jean-Jacques E. Slotine and Weiping Li. Adaptive manipulator control: a case study. *IEEE Transactions on Automatic Control*, 33(11):995-1003, 1988.
 - [26] Reza Fotonhi-C., Walerian Szyszkowski, and Peter N. Nikiforuk. Adaptive control of rigid and flexible manipulators: a survey. *IEE Proceedings-Control Theory and Applications*, 1998. submitted.

An Implementation of the Autonomous Container Transporter

Young Jin Lee¹, Nam Huh¹, Young Jin Yoon¹, Man Hyung Lee², and Jong Il Bae³

¹ Dept. of Intelligent & Mechanical Engineering, Pusan National University

² School of Mechanical Engineering, Pusan National University

³ Dept. of Electrical Engineering, Pukyong National University

¹yjlee4@hyowon.cc.pusan.ac.kr

¹clown@hyowon.cc.pusan.ac.kr

¹yoonyj@hyowon.cc.pusan.ac.kr

²mahlee@hyowon.cc.pusan.ac.kr

³jibae@pine.pknu.ac.kr

Abstract

To improve the productivity in the harbor, successful development of an ACT(Autonomous Container Transporter) is needed. Well-designed steering and velocity control systems are the key factor for the development of the ACT. In this paper, a research concerning the achievement of the steering control is introduced. To get an information on the guide line that the ACT should track, the vision system is applied. By using neural network, proper steering angle is gotten fast with less influence of the image disturbance. A simulation based on the ACT kinematics is performed with the gotten steering angle, and it shows satisfactory results.

1. Introduction

An ACT may be defined as an unmanned vehicle which transport a container from the crane to the specific position in a harbor. Recently, many concerning fields of the harbor management automation are researched to improve the productivity. As a aspect of the automation, the research on the development of the ACT is introduced in this paper. The purpose of the research is that by successful development of the ACT, we can transport more cargoes in the given time, and it is a straightway to the improvement of the productivity in the harbor. The well-designed ACT should not only be stable but also perform fast steering and velocity control. To design such controller, we have to know the dynamics of the plant, select proper control algorithm, and determine sensors and design procedures using chosen sensors.

In this paper, the selection of the sensors, which provide basic operating signal of the controller system and the simulation based on the both ACT kinematics and sensor signal is presented. The vision system is used as a state sensor of the ACT. It costs less installation price, but the robustness on the image disturbance is not strong. To overcome the disadvantage, the neural network is used to

evaluate proper steering angle based on the vision image signals. It is commonly known that well learned neural network can produce proper output under the disturbance-existing environment. With the learning information, the neural network makes good steering angle in spite of the damaged or noise-effected guide line image.

This paper consists of five chapters: In the chapter 1, the motivation and the purpose of this study is shown. The procedures for the evaluating steering angle using vision image information and the neural network, and the control algorithms of the ACT are introduced in the chapter 2. Chapter 3 presents the simulation results, and finally the conclusion and the further study is discussed in the chapter 4.

2. Steering Control

The vision system configuration used in this paper is shown in Figure 1.

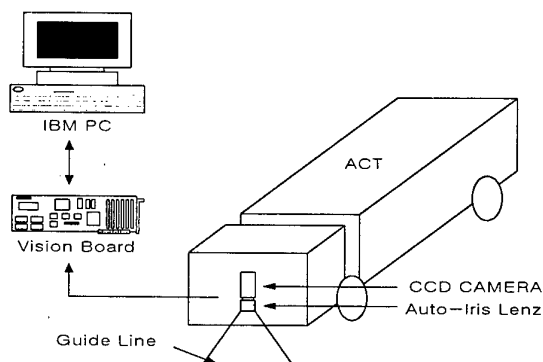


Figure 1. Block diagram of vision system

The detail specification of each system components is as follow:

The detail specification of each system components is as follow:

Table 1. specification of each system components

CCD Camera	Monochrome type by COSMICAR, Japan
Lens	Autoiris by COSMICAR, Japan
Vision Board	MVB03, Korea
Resolution	256 gray level, 640x480 pixel
Host PC	Pentium MMX-233MHz, 32MB RAM

Host PC can perceive the deviation of the ACT from the normal driving trajectory by analyzing the vision information which contains the image of the white guide line. This is shown in Figure 2. With the Figure 2, we can know that two parameters are needed to express the driving state of the ACT : r and θ

r : lateral direction deviate distance of ACT
 θ : moving direction of ACT

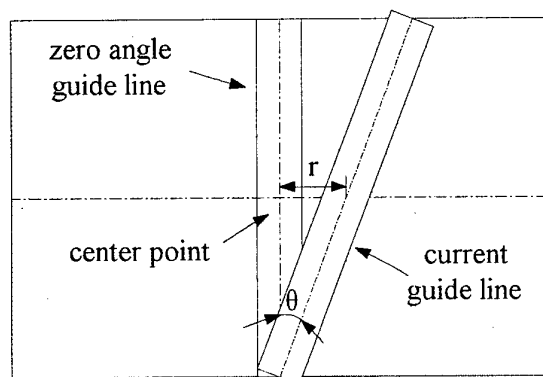


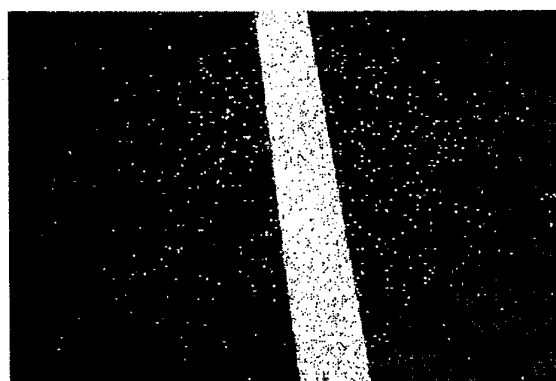
Figure 2. Case of current guide line deviating the center point of vision system

The image processing algorithms are designed to make the ACT go along with guide line by below procedures.

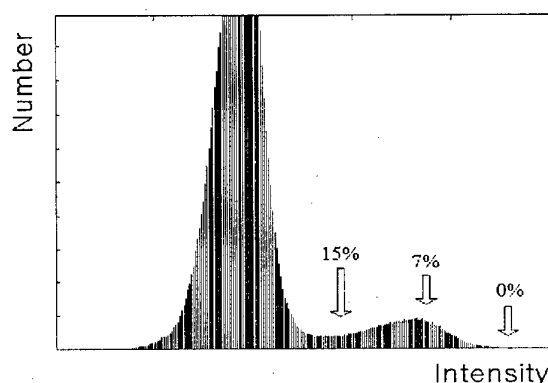
1st procedure : Thresholding of gray level

To extract the information of the guide line from the captured image, the binarization and the segmentation on the image is a must. But the determination of the proper threshold value is hard because it heavily depends on the weather and the environmental condition.

To solve this problem, the threshold value depends on the ratio of (the area of the guide line in the whole captured image) : (the whole area of the captured image.) For example, if guide line occupies 15% area of the image, the threshold value is set to 85% of the intensity value.



(a) Origin image



(b) Histogram of origin image

Figure 3. Input image(gray level) and histogram

2nd procedure : The segmentation of the sub-block

The block segmentation is applied to the binarized image. The reason of the segmentation is that the computing time of the whole-image processing is much longer than that of the segmented image.

The segmentation is not applied to the whole image, but to the highest/lowest and the middle parts of the image. By doing so, enough information to determine the steering angle is taken. We set up the block number of the highest/lowest parts of the image to have double size amount of information compare to the middle block number. Because the key factors which determine the incline of the guide line is start/end point of the guide line, which are allocated at the highest/lowest parts of the image.

Full size of the captured image has a resolution of 640x480 pixels. We set the highest/lowest parts of the block to be a resolution of 20x20 pixel, and the middle parts of the block to be a 40x40 pixel. And the width of the guide line is approximately 80 pixel.

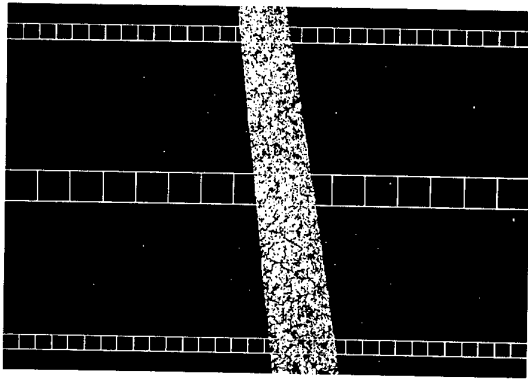


Figure 4. The segmentation of the sub-block

3rd procedure : The binalization of the segmented blocks

In Figure 5, total 80 blocks are binarized. For each block, if the white pixels occupy more than 50% of a block area, then the block is assigned to be one(that means the block is totally considered white), else to be zero(that means the block is totally considered black). As a consequence, 80 length of input bit sequence is obtained.

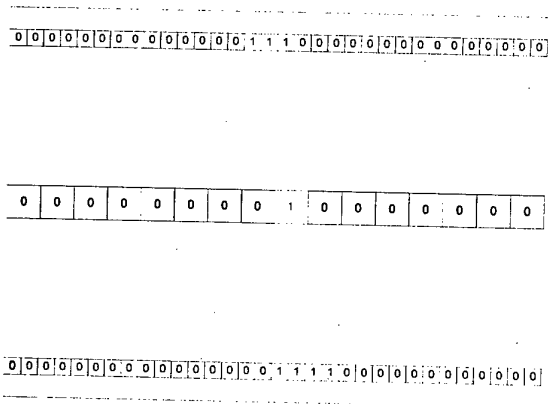


Figure 5. The binalization of the segmented blocks

4th procedure : Input to the neural network

Now, 80 input bit stream is acted as an input of the neural network. To get a steering angle from the captures image, the neural network is used as a 'lookup-table', and the structure of the neural network is shown in the Figure 6.

The obtained image can be classified as two classes: one is what passes the center of the camera, and the other is what passed away from the center of the camera.

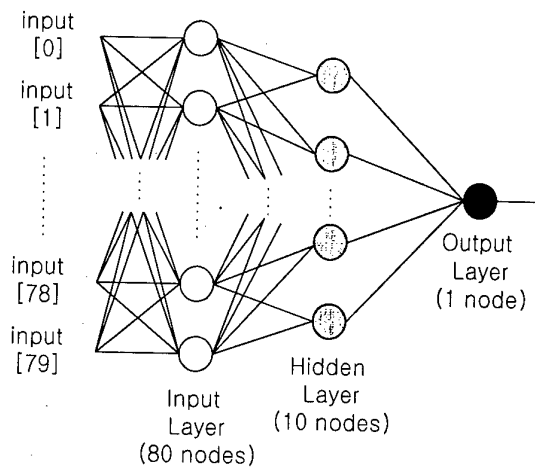


Figure 6. The architecture of NN

Table 2. Structure of NN

Input	3 layer NN
Input Node	80 nodes
Hidden Node	10 nodes
Output Node	1 nodes

We can consider that non-center passing image as a center-passing image with a distance r from the center of camera, so we can express the input to the steering part as below:

Input = θ, r

where the θ is a steering angle evaluated by the neural network, and r is a distance from the center of the camera to the image of guide line.

With above configuration, all possible cases of the guide line images are 29. That means, from the 1st case(the image is allocated from the top-left to the bottom-right of the camera) to the 29th case(the image is allocated from the top-right to the bottom-left of the camera) can be exist. We only take into account the 12th, 13th, 14th, 15th, 16th, 17th, and 18th image under consideration of the actual operating angle range of the front-wheel, and corresponding angle is 14.036(deg), 9.462(deg), 4.763(deg), 0(deg), -4.763(deg), -9.462(deg), and -14.036(deg) respectively.

The angle is evaluated by the next formula:

$$\theta = \text{atan}(x/y)$$

$$x=640-(i-1+Width) \times 640/Column-(i-1) \times 640/Column$$

Width=4, Column=16, i=12...18

$$y=480$$

**5th procedure : Steering control of ACT
consi-dering kinematics analysis**

The ACT knows the angle of inclination between road trajectory and moving direction of ACT and the lateral

direction from image processing and NN. Using these informations, we need the steering control algorithm of the ACT to track working trajectory. So, in the procedure the movement of ACT using in the harbor may obtain the motion equation of ACT from the kinematics analysis. And the ACT is four-wheel driving and front-wheel steering system(Figure 7).

Table 3. Coordinates of ACT

X, Y	Vehicle position
α	Vehicle orientation
$\delta 1$	Left front wheel(LFT) direction
$\delta 2$	Right front wheel(RFT) direction
Θi	Angle deflection each wheel($i=1, \dots, 4$)

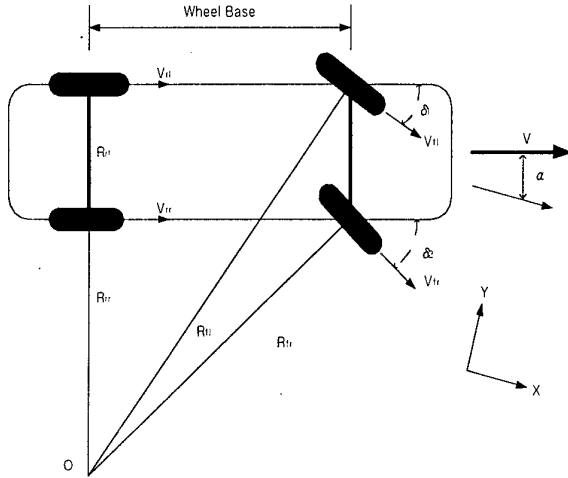


Figure 7. Schematic of ACT Model

We can obtain 9 coordinates(Table 3) for kinematics analysis of the movement of ACT from Figure 7, then each coordinate has dependent relationship. And these coordinates satisfy the follow assumptions to obtain the constraint equations.

1. We ignore dynamic effect of ACT such as the slip of lateral direction and the distortion of tire.
2. Actually the movement of ACT constructs rolling, pitching, and yawing, But yawing is influenced more then rolling and pitching. So, we ignore rolling and pitching.

From these assumption, we induce the follow constraint equations and simplify 2 D.O.F system about the ACT.

Constraint Equation 1 : Point O is 0 velocity point.

$$\frac{d}{L} = \frac{1}{\tan \phi_1} - \frac{1}{\tan \phi_2} \quad (1)$$

Constraint Equation 2 : Center of each wheel rotate the same angular velocity at the point O.

$$\dot{\theta}_1 \sin \phi_1 = \dot{\theta}_2 \sin \phi_2 = \dot{\theta}_3 \tan \phi_1 = \dot{\theta}_4 \tan \phi_2 \quad (2)$$

And we can obtain the follow three constraint equations by the condition that don't occurred the slip of lateral direction in the tire

$$\dot{x} = v_p \cos(\alpha + \phi) \quad (3)$$

$$\dot{y} = v_p \sin(\alpha + \phi) \quad (4)$$

$$\dot{\alpha} = \frac{v_p}{\rho} \quad (5)$$

Using the these constraint equations(Eq.(1)~Eq.(5)), we can obtain the motion equations.

$$x = \int_0^t v_p \cos\left(\frac{1}{L} \int_0^t v_p \sin \phi dt + \phi\right) dt \quad (6)$$

$$y = \int_0^t v_p \sin\left(\frac{1}{L} \int_0^t v_p \sin \phi dt + \phi\right) dt \quad (7)$$

3. Simulation

We simulate guide line, lateral direction is trapezoid type, tracking of ACT. Information of guide line measures the lateral direction distance and angle of inclination by the process as the Figure 8. Then these values are the tracking errors of the ACT. Using these errors, Figure 9 and 10 are results of block diagram(Figure 11), where Figure 9 displays the desired path and the actual path. And Figure 10 is the angle variation of ACT handle. Then, tracking trajectory compensates for using the PID controller.

4. Result

In this paper, a research concerning the achievement of the steering control was performed. To get an information on the guide line that the ACT should track, the vision system was applied. By using neural network, proper steering angle was gotten fast with less influence of the image disturbance. A simulation based on the ACT kinematics was performed with the gotten steering angle, and it showed satisfactory results.

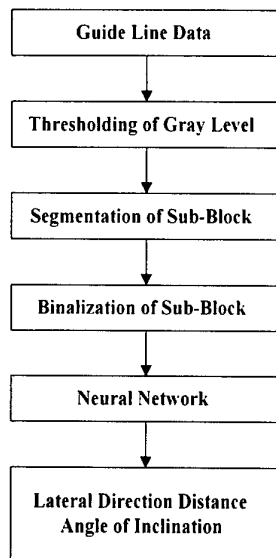


Figure 8. Flowchart

5. Reference

- [1] Min-chul Kim, Steering Control of a Vehicle Based on Kinematic Modeling, *POSTECK*, 1993
- [2] Nasser K., and Norman G., Kelly M., Paul L., A Transportable Neural-Network Approach to Autonomous Vehicle Following, *IEEE Transactions on Vehicular Technology*, Vol 47, No 2, May, 1998, pp. 694-702
- [3] Nack-Young Jang, On the Design of Vision-based Automatic Steering System for Electrically Propelled Vehicles, *KACC '98*, Oct., 1998
- [4] Howard D., Mark B., *Neural Network Toolbox*, Math Work, 1998
- [5] Joon Woong Lee, Lane Recognition Algorithm by an Image Processing, *Journal of Control, Automation and Systems Engineering*. Vol. 4, No. 6, Dec., 1998, pp. 759-764

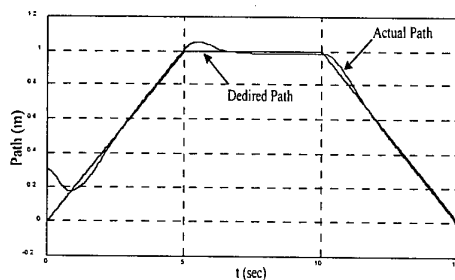


Figure 9. Path Tracking Trajectory

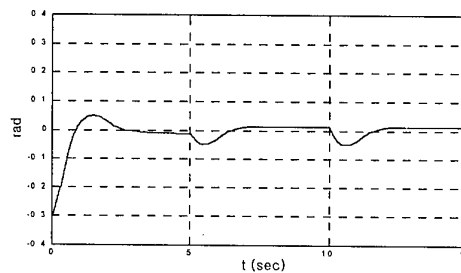


Figure 10. Angle Variation of ACT Handle

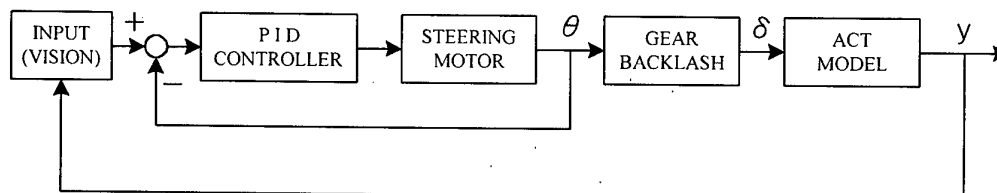


Figure 11. Block Diagram of ACT system

Robotized Palletizing of Wine Glasses

Hakan Altınay, Can Bayar, Gökhan Gök, Gökay Hurmalı, Ağan Şimşek, Dilek Bilgin Tükel
*Altınay Robotics&Automation Inc., Zahit Bey Sok. No 3,
Kızıltoprak, 81030 Istanbul, Turkey
robot@altinay.com.tr*

Abstract

An intelligent robotized wine glass palletizing workcell has been developed for Şişecam Inc. by Altınay Robotics and Automation Inc. The hardware and software design of this mechatronic system includes selecting right mechanical and electronic components which are combinations of different products and creates a solution suitable to every situation. The robotic cell consists of two gantries, two 4 axes SCARA type robots, five servo controlled and two inverter controlled conveyors, pallet and carton separator storage and retrieval units. Also, it includes a quality control station for eliminating non-standard products.

1. Introduction

Robotics is defined as the theory and practice of automation of tasks which were thought to be reserved for a man. Thus, replacing human tasks which are dull, repetitive, hazardous, or beyond the capability of human physical tolerance with robots is the ultimate goal of robotics research [1]. During the last 30 years robots became a widely used and well accepted technology. After 80's, they spread to nearly all industrial production areas. Today, there are 711,500 robots[2] worldwide. They are used mostly for arc welding, spot welding, coating and material handling.

Material handling is one of the most common applications for robots today. Robots are well suited for material handling operations in industrial environments. Loading parts and placing them onto the pallets is called palletization and unloading products from a pallet, called depalletizing. Palletizing/Depalletizing are essential operations in the goods receiving/shipping process of a variety of industries[3]. Glass industry is a good candidate for robotic palletizing because of the repetitive nature of the job and high cycle time requirements. Therefore, the objective of this automation project has been the design of a multiple robot system in order to replace the manual palletizing

process while reducing labor requirements and improving labor conditions.

The constraints of the project are: 1-) The system should be capable of handling 100 glasses per minute and 2-)adaptation process for a new product type should be very short and simple.

The workcell consists of four robots. This makes the system cooperative. Multiple robots performing tasks together in a cooperative manner have advantages over a single robot just as a human using two arms has an advantage over one that uses one arm and as multiple humans have an advantages over a single human. Cooperative robots have many potential applications in assembly and manufacturing. The applications can be grouped as:

- Every robot shares a part of the task in the process: If one robot fails, the others can compensate for it. Therefore, the reability of the manufacturing process increases and process time decreases.
- Robots work on the same object: Carrying a heavy, flexible or long object requires more than one robot.
- Robots disassemble or assemble mating parts: Each robot arm holds a different object. Complex assembly is essentially a two hand job, and can be performed better by a pair of robots working together.

The designed workcell falls into the first category such that every robot shares a part of the task. If there is a problem, the system tries to organize itself according to the problem, such that increasing the speed for compensating the failing part, or carrying glasses to the bufferzone, or buffering the glasses into two rows.

The system is also intelligent, it keeps the necessary data in its database to adapt itself automatically in case of a product change. The only thing that remains to the operator is to select the product type from the operator terminal menus, and to place a few sensors using specially designed interfaces for easy configuring.

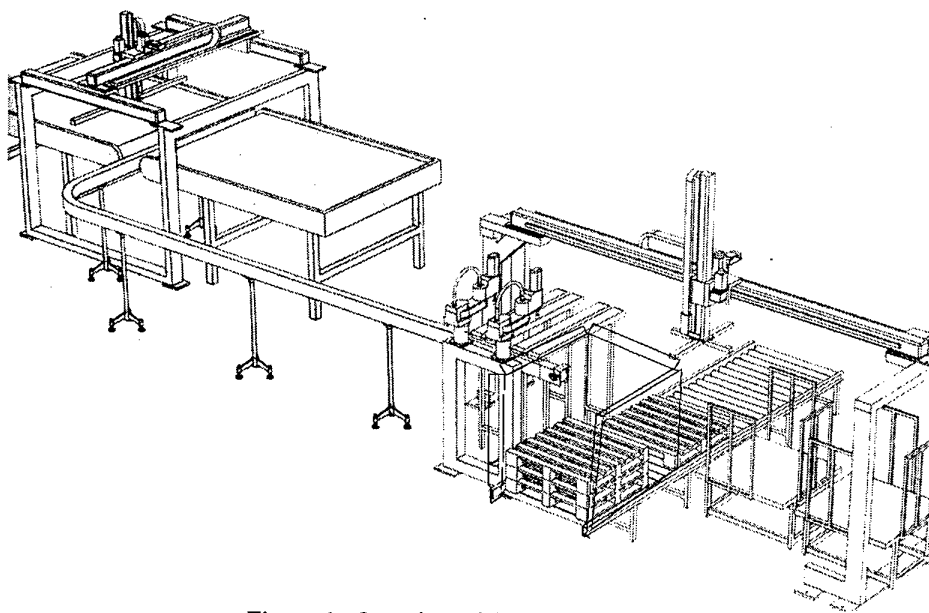


Figure 1. Overview of the designed workcell

2. System architecture

The complete mechanical system (Fig.1) is designed using I-DEAS and DENEb software. The mechanical design of the robotic cell consists of:

2.1. Determination of the components of the workcell.

AKR-XYZ: Three axes gantry robot (Fig. 2) picks glasses from the cooling oven conveyor, and places them onto the L-conveyor while tracking the speed of the conveyor. If a failure occurs on the system, AKR-XYZ places the glasses into a bufferzone, after recovering the problem, the robot loads glasses back from the bufferzone to the L-conveyor.

COBRA-1&2: Two four axes SCARA type ADEPT robots (Fig. 3-4) pick the wine glasses from L-conveyor while tracking the conveyor and place them onto the position controlled conveyors. One COBRA is capable of handling all the production. However, using two COBRAs makes the system more flexible, reliable and the mechanical life of the robots will be longer.

POSCON-1a&1b&2a&2b: There are four position controlled buffering conveyors (Fig.4). COBRA-1 places the glasses onto the POSCON-1a and 1b. COBRA-2 works with the POSCON-2a and POSCON-2b. The robots place the glasses always to the same point, and send a signal that the glass is on the conveyor.



Figure 2. AKR-XYZ: Three axes gantry robot



Figure.3. Four axes SCARA type robot

POSCON proceeds a step whose length is a function of the product type.

After, the accumulated glasses reach a certain number, POSCON proceeds a large step to place the group of glasses to the end of the conveyor, that AKR-XZ can pick them. If there is a jam, it is possible to place two rows of glasses on a single POSCON.

AKR-XZ: Two axes gantry robot (Fig. 5) which picks the equally placed wine glasses from the position controlled conveyors and places them onto the pallets, it should also put carton separators between layers.

PIM: A pallet storage and retrieval mechanism for taking a pallet from the pallet storage unit and placing it to the filling station. When the robot fills the pallet, it will carry the filled pallet to the stretching station. It has to communicate with AKR-XZ.

2.2. Designing robotic hands for AKR-XYZ, AKR-XZ, COBRA1&2

AKR-XYZ: 4 degrees of freedom pneumatic gripper is designed for this robot (Fig. 6a). There are 10 sensors for check hand status. It could handle disordered glass groups.

AKR-XZ: very flexible and adjustable mechanic hand (Fig. 6b) is designed for this robot. It is possible to pick up to 24 wine glasses with this hand. Also, carton separators can be picked. It is equipped with 3 sensors.

COBRA-1&2: have vacuum grippers (Fig. 6c) and sensors to check the status

2.3. Selecting conveyors

Belt conveyors for POSCON, roller conveyor for pallet retrieval unit, plastic panel belt conveyors for L-conveyor and rib-flex conveyor for bufferzone are chosen.

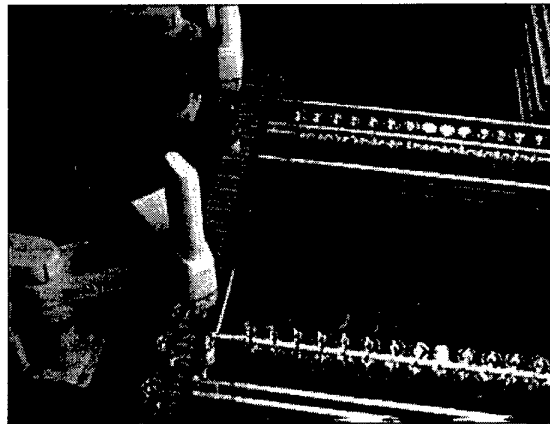


Figure 4. COBRA 1&2 and POSCON 1a&1b&2a&2b

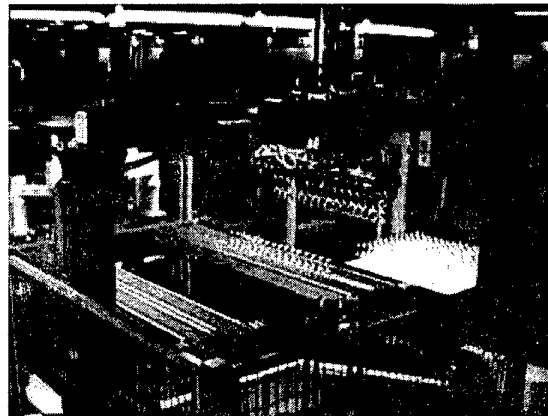


Figure 5. AKR-XZ: Two axes gantry robot

2.4. Interfaces and storage units

- robots' base, carton storage units
- sensor connection interfaces -adjustable measuring systems for quality control station are designed.

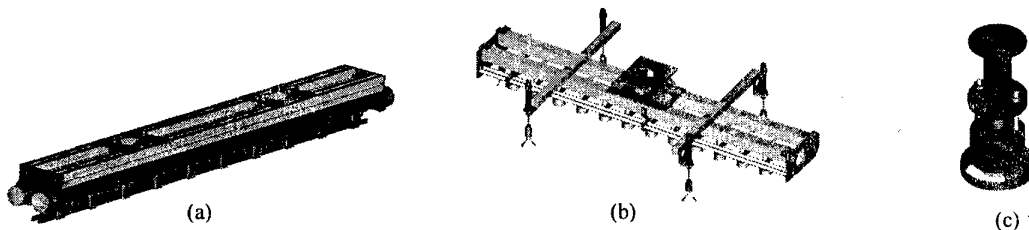


Figure 6. Designed robotic hands for AKR-XYZ(a), AKR-XZ(b), COBRA

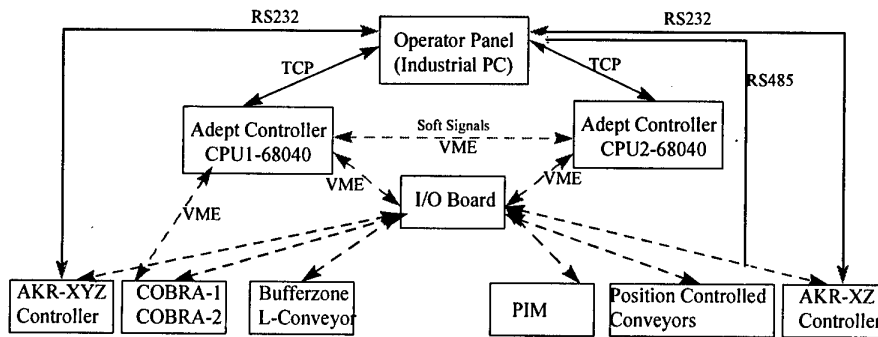


Figure 7. Hardware overview

3. Software architecture and control

The software is the key element to make the designed workcell flexible, reliable and robust under new manufacturing conditions. Decentralized hardware (Fig. 7) and software configurations (Fig. 8) are designed for optimum performance. A user-friendly man-machine interface is developed on an industrial PC. Each robotic unit has its own controller, but a multiprocessor controller is the brain of the system.

There are total 17 parallel processes running on the system. Communications between different processes are possible via signals and global variables. The software configuration is shown in Fig.8.

The palletizing process starts after determining number of rows, columns and layers in a pallet. The operator may select the values suggested by the computer which is based on maximum possible glasses can be placed in a pallet or he can enter values depending on the customer or the transportation needs.

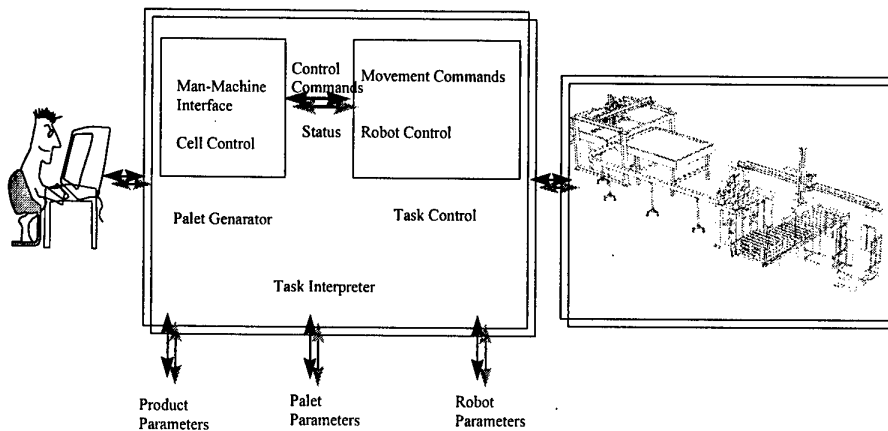


Figure 8. Overview of the software scheme

According to the glass model and the pallet data, man-machine interface computer calculates all the robot pick and place coordinates and downloads those data via serial communication ports or via Ethernet to the robot controllers and one axis controllers of the conveyors.

3.1. Man-machine interface

A menu driven graphical user interface (Fig. 9) is developed on the industrial PC.

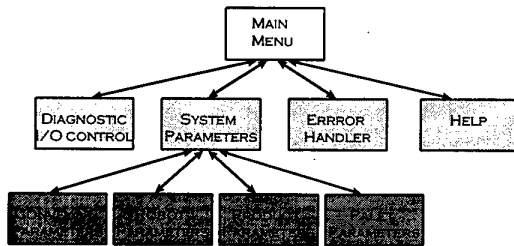


Figure 9. Menu structure of man-machine interface program

Operator commands are interpreted by the task interpreter and converted to the robot controller commands. The operator can monitor several robot parameters and also physical I/O values and alters them, he can also change the robot parameters such as pick and place points, he can select a new product(glass), according to this new information all the robot points will be adapted automatically. He can also create or update pallet parameters and after his confirmation the system again organize itself. All the confirmed data are stored in a database such that in the future, the operator only selects that record for the same product and the pallet.

3.2. Robot controllers

Every robot has its own industrial controller. The low level part of the software is written on the industrial controllers using their own languages.

3.2.1. ADEPT MV controller. The Adept MV series controllers are based on the VME bus specification. The controller used for this project has dual 68040 microprocessor. This controller is the heart of the system. The MV Controller is suitable to implement flexible robot cells because of its open architecture. It is possible to control two SCARA type 4 axes robots, a pallet retrieval-storage unit, conveyors and to do higher

level controls for gantries and communication between operator panel by ADEPT MV controller.

3.2.2. HNC-P384 controller. Gantry robots have Hirata HNC controllers. These controllers are simple point-to-point controllers, they need higher level controllers above them.

3.3. One axis controllers

POSCON 1a&1b&2a&2b have one axis servo controller UNIDRIVE with UD70 position control unit from Control Techniques Inc.. L-conveyor has also UNIDRIVE servo controller without UD70, position controller. The conveyors of the bufferzone and pallet storage and retrieval mechanism are inverter controlled.

3.4. Conveyor tracking

The three axes gantry robot (AKR-XYZ) and SCARA robots (COBRAs) have conveyor tracking capability. To determine the instantaneous position and speed of a belt, the conveyor is equipped with an encoder to measure its position and speed. Conveyor tracking help robot to pick and place glasses from the belt with the speed of the belt without disturbing the balance of the glasses.

3.5. Coordinator

This high level controller commands to the system components how to behave if there is a problem or a jam in the system.

Problem-1: One of the SCARA robots has a failure

The other SCARA robot compensate the failure and loads all the glasses from L-conveyor to its own position controlled conveyors. To prevent jam, AKR-XYZ (three axes gantry robot) picks the glasses from the cooling oven and replaces some of them onto the bufferzone and some of them onto the L-conveyor according to the ratio selected by the operator.

Problem-2: Two of the SCARA robots have failure

L-conveyor will be stopped. AKR-XYZ picks all the glasses from the cooling oven and replaces them onto the buffer-zone. When the problem is eliminated it will load glasses from the cooling conveyor and buffer-zone according to the ratio determined from the operator to the L-conveyor. The speed of the L-conveyor will be increased in this case.

Problem-3: AKR-XZ has a problem

AKR-XYZ picks all the glasses from the cooling oven and replaces them onto the bufferzone. SCARA robots continue to work until their conveyors are filled. When the problem is eliminated the glasses in the bufferzone will be unloaded like in the previous case.

Problem-4: AKR-XYZ has a problem

The end of the system continues to work until all the glasses are palletized and waits till AKR-XYZ is available again.

Problem-5: One of the position controlled conveyors has a problem

SCARA robots will not use that conveyor and continue to work with the others until it is available again.

3.7. Quality control station

The variance in height of the wine glasses will be a problem for palletizing. If they are higher than the standard they may be broken when a higher layer comes. If they are shorter, it is possible that robots could not pick it. To prevent unacceptable variance in the height of the wine glasses a quality control station was developed. Two optical sensors determine if the glass is standard and if it is a nonstandard product, it will not be processed and system let it go to the recycle pool.

3.8. Safety

The fence system for the safety is standard in all the industrial robotic workcells. For this palletizing workcell also a fence system is designed considering the maximum safety of the people and the ergonomics for the operator.

For the safe operation, the parts of the system such as robotic hands which have interaction with the environment have equipped with touch sensors in order to prevent them to insert excessive forces.

4. Conclusion

A fully automatic system for palletizing of wine glasses has been designed and developed by Altınay Robotics&Automation Inc. This research project has had a total duration of one year. It proves that new robotic technology can be introduced to the industry with good results. The main contribution of this developed system is its flexibility to product type changes, and fault tolerance capability against manufacturing problems.

References

- [1] Tükel Bilgin, D., *Actuation Redundancy Control of Two Cooperating Industrial Robots*, PhD Thesis, Dept. of Mechanical Engineering, Katholieke Universiteit Leuven, Belgium, 1997, 97D4
- [2] IFR Reports, *World Industrial Robots, 1998*, United Nations Publications, 1998
- [3] Sakakibara, S., "The Current State of Packaging in Japan", *World Industrial Robots 1997*, United Nations Publications, 1997, pp: 233-237
- [4] Tükel Bilgin, D., Dutré, S., De Schutter, J., "Experiments with teleoperated control of two coordinated industrial robots", *Proc. of Int. Conference on Recent Advances in Mechatronics, Istanbul*, pp: 1030-1035

Acknowledgment

The authors are grateful to Şişe Cam Inc. and especially to Mr. Tuğrul Misoğlu, business development manager, for his help and support during the realization of this project.

An Example of Failure Tolerance through Active Braking

James D. English and Anthony A. Maciejewski

Purdue University
1285 Electrical Engineering Building
West Lafayette, Indiana 47907-1285

ABSTRACT

For a manipulator operating in a hazardous or remote environment, an important concern is its capability after a component failure, since retrieval or repair is not always possible. Methods have been presented in the literature for optimizing capabilities after specific types of failures. However, techniques for achieving failure tolerance when conversion between failure types is possible has not been fully explored. This article presents an approach to improving postfailure performance by converting between locked-joint failures and free-swinging failures through active braking. When a manipulator is moved slowly, gravitational forces can be used to control the failed joint in free-swinging mode, allowing the problem to be cast as a kinematic one.

I. INTRODUCTION

Failure tolerance for robotic manipulators has been widely addressed, often with a focus on using kinematic redundancy. A type of failure often addressed is one resulting in a joint locking. Methods for designing a manipulator with a desired postfailure workspace or a desired level of dexterity after a locking failure have been presented [1, 2, 3], as have general methods for preparing kinematically redundant manipulators for the possibility of a failure [4, 5, 6]. Similar issues have been addressed for free-swinging failures (those for which actuator torque is lost). Methods of preparing for a free-swinging failure were presented in [7, 8], and a study of postfailure capabilities related to design was presented in [9]. These techniques will be combined here to maximize the postfailure capability of a manipulator by choosing between locked and free-swinging modes of operation and using gravity to control the free-swinging joint when the brakes are released. The two failure modes are illustrated in Fig. 1.

Considerable work has been done addressing the related issue of controlling a manipulator with free-swinging joints using dynamic coupling, both with brakes and without. In [10], conditions of integrabil-

This work was supported by a NASA graduate student research fellowship (grant number NGT9-2) and by Sandia National Laboratories under contract number AL-3011.

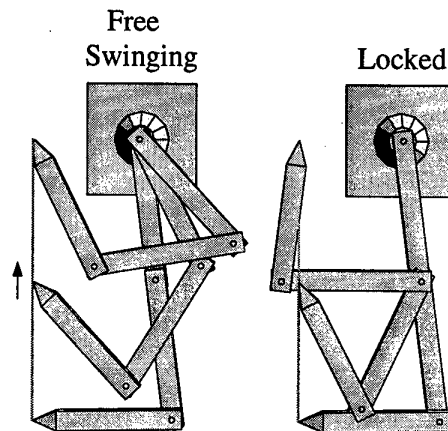


Fig. 1. A three-link planar positioning manipulator is shown tracing a line with joint one free-swinging (left) and locked (right). In the free-swinging case, the arm traces the line while maintaining the composite center of mass of the arm directly below joint one, while in the locked case, the arm traces the line without moving joint one. This article will present ways of using and switching between these two failure modes, by activating and releasing the brakes on the joint whose actuator has failed, to optimize post-failure performance.

ity (i.e., reduction to a holonomic constraint) for free-swinging joints were investigated and methods of stabilizing manipulators without brakes on equilibrium manifolds were presented. In [11, 12] active-braking methods were presented based on dynamic coupling. Operational space methods were developed in [12]. Optimal choices of braking sequences for multiple free-swinging joints were given in [13], and robust methods were presented in [14]. These articles focus on dynamically controlling passive joints about equilibrium points, not on finding the equilibrium points, and not on exploiting gravitational forces.

This article addresses a complementary issue: that of controlling passive joints using gravity alone. Methods are presented for converting, through repeatedly activating and releasing individual joint brakes, between locked-joint failures and free-swinging failures

for manipulators under gravitational forces. Manipulators used in hazardous and remote environments—those where failure tolerance is likely to be an issue—are usually slow moving, and this slow-moving assumption allows the gravitational-force-based control problem to be cast as a kinematic one.

The organization of this article is as follows: Section II will present the swing angle, a key kinematic parameter. Then Section III will give velocity-control methods for both free-swinging and locked joint failure modes; Section IV will look at ways to best switch between failure modes by activating and releasing the joint brakes; and Section V will illustrate the methods through an example.

II. THE SWING ANGLE

Let an n -degree-of-freedom manipulator's joint variables be given by

$$\mathbf{q} = [q_1 \ q_2 \ \dots \ q_n]^T. \quad (1)$$

A fundamental kinematic parameter for the developments in this article is the swing angle. The swing angle $\hat{\theta}_i$ is defined as the angle through which joint i would move to settle into a stationary configuration if its actuator torque were removed [8]. For a viscous friction model, the swing angle equals the smallest-magnitude angular difference between the actual value of joint i and, with the other joints fixed, a value that gives the lowest potential energy (with the value set to π when the smallest magnitude angular difference is $\pm\pi$). The viscous-friction-model swing angle will be used here.

A. The Value and Gradient Calculations

To establish the swing angle, let M_i be the composite mass of links i through n , calculated independently of joint type as follows:

$$M_i = m_i + M_{i+1}; \quad M_n = m_n. \quad (2)$$

Here m_i is the mass of link i . Using these values, the composite first-moment-of-inertia vector \vec{s}_i^* as expressed in the i^{th} D-H frame can be calculated using

$$\vec{s}_i^* = {}^i\mathbf{R}_{i+1}(\vec{s}_{i+1}^* + \vec{s}_{i+1} + M_{i+1}\vec{p}_{i \rightarrow i+1}); \quad \vec{s}_n^* = \vec{0}, \quad (3)$$

where ${}^i\mathbf{R}_{i+1}$ is the 3×3 rotation matrix representing D-H frame $i+1$ in frame i ; \vec{s}_ℓ is the first-moment-of-inertia vector for link ℓ referred to and expressed in its own D-H frame; and $\vec{p}_{i \rightarrow \ell}$ is the vector from the origin of D-H frame i to the origin of frame ℓ , expressed in frame ℓ .

Let

$$u_{i,1} = \hat{z}_{i-1} \cdot (\vec{g} \times \vec{s}_{i-1}^*), \quad (4)$$

and

$$u_{i,2} = (\vec{s}_{i-1}^* \times \hat{z}_{i-1}) \cdot (\hat{z}_{i-1} \times \vec{g}), \quad (5)$$

where \vec{g} is the upward pointing gravity vector. Then provided neither \vec{s}_{i-1}^* nor \vec{g} is parallel to \hat{z}_{i-1} , these allow the swing angle to be calculated as

$$\hat{\theta}_i = \text{Atan2}[u_{i,1}, u_{i,2}], \quad (6)$$

where the range of Atan2 is $(-\pi, \pi]$. If either \vec{s}_{i-1}^* or \vec{g} is parallel to \hat{z}_{i-1} , all values of q_i give the same potential energy, and thus

$$\hat{\theta}_i = 0. \quad (7)$$

If \vec{s}_{i-1}^* or \vec{g} is parallel to \hat{z}_{i-1} or $\hat{\theta}_i = \pi$, the gradient of $\hat{\theta}_i$ is either 0 or undefined. Otherwise, from (6), the entries of $\nabla \hat{\theta}_i$ are calculated as follows:

$$\frac{\partial \hat{\theta}_i}{\partial q_j} = \frac{1}{u_{i,1}^2 + u_{i,2}^2} \left(\frac{\partial u_{i,1}}{\partial q_j} u_{i,2} - \frac{\partial u_{i,2}}{\partial q_j} u_{i,1} \right). \quad (8)$$

Methods for calculating $\frac{\partial u_{i,1}}{\partial q_j}$ and $\frac{\partial u_{i,2}}{\partial q_j}$ are given in [8].

B. Dynamics at Low Velocities

Inherent in the definition of the swing angle $\hat{\theta}_i$ is the requirement that the joints excluding joint i be stationary. In much of the remainder of this article, the swing angle will be applied to a moving manipulator as an approximation. A discussion of the quality of this approximation will be given here.

For a viscous friction model, the differential equation governing the motion of the arm is expressed as

$$\tau = \mathbf{M}(\mathbf{q}) \ddot{\mathbf{q}} + \mathbf{C}(\mathbf{q}, \dot{\mathbf{q}}) \dot{\mathbf{q}} + \mathbf{V}(\mathbf{q}) \dot{\mathbf{q}} + \mathbf{g}(\mathbf{q}). \quad (9)$$

Here, τ is the vector of applied joint torques; $\mathbf{M}(\mathbf{q})$ is the manipulator inertia matrix; $\mathbf{C}(\mathbf{q}, \dot{\mathbf{q}})$ is the matrix specifying centrifugal and Coriolis effects, each row i of which has the form $\dot{\mathbf{q}}^T \mathbf{C}_i(\mathbf{q})$; $\mathbf{V}(\mathbf{q})$ is the viscous-friction matrix; and $\mathbf{g}(\mathbf{q})$ is the vector of joint torques due to gravity. It is assumed that the manipulator's control law (feedback through τ) allows accurate tracking of a prescribed trajectory for the healthy joints.

Let joint i be free swinging and let ϵ_i be defined such that

$$q_i = \hat{\theta}_i|_{q_i=0} + \epsilon_i. \quad (10)$$

Then, assuming the healthy joints are stationary, (9) gives, through entry i of the vector equation,

$$0 = M_{ii}\ddot{\epsilon}_i + V_{ii}(\epsilon_i)\dot{\epsilon}_i + \|\bar{s}_{i-1}^* \times \hat{z}_{i-1}\| \|\hat{z}_{i-1} \times \bar{g}\| \sin(\epsilon_i), \quad (11)$$

where the following were used: $\tau_i = 0$ (because joint i is free swinging), M_{ii} is not a function of ϵ_i , and entry i , i of C_i is zero. If joint i is free swinging with the motor engaged, M_{ii} and V_{ii} should reflect the motor inertia and friction. Equation (11) is an approximation for a slow-moving arm—provided ϵ_i and its first and second derivatives are bounded, the disturbance to (11) can be made arbitrarily small by time scaling the trajectory of the healthy joints. If $|\epsilon_i|$ is assumed small and V_{ii} changes little with ϵ_i , then (11) can be approximated by the following normalized linear differential equation:

$$0 \approx \ddot{\epsilon}_i + \frac{V_{ii}^*}{M_{ii}}\dot{\epsilon}_i + \frac{1}{M_{ii}}\|\bar{s}_{i-1}^* \times \hat{z}_{i-1}\| \|\hat{z}_{i-1} \times \bar{g}\| \epsilon_i \quad (12)$$

where V_{ii}^* is the nominal value. Note $M_{ii} \neq 0$ because M is positive definite. This system acts as one under a proportional plus derivative control law driving ϵ_i to zero (and therefore q_i to $\theta_i|_{q_i=0}$). It has a damping ratio ζ , undamped natural frequency ω_n , and time constant τ_c given by the following:

$$\zeta = \frac{V_{ii}^*}{2\sqrt{M_{ii}\|\bar{s}_{i-1}^* \times \hat{z}_{i-1}\| \|\hat{z}_{i-1} \times \bar{g}\|}} \quad (13)$$

$$\omega_n = \sqrt{\frac{1}{M_{ii}\|\bar{s}_{i-1}^* \times \hat{z}_{i-1}\| \|\hat{z}_{i-1} \times \bar{g}\|}} \quad (14)$$

$$\tau_c = 2\frac{M_{ii}}{V_{ii}^*} \quad (15)$$

Provided the manipulator's motion is slow enough that the disturbance to (12) is minimal, q_i can be viewed as tracking $\hat{\theta}_i|_{q_i=0}$ in much the same way as the healthy joints can be viewed as tracking their desired values. If fast motion of the arm (relative to τ_c) is desired, for large ζ , joint i will tend to lose tracking and lag behind, and for small ζ , the joint will tend to oscillate. However, even if this occurs, the arm can be stopped at key points and allowed to settle. Very fast motion may invalidate (11) and marginalize the usefulness of it (and therefore (12)) in predicting behavior.

III. SINGLE-MODE KINEMATICS

Prior to focusing on the process of switching modes, in this section, kinematic methods will be presented for postfailure control in the presence of a single mode of failure.

For a healthy arm, the positional-kinematic equation that a manipulator configuration reach a hand pose T_{hand} is given by

$$f(q) = T_{\text{hand}}, \quad (16)$$

where $f(\cdot)$ is the mapping from configuration to hand pose. Because (16) is typically difficult to solve, a linearization is often made based on the manipulator Jacobian equation. If \dot{x} is a representation of the hand's linear and/or rotational velocity and the corresponding manipulator Jacobian is given by

$$J = [j_1 \ j_2 \ \dots \ j_n], \quad (17)$$

then the manipulator Jacobian equation is

$$\dot{x} = J\dot{q}. \quad (18)$$

For solving (18) given a desired \dot{x} , one can apply any number of techniques using a suitable joint-rate weighting matrix. This weighting matrix will be labeled $W(q)$ —it is symmetric and if positive definite defines a metric on the \dot{q} space through

$$\eta(\dot{q}) = \sqrt{\dot{q}^T W \dot{q}}. \quad (19)$$

Different modes of failure in this system will be addressed below, and their impact on these equations will be discussed.

A. Locked Joint

Assume a failure at joint i . When the failed joint is locked, a manipulator configuration that reaches hand pose T_{hand} must satisfy (16) and

$$q_i = \ell_i, \quad (20)$$

where ℓ_i is the locked value. The velocity equation becomes

$$\dot{x} = {}^iJ\dot{q}, \quad (21)$$

where iJ is formed by removing column i from J ; i.e.,

$${}^iJ = [j_1 \ \dots \ j_{i-1} \ j_{i+1} \ \dots \ j_n], \quad (22)$$

and ${}^i\dot{q}$ is formed by removing element i from \dot{q} . For trajectory generation, (21) can be solved for ${}^i\dot{q}$ which can be integrated to find ${}^i\dot{q}$ while q_i remains constant.

The induced weighing matrix for ${}^i\dot{q}$ is iW , formed by removing row i and column i from W . Clearly, ${}^i\dot{q}^T {}^iW {}^i\dot{q} = \dot{q}^T W \dot{q}$ when q_i is constant. If W is positive definite, then iW is also.

B. Free-Swinging Joint

When joint i is in free-swinging mode, the manipulator configuration to reach a hand pose T_{hand} while stationary must satisfy (16) and

$$\hat{\theta}_i(\mathbf{q}) = 0, \quad (23)$$

where $\hat{\theta}_i$ is the swing angle.

For a slow-moving manipulator $\dot{\hat{\theta}}_i(\mathbf{q}) \approx 0$. Provided neither \tilde{s}_{i-1}^* nor \tilde{g} is parallel to \hat{z}_{i-1} , this gives, since element i of $\nabla \hat{\theta}_i$ is -1 ,

$$\dot{q}_i \approx {}^i\dot{\mathbf{q}}^T \nabla \hat{\theta}_i, \quad (24)$$

where ${}^i\nabla \hat{\theta}_i$ equals $\nabla \hat{\theta}_i$ with entry i removed.

The velocity equation for a slow-moving manipulator then becomes

$$\dot{\mathbf{x}} \approx {}^i\mathbf{J}^i \dot{q}_i, \quad (25)$$

where

$${}^i\mathbf{J} = {}^i\mathbf{J} + \mathbf{j}_i \nabla \hat{\theta}_i^T. \quad (26)$$

Thus, when the manipulator is slow moving, the velocity equation has the same structure for a free-swinging failure in (25) as for a locking failure in (21). The difference between the locked-joint and the free-swinging Jacobians is the rank-one matrix $\mathbf{j}_i \nabla \hat{\theta}_i^T$. For trajectory generation, (25) can be solved for ${}^i\dot{\mathbf{q}}$, which can be integrated to find ${}^i\mathbf{q}$. An updated value of ${}^i\mathbf{q}$ can then be used with the previous value of q_i to solve for the associated swing angle to be added to the previous value of q_i to get the new value.

The weighing matrix induced by a free-swinging failure is

$${}^i\hat{\mathbf{W}} = {}^i\mathbf{W} + W_{ii} \nabla \hat{\theta}_i \nabla \hat{\theta}_i^T + {}^i\mathbf{W}_i \nabla \hat{\theta}_i^T + \nabla \hat{\theta}_i {}^i\mathbf{W}_i^T, \quad (27)$$

where W_{ii} is diagonal entry i of \mathbf{W} and ${}^i\mathbf{W}_i$ is column i of \mathbf{W} with entry i removed. With this definition, ${}^i\dot{\mathbf{q}}^T {}^i\hat{\mathbf{W}} {}^i\dot{\mathbf{q}} \approx \dot{q}^T \mathbf{W} \dot{q}$ when q_i is free-swinging. As was the case for ${}^i\mathbf{W}$, if \mathbf{W} is positive definite, then ${}^i\hat{\mathbf{W}}$ is also.

IV. SWITCHING BETWEEN MODES

A locked-joint failure cannot be arbitrarily converted to a free-swinging failure without undesirable dynamic effects. Equation (25) does not apply when the swing angle is large because acceleration- and Coriolis-based forces are manifest and the joint swings, possibly violently. Thus, the primary issue when making this

type of conversion is ensuring that the swing angle is at (or at least near) zero.

Conversely, when the manipulator is operating in free-swinging mode and is slow moving, a brake can be applied at any time with minimal dynamic effects. Thus, (25) can be converted to (21) whenever ${}^i\mathbf{J}$ loses rank, for example. The important parameter when this type of conversion is made is the actual value of q_i —it will be frozen until another conversion. Thus, the primary issue for a free-swinging-to-locked conversion is setting the value of the failed joint.

These two issues of setting the swing angle to zero in a locked-joint manipulator and setting the joint angle to a desired value in a free-swinging manipulator are in fact the same positional kinematic problem—finding a configuration giving both $\hat{\theta}_i = 0$ and $q_i = \ell_i$ for some ℓ_i . It will be shown here that for a slow-moving manipulator they are amenable to the same form of velocity-kinematic equation.

A. Locked to Free Swinging

Since this type of conversion should be made when the value of the swing angle is zero, the focus here is on finding a configuration of the failed, locked-joint manipulator that gives a vanishing swing angle. If the arm's dynamic and kinematic parameters are well known, this is essentially a root-finding problem for which any number of techniques can be applied.

Here the problem will be cast as a familiar velocity-kinematic equation. This has the advantage of general applicability and quality, if not completeness, of its solution. It can be used with feedback from sensors to refine solutions when the arm's parameters are in doubt.

When joint i is locked, the governing velocity-kinematic equation is given by

$$\dot{\hat{\theta}}_i = {}^i\nabla \hat{\theta}_i^T {}^i\dot{\mathbf{q}}. \quad (28)$$

Values of ${}^i\dot{\mathbf{q}}$ for control can be found in a number of ways, with possible inclusion of additional constraints.

For example, one approach is to use a weighted pseudoinverse based on ${}^i\mathbf{W}$. This allows $\hat{\theta}_i$ to be differentially changed with the minimum joint-rate measure as given by (19). If ${}^i\mathbf{W}$ is positive definite and provided ${}^i\nabla \hat{\theta}_i \neq 0$, this solution for a desired value of $\hat{\theta}_i$ can be found as follows:

$${}^i\dot{\mathbf{q}} = \frac{\dot{\hat{\theta}}_i}{{}^i\nabla \hat{\theta}_i^T {}^i\mathbf{W}^{-1} {}^i\nabla \hat{\theta}_i} {}^i\mathbf{W}^{-1} {}^i\nabla \hat{\theta}_i. \quad (29)$$

Equation (29) can be used with torque feedback to set the swing angle accurately to zero. The swing angle can be found for small values $(-\frac{\pi}{2} \leq \hat{\theta}_i \leq \frac{\pi}{2})$ using

$$\hat{\theta}_i = \sin^{-1} \left(\frac{-g_i}{\|\hat{s}_{i-1}^* \times \hat{z}_{i-1}\| \|\hat{z}_{i-1} \times \hat{g}\|} \right), \quad (30)$$

where g_i is the measured torque at joint i .

B. Free Swinging to Locked

The primary goal for this type of conversion is to lock the joint at the appropriate value. So the focus is on seeking a configuration of the failed, free-swinging manipulator that gives the desired value of the failed joint. The velocity-kinematic equation for this focus is

$$\dot{q}_i \approx {}^i\nabla\hat{\theta}_i^T \dot{\hat{q}}, \quad (31)$$

and this can be directly used with measured joint position feedback. It has the same form of solution as did the locked-to-free-swinging conversion. So, again as an example, if ${}^i\hat{W}$ is positive definite and provided ${}^i\nabla\hat{\theta}_i$ is defined and not equal to zero, a healthy-joint-rate solution giving a desired value of \dot{q}_i can be found using

$$\dot{\hat{q}} = \frac{\dot{q}_i}{{}^i\nabla\hat{\theta}_i^T {}^i\hat{W}^{-1} {}^i\nabla\hat{\theta}_i} {}^i\hat{W}^{-1} {}^i\nabla\hat{\theta}_i. \quad (32)$$

V. EXAMPLE

The simple planar redundant arm shown in Fig. 1 will be used as an illustrative example. Its link lengths are 1 m, the link masses are 10 kg, the center of mass of each link is at the center of the link, and the link inertias are modeled as thin rods.

A. Switching Strategy

To illustrate a strategy for postfailure operation through switching, assume that a failure of joint one has occurred. The beginning configuration is the top one from the right-hand side of Fig. 1. The goal is to reach the point $\{-2.5, 0\}$. To achieve this, it is necessary to use a mode-switching scheme. To reach $\{-2.5, 0\}$, q_1 must be greater than $\cos^{-1}(-\frac{13}{20})$ and less than $\pi - \cos^{-1}(-\frac{13}{20})$. The intersection of this range of values with those possible for joint one after a free-swinging failure gives $\tan^{-1}(\frac{3}{4}) \leq q_i \leq \pi - \cos^{-1}(-\frac{13}{20})$.

Let the joint-rate weighting matrix be given by $W = \text{diag}(9, 4, 1)$ which is an appropriate choice for reducing the relative burden on the inboard joints. A switching sequence based on using this value of W in (29) and (32) for moving q_1 and relocking it in this range to achieve the task is shown in Fig. 2.

B. Joint Trajectory Generation

In this section, postfailure operation through joint trajectory generation will be explored. The failure for

this example lies in joint one. The joint-one swing angle is given by

$$\hat{\theta}_1 = \text{Atan2} \left[\begin{aligned} &-(5 \cos(q_1) + 3 \cos(q_1 + q_2) + \cos(q_1 + q_2 + q_3)), \\ &-(5 \sin(q_1) + 3 \sin(q_1 + q_2) + \sin(q_1 + q_2 + q_3)) \end{aligned} \right] \quad (33)$$

and, provided $\hat{\theta}_1 \neq \pi$, the gradient is given by

$$\nabla\hat{\theta}_1 = \begin{bmatrix} -1 \\ \frac{-10-15 \cos(q_2)-6 \cos(q_3)-5 \cos(q_2+q_3)}{35+30 \cos(q_2)+6 \cos(q_3)+10 \cos(q_2+q_3)} \\ \frac{-1-3 \cos(q_3)-5 \cos(q_2+q_3)}{35+30 \cos(q_2)+6 \cos(q_3)+10 \cos(q_2+q_3)} \end{bmatrix}. \quad (34)$$

The motor will be assumed disconnected from the failed joint for this simulation experiment, so M_{ii} is the diagonal entry of the mass matrix induced by the inertia of the manipulator's links, and it is assumed that $V_{ii} = 15.0$.

A trajectory was generated using the method given in Section III-B for an end-effector path given by the line segment from $(-0.75, -2.0, 0.0)$ to $(-0.75, 0.0, 0.0)$. This is the path shown in Fig. 1, and it lies well within the joint-one free-swinging postfailure workspace. To form an end-point trajectory from this path, a trapezoidal velocity profile was used, with a 20% speed-up and 20% slow-down time. Three configurations along the idealized joint path for this trajectory are shown on the left side of Fig. 1. For this joint path, $\zeta \in [0.046, 0.145]$ and $\omega_n \in [2.40, 3.08]$; both start at the low end and finish at the high end of their ranges. Thus the system would be expected to be underdamped and oscillate with 2.0 to 2.6 seconds per cycle (with the lower value at the end of the trajectory). And this is in fact what is seen in dynamic simulations. The error in joint one for four trajectory times is illustrated in Fig. 3.

VI. SUMMARY

This article presented ways to exploit a manipulator's postfailure capabilities when conversion between free-swinging and locked-joint failure modes is possible. Velocity-control methods were discussed for both types of failures, and ways of effectively converting between the two types were presented. An example illustrating switching strategies and postfailure operation was given.

REFERENCES

- [1] A. A. Maciejewski, "The design and control of fault tolerant robots for use in hazardous or remote environments," *Proc. Fourth ANS Topical Meeting on Robotics and Remote Systems*, pp. 633-642, (Albuquerque, NM), Feb. 24-28, 1991.
- [2] C. J. J. Paredis, W. K. F. Au, and P. K. Khosla, "Kinematic design of fault tolerant manipulators,"

Computers and Electrical Engineering, vol. 20, no. 3, pp. 211-220, May 1994.

- [3] C. J. J. Paredis and P. K. Khosla, "Mapping tasks into fault tolerant manipulators," *Proc. 1994 Int. Conf. on Robotics and Automation*, pp. 696-703, (San Diego, CA), May 8-13, 1994.
- [4] C. L. Lewis and A. A. Maciejewski, "Dexterity optimization of kinematically redundant manipulators in the presence of failures," *Computers and Electrical Engineering*, vol. 20, no. 3, pp. 273-288, May 1994.
- [5] R. G. Roberts, "On the local fault tolerance of a kinematically redundant manipulator," *J. Robotic Systems*, vol. 13, no. 10, pp. 649-661, 1996.
- [6] C. L. Lewis and A. A. Maciejewski, "Fault tolerant operation of kinematically redundant manipulators for locked joint failures," *IEEE Trans. Robotics and Automation*, vol. 13, no. 4, pp. 622-629, Aug. 1997.
- [7] J. D. English and A. A. Maciejewski, "Euclidean-space measures of robotic joint failures," *Proc. 1997 Int. Conf. on Robotics and Automation*, pp. 2894-2901, (Albuquerque, NM), April 20-25, 1997.
- [8] J. D. English and A. A. Maciejewski, "Fault tolerance for kinematically redundant manipulators: Anticipating free-swinging joint failures," *IEEE Trans. Robotics and Automation*, vol. 14, no. 4, pp. 566-575, Aug. 1998.
- [9] J. D. English and A. A. Maciejewski, "Robotic workspaces after a free-swinging failure," *J. Intelligent and Robotic Systems*, vol. 19, no. 1, pp. 55-72, May 1996.
- [10] G. Oriolo and Y. Nakamura, "Control of mechanical systems with second-order nonholonomic constraints: Underactuated manipulators," *Proc. 30th Conf. on Decision and Control*, pp. 2398-2403, (Brighton, United Kingdom), Dec. 11-13 1991.
- [11] H. Arai and S. Tachi, "Position control of a manipulator with passive joints using dynamic coupling," *IEEE Trans. Robotics and Automation*, vol. 7, no. 4, pp. 528-534, 1991.
- [12] H. Arai, K. Tanie, and S. Tachi, "Dynamic control of a manipulator with passive joints in operational space," *IEEE Trans. Robotics and Automation*, vol. 9, no. 1, pp. 85-93, 1993.
- [13] M. Bergerman and Y. Xu, "Optimal control of manipulators with any number of passive joints," *J. Robotic Systems*, vol. 15, no. 3, pp. 115-129, 1998.
- [14] M. Bergerman and Y. Xu, "Robust joint and cartesian control of underactuated manipulators," *ASME J. Dynamic Systems, Measurement, and Control*, vol. 118, pp. 557-565, 1996.

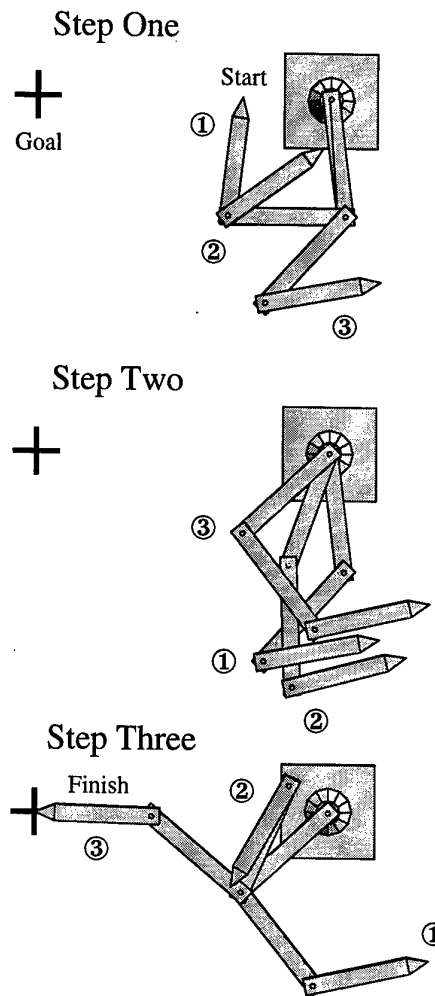


Fig. 2. Three configurations for each of three steps of a switching strategy are shown. The goal is to reach $\{-2.5, 0\}$, shown by cross hairs. In step one, the manipulator is moved using (29) from its initial configuration to a configuration giving a zero swing angle, where the brake is released. In step two, the arm is moved using (32) to place joint one at the desired value, where the brake is reapplied. In the final step, the manipulator is moved to the desired hand position by solving (18) for joint rates that give straight-line end-point motion.

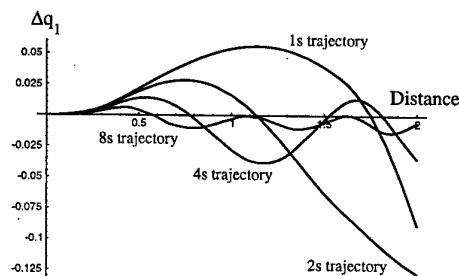


Fig. 3. The joint-one error as the arm traced the two-meter vertical trajectory shown in Fig. 1 with joint one free swinging.

Measurement of Dynamic Characteristics of Traction Drive and High-Precision Control of Traction Drive Servomechanism

Lei Wang, Takashi Emura and Syuichi Oomori

Department of Mechatronics and Precision Engineering, Tohoku University

Aoba-Yama 01, Aobaku, Sendai, 980-8579, Japan
{wang, emura, oomori}@emura.mech.tohoku.ac.jp

Abstract

This paper describes a study of high-precision servomechanisms using traction drive and proposes a method to detect slip velocity with high accuracy and high resolution. A new two-phase type PLL using non-sinusoidal signals was used for detecting this slip velocity. We applied the proposed method to measure frequency characteristics of torque transmission in traction drive, and obtained frequency characteristics by using cross correlation method. Experimental results of servo-control based on the measured characteristics to improve stability and load characteristics of servomechanisms by slip-velocity feedback are also presented.

1 Introduction

High-precision servomechanisms require high-accuracy reduction mechanisms for torque matching. The usual reduction mechanisms are gear reducers. However, the gear reducers have large transmission error due to the backlash, profile error, pitch error of gears. If the frequency components of transmission error are distributed only in lower frequency range, it is easy to compensate by varying motor velocity. On the other hand, if the frequency is beyond the response frequency of servomotors, it becomes difficult to compensate. Unfortunately, transmission errors of reduction gears are distributed over wide frequency range so that it becomes difficult for us to achieve high-accuracy servo-control by using reduction gears.

Traction drive has excellent transmission characteristics compared with reduction gears. Backlash of traction drive is negligible and the frequency components of transmission error are small in high frequency range. Actually, traction drive contains only transmission error associated with shaft eccentricity that has low frequency. This is significant to high-precision servomechanisms because the transmission error can be compensated more easily than gear reducers. Therefore EMURA applied traction drive to a constant-velocity servomechanism. The authors developed a high-precision servomechanism and demonstrated the performance of traction drive for high-precision servomechanisms by experimental results[1].

Traction drive transmits torque by viscous force of fluid film formed between two rolling rollers[2]. Torque transmission of traction drive is accompanied with slip between the two rollers. The torque transmission characteristics versus slip are very important to the servomechanisms that use traction drive. Applying traction drive to positioning servomechanisms, we have to carry out feedback control of rotary angle of output axis. This means that the slip takes place inside feedback loop and affects the performance of the servomechanisms. In the experiments of servo-control, we observed resonant oscillations caused by the slip. Therefore it is important to understand torque transmission characteristics versus slip. The transmission characteristics of traction drive have been investigated by many researchers[3] and in the case of steady transmission torque it has become well known that the torque is approximately proportional to the slip ratio. However, most of reported results are only about static characteristics and the dynamic characteristics have not yet clarified, because it is very difficult to measure the dynamic characteristics. On the other hand, the dynamic characteristics of torque transmission are very important to the dynamic performance of servomechanisms.

Therefore, in this study, the authors investigated the transmission characteristics versus slip by experiments. Slip between the two rollers is very small so that it is difficult to detect with high accuracy by using conventional methods, in particular, at a high-velocity rotation. Emura proposed to use non-sinusoidal 2-phase type PLL for high-resolution detection of slip velocity[4]. This method used two encoders mounted on input axis and output axis respectively. By interpolating the phase of the two encoders, we are able to detect the difference of rotary velocity between the two rollers with high accuracy and high resolution. However, the eccentricity and run-out of rollers induce large ripples to the velocity difference, and the output of detection circuits contains large error. In this study, cross correlation method was used to remove such error for precise investigation of the frequency characteristics of torque transmission.

The experimental results showed that the torque transmission characteristics have large nonlinearity and the linear range is very small. The nonlinearity of torque transmission induces unstability like oscillations to servomecha-

nisms and the robustness for load fluctuation becomes poor. To improve the stability and load characteristics, we proposed a slip-velocity feedback control to the servomechanism basing on the measured torque transmission characteristics. The experimental results showed that the stability and load characteristics of the servomechanism were significantly improved.

This paper describes a new method measuring the dynamic characteristics of transmission torque and gives experimental results of servo-control based on the measured dynamic characteristics.

2 Measurement of Slip Velocity

2.1 Slip Velocity of Traction Drive

The traction drive type reducer used in the servomechanism is shown in Fig.1. Two rollers are pressed against each other by pressing force F_r and are coupled by traction force F_t . The rollers are lubricated by traction oil. The other notations of Fig.1 are as follows.

θ_1 : rotary angle of driving shaft
 θ_2 : rotary angle of driven shaft

R_1 : radius of driving roller
 R_2 : radius of driven roller
 T_m : torque of driving motor
 T_l : load torque.

Slip between the two rollers occurs when torque is transmit-

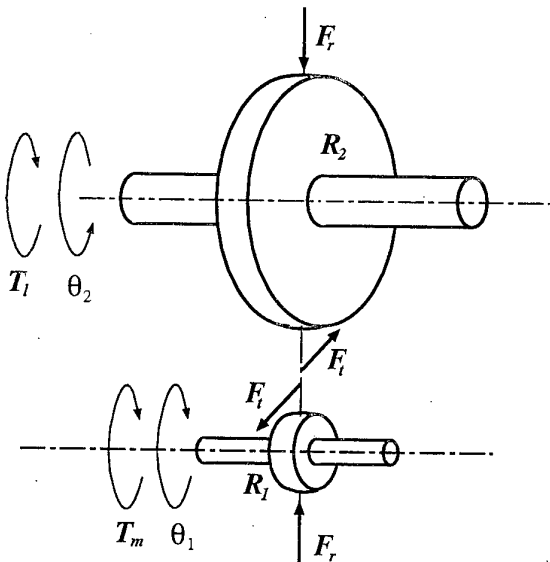


Fig. 1. Reducer that uses traction drive.

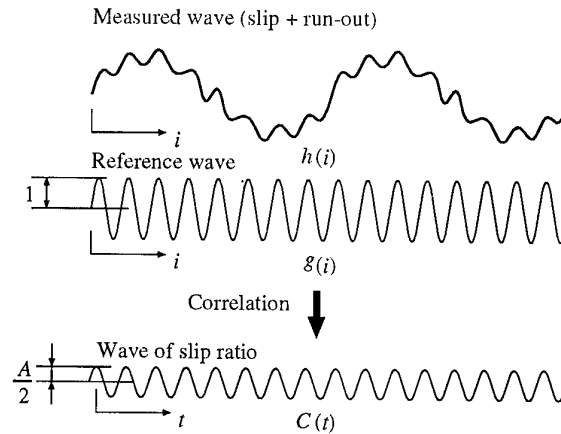


Fig. 2. Detection of slip velocity by cross correlation.

ted. The slip ratio S is defined as follows.

$$S = \frac{2(R_1\dot{\theta}_1 - R_2\dot{\theta}_2)}{(R_1\dot{\theta}_1 + R_2\dot{\theta}_2)} \quad (1)$$

For a constant-velocity servomechanism, the average velocity $(R_1\dot{\theta}_1 + R_2\dot{\theta}_2)/2$ is kept constant, thus it is enough for us to detect the difference of rotary velocity $R_1\dot{\theta}_1 - R_2\dot{\theta}_2$. Two encoders were mounted to each axis. The output pulse trains of encoders have the phase of the pulses proportional to rotation angle. To know the velocity difference of the two axes, we only need to detect phase difference of the two pulse trains.

In order to obtain high-accuracy detection, high-resolution encoders are required. However, because high-resolution encoders can not rotate at high rotary velocity, we have to use low-resolution encoders. Therefore the authors used non-sinusoidal 2-phase type PLL method to interpolate the low-resolution output of encoders for high-resolution detection. This method compares the phase difference between two pulse trains and output a pair of triangular waves with their phase proportional to slip velocity. The triangular waves were interpolated with high accuracy and high resolution by 2-phase type PLL. The slip-velocity detector that uses non-sinusoidal 2-phase type PLL was described in detail in [4].

2.2 Detection of Slip Velocity Using Cross Correlation

By using above-mentioned method, we can investigate the frequency response of torque transmission. In the experiments, we controlled the driving roller to rotate at a constant velocity, and gave load torque of sinusoidal wave to output axis. By detecting the slip velocity with high resolution, we can know the relation of transmitted torque and slip veloc-

ity. However, from (1), it is easy to find that the run-out of the rollers induces error to the detection. This situation is shown in Fig.2, where the reference wave is used for producing load torque. When slip is small, slip velocity has the same frequency as that of load torque. However the measured data contain components associated with eccentricity of rollers. To remove the error we used cross correlation method expressed as follows.

$$C(t) = \frac{1}{N} \sum_{i=0}^{N-1} g(i+t)h(i), \quad (2)$$

where, $h(i)$ is sampled data from slip-velocity detector, $g(i) = \sin(ki)$ is the reference signal that has the same frequency as given load torque, N is the total number of reference data, i is an integer, and t indicates time lag. For example, the output of slip-velocity detector contains slip-velocity signal $A \sin(ki)$ and error $B \sin(mi)$ caused by run-out of rollers, then we have

$$\begin{aligned} C(t) &= \frac{1}{N} \sum_{i=0}^{N-1} \sin\{k(i+t)\} \{A \sin(ki) + B \sin(mi)\} \\ &= \frac{A}{2} \cos(kt) + \frac{1}{N} \sum_{i=0}^{N-1} [-A \cos\{2k(i+t)\} \\ &\quad + B \sin\{k(i+t)\} \sin(mi)], \end{aligned} \quad (3)$$

where, $k \neq m$. If N is large, we have $\lim_{N \rightarrow \infty} C(t) = A \cos(kt)/2$. This means that we can carry out the measurement very precisely by using sufficient number of data. Fig.3 shows the experimental results. The output of slip-velocity detector contains components associated with load torque and other components with different frequency. The

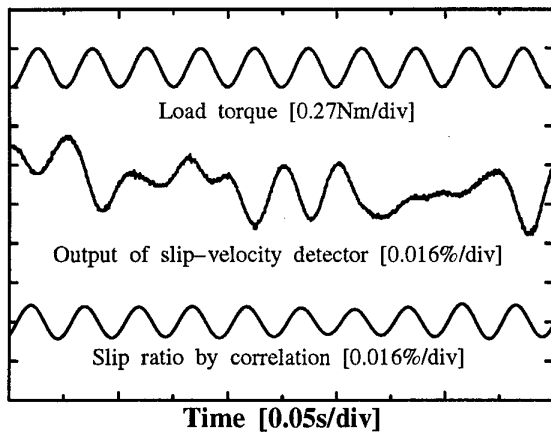


Fig. 3. Measured results with cross correlation.

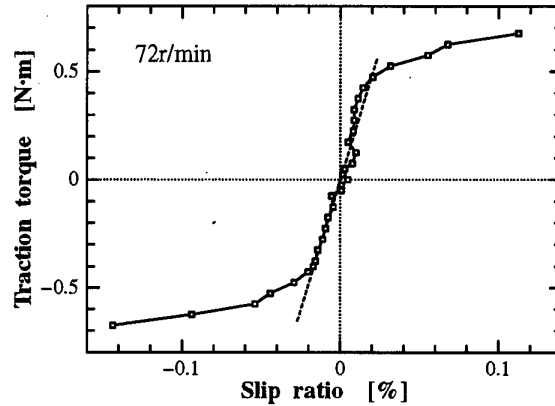


Fig. 4. Measured torque transmission characteristics

components with different frequency from load torque were effectively removed by the cross correlation. From the results, we made certain that the error caused by run-out of rollers is removed and slip-velocity can be obtained by cross correlation method.

2.3 Frequency Characteristics of Torque Transmission

In this study, torque transmission characteristics of a traction drive used for a servomechanism were investigated by experiments. Radii of driving roller and driven roller of this traction drive are 0.018m and 0.11664m. The reduction ratio of this traction drive is 6.48. The encoder of driving shaft generates 5 000 of two-phase square pulses per revolution (ppr) (quadrupled resolution is 20 000 ppr) and the encoder of driven shaft generates two-phase square pulses of 32 000 per revolution (quadrupled resolution is 129 600 ppr). Because the designed reduction ratio is 6.48, we get the equal resolutions for both shafts. In the experiments, input axis was controlled to rotate at a constant velocity as described above.

For comparison with frequency characteristics of torque transmission, static characteristics were measured. In the experiments, a constant load torque was imposed on the output axis and the slip ratio was obtained by averaging the output of slip-velocity detector. Fig.4 is an example of measured static characteristics of torque transmission, where rotary velocity of output axis is 72rpm. The results showed that the torque transmission characteristics have strong non-linearity. When slip ratio is small ($|S| < 0.02\%$) the torque is proportional to slip ratio and the torque gets saturated when slip becomes large ($|S| > 0.02\%$). The maximum transmission torque of linear range is about 0.5N·m. This means that the servomechanism can not transmit large torque so as to keep slip ratio small in linear area. This is

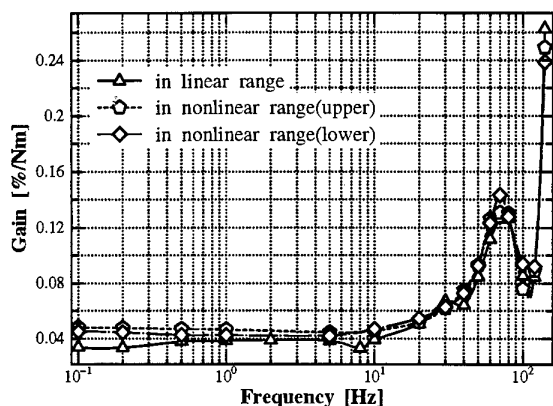


Fig. 5. Frequency characteristics of torque transmission.

because larger torque is not available when slip increases.

In the investigation of frequency characteristics of torque transmission, we changed the load torque with sinusoidal shape and with the frequency range from 0.1 Hz to 180 Hz. Slip ratio was detected using cross correlation method. The cases of load torque of small amplitude 0.13N·m and large amplitude 0.32N·m were investigated. When amplitude is smaller than 0.25N·m, the torque transmission is in linear range according to static characteristics shown in Fig.4. Fig.5 shows the measured frequency characteristics of torque transmission, where the slip ratio was normalized by the pick to pick value of load torque. For the case of linear range, when frequency is lower than 0.2Hz, torque transmission characteristics are the same as that of static characteristics. Slip ratio increases with the increase of the frequency and normalized slip ratio increases rapidly in the high frequency range. However, the slip ratio remains in the linear area if the frequency of load torque is lower than 10Hz. According to static characteristics, when the normalized slip ratio is larger than 0.04%/(N·m), the torque transmission is beyond linear range to nonlinear area. The results mean that slip ratio becomes large more easily under changing transmission torque.

For the case of large load torque, torque transmission is in nonlinear area according to static characteristics. This can be observed from Fig.5 where the normalized slip ratio is larger than 0.04%/(N·m) even in low frequency range. The slip does not increase when the frequency is lower than 10Hz. While the frequency becomes higher than 20Hz, normalized slip ratio increases rapidly. From Fig.5, we can also observe that the frequency characteristics of torque transmission behave the same for large load torque and small load torque. This means that torque transmission was in nonlinearity in both cases of small and large load torque. From the experimental results, we have the conclusions that torque characteristics become nonlinearity more easily when the

transmission torque changes rapidly so that over-large slip occurs.

3 Servo-Control of Traction Drive Based on Measured Torque Transmission Characteristics

Based on the measured torque transmission characteristics, we know that slip ratio becomes large when traction drive transmits large torque. The large slip results in resonant oscillations to the positioning servomechanisms. Moreover, over-large slip will cause damages to roller surfaces. This is fatal to a high-precision servomechanism. In high-accuracy positioning control, high feedback gain is always used. When there is positioning error that is usually caused by load torque change or some other disturbances, the servomechanism needs traction drive which can transmit large torque to suppress the tracking error. Consequently, large slip between rollers takes place. In such time, over-large slip occurs and results in resonant oscillations.

3.1 Feedback of slip velocity

To avoid these phenomena, it is required to suppress the slip ratio. Therefore, we introduced a slip-velocity feedback

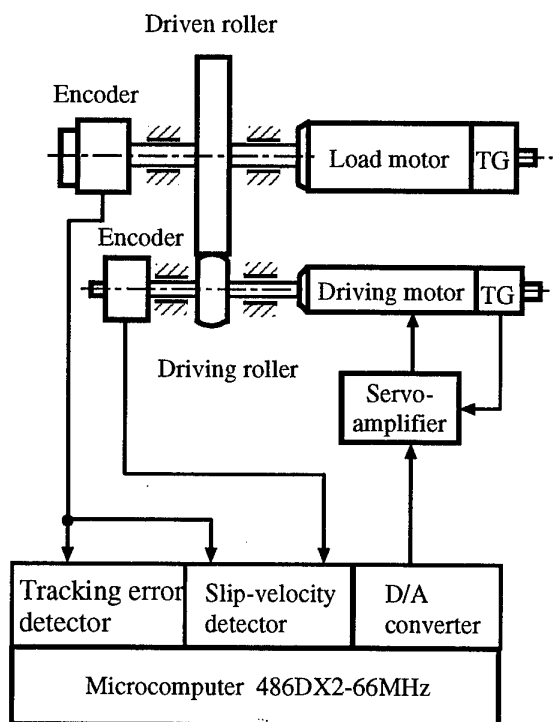


Fig. 6. Setup for experiments.

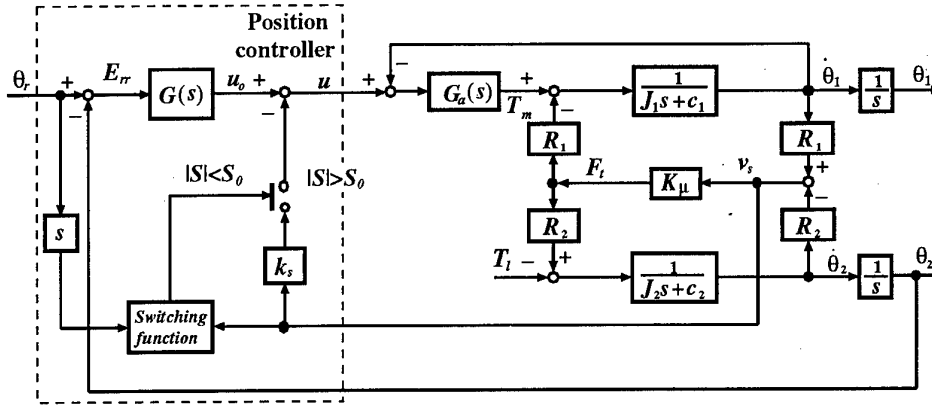


Fig. 7. Block diagram of servomechanism.

control to the servomechanism. This method uses a control strategy that when the slip ratio becomes large the controller carries out feedback of slip velocity. The reason that slip-velocity feedback is not carried out for small slip ratio is that when slip velocity is small the detection error becomes comparatively large and induces error to the servo control. The control strategy is expressed as follows.

$$\begin{cases} u = u_o & |S| < S_0 \\ u = u_o - k_s v_s & |S| > S_0 \end{cases} \quad (4)$$

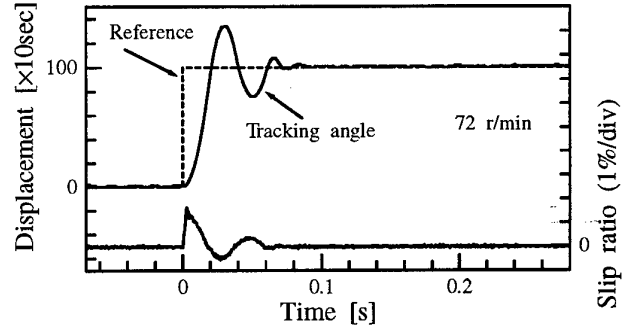
where, v_s indicates slip velocity, k_s is feedback gain, u is controller output, u_o is the controller output without slip-velocity feedback, and S_0 is a constant less than the slip ratio when torque reaches saturation.

3.2 Control system

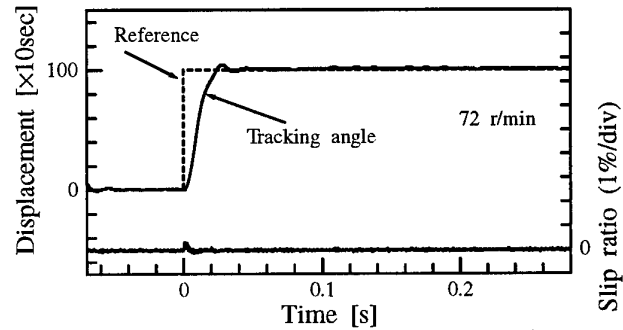
Implementation for the experiments is shown in Fig.6. The driving roller is driven with a DC servomotor. Two encoders are mounted on the driving shaft and driven shaft. Slip-velocity detector uses non-sinusoidal 2-phase type PLL to interpolate the phase difference of the two encoders. The positioning servo controller uses a tracking error detector that can interpolate the rotary angle of output axis to high resolution[1]. In the experiments we achieved a resolution of 0.625sec.

Block diagram of the servomechanism is shown in Fig.7, where

- θ_r : reference input
- J_1 : moment of inertia of driving shaft
- J_2 : moment of inertia of driven shaft
- c_1 : viscous damping coefficient of driving shaft
- c_2 : viscous damping coefficient of driven shaft
- K_μ : viscous friction coefficient of traction drives



(a) without slip-velocity feedback



(b) with slip-velocity feedback

Fig. 8. Experimental results of slip-velocity feedback control.

- $G_a(s)$: transfer function of servomotor and servo-amplifier
- $G(s)$: transfer function of position controller
- v_s : slip speed $R_1 \dot{\theta}_1 - R_2 \dot{\theta}_2$.

This system is basically for a positioning servo control.

We added slip-velocity feedback to the basic system. Switch function is according to Equation (1) and (4), where the average velocity of the two roller $(R_1\dot{\theta}_1 + R_2\dot{\theta}_2)/2$ was approximated by $R_2\dot{\theta}_r$. Positioning control and slip-velocity feedback control were achieved by using a microcomputer. Because the switch function of slip-velocity feedback control requires high-speed operations, we set the sampling period of control to 10^{-4}s^1 .

3.3 Step response of servomechanism

To investigate the stability of the servomechanism, experiments of step response were carried out. Fig.8 shows the experimental results of step response of the servomechanism. The amplitude of angular step input is 1000sec . From the results shown in Fig.8, we can see that, without slip-velocity feedback, the slip ratio became larger than 1.5% instantaneously and large overshoot appeared to make the settle time of 5% longer than 0.08s. While, by the control method with slip-velocity feedback, the slip ratio was controlled to less than 0.3% and the settle time became 0.04s. The results indicate that the dynamic characteristics are improved significantly by slip-velocity feedback.

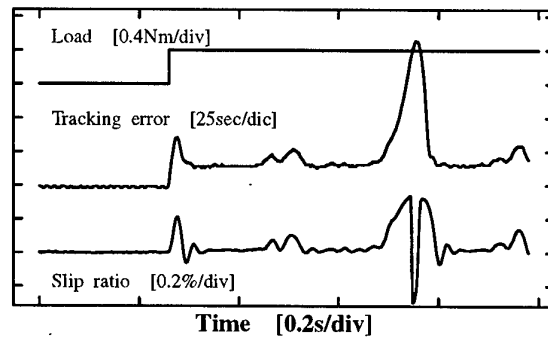
3.4 Load characteristics of servomechanism

Load characteristics are very important for servomechanisms. Because the nonlinearity of torque transmission of traction drive, load characteristics of servomechanisms that use traction drive are very poor when load torque is large. Fig.9 is the experimental results of load characteristics. In the experiments a load torque of step change was added to the output axis through load motor. From Fig.9(a), we can find that large tracking error appears instantaneously. This is because that slip becomes large and torque transmission reached the nonlinear area. The slip ratio is large than 0.02% during instantaneous period of load torque and existence of other disturbances. Over-large slip can be suppressed by introducing slip-velocity feedback. Fig.9(b) shows the experimental results with slip-velocity feedback control. Because the over-large slip did not take place, no large tracking error appears instantaneously as that in Fig.9(a). Therefore, we can confirm that slip-velocity feedback control is useful to improve load characteristics of servomechanisms that use traction drive.

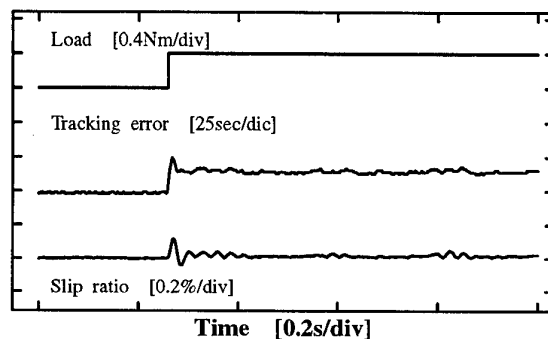
4 Conclusions

In this study, the authors investigated the torque transmission characteristics of the traction drive. The cross correlation method was used for detecting frequency re-

¹sec is used to stand for second of rotary angle and s for second of time in this paper.



(a) without slip-velocity feedback



(b) with slip-velocity feedback

Fig. 9. Improvement of load characteristics by slip-velocity feedback control.

sponse of slip ratio. Considering the measured torque transmission characteristics, we introduced slip-velocity feedback method to improve the dynamic characteristics of servomechanisms. The experiments confirmed the effectiveness of proposed method.

5 Acknowledgements

The authors would like to thank Mr. Masatoshi Suzuki for his cooperation for making the experimental apparatus. A part of this research work was supported by the Grant in Aid for Scientific Research of the Ministry of Education in Japan. The authors express many thanks to this grant.

References

- [1] T. Emura, L. Wang and X. Chen, "Application of Traction Drive to Constant-velocity Servomechanisms," Proc. of The 5th UK Mechanics Forum International Conference, vol.2, pp. 227-232, 1996.
- [2] D. Dowson and G. R. Higginson, "Elastohydrodynamic Lubrication," Pergamon Press London, 1966.
- [3] B. O. Jacobson and B. J. Hamrock, "Non-Newtonian Fluid Model Incorporation of Rectangular Contacts," Trans.ASME, J.Tribol.,106(1984), 275.
- [4] T. Emura and L. Wang, "High-Speed and High-Resolution Detection of Slip Velocity of Traction Drive by Two-Phase Type PLL," JSME Proc. No.971-1, 1997.

A

Data Structure for the Organization by a Robot of Sensory Information

A. Bugra KOKU, Richard Alan PETERS II

Vanderbilt University, Electrical and Computer Engineering Dept.

{koku, rap2}@vuse.vanderbilt.edu

Abstract

This paper both presents the current approach of Intelligent Robotics Laboratory (IRL) to intelligent robotics systems at Vanderbilt University and outlines the upcoming research issues which tend to realize intelligently behaving humanoid robots in a distributed computing environment by making use of the most recent technologies.

1. Introduction

The rapid growth of the power of computers, and concurrent decline in their cost, has increased dramatically the potential of robots to interact naturally with the world. Until recently robots were useful only in highly structured environments such as an assembly line, where they could perform repetitive tasks. They have been quite unlike animals, which must react and adapt to survive while pursuing their goals in a dynamic environment. An animal can react and adapt because it can sense the world, it has some concept of how its actions affect the world, and when its actions do not have the desired effect, it can change them (or it dies). Fast, cheap computers probably can now (or will soon be able to) process sensory data in sufficient quantity quickly enough to permit a robot to adapt to a natural, unstructured environment.

Such adaptability requires more than raw computational power. It requires the robot's sensory system to be properly organized, it requires sensing to be appropriately coupled to the robot's actions, and it requires that the actions of the robot in response to specific sensory input be changeable by the robot itself. Proper organization is necessary to permit simultaneous sensing in a number of different modalities and to enable shifts of attention from one task to another in response to external events and internal status. The coupling of sensing to action embeds the robot in its environment; it links the sensual to the corporeal so that the geometry and dynamics of the external world can be understood in terms of those of the robot. A mapping from sensory input to action that is malleable by the robot is necessary for learning, and learning is the essence of adaptability.

This paper concerns the logical organization of a sensory system for a humanoid robot. The robot is ISAC, developed at the Center for Intelligent Systems at Vanderbilt University. ISAC has two 7-DOF arms, an active, stereo, color, vision system, 6-axis force-torque sensors at the wrists, simple haptic sensors on the fingers of its anthropomorphic hand, haptic sensors and proximity sensors on the palm of the hand, and ISAC has an array of infrared motion detectors on its torso. The robot has sound input which is currently being modified to permit sound source localization. Data from these sensors will be processed as if it is projected on a sphere that surrounds the robot. Albus named the structure an EgoSphere [1]. We refer to it as a **Sensory EgoSphere** or **SES**.

In theory, the sensors and low-level sensory processing algorithms commonly in current use can provide an extensive set of spatial features at any point on the SES. For example each point could have light intensity, hue, color saturation, edge intensity, edge orientation, depth to first surface, motion direction, speed, etc. But in reality, such extensive sets of information are too large to permit real-time processing. The complexity of sensory information processing can be reduced through the use of attentional networks [2]. These are sensory processing algorithms that detect data of potential interest as a function of the task at hand. They are de facto information filters. By directing the computational resources to important but limited and localized sets of sensory data at any one time, an AN causes the rest of the data to be ignored. Shifts in attention permit exploration of the environment. By continuously monitoring several different sensory modalities with ANs that are capable of interrupting each other, attention may be redirected from one location to another. For example, a sudden loud sound detected at one location by an audio AN could interrupt image analysis at another location and cause the visual AN to shift attention to the direction of the sound.

2. The Learning System Architecture

This section will introduce the techniques that are currently in use in our robotics system.

2.1. Intelligent Machine Architecture (IMA)

IMA, being the backbone of all the software written in IRL, is a software system design paradigm that permits the concurrent execution of software agents on separate machines while facilitating extensive inter-agent communication. In other words, IMA is a distributed software architecture specifically designed for generating intelligent machine applications [3].

IMA runs under MS Windows NT 4.0 and makes use of DCOM to manage the inter-agent communications. DCOM (Distributed Component Object Model) is a service of MS Windows NT which allows remote objects to be treated as local, namely, it is the framework of distributed computing.

Agents are loosely coupled, which facilitates parallel processing. For larger systems, IMA takes advantage of both distributed and symmetric multiprocessing computer systems more effectively than do monolithic architectures. Each agent acts locally based on its internal state and provides a set of services to other agents through various relationships. The loosely couple, asynchronous operation of decision-making agents simplifies the system model at high level. Whereas over-simplification of the higher levels of a system can lead to non-robust operation, a collection of asynchronously executing agents is more stable. It provides an abstraction that eliminates many concerns about synchronization, because the architecture provides each agent with a knowledge of time that allows each local decision process to evaluate information based on its age relative to that agent. The agents in IMA work like a group of control loops, continually sampling inputs, updating states and computing new outputs [3].

IMA was designed

- to facilitate distributed implementation,
- to be interface driven, and
- to allow software module reusability [4].

IMA is different from traditional software systems in that:

- IMA uses a system level model that is agent based
- IMA uses an agent level model that is component-object based

As a result of this, each resource, task or domain element can be modeled as a software agent. This two level architecture allows the generation of reusable, extensible programs from the software-engineering point of view and also introduces parallelism, scalability, reactivity and robustness from the systems engineering point of view [5].

With this agent-based architecture, along with the properties of reusability and scalability, many basic routines have been created for the IRL database. New applications may only need to introduce some additional agents to

handle the new situation while benefiting from many of the previously written agents.

2.2. Spreading Activation (SA)

Classical AI approaches, being deliberate and centralized, have some drawbacks. As a result of being deliberate, any failure throughout the application of a plan results in re-planning from scratch. Also, centralized systems are heavily dependent on the performance of the central unit. If it fails, then the whole system fails. On the opposite side of the planning spectrum are reactive planners. A fully reactive system does not have to go back and start from scratch when the current action fails. It simply chooses the second best action towards achieving its goal. This type of behavior has some advantages over deliberate planners, but suffers from getting stuck at local minimas or vicious circles.

The first attempt to combine deliberative and reactive behaviors in a single adjustable distributed system came from MIT. P. Maes introduced the idea of *Spreading Activation Networks* by which she intended to have a system, the behavior of which could be adjusted to move towards deliberate or reactive behavior by changing a global parameter [6]. This algorithm has an agent-based structure, where the agents are composed of some competence modules. These modules compete to accomplish the agent goals, and the agents try to fulfill the global goal. By the use of some global parameters assigned to the system, a smooth shift between the following properties can be established:

- adaptive \leftrightarrow biased towards ongoing goals
- goal oriented \leftrightarrow situation relevant
- fast \leftrightarrow thoughtful
- conservative \leftrightarrow careless about the goal conflicts

The advantages of this algorithm are:

- the system has a distributed search method
- the system produces simultaneous solutions so there are always fall-back plans available
- its performance can be tuned via some global parameters
- it is fault tolerant.

Besides the advantages, there are some problems the solution of which are not addressed in this approach. The first being the tuning mechanism for the global parameters (the settings of which will effect the overall performance of the system) and the second one is keeping a record of past actions.

The second attempt towards achieving a system that can smoothly be shifted between deliberate and reactive behavior, which is highly inspired by the work of Maes, is done by S. Bagchi. The shortcomings of the initial Spreading Activation Network is investigated in detail and

a new version of this algorithm (a probabilistic approach) is proposed [7].

Spreading Activation Networks rely on the basic principle of passing awards from the goals towards the agents, which is referred as “*utility passes backward*” and the agents apply as candidates for accomplishing a task depending on their abilities and past successes, which is referred as “*probability passes forward*”. Figure 1 shows the links that connect the components of a Spreading Activation Network agent. An agent is composed of a set of preconditions and actions. When the preconditions of an agent are all true, it can initiate an action and change the current state of the world. The resulting states (the post-conditions of the agent) will affect the preconditions of some other agents and the system will evolve itself in this manner.

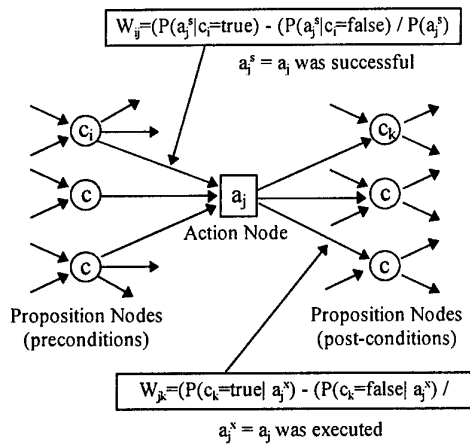


Figure 1. Representation of an precondition, action, post-condition relation (*adapted from [8]*).

The major difference of this study with respect to the initial Spreading Activation Network structure is that the events are handled in a probabilistic manner and some sort of action reports are stored to keep track of the dynamic environment effects and inner dynamics. This not only allows the system to accumulate experience over time and prevents the system from repeating the same mistakes over and over again but also lets the system understand its own dynamics (in other words reliability and/or capability of individual agents composing the SA network). These properties eliminate the shortcomings mentioned for the initial design of the Spreading Activation Networks and makes it a very good real time algorithm.

An important point to note about the SA mechanism introduced so far is the static structure of the network. It is a pre-wired network. It actually, is not static in the sense that, in time, some links may have 0 weights and practically drop out from the network, however, new links are

not formed on the fly depending on the current state of the world. If a new problem is to be handled, a new network design has to be implemented by the programmer. The obvious consequence of this is that, even though the system can learn to pick the best solution that is present in the network, it can never evolve itself towards novel solutions.

A recent research on building Spreading Activation Agents by using the IMA mainframe has been completed in the IRL [4]. Currently this agent structure is being used in our applications.

2.3. Sensory EgoSphere (SES)

Albus defines EgoSphere as

a two dimensional spherical surface that is a map of the world as seen by an observer at the center of the sphere. Visible point on regions or objects in the world are projected on the egosphere wherever the lines of sight from a sensor at the center of the egosphere to points in the world intersect the surface of the sphere [1].

Albus suggests that a 2D egosphere is sufficiently informative for an intelligent agent to model the sensory world. To emphasize its sensory function, we call the structure the **Sensory EgoSphere (SES)** in this text.

Any sensory data that can be localized, (such as the video input stream from an active camera head, a directional sound source, the distance to the closest surface, etc.) can be stored on a SES. It is, therefore, a multiresolution, 2Dx1D map of the robot's environment indexed by elevation, azimuth, and time associated with data specific descriptors (i.e., FFT parameters or verbal descriptors of objects found in an image etc.). From the view point of having different data types with different resolutions, egosphere can be viewed as layers of data wrapped around the egosphere as illustrated in figure 2. A sensory data set of a specific type at a specific SES location can be stored as an object with a timer that indicates its age. Objects at a specific SES location can be deleted from the sphere after a period of time depending on the type of data or the arrival of new up-to-date sensory information can overwrite the older information at the same location. Some quick methods of checking the validity of the currently posted data on the egosphere and the current state of the world is essential. To fulfill this, data specific descriptors are needed. The descriptors are not only needed for checking the correlation with the current state of the world but they are also essential in establishing the links on DBAM (which is introduced in the next section).

Structurally, SES is a multiresolutional (multi-layered) database. Functionally, SES is a multi-user accessible

database. It can be considered to be an associative memory where the association is through proximity. Visible objects that have been recognized can be labeled on the SES, and the labels used as search keys. Any of the agents in the robot can query the database. For example, if the robot is trying to serve a beverage to a person, a possible search in its workspace could be for a *coke can*. In the classical sense, this might be performed through visually searching the environment for the distinctive colors on a coke can or for cylindrical objects. In our case, by passing a query for "coke can" to the SES database the robot can get the most recent location where a coke can was spotted on the egosphere and narrow its visual search space significantly. Later in the paper we describe how SES access might be aided, through learning, to be more efficient.

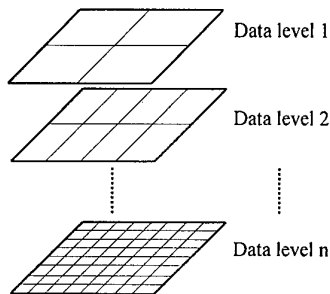


Figure 2. The possible data levels on the egosphere. As an example, Data level 1 may contain sound data, data level 2 may contain sonar data and the last level may contain images captured from the robots environment

The SES provides a natural sense of spatial coherence and continuity to the robot so that imprecise (but entirely natural) interactions with the user such as:

ISAC: *I could not find the spoon.*

USER: *It is right in front of you on the table*
can be made tractable.

This particular interaction uses symbolic information — object labels and location cues — which the robot can use to directly query the database or to restrict its search to specific regions of the EgoSphere

2.4. Database Associative Memory (DBAM):

One important component of our system is an associative memory that is built on a standard database architecture. This will permit, among other things, a symbol to prime or to restrict a search of the SES. The DBAM logically subsumes the SES to provide spatial associations between the objects that surround the robot. The DBAM, further, will associate specific actions with certain objects.

This will enable the robot to decompose a goal into the fundamental actions that it can perform. Our current research focuses on the spatial association.

Whereas the SES provides spatial association — implicit association through proximity and direction — among the data in it, other components of the DBAM provide symbolic associations. Our initial design includes an association lookup table (ALT) to keep track of associations such as the name of an object with its SES locations. Later, it will probably be necessary to trace associations through more complex structures.

Figure 3 illustrates these concepts. The following two scenarios may clarify how SES and DBAM will work to gather.

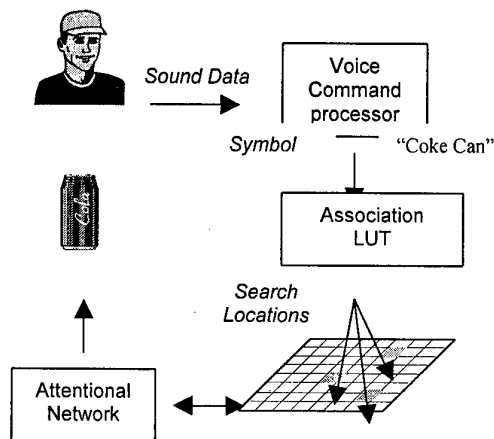


Figure 3. An instance form DBAM illustrating symbolic and spatial association among SES data and ALT.

One of the very basic ways to start interaction with the robot, is to go near it and talk to it (i.e., "Hello ISAC, how are you today?"). This can start a chain of events: sound localization routines will determine where the sound came from, the sonar sensors will try to locate where the motion is and the camera head of the robot will try to find the face of the user and establish an eye-to-eye contact with the user. Also, the user identification routines will try to identify the person and at the end, a similar association to the one shown in figure 3 can be established.

A second situation that may arise throughout an interaction is to find something in the environment during the interaction with a user. As previously stated, suppose that, the robot is to serve coke to the user. On searching for the coke can, the DBAM will provide the locations where the coke can was found previously on the SES. As previously mentioned, each data on SES will be time-stamped and therefore, the DBAM will provide locations of the coke can starting from the most recently located one.

Each record in the DBAM has a numerical activation level. This number can be modified by other agents such as sensing, learning, or task control agents. Each record is linked to others that are in some way related. The link is weighted by the activation level of the record linked to. The links between some DBAM records can be modified by spreading activation (SA) during task execution or through reinforcement learning (RL) conditioned on the success or failure of a task.

3. Learning in the SES and DBAM

An intelligent system should be able to learn from its own experience. It should remember what it saw before and be able to refer to previous events. It should not repeat mistakes. It should be able to learn new skills through observation and repetition. These ideals are far from being met. However, machine learning is currently possible; one can design a system that can learn some things.

Non declarative memories can be formed through trial and error with SA and RL to train sensory-motor coordination maps or task sequence specifications. Such memories enable the robot to work smoothly with its environment while take its own physical structure to best advantage.

Declarative memories are those in which various objects are related to one another, or in which episodes are correlated and associated with objects. This type of memory also permits the association of a goal with the purposive qualities of known objects.

The formation of a declarative memory requires two phases, data acquisition and memory consolidation. Various sensory data is acquired as the robot interacts with its environment. Some of this information is obtained in the course of task execution and is directly coupled to actions performed. Extraneous information, may also be recorded. This is information that may not be directly related to the task at hand, but might be useful in other contexts.

Memory consolidation (MC) is the process whereby the robot forms associations between recently acquired data and previously stored memories. The process will run when the robot is otherwise unoccupied. Recent data will be compared to existing DBAM records. For example, objects data from imagery could be compared to existing object descriptions and if recognized, the new objects would be relabeled. If not, they could be stored as new records. Data acquired during a task execution could be replayed in sequence to form associations based on temporal proximity. The set of such links between data records would constitute a pattern which could be compared to other learned data sequences. Measures of their simi-

larities could be used to link different tasks. The similarities between the MC process just described and dreaming in humans is worth further study.

Figure 4 shows the bi-directional data flow between the memory and the learning units. The formation of associations within the DBAM and SES is the most critical part of our current research. SA provides learning over the established database. Memory consolidation

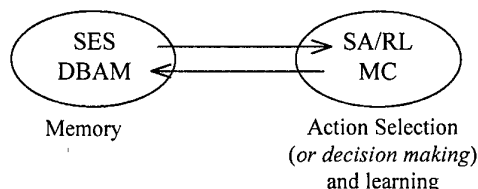


Figure 4. There is bi-directional data flow between SES and SA network.

As a result, the DBAM/SES, the SA/RL network, and the MC procedure provide a mapping from sensory inputs to actions, from objects to objects, and from task to task.

4. Goal: The Shifting of Intelligence from the Programmer to the Robot

A limitation of current SA networks is that they are pre-wired. New states are not added; only the probabilities of changing current states are modified. One can build a SA network by linking software modules. To enable the robot to handle a new task, a programmer can build a network with available modules. It would be much more useful if, by examining associations in the DBAM, the SA network could link new states into itself.

An easy but inefficient solution to this problem is to form a huge network wherein all available modules are linked to each other. Incompatible module dynamics would eliminate many of these links by default. The system would have to be run to evolve itself in time. But such a procedure would probably require human feedback and is likely to require large time intervals. It also requires a good, if not complete, knowledge of all the present modules. Hence the obvious solution is inefficient, lacks scalability, and precludes the introduction of new computational modules.

To create a dynamically linked SA network would require

- an inter-modular communication schema
- a command to action mapping mechanism

The inter-modular communication enables the system to know itself. There are languages present that are designed to manage inter-agent communication such as KQML [9]. Such a language enables software modules to communi-

cate their objects, and pre- and post- execution conditions to each other. It also should possess a descriptor grammar that enables one module to understand the actions of another.

Our approach to system development at the IRL does rely on the systems ability to learn everything from experience. Nor are we attempting to create a high-level symbolic AI. Instead, we approach the development toward both ends from the center. We are designing cognitive structures that will enable the robot to make immediate use of domain knowledge and specific action plans, yet enable it to react to unforeseen occurrences and to evaluate outcomes to modify both knowledge and plans.

5. Conclusion

Current research on robotic control systems performed at the Intelligent Robotics Laboratory of the Center for Intelligent Systems at Vanderbilt University was described. A system including a Database Associative Memory, a Sensory EgoEphere, a Spreading Activation network that uses Reinforcement Learning, and a Memory Consolidation procedure are being designed. It is thought that this system can provide a robot with a sensory-input to action-output mapping. The structure of system is described and future research proposed to enable the system to learn autonomously.

6. References:

- [1] Albus, J. S., "Outline for a theory of intelligence" *IEEE Trans. Syst. Man and Cybern.*, vol. 21 no. 3, 1991
- [2] J. A. Driscoll, R. A. Peters II, and K. R. Cave, "A visual attention network for a humanoid robot," *IEEE/RSJ International Conference on Intelligent Robotic Systems*, Victoria, B. C., Canada, October 12-16, 1998.
- [3] R. T. Pack, "IMA: The Intelligent Machine Architecture", *Ph.D. Thesis*, Vanderbilt University, Nashville, TN, 1998.
- [4] R. M. Watson, "Distributed Task Sequencing for a Humanoid Robot using Spreading Activation Networks", *M.Sc. Thesis*, Vanderbilt University, Nashville, TN, 1998.
- [5] R. T. Pack, D. M. Wilkes and K. Kawamura, "Software Architecture for Integrated Service Robot Development", *IEEE Conf. On Systems, Man and Cybernetics*, Orlando, pp. 3774-3779, Sept. 1997.
- [6] P. Maes, "How to do the right thing", *Connection Science Journal*, 1 (3): 291-323, 1989.
- [7] S. Bagchi, "Planning Under Uncertainty by Spreading Activation Through an Adaptive Probabilistic Network", *Ph.D. Thesis*, Vanderbilt University, Nashville, TN, 1994.
- [8] S. Bagchi, G. Biswas, K. Kawamura, "Generating Plans to Succeed in Uncertain Environments", *Second International Conference on AI Planning Systems*, Chicago, IL, AAAI Press, 1994.
- [9] ARPA Knowledge Sharing Initiative, "Specification of the KQML agent-communication language", External Interfaces Working Group working paper, July 1993.
- [hudl] D. M. Wilkes, R. T. Pack, A. Alford and K. Kawamura, "HuDL, A Design Philosophy for Socially Intelligent Service Robots", *AAAI Symposium in Socially Intelligent Agents*, November 97.

Design of a MEMS SIX DOF Accelerometer

Oren Masory and Jean-Pierre Alfano

Mechanical Engineering Department
Florida Atlantic University
Boca Raton, Florida 33431
masoryo@fau.edu

Abstract.

This paper describes the design of an accelerometer capable of measuring the linear and angular accelerations in a cartesian system. To arrive to the final dimensions and geometry, which will satisfy the requirement under fabrication constraints, an iterative finite elements structural analysis was performed. Also, modal analysis of the proposed structure was performed in order to determine the best locations for capacitance sensing pads. The stiffness matrix of the sensor's structure was found and used to determine its theoretical capabilities.

It was found that the sensor has a high accuracy if used to measure the three components of linear accelerations (average detection error 0.02%), or only the three components of angular ones (average detection error 0.44%). However, when all six acceleration's components have to be measured, the average error increases to about 3%.

1. Introduction

Some recent accelerometers are designed and fabricated using Micro-Electro-Mechanical-Systems (MEMS) technology. Practically all MEMS accelerometers consist on a mass attached to the substrate through a flexible structure. The displacement measurement of the mass and the stiffness of the structure are used to determine the magnitude of the acceleration.

Generally the structure is composed of folded beam in order to reduce the device size and due to fabrication constraints. A capacitance transducer where one plate is fixed and the other is attached to the mass measures the mass displacement.

The goal of designing six DOF accelerometers has been driven by the fact that existing accelerometers are

uniaxial - detect acceleration along one axis. Moreover, no existing accelerometer architecture is also capable of detecting both linear and angular loads at the same time.

Analog Devices fabricates several models of single-axis accelerometers [4]. One of its products features twin sensors, perpendicular to each other, fabricated on the same die, which make it possible to detect accelerations in both the x and y directions[5].

Neuw Ghent Technology Inc. and Crossbow Inc. associate up to three single-axis sensors to have a multi-axis detection device [7,11].

2. Sensor Geometry

MEMS fabrication technology is limited to two dimensional structures. Thus, in order to detect accelerations in the three perpendicular directions, the structure behavior along the third axis (perpendicular to the substrate plane) should be analyzed.

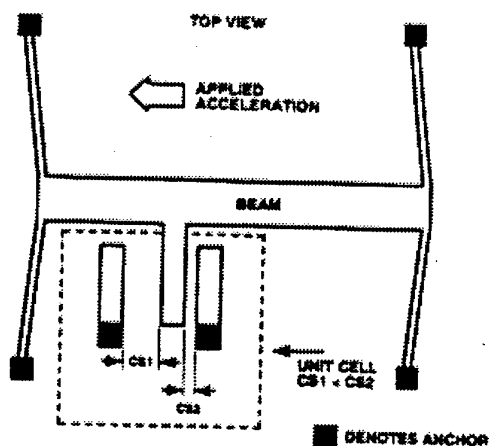


Fig.1. Analog Devices ADXL50's accelerometer.

The geometry of the proposed sensor consists of central movable mass linked to the substrate by eight tethers, four for each detection axis, as shown in Figure 2. The dimensions of the sensors were constrained by the MEMS Design Rules, which are dictated by the micromachining fabrication process. These design rules are defined by the resolution and alignment capabilities of the lithography system. Generally, they define the minimum features sizes and spaces, and the minimum overlap and spacing between relevant levels. The rules affecting the sensor geometry are detailed in the Table 1.

3. Structure Analysis

The ADXL181 accelerometer is rated $\pm 500g$, but in order to insure its reliability it was tested under mechanical shocks and drops with peak acceleration of 1500g and 4000g respectively.

Table 1: Design rules effecting the sensor's geometry

Parameter	Minimum or Mandatory Value [μm]
Tethers width	2.0
Anchors height	2.0
Structure thickness	2.0 or 3.5
Poly1 enclose Anchor1	4.0
Poly0 enclose Poly1	4.0

Similarly, the sensor was designed to withstand acceleration, in all three axes, up o 3000g. At this level of loading the stress should be below the fracture stress of polysilicon (3GPa [3]), and the deflection in Z direction should be below 2 (the layer thickness). After few design iterations the sensor's dimensions were finalized as shown in Figure 2. Note the thickness of the sensor is 3.5 μm that correspond to double layer of polysilicon.

A finite elements program, ANSYS, was used to analyze the structure. The model consisted of 1267 4 nodes solid pyramid elements with 6 DOF. It was found that at 3000g loading the maximum deflection in the sensor's plane (X-Y) was 0.005 μm and 0.015 μm in the perpendicular direction to its plane (Z). These results are in the same order magnitude of the commercial sensor described above. Also, maximum principal stress was under 0.5% the fracture strength of polysilicon.

4. Location of Capacitance Pads

The best locations for the capacitance pads were determined by modal analysis of the structure. The first

six mode shapes and the corresponding frequencies are given in Table 2 and are shown in Figure 3.

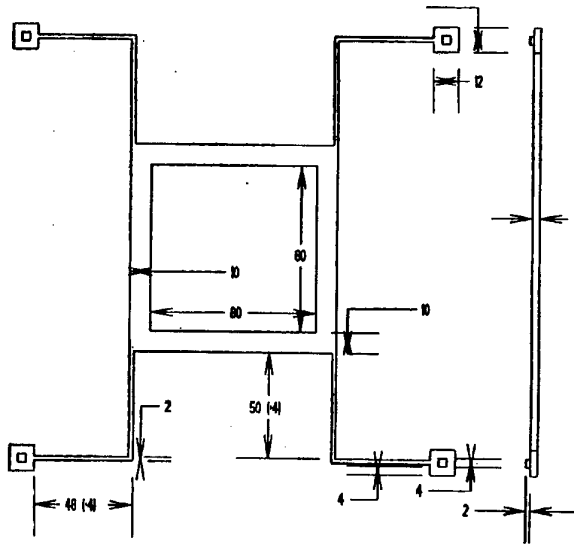


Fig. 2. Drawing of the sensor.

To detect the six components of an acceleration vector, minimum of six measurements are required, which in imply six capacitance pads. However, in order to detect angular acceleration about the X or Y axes it is necessary to use at least two sensing pads as illustrated in Figure 4.

The sensor has seven sensing pads as illustrated in Figure 5.

Table 2. First six mode shapes of the sensor.

Mode	Frequency [kHz]	Description
1	37.547	Deflection in Z direction
2	55.693	Rotation about Y axis
3	61.096	Deflection in Y direction
4	63.032	Deflection in X direction
5	74.681	Rotation about Z axis
6	102.132	Rotation about X axis

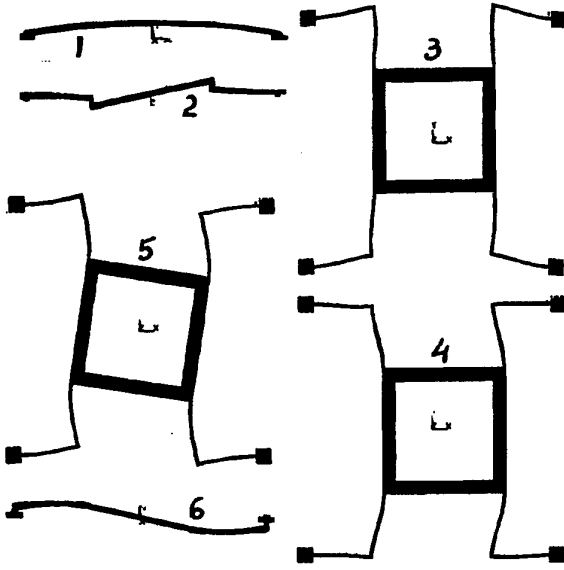


Fig. 3. Structure mode shapes.

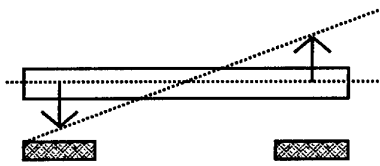


Fig. 4. Use of two pads for angular acceleration measurements.

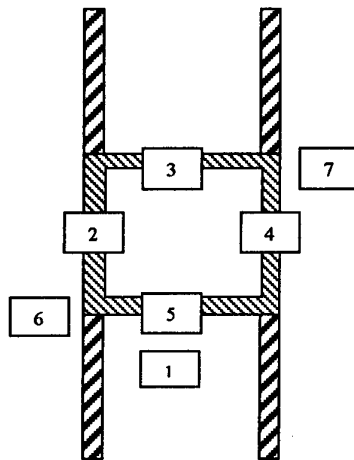


Fig. 5. Locations of the sensing pads.

5. Sensor's Stiffness Matrix

First the compliance the matrix, C , of the sensor was determined by calculating a combination of deflections at the detection pad locations while the sensor is exposed to a unit acceleration in a single direction. This will produce one column of the matrix as shown in Eq. 1.

$$\begin{bmatrix} \delta_x \\ \delta_y \\ \delta_z \\ \lambda_x \\ \lambda_y \\ \lambda_z \end{bmatrix} = \begin{bmatrix} C_{11} & 0 & 0 & 0 & 0 & 0 \\ C_{21} & 0 & 0 & 0 & 0 & 0 \\ C_{31} & 0 & 0 & 0 & 0 & 0 \\ C_{41} & 0 & 0 & 0 & 0 & 0 \\ C_{51} & 0 & 0 & 0 & 0 & 0 \\ C_{61} & 0 & 0 & 0 & 0 & 0 \end{bmatrix} \begin{bmatrix} a_x \\ 0 \\ 0 \\ 0 \\ 0 \\ 0 \end{bmatrix} \quad (1)$$

The entries δ and λ , which corresponds to linear and angular acceleration at the prospective directions, are given below:

$$\delta_x = \frac{1}{2}(d_6 + d_7) \quad (2)$$

$$\delta_y = d_1 \quad (3)$$

$$\delta_z = \frac{1}{4}(d_2 + d_3 + d_4 + d_5) \quad (4)$$

$$\lambda_x = \frac{1}{2}(d_3 - d_5) \quad (5)$$

$$\lambda_y = \frac{1}{2}(d_2 - d_4) \quad (6)$$

$$\lambda_z = \frac{1}{2}(d_6 - d_7) \quad (7)$$

The terms d_i , $i=1..7$ are the displacement at the pads' locations, calculated as the average of the displacements of all pad's nodes.

The stiffness matrix was obtained by taking the inverse of the compliance matrix C . As indication of the separation between the acceleration components, the condition number of the stiffness matrix was determined. The condition number found to be equal to 145.60. Lower values of the condition number indicate better sensor. To lower the condition number of the stiffness matrix additional pads should be considered [1].

6. Estimation of Detection Errors

To characterize the performance of the sensor, once the stiffness matrix was determined, the sensor was exposed to known accelerations, the displacements at the pads were calculated and used to determine the acceleration using the stiffness matrix.

Three different cases were considered for this comparison :

1. Detection of both linear and angular acceleration components (6 outputs).
2. Detection only linear acceleration components (3 outputs).
3. Detection of only angular acceleration components (3 outputs).

For the first case, linear accelerations in the range of 0-500g and angular acceleration in the range of 0-1E6 rad/s² were applied. Nine different loading were used, which resulted in an average detection error of 1.375% with a maximum value of 17.3% for the detection of the angular acceleration component about the X axis.

For the second case, the same range of linear accelerations were applied in nine different loading which resulted in an average detection error of 0.02%.

Similarly, nine three-component angular accelerations were applied on the model, which resulted in an average detection error of 0.44%.

7. Conclusions

The structure of micromachined polysilicon sensor capable of detecting both linear and angular accelerations, was proposed.

Finite element solution of the sensor's model indicate that it is possible to detect a full acceleration vector with accuracy of few percents. This performance can be improved by adding more sensing pads.

Eventually, the structure has to be fabricated with all supporting circuit and then tested in order to evaluate its performance. But the simulation results presented here is a good starting point for the design-fabrication process.

8. References

- [1] C. M. Subramanian, "Development of a graphical user interface for a Stewart platform." Master of Science and Engineering Degree Thesis, Dept. Mech. Eng., Florida Atlantic University, pp 50-52, July 1993.
- [2] G. de Jong, "Smart Capacitive Sensors, Physical, Geometrical and Electronic Aspects", *Delft University Press*, 2628 CN Delft, The Netherlands, 1994.
- [3] S. Bart, J. Chang, T. Core, L. Foster, A. Olney, S. Sherman, W. Tsang, "Design Rules for a Reliable Surface Micromachined IC Sensor", *1995 International Reliability Physics Proceedings, IEEE Catalog No. 95CH3471-0*.
- [4] "Accelerometer Data Sheets, Application Notes and Worldwide Sales Directory", © *Analog Devices Inc.*, 1995.
- [5] H. Samuels, "Single and Dual-Axis Micromachined Accelerometers", *Analog Dialogue, Volume 30, Number 4*, pp3-7, 1996.
- [6] D. A. Koester, R. Mahadevan, K. W. Markus, "Multi-User MEMS Processes, Introduction and Design Rules", *MCNC, MEMS Technology Applications Center, Research Triangle Park, North Carolina 27709, October 1994, Rev.3*.
- [7] "Low g Accelerometer Solutions", *Neuw Ghent Technology, LaGrangeville, NY 12540-5705*.
- [8] R. Allan, "Silicon MEMS Technology is coming of age commercially", *Electronic Design*, pp75-88, January 1997.
- [9] T. W. Kenny, H. K. Rockstad, J. K. Reynolds, W. J. Kaiser, "Technical Support Package on Dual-Element Tunneling Accelerometer with Dual Feedback", *NASA Tech Brief, Vol.21, No.2, Item#98, February 97*.
- [10] P. M. Echternach, U. E. Israelsson, "Technical Support Package on Micromachined Cryogenic Capacitive Pressure Transducers", *NASA Tech Brief, Vol.21, No.2, Item#68, February 97*.
- [11] "CXL04M3 Triaxial accelerometer", *Crossbow Technology Inc, Berkeley, CA 94708*.
- [12] T. A. Core, W. K. Tsang, S. J. Sherman, "Fabrication Technology for an Integrated Surface-Micromachined Sensor", *Solid State Technology, October 1993*.
- [13] J. Bryzek, K. Petersen, W. Mc Culley, "Micromachines on the march", *IEEE Spectrum*, pp20-31, May 1994.
- [14] B. Riedel, "A Surface-Micromachined, Monolithic Accelerometer", *Analog Dialogue, Volume 27, Number 2*, pp3-7, 1993.
- [15] E. Hoffman, B. Warneke, E. Kruglick, J. Weigold, K. S. J. Pister, "3D Structures with Piezoresistive Sensors in Standard CMOS", *Presented at MEMS '95, Amsterdam, The Netherlands, UCLA MEMS TRN 95-1, December 94*.
- [16] Jarlath McEnthee, "Properties of Polysilicon", <http://bell.mma.edu/~jmcent/siliconprop.htm>.

Three-Dimensional Target Tracking Using An Adjustable Infrared Sensor Configuration

Ali Safak Sekmen, Mark Cambron, and Mitch Wilkes

*Intelligent Robotics Laboratory
Department of Electrical and Computer Engineering
Vanderbilt University, Nashville, TN 37235
Sekmen,mac,wilkes@vuse.vanderbilt.edu*

Abstract

A low cost adjustable infrared sensor configuration consisting of five identical passive infrared motion detectors has been added to a service robot, ISAC. The intersections and unions of the motion detectors are used to track a moving object in three dimensions. Each motion detector is placed on a 5-inch long square piece of wood. The infrared motion detectors produce a 5V output when they detect a moving object in three dimensions. Otherwise, an output of 0V is produced. ISAC has a camera head containing two cameras. Four bits of information are extracted from the measurements. These are the tilt and pan angles of the camera head of ISAC and pan angles of the left and right cameras of the camera head.

1. Introduction

For a service robot, it is very important to be able to track the person it serves. Moreover, it may be serving more than one person. In this paper, an infrared sensor configuration for target tracking is introduced. This configuration has been added to a service robot called ISAC [1,2].

In robotics, acoustic sensors are generally used for applications such as robot navigation [3,4], target tracking [5,6], obstacle avoidance [7], and mapping [8,9]. They provide a simple means of determining locations of objects. Kuc did three-dimensional tracking using qualitative bionic sonar [5]. However, sonar sensors have some limitations. For example, their high beamwidth makes it difficult to localize objects correctly. In addition, multiple reflections are sometimes difficult to interpret. When infrared sensors are used alone, it is not possible to obtain sharp position information. Since both infrared and sonar sensors have their own disadvantages, Flynn combined sonar and infrared sensors for mobile robot navigation [10].

The importance of target tracking is also evident in videoconferencing systems. Cameras in current videoconferencing systems are generally controlled manually by the user. Voice source localization is often used to solve this problem. However, if the speaker moves but does not talk, then there may be a delay for the camera to track the speaker. Sound localization has other problems such as noise and reverberation, and the influence of specular reflection from the flat surfaces of furniture such as a table [11].

ISAC (shown in Figure 1) is a service robot. It has a camera head consisting of two cameras (left and right). The sensor configuration is placed on the body of ISAC. An advantage of this sensor configuration is that it does not only use the intersections of the beam patterns it also uses the union of them. In this study, we show how an adjustable infrared sensor configuration can be used to obtain some position information.

In the next section, the system configuration is described. Section 3 describes the method for the pan and tilt calculations of the camera head and left and right cameras of the head. Section 4 explains the vision system of ISAC. In Section 5, the tracking results for one and two moving objects are presented. In Section 6, some conclusions are given.

2. System Configuration

The transducer in our infrared system is a 7800-KT PIR detector which is a sensor module developed for human body detection. It can detect the movement of body heat in the horizontal direction, up to 190 cm away with nearly 180° field of view. The sensor configuration is shown in Figures 2 and 3. Note that the angles between the wood pieces can be adjusted.

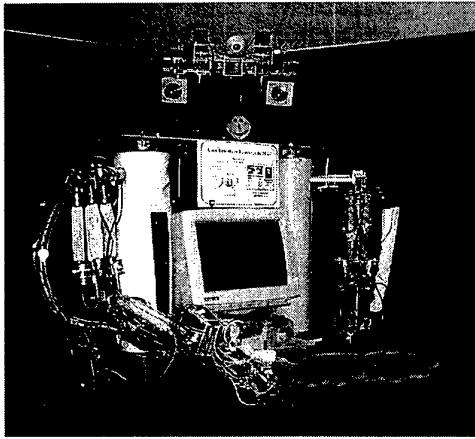


Figure 1. Dual arm humanoid robot (ISAC).

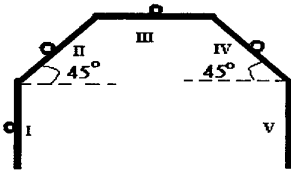


Figure 2. Top view of sensor configuration.

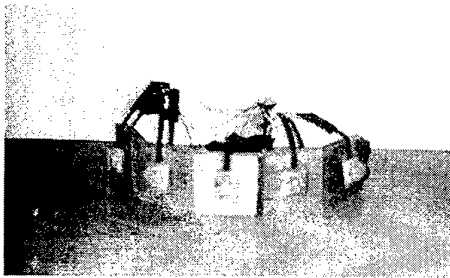


Figure 3. Adjustable sensor configuration.

Figure 4 illustrates the range of one of the detectors. Its detection region can be thought as a half elliptic surface with a horizontal length of 190cm and a vertical length of 75cm. The vertical range is not shown in Figure 4. Each detector produces 5V when a body moves in its range otherwise the output is 0V.

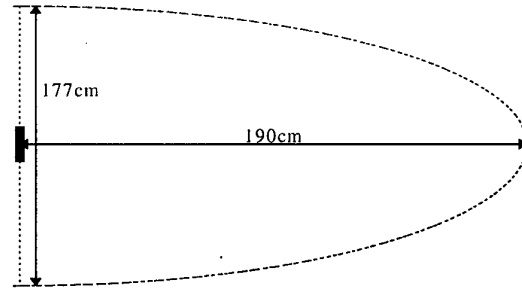


Figure 4. Range of one of detectors (top view).

3. Method For Tracking

Figure 5 illustrates the intersections and unions of the ranges of the detectors. The main idea is to decide which sensors can detect a human body in which regions. Table 1 shows the regions and the transducers that are active in these regions.

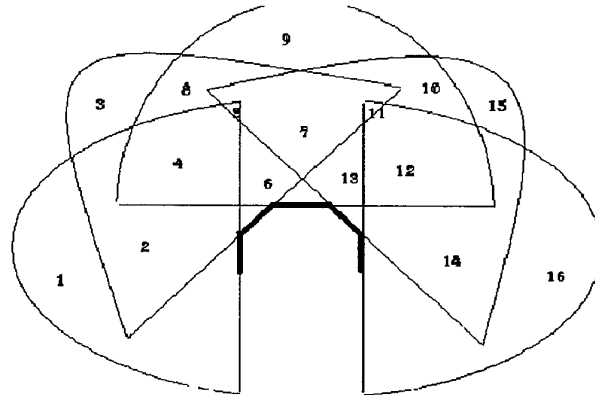


Figure 5. Union of sensitivity regions.

One interesting point derived from Table 1 is that there are some situations in which there cannot be only one moving object. For example, if there is only one person, there is no way for sensors I-V, I-IV, I-III, II-V, II-IV, III-V, I-II-V, I-II-IV, I-III-IV, I-III-V, I-IV-V, II-III-V, II-IV-V, I-II-IV-V, I-II-III-IV-V to be activated simultaneously. We call these regions impossibility regions. In these cases, it means there are two or more people moving around. Since ISAC has two cameras (left and right) we can easily calculate the angles, that the cameras must turn in those regions. For example, if I-II-IV-V are active simultaneously, we assume there are two people and one of them is in Region 2 (I and II active), and the other is in Region 14 (IV and V are active).

Table 1. Active detectors in specified regions.

REGION	DETECTORS
1	I
2	I-II
3	II
4	I-II-III
5	I-II-III-IV
6	II-III
7	II-III-IV
8	II-III
9	III
10	III-IV
11	II-III-IV-V
12	III-IV-V
13	III-IV
14	IV-V
15	IV
16	V

Note that the sensor configuration and the camera head are not on the same level. According to Table 1, the pan angles of the cameras and the pan and tilt angles of the camera head are calculated. The camera head is pointed to the center of the region in which the person is detected. For example, when the person moves from Region 4 to Region 3, the pan angle of the camera head does not change whereas the tilt angle decreases. In some regions the pan angles of the right and left cameras are the same (e.g. Region 4) while in some regions they are different (e.g. Region 1). For example, for Region 1, the camera head is pointed to the center (by adjusting the pan and tilt angles of the camera head), the right camera is pointed to the upper section of Region 1, and the left camera is pointed to the lower section.

4. Camera Fixation

Vision is often necessary for robots that work with and around humans. The active vision system locates a face from stereo images and fixates upon it. Fixation is the process of centering each camera on a target point (a face in this example). This behavior is similar to that of a human turning their head as someone walks in front of him or her. An active vision system solves many vision problems [12]. In particular, the tracking of an object in stereo facilitates segmentation and distance estimation while greatly reducing image clutter.

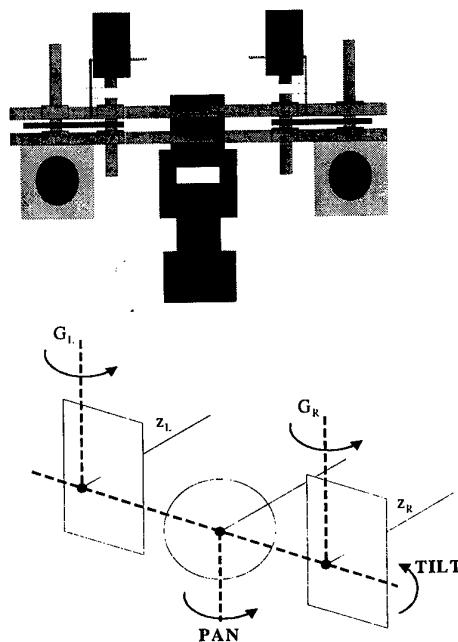


Figure 6. Vision System.

The active vision system (Figure 6) is composed of a 4 degree of freedom camera head and 2 color CCD cameras. Figure 6 shows a simple schematic illustrating the axes of movement of the camera head. The 4 DOF are pan, tilt, left verge, and right verge.

The union and intersection of the detectors give a location area in which the person is located (Section 3). The cameras then move to a predetermined location in which the cameras are looking to the center of the given area. At this point a human tracking behavior takes over control of the pan tilt head. It is desirable to fixate upon the human and look them eye-to-eye (or at least camera-to-eye).

The goal of the color module is to help locate a face in a set of stereo color images and guide the camera head to center it in both cameras. To accomplish this, skin tone color models were created. The color segmentation routine separates pixels into candidate skin-tone pixels and non-skin-tone pixels. Pixels are segmented by determining if they fall within a pre-defined RGB color model space [13]. From this process a binary image mask is created.

Given the location of the skin-tone centroid in the mask image, the camera tracker then moves the camera head to guide the centroid towards the center of the image. The cameras move according to a direction vector generated by the distance from the skin-tone centroid to the center of the image view. The amount of the cameras'

movement is proportional to the magnitude of the direction vector. The y-component of the direction vector controls the tilt motor and the x-component controls the verge motors. Once the target has reached the center, the tracker is acknowledged that the target has been fixated and then stops moving camera head. Once a skin color blob is fixated upon we check for faces by using a template matching routine [14]. A confidence measure is used to indicate the success of the fixation routine.

5. System Performance

The signals from the sensor configuration were sampled every 2 seconds. The results of tracking one person were very good. The person was always in the view range of at least one of the cameras. The cameras tracked the person with 100% accuracy in all regions except for regions 5 and 11 of which the boundaries are not sharp. When there were two persons in the impossibility regions, the results were satisfying. One of the cameras looked at one person while the other looked at the other person. When the people were outside the impossibility regions, the results were not so good since there are some regions in which it is not possible to be able to track two persons. For example, if one of the people is in Region 1 while the other is in Region 2, the two cameras are going to look at Region 2 since the first and second detectors are activated simultaneously.

6. Conclusion

An adjustable passive infrared sonar configuration has been described by which ISAC can track one or more persons by calculating the camera angles according to the qualitative data coming from this configuration. The system performance can be improved by increasing the number of detectors and the angles between the detectors. If a circular configuration is used with a large number of detectors, then ISAC can track a person moving around it. Moreover, if different kinds of detectors that have greater range are used in the configuration, then the system can be extended to be used in videoconferencing systems.

References

- [1] D.M. Wilkes, A. Alford, R.T. Pack, T. Rogers, R.A. Peters II, and K. Kawamura, "Toward Socially Intelligent Service Robots", *Applied Artificial Intelligence*, 1999, vol. 12, pp 729-766.
- [2] K. Kawamura, D.M. Wilkes, R.T. Pack, M. Bishay, and J. Barile, "Humanoids: Future Robots for Home and Factory", *Proceedings of the First International Symposium on Humanoid Robots*, Tokyo, 1996, pp 53-62.
- [3] A. Elfes, "Sonar based real-world mapping and navigation", *IEEE Transactions on Robotics and Automation RA-1*, 1987, vol.1, pp. 31-41.
- [4] R. Kuc and B.V. Viard, "A physically-based navigation strategy for sonar-guided vehicles", *Int. J. Robotics Res.*, April 1991, vol. 10, pp. 75-87.
- [5] R. Kuc, "Three-dimensional tracking using qualitative bionic sonar", *Robotics and Autonomous Systems*, 1993, vol. 11, pp. 213-219.
- [6] I.E. Dror, M. Zagaeski, and C.F. Moss, "Three dimensional target recognition via sonar: a neural network model", *Neural networks*, 1995, vol.8, pp. 149-160.
- [7] B. Barshan and R. Kuc, "A bat-like sonar system for obstacle localization", *IEEE Trans. On Systems, Man, and Cybernetics*, 1992, vol. 4, pp.636-646.
- [8] A. Ohya, T. Ohno, and S. Yuta, "Obstacle detectability of ultrasonic ranging system and sonar map understanding", *Robotics and Autonomous Systems*, 1996, vol. 18, pp. 251-257.
- [9] O. Bozma and R. Kuc, "Building a sonar map in a specular environment using a single module transducer", *IEEE trans. Pattern Anal. Machine Intell.*, 1991, vol. 13, pp. 1260-1269.
- [10] A.M. Flynn, "Combining sonar and infrared sensors for mobile robot navigation", *Int. J. robotics Res.*, 1998, vol. 7, pp. 5-14.
- [11] H. Wang, p. Chu, "voice source localization for automatic camera pointing system in videoconferencing", *ICASSP*, 1997.
- [12] J. Barile, M. Bishay, M. Cambron, R. Watson, R.A. Peters II, K. Kawamura, "Color-based initialization for human tracking with a trinocular camera system", *Proceedings of the IASTED International Conference on Robotics and Manufacturing*, Cancun, Mexico, May, 1997.
- [13] B. Qiu, "Face and Facial Feature Detection in a Complex Scene", *Masters Thesis*, Vanderbilt University, 1997.
- [14] D. Ballard, "Animate Vision", *Artificial Intelligence*, 1991, vol 48, pp. 1-27.

Radius of Curvature and Location Estimation of Cylindrical Objects with Sonar using a Multi-sensor Configuration

Ali Safak Sekmen

Department of Electrical and Computer
Engineering, Vanderbilt University,
Nashville, TN 37235 USA
sekmen@vuse.vanderbilt.edu

Billur Barshan

Department of Electrical Engineering
Bilkent University
Bilkent, 06533 Ankara TURKEY
billur@ee.bilkent.edu.tr

Abstract

Although acoustic sensors are inexpensive and convenient to use in time-of-flight (TOF) ranging systems, they have some important limitations one of which is their low angular resolution that makes localization difficult. In this paper, an adaptive multi-sensor sonar system is introduced to compensate for the low angular resolution and improve the localization accuracy. The sensor configuration is used to estimate the radius of curvature and location of cylindrical objects. Sensitivity analysis of the curvature estimate with respect to some measurement errors and certain system parameters is provided. Two methods of TOF estimation are used and compared: thresholding and curve-fitting methods. Theory and simulations are verified by experimental data from a real sonar system. The adaptive configuration improves the estimates by 35-45% and the curve-fitting method, compared to the thresholding, brings an improvement of about 30% in the absence of noise and 50% in the presence of noise. The radius of curvature estimation is shown to be useful for target discrimination.

1. Introduction

One of the major limitations of acoustic sensors is their high beamwidth that reduces the localization accuracy. An adaptive sonar sensor configuration consisting of three transmitter/receiver ultrasonic transducers is used to increase the localization accuracy. With this configuration, the radius of curvature and location of cylindrical objects are estimated. The radius of curvature estimate can be used to differentiate basic types of reflectors. For large values of radius, the target can be assumed to be a planar wall, and for values close to zero, it can be assumed to be an edge.

Sonar sensors have been widely used in robotics applications including underwater robotics. Several researchers used different sensor configurations. Kuc used a system which adaptively changes its position and

configuration in response to the echoes it detects [1]. In [2], Kleeman and Kuc classified target primitives as plane, corner, edge, and unknown. Flynn combined infrared and sonar sensors to compensate for the high beamwidth of sonar sensors [3]. In [4], Sabattini illustrated that advanced filtering techniques are required for making sonar data more accurate and reliable. Peremans *et al* used a linear configuration with three ultrasonic transducers [5].

When the reflection point of the object is not along the line-of-sight (LOS) of the ultrasonic transducer, there is an exponential decline in the amplitude of the reflected sonar signal which decreases the signal-to-noise (SNR). Depending on the orientation of the target, the transducers of the configuration are rotated towards the target to obtain more accurate estimates.

In Section 2, the adaptive sensor configuration is described and the reason to use this configuration is explained. The radius of curvature and location estimation algorithm is presented in Section 3. Two methods of TOF are described in Section 4. Section 5 provides sensitivity analysis of curvature estimation. The simulation results are presented in Section 6. In section 7, the experimental results are illustrated. Finally, some conclusions are drawn in Section 8.

2. Multi-sensor Sonar Configuration

For a cylindrical target at range z and making an angle α with the LOS of an ultrasonic transducer, the received time signal reflected by the target is a sinusoidal enveloped by a Gaussian which is given by [6]:

$$S_{c,\alpha}(t) = \rho_c \frac{A_{\max} z_{\min}^{3/2}}{z^{3/2}} e^{-\frac{\alpha^2}{\sigma_a^2}} e^{-\frac{(t-t_0-3t/f_0)^2}{2\sigma_t^2}} \sin[2\pi f_0(t-t_0)] \quad (1)$$

where z is the distance between the transducer and the surface of the object, ρ_c is the reflection coefficient

which increases with the radius of curvature, A_{\max} is the maximum amplitude, $z_{\min} \cong a^2 / \lambda$ (a is the radius of the transducer aperture), α is the deviation angle from the LOS, $\sigma_\alpha = \alpha_s / 2$ (α_s is the half beamwidth angle), t_s is the time-of-flight, f_s is the resonant frequency, and $\sigma_t = 1 / f_s$.

Equation (1) shows that when the deviation angle between the object and sensor is not zero ($\alpha \neq 0$), there is an exponential decline in the amplitude of the reflected sonar signal. Hence, as the deviation angle increases, SNR decreases. Therefore, sonar data is most reliable when the target lies along the LOS of the transducer, and at nearby ranges due to the $1/z^{3/2}$ term in Equation (1). In this study, a sensor configuration composed of three ultrasonic transducers is used as shown in Figure 1. First, linear configuration of these sensors are used and some measurement are taken, and then, the transducers are rotated around their center according to these measurements to make them perpendicular to the target.

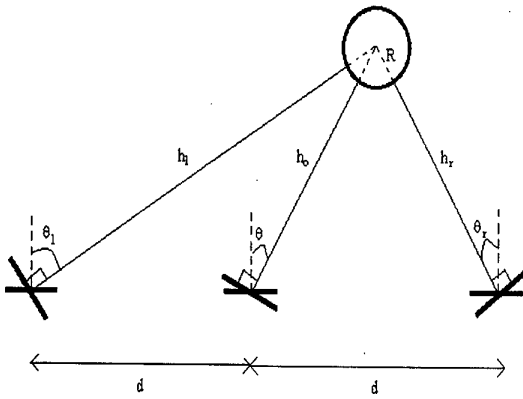


Figure 1. The sensor and target configuration.

3. Algorithm

A cylindrical object with radius R and orientation ϕ is considered. The radius of curvature (R), the distance between the central transducer and the center of the target ($r = h_o + R$), and the deviation angle of the central transducer (θ) are estimated as follows:

- The following measurements are taken by the transducers:

$$\begin{aligned} \hat{h}_o &= \frac{ct_s}{2} = r - R + n_o \\ \hat{h}_r &= \frac{ct_r}{2} = \sqrt{r^2 + d^2 - 2dr \sin \theta} - R + n_r \\ \hat{h}_l &= \frac{ct_l}{2} = \sqrt{r^2 + d^2 + 2dr \sin \theta} - R + n_l \end{aligned} \quad (2)$$

where h_o , h_r , and h_l are the distances between the surface of the object and the central, right, left transducers respectively. t_s , t_r , and t_l are the TOFs for the central, right, and left transducer respectively. d is the transducer separation. n_o , n_r , and n_l are noise terms that can be modeled as spatially uncorrelated Gaussian noise since the noise correlation coefficient is small for the acoustic transducers (most of the noise on the sensors is dominated by the thermal noise) [5].

- The probability density function of the measurement vector \hat{z} is given as:

$$p_z = \frac{1}{2\pi|C|} \exp \left\{ -\frac{1}{2} [\hat{z} - h(r, \theta, R)]^T C^{-1} [\hat{z} - h(r, \theta, R)] \right\} \quad (3)$$

where the vectors \hat{z} , $h(r, \theta, R)$, and the error correlation matrix C are given by

$$\hat{z} = \begin{bmatrix} \hat{h}_o \\ \hat{h}_r \\ \hat{h}_l \end{bmatrix}, \quad h(r, \theta, R) = \begin{bmatrix} r - R \\ \sqrt{r^2 + d^2 - 2dr \sin \theta} - R \\ \sqrt{r^2 + d^2 + 2dr \sin \theta} - R \end{bmatrix} \quad (4)$$

$$C = \begin{bmatrix} \sigma_{n_o}^2 & 0 & 0 \\ 0 & \sigma_{n_r}^2 & 0 \\ 0 & 0 & \sigma_{n_l}^2 \end{bmatrix} \quad (5)$$

- The r , θ , and R values maximizing Equation (3) are the maximum likelihood estimates which can be found by taking the inverse of $\hat{z} = h(\hat{r}, \hat{\theta}, \hat{R})$ as:

$$\hat{r} = \frac{2d^2 + 2(\hat{h}_l + \hat{h}_r)\hat{h}_o - 2\hat{h}_o^2 - \hat{h}_l^2 - \hat{h}_r^2}{2\hat{h}_r^2 + 2\hat{h}_l^2 - 4\hat{h}_o^2} \quad (6)$$

$$\hat{\theta} = \sin^{-1} \left[\frac{\hat{h}_l^2 - \hat{h}_r^2 + 2(\hat{h}_l - \hat{h}_r)\hat{R}}{4d(\hat{h}_o + \hat{R})} \right] \quad (7)$$

$$\hat{R} = \frac{(\hat{h}_r^2 + \hat{h}_l^2) - 2(\hat{h}_o^2 + d^2)}{4\hat{h}_o - 2(\hat{h}_r + \hat{h}_l)} \quad (8)$$

- The deviation angles for the right and left transducers are given by

$$\hat{\theta}_r = \sin^{-1} \left(\frac{(\hat{h}_r + \hat{R})^2 - (\hat{h}_l + \hat{R})^2 + d^2}{2d(\hat{h}_r + \hat{R})} \right) \quad (9)$$

$$\hat{\theta}_l = \sin^{-1} \left(\frac{(\hat{h}_r + \hat{R})^2 - (\hat{h}_l + \hat{R})^2 + d^2}{2d(\hat{h}_l + \hat{R})} \right) \quad (10)$$

- The left, central, and right transducers are rotated by $\hat{\theta}_l$, $\hat{\theta}$, and $\hat{\theta}_r$ respectively and r , θ , and R are estimated again.

4. TOF Estimation

In this study, two methods of TOF estimation are used. The first one, *thresholding*, is the most common method in TOF ranging systems. When a pulse transmitted by the sensor encounters an object, an echo is produced and the TOF of the pulse is considered to be the first time value at which the amplitude of the echo exceeds a preset threshold value. Although the thresholding method is very fast, it is not accurate enough for some applications. The second method of this study, *curve-fitting*, is employed to decrease the error in TOF estimation by thresholding. In this method, a parabolic curve of the form $a_e(t - t_e)^2$ is fitted to the onset of the sonar echo. First initial estimates of the two parameters a_e and t_e are obtained by using samples of the signal around the thresholding point. Initial estimate for t_e is found by simple thresholding, and a_e is estimated from the second derivative approximation around the thresholding point [7]. The iterative Lavenberg-Marquart nonlinear least-square algorithm is initialized by these values. To estimate a_e and t_e , 50 samples of echo around the threshold point have been used in simulations and experiments. The methods are illustrated in Figure 2.

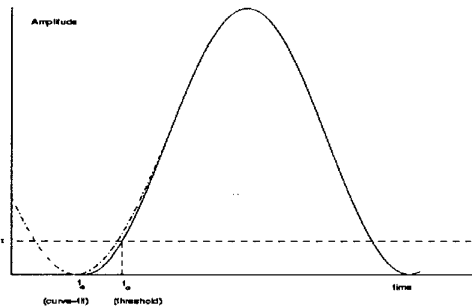
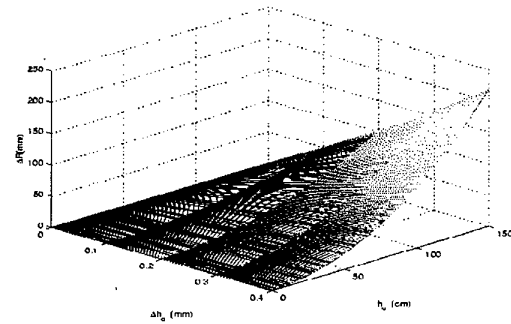


Figure 2. TOF estimate.

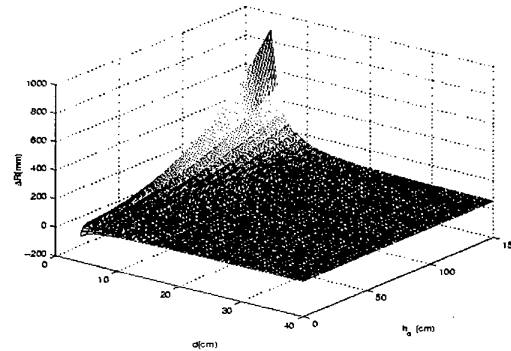
5. Sensitivity Analysis

To illustrate how some measurement errors and certain system parameters affect the radius of curvature estimate, a sensitivity analysis has been provided. A small perturbation is added to a variable and the change in the radius of curvature estimate has been observed. For example, the error, Δh_l , in the left transducer measurement affects the curvature estimate as:

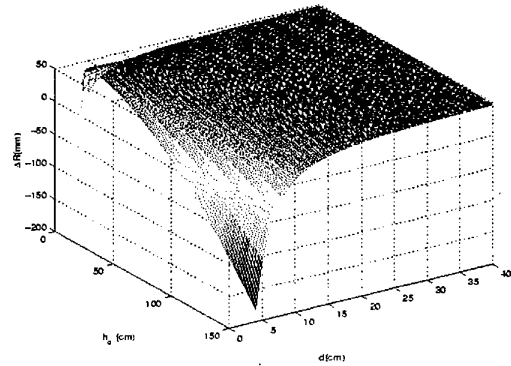
$$\Delta R = \frac{(h_r^2 + (h_l + \Delta h_l)^2) - 2(h_e^2 + d^2)}{4h_e - 2(h_r + h_l + \Delta h_l)} - \frac{(h_r^2 + h_l^2) - 2(h_e^2 + d^2)}{4h_e - 2(h_r + h_l)} \quad (11)$$



(a)



(b)



(c)

Figure 3. Sensitivity analysis.

For sensitivity analysis, a stationary cylindrical object at $\theta = 0^\circ$ with radius 5 cm is considered. Figure 3(a) illustrates the effect of an error, varying between 0-0.4 mm, in h_r . The transducer separation is set to 10 cm. The error in R increases linearly with Δh_r and nonlinearly with h_r itself. Also, a positive error in h_r leads a positive error in R since for constant h_r and h_t , increasing h_r causes an overestimate as shown in Figure 1. Figure 3(b) and (c) display the effect of d on the R estimate when the constant errors $\Delta h_r = 0.18$ mm and $\Delta h_t = 0.18$ mm are added respectively. For small values of d/h_r , the error is high since the resolution provided by the differential TOF information between the central and surrounding transducers will not be sufficiently large to estimate the curvature reliably. Hence, as range increases, the transducer separation should also be increased to achieve a higher resolution.

6. Simulation Results

The reflected sonar signal is modeled by Equation (1) for the simulations with $A_{\max} = 1$, $z_{\min} = 5.8$ cm, $\rho_r = 0.45R - 0.022$, $f_s = 49.4$ kHz, $c = 343.5$ m/s. For simulations, 100-iteration Monte-Carlo simulation study is employed and the curve-fitting TOF estimate method is used. First, the linear configuration of the transducers are used to estimate the range, deviation angle, and radius of curvature by Equations 6-8 respectively. Then, the central, left, and right transducers are rotated around their centers by the angles found by Equations 7, 9, and 10 respectively. Finally, the estimates for rotated configuration are calculated again by using Equations 6-8. From now on, the first estimate corresponds to the estimate taken by the linear configuration, and second estimate corresponds to the estimate taken by the rotated configuration. In all simulations, dashdot (or dot) and dashed lines indicate the mean of the estimate and $\pm\sigma$ (standard deviation) for the linear and rotated positions respectively.

Figures 4(a) and (b) illustrates the radius of curvature estimates when the thresholding method is used in the absence and presence of noise respectively. The first estimate worsens after $d = 37$ cm in the absence of noise while second estimate continues improving. The error in the first estimate is 22.8% while it is 9.2% for the second estimate. In the presence of noise, the second estimate provides approximately 40% better results. Also, the standard deviation is less for the second estimate. Figures 5(a) and (b) shows the same results when the curve-fitting method is used to estimate TOF in the absence and presence of noise respectively. In the

absence of noise, the first estimate gets worse after 43cm (it was 37 for the thresholding method). The error is 11.2% for the first estimate and it is 0.4% for the second estimate. In the presence of noise, the second estimate is better than the first estimate. Comparison of Figure 4(b) and 5(b) shows that the curve-fitting method provides better estimates than that of the thresholding method. The improvements are approximately 60% and 20% for the first and second estimates respectively.

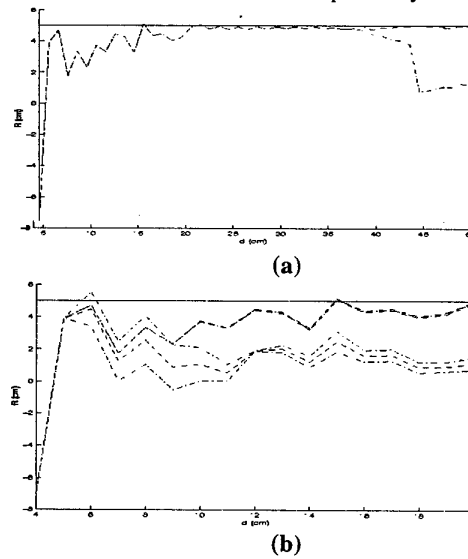


Figure 4. R estimate versus d with thresholding in the absence (a) and presence (b) of noise.

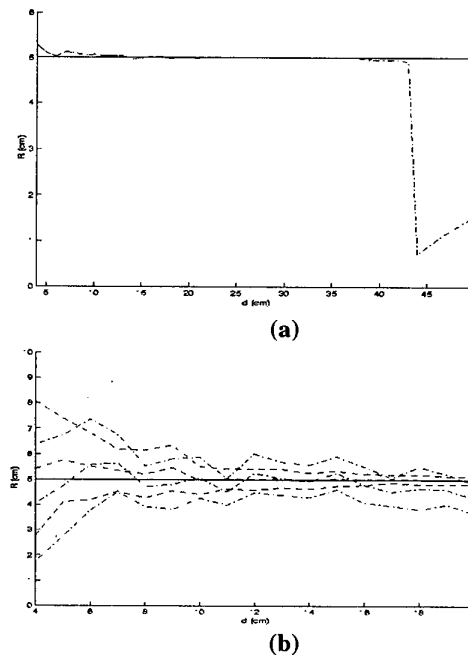


Figure 5. R estimate versus d with curve-fitting in the absence (a) and presence (b) of noise.

Figure 6(a) illustrates the range estimate r versus transducer separation d . The curve-fitting method is employed for TOF estimates. The first estimates improve until $d = 12$ cm and then it worsens since now the target is located at a very low SNR region. $R = 5$ cm, $\theta = 5^\circ$ are considered. Figure 6(b) shows the range estimate r versus deviation angle θ . $R = 5$ cm and $d = 10$ cm are considered. When $\theta = 6^\circ$, the left and when $\theta = 12^\circ$, the right transducer start measuring wrong.

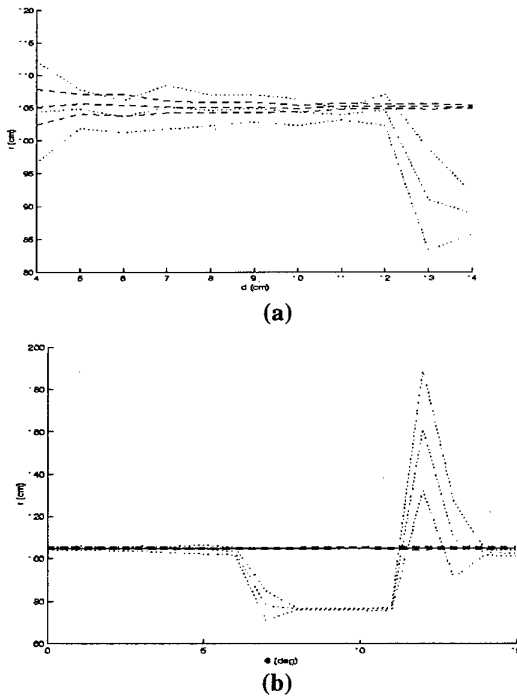


Figure 6. r estimate versus (a) d (b) θ .

7. Experimental Results

7.1. Experimental Set-up

The set-up is constructed for 3D applications. The unit consists of five transmitter/receiver Polaroid transducers with the resonant frequency 49.4 kHz. The central transducer is flanked by four transducers symmetrically as shown Figure 7. Only the left, central, and right transducers are used for the experiments. A 4-channel DAS-50 A/D card with 12-bit resolution and 1 MHz sampling frequency is used to sample the echo signals.

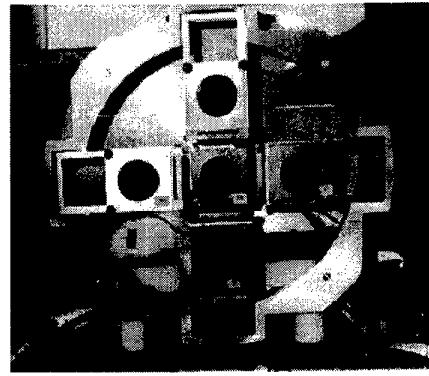


Figure 7. The experimental set-up.

7.2. Results

Table 1 displays some experimental results for the radius of curvature estimate of a cylindrical object with radius 50 mm when the transducer separation is 10 cm. The curve-fitting method is employed for TOF estimate. In the table, \hat{R}_1 and \hat{R}_2 correspond to the radius of curvature estimates of the linear and rotated configurations respectively. It is concluded that the estimates are improved by the adaptive configuration.

Table 1. Experimental results for a cylinder of $R = 50$ mm and $d = 7.5$ mm.

h_o (mm)	$E(\hat{R}_1)$ (mm)	$\sigma_{\hat{R}_1}$ (mm)	$E(\hat{R}_2)$ (mm)	$\sigma_{\hat{R}_2}$ (mm)
300	48.27	6.84	48.93	4.10
400	51.13	10.08	50.27	6.25
500	49.17	15.23	49.44	9.29
600	52.33	22.43	51.79	13.24
700	44.96	27.61	46.63	16.57
800	44.55	35.02	48.36	21.52
900	50.64	45.42	50.25	26.80
1000	59.87	57.41	55.48	33.39

8. Conclusion

In this study, radius of curvature and location estimates of cylindrical objects by a multi-sensor sonar system has been investigated. Two methods of TOF has been used and it has been shown that the curve-fitting method improves TOF estimate. Moreover, the adaptive configuration decreases the effect of low angular resolution of sonar sensors considerably. The results are useful for target discrimination especially for primitive types such as walls and edges. For high values of

curvature, the target is assumed to be a planar wall, and for values close to zero, the target is assumed to be an edge. The method can be generalized to spherical objects as well [8].

References

- [1] R. Kuc, "Fusing binaural sonar information for object recognition", *Proceedings of IEEE/SICE/RSJ international Conference on Multisensor Fusion and Integration for Intelligent Systems*, 1996, pp. 727-735.
- [2] L. Kleeman, and R. Kuc, "Mobile robot sonar for target localization and classification", *International Journal of Robotics Research*, August 1995, vol. 14, pp. 295-318.
- [3] A. M. Flynn, "Combining sonar and infrared sensors for mobile robot navigation", *International Journal of Robotics Research*, December 1988, vol. 7, pp. 5-14.
- [4] A. M. Sabatini, "A digital signal processing technique for compensating ultrasonic sensors", *IEEE Transactions on Instrumentation and Measurement*, 1995, vol. 44, pp. 869-874.
- [5] H. Peremans, K. Audenaert, and J. M. Van Campenhout, "A high resolution sensor based on tri-aural perception", *IEEE Transaction on Robotics and Automation*, February 1993, vol. 9, pp. 36-48.
- [6] B. Barshan, *A Sonar-Based Robot for Bat-like Prey capture*, PhD thesis, Yale University, New Haven, CT, December 1991, University of Michigan Microfilms, order number 9224325.
- [7] B. Barshan, and R. Kuc, "A bat-like sonar system for obstacle localization", *IEEE Transactions on Systems, Man and Cybernetics*, July/August 1992, vol. 22, no. 4, pp. 636-646.
- [8] B. Barshan, A. S. Sekmen, "Radius of curvature estimation and localization of targets using multiple sonar sensors", *The Journal of the Acoustical Society of America*, April 1999, vol. 105, no. 4.

A Study of Q-Learning Method in Multi-Agent System

Fang Yuan Shao Shihuang Geng Zhaofeng

Institute of Electrical Engineering, China Textile University, Shanghai 200051, China

E-mail: yfang@ctu.edu.cn

Abstract

Coordination, the process by which an agent reasons about its local actions and the anticipated actions of others to try and ensure the community acts in a coherent manner, is perhaps the key problem of the discipline of multi-agent systems. In this paper we use the Q-learning method to guide the agents to act cooperatively in multi-agent systems. A special Q-function consists of two parts, one denotes agent's individual pursuit and the other denotes the cooperative requirement, is proposed. And we use the pursuit problem as our testbed system. In the testbed system, agents have been created which choose their actions by maximizing the Q-values of them. The result of our simulation is good.

1. Introduction

Modern applications of computing arise most frequently in environments that are open, heterogeneous, distributed, dynamic, large, and with autonomous components. For these reasons, they require solutions that marry artificial intelligence (AI) and traditional techniques to yield extensibility and flexibility. Agents are an issue of this marriage. Currently, many agent approaches are centralized in a single agent. However, centralization has obvious shortcomings in accommodating the above properties of open environments. Consequently, there has been increasing interest in multi-agent systems, which can yield the benefits of intelligent agent while preserving openness and scalability.

What sets multi-agent systems apart from single agents is that they require the agents to behave in a coordinated manner, agents must follow some protocol even to compete effectively. Therefore, the designer of a multi-agent system must handle not only the application-specific aspects of the various agents, but also their interactions with one another. Current approaches to constructing multi-agent systems offer no special coordination support to the designer, who must manually ensure that the agents interact appropriately. This can lead to unnecessarily rigid or sub optimal designs, wasted development effort, and sometimes to the autonomy of the agents being violated. These limitations,

in effect, subvert many of the features that make multi-agent systems attractive in the first place.

Researchers in the field of Distributed Artificial Intelligence (DAI) have developed a variety of agent coordination schemes under different assumptions about agent capabilities and relationships, such as, intelligent tutoring systems[1], traffic or air-traffic control[2], virtual theater[3], realistic virtual training environments[4], virtual interactive fiction[5]. Most of those researches hitherto have been focused on enabling individual agents to cope with the complexities of those dynamic domains. One promising approach that has emerged is the use of hierarchical reactive plans. Reactive plans are qualified by preconditions, which help select plans for execution based on the agent's current high-level goals/tasks and beliefs about its environment.

Millind Tambe[6] studied Multi-Agent System based on the concept of team not on individuals. His model is based on joint intention framework, which implemented cooperation using the concept of teamwork.

This paper is focus on applying Q-learning method on the coordination problem among the agents of multi-agent system.

2. Coordination

Multi-agent systems are a particular type of DAI system, in which autonomous intelligent agents inhabit a world with no global control or globally consistent knowledge. These agents may still need to coordinate their activities with others to achieve their own local goals. It is widely believed that a group of cooperating agents engaged in problem solving can solve a task faster than either a single agent or the same group of agents working in isolation from each other.

Coordination is central to multi-agent systems, without it any benefits of interaction vanish and the group of agents quickly degenerates into a collection of individual with a chaotic behavior. Agents could benefit from receiving information about what others are doing or plan to do, and from sending them information to influence what they do. But the capabilities needed for collaboration cannot be patched on but must be designed in from the start.

Almost all of the coordination schemes developed to date assume explicit or implicit sharing of information. In the explicit form of information sharing, agents communicate partial results, speech acts, resource availabilities, etc. to other agents to facilitate the process of coordination. In the implicit form of information sharing, agents use knowledge about the capabilities of other agents to aid local decision-making. We believe that the less an agent depends on shared information, and the more flexible it is to the on-line arrival of problem-solving and coordination knowledge, the better it can adapt to changing environments.

As flexibility and adaptability are key aspects of intelligent and autonomous behavior, we are interested in investigating mechanisms by which agents can acquire and use coordination knowledge through interactions with its environment (that includes other agents) without having to rely on shared information.

Coordination strategy among the agents of multi-agent systems can be classified to explicit strategy and implicit strategy. In explicitly cooperative systems, the agents interact and exchange information or perform actions so as to benefit other agents. On the other hand, implicitly cooperative agents perform actions that are a part of their own goal-seeking process but these actions affect the other agents in beneficial ways.

We implement the cooperation among the agents by an implicit strategy, which is based on a kind of co-learning method. Each agent sends signal to relative agents, and the agent can calculate the cooperative value by the signal sent from its partner.

3. Reinforcement Learning

Reinforcement learning, learning procedure of which is driven by scalar values given to the learner to reinforce its behavior, is a promising area of machine learning.

In reinforcement learning problems[7], reactive and adaptive agents are given a description of the current state and have to choose the next action from a set of possible actions so as to maximize a scalar reinforcement or feedback received after each action. The learner's environment can be modeled by a discrete time, finite state, Markov decision process that can be represented by a 4-tuple (S, A, P, r) , where $P: S \times S \times A \rightarrow [0, 1]$ gives the probability of moving from state s_1 to s_2 on performing action a , and $r: S \times A \rightarrow \mathcal{R}$ is a scalar reward function. Each agent maintains a policy, π , that maps the current state into the desirable action(s) to be performed in that state. The expected value of a discounted sum of future rewards of a policy π at a state x is given by $V_\gamma^\pi = E\{\sum_{t=0}^{\infty} \gamma^t r_{x,t}^\pi\}$, where $r_{x,t}^\pi$ is the random variable corresponding to the reward received by the learning agent t time steps after it starts using the policy π

in state s , and γ is a discount rate ($0 < \gamma < 1$). Various reinforcement learning strategies have been proposed using which agents can develop a policy to maximize reward accumulated overtime.

Watkins firstly applied the Q-learning[8] algorithm to multi-agent system. The Q-learning algorithm is designed to find a policy π^* that maximizes $V_\gamma^\pi(s)$ for all states $s \in S$. The decision policy is represented by a function,

$$Q: S \times A \rightarrow \mathcal{R}$$

which estimates long-term discounted rewards for each state-action pair. The Q values are defined as

$$Q_\gamma^\pi(s, a) = V_\gamma^{a;\pi}(s)$$

where $a;\pi$ denotes the event sequence of choosing action a at the current state, followed by choosing actions based on policy π . The action, a , to perform in a state s is chosen such that it is expected to maximize the reward,

$$V_\gamma^{\pi^*}(s) = \max_{a \in A} Q_\gamma^{\pi^*}(s, a) \text{ for all } s \in S.$$

If an action a in state s produces a reinforcement of R and a transition to state s' , then the corresponding Q value is modified as follows:

$$Q(s, a) \leftarrow (1-\beta)Q(s, a) + \beta(R + \gamma \max_{a' \in A} Q(s', a'))$$

The update rule above is used to guide the agents' selections of action.

There are also some other works related to learning in multi-agent system. Tan [9], and Sen and Sekaran[10] represent works in multi-agent reinforcement learning systems.

Shoham and Tennenholtz[11] discuss co-learning and the emergence of conventions in multi-agent systems with simple interactions.

We address the coordination problem in multi-agent system. The Q-learning method is employed and a special Q-function is defined. The calculation of Q-value depends on not only how to achieve the agent's local goal quickly but also how to maintain the coordination with its partner. Agents select actions according to the Q-value, what can lead to good Q-value is selected in every turn.

4. Implementation

Some previous works on using learning techniques to coordinate multiple agents have mostly relied on using prior knowledge, or on cooperative domains with unrestricted information sharing. Even previous proposals for using reinforcement learning for coordinating multiple agents[9] have relied on explicit information sharing. We concentrate on systems where agents share no problem-solving knowledge and each agent is using reinforcement learning techniques to optimizing its own environment reward.

Agents employing Q-learning method decide its actions according to the Q-value. To consider the coordination of

agents, the Q-value should not calculate only based on the agents' local benefit. Otherwise the coordination of agents will not be achieved. So we combine the cooperative factor and local factor to calculate the Q-value. The special Q-function in this paper consists of two parts. One part (presented as V_{perceive}) denotes the value calculated by the perceptual information (i.e. local factor), and the other denotes the value (presented as $V_{\text{coordinate}}$) calculated by the information sent by the partners (i.e. cooperative factor). The formula used to calculate Q-value is:

$$Q = \varepsilon V_{\text{perceive}} + (1 - \varepsilon) V_{\text{coordinate}}$$

where,
 $\varepsilon \in (0, 1)$.

5. Experiment--pursuit problem

We use the pursuit problem as our simulation example. The pursuit problem is a well-known tested problem from the Distributed Artificial Intelligence literature. We based our implementation on the description of the game and definitions of performance measures that are described in literature [12].

The example we consider here is the situation that four predators pursuit one prey in a grid world. The prey chooses randomly between its possible actions: staying where it is, or moving one of the four directions(or less, if some directions are blocked). Diagonal moves are not allowed. The predators are placed at random positions. At each time-step, the prey may move first. Then the predators move. They move one by another, thus avoiding collisions. Possible outcomes are capture, stalemate and escape. A capture occurs when the four positions around the prey (left, right, above and below) are occupied by predators.

Each predator can perceive the environment and can calculate the distance between itself and prey, and receive the signal from its neighbors. We believe that the capture situation can not be attained if the predator select their actions only based on how to minimize the distance between themselves and prey. It is also important that the predators employ the cooperative action at each time-step. So we use a special Q-function that compose of each predator's individual goal (i.e. minimizing the distance between prey and itself) and the coordination factor(i.e. maintaining the suitable angle between predators) to calculate the Q-value that guide each predator's selections of actions. To our 4-predators example, the proper angle for capture between the predators is $\pi/2$.

Let us use A_1, A_2, A_3 and A_4 denote four predators and P denotes prey, and suppose that A_1 has two neighbours A_2 and A_3 . Then the Q function which A_1 use is as the following:

$$Q = \varepsilon D + (1 - \varepsilon) V$$

where,
 $\varepsilon \in (0, 1)$;

$D = 1/\text{Distance}(A_1, P)$; And $\text{Distance}(A_1, P)$ denotes the distance between prey and A_1 ;

$$V = (\text{Distribution}(A_1, A_2) + \text{Distribution}(A_1, A_3))/2;$$

$$\text{Distribution}(A_i, A_j) = 1 - \frac{\left| \frac{\pi}{2} - \text{Phi}(A_i, A_j) \right|}{2\pi - \frac{\pi}{2}}$$

The formula contains an important parameter ε . This had to be fixed first. This parameter ε is initially set to zero. With such a parameter, the agents judge the coordination with their neighbors to be useful when they maximize their distribution around the prey. This yields no prey-following behavior, but causes the agents to try to maintain angles of 90 degrees. Then let the parameter ε increase gradually. Even at low value of the parameter ε (e.g. $\varepsilon = 0.08$), the predators move towards the random moving prey. Sometimes, the agents would converge to the orthogonal positions around the prey (i.e. left, right, above, and below it), a capture situation occurs, but in many cases they converged to the diagonal positions, a stalemate situation occurs, as is shown in figure 1.

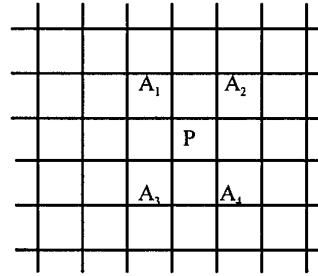


Figure 1 A stalemate situation; the parameter ε is too low

As the angles between the agents are also optimal in this situation, it is another stale configuration. However, in the 4-connected pursuit problem we investigate here, only the first one is a capture situation(i.e. the four orthogonal positions around the prey are occupied by predators). It turns out that raising the parameter ε yields just result. With the parameter value of 0.15, we tested the performance of the system. This turned out to be satisfactory for our purpose.

Figure 2 shows another stalemate situation. The reason for this stalemate is opposite to the stalemate situation described above. Here, the parameter ε was too high($\varepsilon=1$). We went to lower this parameter gradually to increasing

the influence of distribution factor until this stalemate situation disappeared. This first occurred at $\epsilon = 0.95$.

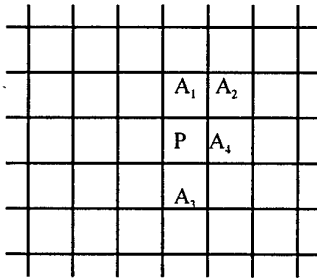


Figure 2 Another stalemate situation; the parameter ϵ is too high

We do our simulations at an IBM compatible PC, programming with Microsoft Visual C++ on the platform of Windows 95.

Our simulations run 100 trials in the various grid worlds, including 40×40 grid, 50×50 grid, 60×60 grid. In all of these situations, we firstly suppose that the prey moves to the position that is furthest away from the nearest predator and rests in 10% of its moves, instead of randomly choosing between the allowed options. The four predators act one by one, and they always select the action that can maximize the Q-value at every time-step.

The final results show that the success ratio is 100%.

6. Conclusion

In this paper we use a Q-learning method with special Q-function to discuss the coordination in multi-agent system. The main idea of this paper is to build the Q-function that combine the local factor and cooperative factor, and try to make the agents employing Q-learning technique with such Q-function coordinate their actions. The experiment results show that this idea is effective.

References

- [1] J.R. Anderson, C.F. Boyle, A.T. Corbett, and M.W. Lewis, "Cognitive Modeling and Intelligent Tutoring", *Artificial Intelligence*, 1990, Vol. 42, pp: 7-49.
- [2] A.S. Rao, and G. Murray, "Multi-agent Mental-state Recognition and Its Application to Air-combat Modelling", In *Proceedings of the Workshop on Distributed Artificial Intelligence (DAI-94)*, Menlo Park, Calif: AAAI press, 1994.
- [3] B. Hayes-Roth, L. Brownston, and R.V. Gen, "Multi-agent Collaboration in Directed Improvisation", In *Proceedings of the International Conference on Multi-agent Systems*, 1995.
- [4] K. Pimentel, K. Teixeira, *Virtual Reality: Through the new looking glass*, Blue Ridge Summit, PA: Windcrest/McGraw-Hill, 1994.
- [5] J. Bates, A. B. Loyall, and W. S. Reilly, "Integrating Reactivity, Goals and Emotions in a Broad Agent", *Technical Report CMU-CS-92-142*, School of Computer Science, Carnegie Mellon University, May 1992.
- [6] M. Tambe, "Teamwork in Real-world, Dynamic Environments", In *Proceedings of the International Conference on Multi-agent Systems (ICMAS)*, 1996.
- [7] A. B. Barto, R. S. Sutton, and C. Watkins, "Sequential Decision Problems and Neural Networks", In *Proceedings of 1989 Conference on Neural Information Processing*, 1989.
- [8] C.J.C.H. Watkins, "Learning from Delayed Rewards", PhD thesis, King's College, Cambridge University, 1989.
- [9] M. Tan, "Multi-Agent Reinforcement Learning: Independent vs. Cooperative Agents", In *Proceedings of the Tenth International Conference on machine learning*, 1993, pp: 330-337.
- [10] S. Sen, and M. Sekaran, "Learning to Coordinate without Sharing Information", In *Proceedings of the Twelfth National Conference on Artificial Intelligence*, WA: AAAI, Seattle, 1994, pp: 426-431.
- [11] Y. Shoham, and M. Tennenholtz, "Emergent Conventions in Multi-Agent Systems: Initial Experimental Results and Observations", In *Proceedings of KR-92*, 1992.
- [12] L.M. Stephens, and M. B. Merx, "The Effect of Agent Control Strategy on the Performance of a DAI Pursuit Problem", In *Proceedings of the 1990 Distributed AI Workshop*, 1990.

The Improvement of Genetic Algorithm using Boltzmann Selection

Yoo-Shin Kim, Gi-Souk Yoon, Jae-Woo Kim

Department of Electronics Engineering, Pusan University, South Korea
kimys@hyowon.cc.pusan.ac.kr

Abstract

In this paper, we propose a method to improve Genetic Algorithm using Boltzmann selection which Michael has suggested. But Michael uses temperature schedule (the initial temperature, the cooling rate), which can be applicable only to the limited range of problems.

We propose a new method to find the critical temperature and the cooling rate as parameters of the temperature schedule. The critical temperature can be derived from the distribution of each individual's fitness. Through the application of the island model where each island has differing cooling rate, it is proved that it is unnecessary to find the optimal cooling rate. The simulation on the TSP's with various city sizes proves the proposed critical temperature correct.

1. Introduction

To solve the optimization problem, researches based on natural phenomena (the physical or biological process) has been conducted. For example, the GA (Genetic Algorithm) and the SA (Simulated Annealing) take their idea from the evolution and the annealing process, each other. The GA [8][9][10] is a searching algorithm that has its origin on the evolution by "the natural selection". The GA uses operators like reproduction, crossover, and mutation, etc. During the process, it forces individuals with relatively high fitness survive. The SA [6][7] simulates the annealing process of solid using statistical physics method. By giving some probability to transit to higher-energy states, it can escape from local minima.

The SA is naturally serial processing algorithm and difficult to implement on parallel systems with appreciable linear speedup. Many approaches have been tried to make SA applicable to parallel system.

Hyeon-Joong [2] introduced a population-oriented SA, where each individual in the population can intelligently have its own annealing schedule in an adaptive fashion.

Saul [5] decomposed annealing algorithms of a multiprocessor design into subtask, which could be run on an experimental shared-memory multiprocessor.

To solve job shop scheduling, Krishna [1] developed distributed SA algorithms (the temperature modifier, the locking edges and the modified locking edges algorithms).

Recently, researches about hybrid approaches that combined the power of the GA and the SA have been conducted.

Hao Chen [4] applied GSA (Genetic Simulated Annealing) to SIMD (Single Instruction stream-Multiple Data stream) machine to solve the TSP and the Error Correction Code Design.

Michael [9] suggested the Boltzmann selection for the GA. He showed that the translation invariance property of the Boltzmann selection, and introduced the temperature as the convergence control parameter, and explained why the Boltzmann selection outperforms the general-used proportional selection on some problems. But he determined the temperature schedule by performing experiments on just one problem.

In this paper, a new temperature schedule for the GA using the Boltzmann selection to improve GA

2. GA using Boltzmann selection

2.1. Terms

A population consists of many individuals. Generally, the GA uses a fixed population size.

Each individual represents one instant of given optimization problem and has a chromosome having information of the instant.

A chromosome composes of a fixed size of alleles, which is usually a bit or an integer.

In the TSP (Travel Salesman Problem) which is the test problem used in this paper, the chromosome is simply a list of the positions about N cities. For example of 10-city, 9 5 4 2 1 3 8 6 7 means that the visiting order is 9, 5, 4, so forth.

The fitness of an individual in a GA is the value of the objective function for its phenotype. The GA objective is

to find maximum fitness in the solution space according to the given problem.

2.2. GA using Boltzmann selection

1. Initialization

The initial population consists of a number of individuals with random allele values. In the TSP, random visiting orders are used.

2. Calculation fitness

Before selection procedure, the fitness of individual should calculated.

3. Selection

The selection probability of the Boltzmann selection is as follows.[9]

$$P_j = \frac{e^{\frac{f_j}{T}}}{\sum_k e^{\frac{f_k}{T}}} \quad (1)$$

P_j : the selection probability of the j-th' individual

f_j : the fitness of the the j-th' individual

In selection procedure, two individuals are selected for crossover, the next procedure.

4. Crossover

In crossover procedure, the selected individuals exchange its information with the probability of the parameter 'crossover rate' by the crossover operator and generate child solutions.

In the TSP, the simple standard crossover operator would be almost guaranteed to generate invalid solution. The PMX[8] method ensures that all child solutions generated are legal.

Consider the following example for 10 city.

A : 9 8 4 | 5 6 7 | 1 3 2 0

B : 8 7 1 | 2 3 0 | 9 5 4 6

-> By the crossover operator(PMX)

A' : 9 8 4 | 2 3 0 | 1 6 5 7

B' : 8 0 1 | 5 6 7 | 9 2 4 3

where, the A and the B are chromosomes of two selected individuals. The section bounded by the two | is the crossover section, which is randomly chosen. The PMX operator performs position-wise exchanges, in the bounded crossover range. In the example, the '5' in the A exchanges the '2' in the A not the B.

5. Mutation

After the crossover operation, with the probability of the parameter "mutation rate" alleles of the child individual are mutated(changed). In the TSP, a subsequence of the tour is chosen and the order is reversed.

6. Loop

The 1~5 procedures are repeated until all individuals converged during the given iteration number.

3. Temperature schedule

3.1. Temperature

The Boltzmann selection does not the selective pressure in high temperature. In a sufficiently high

temperature, $\frac{f_j}{T}$ is approximately zero. So $P_j = 1 / \#$ of

individuals. The selection probabilities of each individual are same, and there is little selective pressure[9].

But in a sufficiently low temperature, the Boltzmann selection would select individual with the maximum fitness. Other individuals may have relatively low probability. In this case, the selective pressure is high.

Therefore, the temperature acts like the parameter that controls the degree of the selective pressure (the convergence control parameter).

In high temperature, low selective pressure lets an individual (solution) search the solution space freely. As the temperature becomes lower, the selective pressure becomes higher, so 'good individual' with higher fitness has higher probability to survive(selected) and crossover.

3.2. Critical temperature

The following temperature schedules are generally used for an annealing algorithm.

$$T_i = (T_{cooling\ rate})^i T_0 \quad (2)$$

The temperature schedule (2) has two parameters: the initial temperature and the cooling rate. These parameters are found usually by 'trial and error' or many experiments.

As explained above, in high temperature at initial stage, there is no difference between the selection probabilities of 'good individual'(with higher fitness) and 'bad individual' (with lower fitness). Therefore individuals in the population are inclined to search the solution space freely by the mutation pressure. As the temperature becomes lower, the selection pressure is

higher. At a certain temperature, the mutation pressure becomes relatively much lower than before. This temperature is called the critical temperature.

Using this critical temperature as the initial temperature, wasteful annealing time in high temperature can be removed and the problem of the premature convergence in low initial temperature can be solved. But, Michael ignored such an important critical temperature. He chose the temperature through which the best individuals can be selected only by repeated experiments on just one problem as initial temperature and applied it to other problems. [9].

In this paper, to derive the critical temperature, a new selection constant α is introduced as follows.

$$\alpha = \frac{P_{\max}}{P_{\min}} \quad (3)$$

α : the selection constant

P_{\max} : selection probability of the maximum fitness individual

P_{\min} : selection probability of the minimum fitness individual

α is a ratio of selection probabilities between the maximum and the minimum fitness individual. The eq. (3) and the eq. (1) can be combined into eq. (4)

$$\alpha = \frac{P_{\max}}{P_{\min}} = \frac{e^{\frac{f_{\max}}{T}}}{e^{\frac{f_{\min}}{T}}} = e^{\frac{f_{\max} - f_{\min}}{T}} \quad (4)$$

If the difference between the maximum and the minimum fitness is known, using the eq. (4), the selection constant α can be found.

When the selection constant α reaches a certain value, the selective pressure meets the mutation pressure and the mean values of the fitness begins to decrease. This is the critical temperature point. Thus, if the α value at the critical temperature is known, the critical temperature can be easily found using the following the eq. (5), which is easily derived from the eq. (4).

$$T_c = \frac{(f_{\max} - f_{\min})}{\ln \alpha_c} \quad (5)$$

T_c : the critical temperature

$f_{\max} - f_{\min}$: the difference between the maximum and the minimum of fitness

α_c : the α value at the critical temperature

From the simulation performed later, valid α_c value is e .

3.3. Island model & cooling rate

The cooling rate is defined as the rate of temperature decreasing per one generation. The range of cooling rate is between 0.9 and 1. If the cooling rate is near 1, the temperature would be decreasing slowly, and individuals search the solution space sufficiently for a long time, and the annealing time becomes sufficiently long. Therefore optimum solution can be found easily. But the time of the convergence is too long.

Otherwise, the temperature would be decreasing quickly, and without searching the sufficient range of searching space, it can easily get into the local minima. So the bad solution can be obtained. But in this case, the solution can be found quickly.

The island model using several cooling rates can solve this tradeoff. The island model is a good evolution model using several isolated islands. And in this model the individuals migrate through the islands with a certain ratio.[10]

In this paper, cooling rates applied to each island are 3 values: small, medium, near 1(for example, 0.9, 0.99, 0.999). In each island, 1% of its population per generation migrate to the island with the next smaller cooling rate per one generation [3]. At island with the lowest cooling rate, no migration from the island to other island occurs.

The island with the lowest cooling rate would converge fastest but good solution is not guaranteed. The individual from the island with higher cooling rate migrates and the individuals which migrate from the island with higher cooling rate to the island lower cooling rate can be selected, crossovered and escape from local minima. Therefore, using the island model with differing cooling rates can show fast convergence and good solution.

3.4. The proposed algorithm

The algorithm using the proposed temperature schedule as following.

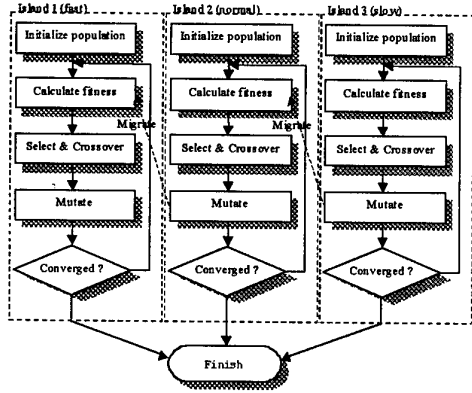


Figure 1. the flowchart of the proposed GA algorithm

1. initialize
 - 1.1. calculate the initial temperature by the eq. (5)
 - 1.2. generate random individuals in the population of the each island
 - 1.3. set the crossover rate, the mutation rate
- 2 evolve each island by one generation
 - 2.1 select two individuals using the Boltzmann selection
 - 2.2 crossover the individuals with the probability of the crossover rate
 - 2.3 repeat the 2.1~2.2 processes until generate all individuals in the population
 - 2.4 mutate all individuals in the population with the probability of the mutation rate.
3. multiply each cooling rate by $T_{cooling\ rate, fast}$, $T_{cooling\ rate, normal}$, $T_{cooling\ rate, slow}$
4. migrate randomly selected 1 % from each island to next lower cooling rate island
5. The 1~4 procedure are repeated until all individuals converged or in the given iteration number.

4. Simulation

4.1. Parameters

Parameters used in the simulation are as follows.

Number of individuals per island : 100

Mutation rate : 0.1

Crossover rate : 0.6

$T_{cooling\ rate, fast}$: 0.9,

$T_{cooling\ rate, normal}$: 0.99

$T_{cooling\ rate, slow}$: 0.999

4.2. Critical temperature

To show the proposed temperature correct, the TSPs with 100 individuals are simulated. In this case, no island model applied to the simulations.

The figure 2 is graphs for 10, 50, 100, 200, 1000 city with the initial temperature $T_{ini} = (f_{max} - f_{min}) \times 1000$ and the cooling rate is 0.9995 and iteration number is 50,000. Three kind of fitness (the maximum, the minimum, and the mean value about the population) is plotted. The direction of the generation is from right to left.

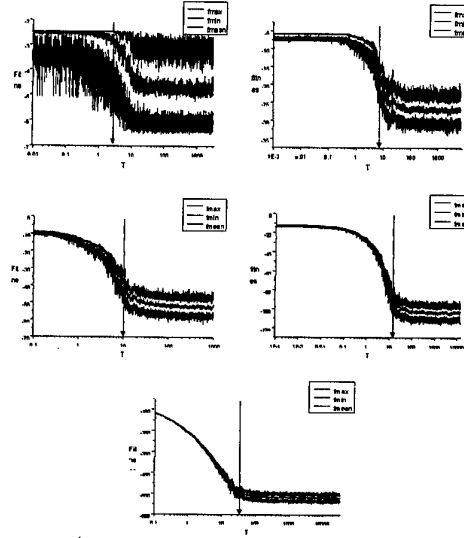


Figure 2. the fitness graphs versus the temperature for the 10, 50, 100, 200, 1000 city TSPs

Following table is the mean values of $f_{max} - f_{min}$ while first 1000 iteration.

Table 1. the mean values of $f_{max} - f_{min}$ with various city sizes

Number of City	Mean of f_{max}	Mean of f_{min}	Mean of $f_{max} - f_{min}$
10	-3.17718	-6.09914	2.92196
50	-23.01106	-30.77153	7.76047
100	-47.12069	-57.45719	10.3365
200	-96.13731	-110.47499	14.33768
1000	-502.2578	-534.57958	32.32178

Vertical arrow-lines are drawn to the figure according to the mean values of the table 1. The critical temperature with rapid decrease and vertical lines are near agreed. This fact shows that experimental value of α is e . Thus, the eq. (5) can be simplified as follows.

$$T_c = f_{\max} - f_{\min} \quad (6)$$

For the 10 city TSP, the critical temperature from the eq. (6) is somewhat incorrect, lower than the temperature shown by the graph. In the case of small number of city, while high temperature, the probability of finding good solution is higher than bigger city size case. So, fitness values become larger in the higher temperature than the temperature calculated by the eq. (6).

4.3. Cooling rate

Table 2. compare the proposed temperature schedule with other various schedules

	Cooling rate	Initial temperature		
		100	10	1
General temperature schedule	0.9	3289,- 8.5143	3512,- 8.57301	3231,- 8.54775
	0.99	3840,- 8.49933	4416,- 8.49171	3167,- 8.53157
	0.999	9904,- 8.91667	9686,- 8.41409	8768,- 8.49519
Proposed method	Proposed cooling rate	5112,-8.36853 (the eq.(6) is used for the initial temperature)		

Above table summaries mean values of the result(the iteration number when occur best fitness and its fitness value) of 15 repeated simulation on the 100-city TSP and 10000 iteration using general schedules and the proposed schedule.

As shown by the table 2, the general schedule with the initial temperature 10 and the cooling rate 0.999 shows the best fitness, but the calculation time is long. When the initial temperature is 10 and the cooling rate is 0.99, the fitness of the solution is ranked the second and the calculation time is half of best case. According to the application, if fast convergence is important, the latter schedule is proper, if optimum fitness is important and the calculation time is unimportant, former schedule can be used. The decision of the temperature schedule like above processing should be performed whenever the Boltzmann selection applies to the application

Even through the proposed method have no need to take time to find the temperature schedule above, it shows the best fitness in the table 2. But the calculation time is not yet best.

4.4. Examples of the TSP results

The figure 3 shows results of proposed algorithm with 10, 50, 100, 200 city TSPs and 10000 iteration.

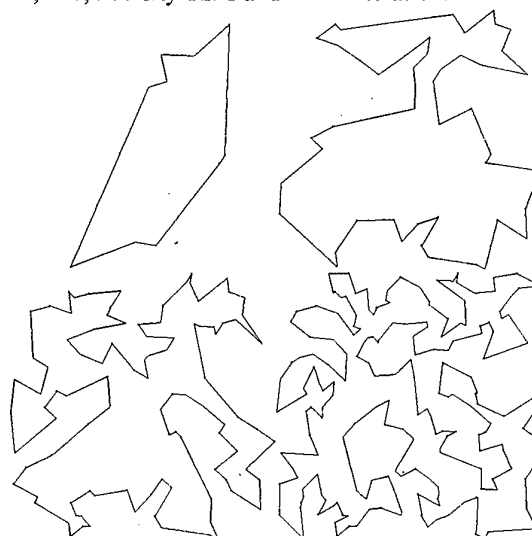


Figure 3. the example of 10, 50, 100, 200-city

5. Conclusion

This paper presents the temperature schedule of the GA using the Boltzmann selection. The proposed schedule consists of the critical temperature derived from the distribution of the individuals' fitness and the island model having different cooling rates.

For more than 100 city TSP, the critical temperature is nearly correct. The proposed schedule shows better fitness than other general schedules by the simulation.

6. Reference

- [1] K. Krishna, K. Ganeshan, and D. Janaki Ram, "Distributed Simulated Annealing Algorithm for Job Shop Scheduling," *IEEE Transactions on System, Man, and Cybernetics*, vol. 25, no.7, pp1102-1109, July 1995
- [2] Hyeon-Joong Cho, Se-Young Oh, and Doo-Hyun Choi, "Population-oriented simulated annealing technique based on local temperature concept", *Electronics Letters*, vol. 34, No. 3, pp. 312-313, 1998
- [3] Theodore C. Belding, "The Distributed Genetic Algorithm Revisited," *Proceedings of the sixth international conference on Genetic Algorithms 1995*, pp114-121, July 1995
- [4] Hao Chen, Nicholas S. Flann, and Daniel W. Watson, "Parallel Genetic Simulated Annealing : A Massively Parallel SIMD Algorithm," *IEEE Transactions on parallel and distributed Systems*, vol. 9, no.2, pp126-136, February 1998

- [5] Saul A. Kravits, and Rob A. Rutenbar, "Placement by Simulated Annealing on a Multiprocessor," *IEEE Transactions on computer-aided design*, vol. CAD-6, no.4, pp534-549, July 1987
- [6] S. Kirkpatrick, C. D. Gelatt, Jr., M. OP. Vecchi, "Optimization by Simulated Annealing," *Science*, Volume 220, pp671-680, May 1983
- [7] R. H. J. M. Otten, L. P. P. P. van Ginneken, "The Annealing Algorithm," Kluwer Academic Publishers, 1989
- [8] D. E. Goldberg, "*Genetic Algorithms in Search Optimization and Machine Learning*," New York, Addison Wesley, 1991
- [9] Michael de la Maza, "The Boltzmann Selection Procedure," *Practical Handbook of Genetic Algorithms : New Frontiers Volume II*, vol. 2, chap.5, pp111-139, CRC Press, 1995
- [10] Conor, Ryan, "Niche And Species Formation in Genetic Algorithms," *Practical Handbook of Genetic Algorithms : Applications Volume II*, vol. 2, chap.2, pp 57-75 ,CRC Press, 1995

Designing Intelligent Multiparameterised Devices : a Mechatronics Field

Geneviève Bosvieux Coilliot

*Laboratoire d'Artois Mécanique et Habitat
Université d'ARTOIS,
rue de l'Université, 62408 BETHUNE, Fr
Email : bosvieux@univ-artois.fr*

Jean Louis Tournier

*Laboratoire d'électronique
ENSEEIH
2, rue Camichel, 31071 TOULOUSE, Fr
Email : tournier@len7.enseeiht.fr*

Abstract

In this paper we are interested with human expression and communication through Man Machine Interaction and with the trends that improve human-friendly interfaces for new processes taking into account kansei technologies. These technologies are a central part of the development of new interfaces. Besides the design of new tools and new 'intelligent' functions, specially based on gesture interaction, is showing the importance of co-designing the systems (hardware part and software part).

Human wants to be able to work his way.

Man-Machine Customization is a Mechatronics field.

Let us give a simple gesture example such as a japanese word written with calligraphy, which means 'silk'. There are rules to write this kind of word. (Fig.1)



Fig. 1 : 'Silk' in japanese.

1. Introduction

Making and using the computers and all computer-assisted machines and devices is more and more a mechatronics field. The introduction of multiparameterised capture tools has brought new possibilities in various domains such as robotics, CAD systems, art, computer assisted painting.

Though many people think that computer graphics possibilities are now sufficiently convenient for artists and designers, such as car designers, we think that there are still many devices missing allowing natural gesture and intelligent interaction.

With a computer environment you cannot realize that sort of symbol and drawing with rapid and simple direct brush strokes; it is no more possible using latin letters as following (fig. 2). The reason is that to render that kind of writing or painting, the gesture and the brush have to be working together allowing a vivid stroke.

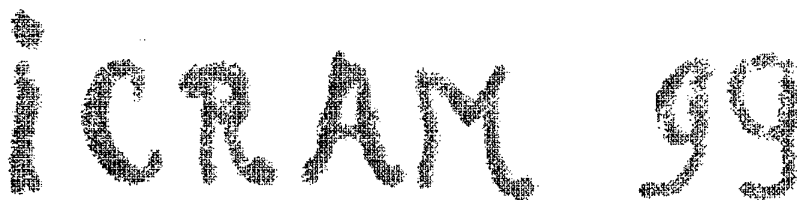


Fig. 2 : Calligraphy mode

In various cultures calligraphy expressed the need of shared knowledge [1], with art and beauty, using specific brushes in slightly different manners. There are precised rules for all the cycle : in the preparation of the tools, in the use and in the drawing.

We intend to realize such a kind of brushes and more generally capture tools with 'intelligent' possibilities, in design, in painting and in robotics [2]. In a general way, we want to have in hands tools easy to use, gesture sensitive, customizable and efficient.

We shall see successively the problem position, the state of the art, the notion of customization and kansei, the proposed 'intelligent' devices, and the 'SMART PEN' presentation.

2. The problem position

Nowadays, new technologies are everywhere, in personal and in working life. We may consider with Aart BIJL [3] several aspects :

- what do people have to know in order to use these new technologies?
- and how does that fit with whatever else people know and do?

We may consider as well :

- what does it bring to people? Such as easiness, pleasure in using functions, possibility of creation for architects, artists,...
- which new functions are being created, and/or have to be created that will allow new customs.

In man-machine interaction, some of these functions are based on the use of new multiparameterised intelligent capture tools, allowing to take into account gesture interaction.

We believe that many new devices are still to be created for gesture rendering. Workshops are now concerned with only gesture man machine interaction [4].

Some systems allow mixed interaction with voice and gesture for example, as we say 'give me a pen' and then write.

One of the new trends is to allow the art people to use their senses and their sensibility in man-machine interaction.

3. The state of the art

3.1. Twenty years for a mouse

Capture tools are not easy to be developed. So, it took twenty years to the mouse invented by Douglas Englebert to become of ordinary use. Some devices are being created, that are no more on the market place. It was the case for the Max digitiser, with seven degrees of freedom [5]. We think that various reasons such as the cost of devices and applications, the lack of drivers available, the lack of power of the computer machines a few years ago, were stopping the realization of interesting devices. Internet technologies will allow easier integration.

3.2 In Graphics domain

Already fifteen years ago, 126 levels in half a centimeter flexibility of a pen pressure were proposed; they could not be discernible.

The effect of just an added parameter to x-y selection could not be calculated in realtime, with usual environments, so it was unpleasant and inefficient to use the pressure of such a pen.

Other parameters were first simulated with potentiometers, then, added inside the pen for gesture rendering [2], associated with graphic tablets, or captured with CCD cameras.

In man machine interaction (MMI), and specially in Graphics computer arts, there are two kinds of processes : those calculated in real time, and those whose effect is delayed. The brush stroke should leave a trace in real time, even if that trace is changing with the time, such as in real water painting : the result is different when the paper is drying!

Graphic palettes such as Quantel, are giving very rich possibilities using image treatment and synthesis, but gesture subtlety is not yet sufficiently expressive.

A special domain is graphic creation for 2D and 3D cartoons.

3.3 In Robotics

Many multiparameterized tools are designed for robots activities. Robots now use multimodal input devices [6] and emotional effects. Teams are working on friendly robots to improve human-robot communication [7].

Next IEEE/Conference on Intelligent Robots and Systems (IROS 99) interest is on 'Human and Environment Friendly Robots with High Intelligence and Emotional Quotients' [8].

3.4. The general context

These new interfaces for personal and cooperative work take into account various developments in many domains :

- in mechatronics design,
- in techniques for creating and using 3D, in real, Virtual and Augmented Reality worlds, [9,10]
- in context-based systems, 'intelligent' systems using methods such as fuzzy logic, clustering, soft computing, reinforcement learning,
- in the interaction and cooperation, using cognitive sciences, affective engineering,
- in techniques for handwriting and typewriting recognition (OCR, online character recognition), for latin, japanese and chinese writing. They should benefit of multiparameterised capture tools.
- in techniques bringing new possibilities of *customization*, in communications and cooperation, using telecommunications, the Internet technologies, such as VRML extensions.

These studies allow the design and use of new 'intelligent' devices for human interfaces.

4. Customization and Kansei

We have presented previously the necessity of customization in MMI [11]. It is a topic among the streams that carry out the new interfaces and processes. - For example, half of the people who buy the new Macintosh Inc. IMAC get a Internet connection the same day, surely because of the connection mode simplicity - not a complicate specialist operation.

So, if men try to improve the cycle impression-expression, besides, analyses and modelisation transfer partly human impression and decision to machine control. This is one of the objectives of kansei technologies.

These two streams will tend to improve M-M interaction.

4.1 'DEVICE' : a human-friendly interface

With Sheffield university we have proposed 'DEVICE' (Design Environment with Visual Interaction and Creative Expression) [12], a human-friendly interface : a user-definable menu allows to link gesture multiparameterised capture and its interpretation for driving processes in design and painting and robotics. The user is able to enter in a personal way and simultaneously information on the objects and on the way to decode them.

In Robotics, the method allows to give importance to natural aptitudes, and knowhow and to build 'testbeds' for trying new devices [6].

4.2. Three levels for customization

In designing and/or carrying out computer assisted processes, we have three levels interacting where customization intervenes : construction, use and control or decision.

4.2.1. customization through the construction of the tools. starting from a multiparameterised *capture* one builds the models of the command, the task and the context. Construction is defined by the user graphically, without programming [2].

In painting, we define paper or surfaces, inks and colors, and brushes or pens allowing gesture multiple capture; we build their specifications and rules of action and interaction.

The user sensitiveness is required. He tries and if the effect is not satisfying, he or she can begin again the construction, as a painter is choosing his tools and palettes.

4.2.2. customization in the way of using the tools.

We gave in [6] the qualities required for man machine interaction tools; the tools should be 'well in hand'. If you change the way you are moving or activating a brush or a tool, the result should be different, as with real mechanical or simple tools: robots, hammers, knives,

So, playing the violin can give an idea of the fact that 'easy to use' or 'easy to interpret' are full of meaning. Personal qualities and training are the base for a good result. The violin interpretation takes into account many physical, mental, emotional, fashionable considerations.

The 'hyperviolin' (fig.3) was designed to measure human performance (testbed), to build ever-more-powerful entertainment interactive systems for the general public. It is a kansei analyse [13].

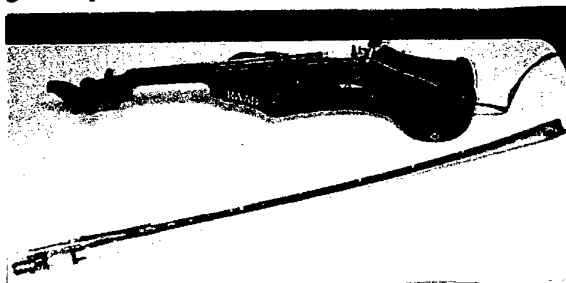


Fig.3 : A kansei 'hyperinstrument'

4.2.3. customization for the control. In context-based systems, with many degrees of freedom (DOF) and sensors, the control is permanent; the part depending of the man decision is reduced by the machine control. Context parameters should be accessible to help the user in his decision.

Driving cars, planes or online robots, painting, playing music, are self-controlled activities. They use conscious and unconscious levels of control; with left side and right side of the mind [14].

4.3. 'DEVICE' and Kansei technology

In each of these three levels of the 'Device' method, perception and sensitivity may guide first the customers.

The capture with several degrees of freedom emphasizes the gesture and facilitates personal expression. It is as well a mean to analyse this expression, like with the hyperinstruments.

Furthermore, the 'DEVICE' method can be extended to the case of multimodal input : co-verbal gesture, or fusion of gesture with other modalities, vision and other senses [4].

The architecture of the systems, the level of fusion, the temporality, the priorities, the representation of this multimodality have to be studied.

Through a user-definable menu, this environment taking into account in a general way sensibility for personal creation of functions [15], activated by gesture and other senses, allows the user to enter in the machine his analyse and to precise preferences in the construction of the tools and in their use; we are in phase with Kansei engineering technology.

"KANSEI is a human ability to derive images from stimulation, and to express them. Also, KANSEI is affected by human knowledge and emotion." [13].

This kansei technology tries to analyse the way people use their senses to realise or to do something - find the defects in a production of glasses, pronounce vowels, playing the violin, why not painting...

Human wants to be able to work his way, when possible. In this study it implies that human likes to feel he has some influence on what he is doing; he is free to do things the way he wants; we try to give him the means to do so in specific domains. Even with CAD systems, people take different ways to realise the same object.

5. The proposed 'intelligent' devices.

We have designed several input devices. They are being developped with Lille and with Toulouse Universities. They are needed for painting and to extend our cursive handwriting simulation using personally designed alphabet and symbols. The letters are joined with splines [15]. The cursive rendering had to be improved in a user-definable way : the distance between two letters, solutions to avoid monotony...

In previous papers, we have proposed several kinds of 'intelligent' devices [16,17].

6. The system proposed by TOULOUSE

The system proposed by the Electronic Laboratory of the Ecole Nationale Supérieure d'Electronique d'Electrotechnique d'Informatique et d'Hydraulique de Toulouse (ENSEEIH) is based on the registering by triangulation.

On a pen 'SMART PEN' with which one can register and reproduce movement, we fixed three laser diodes in a pyramidal geometry (fig. 4).

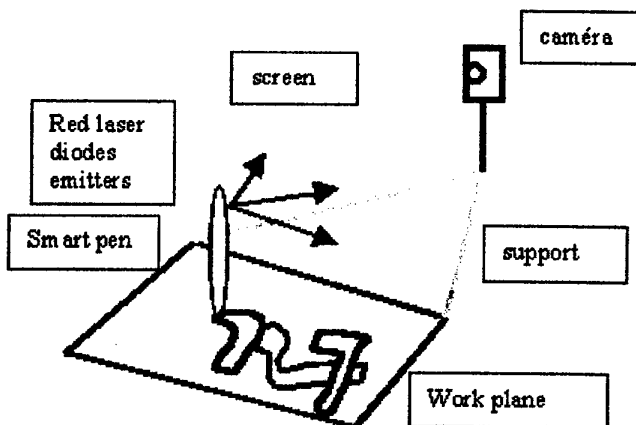


Fig. 4 : Three laser diodes on SMART PEN

These three diodes create three traces on a translucent screen. A video camera records the traces images. The center of gravity is calculated by a system of image treatment; a localisation calculation allows to get the position and orientation of 'SMART PEN'.

This 3D localisation system using laser marking is the object of a european patent (ref. n°EP 0 385 528 B1). Localisation has been the object of many studies in both cognitive and technical points of view [10,18,19].

The registration of the hand real movement, in position and in orientation, allows to reproduce for example the graphics created by a pen that should be a the tip of the 'SMART PEN', in the same way as this drawing was created.

The Electronic Laboratory of the ENSEIHT and the Microelectronic System Design team are working on the project.

- on the one hand, on the optimization of the image process for a real time process, this for the 3D localisation data collection and process,
- on the other hand, on the real time reproduction of the created drawing.

The modularity of the process will allow the optimisation following the technological evolution, because the team is working on the part 'optimisation of the process' to do the best between 'the algorithm and the circuit'.

The quick evolution of the FPGA (Fields Programmable Gates Array), allows to face quick adaptations cheaper than those imposed by the ASIC (Applications Specific Integrated Circuits).

We are in the realisation phase of a prototype which will allow us to validate our proposed concepts in C.A.D, on the 3D localisation part (AUTOCAD), and on the electronic design part (circuits CAD).

7. Conclusion

M-M interaction is a mechatronics field. One of its new trends concerns customization. Next IEEE/Conference IROS 99 is on 'Human and Friendly Robots with high Intelligence and emotional quotients'.

To realise customisation, we have proposed previously 'DEVICE', a user definable menu based on the interpretation of gesture multi-parameters and the design of new tools and new 'intelligent' functions.

We analyse our proposition face to kansei technologies. The generalisation of our method to various senses is going in the way of these kansei technologies applied to computer interactive systems. They are a central part of the development of new multimodal interfaces.

We present a device, SMART PEN allowing the reproduction of a created drawing, for the realisation of computer painting with live brush strokes.



References

- [1] L. Bonfante et al.: La Naissance des écritures, du cunéiforme à l'alphabet, 1994, Scuil ed.
- [2] G. Bosvieux Coilliot, Gesture and Interactivity Tools for Robots Adaptability and Learning, *1st French Japanese Congress of Mechatronics* Besançon, pp 21-23 Oct.1992
- [3] A.Bijl, 'Information Technology : using computers', RSTC, Vol. 2, n°2, 1993, p.191-257, Hermès ed.
- [4] GW'99, 3rd gesture Workshop, 17-19 Mars 99, Paris
- [5] « MAX » Digitiser: Terminal Display Systems, Lower Philips Road Blackburn Lancashire BB1 5TH England, 1989.
- [6] G. Bosvieux Coilliot, D. Boissier, Personalization in Human-Machine Systems: a model', *Workshop on Motion Control*, Berkeley, March 20-23 1994, pp 83-92
- [7] 'RO-MAN'98, 7th IEEE Int. Workshop on Robot and human communication, Sept.30-Oct.2 1998, Takamatsu, Japan
- [8] IEEE/Conference on Intelligent Robots and Systems (IROS 99), Hiroshima, Oct. 17-21, (to pub.)
- [9] J.L.Tournier, J.David, M.Cattoen: 2° Japan-France Congress on mechatronics, Takamatsu, Japan, nov 1-3, 1994, '3D localisation system', Vol 2, p 643.
- [10] J.L.Tournier, et al, 2° Mechatronics, 'Modeling of six parameters 3D localisation system : Appli. : radiotherapy, correl. of medical images' Kitathyushu, 6-8 oct 1998. Vol 1, p 85..
- [11] P. Szalapaj, G. Bosvieux, 'Customising Cooperative Design' *Fifth EurolA 95*, Lyon, 12-14 Déc, p. 391-400
- [12] G. Bosvieux-Coilliot, P.J. Szalapaj, D. Boissier, 'Design Environments with Visual Interaction and Creative Expression', *ICED '95*, Prague, Czech Rep, 1995, pp. 650-655.
- [13] Kansei, the Technology of Emotion Workshop, 1997
- [14] B. Edwards: Drawing on the Right Side of the Brain, 1989, Tarcher Perigee ed.
- [15] G. Bosvieux-Coilliot, 'Customisation for Human-friendly MMI. A Handwriting example.'RO-MAN'98, 7th IEEE Int. Workshop Sept.30-Oct.2, 1998, Takamatsu, Japan. P 588-591
- [16] G. Bosvieux Coilliot, V. Cordonnier, GICOM: Gesture interactivity in a constructor of menu, *SID'90 (Symp. of the Soc. for Inf. Display)*, Las Vegas May 90, pp 173-176
- [17] G. Bosvieux-Coilliot, 'Computer assisted handwriting and painting', *2nd EUROPE-ASIA MECHA-TRONICS*, Kitakyushu, JAPAN, Oct 6-8, 1998, p. 141-144
- [18] J.L.Tournier, J.David, M.Lescure, 1° Europe-Asia Congress on mechatronics, 'Kinesigraph, application, virtual hand' Besançon, oct 1996. Vol 1, p 191.
- [19] S.Perrin : modélisation-simulation de caméra CCD, thèse, LAI-INSA-Lyon, dec 1996

An Expert System for the Prediction of Faults and Wearing in Roller Bearings, Gears and Drill Bits via Signature Analysis in the Frequency Domain

Ata Muğan, Alper Bozdoğan, Murat Doğan and Muzaffer Erdal
Istanbul Technical University, Department of Mechanical Engineering
Gümüşsuyu 80191, Istanbul, TURKEY
mugan@itu.edu.tr

Abstract

In this study, vibration signals of roller ball bearings, gears and drill bits are studied in the frequency domain to determine the condition of them. Signal generation models, characteristics of a specific fault type and signature of wearing are investigated. Power spectrum of the signals produced by these models are computed that are typical for a given fault type. By use of these signal generation models, an algorithm is developed for predicting a fault type and wearing.

1. Introduction

Vibration monitoring is an act of extracting information by using vibration signals of a machinery, which contain information about the condition of the machinery's components. As these signals carry information about the forces that created them and about the structural path through which they propagated, they can be used for predicting the condition of the components. The advantages of vibration and acoustic monitoring are as follows: it is nondestructive and nonintrusive, could be implemented on-line, and instrumentation can be done by off-the-shelf reliable devices. A review about these techniques can be found in [1] and [2].

The study presented here is formed of three application fields: diagnosis of faults in roller ball bearings, diagnosis of faults in gears, and diagnosis of wearing in drill bits. The outline of this paper is as follows: in the first part, the roller ball bearings are considered, and the following signal generation models are obtained following the works [4], [6], [7]: rotational speeds and frequencies of inner and outer races, the cage and the balls, the frequency generation model of a localized defect in a race, effect of loading distribution, effect of the ellipticity of the races, effect of unequal rotating elements, and effect of a misaligned race. In the second part, the gears are studied, and the following signal generation models are considered [5], [8]: spectral distribution of tooth-tooth variation,

eccentricities of the gears, effect of misaligned or bent shaft. The methodologies followed for the analysis of signals of gears and roller ball bearings are identical as follows: firstly, signal generation models are derived and then simulated by use of the Matlab software; the simulation results are compared with the predictions based on analytical models and with some experimental data. In the third part, following the work [3] drill bit wearing is considered in frequency domain. Finally, a diagnosis program written in the Matlab that analyzes the frequency spectrum of a given signal to detect the possible faults and wearing is presented. Vibration monitoring is commonly used for prediction of faults; however, it is generally attempted to establish connections between the peaks in the power spectrum or cepstrum and rotational frequencies of the elements. In our approach, the signal pattern of a fault is searched in the power spectrum and cepstrum, which is more suitable for automation.

2. Vibration generation models for roller-ball bearings

In this section, following [4], [6] and [7], simplified models for vibration generation mechanisms in a roller ball bearing are presented. For the rolling motion, generated signals have the following frequencies

$$f_c = \frac{1}{2} f_{ir} (1 - \gamma) + \frac{1}{2} f_{or} (1 + \gamma) \quad (1)$$

$$f_b = \frac{d_b}{2d_p} (1 - \gamma)(1 + \gamma)(f_{or} - f_{ir}) \quad (2)$$

where $\gamma = (d_b / d_p) \cos \alpha$, d_b and d_p are the ball and pitch diameters, α is the contact angle, and f_c , f_b , f_{or} and f_{ir} are respectively the rotational frequencies of the cage, rollers, and inner and outer rings.

Vibration generation model for a single localized defect i can be expressed as follows

$$x_i(t) = \sum_j g_i(t - jT_i)U(t - jT_i) \quad (3)$$

where j is the index of the period, $g_i(t)$ is the vibration response upon the impacting with the defect and T_i is the

repetition period. For instance, for a defect on the outer ring, $f_{or} = 0$ and K rolling elements, $T_i = 1/(Kf_c)$. Note that $x_i(t)$ has components with discrete frequencies of n/T_i , $n = 1, 2, 3, \dots$. On the other hand, the intensity of the impulse generated by the localized defect is proportional to the load on the rolling element at the time of impact. Therefore, the loading distribution is multiplied by the intensity

$$Q = Q_{\max} \left(1 - \frac{1}{2\varepsilon} (1 - \cos\phi) \right)^m \quad (5)$$

where ε is the load distribution factor, m is a factor in the range 1-1.5 depending on the type of rolling element, and the variations of the load as a function of the number of rolling elements in the loading zone are neglected. For a rotating inner ring, $\phi = 2\pi f_{ir} t$ as long as it stays within the loading zone, that results in a time-dependent periodic loading function $Q(t)$. For example, for an impact frequency f_i and rotating outer ring at frequency f_{or} , we obtain the signals having the following frequencies: nf_i for impacting frequencies, and $nf_i \pm mf_{or}$ for the sidebands, whose magnitudes depend on the load.

In case of unequal rotating elements, the contact force will have the frequencies nf_i and nKf_i , whose magnitude proportionality factors are respectively $(P_i - P_0)/(P_0 n^2)$ and $(1/nK)^2$. On the other hand, a misaligned race will produce signal components of the frequencies nKf_i and $nKf_i \pm 2f_r$, whose magnitude proportionality factors are $(1/nK)^2$ and $\beta/(nK \pm 2)^2$. Finally, an elliptic race would yield signals of the nKf_i and $nKf_i \pm f_r$, whose magnitude proportionality factors are $(1/nK)^2$ and $\beta/(nK \pm 1)^2$. In these formulas, P_0 is the equal contact forces on an element, $P_i - P_0$ is the unequal element force, β is a constant to represent defect severity. Note also that a good bearing generates frequencies of nKf_r due to balls entering and leaving the loading zone whose magnitude proportionality factor is $(1/nK)^2$.

3. Vibration generation models for gears

In this section, vibration generation models of a gear pair are presented following the works [5], [8]. Note that there exist forces with the basic period $1/f_b$ due to tooth meshing, where $1/f_b$ is the time necessary for N rotations, defined by the minimum number of rotations of the smaller gear necessary to achieve the said recurrence. Hence, N is defined as the numerator of the fraction (>1) describing the gear ratio after dividing out all common factors from the numerator and denominator [2]. In sum, f_b is the frequency of tooth-tooth variation of the force,

and f_m is the mesh frequency.

On the other hand, eccentricities in the driving and driven gears 1 and 2 having the rotating frequencies f_1 and f_2 would generate signals of the following frequencies

$$f = \begin{cases} k_1 f_m \pm l_1 f_1 \\ k_2 f_m \pm l_2 f_2 \end{cases} \quad (6)$$

that have peaks around the multiples of f_m , where k_1 , k_2 , l_1 and l_2 are all integers. Note also the following frequency components: mechanical looseness $2f_r$, damaged gear and imbalance f_r , and misaligned or bent shaft f_r and often $2f_r$.

4. Effects of wearing

It is observed in experimental data that due to wearing the magnitude of the power spectrum of the vibration signals increases up to full acoustic emission range. For instance, typical power spectrum plots that belong to the vibration signals in drilling of AISI 1045 steel by using a 9.5 mm HS drill are given in Figures 1 to 3. Observe that the average power spectrum level of vibration signals of drill bits increases almost uniformly in all frequency ranges as wearing develops. Thus, drill bit wearing can be determined by monitoring the vibration or acoustic signals and analyzing them in the frequency domain.

5. Frequency domain signatures of signal models

The frequency domain signatures of signal generation models presented in Sections 2 and 3 will be given in this section through examples.

5.1. Roller ball bearing models

Consider a roller ball bearing ORS 6413 in a gear box having the following specifications: $n_r = 1450$ rpm, $K=12$, $d_p = 160$ mm, $d_b = 29$ mm, $\alpha \cong 30^\circ$, and the outer race is constant while the inner race is rotating with the shaft. Accordingly, (1) and (2) yields that $f_{ir} = 0$, $f_{ir} = f_r$, and $\gamma = (d_b / d_p) \cos\alpha = 0.15735$, $f_c = 10.182$ Hz, $f_b = 2.141$ Hz; hence, corresponding power spectrum would have two peaks at $f_c = 10.182$ Hz if a local defect exists on the outer race and $f_b = 2.141$ Hz if a local defect exists on a ball. On the other hand, a good bearing would have frequencies at $nKf_r = 145n$ Hz having the magnitude proportionality factor $1/(nK)^2$, $n = 1, 2, 3, \dots$, whose time vs. vibration signal plot and corresponding power

spectrum are respectively shown in Figures 4 and 5.

For unequal element forces, $P_i = 103 \text{ kN}$ and $P_j = 25.75 \text{ kN}$. Then, corresponding frequencies are nKf_i and nf_j , whose magnitude proportionality factors are respectively $1/(nK)^2$ and $(P_i - P_j)/(P_i n^2)$, $n = 1, 2, 3, \dots$. Its time vs. vibration signal plot and corresponding power spectrum are respectively shown in Figures 6 and 7.

For a misaligned race, corresponding frequencies are nKf_i and $nKf_i \pm 2f_r$, whose magnitude proportionality factors are respectively $1/(nK)^2$ and $\beta/(nK \pm 2)^2$, $n = 1, 2, 3, \dots$. Its time vs. vibration signal plot and corresponding power spectrum are respectively shown in Figures 8 and 9. Similarly, the frequencies of an elliptic race are nKf_i and $nKf_i \pm f_r$, whose magnitude proportionality factors are respectively $1/(nK)^2$ and $\beta/(nK \pm 1)^2$, $n = 1, 2, 3, \dots$. Its time vs. vibration signal plot and corresponding power spectrum are respectively shown in Figures 10 and 11.

5.2. Gear models

Consider a gear pair in a gear box having the following specifications: $n_1 = 1450 \text{ rpm}$, number of teeth of the driving gear $z_1 = 20$ and number of teeth of the driven gear $z_2 = 100$. Accordingly, the reduction ratio $i = 5$, $f_b = 24.166 \text{ Hz}$ and $f_m = if_b$, whose power spectrum is shown in Figure 12. Notice tooth-tooth variations and modulation effect.

Eccentricity in one of the gears would generate a signal in time domain shown in Figure 13 whose power spectrum is given in Figure 14. Finally, the signal originating from a local defect in a tooth and its power spectrum are respectively given in Figures 15 and 16.

6. The expert system for fault diagnosis

In this section, an expert system for fault diagnosis that utilizes the signal generation models presented in Sections 2 and 3 to predict faults is presented. The expert system program developed in Matlab works in the following manner: first, given the necessary information about the system, the potential frequency components, i.e., the location of peaks in frequency domain, are calculated for each fault type. By using this result, the program fits a spline between the two peaks of the signal generation model for a fault candidate plus *a priori* white noise input. Then, these peaks are searched and the deviation from the spline is calculated in the power spectrum or cepstrum of the vibration signals. If it matches with the experimental data and the value of the peak is higher than a threshold value, the program gives a warning. In order to detect wearing, the average of spectrum of the raw data is

calculated and compared with a priori threshold values to determine the condition of the component.

7. Conclusions

In this work, signal generation models in roller ball bearings and gears are derived, and simulated by use of the Matlab software. The simulation results are compared with the predictions based on analytical models and with some experimental data in literature. It is found that the signal generation models are sufficient to be employed for detecting associated signal sources, which explain the underlying mechanisms behind the signals and their results match with the experimental results. Then, an algorithm for detecting the faults considered in this study is tested on experimental data. Unlike common vibration monitoring applications that usually attempt to establish connections between the peaks in the power spectrum or cepstrum and rotational frequencies of the elements, the signal pattern of a fault is searched in the power spectrum and cepstrum in our approach, which is more suitable for automation.

It is observed that the proposed approach works well if the signals associated with the faults are distinct in the frequency domain and signal-to-noise ratio is high. In addition, using power cepstrum rather than power spectrum of the experimental data for diagnosis yield better results. If two faults have the same frequency component, time domain techniques are necessary for detecting the faults. On the other, it is possible to detect the faults by using the signal generation models; however, a good knowledge about the sample space and threshold values of frequency components is needed to decide about a machinery whether it is faulty or not.

8. References

- [1] R. B. Randall, *Frequency Analysis*, Brüel & Kjaer, Denmark, 1987.
- [2] S. Braun, *Mechanical Signature Analysis*, Academic Press, London, 1986.
- [3] S. Braun, E. Lenz and C. Wu, "Signature Analysis Applied to Drilling", *Trans. ASME J. Mech. Design*, 104 (2) 1982, pp. 268-276.
- [4] T. A. Harris, *Roller Bearing Analysis*, Wiley, New York, 1966.
- [5] W. D. Mark, "Analysis of Vibratory Excitation of Gear Systems: Basic Theory", *J. Acoust. Soc. Am.*, (Part I) 63 (5) 1978, pp. 1409-1430; (Part II) 66 (6) 1979, pp. 1758-1787.
- [6] P. D. McFadden and J. D. Smith, "Model for the Vibration Produced by a Single Point Defect in a Rolling Element

Bearing", *J. Sound and Vibra*, **96** (1) 1984, pp. 69-82.

[7] L. D. Meyer, F. F. Ahlgram and B. Weichbrodt, "An Analytical Model for Ball Bearing Vibrations to Predict Vibration Response to Distributed Defects", *Trans. ASME J. Mech. Design*, **102** (2) 1980, pp. 205-210.

[8] D. W. Osuagwu and D. W. Thomas, "Inter-modulation and Quasi-periodic Instability in the Diagnosis of Rolling Element Incipient Defects", *Trans. ASME J. Mech. Design*, **104** (2) 1982, pp. 296-302.

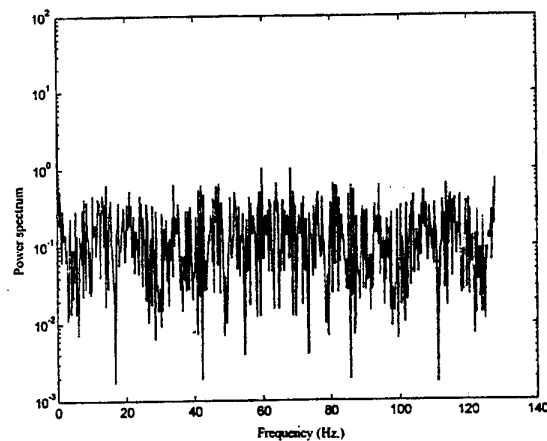


Figure 3. Worn drill.

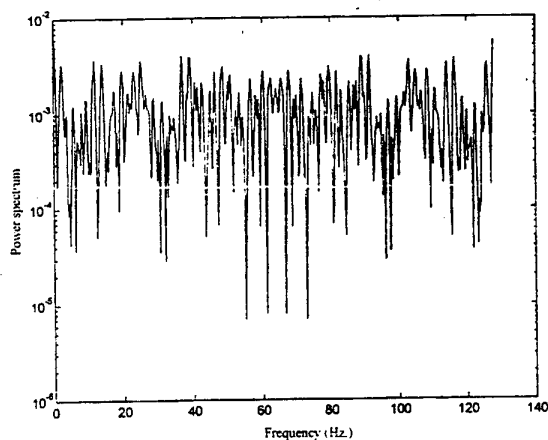


Figure 1. Sharp drill.

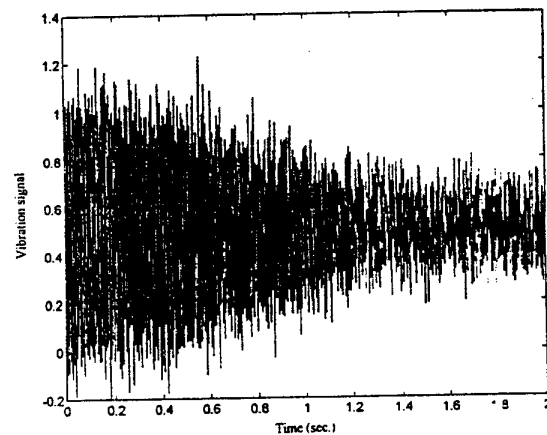


Figure 4. Good bearing signal.

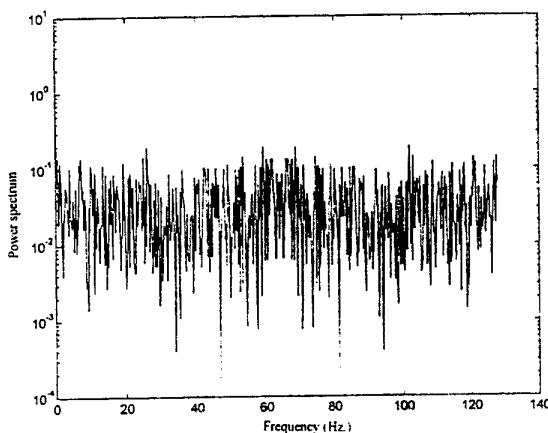


Figure 2. Partially worn drill.

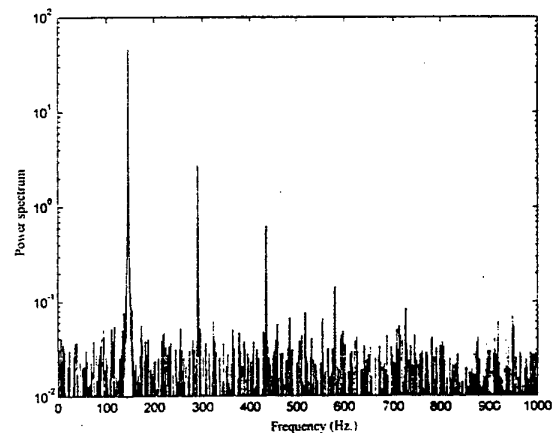


Figure 5. Power spectrum of the signal in Figure 4.

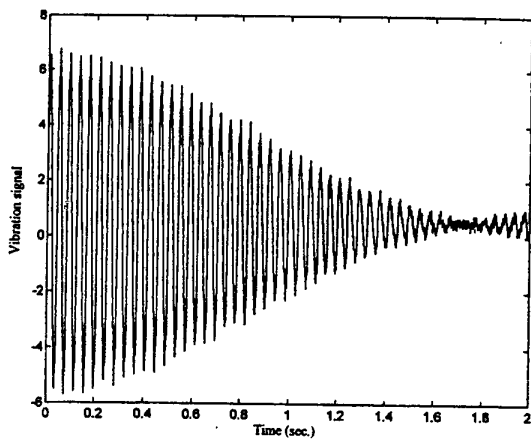


Figure 6. Unequal element force signal.

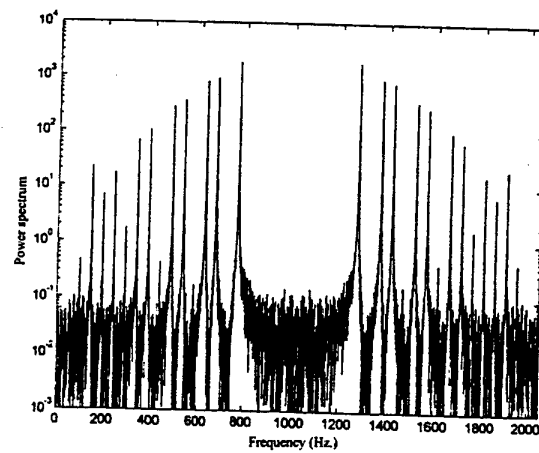


Figure 9. Power spectrum of the signal in Figure 8.

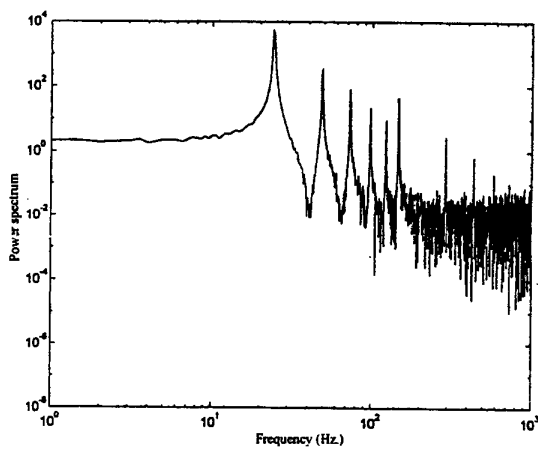


Figure 7. Power spectrum of the signal in Figure 6.

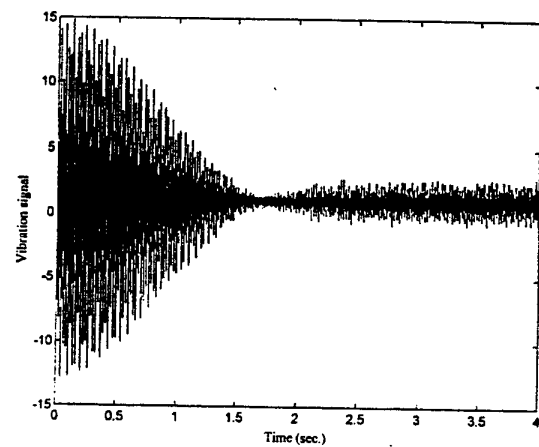


Figure 10. Elliptic race signals.

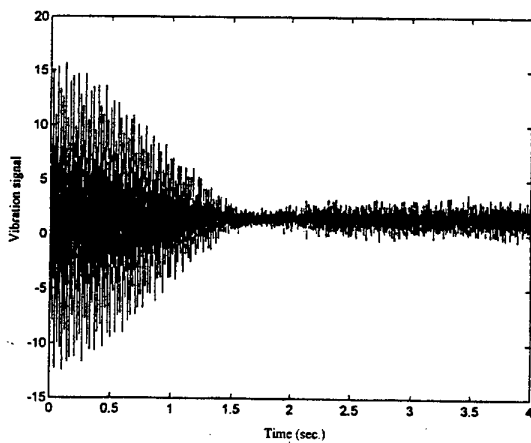


Figure 8. Misaligned race signals.

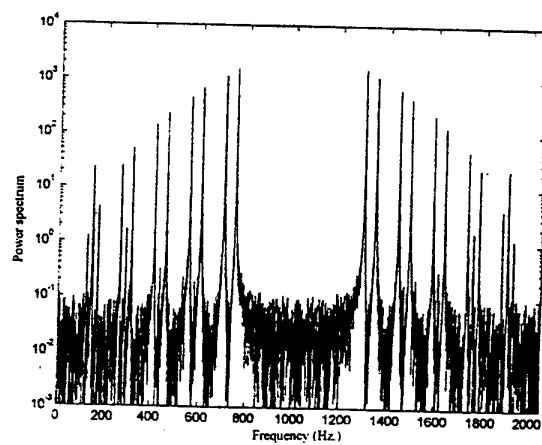


Figure 11. Power spectrum of the signal in Figure 10.

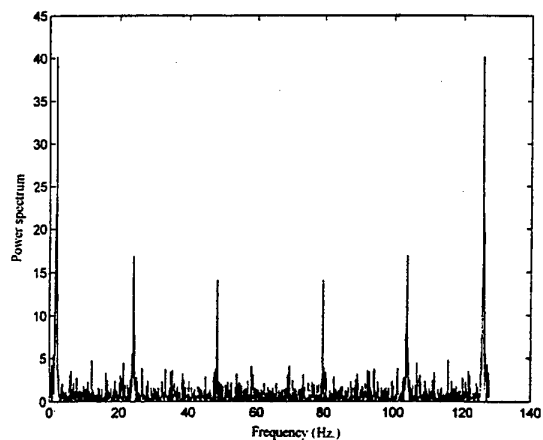


Figure 12. Spectrum of the signal due to tooth meshing.

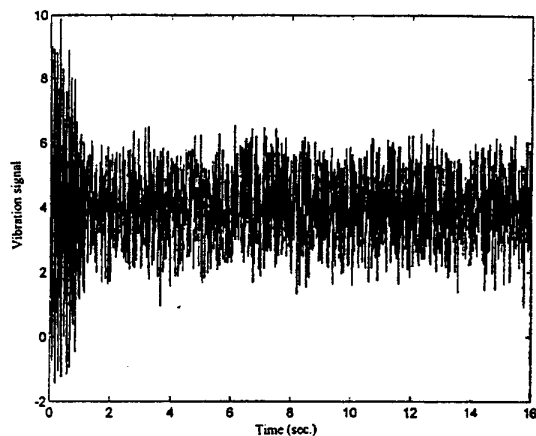


Figure 15. Signal originating from a local defect in a gear.

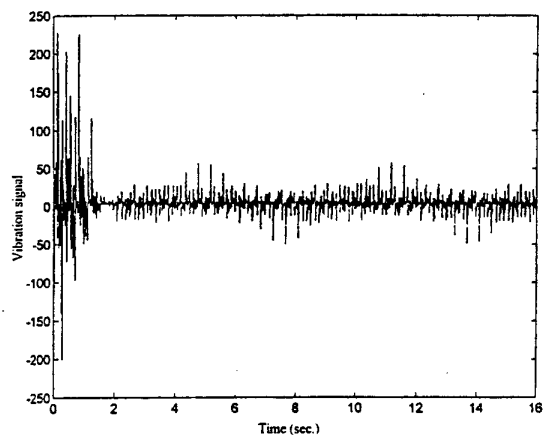


Figure 13. Signal in case of the eccentricity in a gear.

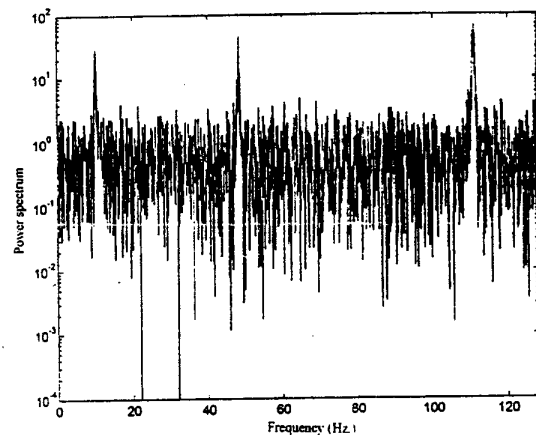


Figure 16. Spectrum of the signal in Figure 15.

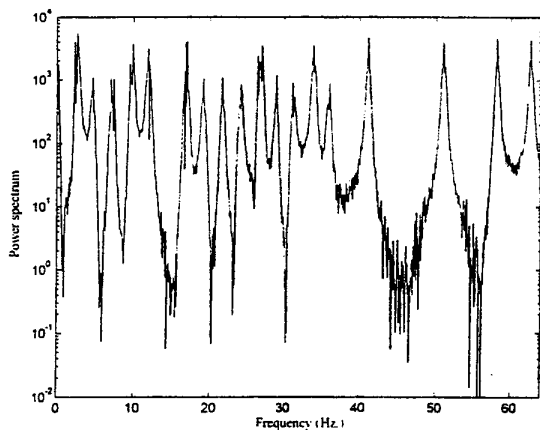


Figure 14. Spectrum of the signal in Figure 13.

The Intelligent Environment For Real -Time Systems Design

Golovina Elena

*Moscow Power Engineering Institute (MPEI),
14, Krasnokazarmennaja St., Moscow 111250, Russia
E-mail: gol@apmsun.mpei.ac.ru*

Abstract

An approach to the construction of a intelligent environment for a real-time systems development based on a object-oriented technology have been considered. Multi-layer logic is selected as the knowledge representation formalism. The intelligent tool for real-time systems development on the stages of analysis and design have been constructed.

1. Introduction

At the present time the designing of the environments for real-time systems development is a necessity. This environment must be integrated system intended for automating the entire life cycle of the real-time systems from the analysis stage to that of maintenance. The intelligent approach to design of the real-time systems development environment based on a object-oriented technology is now the most perspective one.

We will consider one approach to the design of the an intelligent environment for the development of the real-time systems.

2. The Approach to Design of Real-Time Systems Development Environment

We will consider the life cycle of the real-time systems development based on the object-oriented technology[1,2]. The object classes, the object, the relations between them and the object classes behaviour are describe on the analysis stage of the object-oriented systems development life cycle. The structures of the objects and them activities are give on the design stage of the considering life cycle. The program code of the object-oriented system is create

on the programming stage of the considering life cycle, also the testing of the program code is make. The inculcatment and the renovatment of the object-oriented system is make on the maintenance stage.

At present time the designing of the environment for the development of the real-time systems based on the object-oriented technology is a necessity. The creation of an intelligent environment has a number of advantages compared with the traditional approach to the development of a workbench, among which we can distinguish the following:

- the opportunity to represent knowledge that constitutes a generalization of the developer experience accumulated in the process of the object-oriented systems design, and access to this knowledge in the process of the object-oriented systems development;
- the creation of new knowledge about from knowledge represented in the workbench, which can help to developer in designing the system;
- the opportunity to verify consistency of knowledge;
- the opportunity to obtain answers to questions relating to the states of the developing object-oriented system (for example, which the object classes and object have been designed, and which have not, what kinds of errors have occurred, etc.) and its workbench (what kinds of failures have occurred in the hardware and software products, what kind of emergencies, etc.), which facilitates the the object-oriented system design procedure;
- the opportunity to predict the results of design operations;
- the opportunity to select repeatedly used the object classes that satisfy specified requirements.

The central moment of the real-time systems development is problem domain modelling. At the present time is a necessity the modelling of the hierarchical problem domains, having complex

control processes. For a modelling of the modern problem domains the choice the knowledge representation models, which is available for the description of them, is necessary.

3. A Formal Model of a Problem Domain

As a formal model of a modern problem domain we are proposing a hybrid model that combines the "program engineering" paradigm [1,2,3,4] and the "knowledge engineering" one [5,6], i.e. an object-oriented approach [7,8] and procedures, and a model for representing knowledge about a problem domain, should be used in order to represent the formal description of the problem domain in the intelligent tool of modelling [9,10,11,12].

We are proposing the hybrid model, based on logical model and product model, as a knowledge representation in a modern tool of the processes modelling. A logical model based on multi-layer logic (briefly MLL) [13,14] should be used as a formalism of the modelling of a static aspect of a problem domain. A production model should be used as a formalism of the simulation of a dynamic aspect of a problem domain.

MLL is an integration of the logical approach and an approach based on semantic networks. It may be considered as an object-oriented first-order predicate calculus that describes knowledge structuring and aggregation.

To represent the IS-A and Part-of hierarchies in MLL we use the hierarchical abstraction [13], which is given in the form of a graph whose vertices correspond to classes of objects or their representatives, and whose edges correspond to the "class-subclass" relations or to "part-whole" relations. A hierarchical abstraction consists of several levels. The concept of a level in a hierarchical abstraction corresponding to the "class-subclass" relation is based on the inheritance of properties. In the hierarchical abstraction corresponding to the "part-whole" relation, the concept of a level is based on the principle of decomposition. The class of objects and the classes of which a domain consists are arranged on different levels. The attributes of classes of objects or their representatives (objects) and the relations between classes of objects, excluding the structure relations, may be described in the hierarchical abstraction either as individual predicates or as well-formed formulas (WFF).

To represent the Part-of hierarchies of representatives in MLL we use the hierarchical structure [13]. As in the hierarchical abstraction, the concept of a level is based on the inheritance of properties. Classes of objects in relation that inherit properties are arranged on different levels. Thus, classes of objects and their representatives, linked

together by the relation "Element-of", are arranged on different levels, while classes of objects that are linked together by the relation "Component-of" are all on the same level, since they do not exhibit any inheritance of properties.

The hierarchical abstraction allows to describe a control object on the various control levels. The own methods of the object-oriented modelling of real-time systems and the own visual tools are used on the every control level. Us, the hierarchical abstraction is the integrated center between the various modelling methods and the various visual tools, allowed to made the transitions from one of the control level to other or from ones of the modelling methods to others. This approach allows to increase the visual power of the modelling tools and, therefore, to increase the control efficacy.

By a slash we will mean a kind of delimiter used in prefix of a formula. Thus, the simple slash (Qx/X) is used to denote that x is an element of the set X ($x \in X$), the simple "thick" slash ($Qx//X$) denotes that x is defined on a set whose elements are the components of the object X ($X \nabla x$), while the double slash ($Qx//X$) denotes that x is defined on a set whose elements are part of the object X ($X \triangleright x$) [13].

We was developed the extension of MLL syntax, which allows to increase efficacy of the deductive inference. The extended MLL syntax is represented.

Alphabet :

- (1) constants: a, b, c, \dots, X, Y, Z (constant sets)...
- (2) variables: x, y, z, \dots
- (3) function symbols: f, g, h, \dots
- (4) predicate symbols: P, Q, R, \dots
- (5) quantifier: \forall, \exists
- (6) logic connectives: $\neg, \&, \vee, \rightarrow, \leftrightarrow$
- (7) auxilliary symbols: $\#, *, /, //, \{, \}, (,)$

Terms:

- (1). Any constant and variable are terms.
- (2). If f is a n -ary function symbol and t_1, t_2, \dots, t_n are terms, then $f(t_1, t_2, \dots, t_n)$ is a term.
- (3). All terms are obtained by applying the rules (1) and (2).

Rules of designing WFF for extended MLL syntax is represented.

F1. If P is a n -ary predicate symbol and t_1, t_2, \dots, t_n are terms, then $P(t_1, t_2, \dots, t_n)$ is WFF.

F2. If F and G are WFF. $\neg F, F \& G, F \vee G, F \rightarrow G$ are WFF.

F3. If F is a WFF and x is an object variable, then

- (1). $(\forall x / y)F$ and $(\exists x / y)F$ are WFF, where y is a constant or variable.

(2). $(\forall x / y)F$ and $(\exists x / y)F$ are WFF, where y is a constant or variable.

(3). $(\forall x // y)F$ and $(\exists x // y)F$ are WFF, where y is a constant or variable.

(4). $(\forall(x/Z) // y)F$ and $(\exists(x/Z) // y)F$ are WFF, where y is a constant or variable, Z is a constant set.

F4. There are no other rules of designing WFF.

An inference algorithm for extended MLL syntax has been developed.

At the present time KM (Knowledge Model) tool as real-time systems development tool on the stages of analysis and design based on deductive inference in MLL was designed.

4. A Hierarchical Abstraction and a Production Model

To represent the control process in hierarchical problem domain we use the hierarchical abstraction. The hierarchical abstraction allows the production rules to break on the blocks in corresponding to the elements of the abstraction and to use the mechanism of the production rules inheritance. This mechanism is considered. Let us the hierarchical abstraction, which describes a "Airport" problem domain, is given. This hierarchical abstraction consists of the 3-th layers of the partitioning, a namely:

- 1-th layer - "airport" class;
- 2-th layer - "radiolocation station" (RLS) class, "airplane" class;
- 3-th layer - RLS class representatives, "airplane" class representatives.

The production rules are broken on the blocks in corresponding to the layers in the hierarchical abstraction, a namely:

- the production rules, which describe the management process of the whole airport, is included in the block of the 1-th layer;
- the production rules, which describe the RLS class management process and the "airplane" class management process, is included in the block of the 2-th layer;
- the 3-th layers blocks number is defined by the number of the representatives of RLS class and "airplane" class.

The production rules, which is given specify management laws by the airplane and RLS, is included in the blocks of the 3-th layer. The other production rules, which is given common management laws by the RLSs and airplanes, can be received owing inheritance mechanism.

Thus, the hierarchical abstraction allows to describe the production rules hierarchy and to use the inheritance principle of the production rules, similar the mechanism of inheritance of properties in ISA-hierarchy.

5. KM as a Intelligent Tool of Real-time Systems Development on Analysis and Design Stages

KM as a intelligent tool of real-time systems development on analysis and design stages is developed. KM tool allows :

- to construct the ISA-hierarchy of object classes;
- to define the object classes attributes and the relations between object classes;
- to construct the Part-of -hierarchy of object classes;
- to define the classes representatives;
- to construct the representatives Part-of -hierarchy;
- to browse the class objects and the hierarchies;
- to describe the logic formulas;
- to receive answer to queries.

The main components of the system KM are:

- subsystem of the problem domain models controlling;
- subsystem of modelling;
- subsystem of browser;
- knowledge base;
- subsystem of the deductive inference.

The example of the logic formula, represented in the knowledge base, is considering.

Example.

A program component x , including in the control support system (CSS) $\#P$, provides landing an airplane y , assigned to the airport $\#A$, if there are:

- PC t , in which x operates;
- a radio-location station (RLS) s , connected with PC t ;
- information flow $\#I1$, containing message flow $t1$, accepted by RLS s and containing message class $r1$, describing an airplane y and processing by a program component x ;
- information flow $\#I2$, produced by a program component x and accepted by an airplane y , containing message flow $t2$, transferring RLS s , in which there is a message class $r2$, containing information about airplane landing y .

The structures of the problem domain is represented in Fig. 1.

Formalization in MLL with extended syntax:

```
( $\exists(x/\text{program\_component})//\#P$ )
( $\forall(y/\text{airplane})//\#O$ )
( $\exists(s/\text{RLS})//\#A$ )( $\exists(t/\text{PC})//\#A$ )
( $\exists(t1/\text{message\_flow})//\#I1$ )
( $\exists(r1/\text{message\_class})/t1$ )
( $\exists(t2/\text{message\_flow})//\#I2$ )
```

$(\exists(r2/message_class)/t2)$

Operate(x,t) & Connect(s,t) & Accept_RLS(s,t1)
& Describe(r1,y) & Process(x,r1) &
Transfer_RLS(s,t2) & Produce(x,r2) &
Accept_airplane(y,r2) \rightarrow Landing(x,y)

The subsystem of deductive inference, based on inference in MLL, is served for:

- logical verification of information represented in the knowledge base;
- obtaining attribute values and extensions of relations what allows to "compress" the extensional component of the knowledge base;
- receiving the new knowledge from knowledge, represented in the knowledge base;
- obtaining answers to queries.

The conceptual language for modeling of hierarchical problem domain was developed. The translator of queries with conceptual language to MLL has been designed.

The system KM supports "a free connection" [15] of KB and DB under Paradox DBMS. Such implementation of the system KM provides using all opportunities Paradox DBMS such as distributed processing, high performance, complex verification, supporting of integrity and safety of data, failure and recovery of DB, supporting of very large DB.

The system KM is running under Windows'95. The development language of the system KM is Borland C++.

6. Acknowledgments

We would like to thank our Teacher prof. Vadim Nikolaevitch Vagin for big help in this work.

7. Conclusions

We have considered a approach to constructing an intelligent tool of real-time systems development on the analysis and design stages. The hybrid model, based on logic model and production model, for description of management processes in a hierarchical problem domain is proposed. The intelligent tool based on the hybrid model is developed.

This work was supported by the Russian Fund of Fundamental Researches (project code 99-01-00049).

8. References

- [1] Cooling J.E. *Software Design for Real-time Systems*. - Chapman and hall (University and Professional Division), 1991.
- [2] Peter A.Ng., Raymond T. Yeh eds. *Modern Software Engineering. Foundation and Current Perspectives*. - VAN NOSTRAND REINHOLD, New York, 1990.
- [3] Harel D. et al. "Statemate: a Working Environment for the Development of Complex Reactive Systems." *IEEE Transactions on Software Engineering*, Vol. 16, No. 4, 1990, pp.403-413.
- [4] Robert V. R., Walker J., Golin E.J. "Early Experience with the Visual Programmer's Workbench." *IEEE Transactions on Software Engineering*, 1990, vol.16, No.10, pp. 32-56.
- [5] Eisenstadt M., Domingue J., Rajan T., Motta E. "Visual Knowledge Engineering." *IEEE Transactions on Software Engineering*, 1990, Vol.16, No. 10 (Oct.).
- [6] Symods A.J. "Creating a Software-Engineering Knowledge Base." In *Software Development Computer-Aided Software engineering (CASE)*, Chirofsky E.J ed.- IEEE Computer Society press technology series, 1992.
- [7] Gibson E. "Objects - Born and Bred".- *BYTE*, 1990, October.
- [8] Shlaer S. and Mellor S.J. " *Object Lifecycles: Modeling the World in States*", Prentice-Hall, Englewood Cliffs, N.J., 1992.
- [9] Eisenstadt M., Brayshaw M. "A Knowledge Engineering Toolkit." *BYTE*, 1990, vol. 15, No.10, 12.
- [10] Yokoyama T. "An object-oriented and constraint-based knowledge representation system for design object modeling." *ICOT Research Center*, Tokyo, Japan, 1989.
- [11] Vagin V.N., Golovina E.Yu, Salapina N.O. "Intelligent CASE for Decision Making Systems". In *Proceedings of JCKBSE'96. Second Joint Conference on Knowledge-Based Software Engineering*. (Sozopol, Bulgaria, September 21-22), 1996, pp.122-127.
- [12] Vagin V.N., Viktorova N.P., Golovina E.Yu. "Multi-layer Logic as a Knowledge Representation Model in the CASE System." *Journal of Computer and Systems Sciences International*. -1995, Vol.33, No.3, pp.72-83.
- [13] Ohsuga S., Yamauchi H. "Multi-layer logic - a predicate logic including data structure as knowledge representation language." *New generation computing*, 1985, Vol.3,-NO.4, pp.451-485.
- [14] Ohsuga S. "Toward intelligent CAD systems." *Computer Aided Design*, 1989, Vol.21,-NO.5, pp. 315-337.
- [15] Yamauchi H., Ohsuga S. "Loose coupling of KAUS with existing RDBMSs." *Data & Knowledge Engineering*, 5, 1991, pp.227-251.

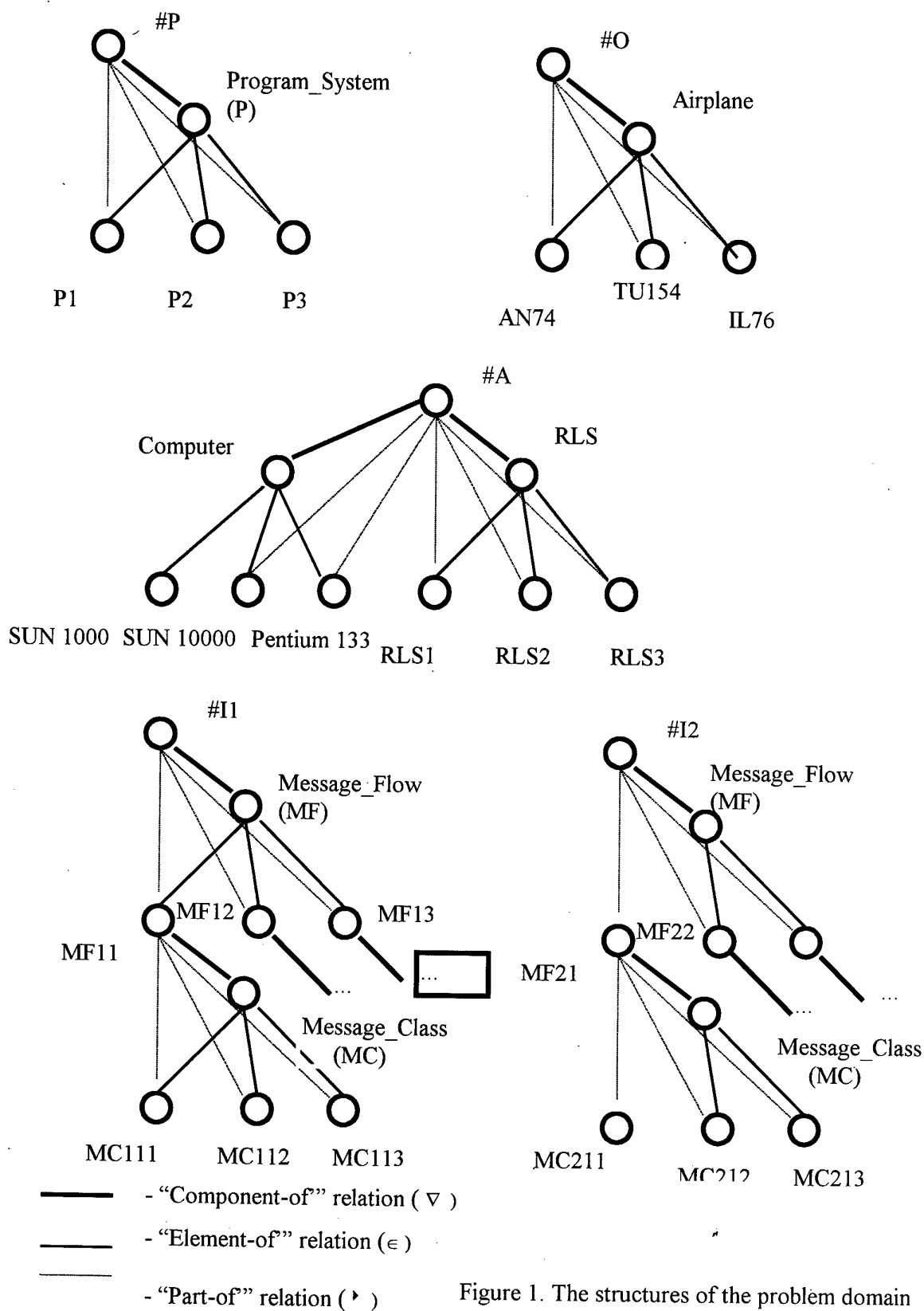


Figure 1. The structures of the problem domain

Decentralized Controllers for SCARA Robot Trajectory Tracking: an Experimental Comparison *

Antonio Visioli[¶] Bruno Zappa[§] Giovanni Legnani[§]

[¶]Dipartimento di Elettronica per l'Automazione
University of Brescia - Italy
e-mail: visioli@bsing.ing.unibs.it

[§]Dipartimento di Ingegneria Meccanica
University of Brescia - Italy
e-mail: {legnani,zappa}@bsing.ing.unibs.it

Abstract

We present an experimental comparison between different decentralized controllers for the trajectory tracking of a two degrees-of-freedom SCARA robot, which is one of the most adopted in industrial settings, especially for assembly tasks. Specifically, a nonlinear three term control law and the Discontinuous Integral Control, which is a kind of Variable Structure Control, are examined and compared with the typical PID control. The parameters tuning aspect, as well as the choice of the control frequency in the digital implementation and the chattering effect have been analyzed. Results show how the Discontinuous Integral Control is a good candidate in replacing PID control in industrial environments.

1 Introduction

It is well-known that dexterous and skilled motions in industrial manipulators need reliable and robust control in order to assure an accurate path tracking. Although in general a robot manipulator is an highly nonlinear and coupled system, nonlinear model-based controllers are not generally adopted in industrial environments, because the estimation of a sufficiently accurate model, that guarantees high performances, is a very hard task and adaptive control laws [1] seem difficult to be applied because their performances are limited by the presence of noise and of unstructured uncertainties.

Hence, in spite of the great effort provided by researchers and of the number of innovative solutions, concerning centralized controllers, that have been proposed in the last decade, independent joint controllers appear at the moment to be the most preferred choice in industrial settings, because of their simplicity and

also for their fault tolerance features, since in the case of a component failure only one joint is affected and the robot can be retrieved in a safe position by means of the others. In this context, several decentralized control schemes have been presented in the literature (see e.g. [2, 3, 4, 5, 6]). However, the most adopted is still the linear Proportional-Integral-Derivative (PID) controller. This seems to be due to the fact that PID controllers provide satisfactory performances for point-to-point motions and industrial operators have great experience on their use and on the tuning of the parameters. Moreover, many theoretical and simulation works have been published on decentralized control schemes different from PID, but not many experimental results have been discussed in the literature [7, 8] and there is a lack of a detailed framework regarding the use of the new control laws. The aim of this paper is to analyze and compare, from an experimental point of view, different decentralize controllers in order to provide information on their use and the results they can achieve in trajectory tracking of a two degrees-of-freedom SCARA robot, which is widely adopted in industry for assembly tasks. The selected control laws appear to be simple, easy to implement and suitable for industrial applications; they do not require the knowledge of the robot dynamics and the stability proof is obtained under mild conditions. These controllers are: a) a nonlinear three-term controller proposed by Tarokh [9]; b) the Discontinuous Integral Control, which is a kind of sliding mode variable structure control, both in the continuous and discretized version [10, 11, 12]. Their performances have been compared with the typical PID control, which has been implemented in different configurations. Specifically, both the scheme with a single digital position loop and the scheme with an inner velocity control loop (both in the analog and digital version) and an outer digital position loop

*Partial support for this research has been provided by MURST.

have been implemented. All the controllers, with the exception of the PID with analog velocity loop, require motor drives configured in torque-mode.

2 Decentralized control

The dynamic model for a n -joint manipulator can be written as follows:

$$M(q)\ddot{q} + C(q, \dot{q}) + g(q) + f(\dot{q}) + u_d(t) = u(t)$$

where q is the $n \times 1$ joint angle vector, $u(t)$ is the $n \times 1$ input torque vector (control variable), $M(q)$ is the $n \times n$ inertia matrix, $C(q, \dot{q})$ is the $n \times 1$ vector representing the centrifugal and Coriolis terms, $f(\dot{q})$ is the $n \times 1$ vector of the frictional terms, $g(q)$ is the $n \times 1$ vector of the gravity terms, and $u_d(t)$ is a $n \times 1$ vector representing unknown disturbances and unmodelled dynamics. Using a decentralized or independent joint control scheme means that the torque to be generated by the motor is evaluated depending only on its position error $e(t) = q_d(t) - q(t)$ and its time derivatives, that is:

$$u_i = u_i(e_i(t), \dot{e}_i(t)), \quad i = 1, \dots, n.$$

The coupling among the links, as well as variations of the inertia and other parameters, are seen as disturbances to be attenuated.

2.1 PID control

The well-known general expression of a PID controller is the following:

$$u(t) = K_p \left(e(t) + \frac{1}{T_i} \int_0^t e(\tau) d\tau + T_d \frac{de(t)}{dt} \right), \quad (1)$$

where K_p is the proportional gain and T_i and T_d are, respectively, the integral and derivative time constants. Many tuning rules have been devised along the last fifty years [13] and the characteristics of the overall controller are generally well understood by control practitioners. In typical industrial settings, PID control for DC and brushless motors actuating a robot manipulator consists of two nested control loops, that is an inner loop for velocity control and an outer loop for position regulation. The velocity control loop is generally implemented, either analogically or digitally, directly in the drive of the motor, and it is tuned before the position control loop, which is always implemented by a digital microprocessor. The output of the velocity control loop is the motor torque reference signal. The motor torque is also controlled by a closed-loop system whose tuning is however not available to the

user. In this paper we implemented the velocity control loop both in an analog and a digital configuration (in the latter case the control frequency is ten times the control frequency of the position control loop). Furthermore, a control scheme with a single position loop control has also been examined.

2.2 Tarokh's nonlinear three term control

The nonlinear control law proposed by Tarokh in 1996 [9], is described by the following three-term expression of the torque to be applied to the motor of the i -th joint:

$$u_i(t) = k_i \eta_i(t) + p_i \eta_i(t) \int_0^t \eta_i^2(\tau) d\tau + q_i \operatorname{sgn}(\eta_i(t)) \int_0^t |\eta_i(\tau)| d\tau \quad i = 1, \dots, n \quad (2)$$

where u_i is the torque applied to the motor of the i -th joint, k_i , p_i and q_i are constant scalar gains, and $\eta_i(t)$ is defined as

$$\eta_i(t) = \lambda_i e_i(t) + \dot{e}_i(t) \quad i = 1, \dots, n$$

where λ_i is a positive scalar constant. The asymptotic stability of tracking error is demonstrated by using the Lyapunov stability theorem. Theoretical and simulation results show that this control system is robust to torque disturbances and unmodelled dynamics and hence it appears particularly suitable to be applied in practical cases. It has to be noticed that the last control torque component in (2) contains a signum function that can result in an undesirable chattering effect. This can be avoided, preserving the asymptotic stability [14], by replacing the signum function with a saturation function of the form:

$$\operatorname{sat}(\eta_i) = \begin{cases} \eta_i/\varepsilon, & |\eta_i| < \varepsilon \\ \operatorname{sgn}(\eta_i), & \text{otherwise} \end{cases}$$

where ε is the boundary layer thickness.

2.3 Discontinuous integral control

Variable-structure sliding mode control of nonlinear multivariable systems has been widely investigated in the last decades because of its inherent robustness to external disturbances [15]. In this context, the recently developed discontinuous integral control (DIC) [10, 11, 12] appears to be particularly suitable to be applied to mechanical systems. An integrator with a nonlinear switching input is added in the control law to track the unknown disturbances. In this way, the chattering introduced by the characteristic switching term of the variable structure controller is reduced since it has only to compensate the difference between the real

disturbance and its estimation. The following typical sliding surface is chosen:

$$\sigma(t) = ce(t) + \dot{e}(t)$$

where $c > 0$. Then, for the continuous-time case, the expression of the torque command can be written as ($i = 1, \dots, n$):

$$\begin{aligned} u_i(t) &= l_i \sigma(t) + k_i \text{sgn}(\sigma_i(t)) + \tilde{\psi}_i(t) \\ \dot{\tilde{\psi}}_i(t) &= h_i \int_0^t \text{sgn}(\sigma_i(\tau)) d\tau \end{aligned} \quad (3)$$

where l_i , k_i and h_i are constant parameters and $\tilde{\psi}_i(t)$ is an estimation of an external disturbance $\psi_i(t)$ which is assumed to be continuous and satisfying the following conditions:

$$|\psi_i(t)| < \Delta_0; \quad |\dot{\psi}_i(t)| < \Delta_1.$$

If l_i , k_i and h_i are chosen in such a way that

$$l_i > 0; \quad k_i > 0; \quad h_i > \Delta_1; \quad h_i l_i k_i > \Delta_1^2(1 - \ln 2);$$

then the controlled system is demonstrated to be globally stable and after a finite time a sliding mode arises on the surface σ_i , so that the error asymptotically converges to zero. In a digital implementation, the discretisation of expression (3) can be slightly modified in order to prevent oscillations when the estimation of the disturbance is constant [12]. It follows that the torque command for the discretised discontinuous integral control (DDIC) can be written as:

$$\begin{aligned} u_i(n) &= k_i \text{sgn}(\sigma_i(n)) + \tilde{\psi}_i(n) \\ \tilde{\psi}_i(n) &= \tilde{\psi}_i(n-1) + k_{e_i} \left[\frac{\Delta \sigma_i(n)}{T_s} + k_i \text{sgn}(\sigma_i(n-1)) \right] \end{aligned} \quad (4)$$

where $\Delta \sigma_i(n) = \sigma_i(n) - \sigma_i(n-1)$, T_s is the sampling time, k_e is a new design parameter and

$$\left[\frac{\Delta \sigma_i(n)}{T_s} + k_i \text{sgn}(\sigma_i(n-1)) \right] = \gamma_i(n)$$

can be viewed as a disturbance estimation error. Denote by Δ_ψ the discrete derivative of the disturbance. Choosing the amplitude of the switching term k_i such that $k_i > \Delta_\psi T_s$ a discrete sliding mode occurs in the system.

3 Experimental setup

The previously described decentralized controllers have been adopted for the trajectory tracking of a SCARA (Selective Compliance Assembly Robot Arm) robot, shown in Figure 1, which is widely used in industrial environments for assembly and pick and place tasks. The manipulator, denominated ICOMATIC

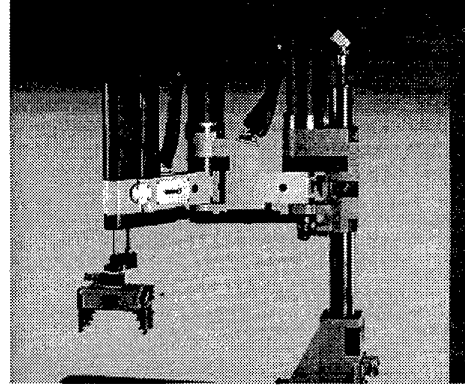


Figure 1: The SCARA ICOMATIC 03 situated in the Applied Mechanics and Robotics Laboratory of the University of Brescia.

SCARA 03, was built by ICOMATIC of Gussago (Brescia, Italy) and it is installed in the Applied Mechanics and Robotics Laboratory of the University of Brescia. It has three degrees-of-freedom, but only the first two has been utilized in the experiments since the third, which is devoted to move the end-effector up and down, is completely decoupled from the others from a dynamic point of view.

The two rotoidal joints are actuated by two direct current motors with Harmonic Drive reduction gears, which assure a good dynamic decoupling between the two links (whose length is 0.33m). For a detailed analysis of the robot kinematics and dynamics, see [16]. Position measurements are obtained by incremental encoders (one encoder step is equal to $\pi \cdot 10^{-5}$ rad), and velocity measurements by tachometers or simply deriving the encoder signal. The system is controlled by means of a build on purpose controller which consists of a PC Pentium 133 with I/O boards. The control software runs under QNX operating system, which assures real-time functionalities and a control loop frequency of 1kHz (in the digital PID velocity control loop the control frequency is 10kHz).

For the evaluation of the tracking error performances, two kinds of trajectory, which cover a large portion of the robot workspace, has been utilized: a circular trajectory, centered in (0,0.5) and with diameter equal to 0.2m, to be accomplished in 3s, and a linear trajectory, from (-0.3,0.5426) to (0.6,0.1574), to be accomplished in 6s. The trajectories are represented, in the Cartesian space, in Figures 2 and 3. It is worth stressing that they require significantly different torque levels to the motors.

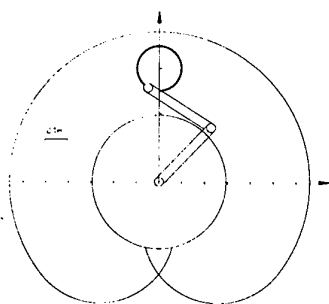


Figure 2: Cartesian space representation of the circular trajectory, to be accomplished in 3s.

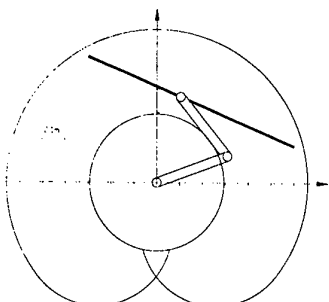


Figure 3: Cartesian space representation of the linear trajectory, to be accomplished in 6s.

4 Results

4.1 Tuning of the parameters

Between the decentralized control laws presented in Section 2, a well-settled tuning procedure exists only for the PID control law. On the contrary, for the Tarokh's controller and for the Discontinuous Integral Control (both in its continuous and discretized version), the physical meaning of the different terms of the controller expression are not very clear and practical tuning procedures are not provided in the literature.

For this reason, a set of experiments has been performed for these three controllers, in order to determine a method for the tuning of their parameters.

For obvious safety reason, it is necessary to guarantee that actuators limits are not exceeded and that no significant overshoot occurs in a step response. However, under this latter point of view, it has been found that only the PID-based controllers are critical. In fact, no overshoot is present in a step response adopting the other analyzed controllers, disregarding the values of their parameters.

For the PID, the inner velocity loop, when it is present in the control scheme, has been tuned before the outer position loop. The values of the proportional, integral and derivative constants have been found by starting

from the well-known Ziegler-Nichols rule and then refining them by hand. Specifically, the derivative action in the velocity loop (when it is implemented in software) and the integral action in the position loop have been set to zero and the proportional and the derivative actions in the position loop have been significantly increased. It has to be remembered that the velocity loop is based on the velocity measure made by the tachometer, which provides a noisy signal, and the noise can be undesirably amplified by the derivative action so that it is opportune to switch it off. Regarding the single loop PID control, all the three actions have to be employed to assure the best tracking performance.

For the Tarokh's controller, the PD part $k\eta$ has been tuned at the beginning analogously to the position loop in the PID control scheme. Then, the two other critical parameters p and s have been considered. The most significant for the adopted systems is p that have been tuned increasing it until the performances worsen. The same method has been applied to s . Finally, parameter ε has to be chosen taking into account the trade-off between the accurate tracking and the chattering effect, although it is not very crucial. A chattering level close to the one achieved by the PID control has been allowed.

In the Discontinuous Integral Control, again the PD term can be tuned as usual. Then, it is necessary to increase h as much as possible, until the performances stop improving. A high value of h permits the reduction of the amplitude k of the switching term and therefore to limit chattering. Hence, in the tuning of k the trade-off between the chattering and the accurate tracking has to be considered, but the presence of the integral term cause an excessive increasing of k to be useless with an evident benefit on the mechanical system.

In the discretized version of the DIC, the parameter is k_e , unlike h in the continuous version, has to be kept sufficiently small in order to avoid chattering again. From a practical point of view k_e can be increased, starting from very small value, until the tracking error does not decrease.

4.2 Trajectory tracking errors

After the controllers have been tuned, they have been used for the tracking of the trajectories presented in Section 3. The performances have been evaluated with respect to different indexes. For each motion, the maximum and mean absolute errors (in encoder steps) have been calculated for each motor separately. Then, according to the ISO 9283 standard [17], the tracking error of the end-effector (in mm) has been calculated

Controller	Joint 1		Joint 2	
	max	mean	max	mean
PIDS	6	0.954	9	1.400
PIDD	4	0.774	12	1.233
PIDA	78	16.18	131	22.53
TAROKH	13	3.706	20	6.234
DIC	4	1.106	20	3.275
DDIC	7	1.828	18	4.340

Table 1: Joint tracking errors (in encoder steps) for the circular motion of 3s.

Controller	Joint 1		Joint 2	
	max	mean	max	mean
PIDS	6	1.057	9	1.471
PIDD	11	0.961	5	0.894
PIDA	48	15.75	44	14.02
TAROKH	12	4.680	16	5.714
DIC	7	1.507	7	1.822
DDIC	9	2.284	11	3.222

Table 2: Joint tracking errors (in encoder steps) for the linear motion of 6s.

as the minimum difference (with sign) between the real end-effector position and the reference trajectory. Furthermore, an additional parameter has also been utilized; it is an error index defined as:

$$\text{e.i.} = \bar{e} + 3\sigma_e$$

where \bar{e} is the average value of the absolute error and σ_e is the standard deviation of the absolute value of e . The definition of e.i. is inspired by the concept of accuracy and repeatability (ISO 9283 standard [17]). It has to be stressed that the end-effector tracking errors are determined by applying the direct kinematic to the joint positions, so that no direct measurements of the gripper position has been performed. Hence, we refer to the tracking errors due to the control action only, disregarding elasticities in the joints and calibration errors. Results are exposed in Tables 1, 2 and 3, where PIDS denotes the single PID position loop control, and PIDD and PIDA denote the double loop control with digital and analog velocity control respectively.

4.3 Discussion

From the above results it appears how the tracking errors obtained with the traditional PID control with an analog velocity control loop are significantly improved by using a full digital controller. This can be due to the difficult in tuning the analog loop in the drive. In this context, tracking performances achieved by using a PID control and DIC are very similar, whilst

Cont.	Circular			Linear		
	max	mean	e.i.	max	mean	e.i.
PIDS	0.105	0.017	0.065	0.081	0.017	0.059
PIDD	0.054	0.010	0.038	0.049	0.009	0.030
PIDA	0.703	0.293	0.977	0.374	0.184	0.554
TAR.	0.145	0.037	0.117	0.102	0.027	0.087
DIC	0.105	0.021	0.089	0.053	0.012	0.039
DDIC	0.081	0.021	0.066	0.073	0.020	0.065

Table 3: End-effector tracking errors (in mm) for the two trajectories.

Tarokh's controller seems not as good as the others. However, it has to be said that from other experiments on a different system with a more significant coupling between the links ([18]), it comes out that the Discontinuous Integral Control (both in the continuous and discretized version) is the most robust to external disturbances.

In order to better evaluate the performances of the controllers, it is worth analyzing the torque signal in the different cases. In fact, it is well known that robot life-span generally decreases when the system has to cope with vibrations, and torque vibrations can excite mechanical vibrations resulting in performance degradation and motor overheating. To give a measure of the chattering amplitude, the torque signals have been digitally filtered off-line using a high pass filter (with cut-off frequency of 150Hz and attenuation of 40dB at 130Hz) and then the mean of the absolute values has been evaluated, obtaining a "chattering index" c.i. reported in Table 4. It can be seen how the PID with the analog velocity loop has a low chattering and also how the DIC is better than the DDIC and in general provides no significant oscillations, compared with the other controllers.

A further study has been done in order to verify the dependence of the tracking errors with respect to the sampling time. It has been found that for all the controllers the tracking error increases when the sampling interval increases, but performances are still acceptable until 5ms. For larger sampling intervals, the tracking error can dramatically worsen, for all the examined controllers. As an example, the maximum and mean absolute errors of the end-effector for the Discontinuous Integral Control applied to the tracking of circular motion, as the sampling interval increases from 1 to 10ms, are plotted in Figure 4.

Finally, it has to be stressed that the presence of the tachometer is not strictly necessary to assure good tracking performances. In fact, for all the implemented controllers, experiments have been done substituting the velocity measure with a simple differentiation of the encoder measure. It has been checked that for all

Controller	c.i.
PIDS	0.146
PIDD	0.121
PIDA	0.041
TAROKH	0.514
DIC	0.088
DDIC	0.478

Table 4: Chattering index for the different experiments.

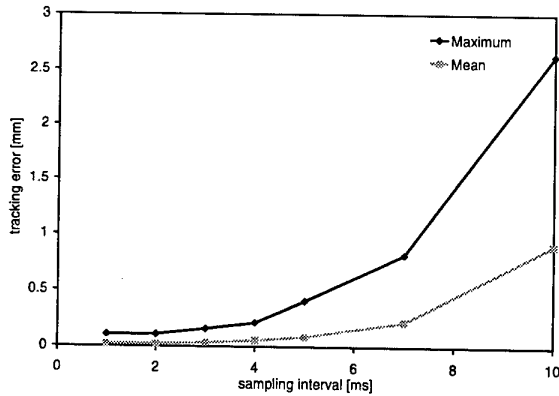


Figure 4: Maximum and mean absolute tracking errors of the end-effector with different control sampling intervals (DIC for the circular trajectory).

the controllers there is not an increasing of the tracking error, so that the cost of the overall control system can be reduced eliminating these sensors.

5 Conclusions

In this paper, different advanced decentralized controllers for the trajectory tracking of an industrial two degrees-of-freedom SCARA robot manipulators have been compared from an experimental point of view. Despite their simple structure, which allows a low-cost implementation, and the easiness in the tuning of the parameters, results show how they can achieve in general very good performances (less than 0.1mm of maximum tracking error for the end-effector). It also appears how for the considered SCARA robot, in which the dynamic coupling between the two links is significantly reduced by the use of Harmonic Drive reduction gears, it is not easy to improve the performances obtained using a PID controller. However, the Discontinuous Integral Control seems to be particularly suitable to be adopted in industrial environments, since, in addition to the very good tracking performances, it is very good in rejecting external disturbances and it keeps the chattering at a low level. Furthermore, the computational effort it requires is low with respect to the typical PID-based control, since only one control loop has to be implemented.

References

- [1] J.-J.E. Slotine, W. Li, "On the adaptive control of robot manipulators", *Int. J. of Robotics Research*, 6, 49-59, 1987.
- [2] D. Gavel, T. Hsia, "Decentralized adaptive control of robot manipulators", *Proc. IEEE Int. Conf. on Rob. and Aut.*, Raleigh, NC, 1230-1235, 1987.
- [3] H. Seraji, "Decentralized adaptive control of manipulators: theory; simulation and experimentation", *IEEE Trans. on Rob. and Aut.*, 5, 49-59, 1987.
- [4] L. Fu, "Robust adaptive decentralized control of robot manipulators", *IEEE Trans. on Aut. Cont.*, 37, 106-110, 1992.
- [5] R. Colbaugh, H. Seraji, K. Glass, "Decentralized adaptive control of manipulators", *J. of Robotic Systems*, 11, 425-440, 1994.
- [6] M. Tarokh, "Decentralized digital adaptive control of robot motion", *Proc. IEEE Int. Conf. on Rob. and Aut.*, Cincinnati (OH), 1410-1415, 1990.
- [7] L. Cai, X. Tang, "A model-free decentralized control for robot manipulators", *Proc. IEEE Int. Conf. on Rob. and Aut.*, 3106-3111, 1997.
- [8] Y. Tang, G. Guerrero, "Decentralized robust control of robot manipulators", *Proc. American Cont. Conf.*, 922-926, 1998.
- [9] M. Tarokh, "A decentralized nonlinear three-term controller for manipulator trajectory tracking", *Proc. IEEE Int. Conf. on Rob. and Aut.*, Minneapolis (MN), 3683-3688, 1996.
- [10] A. Nersisian, R. Zanasi, "A modified variable structure control algorithm for stabilization of uncertain dynamical systems", *Int. J. of Robust and Nonlinear Control*, 3, 199-209 (1993).
- [11] R. Zanasi, "Sliding mode using discontinuous control algorithms of integral type", *Int. J. of Control*, 57, 1079-1099 (1993).
- [12] C. Bonivento, M. Sandri, R. Zanasi, "Discrete variable- structure integral controllers", *Automatica*, 34, 355-361, 1998.
- [13] K. Aström, T. Hagglund, *PID controllers: theory, design and tuning*, (ISA Press, USA), 1995.
- [14] F. Esfandiari, H. K. Khalil, "Stability analysis of continuous implementation of variable structure control", *IEEE Trans. on Aut. Cont.*, 36, 616-620, 1991.
- [15] "Special Issue on Sliding Mode Control", *Int. Journal of Control*, V. I. Utkin, Guest Ed., May 1993.
- [16] A. Visioli, "Control strategies for industrial robot manipulators", PhD thesis, University of Brescia, 1999.
- [17] ISO 9283:1991, "Manipulating industrial robots: performance criteria and related testing methods".
- [18] G. Legnani, A. Visioli, "Experimental valuation of decentralized controllers for industrial robot manipulators", *Proc. IEEE Int. Conf. on Cont. Applications, Trieste (I)*, 567-571, 1998.

A Novel Approach to Computed Torque Based Robot Control

Meliksah Ertugrul

TÜBITAK Marmara Research Center,
Robotics and Automation Group,
41470, Gebze, TURKEY

melik@mam.gov.tr

Okyay Kaynak

UNESCO Chair on Mechatronics and
Mechatronics R & A Center, Bogazici
University, Istanbul, TURKEY

kaynak@boun.edu.tr

M. Ragip Basbug

Gebze Institute of Technology,
Computer Engineering Department,
Gebze, TURKEY

ragip@penta.gyte.edu.tr

Abstract

A variety of robot controllers appear in the literature. However, computed torque (or inverse dynamics) with a secondary controller (PID) is still the most used technique by the industry. In this paper, a novel sliding mode approach to computed torque based robot control is proposed. Firstly, the parallelism between the equivalent part of the sliding mode control and the inverse dynamics is investigated. In sliding mode, the equivalent control has an effect identical to the inverse dynamics. In this paper, the corrective term of the SMC is used as the secondary controller instead of PID controller and equivalent part is replaced with the computed torque. The novel controller can be designed for nonlinear systems without linearization around an operating point. Experimental studies carried out on a direct drive robot indicate that the controller results in a robust response and is suitable for industrial applications.

1. Introduction

The robot control problem for the gross (free) motion is a servo problem in which the center of mass of the robot end effector is made to track the reference values representing the desired trajectory. The inputs to the robot can be chosen as the generalized torques produced by the actuators, and the outputs to be controlled are the positions, velocities and accelerations [1]. To make the robot track the desired nominal trajectory, the generalized torque applied to the system should have the appropriate (nominal) values that result in the desired motion under ideal conditions. The controller generating these values

can be referred to as the *primary controller*. Thus, it compensates for the nonlinear effects, and attempts to cancel the nonlinear terms in the model. Since the mathematical model used is usually not exact, and since the system is subject to disturbances, undesirable deviations (errors) of the actual motion from the nominal trajectory can be corrected by means of an additional controller called a *secondary controller* [1].

Variable structure systems with a sliding mode were first proposed in early 1950's, but it was not until the seventies that sliding mode control (SMC) became more popular. It nowadays enjoys a wide variety of application areas. The main reason of this popularity is the attractive superior properties of SMC, such as good control performance even in the case of nonlinear systems, applicability to MIMO systems, design criteria for discrete time systems, etc. The best property of the SMC is its robustness. Loosely speaking, a system with a SMC is insensitive to parameter changes or external disturbances [2].

SMC design that is based on the selection of a Lyapunov function yields two parts: equivalent control and corrective control [3]. In this paper, the relation between the inverse dynamics and the equivalent control is presented. In sliding mode, equivalent control has an effect identical to the inverse dynamics (computed torque). The motivation of showing the equivalence is to use the corrective term of the SMC as secondary controller. In this paper, the primary controller is again the inverse dynamics while the secondary controller is the corrective term of SMC, instead of a PID controller.

The paper concludes with the presentation of some experimental results obtained for the control of a direct drive scara type robot.

2. Sliding Mode Control

In the application of Variable Structure System theory to control nonlinear processes it is argued that one only needs to drive the error to a "switching" or "sliding" surface, after which the system is in "sliding mode" and will not be affected by any modelling uncertainties and/or disturbances [2,3]. Intuitively, VSS with a sliding mode is based on the argument the control of 1st-order systems (i.e., systems described by 1st-order differential equations) is much easier, even when they are nonlinear or uncertain, than the control of general nth-order systems [4].

2.1 The System (Plant)

Consider a nonlinear, non-autonomous, multi-input multi-output system of the form,

$$\dot{x}_i^{(k_i)} = f_i(X) + \sum_{j=1}^m b_{ij} u_j \quad (1)$$

where $x_i^{(k_i)}$ indicates the k_i th derivative of x_i . The vector U of components u_j is the control input vector and the state X is composed of the x_i 's and their first (k_i-1) derivatives. Such systems are called square systems since they have as many control inputs as outputs x_i to be controlled [4]. The system can be written in a more compact form as letting

$$X = [x_1 \ \dot{x}_1 \ \dots \ x_1^{k_1-1} \ \dots \ x_m \ \dot{x}_m \ \dots \ x_m^{k_m-1}]^T \quad (2)$$

$$U = [u_1 \ \dots \ u_m]^T \quad (3)$$

and assume, X is $(nx1)$. The system equation becomes,

$$\dot{X}(t) = F(X) + BU(t) \quad (4)$$

where B is $(n \times m)$ input gain matrix.

2.2 Sliding Surface

For the systems given in (4), generally, sliding surface, S , $(mx1)$ is selected [3] as given below,

$$S(X, t) = G(X^d(t) - X(t)) = G E \quad (5)$$

X^d represents the desired (reference) state vector and G is (mxn) slope matrix of the sliding surface. The aim in SMC

is to force the system states to the sliding surface. Once the states are on the sliding surface, the system errors converge to zero with an error dynamics dictated by the matrix G .

2.3 Sliding Mode Controller Design

In this section, the design of a SMC based on the selection of a Lyapunov function is presented [3]. The control should be chosen such that the candidate Lyapunov function satisfies Lyapunov stability criteria. As a result of the design, the SMC controller is obtained as;

$$U(t) = U_{eq}(t) + U_c(t) \quad (6)$$

where $U_{eq}(t)$ is the equivalent control and written as,

$$U_{eq}(t) = -(GB)^{-1} \left(GF(X) - \frac{d(GX^d)}{dt} \right) \quad (7)$$

and $U_c(t)$ is the corrective control term and written as,

$$U_c(t) = (GB)^{-1} D h(S) = K h(S) \quad (8)$$

where $h(S)$ is the saturation function and defined as,

$$h(S_j) = \begin{cases} S_j & \text{if } -1 < S_j < 1 \\ \text{sign}(S_j) & \text{otherwise} \end{cases} \quad (9)$$

The details of the controller design can be found in [3].

3. Sliding Mode Approach to Computed Torque

The proposed controller is a combination of the computed torque control and the sliding mode control. The equivalent control part of SMC is replaced by the computed torque, based on the equivalence of these two terms under sliding mode condition. In this part, firstly, equivalence condition will be presented. Secondly, the structure of the proposed controller will be explained and at the end, the closed loop system behaviour will be presented.

3.1 Parallels between Inverse Dynamics and the Equivalent Control

As stated earlier, the sliding mode control converts the nth order system equations to the 1st order equations. The

new dynamics equation while in sliding mode can be written as,

$$\frac{dS}{dt} = 0 \quad (10)$$

By solving (10) for desired control signal, one will obtain the following,

$$\frac{dS(X^d, U^d, t)}{dt} = 0 \quad (11)$$

With using (5) and (4), the equation (11) can be computed as,

$$\frac{dS}{dt} = \frac{d(GX^d)}{dt} - G(F(X^d) + BU^d) = 0 \quad (12)$$

Solving (12) for desired control signal,

$$U^d = -(GB)^{-1} \left(GF(X^d) - \frac{d(GX^d)}{dt} \right) \quad (13)$$

is obtained. If the system is in the sliding mode, this means the system perfectly follows the desired trajectory, and $F(X^d)$ term can be replaced with $F(X)$ which is the actual value. As a result, the desired control signal becomes the equivalent control.

$$U^d \approx U_{eq} = -(GB)^{-1} \left(GF(X) - \frac{d(GX^d)}{dt} \right) \quad (14)$$

A direct approach to show the equivalence of the inverse dynamics and the equivalent control is as follows; the system equation given in (4) can be solved for desired control signal as given below,

$$\dot{X}^d(t) = F(X^d) + BU^d(t) \quad (15)$$

B is not a square matrix, so equation (15) is transformed by multiplying with a transformation matrix G,

$$G\dot{X}^d(t) = GF(X^d) + GBU^d(t) \quad (16)$$

If (16) is solved for the desired control, it will be obtained as given in (13).

As a conclusion, in sliding mode, the equivalent control is an equivalence to the inverse dynamics.

3.2. The Structure of the Proposed Controller

The structure of the proposed controller is similar to a typical robust controller which is composed of a nominal part, or inverse control law, and a corrective term aimed at

dealing with model uncertainty or parameter variations. In this paper, the corrective term is selected as the corrective term of the SMC based on the equivalence of the inverse control and the equivalent control under sliding condition.

As is clear from Fig.1, the controller is represented as given below,

$$U(t) = U^d(t) + U_c(t) \quad (17)$$

where, $U^d(t)$ is given in (13), and $U_c(t)$ is given in (8).

3.3. Closed Loop System Behaviour

If the controller (17) is applied to system given in (4), the closed loop system dynamics become,

$$\dot{X}(t) = F(X) + B(U^d + U_c) \quad (18)$$

Equation (18) is multiplied by G matrix, and $U^d(t)$ is replaced by (13) and $U_c(t)$ is replaced by (8),

$$G\dot{X}(t) = GF(X) + GB \left(-(GB)^{-1} \left(GF(X^d) - \frac{d(GX^d)}{dt} \right) + Kh(S) \right) \quad (19)$$

$$G\dot{X} - G\dot{X}^d = GF(X) - GF(X^d) + Dh(S) \quad (20)$$

If the system perfectly follows the desired trajectory, $GF(X^d)$ term will cancel $GF(X)$ term and using (5), the closed loop behaviour is obtained as below,

$$\dot{S} = -Dh(S) \quad (21)$$

This is the same case as SMC [3], and the solution for (21) implies that

$$\lim_{t \rightarrow \infty} S(t) = 0 \quad (22)$$

Although $S(t)$ goes to zero when time goes to infinity, it goes into boundary layer at a finite time.

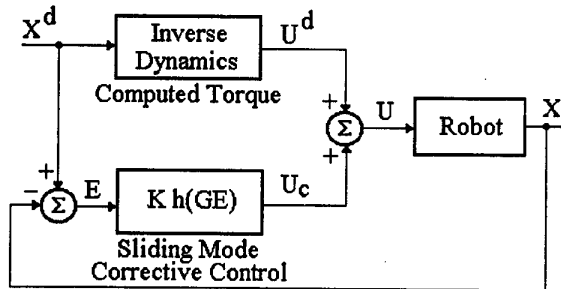


Figure 1. Overall control system

4. Robotics Application

In order to study the performance of the controllers proposed, extensive experimental studies are carried out on a two degrees of freedom, direct drive, scara type manipulator, manufactured by Integrated Motion Corporation (see figure 2).

4.1 Robot Dynamics

The robot model is written as,

$$M(q)\ddot{q} + C(q, \dot{q})\dot{q} + f_c = \tau \quad (23)$$

where,

$M(q)$: (2x2) Inertia matrix,

$C(q, \dot{q})$: (2x2) Coriolis terms,

τ : (2x1) torque vector,

q, \dot{q}, \ddot{q} : (2x1) position, velocity, acceleration vectors,

f_c : (2x1) Coloumb friction force,

$q = [\theta_1 \ \theta_2]^T$ and θ_i : joint angles, ($i=1,2$).

The details of the dynamics can be found in [5].

The model in (23) can be written in the state-space form representation as,

$$\begin{bmatrix} \dot{x}_1 \\ \dot{x}_2 \end{bmatrix} = \begin{bmatrix} x_2 \\ -M^{-1}(C x_2 + f_c) \end{bmatrix} + \begin{bmatrix} 0 \\ M^{-1} \end{bmatrix} u \quad (24)$$

where,

$$[x_1 \ x_2]^T = [q \ \dot{q}]^T = [\theta_1 \ \theta_2 \ \dot{\theta}_1 \ \dot{\theta}_2]^T \text{ and } u = \tau$$

Equation (24) is in the form of (4), and the proposed method can be applied.

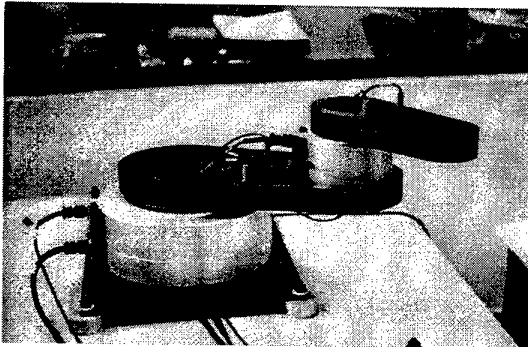


Figure 2. The experimental direct drive scara robot

4.2 The Experimental Setup

The control workstation has an open architecture, enabling the modifications of the control algorithm. The latter can be written and compiled in C-language in a personal computer equipped with a 80486 CPU. The compiled form of the proposed control algorithm is downloaded to a DSP based servo-controller. A TMS320C30 DSP is used which is a floating point DSP with a 32-bit architecture. Necessary torques to track a desired trajectory are computed by software and written to DACs of the board. The motor driver, functionally, converts the complex variable reluctance motor into a system that behaves like a high torque, low velocity DC motor. It also amplifies the controller output to a level that is capable of driving the direct drive motors. The only available feedback signals are the angular positions which are measured by encoders with 153 600 counts per actuator revolution. The angular velocities are computed by differentiating the measured positions. The architecture of the controller is presented in Fig. 3.

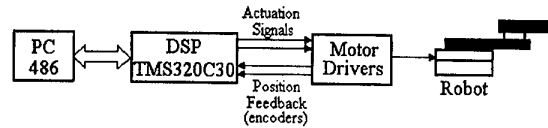


Figure 3. The controller structure

4.3 Experimental Results

The experimental results are presented from Fig. 4 to 9, where the solid and the dashed curves are related to the base and elbow link, respectively. The desired state trajectories used are depicted in Fig. 4. The angular errors are presented in Fig. 5. It should be pointed out that the initial position errors are deliberately introduced to see the system behavior (see Fig. 6 and Fig. 7) when the system is not on the sliding surface. Theoretically, when the states reach to the origin on the phase plane, they should stay there. However, in DSP-based discrete time applications, due to the fact that the system is open loop for the duration of the sampling time, they deviate from origin. When the control for the next sampling time is applied, the states again move towards the origin. In other words, the proposed controller establishes a stable domain of attraction around the origin. The control signals that are applied to the robot are presented in Fig. 8. The computed torque values are presented in Fig. 9. It can be seen that the proposed controller results in very good trajectory following performance.

Experimental studies with the well known computed torque with a PD control and direct computed torque (without PD) are also carried out. The results in terms of RMS and absolute value of the peak errors are compared with the proposed approach, and summarized in table 1. This comparison is made based on zero initial condition errors as differ from the presented figures. . In the design of all controllers, the parameters of the robot as given by the manufacturer, are used. The parameters of the PD controller are tuned to obtain the best results. As can be seen form the table, the proposed novel architecture results in minimum errors.

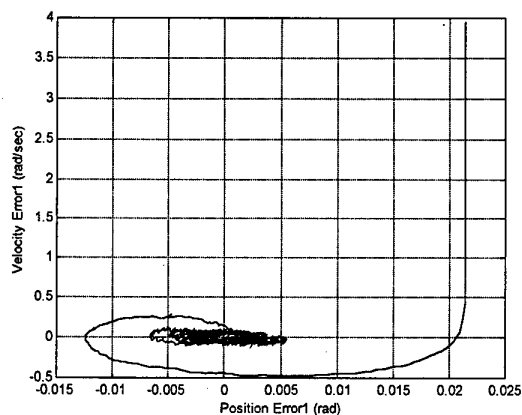


Figure 6. Phase plane motion for the base link

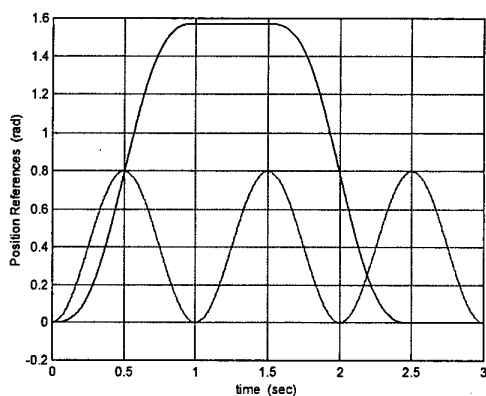


Figure 4. Reference angular position trajectories

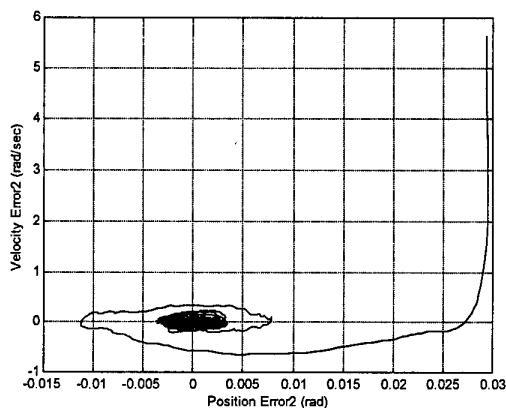


Figure 7. Phase plane motion for the elbow link

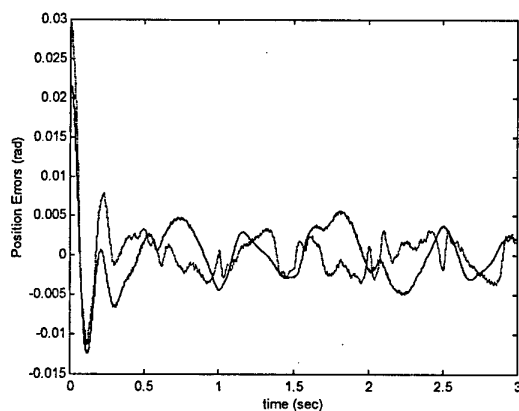


Figure 5. Angular errors for the base and the elbow links

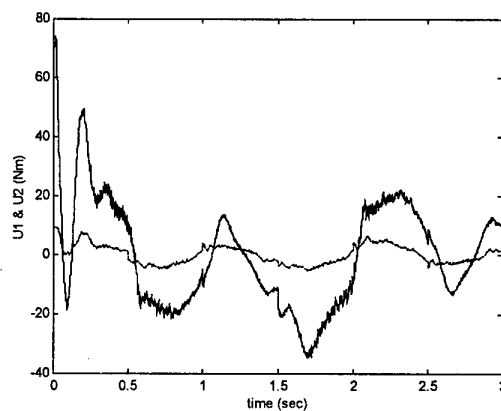


Figure 8. Controller outputs

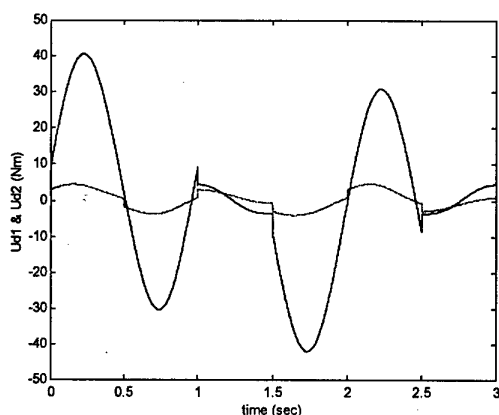


Figure 9. Computed torques

Table 1. A comparison of the methods based on RMS and absolute value of the peak errors

Methods	Base		Elbow	
	RMS	Peak	RMS	Peak
Proposed Controller	0.0029	0.0057	0.0019	0.0037
Computed Torque + PD	0.0036	0.0084	0.0033	0.0088
Computed Torque	0.2601	0.4341	0.2815	0.5833

5. Conclusions

In this paper, a novel approach to computed torque based robot control is proposed. Firstly, the parallelism between the equivalent part of the sliding mode control and the inverse dynamics is presented. In sliding mode, the equivalent control has an effect identical to the inverse dynamics (computed torque). In this paper, the corrective term of the SMC is used as the secondary controller instead of PID controller.

The proposed controller has the following advantages:

1. It can be designed for nonlinear systems without linearization around an operating point,
2. There is no need to measure (or compute) the actual values of the joint accelerations of the robot, as the case in SMC.

3. The novel controller is intuitively more robust than PID controller but less than SMC.

Experimental studies carried out on a direct drive robot arm indicate that the proposed controller is a good alternative to the computed torque plus PID controller for industrial robotic applications.

References

- [1] Koivo, A.J., *Fundamentals for Control of Robotics Manipulators*, John Wiley, 1989
- [2] Hung J. Y., "Variable Structure Control: A survey", *IEEE Transaction on industrial Electronics*, Vol.40, no.1, pp.2-22, February, 1993.
- [3] Ertugrul M., Kaynak O., Sabanovic A., Ohnishi K. "A Generalized Approach For Lyapunov Design Of Sliding Mode Controllers For Motion Control Applications", *Proceedings of 4th International Workshop on Advanced Motion Control, AMC'96*, pp.407-412, Mie, Japan, March 1996.
- [4] Slotine J. J. and Li W., "Applied Nonlinear Control", *Prentice Hall Inc.*, New Jersey, 1991.
- [5] Direct Drive Manipulator R&D package *User's Guide*. Integrated Motion Incorporated, Berkeley CA.

Neural Network Based Robot Controllers

Ertugrul Akbas

TUBITAK, UEKA, 41470,
Gebze, TURKEY

ertugrul@mam.gov.tr

Meliksah Ertugrul

TUBITAK MRC, ITRI,
41470, Gebze, TURKEY

melik@mam.gov.tr

Okay Kaynak

Bogazici University,
Istanbul, TURKEY

kaynak@boun.edu.tr

Yagmur Denizhan

Bogazici University,
Istanbul, TURKEY

denizhan@boun.edu.tr

Abstract

In this paper, two different well-known neuro-controller algorithms and a novel approach are presented and compared based on trajectory tracking performance, computational complexity, design complexity, RMS errors, necessary training time in learning phase and payload variations. The control schemes are simulated on a two degrees of freedom direct drive SCARA robot. In the applications of the neuro-controllers, one has to take into account the difficulties related to the implementation of the efficient neural network training strategy. In this paper, it is concluded that which controller is better for different situations.

1. Introduction

Nowadays, various control techniques are available for robot manipulators in the literature. Major problem of robot control includes kinematics, dynamics, path planning, and motion control.

The different control schemes try to solve one of them or many of them. The ones examined in this paper are neuro-controllers. The major attraction of neural network approach may be attributed to their learning and adaptiveness features. In the literature, a number of recent research show that neural networks are capable to tackle with various nonlinear discrete and continuous control tasks. Currently, neural networks are used in two main areas of application: approximation and classification problems. Numerous network architectures (back-propagation, radial basis, recurrent, self-organizing) and training strategies (supervised and unsupervised) are being considered [1-8]. However, a brief comparative explanation about their performance was not given until this paper.

A popular topic on NN robot control is the use of NN to compute the inverse dynamics or inverse kinematics with learning. Psaltis et al.[4], Guez and Ahmad [5] are the

workers who implemented those architectures. Also Elsley [6], Grossberg and Kuperstein [7], Fukuda [8] are the other important workers on this area. The proposed control algorithm are named direct inverse modelling architecture. Two types direct inverse modeling architecture are applied to robotics applications: DIMA I, which is off-line and DIMA II which is on-line. They are both supervised learning algorithms.

Kawato et al.[1] investigate hierarchical neural network model for voluntary movement with applied to robotics. He claims that a computational model for voluntary movement deals with three computational tasks: (1) trajectory determination, (2) coordinates transformation, and (3) motor command generation. The major part of the architecture used by Kawato is the inverse dynamic model. Kawato used NN in inverse dynamic model and a PID controller and the sum of these outputs are send to the plant as input.

A novel approach about sliding mode control is proposed by Ertugrul and Kaynak. In their work, they show the equivalence of the inverse dynamics and the equivalent control [2,3]. The equivalent part is computed by NN instead of exact calculation.

In this paper, direct inverse modelling architecture (DIMA) [4], feedback error learning architecture (FELA) [1] and a novel approach which is a neuro-sliding mode control [2,3] are compared according to:

1. Trajectory tracking performance,
2. Computational complexity,
3. Design complexity,
4. RMS Errors,
5. Necessary training time in learning phase,
6. Payload variations.

Simulation results obtained from the trajectory control of a scara type direct drive robot are presented and compared.

2. Neuro-Controllers

In this paper, two well-known neuro-controllers and a novel approach are compared. The first one is direct inverse modeling architecture with radial basis functions network. The second one is feedback error learning architecture and the last one is neuro-sliding mode control.

2.1 Direct Inverse Modeling Architecture (DIMA)

The direct inverse control aims to control the plant by using its inverse dynamics. The neural network receives the plant output as its input and the plant input as output [4]. The model is trained by inputting to the controller a sequence of control signals. Although, there is a feedback path between the plant output X and the vector of inputs U of this control plant is open loop in the sense that it does not take into consideration the error between the plant output X and the desired output. The main difficulty in applying this learning method is to choosing the training signal U . The plant must be brought into the desired operating region where the controller will have to operate.

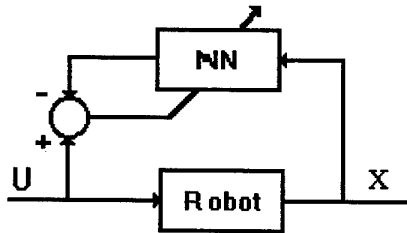


Figure 1. Direct Inverse Modelling Architecture (DIMA)

2.2 Feedback Error Learning Architecture (FELA)

The structure of FELA is shown in Fig. 2, which is proposed by Kawato et al [1]. In this architecture, the neural network is used as a feed-forward controller and trained by using the output of a feedback controller as error signal. The total control input U to the robot is equal to:

$$U(t) = U_F(t) + U_N(t) \quad (1)$$

where $U_F(t)$ and $U_N(t)$ are feedback controller and neuro-controller outputs, respectively.

The architecture requires qualitative priori knowledge about the plant dynamics. The input to the neuro-controller is firstly given as an input to the functions which makes the plant dynamics nonlinear. So the necessary knowledge is the functions that makes the plant nonlinear.

According to Kawato et al.[1], the FELA architecture possesses the following advantages over the other architectures:

1. Learning and control are performed simultaneously,
2. Back propagation of the error signal through a forward model of the plant is not required,
3. The learning is goal-directed and can resolve any ill-posedness of the problem at hand.

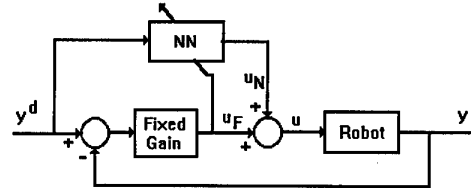


Figure 2. Feedback error learning architecture (FELA)

2.3 Neuro Sliding Mode Control

In the application of Sliding Mode Controllers, the main problem which is encountered is that a whole knowledge of the system dynamics (or inverse dynamics) and the system parameters is required to be able to compute the equivalent control. This is actually very rare in practice. A feed-forward neural network is proposed to compute the equivalent control in [2]. The weights of the net are updated such that the additional control term of the sliding mode goes to zero. Gradient decent method is used for the weight adaptation.

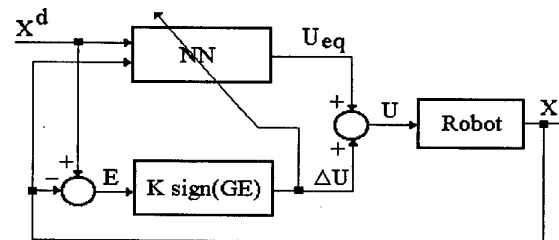


Figure 3. Neuro sliding mode control

3. Robotics Application

In order to study the performance of the controllers proposed, extensive simulation studies are carried out on a two degrees of freedom, direct drive, SCARA type experimental manipulator, manufactured by Integrated Motion Corporation (see figure 4).

3.1 Robot Dynamics

The robot model is written as,

$$M(q)\ddot{q} + C(q, \dot{q})\dot{q} + f_c = \tau \quad (2)$$

where,

$M(q)$: (2x2) Inertia matrix,

$C(q, \dot{q})$: (2x2) Coriolis terms,

τ : (2x1) torque vector,

q, \dot{q}, \ddot{q} : (2x1) position, velocity, acceleration vectors,

f_c : (2x1) Coloumb friction force,

$q = [\theta_1 \ \theta_2]^T$ and θ_i : joint angles, ($i=1,2$).

The details of the dynamics can be found in [2].

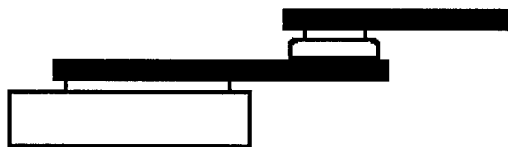


Figure 4. The structure of Direct Drive Scara

3.2 Simulation Results

The simulation results are presented in Figs. 5-12. The solid and dashed lines belong to first and second link, respectively. A comparison of the controllers based on the simulation results is presented in table 1.

3.2.1 Neuro-SMC. Neuro-SMC application algorithm is applied on behalf of computation of equivalent control.

The algorithm is given below

1. Initialization of the weights of NN.
2. Computation of hidden layer and net outputs.
3. Computation of AU.
4. Application of computed control to the robot.
5. Measurement of outputs of the robot.
6. Update the weights of neural network.

In order to compare the effects of payload change while the robot is working 40 kg payload was added and the effects of this payload to the end effector were examined. The payload was added at $t=10$ sec while the whole simulation takes 20 sec. The simulation results can be seen in Figs. 7-8

3.2.2 DIMA. Direct inverse modelling architecture is the one that is applicable to the most of the known robotic applications. The simulations are done under the conditions that has 3 layers of NN which has one hidden layer and the number of nodes are 6-4-2 respectively and the most important criteria is the training method which is RBF in this case.

The effect of payload change was examined with 40 kg payload and it was added at $t=10$ sec while the whole simulation takes 20 sec. The simulation results can be seen in Figs. 9-10.

3.2.3 FELA. Feedback error learning architecture has many successful examples in robotic applications. Therefore it is trustful and also applicable method. FELA has an on-line learning structure and was trained using RBF NN and the NN has 3 layers (one hidden) and it has 6 neuron in the input layer, 10 neuron in hidden layer and 2 neuron in output layer.

The effect of payload change was examined with 40 kg payload and it was added at $t=10$ sec while the whole simulation takes 20 sec. The simulation results can be seen in Figs. 11-12.

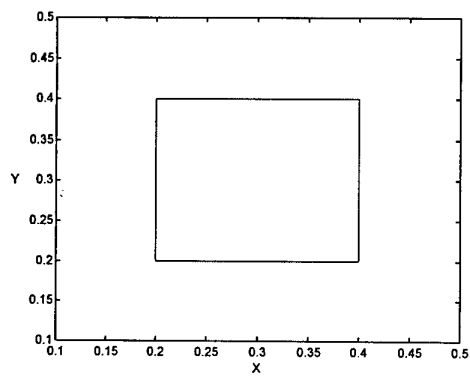


Figure 5. End effector reference on X-Y plane

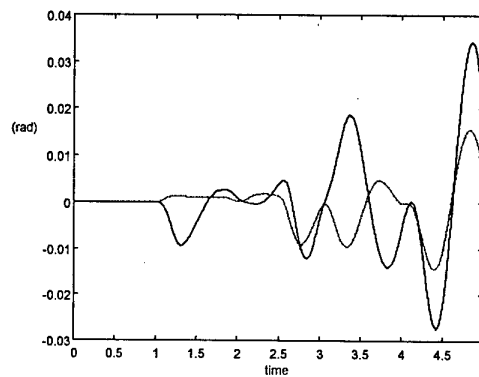


Figure 8. Position errors of Neuro-SMC after payload

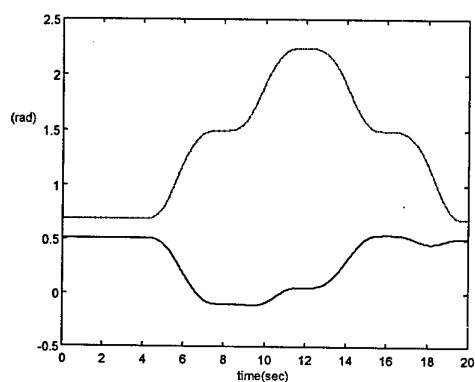


Figure 6. Joint space reference

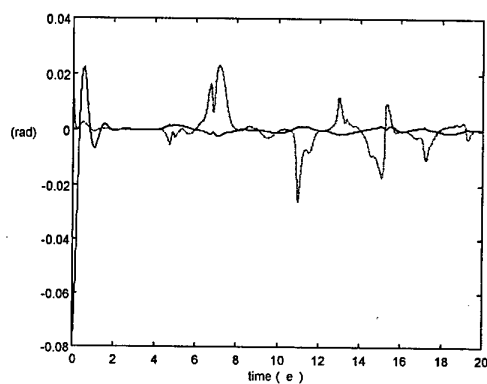


Figure 9. Position errors for DIMA

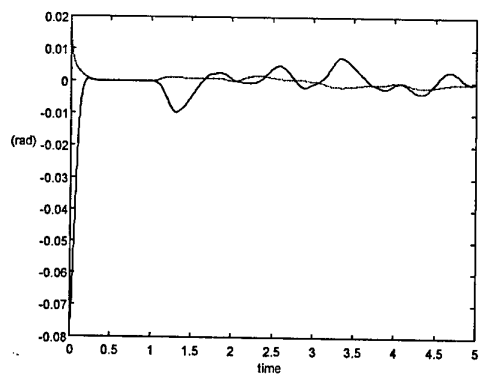


Figure 7. Position errors of Neuro-SMC

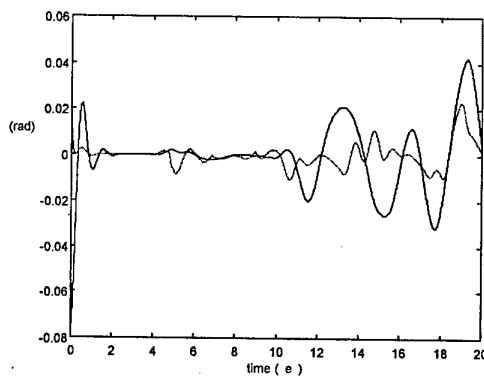


Figure 10. Position errors of DIMA after payload

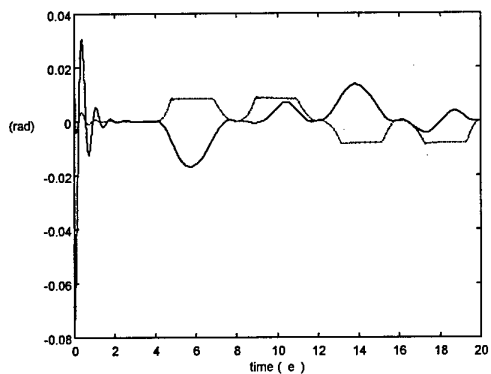


Figure 11. Position errors of FELA

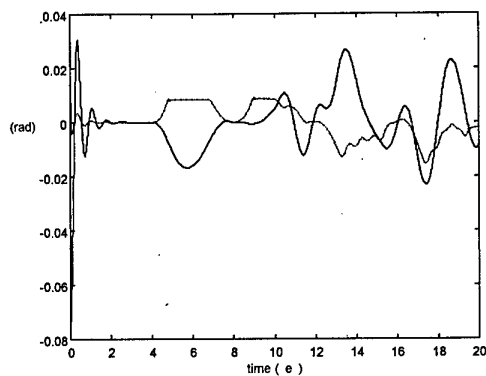


Figure 12. Position errors of FELA after payload

Table 1. Comparison of the neuro controllers

METHODS	DIMA WITH RBF	FELA	NEURO SMC
Computation Time	20	X	X
Necessary Knowledge	X	Qualitative priori knowledge	X
Convergence Time	1200 epochs	1200	1200
$RMS(\theta_1)$	0.0068	0.0085	0.0061
$RMS(\theta_2)$	0.0022	0.0058	0.0011
$Peak(\theta_1)$	0.0755	0.0755	0.0754
$Peak(\theta_2)$	0.0145	0.0145	0.0140
After Payload Change			
$RMS(\theta_1)$	0.0150	0.0116	0.086
$RMS(\theta_2)$	0.0053	0.0059	0.0043
$Peak(\theta_1)$	0.0755	0.0755	0.0343
$Peak(\theta_2)$	0.0231	0.0157	0.0157
Training Method	Off-line	On-line	On-line
Parameters	NN structure		NN structure

4. Conclusion

In this paper, the neural network based robot controllers are compared. From the obtained results, it may come to a conclusion that in which condition the proposed controller is better than the others or which neuro controllers are suitable for the current situation. Between the compared controllers, according to the table 1, the performance of the neuro sliding mode controller is the best with and without payload variations. And also it has one great advantage that is an on-line controller, which means that control and learning takes place at the same time. The RMS and the peak values are much smaller than DIMA and FELA with and without payload (see table 1).

As a conclusion, the superiority of the novel approach is shown in a simple but easily generalizable case in the table. The approach proposed has advantages on both design and application phase for trajectory control of a direct drive robotic manipulator.

References

- [1] Kawato M., Uno Y., Isobe M., Suzuki R. A., "Hierarchical model for voluntary movement and with application to robotics", IEEE Control System Magazine, pp.8-16, April 1988.
- [2] Ertugrul M., Kaynak O., "Neural Computation of the equivalent Control in Sliding Mode for Robot Trajectory control Applications", Proc. of IEEE International conference on robotics and automation, pp.2042-2047, May 1998.
- [3] Ertugrul M., Kaynak O., "Neuro-Sliding mode control of Robotic manipulators" International conference on advanced robotics, pp. 951-956, July 1997, California, USA
- [4] D.Psaltis, A. Sideris, A. Yamamura, "Neural Controllers ", Proc. IEEE Int. Conference on Neural networks, 1987
- [5] A. Guez, Z. Ahmad, "Solution to inverse problem in robotics by neural networks", Proc. Int. Conference on Neural Networks, 1988
- [6] R. Elsey, "A learning architecture for control based on back-propagation neural-networks", IEEE conf. On Neural Networks, Vol.2, pp.584-587, 1988.
- [7] S. Grossberg and M.Kuperstein, " Neural Dynamic of Adaptive sensory-motor Control", Elmsford, NY: Pergamon Press, 1989.
- [8] T. Fukuda et al., "Neural Servo controller; Adaptation and Learning", Proc. IEEE Intl. Workshop Advanced Motion contr. Pp.107-115, 1990.

Fuzzy Identifier based Inverse Dynamics Control of a Direct Drive Manipulator

Kemalettin Erbatur⁺ Okyay Kaynak⁺⁺

⁺ TUBITAK Marmara Research Centre, Gebze-Kocaeli, Turkey erbatur@mam.gov.tr
⁺⁺ Bogazici University, Bebek-Istanbul, Turkey, kaynak@boun.edu.tr

Abstract

A method using fuzzy logic and neural networks for the identification and control of robot dynamics is presented in this paper. Fuzzy identifiers are employed to match the centripetal, Coriolis and inertial effects in the robot dynamics model. Fuzzy logic systems used are represented as three-layer feed-forward neural networks. Fuzzy system parameters are adjusted via back-propagation. An on-line tuning algorithm is employed. Implementation results obtained with a two degrees of freedom SCARA type arm with special attention to rule base construction are presented.

1. Introduction

In the trajectory control of robotic manipulators, the main difficulty is that the dynamics involved is coupled and nonlinear. Two different main methodologies can be applied to overcome the problems introduced by this difficulty. The first is to design robust controllers using minimum information about the dynamics and the second is to use a model which is as close as possible to the real one to predict and counteract the various nonlinear effects inherent. The problem of the first approach is that the resulting controller can be too conservative. The main drawback of the second approach is the need for an accurate plant model. Once having obtained a dynamics model, however, various control structures can be employed. Although linearized models can perform well to some extent, nonlinear model based controllers prove to be more successful in trajectory tracking. A method for obtaining such a model is presented in this paper. To match the centripetal, Coriolis and inertial effects in the robot dynamics model [1-2], fuzzy logic systems which are represented as three-layer feed-forward neural networks are used. The representation used is given in [3-4], where back propagation is used to tune fuzzy system parameters. Similar representations of fuzzy systems as neural networks can be found in [5-8]. Various controller

schemes using a dynamics model obtained by neural network training are reported [9-10]. The control method proposed in this paper, similar to [11-12], is suitable for on line parameter adjustment. In this algorithm, the dynamics parameters are learned while the robot arm is partly controlled by a simple PD control algorithm. The identification process is continuously active to act against disturbances and dynamics changes like in the case of a sudden grasping of an unknown payload.

One of the main objectives considered is to keep the fuzzy system simple with a small number of rules and free of redundant inputs to have applicability in real time. Any deficiency in the rule base is aimed to be compensated by the fast learning capacity of the system.

The next section considers fuzzy modeling of the robot dynamics without going into tuning issues. Section 3 details the three-layer feed-forward neural network representation of the class of fuzzy systems which will be used in this paper together with the back-propagation algorithm and briefs the on-line identification method. Section 4 introduces dynamics properties of the SCARA type arm and presents implementation results obtained on the two main joints of the robot. Conclusions are given in the last section.

2. Robot dynamics representation via fuzzy logic

Dynamics equations of a robot can be represented in the following form

$$D(q)\ddot{q} + C(q, \dot{q})\dot{q} + g(q) = u. \quad (1)$$

Here D is the cumulative inertia matrix of the manipulator and the motors, C is the matrix for Coriolis and centripetal forces, friction effects, g is the gravity effect, $u \in R^n$ is the vector of generalized force or torque inputs and $q \in R^n$ is the vector of joint positions, where n is the number of the degrees of freedom. This equation can be interpreted as n functions of the $3n$ variables

$q_1, \dots, q_n, \dot{q}_1, \dots, \dot{q}_n, \ddot{q}_1, \dots, \ddot{q}_n$, i.e. the components of q , \dot{q} and \ddot{q} . The relations from joint angular positions, velocities and accelerations to torques can be divided further into subsystems. This is illustrated in Fig. 1.

Modeling the whole dynamics as a single fuzzy system and modeling the individual subsystems as local fuzzy systems are two approaches to take. The first approach is favorable when information about the subsystems is lacking. Matching the dynamics for such a system is then solely through a learning process. The number of rules sufficient to identify a model is experimentally obtained. Modeling subsystems individually is preferable when information is present to some extent. In our case the general structure of the robot is assumed to be known. Thus, valuable information about the number of inputs of the specific subsystems and the ranges of the inputs can be exploited. This is where the human knowledge enters to the modeling process. In fact, incorporating human knowledge to model structure design is the main reason why fuzzy systems are employed for identification.

Although using fuzzy input output relations for the subsystems is useful in rule base reduction, going too deep to each and every term in the dynamics equation would complicate the model structure and is most of the time not possible at all since exact knowledge about the dynamics is not available.

Figure 1. Decomposition of the robot dynamics into subsystems.

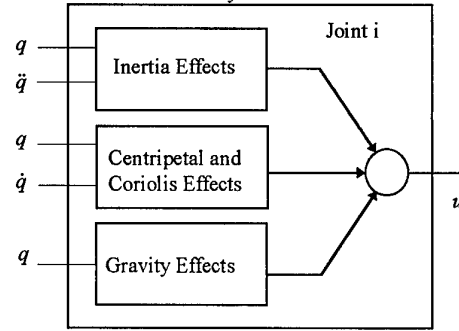


Figure 2. Subsystems used for individual joints

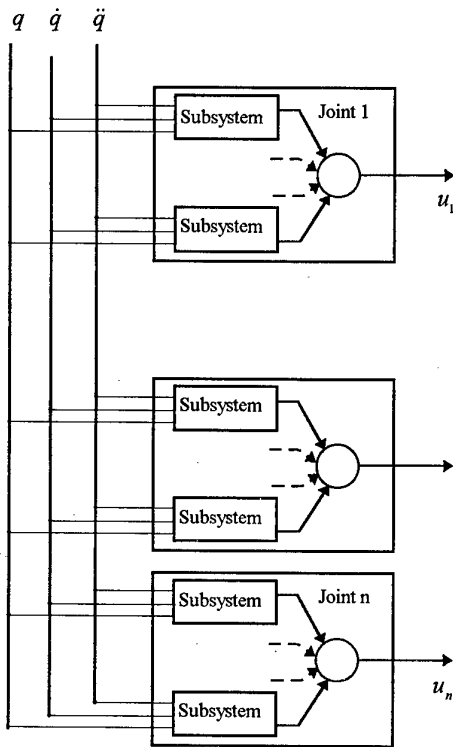
The inertial, centripetal and Coriolis effects for each joint are considered as subsystems to be modeled in this paper. Gravity effects in Fig.2 applicable for a more general robot structure are not present in the first two degrees of freedom of the SCARA configuration. Friction effects are not modeled. The minimum number of rules is tried to be obtained. The on-line tuning algorithm will then be responsible to compensate for differences in the parameters and the structure by very quickly adjusting fuzzy system parameters. This tuning algorithm is explained in the next section.

3. Back-propagation tuning

The fuzzy systems which will be used in this paper are of the form (2).

$$f(\underline{x}) = \frac{\sum_{l=1}^M \bar{y}^l \left[\prod_{i=1}^n a_i^l \exp \left(- \left(\frac{x_i - \bar{x}_i^l}{\sigma_i^l} \right)^2 \right) \right]}{\sum_{l=1}^M \left[\prod_{i=1}^n a_i^l \exp \left(- \left(\frac{x_i - \bar{x}_i^l}{\sigma_i^l} \right)^2 \right) \right]} \quad (2)$$

This function characterizes a fuzzy system with center average defuzzifier, product inference rule, singleton fuzzifier and Gaussian membership functions. Here M is the number of rules, \bar{y}^l stands for the output constant of rule l , n is the number of input variables, x_i is the i th input variable, \bar{x}_i^l is the center of the membership function for x_i for rule l , σ_i^l represents the width and a_i^l the height of this membership function. Gaussian membership functions are differentiable. This feature is required in the back-propagation algorithm. The function in (2) can be represented with a three-layer feed-forward neural network structure shown in Fig.3 [4].



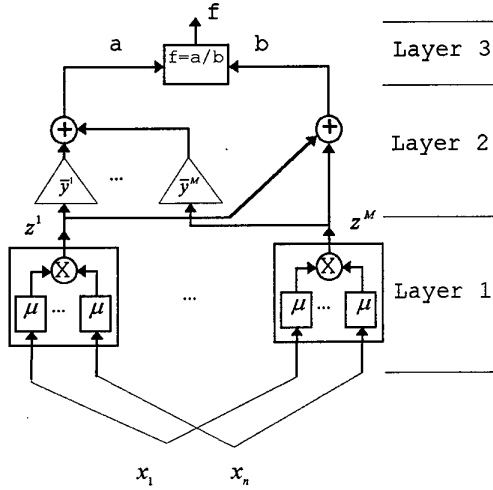


Figure 3. The three-layer feed-forward nn architecture

In Fig.3, μ stands for the membership functions described above. Triangles represent gains.

With the motivation that systems of the form (2) are universal approximators [4,15], [4] develops a back-propagation training algorithm for this class of fuzzy systems as in the following.

For a given input-output pair (\underline{x}^p, d) with $\underline{x}^p \in R^n$ and $d \in R$, a measure of the modeling error of a fuzzy model $f(x)$ of the form above can be defined by

$$E = \frac{1}{2} [f(\underline{x}^p) - d]^2. \quad (3)$$

In order to minimize this error, assuming that all the a_i^l terms are equal to 1, fuzzy system parameters will be varied according to the back-propagation rules below.

$$\begin{aligned} \bar{y}^l(k+1) &= \bar{y}^l(k) - \alpha \frac{\partial E}{\partial \bar{y}^l} \bigg|_k \\ &= \bar{y}^l(k) - \alpha \frac{f-d}{b} z^l \end{aligned} \quad (4)$$

$$\begin{aligned} \bar{x}_i^l(k+1) &= \bar{x}_i^l(k) - \alpha \frac{\partial E}{\partial \bar{x}_i^l} \bigg|_k \\ &= \bar{x}_i^l(k) - \alpha \frac{f-d}{b} (\bar{y}^l - f) z^l \frac{2(x_i^p - \bar{x}_i^l(k))}{\sigma_i^{l2}(k)} \end{aligned} \quad (5)$$

$$\begin{aligned} \sigma_i^l(k+1) &= \sigma_i^l(k) - \alpha \frac{\partial E}{\partial \sigma_i^l} \bigg|_k \\ &= \sigma_i^l(k) - \alpha \frac{f-d}{b} (\bar{y}^l - f) z^l \frac{2(x_i^p - \bar{x}_i^l(k))^2}{\sigma_i^{l3}(k)} \end{aligned} \quad (6)$$

Here α is a constant step size. The variable b is defined in Fig.3 and f stands for the function $f(\underline{x}^p)$ in (3).

This scheme is used in the mechanism of fuzzy identifiers [4]. [4] reports a better performance of fuzzy identifiers when compared with neural identifiers in [14]. This training method will be used in the controller structure shown in Fig.4.

The controller structure is similar to the controller in [11] in that the dynamics identifier is tuned by the difference of the total torque input to the robot and the torque output of the dynamics model. This difference is the output of a simple PD controller. The PD control signal diminishes as the dynamics is learned. [11] uses pure neural networks whereas fuzzy identifiers are used in the present paper for identification purposes.

4. Implementation results

The structure and properties of the robotic manipulator that is used in the simulations is described in the following and the difficulties in its control are outlined. The experimental robot is a two degrees of freedom SCARA type arm [15], the structure of which is shown in Fig.5, its parameters being listed in Table 1 in standard (m sec kg) units.

The dynamics equations of this manipulator are given by the following equation.

$$M(q)\ddot{q} + V(q, \dot{q}) + F = u. \quad (7)$$

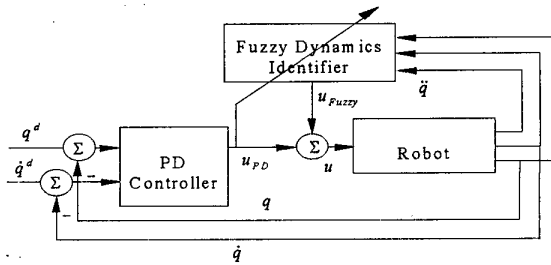


Figure 4. On-line identification and control with the feedback error learning scheme

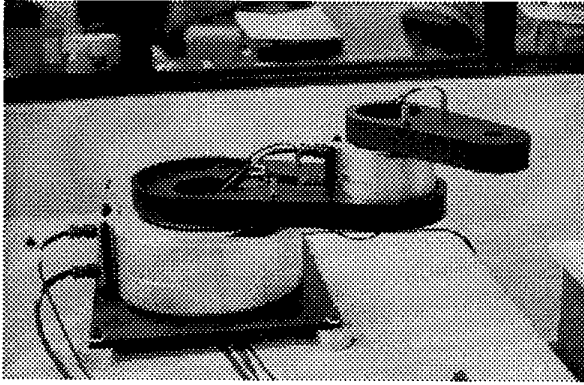


Figure 5. The direct drive arm

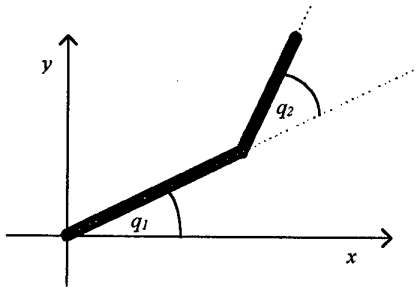


Figure 6. Assignment of joint angles

Table 1. Dynamics parameters of the robot

Motor 1 Rotor Inertia	0.267	Arm 1 Length	0.359
Arm 1 Inertia	0.334	Arm 2 Length	0.24
Motor 2 Rotor Inertia	0.0075	Arm 1 CG Distance	0.136
Motor 2 Stator Inertia	0.040	Arm 2 CG Distance	0.102
Arm 2 Inertia	0.063	Axis 1 Friction	4.90
Motor 1 Mass	73.0	Axis 2 Friction	1.67
Arm 1 Mass	9.78	Torque Limit 1	245.0
Motor 2 Mass	3.0	Torque Limit 2	39.2
Arm 2 Mass	4.45		

In this expression q is the vector of joint angles q_1 and q_2 shown in Fig.6. u is the torque vector applied to the joints, M is the inertia matrix, V is the vector of centripetal and Coriolis forces, F stands for Coulomb friction. M and V can be written explicitly as

$$M(q) = \begin{pmatrix} p_1 + 2p_3 \cos(q_2) & p_2 + p_3 \cos(q_2) \\ p_2 + p_3 \cos(q_2) & p_2 \end{pmatrix} \quad (8)$$

$$V(q, \dot{q}) = \begin{pmatrix} -\dot{q}_2 (2\dot{q}_1 + \dot{q}_2) p_3 \sin(q_2) \\ \dot{q}_1^2 p_3 \sin(q_2) \end{pmatrix} \quad (9)$$

where $p_1 = 3.1877$, $p_2 = 0.1168$ and $p_3 = 0.1630$. These values are computed by considering the various mass, length and inertia parameters of the arm and the direct drive motors in Table 1. The expressions (8-9) and the parameters above are given to present a detailed description of the dynamical system but they are not used in the controller structure.

A TMS320C30 DSP based system is used to control the arm [15]. The user interface is on a 80486 PC machine. C language servo routines are compiled in this environment and downloaded to the DSP. Sampling times in the range of 50-100 microseconds can be achieved for simple control methods. The sampling time used in this work is 3 ms. The torque motors used provide position signals with a resolution of 153600 pulses/rev.

This robot exhibits highly nonlinear characteristics and there exists a high degree of coupling between the links. Conventional independent joint PD and PID controllers therefore prove to be inadequate when a high performance trajectory following is a requirement, especially when the motion is fast. In the following, details are given on how a simple, on-line adapting inverse dynamics controller is designed and implementation results are presented.

The following information about the robot model is used to obtain a simple rule base. In general six inputs, the two joint positions, two joint velocities and two accelerations, are involved in the dynamics. For the described structure, the base joint position does not enter dynamics equations and therefore we have to deal with 5 inputs only. To simplify the rule base, two fuzzy sets are used to characterize the size of each input variable and two rules per input variable are used for each subsystem. The elbow position, since it enters expressions describing inertial effects and since it also appears in Coriolis and centripetal force relations, is represented by four fuzzy sets. Four rules are dedicated to incorporate the effect of the elbow position to the dynamics of the robot. Although most of the time outputs depend on more than one input simultaneously in a coupled manner, simultaneous evaluation of input variables is not carried out. In cases with more than one possible outputs, one of them is selected randomly when generating the initial rule base. This resulted in a simple rule base, which could hardly perform by itself without adaptation. This rule base, however, has a sufficient number of rules for the adaptation algorithm to work on and create outputs to match the dynamics of the controlled plant. Table 2 shows the inputs for the individual subsystems. In this table D1 stands for the inertial effects, C1 is centripetal and Coriolis forces for the base. D2 and C2 are similarly defined for the elbow joint. The parameters to be adjusted

are the centers and widths of the input membership functions and the output constants for rules.

Table 2. Inputs and parameter numbers for subsystems

Sub-system	Inputs	Number of rules	Number of parameters
D1	$q_2, \dot{q}_1, \ddot{q}_2$	6	36
C1	$q_2, \dot{q}_1, \dot{q}_2$	6	
D2	$q_2, \ddot{q}_1, \ddot{q}_2$	6	
C2	$q_2, \dot{q}_1, \dot{q}_2$	6	36

In the last column of Table 2, the numbers of the parameters to be adjusted for each joint are given.

At this level of the design, considering the computed robot model, smaller subsystems inside the four subsystems can be defined. However, this would complicate the rule base instead of making it simpler and no further subsystems inside the mentioned ones are assigned in the presented work. The initial membership widths are all equal to 1. Initial centers for positions are chosen in the 45° neighborhood of the zero position indicated in Fig.6. Output constants are very roughly initialized in a "assign zero or maximum" manner even disregarding possible sign changes. The only information used about the dynamics in the output constant initialization is knowledge of the general structure and a rough knowledge of the link weights. In that way, the performance of the fuzzy identifier with minimum information available will be tested. The reference curves applied for the joints given in Fig.7 are applied to the joints simultaneously.

Due to lack of space, only resulting error and torque curves for the base joint are presented in the figures. Similar performance is obtained for the elbow. A step disturbance torque is applied to the base to test the recovery performance of the proposed method. The magnitude 20 % of the maximum torque output which can be achieved by the base motor. The step disturbance is shown in Fig. 8. To present a comparison with conventional control techniques, experiments are carried out with a well tuned PID controller as well.

Figure 9 shows the error curve obtained by the PID controller. The peak on the error curve is due to the applied disturbance. In Fig. 10, the error curve with the fuzzy identifier method is given. It can be observed that the recovery after the disturbance is faster and the error caused by the disturbance is smaller when comparing with the PID controller.

As mentioned above and illustrated in Fig. 4, the total control input in the fuzzy identification method consists

of the output of the fuzzy system and a PD control input. Fig. 11 shows that the fuzzy identifier output converges to the total control input and the PD control signal diminishes. The fuzzy model takes over the controlling task quickly although its initial parameters, by purpose, are not selected suitable for convergence.

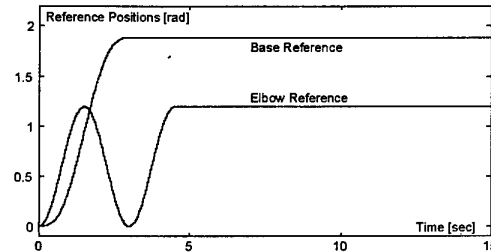


Figure 7. Reference positions used for base and elbow joints.

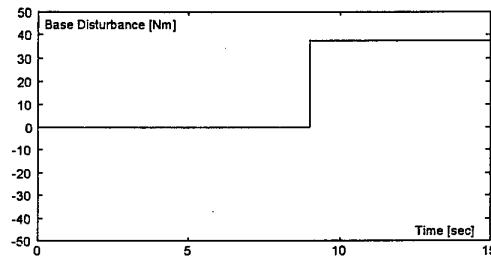


Figure 8. Step disturbance applied to the base. The height of the step corresponds to 20 % of the torque output capacity of the base direct drive motor.

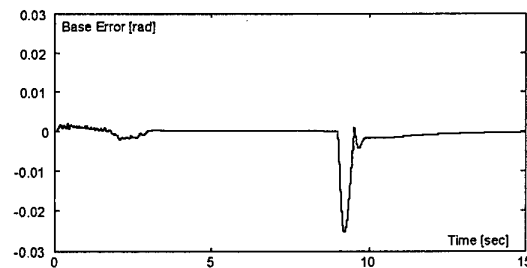


Figure 9. Base joint position error. PID control.

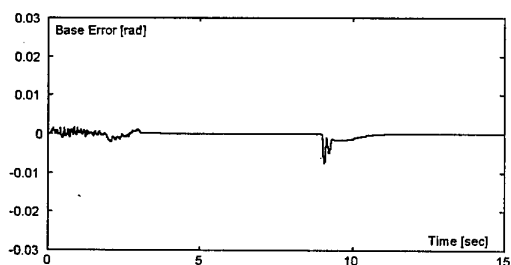


Figure 10. Base joint position error. Fuzzy identifier method.

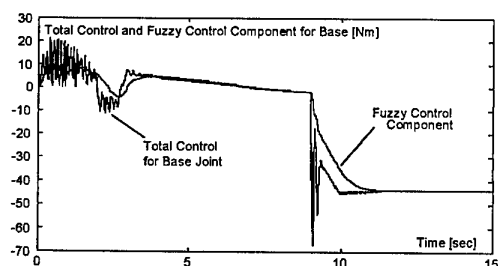


Figure 11. Total control input (gray curve) and its fuzzy control component (solid black) for the base joint. Fuzzy identifier method.

5. Conclusions

An on line robot dynamics learning and control method is presented in this paper. The suggested scheme uses only limited information about the manipulator. By the use of fuzzy logic, this information is incorporated in the model structure. Rule base reduction is carried out in design and equipped with the back-propagation algorithm presented, the fuzzy logic system with a small number of rules performs well in identifying an inverse model. The fact that the adjusted fuzzy system variables have clear physical interpretations has been intensively used in the model development. This is a significant advantage of the fuzzy identifier over neural identifiers. Experimental work indicated good identifying performance of the method.

References

- [1] Spong, M., M. Vidyasagar, "Robot Dynamics and Control", John Wiley and Sons, 1989
- [2] Koivo, A. J., "Fundamentals for Control of Robotic Manipulators", John Wiley and Sons, 1989

- [3] Wang, L. X., "Design and Analysis of Fuzzy Identifiers of Nonlinear Dynamic Systems", IEEE Trans. on Automatic Control, Vol. 40, pp. 11-23, 1995
- [4] Wang, L. X., "Adaptive Fuzzy Systems and Control-Design and Stability Analysis", PTR Prentice Hall, Englewood Cliffs, New Jersey 07632, 1994
- [5] Jang, J. S. R., "Self-Organizing Fuzzy Controllers based on Temporal Back Propagation", IEEE Transactions on Neural Networks, Vol. 3, No. 5, September, 1992
- [6] Nauck, D., F. Klawonn, R. Kruse, "Fuzzy Sets, Fuzzy Controllers, and Neural Networks", in Scientific Journal of the Humbolt University of Berlin, Series Medicine 41, No. 4, 1992, pp. 99-120
- [7] Ichihashi, H., "Learning in Hierarchical Fuzzy Models by Conjugate Gradient Method Using Back Propagation Errors", Proc. Intelligent Systems Symp., 1991, pp. 235-240
- [8] Fukuda, T., "Theory and Applications of Neural Networks in Industrial Control Systems", IEEE Trans. On Industrial Electronics, Vol. 39, No. 6, December 1992, pp. 472-489
- [9] Hunt, K.J., D. Sbarbaro, R. Zbikowski, P.J. Gawthrop, "Neural Networks for Control Systems-A Survey", Automatica Vol. 28, No. 6, pp. 1083-1112, 1992
- [10] Tzafestas, S. G., "Neural Networks in Robotics: State of the Art", IEEE Int. Conf. On Industrial Electronics, 1995
- [11] Kawato, M., Y. Uno, M. Isobe, R. Suzuki, "Hierarchical Neural Network Model for Voluntary Movement with Application for Robotics", IEEE Control Systems Magazine, April 1988, pp.8-16
- [12] Bekey, G. A., "Robotics and Neural Networks", in Neural Networks for Signal Processing, Kosko. B., Prentice hall, 1992
- [13] Wang, L. X., "Fuzzy Systems are Universal Approximators", Proc. IEEE Int. Conf. Fuzzy Systems, San Diego, pp. 1163-1170, 1992
- [14] Narendra, K. S., K. Parthasarathy, "Identification and Control of Dynamical Systems Using Neural Networks", IEEE Trans. on Neural Networks, 1, No. 1, (1990), pp. 4-27
- [15] Direct Drive Manipulator R&D Package User Guide, Integrated Motions Incorporated, 704 Gillman Street, Berkeley California 94710

Development of a Model for Internet Commerce Implementation in Intelligent Manufacturing Management

Ergun Gide

School of Management

University of Technology, Sydney, Australia

E-mail: Ergun.Gide@uts.edu.au

Fawzy Soliman

School of Management

University of Technology, Sydney, Australia

E-mail: Fawzy.Soliman@uts.edu.au

Abstract

Manufacturers have been living under the pressure of both strategic and organisational challenges that come from the Information Technology (IT) all around the world especially for the last five years. In this rapidly changing world demand to produce, expand, develop, and advance has become overwhelming. International competition for goods and services has gone far beyond national boundaries. Change affects people, technology, organisational structures, information management, and of course the way manufacturers operate. This paper examines the importance of Internet Commerce and attempts to develop a model for its implementation in intelligence manufacturing management. It is believed that this model is effective for manufacturing management in this rapidly changing global business environment and for the 21st century.

1. Introduction

The Internet-Based Electronic Commerce (in short form Internet Commerce or E-Commerce) is rapidly emerging as an entirely new method to conduct business and to interact with customers, suppliers and partners. Electronic Commerce covers many aspects of buying/selling relationships. Electronic Commerce covers many operations within production processes. Manufacturers (from small to very large) are scarcely implementing E-Commerce over the Internet to gain strategic advantage over their rivals and not to be out of business in this very rapidly changing and competitive global business environments (Cronin, 1996).

The Internet Commerce has become essential for the survival of manufacturing companies entering the virtual distribution marketplace. The business-to-business and business-to-consumer segments of the E-Commerce contain both common and differing characteristics that

must be understood to succeed in implementation (Gide & Soliman, 1998).

A number of dominant industries have jumped on the Internet bandwagon. Examples are: the IT industry, manufacturers, publishers, retailers, banks and financial institutions, airlines and others as shown in the following table (Table 1).

Table 1. Examples of businesses using the Internet-based e-commerce

Business	Application of Internet-Based E-Commerce
Manufacturing	Thousands of manufacturers use E-Commerce from supplier relations to customer service.
Retail	Many retailers are now using E-Commerce on the Internet with thousands of on-line products and services are offered.
Airlines	Hundreds of airlines have Web sites and doing business with E-Commerce from order receiving to payment for the ticket.
Banks	There are more than 200 banks on the Web from 30 countries.
Media & Publishing	Many publishing houses have developed Web versions of traditional print media, and entirely new Electronic Magazines.

According to the inaugural report from Forrester Research's Business Trade & Technology Strategies service, the value of goods and services traded between companies over the Internet is expected to skyrocket from \$8 billion this year to \$327 billion in the year 2002. According to the same report, businesses are aggressively adopting inter-company trade over the Internet because they want to cut costs, reduce order-processing time, and improve information flow.

Mougayar (1997) noted that perhaps the most significant outcome of E-Commerce is the positive

change it brings to buyer-seller relationships. The most successful users of E-Commerce have recognized that increased familiarity with customers, dealers or suppliers afforded by joint systems leads to collaborative behaviours, which improve economic performance for both partners. Organisations that want to stay in business beyond to the turn of the century must re-evaluate every aspect of their strategy and operations and incorporate these technological changes.

Full implementation of Electronic Commerce over the Internet is very much in its infancy despite there has been phenomenal growth in commercial presence on the Internet in recent times. In the last 2 years the commercial domain registrations on the entire Internet have grown to represent some 85% of all organizations. Electronic trading opportunities offer businesses the chance to compete for an international scale. These Electronic Trading Opportunities, are being expanded to Web sites and many trading forums emerging.

E-Commerce implementation varies significant by industry. According to a recent survey, retailers and wholesalers were far more likely to implement E-Commerce compared with manufacturers. In addition, consumer goods industries led industrial goods industries in E-Commerce implementation. E-Commerce implementation by manufacturers is accelerating, driven by successes of early adopters. Costs associated with E-Commerce implementation are level of system integration and communication, hardware and software and staff training costs. A typical E-Commerce business transaction cycle in a supplier-retailer-customer (consumer) channel could include electronic transmission of purchase order, customer-buying schedule, advanced shipping notice, invoice and electronic funds transfer of payment (EFT) or e-cash.

2. Globalization Effects

The 1990s and beyond will present both strategic and organizational challenges to manufacturing operations management. On the one hand, corporations are being forced to develop strategies that will allow them to be efficient, responsive, and innovative. The global economy is rapidly evolving into an integrated economic system, which presents tremendous opportunities to aggressive global manufacturers while threatening the very existence of the mediocre manufacturer. Competitive survival depends on the firm's ability to understand the changing global environment and to adopt the emerging rules of global strategy (Soliman & Gide, 1997).

Globalization has been a product of change caused by economic, technological, and competitive factors. Three principal economic forces have driven companies and

industries toward globalization: economies of scale, economies of scope, and national differences in the availability and cost of resources. These forces have caused companies to specialize and standardize their products. This competitive strategy has become known as *global chess* and can only be played by companies that message their worldwide operations as interdependent units implementing a coordinated global strategy (Alkhafaji, 1995). One of the more salient aspects of the new global marketplace is the "*borderless world*" - a world in which capital is more mobile than ever and relevant competitive response times have been dramatically reduced (Ohmae, 1989). This borderless world has made the need for decision making based on coordinated global strategies more compelling than ever.

Vastag (1994) stress that in this rapidly changing world, not only internal manufacturing processes but also its external logistical infrastructure need to be changed. Manufacturers require new supporting infrastructures to compete successfully in quickly changing global markets demanding flexibility and timely delivery. The movement of synchronized manufacturing and an elimination of buffer stock mandate improved processes - including the procurement of the right material, at the right place, at the right time. Most authors agree that *time* and *flexibility* will be the new driving forces of competitiveness, and quality is becoming more and more an order qualifier rather than order winner.

According to Stalk and Hout (1990), time-based competitors built their companies around customer needs by redesigning and compressing work processes in order to more directly provide those needs. Time-based are effective in minimizing costs and maximizing the value added to customers because longer development times, cycle times, and lead times invariably cause higher costs. Stonich (1990) stresses that implementing a time-based strategy requires drastic changes in company culture, structure, systems, and the way the work is accomplished. The plan that he offers for becoming a time-based competitor is centered on establishing, planning, and assessing the feasibility of a time-based strategy. According to Fawcett (1992), integration of logistics into the design and management of global manufacturing networks is critical to the success of a global manufacturing strategy. Therefore, the role of the Internet based E-Commerce in manufacturing can not be underestimated and should be taken into account to survive and become competitive in the world market.

3. E-commerce over the Internet

Full implementation of Electronic Commerce over the Internet is very much in its infancy. A limited number of

pilots to provide a trading scenario have taken place in the US and other countries. However, there has been phenomenal growth in commercial presence on the Internet in recent times. In the last 2 years the commercial domain registrations on the entire Internet have grown to represent some 85% of all organizations. Facts and figures from industry show that:

- Internet-Based E-Commerce is expected to reach \$150 billion by the year 2000 and more than \$1 trillion by the year 2010;
- Sales generated via the Web have grown from \$17.6 million in 1994 to nearly \$400 million in 1995 (a growth rate of over 2100%);
- The number of sites using the Internet for product transactions has increased from 14% in 1995 to 34% in 1996 and to a projected increase of 44% in the next 3 years.

Electronic trading opportunities offer businesses the chance to compete for an international scale. These Electronic Trading Opportunities, are being expanded to Web sites and many trading forums emerging. The Internet has reduced the number of letters, voice calls and faxes around the globe. Thirty per cent of Internet users in one survey stated that Internet usage had resulted in new business opportunities and 43% said that it has increased productivity.

4. Driving Forces for E-Commerce

Companies start their E-Commerce owing to different reasons. However, based on the literature survey, there are some typical driving forces for companies to embark on E-Commerce implementation. According to the ABC News (February 1998), the E-Commerce implementation across the Australian businesses doubling every six months due to increase of sales motivation. Various surveys around the world and in Australia show that sale focused motivational elements were the major driving forces to E-Commerce implementation (Gide & Soliman, 1997). Some of these elements are:

- Reduce cost of operations
- Increase sales and profit
- Pressure from major customers' and suppliers' request
- Satisfy the needs of customers
- Ability to capture more market share
- Pressure from competitors (rivals)
- Reach potential customers
- Improve company's image
- Electronic (paperless) work
- Increase productivity
- Pressures from globalization

- Achieve competitive advantage

It is clear that the pro-active drives in E-Commerce implementation are related somehow to the Just-in-Time (JIT) philosophy. Thus, E-Commerce can be treated as an effective tool, which contributes, to the JIT process.

5. Manufacturing Benefits of E-Commerce Implementation

According to Mougayar (1997) there are various types of key measurements that must be tracked prior to embarking on a full implementation. Some of the important key elements to measure business value are:

- ♦ Reducing costs.
- ♦ Process simplification.
- ♦ Improving customer service.
- ♦ Generating new revenue.
- ♦ Taking faster decisions.

With Internet Commerce already headed for \$8 billion in 1997, up 1,000% from 1996, Forrester looked at which industries are at the center of the dramatic growth. Three different company types were identified as shown in the following table (Table 2).

Table 2. Percentage distribution of usage of Internet-based e-commerce within three industries.

Industry Type	1997	1997
	% Sales	\$Billion
Manufacturers of electronics and aeroplane parts	37.5%	3
Vendors of computer-related and office supplies	37.5%	3
Services and utilities providers	25%	2
Total	100%	8

6. Current Challenges to Internet-Based E-Commerce

Like any other IT tools, E-Commerce is not without drawbacks and limitations. There are two main drawbacks or challenges in using Internet-Based E-commerce, these are: security issues and payment tools.

On the other hand, challenges from the internal organization caused one of the biggest obstacles to the E-Commerce. This is because E-Commerce can be treated as a stimulus in a revolution. Some companies do not

have a clear budget on E-Commerce implementation. However, the managers would provide the necessary resources if E-Commerce comes to the priority of the company targets. The various internal difficulties encountered by the companies during the E-Commerce implementation process are: lack time, lack clear budget, benefits can not be evaluated, overloading of work, compete for resources, insufficient training, not supported by employees. External difficulties came from three sources; customers, suppliers and consultants.

Some international surveys show many manufacturers found that, full E-Commerce implementation was expensive, time consuming, too formalized and impersonal. The direct costs of obtaining and maintaining E-Commerce are the computer software and hardware and IT consultation fees. Some businesses do not consider that the implementation can induce new orders although E-Commerce can improve the quality image of the company. Accordingly, some manufacturers considered that the relatively high initial software and hardware costs of full implementation and security and privacy concerns would prevent them from starting the E-Commerce, no other factors appear to have a dominant effect. However, some other common drawbacks include the followings:

- Lack of knowledge on E-Commerce
- The belief that total benefits cannot cover total costs
- Inappropriateness of E-Commerce in their industry
- E-Commerce will not be supported by employees
- Extensive IT/IS changes are required
- Top management doesn't know E-Commerce and hence doesn't recognize its benefits.

Accordingly, companies with larger employee size are more likely to implement E-Commerce or to be in the process of implementation. This suggests that the accessibility to other sufficient resources in larger companies enable them to start the implementation process earlier and obtain the system quicker than the comparatively smaller companies.

7. Managerial Implications of E-Commerce Implementation

To date the major benefits from the Internet include improved internal and external communications. The Web has specifically brought a new marketing medium and enhanced information resource. Innovative applications are starting to appear which allow for sales and database interrogation. Other benefits such as e-mail and file transfer functionality, Web utilization gave many companies '*Internet presence*' and provided them with opportunities to develop and expand new services. In manufacturing, traditionally Design Engineering,

Procurement and Production Departments communicate with each other using paper based methods. However the introduction of Internet-Based E-Commerce and its superiority of over traditional EDI is adding new dimension to reducing the cost of manufacturing (Soliman & Gide, 1997).

Research shows that resource availability plays a vital role in enabling manufacturers to start E-Commerce implementation. The motivations from implementation are sales focused and internal focused. Sales focused motivation is defensive in market survival and offensive in acquiring competitive advantages. Internal focused motivation is originated from the desire of senior management that internal benefits can be obtained on the successful implementation of E-Commerce over the Internet. A commitment of the decision-maker to E-Commerce facilitates a more direct and quick allocation of resources to the process. With the influence of senior management, a more committed workforce is expected. This would ultimately lead to better results of the E-Commerce implementation.

Moreover, senior management of many organizations have in common the desire enforces the persistent commitment of management by devoting the time and providing the resources to support the E-Commerce process. Gaining management commitment and communicating that commitment credibly to employees is one of the success factors for achieving E-Commerce implementation.

8. Developing a Model of E-Commerce Implementation

To cope with these driving forces, people (executive/employee) involved in the system are identified as a factor for the successful implementation of the E-Commerce. In this model, external forces (customer expectation/satisfaction) and internal forces (strategic/competitive benefits) provide the impetus for implementation. These are realized in market/customer demand and implementation of processes, both of which require the commitment and involvement from the personnel in the company.

There is a need for improving the understanding (know-how), belief/trust and communication channels and these form the fundamental element in the strategy of E-Commerce implementation. More importantly, the continuous commitment of people is necessary to ensure that the implementation can be maintained in subsequent review procedures. A model for visualizing the success factor and providing the basis for developing the strategy is illustrated in the Figure 1 below.

8.1. Success Factors of E-Commerce Implementation

According to the research major forces behind E-Commerce implementation are market/customer demand and benefits derived from the implementation and competitive advantage. Most manufacturers started their E-Commerce implementation in response to their customers' request: the requirement of the potential customers. These provide the practical evidence that market/customer demand is the major drive-initiating people commitment toward E-Commerce. Manufacturers seeking E-Commerce implementation also believe that they can achieve competitive advantage over their competitors. In fact, the research shows that E-Commerce user manufacturers are picking up market shares from other non-user suppliers. Also, E-Commerce user manufacturers are seeking company growth by expanding new overseas (global) markets in which E-Commerce usage is a must (Gide & Soliman, 1998).

The continuous demand of E-Commerce is the result of promotion of the quality by government, customers, suppliers, competitors, and industries. However, people will only adopt E-Commerce, which is beneficial and practical to their organizations. There are internal driving forces, which are additional to the external forces to push the manufacturers toward the need to implement E-Commerce over the Internet.

8.2. Successful E-Commerce Implementation Processes

The successful E-Commerce implementation strategy in manufacturing relies on management and employee commitment and active involvement. This requires detailed planning of the activities. The model in Figure 1 is realized through the process elements, which are closely related to critically affecting the behaviour of people (executive/staff/employee).

Management should make an informed decision to implement E-Commerce. This commitment is essential because the E-Commerce process requires not only the involvement of the management, but also the resources that only the management can allocate. In small manufacturers, it is not always a case to establish a formal E-Commerce information management project team as in large corporations. However, the information manager or executive/senior manager is the one who has responsibility to ensure that the E-Commerce requirements are successfully implemented as planned.

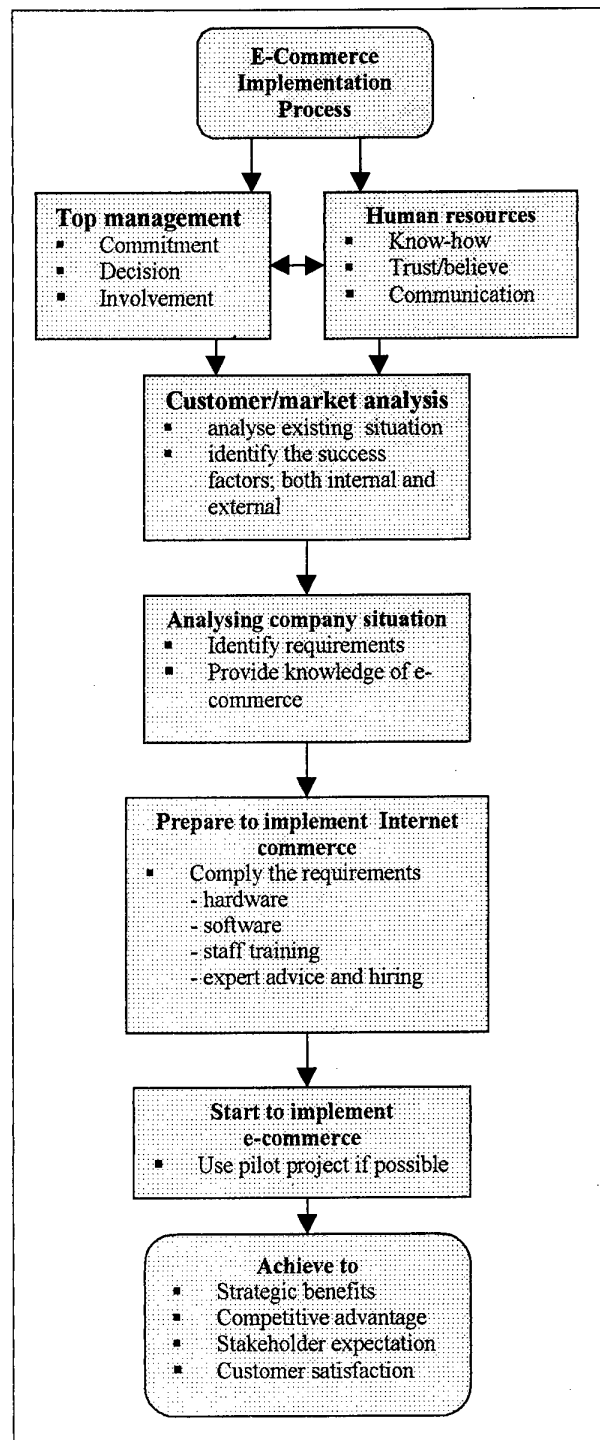


Figure 1. A Model for successful e-commerce implementation over the Internet

Accordingly, the information technology manager/s or external IT consultant/s should provide training sessions on E-Commerce knowledge. Besides, it is an effective way to visualize the management commitment toward E-Commerce implementation. The fundamental process towards successful implementation of E-Commerce is shown in Figure 1.

Along with the adaptation process, the organization needs to determine its starting point to continuously measure progress and evaluate the benefits gained from E-Commerce implementation (Gide & Soliman, 1998). Gaps of process steps can be identified when comparing the current system with the E-Commerce requirements. It enables the management to determine the necessary efforts and resources to be allocated to the areas of importance.

9. Conclusions

This research is designed to propose a model for successful implementation of E-Commerce over the Internet in manufacturing industry. This paper also examines the importance of Internet Commerce in the context of implementation strategies.

Commerce over the Internet is very much in the early stages. Therefore, success in Internet-Based Electronic Commerce depends on how organizations strategically position their products and services through other Internet-based electronic communities and intermediaries, as well as on how they facilitate the interactions with their customers, suppliers, and partners.

The main obstacles to E-Commerce implementation for manufacturers are security, privacy, payment tools, cultural and technical. Cultural issues are challenges linked to a major re-engineering exercise accompanied by resistance to change. Technical issues are high implementation costs, inadequate resources and insufficient external assistance. However, it is expected that Internet will made major advances into redefining manufacturing away from physical driven processes and towards an information-intensive system.

10. References

1. ABC (*Australian Broadcasting Corporation*) News, 18th of February 1998.
2. Alkhafaji, A. F., *Competitive Global Management*, US, St Luice Press, 1995.
3. Cronin, M. J., *Global Advantage on the Internet*, Van Nostrand Reinhold, USA, 1996.
4. Fawcett, S., "Strategic Logistics in Coordinated Global Manufacturing Success," *International Journal of Production Research*, Vol. 30, No. 4, pp. 1081-99, 1992.
5. Forrester Research's Business Trade & Technology Strategies Service, (<http://www.internetnews.com/ec-news/cur/1997/07/3005-bb.html>)
6. Gide, E., and Soliman, F., "A Model for the Implementation of E-Commerce Over the Internet in Manufacturing Industry," in *the Proceedings of IMS'98 International Conference*, Sakarya, 6-7 August 1998, pp. 801-811.
7. Gide, E., and Soliman, F., "Analysis of Conducting Business on the Internet," in *the Proceedings of Inet-tr'97 Conference*, Ankara, 21-23 November 1997.
8. Gide, E., and Soliman, F., "Key Drivers for using the Internet in Australia," in *the Proceedings of Inet-tr'97 Conference*, Ankara, 21-23 November 1997.
9. Mathieu, R. G., "The Internet: Information Resources for Industrial Engineers," *Industrial Engineering*, Vol. 27, No. 1, pp. 49-52, January 1995.
10. Mougayar, W., *Opening Digital Markets*, CyberManagement, Canada, 1997.
11. Ohmae, K., "Managing in a Borderless World," *Harvard Business Review*, Vol. 67, No. 3, pp. 151-61, May-June 1989.
12. Soliman, F., and Gide, E., "Impact of Internet Based E-Commerce on Manufacturing and Business Operations," in *the Proceedings of Inet-tr'97 Conference*, Ankara, 21-23 November 1997.
13. Stalk, G. Jr., and Hout, T. M., "How Time-Based Management Measures Performance," *Planning Review*, November-December 1990.
14. Stonich, P. J., "Time: The Next Strategic Frontier," *Planning Review*, November-December 1990.
15. Vastag, G., and et al., "Logistical Support for Manufacturing Agility in Global Markets," *International Journal of Operations and Production Management*, Vol. 14, No. 11, pp. 73-85, 1994.

Gain-Scheduled Adaptive Control of Unreliable Manufacturing Systems with Variable Demands

B. Porter and P.Y. Mok

Department of Industrial and Manufacturing Systems Engineering

The University of Hong Kong, Hong Kong

E-mail: bporter@hkucc.hku.hk, tracy_mok@cheerful.com

Abstract

It is shown that genetic algorithms can be employed to determine the optimal short-run inventory levels in unreliable manufacturing systems. Furthermore, it is indicated that such inventory levels can be used as the set-points of gain-scheduled adaptive controllers for such systems. The performance of such a gain-scheduled adaptive controller is illustrated for a particular unreliable manufacturing system subjected to a particular piecewise-constant demand. It is demonstrated that the performance of this adaptive controller is superior to that of a genetically optimised non-adaptive controller in this case.

1. Introduction

In modern industry, it is important that manufacturing systems be controlled optimally so as to minimise inventory costs whilst meeting production schedules [1] [2]. However, the dynamical behaviour of manufacturing systems is typically very complex and the synthesis of optimal control policies for such systems is accordingly rather difficult. This difficulty is exacerbated in the case of unreliable manufacturing systems by the presence of failure-prone machines. Indeed, in the case of such unreliable systems, theoretical results are currently available only in the case of single-machine manufacturing systems producing either a single part-type [3] [4] or multiple part-types [5]. These results also apply only to the minimisation of expected costs incurred in the long run for constant demand rates. Nevertheless, these results [3] [4] [5] provide very important information regarding the optimal inventory levels to be used in unreliable manufacturing systems.

In this paper, it is shown that genetic algorithms can be employed to determine the optimal inventory

levels to be used in such systems in the short run. It is shown that such optimal short-run inventory levels depend (for given maximum production rate, mean time between failures, mean time for repair, and inventory weighting parameters) on the demand rate as well as on the initial state of a manufacturing system. This genetic stochastic optimisation procedure readily provides a 'look-up' table that can be used for the gain-scheduled adaptive control of unreliable manufacturing systems with variable demands. Thus, consider that such a manufacturing system is subjected to a piecewise-constant demand; then, given the state of the system at the beginning of a piecewise-constant interval of demand, the corresponding optimal short-run inventory level can be immediately determined from the relevant 'look-up' table. This optimal inventory level can then be used as the set-point for a crisp-logic (or fuzzy-logic) controller [6] [7] [8] until the beginning of the next piecewise-constant interval of demand. This process can be repeated indefinitely and thus provide gain-scheduled adaptive control for unreliable manufacturing systems with variable demands.

The performance of such a gain-scheduled adaptive controller is illustrated in this paper for a particular unreliable manufacturing system subjected to a particular piecewise-constant demand. The optimal short-run inventory levels embodied in the gain-scheduled adaptive controller for this system are determined using the genetic stochastic optimisation procedure described in this paper. Such genetically determined optimal short-run inventory levels are compared with the theoretically determined optimal long-run inventory levels of Bielecki and Kumar [4]. It is demonstrated that the performance of the gain-scheduled adaptive controller incorporating the 'look-up' table for the optimal short-run inventory levels is superior to that of a genetically optimised non-adaptive controller in this case.

2. Genetic Optimisation Procedure

The single-machine manufacturing systems under investigation are governed by differential equations of the form

$$\dot{x}(t) = u(t) - d \quad (1)$$

where $x(t)$ is the inventory level, $u(t)$ is the production rate, and d is the demand rate. Such systems are unreliable, with exponentially distributed time-between-failures and times-for-repair having respective mean values T_f and T_r . The maximum production rate is u_{\max} ; and it is assumed, initially, that the demand rate is constant. The inventory level, $x(t)$, is controlled when the machine is 'up' by generating the production rate, $u(t)$, in accordance with the following crisp control rules:

1. If $x(t) > x^*$, then $u(t) = 0$
2. If $x(t) = x^*$, then $u(t) = d$
3. If $x(t) < x^*$, then $u(t) = u_{\max}$

In these rules, x^* is the set-point of the crisp-logic controller. It is desired to find the optimal set-point,

$x_{\text{opt}}^* = x_{\text{opt}}^*(d, x(0))$, such that the expected value of the cost function

$$J(x^*) = \int_0^T \{c^+ x^+(t) + c^- x^-(t)\} dt \quad (3)$$

is minimised, where T is the task time,

$$x^+(t) = \max\{x(t), 0\} \quad (4a)$$

is the finished-parts surplus,

$$x^-(t) = \max\{-x(t), 0\} \quad (4b)$$

is the finished-parts backlog, and c^+ and c^- are weighting parameters. In solving this optimisation problem, it is assumed that both the mean times T_f and T_r are fixed and also that the demand is achievable, i.e., $d < u_{\max}$. It is evident that, when the machine is 'down', the crisp control rules are no longer effective and that the production rate, $u(t)$, is then zero regardless of the value of the inventory level, $x(t)$.

It is difficult to determine the optimal set-point, $x_{\text{opt}}^* = x_{\text{opt}}^*(d, x(0))$, by using conventional optimisation techniques. However, such optimal set-points can be readily found by using genetic algorithms. The crucial step in this genetic

optimisation procedure is the calculation of the expected value of the cost function, $J(x^*)$, defined in equation (3) for specified values of d and $x(0)$. This calculation can be effected by introducing the set, $\{\alpha_1(t), \alpha_2(t), \dots, \alpha_n(t)\}$, of scalar machine-condition variables. Each such variable, $\alpha_j(t)$ ($1 \leq j \leq n$), is equal either to unity (when the machine is 'up') or to zero (when the machine is 'down'). In each machine-condition variable, the times for these transitions between unity and zero (and between zero and unity) are instances of the exponentially distributed times-to-failure and times-for-repair with respective mean values T_f and T_r . Then, for a fixed value of the

set-point, x^* , in the control rules (2), the cost function in equation (3) is evaluated for each of the machine-condition variables in the entire set $\{\alpha_1(t), \alpha_2(t), \dots, \alpha_n(t)\}$ thus producing a set $\{J_1, J_2, \dots, J_n\}$ of corresponding cost functions. The expected value of the cost function over the entire set of n machine-condition variables is then given by the equation

$$E[J(x^*)] = \frac{1}{n} \sum_{j=1}^n J_j(x^*) \quad (5)$$

The Darwinian fitness, $\Phi(x^*)$, of the set-point, x^* , can then be conveniently defined by the equation

$$\Phi(x^*) = 1/E[J(x^*)] \quad (6)$$

Each such set-point can itself be conveniently represented by a string of binary digits in order to facilitate the genetic optimization procedure.

This optimisation procedure begins by randomly generating an initial population of binary strings in which each such string represents a set-point, x^* , in the control rules (2). Evolution is then caused to occur in this population of binary strings in accordance with the standard genetic operations of crossover, mutation, and selection. In this evolutionary process, the Darwinian fitness of each binary string is evaluated by substituting into equation (6) the expected value, $E[J(x^*)]$, of the cost function over the entire set of relevant machine-condition variables. This evolutionary process is allowed to continue until no significant further increase is obtained in the fitness of the fittest binary string. This string is then decoded, and thus provides

the optimal value of the set-point, x_{opt}^* , for the crisp-logic controller for the specified values of d and $x(0)$. It is evident that this genetic optimisation procedure can be repeated for any desired values of d and $x(0)$ within the operational envelope of the manufacturing system. In this way, the entire optimal set-point function, $x_{opt}^* = x_{opt}^*(d, x(0))$, required for gain-scheduled adaptive control can be readily obtained.

3. Illustrative Example

This procedure for the design of gain-scheduled adaptive controllers for unreliable manufacturing systems can be conveniently illustrated by considering the control of a particular single-machine manufacturing system governed by equation (1). In this case, $x(0) = 0$, $T_f = 5s$, $T_r = 1.5s$, $u_{max} = 5$, and the variable demand is piecewise-constant over intervals of duration 20s as shown in Figure 1; in addition, $c^+ = 1$ and $c^- = 2$ in the cost function defined by equation (3). The first stage in this design process is to determine the optimal set-point, $x_{opt}^* = x_{opt}^*(d, x(0))$, of the crisp-logic controller governed by equation (1) such that, for initial state $x(0)$ and constant demand d , the expected value of the cost function

$$J(x^*) = \int_0^{20} \{x^+(t) + 2x^-(t)\} dt \quad (7)$$

is minimised.

The 'look-up' table obtained for $x_{opt}^*(d, x(0))$ in this case, using the genetic optimisation procedure described in Section 2, is displayed in Table 1. In this procedure, the expected value of the cost function defined in equation (7) was evaluated over an entire set of $n=100$ machine-condition variables using equation (5); a population size of 100 was used in the genetic algorithm over 100 generations; and the respective probabilities of crossover and mutation were 0.6 and 0.003.

It is evident from Table 1 that, as the demand increases, the dependence of the optimal short-run inventory level on the initial state of the system becomes increasingly strong. The corresponding values of the optimal long-run inventory levels in this case, as determined by means of the theoretical results of Bielecki and Kumar [4], are shown for comparison in Table 2. These long-run levels are clearly different from the short-run levels shown in Table 1.

Table 2

d	x^*
1	0.00
1.5	0.00
2	0.54
2.5	1.74
3	4.49
3.5	14.63
4	∞

Table 1

$d \backslash x(0)$ x_{opt}^*	-4	-3	-2	-1	0	1	2	3	4	5	6
1	-0.03	-0.03	-0.03	-0.03	-0.03	-0.03	-0.03	-0.03	-0.03	-0.03	-0.03
1.5	-0.03	-0.02	-0.02	-0.02	-0.02	-0.01	-0.02	-0.02	-0.02	-0.02	-0.02
2	0.06	0.01	0.05	0.03	0.11	0.02	0.04	0.00	0.06	0.02	-0.02
2.5	0.51	0.62	0.61	0.64	0.62	0.71	0.63	0.65	0.60	0.56	0.59
3	1.42	1.44	1.41	1.54	1.55	1.61	1.76	1.56	1.51	1.52	1.44
3.5	2.31	2.24	2.45	2.73	2.69	3.08	3.12	3.26	3.27	3.12	3.00
4	4.25	4.05	4.37	4.16	4.00	4.25	4.74	4.84	5.36	5.38	5.95

In any event, the long-run levels cannot be used for gain-scheduled adaptive control because these long-run levels are independent of the initial state of the unreliable manufacturing system. However, the data contained in Table 1 for the optimal set-point function, $x_{opt}^* = x^*(d, x(0))$, can be readily implemented in the gain-scheduled adaptive controller. Thus, during each piecewise-constant interval of demand, the relevant optimal set-point for the crisp-logic controller governed by equation (2) is obtained from the 'look-up' table by using as $x(0)$ the set-point for the previous piecewise-constant interval of demand. This procedure yields, in this case, the piecewise-constant set-point profile shown in Figure 2. The performance of the resulting gain-scheduled adaptive controller can be conveniently assessed by evaluating the expected value, $E[K]$, of the cost function

$$K = \int_0^{140} \{x^+(t) + 2x^-(t)\} dt \quad (8)$$

over an entire set of 100 machine-condition variables for the adaptively controlled unreliable manufacturing system.

This expected value for the adaptive controller is $E[K] = 836.27$, which is smaller than the corresponding value of $E[K] = 856.10$ for the best obtainable non-adaptive controller. This non-adaptive controller was itself optimised by using genetic algorithms to determine the value of the constant inventory set-point ($x^*=2.09$) for the crisp-logic controller that minimises the expected value of the cost function given by equation (8) for the variable demand shown in Figure 1. These values of $E[K]$ clearly indicate that, in this case, the performance of the gain-scheduled adaptive controller incorporating the 'look-up' table for the optimal short-run inventory levels is superior to that of the best non-adaptive controller. However, it is important to note that – in any event – this non-adaptive controller is not practically realisable since its optimisation requires that the entire demand profile be known in advance. It is therefore remarkable that the practically realisable adaptive controller performs so well. Indeed, this would still be true even if – for some particular demand profile – the performance of the adaptive controller were inferior to that of the best obtainable non-adaptive controller.

The time-domain performances of the adaptive and non-adaptive controllers for a typical machine-condition variable are shown in Figure 3 and Figure

4, respectively, whilst the corresponding trajectories for the cost function, K , are shown in Figure 5. It is evident from Figure 5 that, in this case, the accumulated cost for the adaptive controller is significantly lower than that for the non-adaptive controller.

4. Conclusion

It has been shown that genetic algorithms can be employed to determine the optimal short-run inventory levels in unreliable manufacturing systems. Furthermore, it has been indicated that such inventory levels can be used as the set-points of gain-scheduled adaptive controllers for such systems. The performance of such a system has been illustrated for a particular unreliable system subjected to a particular piecewise-constant demand. It has been demonstrated that the performance of this adaptive controller is superior to that of a genetically optimised non-adaptive controller in this case.

References

- [1] B. Porter and C. Allaoui, "Genetic synthesis of optimal control policies for manufacturing systems", *Proc. World Automation Congress*, vol 4, pp 571-578, 1996.
- [2] B. Porter and T. Merzougui, "Evolutionary synthesis of optimal control policies for manufacturing systems", *Proc. IEEE Int. Conf. on Emerging Technologies and Factory Automation*, pp 304-309, 1997.
- [3] R. Akella and P.R. Kumar, "Optimal control of production rate in a failure prone manufacturing systems", *IEEE Trans. Auto. Contr.*, vol 31, pp 116-126, 1986.
- [4] T. Bielecki and P.R. Kumar, "Optimality of zero-inventory policies for unreliable manufacturing systems", *Op. Res.*, vol 36, pp 532-541, 1988.
- [5] J.R. Perkins and R. Srikant, "Scheduling multiple part-types in an unreliable single-machine manufacturing system", *IEEE Trans. Auto. Contr.*, vol 42, pp 364-377, 1997.
- [6] B. Porter and H. Moi, "Hybrid fuzzy/crisp-logic control of manufacturing systems", *Proc. IEEE Conf. on Emerging Technologies and Factory Automation*, pp 663-669, 1996.
- [7] B. Porter and N.N. Zadeh, "Genetic design of fuzzy-logic controllers for manufacturing systems", *Proc. IFAC Conf. on Control of Industrial Systems*, vol 3, pp 347-352, 1997.
- [8] B. Porter and N.N. Zadeh, "Evolutionary design of fuzzy-logic controllers for manufacturing systems", *Annals of the CIRP*, vol 46/1, pp 425-428, 1997.

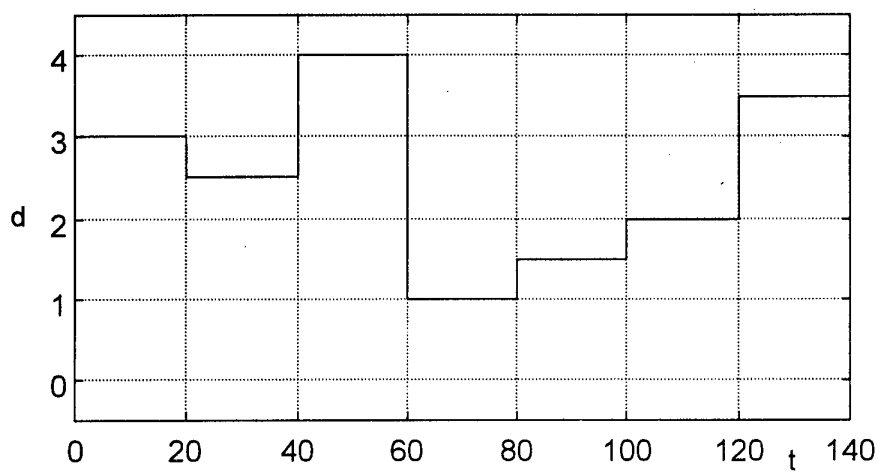


Figure 1: Demand profile

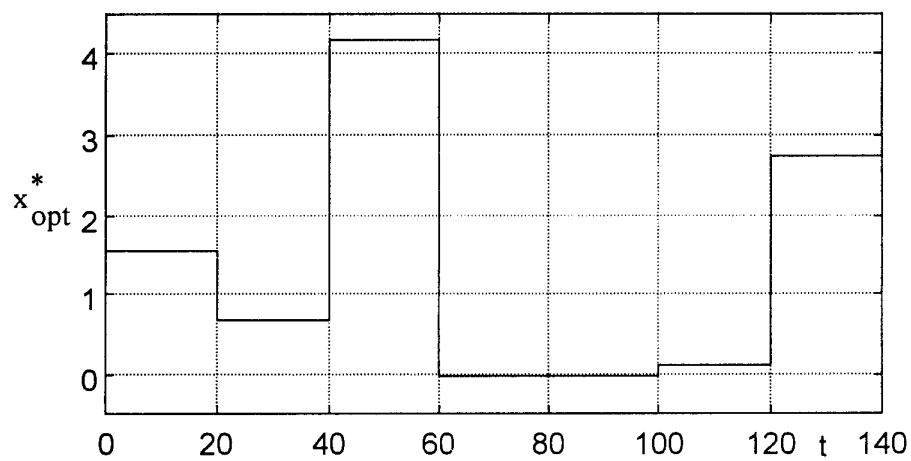
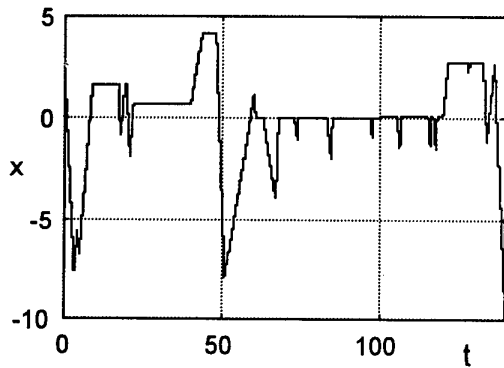
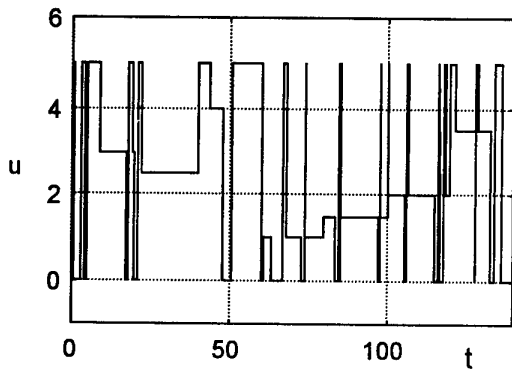


Figure 2: Set-point profile

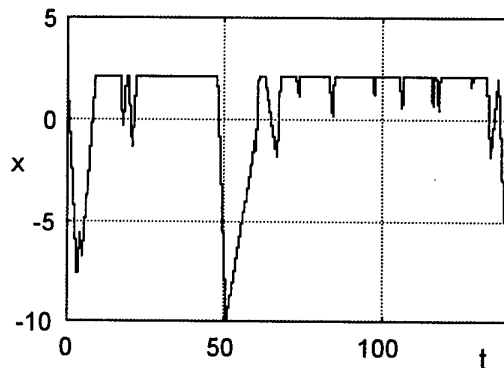


(a)

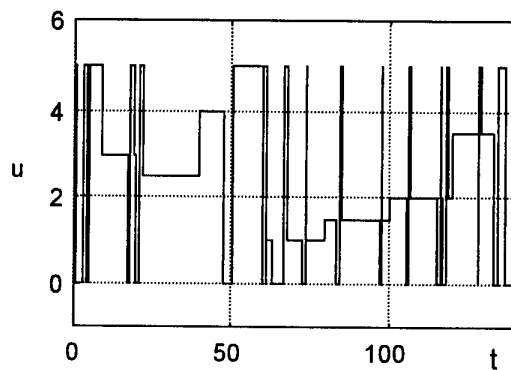


(b)

**Figure 3: Time-domain performance:
adaptive controller**



(a)



(b)

**Figure 4: Time-domain performance:
non-adaptive controller**

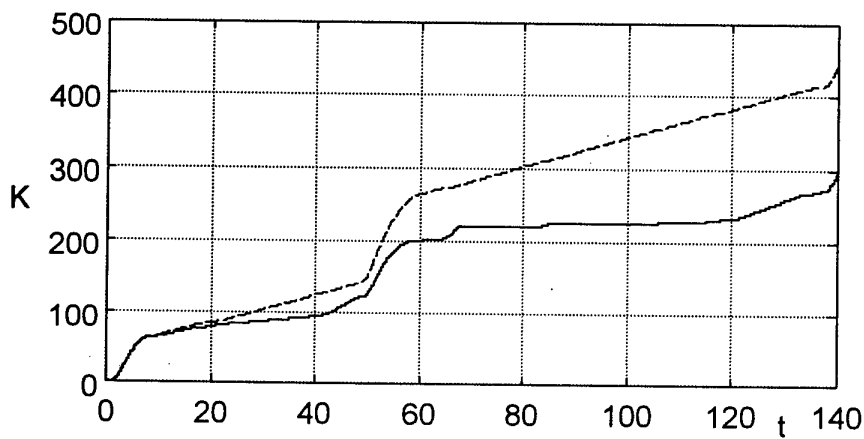


Figure 5: Cost function comparison
(full line = adaptive controller; dashed line = non-adaptive controller)

The Use of Electronic Commerce as a Strategic Tool in Intelligent Manufacturing Systems

Ergun Gide

School of Management

University of Technology, Sydney, Australia

E-mail: Ergun.Gide@uts.edu.au

Fawzy Soliman

School of Management

University of Technology, Sydney, Australia

E-mail: Fawzy.Soliman@uts.edu.au

Abstract

The development of Internet-based E-Commerce offers the most exciting business opportunities in the marketplace. Intelligent manufacturers must re-evaluate every aspect of their strategy and operations from customer service to marketing, product development to retailing, logistics to distribution. That's why the Internet-based E-Commerce is becoming essential for companies entering the cyber-marketplace. This study analyses the use of Internet-based e-commerce as a strategic tool and its possible implication on intelligent manufacturing systems.

1. Introduction

Organisations are facing a rapidly changing dynamic business environment and very fast advances in information technology (IT) while we are approaching to the third millennium. These changes have occurred due to increased global competition, significant advances in international business, and changes in political and economical environments around the world.

Increased internationalization in the business arena has had a major impact on business organizations. Accordingly, business operations all around the world have began moving from the traditional methods of communication to the Internet commerce (Gide & Soliman, 1998). Meanwhile, the business world is witness with the tremendous growth of the Internet and Internet-based Electronic Commerce from manufacturing to retailing, from insurance to health, from banking to travelling, from food to hospitality industry especially for the last two years (Soliman & Gide, 1997). Bottoms (1995) predicts that many executives may soon find their companies in the midst of a major transition from the

utilization of EDI (Electronic Data Interchange) as a strategic tool in supply chain management to a much more comprehensive Internet-based Electronic Commerce strategy.

The value of goods and services traded between companies over the Internet is expected to skyrocket from \$8 billion in 1997 to \$327 billion in 2002 in the US, according to a report from Forrester Research. Businesses are adopting inter-company trade over the Internet because they want to cut costs, reduce order-processing time, and improve information flow.

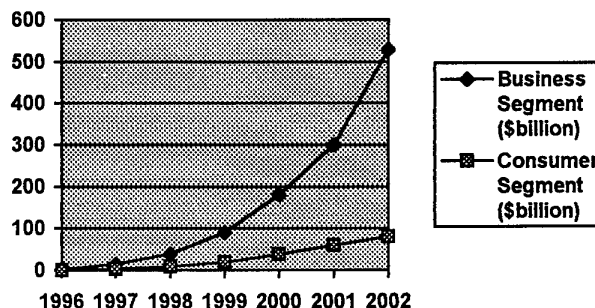


Figure 1. Worldwide Internet commerce revenues (business and consumer segments 1996-2002. source: IDC 1998).

According to a report issued by online researcher eMarketer (July 1998), currently there are approximately 60 million "active Internet users" worldwide, with Americans accounting for 37 million users. If U.S. figures are added for a total worldwide picture, the growth rate will more than quintuple, from 44 million in 1997 to 228 million by year 2002. The worldwide Internet Commerce revenues are shown in Figure 1.

2. The Business Process of Internet-Based E-Commerce in Manufacturing

There are no exact definitions of the Internet-based E-Commerce since it is still immature. However, one definition made by Kalakota (1996), Professor of Management at the University of Rochester and electronic commerce author, as "the process of converting digital inputs into value-added outputs". Basically, the Internet commerce business process involves taking information as raw material and producing value added information-based products or services out of the original raw information as shown in the following figure (Figure 2). So, electronic commerce refers to an on-line production process owned by intermediaries.

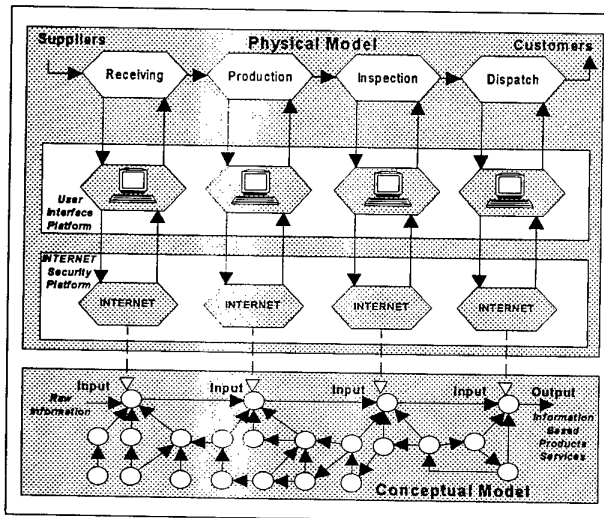


Figure 2. Illustration of the process of adding value to information in a manufacturing setting using the e-commerce.

The figure (Figure 2) shows that the two models (*Physical and Conceptual Models*) in a manufacturing setting are similar. In the Physical Model raw material enters the system and leaves as finished goods. In manufacturing the raw material and converting into finished products, the Internet-Based E-Commerce is used through two platforms (*User and Security Platforms*). In the Conceptual Model raw information is entered in the system and leaves as processed information (Soliman & Gide, 1997). Producers of information interact with services and other processed information, such as orders, payments or instructions. In reality, Internet commerce is about businesses and consumers

adopting a new process or methodology in dealing with each other. These processes are supported by electronic interactions that replace close physical presence requirements and traditional means.

3. The Internet Commerce as a Strategic Advantage

For gaining strategic advantage through Information Technology (i.e. Electronic Commerce) manufacturing managers must understand not just the technology but also the "value chain" in which their company operates. Information technology will have an impact on each activity along the value chain. In fact, information technology is transforming the way value activities are performed and the nature of the linkages among them. These basic effects explain why information technology (Internet) has acquired strategic significance and is different from the many other technological business use. Intelligent manufacturing management via E-Commerce to gain competitive advantage is shown in Figure 3.

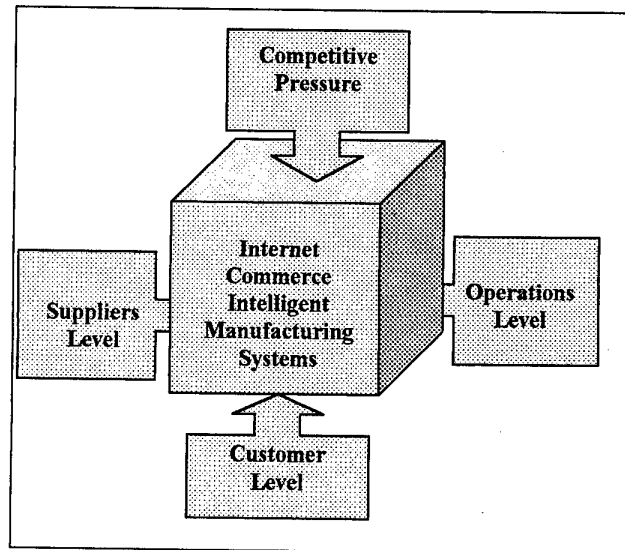


Figure 3. Intelligent manufacturing systems via e-commerce to gain competitive advantage.

The Internet can make a significant contribution to each components of a company's value chain (Cronin, 1994). To uncover and evaluate new avenues for competitive advantage through use of the Internet, companies need to analyze their relationships with suppliers and vendors, the existing role of information in the organization of the company, internal production mechanisms, and the points of contact with customers.

3.1. Internet Commerce Manufacturing: Suppliers Level

The Internet provides very fast, reliable connections to suppliers around the world. Companies can communicate with vendors in any location, without incurring additional communication costs. It is difficult to convey complex bids or cost estimates accurately over the telephone, and if the vendor is in a different time zone even scheduling telephone calls can be problematic. Large amounts of data are also cumbersome to transmit via telefacsimile. Even overnight delivery of information may be too slow when critical decisions are waiting to be made. Many vendors offer electronic pricing and ordering information to overcome these limitations. However, adopting one vendor's proprietary on-line system may limit a company's flexibility to change vendors.

In manufacturing, traditionally Design Engineering, Procurement and Production Departments communicate with each other using paper based methods. However the introduction of Internet-Based E-Commerce and its superiority of over traditional EDI is adding new dimension to reducing the cost of manufacturing. In a typical manufacturing setting Design Engineering Department supply design drawings and specification to Procurement Department to procure material, commence production, and ultimately deliver goods to customers as per orders. There are three types of flows in a general manufacturing setting. These are:

1. Material flow (examples are raw material from supplier, Work-In-Process and Finished Goods);
2. Clerical flow (examples are Drawings, Specifications and Bills Of Materials); and
3. Information flow (examples are information on parts, suppliers, customers and the industry).

Improvement in the movement of raw material, Work-In-Process and Finished Goods is likely to occur as a result of using the Internet-Based E-Commerce. The main benefit to manufacturing lies in using the Internet for the second and third types of flow.

The number of parts used in production could be in the order of thousands of items. These parts are usually purchased from suppliers on the basis of price, quality, and delivery on time and suppliers financial position and reputation in the industry.

Accordingly Material Procurement professionals must be equipped with timely and valuable information on

parts and their suppliers. The Internet-Based E-Commerce provides them with a fast and efficient way of obtaining comprehensive information of the market, feedback from the industry and the performance of suppliers (Soliman & Gide, 1997).

The following figure (Figure 4) illustrates how clerical and production information can be efficiently communicated throughout the supply chain using the Internet-Based E-Commerce.

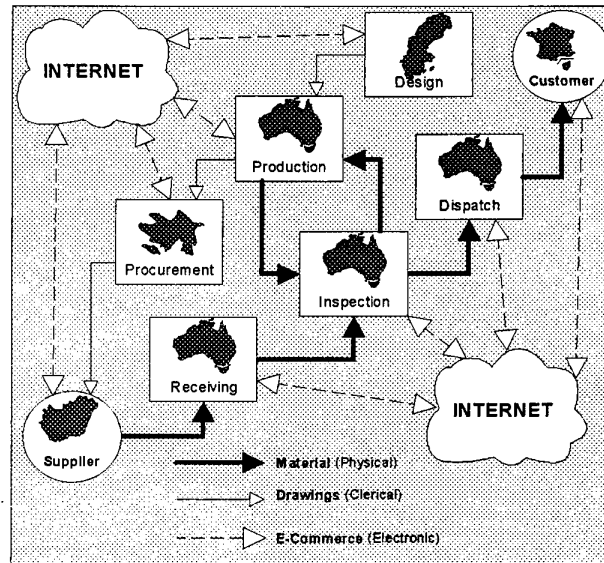


Figure 4. Supply chain communication in manufacturing using Internet-based e-commerce.

On the other hand, electronic distribution of software, publications, and other items provides immediate access to these products. On-line tracking of orders and inventory ensures that companies are aware of delivery dates, and reduces delays in the distribution process. Many companies have found that product support over the Internet significantly reduces the time lost due to system performance problems (Cronin 1994). For some companies, the efficiencies and cost savings generated by dealing directly with suppliers over the Internet have more than justified their investment in the network.

3.2. Internet Commerce Manufacturing: Operations Level

The global connectivity of the Internet offers companies immediate savings in long-distance

telecommunications. A dedicated Internet connection allows unlimited exchange of data and e-mail with locations around the world. Even a low-cost, shared dial-up connection with an hourly use charge is more economical than long-distance telephone charges. In the longer term, the ability to exchange information quickly and easily facilitates the relationships with business partners and customers, encouraging more joint ventures. For employees, connecting to an international information source promotes global awareness. It allows companies to monitor economic and political developments in countries targeted for market expansion.

Furthermore, information resources and discussion groups on the Internet provide employees with direct access to virtually unlimited advice and information. By helping them to answer questions and retrieve relevant materials, the network connection increases their productivity. The Internet also facilitates more effective deployment of human resources. Network links support telecommuting and allow small, remote offices to participate more actively in companywide programs and contribute to joint projects. When project teams are being formed, managers can select members based on their expertise, without regard to geographic location.

3.3. Internet Commerce Manufacturing: Customer Level

The Internet is a powerful tool for market research, for establishing new markets, and for testing customer interest in emerging products. Thousands of discussion groups and bulletin boards are available for keeping in touch with new developments through environmental scanning, as well as for direct contact with customers. Manufacturers and producers of electronic information or software can deliver these items instantly to customers and collect payment on the Internet. Electronic catalogues offer products and services to millions of users browsing through the network. Vendors can offer on-line help services and product support without additional expense of dedicated connections to customers. The Internet allows direct interactions with customers to be spread through many divisions of a company; technical and development staff, documentation providers, production workers, and researchers find out first hand how customers respond to company products. They can address problems and provide customer support as a team.

In addition to that, strategic use of the Internet based on an analysis of the value chain encourages companies to focus on areas where they can measurably improve

performance. If a company decides to distinguish itself through the quality of its customer service organization, the network can be a decisive asset in achieving this goal. If the emphasis is on developing and marketing innovative products, the Internet connection will contribute at a different point in the value chain. The benefits of the Internet will vary from business to business. One thing is certain that for companies seeking competitive advantage, the global network is essential management resource.

4. The Strategic Benefits of the Internet Commerce for Intelligent Manufacturing

In this rapidly changing environment, businesses are taking a look at their own organizations, structures, and processes in an effort to become more competitive. The Internet is a very useful tool for engaging in business activities. Many companies are using e-mail and group conferencing to engage in business process re-engineering projects. Maintaining good communication to exchange data and documents is critical in the re-engineering of business processes. The competitive benefits of the Internet Commerce for intelligent manufacturing are illustrated below in Figure 5.

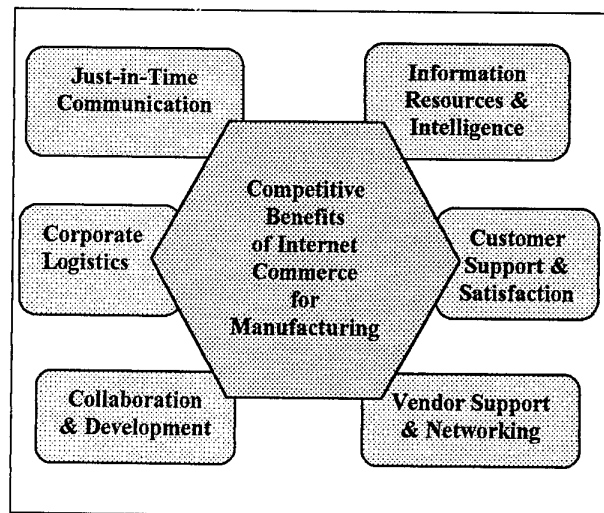


Figure 5. The competitive benefits of the Internet commerce for intelligent manufacturing

In addition, the ability to have the latest information about our marketplace and awareness of the state-of-the-art in our industry allows us to keep our competitive edge. Learning what other companies are doing, knowing the kinds of information available, and discovering new

markets can assist a company in maintaining a competitive advantage.

More companies use the Internet in the search for "best practices." As businesses try to become more competitive, many want to find existing practices that can help them improve their activities. Businesses can also use the communications abilities of the Internet to engage in a Total Quality Management (TQM) plan. Some companies use the Internet to maintain corporate process control across all company locations including even continents. Many companies use the Internet commerce tools to search for successful practices of corporate and product improvement.

4.1. Just-In-Time Communications

The Internet offers a business the opportunity for just in time (JIT) communications with people and organizations across the globe, enlarging the visibility of a business a thousand fold. Being on the Internet allows a company to truly have a world market. Good communications enable more global corporate management control, aiding in consistency of results. Companies can be in touch with suppliers, branches, and subsidiaries in an effort to exert more control over variables. Companies can establish, negotiate, and maintain standards online. As an Internet tool, E-mail is a low cost method for maintaining local, regional, national and international communication. Messages can be exchanged in minutes as opposed to days or even months using regular mail.

4.2. Corporate Logistics

Logistical concerns can dominate production planning and customer service issues for corporate. Since the Internet is the anywhere-anytime-network, employees, suppliers, customers, and others can keep in touch more efficiently. The use of e-mail and teleconferencing facilitates communication between markets. In addition, real - time communication is also possible. Using the Internet for communication removes distance and time barriers. This method reduces the need to be so aware of time zone differences and variations in the phone and mail systems of various countries. Using the Internet lessens logistical concerns because employees do not need to be in the same room or city for meetings. Listserver or group computer-conferencing software is another tool that can improve internal and external communications by helping to overcome logistical concerns.

4.3. Collaboration and Development

The development team and project participants often use the Internet to keep in touch, and to exchange data, programs, and working papers from any locations. The Internet also allows several small businesses to band together much more easily for product development. In another words, formation of partnerships among companies is increasingly common, and the Internet facilitates this collaboration for product design, vendor channels, research, and development. Collaborative approaches have been greatly enhanced by the Internet with its wealth of information, its capacity of supporting telecommuting and time-shifted communication.

4.4. Information Resources and Intelligence

With more than 20 million (1998) machines connected to the Internet, the system has a multitude of databases, Web sites, Usenet, Gopher sites, FTP (File Transfer Protocol) sites, Listserver discussion lists, and conferences, the amount information available is staggering. Scientific and research data is available in large quantities. Furthermore, some manufacturers find that the Internet is useful in helping employees learn new tasks and processes. There are many simulations, manuals, training aids, and tools available for software running on a variety of platforms, from UNIX tutorials to Windows tips and hints. There are also large quantities of instructional materials available on-line regarding the use of the Internet. Furthermore, having the most up-to-date information about markets and the state-of-the-art in industry allows companies to keep or increase their competitive edge. Competitive intelligence can be gained due to access to information on products, materials, new ideas and even the status quo in a given industry. What are other businesses doing? What kinds of information are available? Who are the main competitors in a specific business?

4.5. Customer Support and Satisfaction

One of the prime business uses of the Internet Commerce is in the area of customer support. In this highly competitive and dynamic global marketplace, the company that can reach and satisfy customers will have an advantage- and the Internet Commerce can help in maintaining relationships with customers. With its global reach, the Internet can assist business in locating new suppliers and keeping in better touch with them to aid, for example, in zero inventory planning. Customers can reach a company on their own schedules, 24 hours a day, 365 days a year and be able to obtain information

regardless where they are. Many companies maintain World Wide Web sites, Gophers, and FTP sites for customers use during working and non-working hours.

4.6. Vendor Support and Networking

The Internet provides a fast method for networking with vendors and suppliers, increasing speed and variety in our procurement process. With its global tentacles, the Internet can help businesses locate new suppliers and keeping better touch with them. In addition, small suppliers can network with and compete with larger, better-known suppliers. Furthermore, the Internet assists companies in maintaining low inventory levels because of speed of communications. Relationships with vendors and outlets can also be maintained via the Internet. Companies can arrange product delivery through the Internet, where companies can establish and support actual distribution channels.

5. Conclusions

It is a fact that that Internet-Based E-Commerce is still in its early stages but as we discussed early, it is becoming one of the most important strategic tools for manufacturing management. Businesses of all types and sizes can also find that the Internet serve a large variety of their needs as a strategic tool to gain competitive advantage over their rivals, including marketing, customer and vendor support, the exchange of information, and joint ventures for research and development.

With the aid of the Internet-based E-Commerce, companies also can develop new products, communicate in real time, take orders, receive electronic publications and documents, and retrieve data from specialty databases (Gide & Soliman, 1998). Businesses can find technical advice, establish and maintain business relationships, obtain market intelligence, provide electronic products directly. The Internet will undoubtedly be one of the most important ways of buying and selling goods and services soon.

6. References

1. Active Media (<http://www.activemedia.com>).
2. Cronin, M. J., *Doing Business on the Internet: How the Electronic Highway is Transforming American Companies*, Van Nostrand Reinhold, New York, 1994.
3. eMarketer (www.eMarketer.com).
4. Forrester Research's Business Trade & Technology Strategies Service (<http://www.internetnews.com/ec-news/cur/1997/07/3005-bb.html>).
5. Freeman, E., "How to Move E-Cash Around the Internet," *Datamation*, pp. 58-62, October 1996.
6. Gide, E., and Soliman, F., "Analysis of Conducting Business on the Internet," in *the Proceedings of Inet-tr'97 Conference*, Ankara, 21-23 November 1997.
7. Gide, E., and Soliman, F., "Intelligent Use of the Internet Commerce as a Competitive Advantage in Manufacturing," in *the Proceedings of IMS'98 Conference*, Sakarya, 6-7 August 1998, pp. 813-822.
8. Granger, M. J., and Schroeder, D. L., "Integrating the Internet into the Business Environment," *Internet Research: Electronic Networking Applications and Policy*, Vol. 6, No. 2/3, pp. 85-89, 1996.
9. Hayashi, A. M., "Is Corporate America Ready for E-Commerce?" *Datamation*, pp. 54-56, October 1996.
10. International Data Corporation, IDC (www.idc.com).
11. Kalakota, R., and Whinston, A. B., (1996), *Frontiers of Electronic Commerce*, Addison Wesley, USA.
12. Lynch, D. C., and Lundquist, L., *Digital Money: The New Era of Internet Commerce*, John Wiley & Sons, Inc, USA, 1996.
13. Moody, G., *The Internet with Windows*, Butterworth Heinemann Ltd, Oxford, OX, 1996.
14. Mougayar, W., *Opening Digital Markets*, CyberManagement, Canada, 1997.
15. Open Market Commercial Sites Index (<http://www.directory.net>).
16. Soliman, F., and Gide, E., "Impact of Internet-based E-Commerce on Manufacturing and Business Operations," in *the Proceedings of Inet-tr'97 Conference*, Ankara, 21-23 November 1997.

Contributions of ICT to Machine and Machine System Concepts

Airila, M.
Professor of Machine Design (Mechatronics)
Helsinki University of Technology
Department of Machine Design
Espoo, P.O.Box 4100, FIN-02015 HUT
Mauri.Airila@hut.fi

Abstract

The paper presents and demonstrates some ideas and results related to the application of ICT in machines and machine systems. The research problems presented and the early research results reviewed are based on a technology programme "SMART" which combines the mechatronics research efforts of several universities, research centers and enterprises in Finland. The target of the programme is to develop information technology intensive product concepts and design tools to implement them. The main driving force of the programme is to help SME-sized but globally active companies to achieve competitive advantage through effective incorporation of ICT in their future product concepts.

1. Introduction

This paper presents and demonstrates some challenges which emerge when Information and Communication Technology (ICT) is applied in machines and machine systems. Traditionally, mechatronics is regarded synonymous to robotics. Besides robotics, however, there are numerous potential applications for mechatronics aspects in industries. In the future it will no more be appropriate to speak about mechatronic machines and conventional machines because even simple hand tools can feature active and smart materials, sensors and displays. All machines and devices will be "mechatronized" to some extent.

The Finnish Government has a special strategic tool to encourage technological development and risk-taking especially in SME's. So-called technology programmes are driven by Tekes (Technology Development Center in Finland). The idea is to bring together SME type industries, universities and research centers to work on a relevant research area like mechatronics. A technology programme typically contains several generic projects

which generate public research results. The results are mainly methods and tools, to some extent also new design concepts. Besides generic projects, a programme includes numerous confidential enterprise projects. An enterprise project consists of in-house research and normally also subcontracting from a university laboratory. The results are typically confidential. The volume of a programme may vary from some 2 MECU up to 100 MECU. Financing the programmes is a joint effort of Tekes, industry, universities and research centers.

The discussion in this paper is mainly based on a four-year technology programme "Smart Machines and Systems 2010" ("SMART") which is going on during 1997-2000 with a budget of 8 MECU. The aim is to develop information technology intensive product concepts and design tools to implement them. Some 15 participating industrial enterprises develop their product concepts in confidential company projects. The goal is that the new product concepts provide a firm base for company R&D well into the 21st century. Simultaneously public research projects, driven by some 10 university and research center units, will provide raw material for the confidential projects. Some research topics and primary results from the public projects are reviewed in this paper. The author is responsible for the coordination of this programme.

2. Mechatronics: Fusion of Technologies

Three major technological leaps have occurred in history: the inventions of steam power, electric power, and information power. The steam engine liberated man from the limitations of muscle power, resulting in huge progress in manufacturing industry and transportation. The invention of electric power enabled distributed but effective manufacturing of products on a smaller scale. Information power substituted more flexible automation for the former fixed automation in processes and products. Machines can

take over routine or calculation-intensive intellectual operations to some extent.

Conventional industrial products like process valves, waste water pumps, elevators, paper machine systems, electric generators and forest harvesters typically feature fairly mature mechanical and electro-mechanical design due to the long development history of these domains. However, it is difficult to achieve clear competitive edge with traditional technologies. Exploitation of the potential of information and communication technologies will give new possibilities to enhance traditional products. During the last ten years a lot of effort has been taken worldwide to enhance product concepts on the basis of mechatronics principles. Advanced sensors, more effective control algorithms, increased computing power and increased use of telecommunication technologies have led to better performance, ease of maintenance and more sophisticated user interfaces of new machine generations. Also more effective computer aided design methods, e.g. well-trimmed 3D design software and rapid prototyping technologies, have been launched to facilitate and cut the development process of multitechnological machines and systems. Despite massive research efforts there is still big demand in industry for well-focused basic and applied research mechatronics programmes.

There are many reasons why the development and design of mechatronic machines is relatively difficult compared to conventional industrial products:

- ✓ added-value is made with ICT, and the necessary resources are under a very tough competition worldwide
- ✓ the development culture is multitechnological and nowadays even multiscientific: mechanical engineering, electronics hardware, software, system and control theory, electrical engineering, hydraulics, and human sciences. Traditionally the design and manufacturing cultures have been quite different in various domains.
- ✓ the development of the core technologies in mechatronics is rapid
- ✓ the integration of multitechnological rapidly developing technologies to systems is very challenging

3. Make Dust or Eat Dust

Foreseeing and forecasting the future is not very systematic in conventional machine workshops and SME's. Companies are used to reacting either rapidly or slowly to changes in their environment. Thinking by alternative scenarios, control navigation signs and several

operation alternatives is the proactive way to face the future and may lead to a more agile approach to new opportunities and threats. Some trends in ICT are fairly easy to foresee and do not require any special attention. Some changes like the rapid rise of Internet and its novel industrial application, the high growth rate of advanced digital wireless telecommunication, or the challenge of Linux to Microsoft have been more difficult to foresee. The incubation time of new ICT's is normally fairly long: one may think that practically all the important ICT inventions which will be available in 2010, already exist in some university or research center lab! Alternative scenarios are needed to discover these seeds and to generate enough agility "to be the early bird to catch the worm".

A generic project concentrating on the methods and tools of future research is established in the "SMART" programme. The goal is to develop relevant alternative future scenarios for the participating industrial companies to give background for their product concepts and process development. Especially the application potential of information and communication technologies in the next 15-20 years is the key aspect in the scenarios. It is very common that SME's have a fairly realistic picture of the trends in their core businesses. Outside the key technologies the enterprises' understanding of the prevailing or future technology trends may be poor. Working with alternative scenarios normally opens the eyes of the company management and the R&D people.

4. Modelling of Multitechnological Systems

Modelling, simulation and virtual prototyping have been hot topics in mechatronics research from its beginning. The reasons are easy to see: there is an increasing need to compress the lead time in product development. With more detailed modelling and associated simulation of systems it is possible to decrease the use of mock-ups, physical models and prototypes. Especially physical prototyping is very time and money consuming. The vision is that with sophisticated computer prototyping, "virtual prototyping", one can drop out some iteration stages with normal prototypes. It is not yet realistic to expect that physical prototypes are totally unnecessary. However, with realistic computer screen prototypes they may be postponed to the final meters of the product development process. In the future physical prototypes will be used as the last check of the validity of design results, compared to the past R&D culture where successive physical models, mock-ups and prototypes were needed to validate even the early stages of design.

In mechatronics the buildup of models and virtual prototypes is extremely challenging. Mechatronics is the art of integration, and in modelling this means the development of a common language, design interfaces and design tool compatibility. Non-compatible design languages, methods, tools and software prevail in the main domains like mechanics, electronics, hydraulics, controls etc. Staff for the various domains is recruited from different technological cultures, because strict faculty borders in the universities and other education institutes traditionally separate mechanical engineering, electrical engineering, chemistry and so on. Accordingly, the requirements for design inputs and outputs vary depending on the design domain. Truly concurrent engineering is not possible if you have to transfer data manually from one software to another, or modify the outputs of one software in order to prepare it for the input of another. The vision should be that you have a common digital product model and all the design domains have access to the model. During the design process all the domains contribute to the model in real-time. In simple one-technology products this procedure is already industrial routine but in most mechatronics machines and machine systems just a remote vision.

In the SMART programme the generic problem of submodel integration to the system model is approached through simplified multitechnological pilot cases. For example combined electromagnetic and mechanical modelling and simulation are demonstrated with an electric generator set in the "MAGEN" project. Integrated electro-hydraulic, control systems and mechanical modelling and simulation are tested with a paper machine variable crown roll in the "MATEL" project. Mechatronics modelling of an elevator landing door for condition monitoring purposes is studied in the "MAHIS" project. Especially the interaction of mechanics, sensors and DSP is in the focus of this project. The basic research idea is to learn a lot from these pilot cases and then formulate better generic design methods, rules, tools and data exchange formats for industrial R&D applications in order to approach "the common design language" of all design domains. A brief description of the projects follows. There are also other subprojects which concentrate for example on vibro-acoustic modelling and on modelling of wear of some critical mechanical components.

The major challenge and risk for this project group is the item of generalization. It is not an easy task to draw generic conclusions of the very specific case studies under different technology domains. However, the first step to the correct direction is always the most important one because there is a lot of effort and learning behind it.

4.1. Case MAGEN

Interaction of electro-magnetic and mechanical structure of a generator is modelled using the basic parameters of a commercial generator set. I-DEAS is used as a mechanical design software and an application-specific university software (developed at Helsinki University of Technology, Laboratory of Electromechanics) is used for electro-magnetic field modelling. General understanding of the prevailing phenomena is already achieved and an interface for relevant softwares will be built. This interface will be one building block in the long line where modelling blocks for a mechatronics system are developed in the long run. Some general conclusions will be drawn about the integration of two important technology domains in electro-mechanical design.

4.2. Case MATEL

The interaction between a hydraulic system and a complicated mechanical system with hybrid sliding bearing shoes is studied. The industrial pilot is a paper machine variable crown roll which actually is a massive sliding bearing system with remarkable oil flow and associated massive static and dynamic forces. The oil flow in the bearing and the positions of the bearing shoes are defined by complicated hydro-mechanical phenomena. Understanding of these phenomena and the bearing film formation is increased and the interaction of hydraulic and mechanical forces can be modelled with some precision. The results of this case study will have certain generic implications to other hydro-mechanical modelling and simulation, too.

4.3. Case MAHIS

The industrial case is a normal commercial elevator and especially its landing door. Modelling of the door is an iterative process from a simple kinematic model to a multitechnological complicated model including flexible parts, nonlinearities, actuators and the control system. Modelling is performed with commercial software (I-DEAS and ADAMS) and verified by laboratory measurements with a test door. The final goal is to develop a model which can be used for diagnostics and maintenance purposes. The model and the associated simulation results are used as a reference for normal operation activities. For example, opening the landing door will cause remarkable vibration in some parts of the door. A signal from a sensor fixed on the vibrating area can be analyzed and processed.

When a fault situation appears, a difference between the sensor signal and the modelled signal can be seen. Successful exploitation of this idea requires a huge amount of historical data from the field to determine the tolerances and normal noise of the relevant signals.

The special challenges in this application are e.g. sheet steel structures with large tolerances and flexible elements. Also the environment of an elevator is non-typical compared to most machines because two identical environments do not exist in practice.

5. Advanced user interfaces

User interfaces (UI's) are one of the most potential items to apply ICT on machines and systems. Limitations in current UI's are due to two reasons. First, with traditional technology it was possible just to design user interfaces based on buttons, levers and gauges. It was not possible to integrate any intelligence from the user's point of view. Second, engineering people did not have the methods and tools to deal with the user's values, preferences and limitations. A remote controller of a TV set is a typical example of unsatisfactory UI design: all functions are packed in the same way in the controller without any preferences for the commonly used operations, the signs are too small especially for a dark room, etc.

With ICT, you can enhance the interfaces and take the user's viewpoints better into account. Communication technologies like Internet applications can effectively be used for all kinds of "remote" interfaces. Pilot cases like a welding generator user interface, process valve maintenance interface, elevator user interfaces, a gasoline station delivery pump user interface etc. have been developed simultaneously with a generic research project. Other applications like a forest harvester's training simulator are being developed.

There are two challenging research problems in this field. First, how to translate the user's values and expectations into the technical language. Second, what will the new UI technologies be and how are they applied in machine environments.

6. Dependability of Software and Electronics Hardware

In other public projects dependability and reliability design methods for machine electronics hardware are developed. Simple but systematic methods for producing, testing and documenting real-time software effectively are also studied. Especially new electronics design and testing

methods and tools are demonstrated in industrial pilot cases like forest harvesters and stone crushers. In these cases and applications the reliability requirements for electronics and also for software are much tougher than those typical of most automotive applications. To create product concepts with extensive electronics hardware and software, still maintaining good reliability and functionality, requires a new culture in machine workshops. The "SMART" projects help industrial enterprises to create new design and manufacturing environments.

7. Conclusion

Extensive use of ICT is a potential but difficult way to enhance the competitive edge of conventional machines and machine systems. Mastering the multitechnological development culture of mechatronic products is a big challenge especially to SME's. Active research is a powerful tool to convert new ideas and concepts into engineering practice. Coordinated research efforts can be encouraged by the government and achieved through technology programmes. A lot of research power can be concentrated on research focuses and the cost can be shared between several companies instead of doing redundant research. All research problems cannot be solved during a 4-year programme but many new initiatives can be taken.

The Internet-sites of the programme are:
<http://www.machina.hut.fi/smart/>

Keywords: mechatronics, smart machines, machine intelligence

Training on Programmable Instrumentation for a Curriculum of Electronic Engineering.

P. Marino

Doctor on Telecommunications
Engineering
pmarino@uvigo.es

J. Nogueira

Telecommunications Engineer
nogueira@uvigo.es

H. Hernandez

Electronic Engineer
hhdez@mixteco.utm.mx.

Abstract

The authors present an ATE system designed for teaching practices about programmable electronic instrumentation, by means of GPIB and VXI instruments connected to a local area network (LAN). The aim of this system intended for students of electronic engineering, is the introduction of more relevant technologies involved in hardware instrumentation for ATE applications, besides the handling of their software environments for developing programs.

1.- Introduction.

Teaching electronic instrumentation for engineering students, has a great impact about their basic training on technologies oriented to design systems for: process control, product verification, services operation, quality analysis, etc., over all economic sectors. The growing advance in microelectronics given its continuous reduction in cost and increasing processing power and lower size, with higher performance of software packages, have boosted the presence of powerful systems for automated test equipment (ATE), based on programmable instrumentation [1].

From 1965 when HP Company introduced its HP-IB bus, rack-and-stack programmable instruments were "de facto" standardized, until 1975 when was reached their "de jure" standard called IEEE 488, also popularly named GPIB (General Purpose Interface Bus). The limitation of this standard to bus physical connection (hardware) generated in 1987 an extension of its first version, now called IEEE 488.1, in order to ease instruments programming (software) by means the standardization of: message interchange protocols, data formats and syntax, state reports and general commands for diverse kind of instruments. This new version named IEEE 488.2 was unable for designing ATE systems entirely compatible, and for this reason in 1990 the SCPI (Standard Commands for Programmable Instruments) standard defined a single conceptual model for designing programmable

instruments. Simultaneously with advances in designing software for compatible ATE systems, efforts were made for increasing the processing power of GPIB instruments upgrading the byte rate of bus transfers (less than 1 MBps), until 1987 that a group of electronic instrumentation manufacturers introduced the VXI architecture, which has modular instruments over electronic cards that plug in a chassis (mainframe), able to reach a byte rate of 40 MBps [2].

In 90's decade programmable instrumentation based on GPIB and VXI buses has reached a great spread, allowing ATE systems design with multiple computer platforms and several operating systems, creating the "virtual instrument" concept. Currently the advance impulse for GPIB performances and new architectures for programmable instruments is sustained from manufactures, users and researchers. For example, National Instruments manufacturer introduced respectively the HS488 specification in 1993 oriented to reach a maximum byte rate of 8 MBps in GPIB, and the PXI (PCI eXtensions for Instrumentation) architecture in 1997, based on Compact PCI [3][4], for modular instruments over electronic cards.

2.- ATE system description.

In their digital communications laboratory the authors have designed a programmable instrumentation system (SIP) based on IEEE 488 (GPIB) and VXI (VME eXtensions for Instrumentation) buses, where the GPIB bus connects all programmable instruments to laboratory's PCs by means a LAN [5]. The interface between LAN and GPIB bus is made with the Gateway LAN HP-IB HP E2050 [6]. The VXI bus [2][7][8] is configured in a mainframe for instrument modules in size C cards, and connected to the LAN through the GPIB bus, being its software development tool the environment VEE 4.0 from HP [9][10][11]. The figure 1 shows the ATE system configuration (SIP).

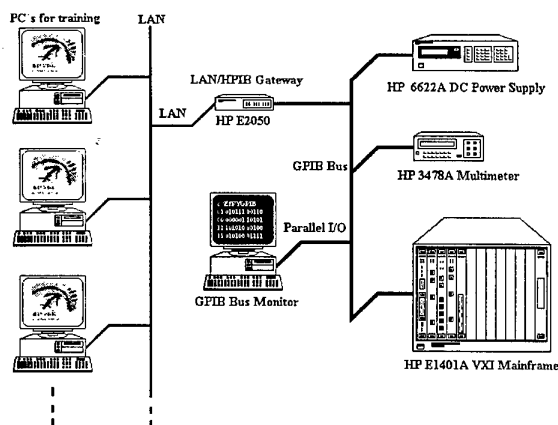


Figure 1. ATE system configuration (SIP) of programmable instrumentation laboratory.

The gateway connects lab's PC network to GPIB bus following client/server model [2], where each PC performs as a client and the gateway as server [6][12][13]. In this way applications running in clients can communicate with instruments based in GPIB bus in a transparent mode through LAN. This allows the access of several students to programmable instruments and sharing in this way the SIP resources. The gateway can be installed in any place of network, depending on instruments location and GPIB's cable length. Instrument identification is reduced to a simple logical address.

Table 1 summarizes the features of equipments that conform the SIP: two GPIB rack-and-stack instruments (DC power supply [14] and multimeter [15]), a VXI mainframe [3][7][16] with eight connected instruments ([14][15] and [17] to [25]), the gateway, and a PC with WATCH_GPIB software developed by the authors that performs the bus monitor function (paragraph 4).

Figure 2 depicts the software/firmware architecture of SIP where each client computer, under operating system Windows 95/NT and with VEE tool, manages the intended programs to control instruments (SICL: Standard Instrument Control Library) and LAN access (TCP/IP). The gateway has the network server software and adequate firmware for implementing the interface between instruments and LAN. The rack-and-stack GPIB instruments include the firmware with bus drivers. Command module (slot 0 of chassis) from VXI mainframe [17][22] incorporates the needed drivers for VXI/GPIB interface. The PC Bus Monitor only takes the signals from GPIB bus lines for displaying them on the screen (paragraph 4).

3.- Development of training program.

The growing technological development in the programmable instrumentation field, has allowed to

authors the implementation of applied research projects with this kind of instruments [1], and applications oriented to teaching electronics. In this way one of largely applications of VXI bus has been the automation of measurement and testing over electronic circuits implemented by the students. Simultaneously have been designed practices oriented to evaluation and analysis of GPIB bus activity. The students have access to SIP through PC's connected to LAN, with the VEE programming tool and SICL libraries (Figure 2), that respectively allow implementing the measurement and testing application and mastering the instruments. Also the students can see the commands and data behavior through GPIB bus by means a PC devoted to this task (Figure 1: Bus Monitor).

Table 1. Features of equipments that conform the SIP.

Instrument	Connection	Characteristics
HP 6622A DC Power Supply	GPIB	2 Outputs of 80 W, at 7V@10 A, 20V@4 A or 50V@2 A, 20V@4A
HP 3478A Multimeter	GPIB	2&4 Wire Ω ; Vdc/ac; 3 A@ 250V
HP E1401A High Power Mainframe	VXI/GPIB	C Size, 13 slots, connector P1/2
HP E1406A Command Module	VXI	GP-IB, RS-232, slot 0; 2MB Ram. Message-based Controller.
HP E1428A Oscilloscope	VXI	2 channels, 1Gsa/s 250 MHz
HP E1410A Multimeter	VXI	2 & 4 Wire Ω , Vdc/ac, True RMS from 20Hz to 1MHz
HP E1420B Universal Counter	VXI	200 MHz / 2ns; 9 digit resolution.
HP E1445A Function Generator	VXI	13 bit resolution, 40 Msa/s; 256 Ksa waveform segment Memory.
HP E1490C Reg. Based Breadboard	VXI	16 bit register-based interface, P2 connector.
HP E1465A 16x16 Relay Matrix	VXI	16x16 two-wire; 1 A, 200V signal switching
HP E2050A Gateway	GPIB/LAN	GPIB Instrumentation via LAN; SICL/VISA support.
GPIB Bus Monitor	Parallel I/O	486 PC, RAM 16 MB, I/O port.

The VEE (Visual Engineering Environment) tool is a graphic programming language particularly designed for driving programmable instruments. When the instruments are connected to GPIB bus, the student send then commands and data following the training program by means a LAN's PC. That PC will receive the replay and will perform data analyzing, displaying graphic results or storing data for a late processing.

For easing the control of programmable instruments in the development of ATE systems, usually are selected high level programming languages such as C, C++, Visual Basic, and so on. In this application is used the VEE programming language that allows simplifying the task of interface design, data acquisition, processing and displaying of results.

There are three control types of instruments in VEE [26][27][28]: Direct I/O, Drivers, and PC Plug-in I/O, which main features are shown in table 2. Laboratory's practices have been designed in order to introduce the students easily about the three control types and adequate

them to application needs and available tools. In this way is justified this application does not use the PC Plug-in I/O alternative given it needs a particular card (VXIplug&play) for implementing the interface, on the contrary to the cases of Direct I/O and Drivers. Although Direct I/O requires the knowledge of SICL's instructions, nevertheless provide a high communication speed and does not need the instrument driver, being for that the control type more frequently used in advanced practices. Otherwise VEE gives a new object called Multidevice Direct I/O that gets the control of several instruments through the edition of only one object. The controllers can be the control panel of the instrument (Panel Driver) or a part of controller (Component Driver). In this application the use of instrument control tools is oriented to teaching, and handling control panels is very important given that students learn to operate the whole choices of each instrument easily. When there is no enough knowledge about SICL's instructions or choices of an instrument, the Component Driver is the best solution because provides higher speed and only send and receive the needed data for implementing a particular task. Also this object has a list of instructions and information for supporting the learning about choices of each instrument.

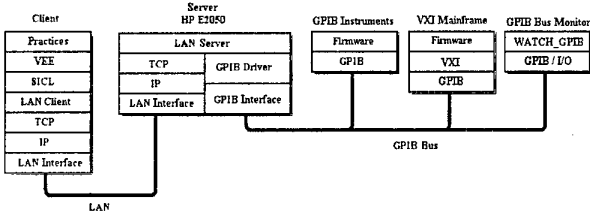


Figure 2. Software/firmware architecture of SIP.

4.- GPIB bus monitor.

The programmable instrumentation GPIB bus is a parallel connection bus in which all devices share the line signals [3][5][29], and requires the existence of some equipment for mastering those signals. Each connected device can listen, talk, control or make combinations of these three functions:

- Listener: This kind of device takes data and command from bus once addressed in this operation mode from the controller.
- Talker: Such as device send data through the bus to active listeners once addressed in this operation mode by the controller. At a given time only one device like this can be active on the bus.
- Controller: Is devoted to manage the bus, send commands, request the state of devices and controlling the data flow. For requesting an action to a device, the controller must put previously its logical address on the bus.

Table 2. Comparison between control types of instruments.

VEE Objects	Access to Instruments	Advantages	Supporting Interfaces
Direct I/O	Direct communication with the instrument	High communication speed. Allows to control anyone instrument.	GPIB, Serial, VXI and LAN.
Plug-in I/O	Requires a controller of the instruments that fits into VXIPlug&play standard	High speed of communication. Controllers are reusable for multiple application programs	GPIB and VXI
- Panel Driver - Component Driver	Requires a controller	Easy of using. Higher communication speed with component driver.	GPIB and VXI

The GPIB Bus Monitor (Figure 1) designed for teaching the IEEE 488 instrumentation bus, allows to display in real time, and without lost of information the signal lines that conform the GPIB bus. Given that a device only can access to the bus when is addressed, the GPIB Bus Monitor must not be a bus device in order to be able for reading its state continuously, and for this reason must not have any address, therefore does not exist from the controller and the whole bus devices point of view.

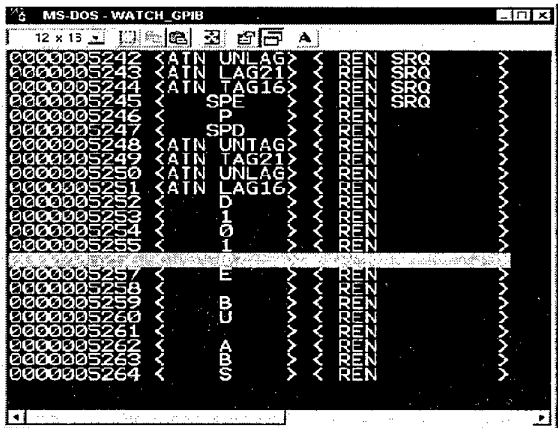


Figure 3. Screen of WATCH_GPIB program.

The GPIB Bus Monitor has been implemented by means of a PC under MS-DOS (Table 1). The GPIB interface cards able to connect a PC to the bus do not allow the access to it in a different time to the card has been addressed by the controller, and therefore are not useful for this purpose. For this reason is used an I/O Card adapted for reading the eight data lines and the eight control lines of GPIB bus. The Bus Monitor runs the WATCH_GPIB program that allows gathering and displaying in real-time the available data on GPIB bus, or displaying stored data in a file (Figure 3). This program loads in the computer memory an interrupt control routine and associates it to parallel port (IRQ7). The line SRQ (Service Request) from GPIB bus [5][8] is used to fire the interrupt routine and read the data from bus. For avoiding the possible loss of data because of GPIB bus higher speed compared with the reading speed of a conventional parallel port, the interrupt routine of WATCH_GPIB

program stops temporarily bus activity until reading the suitable data.

Using the GPIB Bus Monitor the students can visualize the commands and data that is sending through the bus a particular instrument from SIP (Figure 1).

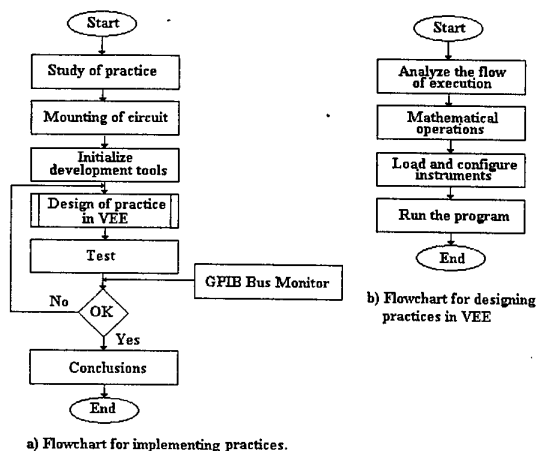


Figure 4. Flowcharts for implementing and designing laboratory practices.

5.- Implementation of practices.

The practices are designed in such a way that students can handle the development environment and visualize the GPIB bus. The two first practices are oriented to introduce them the VEE tool and explaining SIP configuration. Both are shown in auto-learning form and introduce step-by-step the method of using the VEE environment, and the control of instruments for making the practices, according the flowchart of figure 4a.

Following practices allow to students developing their own programs using existing tools, and at any time they can access directly to the SIP for connecting their electronic circuits under test. For example, the practice three is oriented to design a VEE program using the needed instruments for implementing Bode's diagrams (module and phase) of a RC circuit frequency response. Also show to students the choices to identify and compare the three control types of instruments (Table 2), and is explained the way VEE objects are connected, following respectively the flow of execution and sequence. Is emphasized the control of instruments (Figure 4b) with the aim of students can identify correctly the working tools. The results of this practice there are depicted in figure 5. This interaction with development environment allows to students a better use of graphic language and handling powerful mathematical functions provided by VEE.

Other example is practice nine, devoted to the automated testing of electronic boards, in which the

students have a board designed for teaching electronic devices, with the aim of designing a graphical interface able to display the results obtained from testing the whole components of board. Basically the control of instruments is made given input signals to the board and, supported by HP E1465A relay matrix switch module [20], implementing the right connection of instruments for making measurements of resistance, AC/DC voltages and currents, period, frequency and polarity test of diodes. The results are shown in figure 6.

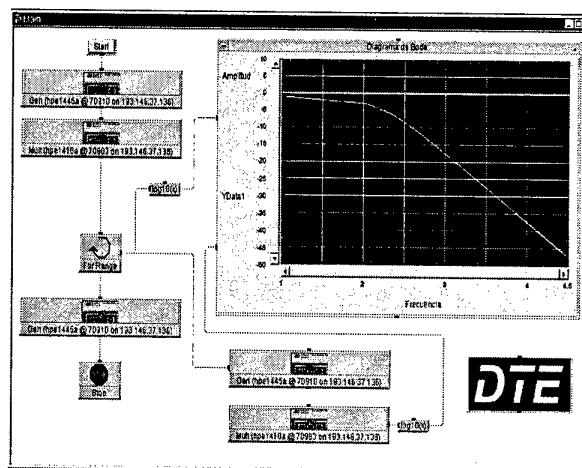


Figure 5. Instance of a practice in VEE

In each practice is optional the use of GPIB Bus Monitor, that shows continuously the bus information, sharing this task with bus monitoring function provided by VEE, that is an useful tool when SICL instructions are applied.

6.- Background requirements.

The set of computer assisted practices designed for teaching programmable instruments to students, requires from them the following previous background:

- Circuits theory.
- Basic electronic foundations and electronic components.
- Experience using manual electronic instrumentation (Oscilloscope, multimeter, function generator, etc.).
- Communication protocols for understanding the SIP configuration which have been trained.
- Performances of HP-VEE working environment.

7.- Results and future developments.

From the point of view of students the results are:

- Accessing to high cost and modern programmable instrumentation equipment.

- Training in the use of programmable instrumentation, currently unavoidable in a growing number of enterprises.
- Knowledge acquisition about a largely used instrumentation bus.
- Use of instrumentation buses like general communication resources if it were needed (i.e.: file transfers between computers).
- Displaying an instrumentation bus control signals, besides implementing electronic circuits testing.
- Generalization of SIP from general purpose practices to more specific ones such as power electronics, engines control, network analysis, etc.

Future developments about new advanced practices and the SIP configuration are:

- Using a VXI register-based breadboard module [25] for designing new compatible instruments (i.e.: A/D and D/A converters, sensors and effectors conditioners, etc.).
- Implementing automatic evaluation of student throughput during their training time.
- Including the new PXI bus for programmable instrumentation (paragraph 1).
- Migrating compatible instrument controllers to VXIplug&play standard currently in growing acceptance, and using VISA (Virtual Instrument Software Architecture) libraries [2][3][30].
- Remote training through Internet over the developed SIP. Experiments with Mixteca Technological University (Oaxaca, Mexico) are started.

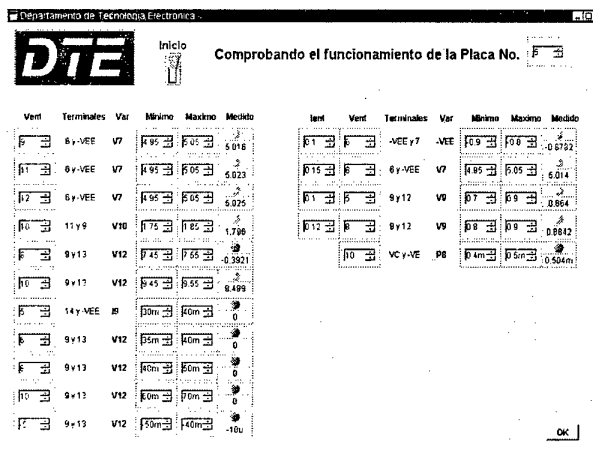


Figure 6. Interface of automated testing program for electronic boards

8.- Conclusions.

The use of communications networks for implementing laboratory practices based on programmable

instrumentation, allow to introduce the electronic engineering students in designing, configuring, and developing distributed ATE systems. This work introduces a programmable instrumentation system (SIP) development with GPIB and VXI instruments connected to PC's by means of a LAN. The training program is started with the introduction to knowledge of VEE programming tool, and follows implementing test and measurements over electronic circuits designed by students. Also are added practices for evaluating and analyzing GPIB's bus signals.

Finally basic knowledge required from students are defined in order to obtain the best progress from practices, and are analyzed the obtained results from the point of view of students. Also are introduced the future developments that authors are involved for improving both programmable instrumentation practices and ATE system that runs them.

9.- Acknowledgements.

This work has been sponsored by R&D NATIONAL SECRETARY AND CICYT from CENTRAL GOVERNMENT (Madrid, Spain) inside of research project, Ref. TIC97-0414.

10.- References.

- [1] Mariño, P. & Domínguez, M. A.: "Image Processing and Automated Testing in Flexible Manufacturing Systems". *Proceedings of the 37th SICE Annual Conference*, IEEE98TH 8377, pp. 1121-1126, Chiba (Japan), July 29-31, 1998.
- [2] HEWLETT PACKARD: *Test System and VXI Products Catalog*. Hewlett-Packard Company, 1997.
- [3] NATIONAL INSTRUMENTS: *Instrumentation Catalogue: Measurement and Automation*. National Instruments, 1998.
- [4] NATIONAL INSTRUMENTS: *PXI Specification Rev.1.0*, National Instruments, 1997.
- [5] Mariño, P.: *Enterprise-wide communications: standards, networks and services*. RA-MA, Madrid (Spain), 1995.
- [6] HEWLETT PACKARD: *HP E2050 LAN/HP-IB Gateway*. Hewlett-Packard Company, 1996.
- [7] Black, J. (editor): *The system engineer's handbook*. Academic Press, 1992.
- [8] Mandado, E., Mariño, P. & Lago, A.: *Electronic Instrumentation*. Marcombo, Barcelona (Spain), 1995.
- [9] HEWLETT PACKARD: *Building an Operator Interface with HP VEE*. Hewlett-Packard Company, 1995.
- [10] HEWLETT PACKARD: *Exploring HP VEE*. Hewlett-Packard Company, 1995.
- [11] HEWLETT PACKARD: *How to Use HP VEE*. Hewlett-Packard Company, 1995.
- [12] HEWLETT PACKARD: *Installing the HP-IB Interface*. Hewlett-Packard Company, 1994.
- [13] HEWLETT PACKARD: *HP 82335, 82340 & 82341 HP-IB Interface*. Hewlett-Packard Company, 1996.

- [14] HEWLETT PACKARD: *Operating Manual, System DC Power supplies, HP models 6621A, 6622A, 6623A, 6624A and 5527A*. Hewlett-Packard Company, 1993.
- [15] HEWLETT PACKARD: *HP 3478A Multimeter: Operator's Manual*. Hewlett-Packard Company, 1988.
- [16] TEKTRONIX: *VXIbus System Specifications* Revision 1.4. Tektronix Inc., May 1992
- [17] HEWLETT PACKARD: *High-Power Mainframe HP E1401A: User's/Service Manual*. Hewlett-Packard Company, 1992.
- [18] HEWLETT PACKARD: *HP E1410A 6 1/2 Digit Multimeter: User's Manual*. Hewlett-Packard Company, 1992.
- [19] HEWLETT PACKARD: *HP E1445A Arbitrary Function Generator*. Hewlett-Packard Company, 1992.
- [20] HEWLETT PACKARD: *16x16, 4x64, and 8x32 Relay Matrix Switch Modules HP E1465A/E1466A/E1467A: User's*
- [21] HEWLETT PACKARD: *C-Size VXIbus Systems: Configuration Guide*. Hewlett-Packard Company, 1994.
- [22] HEWLETT PACKARD: *Command Module HP E1406A: User's Manual*. Hewlett-Packard Company, 1994.
- [23] HEWLETT PACKARD: *Universal Counter HP E1420B: User's Manual*. Hewlett-Packard Company, 1994.
- [24] HEWLETT PACKARD: *Digitizing Oscilloscope HP E1428A: User's Manual*. Hewlett-Packard Company, 1994.
- [25] HEWLETT PACKARD: *HP E1490C C-Size VXIbus Register-Based Breadboard Module: User's Manual*. Hewlett-Packard Company, 1996.
- [26] HEWLETT PACKARD: *HP I/O Libraries*. Hewlett-Packard Company, 1996.
- [27] HEWLETT PACKARD: *Controlling Instruments with HP VEE*. Hewlett-Packard Company, 1998.
- [28] HEWLETT PACKARD: *Getting Started with HP VEE*. Hewlett-Packard Company, 1998.
- [29] Caristy, J.: *IEEE 488 General Purpose Instrumentación Bus Manual*. Academic Press, 1989.
- [30] Helsel R.: *Visual programming with HP VEE*. Hewlett-Packard Professional Books, third edition 1998.
- manual*. Hewlett-Packard Company, 1993.

Method and Software for Teaching Multibody Dynamics in Mechatronics Courses

Doru TALABĂ, Ion VIȘA

University Transilvania of Brașov, ROMANIA

talaba@unitbv.ro, visaion@unitbv.ro

Abstract

The paper presents a method for deriving and integration of the dynamic equations of multibody systems. The method is used in teaching mechanisms for the mechatronic courses taught by the authors at bachelor and master levels. The differential equations are developed for a generic situation, therefore they may be applicable for a large range of mechanisms used in mechatronic systems (vehicles, suspensions, robots etc). The input parameters of the equations are the bodies and kinematic joint positions, the type of each joint, the initial values of the independent generalized coordinates and the forces values. The system of differential algebraic equations is linear in terms of accelerations and joint reactions, which facilitate the numerical integration. The method is implemented in didactical software using a graphic interface conceived in a very popular geometric modeling software - AutoCAD.

1. Introduction

The last developments in the field of Multibody Systems theory led to a large number of commercial software packages available both for research & development and teaching purposes. Most popular of these software (ADAMS, DADS, DYMES, etc) [1, 2, 3, 9] are currently providing a very large range of facilities for various purposes which make them sometime unreachable for teaching purposes both from the price viewpoint and complexity. For this reason, in many cases, teams within the Universities developed their own teaching tools better suited according to their concrete theoretical approach as well as the course curriculum and syllabus of the respective course [1, 5, 7].

In this paper a teaching method for deriving and integration of the dynamic equations of multibody systems is proposed by the authors as well as a software for practical application sessions with students. The teaching is starting from assumption that the students have the basic knowledge in the mechanics of the rigid body in the tri-dimensional space. This is the case after the second study year for most Romanian technical

faculties providing courses in mechanical and mechatronics fields. In this paper the authors present the main theoretical aspects as well as the software elaborated to support the teaching

2. Systems of independent bodies

The systems of independent bodies are defined as a collection of rigid bodies moving in the 3D space without having any link between each other. For this kind of systems, analyzing the motion is simply analyzing the motion of each body separately with the classical theory of the single rigid body motion.

2.1. Kinematics

The spatial position of body is usually given by a number of coordinates usually called generalized coordinates and generically symbolized as q_1, q_2, \dots etc. Even various possibilities to give the position by various number of coordinates are often used [3], for the teaching purposes, the set of six independent coordinates are preferred. The most intuitive one includes the three coordinates of the body associated reference frame (x, y, z) and the orientation of the same frame (ϕ_1, ϕ_2, ϕ_3), with respect to a global reference frame given by Euler or Bryant angles [3]. In this case, to know the body motion means knowing the functions:

$$q_k(t) = 0, \text{ with } k = 1 \dots 6. \quad (1)$$

In a matrix form, this can be written as

$$[q(t)] = 0 \quad (2)$$

Given the motion laws (2) one can obtain the velocity and acceleration laws by simply differentiating them with respect to time once and twice respectively:

$$[J][\dot{q}] = [\tau(q, t)], \quad (3)$$

$$[J][\ddot{q}] = [\psi(\dot{q}, q, t)] \quad (4)$$

where $[J]$ is the Jacobian 6×6 matrix including the coefficients of velocity and accelerations obtained in the differentiation process. All the terms not including the unknown velocities and accelerations are grouped in two column matrices $[\tau]$ and $[\psi]$ the six elements of which are depending only on previously determined parameters.

The equations (3) and (4) are linear in terms of velocity and accelerations, thus easy to solve.

For the case of the independent body systems, the equations (2), (3), (4), remain formally valid. The only difference consists in the form of the matrices which must include the generalized coordinates of all bodies. Thus, for a system of n_b independent bodies, $k = 1, 2, \dots, n_b$ in the equation (1).

2.2. Dynamics

In the dynamic analysis, the number of the given equations (n_e) in the system (1) is less than the total number of unknowns generalized coordinates ($6n_b$). In this case we say that the system have the degree of freedom:

$$L = 6n_b - n_e > 0. \quad (5)$$

that is the system is kinematically undetermined because some of the generalized coordinates have not a known motion equation. The column matrix of the known coordinates will be symbolized as $[q_D]$ as the independent coordinates are included in the vector $[q_i]$ with L elements. As a consequence, the motion corresponding to the L independent generalized coordinates is the result of the external and internal forces action:

$$[m][\ddot{q}_i] = [Q_\alpha] \Rightarrow [\ddot{q}_i] = [m]^{-1}[Q_\alpha]. \quad (6)$$

By simply integrating these accelerations it became easy to determine the velocities and positions of the bodies. Together with the initially given equations of $[q_D]$, the situation became quite similar with that presented at the point 2.1.

3. Multibody Systems with kinematic joints

A more complex case of multibody systems is that in which various type of links and joints relate the bodies to each other. These links influence the degree of freedom of the system and the kinematic and dynamic equations as well.

3.1. Kinematic joints

In mechanical and mechatronic systems very often the multibody systems include kinematic joints which introduce relative constraints between pairs of bodies. In practice a large number of joints types are utilized from the construction viewpoint. A systematization of the joints can be made taking into account whether they are considered in plane or spatial situations, type of contact, number of relative constraints introduced between the two adjacent bodies etc. Most of the joints introduces geometric relations between the generalized coordinates of the adjacent bodies. Some type of joints may introduce

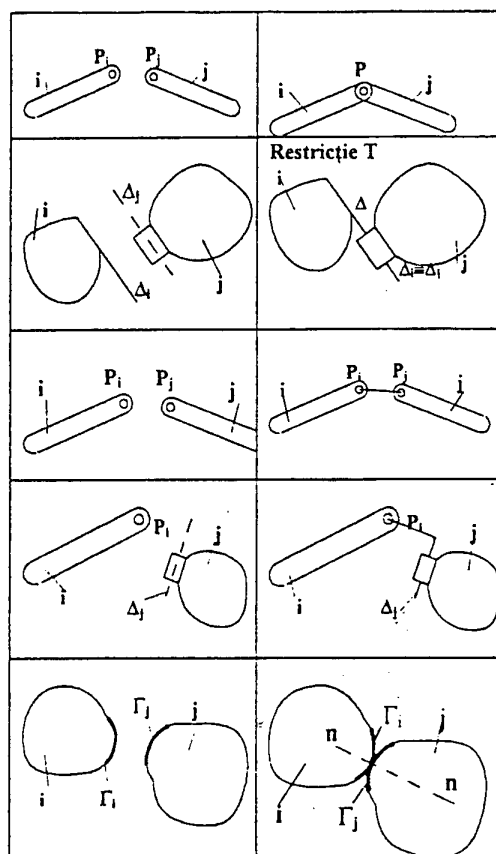


Figure 1. Planar kinematic joints

more complex restrictions (holonomic or non-holonomic, rheonomic or scleronomic etc) but these categories are beyond the scope of the present paper. For the planar mechanisms some usual joints are presented in fig. 1.

From the mathematical viewpoint the joints can be modeled by algebraic equations linking the generalized coordinates of the adjacent bodies. These equations are expressing the geometric restrictions imposed by the joint features. We are going to establish these equations for the revolute joint case (fig.2) just to illustrate the matter. The equations are derived from the geometric condition that guaranties the coincidence between the points P_i and P_j belonging to the two bodies respectively.

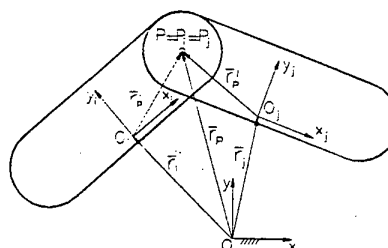


Figure 2. The revolute joint

that guaranties the coincidence between the points P_i and P_j belonging to the two bodies respectively.

$$\begin{aligned}\bar{r}_p &= \bar{r}_{p_i} = \bar{r}_{p_j}, \\ \bar{r}_{p_i} &= \bar{r}_i + \bar{r}_p^i, \quad \bar{r}_{p_j} = \bar{r}_j + \bar{r}_p^j, \\ \bar{r}_i + \bar{r}_p^i - \bar{r}_j - \bar{r}_p^j &= 0.\end{aligned}\quad (7)$$

The vector equation (7) represents the geometric model of the revolute joint. It can be written also in a matrix form, using the linear algebra theory:

$$[\Phi_{ij}] = [\bar{r}_i] + A_i [\bar{r}_p^i] - [\bar{r}_j] - A_j [\bar{r}_p^j] = 0, \quad (8)$$

where A_i and A_j represents the transformation matrices between the body reference frames (i and respectively j) and the global reference frame Oxy .

For the planar case, the equation (8) include two scalar equations, corresponding to the two relative translations restricted between the adjacent bodies: the translations along x and y axis.

In the general case of a spatial multibody system with n_b bodies interconnected with kinematic joints some of the initial $6n_b$ degrees of freedom are kinematically driven like in the case of the independent bodies and other are restricted by the kinematic joints. The remainder degree of freedom represents the degree of freedom of the system. From the mathematical viewpoint the only difference between the driver equations and the joint equations is that the latter are generally pure geometrical (independent with respect to time) and have the general form:

$$[\Phi_{ij}(q_i, q_j)] = 0, \quad (9)$$

as shown for the revolute case (8).

Thus, for a spatial multibody system kinematically determined, $L=0$ and the number of the driver equations with the number of the joint equations is equal to $6n_b$. With the only formal difference given by (9) which came together with (2), the kinematic equations (2), (3) and (4) remain valid and are numerically solvable.

3.2. The dynamic equations

Based on the link release axiom from the Newtonian mechanics, one can replace the joints with corresponding forces and as a consequence the body can be considered in static equilibrium. Thus, the dynamic equations can be written based on the d'Alembert principle stated as following: "The direct applied forces, the reaction forces and the inertial forces acting on a body are in equilibrium" [8], that is

$$[F_{ex}] + [R] + [F_i] = 0, \quad (10)$$

where for the planar case $[F_{ex}]$, $[R]$, $[F_i]$ are column matrices with 3 elements, including the torques.

In the general case, these forces are acting in various points of the body (fig. 3,a). For the vector

composition, it is convenient to reduce these forces with respect to the global reference frame axes in the origin of the body reference frame (fig.3,b). The reduced forces are called *generalized forces* and have a direct correspondence with the generalised coordinates, as following:

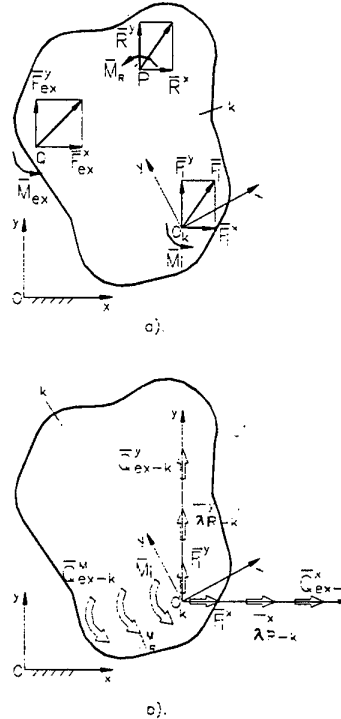


Figure 3. The generalized forces

- The external forces reduced in the point O_i , along the directions of the global reference frame axes are called *external generalised forces* and are symbolised as $[Q_{ex}]$.

$$[Q_{ex}] = \begin{bmatrix} Q_{ex}^x \\ Q_{ex}^y \\ Q_{ex}^m \end{bmatrix}.$$

- The reaction forces from the kinematic joints reduced in the same way are called *generalised reactions* and are symbolised as $[\lambda_R]$.

$$[\lambda_{RM-k}] = \begin{bmatrix} \lambda_{R-k}^x \\ \lambda_{R-k}^y \\ \lambda_{R-k}^z \end{bmatrix} = \begin{bmatrix} \lambda_{R-k} \\ \lambda_{M-k} \end{bmatrix}.$$

- In the case the origin of the body reference frame is not coincident with the mass center, the inertia forces have also to be reduced in the same way and are called *generalised inertia forces* (in fig. 3, for simplicity we considered the origin coincident with the mass centre):

According to the d'Alembert principle, the generalised forces and reactions are in equilibrium:

$$[F_{i-k}] + [Q_{ex-k}] + [\lambda_{RM-k}] = 0 \quad (5)$$

Making the necessary substitutions the equation (5) may be expressed as

$$[m_k][\ddot{q}_k] - [\lambda_{RM-k}] = [Q_{ex-k}], \quad (6)$$

unde

$$[m_k] = \begin{bmatrix} m_k & 0 & 0 \\ 0 & m_k & 0 \\ 0 & 0 & J_k \end{bmatrix} \quad \text{and} \quad [\ddot{q}_k] = \begin{bmatrix} \ddot{x}_k \\ \ddot{y}_k \\ \ddot{\phi}_k \end{bmatrix}$$

The relation (6) represents the general form of the motion differential equation of the rigid body k . In the case of multibody systems the equation (6) is written for each body, thus obtaining the system::

$$[m_k][\ddot{q}_k] - [\lambda_{RM-k}] = [Q_{ex-k}], \quad k = 1 \dots n_b. \quad (7)$$

In matrix form the system (7) may be written as:

$$[m][\ddot{q}] - [\lambda_{RM}] = [Q_{ex}], \quad (8)$$

where

$$[m] = \begin{bmatrix} [m_1] & 0 & 0 \\ 0 & [m_2] & 0 \\ 0 & 0 & [m_{n_b}] \end{bmatrix}$$

is the mass matrix of the system,

$[\ddot{q}]$ - the column matrix of the generalised accelerations, $[\lambda_{RM}]$ the column matrix of the generalised reactions and $[Q_{ex}]$ is the vector of the generalised external forces. For the spatial case the vector of the $6n_b$ generalised reactions can be expressed function on only $c=6n_b-L$ unknown (corresponding to the real number of constraints that is reactions introduced by the kinematic joints). By using a convenient matrix A ($g \times c$).

$$\begin{bmatrix} \lambda_{RM_1} \\ \lambda_{RM_2} \\ \vdots \\ \lambda_{RM_g} \end{bmatrix} = \begin{bmatrix} a_{11} & a_{12} & \dots & a_{1c} \\ a_{21} & a_{22} & \dots & a_{2c} \\ \vdots & \vdots & \ddots & \vdots \\ a_{g1} & a_{g2} & \dots & a_{gc} \end{bmatrix} \begin{bmatrix} \lambda_1 \\ \lambda_2 \\ \vdots \\ \lambda_c \end{bmatrix} \quad (9)$$

where $[\lambda_1 \dots \lambda_c]$ represents c unknown coefficients, which correct the arbitrary chosen values from the matrix $[A]$, the product $[A][\lambda]$ represents the generalised reactions vector (c represents the number of the geometric constraints introduced by the joints).

A matrix ($g \times c$) already numerically available in this stage is the transposed jacobian matrix $[J]^T$. In this case, the relation (9) become

$$[\lambda_{RM}] = [J]^T[\lambda],$$

where $[\lambda]$ is called the Lagrange multipliers vector:

$$[\lambda] = [\lambda_1 \lambda_2 \dots \lambda_c].$$

As a consequence the equation (8) lead to

$$[m][\ddot{q}] - [J]^T[\lambda] = [Q_{ex}] \quad (10)$$

and represents the differential equation of motion of the multibody systems. Together with the kinematic equations of the accelerations it forms the mixed system of differential-algebraic equations (DAE) of motion for a system of interconnected bodies:

$$\begin{cases} [m][\ddot{q}] - [J]^T[\lambda] = [Q_{ex}] \\ [J][\dot{q}] = [\psi] \end{cases} \quad (11)$$

In the spatial case with $c=6n_b-L$ constraints, the system includes as unknowns: $3n_b$ generalised accelerations and c Lagrange multipliers.

Observations

1. The form (11) of the motion equations is in general valid for a multibody system irrespective of the bodies and joints numbers, forces etc. As a consequence for automatically formulate the equations we only need algorithms for the automatic constitution of the matrices $[m]$, $[J]$, $[Q_{ex}]$ and $[\psi]$, first dimensionally and then numerically, starting from the initial data of the multibody system.

2. Related to the case of the system of independent bodies, characterised by the equation

$$[m][\ddot{q}] = [Q_{ex}]$$

the system (11) include furthermore the term $[J]^T[\lambda]$ and the differential equations of the joints. It become clear that by replacing the joints with the set of constraints equations and the set of joint reactions a kinematic chain may be treated in the same way as system of independent bodies (multibody system).

3.3. Numerical integration of the equations

Even in some simple multibody systems analytical solutions of the can be obtained for DAE, in most cases numerical procedures have to be implemented. The solution of the system have to comply with the initial conditions which form the initial solution:

$$[q(t_0)] = [q_0] \quad \text{and}$$

$$[\dot{q}(t_0)] = [\dot{q}_0]$$

The initial solution have to comply also with the constraints equations:

$$\Phi(q_1, q_2, \dots, q_g, t) = 0,$$

$$[J][\dot{q}] = \frac{\partial \Phi}{\partial t}.$$

If the jacobian matrix is a non-singular matrix then we can write the system solution as

$$\begin{bmatrix} [\ddot{q}] \\ [\lambda] \end{bmatrix} = \begin{bmatrix} [m] & [J]^T \\ [J] & 0 \end{bmatrix}^{-1} \begin{bmatrix} [Q_{ex}] \\ [\psi] \end{bmatrix},$$

from which the scalar solution can be extracted

$$\ddot{q}_k = f_k(\dot{q}_1, \dot{q}_2, \dots, \dot{q}_g, q_1, q_2, \dots, q_g, t), \quad k = 1 \dots g. \quad (12)$$

In this way the mixed DAE (11) was reduced to a system of ordinary second order differential equations (12). For the initial position ($t = t_0$), the left side of the equation (12) depends only on the initial data of the motion (initial position and initial velocity) given as input data for the dynamic analysis. Thus $f_{KO} = (\dot{q}_{10}, \dot{q}_{20}, \dots, \dot{q}_{g0}, q_{10}, q_{20}, \dots, q_{g0}, t) = a_k = ct$.

$$\ddot{q}_{KO} = a_k \quad (13)$$

Integrating these equations for with respect to time and with time intervals sufficiently small one can obtain the solutions:

$$\dot{q}_k = a_k \Delta t + c_k \circ i q_k = \frac{1}{2} a_k \Delta t^2 + c_k \Delta t + d_k \quad (14)$$

where c_k and d_k are integration constants depending on the initial conditions. The values determined with (14) will be considered initial conditions for the next step of integration etc.

This method of integration is however unstable because the constraint equations are utilised in the differential form which may lose geometric information. Therefore the constraint equations have to be introduced in the algebraic form in the system. Since the correct solution impose

$$[\phi(q)] = [\dot{\phi}(\dot{q}, q)] = 0 \quad (15)$$

the two terms can be added in any equation without altering the equality. Based on this property Baumgarte proposed a stabilisation method by adding the terms (15) in the DAE system with the weighting coefficients β and γ , such as:

$$\begin{bmatrix} [m] & [J]^T \\ [J] & 0 \end{bmatrix} \begin{bmatrix} [\ddot{q}] \\ [\lambda] \end{bmatrix} = \begin{bmatrix} [Q_{ex}] \\ [\psi] + 2\beta[J]\dot{q} + \gamma^2[\phi] \end{bmatrix} \quad (16)$$

This form of the equations is stable and may be integrated with the method previously indicated. For a good convergence the user have to make a proper choice for the coefficients β and γ .

4. The didactical software

Following the equations derived before a computer package was conceived in a similar manner with the commercial packages having in view to get students familiar with this kind of tools.

The software called AMEC (Analysis of MECanisms) include two modules for the three major stages of the multibody systems automatic analysis: a pre&post-processing module and a processing module.

4.1. The pre&postprocessing module

This module is dedicated first to assist the user in coding the input data into a format and syntax that can

be recognized by the processing module and second to assist the user in interpreting the output data provided by the same processing module also in recognizable format. The module is conceived under AutoCAD software graphic programming language AutoLISP, in order to use the huge popularity of the AutoCAD package among students in Romania.

To this aim, a simple graphic interface was added to the original one of AutoCAD (fig. 4) in order to include "user-friendly" facilities for working with the software entities but without drastically change the usual AutoCAD interface. In this way the students feel familiar with the software from the very beginning.

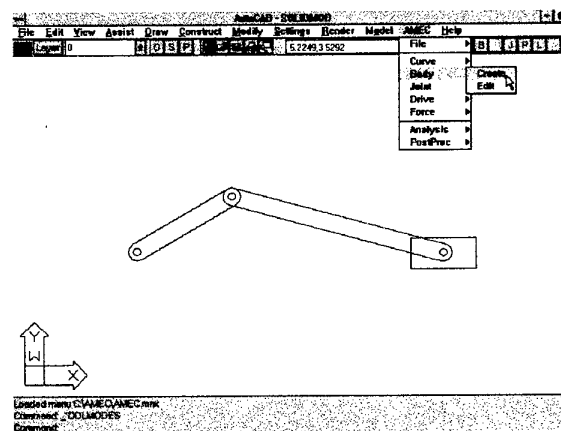


Figure 4. The AMEC graphic interface under AutoCAD

Thus, in modelling session, the multibody system is modeled as a collection of solids with the usual facilities of AutoCAD. Then the multibody system data are collected both automatically from the solid model (the initial position, the mass properties etc - fig. 5) and manually introduced by the user (the forces, joints, drivers etc - fig. 6).

In the next stage the input data are automatically coded in a simple ASCII format with a syntax which easily can be handled afterwards by the students for debugging the model. Thus the data are structured in entities called body, joint etc. For example the entity *body i* include all information regarding that body, *joint i* - all necessary information about joint *i* etc. Then the data are saved in a file on the computer disk with the correct format and syntax. All necessary commands are implemented in a graphic interface with windows easy to handle. Furthermore the students receive before each session a supporting text with a tutorial for the way of using the package.

4.2. The processing module

The processing module is conceived in C programming language. It is runned separately after the pre-processing operation. The operation is quite simple, the only interaction with the user being when indicating the name of the input data file. Then it automatically runs and save result files which may be converted into graphics or animations with the pre&post processing module.

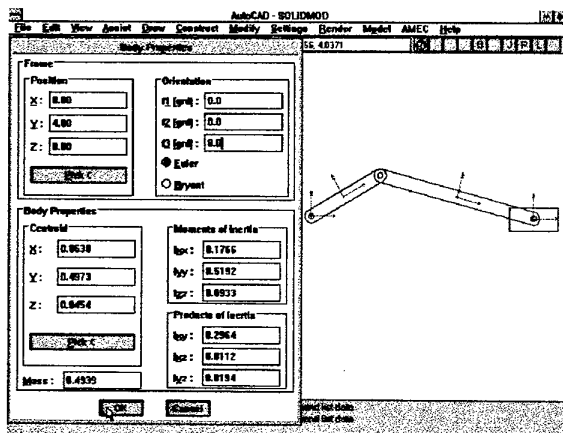


Figure 5. Pre-processing body data window

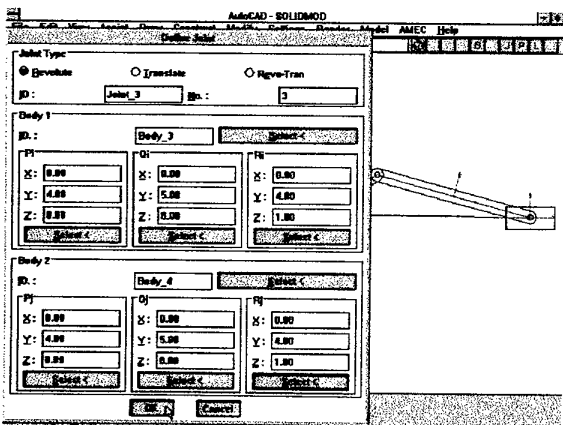


Figure 6. Pre-processing joint data window

12. References

- [1] Haug, E.J. (eds). *Elements and Methods of Computational Dynamics*, Springer Verlag, Berlin - New York, 1984.
- [2] Garcia de Jalón, J., Bayo, Eduardo. *Kinematics and Dynamic Simulation of Multibody Systems. The*

Real-Time Challenge. Springer-Verlag New York, U.S.A., 1993.

[3] Schiehlen, W. *Multibody Systems Handbork*. Springer-Verlag Berlin, Germany, 1990.

[4] Talabă, D., Vișa, I. "Modelarea mecanismului de ghidare cu suspensie independentă tip ARO utilizând softuri performante". *Simpozionului Național ESFA'95*, București, 1995, pp. 277-284.

[5] Talabă, D. "Aspecte ale integrării ecuațiilor dinamice ale mecanismelor modelate ca sisteme multicorp". *The International Symposium on Computer Aided Design of Mechanical Systems, PRASIC'98*, Brașov, 1998, pp.197-202.

[6] Vișa, I. "Aspecte ale modelării utilizată de softurile performante în analiza cinematico-dinamică a mecanismelor articulate". *Simpozionul național MTM*, vol. I, Reșița, 1996, pp. 111-118.

[7] Vișa, I., Talabă, D., Antonya, C. "Software pentru analiza automată a mecanismelor plane". *The International Symposium on Computer Aided Design of Mechanical Systems, PRASIC'98*, Brașov, 1998 pp.223-234.

[8] Voinea, R. *Mecanica rigidelor cu aplicații în inginerie*. Editura Tehnică, București, 1981.

[9] *** EMRC NISA. *DYMES User Reference Manual*, USA, 1992.

Development of a Parallel Inverted Pendulum System for Control Theory Education

Jae Weon Choi, Un Sik Park, and Joo Ho Kim
School of Mechanical Engineering and RIMT
Pusan National University, Pusan 609-735, Korea
choijw@hyowon.pusan.ac.kr

Abstract

In this paper, we develop a parallel inverted pendulum system that has the characteristics of the strongly coupled dynamics of motion by an elastic spring, the time-variant system parameters, and inherent instability, etc. Hence, it is possible to approximate some kinds of a physical system into this representative system and apply the various control theories in order to verify their fidelity and efficiency. For this purpose, an experimental system of the parallel inverted pendulum is implemented in practical, and a decoupling control scheme using the eigenstructure assignment is presented in comparison with the LQR optimal control method for hardware validation. Further more, this system can be utilized as a testbed for control theory education and research purpose through various setups.

1. Introduction

In general, as a typical mechanical system, an inverted pendulum system, which is analogous to launching control of a rocket or a robot system, is suitable for both applying and verifying modern multivariable and nonlinear control theories. Hence, the inverted pendulum is commonly used as a tutorial problem in control theory, where its inherently unstable, highly nonlinear dynamics and damping effect of mechanical friction provide a great potential for applications.

So far, a number of researchers have studied the inverted pendulum for the application of the various control theories to the various kinds of configuration. Control theories such as LQR method [1], neural network [2], variable-structure control, input-output linearization [3], H_∞ control [4], and fuzzy control techniques have been applied to a single type, double-series type [5], and triple-series type inverted pendulum [1].

However, these methods are applied mostly to a SISO inverted pendulum system and there was a few study on dealing with MIMO inverted pendulum systems accounting for dry friction of actuators and robustness with respect to

the perturbation of system parameters or model uncertainties as well.

In this paper, we present a parallel inverted pendulum system, which consists of two identical inverted pendulums, connected each other by a spring. Hence, this system has 2 inputs and 2 outputs and shows a dynamic behavior of strongly coupled motion, which is commonly seen in MIMO systems.

Therefore, this system allows a decoupling control that makes each inverted pendulum operate independently and a decoupling control scheme using eigenstructure assignment is applied in hardware experiments.

It is a distinguished feature of this system that the connecting hinge of a spring between both pendulums is designed to slide along the rod by sliding joints. Hence, this connecting position can be considered as a time-variant parameter. However, the time-variant parameter, which is difficult to describe explicitly, can be considered as the parameter variation or model uncertainty. Therefore, this system allows robust control strategy, so that the effect of the parameter variation or model uncertainty and their robustness can be carefully examined through the experimental system hereafter.

In addition, this system is designed that the mass of the pendulum and the stiffness of a spring can be easily reconfigured to see the effects of system parameters on the control performance for educational purposes.

Finally, we develop the experimental system of the parallel inverted pendulum so as to examine several suitable control strategy for the parallel inverted pendulum system, and then the experimental apparatus is utilized as a testbed for applications of various control theories and development of new control algorithms.

2. Configuration and modeling

This section presents the configuration of the parallel inverted pendulum system and its mathematical modeling. In addition, we examine the several important features of the system.

In this system, two identical inverted pendulums directly mounted on the motor shafts in parallel are connected by an

elastic spring. Hence, the motion of each inverted pendulum is strongly coupled with each other and its control is more difficult due to the increased instability and control inputs. Therefore, this system allows for a decoupling control that has received considerable attentions in multivariable control in recent years.

As the most unique and important feature of this parallel inverted pendulum system, we let the connecting position of a spring is not fixed but varying in time using the joint sliding freely along the rod during the actual operation.

Since this time-variant parameter is difficult to mathematically describe, it can be considered as the parameter variation or model uncertainty, and thus robust control schemes are allowed in this system as well.

Also, we design that the tip mass of each pendulum and the stiffness of the spring can be easily reconfigured, so that the effects of the system parameter on the performance of the control system can be readily examined.

A picture of the parallel inverted pendulum system is shown in Figure 1.

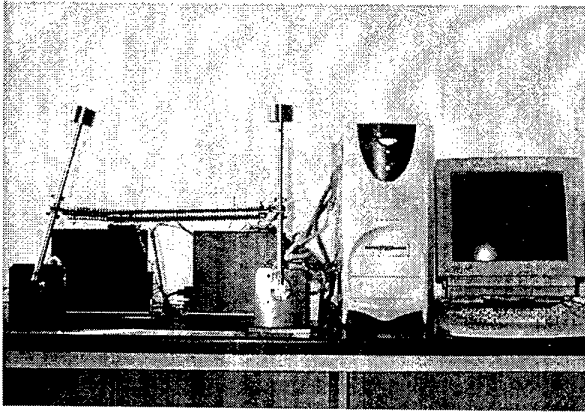


Figure 1. Parallel inverted pendulum system

From these configurations, we derived the mathematical model of the parallel inverted pendulum system.

First, we linearize the system near the equilibrium point assuming a small angular displacement. Also, rigid body motion, lumped mass, and linear spring are assumed and the dynamics of the motor and the mechanical friction in the motor and the spring guider are neglected for simplicity.

The dynamics of the parallel inverted pendulum system are described by the following equations of motion.

$$m_1 l^2 \ddot{\theta}_1 = m_1 g l \theta_1 - k a^2 (\theta_1 - \theta_2) - \tau_1 \quad (1a)$$

$$m_2 l^2 \ddot{\theta}_2 = m_2 g l \theta_2 - k a^2 (\theta_2 - \theta_1) - \tau_2 \quad (1b)$$

In Eq. (1), m_1 , m_2 and θ_1 , θ_2 are the mass and the angular displacement of each inverted pendulum, respectively, and τ_1 , τ_2 represent the input torque of each motor. The length of the inverted pendulum, l , the spring constant, k , and the acceleration of gravity, g , are also

appeared in Eq. (1).

Especially, we let the connecting position of the spring, a , varies arbitrarily in time. However, it is difficult to describe the time-varying characteristic of a , so that we assume that it is invariant and consider as a model uncertainty instead.

Thus, this model can also be rewritten in the state space as follows:

$$x = [\theta_1 \quad \dot{\theta}_1 \quad \theta_2 \quad \dot{\theta}_2]^T \quad (2a)$$

$$\dot{x} = \begin{bmatrix} 0 & 1 & 0 & 0 \\ \frac{g}{l} - \frac{ka^2}{m_1 l^2} & 0 & \frac{ka^2}{m_1 l^2} & 0 \\ 0 & 0 & 0 & 1 \\ \frac{ka^2}{m_2 l^2} & 0 & \frac{g}{l} - \frac{ka^2}{m_2 l^2} & 0 \end{bmatrix} x + \begin{bmatrix} 0 & 0 \\ \frac{-1}{m_1 l^2} & 0 \\ 0 & 0 \\ 0 & \frac{-1}{m_2 l^2} \end{bmatrix} \tau \quad (2b)$$

$$y = \begin{bmatrix} 1 & 0 & 0 & 0 \\ 0 & 0 & 1 & 0 \end{bmatrix} x. \quad (2c)$$

A schematic figure of the parallel inverted pendulum system is shown in Figure 2.

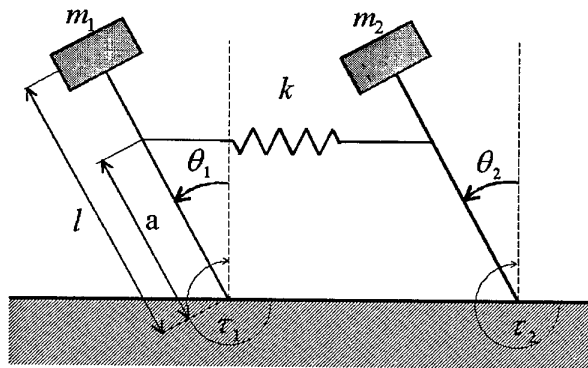


Figure 2. Modeling of the parallel inverted pendulum system

3. Decoupling control theory

In this section, we briefly mention about a decoupling control scheme using eigenstructure assignment (EA) and the command generator tracker (CGT).

The system control designer is often faced with the need to design a multivariable control law in which the objective is to decouple the various outputs from each other, in order to decrease the effects of coupled outputs [6,7].

Eigenstructure (eigenvalues and eigenvectors) assignment is very useful and suitable for achieving this objective. Eigenstructure assignment algorithms can be divided into

two groups; namely, the right eigenstructure (eigenvalues and right eigenvectors) assignment [8] and the left eigenstructure (eigenvalues and left eigenvectors) assignment [9].

Their roles in designing a control system are distinctly different. The mode or disturbance decouplability is governed by the right eigenstructure of a system. On the other hand, the control effectiveness and disturbance suppressibility depends mainly on the left eigenstructure of the system. Therefore, in this work, we use the right eigenstructure assignment scheme for a decoupling control of the parallel inverted pendulum system. In addition, the command generator tracker [10] is used as a servo that makes the inverted pendulum follow the reference input.

Consider a linear time invariant system described by

$$\begin{aligned}\dot{x} &= Ax + Bu \\ y &= Cx\end{aligned}\quad (3)$$

where $x \in R^n$, $u \in R^m$, $y \in R^r$. As previously mentioned, for solving mode-decoupling problems, the right eigenstructure assignment scheme is applied.

To present the right eigenstructure assignment scheme, we define

$$S_{\lambda_i} = [\lambda_i I_n - A : B] \quad (4)$$

and a compatibly partitioned matrix

$$R_{\lambda_i} = \begin{bmatrix} N_{\lambda_i} \\ \vdots \\ M_{\lambda_i} \end{bmatrix} \quad (5)$$

where the columns of the matrix R_{λ_i} form a basis for the null space of S_{λ_i} . For the cases that rank $B = m$, it can be shown that the columns of N_{λ_i} are linearly independent.

The following theorem gives necessary and sufficient conditions for the existence of K which yields the prescribed right eigenstructure.

Theorem 1 [11]: *Let $\{\lambda_1, \lambda_2, \dots, \lambda_n\}$ be a self-conjugate set of distinct complex numbers. There exists a real $(m \times n)$ matrix K such that*

$$(A - BK)v_i = \lambda_i v_i, \quad i = 1, 2, \dots, n \quad (6)$$

if and only if, for each i

- 1) $\{v_1, v_2, \dots, v_n\}$ is a linearly independent set in C^n , the space of complex n -vectors
- 2) $v_i = v_j^*$ when $\lambda_i = \lambda_j^*$
- 3) $v_i \in \text{span}\{N_{\lambda_i}\}$.

Also, if K exists and rank $B = m$, then K is unique, and is computed by using the obtained submatrices N_{λ_i} and M_{λ_i} .

In general, for a system that has repeated eigenvalues, the result of Theorem 1 can be easily extended.

The theorem 1 indicates that the feedback gain K is determined by the closed loop eigenvalues and eigenvectors. The feedback gain K is easily obtained through the following equations by using the right eigenstructure algorithm if the desired right eigenstructure (λ_i, v_i) is already determined.

$$\begin{aligned}v_i &= N_{\lambda_i} z_i \\ K &= [M_{\lambda_1} z_1 \ M_{\lambda_2} z_2 \ \dots \ M_{\lambda_n} z_n] [v_1 \ v_2 \ \dots \ v_n]^{-1}\end{aligned}$$

where z_i is a linear combination coefficient that makes v_i with N_{λ_i} .

The feedforward gain F for guaranteeing zero steady-state errors is obtained by the command generator tracker (CGT), which is one of the explicit models following methods. For the decoupling control problem of the parallel inverted pendulum system, the one pendulum is required to track the command inputs. This may be achieved by choosing an identity model. The output of this model is equal to its input. A control law for this objective is obtained as follows:

$$u = [\Omega_{22} + K\Omega_{12}] u_m - Kx \quad (7)$$

where $[\Omega_{22} + K\Omega_{12}]$ is the feedforward gain, u_m is the command input, K is the feedback gain, and Ω_{ij} are given by

$$\begin{bmatrix} \Omega_{11} & \Omega_{12} \\ \Omega_{21} & \Omega_{22} \end{bmatrix} = \begin{bmatrix} A & B \\ T & D \end{bmatrix}^{-1} \quad (8)$$

In Eq. (8), T is the output matrix C and D is zero matrix. Note that the feedforward gain F is subject to the feedback gain K as seen in Eq. (7).

4. Hardware setup

In this section, the hardware setup of the parallel inverted pendulum system is presented and its validity is proved by experiments. Experimental apparatus for the parallel inverted pendulum system is constructed as follows.

Detailed specifications are listed in Table. 1.

The pivot of each inverted pendulum, which is allowed to rotate about the axis of the motor shaft, is directly mounted on the motor shaft without using a reduction gear to alleviate the mechanical friction of linkage as possible.

The tip mass of each inverted pendulum is 0.4489 kg and 0.4496 kg, respectively, and the mass of rod is small enough to neglect with respect to the tip mass. The hollow stainless steel rod of the inverted pendulum is 0.325m long.

Two inverted pendulums are connected by an elastic

coil spring which has the constant of 340.22 N/m and is guided by a guider to prevent a buckling in contraction. The total mass of the spring including the guider is 0.3875 kg and would not be negligible, hence the equivalent mass at the position of the tip mass is calculated as 0.4868 kg . Since the guider is well lubricated, the friction with the spring can be neglected for simplicity. However, experimental identification of the system parameters such as friction coefficient is important in accurate uncertainty description for the desired performance objective.

Table 1. Parameters of the system and DC servo motor

Inverted pendulum		DC servo motor	
Mass 1	0.4489 Kg	Peak torque	4.94 Nm
Mass 2	0.4496 Kg	Peak current	20.5 A
Spring mass	0.3875 Kg	Mechanical	7 ms
Spring constant	340.22 N/m	Time constant	
Rod	0.325 m	Encoder	1000 ppr

The actuators selected for this experiments were brushless DC servo motors (SM233B) manufactured by Parker Hannifin Corporation with capability of applying 4.94 $N \cdot m$ of peak torque at 20.5 A of peak current (rms), according to the manufacturer's specifications. The motor electrical (0.41 ms) and mechanical time constant (7 ms) are at least two orders of magnitude smaller than the system time constant.

The motors have the built-in incremental photo encoder of 1000 Pulse/Revolution resolution to measure the angular position of the pendulum in the form of pulse signals. Also, 12-bit up/down counter is used to count the pulse signals from the encoder and this digital signal is monitored by the digital computer and a data acquisition system.

DR-8330 board of DARIM system that has 16 channel A/D and 2 channel D/A converter, as well as 16 channel DI/DO, is used for data acquisition and conversion. The real-time digital controller is implemented by C-language routines on a personal computer of 233MHz processor.

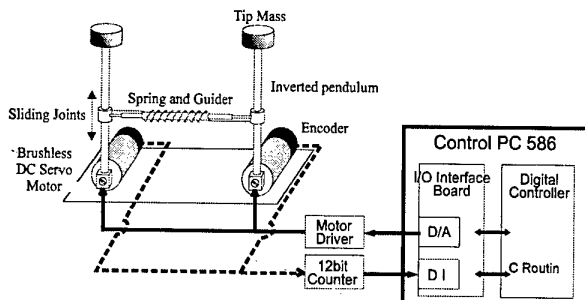


Figure 3. Hardware setup

The operation performed in the DR-8330 board and in C-routines is to sample the digital signal from the encoder by reading the DI channel and generates the analog voltage

to the motor by writing to the D/A channel.

Digital controller closes the control loop and feedback the angular position and velocity of the pendulum from the encoder then generates the command voltage for the motor through the TQ-10 torque servo driver.

This setup is designed to capture the important characteristics of the parallel inverted pendulum system to the best, and it gives the systematic methods for identifying modeling errors for control from experimental data.

5. Hardware experiment

In this section, the performance of the decoupling control system is investigated by hardware experiments. The objective of this experiment is to demonstrate the decoupling controlled system and verify its control law, and more of it is the development of the parallel inverted pendulum system itself.

For the decoupling control, one of the inverted pendulums is need to be oscillated arbitrarily. Hence, a servo controller such as the command generator tracker (CGT) is employed to make the pendulum oscillate to a given reference input. In the experiments, we give the reference input as a sinusoidal wave of magnitude 0.3 and frequency of 0.25Hz.

In designing a decoupling controller, we assign the eigenvalues of a closed-loop system as follows:

$$\lambda = [-24 \quad -22 \quad -14 \quad -12].$$

Since the position and rate responses of the inverted pendulum should be decoupled and has to be faster than another one, we make $\lambda_{1,2}$ larger than $\lambda_{3,4}$.

Using the algorithm described in the section 3, we can design desired right eigenvectors of the closed loop system as follows:

$$V = \begin{bmatrix} 0.0416 & -0.0454 & 0 & 0 \\ -0.9991 & 0.9990 & 0 & 0 \\ 0 & 0 & 0.0830 & -0.0712 \\ 0 & 0 & -0.9965 & 0.9975 \end{bmatrix}.$$

In V , each element having zero value is assigned for achieving the desired decoupling objective.

Then, the feedback gain that satisfies the desired eigenvalues and eigenvectors of the closed loop system can be obtained by an appropriate eigenstructure assignment method.

$$K = \begin{bmatrix} 22.1357 & 2.4138 & 7.1531 & 0 \\ 7.1531 & 0 & 3.2449 & 1.3643 \end{bmatrix}$$

In the gain K , elements of K_{13} , K_{14} and K_{21} , K_{22} represent the degree of correlation of two inverted pendulums and affected mainly by the system parameters as the spring constant, mass and length of the rod. By

assigning the desired eigenvectors for the decoupling control, K_{14}, K_{22} go to zero, and K_{13}, K_{21} are the same as 7.1531 that represents the degree of the correlation. Neither eigenvalues nor eigenvectors of the closed system do affect these elements in feedback gain.

By feedback, the effect of this correlation can be compensated, and the required decoupling objective can be achieved.

Moreover, a feedforward gain for a servo controller is obtained by the algorithm given in section 3 as follows:

$$F = \begin{bmatrix} 27.7065 & 0 \\ 0 & 8.8157 \end{bmatrix}.$$

The sum of Frobenious norm of the feedback and feedforward gains is shown to compare with that of the LQR control gain.

$$\begin{aligned} \text{norm}_{EA} &= \|K\|_{Fro} + \|F\|_{Fro} \\ &= 24.7091 + 29.0752 = 53.7844 \end{aligned}$$

Next, this experiments result is compared with the LQR optimal method to verify the control performance of the decoupling control.

When the design parameter R in the LQR method is $\text{diag}\{0.0043, 0.0043\}$, the Frobenious norm of the gains is almost same as the decoupling control scheme using eigenstructure assignment, and the feedback and the feedforward gains are given as follows.

$$G = \begin{bmatrix} 12.0255 & 15.2912 & 4.8885 & 0.0168 \\ 4.8885 & 0.0168 & 12.0255 & 15.2912 \end{bmatrix}$$

$$H = \begin{bmatrix} 17.5963 & -2.2646 \\ -2.2646 & 17.5963 \end{bmatrix}$$

$$\begin{aligned} \text{norm}_{LQR} &= \|G\|_{Fro} + \|H\|_{Fro} \\ &= 28.3666 + 25.0902 = 53.4568 \end{aligned}$$

The results of experiments in time domain response are shown in Fig. 4 and Fig. 6 for the decoupling control using eigenstructure assignment and the CGT, and Fig. 5 and Fig. 7 for the LQR method using LQ servo.

In the experiments, we let the spring connecting position be fixed since we show the efficiency of the decouplability alone in this paper. However, the time-variant characteristics of the freely sliding spring connecting position is surely considered for the robust control hereafter.

It is clear from experiments that the results demonstrate a good agreement with the theoretical predictions and show a good performance of the controller to decouple the motions of the parallel inverted pendulum.

Experimental data show that pendulum which is to be standstill slightly oscillate as seen in Figure 4 and Figure 5. This is due to the hardware problem such that the time constant of the system is not fast enough to respond

adequately to the decoupling command. Since the time constant is directly related to the inertia of the system and capability of the actuator, this drawback can be easily improved by the hardware tuning.

The nonlinear effects and model uncertainties due to neglecting the friction of the motor and the guider did not cause significant changes in the results of hardware experiments. The brushless DC servo motor and data acquisition board appear to be effective and inexpensive for controller implementation.

The decoupling control using eigenstructure assignment with the CGT is compared with the LQR optimal method using LQ servo, which shows similar decoupling effect in the experiments. However, the LQR control gives more weight on stabilizing the pendulum itself and the decoupling control gives more weight on compensating the correlation. Therefore, the LQR control needs more control input than the decoupling control to achieve the same performance. From the performance stand point, the decoupling control using eigenstructure assignment shows the better decouplability.

One of the important lessons in the hardware experiments is the need for the accurate system modeling and system identification. Also, the experiments proved again that the control problem is often dependent on system modeling, actuator and sensor capability, and controller implementation.

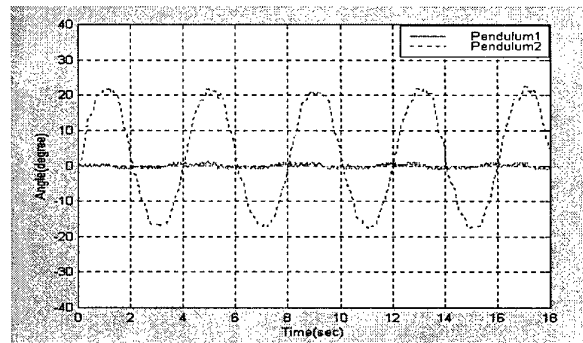


Figure 4. Angular displacement (EA + CGT)

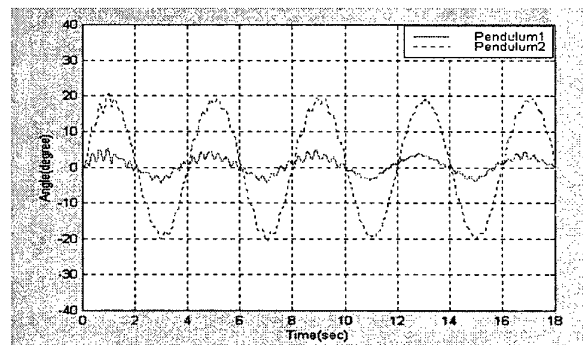


Figure 5. Angular displacement (LQR + LQ servo)

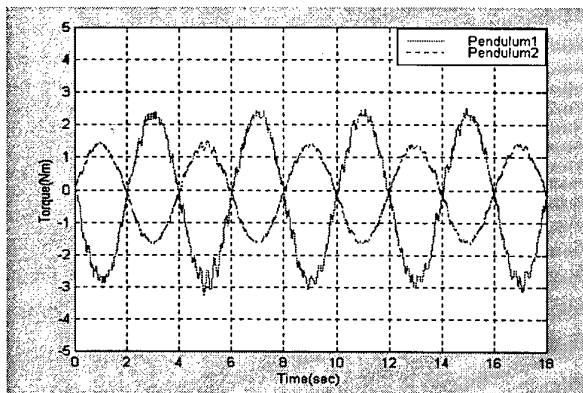


Figure 6. Input torque (EA +CGT)

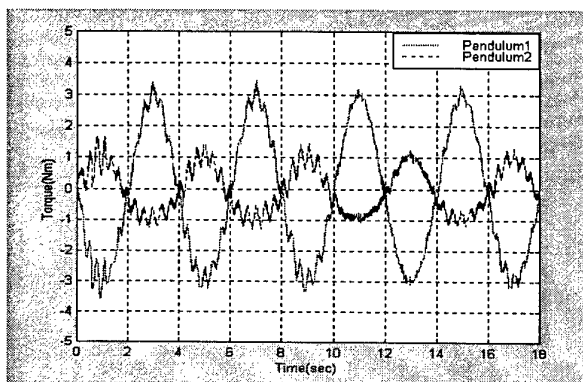


Figure 7. Input torque (LQR + LQ servo)

6. Conclusions

In this paper, a parallel inverted pendulum system is implemented and a decoupling control scheme using eigenstructure assignment with CGT is experimentally demonstrated and shows a good performance.

Despite of the assumption of a linear system and the neglect of the mechanical friction, the hardware experiments show good agreement with theoretical predictions.

Hereafter, this experimental system will be utilized as a testbed for control theory education and evaluation of new control algorithms.

7. References

- [1] K.G. Eltohamy and C.Y. Kuo, "Nonlinear Optimal Control a Triple Link Inverted Pendulum with Single Control Input", *International Journal of Control*, Vol. 60, No. 2, 1998, pp. 239-256.
- [2] C.W. Anderson and "Learning to Control an Inverted Pendulum Using Neural Networks", *IEEE Control and System Magazine*, Vol. 9, No. 3, 1989, pp. 31-37.
- [3] R. Gurumoorthy and S.R. Sanders, "Controlling Non-minimum Phase Nonlinear System - The Inverted Pendulum on a Cart Example", *Proceedings of the 32th IEEE Conference on Decision and Control*, 1993, pp. 680-685.
- [4] G.W. Vander Linden and P.F. Lambrechts, " H_{∞} Control of an Experimental Inverted Pendulum with Dry Friction", *Proceedings of the 31th IEEE Conference on Decision and Control*, 1992, pp. 123-128.
- [5] K. Furuta, T. Okutani, and H. Sone, "Computer Control of a Double Inverted Pendulum", *Computer and Electronic Engineering*, No. 5, 1978, pp. 67-84.
- [6] A. Snell, "Decoupling Control Design with Applications to Flight", *Journal of Guidance, Control, and Dynamics*, Vol. 21, No. 4, 1998, pp. 647-655.
- [7] G. M. Siouris, J. G. Lee, and J. W. Choi, "Design of a Modern Pitch Pointing Control System", *IEEE Transactions on Aerospace and Electronic Systems*, Vol. 31, No. 2, 1995, pp. 730-738.
- [8] J. W. Choi, "A Simultaneous Assignment Methodology of Right/Left Eigenstructure", *IEEE Transactions on Aerospace and Electronic Systems*, Vol. 34, No. 2, 1998, pp. 625-634.
- [9] J. W. Choi, "Left Eigenstructure Assignment via Sylvester Equation", *KSME International Journal*, Vol. 12, No. 6, 1998, pp. 1034-1040.
- [10] M. J. O'Brien and J. R. Broussard, "Feedforward Control to Track the Output of a Forced Model", *Proceedings of the 17th Conference on Decision and Control*, 1978, pp. 1149-1155.
- [11] A. N. Andry, E. Y. Shapiro, and J. C. Chung, "Eigenstructure Assignment for Linear Systems", *IEEE Transactions on Aerospace and Electronics Systems*, Vol. 19, No. 5, 1983, pp. 711-729.

Remote Learning: A World-Wide-Web operated Robot Arm

Matanya Elchanani
matanya@bridgeport.edu

Department of Computer Science and Engineering

University of Bridgeport

Bridgeport, CT 06604

Tarek M. Sobh
sobh@bridgeport.edu

Abstract

The World-Wide-Web has been used extensively in the past few years of its existence for data exchange, and information gathering. Web on-line control, on the other hand, is a new emerging field which has not yet been fully exploited and holds in it a great impact on currently available control systems. This paper discusses an application of on-line INTERNET control service - a WWW controlled robotic manipulator arm.

1 Introduction

The WWW application is an actual real-time, on-line application in which the user interacts with a robot controller in real time using the World-Wide-Web as the medium. The project itself was conceived with the following ideas in mind:

1. A simple client side interface that will use only a form capable web browser.
2. User friendly interface.
3. Structural configuration that will allow fast updates for both user interface and hardware change.
4. Web interface that will allow easy implementation of distant-learning tutorials and exercises using the robot interface.

The above last requirement is quite unique in this application. A major consideration for this project was to be targeted towards distant-learning programs in the field of control and robotics, although such an interface is readily implementable in other fields as a distant-learning aid.

2 General System Description

As mentioned earlier, the client side interface is comprised solely of a forms capable web-browser such as Netscape Navigator V.2 or Internet Explorer V.3. The lack of proprietary software or hardware on the client side enables every user with web access to fully control the hardware, regardless of its platform (except of the above minimal requirements). In order to start a link with the robot, the user simply points the web browser to the robots web page. From there on, the user is guided through a series of screens that eventually end up in an input page (such as a form or a sensitive map page). When the user satisfies the input page request (by either inputting numerical data or clicking on a sensitive map image), the data is being sent as a form GET method to the server side interface. At the server side, the users data is processed and is being used to activate the robot arm. After the arm has ceased moving, two video cameras are being used to grab an image of the robot and feed it back to the user as an indication for the end of movement and as an opening argument for the next command. The server side interface is comprised out of three main parts that communicate with each other to accomplish the bi-directional interface between the user and the robot arm. The following are brief descriptions of the server side parts:

2.1 The web server interface.

The web server interface is a series of HTML pages that are being used as the visual interface with the user. Depending on the user selection, different pages will be selected, until, eventually, a page containing an input field will be selected. When the SEND button in the page will be pressed, the page will launch a generic CGI program that will receive the data entered in the page, and according to the page that launched it will decide upon the next action. In any case, the

CGI program will open an INTERNET stream socket link[1] to the ROBOT SERVER (see next part) that will be used as a data path for the flow of commands to the robot and visual feedback back to the user. No checks are being done on the commands sent to the robot server. At an early stage it was decided that most processing and command parsing will take place on the robot server PC (which is a dedicated machine) and not on the web server machine (which is a public, general purpose machine).

2.2 The robot server.

The robot server is a Pentium PC that hosts the robot server program. This program is the heart of the system and most of the processing is done here. The PC is equipped with an RS232 interface that is used to communicate with the robot controller, an ethernet card which is being used to communicate with the web server interface (see above), and a dual input VGA frame grabber attached to two Black & White video CCD cameras to enable visual feedback. The program is an event driven loop which senses mainly a dedicated INTERNET socket for requests (which are coming from the web server interface). The program idles as long as no requests are sensed. Whenever a request is received over the socket, the program wakes up and parses the request. The current version of the program supports two types of requests, a visual only, and a movement/visual one. A visual only request will initiate an image grabbing session that will grab the arms image using either of the cameras (depending on the request) do some processing on it (also dependent on the request - see stereoscopic interface), convert the image to a JPEG format and send it back to the web server interface. A movement/visual request will first be parsed and checked to be a legal movement command for the robots controller. It will then be passed to the inverse kinematics module[2] which will extract the new joint angles required for the new position from the 3D positional parameters given to it. The joint angles will be checked out against the current ones to validate that no limits are exceeded and finally a movement command will be sent to the controller via the RS232 interface. The main program loop will then wait on the robot to complete its movement and will initiate a visual request (see above).

2.3 The robot unit

The robot unit is comprised out of an SIR-1 semi-industrial grade articulated manipulator arm with five degrees of freedom (out of which only three are being



Figure 1: The coordinate system interface

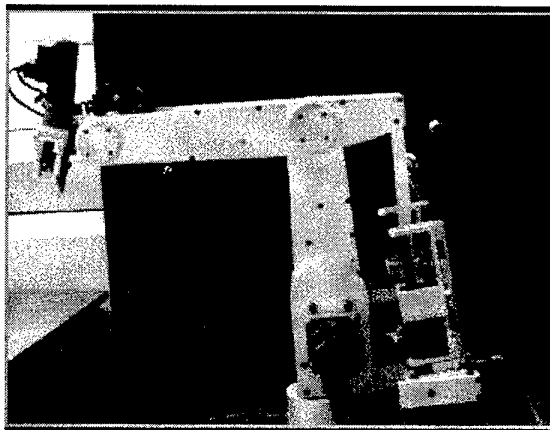


Figure 2: The stereoscopic visual interface - state 1

used now), and the robots controller. The controller is a CPU controlled unit that is connected to the arms motors and to a variety of position and speed sensors mounted on the arm. The controller can receive commands to move the robot from either a control panel or using a special command language through an RS232 port.

3 The user interface

As written earlier, the modularity of the system enables the creation of different user interfaces which are using the same link to operate the robot. Currently, two user interfaces are available: the coordinate system interface (see figure 1), and the stereoscopic visual interface (see figure 2 and figure 3). The coordinate

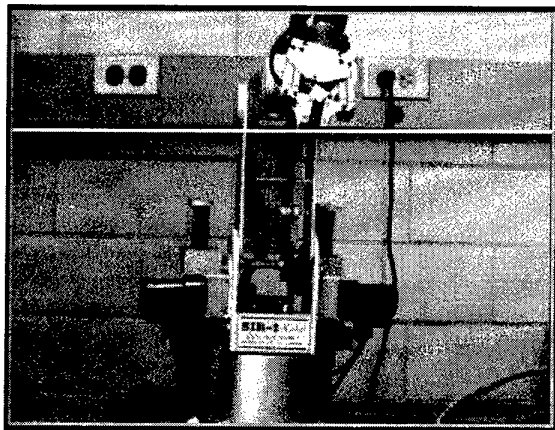


Figure 3: The stereoscopic visual interface - state 2

system interface uses a page that requests the coordinates of a 3D point to which the robot will be moved. When the user presses the MOVE button, a movement/visual request (see above) is being sent to the robot server. After the robot has reached its final position, the new position image is being sent back to the user. A HOME button is also available which causes the robot to move to its cold-start home position. The stereoscopic interface, on the other hand, starts with a visual request at the moment the page is requested. This enables the user to get the latest, most updated picture of the robot. After the image is grabbed from the main camera (a camera positioned in front of the arm) it is being sent as a sensitive image back to the user (figure 2). The user is then given the choice to click on the sensitive image to determine the initial X-Y coordinates of the requested position. when the user clicks on the image, the web server interface saves the coordinates entered and sends another visual request from the robot server. This time though, the image is grabbed from a second camera placed on the same horizontal plane as the main camera, but at a 90 degree angle from it. The robot server uses the Y coordinate information from the above user input to interpolate a white line across the image to mark the requested X-Y 2D point over the rotated image. The image is then sent to the web server interface which raps it with a HTML package. It also puts hidden HTML fields into which the previously selected X-Y coordinates are placed, so they will be passed with the final user request. Eventually, the user receives another image of the robot which is the 90 degree side view with a white line, representing his previous selection (figure 3). The user is requested to click again over the image, thus, setting the new images X coor-

date. this coordinate is basically the Z coordinate (X system, rotated 90 to be perpendicular to the X-Y plane). The request received contains the Z coordinate, together with the X-Y coordinates (embedded as hidden HTML fields), and is being sent as a movement/visual request to the robot server. The robot server is using this data to move the robot to the new position and finally send the resultant picture back to the user.

4 Future additions

The WWW operated arm is a dynamic on-going project. Currently, there are a few additions that are to be considered to be added to the system:

- **Queuing system:** During the writing of this paper, extensive work is being done in creating a queuing system for user control and authentication. For the short duration of its life, the WWW robot had received thousands of hits and an urgent need for a queuing system was noticed. The queuing system we are designing relies solely on a state machine comprised out of the user's own web pages. Each viewed page contains a special magic cookie (inside a hidden field) which is decrypted in the server and carries information on scheduling, expiration, priority and user level.
- **Java based interface:** A Java based interface is also considered as a future addition. The interface would help to move some of the complex inverse kinematics calculations from the robot server to the users machine.
- **Live Video:** For wideband Internet connections, a live video frames stream of the robot's movement would enhance the understanding of what is actually happening on the robot side. We are still considering either a server push, or a Java video console. With both of the considered options, our prime directive is a non proprietary client side software.
- **More Distant Learning:** Expending the project into the general sciences. For example, using the robot and interface in a distant learning chemistry lab experiment set (we are actually working now on this one)

5 Related Information

Information about this project and other robotics related projects is provided on the University of Bridgeport's Robotics and Intelligent Sensing and Control laboratory web page at: <http://www.bridgeport.edu/~risc>.

Feel free to visit us at the above page, or go directly to the WWW robot arm page at: <http://www.bridgeport.edu/~matanya/robi> (please remember that as this project is in its early stages of development, it is mostly off-line and under constant module and interface change).

References

- [1] Stevens, W. Richard. *Unix Network Programming*, Prentice Hall, Englewood Cliffs, N.J., 1990.
- [2] Spong, W. Mark, *Robot Dynamics and Control*, John Wiley & Sons, N.Y., 1989.

Interferogram analysis with neural networks

A.S. Yak¹, A.N. Poo, S.S. Keerthi

National University of Singapore
Mech. & Prod. Engrg. Dept., Kent Ridge Crescent, Singapore.
mpepooan@nus.edu.sg, mpessk@nus.edu.sg

¹ Philips Singapore Pte. Ltd.,
620A Toa Payoh Lorong 1, Singapore 319762.
asyak@magix.com.sg

Abstract

Measurement of optical lenses during its prototyping and failure analysis requires its wavefront error to be determined in the sub-micron range. Reconstruction of the optical wavefront through the analysis of lateral shearing interferograms is done with radial basis function neural networks instead of the analytical inverse matrix approach. Noisy interferograms, which pose a problem for the inverse matrix approach, are simulated and tested in the proposed neural networks approach.

1. Introduction

In the analysis of lateral shearing interferograms resulting from optical wavefront measurements, limitations of the common approach utilising inverse matrices include range and noise issues. The range problem is relevant to aberrations in prototype lenses or out-of-specification lenses where it may be very wide, while noise problems are common in the interferometry system optics and the test piece. Besides these considerations the analysis must be able to handle complicated interferograms containing combinations of aberrations found in the test piece.

The present techniques for analysing interferograms include the phase stepping analysis, and Zernike polynomial fitting through inverse matrices approach [1]. The inverse approach is very effective for very small range of near perfect wavefronts, however it encounters non-deterministic problems when the wavefronts are complicated by mixture of aberrations or by noise e.g. dirt on the lenses. In this paper the radial basis function (RBF) networks are used to analyze the interferogram with the aim of improving the analysis in the presence of noise in the optical system.

The analysis is in two parts. The first part of the analysis is to identify and classify the types of aberration present represented in the interferogram. The second part is to

quantify these aberrations. In this paper the interferograms are first simulated. This are then used for training of the neural networks. Noise is also added to the simulated interferogram during the training phase to simulated actual interferograms that are noisy.

2. Aberrations and Interferograms

Two main forms of interferometry are used for measurement of aberrations of optical systems/components – the lateral shearing and Twyman-Green setups, see figure 1. Lateral shearing interferometry has many advantages over the Twyman-Green setup, such as immunity from vibration of setup, accuracy and range of measurement through variable shear techniques. However the resulting lateral shearing interferogram also poses some peculiarities. For instance, the interferogram for defocus and astigmatism are similar, therefore the interferogram has to be analyzed in two orthogonal shears in order to properly classify these two aberrations. Also the lateral shearing interferogram, being obtained from the interference of one beam shifted in parallel with another part of the same beam, complicates the analysis as compared to the more straightforward Twyman-Green interferograms. Examples of lateral shearing interferograms are shown in figure 2 where they are simulated.

3. Zernike polynomials representation of aberrations

The circle polynomials of Zernike are commonly used to represent wavefront aberrations in optical systems. The reasons include the orthogonality of these polynomials (over interior of unit circle) and their invariance properties, both simplifying the wavefront fitting analysis process in a rotationally symmetric optical system [2]. The polynomial representation of the wavefront is also in the form of balanced aberration; this is very useful in the

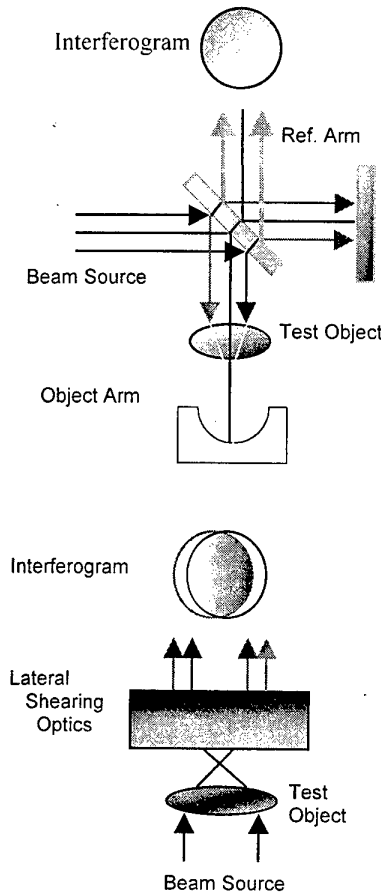


Figure 1. Two main forms of interferometry set-up. The top figure shows the Twyman-Green interferometry set-up and the bottom shows the lateral shearing interferometry set-up.

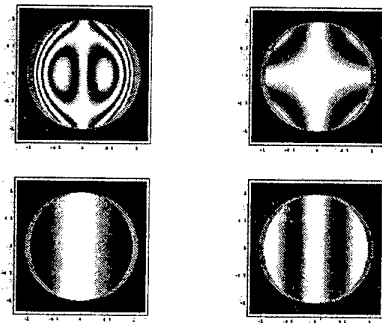


Figure 2. Lateral shearing interferograms for *Spherical Aberration* 3λ (top left), *Coma* (Y) 3λ , *Astigmatism* (0°) (bottom left) 3λ , and *Defocus* 3λ (bottom left).

tolerance analysis of an optical system.

Wavefront OPD error $W(\rho, \theta)$ can be represented by a Zernike expansion in cylindrical coordinates (ρ, θ) as

$$W(\rho, \theta) = \sum_{n=0}^k \sum_{m=0}^n a_{nm} Z_n^m(\rho, \theta) \quad (1)$$

where

a_{nm} are the Zernike coefficients, and

$Z_n^m(\rho, \theta)$ are the Zernike polynomials

n and m are the order and degree of the polynomials respectively.

From equation (1) the wavefront variance with zero mean (mean is arbitrary) is then,

$$\sigma_f^2 = \frac{1}{\pi} \int_0^1 \int_0^{2\pi} W^2 \rho \, d\rho \, d\theta \quad (2)$$

where σ_w is the rms of the wavefront error.

And the fit variance, describing the error of fitting a measured wavefront W' to the actual W , is

$$\sigma_f^2 = \frac{1}{\pi} \int_0^1 \int_0^{2\pi} (W' - W)^2 \rho \, d\rho \, d\theta \quad (3)$$

Then the optimal fit is obtained from partial differential of σ_f^2 with respect to each coefficient a_{nm} . Given the orthogonality of Zernike polynomials, it can be shown that [1],

$$a_{nm} = \frac{2(n+1)}{\pi} \int_0^1 \int_0^{2\pi} W' Z_n^m \rho \, d\rho \, d\theta \quad (4)$$

The intensity of a measured interferogram in a Twyman-Green interferometer can be described as,

$$I_{tg}(\rho, \theta) = I_0 + I_0 \gamma \cos\left(\frac{2\pi}{\lambda} W'\right) \quad (5)$$

And the intensity of a Lateral Shearing interferogram is,

$$I_{ls}(\rho, \theta) = I_0 + I_0 \gamma \cos\left(\frac{2\pi}{\lambda} \Delta W'\right) \quad (6)$$

In the Twyman-Green interferometer $I_{tg}(\rho, \theta)$ is imaged by a CCD camera and W' is obtained equation (5). Zernike coefficients are then derived through the optimal fit equation (4). This is fairly simple compared to the lateral shearing interferometer where $I_{ls}(\rho, \theta)$ is similarly imaged but the derivation of Zernike polynomials for W' is complicated by the lateral shear.

In Lateral Shear (x -shear), the measured $\Delta W'$ is related to W through the shear ratio as

$$\begin{aligned} \Delta V'_x(x, y; s) &= V'(x+s, y) - V'(x-s, y) \\ &= \sum a_{nm} \Delta X_{x,n}^m(x, y; s) \end{aligned} \quad (7)$$

where

V' is the Cartesian coordinate equivalent of W' ,

s is the shear ratio; $\frac{1}{2}$ distance between centers of interference beams,
and

$\Delta X_{x,n}^m(x, y; s)$ is the difference Zernike polynomial term.

The resolution of the interferometry system is improved by an order with *phase stepping*, where a series of interferogram is used instead of only one. In the simplest method the interference pattern is stepped as follows,

$$I(\rho, \theta) = I_0 + I_0 \gamma \cos\left(\frac{2\pi}{\lambda} \Delta W' + \frac{2m\pi}{N}\right) \quad (8)$$

where m is the step number and N is the total number of steps.

4. Analytical wavefront reconstruction

There are two broad wavefront reconstruction techniques. The first technique is the zonal technique where the least square fit of a wavefront on a grid of measured difference-front points is used. This method is more suitable for surface errors, which do not assume any shape in particular. The second technique is the modal phase reconstruction method such as fitting of wavefront error using the Zernike polynomials [1] for identifying and quantifying lens aberrations. The latter approach of wavefront representation is applied in this paper with the results quantified in Zernike polynomial coefficients

5. Wavefront reconstruction with neural networks

In this paper the radial basis neural network is used for the reconstruction of lateral shearing interferograms. The most common form of RBF neural networks is originally proposed by Broomhead and Lowe [3] and has form as shown in figure 4. This network may be expressed as a linear model for the function $y(x)$ of the form

$$f(x) = \sum_{j=1}^m w_j h_j(x) \quad (9)$$

The RBF network is linear if the hidden functions, also called the basis functions, are fixed functions. If the basis functions are allowed to move or change in size (e.g. the radial basis functions' centers are not fixed), then the RBF network is non-linear. In this paper the linear RBF networks will be used.

A special class of function, known as radial functions, is used for the hidden functions. The main characteristic of radial functions is that it is monotonically either decreasing or increasing from a center point. One common form of radial basis functions is the Gaussian function, which in scalar form, is expressed as

$$h(x) = \exp\left(-\frac{(x-c)^2}{r^2}\right) \quad (10)$$

where its parameters are $c = \text{center}$
 $r = \text{radius}$

Gaussian RBF is commonly chosen for RBF neural networks as it gives local response and does not tends to infinity. This is unlike multiquadric-type RBFs which gives global response and tends towards infinity if it is too far off the centre. Multiquadrics are of the form

$$h(x) = \frac{\sqrt{r^2 + (x-c)^2}}{r} \quad (11)$$

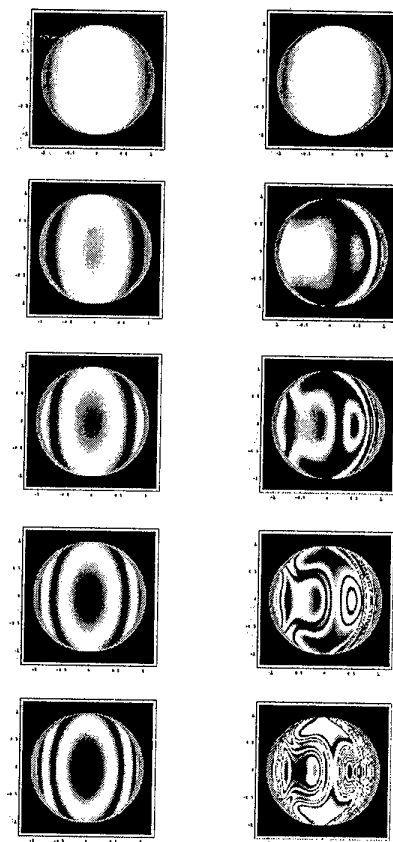


Figure 3. The top row shows the lateral shearing interferograms of coma (X) in various degrees of severity (0.6λ , 1.2λ , 1.8λ , 2.4λ from left to right). The bottom row shows the phase stepping (5 equal steps) images of the 0.6λ coma (X) interferogram.

The approach in this paper is to use a group of sub-RBF networks for the analysis of the lateral shearing interferogram. Each of the sub-RBF networks is trained to identify and quantify one form of wavefront error i.e. op-

tical aberrations. The analysis is in two parts. The first part of the analysis is to identify and classify the types of aberration from the interferogram. The second part is to quantify these aberrations. In this paper the interferograms are first simulated using equation (6). These are then used for training of the RBF networks. Noises are added to the simulated interferograms during the training and testing of the networks to simulated actual interferograms.

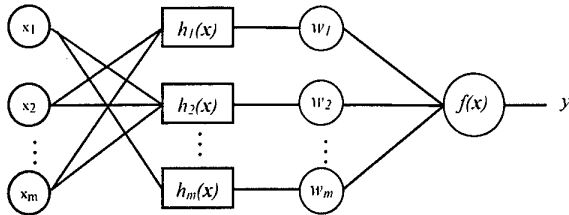


Figure 4. Radial Basis Function Network. w_j represents the weights of the network and h_j are the hidden functions.

5.1. Reconstruction of interferogram without noise

In this section interferograms without noise are reconstructed with neural networks. This is an ideal case study because there is always noise in practice, however it forms the basis for the use of neural networks in the reconstruction process. To reconstruct the noiseless interferogram the least squares method is used during the training phase of each sub-RBF network, see figure 5.

In Linear RBF network, supervised learning can be done using least squares method in which the best weights are solved from the training set through deriving and solving a set of equations (assuming that there is no redundancy in this set of equations). In this analysis it is assumed that noise is negligible in the training data set. Noise will be considered in the regularization networks to be shown in the next section.

Consider the linear network model

$$f(\mathbf{x}) = \sum_{j=1}^m w_j h_j(\mathbf{x}) \quad (12)$$

with the training set $\{(\mathbf{x}_i, \hat{y}_i)\}_{i=1}^p$. The weights of the model are obtained through the least squares method by minimizing the sum-squared-error with respect to the weights. Thus the sum-squared-error is

$$S = \sum_{i=1}^p (f(\mathbf{x}_i) - \hat{y}_i)^2 \quad (13)$$

and to minimize it (for the weight w_j), set

$$\frac{\partial S}{\partial w_j} = 2 \sum_{i=1}^p (f(\mathbf{x}_i) - \hat{y}_i) \frac{\partial f}{\partial w_j}(\mathbf{x}_i) = 0 \quad (14)$$

where

$$\frac{\partial f}{\partial w_j}(\mathbf{x}_i) = h_j(\mathbf{x}_i) \quad (15)$$

Substituting this into the derivative of the sum-squared-error, we thus arrive at the following set of equations

$$\sum_{i=1}^p f(\mathbf{x}_i) h_j(\mathbf{x}_i) = \sum_{i=1}^p \hat{y}_i h_j(\mathbf{x}_i) \quad (16)$$

Using equations (11) and (15) the set of weights can be solved for the network, and a unique solution can be found unless there is redundancy. In the presence of noise in the training or test set, redundancy will arise, in which case regularization and subset selection will be required.

It is important that the interferogram images first be preprocessed before they are used for reconstruction. Here the interferogram set for training are prepared so that it represent a uniform distribution of the interferograms to be reconstructed. The images are also normalized and no redundant images are used in the training set. These steps help to ensure better results.

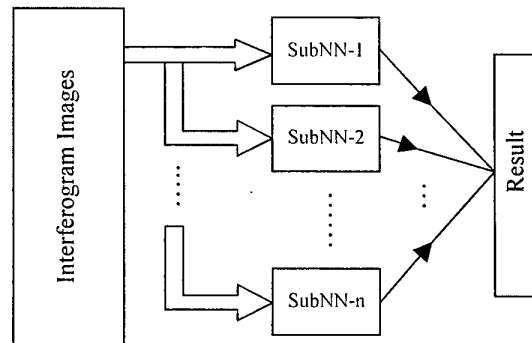


Figure 5. Neural networks structure for interferogram reconstruction. Each *SubNN* module is a radial basis function neural network similar to figure 4.

5.1.1. Results.

In the first experiment, the nodes are chosen with the same number of nodes as the interferogram image inputs. The wavefront error of the reconstructed interferogram shows errors of less than 5% for aberrations ranging from 2 to 5 λ_{p-v} . Each interferogram is represented by 1600 pixels and 240 hidden functions are used per sub-RBF network. Please refer to table 1 for the results. The interferograms are for spherical aberration with 0.1 shear ratio.

5.2. Reconstruction of interferogram with noise

The contrast between a clean and noisy interferogram used in the simulation is shown in figure 6. The noisy interferogram from simulation are close to the actual interferograms obtained from the interferometer, as shown in figure 7. The advantage of using of neural networks for reconstruction of interferogram lies in its ability to handle

noisy images. To reconstruct the wavefront from noisy interferograms the supervised learning with cross-validation and regularization methods are employed to train the RBF networks.

Network learning is essentially a problem of surface reconstruction or approximation in a multi-dimensional space given a training data set. This is a form of inverse problems and are either well-posed or ill-posed. Ill-posed problems are those where no unique solution exists due to insufficient information/training data to constrain one. Ill-posed inverse problems are due to *non-uniqueness* and/or *non-continuity*, arising for instance from the presence of noise in the input training data

To make the problem well-posed so that *generalization* to new data is feasible, the regularization method *ridge regression* [4, 5] is used. Ridge regression, or weight decay, essentially involves adding a penalty term to the sum-squared-error and helps to lessen unimportant network connections. This is done by adding a term to penalise large weights in the sum-squared-error, resulting in the following cost function

$$C = \sum_{i=1}^p (\hat{y}_i - f(\mathbf{x}_i))^2 + \sum_{j=1}^m \lambda_j w_j^2 \quad (17)$$

where $\lambda > 0$ is the regularisation parameter. Therefore a network with small weights is preferred to that with large weights, lessening the network's sensitivity to noise.

The number of hidden nodes, m , of the network must be selected with care to ensure good results. If m is too large then noise will be fitted into the model. This parameter is chosen through a model selection criterion based on the cross-validation method [4].

5.2.1. Results. Simulation results with noisy interferograms with spherical aberrations ranging from 2 to 5 λ_{p-v} show that the reconstructed wavefront error is below 21%. The simulated random noise level is 1.5% of peak image intensity. 480 hidden functions are used per sub-RBF network and each interferogram is represented by 1600 pixels. Three forms of aberrations were tested, spherical aberration, astigmatism and coma (both X and Y shear).

6. Conclusions

The RBF network is found to be a suitable method for reconstruction of wavefront from lateral shearing interferogram. This method has been shown to provide acceptable results for noisy interferogram images found in actual measurements for aberrations in the range of 2λ to $5\lambda_{p-v}$. It is expected that aberrations in the diffraction limited range will present similar results when the shear ratio is increased. This and further experiments on measured interferograms will form future works in the area.

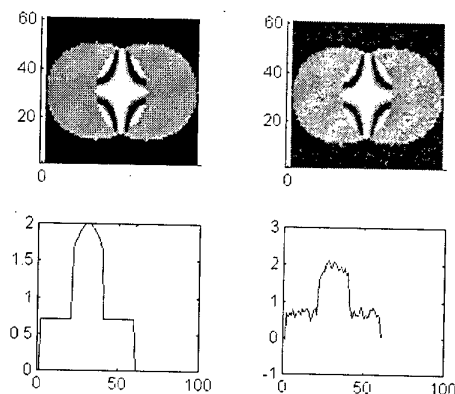


Figure 6. Coma (y) without noise (top left) and with noise (top right). The graphs below them are plots of the intensity profile across the centre of the interferograms.

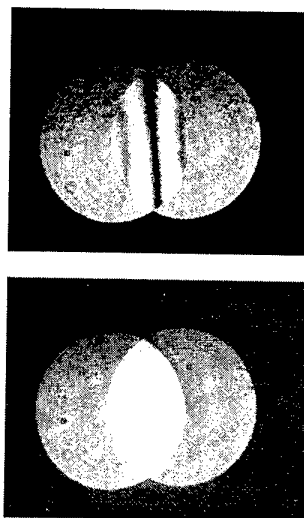


Figure 7. Interferograms obtained from a lateral shearing interferometer. see figure 8. The left has a defocus and the right is a near diffraction limited interferogram.

7. References

- [1] G. Harbers, P.J. Kunst, G.W.R. Leibbrandt : Analysis of lateral shearing interferograms by use of Zernike polynomials, *Applied Optics*, Vol.35, No.31, 1996.
- [2] M. Born, E. Wolf. *Principles of Optics*, Cambridge University Press, 1997.
- [3] Broomhead, D.S., Lowe, D., Multivariable functional interpolation and adaptive networks", *Complex Systems* 2, pp.321-355, 1988.
- [4] Orr, Mark J.L., "Regularisation in the selection of radial basis function centres", *Neural Computation*, vol.7, no.3, pp.606-623, 1995.

[5] Hoerl, A.E., Kennard, R.W., "Ridge regression: Biased estimation for nonorthogonal problems", *Technometrics*, vol. 12, no. 3, pp.55-67, 1970.

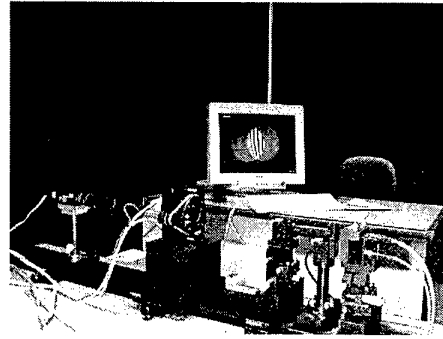


Figure 8. Later shearing interferometer used for aberration measurements.

Training Step	Basis function radius, r	MSE	% Reconstruction Error			
			2λ	3λ	4λ	5λ
SA						
1	0.01	0.04	13.40	0	-6.70	-10.72
1	0.1	0.04	13.40	0	-6.70	-10.72
1	1	0.04	13.40	0	-6.70	-10.72
1	10	0.04	13.40	0	-6.70	-10.72
0.5	0.01	0.01	9.40	0	-4.70	-7.52
0.5	0.1	0.01	9.40	0	-4.70	-7.52
0.5	1	0.01	9.40	0	-4.70	-7.52
0.5	10	0.01	9.40	0	-4.70	-7.52
0.1	1	7.8E-04	5.50	0	-2.70	-4.40
0.05	1	3.2E-04	4.92	0	-2.46	-3.93

Table 1. Results of reconstruction of clean interferogram with neural networks.

			% Reconstruction Error			
Training Step	Basis function radius, r	MSE	2λ	3λ	4λ	5λ
SA						
0.05	1	0.0027	20.4	6.9	-0.5	-4.7
AST						
0.05	1	0.002	11.9	0.0	-5.9	-10.3
C _{Ax,y}						
0.05	1	0.0019	11.5	0.0	-6.3	-9.6

Table 2. Results of reconstruction of interferograms with noise.

slee@hyowon.pusan.ac.kr

This paper presents a lane recognition technique that utilizes a neural network. This technique combines the conventional image processing and the principle of neural network. The technique is applied to images obtained from highways and unpaved roads. The images are filtered to reduce the noise and then fed to a multi-layer feed-forward network that is trained with the road images in advance. The neural network produces its output indicating the direction of road ahead of the vehicle. This technique can be used for a driver warning system that can alert the driver when the car is moving out of its lane without turning on the turn signal.

Among the effort to develop more intelligent and safer vehicle, a key area is the lane. If a car can detect the lane that it has to follow, it is possible to warn the driver when he or she steers out of the lane without turning on the turn signal. Also, the lane recognition ability can be a crucial factor in realizing an autonomous vehicle [1-3]. For this purpose, a vision system is a popular choice because it can provide detailed information about the road ahead[2].

This paper presents the development of a lane recognition technique that combines traditional image processing and neural network[4]. In this research, images from highways and unpaved roads have been processed to be suitable for neural network input. These processed images have been used by a multi-layer feed-forward network to determine in which direction the lane is turning.

The process begins with filtering a captured image of the road by using a band-pass filter whose thresholds are

adjusted to capture only the lane markings painted on the road for highway images. For unpaved road, color information of images is used for the band-pass filter to eliminate portions other than the road. In order to reduce scattered noise on the image, expansion and contraction method was used where a black pixel surrounded by white pixels is converted to white and vice versa.

The highway image after these filters has white lane markings that covers a small portion of the image and may not provide sufficient information for neural network. Therefore, the gap between lane markings is filled with white pixels. This filling process starts from the bottom center of the image and transverses both left and right until a white pixel is reached. The midpoint of the white pixels becomes the starting point of the filling process for the row just one pixel above the current one. For the rows where the lane marking is not present, the lane marking is linearly extrapolated, as shown in Figure 1, based on the lane markers identified already. For the images from unpaved roads, this kind of filling process is not required because the filtered image has a substantial area with white pixels.

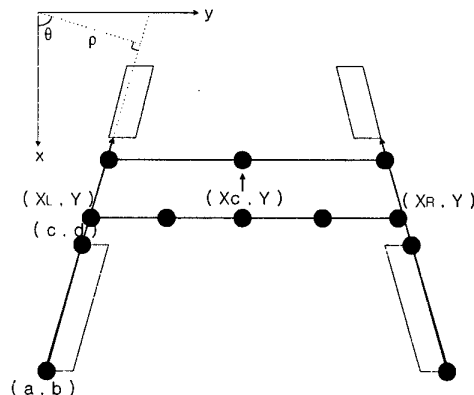


Figure 1. Lane filling

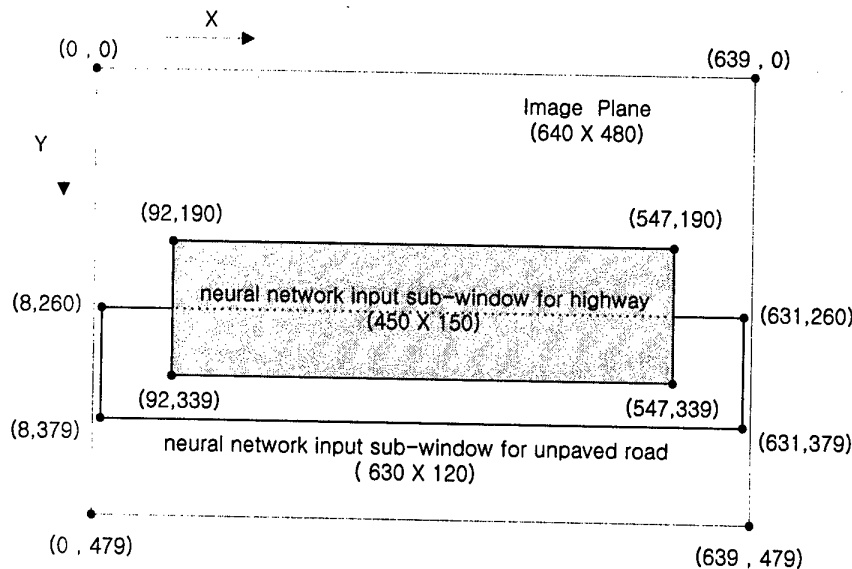


Figure 2. Neural network input windows

The next step is to select a subwindow for neural network input. The input windows are shown in Figure 2 where the input window for unpaved road is a little lower in the image plane and larger than that for highway because the vehicles are driven slower on unpaved road and the unpaved road tends to have smaller radius of curvature. The input window is further divided into thirty-six cells that are arranged in a three-by-twelve array. Each cell is given a value that is the ratio of the number of white pixels to the total number of pixels in the cell.

These values are fed into a feed-forward neural network shown in Figure 3. The neural network has thirty-six input nodes, forty nodes in the hidden layer, and fifteen output nodes. The output nodes are grouped into five different directions, i.e., sharp left turn, left turn, straight, right turn, and sharp right turn. When the peak value appears from output nodes 1 to 3, it is interpreted as a sharp left turn while peak values appearing from nodes 4 to 6, 7 to 9, 10 to 11, and 12 to 15 are left turn, straight, right turn, sharp right turn, respectively. The reason to use the node number producing a peak value rather than the individual output values is to make the result more robust to various noises. The neural network is trained with well-known back-propagation learning algorithm using a set of five typical road images and corresponding human interpretation. The expected output is organized in such a way that a node generates the peak value of 1 and the output value is decreased by 0.25 for the nodes away from the peak node. For example, the node 5 is trained to generate the value of 1 for a left-turning road

while the value of 0.75 should be obtained from nodes 4 and 6, 0.5 from nodes 3 and 7, 0.25 from nodes 2 and 8, 0 from all others.

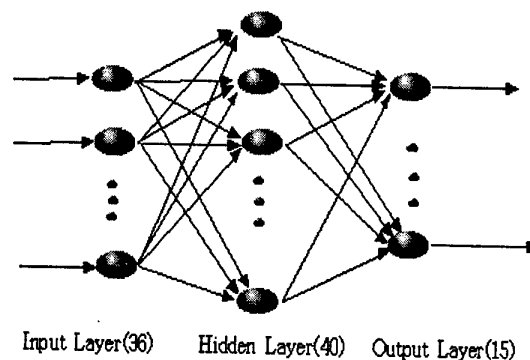


Figure 3. Multi-layer feed-forward network

The steps involved in recognizing the road direction are summarized in Figures 4 for both highway and unpaved road.

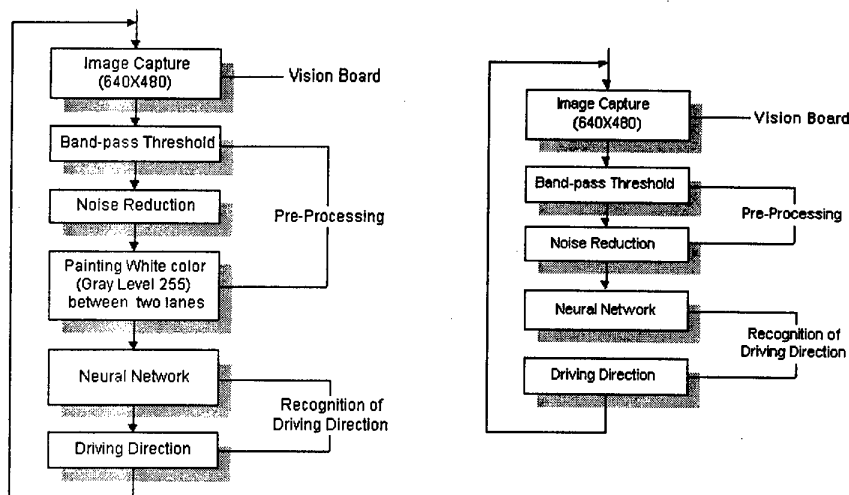


Figure 4. Lane recognition flowchart for highway(left) unpaved road(right)

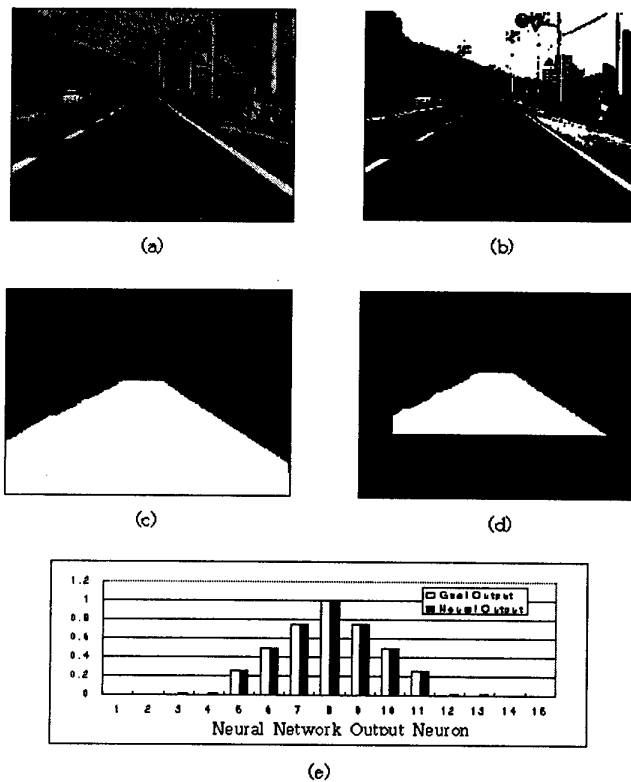


Figure 5. Straight road for neural network training

3. Experimental Results

3.1. Highway Images

After training the neural network, the images used for training were fed into the network in order to verify the ability to recall what has been learned. Figure 4(a) shows one of the training images while Figures 4(b) to 4(d) show the transformed images after filtering, gap filling, and windowing, respectively. In Figure 4(e), the white bars are the training data for the image and the black ones are the outputs of the neural network that closely follows the training data.

In order to check the performance for the untrained image, the image of a straight section of a highway on a rainy day has been used. The original image is shown in Figure 5 along with the neural network input image and outputs. The peak value of the outputs appears from node 8 indicating that it is a straight section

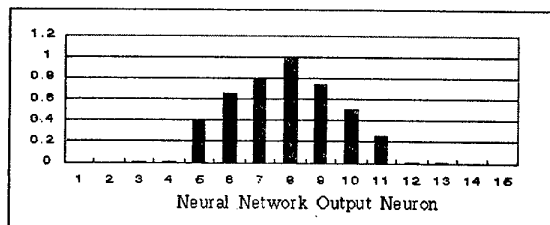
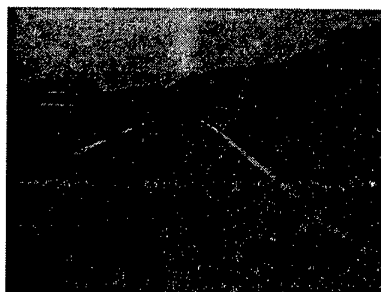


Figure 6. Straight highway

For a curved section of a highway, such images shown in Figure 6 are used to test the performance. Figure 6 shows the original image, input image to the network, and the outputs. The outputs are not exactly matching the ideal outputs, but the peak value is appearing from the node 5 as expected.

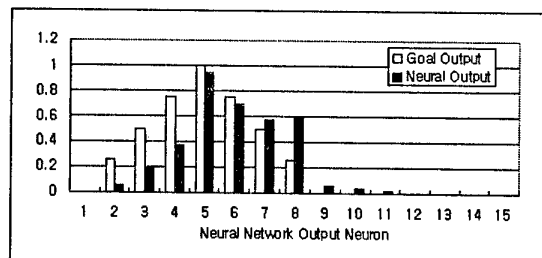


Figure 7. Left-turning highway

3.2. Unpaved Road Images

In Figure 7, a section of unpaved road is shown along with the image for the neural network that has gone through the filtering and windowing. The peak output is from node 5 indicating that the road curves to the left.

Similar tests have been carried out with one hundred untrained images each for highway and unpaved road. For highway, the network was able to determine the road direction correctly for 82 images while the correct outputs were obtained for 95 unpaved road images.

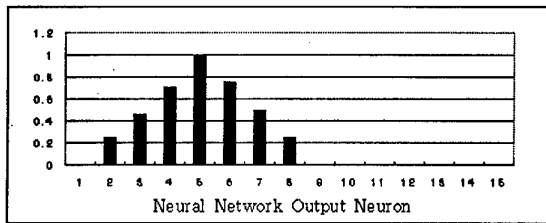
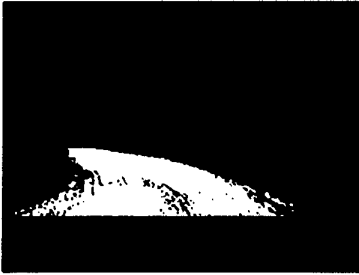
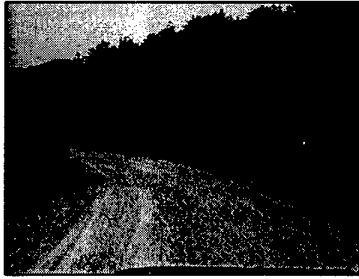


Figure 8. Unpaved road

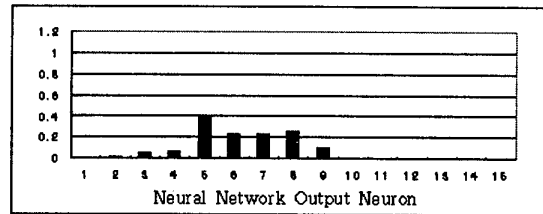
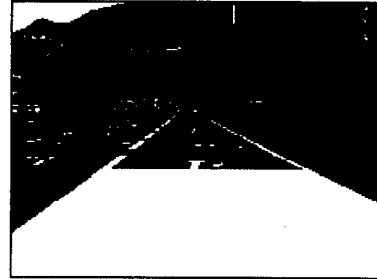
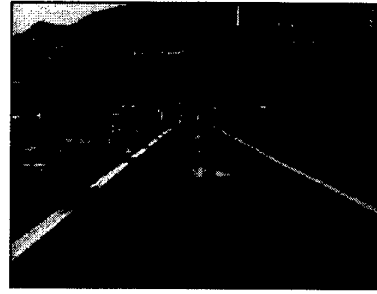


Figure 9. Arrow painted on the road

4. Conclusions

This research focuses on detection of road direction based on images captured on highways and unpaved roads. For this goal, traditional image processing techniques such as band-pass filter and expansion/contraction filter are combined with the principle of neural network. These filters are used to capture the necessary portion of the image and to reduce the noise present in the image. After the processed image within a subwindow is subdivided into thirty-six cells, cell values are computed and fed into a feed-forward neural network with fifteen output nodes. The neural network is trained to recognize five different shapes of the road. The neural network is found to be able to recall the trained image very well and to interpolate for the untrained images. However, the network has difficulties with the untrained images that contain severe noise such as shadows and letters on the road and further research is needed to overcome this shortcoming.

All the incorrect outputs were caused by severe noise in the image that includes other vehicles, letters and arrows painted on the road, and shadows of objects standing at the roadside. Figure 8 shows such an image where an arrow is painted on the road. Due to this extra marking on the pavement, the filling process between lane markings was stopped prematurely, which resulted in an incorrect output. In order to circumvent this problem, an algorithm may be included in the filling process to ignore white pixels within the identified lane markings.

The time required to determine the road direction is within 200msec that looks promising for the implementation as a part of a driver warning system or a autonomous vehicle.

5. References

- [1] Shumeet Baluja, "Evolution of an Artificial Neural Network Based Autonomous Land Vehicle Controller," IEEE Trans. Syst., Man, Cybern., vol.26, pp405-463, 1996
- [2] Toshiaki Kakinami, Jun Sato, Mitsuyoshi Saiki, and Kunihiko Soshi, "Autonomous Vehicle Control System Using an Image Processing Sensor," SAE, 1995
- [3] Wei LI, Xiaojia JIANG, Youngqiang WANG, "Road Recognition for Navigation of an Autonomous Vehicle By Fuzzy Reasoning," IEEE, 1996
- [4] Keon-Myung Lee, Dong – Hoon Kwak, and Hyung Lee – Kwang, "Fuzzy Inference Neural Network for Fuzzy Model Tuning," IEEE Trans. Syst., Man, Cybern., vol26, No.4, August 1996

Neural Network Control of a Fieldbus Pilot Plant System

Fazlur Rahman M.H.R., Philip S M Chin, Yang Rong Huan & Pee Suat Hoon
Dept. of Electrical Engineering, Singapore Polytechnic, Singapore.
F.RAHMAN@sp.edu.sg

Abstract

The application of Artificial Neural Network (ANN) control of a Fieldbus Pilot Plant System is considered in this paper. The pilot plant fitted with Foundation™ Fieldbus devices is modelled using ANN. A novel feedback linearisation technique using neural networks is proposed to control the neural network model of the pilot plant. Simulation results are presented to demonstrate the effectiveness of the technique used.

1. Introduction

The use of process instrumentation with digital communication facilities enables the plant operator a number of advantages. The possibility to control, configure and monitor the performance of the instrumentation from a central control room reduces the need for local inspections, thus economising and saving time. By connecting together instrumentation via a bus, the plant can be operated as a decentralised, modular units.

The main advantage of using Foundation™ Fieldbus is that it utilises only a single pair of wire for connection from the Fieldbus devices to the controller as illustrated in Figure 1. This in turn drastically reduces the cost of wiring, control hardware, I/O cards for PLCs and space in control cabinets, expansions, maintenance etc. as compared with the existing technologies viz., pneumatic, analog and distributed control. Other added features of Fieldbus technology are simpler man-machine interface, easy configuration of the system, enhanced system performance, intrinsic safe and interoperability.

Neural networks can be used favourably in modelling, identification and control of unknown non-linear plants [1-5]. To prevent modelling difficulties for complex physical systems, the ANN method of learning and control provides a basic framework for the design of controllers for unknown nonlinear systems. ANN can be viewed as the nonlinear dynamic mapping of control inputs onto observation outputs. The capability of the neural networks to approximate large classes of non-linear functions sufficiently accurately makes them prime candidates for use in dynamic models for the representation of non-linear process plants.

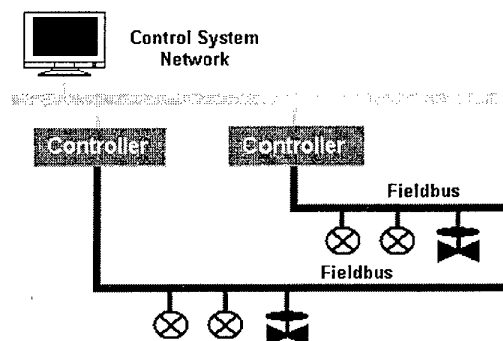


Figure 1: Fieldbus System

In most of the work, arbitrary nonlinear plants have been approximated using ANN. But it is well known that one cannot generalise the nonlinear problem because the nonlinearity is unique in different applications. Process plants have been studied extensively and their nonlinearity has been characterised but this knowledge has not been utilised in the application of ANN to process control. Our approach is unique and has an added advantage of applying neural networks for modelling and control of a Fieldbus system, since abundant information is available from Fieldbus instruments than available from conventional type of instrumentation system. This information can be effectively used to characterise the structure of ANN model and utilise the full capability of ANN to approximate what is unknown [6]. The information allows one to model a system faster, more accurately and also to control it effectively.

Controlling non-linear systems by using a linear controller via feedback linearisation is centred around geometric theory [7]. However, applicability of this method is quite limited since the theory depends on exact knowledge of non-linearities of the system and realisation of non-linear transformation tends to become difficult when the complexity of the system increases. This limitation in turn has motivated the use of feedback linearisation using ANN [8-9]. A novel ANN structure for feedback linearisation of the ANN plant model is proposed in this work. A fixed linear controller is then used to control the linearised pilot plant model.

The paper is structured in the following manner. The next section discusses the system modelling of the Fieldbus pilot plant. In Section 3, input-output linearisation is discussed. In Section 4, ANN implementation for modelling and feedback linearisation is demonstrated with the aid of simulations. Application of linear controller is dealt in Section 5. Finally we conclude our work in the conclusion section.

2. Modelling of the Pilot Plant

In our work, neural networks are used to model the pilot plant equipped with Foundation™ Fieldbus devices as shown in Figure 2. The pilot plant is divided into two major subsystems a heat exchanger system and a batch process system. The pilot plant is installed in the laboratory.

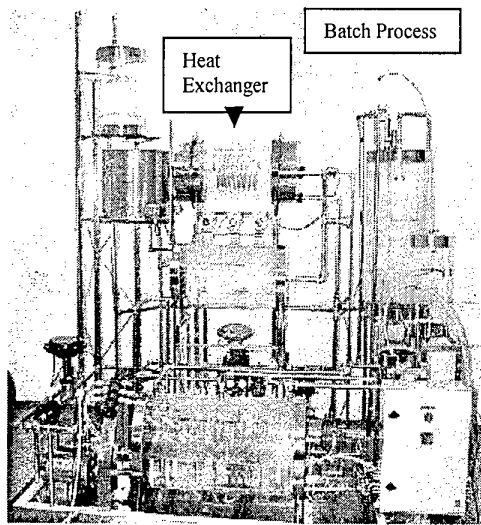


Figure 2: Pilot plant equipped with Fieldbus devices

In this paper we model and control only the heat exchanger system using neural networks. The schematic diagram of the shell and tube heat exchanger is given in Figure 3.

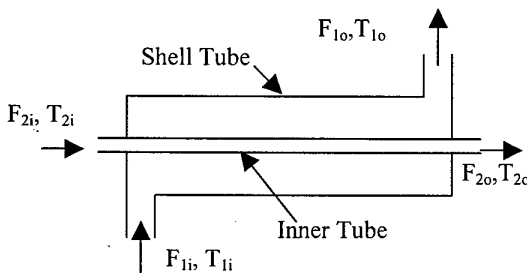


Figure 3: Schematic of a Heat Exchanger

The heat exchanger consists of a shell tube and an inner tube. The heat transfer process takes place from the shell tube to the inner tube. The inlet and outlet temperatures of the shell tube are T_{1i} and T_{1o} . The load disturbances are feed flow of the inner tube F_{2i} and inlet temperature of the inner tube T_{2i} . The shell tube inlet flow is F_{1i} and the outlet temperature of the inner tube is T_{2o} . In the heat exchanger, the liquid flows through the inner tube and it is heated by another liquid that flows around the tube as shown in Figure 3.

The unknown nonlinear system (heat exchanger) to be modelled is expressed by

$$\begin{aligned} y(t+1) &= f[y(t), y(t-1), \dots, y(t-n), \\ &u(t), u(t-1), \dots, u(t-m)] \end{aligned} \quad (1)$$

where $y(t)$ is the scalar output of the system, $u(t)$ is the vector input to the system, $f[\cdot]$ is the unknown nonlinear function to be estimated by the neural network and n and m are the known structure orders of the system. General nonlinear modelling techniques have been studied, such as NARMAX [10], for the identification of this nonlinear function. Based on the theoretical results of Cybenko [11] and Funahashi [12], it has been suggested that feedforward networks, such as the multilayer perceptrons, can be trained to form any realisable vector function $f[\cdot]$ and hence any nonlinear model.

2.1 Neural Modelling

A three layer neural network (input, hidden and output) is used for learning purpose and the standard algorithm [13] and [14] is employed to train the weights. The activation functions are hyperbolic tangent for the second layer and linear for the output layer. Let the input to the neural network be denoted by

$$\begin{aligned} q &= [y(t), y(t-1), \dots, y(t-n), \\ &u(t), u(t-1), \dots, u(t-m)] \end{aligned} \quad (2)$$

and expressing the neural network model for the unknown system (1) as

$$\begin{aligned} \hat{y}(t+1) &= \hat{f}[y(t), y(t-1), \dots, y(t-n), \\ &u(t), u(t-1), \dots, u(t-m)] \end{aligned} \quad (3)$$

where $\hat{y}(t+1)$ is the output of the neural network and \hat{f} is the estimate of f . The backpropagation algorithm guarantees that

$$y(t+1) - \hat{y}(t+1) = \delta, \delta \ll 1 \quad (4)$$

Let the cost function J be defined as follows:

$$J = \frac{1}{2} e^2(t+1) \quad (5)$$

where

$$e(t+1) = y(t+1) - \hat{y}(t+1) \quad (6)$$

The control signal $u(t)$ should be selected to minimise the cost function J . Using the neural network model, (3) can be rewritten to give

$$\hat{y}(t+1) = w_2 [\tanh(w_1 q + b_1)] + b_2 \quad (7)$$

where w_1 , w_2 , b_1 and b_2 are the weights and bias matrices of the neural network respectively [13]. To minimise J , the input $u(t)$ is calculated recursively using the gradient descent rule

$$u(t+1) = u(t) - \eta \frac{\partial J}{\partial u(t)} \quad (8)$$

where $\eta > 0$ is the learning rate. It can be observed that the controller relies on the approximation made by the neural network. Therefore it is necessary that the neural network output $\hat{y}(t+1)$ approaches the real system output (heat exchanger) $y(t+1)$ asymptotically. This can be realised by keeping the neural network training online. Differentiating (5) with respect to $u(t)$, it can be shown that

$$\frac{\partial J}{\partial u(t)} = -e(t+1) \frac{\partial \hat{y}(t+1)}{\partial u(t)} \quad (9)$$

where $\partial \hat{y}(t+1) / \partial u(t)$ is known as the gradient of the neural network model with respect to $u(t)$. Substituting (9) into (8), we have

$$u(t+1) = u(t) + \eta e(t+1) \frac{\partial \hat{y}(t+1)}{\partial u(t)} \quad (10)$$

The gradient is analytically evaluated using the known neural network structure (7) as follows:

$$\frac{\partial \hat{y}(t+1)}{\partial u(t)} = w_2 [\sec h^2(w_1 q + b_1)] w_1 \frac{dq}{du} \quad (11)$$

where

$$\frac{dq}{du} = [0, 0, \dots, 0, 1, 0, \dots, 0]^T \quad (12)$$

is the derivative of the input vector q with respect to $u(t)$. Finally (10) can be written as

$$u(t+1) = u(t) + \eta e(t+1) w_2 [\sec h^2(w_1 q + b_1)] w_1 \frac{dq}{du} \quad (13)$$

Eq. (13) can now be used in the software program for real-time control.

3. Input-Output Linearisation

In this section, we discuss feedback linearisation of the neural network model via suitable transformation based on the input-output data which are accessible for measurements.

Many advanced controllers make use of rigorous models to overcome the difficulties of controlling nonlinear processes. However, it is usually a very difficult and time consuming task to rigorously model the process over the whole operating range. Because of this fact, many linear controllers are used for controlling nonlinear processes in the industries. The local dynamics of the nonlinear system varies significantly depending on the operating range. When the linear controllers are applied to a nonlinear system, the linear controllers are conservatively tuned to ensure the stability in the whole operation range. Around the operation range with slower dynamics, the control performance can deteriorate significantly. Hence, these linear techniques have inherent limitations in controlling nonlinear systems.

It is expected that if the process to be controlled by the linear controller can be linearised, the closed-loop performance will improve. The desired transformation for linearisation is realised with a multilayer neural network which is trained using the input-output data.

We consider the nonlinear neural network plant model $[NN_p]$ and the linearising transformation $[NN_T]$ as shown in Figure 4 to feedback linearise the neural network model. The control input u is the flow rate. We train the network NN_T based on the error between the output $y(t+1)$ which is in the controllable canonical form [15] and the output of the neural network model $\hat{y}(t+1)$.

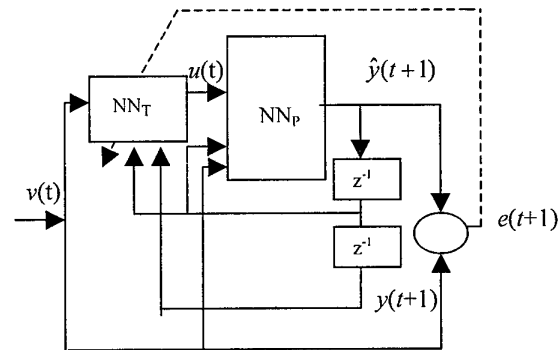


Figure 4: Input-output Linearisation Structure 1

The linearisation problem is now to train the neural network model input $u(t)$ based on the error $e(t+1)$. The network NN_T cannot be directly trained based on its output error using Figure 4, a novel neural network structure given in Figure 5 is used. A Theorem in [16] is derived to basically show the equivalence of Figure 4 and Figure 5.

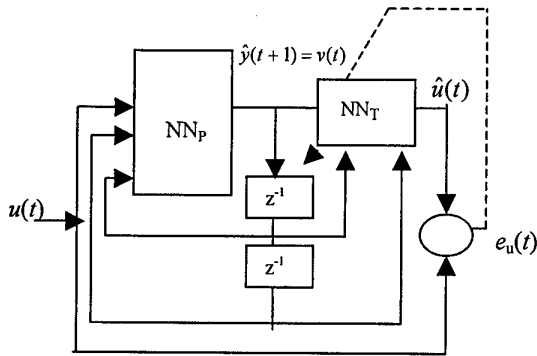


Figure 5: Input-output Linearisation Structure 2

4. Neural Network Implementation

Now we configure the neural network structure for modelling the heat exchanger plant which is of the form

$$y(t+1) = f[y(t)y(t-1), u_1(t), u_1(t-1), u_2(t), u_2(t-1)] \quad (14)$$

where $[u_1(t), u_2(t), y(t)]$ represents the input-output terms of the multi-input single output (MISO) heater exchanger plant at time t . The function $f: R^6 \rightarrow R$. In this neural network model, the output of the plant at time $t+1$ depends both on its past values of output and input.

For identification of the heat exchanger, a neural network model $N_{6,8,1}^3$ is constructed, where the superscript 3 represents the number of layers, the subscripts 6,8,1 represent the number of input nodes in the input layer, number of processing elements in the hidden layer and number of units in the output layer respectively. The output is the outlet temperature of the heat exchanger at time $t+1$. A one step delayed output and input signals are used to determine the future output. On-line data of the heat exchanger is used for neural network modelling.

Figure 6 shows the output of the process plant and the model during training phase, where the identification procedure was carried out for 20,000 iterations using random steps. The input and output data is normalised. A step size of 0.1, momentum factor of 0.8, learning rate

of 0.1, 0.01 and 0.001 were used for 5,000, 10,000 and 20,000 iterations respectively.

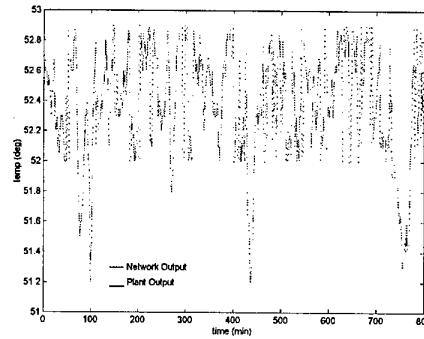


Figure 6: Training Result

Figure 7 shows the output of the plant and the model during the testing phase. The data used for testing the neural network model was different from that used during the training phase.

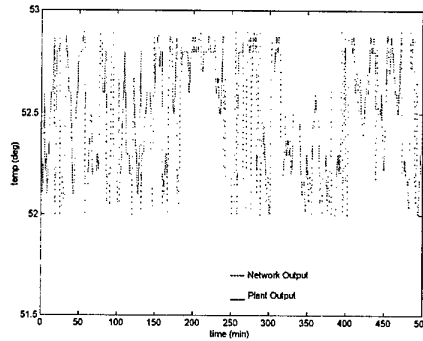


Figure 7: Testing Result

4.1. Linearisation

The performance of the input-output linearisation scheme on the heat exchanger model is presented here. To accomplish input-output linearisation of the neural model NN_P the network NN_T is trained using the structure shown in Figure 5. For the network NN_T we have used $N_{4,2,2}^3$ three layered neural network with four input nodes in the input layer, 2 nodes in the hidden layer and 2 output nodes in the output layer. The input vector $v(t)$ to NN_T comprises of the output temperature of the neural model NN_P and its delayed values. The output that has to be tracked by NN_T is the flow rate $u(t)$ and its delayed value. A random flow rate $u(t)$ and its delayed value $u(t-1)$ uniformly distributed over the dynamic input range for the plant emulator NN_P was used to drive the structure shown in Figure 5.

The error $e_u(t) = u(t) - \hat{u}(t)$ summed over different training steps were used as a performance index and adjustment of the weights of NN_T was performed at the end of each sequence to decrease the error. Different variable step sizes were used to adjust the weights of the network NN_T . After sufficiently training the network NN_T to the desired accuracy using Figure 5 then the over all system (Figure 4) can be assumed to have been trained to track the linear system which is in the controllable canonical form.

5. Implementation of PI Controller

In the previous section, it was demonstrated that a nonlinear system can be identified and feedback linearised using neural networks from its input-output data. Now that the characteristics of the linearised neural network model is known, we proceed to control the linearised neural network model using a PI controller. Figure 8 illustrates the controller configuration used to control the linearised system.

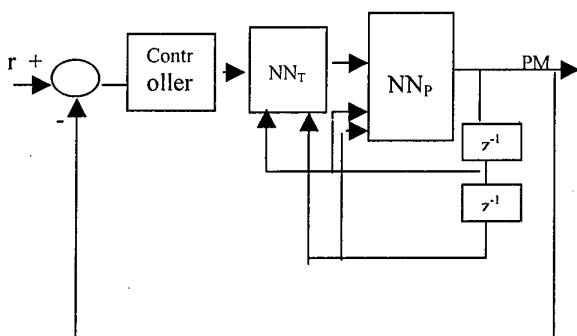


Figure 8: PI Controller & the Linearised System

The PI controller tuning parameters was properly set based on the conventional control theory, the IMC based PID tuning rule. The set point was set to 52.32, proportional gain $K_c = 45$, and the integral time $\tau_i = 0.4$ min. Figure 9 illustrates the time domain response of the linearised system around the equilibrium point with the PI controller in action.

6. Conclusion

This paper has demonstrated that a non-linear pilot plant fitted with Fieldbus equipment can be identified and feedback linearised using neural networks from its input-output data. Performance evaluation of the linearising network from the closed loop control point of view is done. The proposed linearising scheme attempts to

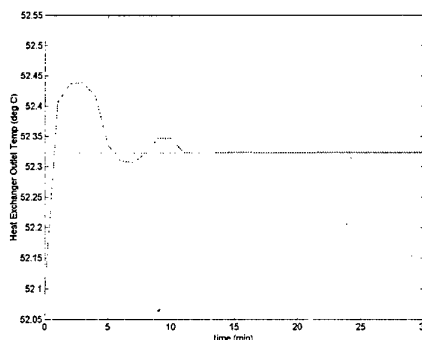


Figure 9: Response of Linearised System with PI Control

simplify, in effect, the control of a non-linear dynamic system by first linearising it and then applying a fixed linear controller, such as, a PI controller to it. The effect of linearising network indirectly measured by the ease of control achieved through an order of magnitude improvement in the proportional and integral gain settings achievable is shown in the paper.

7. References

- [1] K.S. Narendra and K. Parthasarathy, "Identification and control of dynamical systems using neural networks," *IEEE Transactions on Neural Networks*, vol. 1, no.1, pp. 4-27, 1990.
- [2] K.J. Hunt, D. Sbarbaro, R. Żbikowski, and P.J. Gawthrop, "Neural network for control systems-a survey," *Automatica*, vol.28, no.6, pp. 1083-1112, 1992.
- [3] Gordon Lightbody and George W. Irwin, "Nonlinear Control Structures Based on Embedded Neural System Models," *IEEE Transactions on Neural Networks*, vol. 8 no. 3 pp. 553-567, 1997.
- [4] Gerard Bloch, Franck Sirou, Vincent Eustache and Phillippe Fatrez, "Neural Intelligent Control for a Steel Plant," *IEEE Transactions on Neural Networks*, vol. 8, no. 4, pp. 910-917, 1997.
- [5] Jose R. Noriega and Hong Wang, "A direct Adaptive Neural-Network Control for Unknown Nonlinear Systems and its Application", *IEEE Transactions on Neural Networks*, vol. 9, no. 1, pp. 27-33, 1998.
- [6] Dan Hammerstrom, "Working with Neural Networks," *IEEE Spectrum*, vol. 30, no. 7, pp. 46-53, 1993
- [7] A. Isidori, "Nonlinear Control Systems An Introduction," *Springer-Verlag*, 1989.
- [8] A. Delgado, C. Kambhampati, and K. Warwick, "Dynamic input/output Linearisation using Recurrent Neural Networks."

Proceedings of the International Conference on Neural Networks, vol.3, pp. 1721-1726, 1996.

[9] Suk-Joon Kim, Minho Lee, Sunwon Park, Soo-Young Lee and Cheol Hoon Park, "A Neural Linearizing Control scheme for Nonlinear Chemical Processes," *Computers & Chemical Engineering*, vol. 21, no.2, pp. 187-200, 1997.

[10] S. Chen and S.A. Billings, "Representation of Nonlinear systems: The NARMAX model," *International Journal of Control*, vol.49, no.3, pp. 1013-1032, 1989.

[11] G. Cybenko, "Approximations by Superpositions of a Sigmoidal function," *Math. Signals Syst.*, vol. 2, pp.303-314, 1989.

[12] K. Funahashi, "On the Approximate Realization of Continuous Mappings by Neural Networks," *Neural Networks*,

vol. 2, pp. 183-192, 1989.

[13] B. Widrow and M.A. Lehr, "30 years of Adaptive Neural Networks: Perceptron, Madaline and Backpropagation," *Proceedings of IEEE*, vol. 78, pp. 1415-1441, 1990.

[14] F.M. Silva and L.B. Almeida, "Speeding up Backpropagation," *Advanced Neural Computers*, pp. 151-158, 1990.

[15] I. Nagarath and M. Gopal, "Control Systems Engineering," *Wiley Eastern Limited, New Delhi*, 1982.

[16] Fazlur Rahman M.H.R. and Devanathan R., "Dynamic Neural Networks for Input-Output Linearisation," *Proceedings of IEEE International Conference on Neural Networks*, vol.4, pp. 2214-2219, 1996.

Sequential Task Execution in a Prosthetic Limb using an Artificial Neural Network

S. Srinivasan
Department of Electrical Engineering
Singapore Polytechnic
500 Dover Road
Singapore 0513
Email: shankar@sp.edu.sg

A. Bradley
Department of Communication
and Electronic Engineering
RMIT City Campus, Victoria
Australia 3001
Email: alanb@rmit.edu.au

Abstract

Recent advances in computing technology along with improvements in signal processing techniques provide exciting opportunities for the development of highly functional rehabilitative aids for the disabled. This paper reports the use of an artificial neural network (Jordan's Sequential network) for use in a myoelectric prosthetic arm to facilitate fault-tolerant pattern recognition and simple sequential tasks. Initial experiments with this technique have yielded promising results and indicate that the technique has a very good potential for an effective rehabilitation of the functionally disabled in terms of their employability, independence, and self-esteem.

1. Introduction

New computing paradigms (such as neural networks & fuzzy logic) along with availability of low-cost digital signal processing chips provide exciting opportunities for the development of highly functional rehabilitative aids for the disabled. In this context, this paper reports the use of Jordan's Sequential Neural Network [1] for use in a myoelectric prosthetic arm to facilitate fault-tolerant pattern recognition and multifunctional activations.

Myoelectric prostheses utilise the *myoelectric signals* (MES) which originates within the remnant muscles of the limb stump for control purposes. The MES being a very low magnitude, low frequency stochastic signal (< 5 mV) requires statistical means for effective characterisation and processing for control purposes. Typically time domain parameters (*mean, variance* etc.) [2] and frequency domain parameters (*mean frequency, median frequency* etc.) have been employed to relate the MES to the movement parameters such as *force* and *velocity of contraction* of the respective source muscle(s) [3]. The control of a powered prosthetic limb using a MES would therefore have to rely on the variation of such parameters of the signal with the contraction level (force) of the remnant (source) muscles.

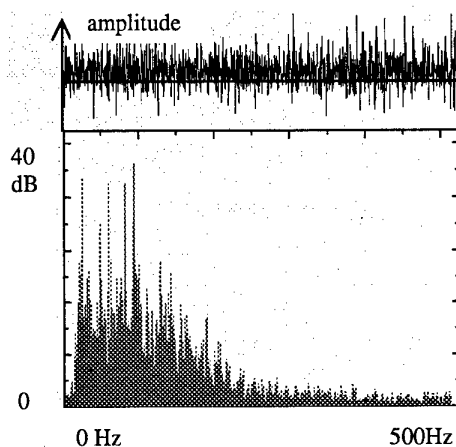


Figure 1. Illustration of the MES time domain waveform along with its power spectrum.

Previous control techniques utilised these parameters to control single functions (such as grasping, turning or releasing etc.) which very soon exhausts the amputee in the execution of even a simple manipulation task. With the advancement of new processing paradigms such as artificial neural networks and fuzzy logic and the availability of low-cost signal processing chips, it is now possible to develop functionally dexterous and light-weight prostheses. Specifically it is reported here that the ability of the Jordan's network to learn and faithfully recall sequences of signal patterns indicates its usefulness for the development of a multifunctional prosthetic limb with minimal control parameters.

2. Methodology

In the myoelectric control scheme amputation is considered as removal of the output portion of the musculoskeletal system, and of associated feedback pathways, leaving a muscle remnant(s) which is still capable of contracting, but has no remaining mechanical function. For the control purposes, the MES is obtained from these remnant muscles, using suitable *surface*

electrodes, in the portion of the limb superior to the point of amputation.

For the case of a 'lower arm amputee', the MES could be obtained from the six muscles spanning the elbow joint. However, for higher level amputees the number of input signals available would reduce dramatically. This necessitates the use of a new technique to maximise the movements effected for any given activation and indeed the current technique is indicated to provide such a capability. The figure below illustrates the basic aspects of the myoelectric control scheme:

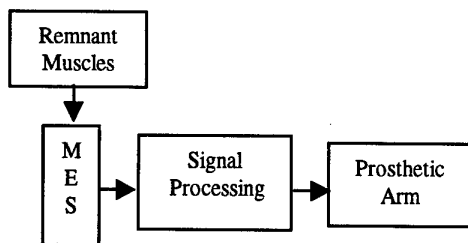


Figure 2. A basic block diagram of the myoelectric control scheme.

The basic processing methodology is illustrated below (Figure 3). The MES as acquired from surface electrodes has a very low amplitude, typically, below 5 mV. This necessitates the use of high-gain differential amplification with a high common mode rejection ratio and a high input impedance. The MES was obtained from four healthy subjects, using Ag/AgCl electrodes, from the upper arm region over the *biceps brachii*. Following acquisition the signals were amplified with a bio-instrumentation amplifier with a gain of 1000 and a CMRR of 86 dB.

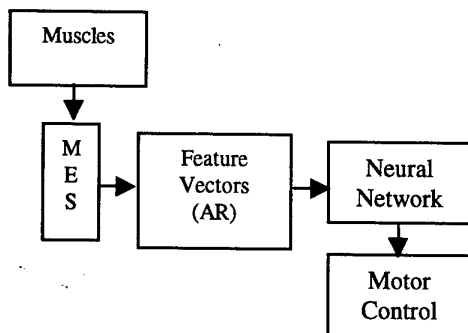


Figure 3. Schematic diagram of the acquisition of the MES and its processing.

Following the amplification as described above, suitable characteristic features (feature vectors) of the MES, were needed to be extracted so as to facilitate

distinguishing between different contraction levels. In this case, different feature vectors would enable effecting different motions or motion sequences in the prosthetic limb. Since the environment would be noise-ridden, the decision algorithm should ensure minimum control error or maximum information transfer between the MES feature vectors and the effectors (typically motors at the joints of the limb). Accordingly, the Jordan's sequential network was employed as the appropriate decision making module. Its inputs would be the different sets of feature vectors to be classified and correctly detected and its outputs would be the appropriate sets of control signals to the prosthetic limb's actuator motors.

To facilitate the feature extraction process, the MES was formulated as a auto-regressive (AR) model as follows:

$$y_k = \sum_{i=1}^m a_i y_{k-i} + w_k, \quad k = 0, 1, 2, \dots$$

where the a_i are the m AR coefficients and the residual w_k being a white noise sequence (totally uncorrelated). Though in theory the value of m is infinite, it has been found that a value of $m=4$ is sufficiently accurate for the purpose of control and spectral analyses [4].

In the case of upper-limb prostheses, there are several functions possible viz. elbow extension and bending, wrist pronation and supination, grasping and ungrasping. Since we were interested in exploring the ability of the proposed control technique to correctly execute learned trajectories despite noisy input features, only the actions of elbow bending, extending and wrist pronation and supination were allowed while the hand was held permanently clasped.. In the actual implementation, these different 'limb functions' are to be activated by the user's generating a different trained muscle activating pattern at the remnant muscles in the vicinity of the electrode site. The latter muscle activation patterns, yielding different sets of a_i need not be related to the desired limb function. The amputee or the paralysed user is however trained to remember the correspondence between the individual muscle activation pattern (at the electrode's vicinity) and the appropriate sequence of motions.

3. Results and discussion

For this project the prosthetic limb was fixed to a suitable platform such that the hand was capable of executing a trajectory on a 2 dimensional plane held orthogonal to the limb's central axis. The acquisition and processing of the MES to yield the feature vectors

and the sequential network's control signals were all performed in a personal computer suitably interfaced to the myoelectric arm.

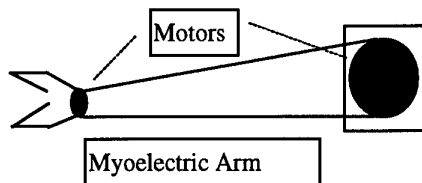


Figure 4. Schematic diagram of the set-up employed in testing the proposed control technique.

All the four subjects were then requested to perform a elbow flexion and pronation and were further required to maintain a similar state of contraction as much as possible over several trials. The AR coefficients for each of the MES samples, obtained from each of them over four trials, were then extracted for further processing.

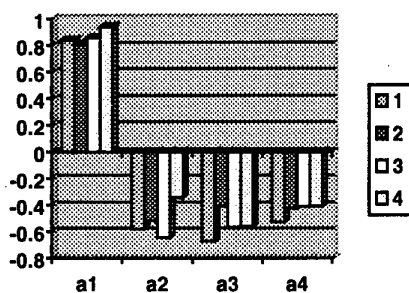


Figure 5. Illustration of the AR coefficients obtained from the MES of a single subject upon four different trials during flexion.

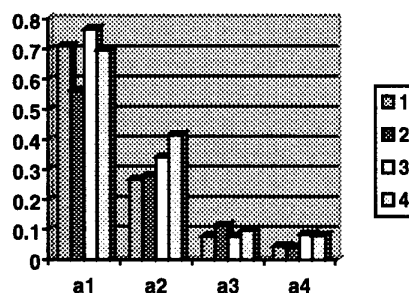


Figure 6. Illustration of the AR coefficients obtained during pronation.

The figures above are an example of the AR coefficients obtained from the MES of a single subject upon four different trials and for the two different

functions associated with the biceps muscle (flexion and pronation).

Following their acquisition, the AR coefficients (the feature vectors) were suitably preprocessed for input to the decision making module, namely, the Jordan's sequential neural network (illustrated below in Figure 7) which employs the back-propagation learning algorithm. For each individual subject (user), the network was made to *learn* the association between the pre-processed feature vectors and a series of control signals which when input to the prosthetic limb's motors would yield different sequences of motion in three-dimensional space. Thus when employing the identified parameters or coefficients to discriminate between limb functions, a decision, relating an identified coefficients vector $a = [a_1, a_2, \dots, a_n]$ to a given limb function, was to be made by the neural network based on the similarity of the feature vector to the learned ones.

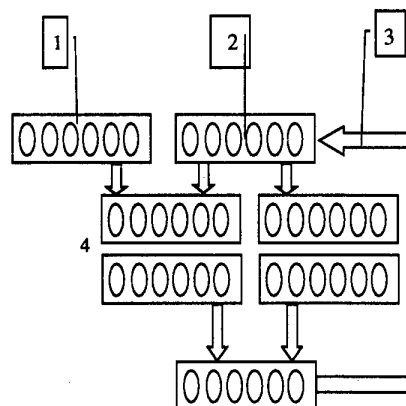


Figure 7. Illustration of the Jordan's Sequential Network. '1' refers to the State Units which are input with AR coefficients, '2' refers to the Input Units which have the different states of the trajectory, '3' refers to the feedback of the past output and '4' refers to the two layers of Hidden Units.

The figure below illustrates the close correspondence between one of the desired trajectories required of the prosthetic arm and that actually executed by it.

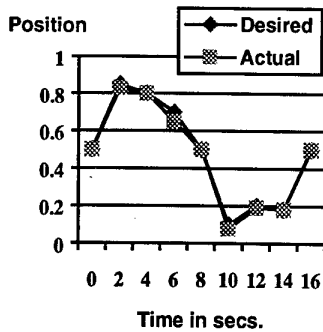


Figure 8. Illustration of one of the desired and the corresponding trajectory executed by the prosthetic limb.

Furthermore, the Jordan's sequential network exhibits the property of *limit cycle behaviour* in that, given any starting, it is capable of reverting to the learned trajectory which closely matches with the given starting position. This is also exhibited in the case of any *faults* which may occur in the midst of the execution of any of the learned trajectories. Indeed for the given trajectory above, the illustration below shows the two cases of the novel starting position and a fault occurrence suitably amended to yield the learned trajectory.

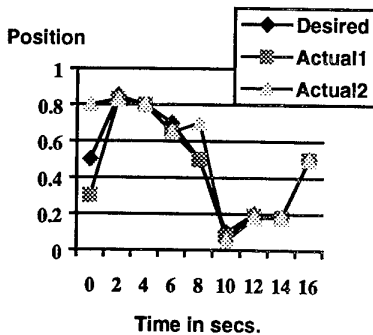


Figure 9. Illustration of the *limit cycle behaviour* of the sequential network - Curve 'Actual1' has a different starting position while curve 'Actual2' also has a different starting position and a fault in between its execution.

The average prosthetic arm would allow the user only one specific motion (example, grasping or releasing) leading to early exhaustion in the execution of even a simple manipulative task [5]. The addition of the sequential network allows the user the option of programming specified movements into the neural network which may be activated by generating a specific pattern of myoelectric signal. For example, the user may perform all movements associated with opening a

microwave oven simply by generating the MES signal pattern usually associated adducting the upper arm hard into the side of the body. Furthermore, the use of the sequential neural network allows the input of a pre-determined sequence of control signals to a combination of one or several motors in the myoelectric limb. This technique could be extended to the case of partly paralysed persons to activate a powered-braces system or a set of appropriately positioned electrical stimulation electrodes.

4. Conclusions

It is imperative that the functionally disabled people be provided with prospects of securing, retaining places and advancing in educational and training institutions, employment and recreation otherwise denied to them as equal members of the society because of their disabilities. The proposed scheme intends to meet this need in a small but hopefully effective manner in restoring the self-dependency and self-esteem of the disabled people. It is also in tune with the need for introducing state of art technology into the current prosthetic and orthotic techniques. It specifically promises to offset the currently available bulky and physically exhausting prostheses by incorporating state of the art processors and techniques. Initial experiments have yielded promising results warranting further investigation into the real-time processing and testing with amputee subjects.

The lack of sensory feedback to the central nervous system is a significant limitation to the new technique as well as the currently popular prostheses. Solutions can be arrived at by employing the new and forthcoming sensor technologies [6][7], and the increasing amount of knowledge in the field of neurophysiology and signal processing [8].

References:

1. Srinivasan, S et al., "A movement pattern generator model using artificial neural networks", *IEEE Transactions on Biomedical Engineering*, Vol.39, No.7, 1992, pp. 716-722.
2. Basmajian, J.V. and DeLuca, C.J., *Muscles Alive*, 5th Ed., Williams and Williams, Baltimore, 1985.
3. Christensen, H. and Frederiksen, A.F., "Power spectrum and turns analysis of EMG at different voluntary efforts in normal subjects", *Electroencephalography and Clinical Neurophysiology*, Vol.64, 1986, pp. 528-535.
4. Graupe, D et al., "A multifunctional prosthesis control based on time series identification of EMB signals using

microprocessors", *Bulletin of Prosthetics Research*, 1977, BPR 10-27.

5. Millstein, S.G et al., "Prosthetic use in adult upper limb amputees: a comparison of the body powered and electrically powered prostheses", *Prosthetics and Orthotics International*, Vol.10, 1986, pp. 27-34.

6. Burdea, G. et al., "Diagnostic/rehabilitation system using force measuring and force feedback dexterous masters", *Proceedings of the Medicine meets Virtual Reality Conference*, USA, 1992, pp. 10-18.

7. Neuman, M.R. et al., "Fabricating biomedical sensors with thin-film technology", *IEEE Engineering in Medicine and Biology Magazine*, Vol.13, No.3, 1994, pp. 409 – 419.

8. Rioul, O and Vetterli, M., "Wavelets and Signal Processing", *IEEE SP Magazine*, pp. 14-38, 1991.

A Robust Fuzzy Controller for a Class of Multiple Hyperredundant Cooperative Robots

Mircea Ivanescu*, professor, PhD

Nicu Bizdoaca*, lecturer

*Automatic and Computer

Department, University of Craiova, Romania

Nirvana Alina Popescu**, assistant professor

Decebal Popescu**, assistant professor

** Computer Department, University

"Politehnica", Bucharest, Romania

Email: rector@alpha.comp-craiova.ro

Abstract

The local control for a multi-chain robotic system formed by tentacle manipulators grasping a common object with hard point contacts is proposed to solve using a robust control system.

The stability and robustness of a class of the fuzzy logic control (FLC) are investigated and a robust FLC is proposed with uncertainties of the load.

The two-level hierarchical control is adopted. The upper level coordinator gathers all the necessary information to resolve the distribution force. Then, the lower-level local control problem is treated as an open-chain redundant manipulator control problem.

The fuzzy rules are established. Simulation results are presented and discussed.

1. Introduction

The coordinated operation of two or more robots is a field of research activity which opens up new fields of applications in assembly automation and flexible manufacturing systems.

A tentacle manipulator is a manipulator with a great flexibility, with a distributed mass and torque that can take any arbitrary shape. Technologically, such systems can be obtained by using a cellular structure for each element of the arm.

A multiple chain tentacle robotic system is more complicated. The first problem is the global coordination problem that involves coordination of several tentacles in order to assure a desired trajectory of a load. The second problem is the local control problem, which involves the control of the individual elements of the arm to achieve the desired position. The force distribution is a subproblem in which the motion is completely specified and the internal forces/torques to effect this motion are to be determined. To resolve this large-scale control problem, a two-level hierarchical control scheme[4] is

used. The upper-level system collects all the necessary information and solves the interchain coordination problem, the force distribution problem. Then, the problem is decoupled into j lower-level subsystems, for every arm. The local fuzzy controllers are assigned to solve the local control. In order to obtain the fuzzy control an approximate model of the tentacle arm is used.

The stability and robustness of the FLC are investigated and a robust FLC is proposed with respect to the robustness of the load uncertainties. The control strategy is based on the Direct Sliding Mode Control (DSMC) which controls the trajectory towards the switching line and then the motion is forced directly to the origin, on the switching line. A fuzzy controller is proposed and the fuzzy rules are established by using the DSMC procedures. Efficiently considerations of the method are discussed. Numerical simulations for several control problems are presented.

2. Cooperative Robots Model

A multiple-chain tentacle robotics system is presented in Figure 1.

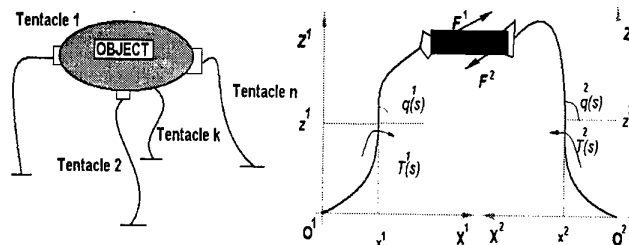


Figure 1

With the chains of the system forming closed-kinematics loops, the responses of individual chains are tightly coupled with one another through the reference member (object or load). The complexity of the problem is considerable increased by the presence of the tentacle

manipulators, $(TM^j, j = 1 \dots k)$, the systems with, theoretically, a great mobility, which can take any position and orientation in space [1,2]. In the Figure 1.b is presented a plane model, a simplified structure which can take any shape in XOZ plane. The dynamic equations for each chain of the system are [1]:

$$TM^j: \rho_j A^j \int_0^s [\sin(q^j - q'^j) \dot{q}'^j{}^2 + \cos(q^j - q'^j) \ddot{q}'^j] ds' + \rho A g \int_0^s \cos q^j ds' + \tau^j = T^j, j = 1, 2 \quad 2.1$$

$$\int_0^{L^j} \tau^j ds = F_x^j \int_0^{L^j} (-\sin q^j) ds + F_z^j \int_0^{L^j} \cos q^j ds, j = 1, 2 \quad 2.2$$

where we assume that each manipulator (TM^j) has a uniform distributed mass, with a linear density ρ^j and a section A^j . We denote by s the spatial variable upon the length of the arm, $s \in [0, L^j]$. We also use the notations: q^j - Lagrange generalized coordinate for TM^j (the absolute angle), $\dot{q}^j = \dot{q}^j(s, t)$, $s \in [0, L^j]$, $t \in [0, t_f]$, $q'^j = q^j(s', t)$, $s' \in [0, s]$, $t \in [0, t_f]$, $T^j = T^j(s, t)$ - the distributed torque over the arm; $\tau^j = \tau^j(s, t)$ - the distributed moment to give the desired motion specified on the reference member. All these sizes are expressed in the coordinate frame of the arm TM^j . The k integral equations are tightly coupled through the terms τ^j , F_x^j , F_z^j where all of these terms determine the desired motion. We propose a two-level hierarchical control scheme [4,5] for this multiple-chain robotic system. The control strategy is to decouple the system into k lower-level subsystems that are coordinated at the upper level. The function of the upper-level coordinator is to gather all the necessary information so as to formulate the corresponding force distribution problem and then to solve this constrained, optimization problem such that optimal solutions for the contact forces F^j are generated. These optimal contact forces are then the set-points for the lower-level subsystems. We consider the hard point contact with friction and the force balance equations on the object may be written as: $F^0 = \sum_j {}^0D_j F^j$ 2.3

where: F^0 - the resultant force vector applied to object expressed in the inertial coordinate frame (0),

0D_j - the partial spatial transform from the coordinate frame for the arm TM^j to the inertial coordinate frame (0).

The object dynamic equations are obtained by the form $M_0 \ddot{r} = GF^0$ 2.4

where M_0 is inertial matrix of the object and r defines the object coordinate vector $r = (x, z, \varphi)^T$

2.5

and $r(t)$ represents the desired trajectory of the motion.

The inequality constraints which include the friction constraints and the maximum force constraints may be associated to (2.3), $\sum A^j F^j \leq B$ 2.6

where A^j is a coefficient matrix of inequality constraints and B is a boundary-value vector of inequality constraints. The problem of the contact forces F^j can be treated as an optimal control problem if we associate to the relations (2.3) - (2.6) an optimal index $\Psi = \sum_j C^j F^j$ 2.7

This problem is solved in several papers [4,5,6] by the general methods of the optimization or by the specific procedures [7]. After all of the contact forces F^j are determinate, the dynamics of each arm TM^j are decoupled. Now, the equations (2.1), (2.2) can be interpreted as same decoupled equations with a given $\tau^j(s)$, $s \in [0, L^j]$ acting on the tip of the arm.

3. Approximate model

A discrete and simplified model of (2.1), (2.2) can be obtained by using a spatial discretization.

$$s_1, s_2, \dots, s_N; \quad s_i - s_{i-1} = \Delta; \quad 3.1$$

$$|q^j(s_i) - q^j(s_k)| < \varepsilon; \quad i, k = 1, 2, \dots, n^j \quad 3.2$$

where ε, Δ are constants and ε is sufficiently small.

We denote $s_i = i\Delta$, $L^j = n^j\Delta$, $q_i^j(s_i) = q_i^j$,

$$T^j(s_i) = T_i^j, \tau^j(s_i) = \tau_i^j \quad 3.3$$

and considering the arm as a lightweight arm, from (2.1), (2.2) it results [2]:

$$M^j \ddot{q}^j + C^j \dot{q}^j + D^j(q^j) F^j = T^j \quad 3.4$$

where M^j , C^j are $(n^j \times n^j)$ contact diagonal matrixes, D is $(n^j \times 2)$ nonlinear matrix [2,13]

$$F^j = \text{col}(F_x^j, F_z^j) \quad 3.5$$

$$q^j = \text{col}(q_1^j \dots q_{n^j}^j) \quad 3.6$$

$$T = \text{col}(T_1^j \dots T_{n^j}^j) \quad 3.7$$

In the equation (3.4), F^j assures the load transfer on the trajectory. The uncertainty of the load m defines an uncertainty of the force F^j .

$$\text{We assume that } |F^{MJ} - F^j|_i \leq \rho_i; i = 1, 2 \quad 3.8$$

Where F^{MJ} is an estimation of the upper bound of the force.

4. Fuzzy control

The control problem asks for determining the manipulatable torques (control variables) T_i^j such that the

trajectory of the overall system (object and manipulators) will correspond as closely as possible to the desired behavior. In order to obtain the control law for a prescribed motion, we shall use the closed-loop control system from Figure 2.

Let q_d^j the desired parameters of the trajectory, F_d^j the desired force applied to the j -contact point of the object, and q^j, F^j the same sizes measured on the real system. For a bounded smooth trajectory, a tracking error is:

$$e = q - q_d \quad 4.1$$

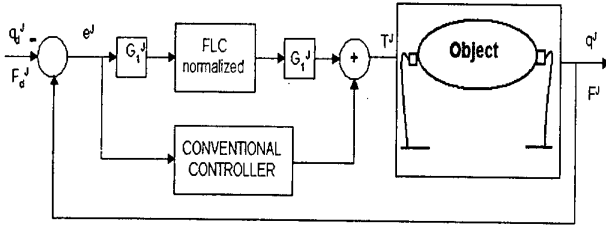


Figure 2

The control system contains two parts: the first component is a conventional controller which implement a classic strategy of the motion control based on the Lyapunov stability and the second is a FLC.

A fuzzy control is proposed by using the control law in the neighborhood of the switching line (Table 1 and Figure 3)

as a variable structure controller.

The physical meaning of the rules is as follows: the output is zero near the switching line (s), the output is negative above the switching line, the output is positive below the diagonal line, the magnitude of the output tends to increase in accordance with magnitude of the distance between the switching line and the state (e^j, \dot{e}^j) .

We consider that all input/output fuzzy sets are assumed to be designed on the normalized space:

$$e_{i,N}^j, \dot{e}_{i,N}^j, T_{i,N}^j \in [-1, 1], i = 1, 2, \dots, n^j \quad 4.2$$

$\dot{e}^j \setminus e^j$	NBE	NSE	ZRE	PSE	PBE
PBDE	ZRC	NBC	NBC	NBC	NBC
PSDE	PBC	ZRC	NSC	NSC	NBC
ZRDE	PBC	PSC	ZRC	NSC	NBC
NSDE	PBC	PSC	PSC	ZRC	NBC
NBDE	PBC	PBC	PBC	PBC	ZRC

Table 1

and the input/output gains $G_1^j = [G_e^j, G_{\dot{e}}^j]$ and G_c serve as scale factors between the normalized space and the corresponding real space of the process

$$e_{N,i}^j = G_{ei}^j e_i^j \quad 4.3$$

$$\dot{e}_{N,i}^j = G_{ei}^j \dot{e}_i^j \quad 4.4$$

$$T_{N,i}^j = G_{ci} T_i^j \quad 4.5$$

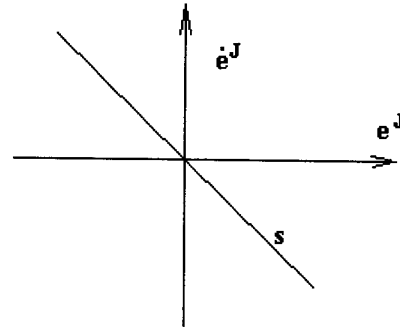


Figure 3

If we consider that the switching line s in the space of normalized values is defined by the diagonal:

$$\dot{e}_{N,i}^j + e_{N,i}^j = 0 \quad 4.6$$

it corresponds to the following diagonal line in the real error phase plane [15],

$$s_i^j = \dot{e}_i^j + \sigma_i^j e_i^j = 0, \quad \sigma_i^j = \frac{G_{ci}^j}{G_{ei}^j} > 0 \quad 4.7$$

$$\dot{e}^j + \sigma e^j = 0 \quad 4.8$$

where $\sigma = \text{diag}(\sigma_1, \sigma_2, \dots, \sigma_{n^j})$

The memberships of the input/output variables are represented in Figure 4, where NB, NS, ZR, PS, PB define the linguistic variables: NEGATIVE BIG, NEGATIVE SMALL, ZERO, POSITIVE SMALL, POSITIVE BIG, respectively.

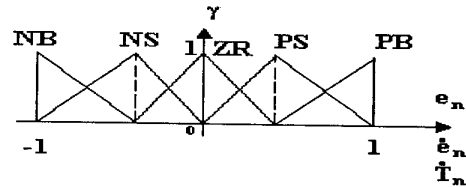


Figure 4

Theorem 1.

The closed-loop system of Figure 2 is stable if the control is defined by

$$T^j = -K^j s + H^j(e, q_d, F^M) + u_F^j \quad 4.9$$

where K^j is a $(n^j \times n^j)$ symmetric positive definite matrix, which satisfies condition

$$K^j - M^j \sigma^j + C^j \text{ positive definite matrix} \quad 4.10$$

and u_F is the output vector of the fuzzy controller

$$u_{Fi}^j = -k_{Fi}^j \text{sgn } s_i^j \quad 4.11$$

$$k_{Fi}^j \geq |H(e, q_d, F) - H^j(e, q_d, F^M)|_i \quad 4.12$$

Proof. See Appendix 1.

The Theorem 1 determines the conditions which assure the motion control in the neighborhood of the switching line. In order to accelerate the motion on the switching

line, we can use the DSMC (Direct Sliding Mode Control). The DSMC was presented in [14] and it establishes conditions which force the trajectory along the switching line, directly toward the origin (Figure 5).

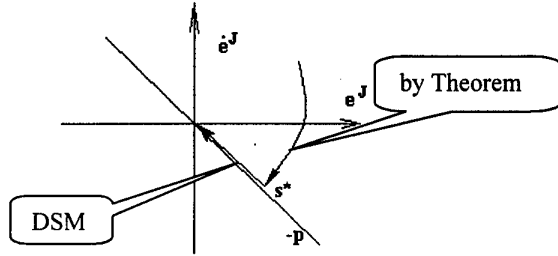


Figure 5

In the first part of the motion defined by Theorem 1, we considered that the switching line has the slope $-\sigma_i$. The DSMC can require a new switching line,

$$s_i^* = \dot{e}_i^J - p_i^J e_i^J = 0 \quad (4.13)$$

Proposition

The DSMC control is assured if the coefficient k_i of the controller verifies the condition,

$$(c_i + k_i)^2 \geq 4m_i(\sigma_i(-m_i\sigma_i + c_i + k_i) + h_i) \quad (4.14)$$

Proof. See Appendix 2.

The DSMC control can introduce a new fuzzy output variable, the coefficients k_i . In the first part of the motion k_i verifies only the condition (4.10). When the trajectory penetrates the switching line s_i^* , the k_i are increased in order to verify (4.14)

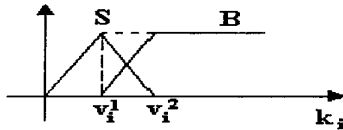


Figure 6

In Figure 6 and Table 2 are presented the memberships functions for k_i and fuzzy rules, where we defined as v_i^1 , v_i^2 the average values which verify the condition (4.10) and (4.14), respectively.

$\dot{e}^J \setminus e^J$	NBE	NSE	ZRE	PSE	PBE
PBDE	B	S	S	S	S
PSDE	S	B	S	S	S
ZRDE	S	S	B	S	S
NSDE	S	S	S	B	S
NBDE	S	S	S	S	B

Table 2

5. Numerical Results

The purpose of this section is to demonstrate the effectiveness of the method. This is illustrated by solving a fuzzy control problem for a two tentacle manipulator system which operates in XOZ plane (Figure 7)

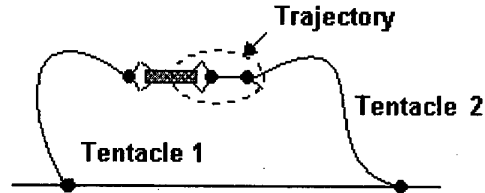


Figure 7

These two manipulators form a closed-chain robotic system by a common object which is manipulated. An approximate model (3.4) with $\Delta=0.06$ m and $n^J=7$ is used ($J=1,2$).

Also, the length and the mass of the object are 0.2 m and 1 kg, respectively.

The initial position of the arms expressed in the inertial coordinate frame are presented in Table 3.

TM^J	$q_1^J(0)$	$q_2^J(0)$	$q_3^J(0)$	$q_4^J(0)$	$q_5^J(0)$	$q_6^J(0)$	$q_7^J(0)$
TM^1	$\pi/6$	$\pi/3$	$7\pi/12$	$2\pi/3$	$\pi/15$	$15\pi/8$	0
TM^2	$5\pi/6$	$4\pi/5$	$4\pi/5$	$3\pi/4$	$3\pi/4$	$2\pi/3$	π

Table 3

The desired trajectory of the terminal points is defined by:

$$x = x_0 + a \sin \omega t$$

$$z = z_0 + b \cos \omega t$$

With $x_0=0.2$ m, $z_0=0.1$ m, $a=0.3$ m, $b=0.1$ m, $\omega=0.8$ rad/s.

The trajectory lies the work envelopes of the both arm and does not go through any workspace singularities. The maximum force constraints are defined by:

$$F_X^J \leq F_{MAX} = 50N \quad F_Z^J \leq F_{MAX} = 50N$$

$$\text{and the optimal index } \min \left(\sum_J F_X^{J^2} \right), \min \left(\sum_J F_Z^{J^2} \right)$$

are used.

The uncertainty domain of the mass is defined as

$$0.8kg \leq m \leq 1.4kg$$

The solution of the desired trajectory for the elements of the arms is given by solving the nonlinear differential equation [13]

$$\dot{q}_d^J(t) = [J^{JT}(q) \quad J^J(q)]^{-1} J^{JT}(q) \dot{w}(t)$$

Where $w=(x,z)^T$ and $J^J(q)$ is the Jacobian matrix of the arms ($J=1,2$).

A conventional controller with $k_i^J=0.5$ ($i=1,..,7, j=1,2$) is determined.

A FLC is used with the scale factors selected as

$$G_{e_i}^J = G_{e_i}^J = 10, \quad i=1,..,7, J=1,2.$$

The conventional and DSMC procedures are used and new switching line is computed. The condition (4.14) is verified and the new switching line is defined for $p_i^J=1.03 : i=1,..,7, J=1,2$.

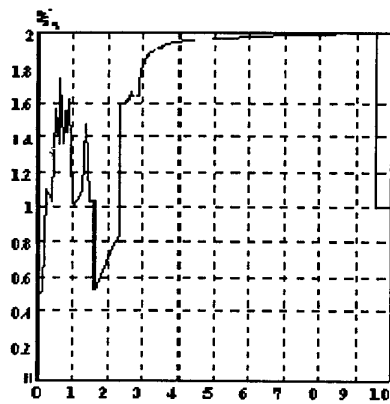


Figure 8

In Figure 8 is presented the evolution of k_5^1 for a DSMC procedure and the evolution of the position error e_5^1 and the position error rate \dot{e}_5^1 are presented in Figure 9.

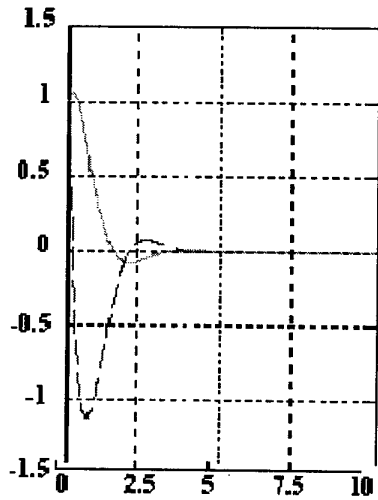


Figure 9

Figure 10 represents the trajectory in the plane (e_5^1, \dot{e}_5^1) for conventional procedure and Figure 11 the same trajectory for a DSMC procedure for a new switching line. Figure 12 presents the final trajectory. We can remark the error during the 1th cycle and the convergence to the desired trajectory during the 2nd cycle.

6. Conclusion

The two level hierarchical control procedure is constructed in this paper to solve the large-scale control problem of a chain robotic system formed by tentacle manipulators grasping a common object. The upper-level the inter-chain coordination problem, the force distribution. Then, the problem is decoupled into j lower-level subsystems, for every arm. The local fuzzy controllers are assigned to solve the local control. The stability and robustness of a class of the fuzzy logic

control (FLC) are investigated and a robust FLC is proposed in order to cancel the uncertainties of the load.

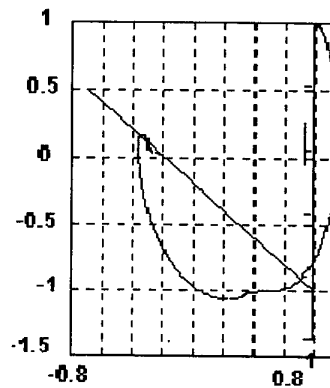


Figure 10

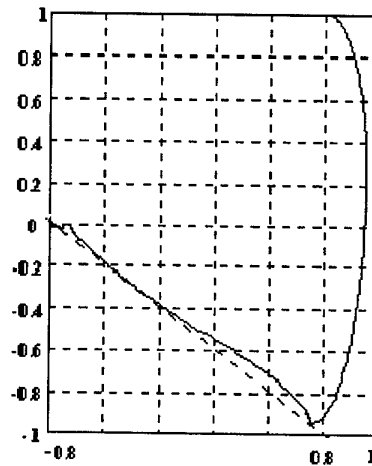


Figure 11

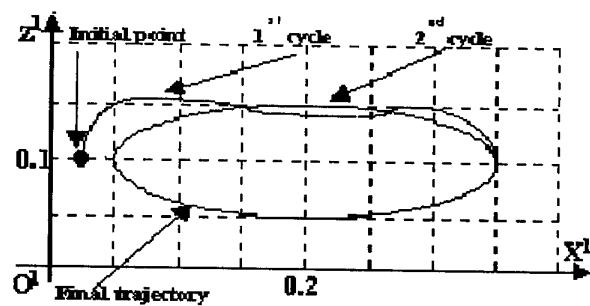


Figure 12

A DSMC procedure is used and the fuzzy rules are established. The simulation problem for two closed-chain tentacle robotic systems has also been studied.

REFERENCES

- [1] M., Ivanescu, "Dynamic Control for a Tentacle Manipulator", *Proc. of Int. Conf.*, Charlotte, USA, 1984.
- [2] M., Ivanescu, "A New Manipulator Arm: A Tentacle Model", *Recent Trends in Robotics*, Nov. 1986, pp. 51-57.
- [3] L. M., Silverman, "Inversion of Multivariable Linear Systems", *IEEE Trans. Aut. Contr.*, Vol AC - 14, 1969.
- [4] Fan-Tien Cheng, "Control and Simulation for a Closed Chain Dual Redundant Manipulator System", *Journal of Robotic Systems*, pp. 119 - 133, 1995.
- [5] Y.F., Zheng, J.Y.S., Luh, "Optimal Load Distribution for Two Industrial Robots Handling a Single Object", *Proc. IEEE Int. Conf. Rob. Autom.*, 1988, pp. 344 - 349.
- [6] M. T., Mason, "Compliance and Force Control", *IEEE Trans. Sys. Man Cyb.*, Nr. 6, 1981, pp. 418 - 432.
- [7] F. T., Cheng, D. E., Orin, "Optimal Force Distribution in Multiple-Chain Robotic Systems", *IEEE Trans. on Sys. Man and Cyb.*, Jan., 1991, vol. 21, pp. 13 - 24.
- [8] F. T., Cheng, D. E., Orin, "Efficient Formulation of the Force Distribution Equations for Simple Closed - Chain Robotic Mechanisms", *IEEE Trans on Sys. Man and Cyb.*, Jan. 1991, vol. 21, pp. 25 -32.
- [9] Li-Chun T. Wang, "Time-Optimal Control of Multiple Cooperating manipulators", *J. of Rob.Sys.*, '96, 229-241.
- [10] D.E., Khatib, "Coordination and Descentralisation of Multiple Cooperation of Multiple Mobile Manipulators", *Journal of Robotic Systems*, 13 (11), 755 - 764, 1996.
- [11] R. J., Schilling, "Fundamentals of Robotics", *Prent. Hall*, '90.
- [12] T.J., Ross, "Fuzzy Logic with Engineering Applications", *Mc.Grow Hill*, Inc., 1995.
- [13] M., Ivanescu, V., Stoian, "A Variable Structure Controller or a Tentacle Manipulator", *Proc. of the 1995 IEEE Int. Conf. on Robotics and Aut.*, Nagoya, Japan, May 21 - 27, 1995, vol. 3, pp. 3155 - 3160.
- [14] M., Ivanescu, V., Stoian, "A Sequential Distributed Variable Structure Controller for a Tentacle Arm", *Proc. of the 1996 IEEE Intern. Conf. on Robotics and Aut.*, Minneapolis, April 1996, vol. 4, pp. 3701 - 3706.
- [15] Soo Yeong Yi, "A robust Fuzzy Logic Controller for Robot Manipulators", *IEEE Trans. on Systems, Man and Cybernetics*, vol 27, No 4, 706-713, 1997

APPENDIX 1

We consider the dynamic model of the manipulator defined by (3.9). The parameter s^j from (4.7) represents an error measure of the closed-loop control.

$$s = \dot{e} + \sigma e \quad A1.1$$

Where we cancelled the upperscript j, for the simplicity. From (3.9) and (4.1) we obtain:

$$M(\ddot{e} + \ddot{q}_d) + C(\dot{e} + \dot{q}_d) + D(e + q_d)F = T \quad A1.2$$

$$M\dot{s} - M\sigma s + M\sigma^2 e + Cs - C\sigma e + D(e + q_d)F = T$$

we separate the linear part of s, it results,

$$M\dot{s} - (M\sigma - C)s + H(e, q_d, F) = T \quad A1.3$$

where H is a $(n^j \times 1)$ nonlinear vector defined on the trajectory parameters q_d, e, F .

In order to prove the stability of the closed-loop system, we use a Liapunov function by the form

$$V = \frac{1}{2} s^T Ms \quad A1.4$$

Differentiating (A1.4),

$$\dot{V} = s^T M\dot{s} \quad A1.5$$

If we substitute (A1.3) we obtain

$$\dot{V} = s^T M [M^{-1}(M\sigma - C)s - M^{-1}H(e, q_d, F) + M^{-1}T] \quad A1.6$$

By using the control law of T, (A1.6) becomes

$$\dot{V} = s^T (k - M\sigma + C)s + s^T [H(e, q_d, F^M) - H(e, q_d, F)] + s^T u_F \quad A1.7$$

And using (4.11), [15],

$$\dot{V} \leq -s^T (k - M\sigma + C)s + \sum_i s_i \|H(e, q_d, F^M) - H(e, q_d, F)\|_i - k_{F_i} \quad A1.8$$

If we introduce the condition (4.12) and we denote by λ_{\min} the minimum eigenvalue of $(K - M\sigma + C)$, it results,

$$\dot{V} \leq -\lambda_{\min} \|s\| \quad A1.9$$

(Q.E.D)

APPENDIX 2

We consider the dynamic model (A1.3) in the area around switching line ($u_{Fi}=0$),

$$M\dot{s} - (M\sigma - C)s + H(e, q_d, F) = -Ks + H(e, q_d, F^M) \quad A2.1$$

From (A1.1) and using the properties of the matrices M, C, K, S (diagonal matrices) we obtain,

$$m_i \ddot{e}_i + (c_i + k_i) \dot{e}_i + (-m_i \sigma_i^2 + c_i \sigma_i + k_i \sigma_i) e_i + (H(e, q_d, F) - H(e, q_d, F^M))_i = 0 \quad A2.2$$

but

$$(H(e, q_d, F) - H(e, q_d, F^M))_i = (\Delta H)_i \cong \frac{\partial H}{\partial F} \frac{\partial F}{\partial q_i} e_i \quad A2.3$$

We denote this term as

$$(\Delta H)_i = h_i(q_d, e) e_i \quad A2.4$$

From (A2.2), (A2.4) we obtain the switching line,

$$\frac{\dot{e}_i}{e_i} = -p_i = \frac{1}{m_i e_i} \left[-(c_i + k_i) e_i - \sigma_i (-m_i \sigma_i + c_i + k_i) e_i - h_i(q_d, e) e_i \right] \quad A2.5$$

This equation determines the slope p_i if the following condition is verified [14],

$$(c_i + k_i)^2 \geq 4(\sigma_i (-m_i \sigma_i + c_i + k_i) + h_i) m_i \quad A2.6$$

Linearization of the Load Characteristics of a Converter Through Fuzzy Compensation

Amr El-Zawawi, M.A.Wahba, and O.A.Sebakhy

*Department of Electrical Engineering,
Faculty of Engineering, University of Alexandria
Alexandria 21544, Egypt.*

E-mail : sebakhy@alex.eun.eg

Fax : (203) 5971853

Abstract

A fuzzy compensator is designed and implemented to linearize the nonlinear load characteristics of a single phase, half controlled ac to dc converter under discontinuous current conduction. The fuzzy compensator uses the converter-firing angle α and the average load current as input universes of discourse. Its output is a binary coded digital signal representing the compensated firing angle α_c . The experimental results show considerable improvement of the motor load characteristics over all the discontinuous conduction regions.

1. Introduction

Because of the nonlinear load characteristics of the converter encountered under discontinuous conduction states of armature current, as depicted in figure (1), it has been difficult to properly adjust the gain of the armature current controller to meet different load conditions. In other words, when the gain of the controller is adjusted to be optimum for continuous current conduction, at discontinuous conduction the closed loop response is observed to become sluggish due to parameter variations of the controlled drive. Conversely, when the controller gain is adjusted so that it is optimum for discontinuous mode of conduction at a certain operating point, the closed loop response will tend to become unstable under continuous current conduction. To overcome this difficulty, two possibilities are conceivable; either using a control system with adaptive gains or designing a nonlinear compensation circuit in an attempt to linearize the converter load characteristics.

Konishi et al. [1] tried to solve this problem by

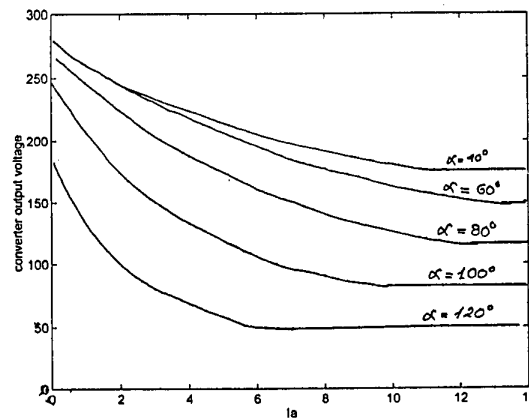


Figure (1) . Load characteristics of the converter

fixing the firing angle and linearizing the load characteristics in case of discontinuous conduction using function generators in the feedforward path of the controller. This was a trial and error technique which is tedious and sensitive to the operating conditions. Kannel et al.[2] proposed a solution which depends on pre-calculation of the output behavior of the system, the current wave form, on the basis of the next switching state, assuming that the converter act as an ideal switch. Then, the actual value of the system is compared with the pre-calculated value. When they are equal the correct converter firing angle is selected and released .Hasegawa et al.[3] proposed a feedback compensator, which becomes active when a discontinuous current mode is detected. This compensator functions as a variable feed back gain of the current PI controller. Naitoh et al. [4] proposed a first order model reference adaptive

control (MRAC). The proposed algorithm was very complex and time consuming as it is based mainly on Popov's hyperstability theorem. Ohmae et al. [5] obtained a fast response current controller by employing a nonlinear compensation sub-loop. The nonlinearity during discontinuous conduction was compensated by incrementing the firing angle α by $\Delta\alpha$ to maintain the same converter gain of continuous conduction. The disadvantages of this method are:

1. It is difficult to design a nonlinear compensation sub-loop that works at all motor operating points.
 2. The motor armature current stability is highly sensitive to deviations in sub-loop gain.
 3. The conventional look-up table method to determine $\Delta\alpha$ needs large memory requirements.
 4. Interpolation, which is time consuming, is always needed when using look-up tables.
 5. A dual mode logic was needed to carry out the nonlinear compensation under the discontinuous conduction state only when there is a large deviation from the reference to avoid instability due to over compensation under continuous conduction.
- To overcome the disadvantages of this method, a simulation study was performed in an attempt to make use of the fuzzy set theory [6]. The fuzzy compensator relies on the same concepts of load characteristic linearization presented in [5]. In this paper, the practical implementation of a fuzzy compensator is applied on a separately excited dc motor driven by a half-controlled, single phase converter bridge. This particular choice was favored by the wide spread of its armature current discontinuity region. In section II, an explanation of the fuzzy compensation algorithm is shown, assuming some background of the fuzzy set theory. Section III, gives a brief explanation of the practical firing circuit. The experimental setup presented in section IV is used to verify the effect of the fuzzy logic compensation in linearizing the converter load characteristics. Finally, the conclusions are drawn in section V.

2- Fuzzy Linearization Algorithm

Since fuzzy compensation is well-suited for nonlinear systems, a fuzzy algorithm is used to generate a suitable increment $\Delta\alpha$ to the firing angle α to linearize the load characteristics of the converter over the discontinuous region. The value of $\Delta\alpha$ depends on the firing angle α and the average armature current I_a . The target of the linearization is to keep the motor armature voltage constant under discontinuous conduction mode of operation.

The universe of discourse of both the armature current I_a and firing angle α cover the

discontinuous conduction region. Figure (2) shows the membership functions of the fuzzy variables I_a , α and $\Delta\alpha$. A 50% overlap has been provided to insure that no more than four rules are fired for any input data pair (α and I_a).

The rule base is developed using heuristic reasoning. The set of rules for fuzzy compensation is given by table (1), where all the symbols are defined in the usual logic using context free linguistic terms.

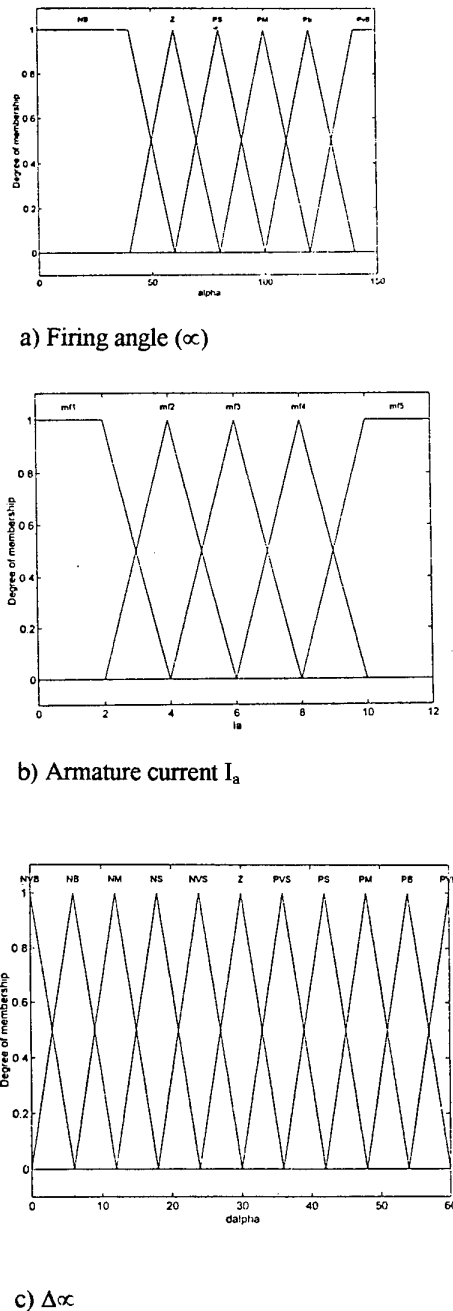


Figure (2) - Membership functions for $\Delta\alpha$ compensation

Table (1)- Rule base for the fuzzy compensator

α Ia	NB	Z	PS	PM	PB	PVB
Mf1	PVB	PM	PVS	Z	NS	NB
Mf2	PM	PVS	NVS	NS	NM	NVB
Mf3	PVS	NVS	NS	NM	NVB	NVB
Mf4	NVS	NS	NM	NB	NVB	NVB
Mf5	NM	NM	NB	NVB	NVB	NVB

Due to the fact that this is a real time application, the rule base was implemented in the software algorithm as a matrix outside the program loop rather than in the traditional set of the IF.....THEN rules. The size of this matrix depends on the partitioning of the input universes of discourse. This size has no bearing on the run time since only the fired rules are read from the matrix.

The algorithm for fuzzy linearization can be summarized as follows:

1- Calculate the interval indices I and J for α and Ia respectively to identify two rules out the four fired rules.

$$I = \text{Int.} ((\alpha - 20) / 20)$$

$$J = \text{Int.} (Ia / 2)$$

2- Calculate the degree of membership of α and Ia for the fuzzy subsets identified by I and J .

$$(\alpha)_I = (20 I + 40 - \alpha) / 20$$

$$(Ia)_J = (2J + 2 - Ia) / 2$$

Then evaluate the degree of membership for the remaining two rules in subsets (I+1) and (J+1) by the complement relations

$$(\alpha)_{I+1} = 1 - \mu (\alpha)_I$$

$$(Ia)_{J+1} = 1 - \mu (Ia)_J$$

3- Calculate the degree of membership contributed by each rule using the MIN operator.

$$R(x,y) = \text{Min} (\mu (\alpha)_x, \mu (Ia)_y)$$

where,

$$x = I \text{ and } (I+1)$$

and

$$y = J \text{ and } (J+1)$$

4- Calculate the crisp output value of $\Delta\alpha$ using the weighted height defuzzification method [7].

$$\alpha_c = \frac{\sum \mu R(x,y) * \Delta\alpha(x,y)}{\sum \mu R(x,y)}$$

where $\Delta\alpha_{(x,y)}$ = height of the output membership function of the rule (x,y).

3.The Firing Circuit

The implementation of the firing circuit requires the coordinated operation of the following modules :-

1. A Zero Voltage Crossing Detector (ZVCD).
2. A Delay Circuit.
3. A Pulse Conditioning Circuit.
4. A Pulse Distribution Circuit .

The required logic is simple and can be summarized as follows :

At the beginning of each half cycle of the supply voltage, the ZVCD circuit will initiate a pulse used as a reference point for counting the delay. The computer sends the required delay α_c binary coded as a byte. Two cascaded synchronous 4-bit counters count the required delay. The count is triggered by the ZVCD signal and a delayed pulse is released at the end of the count. This pulse is widened, synchronized with the clock pulses and sliced by the pulse conditioning circuit. The resulting pulses are amplified and distributed to the appropriate thyristor by the pulse distribution circuit.

Figure (3), gives a complete overview of the firing circuit showing the relationship between its different modules.

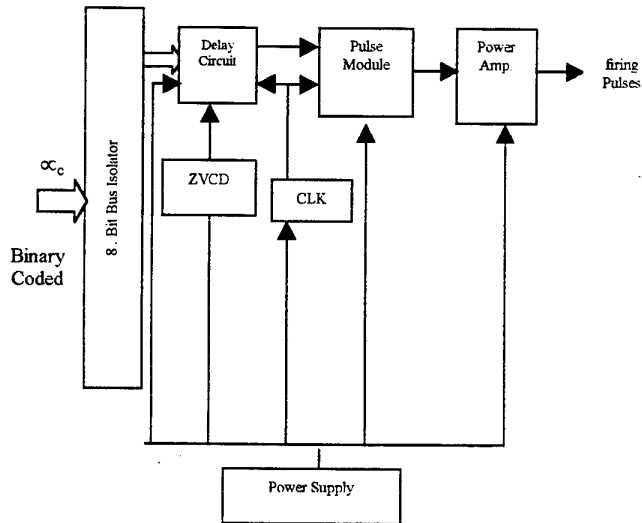


Figure (3) - A Block diagram of the firing circuit

4. Real Time Implementation

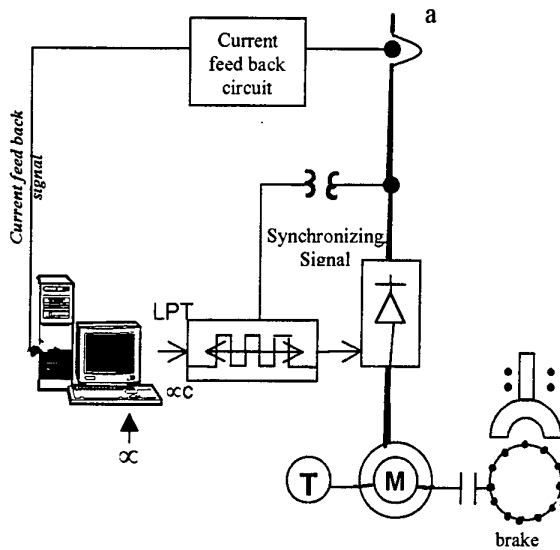


Figure (4) - Single line diagram of the fuzzy compensated dc drive system.

The experimental set up is illustrated in figure (4). The system consists of a 2kW, 11.7 Amp, 1500 r.p.m. separately excited dc motor driven by a half-controlled converter. The motor is loaded using an electromagnetic brake. The converter is fired through a digital phase control firing circuit. A personal computer provided with a data acquisition card converts a signal proportional to the average value of the motor armature current I_a and computes - using fuzzy compensation algorithm - the firing angle offset $\Delta\alpha$. This latter is added to the firing angle α to form the compensated firing angle α_c . Figures (5) and (6) give the experimental results of the implementation of the fuzzy compensator at different firing angles.

The results show considerable improvement of the motor load characteristics over all the discontinuous conduction regions, as the armature voltage approaches the constant value observed under continuous conduction.

Figure (6) shows the pronounced effect of the fuzzy compensation in the reduction of the motor speed regulation under discontinuous conduction.

It is important to mention that, only one set of fuzzy rules can linearize the converter load characteristics for different operating points.

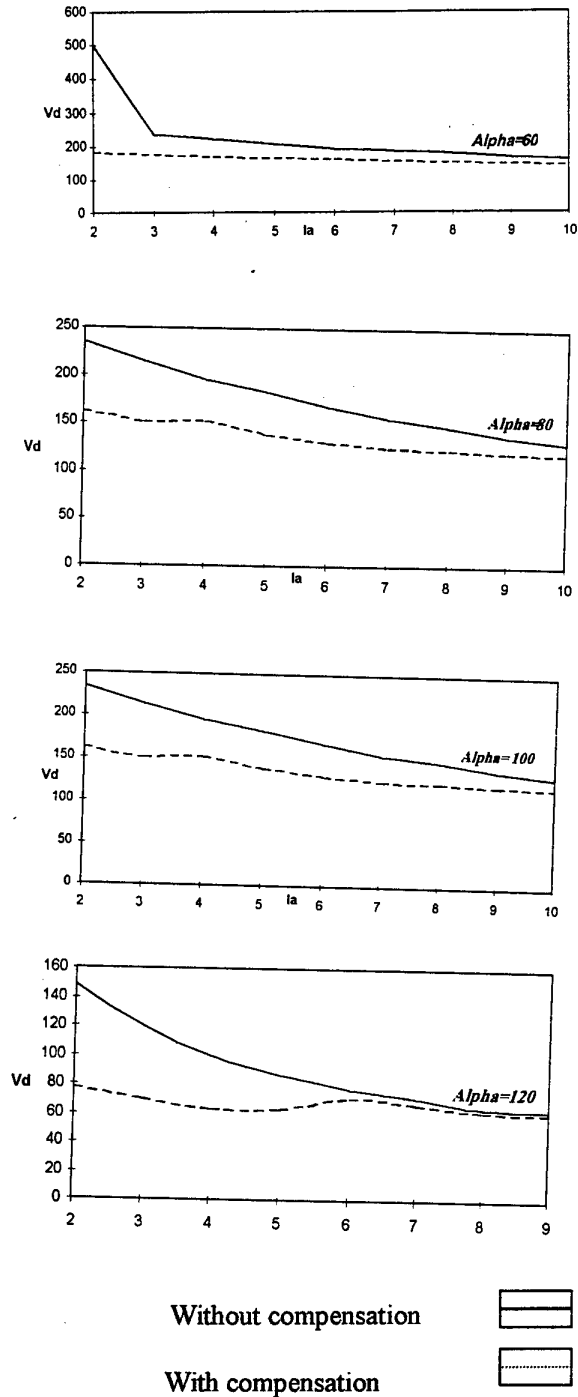
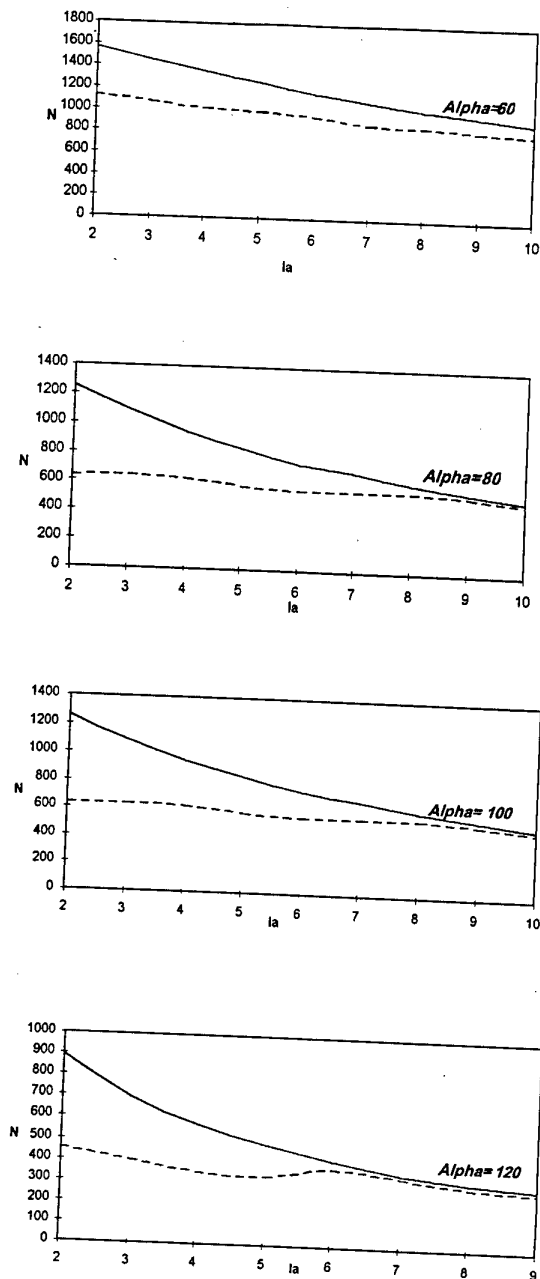


Figure (5) . Effect of the fuzzy compensator on the armature voltage (V_d).



without compensation



with compensation



Figure (6) . Effect of fuzzy compensator on motor speed (N).

Therefore, a major problem for discontinuous operation is solved, that is, the adaptation of the controller parameters for any variation of the operating point. Furthermore, no look-up tables are needed any more. Interpolation is inherently embedded within the fuzzy membership functions. It is intended, in the future work, to use this algorithm as a part of a closed loop computer controlled drive, its execution time for one program loop - containing the A/D conversion of two variables (speed and current), the application of a digital PI algorithm twice in addition to the fuzzy compensation algorithm - must be minimized. The storage of the rule base as a matrix reduced the run time; using a pentium processor 133 MHz; down to 0.24 ms as shown in figure (7).

hp stopped

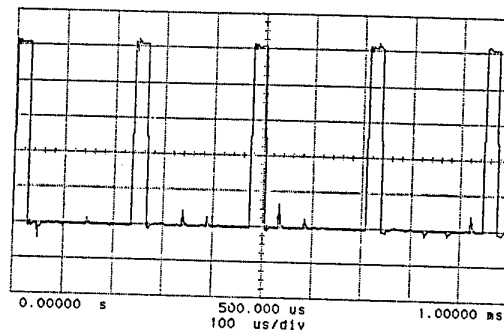


Figure (7) . The experimental run time

5. Conclusions

A fuzzy compensator is used to linearize the load characteristics of a half-controlled converter drive a separately excited dc motor. The experimental results clearly indicate a successful linearization of the converter characteristics for different values of both the firing angle and the armature current. That is, when using such a compensator only one controller will perform adequately over both continuous and discontinuous modes of operation. Further more, storing the fuzzy rule as a matrix reduces greatly the execution run time.

References

- [1] T. Konishi, K.Kamiyama, and T.Ohmae, "A Performance Analysis of Microprocessor Based Control Systems Applied to Adjustable Speed Motor Drives", IEEE Trans. Ind. Appl., Vol.16, No.3, May / June 1980 .
- [2] B.Kennel and D.Schroder, "A New Control Strategy for Converters, " ICEM 82, Grenoble, France.
- [3] T.Hasegawa, T.Nakagawa, H. Hosoda, R. Kuraasawa, and H. Naitoh, "A Microcomputer- Based Thyristor Leonard System Having Powerful RAS Function", IEEE Trans. Ind. Elect., vol.31, No.1, Feb. 1984.
- [4] H.Naitoh, and S. Tadakuma, " Microprocessor-Based Adjustable Speed DC Motor Drives Using Model Reference Adaptive Control", IEEE Trans. Ind. Appl., vol.23, No.2 March / April 1987.
- [5] T.Ohmae , T. Matsuda, T. Suzuki, N. Azusewa, K. Kamiyama and T. Konishi "A Microprocessor Controlled Fast Response Speed Regulator with Dual Mode Current Loop for DCM Drives", IEEE Trans. Ind. Appl., vol.16, No. 3, May/June 1980.
- [6] G. Sousa and K. Bose, "A Fuzzy Set Theory Based Control of a Phase Controlled Converter DC Machine Drive", IEEE Trans. Ind. Appl., vol. 30, No. 1, Jan/Feb. 1994.
- [7] T. Ross, "Fuzzy Logic with Engineering Applications", McGraw - Hill, 1995.
- [8] Fuzzy Systems Toolbox for use with MATLAB. Natick, MA : the Mathworks , 1994 .

Do Fuzzy Controllers Have Advantages over Neural Controllers in Microprocessor Implementation

Bogdan M. Wilamowski and Jeremy Binfet
Department of Electrical Engineering
University of Wyoming
wilam@ieee.org and binfet@uwyo.edu

Abstract

The purpose of this document is to compare several controllers for the same desired control surface implemented in the popular HC11 micro-controller using various fuzzy and neural network architectures. Several neural network architectures were developed and optimized with a help of SNNS - Stuttgart Neural Network Simulator. The microprocessor code for all cases was obtained using the ICC11 C-compiler.

It was proven in the case of neural controller implemented on a microprocessor the code is simpler, much shorter, the processing time is comparable, and the control surfaces obtained with neural controllers are far superior. Control surfaces obtained from neural controllers also do not exhibit the roughness of fuzzy controllers that can lead to unstable or raw control.

The only drawback of neural controllers is that the design process is more complicated than that of fuzzy controllers. However, this difficulty can be easily overcome with proper design tools.

1. Introduction

In recent years, a significant amount of research has been devoted in the development of fuzzy controllers [2][3][4][7][8][14][15][16]. Fuzzy controllers are especially useful for nonlinear systems, which are difficult to describe by mathematical model. Fuzzy controllers are easy to implement. Membership functions and fuzzy rules are chosen arbitrarily and therefore fuzzy controllers are often good but not optimal. Fuzzy controllers can be significantly improved when they are tuned with neural network [5] or genetic algorithm [6].

2. Implementation of Fuzzy Controllers Using Microprocessors.

Microprocessors use primarily trapezoidal membership functions. In order to store the function only four bytes are required x_1 , x_2 , x_3 , and x_4 (see Fig. 1). The triangular membership function is a special case of trapezoidal where $x_2 = x_3$.

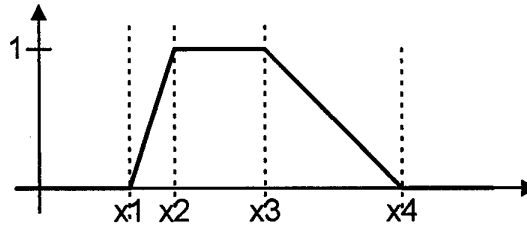


Fig. 1. Representation of the membership function in microprocessor.

Programming the fuzzy controller is relatively simple. It only requires the description of the rule table. For all combinations of input membership functions, a given output membership function must be assigned. The block diagram for Zadeh type [1] controllers is shown in Fig. 2, while required modifications for the Sugano-Tagagi controller are shown in Fig 3.

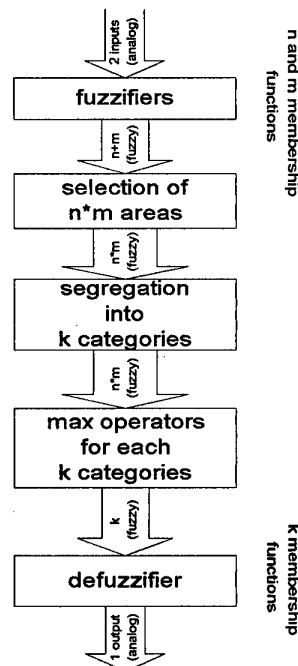


Fig. 2. Block diagram for Zadeh type controller

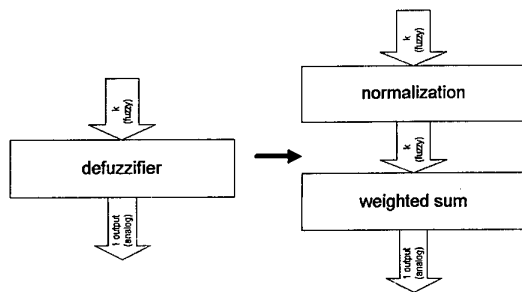


Fig. 3. In Tagagi-Sugeno controller normalization and weighted sum routines replace the defuzzification routine.

All fuzzy controllers were implemented on Motorola's 68HC711E9 microcontroller. This is a low cost, 8-bit microprocessor. The on-board features of the HC711 are 512 bytes of RAM and EEPROM and 12K bytes of UV erasable EPROM. The processor was used with an 8 MHz crystal, allowing an internal clock frequency of 2 MHz. A serial port along with an RS232 interface enables code to be down loaded from a computer. ICC11 for Windows V5 was the compiler used to program the HC711E9. It is capable of converting C or assembly code into the *.S19 file which is downloaded to the microprocessor. ICC11 also has a terminal window for interfacing with the HC711.

Table 1. Error comparison for various type of fuzzy controllers

	Approach used	error SSE	error MSE
1	Zadeh fuzzy controller with trapezoidal membership function (7*7 input and 7 output)	908.4	0.945
2	Zadeh fuzzy controller with triangular membership function (7*7 input and 7 output)	644.4	0.671
3	Zadeh fuzzy controller with Gaussian membership function (7*7 input and 7 output)	562.0	0.585
4	Tagagi-Sugeno fuzzy controller with trapezoidal membership function (7*7 input)	296.5	0.309
5	Tagagi-Sugeno fuzzy controller with triangular membership function (7*7 input)	210.8	0.219
6	Tagagi-Sugeno fuzzy controller with Gaussian membership function (7*7 input)	294.2	0.306

For all controllers shown in Fig. 5 to 10 the same rule table was used and only the shape of membership functions are different. Also, two different defuzzification processes were used. The first three examples used the Zadeh [1] approach and for the following three examples, the Tagagi-Sugeno [2] approach was implemented. All controllers were designed to emulate the control surface shown in Fig. 4. Three different membership functions were used: trapezoidal (Fig. 5 and 8), triangular (Fig. 6 and 9), and Gaussian (Fig. 7 and 10). Error comparisons are shown in Table 1. In that respect the Tagagi-Sugeno approach is far superior over the Zadeh one. The Tagagi-Sugeno algorithm has noticeably large memory requirements. The smoothest results are obtained for the Gaussian type membership functions. Unfortunately it is very difficult to implement Gaussian function on microprocessor. Computation of Gaussian function is very time consuming and it can be used only for slow controllers where time is not the critical issue.

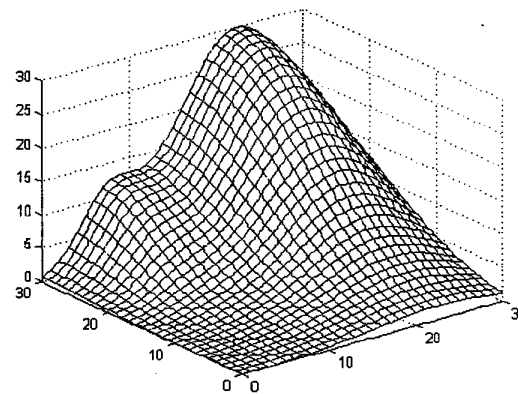


Fig. 4. Required control surface

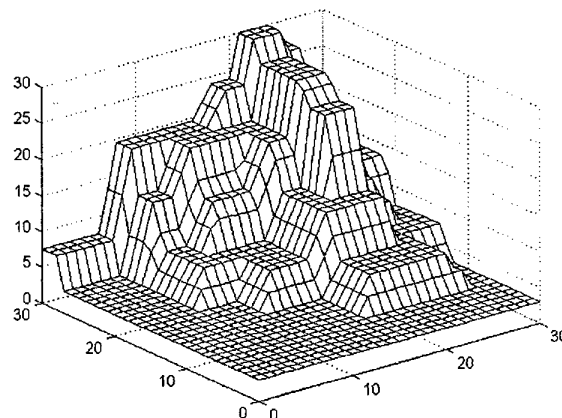


Fig. 5. Control surface obtained with trapezoidal membership functions and Zadeh approach.

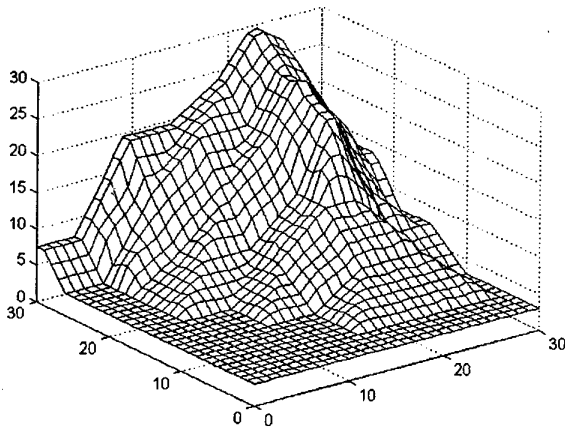


Fig. 6. Control surface obtained with triangular membership functions and Zadeh approach.

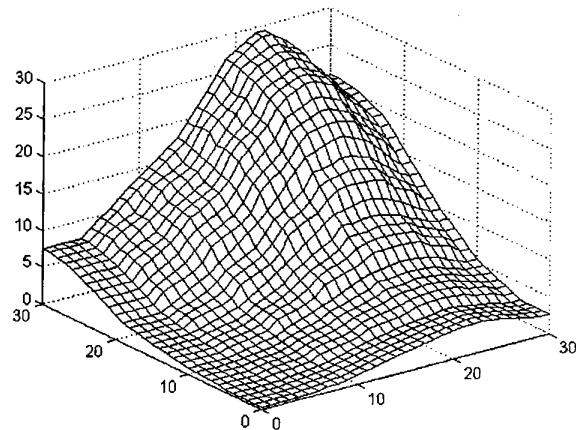


Fig. 9. Control surface obtained with triangular membership functions and Tagagi-Sugeno approach.

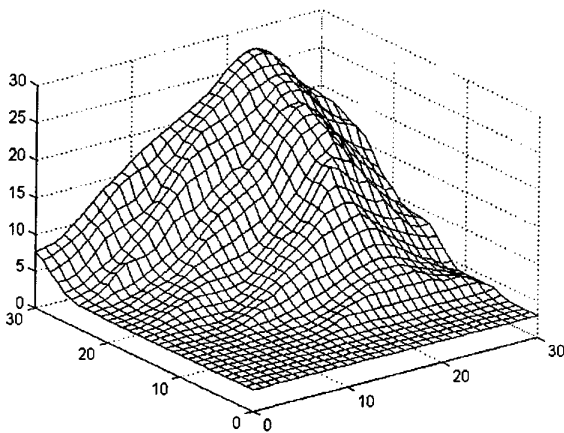


Fig. 7. Control surface obtained with Gaussian membership functions and Zadeh approach.

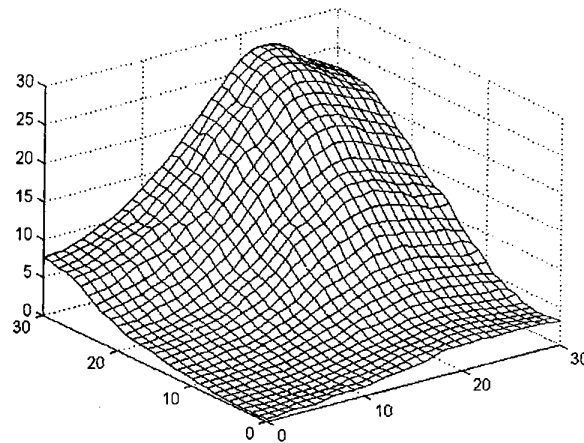


Fig. 10. Control surface obtained with Gaussian membership functions and Tagagi-Sugeno approach.

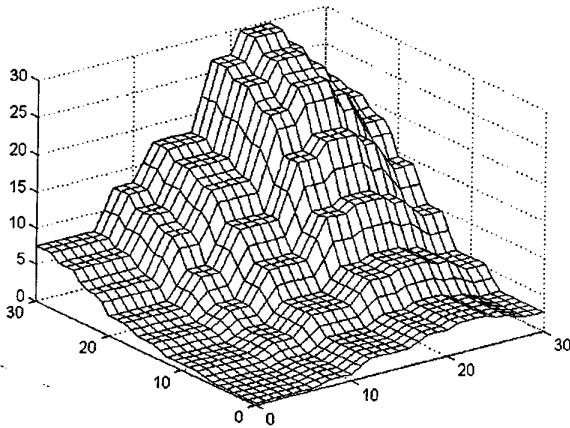


Fig. 8. Control surface obtained with trapezoidal membership functions and Tagagi-Sugeno approach.

3. Implementation of Neurocontrollers Using Microprocessors.

Neural network implementations usually require computations of sigmoidal functions [7][8][12][13]

$$f(net) = \frac{1}{1 + \exp(-net)} \quad (1)$$

for unipolar neurons, or

$$f(net) = \tanh(net) = \frac{2}{1 + \exp(-2net)} - 1 \quad (2)$$

for bipolar neurons. This function is relatively difficult to compute and such implementation on a microprocessor is difficult. If the Elliott function is used:

$$f(net) = \frac{net}{1 + |net|} \quad (3)$$

instead of the sigmoidal, then the computations are relatively simple and the results are almost as good as in the case of sigmoidal function. Fig. 11 shows comparison of sigmoidal and Elliot functions.

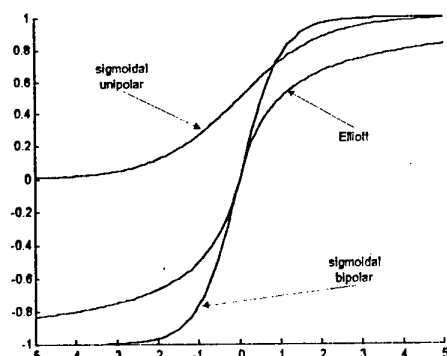


Fig. 11 Various shapes of activation functions

Neural controllers were also implemented on Motorola's 68HC711E9 microcontroller with the code written in C language. Block diagram of neurocontroller is shown in Fig. 12.

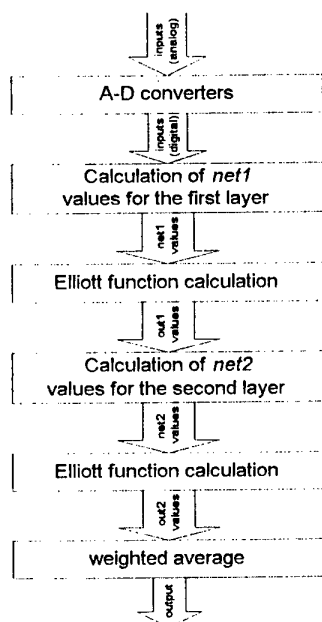


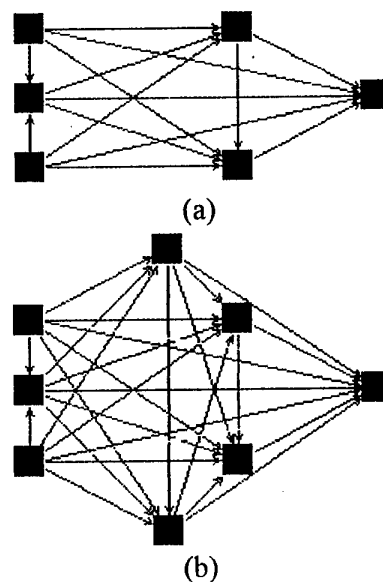
Fig. 12 Block diagram of neurocontroller implemented on Motorola 68HC711E9

During a design process of a fuzzy controller, the designer must know what output should be expected for given input values. More precisely, what the output value is for a given combination of input membership functions. The exact same information can be used to train the neural network. This of course must be done by specially written program, or by using ready software. In our case we have used Stuttgart Neural Network Simulator SNNS [18]. This

software is available free of charge from <http://www.informatik.uni-stuttgart.de/ipvr/bv/projekte/snns/snns.html> and it may run in both platforms UNIX and Windows. The Elliott activation function also implemented in the program SNNS (Stuttgart Neural Network Simulator). Using the dedicated software and the proper architecture, the required weights for each neurons can be found. First, the pattern file has then loaded. SNNS then trains a network for the desired control surface. Many network configurations were tested. The goal was to keep the network as simple as possible while achieving the lowest possible error. Different types of networks that were tested include a) multiple neurons in one hidden layer, b) multiple neurons in cascade and c) multiple neurons in multiple hidden layers. RProp was the training algorithm used to train the networks. It proved to have the fastest convergence time and provided the lowest errors.

For the given control surface shown in Fig. 4, several different controllers that are shown in Table 2 were implemented in the Motorola 68HC711E9 microprocessor. In order to simplify the computation for the neural architectures with limited microprocessor functions, the Elliott function (3) was used instead of the traditional sigmoidal activation function. Several neural network architectures were developed and optimized with a help of SNNS - Stuttgart Neural Network Simulator. The microprocessor code for all cases was obtained using the ICC11 C-compiler. Of course more optimal code can be written directly in assembly language, but relative ratio of codes and processing times should be similar.

Depending on the complexity of neural networks, various levels of accuracy were obtained. Fig. 13 shows implemented neural network architectures and Fig. 14 shows obtained control surfaces for these architectures



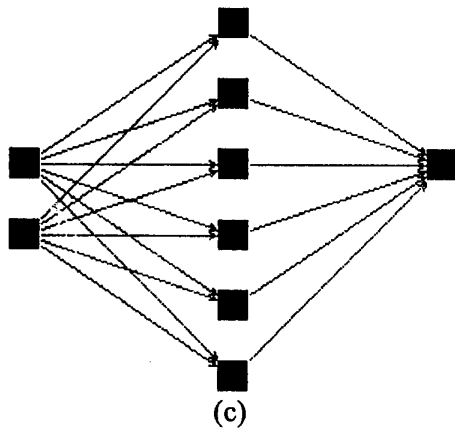


Fig. 13 Various neural network architectures developed for the required control surface of Fig. 4: (a) with 3 hidden neurons, (b) with 5 hidden neurons, and (c) with 6 hidden neurons organized in one hidden layer.

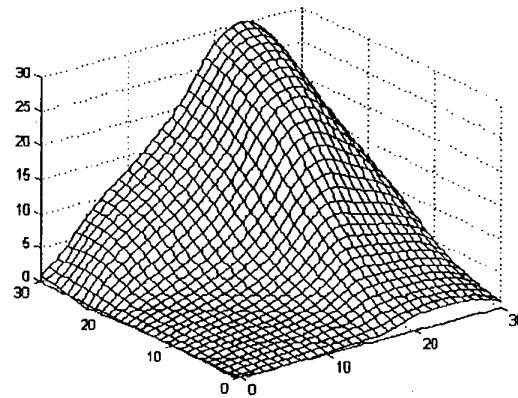
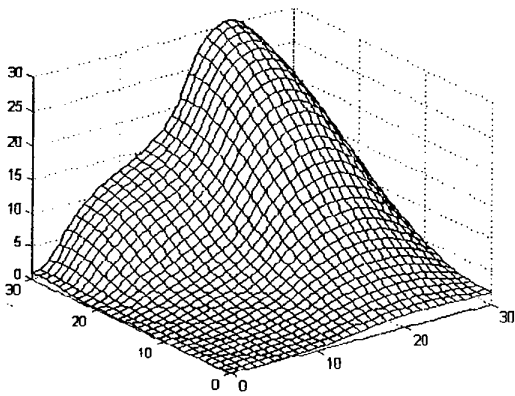
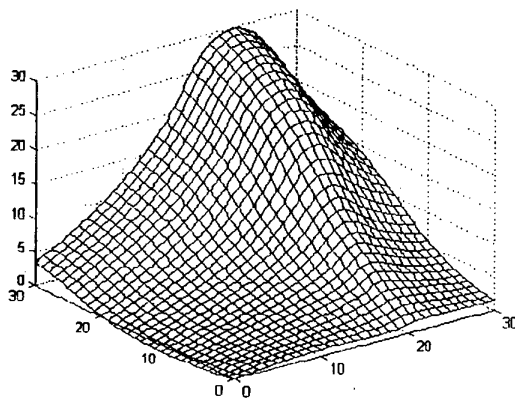


Fig. 14 Control surfaces of neuralcontroller: (a) with 3 hidden neurons, (b) with 5 hidden neurons, and (c) with 6 hidden neurons organized in one hidden layer.

Table 2. Error comparison for various type of neural controllers

	Approach used	error SSE	error MSE
1	Neural network with 3 neurons in cascade (Fig 13 (a))	0.5559	0.000578
2	Neural network with 5 neurons in cascade (Fig 13 (b))	0.0895	0.000093
3	Neural network with 6 neurons in one hidden layer (Fig 13 (c))	0.2902	0.000302

4. Comparison of fuzzy and neural approach

It is shown that it is much simpler to implement a desired control surface in a microprocessor using a neural network structure rather than using a fuzzy type of controller. The only drawback of neural controllers is that the design process is more complicated than that of fuzzy controllers. However, this difficulty can be easily overcome with proper design tools.

It was proven that in the case of neural controller implementation using a microprocessor, the code is simpler, much shorter, the processing time is comparable, and the control surfaces obtained with neural controllers are far superior. Control surfaces obtained from neural controllers also do not exhibit the roughness of fuzzy controllers that can lead to unstable or raw control.

5. Conclusion

Fuzzy controllers do have several advantages such as simple rule based design, but they usually produce relatively raw control surfaces, which are not acceptable for precision control. This obstacle can be overcome by several means. Instead of the triangular or trapezoidal

membership functions, Gaussian-like functions could be used. Better results are also possible with Tagagi-Sugeno fuzzy controllers.

One severe disadvantage of a fuzzy system is its limited ability of handling problems with multiple inputs. Fuzzy systems work well with two inputs. However, with an

increase in the number of inputs, the size of the rule table grows exponentially. Because of this, three inputs is a practical limit. In the case of neural networks, the number of inputs can be much larger.

Table 3. Comparison of various fuzzy and neural controllers

	Type of controller	length of code in bytes	processing time (ms)	Error MSE
1	Zadeh fuzzy controller with trapezoidal membership function (7*7 input and 7 output)	2324	1.95	0.945
2	Zadeh fuzzy controller with triangular membership function (7*7 input and 7 output)	2324	1.95	0.671
3	Zadeh fuzzy controller with Gaussian membership function (7*7 input and 7 output)	3245	39.8	0.585
4	Tagagi-Sugeno fuzzy controller with trapezoidal membership function (7*7 input)	1502	28.5	0.309
5	Tagagi-Sugeno fuzzy controller with triangular membership function (7*7 input)	1502	28.5	0.219
6	Tagagi-Sugeno fuzzy controller with Gaussian membership function (7*7 input)	2845	52.3	0.306
7	Neural network with 3 neurons in cascade (Fig 13 (a))	680	1.72	0.000578
8	Neural network with 5 neurons in cascade (Fig 13 (b))	1070	3.3	0.000093
9	Neural network with 6 neurons in one hidden layer (Fig 13 (c))	660	3.8	0.000302

6. References

- [1] L. A. Zadeh, Fuzzy sets. *Information and Control*, New York, Academic Press vol 8, pp. 338-353, 1965.
- [2] T. Takagi and M. Sugeno, Derivation of Fuzzy Control Rules from Human Operator's Control Action. *Proc. of the IFAC Symp. on Fuzzy Inf. Knowledge Representation and Decision Analysis*, pp. 55-60, July 1989.
- [3] Kosko B., (1993) *Fuzzy Thinking, The New Science of Fuzzy Logic*. Hyperion, New York.
- [4] Passino, K. M., S. Yurkovich, *Fuzzy Control*, Addison-Wesley, 1998.
- [5] Tapkan, Baskin I. and Bogdan M. Wilamowski, "Trainable Functional Link Neural Network Architecture", presented at ANNIE'95 - Artificial Neural Networks in Engineering, St. Louis, Missouri, USA, November 12-15, 1995; also in *Intelligent Engineering Systems Through Artificial Neural Networks* vol. 5, pp. 185-190, ASME PRESS, New York 1995.
- [6] Cupal, J. J. and B. M. Wilamowski, "Selection of Fuzzy Rules Using a Genetic Algorithm," proceedings of World Congress on Neural Networks, San Diego, California, USA, vol. 1, pp. 814-819, June 4-9, 1994.
- [7] Wilamowski B. M. "Neuro-Fuzzy Systems and its applications" tutorial at 24th IEEE International Industrial Electronics Conference (IECON'98) August 31 - September 4, 1998, Aachen, Germany, vol. 1, pp. t35-t49.
- [8] Wilamowski, B. M., "Neural Networks and Fuzzy Systems" chapters 124.1 to 124.8 in *The Electronic Handbook*. CRC Press 1996, pp. 1893-1914.
- [9] Fahlman, S. E. and C. Lebiere. 1990. "The Cascade Correlation Learning Architecture", *Adv. Ner. Inf. Proc. Syst.*, 2, D. S. Touretzky Ed. Los Altos, CA: Morgan, Kaufmann pp. 524-532.
- [10] Ota, Y. and B. M. Wilamowski, "CMOS Implementation of a Voltage-Mode Fuzzy Min-Max Controller", *Journal of Circuits, Systems and Computers*, vol. 6, No 2, pp. 171-184, April 1996.
- [11] Choi J., B.J.Sheu, and J.C.F. Chang, (1994) A Gaussian Synapse Circuit for Analog VLSI Neural Networks. *IEEE Trans. on Very Large Scale Integration (VLSI) Systems*, vol. 2, no. 1, pp. 129-133.
- [12] Hornik, K., "Multilayer Feedforward Networks are Universal Approximators," *Neural Networks*, v.2, pp 359-366, 1989.
- [13] Funahashi, K., "On the Approximate Realization of Continuous Mappings by Neural Networks," *Neural Networks*, v.2, pp 183-192, 1989.
- [14] Wang, L., *Adaptive Fuzzy Systems and Control, Design and Stability Analysis*, PTR Prentice Hall, 1994.
- [15] Efe, M. O., O. Kaynak, "A Novel Computationally Intelligent Architecture for Identification and Control of Nonlinear Systems," *The 1999 IEEE Int. Conf. on Robotics and Automation, ICRA'99*, May 10 - 15, Detroit, Michigan, U.S.A.
- [16] Efe, M. O., A. B. Koku, O. Kaynak, "Comparison of Soft Computing and Conventional Methodologies in Control of Servo Systems", *Int. Conference on Industrial Electronics, Control and Instrumentation, IECON'98*, August 31 - September 4, Aachen, Germany, v.1, pp 75-80, 1998.
- [17] Wilamowski B. M. and R. C. Jaeger, "Neuro-Fuzzy Architecture for CMOS Implementation" accepted for *IEEE Transaction on Industrial Electronics*.
- [18] Stuttgart Neural Network Simulator SNNS <http://www.informatik.uni-stuttgart.de/ipvr/bv/projekte/snns/announce.html>

Grey-Fuzzy Implementation of a DSP-Based Induction Motor Drive

Hung-Ching Lu and Cheng-Hung Tsai

Department of Electrical Engineering, Tatung Institute of Technology

luhung@ctr3.ee.ttit.edu.tw

Abstract

A DSP-based magnetic flux controlled induction motor drive with a grey-fuzzy controller is designed and implemented. This paper investigates the possibility of applying grey and fuzzy algorithms in a DSP-based induction motor controller, which requires faster and more accurate response compared with a traditional fuzzy controller. The proposed controller contains two main parts. The first one is the grey prediction controller, which uses the modified grey model, and the other is the general fuzzy logic controller. The experiments are performed by controlling the induction machines, that it is executed by the digital signal processor (TMS320C30). From the experimental results, the good dynamic speed performance and torque regulation characteristics will be obtained. It also shows the robustness of the fuzzy logic and predictive ability of the grey model.

1. Introduction

Because the high speed digital signal processor has the characteristic to access a high accurate computation within a short sampling period, the speed and the torque control with a high precision of induction machines have been widely applied to various areas of the industrial control system. The control strategy for induction motor is usually carried out by the proportional-integral (PI) method. The strategy will be good enough as long as the speed and accuracy requirements of the control system are not critical. The usual way to optimize the performance is to tune the PI gains, but this cannot cope with a varying control environment or system nonlinearity. Therefore, it is important to develop an effective control technique for precise speed and torque control.

In recent years, adaptive theory has been widely employed to design a controller for induction motor [1]-[3]. They have developed a new control scheme which combines the direct adaptive control law with a variable-structure control law for nonlinear induction motor drive. This adaptive control combination has been shown to improve the transient behavior and the robustness with

respect to the external input disturbance and unmodelled dynamics, and also to overcome the chattering problem which is one of the main drawbacks of the variable-structure method. However, the application of adaptive control approach still needs some knowledge about the system order and range of variations, and its output response has oscillatory features during the initial learning interval.

Since the dynamic model of vector control for induction motor with decouple is very complicated, model-based traditional controllers face on-line computation problems during their implementation. Hence the development of model free intelligent controllers is attracting recent attention, in particular. Fuzzy logic control is a promising approach. However, the application of fuzzy logic control still needs considerable effort to find the appropriate membership functions and fuzzy rules, especially when the system is complicated or rapidly changing. These significantly increase the difficulties in designing a traditional fuzzy controller for induction machines.

With the recent development of grey theory and microprocessors, the grey control theory is being increasingly, applied in various fields of engineering [4]-[6]. In this paper, a grey prediction algorithm is employed to estimate the system's next step output for a look-ahead fuzzy controller, which is based on the predictive speed error and error change. Therefore, the proposed control strategy will reduce the difficulties in implementing the fuzzy controller and use a predictor to pre-compensate the system output error instead of post-compensation. This strategy also effectively improves the time delay problem of control system.

2. Derivation of the Fuzzy Controller with Grey Prediction for Motor Drive

Generally, the requirements for a better performing motor drive system are: (i) fast tracking of a set point without overshoot; (ii) the maximum speed dip and restore time due to load change must be kept as small as possible; and (iii) the steady-state errors must be zero. In order to achieve the object (i), the fuzzy control

algorithm is suitable. The grey predictive ability will respond to the trend of the error in advance under load disturbance condition, so it can solve the problem (ii). To overcome (iii), the outer speed feedback loop must be added. Since the dynamic drive system model is not necessary for the grey-fuzzy controller design, and the performance of the grey-fuzzy controller is robust, it is very suitable for this application. The block diagram of the proposed controller is shown in Fig. 1. In the following, the development of the grey model and the fuzzy controller is described.

2.1 Grey System [7]

Grey theory treats any random variations as a variation in the grey value in a certain range, and the random process is considered as a time-varying grey process in a certain range. In spite of using statistical regulation, the grey theory employs the method of data generating to obtain a more regular generating sequence from the initial random data. The grey prediction is hence to establish a grey model extending from the past information to the future, based upon the past and present known or undetermined information. Then, the grey model can be used to predict the future variation in the system. The specific feature of establishing a grey model is the use of discrete time sequence data to build up an ordinary differential equation.

During the operation of this method, accumulated generating operation and inverse accumulated generating operation are the basic tools for searching the grey model. The orders of these operations depend on the order of the differential equation of the grey model and the number of grey variables. The general form of a grey model is $GM(n, h)$, where n is the order of the ordinary differential equation of the grey model and h is the number of grey variables. The computing time of generating operation increases exponentially with respect to the equation order n and variable numbers h . In addition, better prediction accuracy is also not assured by using large n and h values. Hence, the $GM(1,1)$ model is extensively employed in numbers of grey systems for prediction application.

The $GM(1,1)$ grey model, i.e., a single variable first order grey model, is summarized as follows:

Step 1:

Given the initial data

$X(0) = [x(1), x(2), \dots, x(n-1), x(n)]$, where $x(i)$

corresponds to the system output at time i . We try to predict the next $x(n+k)$, $k \geq 1$.

Step 2: From the initial $X(0)$ a new sequence $X(1)$ is generated by the accumulated generating

operation, where $X(1) = [x^1(1), x^1(2), \dots, x^1(n)]$ and is derived as follows:

$$x^1(k) = \sum_{m=1}^k x(m). \quad (1)$$

Step 3: From $X(1)$ we can form the following first order differential equation:

$$\frac{dx^1}{dt} + ax^1 = u. \quad (2)$$

Step 4: From Step 3 we have

$$\hat{x}^1(k+1) = \left(x(1) - \frac{u}{a} \right) e^{-ak} + \frac{u}{a} \quad (3)$$

$$\hat{x}(k+1) = \hat{x}^1(k+1) - \hat{x}(k), \quad (4)$$

where

$$\hat{a} = \begin{bmatrix} a \\ u \end{bmatrix} = (B^T B)^{-1} B^T y_N, \quad (5)$$

$$B = \begin{bmatrix} -0.5(x^1(1) + x^1(2)) & 1 \\ -0.5(x^1(2) + x^1(3)) & 1 \\ \dots & \dots \\ -0.5(x^1(n-1) + x^1(n)) & 1 \end{bmatrix} \quad (6)$$

$y_N = [x(2), x(3), \dots, x(n)]^T$, and $\hat{x}(k+1)$ is the predicted value of $x(k+1)$ at time $k+1$.

From the above, we know that the GM is restrictive and that only non-negative information is available for it. Hence, it is necessary to overcome this drawback. In [8], the proposed scheme adds a bias to the series; thus, all elements can be pulled up and be avoided being negative. This method is very simple and is easy to implement in a DSP chip.

Since the grey model prediction is a local curve fitting extrapolation scheme, at least four data sets are required for the first-order single-variable grey prediction model to offer a fairly accurate grey prediction. According to the literature [9] and our experimental experience, five data sets can yield a more accurate prediction value than other choices. However, the prediction accuracy is not proportional to the number of data sets, while the corresponding computing time increases exponentially. Therefore, in this study, the most recent five output data are accumulated to predict the next

step output by using a grey model. These data sets are substituted into equations (5) and (6) for solving the grey parameters a and u recursively. This principle is similar to that of the forgetting factor parameter of identification algorithm. Then the system next-step output can be predicted by substituting the grey parameters into equation (3). This predicted output of the next-step is employed to calculate the predicted next-step speed error and error change in the look-ahead fuzzy control strategy.

2.2 Fuzzy Logic Control

The control performance of a traditional controller fully depends on the accuracy of the known dynamic model of the system. However, since the complex systems with several variables are difficult to model appropriately for their dynamic characteristics, a model-free intelligent controller is hence introduced here to solve this kind of problem by using the fuzzy set theory. The main feature of fuzzy logic controller is to choose appropriate linguistic fuzzy rules table established from human control experience and database, by using decision-making process. These fuzzy rules are then transformed into a control type of human thinking according to fuzzy logic and fuzzy set operation. The fuzzy set theory was first proposed by Zadeh [10], and subsequently there has been many control applications based on this theory [11-14]. In most of these applications, the main design objective is to construct a fuzzy system to approximate the desired control action. The fuzzy set theory has also employed as an alternative to traditional modeling and control designs for providing suitable representation of the system [15].

Fuzzy logic control applies the fuzzy set theory to simulate the logical reasoning of human beings. The major parts of the fuzzy controller are a set of linguistic control rules, composed of fuzzy rules, and an inference engine to digest these rules. These rules offer a transformation between the linguistic control knowledge of an expert and the automatic control strategies of an activator. Every fuzzy control rule consists of an antecedent and a consequent; a general form of the rules can be expressed as

$$R_i: \text{IF } X \text{ is } A \text{ and } Y \text{ is } B, \text{ THEN } U \text{ is } C,$$

where R_i is the i th rule, X and Y are the states of the system output to be controlled and U is the control input, A , B and C are the corresponding fuzzy subsets of the input and output universe of discourse.

The importance is the outputs of each rule depends on the membership functions of the linguistic input and output variables. The membership functions

corresponding to the speed error and flux error can be divided into unequal spans, in congruence with the system characteristics. The range of the fuzzy variables can also be adjusted according to variations in the system. According to the characteristics of system dynamics, the appropriate fuzzy rules can be established and adjusted by using a prescriptive algorithm to maintain the system step response within a band [16]. In addition, the fuzzy rules and scaling factors can be planned and adjusted on the basis of the fuzzy phase plane analysis by incorporating the closed-loop system output error in the domain of fuzzy logic control rules [17]. In the present study, 49 fuzzy rules are employed to control the induction machine as listed in table I.

The input variables of the fuzzy controller are the predictive speed error and error change of speed error for the next step. The membership function used in this study the fuzzification is of triangular type, which can be expressed as

$$\mu(x) = \frac{1}{W}(-|x - \beta| + W) \quad (7)$$

where W is the span of distribution of the membership function and β is the parameter corresponding to value 1 of the membership function. The height method is employed to defuzzify the fuzzy variables in order to obtain the control input. The equation can be described as

$$y = \sum_i w_i y_i / \sum_i w_i, \quad w_i = \prod_j \mu_{A_j}(x_j^0) \quad (8)$$

where $\mu_{A_j}(x_j^0)$ is the linguistic value of the fuzzy set variable, w_i is the weight of the corresponding activated rule, y_i is the resulting fuzzy control value of the i th fuzzy rule and y is the net fuzzy control action.

3. The Magnetic Flux controlled Induction Motor Drive

In order to evaluate the performance of the proposed controller based upon the system response, a magnetic flux controlled induction machine is designed and constructed in our laboratory. The magnetic flux pulse-width-modulation (PWM) method is shown in Fig. 2. It is based on eight kinds of space vectors from an inverter bridge. In the figure, the on (off) state of the upper inverter bridge denotes "1" ("0"). There are six nonzero vectors V1~V6 that have length and two zero vectors V0 and V7 that have no length because the inverter bridge produces zero voltage. The space voltage

vector is selected at every time interval so that the flux vector produced from the inverter output line-to-line voltage may move along an ideal circle.

To select proper voltage vectors, the selection rule [18] should be taken into consideration. The selection of the voltage vectors is finished in advance and the whole patterns are burned into a ROM table. The relation between the output voltage and the DC link voltage is expressed as [19]

$$V_{PWM} = \sqrt{\frac{3}{2} \times \frac{3}{\pi} \times \frac{4}{\pi} \times (1-r) \times \frac{E_{dc}}{2}}, \quad (9)$$

where V_{PWM} is the rms fundamental component of the output voltage, E_{dc} is the dc link voltage of the inverter, and r is the portion of zero vectors. Let

$$M = \frac{3}{\pi} \times \frac{4}{\pi} \times (1-r), \text{ then}$$

$$V_{PWM} = \sqrt{\frac{3}{2} \times M \times \frac{E_{dc}}{2}}, \quad (10)$$

where M can be termed as the voltage modulation factor.

Finally, the induction motor is driven by a PWM transistor inverter wherein the current feedback loop is employed. Fast and stable current controlled by PWM is achieved by using a pulse number high enough to limit the current ripple to an allowable value with the help of the leakage inductance. The frequency is determined by the rotating speed of the rotor and slip frequency. The rotor speed is detected by an encoder mounted on the shaft.

4. Experimental Results

Since induction machines exhibit obvious nonlinear behaviors, the application of a traditional PI controller needs intricate gain adjustment for each situation. Hence fuzzy logic control is here employed to improve the system robustness and facilitation. However, the fuzzy logic control still needs considerable efforts to find the appropriate membership functions and fuzzy rules for quick speed or torque control. Hence, the grey predictive theory is utilized in this study to predict the system next-step output response for pre-correction by using a look-ahead fuzzy control. This strategy is expected to improve the robustness of the fuzzy controller and to reduce the difficulty in implementing the fuzzy controller.

In this paper, both a traditional fuzzy controller and a fuzzy controller with grey prediction are

implemented individually to an induction motor. The block diagram is shown in Fig. 1 where

$$\begin{aligned} e(k) &= w_r^*(k) - w_r(k), \\ \hat{e}(k+1) &= G(\text{five error data}), \\ \Delta \hat{e}(k+1) &= \hat{e}(k+1) - e(k). \end{aligned} \quad (11)$$

Here w_r is the feedback speed of the motor and w_r^* is the command speed of the motor. In addition, $\hat{e}(k+1)$ is the predictive value of $e(k)$ at the $(k+1)$ th sampling interval, $\Delta \hat{e}(k+1)$ is the difference between $\hat{e}(k+1)$ and $e(k)$, and $G(\cdot)$ is the grey operator. The actual control input for this fuzzy control with grey prediction system is

$$\hat{u}(k) = \hat{u}(k-1) + \Delta \hat{u}(k) \quad (12)$$

In order to demonstrate the performance of the proposed fuzzy controller with grey prediction, experimental results obtained from this controller are compared with those obtained from the traditional fuzzy controller. The membership functions of speed error, error change and control input used here are given in Fig. 3, where α_i is the scaling factor, the subscript $i=1,2$, devotes the speed and flux where the superscript $j=1,2,3$ is used to devote the error, error change and control output. The parameters of the membership functions used in this study are listed in table II.

The hardware of the drive system and the software realization of the proposed grey-fuzzy controller using a TMS320C30 DSP chip is performed. The motor used in this drive system is a 3-phase 60-Hz Y-connected 4-pole 220-V 3-HP induction motor. Fig. 4 shows the dynamic speed responses of both the proposed grey-fuzzy controller and the traditional fuzzy controller in case of a speed command at 80 rpm (equivalent voltage 8v). The results indicate that good speed following response is obtained. It also shows the proposed grey-fuzzy controller has a faster rising time than the traditional fuzzy controller does.

One may say that the fuzzy controller can also obtain the same rising time as can the proposed controller. After tuning the parameters of traditional fuzzy controller, Fig. 5 can be obtained. It is clearly that the two controllers have the same rising time, but an overshoot occurs in the pure fuzzy controller. As for the load regulation characteristics, the same load disturbance is used both in the proposed drive and the traditional fuzzy controller. Fig. 6 shows the dynamic speed responses at a load disturbance under two different operating conditions. Good speed regulation characteristics of the proposed system are also observed in Fig. 6. The experimental

results show that the proposed grey-fuzzy controller gives a better result.

5. Conclusions

The control system design and implementation of a DSP-based grey-fuzzy induction motor drive have been presented in this paper. Based on the proposed scheme, a very fast speed dynamic response under a constant flux condition is achieved. Integrate a fuzzy controller with a grey predictor is designed to obtain good dynamic speed responses and load disturbance regulation characteristics. By using the experience with the motor drive system, the fuzzy algorithms are designed easily and the mathematical grey processing can be simply carried out by the DSP chip. The experimental results also show that good responses is achieved by the proposed grey-fuzzy controller.

6. Acknowledgement

This work was supported by the National Science Council, Republic of China under the grant NSC 88-2213-E-036-017 is gratefully acknowledged.

7. References

- [1] H. Kubota, H. Matsuse and T. Nakano, "DSP-based speed adaptive flux observer of induction motors", *IEEE Transactions on Industry Applications*, Vol. 29, 1993, pp. 344-348.
- [2] C. Schauder, "Adaptive speed identification for vector control of induction motors without rotational transducers", *IEEE Transactions on Industry Applications*, Vol. 28, 1992, pp. 1054-1061.
- [3] G. Yang and T. H. Chin, "Adaptive-speed identification scheme for a vector-controlled speed sensorless inverter induction motor drive", *IEEE Transactions on Industry Applications*, Vol. 29, 1993, pp. 820-825.
- [4] M. Lin, "An application of the GM(1,1) model: the prediction of flight safety", *The Journal of Grey System*, Vol. 1, 1989, pp. 89-102.
- [5] D. S. Yiand and R. Yang, "Grey predictor controller for DC speed control system", *The Journal of Grey System*, Vol. 2, 1990, pp. 189-215.
- [6] J. Liu, C. Wang, D. Xiao and P. Liu, "Application of grey system theory to the forecasting and control of air environmental quality", *The Journal of Grey System*, Vol. 4, 1992, pp. 181-192.
- [7] J. L. Deng, "Introduction to grey system theory", *The Journal of Grey System*, Vol. 1, 1989, pp. 1-24.
- [8] H. C. Lu, "Universal GM(1,1) model based on data mapping concept", *The Journal of Grey System*, Vol. 8, 1996, pp. 307-319.
- [9] J. L. Deng, "Five step modeling of grey systems", *Grey System* (China Ocean Press), 1988.
- [10] L. A. Zadeh, "Fuzzy sets", *Information and Control*, Vol. 8, 1965, pp. 338-353.
- [11] J. Maiers and Y. S. Sherif, "Applications of fuzzy set theory", *IEEE Transactions in Systems, Man, and Cybernetics*, Vol. 15, 1985, pp. 175-189.
- [12] S. A. Mir, d. S. Zinger and M. E. Elbuluk, "Fuzzy controller for inverter fed induction machines", *IEEE IAS Conf. Rec.*, 1992, pp. 464-471.
- [13] P. Rainer, "Control of a redundant manipulator using fuzzy rules", *Fuzzy Sets and Systems*, Vol. 45, 1992, pp. 279-298.
- [14] B. A. M. Wakilen and K. F. Gill, "Use of fuzzy logic in robotics", *Computer in industry*, Vol. 10, 1988, pp. 35-46.
- [15] D. Driankov, H. Hellendoorn and M. Reinfrank, *An introduction to fuzzy control*, Springer-Verlag, Berlin, 1993.
- [16] E. H. Mamdani, and N. Baaklini, "Descriptive method for deriving control policy in a fuzzy logic control", *Electronics Letters*, Vol. 11, 1975, pp. 625-626.
- [17] M. Braae and D. A. Rutherford, "Selection of parameters for a fuzzy logic control", *Fuzzy Sets and Systems*, Vol. 4, 1979, pp. 143-162.
- [18] M. Morimoto, S. Sato, K. Sumito and K. Oshitani, "Voltage modulation factor of the magnetic flux control PWM inverter", *IEEE Transactions on Industrial Electronics*, Vol. 38, 1991, pp. 57-61.
- [19] M. Morimoto, S. Sato, K. Sumito and K. Oshitani, "Voltage modulation factor of the magnetic flux control PWM inverter", *IEEE Transactions on Industrial Electronics*, Vol. 38, 1991, pp. 57-61.

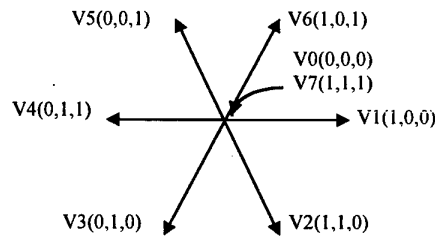


Figure. 2 Voltage vectors made by the inverter.

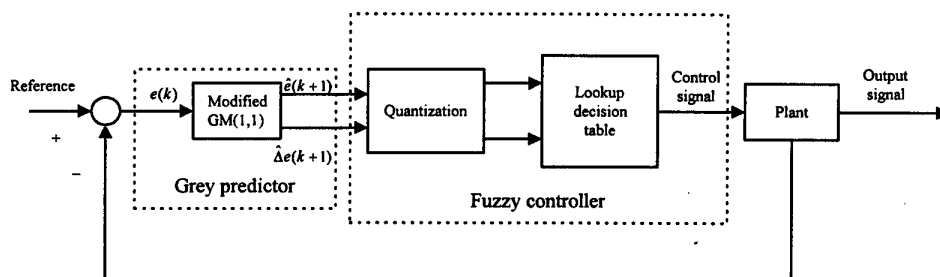


Figure. 1 The block diagram of the proposed grey-fuzzy controller

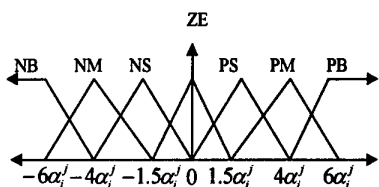


Figure. 3 The membership functions of the traditional fuzzy controller

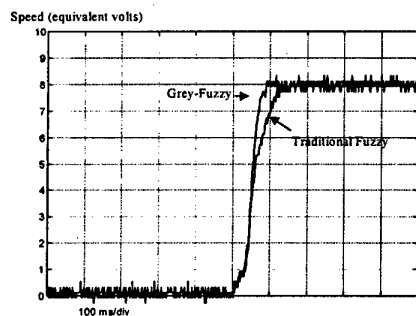


Figure. 4 Speed responses from 0 to 80 rpm (8v) of grey-fuzzy and traditional fuzzy controller

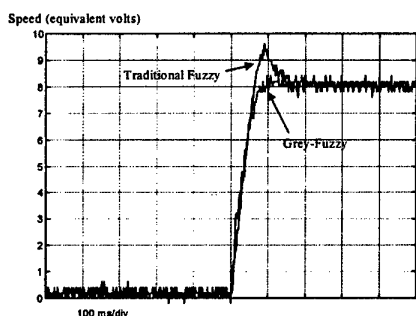


Figure. 5 Speed responses with the same rising time of grey-fuzzy and traditional fuzzy controller

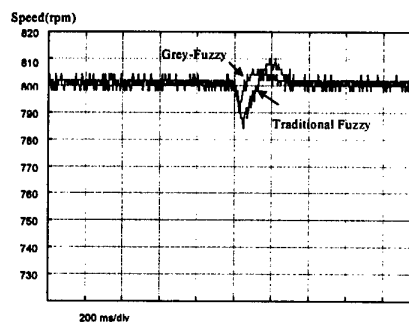


Figure. 6 Load regulation characteristics of grey-fuzzy and traditional fuzzy controller

Table I. The fuzzy control rules of this fuzzy controller

$\Delta \hat{e}$	\hat{e}						
	NB	NM	NS	ZE	PS	PM	PB
NB	NB	NM	NM	NM	NS	NS	ZE
NM	NM	NM	NM	NS	NS	ZE	PS
NS	NM	NM	NS	NS	ZE	PS	PS
ZE	NS	NS	NS	ZE	PS	PS	PM
PS	NS	NS	ZE	PS	PS	PM	PM
PM	NS	ZE	PS	PS	PM	PM	PM
PB	ZE	PS	PS	PM	PM	PM	PB

Table II. The scaling factors of this fuzzy controller

$\alpha_1^1 = 0.3$	$\alpha_2^1 = 0.0.7$
$\alpha_1^2 = 0.14$	$\alpha_2^2 = 0.024$
$\alpha_1^3 = 0.094$	$\alpha_2^3 = 0.01$

UPS Systems Feeding Nonlinear Loads Using Fuzzy Reasoning

Hung-Ching Lu and Ta-Hsiung Hung

Department of Electrical Engineering, Tatung Institute of Technology

luhung@ctr3.ee.ttit.edu.tw

Abstract

This paper presents a fuzzy control scheme for the regulation of pulse-width modulation (PWM) inverters used in uninterruptible power supplies (UPS). The performance is superior to a conventional UPS. Conventional UPS systems operate to protect against such disturbances using complex filtering schemes, often employing large passive components. This paper presents the fuzzy control [1,2] of UPS systems. A prototype has been implemented and tested to verify its performance. The experimental results justify the input and output performance of the proposed system that is better than the conventional control method.

1. Introduction

Uninterruptible power supplies provide electric power for critical functions and equipment when the quality of the normal supply, i.e., utility power, is not adequate or fails entirely. With the rapid growth in the utilization of data processing systems, life care medical equipment, alarm systems, and safety lighting, the demand for high quality uninterruptible power is increasing [3-6]. Further, with the widespread application of high efficiency static power converter devices, many electrical loads are nonlinear, including the above mentioned critical loads, and generate harmonics. Therefore, additional harmonic filtering techniques must be applied in order to maintain a high quality sinusoidal UPS inverter output voltage.

A typical UPS consists of a rectifier supplied battery bank for energy storage and a static inverter-filter system to convert a dc voltage to a sinusoidal ac output (Fig. 1). The inverter is typically operated with a PWM strategy under feedback control to realize the desired output waveform. UPS systems can be off-line, where the load is connected directly to the utility under normal operation, and emergency power is provided by the UPS. The on-line configuration is shown in Fig. 1, where the UPS inverter powers the load continuously.

Control of the UPS inverter switching is important to minimize the total harmonic distortion (THD) of the

output voltage. The difficulty in successful switching control operation stems from the output impedance of the inverter filter [4]. Much attention has been focused on providing a near zero-impedance inverter stage which in theory would provide near zero distortion of the output voltages, independent of the load conditions. Low output filter impedance can be realized via a high inverter switching frequency.

Thus, modern UPS systems minimize the THD of the inverter output voltage through the use of complex filtering schemes employing large passive components. In addition, a number of pulse width modulation techniques have been investigated to compensate for the filter output impedance and reduce the output voltage distortion [5]. Real time PWM control of the inverter output voltages provides the ability to dynamically adapt to changing load conditions.

In this paper, we propose a fuzzy controller to control the inverter switches to generate the required PWM pattern to produce low THD sinusoidal output voltage. The feature of the fuzzy logic control schemes is that even if the mathematical model of the considered system is unknown, fuzzy control still can achieve the control object. The fuzzy control is constructed by the rule-based expert knowledge or experience that is simple to design.

This paper is organized as follows. In Section 2, the configuration of the DC-AC inverter is introduced. In Section 3, the design of proposed fuzzy controller for UPS system is described. The experimental results are presented in Section 4. Finally in Section 5, the general conclusion is formulated.

2. Configuration of the dc-ac inverter

Single-phase voltage source PWM inverters are commonly used in low and medium power UPSs. In such applications, the output of the inverter is usually provided with an LC filter to reduce the inverter output harmonics. In the following, the configuration of DC-AC output stage including single-phase PWM inverter and LC filter is introduced.

2.1 Single-phase PWM inverter

Switch-mode DC-AC power inverters are used in AC motor drives and UPSs where the objective is to produce a sinusoidal AC output with controllable magnitude and frequency [6]. Although several possible inversion schemes exist, today's most applications are dominated by PWM inverters due to their abilities of providing both voltage and frequency control and generating output waveform with low harmonic distortion [7-11].

In the PWM inverter of single phase systems, the most obvious and popular configurations are the half-bridge and the full-bridge inverters shown in Fig. 2 [12]. With the same DC input voltage, the maximum output voltage of the full-bridge inverter is twice that of the half-bridge inverter. This implies that for the same power, the output current and the switch currents are one-half of those for a half-bridge inverter. At high power levels, this is a distinct advantage, since it requires less paralleling of devices.

The full-bridge inverter is shown in Fig. 2(b). If S_a and S_d are turned on and off together by a single pulse width modulator and a single modulation waveform, we can observe that the output voltage V_o switches between $-V_d$ and V_d voltage levels.

2.2 LC filter

PWM uses an analog signal to modulate the width of pulses whose durations are proportional to the amplitude of the modulating signal at that instant. Since most electronic loads are nonlinear and inject harmonic currents into the UPS, additional harmonic filtering techniques must be applied and the inverter must allow for almost instantaneous control over its output AC waveform to reduce the harmonic distortion to acceptable levels. The application of a second order LC type low pass filter shown in Fig. 3 is common practice in the attenuation of the harmonics [13,14]. Design of the output LC filter is dependent on the inverter switching frequency [15]. Individual component size selection depends upon the type of load being applied and the DC bus voltage. When supplying a nonlinear load, the filter output impedance should be minimized by maximizing the capacitor size. Large inductor with low DC bus voltage will make the output voltage feedback sluggish. Too small an inductor will result in large ripple in inductor current, resulting in increased losses. Optimum component values may be determined by using simulation.

2.3 Feedback control of PWM UPS inverter

A typical specification for the output voltage of a UPS is 5 percent THD. To achieve this level, a method can be used is to utilize feedback control of the output voltage waveform to cancel the harmonic distortion. Theoretically, the output impedance of a PWM UPS inverter can be controlled by the gain and bandwidth of the output voltage in perfect coincidence with a sinusoidal reference voltage, in the fact of nonlinear load, then the inverter can be said to have zero output impedance at the frequency components of the load current. Some characteristics of using feedback control are listed below:

1. There appear to be inherent limits to the reduction of output impedance and bandwidth when using discrete-time feedback control. Two controllers have been used effectively: One is to compensate for harmonic disturbances; the other is for fast response with sudden load changes.
2. The highest possible PWM switching frequency should be used, so that the break frequency of the LC filter occurs for outside the range of the load current harmonics. This allows the highest possible control bandwidth.
3. The inverter must be designed with additional voltage capability to compensate for the voltage drop across the filter inductance.

Because zero output impedance is achieved by compensation of forward voltage drop on the output inductor, it will be possible to compensate the voltage drop by measuring the inductor current, and thus to eliminate output voltage variation. Inverter with desired small output voltage variation, must have an additional circuit for compensation of the inductor voltage drop. Equivalent circuit of the inverter output stage is shown in Fig. 3 where the filter real inductor L is represented as an equivalent ideal inductor L in series with its ohmic resistance R_e . From Fig. 4, the inductor voltage drop V_L is given as

$$V_L = I_L(R_e + L \frac{d}{dt}). \quad (1)$$

By measuring the inductor current I_L , a corresponding compensation voltage V_e is obtained, proportional to the inductor voltage drop V_L . By adding this compensating voltage V_e to the input signal V_{inv} , the influence of the inductor voltage drop to the inverter output voltage will be eliminated. If V_e equals to V_L , V_o will equal to V_{inv} . Hence, the output voltage V_o depends on the fundamental of the PWM modulated signal, that is proportional to the sinusoidal reference signal V_{ref} and

compensation signal V_c . Theoretically, such an inverter will have zero output impedance.

3. The fuzzy controller design for UPS system

The most important three inputs of the controller are $V_{err}(k)$, $cV_{err}(k)$, $V_c(k)$ and one output $\Delta T(k+1)$ is used for the PWM pulse width control system. In view of this figure, $V_{err}(k)$ denotes the error between the reference sinusoidal waveform $V_{ref}(k)$, and the output voltage $V_{inv}(k)$ at time instance kT , and $V_c(k)$ denotes the inductor voltage drop, where k is a positive integer and T is the sampling time; $cV_{err}(k)$ denotes the change of the error; $\Delta T(k)$ denotes the output change of fuzzy controller, they are defined as follows:

$$V_{err}(k) = V_{ref}(k) - V_{inv}(k) + V_c(k) \quad (2)$$

$$cV_{err}(k) = V_{err}(k) - V_{err}(k-1) \quad (3)$$

$$\Delta T(k) = F[V_{err}(k), cV_{err}(k)] \quad (4)$$

where $F[\bullet]$ denotes the fuzzy controller.

The control rules for the UPS system are shown in Table 1. In these control rules, seven linguistic sets are applied for the fuzzy variables. The seven linguistic sets are defined as

$$\{ \text{NB, NM, NS, ZE, PS, PM, PB} \},$$

where N is negative, P is positive, B is big, M is medium, S is small, and ZE is zero.

Having defined the linguistic control rules, the membership functions corresponding to each element in the linguistic set must be defined. For simplicity, the trapezoidal functions shown in Fig. 5 are proposed, where the universal sets $V_{err}(v)$ and $cV_{err}(v)$ are all defined at the interval $(-3.6, -3.0, \dots, 3.0, 3.6)$ and $(-1.8, -1.5, \dots, 1.5, 1.8)$. After the above operation is done, then we can get a fuzzy controller in Fig. 6.

As shown above, the output of the plant will feedback to the first stage with the reference signal to generate the error signal. Then, the fuzzy mechanism will generate a suitable ΔT to control the PWM pulse width.

4. Experimental results

The whole system has been established and tested with a laboratory prototype. In all cases the inverter system is supplying a single-phase rectifier-type nonlinear load. The PWM switching frequency is 6 kHz.

Fig. 7 and Fig. 8 show the output voltage and load current waveforms with the deadbeat controller and fuzzy controller respectively for $V_d=200V$, where the DC voltage source is adopted the switching power supply. The total harmonic distortions of the output voltage are equal to 2.5% and 1.2%, respectively. From the result, the voltage drop has significant improvement with the fuzzy controller. When the DC voltage is turned more larger, the load current will be overload. Thus, in the following experiment, the DC voltage source is replaced with an autotransformer and a rectifier.

Fig. 9 and Fig. 10 show the output voltage and load current waveforms with the deadbeat controller and fuzzy controller respectively for $V_d=300V$. The total harmonic distortions of the output voltage are equal to 8.8% and 4.5%, respectively. It is apparent that the fuzzy controller works better than the deadbeat controller.

5. Conclusions

This paper describes an algorithm which applies a fuzzy controller to digital control of the single phase PWM inverter for UPS application. This controller is used to compensate the nonlinear load. The output is fed into the fuzzy logic controller to get a proper PWM switching pattern.

The features of the proposed DC-AC converter are shown below.

1. The experimental results demonstrate the total harmonic distortion of the output voltage can be reduced to less than 5% by feedback control to achieve zero output impedance of the PWM inverter.
2. No matter what the input DC voltage level is, the fuzzy controller has the better performance than the deadbeat controller.

From the experimental results, the proposed fuzzy controller has better transient performance and low total harmonic distortion for nonlinear loads than deadbeat controller.

6. Acknowledgement

This work was supported by the National Science Council, Republic of China under the grant NSC 88-2213-E-036-019 is gratefully acknowledged.

7. References

- [1] C. Lee, "Fuzzy logic in control system: Fuzzy logic controller—Part 1," *IEEE Trans. Syst. Man Cybern.* vol. 20, no.2, pp. 404-418, 1990.

- [2] C. Lee, "Fuzzy logic in control system: Fuzzy logic controller—Part 2," *IEEE Trans. Syst. Man Cybern.* vol. 20, no. 2, pp. 419-436, 1990.
- [3] A. Kusko, *Emergency/Standby Power Systems*. New York: McGrawHill, 1989.
- [4] M. A. Boost and P. D. Ziogas, "Toward a zero-output impedance UPS system," *IEEE Trans. Ind. Appl.*, vol. 25, no. 3, pp. 408-418, May/June 1989.
- [5] C. Hua and R. G. Hoft, "High performance deadbeat controlled PWM inverter using a current source compensator for nonlinear loads," in *PESC '92 Conf. Proc.*, pp. 443-450.
- [6] N. Mohan, T. M. Undeland and W. P. Robbins, *Power Electronics: Converters, Applications and Design*. New York: Wiley, 1995.
- [7] R. S. Lai and K. D. T. Ngo, "A PWM Method for Reduction of Switching Loss in a Full-Bridge Inverter," *IEEE Trans. Power Elec.*, vol. PE-10, no. 3, pp. 326-332, May 1995.
- [8] N. M. Abdel-Rahim and J. E. Quaicoe, "Analysis and Design of a Multiple Feedback Loop Control Strategy for Single-Phase Voltage-Source UPS Inverters," *IEEE Trans. Power Elec.*, vol. PE-11, no. 4, pp. 532-541, July 1996.
- [9] T. Yokoyama and A. Kawamura, "Disturbance Observer Based Fully Digital Controlled PWM Inverter for CVCF Operation," *IEEE Trans. Power Elec.*, vol. PE-9, no. 5, pp. 473-480, Sep. 1994.
- [10] Y. Y. Tzou, "DSP-Based Fully Digital Control of a PWM DC-AC Converter for AC Voltage Regulation," *IEEE IECON Conf. Record*, pp. 138-144, 1995.
- [11] J. Sun, S. Beineke and H. Grotstollen, "DSP-Based Real-Time Harmonic Elimination of PWM Inverters," *IEEE PESC Conf. Record*, pp. 679-685, 1994.
- [12] C. Hua, "Two-Level Switching Pattern Deadbeat DSP Controlled PWM Inverter," *IEEE Trans. Power Elec.*, vol. PE-10, no. 3, pp. 310-317, May 1995.
- [13] H. L. Jou, J. C. Wu and H. Y. Chu, "New Single-Phase Active Power Filter," *IEE Proc. Electr. Power Appl.*, vol. 141, no. 3, pp. 129-134, May 1994.
- [14] P. A. dahono, A. Purwadi and J. Qamaruzzaman, "An LC Filter Design Method for Single-Phase PWM Inverters," *IEEE ICPEDS Conf. Record*, pp. 571-575, 1995.
- [15] M. A. Boost and P. D. Ziogas, "State-of-the-Art Carrier PWM Techniques: A Critical Evaluation," *IEEE Trans. Ind. Appl.*, vol. 24, no. 2, pp. 271-280, Mar./Apr. 1988.

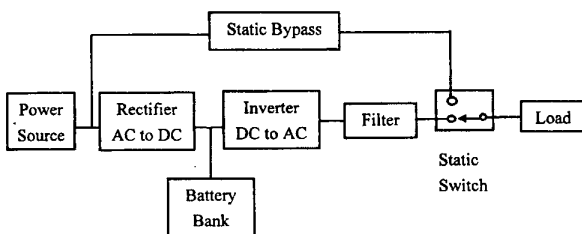


Figure 1 Block diagram of on-line UPS system.

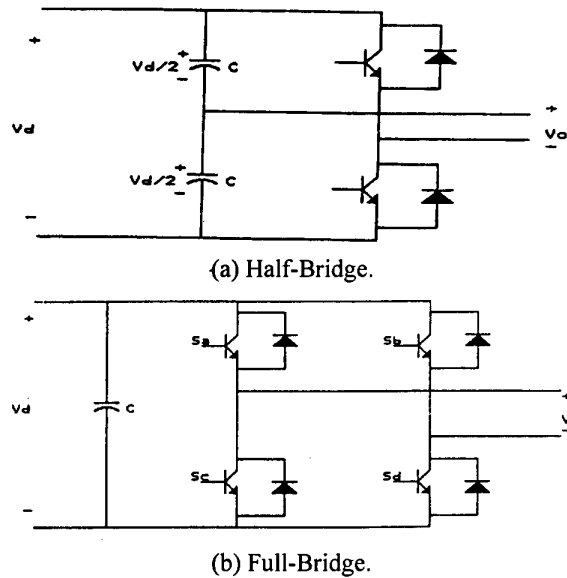


Figure 2 Configuration of single-phase inverter.

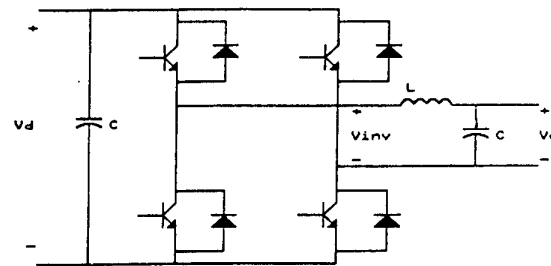


Figure 3 Single phase full-bridge inverter with LC filter.

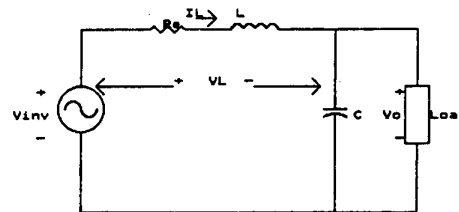


Figure 4 Real inverter output circuit.

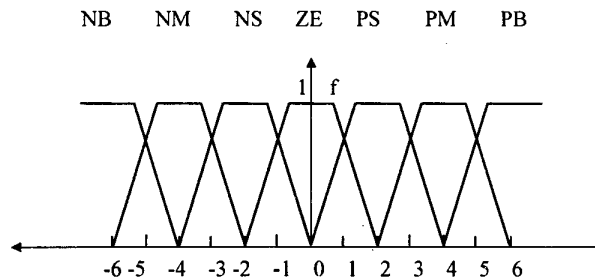


Figure 5 The membership function

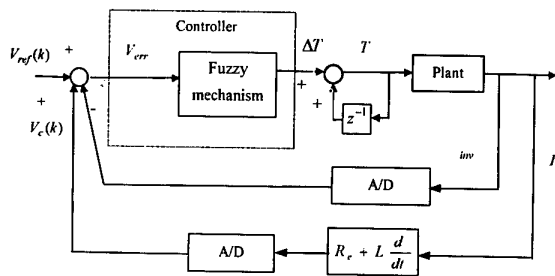


Figure 6 The fuzzy controller

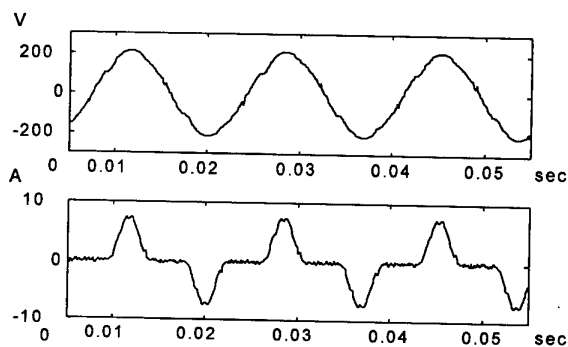


Figure 7 Inverter output voltage and load current waveforms with deadbeat control.

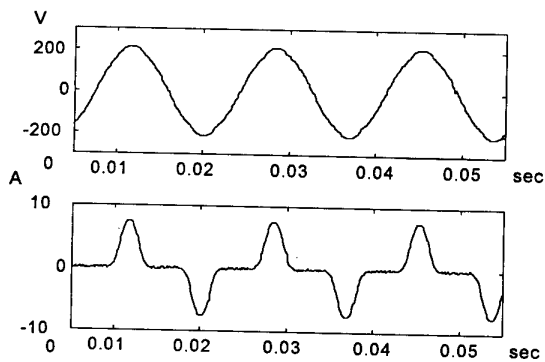


Figure 8 Inverter output voltage and load current waveforms with fuzzy controller.

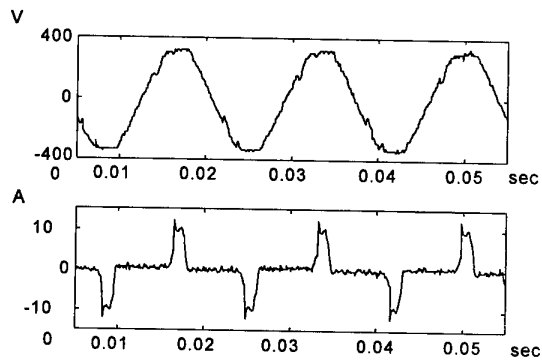


Figure 9 Inverter output voltage and load current waveforms with deadbeat control.

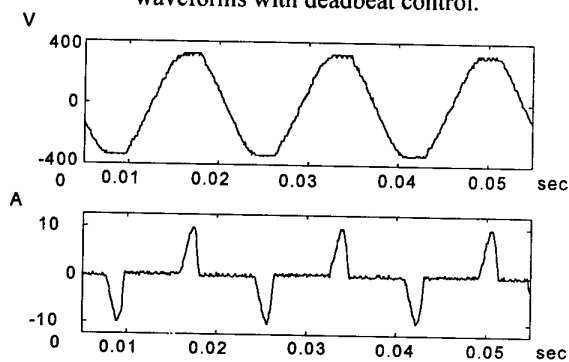


Figure 10 Inverter output voltage and load current waveforms with fuzzy controller.

Table 1. The control rules

$\Delta e \setminus e$	NB	NM	NS	ZE	PS	PM	PB
NB	ZE	PS	PS	PM	PM	PB	PB
NM	NS	ZE	PS	PS	PM	PM	PB
NS	NS	NS	ZE	PS	PS	PM	PM
ZE	NM	NS	NS	ZE	PS	PS	PM
PS	NM	NM	NS	NS	ZE	PS	PS
PM	NB	NM	NM	NS	NS	ZE	PS
PB	NB	NB	NM	NM	NS	NS	ZE

Importance of the Mechanical Flexibility on Behaviour of a Hydraulic Driven Log Crane

Salvador Esqué (Researcher) Timo Käppi (Researcher) Asko Ellman (Professor)
Institute of Hydraulics and Automation - Tampere University of Technology
esque@cc.tut.fi

Abstract

Hydraulically driven crane is a multibody system, which can be studied by the means of simple kinematics transformation matrix method [1] and applied for hydraulic driven crane. However if the elasticity of mechanical structure need to be taken into account the number of degrees of freedom increases significantly and special methods are required. ADAMS-software is a suitable environment for simulating and analysing such systems. Elastic structures can be modelled in FEM-software and then imported to ADAMS where the complete system can be assembled and simulated. This approach leads to precise result but it is a numerically heavy method and requires advanced knowledge on mechanics. The purpose of this study is to evaluate the importance of mechanical flexibility in the case of a typical forest crane. The evaluation is made by comparing the eigenfrequency charts of cranes where flexibility is and is not taken into account.

1. Introduction

Typical hydraulically driven log cranes are constructed with light and long boom structures that can present important deflections during its operation time. Until the latest years, dynamic simulations of cranes were carried using rigid models of the mechanical structures of the crane. Therefore, elastic deformations and damped vibrations were omitted, making the analysis less accurate. The dynamic simulation of flexible-bodies mechanisms involves solving a large second order of coupled differential equation system for each one of the discretizations of the flexible bodies, as it is showed in section (2.3). Therefore coding all the equations of motion for each model is not encouraged.

In this paper, an FEM-software (ANSYS) and dynamic system simulation software (ADAMS) is used to carry out the simulation of a hydro-mechanical system with mechanical flexibility properties. Firstly, the flexible components of the mechanism are modelled in ANSYS.

Then, by performing on them a Modal Analysis, the flexible properties of each body can be extracted and saved as a binary file (Modal Neutral file) directly importable to ADAMS software. The figure 1 illustrates the procedure:

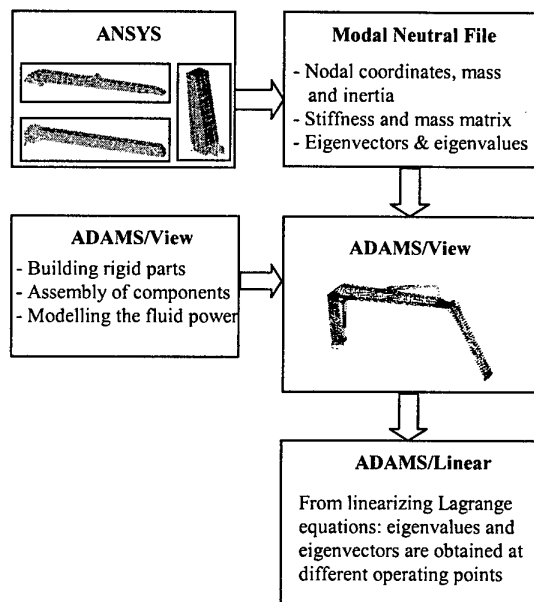


Figure 1. Layout of the flexibility transfer, model assembly and analysis

On the other hand, a rigid model of the same log crane is built in order to compare the simulation results between the two models of the crane. In the rigid model, the flexible properties of the booms spread along the nodes are replaced by the mass and inertia concentrated at each centre mass of the bodies. The rest parts of the model and the fluid power remain modelled in the same way as the flexible model.

2. Method

From ANSYS-software package, every single flexible body is modelled and analysed separately from the others

by using the ANSYS Modal Analysis algorithm. The ANSYS Modal Analysis is able to write a file that contains all the geometrical and mechanical flexible properties of the body analysed. Therefore, this file can be imported to ADAMS, where the elastic body will be created automatically. The MNF is directly importable to ADAMS-software, and the flexible bodies are automatically created.

The next steps consist on creating (in ADAMS-software environment) the cylinders and other rigid bodies, assembling the model, and implementing the fluid power model governing the actuators.

Afterwards, ADAMS/Solve and ADAMS/Linear modules are used simultaneously in order to perform dynamic analysis and to perform eigenanalysis. Dynamic simulation drives the model to an operating point and then the eigenanalysis extract the natural frequencies and their mode shapes. The operation is repeated until reaching all the points desired.

2.1. Modal Analysis

Modal Analysis is the process of determining the inherent dynamic characteristics of a system and using them to formulate a mathematical model of the dynamic behaviour of the system. Modal analysis characterise the deformation of a body due to external vibration input. When the body is excited by external vibration energy, it is deformed in a number of well-defined wave-like patterns or modes. Each mode has its own specific natural frequency (eigenvalue) and shape (eigenvector). The analytical formulation to extract the modes of a flexible body is the following:

The equation of motion for an undamped body expressed in matrix notation is

$$[M]\{\ddot{u}\} + [K]\{u\} = 0. \quad (1)$$

Where $[M]$ and $[K]$ are the mass and stiffness matrices respectively, $\{u\} = \{u_1, \dots, u_N\}$ is the nodal coordinate matrix, N is the number of nodes defining the FEM modelled body, and $\{\ddot{u}\}$ is the nodal acceleration matrix.

For a linear system, free vibrations are harmonic of the form that nodal coordinates can be expressed as

$$\{u\} = \sum_{i=1}^N \{\phi_i\} \cos(\omega_i \cdot t). \quad (2)$$

Where $\{\phi_i\}$ is the eigenvector associated to the i^{th} natural frequency and ω_i is the i^{th} natural circular frequency. Using the equation 2 in the equation of motion 1, the following equation is obtained:

$$(-\omega_i^2 [M] + [K]) \cdot \{\phi_i\} = 0. \quad (3)$$

The equation (3) is satisfied if the determinant of $([K] - \omega^2 [M])$ is zero. This is an eigenvalue problem, which may be solved for up to n values of, ω^2 and n eigenvectors $\{\phi_i\}$, where n is the number of degrees of freedom (DOF). The eigenvalue problem has the form

$$[K]\{\phi_i\} = \lambda_i [M]\{\phi_i\}. \quad (4)$$

ANSYS Modal Analysis computes the mass and stiffness matrix of the body using lumped mass approximation and solves the numeric eigenvalue equation (4), extracting the natural frequencies λ_i and the mode shapes ϕ_i for each mode i .

2.2. Exporting the flexible information to ADAMS

ANSYS and ADAMS have been working together in order to build the capability of exporting the geometrical and mechanical flexible properties of a body modelled in ANSYS to ADAMS. This is possible due to a binary file named Modal Neutral File (MNF) written during an ANSYS Modal Analysis of a single body. The MNF is directly importable to ADAMS-software and contains the following information for each body:

- Nodal coordinates, nodal masses and nodal inertia
- Element topology
- Generalised stiffness and mass matrix
- Nodal displacements (mode shapes) and their natural frequencies

Description of the compatibility between the binary MNF and ADAMS software in different hardware platforms can be found in [2].

The three arms of the hydraulically driven log crane presented in this study have been modelled and analysed separately in ANSYS. Therefore, three MNF have been extracted from the analyses and they have been imported to ADAMS using the interface module ADAMS/Flex, which uses an assumed modes method of modelling flexible bodies.

2.3. Flexible Bodies in ADAMS. Lagrange formulation

ADAMS uses an assumed modes method of modelling flexible bodies called Modal Flexibility. Modal Flexibility assigns a set of mode shapes to a flexible body. During a time analysis the relative amplitude of each eigenvector is

calculated as a state variable. The principle of linear superposition is then used to combine the mode shapes at each step time to reproduce total deformation of the flexible body. This is executed by means of Lagrange formulation.

The nodes of the finite element model imported to ADAMS can be assumed to undergo in linear deformations and rotations as a combination of mode shapes. The position of the j^{th} node is

$$r_j = x + A(s_j + \Phi_j q). \quad (5)$$

Where x is the coordinates vector from the global origin to the local body reference (l.b.r.), A is the orientation between the l.b.r. and the global origin in Euler angles, s_j is the undeformed location of the j^{th} node in the l.b.r., Φ_j is the contribution of the mode shape to the j^{th} node, and q is the vector of modal amplitudes. Now the vector of generalised coordinates for the flexible body can be represented as

$$\xi = \{x \ \psi \ q\}. \quad (6)$$

According to Lagrange formulation, the motion of a body defined by the generalised coordinates in equation 6 can be described as

$$\frac{d}{dt} \left(\frac{\partial L}{\partial \dot{\xi}} \right) - \frac{\partial L}{\partial \xi} + \frac{\partial F}{\partial \xi} + \left[\frac{\partial \Phi}{\partial \xi} \right]^T \lambda - Q = 0. \quad (7)$$

Where L is the Lagrangian, Φ is the matrix of constraint equations, F is the matrix of damping forces, λ is the matrix of the reaction forces vectors in the constraints, and Q is the matrix of external applied forces.

After relating the derivative of the Euler angles ψ with the angular velocity of the l.b.r. relative to the ground through the matrix B , the velocity of a node j on the flexible body can be expressed as

$$v_j = \begin{bmatrix} I & -A(\tilde{s}_j + \tilde{\Phi}_j q)B & A\Phi_j \end{bmatrix} \dot{\xi}. \quad (8)$$

The Lagrangian L can be expanded as $L = T - V$ with

$$T = \frac{1}{2} \sum_{j=1}^N m_j \{v_j\}^T \{v_j\}. \quad (9)$$

$$V = V_g(\xi) + \frac{1}{2} \xi^T K \xi. \quad (10)$$

Combining the equation 8 and equation 9, the kinetic energy of the Lagrangian T simplifies into

$$T = \frac{1}{2} \dot{\xi}^T M(\xi) \dot{\xi}. \quad (11)$$

The gravitational potential energy V_g in equation 10 can be expressed as

$$V_g = \sum_{j=1}^N m_j [x_j + A(s_j + \Phi_j q)]^T g. \quad (12)$$

Therefore, the gravitational force is

$$f_g = -\frac{\partial V_g}{\partial \xi}. \quad (13)$$

The matrix of damping forces F depends on the modal velocities. According to Rayleigh dissipation function:

$$F = \frac{1}{2} \dot{q}^T D \dot{q}. \quad (14)$$

Where D is the damping matrix of the body, and its coefficients have the form

$$d_j = 2\eta_j \sqrt{k_j m_j}. \quad (15)$$

Then, the final expression of the motion of the body according to Lagrange formulation turns from equation (7) to the following in terms of mass, stiffness and damping:

$$M\ddot{\xi} + \dot{M}\dot{\xi} - \frac{1}{2} \left[\frac{\partial M}{\partial \xi} \dot{\xi} \right]^T \dot{\xi} + K\xi + f_g + D\dot{\xi} + \left[\frac{\partial \psi}{\partial \xi} \right]^T \lambda - Q = 0. \quad (16)$$

2.3.1 The extraction of modes

ADAMS/Linear allows ADAMS models to be represented by complex valued eigendata (eigenvalues and mode shapes). ADAMS/Linear carries out a condensation of the flexible structure by using the Modal Analysis method described in section (2.1) to the whole mechanism. Therefore, the flexible mechanism is modelled by two components: The Rigid Body component describing the motion of the Body reference, and a set of Differential Equations describing the structural deflections. The eigendata solution results from solving the general eigenvalue problem of the same form as equation 4. A developed analytical method for obtaining the Linear State Equations can be found in [4].

3. The model

The hydraulically driven log crane simulated is a typical hydraulic crane used in harvesting and log handling forestry machines. Three booms (swing arm, lift arm and stick arm) compose the crane. Three actuators drive the real crane by means of electrically directional valves, conferring the mechanism 3 DOF. However the turning actuator has not been modelled as the contribution of this rotational DOF to the final results has been observed to be negligible.

3.1. Model of the boom structure

The three booms of the crane structure (swing arm, lift arm and stick arm) have been modelled as elastic structures using ADAMS software. 4-node shell elements have been used to model the boom structures flexibility. The swing arm is modelled with 434 nodes, the lift arm with 961 nodes and the stick arm with 599 nodes, conferring to the whole mechanism almost 12 000 DOF.

The three FEM-modelled booms are analysed and exported separately to ADAMS, where the rest of the rigid parts of the crane (load, cylinders and links) are modelled and assembled to the mechanism. A load of 5 000 N is applied at the end of the stick arm.

The ANSYS Modal Analysis has been set up to extract 30 modes associated to the first 30 natural frequencies of each body. ADAMS by default enables all the modes when the MNF is imported. However, in order to increase the efficiency of simulations, only the modes that contribute to the motion to simulate are enabled. An another criterion is to disable the modes that do not significantly contribute to the total strain energy of the flexible body. This task can be carried out automatically by ADAMS.

3.2 Modelling the hydraulic circuit

The hydraulic cylinders are the interface between the mechanism and the fluid power system. The rest of the hydraulic components modelled are the valves and the pump. The scheme of the hydraulic circuit used to transmit power to the log crane is presented in figure 2.

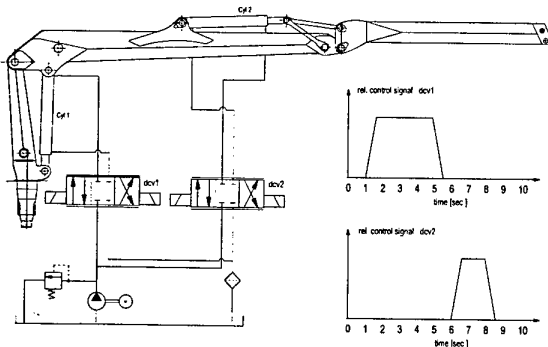


Figure 2. Scheme of the hydraulic circuit and control signal for the valves

The flexible behaviour of the fluid power is described [4] by the dynamic pressure fluctuation in the circuit:

$$\dot{P} = \frac{B_{eff}}{V_c} (Q_c + Q_v). \quad (17)$$

Where B_{eff} is the effective bulk modulus, V_c is the volume in the active chamber of the cylinder plus the volume compressed between the actuator and the valve. Q_c and Q_v are the flow to the actuator chamber and the flow through the valve respectively, and computed as follows

$$Q_c = A_c \dot{X}. \quad (18)$$

$$Q_v = |R_v| K_v \sqrt{P_p - P}. \quad (19)$$

Where A_c is the section area of the cylinder, and \dot{X} is the relative speed between the two chambers. On the other hand, R_v is the relative control signal (see figure 2), P_p is the supply pressure and K_v is the flow coefficient of the control valve that can be written as follows

$$K_v = \frac{Q_{vnom}}{\sqrt{\Delta P_v}}. \quad (20)$$

Where Q_{vnom} and P_v are the flow and the drop pressure respectively when the valve is fully open. The resultant hydraulic force in the cylinder can be set from the following equation

$$F = A_{PL} P_{PL} - A_{MI} P_{MI} - C_{vis} \dot{X}. \quad (21)$$

Where the term $C_{vis} \dot{X}$ is the friction force between seals and the cylinder wall. In this model the viscous friction C_{vis} has been fixed as a constant. However in a more accurate approach [5], the viscous friction would be treated as a variable depending on the sliding velocity and the pressure acting in the cylinder.

3.3 Design of the simulation

The comparison between the rigid model and the flexible model of the log crane is carried out by comparing the natural frequencies extracted in different operating points. Combinations of 20 positions in both actuators have been fixed in order to perform the experiment.

Therefore, a 400-point chart of natural frequencies is obtained for each rigid and flexible models of the log crane. Figure 3 and figure 4 show the range of positions taken by the crane.

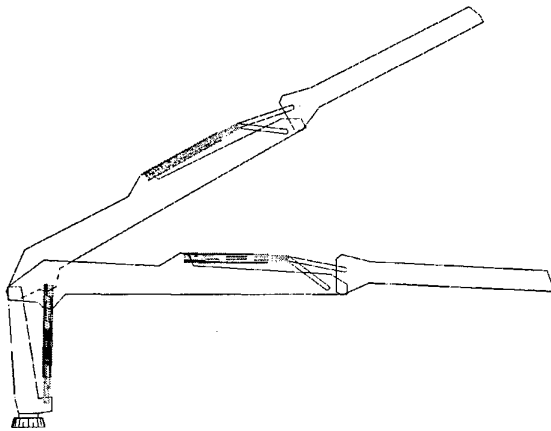


Figure 3. Minimum and maximum stroke among the 20 positions of the lifting cylinder

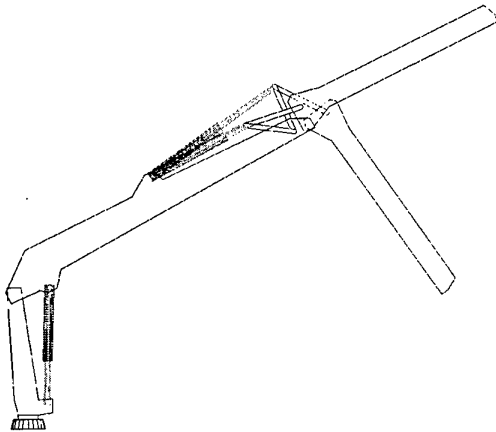


Figure 4. Minimum and maximum stroke among the 20 positions of the piling cylinder

The operating points have been reached by powering the lifting actuator from initial position (minimum stroke) to final position 20 steps. At each one of the 20 lifting cycles, the piling actuator takes a different configuration according to the figure 4 (from horizontal end arm to vertical end arm). Both actuators have been powered according to the control ramps showed in figure 2. Therefore, a linearization of the dynamic equations of motion is carried out along the combination of 20 equally spaced positions of both piling and lifting actuators, obtaining the modes of the system at 400 operating positions of the crane.

4. Results and conclusions

Firstly are presented the modes extracted concerning the two DOF of the crane mechanism. Both rigid and flexible models show identical mode shapes but, on the other hand, their natural frequencies present some differences.

4.1 First mode

The chart in figure 5 shows the natural frequencies belonging to the first mode of the rigid model. The values of natural frequencies are strongly dependent on the position of the stick arm, however the position of the lifting cylinder is not very sensitive to the natural frequencies of the system.

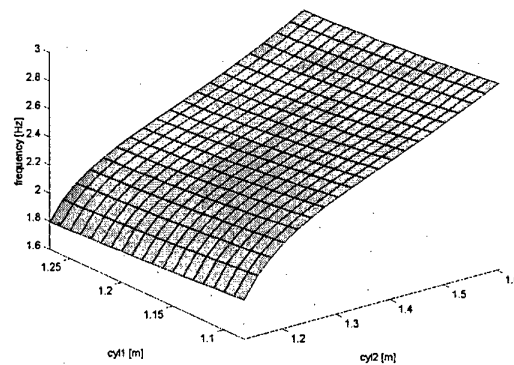


Figure 5. Chart of the natural frequencies of the first mode of the rigid model.

A similar chart (figure 6) is obtained from extracting the natural frequencies in the flexible body.

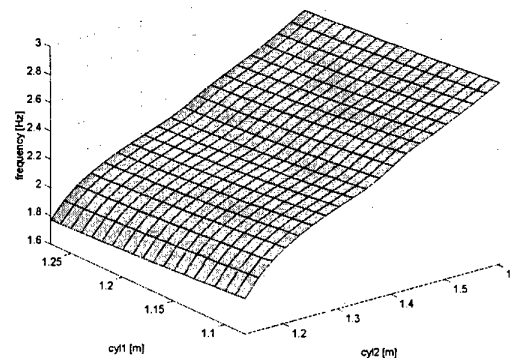


Figure 6. Chart of the natural frequencies of the first mode of the flexible model.

The only detectable difference between rigid and flexible models can be found in a smooth variation of the slope of the surface of the flexible model chart, around an intermediate position of the piling actuator. This fact can be observed in the next chart (figure 7) where the relative error between both natural frequency extractions has been plotted. The maximum difference occurs when the stick cylinder has a stroke of 1330 mm. (intermediate position according to figure 4) and the lifting cylinder is in the lowest position (according to figure 3). In that position the relative error between the natural frequencies of both rigid and flexible models is 4.7 %.

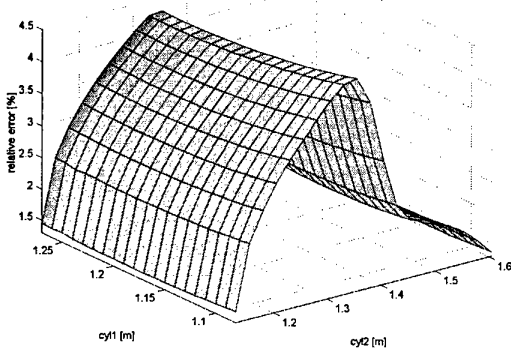


Figure 7. Chart of the relative error between the first natural frequencies of the rigid and the flexible model.

4.2 Second Mode

The natural frequencies obtained from the extraction of the second mode in the 400 positions of the crane are showed in the following charts. In figure 8 the second natural frequency chart of the rigid model is showed.

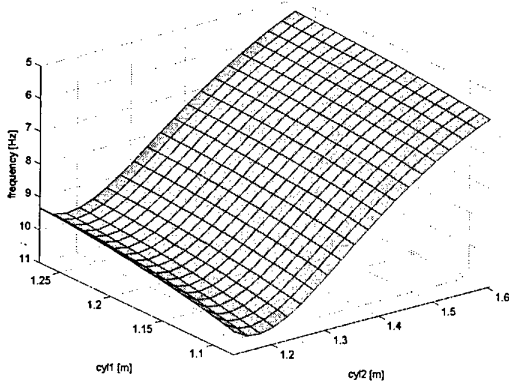


Figure 8. Chart of the natural frequencies of the second mode of the rigid model.

Figure 9 shows the second natural frequency chart of the flexible model. As in the first mode, the position of the lifting cylinder has not an important influence on the discrepancies of the natural frequencies between both models. Comparing the value of the natural frequencies in both rigid and flexible charts, it can be observed that major discrepancies are obtained in the second mode.

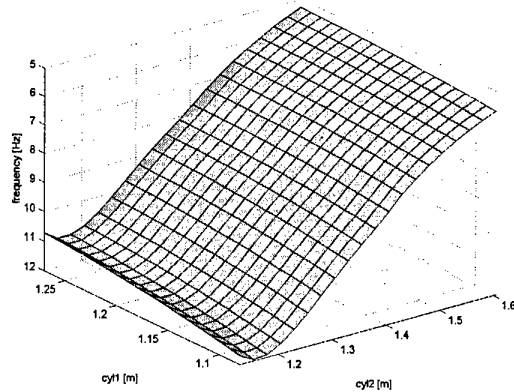


Figure 9. Chart of the natural frequencies of the second mode of the flexible model.

The phenomena can be better observed in figure 10, where the relative error between the natural frequencies of both models is plotted. For extended positions of the stick arm (minimum stroke of the piling actuator) the natural frequencies in the flexible body are up to 14.8% higher than in the rigid model. The divergence decreases when the position of the piling actuator makes the stick arm to reduce the total length of the crane.

The relative error chart obtained in the extraction of the second mode (figure 10) seems to be more logical than the one obtained in the first mode (figure 7). The torque arm of the crane reach the maximum value for extended positions of the stick arm (when the stick arm is parallel to the lift arm). In those positions the stress in the boom structure is also maximum and deformations of the flexible modelled booms are induced. These deformations have a non-negligible rule on the equation of motion of the system, and consequently they are contributing to the values of the natural frequencies.

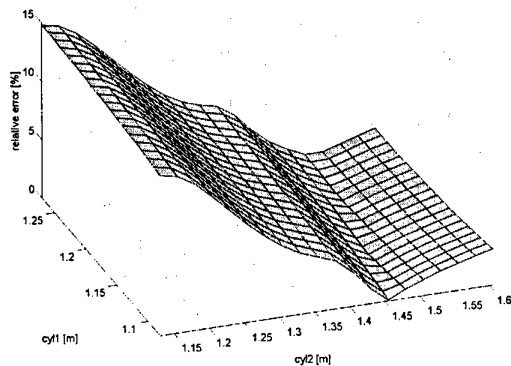


Figure 10. Chart of the relative error between the second natural frequencies of the rigid and the flexible model.

The two first modes presented before were associated to vibrations of the system along the equilibrium position of the two actuators. However, between the two natural frequencies associated to the two DOF of the mechanism, the flexible model presents an intermediate mode. This mode is associated to vibrations of the log crane due to the deformations of the mechanical boom structure. Figure 11 shows the natural frequency chart of the mode shape.

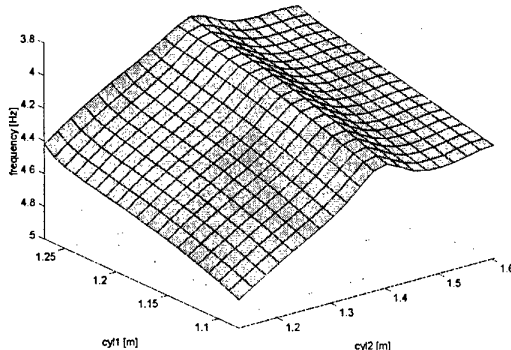


Figure 11. Intermediate mode of the flexible model due to mechanical deformation of the booms.

The mode shape associated to this intermediate mode is characterised by the deformations of the boom structure due to the bending of the lift and stick arm. Figure 12 shows the deformation taken by the structure when it is excited by an arbitrary natural frequency belonging to the intermediate mode shape (figure 11).



Figure 12. Mode shape of an intermediate mode of the flexible model.

4.3 Conclusions

The natural frequencies of a mechanical system use to be a design variable during the machine design process. From the analyses of the results obtained in this paper, it can be concluded that the flexibility component plays an important role in the determination of this dynamic property. The results show that hydraulic flexibility governs the problem and mechanical flexibility deviates the natural frequencies up to a 15 %. Moreover, many other modes can be identified in the mechanical flexible model. For instance a dozen of mode shapes (with natural frequencies contained between 5 Hz and 200 Hz) due to the bending (of lifting and sticking booms) and/or torsion (of the lifting boom) has been found. Other local modes of higher frequency can be also detected although they do not contribute to the general motion of the crane.

The modelling of the flexibility properties should be taken into account when analysing such hydraulically driven mechanisms. Therefore, virtual testing technique can be very suitable as an optimisation tool for drive technology systems of complex kinematics and dynamic equations. The use of both FEM and ADAMS software to model the prototype is the most suitable choice to achieve accurate results.

References

- [1] R.P. Paul, *Robot Manipulators: Programming and Control*, MIT Press 1981
- [2] S. Esqué, *Modelling of flexible structures on ADAMS*, Tampere University of Technology, Master Sc. Thesis, 1998
- [3] D. Minen, D. Catelani, *Flexible Bodies and ADAMS: Methods and Techniques*, Mechanical Dynamics Italy, 1996
- [4] A. Ellman, T. Käppi, M. Vilenius, *Simulation and analysis of hydraulically-driven boom mechanism*, 9th Bath International Fluid Power Workshop, Bath, England 1996
- [5] A. Mikkola, H. Handroos, *Modelling and simulation of a flexible hydraulically driven log crane*, 9th Bath International Fluid Power Workshop, Bath, England 1996

Analysis and Synthesis of Electrohydraulic Servomechanisms

Alexandru MARIN

"POLITEHNICA" University, Hydraulics Department

Splaiul Independentei 313, 79590 Bucharest, Romania, e-mail: marin@hydrop.pub.ro

Ionică CRISTEA, Paul SVASTA

"POLITEHNICA" University, Electronic Technology and Reliability Department

Splaiul Independentei 313, 77206 Bucharest, Romania, e-mail: cristea@cadtiectp.pub.ro

Petrin DRUMEA

Hydraulics and Pneumatics Research Institute

Cutitul de Argint 14, 75212, Bucharest, Romania, e-mail: ihp@fx.ro

Abstract

The paper reveals theoretical and experimental results, concerning the dynamic experimental identification of a proportional valve, destined to replace the moving coil valves (an old generation), belonging to the speed governors of the hydraulic turbines. It was made the experimental validation of the mathematical model, written for the servomechanism equipped with the previously mentioned proportional valve. It was proposed a synthesis method for the PI controller, with additional state feedback, corresponding to a classical servomechanism (containing a moving coil valve).

The experiments, the numerical simulations and the proposed algorithm of synthesis revealed important practical conclusions, concerning the dynamic behaviour of the proportional valve by himself and within the servomechanism and the advantages of the proposed synthesis algorithm.

1. Introduction

The presence of electronic equipment in the electrohydraulic servomechanisms confirms the modern concept of mechatronics [3]. Flexibility of these servomechanisms depends on the hardware and software devices, highly integrated in the concept of total automatic processes (hierarchical control structures).

Modern theoretical and experimental research are focused on structural and design improvement for elements and systems, in association with a coherent methodology for analysis and synthesis of the system controllers.

A very important device in every servomechanism is the electrohydraulic interface (proportional valves and servo valves). These ones were spectacularly developed recently,

great companies (Bosch, Rexroth, Parker) offering proportional valves with high dynamic performances, by using local position controlling loops. The position feedback loop from the spool valve, completed with additional feedback state control increases the stability and improves the transient response [7].

The servomechanisms destined to speed governors for hydraulic turbines include two fundamental non linear aspects (different acting areas of the guide vanes hydraulic cylinder and the "dead band" of the characteristic curve for the proportional valve). The asymmetry of behaviour can be eliminated by using two different controllers, corresponding to each moving direction. A self-learning controlling algorithm is able to compensate different influences on the width of the "dead band", increasing the steady-state and dynamic performances [5].

This paper reveals some theoretical and experimental results, obtained by the authors in the following areas of interest [4]:

- the dynamic experimental identification of a proportional valve, destined to replace the moving coil valves (an old generation), belonging to the speed governors of the hydraulic turbines; it was determined the equivalent transfer function, using the experimental data, previously mentioned;

- the experimental and numerical simulation validation of the mathematical model, written for the servomechanism equipped with the previously mentioned proportional valve;

- the conception of a coherent synthesis method of the PI controller, with additional state feedback, corresponding to a classical servomechanism (containing a moving coil valve).

All numerical simulations implied graphical networks, specific to the software package MATLAB- SIMULINK and TOOLBOX CONTROL MATLAB [9].

2. Experimental dynamic identification of the proportional valve

The proportional valves steady-state characteristics are non linear, with a greater hysteresis than the moving coil valves [4,5]. The low sensibility for impurities, the modern fabrication technology and the cheaper price impose this valve category. In order to diminish the insensitivity and the hysteresis, over the command signal it is superposed a "dither" signal, or it can be controlled the position of the spool valve within a local servomechanism.

The reference model of the 3/3 proportional valve (fig. 1) includes a solenoid and a critical centre flow valve with circular hydraulic inlets on the sleeve [4].

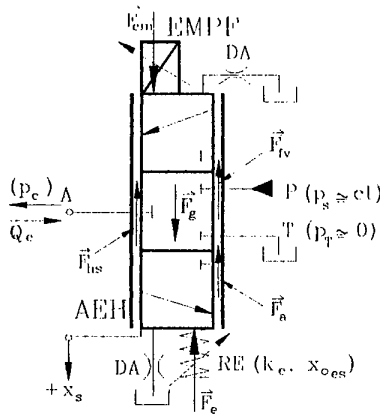


Fig. 1 The symbolic functioning scheme for the proportional valve

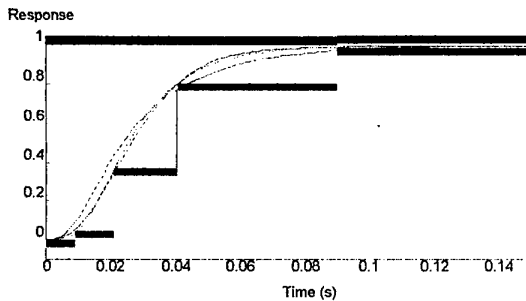


Fig. 2 Step response and the graphical identification scheme

In accordance with the experimental step response (fig. 2) we propose an approximate third order transfer function:

$$H(s) = \frac{Q_c(s)}{i(s)} = \frac{K_{Qi}}{\left(\frac{s^2}{\omega_{n3}^2} + \frac{2\zeta_3}{\omega_{n3}} s + 1 \right) (T_3 s + 1)} \quad (1)$$

An automatic methodology for dynamic identification is implemented in the software package MATLAB-TOOLBOX NCD (NCDBLOCK [9]). This way we determined precisely the values of the coefficients, introduced by equation (1): $K_{Qi}=95,7533 \text{ l/min/A}$; $\omega_{n3}=109,3 \text{ rad/s}$; $\zeta_3=0,6928$; $T_3=16,6 \text{ ms}$.

3. Experimental identification of a servomechanism with proportional valve

The experimental stand scheme of the servomechanism with proportional valve is presented in Figure 3.

The transfer function of the PD electronic controller can be written as follows:

$$H_R(s) = \left(1 + \frac{K'_P}{2} \right) \left[1 + \frac{(K'_D + 10) \times 10^{-3} s}{T_f s + 1} \right] = K_P \left(1 + \frac{T_D s}{T_f s + 1} \right) \quad (2)$$

where: $K'_P = 0 \dots 100$ is a gain coefficient; $K'_D = 0 \dots 100$ is an accordance parameter for the derivative component; $T_f = 10^{-3} \text{ s}$ - "filtering" time parameter, active at low frequencies and at starting of a transient regime; K_P - gain coefficient for the proportional component; T_D - time derivative coefficient.

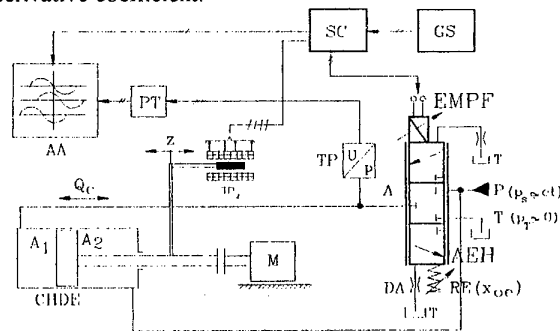


Fig. 3 Experimental testing stand of the servomechanism

The mathematical model of the studied servomechanism (fig. 3) contains the following equations [4]:

- equations corresponding to the proportional valve;
- the continuity equation applied to the flow domain placed between the "A" port of AEH and the high surface chamber of CHDE;
- the dynamic equation applied on the moving part of CHDE.

With the upper mentioned equations we assemble a graphical simulation network and determine the input step response of the servomechanism. The numerical values of the coefficients are: $A_1 = 1963,5 \text{ mm}^2$; $R_{hc} = 20 \text{ MN/m}$; $m_{CH} = 12 \text{ Kg}$; $A_2 = 1159 \text{ mm}^2$; $p_s = 30 \text{ bar}$; $F_{CH} \cong 40 \text{ N}$.

A comparison between the simulated and experimental step responses is presented in Figure 4. The experimental identified values of the accordance parameters for the PD electronic controller are: $K_p = 8,9$ and $T_D = 46$ ms. A very good resemblance exists between the two curves, excepting some differences in the beginning of the transient regime; this differences are connected to the influence of length of the supply line (some pressure variations) [4].

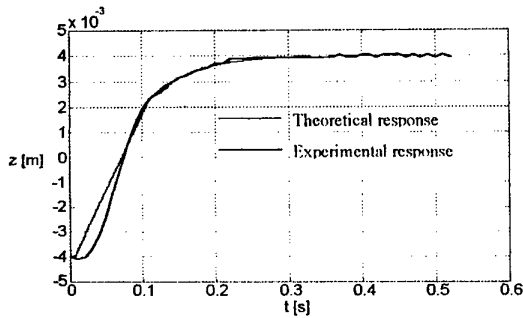


Fig. 4 Theoretical and experimental step responses

4. Synthesis algorithm for the controller of an electrohydraulic servomechanism

The classical electrohydraulic servomechanism destined to the speed governors for hydraulic turbines contains a 3/3 moving coil valve CEHBM, a 4/3 power mechanohydraulic proportional valve AMH, a position transducer TP_2 and an electronic controller RE_z (fig. 5).

The mathematical model corresponding to the dynamics of the servomechanism are [4]:

- the transfer function for the moving coil valve, with state feedback and integrator bloc on the command channel;
- flow equation for the open centre moving coil valve;
- the continuity equation written on the flow domain (Σ) (fig. 5);
- the dynamic equation on the spool of the mechanohydraulic proportional valve AMH.

Starting from these equations we propose a state controller; the transfer function for the fixed part of the system can be written as follows:

$$H(s) = \tilde{H}_{CEM}(s)H_3(s) \quad (3)$$

$$= \frac{g_0 K_0 K' \alpha}{(b_0 s + K_0 K')(\beta_3 s^3 + \beta_2 s^2 + \beta_1 s + \beta_0)}$$

On the command channel we choose a PI controller configuration (fig. 6), in order to ensure the steady-state precision.

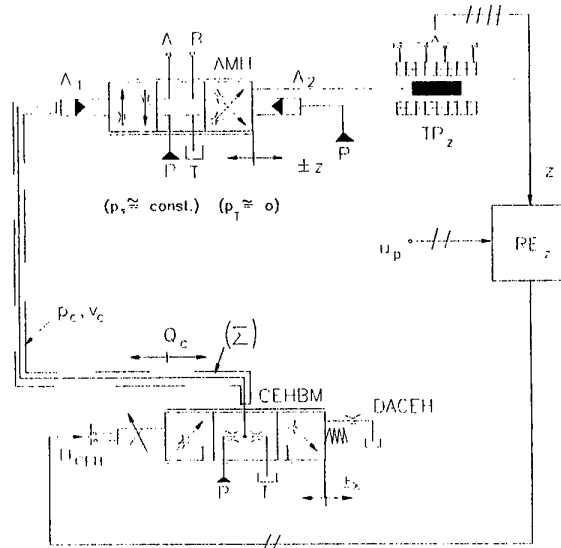


Fig. 5 The structure of the classical electrohydraulic servomechanism

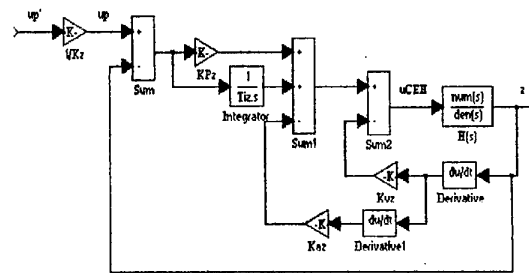


Fig. 6 The state controlled servomechanism equivalent scheme

The transfer function of the state controlled servomechanism can be written as follows:

$$H_{oc}(s) = \frac{z(s)}{u_p(s)} = \frac{g_0 K_0 K' \alpha \left(K_{Pz} s + \frac{1}{T_{Iz}} \right)}{\text{Numitor 2}(s)} \quad (4)$$

$$\text{Numitor 2}(s) = s^5 + \frac{K_0 K' \beta_3 + b_0 \beta_2}{b_0 \beta_3} s^4 +$$

$$+ \frac{K_0 K' \beta_2 + g_0 K_0 K' \alpha K_{az} + b_0 \beta_1}{b_0 \beta_3} s^3 +$$

where:

$$\frac{K_0 K' \beta_1 + g_0 K_0 K' \alpha K_{vz} + b_0 \beta_0}{b_0 \beta_3} s^2 +$$

$$+ \frac{K_0 K' \beta_0 + g_0 K_0 K' \alpha K_{Pz}}{b_0 \beta_3} s + \frac{g_0 K_0 K' \alpha}{T_{Iz} b_0 \beta_3}$$

With the transfer function (4) it is realised a good steady-state precision (zero error for input step response).

The problem to solve is the placement of the proper values corresponding to the following form of the transfer function $H_{06}(s)$:

$$H_{06}(s) = \frac{\frac{p_{52}}{z_2}(s + z_2)}{(s + p_{52})} \times \frac{p_{12}p_{22}p_{32}p_{42}}{(s + p_{12})(s + p_{22})(s + p_{32})(s + p_{42})} \quad (5)$$

With some preliminary numerical simulations we conclude the existence of two dominant poles, corresponding to a second order system, completed with the presence of two complex related poles, characterised by a very low damping factor. The additional pole and zero, p_{52} and z_2 were chosen very close to the origin (a "dipole").

We choose the poles p_{32} and p_{42} like having the modulus of the imaginary part very high (in accordance with the preliminary numerical simulations), the real part being calculated with the formula:

$$\text{Re}(p_{32}) = \text{Re}(p_{42}) = \frac{p_{32} + p_{42}}{2} \quad (6)$$

From the identification of the other coefficients from the transfer functions (4) and (5) we obtain the equations for the accordance parameters of the controller:

$$K_{p22} = \frac{p_{12}p_{22}p_{32}p_{42}p_{52}b_0\beta_3}{z_2g_0K_0K'\alpha} \quad (7)$$

$$T_{12} = -\frac{g_0K_0K'\alpha}{b_0\beta_3} \frac{1}{p_{12}p_{22}p_{32}p_{42}p_{52}} \quad (8)$$

$$K_{v22} = -\frac{1}{g_0K_0K'\alpha} \times \left\{ \begin{aligned} & p_{12}p_{22}(p_{32} + p_{42}) \\ & + p_{32}p_{42}(p_{12} + p_{22}) \\ & + \left(\frac{p_{12}p_{22} + p_{32}p_{42}}{(p_{12} + p_{22})(p_{32} + p_{42})} \right) p_{52} \end{aligned} \right\} \quad (9)$$

$$K_{a22} = \frac{1}{g_0K_0K'\alpha} \times \left\{ \begin{aligned} & p_{12}p_{22} + p_{32}p_{42} \\ & + (p_{12} + p_{22})(p_{32} + p_{42}) \\ & + (p_{12} + p_{22} + p_{32} + p_{42})p_{52} \\ & - K_0K'\beta_2 + b_0\beta_1 \end{aligned} \right\} \quad (10)$$

By accepting the dynamic behaviour of the servomechanism with a second order delay element and imposing ζ_2 and t_{r2} we can calculate the values for the according parameters with the equations (8), ..., (11) [4].

5. Conclusions

The experiments, the numerical simulations and the proposed algorithm of synthesis for the controller of the servomechanism lead to some practical conclusions:

- the dynamic behaviour of the proportional valve corresponds to a third order delay element, over damped; it is possible to accept a second order or even a first order transfer function, depending on the dynamics of the entire system;

- the according controller parameters K_p and T_D of the servomechanism with proportional valve are identically for the mathematical model and in the experimental tests. Choosing a right balance between the parameters we can satisfy the compromise precision-stability, depending on the imposed performances;

- the proposed synthesis algorithm for the classical servomechanisms, dedicated to the speed governors for hydraulic turbines isn't unique, concerning the structure of the controller and the position of the proper values on the equivalent transfer function. The proposed analytical equations facilitate a rapid first dimensioning of the controller and the implementation of a self-learning control structure.

References

- [1] De Santis R.M. - "An Adaptive PI/Sliding Mode Controller for a Speed Drive", Journal of Dynamic Systems, Measurement and Control, September 1989;
- [2] Ikco S., Takahashi T. and Takahashi K. - "Application of the Adaptive Control Theory to the Electrohydraulic Servo System Including Proportional Control Valve", The Third Scandinavian International Conference On Fluid Power;
- [3] Isermann I. - "On the design and control of mechatronic systems", IEEE Robotics and Automation Society, 1996;
- [4] Marin Al. - "Researches concerning the analysis and synthesis of the hydraulic speed governors for the hydraulic turbines", Ph. D. Thesis, "Politehnica" University, Bucharest, 1997;
- [5] Matten N. - "Measures to Significantly Improve the Dynamics of Proportional Directional Valves", The Third Scandinavian International Conference On Fluid Power;
- [6] Niemela E., Zhao T. and Virvalo T. - "Fuzzy Logic Controller Applied on Hydraulic Position Servo", The Third Scandinavian International Conference On Fluid Power;
- [7] Virtanen A. - "The Design of State Controlled Hydraulic Position Servo System", The Third Scandinavian International Conference On Fluid Power;
- [8] Weishaupt E. and Backe W. - "Secondary Speed and Position Controlled Units with Adaption for Pressure and Inertia Load", The Third Scandinavian International Conference On Fluid Power;
- [9] *** - "MATLAB-SIMULINK", Users Guide, Natick Massachussets, The Math Works Inc., 1992.

FORCE TRANSDUCER WITH INTEGRATED ELECTRONICS FOR HYDRAULIC CYLINDER

Ionica Cristea², Mircea Comes¹, Marian Blejan¹, Adrian Mirea¹, Andrei Drumea²

¹ Hydraulic and Pneumatic Research Institute, Cutitul de Argint 14, 75212 Bucharest 4, Romania
phone: +00401/3363990, 013363991 Fax: 01/3373040 E-mail: ihp@fx.ro

² "POLITEHNICA" University of Bucharest, Center for Technological Electronics and Interconnection
Technique, Splaiul Independentei 313, 77206 Bucharest, Romania
E-mail: cristea@cadtieccp.pub.ro

Abstract

This paper presents the realisation of force transducers with 0 – 6300 kN measure range, designed to work with hydraulic cylinders in automatic positioning systems with real force control. These systems are used in materials' stress testing installations as well as in vibrations testing installations for industrial equipment. The constructive solution chosen by the authors is to use displacement sensors with variable reluctance in order to measure the central arrow of an elastic steel membrane. The paper contains an accessible presentation for calculating the sensible items and it presents some experimental-obtained conditions required to obtain high linearity. There is also presented the automated hydraulic testing system of these transducers considering that the measuring range of force is 10 kN ... 630 kN.

1. Introduction

In the last 10-15 years the hydraulic and pneumatic equipment became wide-spread in the industry and the trend is to grow even more and to replace another type of systems (e.g. electrical and mechanical ones). This trend is due to their great advantages – sturdiness and adaptability to a wide range of working conditions, high level forces and torque obtained with relatively low cost

prices and, most of all, the integrability in complex automation systems. Using the proportional elements' techniques and electronically controlled servo- devices, the hydraulic systems can be integrated in computer-controlled automation systems with high precision, excellent response time and smaller dimensions, making them unbeatable in industrial control and robotics. A typical example is represented by the hydraulic servocylinders. The compact actuator-type variant (which includes the cylinder, the servovalve, the position transducer and the electronic regulator) is quite used in mass production by several companies. This solution is based on electrical position feedback and represents the typical mechatronic subsystem. Basically, electric feedback represents an automated system for position adjusting that becomes able to realise a strictly controlled translation displacement using a specific transducer and an electronic regulator. In many cases it is necessary to control also the realised force by introducing a supplementary electrical feedback that uses a force transducer. In some cases it is necessary to be able to measure the pressure difference between the servocylinder's chambers, the acceleration or the velocity, so there are needed specific transducers for these mechanic variables. On the other hand, due to the trend of miniaturisation, the electronic blocks for conditioning the transducers signals are integrated in transducers bodies and this is the way to obtain integrated electronics transducers which offer the big advantage of a high level immunity to electro-magnetic interference (because the output signal is a current and not a voltage).

Considering these concepts, The Research Institute for Hydraulics and Pneumatics (IHP) has started some years ago the design of a full range of sensors with integrated electronics that are used in hydraulic and pneumatic systems. At this time we have pressure transducers till 500 bars, 200 bars differential pressure transducers, 400 mm linear displacement transducers, 5000 RPM rotation transducers, 100 kN force transducers and, in the future, 200 Nm torque transducers. As a common aspect of these transducers, all of them are made with variable reluctance inductive sensors. The advantage of this kind of sensors is their high sensibility, the fact that movable core is also the elastic item and it's not necessary to be in mechanical contact with it.

The present paper describes the 100 kN inductive force transducer, designed and made by the authors in order to use it in hydraulic installations of a stress/vibrations testing machine.

2. Theoretical aspects

Force transducer made at IHP contains elastically diaphragm and variable reluctance displacement sensor. This type of transducer has three sensible items:

- one circular elastic clamped diaphragm made from stainless steel; the measured force is applied to the centre of diaphragm
- the measuring sensor represented by a 14 millimetres diameter ferroxcube potcore placed in front of the diaphragm with an initial gap δ_0
- the reference sensor, identically with the measurement one, but placed in its behind; the magnetic circuit is closed through a stainless steel armature; there is also an adjustable gap for the symmetry of the two sensors.

The main problem is the correct expression of mechanical condition of the diaphragm from the point of view of elasticity theory.

For the elastically diaphragm loaded with a concentrated force, it is recommended to use following calculation formulas:

- for equivalent unit stress calculation:

$$\sigma_e = K \times F / h^2 \quad (1)$$
- for centred deflection of the diaphragm:

$$x_0 = K_1 \times F R^2 / E h^3 \quad (2)$$

where F – central force, E – elastic modulus of the diaphragm's steel, h – diaphragm's thickness, R – diaphragm's outer radius, K and K_1 – R/r_0 ratio depending coefficients, where r_0 is a radius of the central coupling bolt.

The calculation's premises must to foresee the realisation dimension's size with covered domain 10...630 kN using a unitary construction and a commune

electronics. For industrial development it used the solution in which diaphragm's radius and R/r_0 ratio is choosing in three steps and diaphragm's thickness is choosing in depending of load F and radius R .

The transducer presenting in this paper is of thick diaphragm type which has the ratio $x_{\max}/h \leq 0,2$. For this ratio range, the relation (2) is linear.

The changes of diaphragm's central deflection cause the increase or decrease of the sensor's gap and therefore of the inductance value, according to formula:

$$L = \frac{N^2}{\frac{l_m}{\mu_0 \mu_r S_{Fe}} + 2 \frac{\delta_0 \pm x_0}{\mu_0 S_a}} \quad (3)$$

where L – sensor's inductance, N – number of the spool wire, l_m – magnetically circuit's length, S_{Fe} and S_a magnetically field areas, μ_0 and μ_r – magnetically permeability for air and magnetically core, δ_0 – initial air-gap and x_0 – diaphragm's central deflection. For reducing of the errors, it is used a reference sensor. For simplicity it considers equal both areas S_{Fe} and S_a , both initial air-gap, too and consider $l_m / \mu_r \ll \delta_0$. The inductance of the measure sensor can be calculated with formula:

$$L(x_0) = L_0 \frac{1}{1 \pm \frac{x_0}{\delta_0}} \cong L_0 \left(1 \mp \frac{x_0}{\delta_0 \pm x_0} \right) \quad (4)$$

where L_0 is the initial inductance value.

If the two inductive sensors are half-bridged connected and supplied with a sinus voltage with ω_0 frequency and U_0 amplitude and we neglect the ohmic resistance of the coil, then span voltage can be calculated with formula:

$$\Delta U = U_0 \frac{\Delta z}{2z_0} \cong U_0 \frac{\Delta L}{2L_0} \cong \pm U_0 \frac{x_0}{\delta_0 \pm x_0} \quad (5)$$

With a view to obtain a satisfactory linearity, it was necessary to take the some steps: it choose an initial air-gap $\delta_0 \gg x_{\max}$, a ferromagnetic material with high value of μ_r , and a high excitation frequency to obtain $\omega_0 L_0 \gg r_0$ thus is possible to linearize equation (5). Because x_0 is proportional to force, the bridge output voltage is proportional to force, too. The measurement system assure a conversion linearity better as 1%.

3. Construction

The force transducer consist in circular clamped diaphragm made from stainless steel with a central coupling bolt to apply the measured force.

The diaphragm is mounted on the cylindrical undeformable body (fig. 1). This transducer's body contain the two sensors placed in front of centre of diaphragm. An aluminium box fixed on the transducer's body, contain the electronic module for measurement conversion and the output connector.

The more constructive problems must was resolved

- choose of diaphragm's steel
- realisation of rigidity of diaphragm's mounting
- realisation mounting of the central coupling bolt
- fixing of the diaphragm's dimensional tolerances
- fixing of the initial value of the air-gape to obtain a best linearity

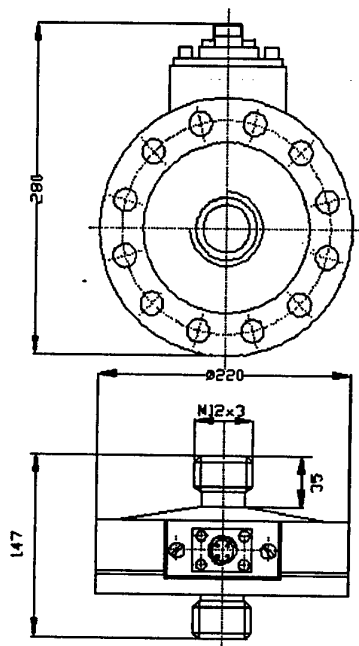


Figure 1. Force transducer

4. Electrical structure

The functional block diagram of the electronic amplifier of the force transducer is given in Fig. 2. The electronic module is realised on a 42X52 millimetres PCB and contains one quadrature oscillator, achieved with two operational amplifiers, providing a very stabile 5 Vrms at 5 KHz sinus signal for the measuring bridge. A cosines signal from second output of the oscillator is passed through two-transistors zero-crossing detector then differentiated by the third transistor, thus obtaining pulses required by a sample and hold circuit made by a FET and a capacitor. The sample pulses are situated on the peak of the sinus signal. The output measure bridge voltage is

amplified by a third operational amplifier and nonlinearities compensated. A fourth operational amplifier is configured as an active low-pass filter and provide to output connector a voltage in the range $-10V \dots +10V$ (unified signal). The four operational amplifiers are integrated in the same chip LM324 which allows a small size PCB. It is possible a zero adjust and an amplifier gain adjust for calibration of the transducer; after calibration the transducer is sealed. The output stage can be eventually configured as current generator in order to obtain an current-unified ($4 \dots 20$ mA) output signal. Power supplies are $+15V$ and $-15V$ stabilized.

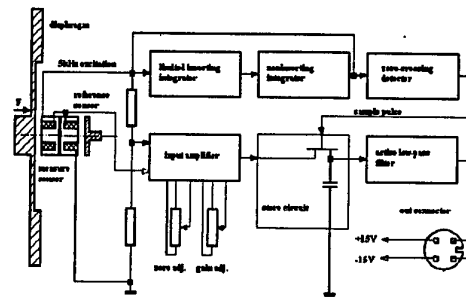


Figure 2. Transducer bloc diagram

In Fig.3 is shown the PCB of the module, componentlayer. The transducer has an output 4 pins circular connector for a 3 wire shielded cable.

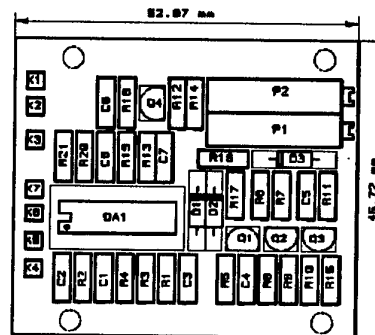


Figure 3. Printed circuit board

5. Experimental works

Force transducer made by IHP was tested in a calibrating stand in conjunction with a high precision reference transducer. Calibrating curve was obtained using a modern data acquisition system. The block

schematics of the hydraulic testing system is shown in Fig.4.

The calibrating stand contains a hydraulic servocylinder with automatic control of both displacement and force. The special electronic control module was also made in our testing laboratory and it can be connected to the stand computer. Using a ramp-type command is possible to obtain on the computer screen the calibrating curve of the transducer as well as the force-deflection curve of the elastic membrane. This last curve allowed us to study the behaviour of different types of membranes in order to achieve optimal solution and to find initial gap between sensor and membrane for optimal global linearity of transducer.

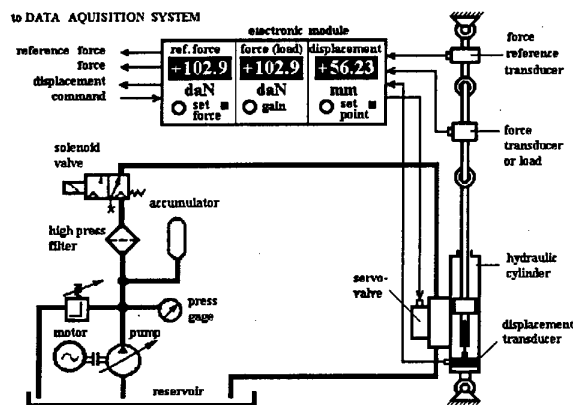


Figure 4. Test stand schematic

The process computer of the stand has a DAS1701AO data acquisition board from Keithley. Using TestPoint software package there were developed virtual instruments for calculating the mentioned curves. In Fig.5 is shown the virtual instrument for calculating calibrating curve of force transducer.

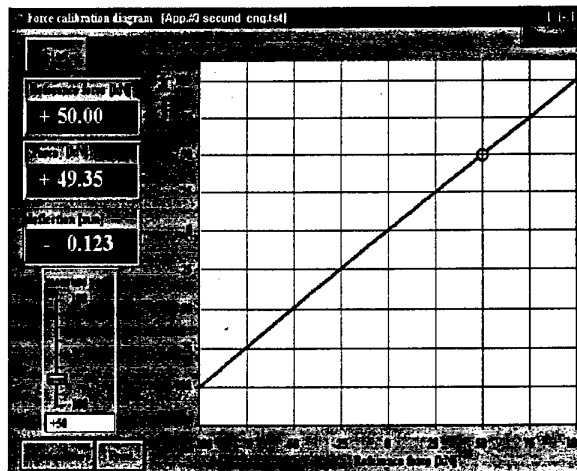


Figure 5. Calibration diagram

6. Conclusions

The experiments on the test stand proved that this type of transducer has high sensibility, linearity (global linearity under 1%) and reliability and very good dynamic behaviour, despite its constructive simplicity and its low cost .One big advantage of this device is the presence of conversion electronics into the body of the transducer, which means high noise immunity. In the future the electronics will be completed with a microprocessor subsystem in order to increase precision and linearity of the transducer, as well as to use a serial communication bus.

References

- [1] G.Ionescu,R.Dobrescu,...Traductoare pentru automatizari industriale, vol I,Editura Tehnica, Bucuresti 1985, p.181-183
- [2] M.Ciugudean,V.Tiponut...Circuite integrate liniare. Aplicatii, Editura Facla,Timisoara 1986, p.71-75
- [3] M.Bodea,I.Mihut...Aparate electronice pentru masurare si control, Editura Didactica si Pedagogica, Bucuresti 1986, p.167-170
- [4] Merritt, H. Hydraulic Control Systems, John Wiley and Sons 1967
- [5] Petrin Drumea, Paul Svasta, Mircea Comes, Ciprian Ionescu, Adrian Mirea, Ionică Cristea. Differential inductive pressure transducer with built-in signal conditioning circuit, MTM Symposium Lvov, Ukraine 1998
- [6] Petrin Drumea, Mircea Comes, Marian Blejan, Adrian Mirea, Paul M.Svasta, Pressure inductive transducer with built-in signal conditioning circuit, XXII IMAPS-POLAND Conference and Exhibition, Zakopane, October 1-3, 1998

Design of an Electro Pneumatic Micro Robot for In Pipe Inspection

Cédric Anthierens, Maurice Bétemps
Laboratoire d'Automatique Industrielle
INSA of Lyon

20, avenue Albert Einstein
69621 Villeurbanne Cedex

cedric.anthierens@lai.insa-lyon.fr / maurice.betemps@lai.insa-lyon.fr

Abstract

This paper presents the different phases from the design of an in pipe micro robot to its implementation. The mechanical part designed in order to satisfy several criteria of performances is detailed. In a second time the modelling and identification of each parameter have been done, simulated and compared to experimental results. Finally the control law of the robot is investigated to optimise the positioning accuracy and the carried load. Perspectives are given to improve the task of the in pipe locomotion by reducing the size of the robot for example.

1. Introduction

Micro robotics is now a growing field which has been pushed ahead by the developments of microelectronics over the last few years. Micro machining such as chemical etching has been a starting point for novel technologies such as micro stereo lithography or LIGA with those very small pieces (few tens of microns) can be machined very accurately.

In the same time, smart materials have been discovered and developed in order to realise many micro actuators and micro sensors.

The miniaturisation of macroscopic robots allows the realisation of micro tasks. Most of applications are based on the manipulation, the locomotion or the handling of tools.

Domains most interested by these micro tasks are medicine, defence, biologic and nuclear.

Micro systems closed than micro robots are widely used in medicine for endoscopy for example. Micro robots designed as ants or flies are studied in order to watch over a hostile land. Such systems need to communicate with each other and take a decision according to several cases. Micromanipulation is an important domain of investigation, because micro robots are useful to assembly other micro systems such as micro motor or else. This research can lead to the creation of

whole micro workshops. For genetic or biologic applications it is required to catch, transport and set down very small organic pieces.

It remains a specific task that is the locomotion in restraint environment. Our investigations specially concern the in-pipe locomotion. Many applications of maintenance such as those of pipelines, canalisation, or nuclear generators of power plant or submarine are targeted. We chose to study the general case of nuclear generator pipes.

2. In Pipe Micro Robot

Many researches are leaded to accomplish an in pipe micro robot. Several micro robots based on a piezoelectric have been designed for in pipe locomotion.

Matsuoka has designed a robot that has 3 legs passive legs always in contact with the pipe side [2]. Its piezoelectric actuator is placed in the body of the robot. It constitutes the only link between legs and a fore mass. This mass is actually a micro sensor. Then the robot moves forward by doing a slow stretching of piezoelectric actuator and a quick contraction hence legs stick and slip on the pipe side. The advantages of this technology are its small size (pipe is 10 mm in diameter), its velocity that can reach 5 cm/s and this system can move reward.

Another kind of micro robot is developed in the French Japanese laboratory LIMMS or in LMA by Minotti. The micro robot has many active legs that push against the pipe side according one direction. The performances of this robot are closed to the precedent one. Piezoelectric actuators usually need a high voltage of supply but can be controlled with high frequency.

Actuators based on the Shape Memory Alloy are very used for in-pipe micro robotic. Indeed two French laboratories work on this technology. In order to inspect rectilinear pipe of 10 to 15 mm in diameter, the inchworm motion seems to be the movement the most suitable. Touaiba has designed an inchworm micro robot that is constituted by a stretching actuator in the body placed

between two parts with legs [1]. The main actuator creates a step and legs are pushed against the pipe sides to assure the support. Actuators are linear and based on a spring of a Shape Memory Alloy (SMA) that can be stressed and stretched according to the temperature of the wire.

Each actuator is controlled by direct current supplied through the SMA wire. To accelerate SMA to reach their initial position, each actuator works in opposite or against a natural spring.

According to another principle, Libersa has designed an inch worm micro robot composed by five modules as a train [8]. Each module is able to push against the pipe side to support the body or to be expanded to create a small motion forward. Each module is successively excited that create a wave hence contact point against the pipe moves forward as a snake.

A module is actuated by SMA wires that deform a passive flexible square structure that is pre-stressed. In this case the displacement create by actuator is amplified by the mechanical structure and each wire works in opposite with another one.

Such actuators are very interesting for micro robotic because they have a good power to weigh ratio and they can be machined with the desired shape. SMA provide very large displacement contrary to piezoelectric. However their main inconvenient is their control where it is quite easy to heat the wire to control its shape but it is more difficult to cold it. This is why they have a long response time.

The last main technology employed for in pipe micro robotics is fluidic. Indeed the pneumatic power can provide high force. For this reason several actuators have been designed to profit of this characteristic.

In the macroscopic world, artificial muscles exemplify an interesting kind of actuator [3]. Indeed such actuators provide a stretching motion when they are supplied by pneumatic pressure. As real muscles, the actuator is inflated hence its section is growing while its length is decreasing. When these actuators are mounted in parallel structure and work in opposite each other, they can supply linear displacement in their main axis and rotation movement around several axis. This characteristic is enable because whole actuator is compliant. This actuator could be used to actuate micro robot arm where each joint can create several rotations.

The Flexible Micro Actuator (FMA) is shaped like a finger [4]. 3 long chambers that can be independently supplied by pneumatic pressure compose its section. When the 3 chambers are excited in the same time the actuator is stretched, in any other cases it is bending in a direction of the chamber that is the least supplied in pressure.

A repeating sequence of the different movement provides an elliptic displacement of the tip of the actuator. Hence it can reproduce the movement of a foot on the ground. This actuator has been miniaturised to realise an

in pipe robot with 5 legs by section in contact with the pipe side. It is composed by twenty legs.

Main advantages of this actuator are the compliance, its various motion and the available force. Its main inconvenient is the supply of the pneumatic pressure that involves a servo valve and a supply pipe for each chamber that requires space.

The last kind of actuator employed for micro robotics is bellows. An in pipe micro robot has been designed by KATO [5] to inspect pipes of 18 mm diameter. It is composed of five rubber bellows independently driven and it is based on the same principle of locomotion as snake detailed above. It reaches 77 mm/s in velocity but its support being assumed by the stick slip motion of the bellows it can not push or pull a mass higher than 200 g.

An inchworm micro robot was conceived with three metal bellows actuators [6]. It moves in circular section 25 mm in diameter and can cross a junction in Y. Its module of elongation is carried out by a system with pulley actuated by two metal bellows. Both modules of blocking ensure the contact against the walls. The robot progresses to 1 mm/s approximately.

According to many implementations developed in our laboratory we have chosen the metal bellows to create an actuator for the in pipe locomotion [7]. Indeed every robot actuated by this technology has allowed to control accurately a position or the available force. It is why a XY table conceived in LAI has been able to create displacement with accuracy better than 2 microns. In another case the metal bellows actuator have been used to control the compliance of a robot arm.

3. Design

The main constraint is the very confined environment ; this is why it must be precisely characterised.

In our case the pipe is rectilinear and has a constant circular cross section of 18 mm of diameter. The actual material of the pipe is steel but for our experimentation we used a transparent pipe made of PVC that allows observing of each motion of the robot.

Finally we chose to study the worst case where the pipe is vertical and the robot has to move up.

An inchworm micro robot is composed by 2 blocking modules that assume the support of the body and one stretching actuator that creates the step displacement (fig.1). The fore blocking module is actuated by micro motor that drives a screw / nut system to brace three legs against the pipe sides. The rear blocking module makes moving 3 legs made as pistons that are actuated by air pressure [7].

The main actuator is composed with metal bellows. It acts like a pneumatic jack except it has no joint between the rod and the cylinder. Such technology limits

the friction that involves a more accurate positioning. In this case contrary to Yoshida's micro robot, we chose to supply pressure out side of the metal bellows. This is the reason why a solid cylinder machined from a bulk of Aluminium is placed around the bellows to carry out the chamber. This characteristic makes that bellows always work in stressed way. Hence that allows to ensure a longer life of the metal bellows and a constant stiffness.

The displacement of the rod represents a step. Inchworm movement is a succession of such steps. A Hall effect sensor has been placed on the back of the cylinder in front of a magnet glued on the rod back. This allows to measure the magnitude of displacement and so the step length.

The general design has shown few difficulties to obtain wanted performances. The most important is the pneumatic and electric power supply. Indeed the robot is supplied by air pressure through 2 different pipes that involves a good airtightness between both chambers (rear blocking module and stretching actuator). The micro motor needs to be supplied with current ; this is why the 3 mm diameter rod has been drilled end to end to allow the insertion of a wire from the back to the head of the robot. Thus this wire is placed through the chamber of the main actuator where it is necessary to avoid leakage. The problem is the same with the 3 wires of the effect Hall sensor.

Note that the robot has been built with standard materials and components then it is relatively cheap.

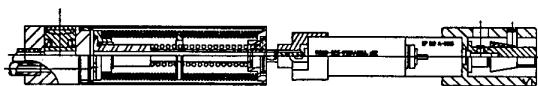


Figure 1. Drawing of the micro robot

4. Design calculations

Design of a complex system such as a micro robot needs to follow several courses. Indeed the most important criterion is the small size because the pipe imposes its internal diameter. Power available to carry heavy loads has been chosen as second characteristic. Accuracy of positioning is placed at the same level of priority. Velocity appears as the last performance required. Many studies work at the opposite. Classification of criteria is very important for the design of complex systems to optimise the device.

4.1. Stretching actuator

In our case the bellows have been chosen according to the supply pressure, the stroke and the stiffness. Stiffness must be high enough to move up the rear mass with tubes and wires. Then bellows must be shorter as possible to be stiff while knowing the stroke is

proportional to the length. The solution held is to place an added spring in parallel of bellows to ensure a strong stiffness. Thus bellows could be very flexible and not too long to provide large step. Note that pressure is high to stress bellows that have to be enough resistant. The length of the robot and the step size depend of loads that it can pull up.

4.2. Rear blocking module

This part has to support the whole mass of the robot plus carried loads. It depends on supply pressure, cross section of piston and friction between tip of legs and pipe sides. The small diameter of pistons (legs) involves once more supplying under high pressure.

4.3. Fore blocking part

It has the same function as the rear blocking part described above. The micro motor and its speed reducer have been chosen firstly for their diameter, secondly for the maximal torque supplied during a short time. Indeed the high reducing ratio plus the screw / nut system make the device irreversible. Then the motor is not supplied while legs are braced against pipe sides. Strength provided at contacts is therefore function of screw characteristics (diameter, thread, screw angle) and inclination of guides on the nut. This device is used in all or nothing. Length of this module depends on the whole mass transported.

4.4. Hall effect Sensor

This sensor estimates the distance between the rod and the cylinder back - i.e. position of the rod - by measuring the magnitude of the magnetic field. Indeed this field is provided by the magnet glued on the rod back.

The magnitude of magnetic field measured is decreasing when distance between magnet and sensor is growing. We searched to obtain a significant signal with a good resolution along the whole stroke of the rod. That depends on the magnetisation or size of magnet and the initial distance to sensor. The sensitiveness of the Hall effect sensor reaches 1 micrometer but according to its characteristic modelled it can ensure measures reliable with an error less than 7 micrometers.

5. Modelling and identification

5.1 Mechanical identification

This work has been done in two times where we firstly have estimated the parameters of the mobile part and secondly the pneumatic part - i.e. the servo valve and the supply pipe to the robot.

The other modules that actuate the legs are not detailed in this paper because they function on all or nothing basis. They have been designed to brace legs against the pipe side in order to support a heavy mass that involves choosing a high power motor and a supply pressure of 20 bars.

The figures 2 and 3 show a rising step and a falling step. The robot is controlled in opened loop. The bold line represents implemented points whereas the continuous line represents simulated points.

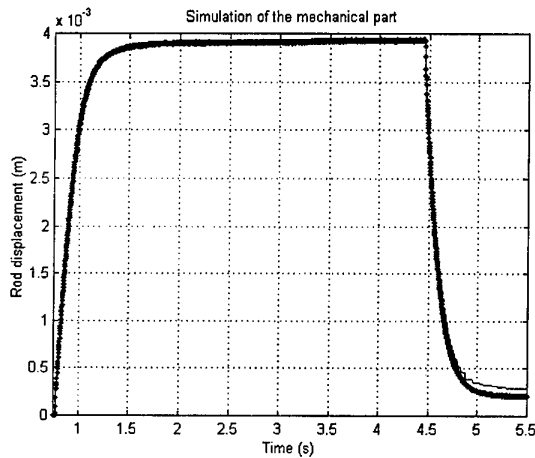


Fig.2. Simulation of the whole mechanical part In opened loop

This implementation can verify the accurate estimation of the moving mass (whole the fore blocking part with legs), the stiffness of the metal bellows actuator (metal bellows plus the added spring), the viscous friction coefficient, and the friction force certainly du to the guidance of the rod.

As these characteristics are known those of the pneumatic part can be identified. The figure 4 illustrates the difference between the modelling and the real process. This graphic confirms a good identification of the gain of flow (K_v) and the gain of pressure (K_p) of the servo valve. The gap between simulated points and implemented points is certainly du to the characteristic linearised of the servo valve.

5.2 Modelling of the whole process

This part has been designed to be very stiff to allow the pulling up of a heavy rear mass. Supply pressure is controlled in order to allow the pushing up of the fore mass with accurate positioning. This relation gives dynamic behaviour :

$$M_s \frac{d^2 x}{dt^2} + b \frac{dx}{dt} + k_e (x - x_0) = S(P - P_{atm}) - M_s g - f$$

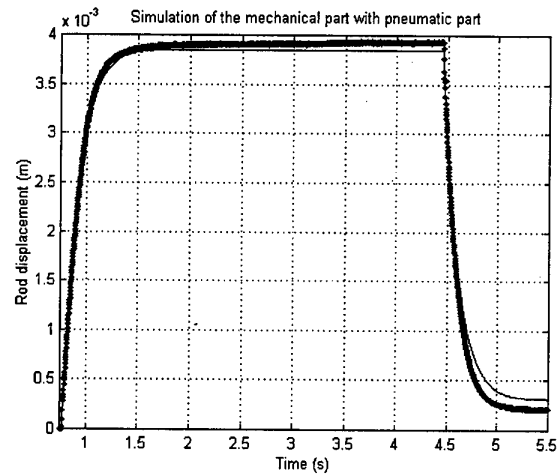


Fig.3. Simulation of the mobile part in opened loop

Where :

- x_0 : initial rod position,
- x : actual rod position,
- S : bellows section,
- P_{atm} : atmospheric pressure,
- P : internal pressure,
- M_s : mass in translation,
- b : viscous friction,
- k_e : equivalent stiffness,
- f : friction.

Metal bellows actuators do not use joint to guide the rod contrary to classical jack then friction is very limited. Pneumatic behaviour is given by the relation based on the mass conservation given below :

$$\frac{dM}{dt} = \frac{V}{rT} \frac{dP}{dt} + \frac{dx}{dt} \frac{SP}{rT}$$

Where :

- $\frac{dM}{dt}$: input massic flow,
- T : temperature,
- γ : specific heat ratio,
- r : air constant,
- V : chamber volume.

As the system is adiabatic and the variations of temperature are very low, model can be linearised at an equilibrium point. Thus it can be represented as a closed loop block diagram drawn below (fig 5).

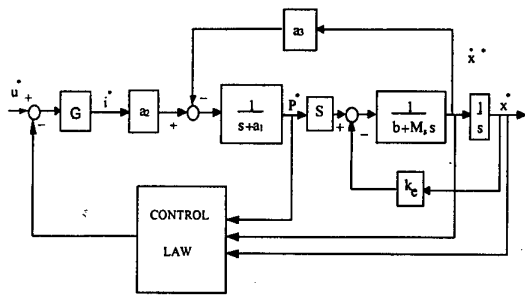


Figure 4. Block diagram of the stretching actuator

Notations :

$$a_1 = \frac{K_p r T \gamma}{V_0} \quad a_2 = \frac{K_v r T \gamma}{V_0} \quad a_3 = \frac{\gamma S P_0}{V_0}$$

6. Implementation and performances

Our device is currently controlled by D-Space environment that uses Matlab and Simulink software. Firstly the micro robot has been tested to realise displacement stairs shaped. During this task the control law employed is a simple PID correction. The figures 5 shows the gap between the simulated lines and experimental points. The figure 6 is a zoom where the line with stars is implemented points and continuous line is the simulated result. This small gap confirms us the good modelling of each part of our device.

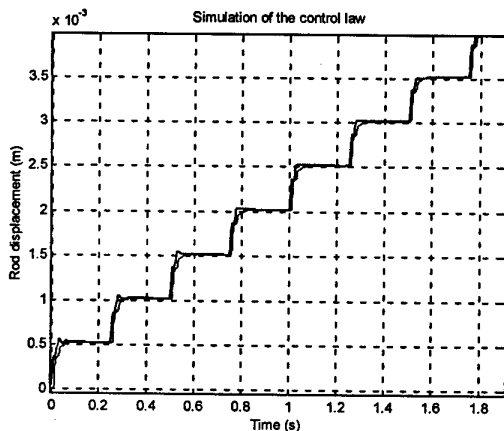


Figure 5. Comparison of the modelling to experimental results in closed loop

After the validation of our whole modelling a control law has been established. Firstly we have chosen to optimise the positioning accurate of the robot in the pipe. The matching of gains of the corrector has allowed reaching a very good positioning accuracy on every step better than 3 micrometers. According to the reliability of

the Hall effect sensor, error of positioning can not exceed 10 micrometers.

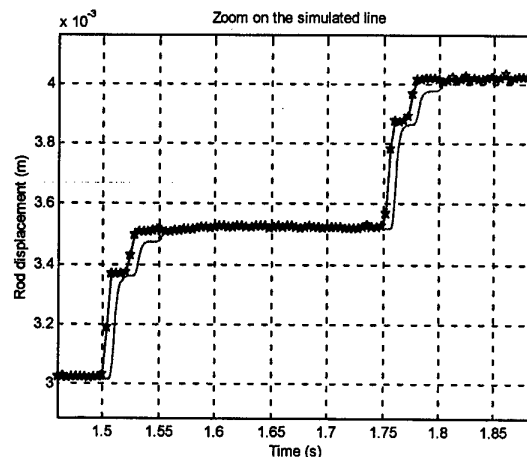


Figure 6. Zoom of the figure 5

The micro robot realises 8 steps of 0.5 mm in size before one change of supports. Currently a step is done each 0.25 seconds but the figure 5 shows that the very short response time of our device could allow to move up very faster while keeping the good positioning accuracy.

Changes of support constitute the most serious problem that limits the global positioning accuracy. Indeed with a low load carried (less than 1 kg) the supports can't slip along the pipe sides but during the change of supports the rod can change a bit of orientation (few degrees around a vertical line). This phenomenon can involve disturbances in measurement of the position of the rod. This is the reason why we currently obtain a 0.5 % error of positioning during a course 80 mm long.

The locomotion can be faster than the precedent one. Indeed the micro robot can move up quickly by creating only steps of 4 mm size. By this way the velocity exceeds 5 mm/s without added load. At this moment this criteria is optimised by the improving of a states feedback control law.

According to the pipe material hence its friction coefficient with legs, the robot is able to support added loads higher than 2 kg without observing a slipping displacement at the contact points. The main actuator has pushed a load of 5 kg while ensuring the positioning accuracy better than 10 micrometers. Obviously the response time is increasing in this case.

The robot can pulled an added load but the efficiency of the stroke is decreased if the metal bellows actuator is not enough stiff. The moving up of the rear part is only assumed by the general stiffness. The design of the robot has foreseen this case ; this is why it is able to replace the added spring by a stronger one and to supply pneumatic pressure up to 20 bars.

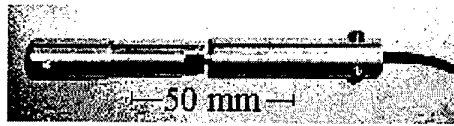


Figure 7. Picture of the micro robot

7. Conclusions and perspectives

A robot for in-pipe locomotion has been designed to move up vertical pipes of 18 mm diameter (locomotion is able in pipe from 16 mm to 20 mm in diameter). Its main advantage is to carry heavy loads higher than 2 kg with an accurate positioning. Modelling of each part (actuators, sensors) has been carried out and implemented results have been compared with behaviour simulated.

Now the control law using states feed back is implemented to control the positioning of the robot in the pipe and to avoid disturbances due to the delay of pressure along the supply pipe.

Behaviours of the micro robot will be still investigated with different conditions (load, velocity...). Another prototype has been designed to realise the same task. This industrial project is shorter (about 80 mm length) than the current one because the fore blocking module is composed with a micro motor of 3 mm diameter. When it will be machined, it will test as the same way as the current robot.

8. References

- [1] Touaibia M., Chaillet N., Bourjault N., "In-Pipe Microrobot System based on Shape Memory Alloy Actuators", *4th Japan-France Congress and 2nd Asia-Europe Congress on Mechatronics*, Fukuoka, 1998, pp 272-7.
- [2] Matsuoka T., Asano M., Mitsuishi S., Nagashima K., Matsui T., "Improvement of Micro Mobile Machine with Piezoelectric Driving Force Actuator", *6th International Symposium on Micro Machine & Human Science*, Nagoya, 1995, pp 211-217.
- [3] B. Tondu and P. Lopez, "Theory of McKibben Muscle : A pneumatic artificial muscle contracting like skeletal muscle", *2nd Japan-France congress on Mechatronics*, Takamatsu, Japan, pp.288-291 (1994).
- [4] Suzumori K., Koga A., Kondo F., Haneda R., "Integrated flexible microactuator systems", *Robotica*, 1996, Vol. 14, pp 493-498.
- [5] Kato, S., Hirayama, T., "Fabrication of a high speed in-pipe mobile micromachine", *4th Japan-France Congress and 2nd Asia-Europe Congress on Mechatronics*, Fukuoka, 1998, pp 429-32.
- [6] Yoshida K., Mawatari H., Yokota S., "An in-pipe mobile micromachine using fluid power traversable branched pipes", *3rd Japan Hydraulics & Pneumatics Society, International Symposium on Fluid Power*, Yokohama, 1996, pp 229-234.
- [7] Anthierens C., Prelle C., Jutard A., Betemps M., "Pneumatic Actuated Microrobot for In-pipe Locomotion", *4th Japan-France Congress and 2nd Asia-Europe Congress on Mechatronics*, Fukuoka, 1998, pp 433-6.
- [8] Libersa, C., Arsicault, M., Lallemand, J.P., Zeghloul, S., "Design study and development of a two -stable equilibrium states SMA-actuated deformable structure. A microrobotics example of application", *4th Japan-France Congress and 2nd Asia-Europe Congress on Mechatronics*, Fukuoka, 1998, pp 478-83.

FLEXIBLE STRATEGY AND THEORY FOR IDENTIFICATION WITH HYBRID ADAPTATION APPLICATION TO MOBILE ROBOTICS

AMAR KHOUKHI

*Institut d'Informatique USTHB, BP32 El-Alia Bab-Ezzouar Alger Algeria
And ESIEE group, 2 Bd Blaise Pascal Cité descartes 93160 Noisy le Grand France*

Abstract

A stochastic program is developed for adaptive control and identification of industrial mobile robot. Our program is executed at two levels: a stochastic trajectory planner (STP) in the first place then a follower trajectory en-line (FTE) based on the complete stochastic dynamic model of the mobile. The modelization is first done in the deterministic case based on the Lagrangien formalism. This gives the stochastic model of the mobile robot. The mobility of the robot is besides considered; first a static mobility is given. Then we consider a dynamic mobility. After that the mobility is randomized and taken as an output of our dynamic system. Our program is one of identification of the doubly stochastic process of hidden Markov chains minimizing the function of information of Kullback-Leibler. The convergence and the consistence of functions of parameters evaluation as well as simulations on the case of the SARAH robot are given to demonstrate the efficiency of our algorithms

Key words:

Dynamic Navigation, Dynamic Mobility, Information of Kullback-Leibler, Identification and Stochastic Control.

1. Introduction

Until now the mobile robotics knew some important developments on the plan material Hardware, notably, systems of vision. Whereas decision level of intelligence and command is reduced to an assessment from the geometric or kinematics models of the mobile generating an organized trajectory of right lines or corn spiral connections. [1], [2], [3] and where the curvature or the acceleration is taken like command. One perceives while the dynamic effects as inertia and mass and various disruptions can not be neglected, that is wished for the high performances.

In [4] the authors had developed a deterministic dynamic model based on the principle of Lagrange-Euler. We follow-up here of a stochastic dynamic model. An original contribution of the present work is the quantification of the mobility and capacity of

maneuverability of the robotics system. Indeed a static mobility function has been considered in [10]. However such a function of mobility is valid only in the case of the stationary robots or manipulators. In the second section one will develop deterministic and stochastic dynamic models of the mobile. In the third section the first level of the stochastic strategy for identification and command is developed. An Iterative Global Algorithm (IGA) based on the minimization of the function of Kullback-Leibler information of processes of doubly stochastic hidden Markovs is considered. This algorithm has been applied to the identification of parameters meaning the various disruptions, notably the variance of the white additive gaussian noise representing uncertainties of measures. This algorithm has been applied with success to ecology [5], to the speech recognition [6][7], to the pictures Markovien models [8], to the numeric communications [9] and in short to robot manipulators [10]. In the fourth section, we will develop the application of an algorithm of recursive identification of parameters and adaptive control (IRCA) to the mobile robots. This algorithm is a truncation of Birkoff ergodic theorem. The interest carried by the application of this strategy to the case of the mobile robots SARAH type. Convergence analysis based on martingal proprieties is followed by developing a new model, new space and new probability measure. We noted the fast convergence of parameters identified and the optimality in precision in the scheduling by IGA and the pursuit by IRCA of the trajectory. The SARAH robot being the robot developed by the unit Genius Advanced Robotics of the atomic energies center Paris [12].

2. Dynamic model of the mobile

The mobile is assimilated to a parallelepiped. The long of the present work will be referred that it is the body of the robot. The wheels of the robot are assimilated to two identical cylinders. Let's consider the following notation (see figures 1, 2)

(a, b, h) Lengths of the axis, and height of the robot respectively.

(r, e) The radius and the thickness of the wheel

(O, X, Y, Z) The axis 3D that origin is at the center of gravity of the robot

O_1 Center of the right wheel

O_2 Center of the left wheel

I_1 and I_2 points of wheel contact with the ground

ω Angular speed of the wheel around the Z axis

V Linear speed of the center of gravity of the robot

V_1 Linear speed of the right wheel

V_2 Linear speed of the left wheel

ω_1 Angular speed of the right wheel

ω_2 Angular speed of the left wheel

2.1 Deterministic model

$$X_{i+1} = X_i + h_i v_i \cos(\theta_i)$$

$$Y_{i+1} = Y_i + h_i v_i \sin(\theta_i)$$

$$\theta_{i+1} = \theta_i + h_i \theta_i$$

$$V_{i+1} = V_i + \frac{h_i}{rM} (C_{1i} + C_{2i})$$

3. Mobility:

The static and dynamic mobilities are defined in the previous articles [10], [13].

Let's recall however their characterizations. Indeed, the static mobility is expressed:

$$M(r) = K \int_0^{2\pi} \left(\frac{r(t)}{r_0(t)} - 1 \right)^n dt$$

The dynamic mobility is :

$$M(r) = K \int_0^{2\pi} P(r, v, \theta, w) \left(\frac{r(t)}{r_0(t)} - 1 \right)^n dt$$

$$P(r, v, \theta, w) = \sqrt{a^2 h_1(t, v) \cos^2 t + b^2 h_2(t, w) \sin^2 t}$$

With

$$t = \arctg\left(\frac{a}{b} \operatorname{tg} \alpha\right)$$

$$\text{And } \alpha = \lambda + \frac{w}{w_{\max}} \frac{\pi}{2}$$

If

$$v \neq 0 \quad h_1(t, v) = h_1(t, w) = 1$$

$$A = b = r(t)$$

If

$$v \neq 0 \quad h_1(t, v) = \frac{1}{3} \operatorname{for} [t\pi(1 - \operatorname{sgn}(v))] > \frac{\pi}{2}$$

$$h_1(t, v) = 1 - \frac{1}{3} \frac{4}{3\pi} [t\pi(1 - \operatorname{sgn}(v))]$$

Elsewhere

3.1 Stochastic mobility

A quantification of the mobility as uncertain variable becomes necessary as we have inherent unavoidable disruptions because of to the intrinsic and extrinsic working space of the mobile.

The intrinsic disruptions are owed to the robot because of proper deteriorations of the machine. The extrinsic disruptions are for the main thing owed peripheral system (camera, sensors...) and to the environment in general as obstacles, other robots and targets.

So the continuous stochastic mobility can be defined from the dynamic mobility as follows

$$Ms(r) = Ks \int_0^{2\pi} P(r, v, \theta, w) \left(\frac{r(t)}{r_0(t)} - 1 \right)^n dt + dw_t$$

With the functions, P, r, r_0 , to identify w_t a Brownian movement.

However, the mobile agents are for the main thing systems to discrete evolution, so a discrete treatment of these systems is necessary.

One is going to consider the discrete version of the model of the stochastic mobility of our mobile which will be given as the output of the system.

$$Ms(r)_{i+1} = Ms(r)_i + Ks \sum_{j=1}^1 p_j(r, v, \theta, w)$$

$$\left(\frac{r(j)}{r_0(j)} - 1 \right)^k + p_M w$$

4. Stochastic dynamic model

The stochastic dynamics mobile generalizes the deterministic mobile dynamic of the robot:

$$X_{i+1} = X_i + h_i v_i \cos(\theta_i) + p_X v_i^1$$

$$Y_{i+1} = Y_i + h_i v_i \sin(\theta_i) + p_Y v_i^2$$

$$\theta_{i+1} = \theta_i + h_i \theta_i + p_\theta v_i^3$$

$$V_{i+1} = V_i + \frac{h_i}{rM} (C_{1i} + C_{2i}) + p_V$$

5 - The first level of the program: The Iterative Global Algorithm (IGA):

For $\Lambda = (\rho_X)$ the IGA, one is going to define an extension of the method proposed by Baum [5] based on the utilization of the function of information of Kullback - Leibler that defines a distance between two values of parameters Λ and Λ' . This is function of entropy.
The algorithm for one parameter is the next one

$$\rho_X = \frac{1}{N} \sum_{n=1}^N \sum_{X_n} \sum_{X_{n-1}} \left[\frac{X_n - X_{n-1} - h_{n-1} V_{n-1} \cos \theta_{n-1}}{L(M_1^N, X_{n-1}, X_n / \Lambda)} \right]$$

$$\frac{L(M_1^N, X_{n-1}, X_n / \Lambda)}{\sum_{X_n} \sum_{X_{n-1}} L(M_1^N, X_{n-1}, X_n / \Lambda)}$$

5.2 the control law

Let's suppose given the initial conditions to the state $n+1$ the law of command is given while using the stochastic gradient by:

$$C_1^{n+1} = C_1^n + \gamma_n \sum_{n=1}^N \sum_{V_{n-1}} \sum_{V_n} \frac{(V_n - V_{n-1}) r M}{h_n} - \frac{h_n}{r M} C_2^n$$

6. The second level of the algorithm Recursive Identification and Adaptive Control (RIAC)

The parameter estimation is given for the same parameter by:

$$\rho_{X_{n+1}} = \rho_{X_n} + \delta_n \sum_{X_n} [X_n - X_{n-1} - h_n V_{n-1} \cos \theta_{n-1}]^2 \alpha_{\Lambda_n} (M_1^N, X_n, X_{n-1})$$

7. Convergence of the stochastic evaluation:

7.1. The new model:

In [13], the author defines a new model, new space and new probability measure

7.2 Theorems

7.2.1 Martingales proprieties

Theorem 1 (A. Khoukhi)

one has the following result
Parameters estimated are martingals

Demonstration:

Similar to the one in [13]. One is going to demonstrate that this integral is squares integrables

Theorem 2 (A.Khoukhi)

Under hypothesis adhoc, ρ_{X_n} is square integrable

$\hat{E}((\rho_{X_n})^2)$ is bounded

But the demonstration of this theorem is a direct consequence of the theorem of J.Neuveu[14]

Theorem 5 (Kabanov, Lipser, Shrayer)

Being given (Ω, F) a measurable space with a following of sigma-algebra $F_n, n \geq 0$ $F_n \leq F_{n+1}$ and being given

P_n and \hat{P}_n

Let's suppose $P_n \ll \hat{P}_n$ and let's put

$\alpha = L_n / L_{n-1}$ With $L_n = d\hat{P}_n / dP_n$ Then \ll

$\hat{P}_n \ll P_n$ (absolutely adjoining)

$$\Leftrightarrow \sum_{n=1}^{\infty} E\left(\left(1 - \sqrt{\alpha_n}\right)^2 / F_{n-1}\right) < \infty$$

Theorem 6 (A.khoukhi)

Under hypothesis adhoc the law of probability P relative to the initial model and the relative probability law to the new model are absolutely adjoining

Demonstration: See [13]

Corollaries: The parameters converged under P

8. Control algorithm:

It is a stochastic algorithm of type corrective-predictive. On the one hand a precise model of the robot identified in real time that gives torque to apply to wheels to assure the desirable movement while holding amount of gaussian structure of the noise. It is called command predictive. On the other hand a proportional integrator derivator determined by nonlinear stochastic approximation with adaptive and chosen gain going asymptotically toward zero.

9. results of simulation:

Studies of simulation have been done on the model of the SARAH robot (Autonomous Robot developed by the unit genius robotics Advanced of the CEA for the cleaning of the embankment of the subway of the Parisian Metro RATP) on a Pentium II using the software of automatic Matrixx

We simulated the movement producing the trajectory starting of (0,0) and reaching the target (4,4) (10,10).

This diagram of simulation is done at a time for iterative global algorithm (AIG) and for the algorithm of recursive identification and the adaptive control (IRCA).

10. Efficiency of mobility

We show many cases study of mobility. In fact, we have two important cases: The case of weak mobility where the mobile has a limited workzone. Mainly, in the presence of obstacles and other machines. The second case is the case of strong mobility where the robot has more freedom in the workzone.

11. Conclusions

In this article two strategies of identification and command global iterative and recursive adaptive are presented. We got some more effective results by the strategies IGA, IRCA. A new function stochastic mobility has also been developed. Our mobility is also taken as an output function in identification and control process.

12. References:

- [1]Y. Kanayama, Y. Yuta, J. Lijima, Y. Amabico: "Constrained Intelligent Robot" Proceedings 2NDDL annuals Conference of Robot Society of Japan, Dec. 1984.
- [2]Y. Kanayama, S. Yuta: "Vehicle Path Specification by has sequence of Street Lines" IEEE Conf. Rob of. and Auto. June 1988.
- [3]J. L. Crowley: "Position for Intelligent Mobile Robot" The GMU Robotics Institute Annual Research Review 1984.
- [4]A. Khoukhi, P. Auslin, J. Bermeduz: "Profil cinématique pour la navigation optimale d'un robot mobile industriel" Report Interns ESIEE. June 1987.
- [5]L. E. Baum, J. A. Eagon: "An Inequality with Application to Statistical Prediction Function for Markov Process to Model of Ecology" Bull. Math. Ame. Society. Vol. No. 3. p. 360 - 363. 1967.
- [6]L. R. Robiner, S. E. Levinson M. Soundhi: "On Application of Vector Quantization and Hidden Markov Models to Independent Isolated Words Recognition". Bell System Technical A.T&T Vol. 62. P. 1075-1105, April 1983.
- [7]S. E. Levinson: "Continuously Variable Duration Hidden Markov Models for Automatic Speech Recognition". Compute Speech and Language Vol. 1. pp 29-45. 1986.
- [8]G. Bertrand: "Modèles markoviens d'images". Report Interns Télécom Paris. Juin 1990.
- [9]A. Khoukhi, H. Korezlioglu: "Application des Algorithmes d'identification des Chaines de Markov Cachées aux Communications Numériques". 11eme Symposium GRETSI Nice Juin 1987.
- [10]A. Khoukhi: "Error Compensating and Stochastic Control Manipulators" Cybernetica Vol 4 1998.
- [11]H. J. Wardenke, J. Schuler: "Mobile Robot Applications" Hand Book of Industrial Robot PUT Press 1986.
- [12]A. Khoukhi: "Constrained Dynamic Navigation of has Mobile Robot". Artificial Intelligence and Information Control Systems of Robot 89. I. Plander Editor Elsevier Science Publishers B.V.
- [13]A. Khoukhi: "Sur the Convergence d'un algorithme stochastique" Rapport Interne USTHB Alger 1998.
- [14]J. Neveu: "Martingales à temps discret". Masson 1982.

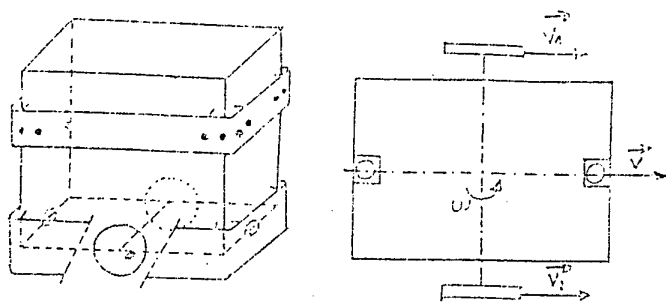


Figure 1 Model of a mobile robot.

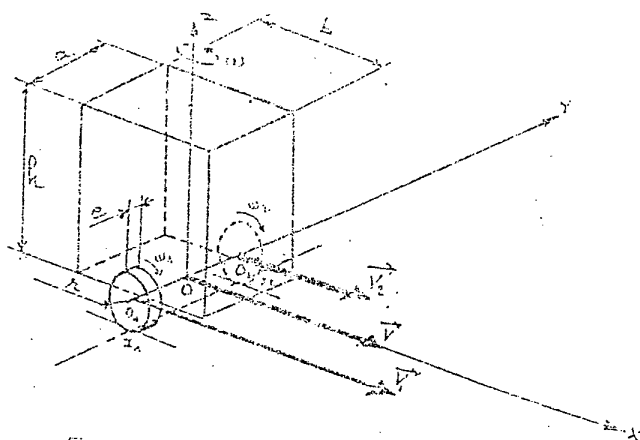
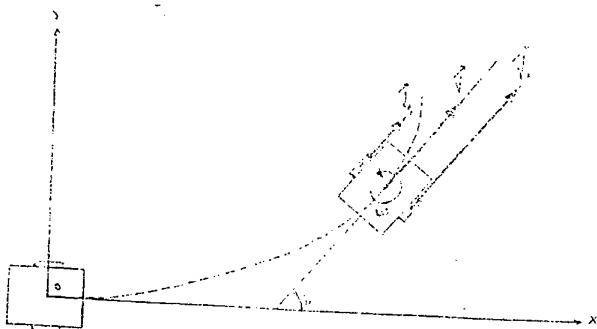


Figure 2 Geometric representation.



Dynamically Stable Control of a Biped Robot

K. Löffler, M. Gienger and F. Pfeiffer

Lehrstuhl B für Mechanik

TU-München, 85747 Garching, Germany

e-mail: loeffler@lbm.mw.tu-muenchen.de

Abstract

The project of a two-legged walking robot is presented. First the mechanical design is described with particular emphasis on the sensors and actuators of the robot. For this system a nonlinear control scheme is proposed that is based on the method of feedback linearization. In order to allow for a "dynamically" stable motion, the reference trajectories are computed so that the system remains controllable throughout the entire gait cycle. In simulations the robot is controlled in a running motion, including phases without ground contact. The simulation results show the good performance of the control strategy in a purely dynamic motion.

1. Introduction

In recent years growing scientific effort has been devoted to the development of two-legged robots that can move similar to human beings. This trend is stimulated by the rapid development of electronics and microcomputing allowing for the implementation of more sophisticated control schemes. In spite of worldwide efforts in the area of human walking, only few machines with acceptable performance have been realized [4, 12, 13]. Still there is no machine that can walk at higher speeds and there is no comprehensive solution to the control problem.

In this paper the principles of dynamically stable walking are discussed and a control strategy for a two legged robot is presented. The control scheme is designed for a biped robot being developed at the TU-Munich.

2. Design of the Robot

The geometry of the robot is based on anthropometric data taken from a male human of the size of 180 cm and a weight of 75 kg [3]. The joint structure (see figure 4) has been chosen to provide the required degrees of

freedom for walking and running on plain and uneven ground. The upper body is connected to the pelvis by a rotational joint. Each hip joint has three degrees of freedom. The knee joint has one degree of freedom, whereas the ankle joint allows two degrees of freedom, pitch and thrust. Furthermore, the arms are connected to the upper body with one active or optional two passive (damped) degrees of freedom, each.

The structure will mainly consist of aluminum, which has particular advantages in terms of the heat conduction and the weight properties. As the weight of the structure itself will be low compared to that of the actuation and the electronics, weight reduction of the actuation has been emphasized.

Therefore, hydraulic, pneumatic and electric drives have been considered. It has been proven that electric actuation has the highest performance-to-weight ratio in the weight region of interest. The good controllability was another reason for choosing electric actuation. The chosen joint components are Neodym-Bor motors with Harmonic Drive gears and ball screws, respectively.

To obtain an optimized design, several iterations have been performed. Figure 1 shows the design of

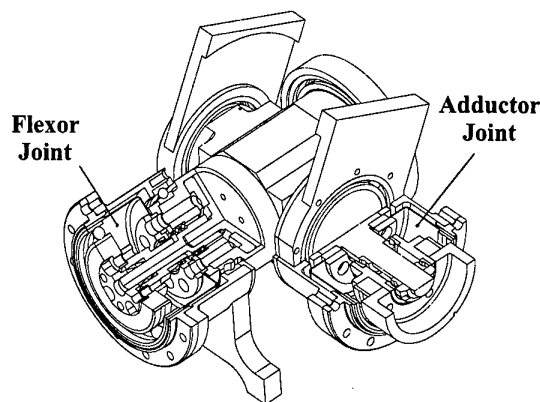


Figure 1: Design of hip joint

the hip joint. The hip contains three active degrees of freedom and has to transmit high torques. The available space is very limited and the demand for integrating three motor - gear - combinations makes it difficult to find an appropriate arrangement. The joint for the internal and external rotation of the shank is integrated in the shank (not shown) and attached to the flexor joint. The adductor joint is actuated by a motor in combination with a toothed belt, which is integrated in the pelvis. The flexor joint and the rotational joint both have a coaxial arrangement of motor and Harmonic Drive gear which is very space efficient. Figure 2

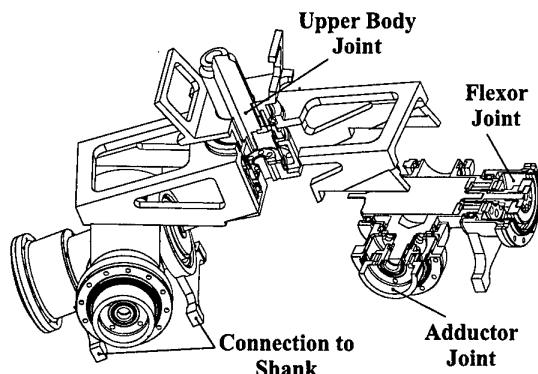


Figure 2: Design of the pelvis

shows the assembled pelvis including both hip joints and the upper body joint. The whole unit weights about 4,600 g. Table 1 shows the transmittable torques.

Table 1: Drive torques of the leg joints

	Average torque	Maximum torque
Hip adductor joint	35,3Nm	147Nm
Hip flexor joint	20,4Nm	147Nm
Hip int. rot. joint	7,8Nm	86Nm
Knee flexor joint	32,5Nm	255Nm
Foot adductor joint	26,0Nm	64Nm
Foot flexor joint	26,0Nm	288Nm

Another important aspect is the design of the feet. Since fast walking as well as running is planned, impacts have to be reduced to a minimum and the time gap between the sensor input and the motor response has to be bridged. Therefore, a damping mechanism is required. It will be realized by integrating elastic elements in the foot.

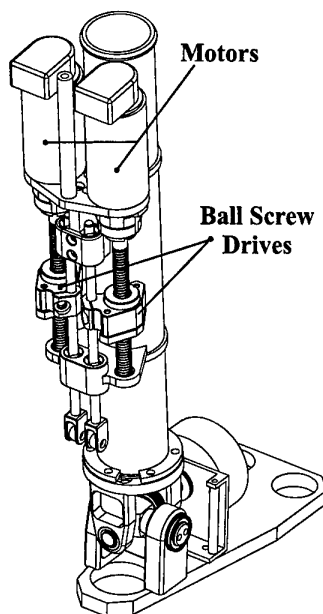


Figure 3: Design of the foot

The foot actuation is realized by two linear drives based on ball screws (see figure 3). This way the high torques in the ankle joint can be realized using two motors in parallel.

3. Sensor System

The sensor system consists of angular velocity and position sensors in each joint. Furthermore, the foot contains three-axis force sensors to measure the ground reaction forces in each of the three contact points. To measure the spacial orientation of the upper body, gyroscopic sensors in combination with inclinometers are installed. To verify the measured results and to determine external forces, three acceleration sensors are used in addition.

The machine hardware will consist of a central PC-board, which is connected to decentral C167-controllers by a CAN-bus system.

4. Control of the Robot

The mathematical model of the plant corresponds to the design of the robot and consists of a system of 16 bodies connected by $m = 15$ rotational joints (figure 4). Then the overall system has $n = m + 6 = 21$ degrees of freedom. When the robot is standing on one leg, the 6 degrees of freedom of the upper body correspond to a specific orientation of the 6 rotational joints of the

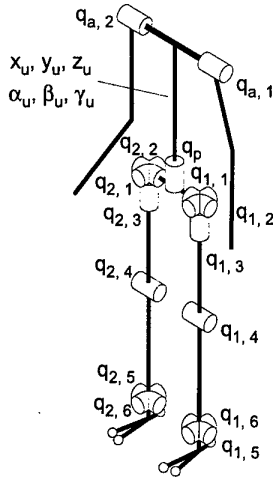


Figure 4: Plant model

supporting leg. Furthermore there is one joint in the pelvis and one joint for each arm, which can be used to compensate dynamic forces.

The controller is designed to not only realize "dynamically" stable walking, but also to allow for "running", which includes "ballistic" phases without ground contact. Since the latter is more complicated than pure walking, we only concentrate on this case in the following. During the gait pattern of "running", the support phases of the feet are alternating with ballistic phases.

4.1. Feedback Linearization

The control of the robot is based on the method of feedback linearization [10, 9], which starts out from the equations of motion:

$$M\ddot{q} + W_1\lambda = h + Q_e \quad (1)$$

Here M is the mass matrix, $q \in \mathbb{R}^n$ is the vector of generalized coordinates and h and Q_e are the gyroscopic and external forces, respectively. The vector $\lambda \in \mathbb{R}^m$ comprises the applied torques of the joints that are projected on the generalized coordinates with the Jacobian W_1 . Given a set of control inputs λ , a linear behavior can be prescribed in m coordinates. Now we first take a look at the "support phase", in which one foot is in contact to the ground, while the other one is swinging to its next stance point. Then the 6 degrees of freedom of the supporting foot are determined by the ground constraints. Therefore all n degrees of freedom of the system are exactly defined. In general the trajectory of the robot can be prescribed in any m

coordinates, as long as there exists a unique transformation to the generalized coordinates. Here a linear behavior is prescribed for vector x_c , which consists of the height of the center of gravity z_s , the spacial orientation of the upper body $\alpha_u, \beta_u, \gamma_u$, the orientation of the arms x_a and of the pelvis joint x_p and the position and orientation of the foot (x_{fl}) that is lifted off and swinging to its next stance point.

$$x_c = \begin{pmatrix} x_u \\ x_p \\ x_a \\ x_{fl} \end{pmatrix} \quad x_u = \begin{pmatrix} z_s \\ \alpha_u \\ \beta_u \\ \gamma_u \end{pmatrix} \quad x_{fl} = \begin{pmatrix} x_{fl} \\ y_{fl} \\ z_{fl} \\ \alpha_{fl} \\ \beta_{fl} \\ \gamma_{fl} \end{pmatrix} \quad (2)$$

A linear PD control law is prescribed in x_c with constant matrices C and D . The deviation from the reference trajectory is denoted $\Delta\dot{x}_c = (\dot{x}_c - \dot{x}_{c,ref})$ for the velocity and $\Delta x_c = (x_c - x_{c,ref})$ for the position, respectively.

$$\ddot{x}_c = \ddot{x}_{c,ref} - D\Delta\dot{x}_c - C\Delta x_c \quad (3)$$

When the system is in a non-singular configuration, the linear control law can be projected on the vector of generalized coordinates:

$$\dot{x}_c = J\dot{q} \quad (4)$$

$$\ddot{x}_c = J\ddot{q} + \dot{J}\dot{q} \quad (5)$$

Introducing (5) in (3) leads to:

$$J\ddot{q} = \ddot{x}_{c,ref} - D\Delta\dot{x}_c - C\Delta x_c - \dot{J}\dot{q} \quad (6)$$

With abbreviations w and W_2

$$w = \ddot{x}_{c,ref} - D\Delta\dot{x}_c - C\Delta x_c - \dot{J}\dot{q} \quad (7)$$

$$W_2 = J \quad (8)$$

we obtain the equations of motion in standard form:

$$M\ddot{q} + W_1\lambda = h + Q_e \quad (9)$$

$$W_2\ddot{q} + w = 0 \quad (10)$$

Solving (9) with (10) for the applied torques λ leads to:

$$\lambda = (W_2M^{-1}W_1)^{-1}(w + W_2M^{-1}(h + Q_e)) \quad (11)$$

4.2. Trajectory Planning

As long as the mathematical model of the plant is close to the real system, stability of the linearized system can be achieved by placing the closed loop poles with matrices C and D . However it is not sure that the supporting foot does not move relative to the ground

throughout the entire support phase. While simulations show that slipping does not occur since the normal forces are high enough to ensure sticking, problems arise from the limitation of the maximum torques that can be transmitted to the ground. When the corresponding torques of the ankle joint reach their limits, the system becomes underactuated. Practically this means that the robot starts tipping over in the sagittal or lateral direction. Therefore it is not possible to prescribe a completely arbitrary reference trajectory in \mathbf{x}_c , but the ground constraints have to be considered in the trajectory. Defining the torques that act between foot and ground with respect to the center of the foot, the constraints on torques T_x and T_y are denoted:

$$|T_y| \leq 0.5 F_z l_x \quad (12)$$

$$|T_x| \leq 0.5 F_z l_y \quad (13)$$

Here l_x and l_y are the length and width of the foot and F_z represents the normal force. In order to ensure that there exists some region around the reference trajectory in which the system does not become underactuated, functions for T_x and T_y are prescribed for the reference trajectory. This procedure is similar to prescribing the path of the "zero moment point" as known from literature [11]. For the lateral plane, the trajectory can be chosen such that the center of gravity is always between the lateral edges of the supporting polygon. For example T_x can be chosen to $T_x = 0$, so that equation (13) is satisfied. However the motion in the sagittal plane cannot be treated in the same way, since the projection of the center of gravity always moves out of the supporting polygon during a natural gait cycle. Therefore a function for T_y is prescribed dependent on the position of the center of gravity \mathbf{x}_c :

$$T_y = -k F_z l_x \quad \text{for } x_c - x_f \leq -\Delta x \quad (14)$$

$$T_y = F_z(x_c - x_f) \quad \text{for } |x_c - x_f| < \Delta x \quad (15)$$

$$T_y = k F_z l_x \quad \text{for } x_c - x_f \geq \Delta x \quad (16)$$

$$\Delta x = k l_x \quad (17)$$

$$k = \text{const.} \quad \text{with } 0 \leq k \leq 0.5 \quad (18)$$

Here x_f denotes the position of the center of the foot. With a larger value of k , the system is getting closer to the underactuated state $|T_y| = F_z l_x$. While this reduces the domain of attraction of the controller, a large value of k leads to a more human-like gait pattern and reduces the variations of the velocity in the sagittal plane.

Besides these constraints, the trajectory has to satisfy additional conditions to ensure that the robot performs a periodic motion. The trajectory of the support phase has to be calculated such that the system reaches a well defined state at the end of the support phase.

Then each ballistic phase starts with the same initial conditions.

$$\mathbf{x}_c(t_i) = \mathbf{x}_{c,1} \quad (19)$$

$$\dot{\mathbf{x}}_c(t_i) = \dot{\mathbf{x}}_{c,1} \quad (20)$$

A trajectory has to be found for \mathbf{x}_c such that equations (14)-(20) are satisfied for the equations of motion (1) when the i th support phase ends at some time t_i . In general there is no analytical solution to this problem, we therefore suggest a numerical approach.

For a given time t_i the trajectories of $m - 1 = 14$ elements of \mathbf{x}_c are prescribed in fifth order polynomials such that equations (19) and (20) are satisfied. Then one component of \mathbf{x}_c results from the constraints (14)-(16) and is therefore dependent on t_i . Here the velocity of the center of gravity in the sagittal plane is chosen as dependent variable. Then the equations of motion can be solved numerically for t_i so that all constraints are satisfied.

The numerical solution requires iterative integration and is therefore computationally expensive. However the determination of the trajectory has to be done only once per gait cycle and does not need to be calculated at the frequency of the digital controller. Furthermore simulation results show that a simplified model of the system is sufficient for the calculation of the reference trajectory.

4.3. Ballistic Phase

When the robot has no contact to the ground, the motion of the system is not influenced by external forces except for the gravitational force. Still a set of m generalized coordinates can be controlled with the m driven joints, while 6 degrees of freedom of the robot cannot be influenced by the controller. A possible set of controllable variables is:

- spacial orientation of the upper body $(\alpha_u, \beta_u, \gamma_u)^T$
- position of the arms and the pelvis $\mathbf{x}_a, \mathbf{x}_p$
- orientation and position of the foot that is swinging to its next stance point \mathbf{x}_{f1}
- orientation of the previous stance foot $(\alpha_{fg}, \beta_{fg}, \gamma_{fg})^T$

By choosing the trajectories of these variables the motion of the robot can be adapted to the human gait pattern. Furthermore it is important to define the position of the foot that is swinging to its next stance point, so that the subsequent support phase starts out with a well defined initial configuration.

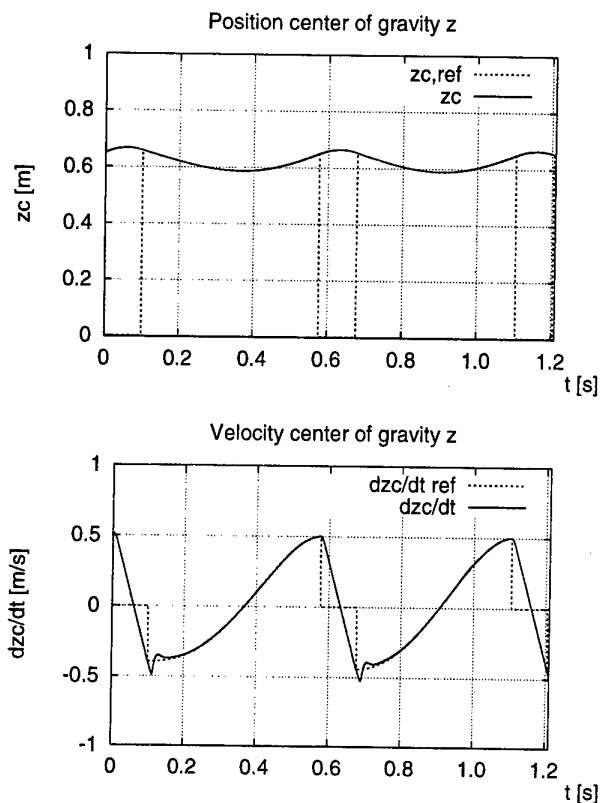


Figure 5: Trajectory z

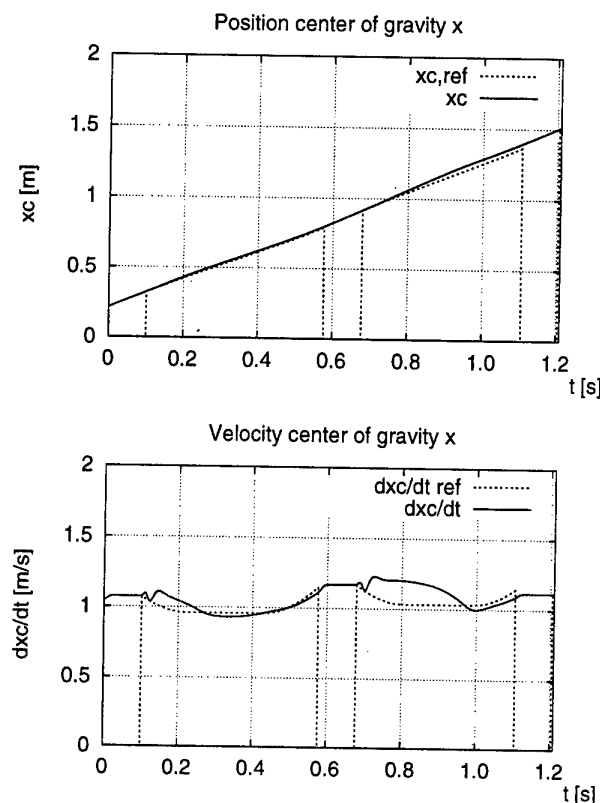


Figure 6: Trajectory x

While these variables can be controlled, the center of gravity follows a ballistic curve defined by the initial conditions. Add to this the position of the previous supporting leg cannot be controlled, but it results from the overall moment of momentum.

Based on these assumptions the control scheme of the ballistic phase is implemented analogous to that of the support phase using the method of feedback linearization. Only the transformation from control variables to generalized coordinates has to be adapted.

5. Simulation Results

The presented control algorithm is evaluated in a multibody simulation program. The corresponding model of the plant has the same structure as the model for the controller. In order to obtain realistic simulation results, the contact situation between foot and ground is modelled in detail. The stick-slip effects are modelled with Coulomb friction.

Here typical results are given for a gait at a speed of $1 \frac{m}{s}$. In order to demonstrate the dynamic stability, the robot is in a "jogging" motion including phases

without contact to the ground. The time for one step is about 0.6s with a ballistic phase of 0.1s. Figure 6 shows the sagittal position and velocity of the center of gravity and the corresponding reference for two steps. The reference is not defined for the ballistic phases and is therefore set to zero for these periods. Due to a simplified model used for the calculation of the reference trajectory, the actual velocity differs from the reference. However the system is controllable so that the reference velocity can be reached at the end of the steps. This leads to an approximately linear increase of the position in the sagittal plane. The vertical position and velocity are shown in figure 5. Since the model is known exactly in the simulation, the resulting velocity is very close to the reference velocity.

The corresponding torques of the driven joints are shown in figure 7 for the knee and hip joint. From about 0.0s to 0.7s the foot is not in contact to the ground. Therefore the torques are relatively low. When the foot touches the ground at $t = 0.7s$ the torque of the knee joint reaches its maximum and stays on a high level during the support phase. The

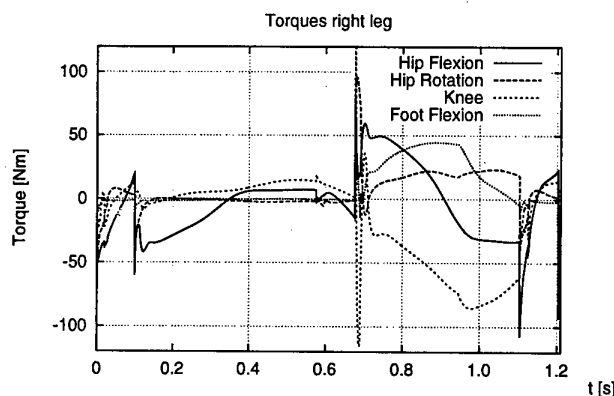


Figure 7: Driving torques

design of the machine and the choice of the motors complies with these requirements. According to the simulation results, the robot is dynamically stable and can handle disturbances effectively. When the system is excited by external forces, the stance points are adapted so that the robot remains stable.

6. Summary

The design and control of a humanoid walking machine are presented. Using the method of feedback linearization, dynamically stable motion can be achieved. The trajectories of the system are calculated at each step numerically. The computational effort is reduced by using a simplified model of the plant. This way the control problem can be solved in real time and is suitable for implementation on a real robot. In the near future friction effects and sensor transfer functions will be considered in the control loop so that model uncertainties can be reduced. With the completion of the real robot, the control strategy will be verified practically.

References

- [1] Föllinger, O.: *Nichtlineare Regelungen I*, R. Oldenbourgverlag, München, Wien, 1993.
- [2] Föllinger, O.: *Nichtlineare Regelungen II*, R. Oldenbourgverlag, München, Wien, 1993.
- [3] Hahn, U.: *Calculation of Anthropometric Data for Human Body Segments*. Implementiert in Programm "Calcm3d", 1994.
- [4] Hirai, K.; Hirose, M.; Takenaka, T.: *The Development of Honda Humanoid Robot*, Proceedings of the 1998 IEEE International Conference on Robotics and Automation, Leuven, Belgium, May 1998, pp. 1321-1326.
- [5] K. Ogata: *Discrete-Time Control Systems*, Prentice-Hall International, Inc., Englewood Cliffs, New Jersey, 1987.
- [6] Weidemann, H.-J.: *Dynamik und Regelung von sechsbeinigen Robotern und natürlichen Hexapoden*, Fortschrittsberichte VDI, Reihe 8, Nr. 362, VDI-Verlag, Düsseldorf, 1993.
- [7] Pfeiffer, F.; Eltze, J.; Weidemann, H.-J.: *The TUM-Walking Machine*, Intelligent Automation and Soft Computing, 1, 1995, pp. 307-323.
- [8] Roßmann, Th.; Pfeiffer, F.: *Control and Design of a Pipe Crawling Robot*, Proc. of the 13th World Congress, of Automatic Control, I. F., ed., San Francisco, USA, 1996.
- [9] Rossmann, Th.: *Eine Laufmaschine für Rohre*, Fortschritt-Berichte VDI, Reihe 8, Nr. 732, VDI-Verlag, Düsseldorf, 1998.
- [10] Slotine, J.-J. E.; Li, W.: *Applied Nonlinear Control*, Prentice Hall, Englewood Cliffs, New Jersey, 1991.
- [11] Vucobratovic, J.; Borovac, B.; Surla, D.; Stokic, D.: *Biped Locomotion: Dynamics, Stability, Control and Applications*, Springer-Verlag, Berlin, 1990.
- [12] Yamaguchi, J.; Takanashi, A.; Kato, I.: *Development of a Biped Walking Robot Adapting to a Horizontally Uneven Surface*, Proc. of the 1994 IEEE/RSJ International Conference on Intelligent Robots and Systems, Munich, Germany, 1994, pp. 1156-1163.
- [13] Yamaguchi, J.; Takanashi, A.: *Development of a Leg Part of a Humanoid Robot - Development of a Biped Walking Robot Adapting to the Human's Normal Living Floor*, Autonomous Robots, 1997, pp. 369-385.

Multi-Agent Based Control for Biped Motion

A.KHOUKHI^{1,2}, R.OUGUIN³, L.KHOUKHI¹, N.ABABOU³

¹Institut d'Informatique USTHB BP32 El-alia Bab-Ezzouar Alger Algérie

²Groupe ESIEE Dépt Automatique 2 Bd Blaise Pascal Noisy le Grand 93400 France

³CDTA 9chemin Med Gacem El Madania Alger Algérie

Abstract :

In this paper the problem of motion control of biped is considered. We develop a new method based on multi-agent strategy. This method deals with organization and coordination aspects in an intelligent modeling of human motion. We propose a cooperative multi-agent model, based on this model. We develop a control kernel named IMCOK (Intelligent Motion Control Kernel), which consists of a controller, coordinator and executor of different cycles of motion of biped. When walking, IMCOK receives messages and sends offers. The articulator agents partially planify the motion of non-articulator agent associated. The system is hybrid and distributed functionally, that is to say that it is constituted of a hybrid agent (cognitive and reactive) which cooperate to accomplish functions of control and command of biped. Cognitive agents communicate with reactive agents (non articulator) in order to generate the motion.

1. Introduction

The study of the motion of walker robots, especially the locomotion of bipeds has been studied by many researchers. The biped can navigate on surfaces, so their applications will be increasing, but the control and the coordination of their movements remain a problem that must be adapted according to methods proposed in the literature[10;], such as Autonomous locomotion[1;], optimization based methods of energy and time-energy Adaptive control algorithms [2][3][4], methods based phase of movement[7]. Recently, many researches investigated biped robots and walking on surface, as robot that can climb a sloping surface[16]. Presented hereafter is using the distributed artificial intelligence (DAI). So researchers in DAI are concerned with understanding and modeling action and knowledge in collaborative enterprises [17]. Hence, we consider principles and foundations of Distributed Artificial Intelligence (D.A.I) in order to build cooperation and communication system between agents.

Multi-Agent Systems (MAS) offer a way to relax the constraints of centralized, planned, sequential control, they offer production systems that are decentralized rather than centralized, emergent rather than planned, and concurrent rather than sequential[18] concerned with the behavior of a collection of

autonomous agents aiming at solving a given problem. So, these intelligent entities (agents) cooperate in order to solve a problem [6,7]. The autonomous agent approach replaces a centralized data base and control computer with a network of agents, each endowed with a local view of its environment and authority to respond locally to that environment [8]. Several taxonomies of multi-agent systems have been published In different areas : production and design [11,12;] Robotics[9], urban traffic [13,14], ethology and biology [15;], . So, multi-agent proposes an intelligent method for control because of its powerful theories[7]. This part is an extension of article [10]. The model is called Multi-agent Biped System (MABS) and the control kernel is called Intelligent Motion Control Kernel (IMCOK). Actually, the coordination between the biped members makes its movement. The present scheme is a representation of a biped .



Figure1 : Schematic representation of biped

2. System description

2.1 Definition

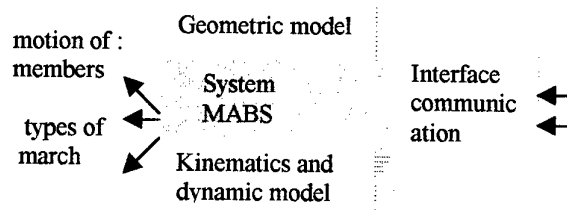


Figure 2 : knowledge of MABS

The MABS system is a multi-agent system within a basis of actors conceived to assure the control over the activity of movement of the biped. The system is hybrid and distributed in terms of function and scheduling ,i.e. it constitutes of a set of hybrid agents (cognitive and

reactive) that cooperate to accomplish functions of control of biped. Agents use a dynamic organization strategy based on the use of the negotiative technique based on communication protocol inter-agent. This technique allows messages exchanging between agents.

2.2 MABS Model

The main features of this model is to permit a scheduling distributed of several agents, and facilitates the communication with the user via the interfacing of communication. Mainly, it gives a new strategy of organization: the parallel communication between agents, the execution of several operations (intra-agents or inter-agents) and the flexibility and extensibility. It allows a distributed scheduling too. It also admits new articulator agents.

2.3 Operation levels

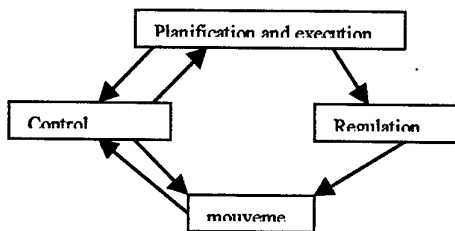


Figure 3 : MABS levels

The scheme below shows the different levels of our architecture, the user can communicate with MABS via interfacing of communication which is the means of communication necessary, for outside knowledge receipt, to the working of the system.

2.3 Procedure of function :

It is based on the following algorithm, followed by every agent:

- Message receiving.
- Scheduling.
- Sending results.

3 Architecture of MABS system

MABS constitutes of (figure 4):

- Kernel (IMCOK) " Intelligent Multi-agent Control Kernel" that is composed of: supervisor agent, percr agent, and equilibrator agent and regulator agent.
- Interfacing of communication
- Articulator agents
- Non-articulator agents

3.1 Articulator agents

These agents are homogeneous in their structures, but differentiate by their associated functions

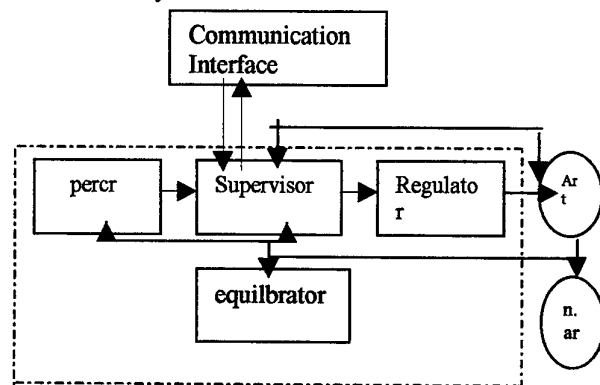


Figure 4: MABS and IMCOK

Architecture

Movement. Our articulator agent has three processes: Process of communication, process of decision and Process of scheduling.

- Process of communication: It receives the message coming from the supervisor or other components by the Process of Input Communication (PIC), it shapes it into Internal Message File (IMF), and transmits the results of scheduling by Process of Output Communication (POC).

- Process of decision: at the receipt of a message from the regulator agent, the articulator agent decides after consulting the scheduling process, whether it sends the control to the non-articulator agent or no. This process also decides on sending the answer (success or failure) to the supervisor, percr and equilibrator.

- Process of scheduling: this process is constituted of library of plans and memory of storage: the necessary data allowing the process of decision either to send a signal of activation or not to the non-articulator agent, are contained in the library of plans (like max and min limit for rotation of the non-articulator agent partner). The ability of articulator agents resides in their plans. In case of fire, the signal of activation is going to automatically reactivate in the memory of storage, what permits to optimize the time of scheduling. Noting that the three processes communication-scheduling-decision function in parallel.

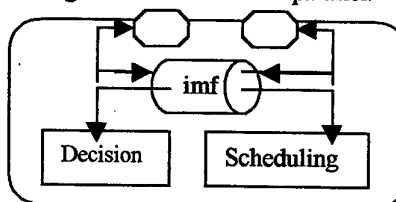


Figure 3: articulator agent architecture

3.2 Non-articulator agents

It doesn't arrange a process of decision. Its primary function is clearly the execution of the movement. So, it represents a reactive agent. It constitutes of *Process of communication*: it receives the activation signal of articulator agent via PIC, and transmits the result of movement to the main articulator agent via PIC.

- *Process of scheduling*: The necessary data allowing the non-articulator agent to plan its trajectory of reference and then to follow it, are contained in the library of plans. After having executed its function, the non-articulator agent sends a signal of result to the articulator agent partner, which transmits it to the percr and supervisor.

3.3 Regulator agent

It constitutes of: process of communication, process of regulation, motor process, process of scheduling.

- *Process of Regulation*: its function is the regulation of speed of the members given by the supervisor. The compliant speeds to the movement are initialized by the programmer under a shape of a speed interval in order to adjust the speeds of non-articulators agents coming from the supervisor.

- *Motor process*: its unique function is the generation of a signal (message) called message motor, as well as the speed of the movement associated to these members.

- *Process scheduling*: this process contains the necessary information to the treatment.

3.4 PERCR agent

. After having received signals of the environment (reversed picture), the cerebellum of our system is going to construct the real picture of the environment, it is the perception of the environment. Then the resulting signal is going to be transmitted to the supervisor's.

PERCR constitutes of: Process of communication, process of scheduling, Process of perception and Process of decision.

Pecr receives two types of signals, one from sensors, the other from the agent's.

- *Process of perception*: this process ensures the perception of the environment signals.

This process arranges a SYstem of Picture Treatment (SYPT) permitting a real reconstruction of the received virtual picture by sensors.

- *Process of scheduling*: it contains a library of plans: One distinguishes two essential data parts: data specified for the perception, which ensures the management of the system of picture treatment (SYPT). And data specified for the control, which ensures the management of the control system by

sending data concerning states of the different members in progress of each cycle of movement (single support, and double support).

- *Process of control (SYMOC)*: SYstem of Movement Control: agent transmits him information on states of agents to control ... at all instants, SYMOC has the monitoring of messages coming from the articulator agents, then treats them transmits a result signal to the supervisor (to inform the user of the state of march)..

3.5 Supervisor agent

The supervisor receives the already quoted signals from agents, treat them and generate new signals of command or answer (structures of solution to problems met by the other agents of MABS). The supervisor communicates with the environment or agents via the process of communication. One distinguishes two types of communications, at the level of the supervisor:

communication intra-supervisor (between its different constituents) effected via the Internal Messages File (IMF), and the inter-supervisor communication (the exchange of messages between the supervisor and the other components of the system) effected via DISI Dispatcheur of Signals, and PIC process of exit communication. Signals coming from the different components are identified and recognized by RISI. All the components of MABS system are managed by their respective managers.

MC: manager of communication
ME: manager of equilibrator
MR: regulating manager
MO: manager of control
MA: manager of articulator agent
MN: manager of non-articulator agent

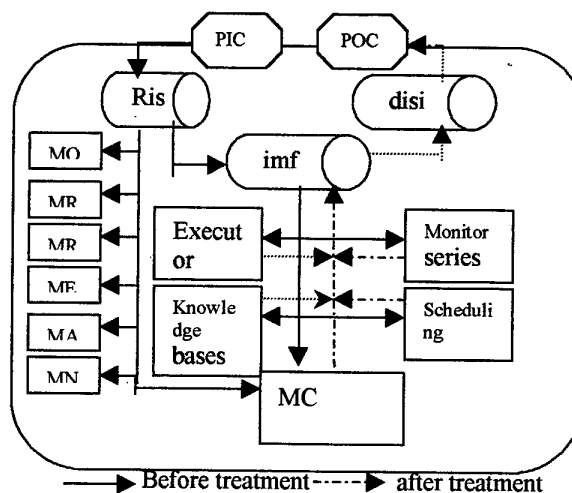


Figure 5: Supervisor agent

We explain little process : The library of plans contains as the command or the necessary tools for the management of the components of the MABS system.

3.5.1 Basis of knowledge

It is the data basis of MABS. Containing all information on the different components of the system (IMCOK , articulator and non-articulators agents), and of each cycle of movement (4 cycles, two for double and two for single support).

3.5.2 Monitor of Series (MS)

Its main role is the coordination between the supervisor actions. This process is still in contact with the executor (while providing him with actions to execute) after consultation of knowledge basis and process of scheduling. One can associate different strategies to plan activities of this monitor:

-- With static priority: once a priority is affected into a program, this one won't change until the end of execution of this program.

-- With dynamic priority: the priority affected into program changes according to the environment of execution of this one (load of system, types of actions to be executed...).

3.5.3 Executor

it is the loaded process of instructions provided by the monitor of series. The strategy of scheduling data to IMCOK is said to be not interrupted [if once the executor is allocated to a program, this one will keep it until the end of its execution or that it is blocked on a resource not yet ready]. The allowance of executor to the program can make it according to the affected priorities to program them automatically (for example one is going to give to every signal coming from an organ a priority, with of course their organization), or by an external manner by the person responsible of exploitation, the priority can be allocated statically or dynamically.

After execution, the result will be transmitted to the dispatcher of signals in order to transmit it to the concerned agent.

3.5.4 Receiver and Identifier of the Signals (RISI) :

Contrarily to the other agents of MABS, the supervisor has a superior workload. That requires a loaded element of identification and to send received messages from the outside into process or the corresponding manager in the supervisor. This element is called RISI.

3.5.5 Dispatcher of Signals (DISI)

Play an important role in the diffusion of signals (either signals that have just been executed, or those that has just been managed without being executed).

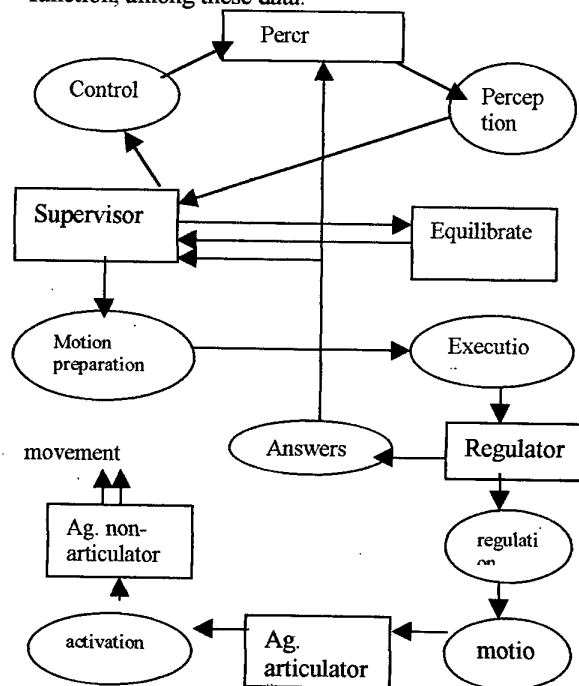
3.5.Managers

ensures the management of agents of the MABS system. The manager sends a message of working to the agent managing. It arrives that during its work, the agent undergoes a problem of state, in this case it informs the corresponding manager in order to solve the problem.

3.5.6 Equilibrator

This process ensures the balance of the biped during the march or during the station. The physical conditions, so that the robot is in state of balance, are that the center of gravity of the body is on the surface of lift (surface taken between elements in contact with the ground). It consists of a process of communication, process of scheduling and process of equilibration.

The equilibrator receives the answer from articulator agents [this answer is the result of the articulator agent decision on information of command (for example the degree of rotation, the degree of bending, the degree of extension...) constituting the signal of command that it receives from the supervisor] via the process of communication, after a treatment, the process of equilibration gives the state of balance of the biped, and transmits them to the supervisor. The plans contain all data allowing the equilibrator to ensure its function, among these data.



The scheme bellow shows the relationships that exist between different agents already quoted .

4. Management of the communication:

The MABS system, according to its architecture and its function, it appears like a very necessary system in matter of communication needs. Indeed, MABS agents communicate between them by sending messages.

Every signal (message) represents the information needed by the agent (a control to be achieved) and as the result of treatment of the previous agent.

5. Simulation :

Inter-agents message exchanging protocol via DDE(Dynamic Data Exchange) through conversation with the server, there by he transmits (transactions) to the server, the latter answers by providing data or services. We choose then , asynchronous transactions. The general form of algorithm is :

```

Client agent
{
  xtype_connect;
  put message in case
  transaction of emission

  read answer
  send xtyp_disconnect
}

server agent
{
  xtyp_connect_confirm

  xtyp_poke

  read data from case
  send answers
}

```

6. References

[1] M.Nilsson "Snake robot" conf. IEEE control systems. Apr 1997, pp. 21-26.
 [2] S.kajita and al. "dynamic walking control of a biped robot along a potential energy conserving orbit" IEEE trans. robotics Automat., vol. 8, no. 4, pp. 431-437, Aug 1992.
 [3] C.Chevallereau, A. Formal'sky, B. Perrin, "low energy cost reference trajectories for a biped robot" IEEE conf. Robotics Auto. May 1998, pp. 1398-1404.
 [4] A. Khoukhi "commande et identification d'une classe de systèmes non linéaires" thèse doctorat, Télécom-Paris, June 1991 Telecom.Paris 1991.

[7] M. Rostami and Guy Bessonnet "Impactless sagittal gait of a biped robot during the single support phase" IEEE conf. Robotics Automat. , May 1998, pp.1385-1391.
 [6] B. Moulin and B.Caib-draa "An Overview of Distributed Artificial Intelligence". In Foundation of distributed Artificial Intelligence, 1996.
 [7] L.Khoukhi "general view and analysis of multi-agent systems". Internal report, USTHB. 1999.
 [8] H. Van Dyke Parunak "Applications of Distributed Artificial Intelligence in Industry" in Foundation of distributed Artificial Intelligence, 1996.
 [9] S. Kagami, and al. "Design and Development of a Legged Robot Research Platform JROB-1" conf. of IEEE robotics Automat., May 1998, pp.146-151.
 [10] L.Khoukhi, A.Khoukhi, R.Ouguini and N.Ababou "Multi-Agent Based Strategy for Biped Motion control" conference computer, algeria, october 1999.
 [11] C. Yu-Yung, L.Fu and C. Yu-Chien "Multi-agent Based Dynamic Scheduling for a Flexible Assembly System" conf. of IEEE Robotics Automat., May 1998, pp.2122-2128.
 [12] S. Liu, L. Fu and J.Yang "Multi-Agent Based Control Kernel for Flexible Automated Production System" conf. IEE Robotics Automa., 1998, pp-2134-2139.
 [13] D. Steiner "An Integrated Environment for Constructing Distributed Artificial Intelligence Systems" Foundation of distributed artificial Intelligence, 1996.
 [14] K.Fischer, J.Muller and M.pischel "A. Geral Testbed Artificial Intelligence Applications". Foundation of distributed Artificial Intelligence, 1996.
 [15] J. Ferber "Reactive Distributed Artificial Intelligence : Principles and Application '96.
 [16] Y.F.Zheng and J.Shen: "Gait synthesis for the SD-2 biped robot to climb sloping surface" IEEE Tran.Robotics Automat., vol. 6, no .1, pp.86-96, Feb 1990.
 [17] Bernard moulin and Brahim Chaib-Draa "An Overview of Distributed Artificial Intelligence " Foundations of Distributed Artificial Intelligence, 1996.
 [18] H. Van Dyke Parunak "Applications of Distributed Artificial Intelligence in Industry", Foundations of Distributed Artificial Intelligence, 1996.

FLEXIBLE MINI-ROBOT WITH AUTONOMOUS MOTION

Francis MUNERATO, Doru
MIHALACHI, Claude LAURENT
University of Metz (France)
munerato,mihalach@
agip.sciences.univ-metz.fr

Constantin NITU, Constantin Daniel
COMEAGA
"POLITEHNICA" University of
Bucharest (Romania)
C.Nitu@me.mecatronica.pub.ro

Waldemar OLEKSIUK, Wieslaw
CZERWIECZ University of
Technology (Poland)
kup_olw@mp.pw.edu.pl

Abstract

We introduce here our works in development of a snake-like redundant micro-robot based on twenty identically segments structure for pipe investigations. Each segment is a parallel mechanism (3 DOF) with 3 DC motors associated with its sensors and controlled by a 16-bit micro-controller. The distributed control system is supervised by a real-time kernel on the host computer communicating via a Can network.

1. INTRODUCTION

The paper presents the development of a mobile robot, acting like an earth-worm, if both ends are free, or like an elephant trunk, if one end is fixed, within the European COPERNICUS project 941306-FMAM. The work was performed by international collaboration between University of Science Metz (France), "POLITEHNICA" University of Bucharest (Romania) and Warsaw University of Technology (Poland).

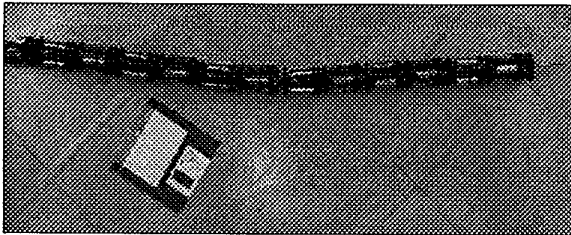


Fig. 1 Robot mock-up

Current evolution of micro and mini-robotics is directed to continuous miniaturization, to increasing of autonomy and flexibility for accomplishing complex tasks in narrow or hardly accessible spaces. Today, industry is faced with the need to increase reliability and reduce the maintenance costs for the complex mechanical systems and equipment (power plants, airplane engines, etc.).

This means a tremendous requirement for technology, which makes possible to perform inspections and repairs in tight spaces, without having to dismantle the plant equipment. If the newly developed robots will be able to remain inside various installations, they could monitor and repair it and maintenance work will be performed without shutting down or dismantling complex machinery. For these purposes, the solution is to transpose the motion principles, which are specific to living world, into technical achievements. The first investigations concerning development of mobile robots, with a snake-

like locomotion, were made in Japan, by Shigeo Hirose, in the early '70-s but there are reported only a few achievements in this field (Japan, USA, Germany). Then, waving still remains an interesting way of locomotion for grounds with variable geometry or difficult to travel through, such as pipes, while it is also an actual subject for research and development.

2. TYPES OF MOTION

The first stage consist in define future modes of motion of the robot in autonomous working, the tentacular working leading to other type of problem.

Grass-snake type displacement: undulation in a horizontal plan.

Advantages: no problem of stability, reduced consumption of energy.

Disadvantages: not negligible rubbing.

Adder type displacement: undulation in a vertical plan.

Advantages: medium energy consumption, reduced rubbing.

Disadvantages: problem of stability.

Cobra type displacement: undulation and extension in a horizontal plan.

Advantages: no problem of stability, speed raised.

Disadvantages: important energy consumption, important rubbing.

Earthworm type displacement: extension in a horizontal plan.

Advantages: no problem of stability, reduced energy consumption, negligible rubbing, medium speed.

Disadvantages: necessary module elongation.

Some investigations have shown that the most interesting solution was a multiple-module robot, able to move like an earthworm. On the basis of simulations undertaken on one model in two dimensions, we have developed this principle of locomotion.

This requirement had led to providing the module with 3 degrees of freedom: 2 rotations (θ, ψ) and 1 translation (ρ). The rotations was necessary for generating the snake-like or earth-worm like motion with bending waves, while the translation was useful for generating the earth-worm motion with elongation

waves, which enables the robot to move into narrow spaces or to increase its velocity on straight trajectory.

In reality, this principle obliged to realize a more complex mechanics, but it would be able to support to support all types of snake-like locomotion presented previously. We left therefore the open way to other types of utilization, particularly in tentacular or trunk mode.

3. MECHANICAL STRUCTURE

The design of the module had several possibilities to be carried out, but the adopted solution was to link 2 platforms with a special 3 DOF joint (Cardan + translation) and 3 linear actuators, ended with spherical joints. As linear actuators, screw-drives and micromotors with gearheads and encoders were used.

This articulation (a scale 2 model has been realized) eliminates mechanical problems like radial parasitic effort and axial torque. The precision is good since one uses kneecaps, as well as the robustness. The overall dimensions of each module are diameter~ 30 mm, height~ 50 mm. The robot body consists of 20 similar modules that mean 60 DOF to be controlled. But they are not yet instrumented.

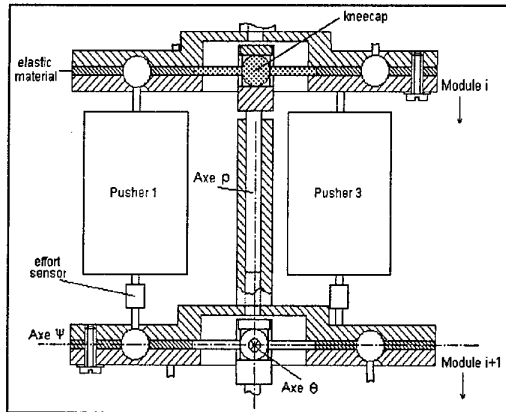


Fig. 2 Three DOF parallel mechanism

Amplitude of angles θ and ψ are limited to 20 degrees and ρ to 1/3 of total length of the module. The reverse mathematical model is simple, which reduce times of calculation. However, the direct mathematical model has no analytic solution, since it is a parallel architecture.

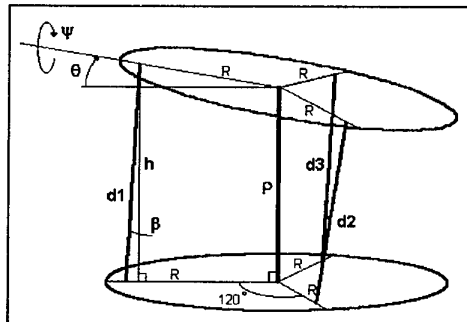


Fig. 3: Module diagram

A significant amount of our research was oriented on the module comportment simulation. The geometrical models are now operationally with respect of the mathematical problems of resolution. The calculation model of torque and effort components is also prepared (see Reflex level) and we are actually working on the algorithm of pipe forward mode. But the problems concerning the effort threshold sampling could be resolved only in the phase of identification on the complete prototype.

Direct Model: $\rho, \theta, \psi = F(d1, d2, d3)$

$$d1 = \sqrt{(-2 R^2 \cos \theta - 2 R \rho \sin \theta + 2 R^2 + \rho^2)}$$

$$d2 = \sqrt{(\sqrt{3} R \rho \cos \theta \sin \psi + \frac{\sqrt{3}}{2} R^2 \sin \theta \sin \psi - \frac{1}{2} R^2 \cos \theta + R \rho \sin \theta - \frac{3}{2} R^2 \cos \psi + 2 R^2 + \rho^2)}$$

$$d3 = \sqrt{(-\sqrt{3} R \rho \cos \theta \sin \psi + \frac{\sqrt{3}}{2} R^2 \sin \theta \sin \psi - \frac{1}{2} R^2 \cos \theta + R \rho \sin \theta - \frac{3}{2} R^2 \cos \psi + 2 R^2 + \rho^2)}$$

Reverse Model (linearized) : $d1, d2, d3 = F^{-1}(\rho, \theta, \psi)$

$$\rho = -1/3 \cdot \sqrt{3 \cdot d1^2 + 3 \cdot d2^2 + 3 \cdot d3^2}$$

$$\theta = \frac{2 \cdot d1^2 - d2^2 - d3^2}{2 \cdot R \cdot \sqrt{3 \cdot d1^2 + 3 \cdot d2^2 + 3 \cdot d3^2}}$$

$$\psi = \frac{-2 \cdot \sqrt{3} \cdot (d2^2 - d3^2) \cdot \sqrt{3 \cdot d1^2 + 3 \cdot d2^2 + 3 \cdot d3^2}}{3 \cdot R \cdot (2 \cdot d1^2 + 5 \cdot d2^2 + 5 \cdot d3^2)}$$

Another solution for direct model is to consider that h is approximately equal to $d1$. Then we can iterate.

4. CONTROL ARCHITECTURE

The developed architecture of the control system of the robot is hierarchically distributed on two main operational levels. At the higher level, a real time nucleus, implemented on a computer plays the role of the supervisor and deals with the trajectory planning, as well with the user interface. At the lower level, a local control system, distributed between the robot modules, allows the control of each module, in order to reach the imposed trajectory. This system provides some degree of autonomy for each module and also presents the advantages of modular construction, consisting of identical control closed loops for each module, possibility of connecting and disconnecting the modules and putting out of operation the defective ones, without stopping the robot action.

Utilization	Application Level	Task planning - Planning - Decision taking	Task
Equipment	Cooperation Level	- Environment interaction - Dialog management - Peripheral devices management	Central Calculator
Effectors	Coordination Level	- Coordination and modules control by function - Gripper management	Robot
Actuators	Action Level	- Combinations of elementary actions by operation - Informations processing - Corrections and adaptation	Module
	Reflex Level	- Asservissements of actuators - Taking of raw informations	Micro-Controller Hardware

Table 1: Control system architecture

The communication between the two hierarchical levels is accomplished by means of a field-bus of CAN

type. The choice of this one was recommended by its guaranteed performances of the communication protocol, especially for real-time applications. The two levels of the control system are organized in several layers, as specified in the next table. For a better visualization, we present the functional analysis structure used and the layers covered by the Copernicus project, which we have developed.

Application level

This level is that of the tasks planning. It is here that been defined objectives to reach, modes of snake-like locomotion, functionment modes, etc.

This level is not included in our project, nevertheless, a minimal application will be developed to govern the robot, with a joystick or a mouse, by an operator ahead the screen connected to the camera of the robot.

Coordination level

This layer is an interface between the robot and its utilization. It allows an application to access to all functions of the robot via requests to the exploitation system.

It manages equally all computer peripheral devices or other (lectors of discs, camera, keyboard, screen, printer, inputs-outputs, etc.), as well as man-machine and machine-machine interfaces.

Cooperation level

At this level are realized commands to the effectors, such as gripper and the whole body itself.

This level is implanted in the central computer and dialogue with the inferior layer by a network that it manages. It is therefore comparable to the spinal cord that transmits orders and executes automatic actions, here, crawling along of a path.

The principle of interpolation currently used is developed here: (note that all the figures are in 2D for more clearness, but calculations are in 3D).

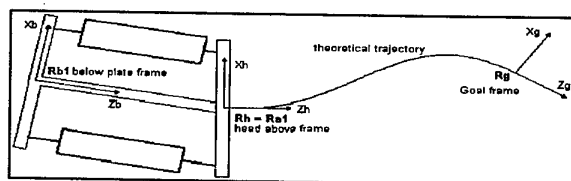


Fig. 4 : Interpolation principles

To each segment of the robot is associated two frames, one on the below plate R_{bi} , and one on the above plate R_{ai} , expressed in an absolute frame associated to the head above frame R_h . This frame is then floating. Note that the below frame R_{bi} of one module is the same as the above plate R_{ai+1} of the backward module. All frame are expressed in a homogeneous matrix form, i.e. position + orientation.

The trajectory to follow is given, by the superior level, in terms of position R_g to reach by the frame R_h associated to the head and expressed in herself. When an order of displacement is received, the frame of the

head and the goal frame allow interpolating a curve tangent to the Z-axis of the two frames and passing by their origins.

We actually use two 3-degree equations for this curve. Since the curves are expressed in head frame, we assume that Z can only increase. If the vector Z_g is oriented in backward direction, another (intermediary) frame R_g must be defined before by the superior level.

The head has to follow this curve with a relative precision of 0,1mm and to remain constantly tangent to the path, but the precision have no real signification when the robot move.

Next elements have to follow "on the best" this curve, without obligation of tangency. So as to not to overload calculations, positions of next elements are calculated by linear interpolation between points of passage of the head. However, this method induces to memorize a considerable number of points. We prefer therefore to memorize only 20 points in a circular table (one point by segment).

A point is added to the table each time that the second segment reach or exceeds its aimed point. The added point corresponds to the theoretical position of the head at this moment. A point is suppressed each time the last segment reach or exceeds its objective. Each segment that reach or exceeds its objective aims then the following point in the table. The table is initialized with original positions of 20 segments at power-on.

The amplitude of the movement is realized by a unique wave going through the head to the tail of the robot. With half-sinuosid sampled in n intervals, we obtain a flowed movement. To each temporal sample, the amplitude of an articulation ρ_{ij} is equal to $A \cdot \sin(j \cdot \pi / n) + \rho_{min}$, where ρ_{min} is the minimal length of one segment. The speed of the movement is a function of n and A is the maximal segment elongation. Only five modules are moving at the same time to the maximum, so n is a multiple of five.

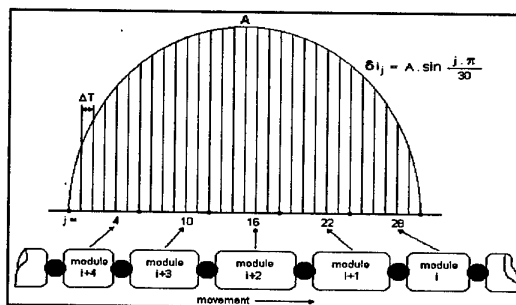


Fig. 5: Movement amplitude

For positioning the head, the amplitude obtained for the first articulation gives ρ . The intersection of a sphere of radius ρ centered in R_{b1} , with the two equations of the trajectory path gives the position R_{n1} to reach for the next sample by the head above frame R_h (calculated by successive approximations). Note that

Rb1 is not the actual Rb1 but the future position of Rb1 for the next sample. Then the tangent to the curve at this point give the orientation of this frame in terms of θ and ψ .

For positioning the backward elements, and only while the head module move, the amplitude of each articulation gives also ρ_i . The intersection of a sphere of radius ρ_i centered in Rbi, with the straight line to the aimed point Pj of segment i gives the position to reach for the next sample by the frame Rai (calculated analytically). In the example below, the above frame plate Rai of the module i is initially in Oi. It must go to Ai. Another methods consist to not aim points Pj themselves, but segments of straight line between points, for a best precision. The solution is a lightly more complex.

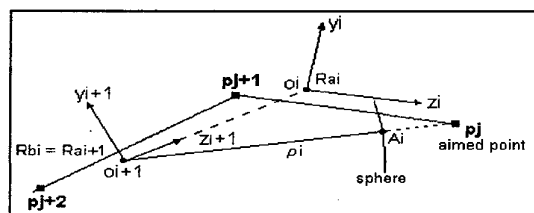


Fig. 6: Module trajectory positioning

The first calculated point is that corresponding to the most behind module, then we goes up towards the head. Each Rai obtained is used to calculate the following ($R_{ai} = R_{bi-1}$). We finish by calculation on the head module developed earlier. Let us note that the most behind module cannot be directed towards its aimed point since θ_i and ψ_i are on Rai and not Rbi.

When the head module don't move, the calculations is a quite more complex because the five modules must move between two fixed points. The forward and the backward modules must not move. Since the distance between these two points is constant, it is impossible that the sum (in 3D) of the calculated elongation of the five modules have the good value. The solution is to modulate the value of the maximal segment elongation A, the relations between the lengths of the five modules remain in sinus forms. This is done by iterations.

When we have all the origins of the frames, we can compute their orientations since their Z axis must point the origin of the preceding segment frame and their Y axis are in the same plan. This gives the θ_i and ψ_i . All the ρ_i , θ_i and ψ_i calculated are then sent to correspondent modules by the net.

Note that when the robot goes in backward direction, the calculations are analogous but not exactly the same because of the rotations \square and \square are on the frame Rbi and no more Rai.

Action level

This level corresponds for us to a complete module of the robot. Each module is composed of a segment

with its three actuators, its proprioceptive position and effort sensors, the electronics of power and a micro-controller managing the module in his totality and conversing with the superior level by a field-bus.

A module possesses certain autonomy and a "free arbiter". It receives orders of displacement and fonctionment modes and returns responses in terms of state and positions reached. It is itself that applied direct and reverse geometrical models and adapts order received to conditions of evolution that it detects by its effort sensors. A module has to be seen functionally like a vertebra that executing "as well as possible" the orders received from the superior level. It can refuse to function in case of failure, but it has to inform the coordination level that will change then the fonctionment mode.

Reflex level

It concerns the control of actuators and the taking of raw information. It is the layer that pilots the equipment and is situated in micro-controllers.

To control speed of each motor of a module, we use the command Pulse Width Modulation. This for reasons of cost and facility of future integration in a VLSI chip. The Siemens micro-controller used is already provided with the necessary circuits.

Two supplementary information are necessary for superior levels. It concerns the horizontally of the robot and lateral efforts applied by each segment of the robot on the pipe.

Let us specify that currently, the robot is not instrumented with these sensors.

Compliant command

The compliant command is necessary in three operating modes:

- ◆ In pipe forward mode, the robot must be able to adapt to the inequalities of the ground and the curves of the pipes. For doing this it uses its own effort traducers to calculate the applying forces on the pipe walls. It drives its actuators in the sense of the best rapprochement of the objective but without overtaking the maximal effort threshold. In this case, the aimed position, given by the higher level, is theoretical and cannot always be reached.
- ◆ The pipe forward mode also, allows solving the problems of robot sliding by jamming in the canalization. In this case the effort threshold will be significantly greater and the top level define a sinusoid trajectory or spiral trajectory with the diameter just a little greater than the one of the pipe, making the robot to exercise an effort on the pipe walls.
- ◆ The inert mode. This mode is useful for the dysfunctional movement of one or more modules. When a module detects a network fault (it can't communicate) or when it receives the order to disconnect itself, this mode allows the robot driving

and ignoring that module. The disconnected module uses its effort sensors for pilot its motors such a way that the module don't oppose any resistance (active reversibility). The module becomes, then, inert.

The problem is that we don't use tactile sensors because technology does not allow a rather high resolution. We prefer use effort sensors instead, so we can't try to determine where are the contact points between the robot module and the pipe.

The effort sensors must be established on the axes of the three push rods $d1$, $d2$, $d3$. When the module meets an obstacle, it undergoes an effort F which break up into a R_z force along Z axis and two torque C_x and C_y around X and Y axis (the other components do not interest us). This effort F also breaks up into three constraints $F1$, $F2$, $F3$ on the three pushers.

We established the mathematical model allowing to calculate R_z , C_x and C_y according to $F1$, $F2$ and $F3$. But this model is complex and does not allow making the difference between the constraints imposed by the force F and those imposed by the adjacent modules. But these two constraints require opposite reactions of the motors. A simpler (and worse) solution would consist to impose a maximum threshold for the constraints $F1$, $F2$ and $F3$ and to integrate it in the control loops of the motors.

Horizontality sensor

A non-negligible problem relates to the need to know the horizontality of the robot, because the robot can roll on itself. It then becomes impossible to direct it without this information. If we know the inclination angle of the robot, we can evaluate the real reference frame of the head and calculate a pseudo reference frame R_h so that its axis X_h is always vertical.

The Polish team built a prototype of 3D-horizontality sensor. This prototype is still too large to be integrated in the head of the robot, but it enables us to work. Currently, this sensor is in phase of characterization, because the vibrations of the robot generate parasitized signals.

5. HARDWARE

The Reflex and Action layers, implemented on each module, are under the responsibility of local 16-bit micro-controller.

Application, Cooperation and Coordination layers are implemented on a host computer (PC Pentium).

The communication between the host computer and the twenty micro-controllers is accomplished by a CAN field bus.

Controller

Each module is equipped with a micro-controller of 16 bits (Siemens C167CR). This one administrates the communication within CAN network and local control on the basis of the sampled trajectory, by the real-time

kernel. Micro-controller also implements the geometrical positioning algorithm and control functions. In the same time, each module informs the central computer about its own evolution.

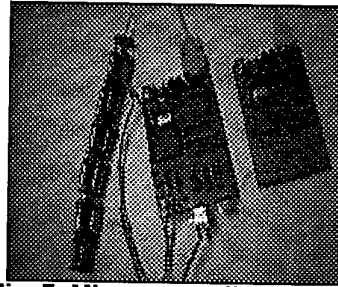


Fig. 7: Micro-controller board

Real-time kernel-Multi-tasking

Specific to embedded applications, a real-time kernel is necessary to allow the administration of distributed applications with a short switching time of different tasks.

The kernel divides the work in several tasks, grouped according to priorities system. Some of the most important tasks are robot trajectory, interpolation and communication with the modules. Other tasks, like monitoring of the robot evolution, corrections and adaptation, prove the user interfaces are have different priority levels.

Concerning the robot motion, the kernel surveys the five parallel moving modules. For each $n/5$ sampling period, this window of five modules is cyclically shifted with one module, beginning from the robot head towards the tail

During the development stage, a real-time system (iRMX) is used, which, will be replaced, in the final stage, with a real-time kernel of smaller size and dedicated to specific problems of robot

Inter-modules communication network

CAN is a new field bus with good performances in development of real-time embedded applications; a quick serial bus (maximum transfer rate of 1Mbit/s for a maximum distance of 40 m). The communication protocol is of CSMA/AMP type and the messages can transport up to 8 bytes of data.

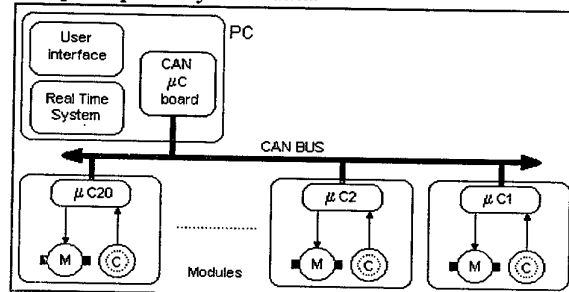


Fig. 8: Network architecture

All the nodes, connected to the CAN network, survey and can receive the bus broadcast messages, labeled with a unique identifier (29 bits, B norm, Extended CAN). The identifiers also determine the

priority degree of the message. CAN provide a good noise protection (differential transmission), as well as a permanent system of transmission errors detection and recovering.

Each robot module is seen as a network node and uses the CAN controller already integrated on the 16 bit Siemens C167CR micro-controller.

Central computer has a CAN communication board, which liberates the computer from the CAN protocol management task. Data to be transmitted are read or written by computer, via DPRAM memory (dual port). Physical connection, in bus topology, is provided by a differential line, opto-electrically coupled assuring a good noise protection.

Central computer broadcasts, into the network, the operations to be carried out by each module, the robot actions sequence and the necessary data (position coordinates, limit values of forces, etc.). Each module responds with its own data and information. At a certain moment, five modules act in parallel, therefore the messages have to be received by all the five modules in action. So, a message is not forced to contain information about receiver, but especially information about the enclosed data. Each node monitors the network and can decide if the enclosed information is interesting or not. This way, the messages could be organized in the so-called dictionaries, depending on the enclosed data (position, speed, force, etc.) and on the priority level.

6. CONCLUSION AND FUTURE WORK

We exposed some techniques and methods used in the design of snake-like robot built in collaboration by three laboratories (French, Romanian, and Polish). The robot is dedicated mainly for small diameter pipe investigations.

First, we presented the mechanical articulated structure based on a parallel mechanism with 3 DOF. Several mock-ups were built and studied for finally adopting the fig. 2 design and for building a 20 segments robot (scale 2:1).

Then the distributed control system architecture is exposed. Methods developed here are tested on the robot structure, but some algorithms couldn't be directly applied since some sensors are not yet enough small to fit on the robot's modules.

Also, some robot systems are not studied in this phase, for examples the vision micro-camera system and the head micro-gripper;

A lot of work still rests to do in integration and miniaturization and will make the object of further communications.

7. BIBLIOGRAPHY

- [1] A. B. Slatkin and J. Burdick. *The Development of Robotic Endoscope*. In Proc. IROS, Pittsburg, PA, 1995
- [2] D. Comeaga, C. Nitu and E. Grecu. *Kinematic and Static analysis of a Snake-like Redundant Microrobot Module*, "Mekatronika'97", vol. 1, pp 37-41, Warsaw, 1997
- [3] D. Paret. *Le bus CAN, Controller Area Network*, Dunod, Paris 1996, ISBN 2 10 003164 3
- [4] E. Paljug, T. Ohm and Samad Hayati. *The JPL Serpentine Robot: a 12 DOF System for Inspection*. In Proc. IEEE International Conference on Robotics and Automation, pp 31433148, 1995
- [5] F. Murerato, M. Siadat, D. Anciaux, C. Laurent. *Architecture and Control System of a Reptilian Micro-Robot*, 3rd France-Japan & 1st Europe-Asia Congress on Mechatronics, Besancon, France, October 1-3, 1996.
- [6] G. S. Chirikjian and J. W. Burdick. *Kinematics of hyper-redundant locomotion with applications to grasping*. In Proc. IEEE Int. Conf. On Robotics and Automation, p. 720-727, Sacramento, CA, April 1991.
- [7] J. Ostrowski, J. Burdick, A. Lewis, R. Murray. *The Mechanics of Undulatory Locomotion: the Mixed Kinematic and Dynamic Case*, IEEE Int. Conf. On Robotics and Automation, 1995
- [8] JP. Merlet. *Parallel Manipulators: state of art and perspectives*; INRIA Sophia-Antinopolis
- [9] Karl L. Papp, Michael Delwisch, Bernard Klaassen. *GMD-Snake: A Semi-Autonomous-Like Robot*, 3rd International Symposium on Distributed Autonomous Robotic Systems (DARS'96), Riken, Saitama, Japan, Oct. 29-31, 1996
- [10] Lee K-M. et Arjunan S. *A three-degrees-of-freedom micromotion in-parallel actuated manipulator*. IEEE Trans. on Robotics and Automation, 7(5):634-641, Octobre 1991
- [11] Luc Tancredi. *De la simplification et la résolution du modèle géométrique direct des robots parallèles*, Thèse de Doctorat, INRIA Sophia-Antinopolis, 1995
- [12] R. Bosch GmbH. *CAN Specification, version 2.0*, part A, B, Postfach 50, D-7000, Stuttgart 1, 1991
- [13] R.S. Desai, C., J. Rosenberg, J. L. Jones. *Kaa An Autonomous Serpentine Robot Utilizes Behaviour Control*, "IROS '95", vol. 3, pp250-255, Pittsburg, PA, August 6-9, 1995
- [14] Shigeo Hirose. *Biologically Inspired Robots (Snake-like Locomotor and Manipulator)*, Oxford University Press; 1993, ISBN: 0 19 856261 6
- [15] T. Lee, T. Ohm. and S. Hayati. *A Highly Redundant Robot System for Inspection*, Proceedings of the Conference on Intelligent Robotics in the Field, Factory, Service and Space "CIRFFSS '94", Huston, Texas, March 21-24, 1994, pp. 142-149
- [16] W. Henning, F. Hickman and H. Choset. *Motion Planning for Serpentine Robots*, "ASCE" Space and Robotics, Albuquerque, New Mexico, 1998
- [17] W. Oleksiuk. *An electric linear actuator-design and investigations*. 4th International Conference "Dynamics and Machine Aggregates", pp. 99-101, Bratislava-Gabcikovo, 1998

A Comparison of Controller Performance for an Autonomous Underwater Vehicle

Ching-Chaw Chiok, Hariharan Krishnan and Chee-Leong Teo
Department of Mechanical and Production Engineering
National University of Singapore
Singapore 119260
Email: engp7494@leonis.nus.edu.sg

Abstract

In this paper, we study the performance of various controllers designed for an Autonomous Underwater Vehicle (AUV). A particular AUV is chosen as a base model for controller design and comparison. Three different controllers are designed to control the speed, the direction heading and the depth of the AUV: PD controller, feedback linearization controller (FBLN) and sliding mode controller (SMC). Computer simulations are carried out to evaluate the performance of the various controllers. Disturbances and parametric uncertainties are introduced to determine the robustness of each of the controllers

1. Introduction

Many researchers have studied the modelling and controller design for Autonomous Underwater Vehicles (AUVs). In [1], [2], [3] (and the references therein), many controller designs have been proposed for AUVs and the performance and robustness of the controllers have been studied. We will not review all the control design methods for the AUVs here and refer the reader to the reference [1], [2], [3] and the references in those papers. In this paper, we compare the performance and robustness of three well known controller design methods: PD controller, Feedback Linearization controller and Sliding Mode controller for an AUV. The controllers are designed to control the speed, the heading angle and the depth of the AUV. Computer simulations are carried out to verify the performance of these various control design methods for an AUV.

2. Dynamic Modelling of an AUV

The dynamic model of an AUV is nonlinear due to rigid body coupling and the complex hydrodynamics associated with underwater operation. The inclusion of terms such as added mass is an important feature of an AUV model since it moves in water. The equations of motion can be derived using Newton's 2nd law and Euler's law of angular momentum.

In accordance to SNAME nomenclature [2], we define

$$\eta = \begin{bmatrix} \eta_1 \\ \eta_2 \end{bmatrix} = \begin{bmatrix} x \\ y \\ z \\ \phi \\ \theta \\ \psi \end{bmatrix} \quad \text{and} \quad v = \begin{bmatrix} v_1 \\ v_2 \end{bmatrix} = \begin{bmatrix} u \\ v \\ w \\ p \\ q \\ r \end{bmatrix}$$

where η is the linear and angular position vector, and v is the velocity vector expressed in a body fixed frame respectively (See Figure 1). The 6 DOF dynamics can be written in compact matrix form as [2]:

$$M\dot{v} + C(\dot{v}, v) + D(v) + g(\eta) = P\tau, \quad (1)$$

where $M \in \mathbb{R}^{6 \times 6}$ is the symmetric and positive definite inertia matrix which includes the added mass, vectors $C, D, g \in \mathbb{R}^{6 \times 1}$ represent centripetal and Coriolis, damping, gravity and buoyancy respectively, $P \in \mathbb{R}^{6 \times m}$ and $\tau \in \mathbb{R}^{m \times 1}$ represents the control inputs of the AUV.

The vehicle's path relative to the earth-fixed coordinate system is given by a velocity transformation [2]

$$\dot{\eta} = J(\eta_2)v, \quad (2)$$

where $J(\bullet)$ is the Jacobian matrix.

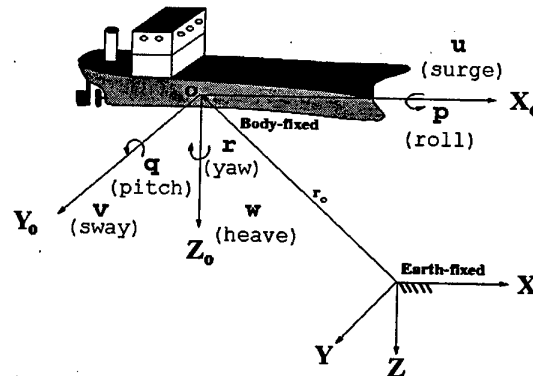


Figure 1: Body-fixed and earth-fixed reference frames.

These 12 equations form the dynamic model of an AUV. The interested reader is referred to [2] for more details on the modelling aspect of an AUV.

3. Simplified Decoupled System

In our study, we use the Naval Postgraduate School AUV II as an example [1] (See Fig.2). The model of the NPS AUV II is the form described by (1) and (2). The value of the model parameters of the AUV II can be obtained from [1]. These equations of motion are modified further in [4].

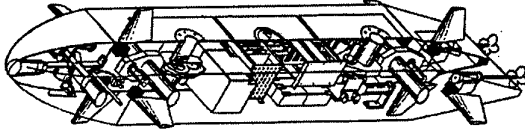


Figure 2: Schematics of the NPS AUV II.

As with current practice in submarine control, the dynamic equations of motion of an AUV can be decoupled into 3 lightly or non-interacting subsystems [1]. This assumption holds true as the shape of the hull of the AUV II is streamlined. Three controllers are designed for the following 3 subsystems:

1. Speed (surge velocity) controller which uses u as the state
2. Direction heading control is determined by the 3 states consisting of v, r, ψ
3. Depth controller makes use of 3 states q, θ, z .

The external control inputs for each of the 3 subsystems are the propeller speed n , the angle of deflection of the rudder δ_r , and the angle of deflection of stern planes δ_s , respectively. These inputs are represented by the vector

$$\tau = [n \quad \delta_r \quad \delta_s]^T. \quad (3)$$

The roll mode is left to be passive.

The equations of motion being used are given next. The interested reader is referred to [1] and [2] for the nomenclature used and the parameter values of the variables.

For speed control, we make use of the surge equation of motion given by [1]

$$(m - \frac{\rho}{2} L^3 X'_u) \dot{u} = \frac{\rho}{2} L^2 u^2 C_{d0} \left[\left(0.012 \frac{n}{u} \right) \left(0.012 \frac{n}{u} \right) - 1 \right]. \quad (4)$$

The equations of motion used to determine the control for direction heading are [1]

$$m[\dot{v} + x_G \dot{r} - y_G r^2] = \frac{\rho}{2} L^4 [Y'_r \dot{r}] + \frac{\rho}{2} L^3 [Y'_v \dot{v} + Y'_r u_0 r] + \frac{\rho}{2} L^2 [Y'_v u_0 v + Y'_{\delta_r} u_0^2 \delta_r] \quad (5)$$

$$I_z \dot{r} + m[x_G(\dot{v} + u_0 r) - y_G(\dot{u}_0 - vr)] = \frac{\rho}{2} L^5 [N'_r \dot{r}] \quad (6)$$

$$+ \frac{\rho}{2} L^4 [N'_v \dot{v} + N'_r u_0 r] + \frac{\rho}{2} L^3 [N'_v u_0 v + N'_{\delta_r} u_0^2 \delta_r] \quad (7)$$

$$\dot{\psi} = r.$$

The 4 equations of motion that are used for the design for the depth controller are [1]

$$m[\dot{w} - u_0 q - x_G \dot{q} - z_G q^2] = \frac{\rho}{2} L^4 [Z'_q \dot{q}] + \frac{\rho}{2} L^3 [Z'_w \dot{w} + Z'_q u_0 q] + \frac{\rho}{2} L^2 [Z'_w u_0 w + u_0^2 (Z'_{\delta_s} \delta_s)] + (W - B) \cos \theta_0 \quad (8)$$

$$I_y \dot{q} - m[x_G(\dot{w} - u_0 q) - z_G(\dot{u}_0 + wq)] = \frac{\rho}{2} L^5 [M'_q \dot{q}] + \frac{\rho}{2} L^4 [M'_w \dot{w} + M'_{uq} u_0 q] + \frac{\rho}{2} L^3 [M'_{ww} u_0 w + u_0^2 (M'_{\delta_s} \delta_s)] - (x_G W - x_B B) \cos \theta_0 - (z_G W - z_B B) \sin \theta_0 \quad (9)$$

$$\dot{\theta} = q \quad (10)$$

$$\dot{z} = -u_0 \sin \theta_0 + w \cos \theta_0. \quad (11)$$

4. Controller Design

For the controller design, we assume that all states are observable and full state feedback is possible.

4.1 PD Controller

From (4), setting $\dot{u} = 0$ gives $u^2 \propto n^2$ at steady-state condition. Therefore, it is found that the propeller speed, n , and the surge velocity are linearly related. In order to design a speed controller, we consider a first order linearization of (4) at operating points n_d and u_d .

A speed controller consisting of a pure P-controller with a feedforward term is proposed. This feedforward term makes use of the knowledge of the linear relationship between propeller speed and surge velocity, while the P-controller is used to reduce the steady state error to zero asymptotically. Therefore, the control law is $n = K_1 n_d + K_{1P}(u - u_d)$, (12)

where n_d is the desired propeller speed related to desired surge velocity u_d , K_1 is the proportional constant, K_{1P} is the proportional constant that has to be chosen carefully to exponentially stabilize (4) so as to reduce the steady state speed error asymptotically to zero.

The direction heading and depth control utilize the linearized equations of motion based on (5)-(7), linearized about the desired surge velocity $u = u_d = 1.0 \text{ m/s}$, while the other equilibrium states are at zero. We propose a rudder controller which is a simple PD controller. Treating the sway velocity v , as negligible, the controller is given by

$$\delta_r = K_{2P}(\psi_d - \psi) + K_{2D}(r_d - r), \quad (13)$$

where ψ_d and r_d are the desired heading and angular yaw rate respectively. Both K_{2P} and K_{2D} are chosen for performance and to ensure exponential stability of the system (5)-(7).

Similarly, the depth controller makes use of the state equations (8)-(11). It should be noted that the heave velocity w , is ignored as simulations have shown it to be negligible. Based on the linearization of (9)-(11), we

propose a depth controller with the control law given by $\delta s = K_{3P}(\theta_d - \theta) + K_{3D}(q_d - q) + G_3(z_d - z)$, (14)

where the constants K_{3P}, K_{3D}, G_3 are chosen to ensure closed-loop stability of the system (8)-(11). The first 2 terms in the controller (14) exponentially control the pitch angle to zero while the last term is used to achieve the asymptotic convergence to the desired depth z_d .

4.2 Feedback Linearization Controller

Consider a simplified system where

$$\dot{\eta} = v \quad (15)$$

$$m\dot{v} + h = \tau \quad (16)$$

Note that in equation (15), v is the velocity of the state to be controlled. The nonlinearities in " h " can be cancelled out by the choice of a suitable control law

$$\tau = m\dot{a}_v + h, \quad (17)$$

which leads to a linear closed-loop system given by

$$\dot{\eta} = v \quad (18)$$

$$\dot{v} = a_v. \quad (19)$$

The commanded acceleration a_v can be selected to be of the form

$$a_v = \dot{v}_d - \lambda_1(v - v_d) - \lambda_2(\eta - \eta_d), \quad (20)$$

where v_d is the desired velocity, η_d is the desired state (position), which gives us the closed-loop system given by

$$\ddot{e} + \lambda_1\dot{e} + \lambda_2e = 0 \quad (21)$$

where $e = \eta - \eta_d$. Note that $\lambda_1, \lambda_2 > 0$ ensures exponential convergence of $e(t)$ to zero.

For speed control, we use (4), which is a special form of (15)-(16). The speed control is chosen similar to the control law (17) where the commanded acceleration is chosen as

$$a_u = \dot{u}_d - \lambda_u(u - u_d), \quad (22)$$

where u_d is the desired speed for the AUV. This results in a closed-loop system given by

$$\dot{u} - \dot{u}_d + \lambda_u(u - u_d) = 0. \quad (23)$$

Thus, if $\lambda_u > 0$, we have exponential convergence of the speed $u(t)$ to the desired speed $u_d(t)$.

For direction heading, we used equations (6)-(7), which are of the same form as (15)-(16). The heading angle controller is chosen similar to the control for (17), where the commanded acceleration is chosen as

$$a_\psi = \dot{\psi}_d - \lambda_{r1}(r - r_d) - \lambda_{r2}(\psi - \psi_d) \quad (24)$$

where ψ_d is the desired heading angle and r_d is the desired heading angle rate.

This results in a closed-loop system given by

$$(\dot{r}_d - \dot{r}) + \lambda_{r1}(r - r_d) + \lambda_{r2}(\psi - \psi_d) = 0. \quad (25)$$

Thus if $\lambda_{r1}, \lambda_{r2} > 0$, we have exponential convergence of the heading angle $\psi(t)$ to the desired heading angle

$\psi_d(t)$.

In order to design the depth controller, we consider equations (9)-(11). Notice that the depth controller is designed in 2 steps. Firstly, we design a pitch controller and secondly, we add an outer loop proportional controller for depth controller.

To devise the pitch controller, we use (9)-(10), which is of the form as (15)-(16). The pitch control law is chosen similar to the form given by (17) where the commanded acceleration is chosen as

$$a_\theta = \dot{\theta}_d - \lambda_{\theta1}(q - q_d) - \lambda_{\theta2}(\theta - \theta_d), \quad (26)$$

where θ_d is the desired pitch angle and q_d is the desired pitch angular rate.

This control law would result in a closed-loop system given by

$$(\dot{q}_d - \dot{q}) + \lambda_{\theta1}(q - q_d) + \lambda_{\theta2}(\theta - \theta_d) \quad (27)$$

Thus if $\lambda_{\theta1}, \lambda_{\theta2} > 0$, we have exponential convergence of the pitch angle $\theta(t)$ to the desired pitch angle $\theta_d(t)$.

Now to control the depth, we have to modify (26) to include an outer loop proportional controller for depth control. Thus for depth control, we modify (26) as

$$a_z = \dot{q}_d - \lambda_{\theta1}(q - q_d) - \lambda_{\theta2}(\theta - \theta_d) - G_\theta(z - z_d) \quad (28)$$

where z_d is the desired depth. Appropriate values of

$\lambda_{\theta1}, \lambda_{\theta2}$ and G_θ are then chosen to guarantee good performance of the closed-loop system with the controller given above.

4.3 Sliding Mode Controller

The approach from [1] is used here for the design of the SMC. The nonlinear system described by the equations that corresponds to each sub-system, i.e. (4), (5)-(7) and (8)-(11), can be rewritten as

$$\dot{x} = Ax + bu + f(x) \quad (29)$$

The first 2 terms of (29) form the linear part while the last term contains the nonlinearities. The linearized equations of motion at operating point corresponding to $u_d = 1.0 \text{ m/s}$, are used to select the sliding surfaces.

In the design for a SMC, we need to define sliding surfaces in state error space. Let this error be denoted by $\tilde{x} = x - x_d$. The sliding surfaces are then given by $\sigma = s^T \tilde{x}$. Global asymptotic stability of the sliding surface dynamics can be guaranteed through defining a Lyapunov function such that

$$V(\sigma(t)) = \frac{1}{2} \sigma^T \sigma. \quad (30)$$

Since $V(\sigma)$ is positive definite and unbounded, global asymptotic stability of $\sigma(t)$ can be assured if

$$\dot{V}(\sigma) = \dot{\sigma}^T \sigma < 0 \quad (31)$$

The control law of each of the sub-systems (i.e. corresponding to (4), (5)-(7) or (8)-(11)) is chosen to be of the form

$$u = \hat{u} + \bar{u}. \quad (32)$$

The nominal control is chosen as

$$\hat{u} = -kx \quad (33)$$

and \bar{u} is the sliding control law which is determined next. If the pair (A, b) is controllable, substituting equation (33) into (29) gives

$$\dot{x} = A_C x + b\bar{u} + f(x) \quad (34)$$

where $A_C = A - bk$. Premultiplying (34) by s^T and

subtracting $s^T \dot{x}_d$ from both sides, we get

$$\dot{\sigma} = s^T A_C x + s^T b \bar{u} + s^T f(x) - s^T \dot{x}_d. \quad (35)$$

If $s^T b$ is invertible, choosing

$$\bar{u} = (s^T b)^{-1} [s^T \dot{x}_d - s^T \hat{f}(x) - \eta \operatorname{sgn} \sigma], \quad (36)$$

where $\hat{f}(x)$ is the best estimates for the nonlinearities and uncertainties, yields

$$\dot{\sigma} = s^T A_C x - \eta \operatorname{sgn} \sigma + s^T \Delta f(x), \quad (37)$$

where $\Delta f(x) = f(x) - \hat{f}(x)$.

The choice of σ can now be determined. If the vector $s \in \mathbb{R}^3$ is the left eigenvector of the closed-loop dynamics A_C such that $s^T [A_C] = 0$, equation (37) can be simplified as

$$\dot{\sigma} = -\eta \operatorname{sgn}(\sigma) + s^T \Delta f(x). \quad (38)$$

This is possible if the gain vector k is chosen to place the closed-loop eigenvalues of the matrix A_C at $\lambda_1 = 0$, λ_2 and λ_3 are arbitrarily selected based on performance requirements. Substituting (38) into (31) yields

$$\begin{aligned} \dot{V} &= \dot{\sigma} \sigma = -\eta \sigma \operatorname{sgn}(\sigma) + \sigma s^T \Delta f(x) \\ &= -\eta |\sigma| + \sigma s^T \Delta f(x). \end{aligned} \quad (39)$$

Thus, if η is chosen "large" enough, which implies $\dot{V} < 0$, we can be assured of global asymptotic stability while overcoming the nonlinearities and uncertainties represented by the second term on the RHS of (38). Details of the above formulation can be found in [2].

The implementation of the discontinuous switching control $\operatorname{sgn}(\sigma)$ results in chattering. In practice, this is undesirable since it involves a high amount of control activity and may excite unmodeled high frequency dynamics. To achieve smoother switching, a suitably selected value of (Φ) , known as the "boundary layer", can be added. The modified switching law is given by the saturation function $\operatorname{sat}(\sigma/\Phi)$ such that

$$\operatorname{sat}(\sigma/\Phi) = \begin{cases} \operatorname{sgn}(\sigma) & \text{if } |\sigma/\Phi| > 1 \\ \sigma/\Phi & \text{otherwise} \end{cases} \quad (40)$$

This reduces tracking precision, but improves robustness by increasing the bandwidth of the system and reduces the effects of chattering [2]. In this paper, we follow [1] in using the $\tanh(\sigma/\Phi)$ functions for the switching control

instead of the saturation function $\operatorname{sat}(\sigma/\Phi)$ to reduce chattering.

5. Simulation Results

The controllers are designed based on a constant speed which is at $u_d = 1.0 \text{ m/s}$ and by making use of the parameter values of the NPS AUV II given in [1]. We consider these values to form the "nominal" model of the AUV. Parametric uncertainties are introduced by 50% changes in the values of the hydrodynamic derivatives. This is because hydrodynamic derivatives are the most difficult to obtain accurately and thus contribute to the highest possibility of errors in modelling any AUV.

External disturbances are introduced which represent translational sinusoidal waves with respect to the global fixed frame and transformed to the body fixed frame as an additional velocity vector.

Computer simulations are carried out using MatlabTM with a sampling time of 0.1 seconds. This is sufficient for our case, as the time constant for the AUV dynamics is large. Source codes were adapted from [5], with extensive modifications to suit our particular simulation needs.

The tracking reference input is generated based on the equation of a cubic polynomial [6]. This is used instead of a step input to prevent saturation of the input efforts and also to provide a reference input which is continuous as time derivatives are needed for the controllers.

The gains for all 3 controllers, that is the PD controller, the feedback linearization controller, and sliding mode controller, have been adjusted such that all the input efforts would be of the same range. This is done so as to make a fair comparison among the 3 different schemes. Representative results from our simulations will be discussed in this section. Each figure shows the surge velocity u in metres per second, the yaw (direction heading) in degrees and the depth Z in metres respectively. The bottom 3 graphs show the propeller speed n in RPM, the rudder and stern planes deflection angles in degrees.

First, with surge velocity at 1.0 m/s , the desired direction heading is commanded from 0° to 20° in 30 seconds and the desired depth is commanded from 0 m to 2 m in 50 seconds. We see from Figure 4 that all 3 controllers have similar performance. As expected, all 3 controllers perform well at this operating condition.

Next, we examine the performance of the controllers under modelling uncertainties. The controller is designed based on the nominal model of the AUV. But for simulation, the model used has a 50% larger value for hydrodynamic parameters. Figure 5 shows the simulation with $u = 1.0 \text{ m/s}$, the desired direction heading changing from 0° to 20° in 30 seconds and the desired depth changing from 0 m to 2 m in 50 seconds. We see that the AUV is stable with all 3 controllers.

For figure 6, a sinusoidal disturbance of low frequency and small amplitude is applied along the Y- and Z-axes to the nominal AUV model so as to simulate environmental disturbances. The operating surge velocity is $u = 2.5 \text{ m/s}$, with the direction heading changing from 0° to 20° in 30 seconds, and the desired depth changing from 0 m to 2 m in 50 seconds.

All 3 controllers, which are designed based on the nominal model, are able to stabilize the AUV to the desired set points. The speed control used in the PD-controller outperforms the other 2 possibly due to the presence of the feedforward term. Both the SMC and FBLN controllers display good overall performance in the other 2 objectives.

From the various responses of the AUV, we can observe some interesting results. The PD controller does not perform as required when the operating surge velocity is significantly higher than $u = 1.0 \text{ m/s}$. The linearization of the nonlinear model is not robust enough to handle a wide range of operating conditions. While for the case of SMC and FBLN, they are robust as their designs are based on the nonlinear model of the AUV, which retain important nonlinear dynamics.

6. Conclusion

The comparisons of the 3 control schemes applied to an AUV have reinforced several points we already know. Using a simple PD controller for a nonlinear plant may give rise to stability problems if the operating condition is far away from the linearized point. The use of FBLN allows the full knowledge of the nonlinear plant to be

used. Together with SMC, the 2 schemes show improved capabilities over the simple PD. Although SMC tends to be more involved while implementing the control law, it has the added advantage of not needing the exact modelling parameters.

7. References

- [1] A J Healey and D Lienard, "Multivariable Sliding Mode Control for Autonomous Diving and Steering of Unmanned Underwater Vehicles", *IEEE J of Oceanic Engineering*, Vol. 18, No. 3, July 1993, pp.327-339
- [2] T I Fossen, *Guidance and Control of Ocean Vehicles*, New York-Wiley, 1994
- [3] J Yuh, "Modeling and Control of Underwater Robotic Vehicles", *IEEE Transactions on Systems, Man and Cybernetics*, Vol. 20, 1990, pp.1475-1483
- [4] D P Brutzman, *A Virtual World for an Autonomous Underwater Vehicle*, PhD Dissertation, NPS, Monterey, California, December 1994. Also available at <http://www.stl.nps.navy.mil/~brutzman/dissertation/>
- [5] Trygve Lauvdal and T I Fossen, *Matlab Simulation Program for Marine and Flight Vehicles*, Department of Engineering Cybernetics, Norwegian U. of Science and Technology, Trondheim, Norway. Available at <http://www.itk.ntnu.no/SIMULATOR/index.html>
- [6] J J Craig, *Introduction to Robotics - Mechanics & Control*, Addison Wesley, 1988

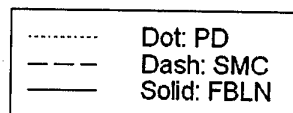


Figure 3: Legend for Figures 4 to 6

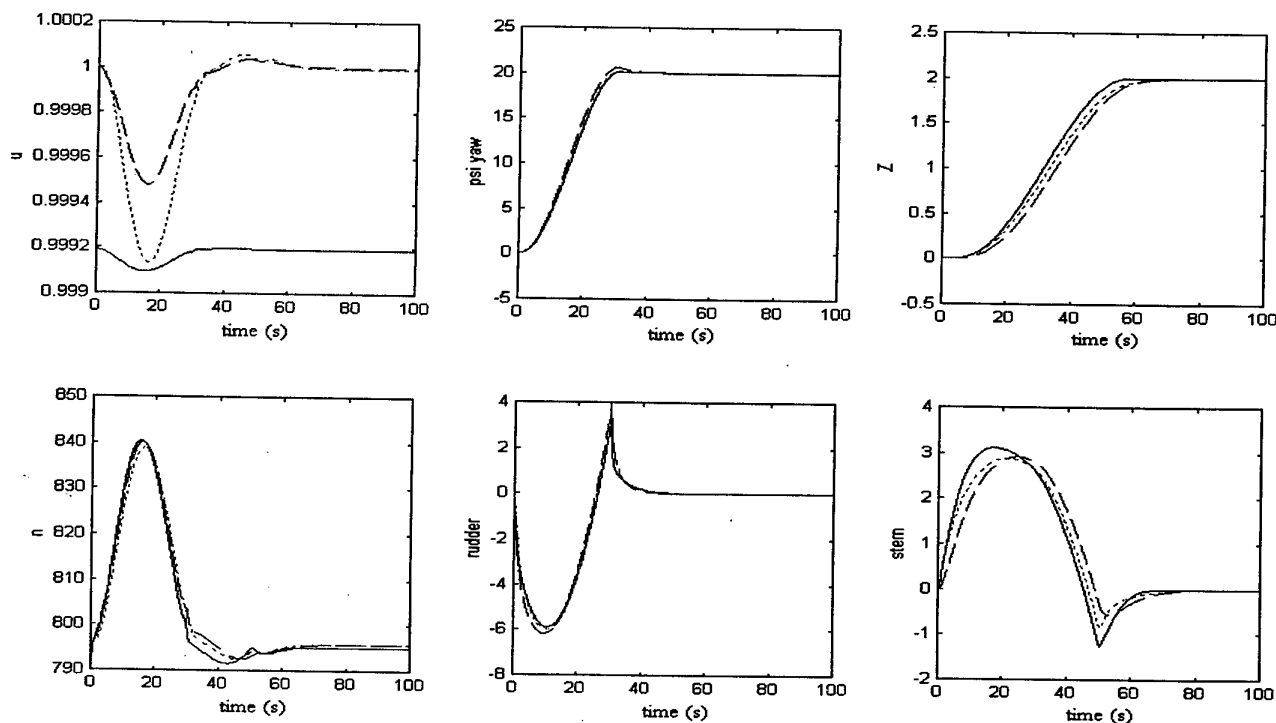


Figure 4 Graph showing response of AUV model, with direction heading from $\psi = 0^\circ$ to $\psi = 20^\circ$ in 30 sec and depth change from $z = 0 \text{ m}$ to $z = 2 \text{ m}$ in 50 sec.

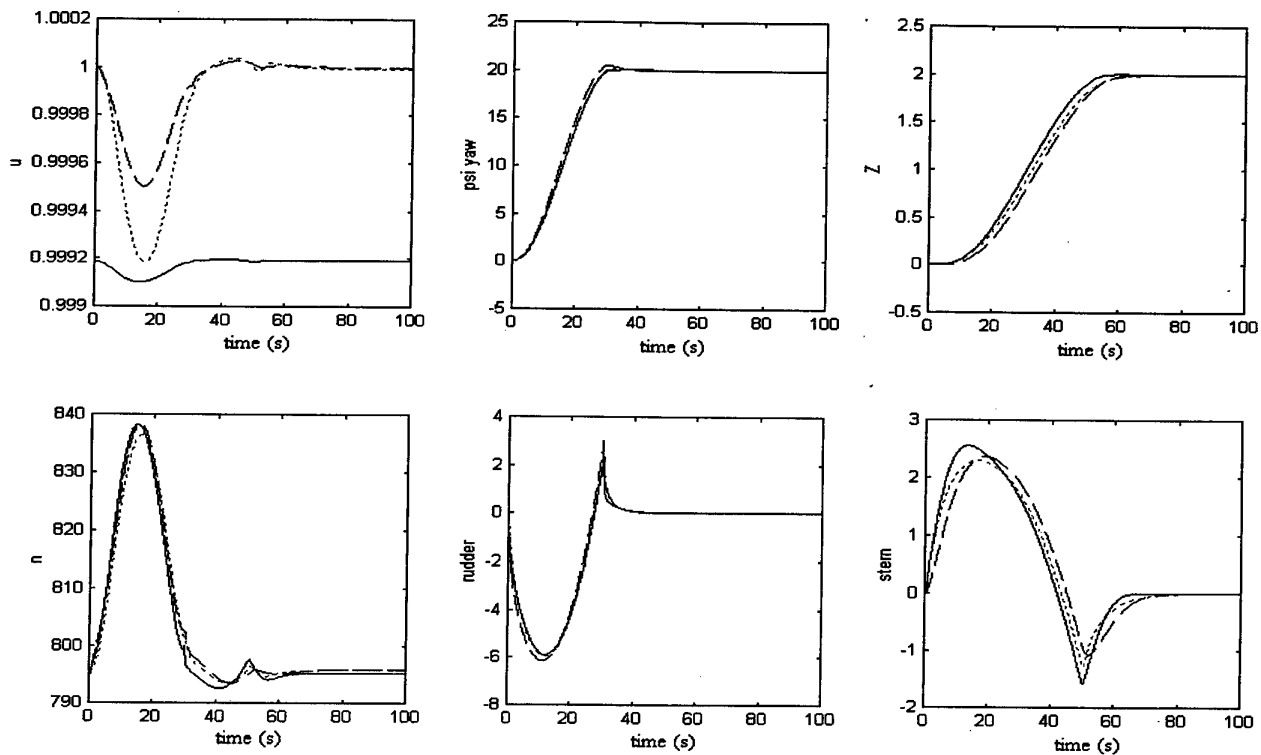


Figure 5 Graph showing response of AUV model in the presence of hydrodynamic parameter uncertainties, with direction heading from $\psi = 0^\circ$ to $\psi = 20^\circ$ in 30 sec and depth change from $z = 0m$ to $z = 2m$ in 50 sec.

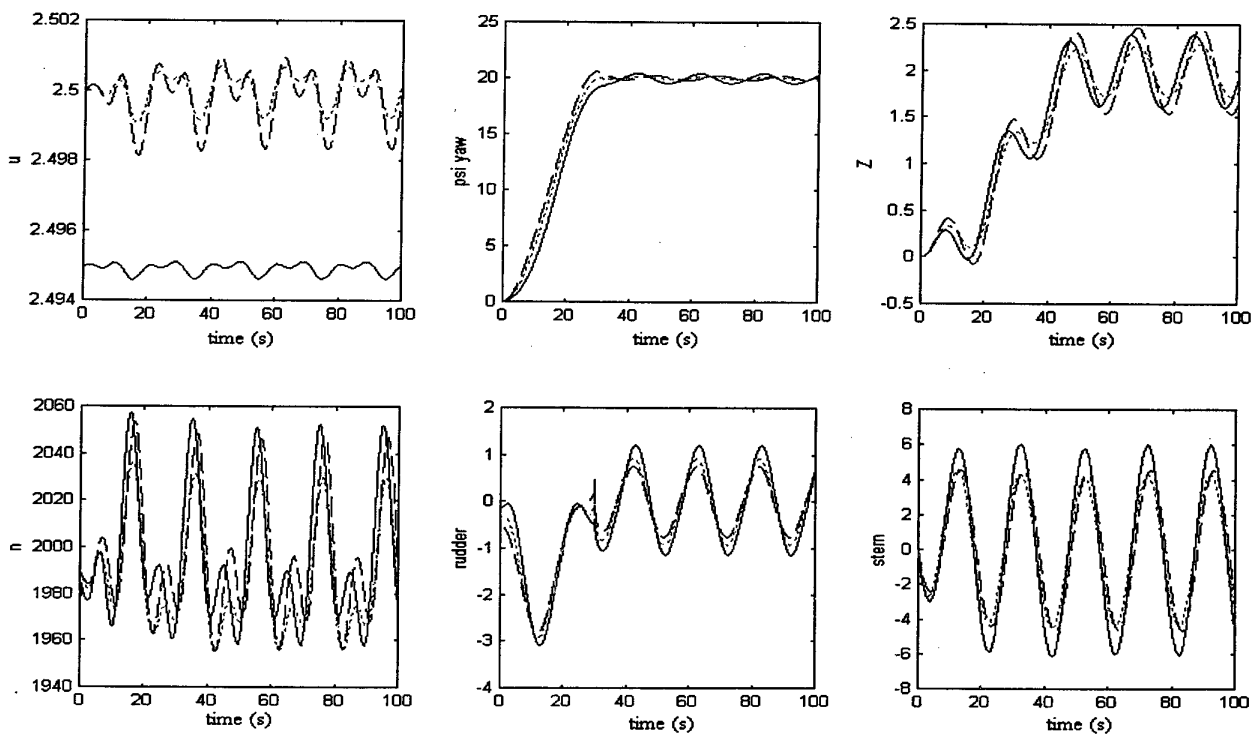


Figure 6 Graph showing response of AUV model under disturbances, with direction heading from $\psi = 0^\circ$ to $\psi = 20^\circ$ in 30 sec and depth change from $z = 0m$ to $z = 2m$ in 50 sec.

A Novel Speed Control Technique for Single-Phase Induction Motor

A.S.ZEIN EL-DIN and A.E.EL-SABBE

Department of Electrical Engineering, Faculty of Engineering, Shebin El-Kom, Egypt,
Tel. (048)221549, Fax.: (048) 235695, e-mail: IN%"et001@shebin.eun.eg".

Abstract

In this paper, a novel speed control of a single phase induction motor is proposed using a modified inverter. Three MOSFETs are used for controlling the flux linkage of a single phase transformer, its secondary winding is connected in series with the motor. On-line Bang-Bang speed control of motor scheme is implemented using a microprocessor to derive the inverter. A mathematical model for the single-phase induction motor is presented, which is used to build up a simulation program for a certain desired speed. Experimental results have been carried out to investigate the motor performance with the controller. Good agreement has been obtained between simulation and experimental results.

Keywords

Microprocessor, Flux linkage, MOSFET, Bang-Bang control, and single-phase induction motor.

1.Introduction

The high-performance inverter technology realizes many new application fields. The dc/ac static inverters permit feeding the complex systems, providing a low rate of harmonic distortion, high efficiency, rapid dynamic response and competitive cost. The great inconvenience found in these inverters lies in the great power dissipation during turn on and turn off of the semiconductors, and in turn limiting the inverter frequency. This problem prevents the reduction of weight, volume and cost for the system as a whole [1-4].

Pulse-Width Modulation (PWM) schemes for dc-ac power conversion have received much attention in the last two decades. Many PWM schemes have been developed and implemented successfully for different applications. Variable-speed induction motor drives have found widespread use of pulse-width modulation inverters. In many applications, a further cost reduction for the drive is an important aspect and, thus, a reduction of the number of power semiconductors in the converter should be a main

consideration [5-6]. In recent years, numerous pulse width modulation pattern generation techniques have been developed for improving the performance [2-7]. When an induction motor fed by a voltage source inverter, the applied stator voltage wave forms contain harmonics generated by the PWM technique and the system stability will be affected by these harmonics especially at low frequencies.

This paper presents a speed control of a single-phase induction motor fed by the proposed inverter. Such a system can be used in the industrial applications, which required smooth variation of speed with high response, also in controlling speed of car vehicles, and robot motion. The proposed systems requires only three MOSFETs and gives an output ac voltage can be controlled in a wide range to give smooth variation of motor speed.

2. System operation and analysis

In this section, the proposed system shown in Fig. 1, is described and analyzed. MOSFETs 1 and 2 transfer the input voltage to the output load (motor) through step-up transformer, which having a rating more than the load rating. MOSFET 3 connected in parallel across the load (transformer primary) to prevent any opposite voltage in the output, either in positive or negative half cycle, also to reduce the output spikes and improving the output voltage V_L . The MOSFETs switching are controlled by using PWM technique. The driver circuits (shown in Fig.2) are feeding from a microprocessor to arrange the switching process, according to the reference control voltage (Ref) and feed back signal from the motor speed (N) through a tachogenerator. MOSFET 3 is switched on if and only if either MOSFET 1 or MOSFET 2 is turned off to prevent the opposite voltage due to the load inductance (transformer and motor).

A square wave signal with 50 Hz to the microprocessor is used to achieve synchronization between the MOSFETs pulses and the applied voltage to the motor. This circuit is used if an ac supply exists to recognize the frequency of the

waveform of the output voltage, but, in case of the absence of the ac supply, a timer is used to achieve a fixed load voltage frequency. Comparing between reference speed (Ref.) and the motor speed (tachogenerator feed back signal) through summing circuit used to give the error signal e , A/D circuit transfers the error signal e to the microprocessor for arranging the MOSFETs switching. Applying bang-bang control action [6] as follows; if $e > \text{zero}$ hence turn on MOSFETs 1 or 2, depending on positive or negative load voltage, otherwise if $e \leq \text{zero}$ hence turn off MOSFETs 1 or 2.

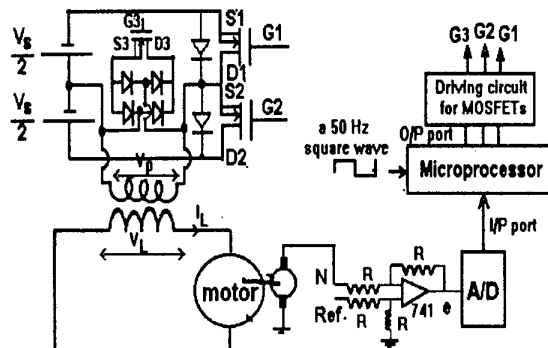


Fig. 1 A schematic diagram of the proposed system

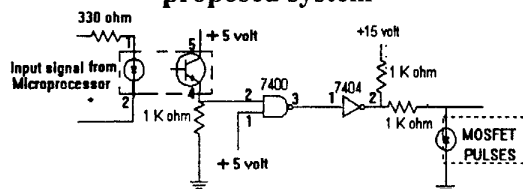


Fig. 2 Driver circuit for MOSFET

3. Motor mathematical model

For running capacitor single phase induction motor, the motor equations in d-q axis (Fig. 3) can be written as follows:[9]

$$V_m = (R_m + L_m \rho) i_m + M \rho i_\alpha$$

$$V_m - V_c = (R_a + L_a \rho) i_a + A_s M \rho i_\beta$$

$$0 = M \rho i_m - A_s M \frac{d\theta}{dt} i_a + (R_r + L_r \rho) i_\alpha - L_r \frac{d\theta}{dt} i_\beta$$

$$0 = M \frac{d\theta}{dt} i_m + A_s M \rho i_a + L_r \frac{d\theta}{dt} i_\alpha + (R_r + L_r \rho) i_\beta$$

$$\text{where } V_c = \frac{1}{c} \int i_a dt$$

The instantaneous electromagnetic torque may be expressed in terms of substitute variables as:

$$T_e = P M (i_\beta i_m - i_\alpha i_a A_s)$$

The equation of motion can be written as follows:

$$J \frac{d\omega_r}{dt} = T_e - T_L - K \omega_r$$

The present model is valid for both steady-state and transient conditions.

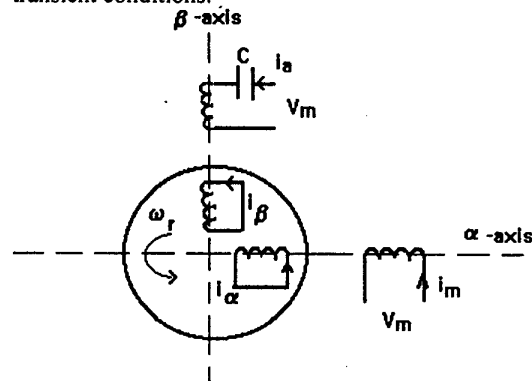


Fig.3 Representation of single-phase induction motor

4. System performance and results

In order to evaluate the performance of the proposed system, dc source used with suitable value and must be free of ripples and accepted recovery power such as car batteries, where the dc voltage supplied inverter has great influence of its operation. An experimental circuit has been built according to Fig. 1 and tested at the laboratory to evaluate the motor performance under different conditions of operation.

For single phase running capacitor induction motor with parameters shown in Appendix (a), two batteries of 12 volt each ($V_s/2$) are used as a dc source, power devices are MOSFETs, type IRFP740. A pulse width modulation control is achieved using microprocessor 8085, and Bang-Bang control technique Algorithm is used, an Assembly program is written and stored in an EPROM interfaced with the microprocessor to achieve that technique. Figures 4-7, show the experimental and simulation waveforms of the motor speed, terminals voltage and current during startup period and steady state interval at reference speed = 1040 r.p.m., the spikes in the experimental waveform may be due to the

motor and transformer inductance. The motor performance under steady state condition is shown in Figs.8-9. When a change in the reference speed is occurred, the motor response is shown in Figs. 10,11. It is noticed that the motor response follows the reference speed. This means that the proposed controller is accurate and smooth on the period of change. Figures 12,13 show the motor response when the load torque is changed by 60 % of full load torque.

5. conclusion

This paper describes a novel method of speed control of an ac motor (single-phase running capacitor induction motor) by adjusting the flux linkage between two magnetic coils using a modified inverter and Bang-Bang control. This strategy influences the effective equivalent inductance of two coils connected in series with the motor, consequently control the motor applied voltage. Simulation and experimental study have shown that, by this method of control the speed of the motor can be changed smoothly from zero value to the rated speed with high response.

6. References

- 1- S.Y.R. Hui, Opperman and S. Sathiakumer, "Microprocessor-Based random PWM schemes for dc-ac power conversion", IEEE Transaction on power electronic, vol. 12, No. 2, March 1997, pp 253-260.
- 2-Michihiko and Koosuke, "inductor commutation soft switched PWM inverter driven by frequency modulated PWM signal", IEEE Transaction on power electronic, vol. 13, No. 1, January 1997, pp 67-74.
- 3-Falconds Jose Mendes De Seixas and Denizar Cruz Martins, "The ZVS-PWM commutation cell applied to dc-ac converter", IEEE Transaction on power electronic, vol. 12, No. 4, July 1997, pp 726-733.
- 4-Frede Blaabjerg, Sigurdur Freysson, Hans- Hernik Hansen and S.Hansen, "A new optimized space vector modulation strategy for a component-minimized voltage source inverter", IEEE Transaction on power electronic, vol.12, No.4, July 1997, pp704-714
- 5-Awad El-sabbe and Ashraf Zein El-Din, "Speed control of a single phase ac motor by using ac voltage regulator", accepted in MEPCON' 98, El-Mansoura -Egypt, 14-16 December 1998

- 6-S.A.Mahmoud, A. S.Zein El-Din and A .E. El-Sabbe, "PLC-Based control of UPS", Accepted in PEMC' 98, Techequ republic, 8-10 September 1998
- 7-J.Marcos Alonson, Cecilio Blanco and Manuel Rico, " Analysis, Design, and optimization of the LCC resonant inverter as a high intensity discharge lamp ballast", IEEE Transaction on power electronic, vol. 13, No. 3, May 1998, pp 573-585.
- 8-David Leggate and Russel J. Kerkman, "Pulse-Based dead-time compensator for PWM voltage inverters", IEEE Transaction on power electronic, vol.14, No.2, April 1997, pp.191-199 [9] A. S.Zein El-Din and A .E. El-Sabbe and S.A.Mahmoud, "A novel ac voltage regulator", IECON98, 24 th Annual conference of the IEEE Industrial Electronics Society, Aachen-Germany, Volume 2/4, August 31-September 4, 1998, pp.607-611
- [10] S.S.Shokralla and A.M.Kinawy, "Perturbation analysis of a single-phase capacitor induction motor in time and frequency domains", Eng. Research bull. Faculty of Eng., Menoufia university, Vol. 16, No.2, pp.179-201, 1993.

7. Appendix (a)

The single phase running capacitor induction motor has :

110 volt. rated voltage., 0.5 amp rated current and 2770 r.p.m. rated speed, $L_s=L_r= 0.25$ H, $R_r=50 \Omega$, $R_c=69.76 \Omega$, $M=0.6$ H, $C=3 \mu F$, and $A_s = 1$
Transformer rated current: 3 amp

Symbols

- A_s : Auxiliary to main winding turns ratio.
 i_a, i_m : Auxiliary and main winding current.
 i_{α}, i_{β} : rotor current in α and β axis;
 J : Moment of inertia in $Kg.m^2$
 L_a, L_m, L_r : Auxiliary, main and rotor winding self inductance.
 M : Main to rotor mutual inductance.
 K : Friction constant.
 P : number of pair poles.
 p : d/dt
 R_a, R_m, R_r : Auxiliary, main and rotor winding resistance.
 T_e : Electromagnetic developed torque.
 T_l : Load torque.
 V_s : Supply voltage
 V_c : capacitor terminal voltage.
 V_m : Amplitude of a.c. Input voltage
 Θ : Electrical angle between stator and rotor.
 ω_r : Motor speed in rad./sec = $d\Theta / dt$

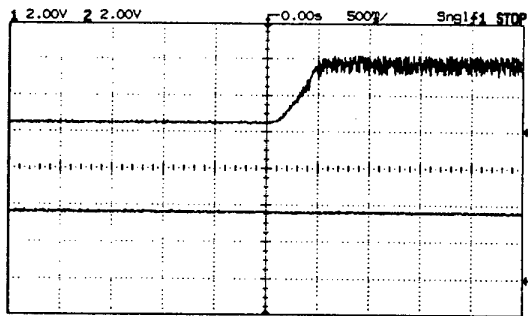


Figure 4 Experimental results of
Ch.1 Motor speed
Ch.2 Reference speed

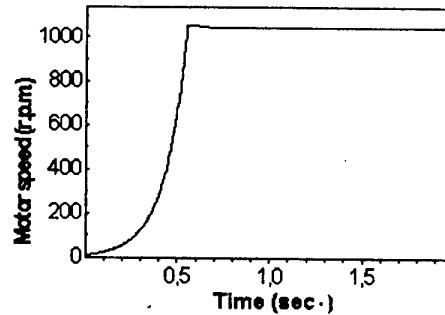


Figure 5 Motor speed (Simulation result)

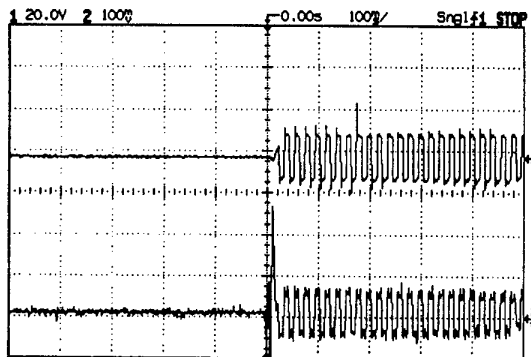


Figure 6 Start up of motor terminal voltage and current (Experimental results)

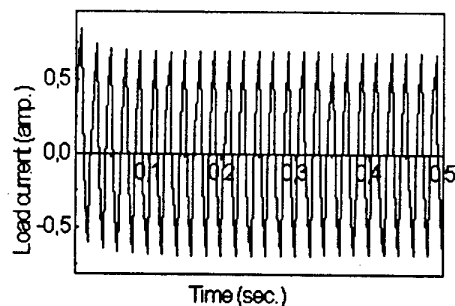
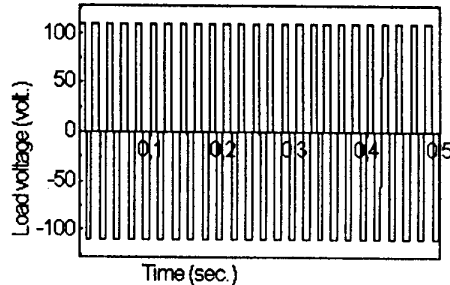


Figure 7 Start up of motor terminal voltage and current (Simulation results)

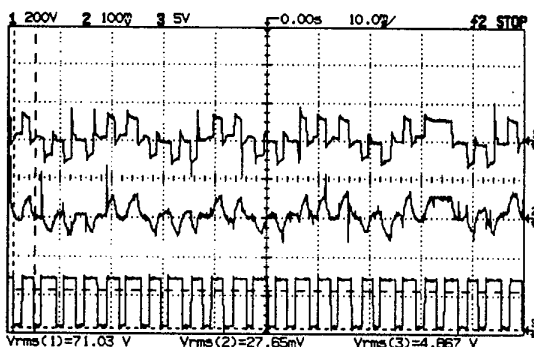


Figure 8 Steady state of motor wave forms (Experimental results)

Ch.1 Motor terminal voltage
Ch.2 Motor current
Ch.3 MOSFET 3 pulses

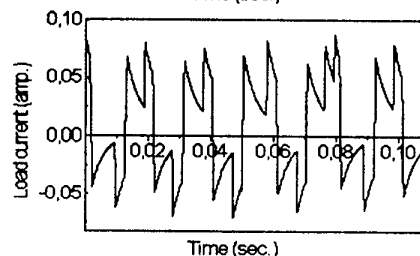
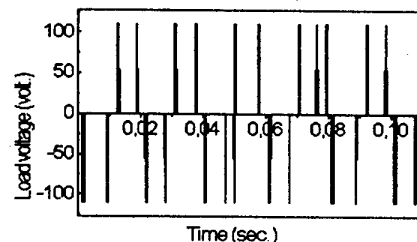


Figure 9 Steady state of motor wave forms (Simulation results)

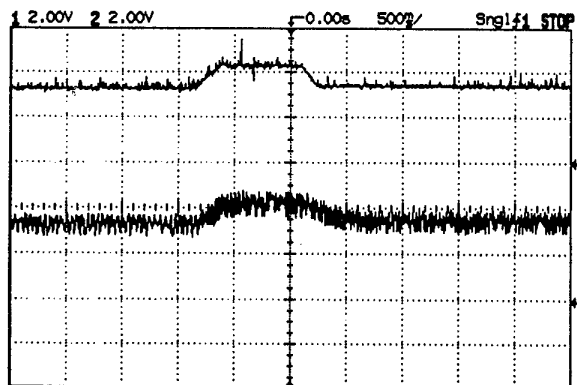


Figure 10 Experimental results (variation of reference speed)

Ch1. Reference speed
Ch2. Motor speed

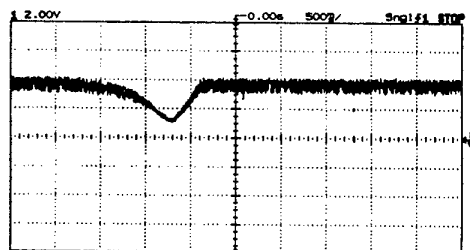
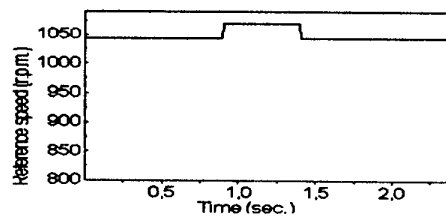
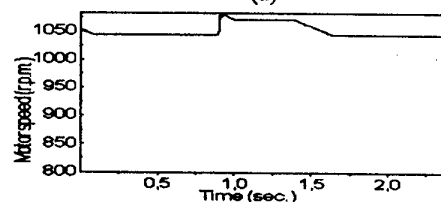


Figure 12 Experimental result of motor speed (variation of load torque)



(a)



(b)

Figure 11 Simulation results (variation of reference speed)

(a) Reference speed
(b) Motor speed

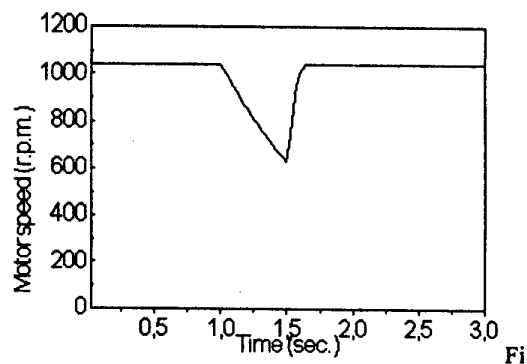


Figure 13 Simulation result of motor speed (variation of load torque)

Design of LMI-based H^∞ servo controller for Cold Tandem Mill

In Soo Kim¹, Yu Shin Chang¹, I Cheol Hwang² and Man Hyung Lee³, and Jong Il Bae⁴

¹Graduate School of Mechanical and Intelligent Systems Engineering, Pusan National University

²Dep't of Mechanical Engineering, Dongeui University

³School of Mechanical Engineering and ERC/Net Shape & Die Manufacturing, P.N.U.

⁴Department of Electrical Engineering, Pukyong National University

¹{iskim1,yschang}@hyowon.cc.pusan.ac.kr

²ichwang@hyomin.dongueui.ac.kr

³mahlee@hyowon.cc.pusan.ac.kr

Abstract

This paper is study on the design of H^∞ servo controller for cold tandem mill, using LMI (Linear Matrix Inequality)-based techniques. The controller improves the performance of AGC(Automatic Gauge Control) system based on Taylor linearized model of cold tandem mill and satisfies robust stability, the restraint of disturbance and robust tracking property. The H^∞ servo control problem is modified as an usual H^∞ control problem, and the solvability condition of H^∞ servo control problem depends on the solvability of modified H^∞ control problem. But this modified problem dose not satisfied standard assumptions for H^∞ control problem, it can be solve by using LMI techniques. Consequently, the comparison of the performance between our H^∞ servo controller and the existing PID/FF(FeedForward) controller shows the usefulness of this study.

1. Introduction

For the improvement of mill product quality in cold rolling process, there has been much research related to the development of AGC system to improve the performance of the existing gauge control system. In especial, the new mathematical models for cold tandem mill and control systems, which are applied with modern control theories, such as optimal control, robust control, etc, have been developed. Recently, there have been many studies on the design of robust H^∞ control system considering interstand interference in cold tandem mill^[1].

An H^∞ control is the method of control design which has a performance index containing uncertainties, such as disturbances, modeling errors occurred from the variation of system parameters or the model approximation. An LMI-based H^∞ control particularly has been researched lately. If the uncertainties are considered as the unstructured form, these are specified to the form of weighting function in frequency domain. The importance

of determining uncertainties has been perceived in the H^∞ control, so the research on identifying mathematical model with input and output data has been achieved briskly.

At first, we analyze the dynamic characteristics of cold tandem mill as a basic procedure of our study. The interrelation between input and output data for model identification and the effect of uncertainties to our system can be determined from the results of these analyses. And then, we determine a mathematical model of cold tandem mill using model identification, based on these dynamic analyses. In our paper, MOESP (MIMO output-error state space model identification) algorithm which is useful to MIMO system identification is applied to construct the mathematical model^[1]. First, a nominal model is identified from input and output data without uncertainties, and then, an uncertain model is identified from input and output data containing uncertainties. The modeling error can be determined by calculating the error between the nominal and the uncertain model. And the maximum singular value plots of both the modeling error and the disturbance are shown in this paper. Finally, stable weighting functions for designing H^∞ servo controller are determined by these maximum singular value plots.

In order to design the H^∞ servo controller which satisfies robust stability, restrain disturbance and has robust tracking property, the H^∞ servo control problem is modified as an usual H^∞ control problem with internal model which contains the mode of reference input model^[3]. But the modified generalized plant in this H^∞ control problem does not satisfy the assumptions of DGKF^{[3],[6]}. Hence, the LMI-based solution to the H^∞ control problem is applied to solve our H^∞ control problem^{[4],[5]}.

This paper consists of four chapters. Chapter 1, an introduction, gives brief reviews of previous study and the purpose of this paper. The dynamics of cold tandem mill and the simulation results are introduced in the chapter 2. Chapter 3 presents the model identification for

2. The dynamic characteristic of TCM

In this chapter, as a basic process of designing the H^∞ servo controller, we analyze the dynamic characteristics of cold rolling process using a computer simulation with some empirical formulas of the TCM. Through this simulation, we grasp the motion of the cold rolling process and determine the relation of input and output signal for model identification of the TCM. The three-stand the TCM considered in this study is shown schematically in Fig. 1.

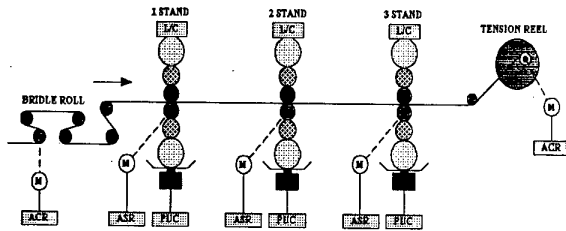


Figure 1. Schematic of three-stand the TCM

Some typical empirical formulas of the TCM used in the simulation for the dynamic analyses are given by

- Rolling force equation (P_i) : Hill's approximation^[7]

$$P_i = k_{pi} Q_{pi} \kappa_i b_i \sqrt{R_{Di} (H_i - h_i)} \quad (1)$$

- Delivery strip thickness (h_i), Back unit tension (τ_{bi})

$$h_i = \frac{P_i}{K_i} + S_i \quad (2)$$

$$\frac{d\tau_{bi}}{dt} = \frac{E}{L_i} \left(\frac{h_i}{H_i} (1 + f_i) V_{Ri} - (1 + f_{i-1}) V_{Ri-1} \right) \quad (3)$$

- Forward slip coefficient (f_i) : Bland & Ford equation^[8]

$$f_i = \frac{R_{Di}}{h_i} \Phi^2 \quad (4)$$

$$\Phi = \sqrt{\frac{h_i}{R_{Di}}} \tan \left(0.5 \sin^{-1} \sqrt{r_i} + \frac{1}{4\mu_i} \sqrt{\frac{h_i}{R_{Di}}} \ln \left(\frac{(1 - \frac{\tau_{bi}}{S_{bi}})(1 - r_i)}{(1 - \frac{\tau_{fi}}{S_{fi}})} \right) \right)$$

The simulation which is composed the empirical formulas of the TCM is essential to the analysis of the dynamic characteristics, such as nonlinearities in rolling process, interstand transport delays, interaction between delivery strip thickness and back-tension. Using this simulation, the interrelation between input and output data for model identification and the effect of uncertainties to TCM can be determined. The set-up values for the TCM for the simulation are shown in Table 1. Input variables are roll gap and roll speed, output variables are delivery strip thickness and back unit

tension. As a result of the simulation, we show the simulation results of the behavior of delivery strip thickness resulted from the variation of roll gap and the occurrence of roll eccentricity. The simulation was carried out in MATLAB.

Table 1. The set-up values for the TCM

	1 STD	2 STD	3 STD
Entry strip thickness(mm)	2.6	2.12	1.57
Delivery strip thickness(mm)	2.12	1.57	1.17
Back unit tension(kgf/mm ²)	2	12.7	17.1
Forward unit tension(kgf/mm ²)	12.7	17.1	10
Work roll radius(mm)	273	273	273

The variations of delivery strip thickness resulted from increase of roll gap to +0.1mm(5% from set-up value) at 0sec and resulted from sinusoidal roll eccentricity of work-roll in the first-stand are shown in Fig. 2 and Fig. 3.

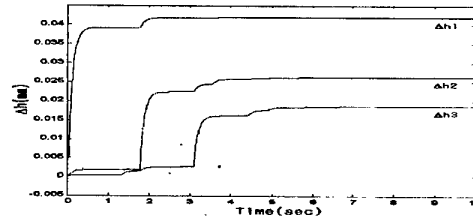


Figure 2. Time response of delivery strip thickness in the each stand

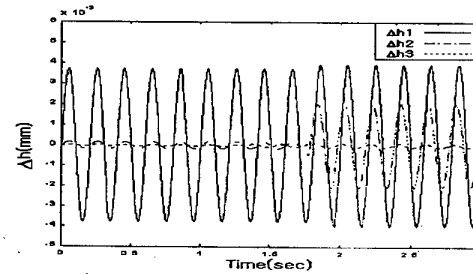


Figure 3. Time response of delivery strip thickness in the each stand

As a result of this simulation, we concluded that the variations of the roll gap, the roll speed and the disturbances(such as the roll eccentricity, the variation of the entry strip thickness, etc) in the first stand affect greatly the delivery strip thickness and back tension in each stand of the TCM.

3. Model identification

In order to construct the mathematical model to design the H^∞ servo controller, we identify the model of the TCM using the MOESP algorithm^[2]. In especial, to obtain the independent model of each stand which has natural properties of the TCM, the model is identified with the input and output data which determined from the dynamic analyses in the chapter 2. The identified model is discrete-time linear time invariant state-space model by

$$\begin{aligned} x(k+1) &= Ax(k) + Bu(k) \\ y(k) &= Cx(k) + Du(k) \end{aligned} \quad (5)$$

The MOESP algorithm is based on subspace model identification. From input and output data, block Hankel matrices are constructed, state-space model A, B, C and D are calculated through the RQ factorization and SVD(Singular Value Decomposition)^[9].

An implementation of the MOESP algorithm is given by

Step 1 : Construct the Hankel matrices Y_k, U_k from the input and output data.

$$Y_k = \begin{bmatrix} y(k) & \cdots & y(k+N-1) \\ y(k+1) & \cdots & y(k+N) \\ \vdots & \ddots & \vdots \\ y(k+i-1) & \cdots & y(k+i+N-2) \end{bmatrix} \quad (6)$$

$$U_k = \begin{bmatrix} u(k) & \cdots & u(k+N-1) \\ u(k+1) & \cdots & u(k+N) \\ \vdots & \ddots & \vdots \\ u(k+i-1) & \cdots & u(k+i+N-2) \end{bmatrix} \quad (7)$$

Step 2 : Achieve the RQ factorization of the block Hankel matrices \hat{Y}_k, U_k

$$\begin{bmatrix} U_k \\ \hat{Y}_k \end{bmatrix} = \begin{bmatrix} R_{11} & 0 \\ R_{21} & R_{22} \end{bmatrix} \begin{bmatrix} Q_1 \\ Q_2 \end{bmatrix} \quad (8)$$

$$R_{11} \in \mathcal{R}^{(m \times m)}, R_{21} \in \mathcal{R}^{(l \times m)}, R_{22} \in \mathcal{R}^{(l \times l)}$$

Step 3 : Compute the SVD of the matrix $R_{22} \in \mathcal{R}^{(l \times l)}$

$$R_{22} = \begin{bmatrix} U_n & U_n^\perp \end{bmatrix} \begin{bmatrix} \Sigma_n & 0 \\ 0 & \Sigma_2 \end{bmatrix} \begin{bmatrix} V_n^T \\ (V_n^\perp)^T \end{bmatrix} \quad (9)$$

$$U_n : (l \times n), U_n^\perp : (l \times (l-n)), \Sigma_n : (n \times n)$$

Step 4 : The system matrices denoted by A, B, C and D can be computed from the following set of equations

$$C = U_n(1:l,:), U_n^{(0)} A = U_n^{(2)}, X_y = X_u \ominus, (\ominus = \begin{bmatrix} D \\ B \end{bmatrix}) \quad (10)$$

$$X_y = \begin{bmatrix} L(:,1:m) \\ L(:,m+1:2m) \\ \vdots \\ L(:,m(i-1)+1:mi) \end{bmatrix}, L = (U_n^\perp)^T R_{21} R_{11}^{-1}$$

$$X_u = \begin{bmatrix} U_n^\perp(1:l,:)^\top & \cdots & U_n^\perp(l(i-1)+1:l,:)^\top \\ U_n^\perp(1+l:2l,:)^\top & \cdots & 0 \\ \vdots & \ddots & \vdots \\ U_n^\perp(l(i-1)+1+l:l,:)^\top & \cdots & 0 \end{bmatrix} \begin{bmatrix} I_l & 0 \\ 0 & U_n^{(0)} \end{bmatrix}$$

where $U_n^{(0)}$ is the submatrix composed of the first $(i-1)l$ rows of the matrix U_n and $U_n^{(2)}$ is the submatrix of the $l+1$ rows to li rows of the matrix U_n .

The delivery strip thickness of the first stand model identified from the input data (the roll gap and roll speed of the first stand) and output data (the delivery strip thickness and back unit tension of the first stand) appears in Fig. 4. A solid line is the delivery strip thickness used to identify model and a dotted line is the delivery strip thickness comes of identified the first stand model. The error between two thicknesses in Fig. 4 is shown in Fig. 5.

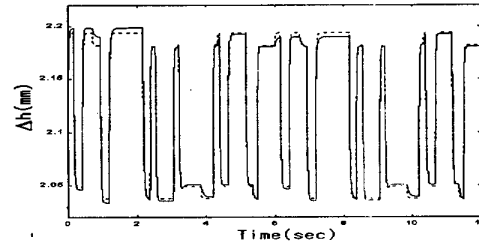


Figure 4. The delivery strip thickness of the identified model.

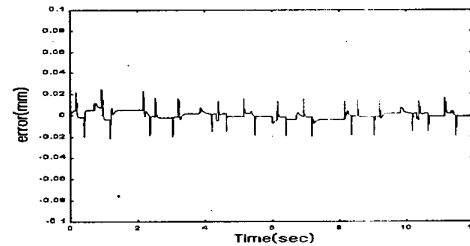


Figure 5. The error of two delivery strip thicknesses.

The identified model(the nominal model) of the first stand is given by

$$\begin{aligned} A &= \begin{bmatrix} 0.9959 & 0.10 \\ 4.745 \times 10^{-3} & 0.8839 \end{bmatrix} & B &= \begin{bmatrix} 3.98 \times 10^{-2} & 1.19 \times 10^{-5} \\ -4.61 \times 10^{-2} & -1.38 \times 10^{-5} \end{bmatrix} \\ C &= \begin{bmatrix} 0.465 & -0.59 \\ 0.534 & 0.462 \end{bmatrix} & D &= \begin{bmatrix} -7.46 \times 10^{-5} & -4.02 \times 10^{-8} \\ -3.42 \times 10^{-7} & -2.3 \times 10^{-10} \end{bmatrix} \end{aligned}$$

The identification of the uncertain model achieves by using the input and output data containing uncertainties, and the modeling error can be determined by calculating the error between the nominal model and the uncertain model. The maximum singular value plot of the

modeling errors (such as the variation of coefficient of friction between roll and strip, the variation of deformation resistance of strip) and the plot of the disturbance (such as the variation of entry strip thickness, roll eccentricity) are shown in Fig. 6 and Fig. 7. In next chapter, stable weighting functions for designing H^∞ servo controller can be determined by these maximum singular value plots.

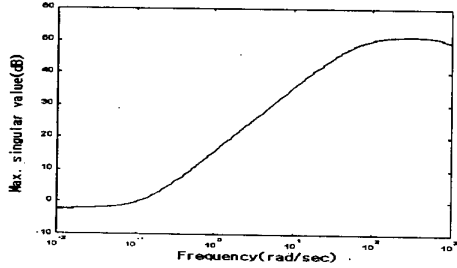


Figure 6. The maximum singular value of the modeling error.

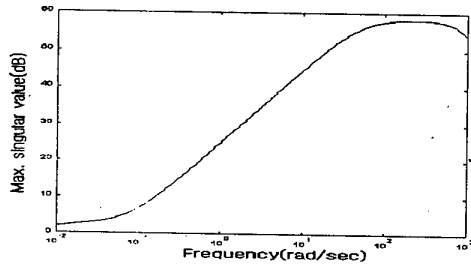


Figure 7. The maximum singular value of the disturbance.

4. H^∞ servo controller for TCM

The H^∞ servo problem for designing the controller which achieves the robust tracking property (the delivery strip thickness robustly tracks the command input, i.e. the given set-up value without steady-state error) is defined as follows^[3].

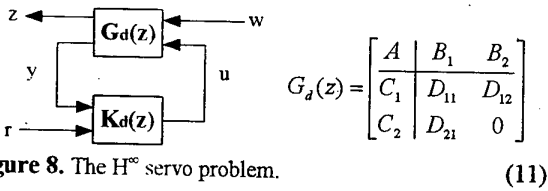


Figure 8. The H^∞ servo problem.

[H^∞ servo problem]

Consider a two degree-of-freedom control system depicted in Fig. 8. For a given generalized plant $G_d(z)$ in (11) and a reference model, find a controller $K_d(z)$

$$u = K_d \begin{bmatrix} r \\ y \end{bmatrix} \quad (12)$$

- (s1) $K_d(z)$ internally stabilizes $G_d(z)$
- (s2) $\|T_{zw}(z)\|_\infty < \gamma$, $T_{zw}(z)$: transfer function from w to z .
- (s3) $K_d(z)$ achieves the robust tracking property for the reference model

$K_d(z)$ denotes the controller to be designed, $w(t) \in \mathbb{R}^1$ denotes the disturbance input, $u(t) \in \mathbb{R}^{m_2}$ denotes the control input, $z(t) \in \mathbb{R}^{p_1}$ denotes the controlled output, $y(t) \in \mathbb{R}^{p_2}$ denotes the measured output, and $r(t) \in \mathbb{R}^{p_2}$ denotes the reference input, respectively.

The H^∞ servo problem is modified as an usual H^∞ control problem with internal model $\Sigma(z)$ which contains the mode of reference input model. In this paper, we consider the case of step reference input, hence we can set $\Sigma(z)$ and the modified generalized plant $\hat{G}_d(z)$ by

$$\Sigma(z) = \begin{bmatrix} I_{p_2} & I_{p_2} \\ I_{p_2} & 0 \end{bmatrix} \quad (13)$$

$$\hat{G}_d = \begin{bmatrix} I_{p_1} & 0 \\ 0 & I_{p_2} \\ 0 & \Sigma \end{bmatrix} G_d = \begin{bmatrix} \hat{A} & \hat{B}_1 & \hat{B}_2 \\ \hat{C}_1 & \hat{D}_{11} & \hat{D}_{12} \\ \hat{C}_2 & \hat{D}_{21} & 0 \end{bmatrix} \quad (14)$$

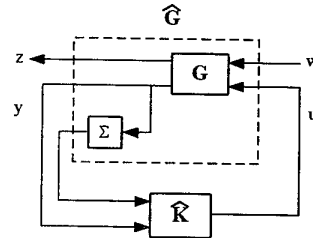


Figure 9. The H^∞ control problem equivalent to the H^∞ servo problem.

Consequently, we will solve the following H^∞ control problem whose solvability is equivalent to the H^∞ servo problem.

[H^∞ control problem]

For a given generalized plant $G_d(z)$ in (11) and a reference input r , construct the modified generalized plant $\hat{G}_d(z)$ in (14). Find a controller $\hat{K}_d(z)$ satisfying the following two specifications

- (p1) $\hat{K}_d(z)$ internally stabilizes $\hat{G}_d(z)$
- (p2) $\|T_{zw}(z)\|_\infty < \gamma$

The modified generalized plant in (14) does not satisfy the assumptions of DGKF^[6], e.g. $\hat{G}_{12}(z)$ has an

imaginary axis zero and \hat{D}_{21} has not full row rank. Hence, the LMI-based solution to the H^∞ control problem is applied to solve our H^∞ control problem in this paper^{[4],[5]}.

[LMI-based H^∞ control]

The set of H^∞ controllers with closed-loop performance γ can be implicitly parameterized by the solutions of the system of LMI. These solutions of LMI play a role analogous to that of the Riccati solutions in ARE-based H^∞ control. For a given discrete-time generalized plant $\hat{G}_d(z)$ in (14) and the performance γ , the discrete-time H^∞ control problem is solvable if and only if there exist two symmetric matrices $R, S \in R^{n \times n}$ satisfying the following system of LMIs.

$$\begin{bmatrix} N_{12} & 0 \\ 0 & I \end{bmatrix}^T \begin{bmatrix} \hat{A}R\hat{A}^T - R & \hat{A}R\hat{C}_1^T \\ \hat{C}_1R\hat{A}^T & -\gamma I + \hat{C}_1R\hat{C}_1^T \end{bmatrix} \begin{bmatrix} \hat{B}_1 \\ \hat{D}_{11} \end{bmatrix} \begin{bmatrix} N_{12} & 0 \\ 0 & I \end{bmatrix} < 0 \quad (15)$$

$$\begin{bmatrix} N_{21} & 0 \\ 0 & I \end{bmatrix}^T \begin{bmatrix} \hat{A}^T S \hat{A} - S & \hat{A}^T S \hat{B}_1 \\ \hat{B}_1^T S \hat{A} & -\gamma I + \hat{B}_1^T S \hat{B}_1 \end{bmatrix} \begin{bmatrix} \hat{C}_1^T \\ \hat{D}_{11}^T \end{bmatrix} \begin{bmatrix} N_{21} & 0 \\ 0 & I \end{bmatrix} < 0 \quad (16)$$

$$\begin{bmatrix} R & I \\ I & S \end{bmatrix} > 0 \quad (17)$$

where N_{12} and N_{21} denote orthonormal bases of the null spaces of (B_2^T, D_{12}^T) and (C_2, D_{21}) .

Given any (R, S) satisfying (15)-(17), a full-order γ -suboptimal controller $K(z) = D_K + C_K(sI - A_K)^{-1}B_K$ is obtained as follows.

Step 1 : Compute any solution D_K of $\lambda > 0$, with λ given by

$$\Delta = \Delta^T := - \begin{bmatrix} -R & 0 & A + B_2 D_K C_2 & B_1 + B_2 D_K D_{21} \\ 0 & -\gamma I & C_1 + D_{12} D_K C_2 & D_{11} + D_{12} D_K D_{21} \\ * & * & -S & 0 \\ * & * & 0 & -\gamma I \end{bmatrix} \quad (18)$$

Step 2 : Compute the least-norm solutions $\begin{pmatrix} \Theta_B \\ * \end{pmatrix}, \begin{pmatrix} \Theta_C \\ * \end{pmatrix}$

of the linear equations

$$\begin{pmatrix} 0 & 0 & 0 & C_2 & D_{21} \\ 0 & & & & \\ 0 & & & & \\ C_2^T & & & & \\ D_{21}^T & & & & \end{pmatrix} \begin{pmatrix} \Theta_B \\ * \end{pmatrix} = - \begin{pmatrix} 0 \\ -I \\ 0 \\ A^T S \\ B_1^T S \end{pmatrix} \quad (19)$$

$$\begin{pmatrix} 0 & B_2^T & D_{12}^T & 0 & 0 \\ B_2 & & & & \\ D_{12} & & -\Delta & & \\ 0 & & & & \\ 0 & & & & \end{pmatrix} \begin{pmatrix} \Theta_C \\ * \end{pmatrix} = - \begin{pmatrix} 0 \\ AR \\ C_1 R \\ -I \\ 0 \end{pmatrix} \quad (20)$$

Step 3 : Factorize $I - RS$ as MN^T , with M and N invertible, and compute A_K, B_K, C_K by solving

$$NB_K = -SB_2 D_K + \Theta_B^T \quad (21)$$

$$C_K M^T = -D_K C_2 R + \Theta_C \quad (22)$$

$$-NA_K M^T = SB_2 \Theta_C + \Theta_B^T C_2 R + S(A - B_2 D_K C_2)R \\ + \begin{pmatrix} -I & \\ 0 & \\ A^T S + C_2^T \Theta_B & \\ B_1^T S + D_{21}^T \Theta_B & \end{pmatrix}^T \Delta^{-1} \begin{pmatrix} AR + B_2 \Theta_C \\ C_1 R + D_{21} \Theta_C \\ -I \\ 0 \end{pmatrix} \quad (23)$$

[Simulation results]

Now, we design the H^∞ servo controller which satisfies robust stability of modeling errors, restrains disturbances and achieves the robust tracking property of the delivery strip thickness. In this paper, we consider only the first stand of the TCM to design the thickness controller. The generalized plant is shown in Fig. 10.

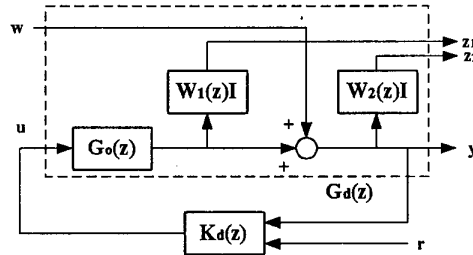


Figure 10. The generalized plant for designing the H^∞ servo controller of the TCM

$$\begin{bmatrix} z_1 \\ z_2 \\ y \end{bmatrix} = \begin{bmatrix} 0 & W_1(z)IG_o(z) \\ W_2(z)I & W_2(z)IG_o(z) \\ I & G_o(z) \end{bmatrix} \begin{bmatrix} w \\ u \end{bmatrix}$$

where $G_o(z)$ is the identified model of the first stand of the TCM, $W_1(z)$, $W_2(z)$ are the weighting functions, and $K_d(z)$ is the H^∞ servo controller to be designed.

The $W_1(z)$, $W_2(z)$ are considered in the form of stable weighting function in frequency domain and determined from Fig. 6 and Fig. 7.

$$W_1(z) = \begin{bmatrix} A_{w1} & B_{w1} \\ C_{w1} & D_{w1} \end{bmatrix} = \begin{bmatrix} 0.905 & 1.0 \\ -0.453 & 4.762 \end{bmatrix}$$

$$W_2(z) = \begin{bmatrix} A_{w2} & B_{w2} \\ C_{w2} & D_{w2} \end{bmatrix} = \begin{bmatrix} 0.986 & 1.0 \\ -0.0453 & 3.2 \end{bmatrix}$$

The comparison of delivery strip thickness controlled the H^∞ servo controller and the PID/FF controller based on the Taylor linearized model is appeared in Fig. 11.

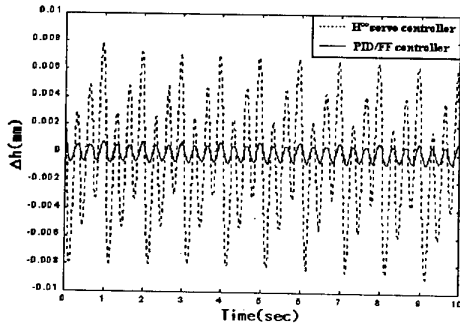


Figure 11. The variation of delivery strip thickness of H^∞ servo controller and PID/FF controller

A dotted and a solid line is respectively the delivery strip thickness resulted from the PID/FF controller and the H^∞ servo controller when the disturbance, the roll eccentricity, occurred in the work-roll of the first stand. The variation of the delivery thickness of H^∞ servo controller is within $\pm 1\mu m$, it shows that the good performance of our H^∞ servo controller in the restraint of disturbance.

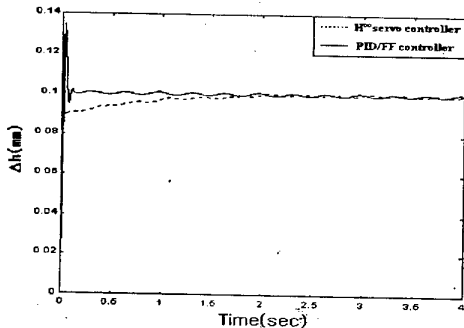


Figure 12. The variation of delivery strip thickness of H^∞ servo controller and PID/FF controller.

Specially, we show the comparison of the tracking performance between the H^∞ servo controller and the PID/FF controller in Fig. 12. For the step reference input of the delivery strip thickness, a dotted and a solid line is respectively the delivery strip thickness of the PID/FF controller and the H^∞ servo controller. As shown in Fig. 12, the steady state error of the output in PID/FF controller does not reduce within $\pm 20\mu m$, but the case of the H^∞ servo controller, the steady state error of the

output is $\pm 8.3\mu m$ and the settling time of the response is 0.12sec.

5. Conclusion

In this paper, we designed the H^∞ servo controller which satisfy the robust stability under the modeling errors, restrain the disturbances and achieve the robust tracking property. The generalized plant in the H^∞ servo controller was modified by the internal model principle, the LMI-based H^∞ control technique was applied to design the H^∞ controller for the modified generalized plant. Consequently, it was shown that the delivery strip thickness robustly tracked the reference input although the modeling errors and disturbances exist.

6. References

- [1] "Special Issue on Control in the Metal Processing Industries," *IEEE Transactions on Control System Technology*, Vol. 6, No. 2, 1998.
- [2] M. Verhaegen and P. Dewilde, "Subspace Model Identification Part1. The Output-Error State-Space Model Identification Class of Algorithm," *International Journal of Control*, Vol. 56, No. 5, pp.1187-1210, 1992.
- [3] J. Hozumi, S. Hara and H. Fujioka, "Robust servo problem with H_∞ norm constraint," *International Journal of Control*, Vol. 66, No. 6, pp.803-823, 1997.
- [4] P. Gahinet, "Explicit Controller Formulas for LMI-based H_∞ Synthesis," *Automatica*, Vol.32, No. 7 pp.1007-1014, 1996.
- [5] P. Gahinet and P. Apkarian, "A Linear Matrix Inequality Approach to H_∞ control," *International Journal of Robust and Nonlinear Control*, Vol. 4, pp.421-448, 1994.
- [6] J. C. Doyle, K. Glover, P. P. Khargonekar and B. A. Francis, "State-Space Solutions to Standard H_2 and H_∞ Control Problems," *IEEE Transactions on Automatic Control*, Vol. 34, No. 8, pp.831-847, 1989.
- [7] R. Hill, "Relations between roll force, torque and the applied tensions in strip rolling," *Proceedings of the Institution of Mechanical Engineers*, Vol. 163, pp. 135-140, 1950.
- [8] D. R. Bland and H. Ford, "The calculation of roll force and torque in cold strip rolling with tensions," *Proceedings of the Institution of Mechanical Engineers*, Vol. 159, pp. 144-163, 1948.
- [9] T. Soderstrom and P. Stoica, *System Identification*, Prentice Hall, 1989.

Intelligent Control of Multiple Mobile Robots Handling a Single Object in Coordination

Kazuhiro Kosuge*, Yasuhisa Hirata*, Manabu Sato*,
Hajime Asama**, Hayato Kaetsu** and Kuniaki Kawabata**

*Department of Machine Intelligence and Systems Engineering, Tohoku University

E-mail:kosuge@irs.mech.tohoku.ac.jp

**Biochemical Systems Laboratory

The Institute of Physical and Chemical Research, RIKEN

Abstract

In this paper, we propose a decentralized motion control algorithm of multiple mobile robots handling an object in coordination like humans. First, we illustrate the principle of the control algorithm using two mobile robots in coordination, and propose a leader-followers type control algorithm for multiple robots using the concept of the "Virtual Leader". Experimental results with omni-directional mobile robots will illustrate the validity of the proposed control algorithm. We then extend the algorithm to nonholonomic mobile robots driven by two wheels by introducing dual caster action to followers. Experimental results using two tracked mobile robots will illustrate how the algorithm works.

1 Introduction

When we would like to transport a large and heavy object, we carry it in cooperation with other people. To utilize multiple robots in coordination is a natural extension of such human behavior to the robots. In this paper, we propose an intelligent decentralized control algorithm of multiple mobile robots handling an object in coordination like humans.

Much research has been already done for the motion control of multiple manipulators handling an object in coordination [1]-[6] etc. However, most of the control algorithms proposed so far have been designed for the centralized control system, that is, a single controller is supposed to control all of the robots in a centralized way. The centralized control system could handle two or three manipulators in coordination, but it is not easy to control many mobile robots in coordination because of its implementation problem and computational burden.

In this paper, we develop a decentralized control algorithm for handling a single object by multiple robots in coordination like humans. The algorithm could be applied to multiple mobile robots in coordination. In the proposed control system, the motion command of the object is given to one of the robots, referred to as a leader. The other robots are referred to as followers. Each follower, which is controlled by its own controller, estimates the motion of the object com-

manded to the leader to transport the object in coordination with the leader. The proposed control algorithm is experimentally applied to omni-directional mobile robots first, and the results illustrate the validity of the proposed control algorithm. The algorithm is also extended to two nonholonomic mobile robots driven by two wheels by introducing dual caster action to the follower. Experimental results using tracked vehicle will illustrate its validity.

2 Principle of Coordination

2.1 Two Robots in Coordination

In this section, we explain the decentralized control algorithm. For the simplicity of explanation, we first consider the case of two autonomous omni-directional mobile robots, each of which has three degrees of freedom of motion. We assume that each robot is controlled by its own controller in a decentralized way. The desired trajectory of the object is given to the leader and the follower estimates the desired motion of the object commanded to the leader.

We assume that each robot has the following dynamics by an appropriate controller as shown in Figure.1.

$$D\Delta\dot{x}_l + K\Delta x_l = f_l - f_l^{in} \quad (1)$$

$$D\Delta\dot{x}_1 + K\Delta x_1 = f_1 - f_1^{in} \quad (2)$$

where $D \in R^{3 \times 3}$ and $K \in R^{3 \times 3}$ are positive definite matrices, $f_l, f_1 \in R^3$ be a forces applied to the robots, $f_l^{in}, f_1^{in} \in R^3$ be a specified internal forces applied to the object by the robots, and $\Delta x_l, \Delta x_1 \in R^3$ be the trajectory deviations of the robots according to the forces applied to the robots. The subscripts l and 1 indicate that the variables with the subscripts are related to the leader and the follower respectively.

Let $x_d, x_{e1} \in R^3$ be the desired trajectories of the leader and the follower respectively and $x \in R^3$ be the real trajectory of the object. Under the assumption that each robot holds the object firmly and no relative motion between the object and each robot occurs, these deviations, Δx_l and Δx_1 , are expressed as follows;

$$\Delta x_l = x - x_d \quad (3)$$

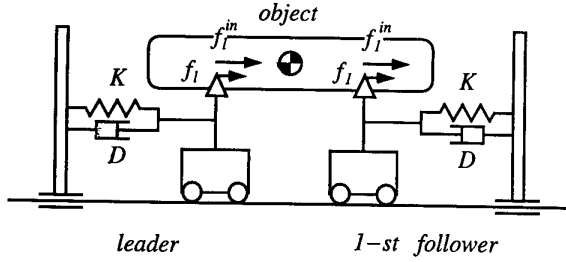


Figure 1: Compliant Motion of Robot

$$\Delta x_1 = x - x_{e1} \quad (4)$$

Under the assumption that the external force applied to the object is negligible, the relationship between Δx_l and Δx_1 is expressed as follows from Eq.(1) and (2);

$$\Delta x_l + \Delta x_1 = 0 \quad (5)$$

Eliminating x from Eq.(3) and (4), we obtain

$$\Delta x_1 - \Delta x_l = x_d - x_{e1} \quad (6)$$

Let Δx_{d1} be the trajectory estimation error of the follower, then, Δx_{d1} is expressed by

$$\Delta x_{d1} = x_d - x_{e1} \quad (7)$$

From Eq.(5), (6) and (7), Δx_{d1} can be written as follows;

$$\Delta x_{d1} = 2\Delta x_1 \quad (8)$$

It should be noted that the follower can calculate Δx_{d1} using the observable variable Δx_1 .

Let us consider how x_d is estimated using Δx_{d1} . Let G_1 be the transfer function, which estimates x_d , as x_{e1} , based on Δx_{d1} as shown in Figure.2(a). From Eq.(7), Figure.2(a) can be rewritten as a feedback system shown in Figure.2(b). To eliminate the steady-state position and velocity estimation errors, the transfer function G_1 is designed as follows;

$$G_1 = \frac{a_1 s + b_1}{s^2} I_3 \quad (9)$$

where $I_3 \in R^{3 \times 3}$ is the identity matrix and a and b are positive real numbers to keep the stability of this feedback system.

2.2 n+1 Robots in Coordination

2.2.1 Forces and Trajectory Deviations

We extend the result in the previous section to a general case. First, we consider the relationship among trajectory deviations. Under the assumption that external force applied to the object is negligible, we have

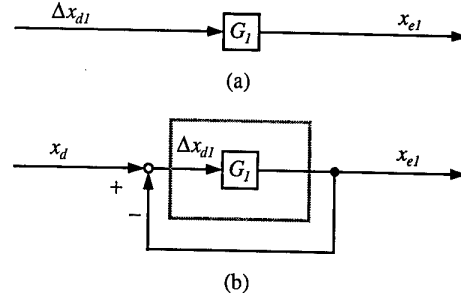


Figure 2: Estimator

the following relations with respect to the forces applied to the object;

$$f_l + \sum_{j=1}^n f_j = 0 \quad (10)$$

$$f_l^{in} + \sum_{j=1}^n f_j^{in} = 0 \quad (11)$$

As time tends to infinity, we obtain the following relationship from (1), (2), (10) and (11), even if the initial value of $\Delta x_l + \sum_{j=1}^n \Delta x_j$ is not zero.

$$\Delta x_l + \sum_{j=1}^n \Delta x_j = 0 \quad (12)$$

2.2.2 Dynamics of Virtual Leader

It is impossible for the i -th follower to estimate the desired trajectory of the leader because the trajectory deviation of the i -th follower, which was used for the estimation of the desired trajectory of the leader in previous case, is affected by motions of all of the robots. Therefore, for the i -th follower, the robots are classified into two groups; one is the i -th follower itself and the other is the rest of the robots including the leader. In this paper, we refer to the rest of the robots as the i -th virtual leader. The i -th virtual leader consists of the leader, and j -th followers

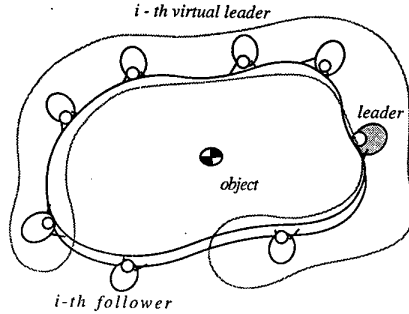


Figure 3: Virtual Leader

($j = 1, \dots, i-1, i+1, \dots, n$) as shown in Figure 3. For the i -th follower, the i -th virtual leader behaves as if it were a real leader. Using the concept of the virtual leader, the i -th follower estimates the desired trajectory of the i -th virtual leader based on the estimation algorithm when two robots handle a single object in coordination.

We can derive the dynamics of the i -th virtual leader as follows;

$$\begin{aligned} D(\Delta \dot{x}_l + \sum_{j=1(j \neq i)}^n \Delta \dot{x}_j) + K(\Delta x_l + \sum_{j=1(j \neq i)}^n \Delta x_j) \\ = (f_l + \sum_{j=1(j \neq i)}^n f_j) - (f_l^{in} + \sum_{j=1(j \neq i)}^n f_j^{in}) \end{aligned} \quad (13)$$

where

$$\sum_{j=1(j \neq i)}^n c_j = \sum_{j=1}^{i-1} c_j + \sum_{j=i+1}^n c_j \quad (14)$$

The trajectory deviation of the i -th virtual leader Δx_{li} is expressed as follows;

$$\Delta x_{li} = \Delta x_l + \sum_{j=1(j \neq i)}^n \Delta x_j \quad (15)$$

As time tends to infinity, we obtain the following relationship, regardless of the desired trajectory given to the leader x_d .

$$\Delta x_{li} + \Delta x_i = 0 \quad (16)$$

The force applied to the i -th virtual leader f_{li} and the internal force applied to the object by the i -th virtual leader, f_{li}^{in} , are expressed as follows;

$$f_{li} = f_l + \sum_{j=1(j \neq i)}^n f_j \quad (17)$$

$$f_{li}^{in} = f_l^{in} + \sum_{j=1(j \neq i)}^n f_j^{in} \quad (18)$$

From (10) and (11), we also have

$$f_{li} + f_i = 0 \quad (19)$$

$$f_{li}^{in} + f_i^{in} = 0 \quad (20)$$

From (15), (17) and (18), (13) is rewritten as

$$D\Delta \dot{x}_{li} + K\Delta x_{li} = f_{li} - f_{li}^{in} \quad (21)$$

It should be noted that (21) expresses the behavior of the i -th virtual leader.

Let x_{di} be the desired trajectory of the i -th virtual leader. Then, Δx_{li} is expressed as

$$\Delta x_{li} = x - x_{di} \quad (22)$$

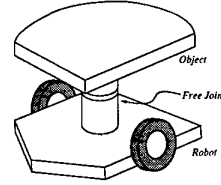


Figure 4: Free joint

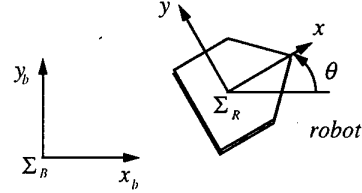


Figure 5: Coordinate system

From (15) and (22), x_{di} is written as

$$x_{di} = x_d - \sum_{j=1(j \neq i)}^n \Delta x_j \quad (23)$$

2.2.3 Estimation

Using the concept of virtual leader, the i -th follower can estimate the desired trajectory of the i -th virtual leader x_{di} based on the estimation algorithm which we discussed in the previous section, because (21) and (22) have the form as (1) and (3).

We define Δx_{di} as the estimation error of the i -th virtual leader estimated by the follower. Δx_{di} is expressed as

$$\begin{aligned} \Delta x_{di} &= x_{di} - x_{ei} \\ &= 2\Delta x_i \end{aligned} \quad (24)$$

It should be noted that Δx_{di} is calculated by each follower based on the observable state of each follower Δx_i . Using this Δx_{di} and the transfer function matrix G_i which we design in previous section, the i -th follower can estimate the desired trajectory of the i -th virtual leader as follows;

$$X_{ei} = G_i \Delta X_{di} \quad (25)$$

We design the transfer function matrix G_i similar to the case of previous section. The transfer function matrix G_i is expressed as follows;

$$G_i = \frac{a_i s + b_i}{s^2} I_3 \quad (26)$$

3 Extension to Mobile Robots Driven by Two Wheels

The decentralized control algorithm discussed in the previous sections has been proposed for robots under holonomic constraints. This decentralized control

algorithm cannot be applied to the mobile robots under nonholonomic constraints because nonholonomic robots cannot generate velocity in all directions. In this section, we extend this decentralized control algorithm to the nonholonomic mobile robot. Consider a mobile robot driven by two wheels as shown in Figure.4. Define the robot coordinate system as shown in Figure.5. The motion of the robot is characterized by the velocity in its heading direction x and the orientation of the robot θ . By appropriately specifying the velocity of each wheel, we can specify the translational motion velocity and the rotational motion velocity $\dot{\theta}$.

3.1 Outline of System

The control algorithm in the previous section was designed under the assumption that each robot holds the transported object firmly. In case of the mobile robots under nonholonomic constraints, the robot could not move on the ground freely if each robot holds the transported object firmly. To solve the problem, we assume that each robot holds the object through a free rotational joint, which is located in the middle of both wheels, as shown in Figure.4.

The mobile robots driven by two wheels cannot be controlled so as to have the dynamics given by Eq.(1) and (2), because it cannot generate velocity in all directions. We consider to use the algorithm in the previous section only along the translational motion direction. The motion command is given to the leader and the follower estimates the desired trajectory given to the leader along the translational motion direction of the follower. For the rotational motion of the robot, we use the idea of the caster action proposed by D. J. Stillwell et al. We extend the caster dynamics and propose the dual caster action.

3.2 Dual Caster Action

The use of the caster dynamics for the tracked vehicle coordination was proposed by D. J. Stillwell et al. He proposed to control a vehicle as if it has a caster dynamics. The real caster has an offset C_{off} between the axis of the wheel and the free joint as shown in Figure.6. The caster turns to the direction of the force applied to the caster by this offset.

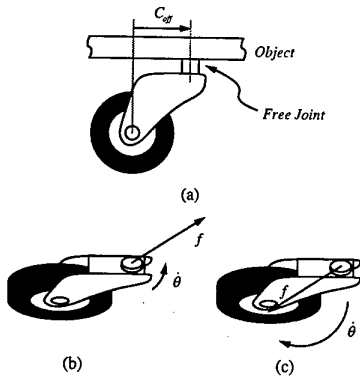


Figure 6: Real caster action

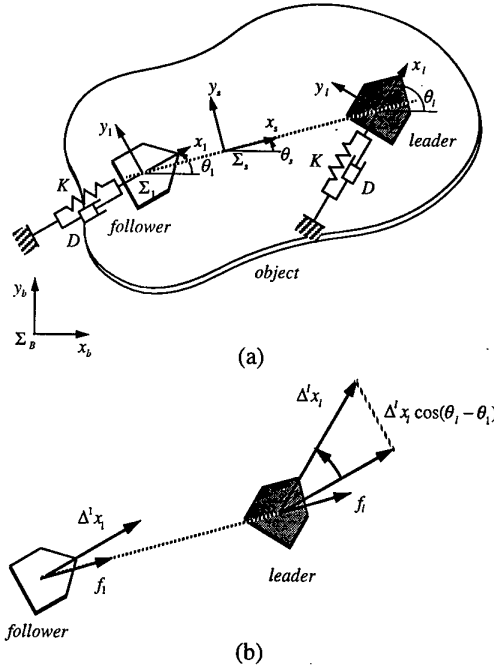


Figure 7: Compliance of each robot

In our system, each robot holds the object through a free rotational joint, which is located in the middle of both wheels, as shown in Figure.4. The caster action is realized by a control software. To mimic the motion of the real caster, the follower is controlled so as to have the following dynamics.

$$D_{cast}\dot{\theta}_1 = C_{off}(-f_{1x}\sin\theta_1 + f_{1y}\cos\theta_1) \quad (27)$$

This caster dynamics is realized by specifying the angular velocity of the follower $\dot{\theta}_1$ so as to satisfy the Eq.(27). Where f_{1x} and f_{1y} are the forces applied to the follower with reference to the base frame Σ_B as shown in Figure.7, θ_1 is the follower orientation with reference to the base frame Σ_B and D_{cast} is the parameter expressing the characteristic of the caster.

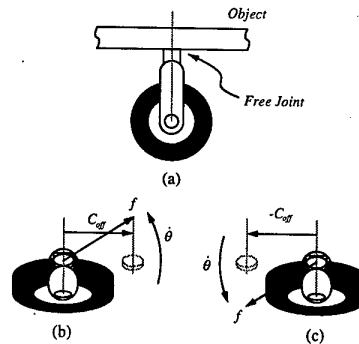


Figure 8: Dual caster action

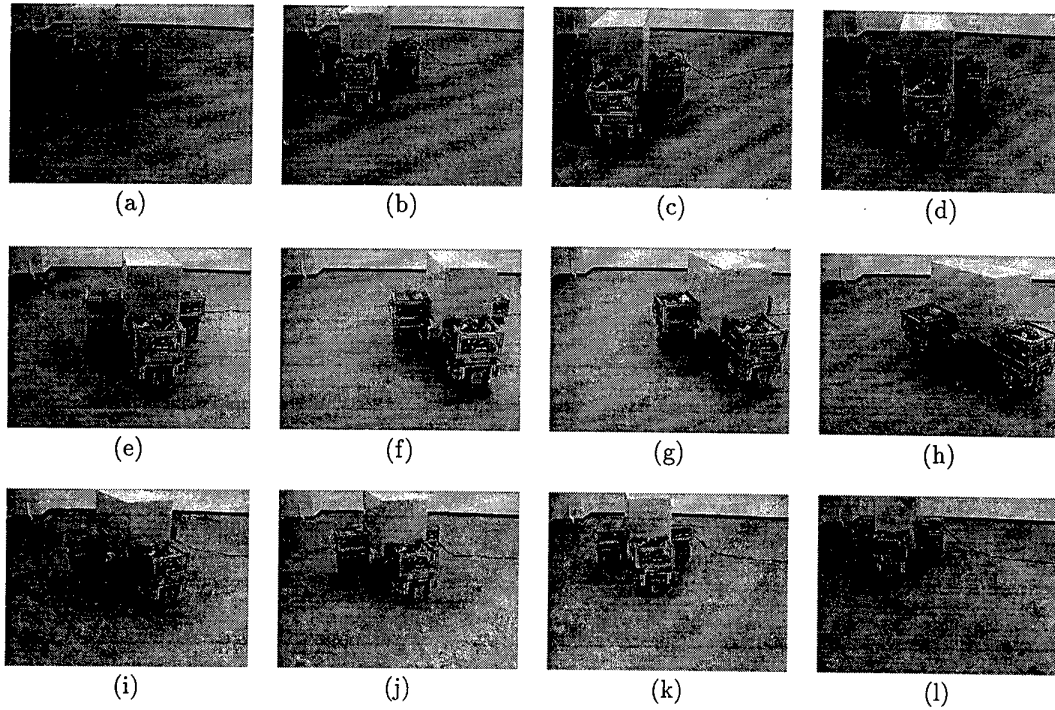


Figure 9: Experimental Result

D_{cast} and C_{off} are positive real numbers.

As long as $f_{1x} \cos \theta_1 + f_{1y} \sin \theta_1 \geq 0$ as shown in Figure.6(b), the follower adjusts its motion direction with the minimum rotational motion, but when $f_{1x} \cos \theta_1 + f_{1y} \sin \theta_1 < 0$ as shown in Figure.6(c), the follower rotates more than 90 degrees. The rotational motion more than 90 degrees brings the follower into a singular configuration of this transportation system in which the direction of the follower is perpendicular to that of the leader. The follower could not generate any velocity along the motion direction of the leader.

To avoid this problem, we consider to control the follower so as to have two different caster actions. That is, we change the position of the virtual caster wheel according to the sign of $f_{1x} \cos \theta_1 + f_{1y} \sin \theta_1$ as follows;

$$D_{cast} \dot{\theta}_1 = C(-f_{1x} \sin \theta_1 + f_{1y} \cos \theta_1) \quad (28)$$

where

$$C = \begin{cases} C_{off}, & \text{for } f_{1x} \cos \theta_1 + f_{1y} \sin \theta_1 \geq 0 \\ -C_{off}, & \text{for } f_{1x} \cos \theta_1 + f_{1y} \sin \theta_1 < 0 \end{cases} \quad (29)$$

Since the follower is controlled by two different caster actions, the action of the follower is referred to as the dual caster action. Using the dual caster action, the follower can align its orientation with the direction of the force applied to the robot without unnecessary over action. The concept of dual caster action is illustrated in Figure.8.

4 Experiment

4.1 Experimental Results using Holonomic Mobile Robots

We did experiments using three autonomous omnidirectional mobile robots, ZEN, developed by RIKEN [9]. Each mobile robot has three degrees of freedom of motion and equip with the Body Force Sensor which is the force/torque sensor located between the drive mechanism and the body of the mobile robot[10]. The leader was given the desired trajectory and each follower estimated the desired trajectory of its own virtual leader using the algorithm proposed in the previous section. The control algorithm was implemented using VxWorks. The sampling rate was 1024Hz. One of the results is shown in Figure.9

4.2 Experimental Results Using Nonholonomic Mobile Robots

The extended decentralized control algorithm was implemented in the experimental system, which consists of two tracked mobile robots. Each mobile robot held the object through a free joint. Given the desired trajectory to the leader, the follower was controlled based on the dual caster action which we proposed in Eq.(28), and estimated the desired trajectory given to the leader along the translational motion direction using the estimator illustrated in Figure.2. The control algorithm was implemented using VxWorks. The sampling rate was 1024Hz. One of the results is shown in Figure.10

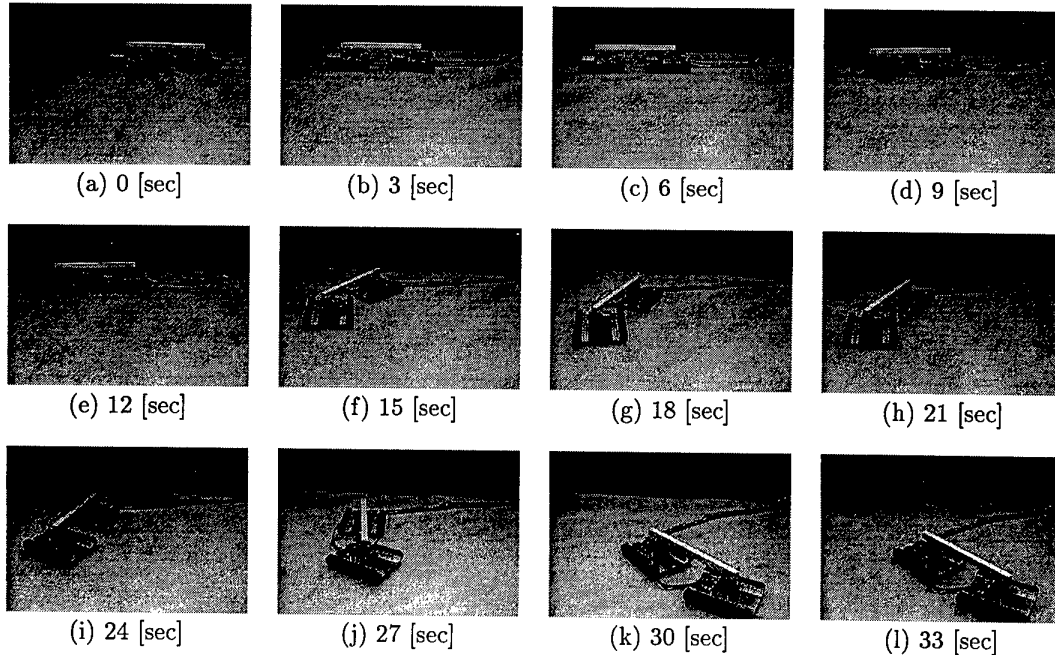


Figure 10: Experimental Result

5 Conclusions

In this paper, we proposed a decentralized motion control algorithm of multiple mobile robots in coordination. The algorithm realizes a natural robot behavior for handling a single object in coordination. The robots handle an object in coordination although only the leader knows how to move. The collective behavior was realized through the estimation of leader's motion by each follower based on information obtained at each follower. The algorithm was extended to non-holonomic mobile robots by introducing the concept of the dual caster action. Experimental results illustrated the proposed algorithms.

References

- [1] E.Nakano, S.Ozaki, T.Ishida, I.Kato, "Cooperational Control of the Anthropomorphous Manipulator "MELARM", *Proc. of 4th International Symposium on Industrial Robots*, pp.251-260, Tokyo 1974
- [2] Y.F. Zheng, J.Y.S. Luh, "Optimal Load Distribution for Two Industrial Robots Handling a Single Object", *Proc. of IEEE International Conference on Robotics and Automation*, pp.344-349, 1988
- [3] M. Uchiyama, "A Unified Approach to Load Sharing, Motion Decomposing and Force Sensing of Dual Arm Robots", *Robotic Research : The Fifth International Symposium*, pp. 225-232, MIT Press, 1990
- [4] Y. Nakamura, K. Nagai, T. Yoshikawa, "Mechanics of Cooperative Manipulation by Multiple Robotic Mechanism", *Proc. of 1987 International Conference on Robotics and Automation*, pp.991-998, 1987
- [5] K. Kosuge, J. Isikawa, "Task-Oriented Control of Single-Master Multi-Slave Manipulator System", *Robotics and Autonomous Systems*, Vol. 12, pp.95-105, 1994
- [6] Daniel J. Stillwell and John S. Bay, "Toward the Development of a Material Transport System using Swarms of Ant-like Robots", *Proc. of 1993 IEEE Int. Conf. on Robotics and Automation*, pp.318-323, 1993
- [7] K. Kosuge, T. Oosumi, "Decentralized Control of Multiple Robots Handling an Object", *Proc. of 1996 IEEE/RSJ Int. Conf. on Intelligent Robots and Systems*, pp.318-323, 1996
- [8] K. Kosuge, T. Oosumi, K. Chiba, "Load Sharing of Decentralized-Control Multiple Mobile Robots Handling a Single Object", *Proc. of 1997 IEEE Int. Conf. on Robotics and Automations*, pp.3373-3378, 1997
- [9] H. Asama, M. Sato, H. kaetsu, K. Ozaki, A. Matsumoto, I.Endo, "Development of an Omni-Directional Mobile Robot with 3 DoF Decoupling Drive Mechanism" *Journal of the Robots Society of Japan*, Vol.14, pp.249-254, 1996(In Japanese)
- [10] K. Kosuge, T. Oosumi, Y. Hirata, H. Asama, H. Kaetsu, K. Kawabata "Handling of a Single Object by Multiple Autonomous Mobile Robots in Coordination with Body Force Sensor", *Proc. of 1998 IEEE Int. Conf. on Intelligent Robots and Systems*, pp.1419-1424, 1998

ROBOPAINT: Multi-robot Painting System for Glass Bricks

Hakan Altınay, Can Bayar, Gökay Hurmalı, Emin Tahralı, Dilek Bilgin Tükel, Gökhan V. Gök,
Ağan Şimşek, Nazik Kurtuldu
Altınay Robotics & Automation Inc. Zahitbey Sok. No:3,
81030 Kızıltoprak Istanbul - Turkey
robot@altinay.com.tr

Abstract

ROBOPAINT, the first multi-robot glass brick painting system in the world has been designed and developed by Altınay Robotics & Automation Inc. The system was planted and is currently functioning successfully in the Mersin Factory of Şişecam A.S. ROBOPAINT automates the whole production line starting from the cooling system to the drying oven. This system takes in raw glass bricks, passes them through certain processes and produces a final usable product at a rate of 10 pieces per minute which is the production speed of the raw glass bricks. This robotic system consists of four subsystems including 2 SCARA robots and 1 cartesian robot.

1. Introduction

The development of robots and automation systems for the industry is due to two main reasons. The first one is to keep people out of unhealthy and hazardous environments and free them from performing "3-d" tasks (dirty, dull, dangerous). The second reason is to be able to produce standard products with high quality. Painting application represents one of the branches which have rapidly switched to robotized and automated systems. The objective of this project has been to design a painting system where the final product will be packed without being touched by a human, therefore having no fingertips on. ROBOPAINT is the only robotized glass brick painting system in the world and has the ability to handle glass bricks of different dimensions.

As a multi-robot system ROBOPAINT possesses the advantages of such systems namely if one of the robots fails, the others can compensate for it, and thus the system is reliable and flexible.

2. Painting Applications

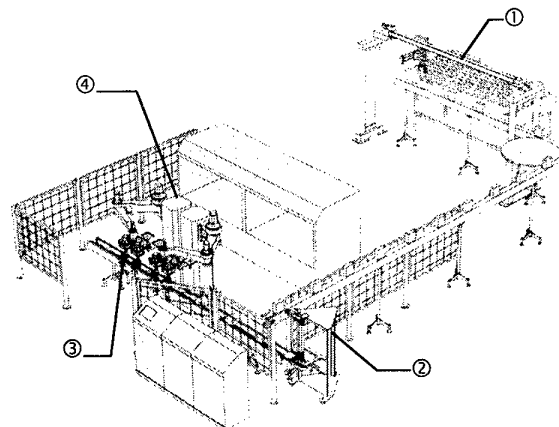
The challenge of building a spray painting booth in conformance with all safety and health codes makes spray painting a natural application for industrial robots. [1] In addition, robots are able to achieve a level of consistency that is difficult to expect human spray painters to duplicate. Although a skilled spray painter is required the first time to teach the robot a painting task, once taught,

the robot will do the spray painting operation repeatedly, with a consistency unattainable by the same expert who taught the robot the first time through.

According to the robot statistics given by UN and IFR (International Federation of Robotics) [2] dispensing applications represent 3% of all robotic applications and painting applications represent 66% of all dispensing applications.

Spray painting methods fall mainly into three categories: manual, hard automation and robotized painting systems. The last one is the hardest to implement but the most useful and flexible.

3. System Structure of ROBOPAINT



- ① : Glass Brick Transferring System
- ② : Glass Brick Rotating System
- ③ : Glass Brick Donating System
- ④ : Robotized Painting System

Figure 1 CAD View of the Whole ROBOPAINT System

The design of the system components shown in figure 1 was done using I-DEAS CAD software. During this project the first SCARA robot used for industrial purposes in Turkey ASC-40 was designed and manufactured.

ROBOPAINT consists of autonomously functioning units. The electromechanical subsystems can be classified as follows:

- Glass Brick Transferring System
- Glass Brick Rotating System
- Glass Brick Donating System
- Robotized Painting System

3.1 Glass Brick Transferring System

The Glass Brick Transferring System consists of a cartesian robot (AKR-40) having maximum capacity of 40 kg, 1 servo and 4 pneumatically controlled axes and a variator controlled L-shaped transferring conveyor as shown in figure 2. The robot hand is controlled by the PLC and can hold the glass bricks firmly without damaging them.

The glass bricks are being produced at rate of 10 pieces per minute. The robot transfers the glass bricks coming from the cooling system in groups of fifteen onto the transferring conveyor one by one. The motion of the conveyor is continuous and the robot leaves the glass bricks onto it while it is moving.

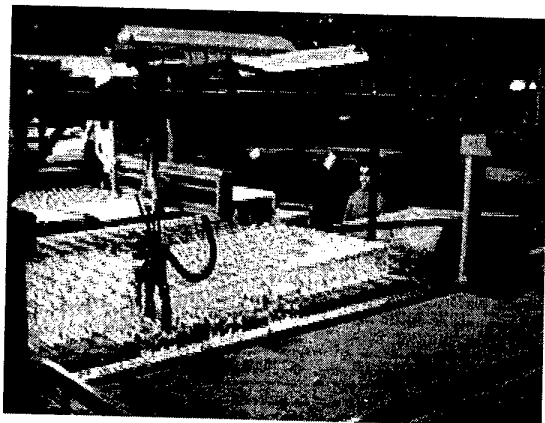
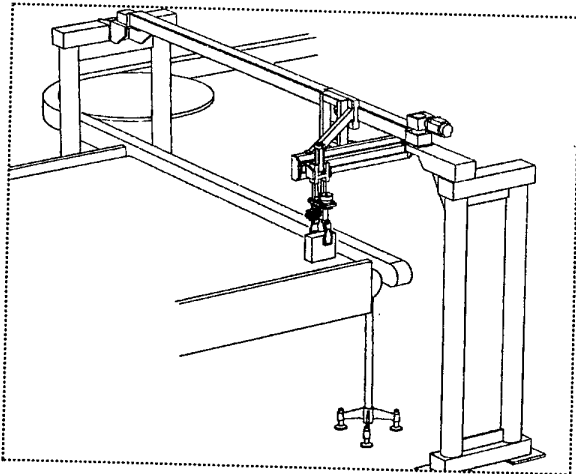


Figure 2 Glass Brick Transferring System-CAD Picture and Real Photo

3.2 Glass Brick Rotating System

The Glass Brick Rotating System is a 4-DOF pneumatically controlled system placed at the end of the Glass Brick Transferring System. The glass bricks are rotated and transferred to the glass brick donating conveyor in a position suitable for the robots to handle them.

When the glass brick reaches the stopper at the end of the transferring conveyor, the glass bricks are stopped, when the sensor placed on the stopper identifies the glass brick the pneumatic piston approaches the glass brick, grabs it and after rotating it 90° leaves it onto the up-and-down moving plate which moves it down to the conveyor height.

There are 4 different movements in the glass brick rotating system.

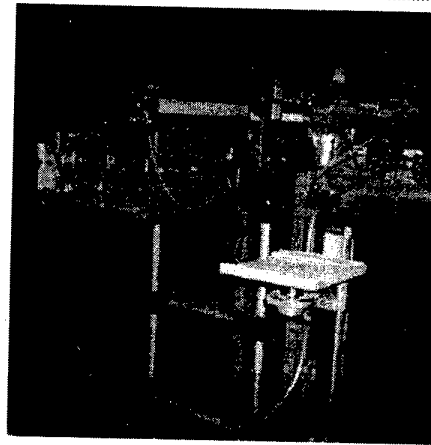
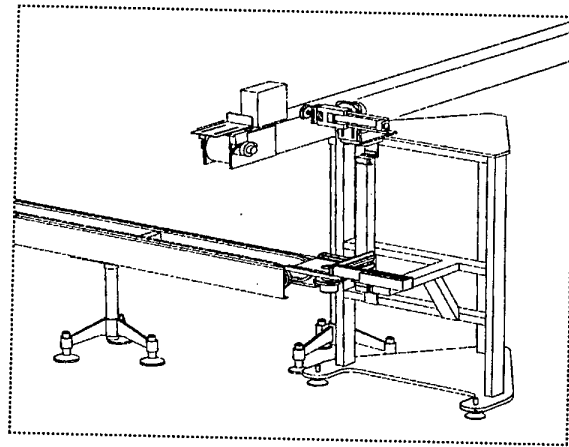


Figure 3 Glass Brick Rotating System CAD Picture and Real Photo

3.3 Glass Brick Donating System

The Glass Brick Donating System consists of a conveyor and indexing units. There are 4 pneumatically controlled donating systems-2 for each robot. The glass bricks are indexed with respect to 4 indexing points and are fed to the robot hands. The glass bricks are released

just when it has been ensured that the robot hand can hold them safely.

Although the indexing systems are working independently, there is no difference between their movements.

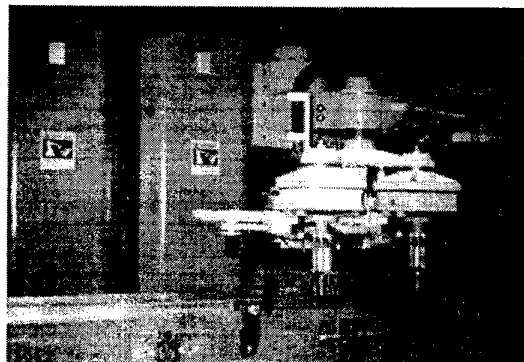
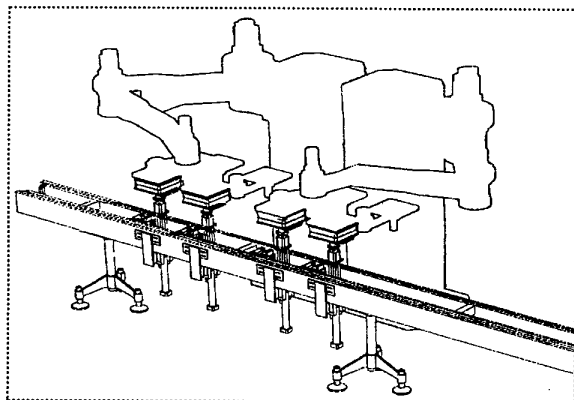


Figure 4 Glass Brick Donating System-CAD Picture and Real Photo

3.4 Robotized Painting System

The Robotized Painting System consists of two 5-DOF SCARA type industrial robots (Altinay ASC-40) and their special hands. When the robot hands are closed just the side surfaces of the glass bricks are uncovered and can be painted. The robot hands have been specially designed for this application and besides the control axes of the robots, they have two pneumatically controlled axes.

The 1st, 2nd and 3rd axes are performing rotary motion and span a circular area in the coordinate system. The 4th axis rotates the fist part of the robot hand and the fifth axis rotates the second part of the robot hand.

The up-down movement of the robot hand covers is pneumatically controlled and the movements of the two robots are symmetric.

The structure and properties of the ASC-40 robot will be given in detail in the following sections.

Although this robot was designed for the application mentioned above, ASC-40 can be used in various other industrial applications such as material handling, assembly, material transfer, etc.

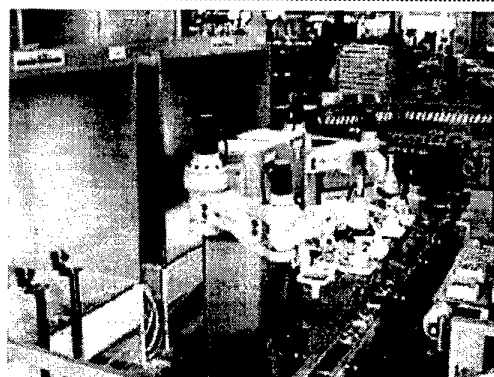
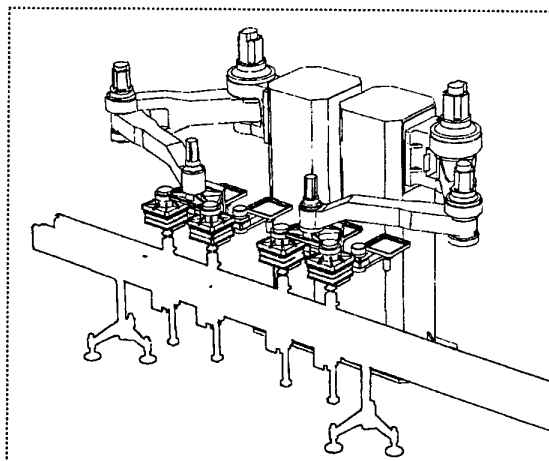


Figure 5 Robotized Painting System

4. The Industrial Robots Used in the Project

Two types of industrial robots have been used in the ROBOPAINT project, namely the cartesian robot used in the Glass Brick Transferring System (AKR-40) and the SCARA type robots used in the Robotized Painting System (ASC-40).

4.1 Altinay AKR-40 Robot

The AKR-40 robot takes the glass bricks from the cooling conveyor and leaves them onto the transferring conveyor. The properties of the robot and its working range are as given in Figure 6 and Figure 7.

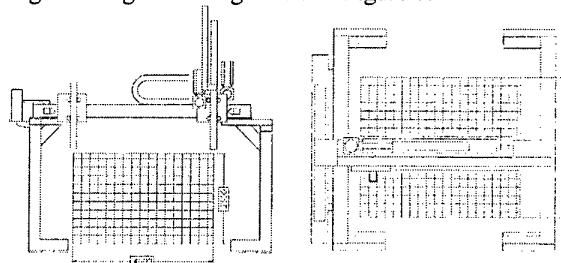


Figure 6 Working Range of the Altinay AKR-40 Robot

Model Name			AKR-40
Architecture			Cartesian
Degree of Freedom			1+4
Motor Driving System			Brushless AC Servo
Motor Driving Capacity			2000 W
Working Range	Arm	1. axis	3500 mm
		2. axis	700 mm
		3. axis	120 mm
		4. axis	$\pm 185\text{ deg}$
		5. axis	$\pm 65\text{ deg}$
Speed	Arm	1. axis	3000 mm/sec
Maximum Payload			40 kg
Repeatability			$\pm 0.5\text{ mm}$
Robot Arm Working Range			9.4 m^3
Ambient Temperature and Hum.			0~40℃
Weight			500 kg

Figure 7 Properties of AKR-40 Robot

4.2 Altinay ASC-40 Robot

The ASC-40 scara robot is active through the painting process. The robot hands cover the glass bricks while the robots are in the painting cabin leaving just the surfaces to be painted uncovered. While the glass bricks are being painted the robot hands turn 360° , 4 times 90° so that the complete circumference of the glass bricks is completely painted.

The properties of the ASC-40 robot are as given in Figure 8 and the working range of the robot is given in Figure 9.

Model Name			ASC-40
Architecture			Scara
Degree of Freedom			5
Motor Driving System			Brushless AC Servo
Motor Driving Capacity			7000 W
Working Range	Arml	1. axis	200 deg
		2. axis	240 deg
	Wrist	3. axis	210 deg
		4. axis	Unlimited
		5. axis	Unlimited
Operation Speed	Arm	1. axis	166 deg/sec
		2. axis	166 deg/sec
	Wrist	3. axis	166 deg/sec
		4. axis	270 deg/sec
		5. axis	270 deg/sec
Maximum Payload			25-40 kg
Repeatability			±0.5 mm
Robot Arm Working Range			9.4 m ³
Ambient Temperature and Hum.			0~40 ℃, 20~80%RH
Weight			~800 kg

Figure 8 Properties of ASC-40 Robot

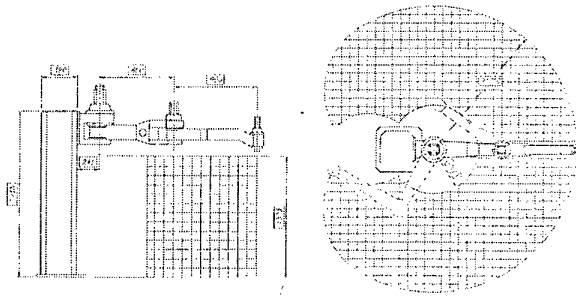


Figure 9 Working Range of the Altinay ASC-40 Robot

At the design stage of the robots the properties have been defined by the requirements of the application, that is why the motors and the reduction gears have been selected by calculating the essential limit values accordingly.

5. The Mathematical Model of the Painting Operation

In order to be able to develop a mathematical model for the painting process a lot of strategies have been tried. The aim is to develop a tool that can calculate the optimal painting trajectory. [3]. The geometry of the paint particles is as shown in Figure 10.

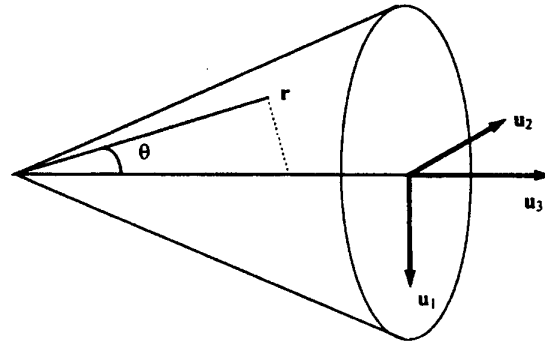


Figure 10 The Geometry of the Paint Distribution

The orthonormal unit vectors $u_1 \dots u_3$ fix the paint gun orientation. The figure shown above is formed of aerosol and when the aerosol reaches the surface to be painted the paint particles stick onto the surface. If the paint distribution area $j(r, u_1 \dots u_3)$ can be determined a prediction using multivariable differential theorems can be made.

$$j(r, u_1 \dots u_3) = Q_0 V / (4Dz) \exp(-VR^2 / (4Dz)) u_3$$

Q_0 : constant,
 V : the speed of aerosol,
 R : Distance from u_3
 D : Diffusion coefficient

6. Conclusion

ROBOPAINT is an innovative system in several aspects:

The idea is new: this is the world's first multi-robot glass brick painting system.

The product developed for this system is new: ASC-40 - the first SCARA robot of Turkey was designed and manufactured by Altinay for this project.

The final product of the system is new: the production of glass bricks in Turkey started with the completion of ROBOPAINT.

7. References

- [1] Asfahl, C. R., *Robots and Manufacturing Automation*, John Wiley and Sons Inc., Singapore, 1992
- [2] *World Industrial Robots 1997*, United Nations, Geneva, 1997
- [3] Tahrali, E., "*A Simulation Method in Robotized Painting*", Istanbul Technical University, Ms. Thesis, Istanbul, June 1998

Development of an Active Worktable for Force Control of Robot Manipulators

Shin-ichi Nakajima

Department of Mechanical and Control Engineering,
Niigata Institute of Technology, Kashiwazaki, Niigata 945-1195 JAPAN
nakajima@mce.niit.ac.jp

Abstract

An active worktable for force control of robot manipulators is designed and fabricated. The active worktable has several degrees of freedom and accommodates its position/force in accordance with the motion of a robot. The worktable is controlled, based on impedance control methods, to achieve compliant motions. Several experiments are carried out to confirm basic effectiveness of the active worktable.

1. Introduction

Compliant motion control is considered to be a key technique for intelligent motion control of robot manipulators. Numerous control schemes have been proposed for force control of robot manipulators [1]. However, applications to practical tasks have not readily progressed. One of the reasons is that most industrial robots to date have been developed on the basis of position control schemes and it is difficult to change the controller for force control.

An approach of adding extra degrees of freedom to a robot manipulator is one of the practical solutions. Based on the idea, active devices to provide the compliance to an end effector have been developed [2,3]. The active end effectors accommodate the position and force, according as the change of environment. However, the weight of an end effector becomes a load to the manipulator and the design is restricted by the payload limitation of robot manipulators.

This article discusses an approach to give the compliance to a workpiece, instead of giving the compliance to manipulators. To make practical the approach, an active worktable, which provides active compliance to a workpiece, is proposed here. The worktable has several degrees of freedom and can perform compliant motion tasks independently to the robot motion.

Developed active worktable has architecture based on a parallel link mechanism powered by DD (direct drive) motors. Since DD motors have many advantages such as

large torque, low friction and low torque ripple, the motors are suitable for force control tasks. Also, the parallel link mechanism can solve problems of supporting heavy DD motors.

In section 2, a design concept of the active worktable is presented. Then, the control systems design for achieving the active compliance is discussed in section 3. To confirm the effectiveness of the system, several experimental results using prototype active worktable are shown in section 4.

2. Active worktable

Fig.1 illustrates the concept of an active worktable. The worktable holds a workpiece and accommodates its horizontal and vertical positions. The table is driven actively to give the compliant motion to a workpiece.

Consider the grinding or polishing a surface by a robot manipulator, for example, it is necessary to design a system with large compliance (small stiffness) in the normal direction, and small compliance (large stiffness) in the tangential direction. The active worktable can change the compliant direction, depending on the surface profile of a workpiece.

Using the active worktable together with an industrial robot, we can achieve the compliant motion tasks without any change of the robot controller.

Fig.2 shows the mechanism of the active worktable.

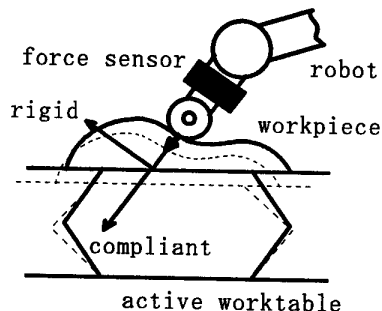


Fig. 1 Concept of an active worktable.

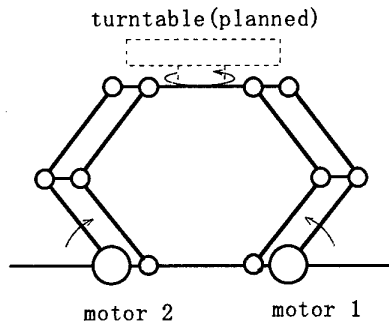


Fig. 2 Two degrees of freedom parallel link mechanism.

The table has a 2 d.o.f. parallel link mechanism driven by two DD motors. The mechanism converts rotary motion of two motors into translational movement of the table. The motion is restricted within a vertical plane. However, for 3D applications, a turntable on the table enables the adjustment of horizontal orientation of a workpiece.

Based on the concept, a prototype active worktable is designed and fabricated as shown in Fig.3. Two DD motors are placed in both side of the parallel link mechanism. The length of links is 176mm and work area of the table is approximately 8cm square.

The specifications of the DD motor are listed in Table 1. As the gravity load is fairly balanced by counterweights attached at motor links, the maximum power of the active worktable is 240 N.

Maximum torque	30 Nm
Friction torque	0.29 Nm
Maximum speed	1.25 rps
Angular resolution	491520 P/rev
Rotor inertia	0.018 Kgm ²

Table 1 Specifications of DD motor (NSK SSB030).

3. Control of the active worktable

3.1. Stiffness control

This section discusses a simple stiffness controller based on the kinematics of an active worktable.

Refer to Fig.4. Kinematics equations of the link mechanism are

$$P_x = \ell \cos \theta_1 - \ell \cos \theta_2 \quad (1)$$

$$P_y = \ell \sin \theta_1 + \ell \sin \theta_2 \quad (2)$$

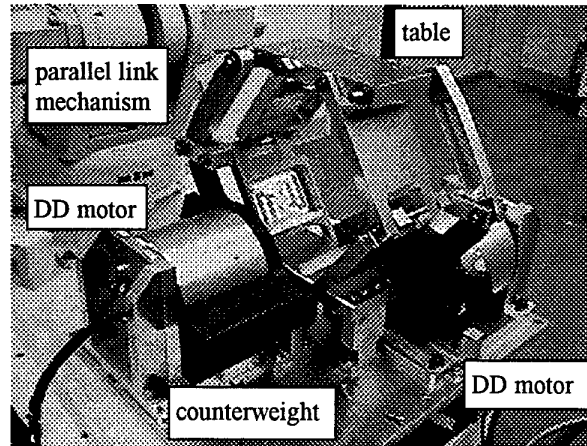


Fig.3 Prototype active worktable.

In order to realize the active compliance, a stiffness control scheme [4] is applied to the mechanism as follows.

Give the relation between the applied force F^s and table deflection X_e^s in the task coordinate frame X_s - Y_s as

$$F^s = K_s X_e^s + D_s \dot{X}_e^s, \quad (3)$$

where $K_s = \text{diag}(K_{sx}, K_{sy})$ is a stiffness matrix and $D_s = \text{diag}(D_{sx}, D_{sy})$ is a damping matrix to ensure the stability of the control system, respectively.

Assuming that dynamic coupled nonlinearities (coriori's force, centrifugal force etc.) are negligibly small and gravity forces can be mechanically compensated by counterweights, torques to realize the target stiffness (3) is determined as follows.

$$T = -J^T (RK_s R^T X_e + RD_s R^T \dot{X}_e), \quad (4)$$

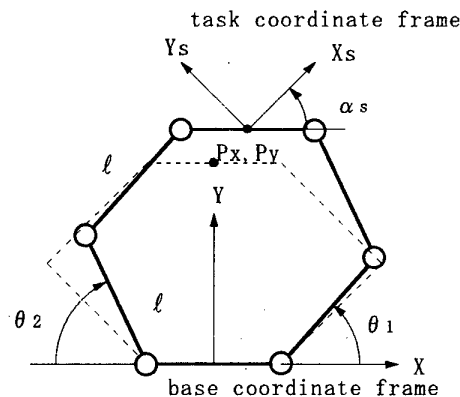


Fig. 4 Kinematics of the parallel link mechanism.

where J is Jacobian matrix of kinematics relation and R is a rotation matrix between the base coordinate frame to task coordinate frame. X_o is table deflection in the base coordinate frame, which is given by reference position X_o and motor angles as

$$X_e = X - X_o = L(\theta) - X_o. \quad (5)$$

where $L(\theta)$ is the kinematics relationship of (1) and (2).

The table velocity is determined as

$$\dot{X}_e = \dot{X} - \dot{X}_o = J\dot{\theta} - \dot{X}_o. \quad (6)$$

3.2 Impedance control

The controller (4) is a position servo in the task coordinate frame and stiffness is determined by position feedback gains. Thus, the controller can achieve arbitrary stiffness without using force feedback. However, the controller has not freedoms to specify the dynamic characteristics. For example, once we choose a small position gain for compliant motion, the transient response of the control system becomes slow.

An impedance control method [5] can be applied when the force information is available in a control loop.

By adding a force feedback to equation (4) as

$$T = -J^T \{ RK_s R^T X_e + RD_s R^T \dot{X}_e - R(K_R - I)R^T F \}, \quad (7)$$

we can realize the following mechanical impedance.

$$M_R \ddot{X}^s + D_s \dot{X}_e^s + K_s X_e = K_R F^s, \quad (8)$$

where M_R is a mass matrix of the mechanism described in the task coordinate frame.

Although M_R is a function of joint angles and varies in accordance with the table configuration, the simplified impedance control (7) cannot specify the mass matrix. However, motor inertias and counterweights determine dominant components of the mass matrix and they do not depend on the table configuration. Consequently, in relatively small work area, the matrix is assumed to be constant. Thus, we can design the controller as follows.

First, we design K_s and D_s at the nominal table configuration to satisfy the dynamic characteristics, then design K_R to realize the necessary stiffness.

Both the stiffness controller and simplified impedance controller need information on the normal direction at contact point. This information is determined by the orientation of an end effector, which is decided in the robot programming process.

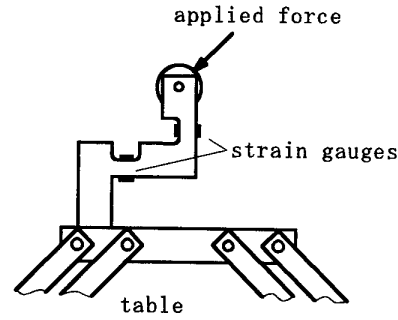


Fig. 5 Two axis force sensor.

Since reference positions of the table are programmable, we can adjust the contact force by accommodating the reference position along the compliant direction. The accommodation also enables the compensation of positioning errors introduced by the uncertainty of fixturing.

4. Experiments

To confirm the basic effectiveness of the system, stiffness of the table was examined using the prototype active worktable.

As shown in Fig. 5, simple force sensor using strain gauges is installed in the table to measure the forces in two directions in the Cartesian coordinate frame. The force information is necessary for the force feedback in the impedance control (7).

The control software was written in C++ and implemented on 200MHz Pentium processor. Sampling frequency of the control system is 200Hz.

4.1. Stiffness control

First, stiffness control (4) was implemented and tested. Stiffness was designed as 5N/mm for compliant direction and 50N/mm for rigid direction. Table deflections caused by the applied force were examined in three different compliant directions, 0° , 45° , 90° respectively.

The results are shown in Fig. 6. (a) is plots of the deflections in the compliant direction and (b) is those in the rigid direction. Although the deflections are slightly larger than expected, a slope of the plots agrees with the designed stiffness. The results show that we can achieve the arbitrary stiffness in steady state without using the force information

4.2. Simplified impedance control

Next, the simplified impedance control (7) was tested. Fig. 7 shows the same results as Fig. 6. The control parameters are chosen as listed in Table 2.

Accuracy of the stiffness is remarkably improved in both directions. The controller not only increases the accuracy of the stiffness control, but also improves the transient characteristics of the system.

Fig. 8 shows step responses of the active worktable. The results show that stable and quick responses are realized by choosing the appropriate K_s and D_s . The rise time of the step responses is less than 40ms for both

Direction	K_s [N/mm]	D_s [Ns/mm]	K_R	Stiffness [N/mm]
Compliant	40	0.8	8	5
Rigid	40	0.8	0.8	50

Table 2 Control parameters.

compliant and rigid direction. The positioning accuracy is 0.1mm for horizontal direction and 0.5mm for vertical direction respectively.

Although the nonlinear terms of the table dynamics are neglected in the control systems design, dynamic interactions are sufficiently small.

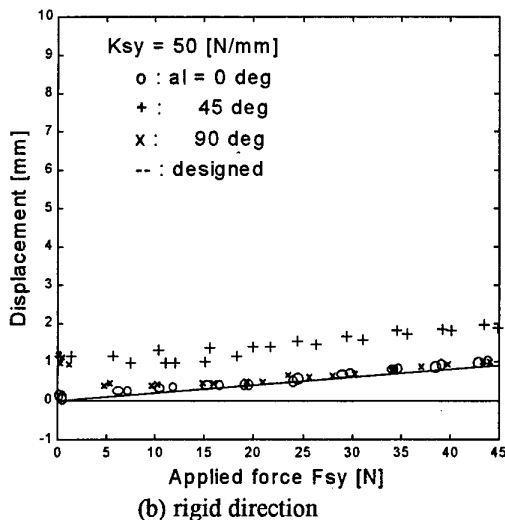
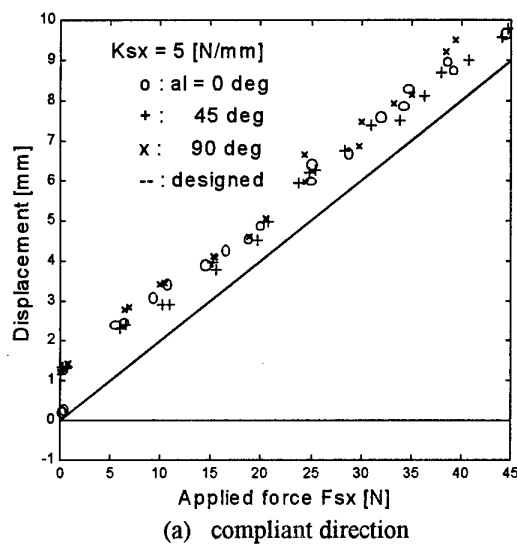


Fig. 6 Experimental results of the stiffness control.

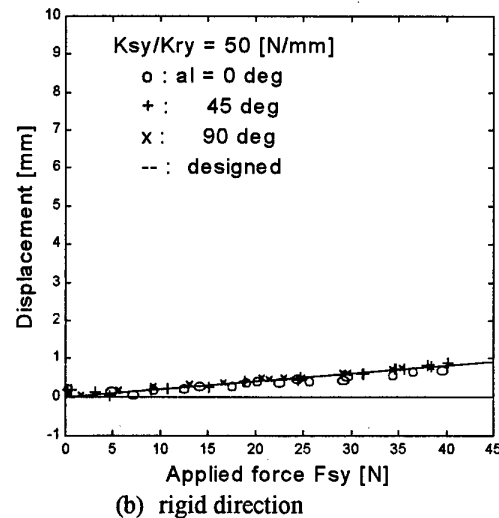
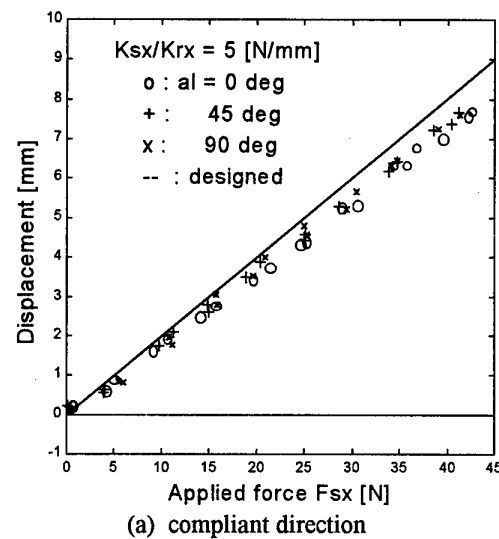


Fig. 7 Experimental results of the simplified impedance control.

5. Conclusion

An active worktable for force control of robot manipulators was designed, fabricated and tested. The active worktable uses a parallel link mechanism driven by DD motors. The table holds a workpiece and accommodates its position/force in accordance with the motion of a robot.

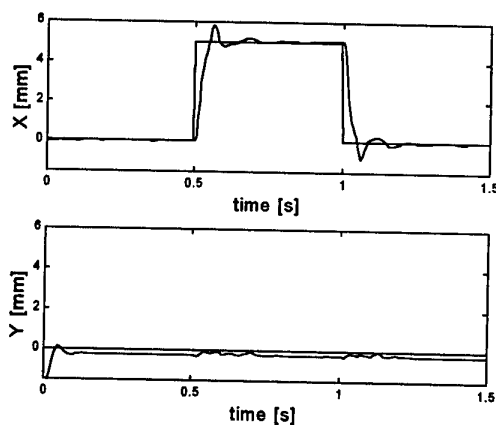
In order to provide a compliant motion to the table, a force control system was designed, based on a stiffness control method. The control system realizes the necessary stiffness in arbitrary task coordinate frame.

The dynamic characteristics of the table were also considered by implementing a simplified impedance control. The controller can realize the arbitrary stiffness without decreasing the dynamics performance.

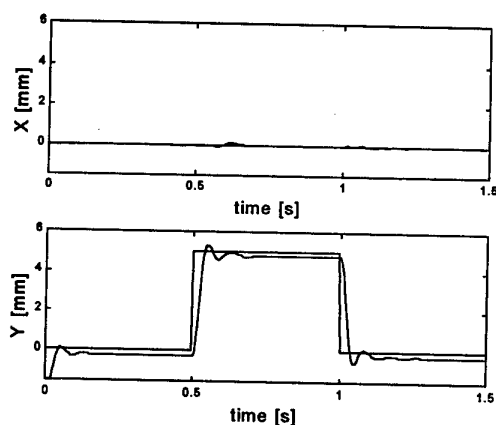
Several experiments were carried out using a prototype active worktable. Experimental results showed the usefulness of the developed worktable for force control of robot manipulators.

6. References

- [1] D. E. Whitney, "Historical Perspective and State of the Art in Robot Force Control", *The International Journal of Robotics Research*, Vol.6, No.1, Spring, pp. 3-14, 1987.
- [2] H. Kazerooni, "Direct-Drive Active Compliant End Effector (Active RCC)", *IEEE Journal of Robotics and Automation*, Vol.4, No.3, pp324-333, 1988.
- [3] G. M. Bone, M. A. Elbestawi, "Robotic Force Control for Debarring using an Active End Effector", *Robotica*, Vol.7 pp. 303-308, 1989.
- [4] J.K.Salisbury, "Active Stiffness Control of Manipulator in Cartesian Coordinates", *Proc. of the 19th IEEE Conference on Decision and Control*, pp. 95-100, 1980.
- [5] N. Hogan, "Impedance Control: An Approach to Manipulation: Part1-Part3", *Trans. ASME, J of Dynamic Systems, Measurement, and Control* Vol.107, pp.1-24, 1985.



(a) step input to horizontal (rigid) direction



(b) step input to vertical (compliant) direction

Fig. 8 Step response of the active worktable.

Development of Soft Planar Actuator using Pneumatic-Rubber Balls

Toshiro Noritsugu and Daijyu Kaneshiro
Faculty of Engineering, Okayama University
toshiro@sys.okayama-u.ac.jp

Abstract

A manipulation of fragile and shapeless objects requires an actuator with enough flexibility and safety not to injure manipulated objects. To cope with such requirements some kinds of soft actuator have been already developed, almost of which utilize the elastic deformation of rubber tube or balloon caused by compressed air pressure. Such a pneumatic rubber actuator can be expected to be effectively used as a flexible and human friendly soft actuator in various fields. In this study, in order to realize a flexible pneumatic carrier system, a soft planar actuator using rubber balls has been developed assuming that the actuator directly contacts with the carried objects. This paper describes a fundamental principle of operation, a control method and experimental results. The results show the effectiveness of the proposed actuator mechanism.

1. Introduction

In various electronic, mechanic and food factories or medical welfare fields, robots which can manipulate fragile and shapeless objects have been required, which should be driven with an actuator provided with enough flexibility and safety not to injure the manipulated objects or human. To cope with such requirements some kinds of soft actuator have been already developed, almost of which utilize the elastic deformation of rubber tube or balloon caused by compressed air pressure [1, 2, 3]. Such a pneumatic rubber actuator can be expected to be effectively used as a flexible and human friendly soft actuator in various fields.

In this study, in order to realize a flexible pneumatic carrier system, a soft planar actuator using pneumatic rubber balls has been developed assuming that the actuator directly contacts with carried object. The actuator consists of a two-layer building pneumatic rubber balls. These balls are divided into five groups, each group repeats expansion and contraction independently controlled with a pressure control valve. By controlling inner pressure of balls, the actuator produces a traveling wave to carry the object contacting

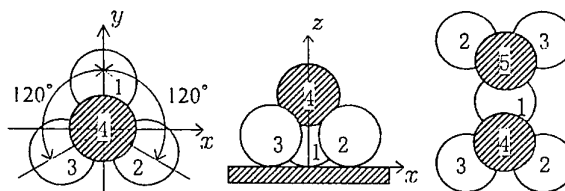
with the actuator owing to the friction force between balls and object.

In this paper, first, a control method of inner pressure of balls to realize the desired operation is described. Next, an open loop position control is constructed, which depends on only the pressure control. Also, a closed loop position control system is constructed by using a camera as a position feedback sensor. The control performances are experimentally investigated.

2. Principle of operation

Figure 1(a) shows a basic component of the actuator. The actuator consists of a two-layer building pneumatic rubber balls. In the lower layer, three balls are placed at an angle 120° apart. An upper ball is attached to the lower three balls. There is no air flow among the balls. The inner pressure of each ball is independently controlled.

Figure 1(b) shows a fundamental construction of the actuator, which is composed of a point symmetric connection of the basic component in Figure 1(a) with a ball 1, comprising seven balls. The lower balls 1, 2 and 3 determine the direction of travelling wave by adjusting the combination of expansion and contraction of each ball. The upper balls 4 and 5 contact with the object and select the carrier direction by adjusting the timing of expansion and contraction for the motion of lower balls.



(a) Basic component (b) Fundamental construction
Figure 1. Fundamental structure of proposed actuator

Figure 2 shows an example of fundamental operation of the actuator, where the object is carried toward the right direction. The left and right figures are top and side views, respectively. Dotted lines indicate the center

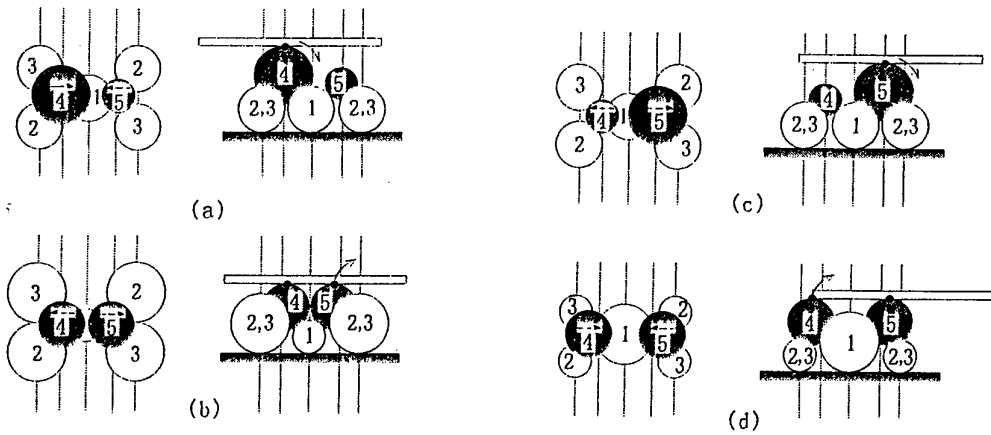


Figure 2. Operation of soft planar actuator

positions of each ball in the state of (a). The principle of operation is described as follows:

- (a) Balls 1, 2 and 3 are in a middle pressure. Balls 4 and 5 are in an expansion and a contraction, respectively. Right after, by contracting ball 1 and expanding balls 2 and 3, balls 4 and 5 are moved toward the center position. The ball 4 carries the object to the direction indicated by an arrow, that is, the right lower direction. At the same time, balls 4 and 5 start contracting and expanding, respectively.
 - (b) Balls 4 and 5 are in the middle pressure, both balls are contacting with the object. By continuing the contraction of ball 4 and expansion of ball 5, the object is handed to ball 5 from ball 4. At the same time, balls 4 and 5 start returning to the original position in the state of (a) by bringing balls 1, 2 and 3 back to the middle pressure. The object can be carried to the right upper direction of the arrow.
 - (c) Balls 1, 2 and 3 are in the middle pressure. Balls 4 and 5 are in a contraction and an expansion. Right after, by expanding ball 1 and contracting balls 2 and 3, balls 4 and 5 are moved apart from the center position. The object contacting with ball 5 is carried to the right lower direction indicated by the arrow. At the same time, balls 4 and 5 start expanding and contracting, respectively.
 - (d) Balls 4 and 5 are in the middle pressure, both balls are contacting with the object. By continuing the expansion of ball 4 and contraction of ball 5, the object is handed to ball 4 from ball 5. At the same time, balls 4 and 5 start returning to the original position in the state of (a) by bringing balls 1, 2 and 3 back to the middle pressure. The object can be carried to the right upper direction of the arrow.
- By repeating the process from (a) to (d), the object can be continuously carried to the right direction.

Figure 3 shows an operation to carry to the other direction, which can be achieved by changing the combination of expansion and contraction of lower balls. In this example, if balls 4 and 5 are contracted and expanded, respectively, in the left figure, and in the right figure balls 4 and 5 are expanded and contracted, respectively, the movement in the right lower direction of the arrow can be achieved by periodically switching of left and right configurations. The combination of expansion and contraction can be adjusted by the pressure control of balls. Both the desired carrier direction and speed can be achieved by the pressure control of lower balls.

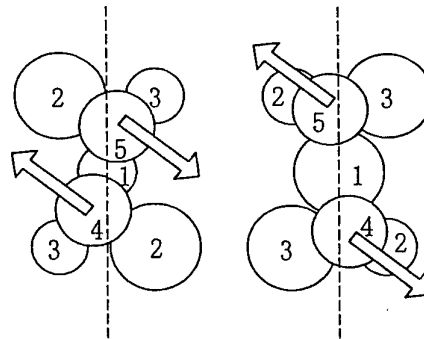


Figure 3. Operation for two dimensional direction

By combining the fundamental structure shown in Figure 1(b), a soft planar actuator comprising 48 balls is constructed as shown in Figure 4. which can carry the object in the arbitrary two dimensional directions on the actuator. This actuator is composed of lots of balls, however, it can be driven with only five pressure control valves because balls with same number are driven with a common pressure.

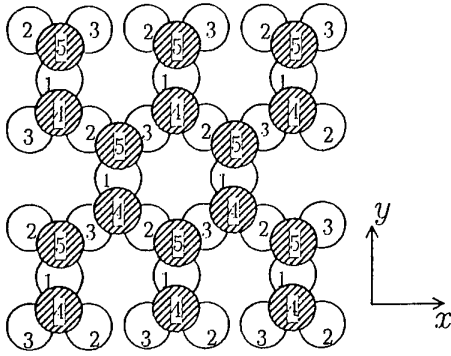


Figure 4. Soft planar actuator comprising 48 balls

3. Pressure control

In order to derive a pressure control strategy, the fundamental construction shown in Figure 1(a) is analyzed. Some variables are defined as follows:

- P_0 : equilibrium pressure
- P_j : inner pressure of ball
- F_j : generated force of ball
- A_j : pressure acting area of ball
- ψ_j : angle between lower and upper balls
- P_x, P_y, P_z : virtual acting pressures in x, y and z directions
- P_s : composition of virtual pressures
- θ : angle of P_s from positive x direction in $x-y$ plane

where, a subscript j ($j=1,2,3$) specifies the amounts of balls 1, 2, and 3. δ denotes a change of each variable from the equilibrium value.

When the inner pressure of ball changes, its generated force (expansive force) also changes. The change of expansive force δF_j induced by the inner pressure change δP_j from the equilibrium pressure P_0 is given by

$$\delta F_j = A_j \delta P_j \quad (1)$$

Figure 5(a) shows the force from the lower ball to the upper ball. The angle ψ_j is assumed not to vary and $\psi_1 = \psi_2 = \psi_3 = \psi$. From the configuration of balls shown in Figure 5(b), the generated forces in x, y and z directions are composed as follows:

$$\delta F_x = -\frac{\sqrt{3}}{2} \delta F_2 \cos \psi + \frac{\sqrt{3}}{2} \delta F_3 \cos \psi \quad (2)$$

$$\delta F_y = -\delta F_1 \cos \psi + \frac{1}{2} \delta F_2 \cos \psi + \frac{1}{2} \delta F_3 \cos \psi \quad (3)$$

$$\delta F_z = \delta F_1 \sin \psi + \delta F_2 \sin \psi + \delta F_3 \sin \psi \quad (4)$$

Assuming $A_1=A_2=A_3=A$, and virtual acting pressures, $\delta P_x = \delta F_x/A$, $\delta P_y = \delta F_y/A$ and $\delta P_z = \delta F_z/A$ are defined. It is supposed that the upper ball is moved toward the composite direction of virtual acting pressures and of which displacement is proportional to the magnitude of composite pressure.

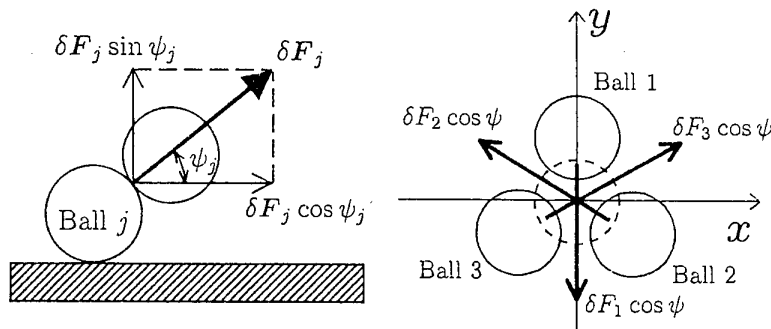
From equations from (1) to (4), the relation between the inner pressure change vector $\delta \mathbf{P} = [\delta P_1, \delta P_2, \delta P_3]^T$ and the virtual acting pressure vector $\delta \mathbf{P}_a = [\delta P_x, \delta P_y, \delta P_z]^T$ can be expressed as

$$\delta \mathbf{P}_a = \mathbf{N} \delta \mathbf{P} \quad (5)$$

where, the matrix \mathbf{N} is given by

$$\mathbf{N} = \begin{bmatrix} 0 & -\frac{\sqrt{3}}{2} \cos \psi & \frac{\sqrt{3}}{2} \cos \psi \\ -\cos \psi & \frac{1}{2} \cos \psi & \frac{1}{2} \cos \psi \\ \sin \psi & \sin \psi & \sin \psi \end{bmatrix} \quad (6)$$

In order to carry the object toward the desired θ direction, the upper balls 4 and 5 have to perform a reciprocating motions in the specified direction of θ . This study deals with only the motion in the horizontal $x-y$ plane, not considering the motion in the z direction.



(a) Relation between lower and upper ball

(b) Horizontal force

Figure 5. Force from lower balls

The magnitude and direction from the positive x direction are represented by δP_s and θ as shown in Figure 6. The relation between δP_a and δP_s , θ is given by

$$\delta P_a = \delta P_s L \quad (7)$$

$$L = \begin{bmatrix} \cos \theta \\ \sin \theta \\ 0 \end{bmatrix} \quad (8)$$

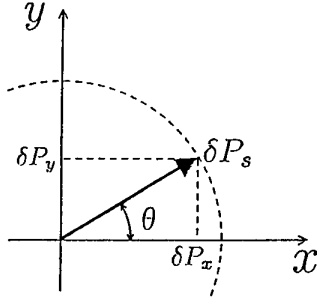


Figure 6. Driving pressure in θ direction

Based on the equations (5) and (7), a pressure control system for lower balls 1, 2 and 3 can be constructed as shown in Figure 7. u_0 denotes the control input to generate the equilibrium pressure P_0 . P are detected pressures. u are control inputs corresponding to δP . C expresses a controller. δP_s is given by a triangular wave with an amplitude of δP_{smax} as a top diagram in Figure 8. The inner pressures of balls 4 and 5 are also controlled by triangular waves synchronizing with the desired pressure of lower balls as shown in Figure 8.

4. Position control system

Figure 9 shows a position control system. X is a position of carried object in the x - y plane, of which desired value is X_r . The pressure control system same as Figure 7 is included as an inner loop. The position control error $X - X_r = [\delta x, \delta y]^T$ is transformed to the virtual acting pressure δP_s and the angle θ as shown in

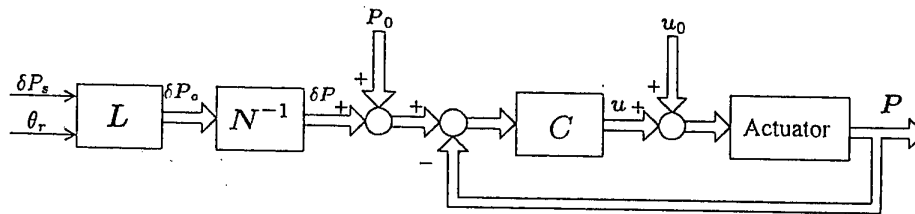


Figure 7. Pressure control system

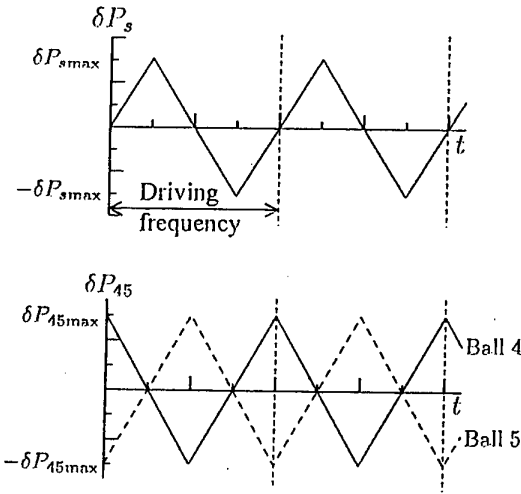


Figure 8. Reference triangular pressures

Figure 10. δP_{smax} is given by

$$\delta P_{smax} = S \delta r \quad (9)$$

where, S is treated as a proportional control gain.

5. Experimental system

Figure 11 shows an experimental system. An experimental planar actuator is constructed by using 48 soft tennis balls, comprising 8 balls as each ball group of 1,4, and 5, 12 balls as each ball group of 2 and 3, respectively.

The inner pressure of each ball group is controlled by a pneumatic servo valve. A supply pressure P_s is 200[kPa]. The detected pressures are fed back to the computer through A/D converter. The position of object is measured with a camera.

6. Experimental results and discussion

In the experimental system, the equilibrium pressure P_0 is 15[kPa] and the angle ϕ is 30° . The controller is PI controller with a proportional gain $k_p=0.03[m^2/N]$ and

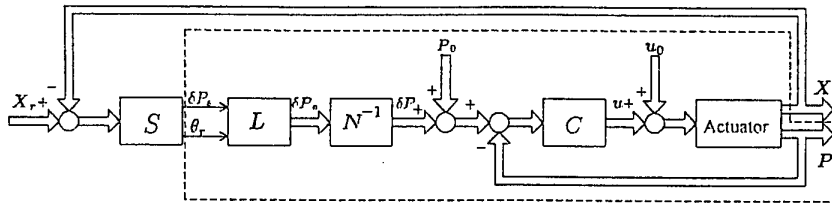


Figure 9. Position control system

an integral gain $k_i=0.5[\text{m}^2/\text{Ns}]$. The amplitude $\delta P_{4\text{max}}$ and $\delta P_{5\text{max}}$ of desired triangular pressure waves of balls 4 and 5 are 25[kPa]. An acrylic board of $350[\text{mm}] \times 350[\text{mm}] \times 2[\text{mm}]$ is used as a carried object.

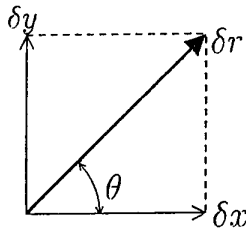


Figure 10. Relation between δx , δy and δP_s , θ

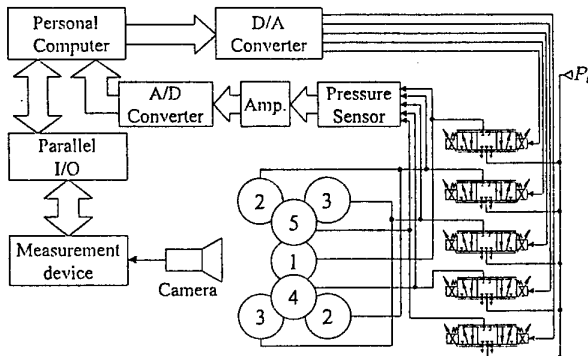


Figure 11. Experimental system

6.1. Pressure response of each ball group

Figure 12 shows the frequency response of each ball group measured for a sinusoidal desired input with an equilibrium pressure of $P_0=15[\text{kPa}]$ and an amplitude of $\delta P=8[\text{kPa}]$. Each group of ball 1, 4 and 5 includes eight balls, respectively. Groups of ball 2 and 3 comprise twelve balls. Balls included in each ball group are simultaneously controlled with a common one servo valve. A satisfactory control performance can be obtained in the frequency range below about 1 [Hz] regardless of number of driven balls.

6.2. Open-loop operation with pressure control

Figure 13(a) shows the carrier distance r of the object at intervals of 20 seconds for various driving frequency, when only the pressure control shown in Figure 7 is executed for the triangle desired pressure wave with an amplitude of $\delta P_{s\text{max}}=32[\text{kPa}]$ and for five desired carrier directions. The experimental results shown in Figure 13 are the average of five measurements. From the results, the driving frequency of 0.4[Hz] and the amplitude $\delta P_{s\text{max}}$ of 32[kPa] are selected as a best driving condition of the experimental actuator where the carrier speed is relatively large and the influence of the carrier direction on the carrier speed is relatively small.

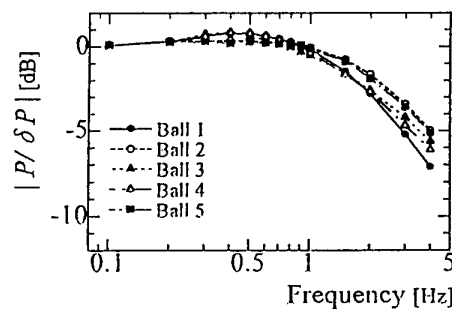


Figure 12. Pressure response of each ball group

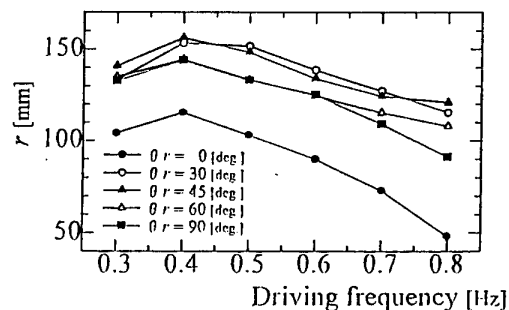


Figure 13. Open-loop characteristics

Figure 14 shows the movement of object during 20[s] for every 30° desired carrier directions θ_r between 0° and 330° under the above driving condition of 0.4[Hz] and $\delta P_{smax}=32[\text{kPa}]$. The respective desired and measured carrier directions are represented by dotted and solid lines. The measured values indicate the center of object. An origin of coordinate is the starting point. The results show that the movement in the arbitrary directions can be obtained, but a certain difference remains between command directions and actual directions probably caused by the assembly error, the individual difference of balls and so on.

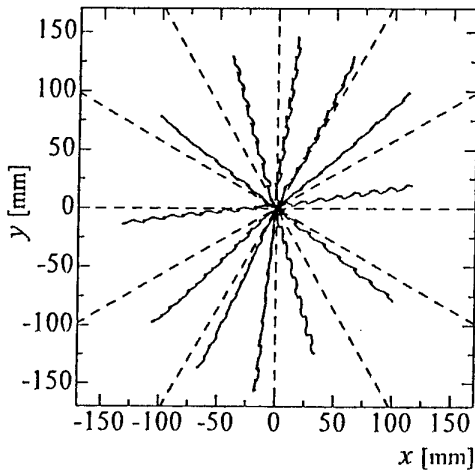


Figure 14. Carrying in various θ direction

6.3. Closed-loop operation with position feedback

The experimental results obtained from the position feedback control system shown in Figure 9, where the driving frequency is 0.4[Hz] and $\delta P_{smax}=32[\text{kPa}]$. Figure 15 shows the step response when the movement of 100[mm] in the x direction and 50[mm] in the y direction. $S=4 \times 10^3 [\text{Pa/mm}]$ in the equation (9). The object can be accurately carried to the desired position.

Figure 16 shows the response for the desired circular trajectory with a radius of 50[mm] and a period of 70[s]. Where, $S=5 \times 10^3 [\text{Pa/mm}]$.

7. Conclusions

A soft planar actuator to carry the object in the two dimensional directions has been developed as a pneumatic carrier actuator with the flexibility. The experimental actuator comprises 48 soft tennis rubber balls. A control method of the inner pressure of balls to

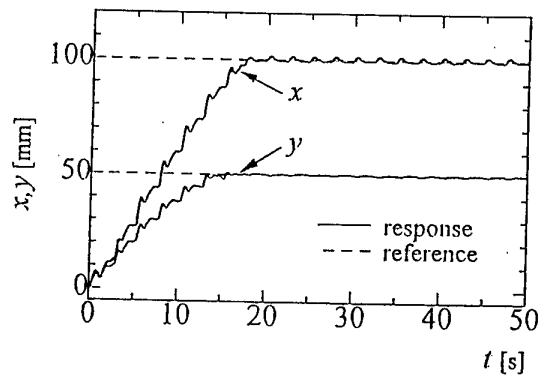


Figure 15. Step response on closed-loop system

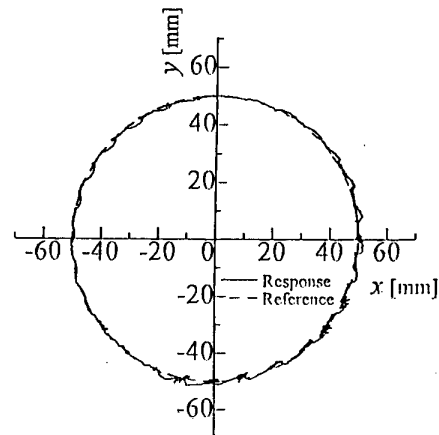


Figure 16. Tracking control for desired circle

carry the object successfully has been proposed. Also a position feedback control system has been constructed with a camera. The proposed actuator can carry the object continuously in the arbitrary two dimensional directions. The experimental results have confirmed the effectiveness of the proposed actuator.

This actuator is suitable for carrying soft and fragile object. The small sized actuator is available, for example, in a semiconductor manufacturing, food industry and so on. Also, the large sized one may be effective in the welfare or medical field, for example, as welfare bed.

8. References

- [1] C.P. Chou and B. Hannaford, "Static and Dynamic Characteristics of McKibben Pneumatic Artificial Muscles", Proc. of IEEE Intl. Conf. on Robotics and Automation, vol.1, 1994, pp.78-84.
- [2] T. Noritsugu, "Pneumatic Actuators", Journal of the Robotics Society of Japan, 15-3, 1997, pp.355-359 (In Japanese)
- [3] T. Noritsugu, "Human-Friendly Soft Actuator", International Journal of The Japan Society for Precision Engineering, 31-2, 1997, pp.92-96

Design and Performance of a new Tactile Sensor for Robotic Underwater Application

A. Bruno¹, G. Cannata², G. Casalino², G. Verruggio³

1 CNR - ITIA, National Research Council - Institute of Industrial Technologies and Automation, Milan - Italy.

2 DIST, Department of Communication, Computer and System Science, University of Genoa - Italy.

3 CNR - IAN, National Research Council - Naval Automation Institute, Genoa - Italy.

E-mail: bruno@itia.mi.cnr.it

Abstract

In this paper the implementation of a simple mechatronic system design of a new robotic underwater tactile sensor is described. We examine the design and the definition of a tactile sensor for manipulation in underwater robotic applications. Different kinds of technology concerning force transducers are reported, in order to better understand the choice of strain gauge technology for this application. The most important features that the sensor has to respect are individuated: the choice of the adapted transducers for this kind of application, the design of the mechanical structure, in terms of the sensitive force surface, the circuitry to conditioning the signals coming from the transducers; the compensation part, in order to work at the different water pressure the water - proof support and the way to better mount it on the gripper of the manipulator. In fact, the final product should be mounted on the fingertip of an underwater manipulator, developed inside an EU- project. After the Force versus Voltage feature of the sensor, some experimental data performed in air are showed: a qualitative shape recognise and a detecting force response versus xy displacement on a single sensor cell.

1. Introduction

In robotic field, it is becoming more and more important to support mechanical robot of several sensing devices in order to get satisfying information of the main physical quantities. This allows to better identify the robot and to develop the right control algorithms. For this reason, it is necessary an accurate study of the devices (component, struments) technology (mechanical, electro-mechanical, solid state, optical) and techniques (data acquisition, data processing). Robotic arms and mechanical hands have a larger and larger field of applications, such as assembling parts, edge following,

fine manipulation, space and underwater application and so on [1] [2] [3]. The purposes of a tactile sensor are described in the following points. The information coming from a tactile sensor [4] [5] can be used for application like object recognition, where it is necessary to determine the location and orientation of object edges and surfaces in order to design a real time closed loop force control. Slip detection [6] is another field where data coming from tactile sensors are processed with frequency analysis based techniques; the position of the centre of the force distribution and the fluctuation of the contact point normal are good parameters to define slipping between robot and object. In this work, we consider the information coming from a tactile sensor, a device that is able to give physical information about interaction forces during the contact. The use of strain gauges transducers for underwater application has been chosen because it is easy to carry on a mechanical structure, which compensate the water pressure. Moreover, they are more robust compared with other kinds. Talking about the underwater tactile sensor prototype, we will use the same technology for the aspect described before, about making a rialable underwater device. Recent research [7] describes the design of a new underwater slip detecting and force sensor mounted on a fingertip, using strain gauges as sensor elements.

The following points describe the development and design of this device. The shape of the sensor is given by the arrangement of 13 cells mounted in a rhomboidal configuration, in order to better acquire a good tactile information about the manipulated object (Figure 2). Transducers were selected in a way such that they have good performances in according to the desired application, to be able to operate correctly in the marine environments. The choice of strain gauges (piezoresistive transducer technology) was preferred to other materials (such as conductive rubber, piezoelectric, capacitive and so on) because it is easier with them to develop a compensation system for underwater application. Any transducers has been mounted in every cells in figure 1. An

electronic circuit is necessary to manage the signals coming from the strain gauges and send them to the signal processing devices using a single wire (weather it is possible). This is accomplished by a 16 channels analog multiplexer. In fact, the arm allows the passage of only eight wires through it, due to the complexity of the internal devices such as motors, reducers, resolvers and so on. Three of them are necessary for the power supply, while one is devoted to the clock. Hence only four wires are available. The idea is to use two of them for the data transmission and the other two for the communication protocol, in order to recognise which channel is being acquired. Two possible approaches are currently under evaluation about transmitting the signals. The first one is simply the posting of the analog signals from the multiplexer output. The second consists of using a digital circuit able to convert analog data into digital ones to be sent through a serial line.

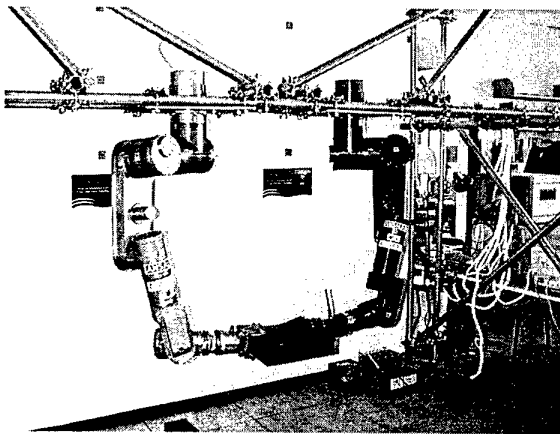


Figure 1. The dual-arm working cell

In the second case, two possibilities are considered: the use of an RS232 protocol with a serial link and the use of a parallel port adopting a custom protocol. In the first case, a custom circuitry is needed in order to demultiplex and synchronize sensor data to make them available as input of the ADC board (IP-330) on the VME bus, which is used for the control hardware. Anyway, it seems that the RS232 protocol solution is the best one, moreover by using a microcontroller to manage the signals both during the A/D conversion and the data transmission phase. The mechanical support must be able to make waterproof the sensor and electronic parts. For this way a metallic support to guest the electronic part has been developed. In the other hand, different kind of rubber are under study, in order to choose the one which is able to better acquire and transmit the normal force on the strain gauges and, in the same time, to make waterproof the system.

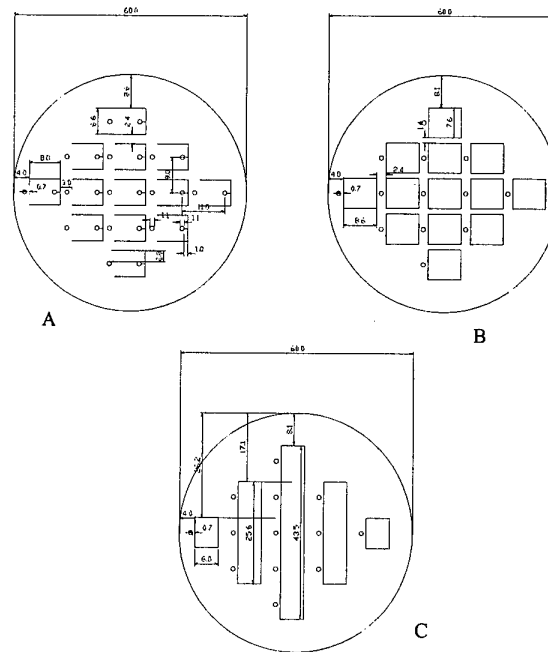


Figure 2 – The tactile sensor surface and support

The AMADEUS Project [8] (Advanced MANipulation for DEep Underwater Sampling) is an UE-funded project within the MAST (MARine Science and Technology) framework. Its aim is to study and develop on-the-edge technology for underwater manipulation of objects. The project is currently in its second phase, aimed at devising, producing and testing two different hardware setups: a hydraulic-actuated manipulator mounted on a Slingsby arm and a 'dual-arm workcell' [9], a couple of mechanical-actuated arms with smaller jaws on top (Figure 1).

The tactile sensor presented in this paper (figure 2) is going to be mounted on the gripper of each arm developed in Genoa, to perform underwater operations in the robotic manipulation field. The 'technical side' of the AMADEUS Consortium is composed of the Heriot Watt University, Edinburgh, responsible for the hydraulic gripper, the DIST Department, University of Genoa and the Naval Automation Institute, Genoa, who share responsibility for the dual arm workcell and the Human Computer Interface [10]. The 'scientific side' is composed of the Institute of Marine Biology of Crete and the University of Barcelona: these latter teams consist of biologists who have established the global features the developed systems should have. In section II we examine the main transducers technology for tactile and force sensors.

In section III we consider the main sensor feature (sensor shape, transducers, conditioning and sampling

circuit, data transmission, mechanical part and underwater features, protective covering rubber and compensator). In section IV, the performance of the sensor is reported, and some experimental results are reported. In section V the conclusion and the consideration about future developments are made.

2. Transducers for tactile and force sensor

The transducers able to be tactile sensor elements [11] are classified by the physical effects by means they convert a pressure/force in a different easy-to-get quantity.

We can consider:

- piezoresistive transducers, where the pressure is converted into a resistance difference, due to the expansion (contraction) of the sensor element (strain gauges, conductive rubber), used in many kind of applications [3] [12] [13];

- piezoelectric transducers, where a contact force is converted into a voltage difference (quartz based sensor); they are also used in micropositioning system for automatic precision assembly [14];

- capacitive transducers, [4] often used in biomedic and robotic manipulation fields, where a capacitive variable array of elements gives the tactile information;

- optoelectronic transducers, where a change of the light magnitude is performed in presence of external pressure [15] [16];

- inductive transducers, which are better used as position sensor rather than tactile sensor, due to their large dimensions. In this case, a pressure difference is detected by inductive effect.

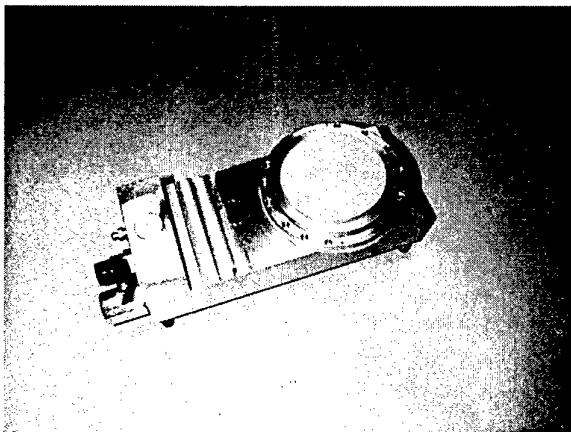


Figure 3 – The underwater tactile sensor

The use of strain gauges transducers for underwater application has been chosen because it is easy to carry on a mechanical structure, which compensate the water pressure. Moreover, they are more robust compared with other kinds. Talking about the underwater tactile sensor

prototype, we will use the same technology for the aspect described before, about making a reliable underwater device. Sensor features

3. The underwater tactile sensor

We are going to design and assemble four underwater tactile sensors based on strain gauges: the sensors will be mounted on the fingertips of the grippers of a dual arm cell for underwater manipulation applications. They will be used to control manipulation and in shape recognition tasks. The following points describe the development of this device.

3.1 Sensor shape

The shape of the sensors is given by the arrangement of 13 cells mounted in a rhomboidal configuration, in order to better acquire a good tactile information about the manipulated object (Figure 2). The strain gauges are placed on each cells of the surface A. This is a kind of steels, 0.5 mm thick. The three parts are fixed together. The part B (Alluminium, 1 mm thick) is necessary to avoid the dependence between the force applied on each cantilever. The part C (Aluminum, 3 mm thick) ensures the joint holding, and works as mechanical lock.

3.2 Transducers

Transducers were selected in a way such that they have good performances in according to the desired application, and they are able to operate correctly in the marine environments.

The choice of strain gauges (piezoresistive sensor technology) was preferred to other materials (such as conductive rubber, piezoelectric sensors, and capacitive sensors) because it is easier with them to develop a compensation system for underwater application. Any transducer has been mounted in every cell in figure 4.

3.3 Conditioning and sampling circuits

An electronic circuit is necessary to manage the signals coming from the strain gauges and send them to the signal processing devices using a single wire (weather it is possible). This is accomplished by a 16-channel analog multiplexer. In fact, the arm allows the passage of only eight wires through it, due to the complexity of the internal devices such as motors, reducers, resolvers and so on. Three of them are necessary for the power supply. Hence only five wires are available. The idea is to use two of them for the data transmission and the other two for the communication protocol, in order to recognise which channel is being acquired. The last one is used as external

clock, even if the analog board provides an own internal clock.

3.4 Data transmission

Two possible approaches are currently under evaluation about transmitting the signals. The first one is simply the posting of the analog signals from the multiplexer output. The second consists of using a digital circuit able to convert analog data into digital ones to be sent through a serial line.

In the second case, two possibilities are considered: the use of an RS232 protocol with a serial link and the use of a parallel port adopting a custom protocol.

In the analog acquisition case, a custom circuitry is needed in order to demultiplex and synchronize sensor data to make them available as input of the ADC board (IP-330) on the VME bus, which is used for the control hardware. Anyway, it seems that the RS232 protocol solution is the best one, moreover by using a microcontroller to manage the signals both during the A/D converting and the data transmission phase. At the present, the first tests on this prototype have been performed with the only analog data acquisition system.

3.5 Mechanical parts and underwater features

The mechanical support must be able to make waterproof the sensor and electronic parts. For this way a metallic support to guest the electronic part has been developed (figure 4). In the other hand, different kind of rubber are under study, in order to choose the best in one, or the one which is able to better acquire and transmit the normal force on the strain gauges and, in the same time, to make waterproof the system.

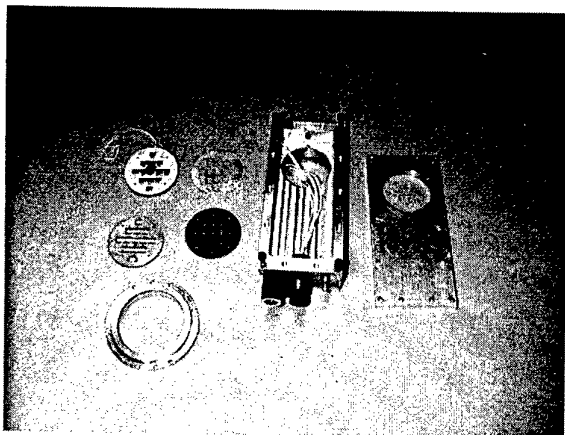


Figure 4. - Main components of the tactile sensor

3.6 Mould

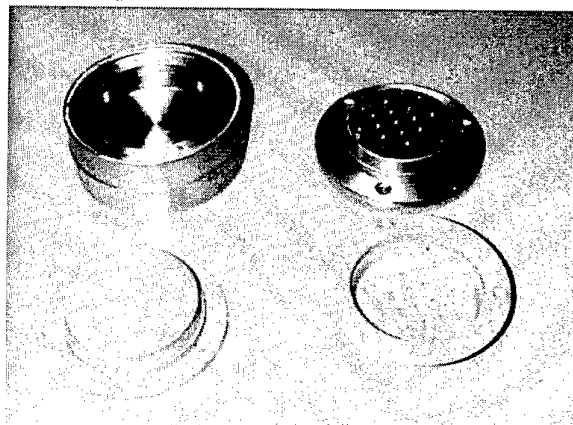


Figure 5 – The mould and the covering rubber

In order to protect the sensor surface, it is necessary to cover it with an elastic material, able to transmit the surface force applied to the transducers, and able to work at the high water pressures. For this reason, a bi-component silicone rubber has been used. The mould in figure 5 has been developed in order to obtained a perfectly compliant shape with the sensor surface. The water retain is obtained with the mechanical support.

3.7 Compensation

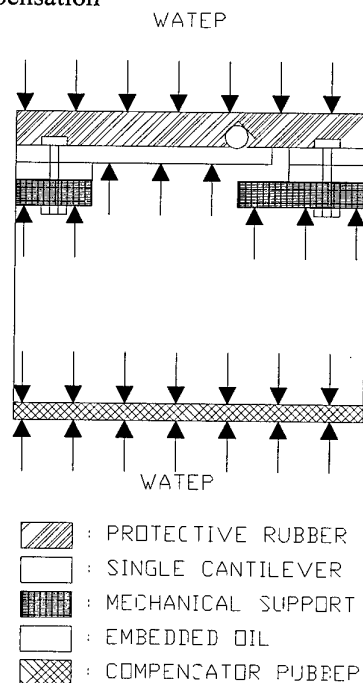


Figure 6 – The tactile sensor section

To get the right performance at different water pressures, it is necessary to completely fill of oil the mechanical support,

or generally, with a not compressible liquid, which provides the right performance of the transducers (they are however covered by a special not invasive rubber) and the embedded electronic. Nevertheless, it must be add a compensator on the base of the mechanical support, as showed in figure 6. It is made of a silicone rubber, more elastic then the protective covering rubber. In this way, the presence of the compensator allows to maintain the cantilever of each cell in the idle position, if the pressure arises.

4. Performance of the tactile sensor

In the graphic in figure 7 it is showed the characteristics measured on a strain gauges mounted in a single cell. The signals have been conditioned by a quarter Whetstone bridge (resistance of the strain gauge and of the other resistance: 350 ohm; power supply: 5 V), and then acquired through a differential amplifier.

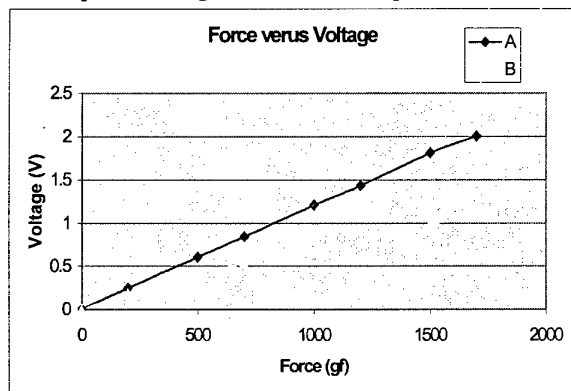


Figure 7 – Voltage versus Force

Gain of the amplifier: 500. The A characteristic has been acquired without any covering rubber on the sensor surface. The B characteristic has been acquired with the silicone rubber covering showed in figure 2. The decreasing of the Voltage magnitude depends from the distribution property of the chosen rubber.

2:1 scale of each cantilever

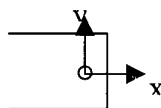


Figure 8 – The cantilever

It has a good linearity. The accuracy is around 50 g, and it could be improve by improving the amplifier and increasing the signal-to-noise ratio.

Two kinds of experiments have been performed on the tactile sensor in air.

The first ones have been oriented on the objects shape recognises. In figure 9 it is showed the response acquired in the presence of a cylindrical shape object on the surface.

The second ones have been conducted in order to study the effect of mechanical filtering in presence of elastic cover [17]. In figure 10 and 11 the horizontal and vertical characteristics are showed. The data have been acquired with a one kilo punctual force, moving on the surface covered with the silicone rubber. The direction of the displacement is showed in figure 8. As showed in figure 10, the characteristic is symmetric with the center, where the strain gage is mounted; the other one (figure 11) is not perfectly symmetric, that's why the force resultant depends on the versus of the displacement

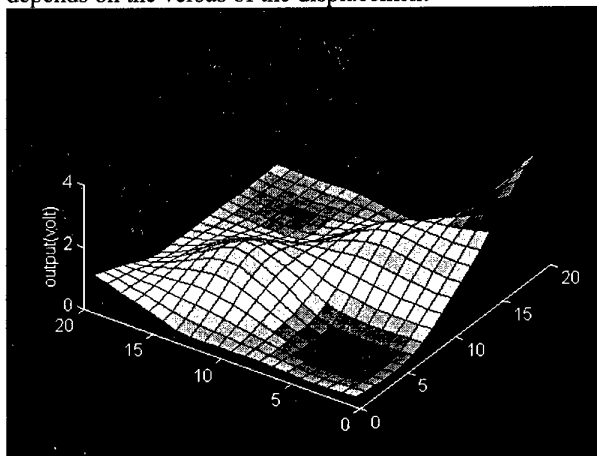


Figure 9 – Local shape recognise

Other tests of the tactile sensor are going to be done, in order to evaluate the performances at different pressure of water. A first test in water has already been performed at the 12 AT pressure in the idle condition (without external contact force on the sensor surface) with good results.

5. Conclusion

The design and the development of a tactile sensor prototype, able to perform robotic application in the underwater manipulation field have been described.

The transducer chosen, the sensitive surface and the mechanical waterproof support have been proposed as a kind of solution concerning a device able to work in hostile environment. Some experimental data have been

reported, among them there are the impulsive force response and the local shapes recognize.

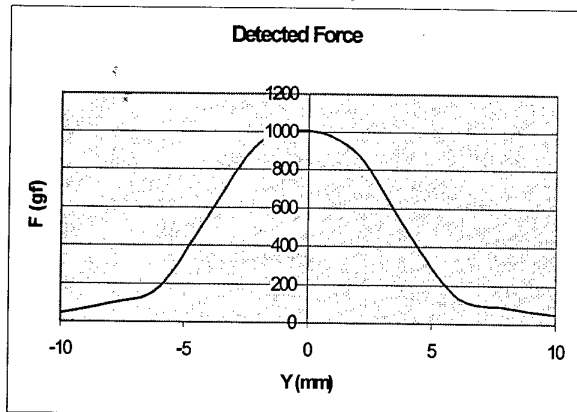


Figure 10 – Force versus Y displacement

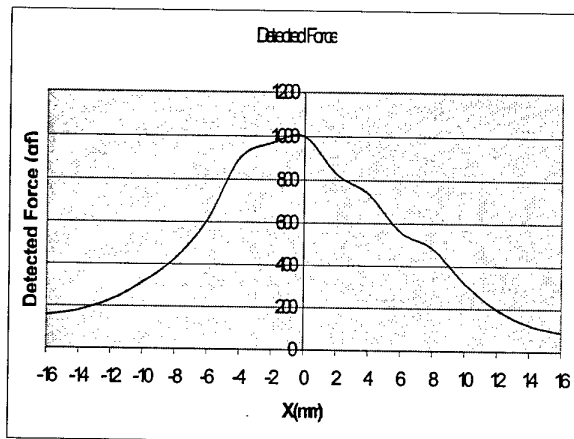


Figure 11 – Force Versus X displacement

This system must be still considered as a prototype. In fact, the sensor needs to be improved in terms of dimension and sensitivity. In fact, the mechanical support should be reduced and the sensitivity of the sensor surface must be increased. So, it is required a detailed study on a more complex mechanical structure, on a more sophisticated electronic technology in order to allow the use of a greater number of cells.

6. Acknowledgement

This work was supported by the EC MAST III AMADEUS 2 project.

7. References

- [1] G.Hirzinger, B. Brunner, J. Dietrich, J. Heindl, "ROTEX - The first Remotely Controlled Robot in Space", *IEEE Int. Conference on Robotics and Automation*, San Diego, California, May 1994.
- [2] M. R. Cutkosky, *Robotic Grasping and Fine Manipulation*, 1985, Kluwer Academic Publisher.
- [3] M.T. Mason and J.K. Salisbury, , *Robot Hands and the Mechanism of Manipulation*, 1985, Cambridge, MIT Press.
- [4] A. Bicchi, "Contact sensing from force measurements", *The International Journal of Robotics Research*, Vol. 12, N.3, June 1993.
- [5] R.S. Fearing , "Tactile Sensing Mechanisms", *The International Journal of Robotics Research*, Vol. 9, No.3, June 1990.
- [6] E.G.M Holweg et al. "Slip Detection by tactile Sensors: Algorithms and experimental Results", *IEEE Int. Conference on Robotics and Automation*, Minneapolis, Minnesota, April 1996.
- [7] D.J. O' Brien, D.M. Lane, "Force and Slip Sensing for a Dexterous Underwater Gripper", *IEEE Int. Conference on Robotics and Automation*, Leuven, 1998.
- [8] D. M. Lane et al. "AMADEUS: Advanced Manipulator for Deep Underwater Sampling", *Special Issue of the IEEE Robotics and Automation Magazine*, December 1997.
- [9] D. Angeletti, G. Cannata, G. Casalino, "The Control Architecture of the AMADEUS gripper", *Int. Journal of Systems Science*, Vol.28, 1998.
- [10] A. Bruno, G. Bruzzone, E. Spirandelli, P. Virgili, "Architecture, Features and Evaluation of effective, multi-purpose Human Computer Interfaces", *IEEE OCEAN '98 International Conference*, (1998), 28th September – 1st October, Nice (France).
- [11] Mark H. Lee "A survey of Robot Tactile Sensing Technology", *The International Journal of Robotics Research*, Vol. 8, No. 3, June 1989.
- [12] A. Cicchetti et al. "An Intrinsic Tactile Force Sensor for Robotic Manipulation", *ICAR*, 1995
- [13] Y. Yamagata, T. Higuchi, "A Micropositioning Device for Precision Automatic Assembly using Impact Force of Piezoelectric Elements", *IEEE Int. Conference on Robotics and Automation*, 1995.
- [14] R. A. Russell, *Robot Tactile Sensor*, Prentice Hall of Australia, 1990.
- [15] N. Maalej, "A Miniature Electrooptical Force Transducer", *IEEE Transaction of Biomedical Engineering*, 1998.
- [16] S. Ozawa et al. "High-Speed Measuring Equipment of Fibre Core Position of Optical Fibber Array Using Piezo Actuator", *IEEE Int. Conference on Robotics and Automation*, 1995.
- [17] M. Shimojo, "Mechanical Filtering Effect of Elastic Cover for Tactile Sensor", *IEEE Transactions on Robotics and Automations*, Vol. 13, No. 1, February 1997.

Development of an Actuator for an Automatic Drum Playing in Drive Motors

Eiji Hayashi
Kyushu Institute of Technology
e-mail haya@mse.kyutech.ac.jp
Masami Yamane
Waseda University

Abstract

A moving coil-type actuator in drive motors was designed and developed to control a drumstick in automatic drum playing. The first purpose of this study was to develop an actuator capable of the fast response. To obtain high magnetic flux in the actuator, a rare earth cobalt magnet is used. The servo system functions by means of position feedback, and it uses a follow-up control that allows the drumstick to follow any input waveform. Further, the optimum position for securing the drumstick is determined by analyzing the base of the model of the rigid body in a plane, additionally the coupling between the drumstick and the rotor is designed.

1. Introduction

In recent years, rapid progress has been made in computing speed and memory in electronic devices. Electronic musical instruments have improved remarkably in their performance, especially regarding their ability to sample the data of various waveforms. However, the sound they produce is not satisfying when compared with the actual sounds of acoustic musical instruments, due to their use of the audio devices. This study aims to develop

an automatic drum-playing device which is able to play the snare drum in the same manner as a human; that is, to perform the snare drum by using a drumstick.

A simple technique of drum playing, involves the drum head being struck near its center with a drumstick, and after this drumstick returning rapidly. In the case of human players, the gripping force of the drumstick is changed from a strong to a soft movement when the drumstick rebounds from the drum head. The drumstick does not keep the drum head from vibrating. In case of an actuator, a fast response and gain control instead of gripping force is needed. First, the purpose of this study is aimed at developing an actuator capable of fast response.

2. Actuator

The actuator was designed and developed to control the drumstick in automatic drum playing. Actuators marketed in the past had utilized a DC motor. However, there were some problems involved in repeatedly and quickly moving the rotor of the actuator within a narrow rotational angle. Voltage drop was caused by the abrasion of the commutator, and heat was caused by the flow of the current through the rotor in the motor. As a result, the

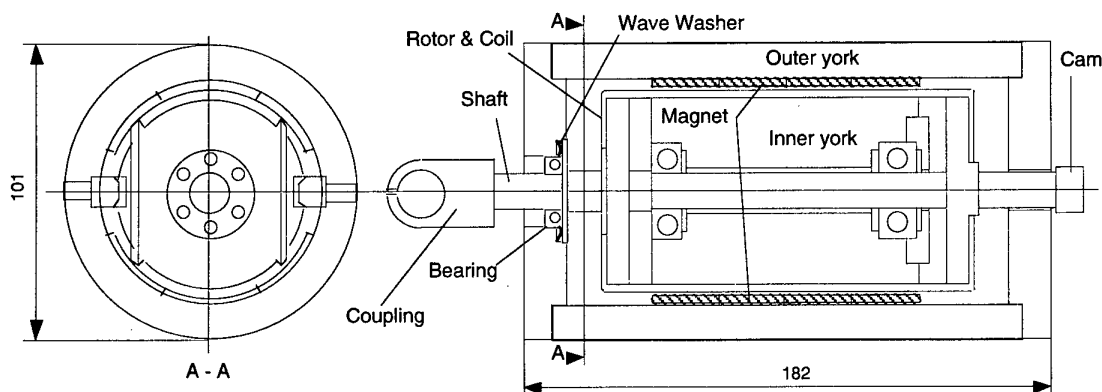


Figure 1. Schematic view of Actuator

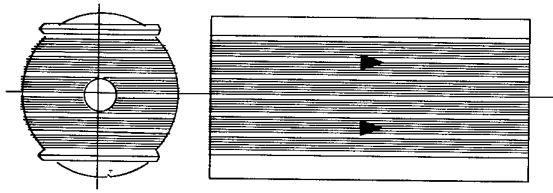


Figure 2. Coil form

character of the actuator remarkably diminished the control of the drumstick. Therefore, further development of the actuator was necessary in order to solve the problems described above. A moving coil-type drive motor [1][2] has been designed for this purpose, as shown in Fig.1.

2.1 Magnetic circuit

The rotor in the actuator is designed as shown in Fig.2. The rotor's core is made of an epoxy resin as in an enameled wire. The rotor core is built in the form of a cylinder in order to be as light as possible. The enameled wire is wound in the direction shown in Fig.2 in order to obtain optimum magnetic flow. The coil resistance of the rotor is 12.6 Ω .

2.1.1 Magnetic flux

High magnetic flux has been obtained in the actuator through the use of a rare earth cobalt magnet. As shown in Fig.3, two magnets were secured in the inside of the outer yoke. The gap between the magnet and the inner yoke is 4 mm, and the magnetic flow in the gap can be expressed by the following equations;

The cross-sectional area of the magnet A_m is

$$A_m = \left(\frac{d_o + d_i}{2} \cdot \frac{\pi \cdot \theta}{360} \right) \cdot L \quad (1)$$

The cross-sectional area of the gap A_g is

$$A_g = \left(\frac{d_i + d_o}{2} \cdot \frac{\pi \cdot \theta}{360} \right) \cdot L \quad (2)$$

The length of the gap L_g is

$$L_g = \left(\frac{d_i - d_o}{2} \right) \quad (3)$$

Using the magnetic flux at the maximum level of the magnetic energy B_d from reading the demagnetization curve, the magnetic flux in the gap can be expressed by the equation

$$B_g = B_d \cdot A_m / A_g \cdot \frac{1}{\sigma} \cdot \frac{1}{f} \quad (4)$$

where σ and f are leakage factors. The conditions of the leakage factors, $\sigma = 1$ and $f = 1$, were used, and Eq.(4) was calculated. As a result, in case of the present

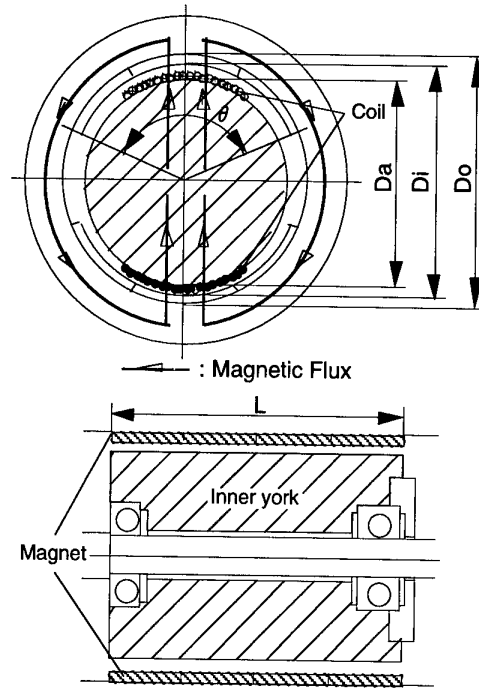


Figure 3. Magnetic circuit

magnetic circuit the magnetic flux in the gap B_g was of the approximate value 0.44 T. The magnetic flux in the gap was measured, and its obtained value was approximately 0.45 T. The error became approximately 2 % by comparing the measured and the calculated data. As a result, the analysis of the magnetic flux was indicated to be applicable under the assumptions regarding the developed magnetic circuit.

2.2 Coupling

Generally, drum players don't perform by gripping the edge of the drumstick by choice. Therefore, the gripping position and the coupling of the drumstick was designed in order to connect the drumstick to the rotor base in consideration of the actual human grip.

The analysis used the model of a rigid body in a plane. The analytical model of the drumstick is shown in Fig.4. In this model, the rebounding motion of the drumstick striking the drumhead demonstrated that the drumhead is struck by the tip of the drumstick. And the drumstick is secured at the center of percussion if its center of percussion could be derived from the analysis. Because the drumstick rotates round the center of percussion on which the impulsive force acts. And then, the drumstick after it was struck the drumhead should be able to rebound naturally as possible. In what follows, the analysis of the center of percussion is discussed.

The drumstick is pivoted at a point other than its center of gravity as shown in Fig.4. The motion can be

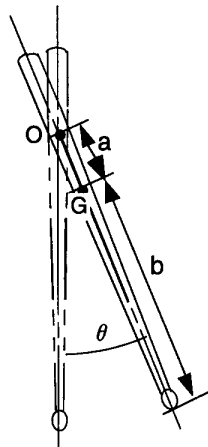


Figure 4. Model of stick

Table 1. Specifications of stick

Item	Unit	Value
a	m	59.0
b	m	225
I_G	$\text{Kg} \cdot \text{m}^2$	5.86×10^{-4}
I	$\text{Kg} \cdot \text{m}^2$	7.16×10^{-3}

given by the equation

$$I \ddot{\theta} = M \cdot g \cdot a \cdot \sin \theta \quad (5)$$

where I is the inertia, g is gravitational acceleration, M is the mass of the drumstick, and a is the distance from the rotational center to the center of the gravity. And by assuming the motion within $\sin \theta \approx \theta$, the period of the natural oscillation τ can be expressed by

$$\tau = 2\pi \sqrt{I / M \cdot g \cdot a} \quad (6)$$

Using Steiner's theorem, the inertia of the drumstick I_G secured at the center of the gravity is

$$I_G = I - M \cdot a^2 \quad (7)$$

When the drumstick strikes the drumhead, the impulsive force acts at the drumstick's tip. At that moment the motion's change is exhibited by the change of angular velocity at any point on the drumstick. But

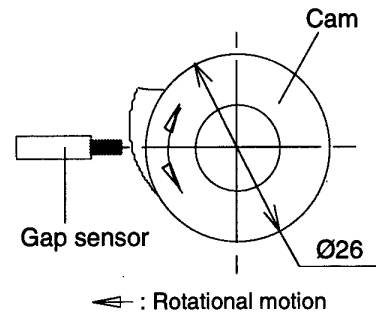


Figure 6. Design of cam

the position of one point on the drumstick remains unchanged; there is only unchange point in the drumstick, this is the center of percussion. Its point can be given by the equation

$$a \cdot b = I_G / M \quad (8)$$

The schematic view of the coupling and the Character of the drumstick, indicated by the symbols of a or b , is shown in Fig.5 and Table.1, respectively. As a result, the center of percussion for the drumstick can be obtained. The drumstick is secured by coupling at the position of the center of percussion. The drumstick can rebound naturally from the drumhead in this coupling design. And also, the drumstick is controlled so that it does not prevent the drumhead from vibrating as freely possible.

2.3 Cam for measuring the position of the rotor

Measuring the position of the rotor was achieved using the mechanism of the cam with an eddy current-type sensor, instead of changing the circular motion of the rotor as the rotor returned. The projecting part of the cam is designed so that the gap between the sensor and the projecting part, as the rotor returns, can obtain ± 0.5 mm to the rotational angle of ± 0.39 rad (see Fig.6), and the output of the sensor is adjusted ± 1.2 V. This mechanism is positioned on the end edge of the rotor.

3. Synthesis of the control system

As shown in Fig.7, the servo system functions by

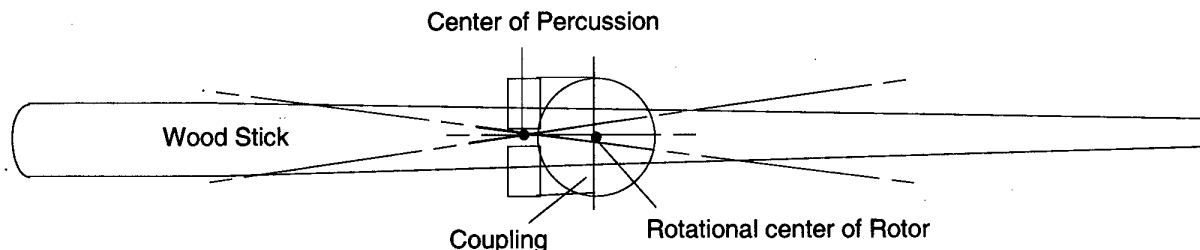
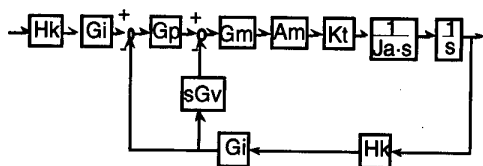


Figure 5. Schematic view of Coupling



Gi : Controller gain
Gp : Position feedback gain
Gm : Manipulation gain
Gv : Velocity gain
Am : Amplifier
Kt : Torque constant
Ja : Actuator inertia
Hk : Position voltage constant

Figure 7. Diagram of servo system

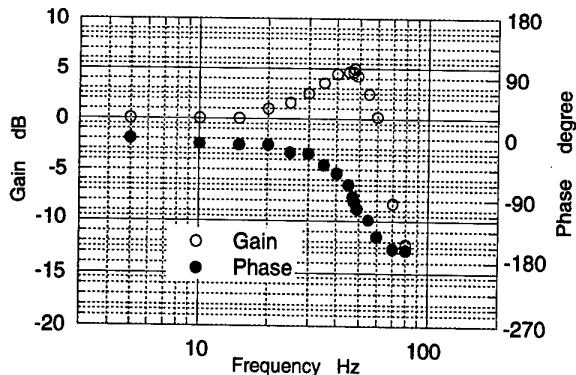


Figure 8. Frequency response

means of position feedback and velocity feedback, measuring the position of the rotor with a eddy current-type sensor described in prior the section, and uses a follow-up control that allows the drumstick to follow any input waveform. The velocity feedback system is achieved by using a differentiator to differentiate the position signal from the sensor. The servo amplifier for the touch actuator is a pulse-width modulated type, with a maximum current of 9 A. As a result of this development, the actuator produces a torque of 0.768 N·m/A, a thrust of 2.86 N/A at the drumstick's tip, and a frequency response of 47 Hz, including the drumstick as shown in Fig.8.

3.1 Drum playing system

The system in Fig.9 is comprised of two actuators with a servo mechanism for each actuator. In the present system, two actuators for the drumsticks are needed to control its motion separately.

In order to control this network of actuators, a two-level, hierarchically structured computer system was introduced. At the slave level, 4 micro-processors are employed to efficiently control the two actuators. The interface between the top level and the bottom is built by utilizing a dual-ported memory in integrated circuit memories, and it is possible to transfer the data quickly

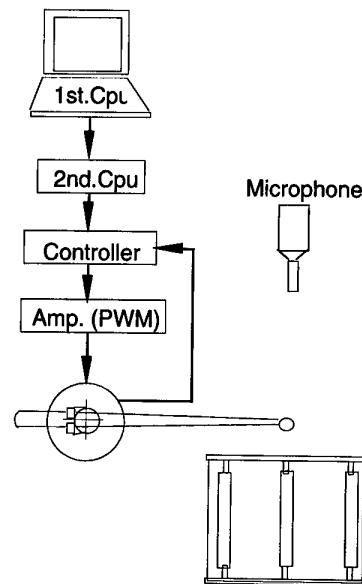


Figure 9. Automatic playing system

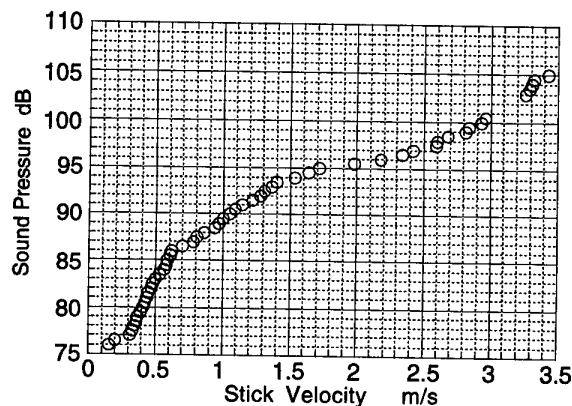


Figure 10. Relationship between stick velocity and sound

from the top to the bottom level. The CPU system in the bottom level is designed and developed by using an 8 bit mode and a D/A convertor of 12 bits.

The top level has to edit musical data and translate it into the actuator's input waveform parameters based on the musical data. At the same time that the individual CPU system in the bottom level translates the input waveform based on the input waveform parameters, it output the waveform to the servo system for the actuator.

4. Basic experiment for drum playing

A constant speed for the input wave form was used so that the drumstick's drumhead-striking velocity can be controlled by its speed. The relationship between the

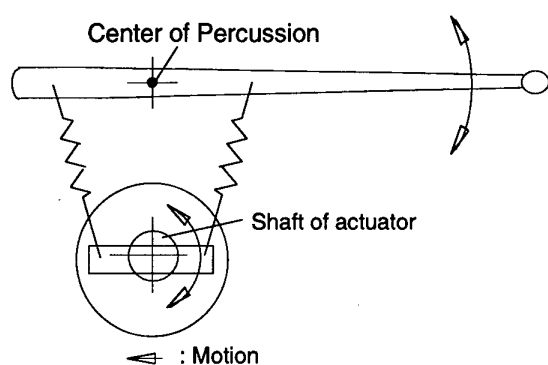


Figure 11. Experimental Model

velocity of the drumstick's tip and the resulting sound pressure was measured using a sound level meter, as shown in Fig.10. The sound level meter was set 1 m above the drumhead. The drumstick speed at its tip indicates it to be in proportion to the sound pressure, though the produced sound is slightly different compared to the sound that a person produces by playing a drum. This phenomenon was particularly exhibited in regard to the strong and soft tones. Therefore, the experimental coupling, which secures the springs, is designed as shown in Fig.11. This mechanism allows the drumstick to act in an up - and down motion by stretching the springs to the right and left. And also, the gripping force cannot be changed as in the case of a human player because of the consistent stiffness of the springs. The servo system of this mechanism was designed in the manner shown in Fig.7. The actuator of this mechanism produced a frequency response of an approximately 30 Hz dynamic range. When the ex-coupling and this mechanism are compared in regard to frequency response, the frequency response of this mechanism is lower by approximately 17 Hz. Yet dynamic range has increased by +5 dB and -5dB in the realms of loudness and softness, respectively. Additionally, the produced sound has a tone bearing a greater similarity to human playing.

Finally, the necessary grip of the drumstick is spring-like, and by utilizing a spring we ensured that the drumstick can be returned naturally and rapidly from the drumhead.

5. Conclusion

- (1) The actuator developed could produce a torque of $0.768 \text{ N}\cdot\text{m/A}$, a thrust of 2.86 N/A at the drumstick's tip, and a frequency response of 47 Hz, including the drumstick.
- (2) When the measured and the calculated data regarding the magnetic flux between the magnet and the inner yoke is compared, we see an approximately 2 % error. Thus, the theoretical equations regarding the magnetic flux apply to the assumptions governing the developed magnetic circuit.
- (3) The drumstick needs to be gripped at the axis of the rotation if it is mounted on a fixed horizontal axis. And the position of the center of percussion could be determined by utilizing a model of a pendulum.
- (4) The actuator could produce stable tones ranging from loud to soft by using a constant speed for the input wave from, and the dynamic range obtained was approximately 29 dB.
- (5) An experimental coupling was developed that added two springs to the mechanism. As a result, loud and soft dynamic range increased by +5dB and -5dB, respectively. And the sound produced could have tones resembling human playing.

Acknowledgment

The authors would like to acknowledge the financial support of the Electro-Mechanic Technology Advancing Foundation.

References

- [1] K.Sekiguchi, R.Amemiya, H.Kubota and M.Yamane, "Development of an automatic drum playing device, Int.Computer music conference, Japan, 1993, pp.428-429.
- [2] E.Hayashi, M.Yamane and H.Mori, "Development of a moving coil actuator for an automatic piano, Int. j. Japan Society for Precision Engineering, Vol.28 No.2, 1994, pp164-169.

A Flexibly Operated Electro-Mechanical Fine Stepper Motor.

E Wong Chun Kay**, E C Partington** and W A Bullough*

* University of Sheffield, Dept. Mech. Eng., Mappin Street, Sheffield

w.bullough@sheffield.ac.uk

** Formerly of the University of Hong Kong, Department of Industrial Engineering

Abstract

A preliminary proof of concept is given for a novel, all electric, linear to rotary motion precision drive which is based on electro or magneto structured fluid clutches and electro strictive driver stacks. In the embodiment utilised for the present exercise the drive is entirely electrostatic.

1. Introduction

Many attempts have been made to design an electronically controllable producer of fine precision rotary motion. Perhaps the handiest example of this lies in the stepper motor in which alas, the regulation of torque at high speeds is severe. This problem is caused principally by the inductive nature of the force producing element: the greater the number of teeth the cogging mechanism has the more complicated the winding structure and, at higher speeds, the more severe the degeneration of the wave form of current. Fine steps and high stepping speed do not come together. In order to overcome these and stiffness limitations a new concept mechanism was investigated.

In theory magneto strictors and a powerful magneto rheological fluid clutch could be used in the drive. For the present purpose on all electrostatic apparatus is used.

2. Machine Concept

The mechanism comprises what are essentially matched, variable stroke, positive displacement piezo drivers which rotate twin cylindrical clutch driver plates (via levers) which are coupled to the load, and operate in tandem by alternate excitation of intervening electro rheological fluid - Figure 1. This shows two piezo drivers that work in synchronism with the clutch in ratchet fashion: as each PZT expands the corresponding clutch is simultaneously excited into an unyielding situation (for a matched load) and the output cylinder rotates by a small amount. As the piezo starts to reverse its direction (because the charge is removed) the clutch excitation is also removed, thus the lever drags back the driver drum to its 'bottom dead centre' Figure 2. In sequence, the twinned driving system takes up

the other barrel thereby advancing the load in continuous fashion.

Speed control can be obtained in two ways, by adjusting the magnitude of the voltage pulse (which gives more or less piezo displacement) and/or changing the frequency of its supply. Reversal of the motion can be obtained by repeating or skipping a pulse. Given the risks inherent in piezo operation in tension the inertial load of the barrel has to be fixed accordingly, the load and the fluid mass being considered to be added to the output barrel mass for this purpose [1]. Nevertheless, given this, the all electronic dual control of the piezo output and perhaps the potential advantage of independent clutch control seem to provide the basis for a precision, flexible and potentially electronically variable configuration of rotary motion device, provided compliance and backlash are restricted.

The main outstanding question at this stage is will such a machine actually work? In the present paper a positive outcome of this question is shown to be forthcoming. The concept is brought before the meeting in order to procure industrial interest towards answering the second most important question - is there a use for such a device? Is it worth developing and if so, at what scale? To aid this advance simple quantitative assessments formulae are given [2] and justified by comparison with preliminary test results.

3. Calculation Procedure

The output displacement from each piezo stack is amplified by the nominal lever advantage L/ℓ to give a linear displacement at the radius of lever connection to the rotating barrel (r). The resulting "ideal" performance formulae are given on Figure 3.

The input values to these formulae come from step pulse signals obtained through a parallel interface card, which are transmitted to a power supply (Kepco) which in turn outputs a zero or high tension step voltage to the ER clutches, so as to perform grip or slip action. Sawtooth signals derived from a 12 bit digital to analogue converter, are transmitted to a proprietary amplifier which outputs a pre set voltage to matched PZT's (Physik Instrumente), thus fixing the magnitude and frequency of the electrostrictor displacement.

Without the amplifying lever the PZT's would have to run at high frequencies to produce even a modest rotational output speed. The present arrangement is designed to run at 1+ radians per second when excited at 200 Hz or less, by virtue of an approximately 10:1 lever. The fluid used was a proprietary mixture of about 10 kPa max yield shear stress, which operated in the 0.5 mm inter electrode channels. The force available from the piezo is about 10,000 N which translates to some 1000 N at the clapper/driver. This corresponds with approximately 300 cm² ER shear plane area (within a factor of safety) at a conservative 2 kV clutch excitation. This arrangement gives approximately 0.5 mm/piezo stroke movement, at the barrel surface.

4. Results and Conclusions

Initial tests at zero output load showed a displacement efficiency (measured/ theoretical output displacement) of up to 83%. The loaded output shaft shows some slippage - Figure 4. No doubt this is due to a combination of solid part and ERF compliance, imperfect timing and the limitations imposed by the constant power driver amplifier [2].

A novel rotary stepper motor is thus in prospect. The precision linear actuator is programmable with speed and stepwidth being adjustable. Additional ERF control offers possibilities in position/velocity working which needs further study and the production of more comprehensive relevant test results - in the intended speed/torque domain.

A magneto rheological suspension could be expected to provide up to ten times more low shear rate yield shear stress (and specific torque) at the same order of viscosity (100/200 mPas), as a typical ERF. It would need a somewhat bigger construction of clutch to enable placement of a magnetic circuit which would probably be limited to an unforced switching response time of approximately 5 milli seconds. The increased performance could presumably be offset by higher weight and cost and possibly lower speed.

5. References

- [1] M. Whittle, R. Atkin and W.A. Bullough, "Fluid Dynamic Limitations on the Performance of an ER Clutch". *Jnl. Non. Newtonian Fluid Mech Vol 57, No. 1*, April 1995, p. 1-25. See also: H. K. Tonsoff & A. Stegman, "ERF Based Linear Drive System" *ibid*, p. 3305-3314.
- [2] E. C. Partington, E. Wong Chun Kay and W.A. Bullough, "An Electrostatic Stepper Motor", *Jnl. Mod. Phy. B, V10, No 23924*, 1996, pp. 2917-2923.

6. Acknowledgments

are due to Croucher Foundation and British Council of Hong Kong for support of research and collaboration, respectively. The experimental work was undertaken at the University of Hong Kong.

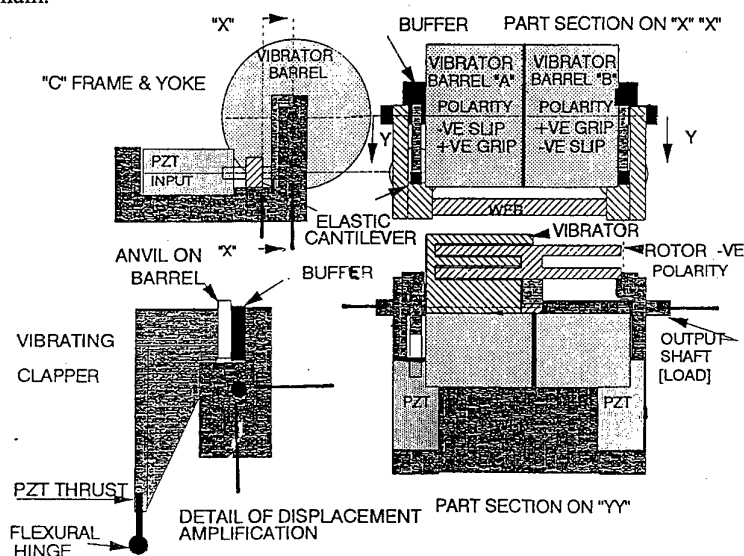


Figure 1. General arrangement of the digital electro static power train: the piezo stacks reciprocate to drive the output drum continuously via ER clutches. The speed of motion can be varied by adjustment of the piezo excitation magnitude and frequency; at low speeds steps down to 0.01° should be possible.

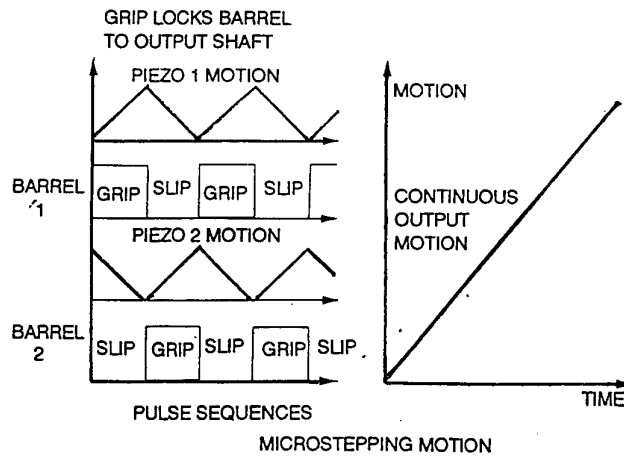
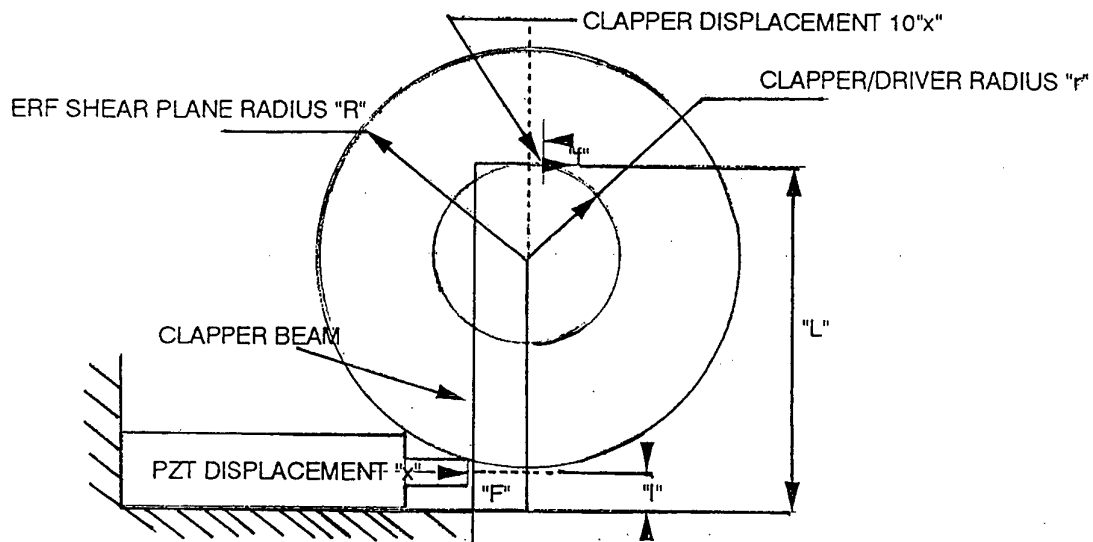


Figure 2. Synchronised motion of piezo's and electro rheological fluid clutches.



DISPLACEMENT AMPLIFICATION = $L/l = 10$

FORCE ATTENUATION $l/L = 1/10$

AVAILABLE TORQUE = $[F] \times [l/L] \times [r]$

TRANSMISSIBLE TORQUE = $[ERF \text{ AREA}] \times [ERF \text{ STATIC YIELD STRENGTH}] \times R$

OUTPUT SPEED = $[FREQUENCY] \times [10x] \times [2 \text{ BARRELS}] \times [1/r]$ RAD/SEC

Figure 3. 'Unloaded' formulae for estimation of ideal (no slip/regulation) performance.

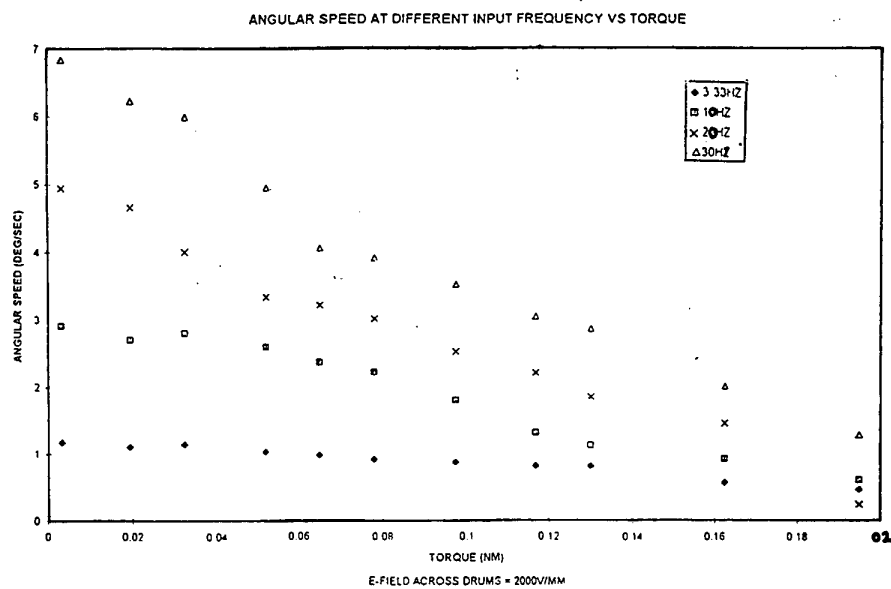


Figure 4. Sample characteristic of the prototype power train on load.

Design a Capacitive and Perseptible Tactile Sensor for Robot Hand

Francisco Flávio Córdova Quiróz

Mauro Francisco Espinosa Coss

*Universidad del Valle de México, Campus Tlalpan, Departamento de Ciencia y Tecnología
San Jan de Dios #6, Col. Exhacienda de San Juan, C.P 14370, México D.F., México*

Tel: (525) 2 38 53 00, Ext: 04202, 04216, 02245, Fax: (525) 6 71 25 91

Email: ffcq@df1.telmex.net.mx, fcordovamredipn.ipn.mx

Abstract

This work take the sensibility hand construction, it is based in two systems, the sensitive system (skin), and the nervous system for the signal transmission, the prototype design satisfy all requirements to select from one exited point to other, such as the pressure on this point to send a computer, comparing [1] that doesn't define the precise exited point.

1. Introduction.

Studying the human arm and hand composition, it's possible observe that is composed of four basic systems, which are the most important to an appropriate and a proper way of working, those systems are :

- Osseous System.
- Muscular System.
- Sensitive System.
- Local and Peripheral Nervous System.

Where each system has special and particular functions, all this systems are synchroniced to work together, and the result is a big and complex system. Now it's describing all systems emphasizing the most important in our work.

1.1. Osseous System

This is in charge of sustaining all our body, it gives consistence and firmness, over the rest of all other systems, comparing this versus a robot then we can say that this is it's structure, see figure #1.

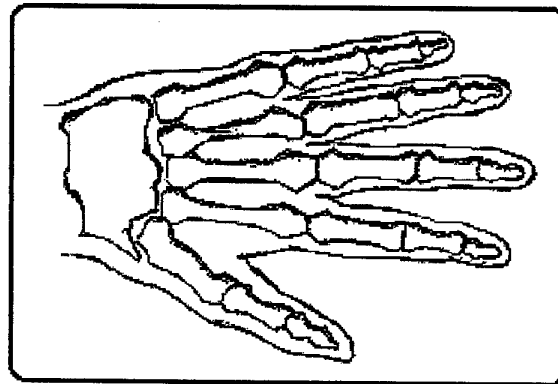


Figure #1. Osseous System

1.2. Muscular System

With the use of this system we obtain all the movements of the human body and we can move and displace any object or body, only if the maximum weight of the object is drawn by force and it is produced by the muscles. whereas in a robot or mechanic arm, we are talking about the force that is produced by the motors of the unit and its structure.

1.3. Sensitive System

The sensitive system is associated with the skin and through this it is possible to detect the next three parameters of main importance to evaluate the different stimulus of the environment, for a Robot it's the sensor and transducers to acquire this stimulus, these parameters are:

- Pressure.
- Temperature.
- Rugosity of the Surface.

1.4 Nervous System

This system is in charge of transmitting the different impulses that receive and send any part of the human body to the brain. This system is formed for an entire organism whose functions are: relationship life, and organic function automatic control.

2. Analysis

The sensitive system or skin has two parts; an external called epidermis and an internal called dermis.

Under the epidermis we can find the dermis that is the most internal layer of the skin. It is formed by living cells, that adopt the form of the closest one for the exterior, they form a surface with entrances and exits called papillas, in the same way we can find nervous terminals in charge of registering the tact stimuli, temperature and pressure.

The skin has little nervous terminals that monitor all actions that we have done on it. Once we have a contact, it transmits a little electrical impulse that goes to the peripheral nervous system, but if the impulse is bigger than a different one, it will go to the nervous central system and then its reflection will activate itself to avoid damages into the contact point, see figure #2.



Figure #2, Nervous Terminals in Charge of Registering the Tact Stimules

The function of these nervous terminals is to protect, and it forms one of the main special senses of the human body, the tact.

Now if we examine the terminals that we have in the skin they act as little switches that indicate the contact point and evaluate the pressure that we are putting on it.

If we separate this effect like electrical phenomenon, we have two separate subsystems, the first one is the tactile subsystem in on/off sensibility form, the second one is the evaluated pressure subsystem, so we will watch that the circuit has been closed, but we haven't quantified the pressure that it's putting on it.

To solve this problem, we can use a pressure membrane as an evaluating element, where the deformation of the membrane sends an electric impulse that is proportional to the total pressure that it's putting on it.

We can also solve this problem using variable capacitors, because if we alter the length that separates the plates of the capacitor, we will vary its capacitive value, and we also have a proportional variation to the pressure that it's putting on it but, this will be considered in the second part of the work.

The nervous system as we see is divided anatomically in two parts: central nervous system, and peripheral nervous system, like shown in the figure #3.

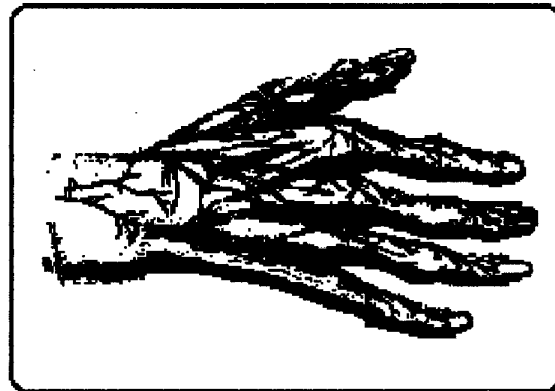


Figure #3, Peripheral Terminal Nervous System

The organs of the central nervous system are: encephalon and spinal marrow, and the organs of the peripheral nervous system are: the nervous properly said. (organs are not mentioned in the study).

The anatomic functional unit of the nervous system is the neuron, which is constituted by a cell body that has several prolongations; the largest is called cylinder axis, and the shortest is called dendrite, see figure #4.

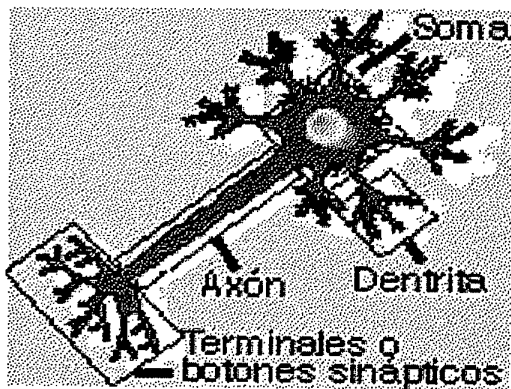


Figure #4, Neural Schematic Diagram

The neural body is the place where functional information occurs, it generates a stimulus or registers it and it is the cylinder axis which works like a conduct way to the stimulus, through the synapsis the stimulus crosses each neuron. The stimulus transmission system is reflected by the cables and the footprints of the physical system.

As well as the quantity of these nervous terminals by square centimeter is too big, due to its short gap between each other, it involves the development of a system that detects each terminal in an independent way.

In our work we realized an arbitrary, and not so detailed division of the human hand surface. that it could have 124 contact points and one evaluation of the pressure that we are putting on it, like shown in the figure #5.

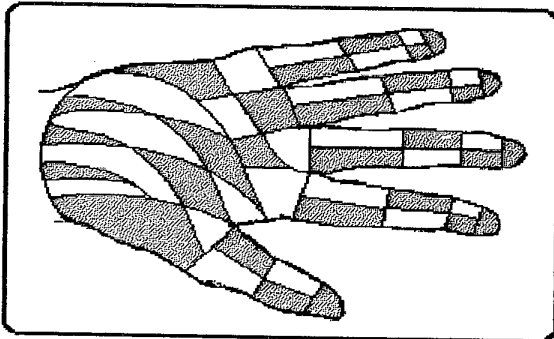


Figure #5. Contact and evaluation Points on the Hand

3. Development

Now it's known the sensitive system, is possible to design a system that realize the same functions, but with on/off sensibility.

Then the sample and control systems for this points it's a keyboard controller, because through this devices it is possible detect the activated points in diferent time. In the study of this devices we find some controller that fulfill own necessity, like the intel controllers [2] which as the 8279, 83C51KB and the 8XC51SL, all this devices are keyboard controllers but the 83C51KB was selected because thus characteristics and ease use like shown the diagram block in the figure #6.

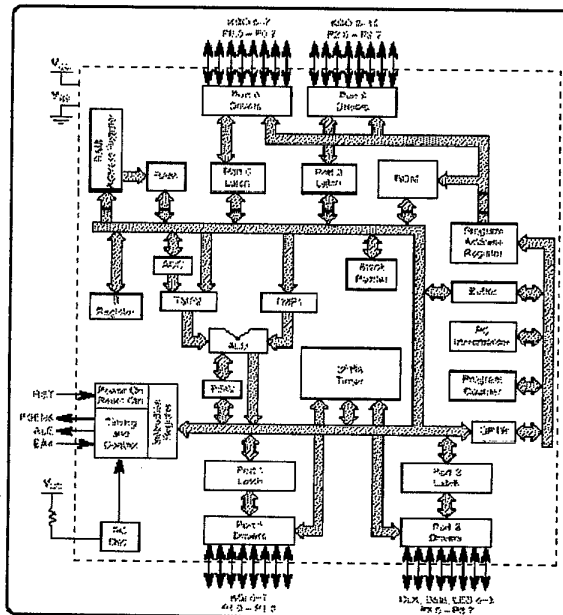


Figure #6. Diagram Block of 83c51 kb Keyboard Controller

For the first stages it's necessary detect the on/off pressure in the exitated point, so the electrical system of the robot hand is the same such a matrix keyboard configuration, shown in the figure #7.

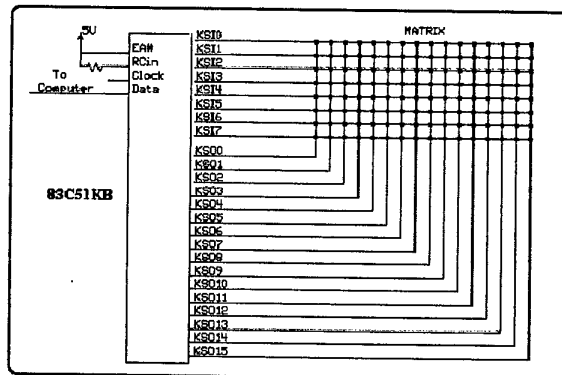


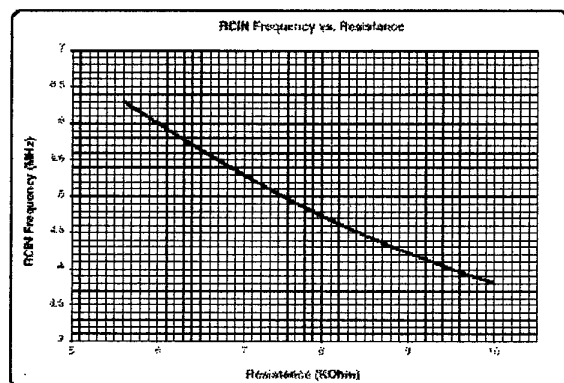
Figure #7. Electrical Diagram to On/Off Pressure in The Robot Hand

Well, the matrix is distributed in all sensitive hand surface, to obtain all the contact point we must to use the 8 scanner input lines "SIL", 1 line for each finger and the rest for the palm, the rest 16 scanner output lines "SOL" it's to made the contact point of each division zone.

Due the 83C51KB works in a frequency of 4 to 6 MHz, then the sample time is in a range of:

$$T_{max} = 4 \mu s \text{ and } T_{min} = 2.6 \mu s$$

This time is better than the response time of the hand, the sample frequency depends of the resistance value connected between V_{cc} and RCin terminal, and is characterized by the graphic #1.



Graphic #1, RCin Frequency (5vdc At Romm Temperature)

In the second stage, is implanted a sensible capacitance device to pressure measurement on the contact point, where the change of capacitance is proportional to the pressure.

So for the pressure measurement we need a Analogical Digital Convert "D.A.C" to evaluate the magnitud of the analogical signal, with this new function the diagram system change, like shown the figure #8.

Due this modifications the 83C51KB controller no is the only device that work in the hand, now we have to desig a new circuit device to solve the next problems:

- Calibration of the Sensitive Device.
- Capacitance Measurement.
- Combination between the Analogical and Digital Signals

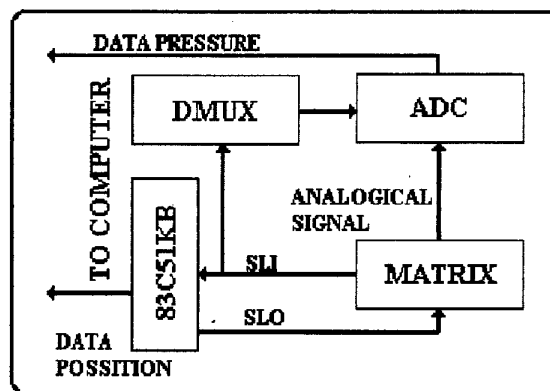


Figure #8, Diagram Block of the New System

To solve this problems, we applicated a capacitive circuit to isolate the signals for each point of the matrix, so one side we get the digital signal and in the other hand the analogical signal, to make ease the pressure meassurement process, because we use the capacitive effect in a filter when the noise doesn't affect, now the circuit used is in the figure #9.

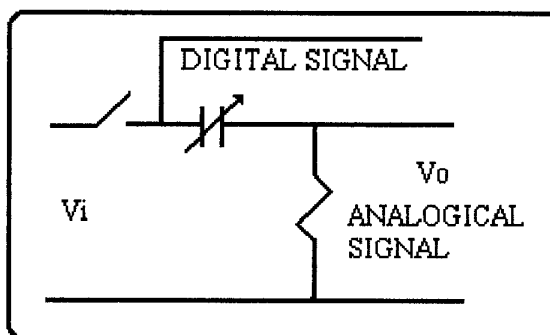
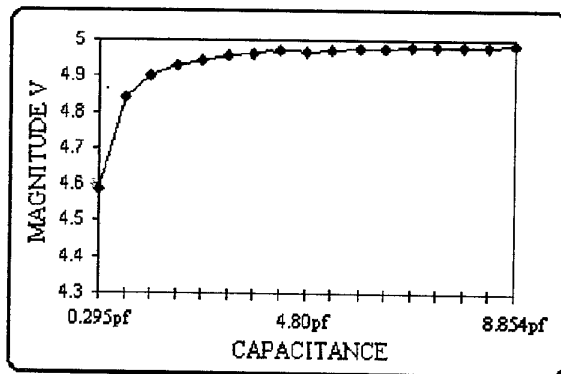


Figure #9, Capacitive Circuit to Isolate the Digital and Get the Analogical Signal

Were the resistance is 1 MOhm and the total impedance is too high, so doesnt afect the digital pulse magnitud, and the output circuit get the analogical signal that is characteriside by the equation of this circuit (1).

$$V_o = \frac{2\pi\nu CR_2 V_i}{1 + 2\pi\nu CR_2} \quad (1)$$

that represent the analogical output magnitude in function of the capacitive variation in a range of 0.2951pf to 8.854pf in a frequency of 6 MHz, like shown in the graphic #2.



Graphic #2. Variation Output Voltage with Capacitance Variation

With this circuit, we have a frequency too, where our principal objective is the magnitude measurement of the analogical signal, for this case we need an embolment detector circuit by improving the system, that is characterized by the next equation (2).

$$V(t) = V_0 e^{-\tau/RC} \quad (2)$$

Where $\tau = RC$ and $\tau = 10/\nu$, now we can see all this functions in the complete circuit, figure #10.

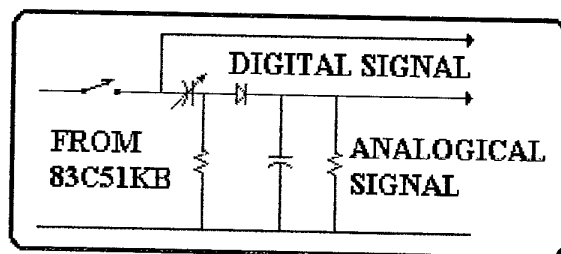


Figure #10. Total Circuit to Obtain the Analogical Signal

4. Conclusions

In the prototype construction, we use digital devices that were not design to this functions, but the adjust fulfill the goal.

Besides the uses the analogical circuit to pressure measurement in any point of the matrix, permits a full integration in a mechanical hand like a human hand in the perceptible tactile function, all that show the function of all the system and the possibility to made complex systems, see figure #11.

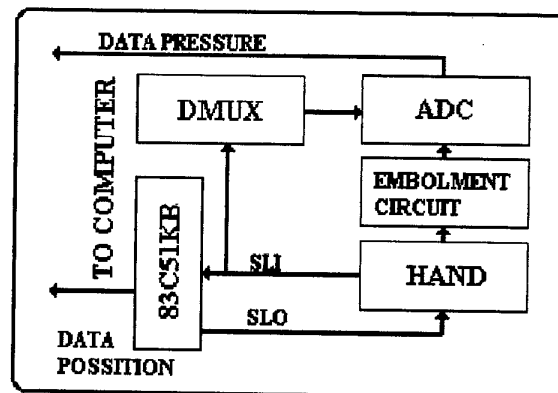


Figure #11. Diagram Block of the Sensitive Tactile System

References

- [1] "Desig And Experiment of an Optical Tactile Sensor for Robot Hands Utilizing a Suspension Shell", T. Okada and S. Tatsuya, Imtc/98, pp 435-440.
- [2] "Periferical Devices". www.intel.com
- [3] "Neuronal Systems"

Dynamic Characteristics of Piezoelectric Multilayer Stack Actuators

Michele Pozzi and Tim King

*School of Textile Industries
The University of Leeds
Leeds LS2 9JT, UK*

e-mail: texmp@leeds.ac.uk, t.king@leeds.ac.uk

Abstract

Piezoelectric actuators have found many applications in mechatronics systems because of their ability to provide large forces in very short times. To overcome the limits of the tiny displacements available, different amplification mechanisms have been envisaged, namely integration of multiple steps ('inchworm'), direct mechanical amplification (simple lever, frames) and transfer of impulse to a projectile. Especially in the last two approaches, the dynamic characteristics of the piezoelectric actuator are of primary importance. Manufacturers' catalogues for commercially available piezo stacks, whilst providing important electrical and basic mechanical compliance data, usually do not give sufficient information on the dynamic behaviour of these devices. This paper provides experimentally observed dynamic performance data for several piezo stacks of differing sizes and from different manufacturers. The observed motion is compared with that predicted by a simple Matlab-Simulink model and suitable model parameters estimated.

1. Introduction

Piezoelectric stack type actuators are beginning to be used in a wide variety of applications on account of their ability to generate large forces very quickly [1]. However, they generate micron-scale displacements. In order to use them in practical machinery applications it is usually necessary to amplify their output motion in some way. There are three commonly applied approaches to increasing output motion.

The first is to integrate many cycles of motion as is accomplished by the 'inchworm' linear motor [2] or, in a different way, by travelling wave (ultrasonic) piezo-motors [3, 4]. The piezo devices are usually driven in a resonant mode. The second method is to use a mechanical amplifier, typically a flexure hinged structure [5]. The third, and currently least exploited approach is to use a 'ballistic' or 'impulse' approach in which the piezo stack

exchanges energy with a 'projectile' which provides the output effort by virtue of its kinetic energy and is capable of moving through a useful distance [6, 7].

In all three displacement increasing approaches the dynamics of the piezo stack are important. However, for the latter two approaches (direct amplification and 'impulse' actuation) a good knowledge of the dynamic characteristics of the piezo stack becomes essential. For amplifiers it is needed in order to optimise the combined piezo-amplifier structure, whilst for impulse devices the energy transfer mechanism needs to be carefully optimised, which requires piezo dynamics information.

It is well known that piezoelectric devices of the previous generation had to be fed with very high voltages, which required special care in the design of the power supply system. Exciting voltages have significantly dropped (typically down to 100 V) in piezoelectric multilayer actuators, where many (60-150) layers of reduced thickness (in the order of 100 μm) are mechanically assembled in series to form a stack while being electrically connected in parallel. Thanks to the reduced thickness of each active layer, the electric field induced by a given potential is greatly increased. 'Soft' piezoelectric materials (like PZT 5) are usually employed in actuator construction, because they provide higher maximum displacements (although with higher hysteresis) - the piezoelectric coupling constant d_{33} is typically between 5 and 7 ($\times 10^{-10}$ m/V) and the electric field can be as high as 1-2 MV/m.

The piezoelectric multilayer actuators examined in this paper are commercially available; they can be seen in figure 1. Actuators A and B are nominally identical except for the cross sections (A is 5x5 mm² and B is 2x3 mm²); they are 10 mm in height with active layers 100 μm thick. Therefore they are expected to have the same resonant frequency and maximum displacement but different output force and capacitance (which affects the dynamic response). Actuator C is 5x5x14 mm³ and has 140 active layers about 100 μm thick. Stack D is 5.2x5.2x3.5 mm³ and has slightly thicker layers (125 μm).

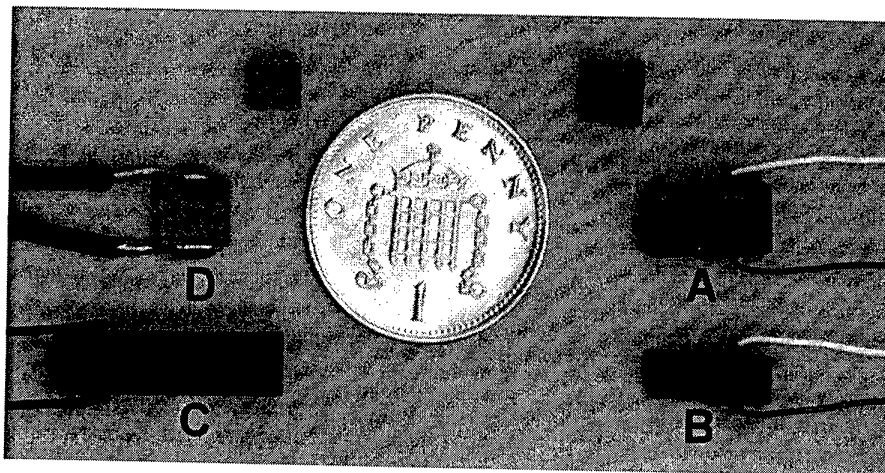


Figure 1: Photograph of some commercial stack piezoelectric actuators from various manufacturers. Experimental results on stacks A to D are reported in this paper.

A simple computational model has been developed with the aim of predicting the dynamic response of the actuators, given some technical data (in figure 2 the version for a completely free stack is reproduced; if the stack is fixed at one end, the mass is multiplied by 4). The system was modelled using Simulink® (a toolbox of the Matlab® software package) with the idea of representing

the mechanical and the electrical sub-systems separately and then taking into account their interaction. As a first approximation, the piezoelectric multi-layered structure is replaced in the mechanical sub-system by a mass-spring system – where the measured mass of the actuator is multiplied by a suitable constant. The parametric values for the model have been obtained from manufacturers'

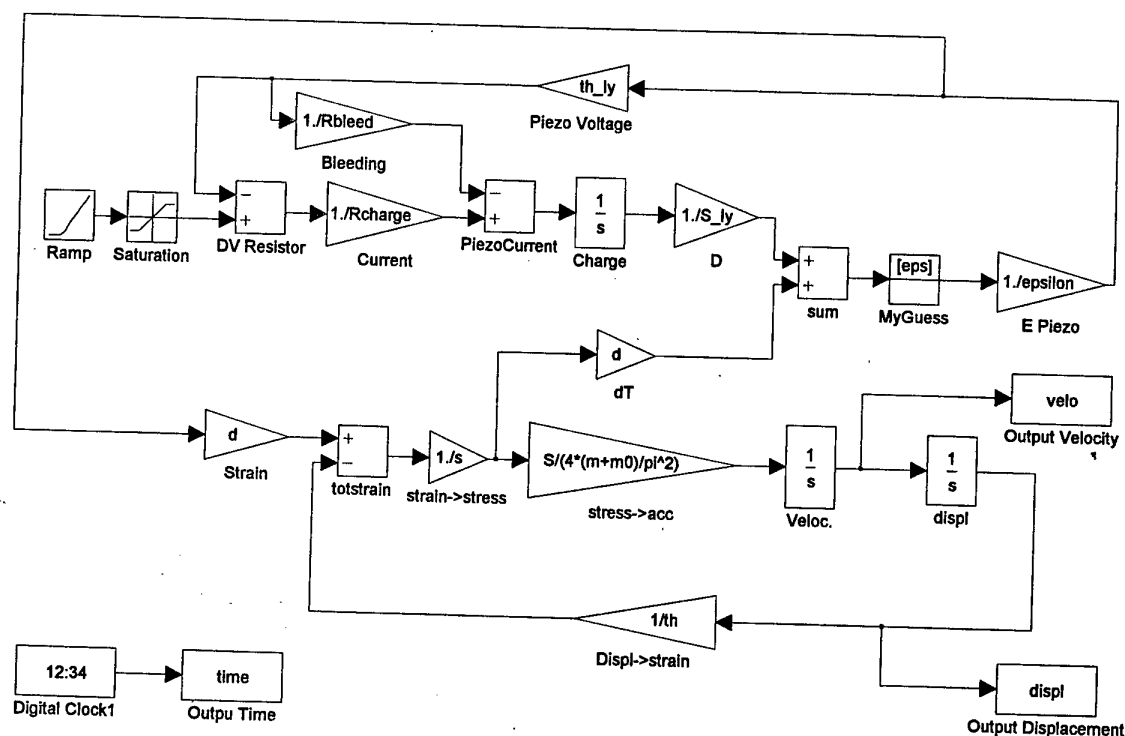


Figure 2: Schematic of the Simulink® model for a stack free at both ends.

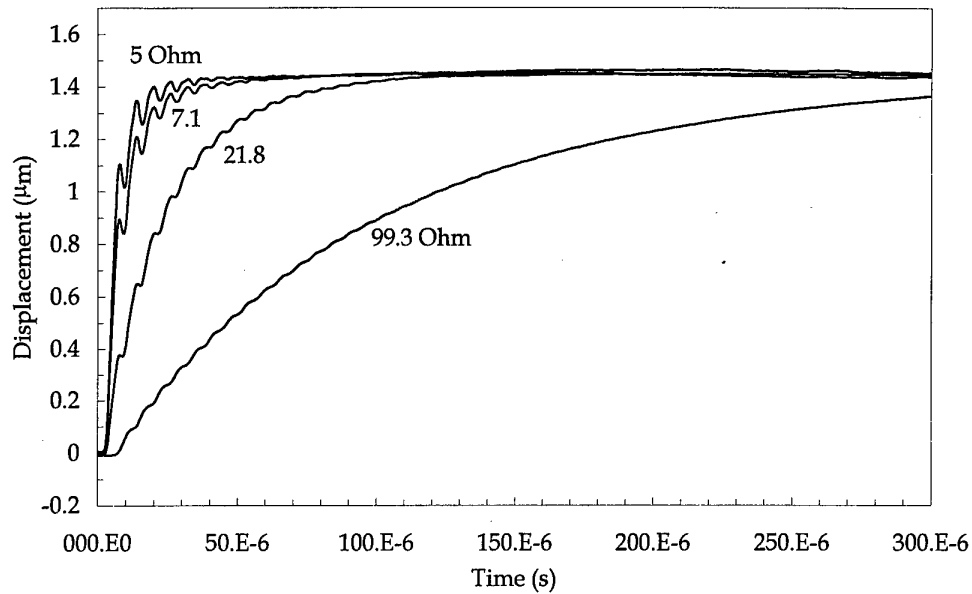


Figure 3: Experimental results on stack A. Both end faces are free, driving voltage is 50 V. The figures near each curve represent the values of the current limiting resistor.

data or deduced from measured quantities (like the capacitance). In the mechanical system the parameter m_0 is added to take into account the mass of inactive layers (typically present at the top and bottom ends of the piezoelectric actuator).

The electrical sub-system is the top part of figure 2. A ramp function with saturation at the maximum exciting voltage simulates the action of the electronic switch. For the MOSFET used in the experiments this ramp is effectively a step and so a ramp rate of 10^7 V/s is used in

the simulations shown here. R_{charge} represents a series resistor which limits the current flow into the piezo actuator which is modelled as a perfect capacitor, although resistive characteristics can be accommodated by modification to the values of R_{charge} and R_{bleed} employed (R_{bleed} nominally models a discharge resistor on our drive circuit, in parallel with the actuator). D is the electric displacement resulting from the charge on the actuator capacitance. To enable Matlab® to solve the algebraic loop a starting value, close to zero, is imposed

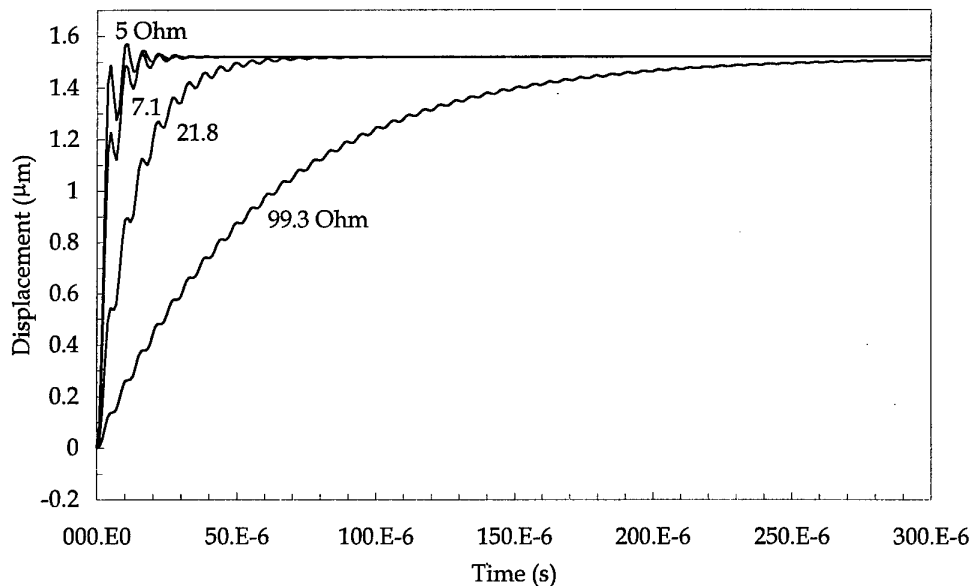


Figure 4: Model output for stack A with both surfaces free and a driving voltage of 50 V. The figures near each curve represent the values of the current limiting resistor.

as MyGuess. The electric field developed is fed from the electrical sub-system to the mechanical one by the link between the EPiezo and Strain blocks. The gain, d , represents the d_{33} value of the piezo material which converts the electric field to strain and this is transformed to stress via the mechanical compliance, s . This is used to determine the force accelerating the lumped-mass of the actuator (S is the cross-section area of the actuator). After integration twice to yield the displacement, this is converted into strain and fed back into the mechanical sub-system. The feedback link between the two sub-systems is completed by transducing the stress, via d , and adding it to the electric displacement. Some features of the model, like the bleeding and the current-limiting resistors and the voltage ramp, are specific for the driving circuit used.

In order to collect experimental data, the piezoelectric stacks were driven by an electronic circuit, featuring a MOSFET with a specific driver IC controlled by a TTL signal, designed to provide very fast switching times. A power unit with very large reservoir capacitor and low impedance supplied a controllable high voltage.

The motion of the top surface of the actuator was monitored using a Polytec Laser Doppler Vibrometer (OFV 512 interferometer + OFV 3001 controller). A piece of retro-reflective tape, of negligible mass, was stuck on the top surface of the actuator to optimise the signal to noise ratio. Velocity range varied from 5 mm/s/V to 1000 mm/s/V depending on the actuator and on the current limiting resistor, while filtering was always off, leading to maximum bandwidths ranging from 250 kHz to 1.5 MHz. The signal from the vibrometer was fed into a 20 MHz oscilloscope triggered by the same TTL signal which drove the MOSFET driver IC; the acquired oscilloscope traces were transferred to a PC for further analysis.

Piezoelectric actuators A to C were tested at 50 V in completely free conditions (by placing them on a very low stiffness material) and at 100 V with the bottom surface glued onto a 20x20x1 mm³ alumina insulating plate, which was in turn glued to a 7 mm thick steel base plate. Piezoelectric actuator D was tested at 155 V.

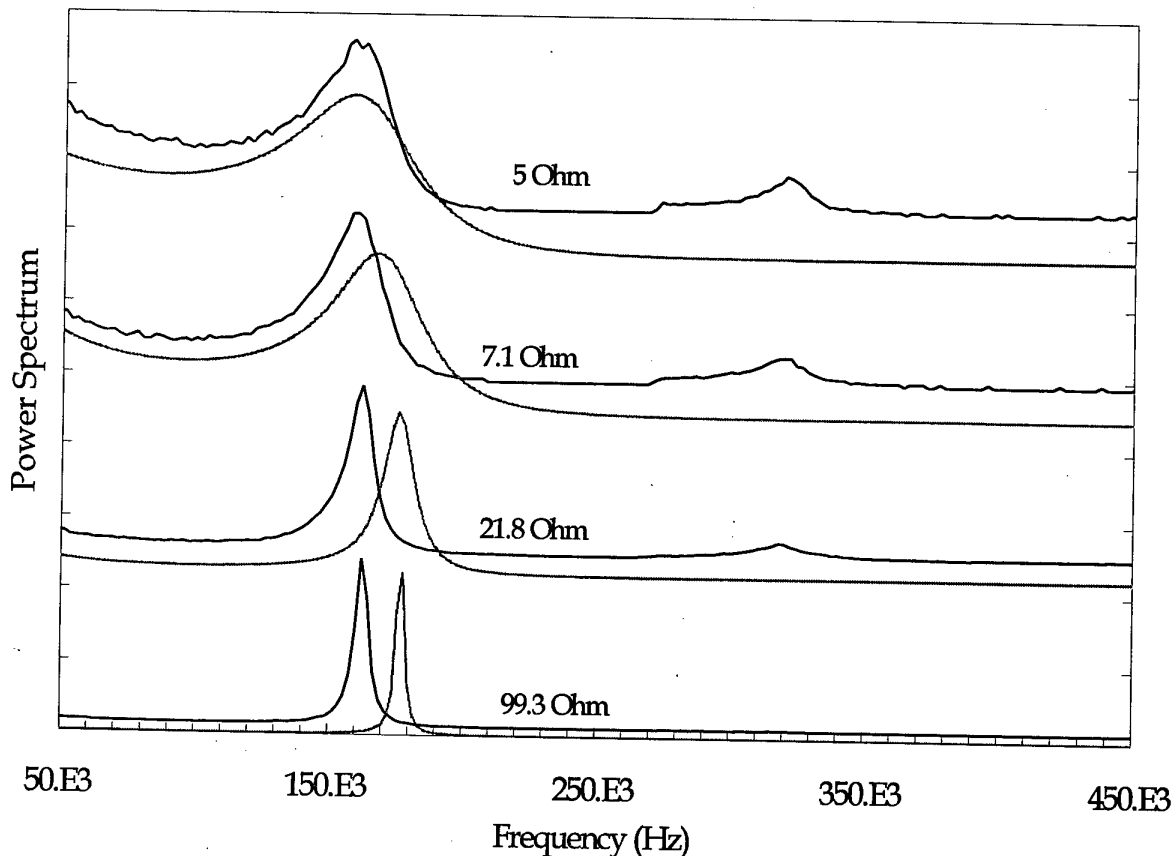


Figure 5: Fourier transform of the curves in figures 3 and 4. Experimental data (black) and model output (grey - lower curve of each pair).

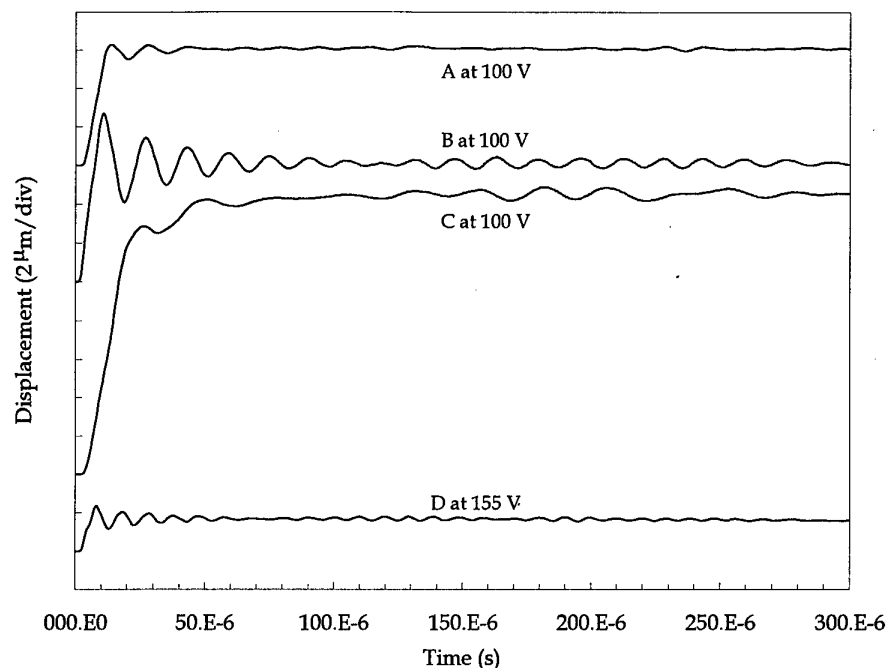


Figure 6: Experimental data on all the tested stacks, driven at the voltages shown, with a current limiting resistor of $5\ \Omega$ and with one end fixed.

2. Results and Discussion

Figures 3 and 4 show the experimental results and the model output for stack A under the same conditions (both

surfaces free, 50 V maximum excitation). It is clear that the model can predict the general behaviour of the piezoelectric stack quite well, except for slightly larger overshooting in the model which could be related to

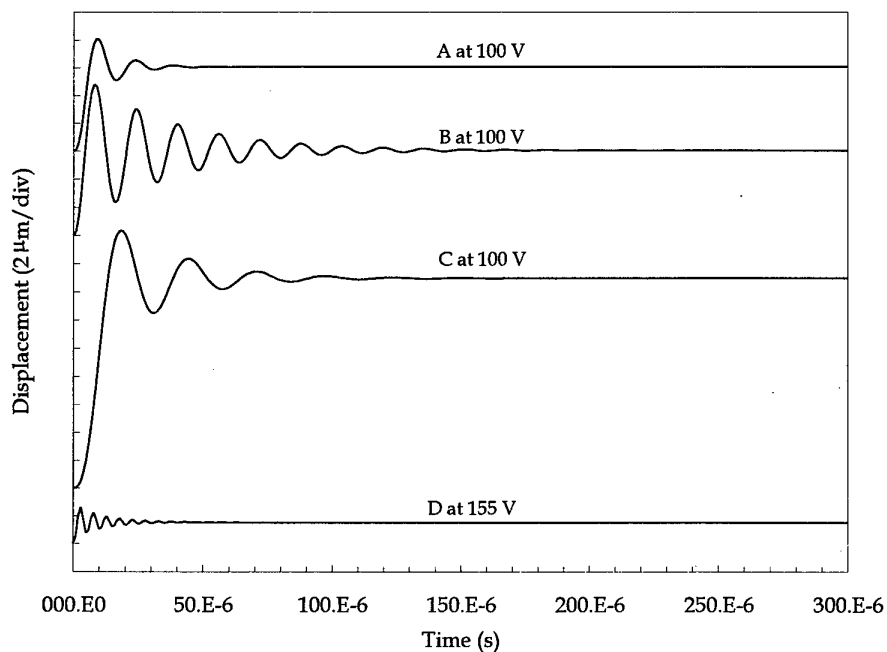


Figure 7: Model output for all the tested stacks with a current limiting resistor of $5\ \Omega$ and with one end fixed (the same conditions as in figure 6).

having neglected any mechanical frictional losses. From figures 3 and 4 the effect of the current-limiting resistor (R_{charge}) can be seen: the lower this value, the faster the response, but at the expense of a higher stressing of the stack. In figure 5 the Fourier transforms of these data are shown. The parameter m_0 of the model was calibrated to match the resonant frequency observed at $R_{\text{charge}} = 5 \Omega$ and set to 0.8 g (the mass of the stack is 2.17 g). It is interesting to notice how the model can predict the shift toward higher values of the main resonant frequency with increasing current-limiting resistor (R_{charge}), although it overestimates this effect (which is much more evident in the experimental results on other stacks, not reported here).

Figures 6 and 7 show the experimental results and the output from the model, respectively, for all the actuators tested, with $R_{\text{charge}} = 5 \Omega$ (note that the curves have been vertically displaced to avoid overlap). Again, a good agreement between measured and predicted data can be noticed, with the aforementioned overshooting.

3. Conclusions

The model can be seen to provide a reasonable approximation to the behaviour of the piezo stacks. However, the simplifying assumption of a lumped-mass model for the multilayer actuator in the mechanical subsystem prevents the model from predicting the higher harmonics which are found in the Fourier transforms of the experimental data. For many engineering applications this will not be problematic and the model will provide sufficiently accurate results for initial design of dynamic piezoelectric actuation systems.

It is hoped that this work will be of use to anyone developing high speed piezo actuators for machinery applications.

4. Acknowledgements

The authors would like to acknowledge the financial support of the UK EPSRC in providing a studentship for M. Pozzi.

5. References

- [1] Spanner K. and Wolny WW., "Trends and Challenges in New Piezoelectric Actuator Applications", *Actuator 96. Proceedings of the 5th International Conference on New Actuators, Bremen, Germany*, 140-146, 1996.
- [2] "The Piezo Book", Burleigh Instruments Inc., New York, USA
- [3] Hagedorn P. and Wallaschek J., "Travelling Wave Ultrasonic Motors Part 1: Working Principle and Mathematical Modelling of the Stator", *J. of Sound and Vibration*, **155** (1), 31-46, 1992
- [4] Wallaschek J., "Piezoelectric Ultrasonic Motors", *J. of Intelligent Materials Systems and Structures*, **6**, 71-83, 1995.
- [5] Xu W. and King T.G., "Flexure Hinges for Piezo-actuator Displacement Amplifiers: Flexibility, Accuracy and Stress Considerations", *Precision Engineering*, **19** (1), 4-10, 1996.
- [6] Chang S.H. and Wang H-C., "A high speed impact actuator using multilayer piezoelectric ceramics", *Sensors & Actuators A-Physical*, **24**, 239-244, 1990.
- [7] Chang et al., "Printer actuated by piezoelectrically generated shock wave", *US Patent N. 5 046 872*, 1991.

Nonlinear System Identification of a Micromanipulator

Quan Zhou*, Pasi Kallio* and Heikki N. Koivo**

**Tampere University of Technology, Automation and Control Institute,
P.O. Box 692, 33101 Tampere, Finland;
Email: quan@ad.tut.fi, kallio@ad.tut.fi*

***Helsinki University of Technology, Control Engineering Laboratory,
P.O. Box 3000, 02015TKK, Finland;
Email: heikki.koivo@hut.fi*

Abstract

A micromanipulator is a precision positioning device that often uses piezoelectric actuators. Piezoelectric actuators have disadvantageous properties such as hysteresis nonlinearity and drift. This paper discusses a hybrid model to describe these properties. The model consists of a dynamic linear part and a static nonlinear part. The dynamic part describes the dynamic response and the drift property. The static nonlinear part adapts the model to the hysteresis nonlinearity and gain nonlinearity. Simulation and experimental results show that the model is able to predict the drift and the nonlinear properties of the actuator, including the minor loop property of hysteresis. This actuator model serves the basis for the nonlinear micromanipulator model.

1. Introduction

A micromanipulator is a precision positioning device having applications in biotechnological operations, the assembly of microelectro-mechanical systems, and the testing of microelectronics circuits [1]. It requires actuators having displacement resolution of nanometers, high stiffness and fast frequency response. These requirements can be fulfilled by using piezoelectric actuators. Therefore, piezo actuators have been widely used in many micromanipulators and other precision positioning devices. However, piezo actuators have such properties as hysteresis nonlinearity and drift, which remarkably reduce their accuracy. As the micromanipulation applications become increasingly demanding, requirements for better control design are also raised. A good manipulator model will help the control design. Such a model, in turn, requires proper dynamic models for the piezo actuators.

The properties of piezoceramic actuators have been studied for many years and different approaches have been used. IEEE Ultrasonics, Ferroelectrics and Frequency

Control Society formulated linearized constitutive relations describing piezoelectric continua, published in 1966 and revised in 1987 [2]. Leigh and Zimmerman discussed an implicit algorithm for predicting the hysteresis behaviour of piezoceramic actuators, employing the trapezoidal rule for stepping the equations forward in time [3]. Jung and Kim presented a feed-forward control method with three different deterministic models to reduce the hysteresis effect in piezoceramic actuators [4]. Ge and Jouaneh modelled the hysteresis nonlinearity of a piezoceramic actuator using numerical Preisach models [5], [6]. Goldfarb and Celanovic developed a generalized Maxwell model of a piezoelectric stack actuator where the static hysteresis was identified as energy storage coupled to rate-independent dissipation and was represented by a generalized elasto-slip model [7]. The emphasis has been on hysteresis nonlinearity: models are often static, and drift modelling is largely ignored.

In this paper, we use a hybrid approach to model the piezohydraulic actuators of a micromanipulator developed at the Tampere University of Technology and the Helsinki University of Technology. The model consisting of a dynamic part and a static part is based on the method presented in [9]. The dynamic part of the model describes the dynamic behaviour of the actuator including the drift property. The hysteresis and gain nonlinearities are modelled statically using neural networks. Here, we extend the hysteresis model such that it is able to take into account not only the major hysteresis loop but also minor loops, which is very important for any practical model.

In the next section, the actuator and the micromanipulator under study will be briefly discussed. Section 3 presents the structure of the hybrid nonlinear model. The simulation and experimental results are presented and discussed in section 4. Section 5 concludes the paper.

2. The micromanipulator

A micromanipulator is a device that facilitates the remote handling of microscopic objects under computer-assisted human control. The operator obtains visual information about the end-effector and micro objects using a microscope and a CCD camera, as shown in Fig. 1. The micromanipulator can be controlled either by using a joystick or a PC keyboard. Automatic operations, such as automatic injections, can be activated using the keyboard.

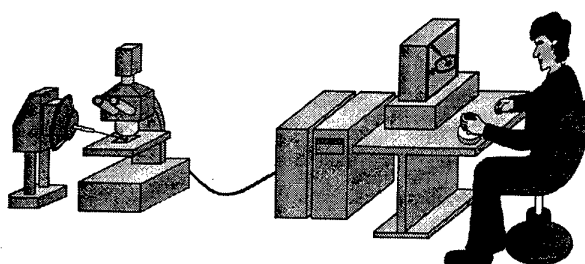


Figure 1: Concept of micromanipulation.

2.1 Actuation system

The actuation system of the micromanipulator consists of a piezoelectric actuator, a small tank and a metallic bellows, as illustrated in Fig. 2 [8]. The piezo actuator is placed in the tank filled with hydraulic oil. When a voltage is applied to the piezo actuator, it deforms. When the actuator buckles, oil flows from the tank to the bellows which elongates, and vice versa: when the actuator gets straightened, oil flows from the bellows to the tank. Since the effective area of the bellows is smaller than that of the actuator, the displacement is magnified. The results of displacement experiments have shown that the movement range of the actuator is about $\pm 250 \mu\text{m}$.

The piezoelectric actuator (RAINBOW™) is structurally similar to unimorph type of elements. The RAINBOW™ actuator is a single element structure consisting of a PZT side and a metallic side [10]. When a voltage is applied opposite to the poling field, the wafer buckles and when the voltage is parallel to the poling field, the wafer straightens.

The bellows is a spring type of passive component where the force required to deform the bellows is directly proportional to the displacement. The bellows can be considered as a linear system.

2.2 Manipulator structure

The manipulator has a Stewart platform [11] type parallel structure consisting of three identical

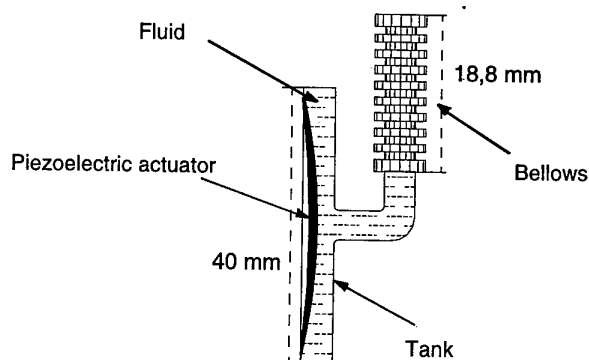


Figure 2: Overview of the actuation system.

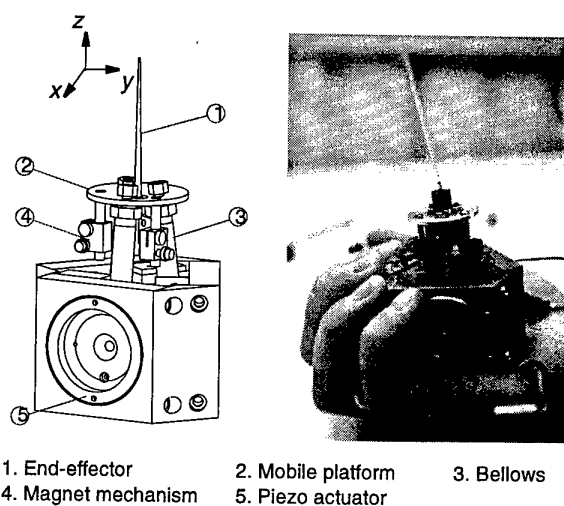


Figure 3: Overview and photograph of the micromanipulator.

piezohydraulic actuation systems as described in [12]. The actuators are connected by a mobile platform resulting in a tripod-like parallel configuration, Fig. 3. The mobile platform is fixed to each bellows using a venting screw and a small nut. The end-effector (needle) is mounted on the platform.

This manipulator differs from the conventional Stewart platform type of structures, since the bending of the bellows facilitates a joint-free structure. Using the bending character of the bellows instead of spherical joints simplifies the structure and the manufacturing process, since especially the manufacture of miniaturised spherical joints is difficult. By changing the lengths of the bellows the orientation of the mobile platform, and thus the position of the end-effector can be controlled.

3. The hybrid model of the piezohydraulic actuation system

In the following, we develop a dynamic model of the piezohydraulic actuator for its z -axis displacement. Since the bellows and the hydraulic system can be considered as a linear amplifier, the specific properties of the piezohydraulic actuator inherit mainly from the properties of the piezoelectric actuator – hysteresis and drift, as shown in Fig. 4 and Fig. 5, respectively. From Fig. 4, it can be noticed that the gain of the actuator is nonlinear. Due to the hysteresis and drift, a linear dynamic model is not sufficient to describe the system behaviour. Therefore, the model parameters have to be changed to cope with the nonlinear features. This paper uses a model structure where parameters of a properly formulated linear dynamic model are scheduled by neural networks. The model structure presented in [9] is improved to take into account the minor hysteresis loops.

3.1 The dynamic part of the actuator model

The step response shown in the Fig. 5 can be described by a linear model containing two time constants, one describing the fast behaviour and the other describing the slow behaviour – the drift – of the system. As shown in Fig. 6, the model consists of two first order transfer functions having time constants T_1 and T_2 , and respectively two gains k_1 and k_2 . The gains determine the contribution of the two parts to the system output. The system can be described by a transfer function having two poles and one zero:

$$G(s) = \frac{(k_1 a + k_2 b)s + ab(k_1 + k_2)}{(s + a)(s + b)} \quad (1)$$

where $a = 1/T_1$ and $b = 1/T_2$.

However, the linear transfer function with fixed parameters is only locally valid due to the nonlinearities of the system. To describe the actuator behaviour over the entire workspace, model parameters must be identified for each operation context.

3.2 The static part of the actuator model

The static nonlinearity part of the hybrid model is responsible for describing the hysteresis of the actuator. It also takes into account the gain nonlinearity. One of the classical models for hysteresis is the Preisach model [13]:

$$x(t) = \iint_{\alpha \geq \beta} \mu(\alpha, \beta) \gamma_{\alpha\beta}[u(t)] d\alpha d\beta \quad (2)$$

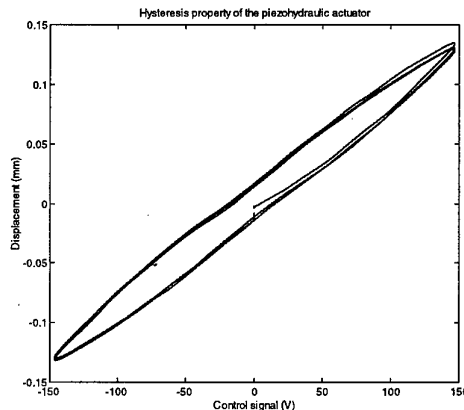


Figure 4: Hysteresis and gain nonlinearity properties of the piezohydraulic actuator.

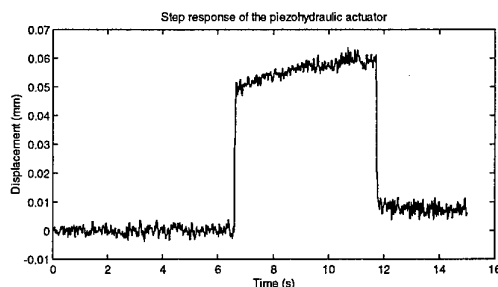


Figure 5: Step response of the piezohydraulic actuator, the drift being obvious.

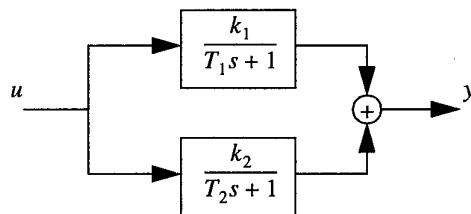


Figure 6: Structure of the dynamic model.

where $x(t)$ is the output response of a piezoceramic actuator; $\mu(\alpha, \beta)$ is a weighing function in Preisach model; α and β correspond to up and down switching values of the input, as shown in Fig. 7; and $\gamma_{\alpha\beta}[u(t)]$ is a binary hysteresis operator whose value is determined by the input operation.

The classical Preisach model can only represent hysteresis nonlinearity which satisfies the wiping-out property and the congruency property. The wiping-out property means that the hysteresis curve does not depend

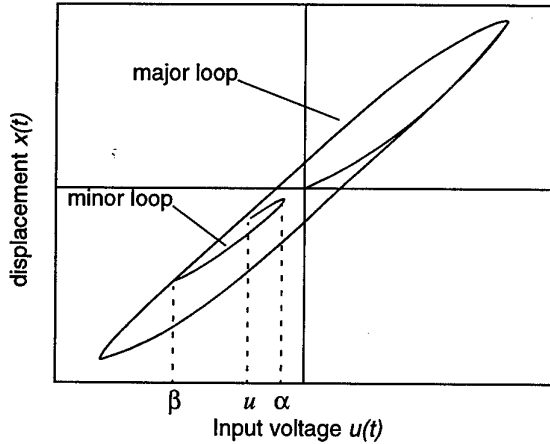


Figure 7: Hysteresis loops.

on how it was approached. The congruency property refers that the change in displacement should be the same for the same control input change. This property is not satisfied e.g. in piezoceramic actuators. A detailed discussion of these properties can be found in [13].

If we regard the Preisach model as a nonlinear function, it could be generalized as:

$$x(t) = f(\alpha, \beta, u(t), \gamma[u(t)]) \quad (3)$$

where α and β correspond to up and down switching values of the input, $u(t)$ is the input signal of the actuator, and $\gamma[u(t)]$ is the direction of the input signal.

Thus, nonlinear mappings such as feed forward neural networks can be used to describe the hysteresis nonlinearity. Moreover, the dynamic model is only valid locally because it depends on the input voltage and history of the inputs. Therefore, the parameters of the dynamic model should be adapted to the hysteresis and gain nonlinearities.

3.3 The hybrid model structure

The dynamic model (1) can be modified to take into account the system nonlinearities by replacing the parameters with functions:

$$G(s) = \frac{\lambda_1(\alpha, \beta, u, \gamma)s + \lambda_2(\alpha, \beta, u, \gamma)}{(s + a)(s + b(\alpha, \beta, u, \gamma))} \quad (4)$$

where

$$\lambda_1 = k_1(\alpha, \beta, u, \gamma)a + k_2(\alpha, \beta, u, \gamma)b(\alpha, \beta, u, \gamma)$$

and

$$\lambda_2 = ab(\alpha, \beta, u, \gamma)[k_1(\alpha, \beta, u, \gamma) + k_2(\alpha, \beta, u, \gamma)]$$

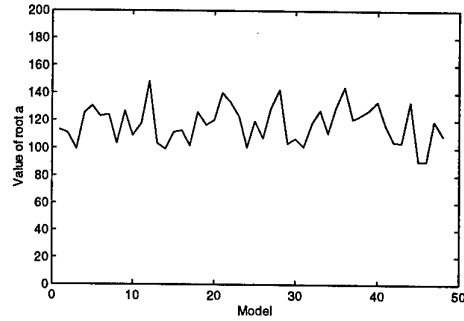


Figure 8: Variation of the parameter a in different models.

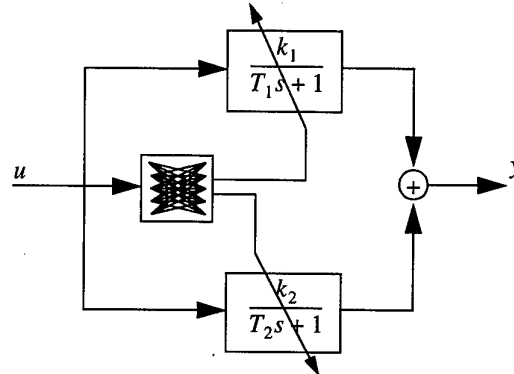


Figure 9: Principle of the hybrid model structure.

The response time of the piezohydraulic actuator is consistency despite the hysteresis nonlinearity. Thus, the parameter a is kept constant. This has been proven in experiments and is demonstrated in Fig. 8 which shows the values of a for 50 different models. Those models are determined from 50 step responses covering the whole workspace of the actuator. The parameters b , k_1 and k_2 are functions of up and down switching values α , β , input signal $u(t)$ and its direction γ . The functions are nonlinear and implemented using neural networks. Other methods can also be used. The hybrid model structure is shown in Fig. 9.

4. Simulation and experimental results

The system response can be divided into multiple windows to determine the parameters of an individual linear dynamic model. Such determination results in a group of dynamic models $G_i(s)$ and groups of model parameters (a_i , b_i , k_{1i} , k_{2i}).

A multi-stage step signal is designed to cover the workspace of the actuator, as shown in Fig. 10. The signal can be divided into multiple windows such that each window contains one step signal. As a result, 316 windows

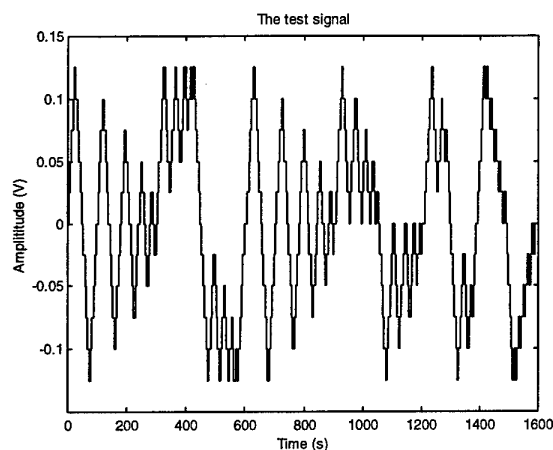


Figure 10: The multi-stage step test signal.

are obtained for the test signal. The a parameter is relatively constant for all ARX models and has determined based on the main loop model [9], which has a mean value of 117.4 and a standard deviation of 13.9, Fig. 8. After determining the gains k_{1i} , the fast dynamic response is simulated and the difference between the measured signal and simulated fast response is computed for each window. The resulting residue is used for identifying an ARX model with one pole for each step response and thus determining b_i and k_{2i} . After the model parameters for each window have been computed, they are used as the training data for neural networks. Three layer feedforward neural networks are used for computing the functions $k_1(\cdot)$, $k_2(\cdot)$ and $b(\cdot)$. Input variables for the networks are α , β , $u(t)$ and γ .

The model is built using the test signal shown in Fig. 10. The simulated output of the model and the testing data match quite well. A segment of the signal is shown in Fig. 11, as the entire signal contains too many steps to be seen the details in a single figure. Fig. 12 compares simulated and experimental results of a linear decaying ramp signal and shows almost indistinguishable difference. When the results are plotted as a hysteresis curve in Fig. 13, the small difference between the experimental results and simulated outputs can be observed. Fig. 14 shows the comparison of an experimental and a simulated response for a signal generated using a joystick, i.e. directly by a human operator. The model output is able to follow the measured curve generally. The modelling errors seen in Fig. 14 come from several aspects. Firstly, the measurement signal is noisy, which brings errors in the parameter determination. The errors in the parameters transfer to the neural network, and in the meanwhile, make the training of the network more difficult. Secondly, the used training signal may not sufficiently excite the actuator.

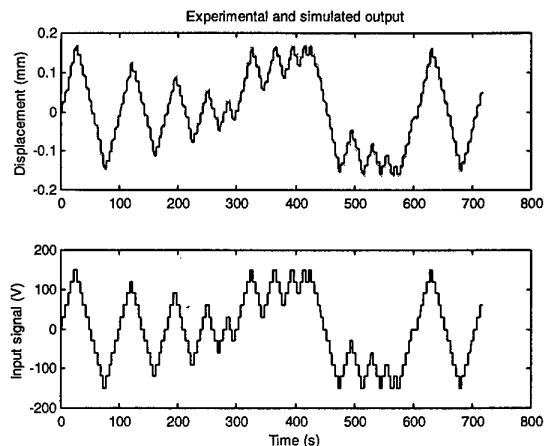


Figure 11: Model matching, measured (gray) and simulated (black) output.

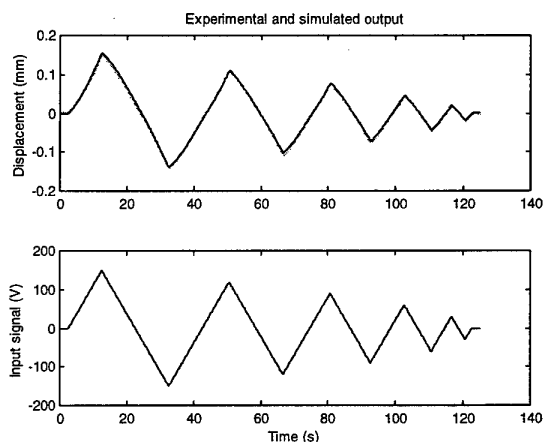


Figure 12: Measured (gray) and simulated (black) output for a linear decaying ramp signal.

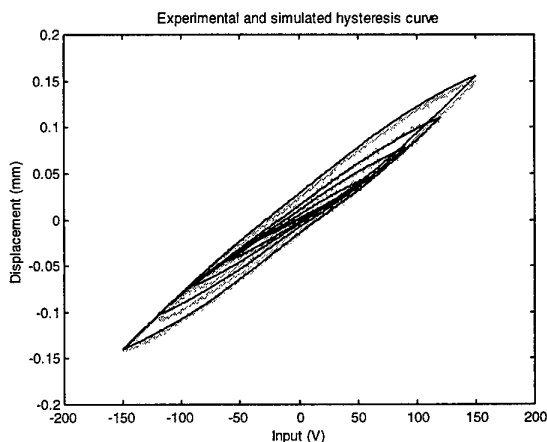


Figure 13: Measured (gray) and simulated (black) hysteresis curves.

Overall, our proposed model describes well the dynamics, the drift and the nonlinear properties of the actuator. The results can be further improved by reducing measurement noise and using more complex pattern in training signal.

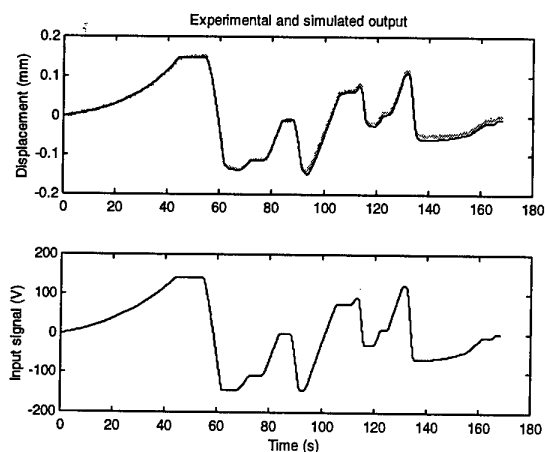


Figure 14: Measured (gray) and simulated (black) response of a free movement test.

The developed actuator model can be utilized in modelling the entire micromanipulator by combining three actuator models together. Since the actuator model describes the dynamics, hysteresis nonlinearity and drift of the micromanipulator, the identification of the manipulator kinematics completes the micromanipulator model.

5. Conclusions

This paper presented a nonlinear dynamic model of a piezohydraulic actuator. The model is able to describe minor hysteresis loops. The structure of the model can conceptually be separated in two parts: a linear dynamic part to model the dynamics and the drift property of the actuator, and a static nonlinear part to adapt the dynamic model to the hysteresis and gain nonlinearities. The hybrid model was generated using a multi-stage step signal. The resulted model was verified on a linear decaying ramp signal and a free movement test. The results have shown that the nonlinear dynamic model is capable of compensating the hysteresis and gain nonlinearities of the actuator as well as the drift property.

The hybrid model presented here has been tested on both the major loop and the minor loop of the hysteresis. By improving the measurement and trying other types of test signal, it is possible to improve the model. The presented nonlinear dynamic model can also act as a part of a micromanipulator model. A micromanipulator model

based on the actuator models will be developed in the future.

ACKNOWLEDGMENT

The authors wish to thank the Technology Development Centre of Finland (TEKES) and the Academy of Finland for funding the project.

REFERENCES

- [1] Kallio, P. and Koivo, H. N., "Microtelemanipulation: a Survey of the Application Areas", *Proceedings of the International Conference on Recent Advances in Mechatronics, ICRAM'95*, Istanbul, Turkey, August 1995, 365 - 372.
- [2] Standards Committee of the IEEE Ultrasonics, Ferroelectrics, and Frequency Control Society, *An American National Standard: IEEE Standard on Piezoelectricity*, The Institute of Electrical and Electronic Engineers, ANSI/IEEE Std. 176-1987, New York, 1987.
- [3] Leigh, T. and Zimmerman, D., "An Implicit Method for the Nonlinear Modelling and Simulation of Piezoceramic Actuators displaying Hysteresis", *Smart Structures and Materials*, AD-Vol. 24/AMD-Vol. 123, ASME, 1991, pp. 57-63.
- [4] Jung, S. and Kin, S., "Improvement of Scanning Accuracy of PZT Piezoelectric Actuators by Feed-forward Model-reference Control", *Precision Engineering* 16, 1994, pp. 49-55.
- [5] Ge, P. and Jouaneh, M., "Modeling Hysteresis in Piezoceramic Actuators", *Precision engineering* 17, 1995, pp. 211-221.
- [6] Ge, P. and Jouaneh, M., "Generalized Preisach Model for Hysteresis nonlinearity of Piezoceramic Actuators", *Precision Engineering* 20, 1997, pp. 99-111.
- [7] Goldfarb, M. and Celanovic, N., "Modeling Piezoelectric Stack Actuators for Control of Micromanipulation", *IEEE Control Systems*, VOL. 17, NO. 3, June 1997, pp. 69-79.
- [8] Kallio, P., Lind, M., Kojola, H., Zhou, Q., Koivo, H., "An Actuation System for Parallel Link Micromanipulators", *Proceedings of the Intelligent Robots and Systems, IROS'96*, Osaka, Japan, November 1996, 856 - 862.
- [9] Zhou, Q., Kallio, P. and Koivo, H. N., 1999. Modelling of Piezohydraulic Actuator for Control of a Parallel Micromanipulator. To be published in 1999 *IEEE International Conference on Robotics and Automation, ICRA'99*, Detroit, Michigan, USA, May 10-15, 1999.
- [10] Haertling, G., "Rainbow Ceramics - a New Type of Ultra-high-displacement Actuator". *American Ceramic Society Bulletin*, Vol. 73, No. 1, January 1994, 93 - 96.
- [11] Stewart, D., "A Platform with 6 Degrees of Freedom". *Proceedings of the Institution of Mechanical Engineers*. Vol. 180, Part 1, No. 15, 1965, pp. 371 - 386.
- [12] Kallio, P., Lind, M., Zhou, Q., Koivo, H. "A 3 DOF Piezohydraulic Parallel Micromanipulator". *Proceedings of the IEEE ICRA'98*, Leuven, Belgium, May 1998.
- [13] Mayergoyz, I., *Mathematical Models of Hysteresis*, New York: Springer-Verlag, 1991.

High mobility hand Prosthesis; A Mechatronic approach

J. L. Pons, H. Rodríguez, R. Ceres
*Instituto de Automática Industrial,
CSIC
Spain
E-mail: Jlpons@iai.csic.es*

D. Reynaerts, I. Luyckx
*Dept. of Mechanical
Engineering, KULeuven
Belgium*

L. Goldenberg
*Alorman Advanced Medical
Technologies Ltd.
Israel*

W. Van Moorleghem
*Memry Europe
Belgium*

Abstract

The development of a human upper limb prosthesis is a multidisciplinary approach involving mechanics, electronics and control in a concurrent manner. As a consequence, better solutions are obtained if a mechatronic approach is adopted. The present paper outlines the work done in the framework of the project MANUS so far. In particular, problems related to the development of a natural HMI based on EMG sensors under a specific electronic architecture are addressed. Likewise, we focus on the particular solution of hand mechanics, electronic architecture and actuators design so that overall functionality is met in accordance with user requirements.

1. Introduction

The topic of robotics hand design has received interest from the scientific community for more than three decades. Initially it was a mean of providing dextrous manipulation capabilities to robotics devices looking for reusability of components, i.e. more general tools. The thorough state of the art achieved in the field of mechanical design and control of such robotics hands made it possible focusing on the application of these devices to technical aids for disabled, in particular, for prosthetic hands.

The problem becomes, however, much more complex. On one hand, while in robotic hands actuator packages can be placed far from the hand itself and therefore can be bulky, prosthetic applications require high miniaturisation in order to integrate all the components in the same room a human hand would take. This imposes the necessity of developing high power density actuator packages. On the other hand, the prosthesis has to be commanded by the

amputee and thus a natural interface should be provided, allowing for enough fast command channels.

Taking the whole implementation into consideration, specific sensing devices, actuators, mechanics and control has to be provided in a concurrent engineering problem. As a consequence, a number of mechatronic topics are inherently involved in such a device. In particular, supporting electronics is to be specifically designed in order to improve actuator and sensing device functionality. Moreover, advanced motion control schemes are also of paramount importance given the fact that some autonomous reactive behaviour of the hand in response to external disturbances (mainly slippage and unknown forces) is necessary.

The present paper introduces the approach followed by the MANUS consortium under the European Community project "Modular Anthropomorphic User-adaptable Hand Prosthesis with Enhanced Mobility and Force Feedback" under contract DE-4205. The MANUS consortium includes scientific technology developers, medical firms as well as user organisations and has been set up in order to provide support to the mechatronic approach proposed in the development of the prosthesis.

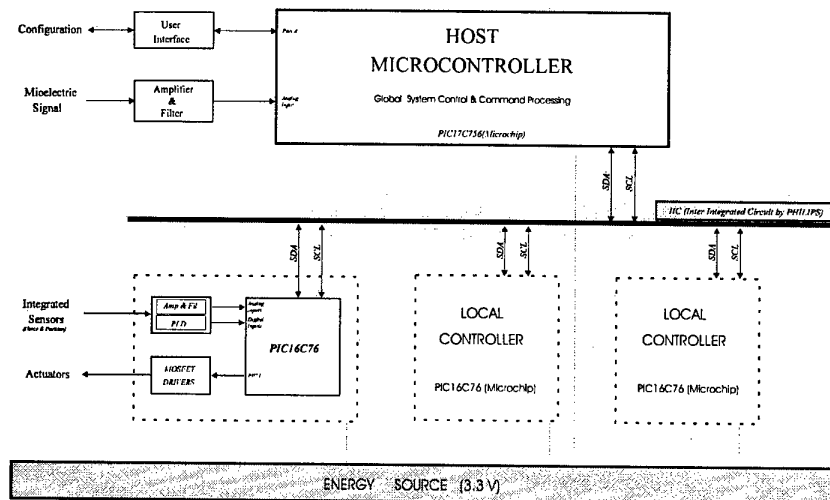
In the following sections we will attend to main subsystems of the hand prosthesis, namely, Electronics and Control, Hand mechanism and Actuation technology focussing in the latter.

2. Electronics & Control

The aim of the project is increasing the functionality of the hand prosthesis by providing a threefold modular approach. The prosthesis should be modular according to the number and kind of grasping modes provided to the

amputee; it has to be modular in the sense of allowing a stepwise extension to the shoulder (in this first version only hand and wrist are addressed); the third modularity aspects accounts for the residual capabilities of the amputee.

In order to solve the problem, an electronic subsystem, referred to as EMG Processor in figure 1 has been implemented. The EMG processor filters, samples and treats the signal to produce a three bit ternary logic code to command the prosthesis. Figure 2 shows the EMG



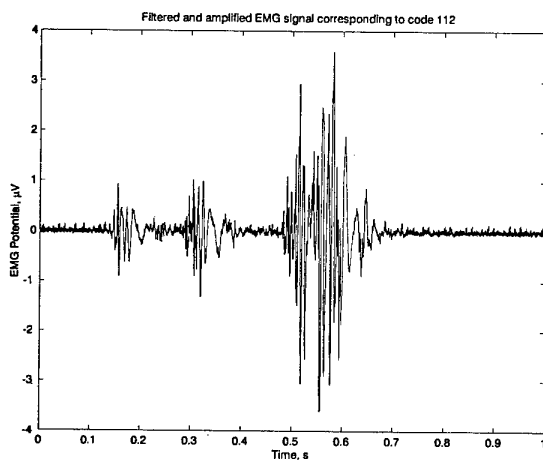
Φιγυρε 1. Ελεχτρονικη συστημα

Regarding this last issue, a natural human-machine interface, HMI, has to be provided. Several alternatives have been considered. Among them two are being evaluated in the project: surface mioelectrical pickups and mioelectrical implanted sensors. In both cases, the signal generated by muscle contraction are registered and coded to command the prosthesis. Since a large number of grasping modes is desired, a high number of codes is

signal from a healthy muscle of a patient with amputation. It has been experimentally checked that, with a short period of training, the amputee can produce desired commands by controlling the muscle contraction is short periods of 0.5 to 1 s.

Following this approach, we have detected 18 valid codes for commanding the signal. All codes starting with 1 or 2 (medium or high muscle contraction) are associated with valid commands. Since electrical potential signal vary from user to user, when the prosthesis is fitted a calibration process starts in which the user is asked to produce a pattern of codes so that signal processing parameters are optimised. It has been checked out that the amplitude of EMG signals corresponding to the same patient vary as a function of muscle fatigue, sweating and a number of other causes. In order to avoid wrong command coding, calibration processes are evenly distributed in time so that processing parameters are always kept updated.

High level control of the prosthesis is performed by the host microcontroller, as shown in figure 1. One of the requirements as specified by users and therapists for increasing the functionality of the prosthesis is involving the users in the control loop of grasping operations. This can be achieved by providing a feel of the grasping force being exerted. The host microcontroller is in charge of computing the hand kinematics transformation according



Φιγυρε 2. EMG σιγναλ χορρεσπονδινγ τ ο χομμανδ 112

needed.

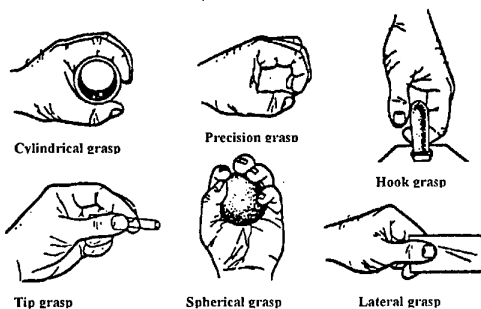
to the exact kinematics of the hand mechanism and the particular control command generated by the user.

3. Hand Mechanism

When designing an anthropomorphous hand for a upper limb prosthesis, a number of general design requirement arise. Designing a hand prosthesis is a clear example of user oriented concurrent design in which ergonomic, functional as well as cosmetic issues must be addressed.

In a first stage of our project, we have identified all these requirements in terms of must and minimum criteria. The definition of requirements is based on a survey conducted on hand prosthesis users belonging to several countries and cultures as well as on prosthesis therapists, [1]. From this study a number of functional requirements arose that can be summarised as follows:

- Desired 5 grasping modes according to figure 2: lateral grasp, hook grasp, precision grasp, cylindrical grasp and spherical grasp. A minimum of 4 grasps are acceptable (spherical grasps are not so useful as the other).
- Maximum grasping time of 1 s.
- Motion range of 90 degrees for finger motion (medium and index).
- Desired grasping force of 100 N.
- Maximum overall weight of 800 gr (for the entire prosthesis device including electronics and actuators), desired weight of 500 gr.



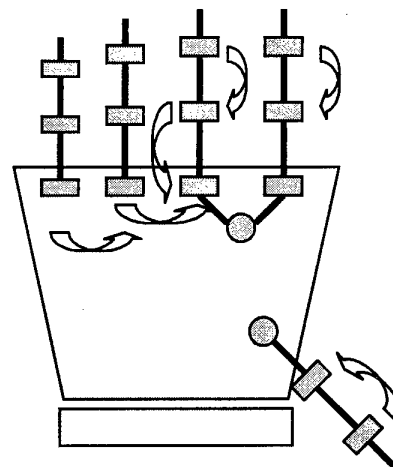
Φιγυρε 3. Σετ οφ απαιλαβλε γρασπινγ μοδεσ

According to these specifications several kinematics configurations have been considered. One of the issues addressed at this stage is the use of adaptive vs. non-adaptive mechanisms. Adaptive mechanisms are mechanisms with a number of degrees of freedom higher than the number of actuators in the hand. As a

consequence it is an underactuated mechanism that relies on differential devices to obtain shape adaptation, i.e. the enveloping surface of the fingers can be adapted to the shape of the object being grasped. A first advantage of these approach is the increased manipulability of the hand.

On the other hand non-adaptive mechanisms have exactly the same number of actuators as the number of degrees of freedom. Generally, for these devices the motion of the different phalanxes of a finger is linked in a fix manner to the motion of the previous phalanxes. A number of mechanisms for doing so are currently well known. They are based on mechanical linkages based on bars [2], on gears and on tendons [3]. Even when no possibility of shape adaptation is present in this type of mechanism, resulting devices are much simpler than adaptive devices.

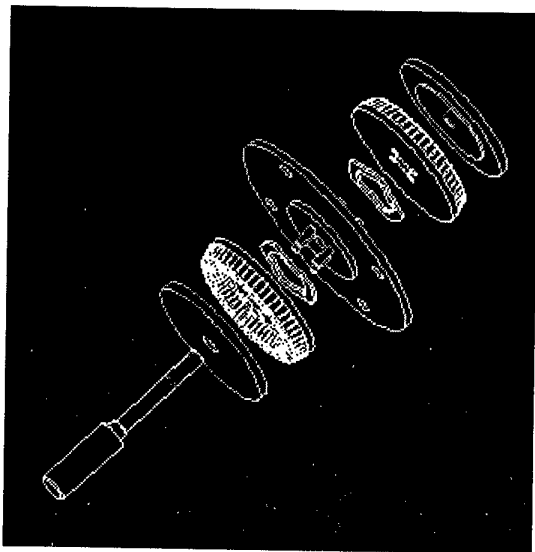
In the framework of MANUS we have analysed both adaptive and non-adaptive mechanisms. Due to severe restrictions on weight and available size (see above) we have finally selected a non-adaptive mechanism with four degrees of freedom. The mechanism comprises three active fingers: index medium and thumb and additionally the wrist is provided with a rotational joint providing pronosupination.



Φιγυρε 4. Κινεματιχο σχιγμε

The motion of index and medium is linked by a differential mechanism so that, when one of the fingers contacts the object to be grasped, the other follows flexing until contact and thus providing an adaptation to object geometry. After studying different kinematics configurations, it was found that an opposition type of hand would provide the basic four grasping modes above introduced. Designing a two-degree of freedom thumb (opposition and flexion) solves this.

Two basic mechanisms for linking the motion of all phalanges for a given finger are being considered: coupling by bars and tendons. Coupling with bars could result in a mechanism with singular positions in its range of motion, therefore a careful design is needed. On the other hand, coupling through tendons avoid the problem of singularities in the motion range but increases the number of components to be included in a very small room, a trade-off should be reached. Also weight is of major concern. Having into account that the overall weight should not increase 800 gr, no more than 100-200gr are left for the hand mechanism.



Φιγυρε 5. Εξπλωδεδ πιεω οφ της ΥΣ μοτορ
πρωτοτυπε

4. Actuation technology

It was already on April, 1982, in the context of a workshop held at MIT, [4], where it was pointed out that "the current actuation technology provides perhaps the most serious, long term impediment to artificial hand design". The same statement holds 17 years after this meeting. In fact, current actuation technologies fail to provide efficient, high power density actuators suitable for artificial hand design. The lack of adequate actuation technologies directly affects the design of dextrous hands. This impediment becomes even stronger if the artificial hand is intended for prosthetics.

In the framework of MANUS a number of possible alternatives have been considered. Initially a number of "traditional" technologies were proposed as backup technologies, while a number of "non-traditional" actuation technologies were proposed for research, ie. Shape Memory Actuators, and Ultrasonic Motors.

In the first stage of the project we have thoroughly studied and compared all of them in terms of efficiency, bandwidth, controllability, available torque and velocity, robustness and specific power. As a result we have concluded that both US motors and Brushless DC motors are the most suited for a hand prosthesis application.

While Brushless DC motors is a well known technology, US motors are still in the state of the art of research in actuation technologies. Therefore our consortium is conducting research towards improving US motors performance mainly in providing a good trade-off between delivered torque and rotation speed and efficiency. We have fully designed a number of prototypes according to our theoretical models to check the effect of a number of parameters on the performance of the actuator, one of them can be seen in figure 5.

Ultrasonic piezoelectric motors are motors of simple structure that use elastic ultrasonic waves to drive a rotor by frictional forces. There are several types of ultrasonic motors, which can be classified depending on its shape and the type and number of vibration modes they use to produce the movement. Among all types of piezoelectric motors, the ring type travelling wave ultrasonic motor (TWUM) has been the most successful and it is being used in commercial applications [5].

Ultrasonic motors driven by travelling waves are based on the fact that when a travelling wave propagates along elastic solid, each particle on its surface moves describing an ellipsis. The ultrasonic travelling waves are produced by electric excitation of a stator made of a piezoelectric material. This motion is then imposed by direct contact to the rotor.

Ultrasonic piezoelectric motors exhibit several features that are very convenient for a prosthetic hand application. Compared to a normal electromagnetic D.C. motor which has a high efficiency but a low torque at high speed, the ultrasonic motor can produce high torque at a low speed with a high efficiency. In addition in these lightweight motors, the torque per unit weight is high and since the inertia of the rotor can be made very small, the control characteristics at start and stop are also good. Moreover, since the rotor is always pushed against the stator to maintain frictional forces, when no electric power is applied the torque and position is held. This last characteristic increases the total efficiency of ultrasonic motors for this application, since no power would be needed when the hand is in its final position.

A double stator travelling wave ultrasonic motor (TWUM), as schematically shown in figure 5, has been designed to obtain a higher operating torque for a given diameter. As shown in the figure, the rotor is made of two outer disks, which are both fixed to the motor shaft so

they move together. Each stator has its own input signal, so there are two independent energy inputs to the two-disc rotor. Thus, the final output torque delivered by the motor is due to the forces acting upon both disks in the contact interface. In addition, since torque and efficiency depend on the pre-load, see [5], the pressure between rotor and stators for this prototype can be adjusted by pressing against the wave springs also shown in the figure. This force is applied by tightening the upper disk until the desired position is reached and then locking it with the nut.

The other components of the motor are the piezoelectric and the engineering plastic rings. Each piezoelectric ring is divided into 18 sectors with alternating polarity. A ring is stuck to each of the stators with a very strong adhesive. On the other hand, engineering plastics are stuck to each disk to provide a wear resistant surface for the contact interface with the stators.

An interesting issue addressed by our design is related to the possibility of optimising the driving voltage to the piezoelectric discs independently. We have to take into account that even when piezoelectric ceramics are very similar, in general there will be, due to manufacturing process, some differences in the resonant frequency of the discs. If discs are excited at different frequencies there would be a net difference of tangential velocities at the contact point where torque and speed is applied to the rotor. But if frequencies are equal, the amplitude of vibration will, in general, differ between stators, causing again the same problem of inefficient torque transmission.

In order to avoid so, amplitude of vibration has to be controlled. This is solved by placing embedded sensors in the piezoelectric ceramic. These embedded sensors are circular sectors of the piezoelectric disc that are used to measure the amplitude of vibration. Amplitude of both piezoelectric discs is compared and controlled so that it remains equal during operation and thus minimising sliding in the contact surface.

Future research includes the optimisation of the stator design, specially the tooth shape, and the rotor stiffness. Such study would require a better understanding of the non-linear contact problem between rotor and stator.

This prototype can be also considered as two parallel coupled actuators. Such configuration has some advantages in force control applications. Beside increasing the output torque, this actuation system can be used to expand the dynamic range and reduce impact forces [6]. For instance, if different stators are used, the resolution would be bounded by the minimum controllable force exerted by the smaller stator and the maximum force of the larger stator. In addition, if instead of a rigid link

between the disks a compliant transmission is used, the forces due to unexpected contact transitions would be reduced.

5. Conclusions

In this paper we have presented an overview of the activities being carried out in the framework of the MANUS project to develop a hand prosthesis. As a whole, the prosthesis can be considered as a complex mechatronic system in which system functionality is enhanced by specifically interrelating mechanisms, electronics and control.

At a level of component or subsystem the same mechatronic approach can be seen. Taking as an example the implementation of Ultrasonic Motors we see how the integration of embedded sensors can be used to optimise the performance of the motor by modifying the vibration pattern of the stator and thus allowing a uniform contact surface.

It is still soon to evaluate the performance of the proposed hand prosthesis, in particular more research has to be conducted on actuation to improve efficiency and speed.

6. References

- [1] Manus Consortium, Manus Project Programme and project deliverables, *European Commission, TELEMATICS Programme*
- [2] Vinet, R., Lozac'h, Y., Beaudry, N. And Drouin, G., *Design methodology for a multifunctional hand prosthesis*, Journal of Rehabilitation Research and Development, Vol. 32, No. 4, pp. 316-324, 1995.
- [3] Reynaerts, D., Control methods and actuation technology for whole-hand dextrous manipulation, *Ph.D. Thesis*, Katholieke Universiteit te Leuven, 1995.
- [4] Hollerbach, J., Workshop on the design and control of dextrous hands, *MIT-AI Memo No. 661*, 1982.
- [5] Ueha, S. And Tomikawa, Y., *Ultrasonic motors: theory and applications*, Pclaredon Press, Oxford, 1993.
- [6] Morrell, J.B., Parallel coupled micro-macro actuators, *MIT-AI Memo No. 1563*, 1996.

Active Video Modules for Launchable Reconnaissance Robots

Kemal B. Yesin

Bradley J. Nelson

Department of
Mechanical Engineering
University of Minnesota
Minneapolis, Minnesota
kyesin1@me.umn.edu
nelson@me.umn.edu

Nikolaos P. Papanikolopoulos

Richard M. Voyles

Department of Computer
Science and Engineering
University of Minnesota
Minneapolis, Minnesota
npapas@me.umn.edu
voyles@me.umn.edu

Donald Krantz

MTS Systems Corporation
Eden Prairie, Minnesota
Don.Krantz@mts.com

Abstract

In this paper we present an active video module that consists of a miniature video sensor, a wireless video transmitter and a pan-tilt mechanism driven by micromotors. The video module is part of a miniature mobile robot that is projected to areas of the environment to be surveyed. A single-chip CMOS video sensor and miniature brushless D.C. gearmotors are used to comply with restrictions imposed by the robotic system in terms of payload weight, volume and power consumption. Different types of actuation are analyzed for compatibility with a mesoscale robotic system. Applications of an active video module are discussed.

1. Introduction

The use of robots to remotely monitor hazardous environments is a primary application for autonomous robotic systems. A joint project between the University of Minnesota, MTS Systems Corp., and Honeywell Inc. is developing a new approach to this robotic task through the use of a novel distributed system of miniature mobile robots. These miniature robots are distributed throughout the environment through two separate methods of locomotion. A gross positioning method launches the robots through the air to an approximate location. After the robots land, fine motion capabilities that the robots possess allow them to move into appropriate reconnaissance positions. These miniature robots, called Launchable Reconnaissance Robots (LRR), contain various types of sensors as payloads and a wireless transmitter/receiver. In this paper we describe the active video module that was designed as a payload for an LRR. This is a challenging task due to the limitations required on size, weight, and power consumption. We discuss the various design issues and new technologies that enabled us to achieve our goal of providing live video information using active video sensors.

1.1. Launchable reconnaissance robots

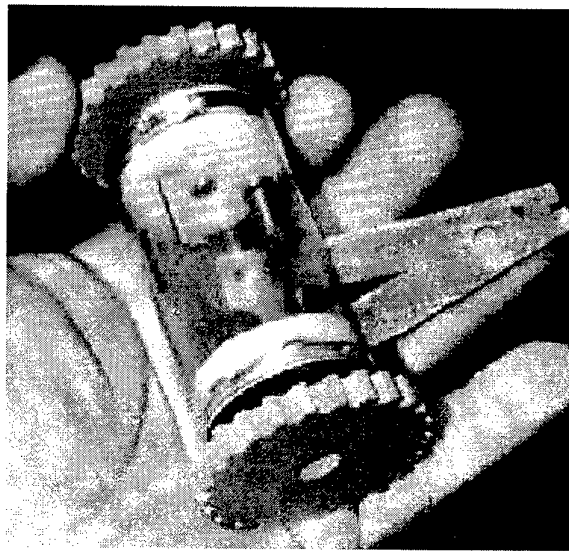


Figure 1. Launchable reconnaissance robot

LRRs are cylindrical in shape with an outer diameter of 40 mm and length of 80 to 100 mm. These dimensions allow the robot to be launched using standard equipment. There are two wheels at both ends of the cylinder that are driven by separate D.C. gear-motors. Another motor is used to retract a spring arm located outside the body. By quickly releasing the spring a hopping action of the robot is achieved. This locomotion method is intended to rescue the robot from obstacles that are too big to move over using the wheels. Figure 1 illustrates a prototype LRR.

The most important components of the LRRs are the various sensors that are carried as payloads within the shell. LRRs have a modular design so that different payload modules can be attached to the base robot for alternative functionality. These modules include vibration and toxic gas

sensors using MEMS technology, microphones, and an active video module.

LRRs can be deployed either by individuals or by more sophisticated and larger mobile robots. They receive commands and transmit information through an RF data link. This allows the robots to form a distributed sensory network over the area of surveillance. Figure 2 illustrates this concept.

1.2. Active Video Module

The active video module consists of a miniature video camera, a wireless video transmitter and a pan-tilt mechanism. The camera is normally concealed inside the body to conserve the tubular form of the shell. It comes out of the body by opening a hatch and retracts when the robot is to be moved. However, the camera can still see through the transparent body of the robot.

The payload volume available for the video module is a semi-cylinder along the tubular body, approximately 35 mm in diameter and 18 mm in length with a total volume of 8.7 cm³. To fit inside such a small volume each component of the module must be miniaturized. Additionally, the maximum power available for payloads from the lithium batteries of the robot is 0.9 W (100mA @ 9V).

In the remainder of this paper we discuss individual elements of the active camera module surveying the available technologies.

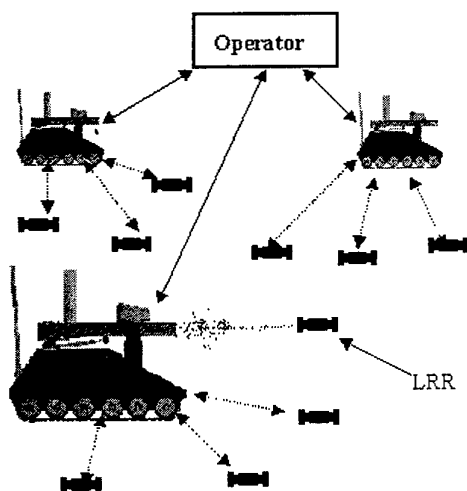


Figure 2. Distributed robotic system

2. Video camera and transmitter

Video is a valuable information source for reconnaissance and surveillance purposes. Live or still images may be captured and sent back to a human operator. A video

camera generates signals according to the light intensity on its sensor. Light rays from the scene are focused on the sensor plate by a lens system. Early video sensors were all tube-type devices and were expensive. An enormous reduction in cost, size and power consumption was achieved by the invention of the CCD sensor.

Another type of video sensor technology, the CMOS sensor, has emerged recently. Both CMOS and CCD sensors are solid-state devices made from silicon. They are based on the same principle of photoconversion to represent incident photons by charge. Unlike the CCD, the CMOS sensor detects the integrated charges in the pixels at the spot, without transferring them, using charge amplifiers made from CMOS transistors. CMOS is a well developed technology and all necessary circuitry for the camera can be integrated in a single chip at a reduced cost and power consumption [7].

An important feature of the sensor is on-chip automatic exposure control circuit. This circuit adjusts the integration time of the pixels (the duration while the photons hit the pixels and charges are collected before they are sampled and flushed) and eliminates the need for external mechanical shutter components. In other words, the camera electronically adjusts to ambient lighting conditions and no mechanical aperture in the lens system is needed. Since the video module will be used both indoors and outdoors this functionality is essential.

The power consumption of single chip monochrome CMOS video sensors on the market are typically between 100-200 mW. The power consumption of CCD sensors is typically 3 to 5 times this figure. The sensor we use is the OV5016 by OmniVision and consumes 20 mA at 5 V.

Color sensors are also available for both CCD and CMOS types. Color images do not contain considerably more information than grayscale images and in the case of the video module the increased power consumption makes this option unattractive.

A pinhole lens with 5.7 mm focal distance is used to focus the image on the video sensor. The resulting sensor-lens package is approximately 15x15x16 mm in size and weighs less than 5 gr.

CMOS vision sensors are also sensitive to near-infrared wavelengths. Using suitable LEDs for illumination, these sensors are useful for nighttime applications.

Table 1 summarizes the specifications of the video camera used in the video module.

Table 1: Video camera specifications

Sensor type	Single-chip monochrome CMOS sensor with 320x240 pixels
Size	15 x 15 x 16 mm
Power consumption	20 mA at 6-9 VDC

Table 1: Video camera specifications

Output	Composite video signal, 2 V p-p at 30 frame/s
Lens	Pinhole lens 5.7 mm focal length

There are a number of wireless video transmitters available on the market, however, only those intended for covert video applications and hobby use are small enough to fit within the payload constraints. We use a miniature transmitter by Micro Video Products, Canada that transmits in the 900 MHz ISM (Industrial, Scientific and Medical) band and consumes 30 mA at 9V. The circuit board is about 24 x 17 x 8 mm in size. Its range was tested to be 150-200 ft line of sight indoors. However, the structure of the building will affect this figure.

3. Actuators

Development of actuators for MEMS is an important research area. Several different actuators utilizing various physical phenomena have been developed. The effect of miniaturization on these actuators is dependent on the type of forces involved in actuation [15].

Common microactuators can be classified as actuators using electromagnetic and electrostatic forces and actuators using a functional element [10]. Examples of actuators with a functional element are piezoelectric and shape memory alloy (SMA) actuators.

Many of these microactuators may be applied to mesoscale systems millimeter to centimeter size. However, their effectiveness in this size may be different than it is in the micro domain. Additionally, some actuators may require high voltages or currents which limits their use in miniature mobile robots. Below, common types of actuators are analyzed from this perspective.

3.1. Electrostatic and electromagnetic actuators

Electrostatic force between two electrodes is proportional to the surface area of electrodes and inversely proportional to the square of the distance between them. Since these two scale equally but opposite to each other electrostatic forces are not effected from miniaturization. When electrostatic forces are compared to gravitational forces, as in the case of micro systems, they are considered suitable for actuation. However, high voltages (over 100 V) are typically needed to drive electrostatic actuators [10]. For a mesoscale system electrostatic forces are usually too weak to generate mechanical action.

Unlike electrostatic forces, electromagnetic forces, commonly utilized in all types of electric motors are effected from scaling by the square of the linear dimension. How-

ever, electromagnetic actuators may still be a good choice for mesoscale systems if the magnetic field density is high. Motors with rare-earth permanent magnets are typically used in such drives. As an example, a brushless D.C. motor by RMB has dimensions of 3 mm diameter and is approximately 10 mm length. Torques of $25 \cdot 10^{-6}$ N-m at 20000 rpm are achievable with this motor [5].

A gearbox at the output of the electromagnetic actuator is often necessary to increase the torque while reducing the speed. Typical reduction rates for commercially available gearmotors with a diameter below 5 mm are from 1:3.6 to 1:125 [6] [12]. A planetary micro gear system is often employed for increased reduction in a small volume. The elements of the gear box are too small to be machined by traditional methods. Wire Electro Discharge Machining (W-EDM) technology allows tooth modulus down to 20 microns using any conductive material. Gears made of Nickel manufactured by the LIGA process are also used in commercial motors [12]. The rotating shafts are usually made of steel and use jewel bearings.

3.2. Piezoelectric actuators

Piezoelectric elements generate strain due to an applied voltage across them. Nanometer resolution and large forces can be generated at frequencies of several kHz. However, the strain generated is around 0.1% and mechanical amplification of displacement is generally required. A mechanism working close to a kinematic singularity may be used to create large displacements from the small strain of the piezo element [4].

Another problem is the requirement of high voltages, typically around 150 V. Although power consumption may be low, special power electronics is required to generate these high voltages from typical battery supply voltages of mobile robots.

One distinct type of actuator using piezoelectric elements is the ultrasonic motor [13]. These types of motors have a rotor that rests on a stator made of piezoelectric elements. The stator is excited by a voltage signal to create travelling waves and cause a rubbing movement between the stator and the rotor. Typical characteristics of these motors are high torque at low speed and high holding torque due to friction between stator and rotor. They are also suitable for hazardous environments since no sparks are produced. The inherent high torque at low speeds eliminates the need for complex gear boxes in many cases.

3.3. Shape memory alloy actuators

Shape memory alloy (SMA) material is a metal alloy (commonly TiNi) with a shape-recovery characteristic. When the material is plastically deformed and then heated

above a certain temperature, it recovers its original shape. This property is utilized to create various kinds of actuators. The SMA material is usually strained by a bias force and upon heating recovers its original shape by acting against the bias force. Stresses of 170 MPa and more can be generated this way. The bias force is adjusted to cause 4% maximum strain to minimize the decrease in the memory effect after many cycles. Tens of millions of cycles are possible at low strain [3].

The SMA provides simple and robust actuation within a small volume and weight. It is intrinsically an on/off type of actuator with two positions for high and low temperature states. However, research has been done to implement electric resistance feedback control in a SMA servo system [9].

One disadvantage of SMA is its relatively slow response especially during the cooling phase which is usually not forced. Bandwidths of approximately 4 Hz have been achieved by differential heating and using SMA wire both as actuator and as mechanical bias for restoration [8]. Another disadvantage for mobile systems with limited power supply is the typical current of several hundred milliamps required to heat the SMA material.

In the case of the active video module, the most restrictive requirements from the chosen actuation type are small volume, low current (100 mA peak), and low voltage (9 V max). The camera weighs less than 5 gr. and enough torque can be generated for the necessary pan and tilt action by any of the three actuation types mentioned above. An ultrasonic motor has good torque, speed, and holding torque specifications for this purpose, however the need for power electronics to increase the voltage and driver circuitry to generate appropriate signals does not comply with the small volume available.

A mechanism driven by a shape memory alloy actuator would have the advantage of simple and thus reliable operation. However, the camera is to be tilted and panned within a range, and intermediate positions must be held without consuming power. SMA actuation can still be useful for simple mechanisms like bistable latches for locking and releasing spring actuated hinges.

An electromagnetic actuator was chosen to drive the pan-tilt mechanism of the active video module. It is a brushless D.C. gearmotor by RMB. The motor has a diameter of 3.4 mm and length of approximately 15 mm. A 3 stage planetary gearbox provides 1:125 reduction and a continuous output torque of 2.2 mNm [6]. The total gear-head efficiency is 60%. Since the motor is brushless, commutation is done externally by a microprocessor based drive circuit, also supplied by the company. However, the on board processor of the robot is likely to take over this job. Peak power consumption is 70 mA at 5 V.

4. Pan-tilt mechanism

The usual design of a pan-tilt mechanism has two actuators for each axis of motion. Usually the pan motor carries the tilt motor and the camera. These types of pan-tilt actuators are frequently used for security monitoring. They are also used by computer vision and robotics researchers for active vision. These systems are generally big, heavy and slow. Additionally they do not incorporate any position feedback sensor. Some alternative designs were made [1], for example a linear stepper motor controlled platform pan-tilt actuator and a spherical pointing motor (SPM). The latter consists of a miniature camera with a permanent magnet mounted on a gimbal. Three sets of coils are wound outside the gimbal in orthogonal directions. By controlling the individual currents to each coil a magnetic field vector of desired orientation is produced. The permanent magnet on the gimbal (and thus the camera) aligns itself with this vector. The camera can be rotated by step sizes of 0.011° . However, the SPM weighs 160 gr. and requires about 1A current.

The active video module transmits live images back to a human operator and the pan-tilt action is also controlled by this operator. Therefore highly accurate motion or position feedback is not essential. On the other hand, the camera should normally be concealed inside the robot body, come out when needed, and retract before the robot moves.

The general design of the pan-tilt mechanism is shown in Figure 3. A tendon attached to a drum at the base controls the tilt action. The camera is attached to a sliding column and is constantly pushed up by a compression spring. Additionally, a torsion spring at the upper drum exerts a continuous moment to tilt the camera towards its maximum tilted position. When the tilt motor releases the tendon the camera first raises up to gain clearance for pan action and then rotates 90 to 180 degrees under the action of the torsional spring. The reverse happens when the tendon is wound back. The whole setup is mounted on a platform which is rotated by a second motor for the pan action. The portion of the transparent shell of the robot which is directly above the camera is separate from the rest and is attached to the camera. Figure 4 shows the operation of the mechanism. Figure 5 shows an early design of the active video module. The camera and the motor are visible.

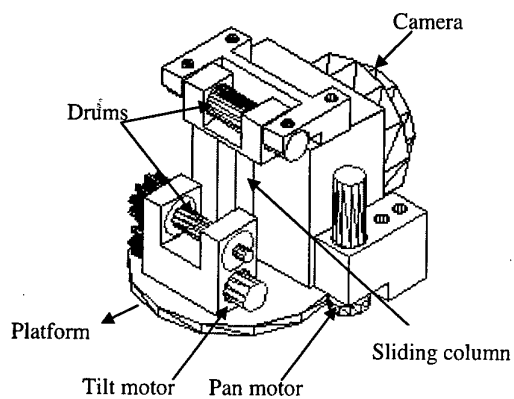


Figure 3. Pan-tilt mechanism

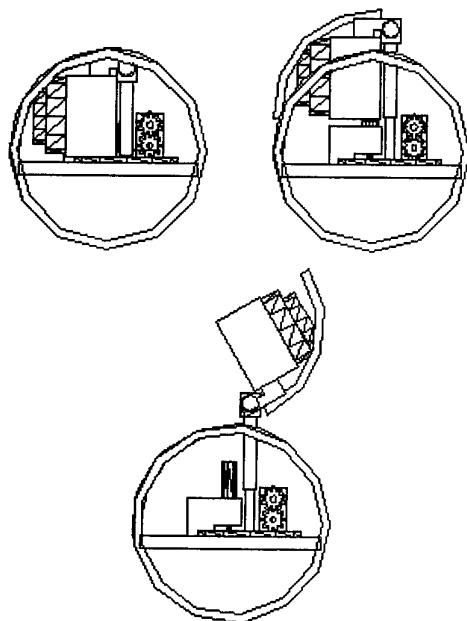


Figure 4. Mechanism operation

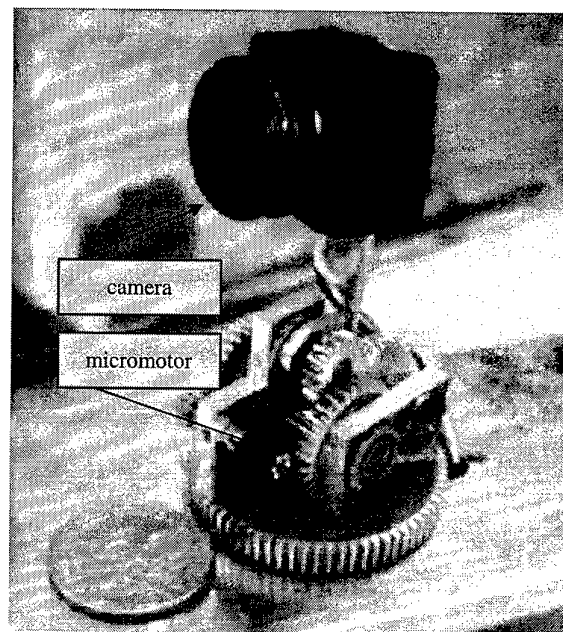


Figure 5. Active video module

5. Applications and future work

The primary application of the launchable reconnaissance robot is surveillance and especially detection of humans. Currently the images acquired from the robots are inspected by human operators but the goal is to bring more autonomous behavior using advances in technology and computer vision.

Image processing is by its nature a computationally expensive task. However, using digital video cameras and powerful microprocessors it is possible to have embedded vision systems suitable for miniature mobile robotic applications. One example is the Eyebot from the University of Western Australia [2]. This platform employs a digital camera with 80x60 pixels and a Motorola 68332 32-bit microcontroller for control of mobile robots and processing of visual data.

Digital transmission with image compression is another advantage of using digital cameras. A micro camera system comprising a CMOS grayscale sensor with 312 x 287 pixels, A/D converter, processing interface and pipelined processing architecture was built into a package size of 20.6 x 15.75 x 14.7 mm [11]. The total processing power of the camera is 70 MIPS (million instructions per second). It can be programmed to perform real-time image enhancement, image encoding or motion triggered acquisition.

Active camera systems have been used for motion tracking. Motion based tracking systems have the advantage of

being able to track any moving object regardless of shape and size [14]. Unlike recognition based systems they can be used effectively in uncontrolled environments.

Our future goals include digital image acquisition, on-board image processing and implementing active vision techniques with the vision module.

6. Conclusion

A miniature active video module for a launchable mobile robot was designed. Different types of video sensors were inspected and various forms of micro actuation were analyzed for their compatibility in a mesoscale robotic system. Applications and future improvements of the video module were discussed.

7. Acknowledgment

This material is based upon work supported by the Defense Advanced Research Projects Agency, Electronics Technology Office (Distributed Robotics Program), ARPA Order No. G155, Program Code No. 8H20, Issued by DARPA/CMD under Contract #MDA972-98-C-0008.

8. References

- [1] B. Bederson, R. Wallace, E. Schwartz, "A Miniature Pan-Tilt Actuator: The Spherical Pointing Motor", *IEEE Transactions on Robotics and Automation*, Vol. 10, No. 3, USA, June, 1994, pp298-308.
- [2] T. Braunl, "Improv and EyeBot Real-Time Vision On-Board Mobile Robots", *Proc. Fourth Annual Conference on Mechatronics and Machine Vision in Practice*, IEEE Comput. Soc., 1997, Los Alamitos, CA, USA, pp. 131-135.
- [3] J. Conrad, J. Mills, *Stiquito Advanced Experiments with a Simple and Inexpensive Robot*, IEEE Computer Society, Los Alamitos, CA, 1998, pp. 301-309.
- [4] A. Cox, E. Garcia, M. Goldfarb, "Actuator Development for a Flapping Microrobotic Microaerial Vehicle", *Proc. SPIE Microrobotics and Micromanipulation Conf.*, Vol. 3519, Boston, Massachusetts, Nov 1998, pp. 102-108.
- [5] Data Sheet for 3mm motor SYE39001, Roulements Miniatures SA, Eckweg 8, CH-2500 Biel-Bienne 6, Switzerland, February 1999.
- [6] Data Sheet for 3mm gearmotor SPE39003, Roulements Miniatures SA, Eckweg 8, CH-2500 Biel-Bienne 6, Switzerland, February 1999.
- [7] P. Denyer, "CMOS vs. CCD", whitepaper by Vision Company, UK, 1999, "www.vvl.co.uk/whycmos/whitepaper.htm".
- [8] K. Gabriel, W. Trimmer, J. Walker, "A Micro Rotary Actuator Using Shape Memory Alloys", *Sensors & Actuators*, Vol. 15, No.1, Switzerland, 1988, pp. 95-102.
- [9] K. Ikuta, M. Tsukamoto, S. Hirose, "Shape Memory Alloy Servo Actuator System with Electric Resistance Feedback and Application for Active Endoscope", *Proc. IEEE Robotics and Automation*, Philadelphia, U.S.A., 1988, pp. 427-430.
- [10] H. Ishihara, F. Arai, T. Fukuda, "Micro Mechatronics and Micro Actuators", *IEEE/ASME Transactions on Mechatronics*, Vol 1, No 1, USA, March 1996, pp. 68-79.
- [11] S. Larcombe, J. Stern, P. Ivey, N. Seed, "A Low Cost, Intelligent Micro-camera for Surveillance", *European Convention on Security and Detection*, IEE, 1995, London, UK, pp. 50-3.
- [12] F. Michel, W. Ehrfeld, U. Berg, R. Degen, F. Schmitz, "Electromagnetic Driving Units for Complex Microrobotic Systems", *Proc. SPIE Microrobotics and Micromanipulation Conf.*, Vol. 3519, Boston, Massachusetts Nov 1998, Boston, Massachusetts, pp. 93-101.
- [13] R. Moroney, R. White, R. Howe, "Ultrasonic Micromotors: Physics and Applications", *IEEE Micro Electro Mechanical Systems An Investigation of Micro Structures, Sensors, Actuators, Machines and Robots*, IEEE, New York, USA, February 1990, pp. 182-187.
- [14] D. Murray, A. Basu, "Motion Tracking with an Active Camera", *IEEE Transactions on Pattern Analysis and Machine Intelligence*, Vol. 16, No. 5, May 1994, USA, pp. 449-459.
- [15] W. Trimmer, "Microrobots and Micromechanical Systems", *Sensors & Actuators*, Vol 19, No. 3, USA, pp. 267-287, September 1989.

RELIABLE MOBILE ROBOT LOCALIZATION AND NAVIGATION USING INCREMENTAL ODOMETRY, A COMPASS AND A GYROSCOPE

Levent Yenilmez

Department of Electronics Engineering
Air Force Academy
Yesilyurt, Istanbul 34807, Turkey
l.yenilmez@hho.edu.tr

Hakan Temeltas

Faculty of Electrical and Electronics Engineering
Istanbul Technical University
Maslak, Istanbul 80626, Turkey
Temeltas@elk.itu.edu.tr

ABSTRACT

We present a localization and navigation system which determines the position and orientation of a mobile robot and navigates it safely using the odometry system, a gyro and a compass measurements. The estimating of the localization using these sensors information was performed by an extended Kalman filter (EKF). Using this kind of sensor fusion, the precise localization information of the mobile robot updated and path-planning can be realized safely by Generalized Voronoi Diagrams (GVD).

1. INTRODUCTION

Precise determination of the actual position and orientation of an autonomous mobile robot is essential in control and path finding [1, 2]. This important task can be accomplished by using dead reckoning [3, 4], landmarks [5-7] or beacons [8, 9] to correct errors in position. In the dead reckoning system the robot's position and orientation are calculated from measurements of wheel motion, also called odometry. Dead reckoning control has some problems like poor mechanical alignment of wheels, slop in gears, noise in sensor signals, errors in sensor signals, wheel slippage and trajectory variations due to surface unevenness. To reduce the problems with dead reckoning, recently, a position and orientation determining strategies are developed by using an ultrasonic ring around an autonomous mobile robot and two ultrasonic position referencing beacons in [10], and only one beacon in [11].

In this work, we introduce an approach to combine the observed sensor data coming from dead reckoning system, a fiber-optic gyroscope also called "laser gyroscope" (Autogyro Navigator) [12] and a magnetic compass (KVH Fluxgate Compass) [13] sensors for exact determination of the position and orientation of a mobile robot in a predefined environment. An extended Kalman filter (EKF) [14-16] algorithm is employed to realize this approach. In addition, measurements data gathered from the ultrasonic and infrared sensors are integrated to avoid the mobile robot from the known / unknown obstacles and plan the target-path using the Generalized Voronoi diagrams (GVD) [17, 18] concept. We apply the our approach to the problem of

location estimation and navigation in mobile robotics using and experimenting with the our laboratory mobile robot Nomad-200. The Nomad-200 is an integrated mobile robot system and has an on-board multiprocessor system consisting of a Pentium 133 and multiple slave microcontrollers. It has also an incremental odometry system, one laser gyroscope and one magnetic compass to localize itself, and sixteen infrared and ultrasonic sensors to obtain a 360-degree sweep horizontally.

The use of gyros in mobile robot applications has become more attractive for position estimation. Komoriya and Oyama used the OF6-3 (Hitachi) optical fiber gyroscope in order to fuse with odometry information [19]. They used a Kalman Filter to fuse these two different sensors information. Barshan and Durrant-Whyte conducted the gyroscopes for the inertial navigation of the mobile robots [20]. They evaluated the performance of the ENV-05S Gyrostar from (Murata) and the other Solid State Angular rate Transducer "Start" gyroscope manufactured by (Gec). They found that these gyros had relatively large drifts like 5° to 15°/min. However, The applying EKF showed that the drift can be reduced the rate of 1° to 3°/min.

Because of its technical maturity and commercial availability, the magnetic compass is an useful alternatif to inertial sensor systems provided it is widely used in mobile robotics applications. Due to the influence on accumulated dead-reckoning errors, to provide a measure of absolute heading of the mobile robot is very important to solve the navigation problems safely. One magnetic compass has an important disadvantage that the magnetic field of the earth is often distorted near high voltage system or big ferromagnetic structures. Also the robot itself distorts this magnetic field. In order to filter these internal and external magnetic field perturbations, we have developed a method.

The Kalman Filter approach is an essential data fusion method to reduce the drift and distortions, and fuse odometry, gyro and compass data in both of the above studies. To produce a detailed model of the sensors is important to use the Kalman Filter efficiently. In our study, we have developed the EKF algorithm (presented in section 3) to process the sensor data sequentially. Each sensor information was taken into consideration separately. So it made the algorithm more flexible and the

measurements could be easily integrated with each other in the EKF algorithm.

In the navigation part in section 4, mobile robot can navigate with a given set of path data from an off-line path planner which uses GVD diagrams and calculates its shortest target path, shown in Fig.2 and 3. In our system there is an active matching algorithm in order to update the robot environment with new obstacles or to delete some known obstacles that are removed anywhere. If any change in the robot environment is sensed, the off-line path planner produces its new path data using the GVD diagrams.

2. SENSING SYSTEM

2.1 Incremental Odometry System

Our robot, Nomad 200 has three wheel synchronous drive non-holonomic system with zero gyro-radius (i.e. the robot can rotate around its center) and equipped with optical shaft encoders. The three wheels controlled by one motor translate together and rotate all together with an other motor. Its shaft encoders give pulses per sampling period. The number of counted pulses are converted to the distance and given as a x, y coordinates of the robot. The robot can only translate along the forward and backward directions. This situation is the non-holonomic constraint and similar to that of a car. The reference point of the mobile robot is the midpoint of the wheels as shown in Figure 1.

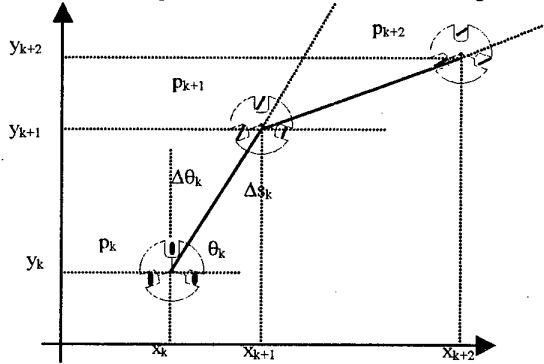


Figure 1. Position of the synchronous mobile robot.

In two-dimensional Cartesian-coordinates system, the robot position and orientation at the $t=kT$ instant can be given as x_k , y_k and θ_k respectively. Using the trigonometric relation, the robot position and orientation can be updated as follows:

$$\theta_{k+1} = \theta_k + \Delta\theta_k \quad (1)$$

$$x_{k+1} = x_k + \Delta s_k \cos(\theta_{k+1}) \quad (2)$$

$$y_{k+1} = y_k + \Delta s_k \sin(\theta_{k+1}) \quad (3)$$

Where $\Delta s_k (=T.v_k)$ is the distance traveled and $\Delta\theta_k (=T.w_k)$ the steering rate between the two sampling point p_k and p_{k+1} . If we examine the equations (1), (2) and (3), we can realize that orientation errors will cause large lateral position errors and this errors will increase proportionally with the distance Δs_k traveled by the mobile robot. For this reason, we used gyroscope and compass to compensate this foremost weakness of odometry.

2.2 Flux-gate Magnetic Compass

In our mobile robot, we have C-100 (from KVH) compass system that uses a state of the art microprocessor controlled flux-gate compass. In the convenient conditions, especially in outdoor applications, accuracy of the 1 degree can be achieved. In terms of its influence on accumulated odometry errors, the robot heading θ_k is the most important between the localization parameters. In an other word, the correct measure of absolute heading is very important to navigate the mobile robot safely.

However, this sensor is often distorted near high voltage lines and big ferromagnetic structures that corrupt the earth's magnetic field.

In the mobile robot applications, the best compass is the flux-gate compass. It measures the horizontal components of the earth's magnetic field strength;

$$H = (h_x, h_y, h_z)^T$$

Where h_x is measured in forward direction, h_y in the mathematical positive cross-direction and h_z in the vertical direction. H-vector in the plane x, y describe a circle. So, the robot heading is given by the transformed x, y components;

$$\theta_{\text{compass}} = \tan^{-1}(h_y / h_x) - \theta_0 \quad (4)$$

Where θ_0 is the initial heading angle of the robot measured by the magnetic compass in the first reading.

2.3 Fiber-Optic (Laser) Gyroscope

Gyroscopes are used to compensate for the foremost weakness of odometry in the mobile robot applications. Any small orientation error in the odometry system will give a growing cumulative position error. In order to prevent this weakness, highly accurate gyros can be used to detect the orientation errors and correct them immediately.

In our system we used a laser gyro which is the "Autogyro Navigator" from Andrew Corp. It is a single-axis interferometric fiber optic gyroscope to support the dead reckoning and GPS receiver systems.

The device measures angular rate, and allows robot-turning angle to be measured accurately. The autogyro produces an output in digital format (16-bit) proportional to angular rotation rate over the range ± 100 degrees per second. One sample (0.1 second) represents 10 degrees of rotation at ± 100 degrees per second rotation rate. With the gyro stationary, the indicated rate is less than 0.2 degree per second. The stationary drift rate depends on the operating temperature range and drifts with time. Using the drift rate " e_{drift} " the angular velocity of the mobile robot can be calculated as follows:

$$w_{\text{gyro}} = C_{\text{gyro}} (e_{\text{gyro}} - e_{\text{drift}}) \quad (5)$$

Where e_{gyro} is the gyro output voltage, e_{drift} the drift voltage, and C_{gyro} transformation constant.

3. LOCALIZATION PROCESS

3.1 Robot Model and Kalman Filtering

In our study, we assume that the angular velocity is constant during one sampling period which is $T=0.1$ sec. in our tests. In this case, any acceleration in the robot will be taken as system noise. The state space variables are the position x, y and the heading θ . We also add the vehicle translation velocity "v" and angular velocity "w" to the state vector x_k as follows:

$$\begin{bmatrix} x \\ y \\ \theta \\ v \\ w \end{bmatrix}_{k+1} = \begin{bmatrix} x_k + \Delta s_k \cos(\theta_k + \Delta\theta_k) \\ y_k + \Delta s_k \sin(\theta_k + \Delta\theta_k) \\ \theta_k + \Delta\theta_k \\ v \\ w \end{bmatrix} \quad (6a)$$

Which can be written as:

$$x_{k+1} = f(x_k, u_k) \quad (6b)$$

For each sampling period ($T=0.1$ sec.) the measurements x_{odo} , y_{odo} are obtained from the wheels encoder, the rotational w_{gyro} from the gyroscope and the robot heading θ_m computed based on $\Delta\theta_{\text{compass}}$ or $\Delta\theta_{\text{gyro}}$ or $\Delta\theta_{\text{odometry}}$ using this simple if statement :

if ($\Delta\theta_c < \Delta\theta_{th1}$) & ($|\Delta\theta_{g-c}| > \Delta\theta_{th2}$) then $\theta_m = \theta_{compass}$
else
if ($\Delta\theta_g < \Delta\theta_{th1}$) & ($|\Delta\theta_{g-o}| > \Delta\theta_{th2}$) then $\theta_m = \theta_{gyro}$
else $\theta_m = \theta_{odometry}$

Where $\Delta\theta_c = (\Delta\theta_{compass})_k = (\theta_{compass})_k - (\theta_m)_{k-1}$
 $\Delta\theta_g = (\Delta\theta_{gyro})_k = (\theta_{gyro})_k - (\theta_m)_{k-1}$
 $\Delta\theta_{g-c} = \theta_{gyro} - \theta_{compass}$
 $\Delta\theta_{g-o} = \theta_{gyro} - \theta_{odometry}$
 $\Delta\theta_{th1} = 1^\circ / T$ (Experimental threshold level-1)
 $\Delta\theta_{th2} = 0.145^\circ / T$ (Experimental threshold level-2)

If we want to summarize these measurements, the observation equation can be expressed as follows:

$$\begin{bmatrix} x_{odo} \\ y_{odo} \\ \theta_m \\ v_{odo} \\ w_{gyro} \end{bmatrix}_k = \begin{bmatrix} 1 & 0 & 0 & 0 & 0 \\ 0 & 1 & 0 & 0 & 0 \\ 0 & 0 & 1 & 0 & 0 \\ 0 & 0 & 0 & 1 & 0 \\ 0 & 0 & 0 & 0 & 1 \end{bmatrix} \begin{bmatrix} x \\ y \\ \theta \\ v \\ w \end{bmatrix}_k \quad (7a)$$

$$y_k = g(x_k) \quad (7b)$$

Our state space model have some inaccuracies α_k and β_k which are, respectively, system and observation noises. In this case, the stochastic system representation can be expressed by the following equations:

$$x_{k+1} = f(x_k, u_k) + \alpha_k \quad (8a)$$

$$y_k = g(x_k) + \beta_k \quad (8b)$$

We assume that these noises are non-correlated, zero-mean Gaussian white noises with covariance matrices Q_α and R_β , respectively.

3.2 Estimation Phase of EKF

The mean of the estimated state vector and related covariance matrix are the probability distribution of the robot state estimation. Given state space model of the system in equation (8a) is in the non-linear form. We should linearize this equation in the form of equation (9) in order to express the uncertainty of his structure.

$$x_{k+1} = \phi_k \cdot x_k + \alpha_k \quad (9a)$$

$$y_k = x_k + \beta_k \quad (9b)$$

Now, let us choose some nominal value of x and call it x_{nom} , and constitute the state space transition matrix ϕ_k :

$$(\phi_k)_{i,j} = \frac{\partial f(x_k, u_k)_i}{\partial x_{k,j}} \bigg|_{x=x_{nom}} \quad (10)$$

Expanding x_{k+1} in a Taylor series about x gives us;

$$x_{k+1} = f(x_{nom,k}, u_k) + (x_k - x_{nom,k}) + \dots \quad (11)$$

Where we have left off the higher order terms. This equation is linear in x in this form without the higher order terms. Therefore, the optimum estimate of x_{k+1} is given as:

$$\hat{x}_{k+1} = f(x_{nom,k}, u_k) + \phi_k (\hat{x}_k - x_{nom,k}) \quad (12)$$

Where as usual \hat{x} is the best estimate of x_k inherited from the previous computing cycle. If we assume that $x_{nom,k} = \hat{x}_k$, then it will give us:

$$\hat{x}_{k+1} = f(\hat{x}_k, u_k) \quad (13)$$

The equation for the covariance matrix of the error in this estimate is as follows:

$$P_{k+1} = \phi_k P_k \phi_k^T + Q_\alpha \quad (14)$$

In our experiments, we saw that standard deviation for the odometry is 1 cm. in 100 cm. and 2 degree in 100 degree.

3.3 Updating the State Estimation

We assume that sensor measurements are obtained from statistically independent sources. Therefore, the covariance matrix of the output noises has a diagonal form. Since state values obtained from our odometry system, the observation matrix is equal to unity matrix. Therefore, y_k in observation equation is exactly equal to state vector x_k . The optimal estimate with our assumption $x_{nom,k} = \hat{x}_k$ is given as:

$$\hat{x}_{k+1} = \hat{x}_k + K_{k+1} [y_{k+1} - \hat{x}_k] \quad (15)$$

Where K_{k+1} is the gain matrix and can be calculated using the equation (15);

$$K_{k+1} = P_k (P_k + R_\beta)^{-1} \quad (16)$$

Let us constitute the P_{k+1} using his equation:

$$P_{k+1} = P_k - (P_k + R_\beta) K_{k+1} K_{k+1}^T \quad (17)$$

In our observations, standard deviation in compass is 0.02 and in gyro 0.01. All variables of the above model can not be observed using our sensor system and then the estimation uncertainty of these variables will diverge unless direct x , y measurements are taken into consideration to reduce these uncertainties.

4. TRAJECTORY GENERATION

In the navigation part, our mobile robot can navigate with a given set of path data from an off-line path planner which uses GVD diagrams [15] and calculates its shortest target path, shown in Figure 2 and Figure 3.

In our system there is an active matching algorithm in order to update the robot environment with new obstacles or to delete some known obstacles that are removed anywhere. If any change in the robot environment is sensed, the off-line path planner produces its new path data using the GVD diagrams.

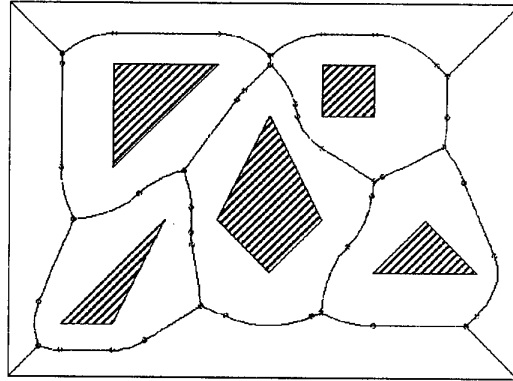


Figure 2. All possible paths with GVD.

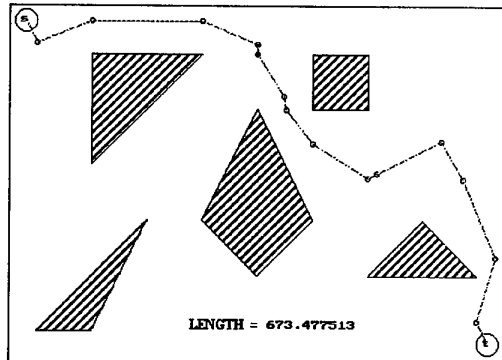


Figure 3. The calculated shortest path.

5. EXPERIMENTAL RESULTS

We implemented and tested the study on our mobile robot Nomad 200. The robot has been primarily based for use as an autonomous robot operating in a structured laboratory or office environment. It has also served as a test platform for studies in real-time. The entire autonomous robot is self-contained (all processing being performed onboard). It has a maximum travel speed on 61 cm/sec. Our laboratory area was surveyed out to a 10 cm. grid with accuracy better than about 1 cm. To extract the mapping, a start and target point were presented, and an absolute localization was presented with incremental odometry, gyro, and compass sensors using the EKF. In addition to, a real-time path planning was generated using the GVD diagrams.

In our localization study, we placed the robot at the initial position $x_0 = 1.8$ m., $y_0 = -1.8$ m., and $\theta_0 = 0^\circ$ in the laboratory workspace which is limited to an area of 5.5x3.5 meters. A special robot trajectory was planned using the polar form for the elliptical equation;

$$x = x_c + r_1 \cdot \cos\theta, \quad y = y_c + r_2 \cdot \sin\theta$$

Where x_c, y_c is the ellipse center, r_1 semimajor axis, and r_2 semi-minor axis as shown in Figure 4.

The length (ρ) of this trajectory is approximately 13.7 meters.

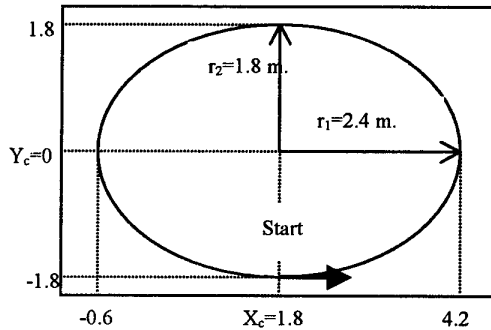


Figure 4. Generated robot trajectory.

In the first part of the localization test, we started the robot from the initial position $(x_0, y_0, \theta_0)^T = (1.8, -1.8, 0)^T$ and turn it in the counterclockwise direction along the elliptical rotation in a travel speed on 35 cm/sec. as shown in Figure 4. In the second part, this scenario was realized in the other direction and at the same speed. After these turns, obtained position and orientation errors on the final point are tabulated in table 1 and table 2. In the tests, all sensors were used to estimate robot localization and track the generated elliptical path. However, the sensor outputs were stored separately to find out the best estimate of the robot localization with different sensor combination.

The error (ϵ) in estimating the position is calculated as;

$$\epsilon_p = \|p - p_e\|_2 \quad (9)$$

That is, the error in estimation is the geometric distance (in meters) between the real position and the estimated position. The expected value of this error will provide us the standard deviation of the estimated position.

The experimental results obtained with EKF algorithm in relation to the sensor groups for this elliptical path are summarized in Table 1 and Table 2. Here, ϵ_p is the deviation of the robot location in the x, y coordinates (Euclidean distance between the starting and final points), ϵ_θ deviation in the robot heading angle. We also calculated the relative distance errors ϵ_p/ρ in order to express the localization errors with respect to the sensor groups. Our test results show that if the odometry system is supported with a gyroscope and a compass, the localization errors can be reduced to minimum level.

Table 1. Localization errors after CCW turn.

Errors	Sensors			
	Odo.	Odo.& Gyro	Odo.& Comps	All
ϵ_p	30.7	10.8	7.5	2.8
ϵ_θ	-12.7	-7.6	3.8	0.7
ϵ_p/ρ	2.25	0.79	0.55	0.20

Table 2. Localization errors after CW turn.

Errors	Sensors			
	Odo.	Odo.& Gyro	Odo.& Comps	All
ϵ_p	42.7	12.3	6.5	2.1
ϵ_θ	-15.1	-8.2	0.7	0.4
ϵ_p/ρ	3.12	0.90	0.47	0.15

In our laboratory area, to realize the navigation of the robot, a start and target point were presented and an off-line path planning was generated using the GVD diagrams as mentioned before. The shortest target path was easily calculated with this method, shown in Figure 5.

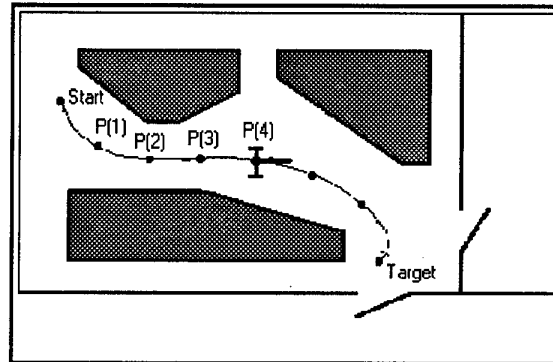


Figure 5 The calculated shortest path using GVD in the laboratory environment.

6. CONCLUSIONS

A complete data fusion and processing system was presented for application in the robotics localizing and navigation field. Our experimental results demonstrated that excellent positioning of low-speed mobile robots can be achieved using an incremental odometry, a fiber-optic gyro and a compass sensors inside any working environments with significant cluttered and noise. System performance comes into view to be close to the best achievable with the current sensor and system models. The obtained result is used to navigate mobile robot safely. In our study, GVD diagrams are used to effectively determine a

sequence of robot motion such that the robot can arrive at its goal position in the shortest time while avoiding obstacles.

Acknowledgment:

This research was funded by Turkish Air Force and Control Section of Istanbul Technical University.

REFERENCES

- [1] Crowley J., "World Modeling and Position Estimation for a Mobile Robot Using Ultrasonic Ranging," IEEE Conf. Robotics and Automation, pp. 674-680, 1989.
- [2] Moutarlier, R. Chatila, "Stochastic Multisensory Data Fusion for Mobile Robot Location and Environmental Modelling," Robotics Research 5th Int. Symp. pp. 85-94, 1994.
- [3] Chenavrier F., and Crowley J. L., "Position estimation for a mobile robot using vision and odometry", Proc. of the IEEE Int. Conf. on Robotics and Automation, pp.2588-2592, Nice, May 1992.
- [4] Nishizawa T., Ohya A., and Yuta S., "An implementation of On-board Position Estimation fo a Mobile robot", Proc. of the Int. Conference on Robotics and Automation, Nagoya, Japan, pp. 395-400, 1995.
- [5] Wiklund U., Andersson U., and Hyypa, "AGV Navigation by Angle Measurements", Proc. of the 6th Int. Conf. on Automated Guided Vehicle Systems, Brussels, Belgium, pp. 199-212, 1988.
- [6] Tsumura T., Okubo H., and Komatsu N., "A 3-D Position and Attitude measurement System using Laser Scanners and Corner Cubes", Proc. of the 1993 IEEE/RSJ Int. Conf. on Intelligent Robots and Systems, Yokohoma, Japan, pp.604-611, 1993.
- [7] Sutherland K.T. and Thompson W.B., "Localizing in Unstructured Environments: Dealing with the Errors", IEEE Trans. on Robotics and Automation, vol.10, no.6, pp.740-754, 1994.
- [8] J.J. Leonard, H.F. Durrant-White, "Mobile Robot Localization and by Tracking Geometry Beacons", IEEE J. Robotics & Autom. , 7, (3), pp(376)-(381), 1991.
- [9] Beom H.R., Koh K.I., and Cho H.S., "The Improvement of Sonar-Based Mobile Robot Localization method by Multiple Beacons", IFAC, 13th Triennial World Congress, pp.199-204, San Francisco, USA, 1996.
- [10] Yenilmez L., and Temeltas H., "Enabling an autonomous mobile robot to determine its actual position and orientation by using an ultrasonic ring," *Forth Int. Conf. on Control, Automation, Robotics and Vision*, Singapore, Dec.1996.
- [11] Yenilmez L., Temeltas H., "Local Positioning of a Mobile Robot Using an Ultrasonic Ring", In *ComCon6 : 6th Int. Conf. on Adv. in Comm. and Cont. Telecommunications/Signal Processing*, pp.203-211, Corfu, Greece, 23-27 June 1997.
- [12] Andrew Corporation, 10500 W. 153rd Street, Orland Park, IL 60462.
- [13] KVH Industries, C100 Compass Engine Product Literature, 110 Enterprise Center, Middletown, RI 02840.
- [14] Maybeck P.S., "Stochastic Models, Estimation and Control", Vol.1, Academic Press, 1979.
- [15] Bar Shalom Y., Fortmann T.E., "Tracking and Data Association", Academic Press, 1988.
- [16] Brooks R. R., Iyengar S. S., "Multi-Sensor Fusion - Fundamentals and Applications with Software-", Prentice-Hall, 1998.
- [17] D. T. Lee, "Generalized Voronoi Diagrams in the Plane," *SIAM J. Comput.*, 10, (1), 73, (1981).
- [18] Takahashi O., and Schilling R.J., "Motion planning in a plane using generalized Voronoi diagrams, "IEEE Trans. Robotics and Autotomation, RA-5, (2), 143, 1989.
- [19] Komoriya, K. And Oyama, E., "Position Estimation of a Mobile Robot Using Optical Fiber Gyroscope (OFG)." International Conference on Intelligent Robots and Systems (IROS'94). Munich, Germany, September 12-16, pp.143-149, 1994.
- [20] Barshan, B. And Durrant-Whyte, H.F., 1995, "Inertial Navigation Systems for Mobile Robots. "IEEE Transactions on Robotics and Automation," Vol.11, No.3, June 1995, pp.328-342.

AUTHOR INDEX

Abe, Y.	129	Czerwicz, W.	396
Adriaens, H.	16	Denizhan, Y.	251
Airila, M.	281	Deyanov, Y.	153
Akbas, E.	68	Dimirovski, G.M.	40
Akbas, E.	251	Dimirovski, G.M.	78
Alexandrescu, N.		Dogan, M.	228
Alfano, J-P.	199	Drumea, P.	366
Altinay, H.	175	Drumea, A.	370
Altinay, H.	425	Dumitriu, A.	74
Anthierens, C.	374	Durna, M.	
Arai, F.	129	Efe, M. O.	57
Asama, H.	419	Elchanani, M.	303
Astrand, B.	135	El-Din, A.S.	408
Avram, M.		Elena, G.	234
Avramov, I.	153	Ellman, A.	359
Bae, J.	170	El-Sabbe, A.E.	408
Bae, J.	123	El-Zawawi, A.	336
Bae, J.	313	Emura, T.	187
Bae, J.	413	English, J. D.	181
Baerveldt, A. J.	135	Erbatur, K.	257
Balavessov, V. A.	153	Erdal, M.	228
Banning, R.	16	Erden, A.	
Barshan, B.	207	Erkmen, I.	
Basbug, M.R.	245	Erkmen, A.	
Bayar, C.	175	Ertugrul, M.	68
Bayar, C.	425	Ertugrul, M.	245
Betemps, M.	374	Ertugrul, M.	251
Binfet, J.	342	Esque, S.	359
Blejan, M.	370	Flavio, F.	456
Bogosyan, S.		Fotouhi-C, R.	148
Bouzouia, B.	159	Fotouhi-C, R.	165
Bozdogan, A.	228	Fransisco, M.	456
Bradley, A.	325	Fukuda, T.	1
Bruno, A.	441	Fukuda, T.	129
Bullough, W. A.	452	Gacovski, Z. M.	40
Cambron, M.	203	Galabov, V.	153
Cannata, G.	441	Gide, E.	106
Casalino, G.	441	Gide, E.	263
Ceres, R.	473	Gide, E.	275
Chang, Y. S.	413	Gienger, M.	385
Chin, P.	319	Gok, G.	175
Chiok, C-C.	402	Gok, G.	425
Cho, K. S.	3	Gokasan, M.	
Choi, J. W.	297	Gramescu, B.	
Coilliot, G. B.	223	Grotjahn, M.	46
Comeaga, C. D.		Guvenc, L.	100
Comeaga, C. D.	396	Haj-Fraj, A.	9
Comes, M.	370	Han, S-H.	123
Coss, M. F.	456	Hayashi, E.	447
Cristea, D.	74	Heimann, B.	46
Cristea, L.	74	Hernandez, H.	285
Cristea, I.	370	Hirata, Y.	419

Hirzinger, G.	2	Louam, N.	159
Hoon, P.S	319	Lu, H-C.	348
Huan, Y.	319	Lu, H-C.	354
Huh, N.	170	Maciejewski, A. A.	181
Hurmali, G.	175	Marin, A.	366
Hurmali, G.	425	Marino, P.	285
Hwang, I. C.	413	Masory, O.	84
Ildiri, G. D.	34	Masory, O.	199
Ivanescu, M.	330	Mihalachi, D.	396
Iwata, H.	94	Mirea, A.	370
Jing, Y.W.	78	Mojsovski, A.	78
Kadri, M.	159	Mok, P. Y.	269
Kaetsu, H.	419	Morita, T.	94
Kallio, P.	467	Mugan, A.	228
Kaneshiro, D.	435	Munerato, F.	396
Kappi, T.	359	Nakajima, S-I	430
Kawabata, K.	419	Nelson, B. J.	
Kay, E. W.	452	Nigrowsky, P.	62
Kaynak, O.	57	Nikiforuk, P. N.	148
Kaynak, O.	78	Nikiforuk, P. N.	165
Kaynak, O.	245	Nitu, C.	
Kaynak, O.	251	Nitu, C.	396
Kaynak, O.	257	Nogueira, J.	285
Keerthi, S.S	307	Noritsugu, T.	435
Kerestecioglu, F.	57	Oleksiuk, W.	396
Khoukhi, A.	380	Oomori, S.	187
Khoukhi, A.	391	Ouiguini, R.	391
Khoukhi, L.	391	Palaz, H.	68
Kim, Y-S.	217	Papanikolopoulos, M.	
Kim, J-W.	217	Parasiliti, F.	88
Kim, J. H.	297	Park, S. T.	3
Kim, I. S.	413	Park, U. S.	297
King, T.	461	Partington, E.C.	452
Kivanc, Z.		Perez, L.A.	473
Koivo, H.N.	467	Peters, R. A.	193
Koku, A. B.	193	Petrella, R.	88
Kolemisevska, T.D.	40	Pfeiffer, F.	9
Kosuge, K.	419	Pfeiffer, F.	385
Krantz, D.		Piazzi, A.	28
Krishnan, H.	402	Pons, J. L.	473
Kubota, N.	1	Poo, A.N.	307
Kurtuldu, N.	425	Popescu, A. N.	330
L. de Koning, W.	16	Popescu, D.	330
Laurent, C.	396	Porter, B.	269
Lee, M-H.	170	Pozzi, M.	461
Lee, M. H.	3	Quan, Z.	467
Lee, C-G.	52	Quiroz, F. F.	456
Lee, S.	313	Rahman M.H.R, F.	319
Lee, J.M.	313	Rodriguez, H.	473
Lee, M.H	313	Saadi, F. A.	380
Lee, M. H.	413	Sakamoto, S.	129
Lee, M-H.	123	Sarioglu, K.	68
Lee, Y. J.	170	Sato, M.	419
Legnani, G.	239	Sebakhy, O. A.	336
Lim, H-S.	52	Sekmen, A. S.	203
Loffler, K.	385	Sekmen, A. S.	207

Shihuang, S.	213	Zhaofeng, G.	213
Shikano, M.	129	Zobel, R.	2
Simsek, A.	175		
Simsek, A.	425		
Sobh, T.	303		
Soliman, F.	106		
Soliman, F.	263		
Soliman, F.	275		
Song, K-H.	52		
Srinivasan, S.	325		
Stankovski, M.J.	78		
Sugano, S.	94		
Svasta, P.	366		
Szyszkowski, W.	165		
Tahralli, E.	425		
Takeno, J.	117		
Talaba, D.	291		
Tanaka, Y.	129		
Temeltas, H.			
Teo, C-L.	402		
Thiemann, A.	46		
Tomizuka, M.	2		
Tournier, J-L.	223		
Tsai, C-H.	348		
Tsai, C-H.	354		
Tukel, D. B.	425		
Tukel, D. B.	175		
Turgut, A.E.			
Turkay, O.	34		
Turner, P.	62		
Tursini, M.	88		
Unel, M.	22		
Vagin, V. N.	112		
Visa, I.	291		
Visioli, A.	28		
Visioli, A.	62		
Visioli, A.	239		
Voyles, R.			
Wahba, M. A.	336		
Wang, L.	187		
Wilamowski, B.	342		
Wilkes, M.	203		
Wolovich, W.	22		
Xiu, D.	84		
Xu, Z.	117		
Yak, A.S	307		
Yamane, M.	447		
Yang, J-H.	142		
Yang, S. Y.	3		
Yenilmez, L.			
Yeremeyev, A. P.	112		
Yesin, K. B.			
Yoon, Y. J.	170		
Yoon, G-S.	217		
Yuan, F.	213		
Zappa, B.	239		